MASS TRANSFER - ADVANCED ASPECTS

Edited by **Hironori Nakajima**

INTECHWEB.ORG

Mass Transfer - Advanced Aspects
Edited by Hironori Nakajima

Published by InTech
Janeza Trdine 9, 51000 Rijeka, Croatia

Publishing Process Manager Alenka Urbancic
Technical Editor Teodora Smiljanic
Cover Designer Jan Hyrat
Image Copyright Shvaygert Ekaterina, 2010. Used under license from Shutterstock.com

First published September, 2011
Printed in Croatia

A free online edition of this book is available at www.intechopen.com
Additional hard copies can be obtained from orders@intechweb.org

Mass Transfer - Advanced Aspects, Edited by Hironori Nakajima
p. cm.
ISBN 978-953-307-636-2

Contents

Preface

In recent years, our knowledge of mass transfer processes has been further extended and applied to various fields of science and engineering, including industrial and manufacturing processes. Since mass transfer is a primordial phenomenon, it plays a key role in scientific research in the fields of mechanical, energy, environmental, materials, bio, and chemical engineering. This book is comprised of selected advanced topics in mass transfer processes in those fields. This book covers both fundamental and applicational aspects of mass transfer in various developing sciences and technologies.

The 35 chapters of this book are divided into six sections. The first section, Chapters 1 - 6, focuses on advanced topics in scientific and theoretical aspects of mass transfer. Chapters 7 - 9 in the second section are devoted to mechanical engineering aspects. Advanced topics in energy and environmental engineering aspects of mass transfer are collected in the third section, containing Chapters 10 - 17. The fourth section, comprised of Chapters 18 - 23, introduces advances in materials engineering. The fifth section, Chapters 24 - 28 covers the advances in the field of bioengineering. The final section, with Chapters 29 - 35 deals with advanced topics regarding chemical engineering.

The authors show the advances in scientific findings and technologies, as well as develop new theoretical models concerning mass transfer. The editor would like to express his sincere gratitude to all authors for their contributions. This book provides valuable references for researchers and engineers who are working in a wide variety of mass transfer sciences and related fields in mechanical, energy, environmental, materials, bio, and chemical engineering. Since the the advances in broad research areas are covered, the topics will be mutually stimulus and informative to the researchers and engineers in different areas.

Hironori Nakajima
Department of Mechanical Engineering
Kyushu University, Fukuoka,
Japan

Part 1

Advances in Scientific and Theoretical Modeling Aspects

1

Mass Transfer Between Stars: Photometric Studies

Phillip A. Reed
Kutztown University of Pennsylvania
U.S.A.

1. Introduction

This chapter discusses photometric methods of studying mass transfer between stars in close binary star systems, and explains how researchers use the variations in the light received from far away stars to determine the properties of the stars and the nature of mass flow between them. A new photometric method of modelling mass transfer in a certain class of binary stars is introduced.

Binary systems undergoing mass exchange are said to be *interacting* and are referred to as *interacting binary stars*. The interacting binaries discussed in this chapter are Algol-type binary stars (see Section 2), or similar systems. Considerable attention in the field of interacting binary stars has recently been paid to systems containg compact objects (white dwarfs, neutron stars, black holes, etc.) and has left many systems of more normal stars, such as Algols, neglected. This circumstance actually provides opportinities for researchers to study those systems that have been studied in the past century, but have been neglected over the last couple decades. Some emphasis in this chapter is placed on a certain class of interacting binary stars that undergo strange variations in light.

Basic concepts such as the *light curve* and *ephemeris* determination are introduced in section 3. Section 4 explains how a time-dependent ephemeris can be detected and used to calculate the rate at which an interacting binary's orbital period is changing due to mass transfer between the stars, and also to calculate the rate as which the mass is transferring. The *ephemeris curve* is an important tool in the photometric study of interacting binary stars because it is used to verify that mass transfer is taking place.

As the study of interacting binaries continues, we're learning more about their evolution. Interacting binaries can even be used as a sort of laboratory for testing current theories of stellar evolution. Throughout our studies, we've learned that mass transfer between stars can be quite variable. Accretion structures have been detected around the mass-gaining component, and it has been determined that the presence and/or stability of the accretion structures depend on several factors including the size and period of the system's orbit. The mass transfer stream in Algol systems with short orbital periods (about 3 days or less) strikes the accreting star more directly and an accretion disk is not likely to form. On the other hand, stable accretion disks do tend to form in systems with longer orbital periods (greater than about 6 days), where the accretion is not as direct. Systems with intermediate periods can exhibit wild variations, on timescales as short as one orbital cycle or less, due to a variable or transient accretion structure resulting from the system's oscillations between states of direct

impact and indirect accretion. It is in these intermediate-period systems that we can find variations due to eccentric and transient accretion structures (Reed et al., 2010). The sources of other variations in these interacting binary systems include magnetic activity cycles in a component of the system or the existence of a third, more distant, star in the system.
The light curve and ephemeris curve are considered in more detail in Sections 5 and 6. Section 5 discusses the possible causes for periodically variable ephemeris curves, which include magnetic activity and the light-time effect of multiple stars in the system. Section 6 explores the outside-of-eclipse variations that can be used to map out the eccentric accretion structures in intermediate-period interacting binary systems.

2. Algols

Algol-type binary star systems are named after the first one discovered, β Persei, or "Algol". The discovery and analysis of β Per and other similar stars posed an apparent problem than became known as the "Algol Paradox", which has relatively recently been understood through the consideration of mass transfer between stars in binary star systems. The paradox arose from the fact that astronomers were finding binary stars consisting of a less massive, but more evolved, star paired with a more massive and less evolved companion. The problem with this combination was that, according to the widely accepted models of stellar evolution, more massive stars are known to evolve more quickly than less massive ones. Since both stars in a given system are born at the same time, the existence of the Algol-type binaries seemed at odds. The answer, of course, is that mass can transfer between stars in close binaries. The more evolved (giant or sub-giant) star donates mass to the less evolved (main-sequence) star, beyond the point of reversing their mass ratio, leading to Algol-type systems.

3. The light curve

The primary tool used in the photomtric study of variable stars is the light curve, which is simply a plot of the brightness of the star versus time. We will focus on light curves of interacting binaries which are eclipsing from Earth's perspective.
On a light curve, the brightness could be given in absolute flux units such as $erg\,s^{-1}cm^{-2}\,\text{Å}^{-1}$, relative flux that is normalized to a specific orbital phase value, or stellar magnitude. Time could be in days (Heliocentric Julian Date, or HJD) or in orbital phase values. Julian Date is a continuous counting of whole days, starting with 1 January 4713 BC, and can be calculated from the calendar date of the observation using a standard algorithm. Many groups, such as the United States Naval Observatory, offer on-line conversions between calendar date/time and Julian Date (http://aa.usno.navy.mil/data/docs/JulianDate.php).
The method of CCD photometry compares the brightness of the target with comparison stars in the same filed of view. Since we use the known magnitudes of the standard, non-varying comparison stars, the primary result of the data reduction is the magnitude of the target at the time of the observation. In order to analyze the light curve using specialized modeling programs such as the Wilson-Devinney code, stellar magnitudes should be converted to relative flux, and HJD shoud be converted to orbital phase.
To convert stallar magnitude to relative flux, the following formula is used:

$$\text{Relative Flux} = \frac{L}{L_{norm}} = 10^{((M_{norm}-M)/2.5)} \tag{1}$$

where M is the measured stellar magnitude of the system at the orbital phase being plotted, and M_{norm} is the stellar magnitude of the the system at the orbital phase that is being used as the normalization phase. The normalization phase is generally chosen to be when the system is not eclipsing and its brightness is near maximum. L and L_{norm} refer to the luminosity of the system at the phases described above. Thus, the relative flux is set to 1.0 at the normalization phase, and is equal to a relative value throughout the rest of the system's orbit.
A binary star system's ephemeris is used to convert the HJD of the observation into an orbital phase value. Before defining the ephemeris, let's consider the observational light curve in Figure 1. Here we have stallar magnitude plotted against HJD.

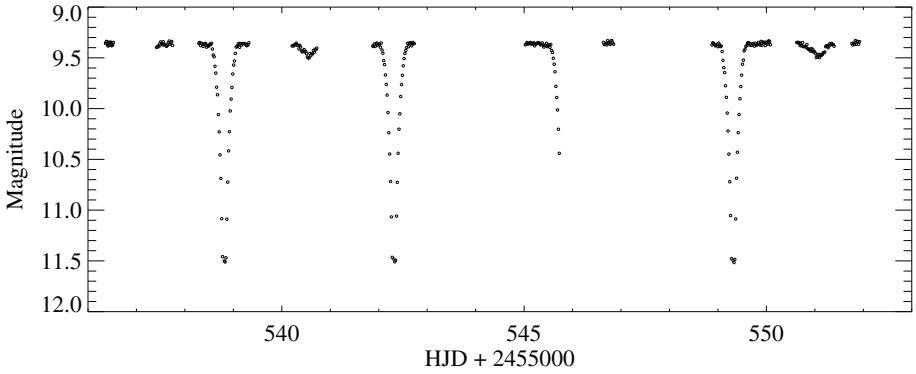

Fig. 1. An example observational light curve of a theoretical binary star system.

This light curve contains data taken over several days time and spans a few complete orbital cycles. The deepest dips in the light curve are due to the *secondary star* (cooler/dimmer) passing in front of the *primary star* (hotter/brighter), and is called the *primary eclipse*. The *secondary eclipse* is not as deep and is caused by the primary star passing in front of the secondary star. We define the center of the primary eclipse as *phase zero* ($\phi = 0$). The rest of the orbital phase values range between 0 and 1, with $\phi = 1$ being the center of the primary eclipse again. For circular orbits, the secondary eclipse occurs at $\phi = 0.5$.
If we analyze the light curve of Figure 1, we would see that the orbital period is 3.50 days, with entire primary eclipses observed at HJD2455538.8125, HJD2455542.3125, and HJD2455549.3125. The *ephemeris* is a formula for calculating future *times of minimum light* (or times of primary eclipses). The ephemeris contains one known time of primary minimum and the orbital period. The ephemeris for this example would look like this:

$$HJD_{Pr.Min.} = 2455538.8125 + 3.5000E \tag{2}$$

where E is an integer equal to the number of complete orbital cycles of the system between the known primary minimum (HJD2455538.8125) and the calculated eclipse time.
So, to convert an observation's HJD to orbital phase, the following procedure is followed. Subtract the known time of primary minimum from the observation's HJD, then divide the difference by the orbital period and truncate the whole number (the decimal part is equal to the orbital phase). For instance, the observation taken at HJD2455546.6702 would be given an orbital phase value like this:

$$\frac{(2455546.6702 - 2455538.8125)}{3.5000} = 2.245 \rightarrow \phi = 0.245 \quad (3)$$

In this example, we will use $\phi = 0.25$ as the normalization phase for converting stallar magnitudes to relative flux values. Figure 2 shows the normalized light curve for the system. Notice that all of the data in Figure 1 are plotted in Figure 2. In practice, it might take several months to years of observations to build a good light curve. A normalized light curve folds all of the available data into one orbital phase and enables all of the data to be used to model the stars in the system.

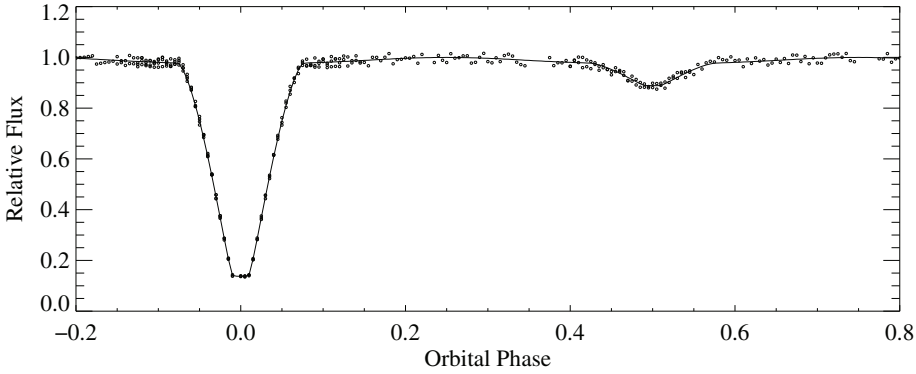

Fig. 2. The normalized light curve of the theoretical binary star system. The solid line is the synthetic light curve produced by the model.

The most widely used method of modelling an eclipsing binary star system is the Wilson-Devinney (W.D.) code (Wilson & Devinney, 1971). The W.D. code's input parameters include the masses, sizes, and surface temperatures of the stars in the system. Other parameters such as *reflection* (the heating of the near side of the cooler star by the hotter star), *limb darkening* (the surfaces of a star that are closer to the center are hotter and brighter than the surfaces that are farther from the star's center), and *orbital inclination* (the orientation of the system's orbital plane relative to our line of sight; an inclination of 90° is edge-on and 0° is face-on) are also standard parameters in the W.D. code.

The theorectical system discussed in this section consists of a primary star with a surface temperature of 12,000 K and a secondary star with a 6,000-K surface temperature. The mass ratio is $q = 0.25$, which means the primary has 4 times the mass of the secondary, and the orbital inclination of the system is 90°. The solid line in Figure 2 shows the synthetic light curve obtained from modelling these parameters with the W.D. code.

Figure 3 illustrates three-dimensional models of the stars at various orbital phase positions. It can be seen that the secondary star has evolved and expanded into a red giant or sub-giant. The secondary star's shape is distorted into a "tear-drop" shape due to the gravity of the nearby primary star. The secondary would be donating mass to the primary star in this case, as is the case with most Algol-type systems.

The W.D. code also allows for *spots* to be incorporated into the modelled light curve. Spots are circular areas on a star's surface and are given a size (radius), location (stellar latitude and

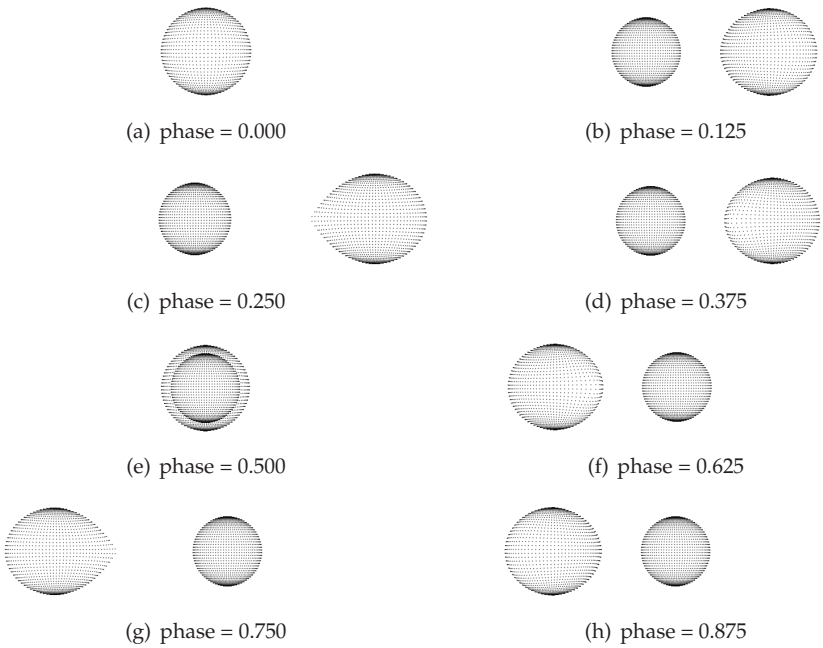

Fig. 3. These are 3-D models of the star system at various orbital phase positions. These models correspond to the synthetic light curve (solid line) plotted in Figure 2, created using the W.D. code.

longitude), and temperature (which could be cooler or hotter than the star's surface). Cool spots are generally used to model regions where magntic field activity has cooled parts of a star's surface, very similar to Sunspots on our Sun. Hot spots have been used to explain "humps" in a binary star's light curve, and are evidence of mass transfer between stars. Hot spots arise from the region where the mass flow stream from the mass losing star impacts the accreting star. This type of modelling has been referred to as *eclipse mapping*.
A new technique, presented in Section 6, actually incorporates large cool spots in the model to estimate the effect of an eccentric accretion structure eclipsing the primary star. This effect may explain the existence of unexpected dips, and other variations, in the light curve outside of primary and seconday eclipses.

4. The ephemeris curve

The most direct photometric evidence for mass transfer between stars in a binary star system is the observed time-dependent change in the orbital period, or ephemeris, of the system. However, the detection of such a change usually takes some time. A changing ephemeris is typically not detectable with any less that a decade or two of data.
The basic idea is that as material is exchanged between stars in an interacting binary system, the center of mass of the system shifts toward the star that is gaining mass. As a result, due the the conservation of angular momentum, the orbital period of the system will also change. If the more massive star is gaining mass (as is the case with most Algol-type systems), we would

expect the orbital period of the system to continually increase. If the mass accreting star is less massive than the mass donor, then we would ecpect the orbital period to decrease over time.
A binary star's ephemeris is used to calculate future times of eclipses, or minima. Let C be the *calculated* time of a future eclipse. When the night of the calculated eclipse time arrives, and we observe the actual time of the eclipse, we can compare the exact *observed* (O) time with the calculated time to see if a possible period change has occurred. An *ephemeris curve* is the value $(O - C)$ plotted against the integer E, from the ephemeris. E is simply the number of orbital cycles that occurred between the two eclipse times.
Consider again the theoretical eclipsing binary system from Section 3, whose 3.5000 - day orbital period is given in its ephemeris (Equation 2) . Figure 4 shows some possible ephemeris curves for that system, which span 9,000 orbital cycles, or about 85 years. Figure 4(a) indicates no observed orbital period change, since O is equal to C and $O - C = 0$ throughout the 85 years of observations. Figure 4(b) also indicates no observed orbital period change, as the best-fit to the ephemeris curve is linear. A linear ephemeris curve, such as this, simply means the orbital period used in the ephemeris is incorrect. One could find an orbital period that, when applied to the ephemeris, would produce a horizontal ephemeris curve (as in Figure 4(a)).
Figures 4(c) and 4(d) both reveal observed period changes. Both are best fit with quadratic functions. The quadratic function would be given by:

$$(O - C) = C_0 + C_1 E + C_2 E^2 \tag{4}$$

where C_0, C_1, and C_2 are the coefficients in each term of the best-fit function. The coefficient C_2 is used to calculate the rate at which the orbital period has been changing. The period change rate, averaged of the 85 years of observations, is:

$$\frac{dP}{dt} = \dot{P} = \frac{2C_2}{P} \tag{5}$$

where P is the orbital period of the ephemeris used to determine the calculated eclipse times. Figure 4(c) indicates an orbital period that is steadily increasing. The coefficient C_2 is positive for that case. The case in Figure 4(d) is that of a negative C_2 and therefore a steadily decreasing orbital period.
A good, real example of a neglected interacting binary star system is R Arae, which was discovered in 1894 but whose first ephemeris curve was published in February 2011 and is shown in Figure 5. The plot contains all known times of primary eclipse spanning the 116 years from R Ara's discovery through the latest observation of 30 May 2010. The ephemeris used for the plot is the one calculated from observations taken in 1986 (Nield, 1991):

$$HJD_{Pr.Min.} = 2446585.1597 + 4.425132E \tag{6}$$

so, it can be seen that in 1986, the orbital period of R Ara was 4.425132 days. The quadratic function that best fits the data is:

$$(O - C) = (0.0538) + (6.371 \times 10^{-5})E + (1.41 \times 10^{-8})E^2 \tag{7}$$

which means the average rate of period change on the 116 years of observations is:

$$\frac{dP}{dt} = \dot{P} = \frac{2C_2}{P} = \frac{2(1.41 \times 10^{-8})}{4.425132} = 5.16 \times 10^{-9} \frac{days}{day} \tag{8}$$

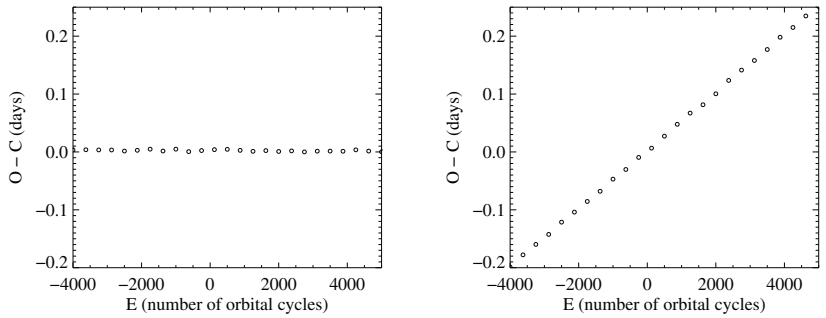

(a) Linear Ephemeris Curve (b) Linear Ephemeris Curve

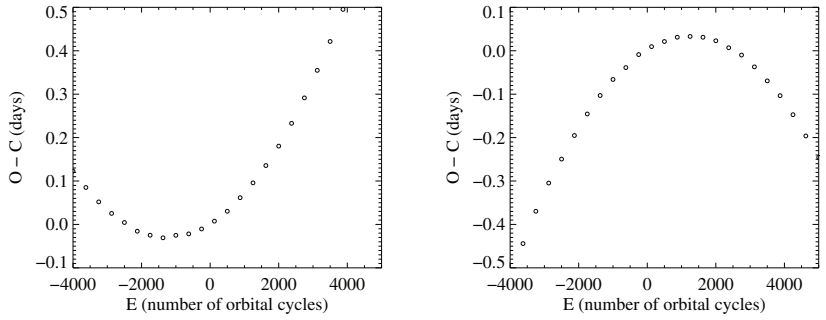

(c) Quadratic Ephemeris Curve (d) Quadratic Ephemeris Curve

Fig. 4. Linear Ephemeris Curves ((a) and (b)) and Quadratic Ephemeris Curves ((c) and (d)).

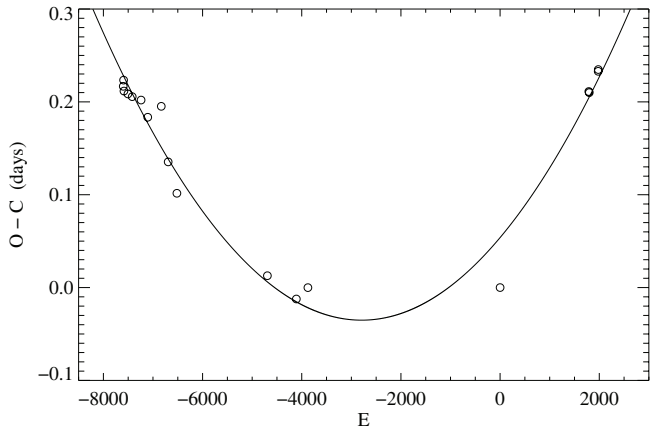

Fig. 5. This is the first ephemeris curve for R Ara. (Reed, 2011)

The average rate of mass transfer from the donating star to the accreting star can be calculated from the period change rate. The calculation requires estimates for the stars' masses and the assumption that the mass transfer is *conservative*. Conservative mass transfer assumes that all material leaving one star is accreted onto the other star, and no mass is lost to interstellar space. Mass transfer is very likely conservative in most Algol-type binaries, but it could deviate from this in the cases of the most active and rapidly interacting systems. The conservative mass transfer assumption, combined with the modified Kepler's laws of orbital motion, leads to the following formula for mass transfer rate:

$$\frac{dM}{dt} = \dot{M} = \frac{\dot{P} M_1 M_2}{3P(M_1 - M_2)} \tag{9}$$

where M_1 and M_2 are the masses of each of the two stars in the binary system.
For the case of R Ara, a spectroscopic study (Sahade, 1952) of the system determined the masses of the stars to be $M_1 = 4M_\odot$ and $M_1 = 1.4M_\odot$. (The symbol "$\odot$" means "Sun", so $1M_\odot$ is equal to the mass of our Sun.)
Applying these masses, and the period change rate (from equation 8), to equation 9, yields:

$$\frac{dM}{dt} = \dot{M} = \frac{\dot{P} M_1 M_2}{3P(M_1 - M_2)} = \frac{(5.16 \times 10^{-9})(4)(1.4)}{3(4.425132)(4 - 1.4)} = 8.37 \times 10^{-10} \frac{M_\odot}{day} \tag{10}$$

Finally, converting days to years for the standard units of "Solar-masses-per-year", we get:

$$\frac{dM}{dt} = \dot{M} = 3.06 \times 10^{-7} \frac{M_\odot}{year} \tag{11}$$

which is actually quite rapid for an Algol-type system. For those unfamiliar with these units, the equivalent mass transfer rate of about 20 trillion tons per second might sound more impressive!
A quadratic ephemeris curve is considered strong photometric support for mass transfer between stars. It certainly proves that the orbital period is changing, and it is widely accepted that mass exchange is the most likely cause.

5. Variable ephemeris curves

The previous section described how the analysis of an ephemeris curve is used to calculate rates of period change and mass transfer in interacting binary stars. This section further discusses ephemeris curves and the additional information they may provide.
Consider the plot in Figure 6(a). The ephemeris curve is fit with a quadratic function, which indicates a steady increase in orbital period, and provides evidence for mass exchange. Notice the scatter in the data follows a periodic pattern. Taking the difference between the data points and the quadratic function yields a plot of the residuals of the fit. The residual plot is shown in Figure 6(b). I sinusoidal function fits the residual plot nicely, which seems to indicate a periodical increase and decrease in the mass transfer rate. A sinusoidally varying ephemeris curve could mean one of two things; either there is a third star in the system, or there is significant magnetic activity.
In the case of a third star in the system, the mass transfer rate is not actually varying, but it is just an apparent *light-time* effect resulting from the fact that light travels at a finite speed. If the close, interacting binary system is orbiting around a third, more distant star, then we will sometimes be observing the interacting system when it is on the near side of the larger orbit. Some observations will take place while the interacting system is on the far side of the

triple star system. This circumstance will lead to alternating changes in the observed times of eclipses. The eclipses observed while the interacting system is on the near side will be detected sooner than those occuring while it is on the far side. If the effect is due to a third star in the system, the periodic variation **must** be precise and repeating.

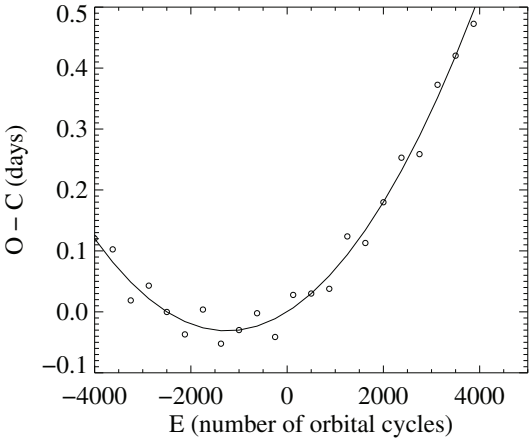

(a) An phemeris curve fitted with a positive quadratic function.

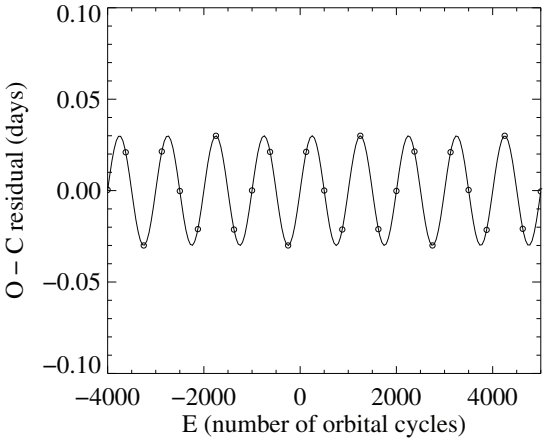

(b) The residuals of the ephemeris curve from Figure (a), fitted with a sinusoidal function.

Fig. 6. This is a periodically variable ephemeris curve.

Periodic variations could also indicate magnetic activity cycles in the evolved star that is donating mass. In this case, the precise repitition of the cycle is not necessary. Our Sun is known to undergo an eleven-year magnetic activity cycle, where the Sun goes through periods

of high activity (Sunspots, Solar flares, prominances, and coronal mass ejections) followed by periods of little to no activity. It is expected that a mass-losing star with strong magnetic activity cycles will donate mass more rapidly during high activity and less rapidly during low activity, which in turn will cause the rate of period change, and therefore the ephemeris curve, to aternate periodically. The period of the sinusiudal residual plot would be equal to the star's magnetic activity cycle period. In the example of Figure 6, the period is 1,000 orbital cycles. If this is for the theoretical star system introduced in Section 3 (orbital period of 3.5 days), the magnetic activity cycle of the star would be approximately 10 years.

Algol-type interacting systems with negative ephemeris curves (as in Figure 4(d)) present another interesting problem. A negative ephemeris curve indicates a decreasing orbital period, but since Algol-type systems consist of a less massive star donating mass to a more massive star, we would expect the orbital period to increase and the ephemeris curve to be positive (as in Figure 4(c)). This contradiction seems to violate the law of conservation of angular momentum.

Possible solutions to this angular momentum problem include *magnetic braking* and non-conservative mass transfer. Magnetic braking is basically the concept that the stars are "dragging" though strong magnetic fields which causes the orbit to decline and the orbital period to decrease. Non-conservative mass transfer implies that some of the mass escaping one star does **not** accrete onto the companion, but rather it either escapes the entire system or forms a *circumbinary* envelope around both stars. The lost mass in the non-conservative mass transfer case would deplete angular momentum from the rest of the system, leading to a negative ephemeris curve.

6. Effects of eccentric accretion structures

The light curves of many Algol-type binary stars show strange variations outside of the primary and secondary eclipses. It has been assumed that these variations arise from mass transfer activity between the stars, but the W.D. code is limited in how it can model such variations. A newly developing photometric method will enable astronomers to use outside of eclipse variations to visualize an eccentric accretion structure surrounding the mass-gaining star.

Experts in the field have determined, using computer modelling and spectroscopic obsverations, that an Algol system's orbital period (and orbital size) plays an important role in the nature of the mass transfer within the system. As introduced in Section 1, "short-period" Algols (orbital periods $\approx$ 3 days or less) have smaller orbits and experience direct impact of mass transferring from one star to the other, while "long-period" Algols ($\approx$ 6 days or longer) have wider orbits and develop stable accretion disks. Intermediate-period Algols are found to oscillate between "stream-like" (similar to short-period systems) and "disk-like" (similar to long-period systems) states (Richards et al., 2010). Many intermediate-period Algols exhibit outside of eclipse variations in their light curves, which are likely caused by the unstable, transient, and eccentric accretion structure that develops.

The accretion structure can at times block the view of the primary star, similar to an eclipse, causing dips in the light curve. These dips can vary in intensity, or even disappear, on timescales as short as a single orbital period. Since entire light curves of Algol systems must be obtained over many week or months, it is very difficult to accurately determine the causes of the variations because it is impossible to continuously observe the system through a complete orbit. Observations from the ground can only be made at night, and that's only when skies are clear and free of clouds.

A good example of such an intermediate-period system is R Ara, whose orbital period is 4.4 days. Ground-based light curves of R Ara exhibit strange dips and other variations. Again, these light curves were built over many weeks of observations. But by using the International Ultraviolet Observer (IUE) satellite, a group of astronomers were able to observe R Ara for 5 consecutive days, which provides and uninterrupted light curve. From space, weather and daylight do not impede observations.

Figure 7 shows the ultraviolet (UV) light curve. The solid circles in the figure are the flux levels at 1320 Å and the open circles are at 2915 Å. Notice that the primary eclipse is deeper at 1320 Å and shallower at 2915 Å, which is as expected. Since the primary eclipse is when the hotter star is eclipsed by the cooler star, it is always deeper at shorter wavelengths. Similarly, a secondary eclipse (eclipse of the cooler star by the hotter star) is always deeper at *longer* wavelengths. In the UV range (shorter wavelength than visual), R Ara's secondary eclipse is expected to be very shallow.

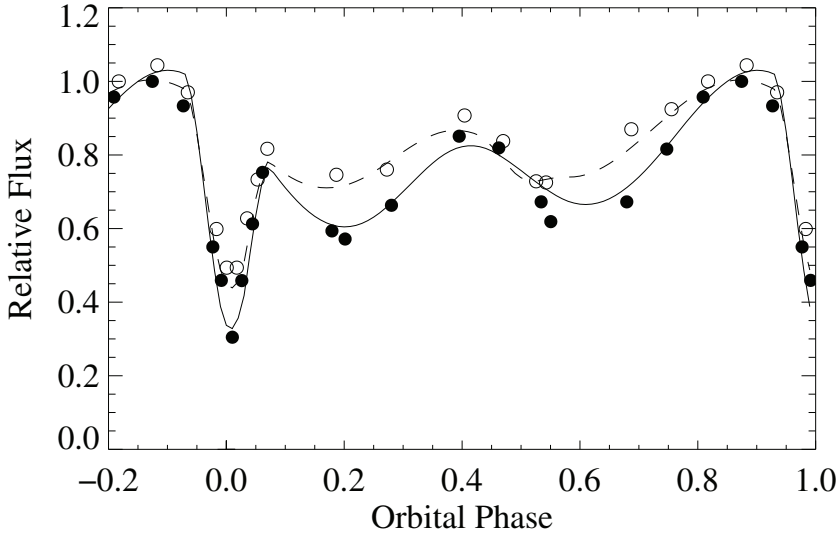

Fig. 7. This is the IUE light curve for R Ara. The solid circles are data points at 1320 Å and the open circles are at 2915 Å. The solid line is the W.D. model at 1320 Å and the dashed line is the model at 2915 Å. (Reed et al., 2010)

Notice the other two "dips" in the UV light curve of R Ara, one around phase 0.2 and the other near phase 0.6. Both of these dips behave like the primary eclipses, that is, they are both deeper at the shorter wavelength and therefore must be due to something cooler than the primary star eclipsing the primary star. Since we know that R Ara's orbital period is steadily increasing due to mass transfer (see Section 4), it is reasonable to assume that there is a cool accretion structure surrounding the primary star, which results from the mass transfer.

Cool "spots" were used in the W.D. code to model the dips in R Ara's UV light curve by treating them as spherical clouds in the line of sight to the primary star. In the model, the stars' surface temperatures are 12,500 K for the primary and 7,000 K for the secondary. The clouds have a temperature of 4,000 K. The inclination of R Ara's orbit, relative to Earth, is 78°. The solid and dashed lines in Figure 7 are the synthetic light curves produced by the W.D. code with the

cool clouds in the model. The solid line is the model at 1320 Å and the dashed line is at 2915 Å.
The locations of the cool clouds (spots) in the model reveal the general geometry of the accretion structure. An illustration of the model for R Ara is shown in Figure 8. The model shows an eccentric accretion cloud surrounding the primary star.

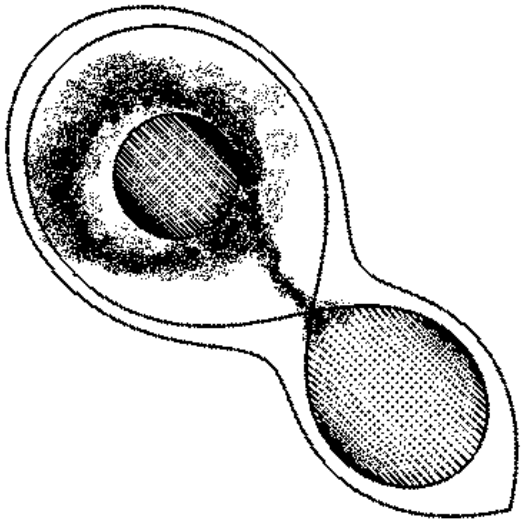

Fig. 8. This is an illustration of the model for R Ara showing an eccentric accretion structure surrounding the primary star.

The eccentric acccretion structure, combined with R Ara's orbital inclination, produces the dips seen in the light curve. Three-dimensional views of the model for R Ara are drawn in Figure 9, showing the locations of the cool spots that best fit the data. When the accretion structure is farthest from the star, around phase 0.4, it is below our line of sight and we are looking over the accretion cloud directly at the primary star. At other times during the orbit, when the accretion structure is closer to the star, the cloud blocks our line of sight to the primary star and we see dips in the light curve.
The fact that the outside of eclipse dips in the light curve are quite variable indicates that the accretion structure is unstable and variable. When the accretion onto the star is more rapid, the accretion structure decreases in size and thickness and the system becomes brighter overall. When the accretion structure builds up again, the dips become deeper.
The question to ask is then, "can the accretion structure be eccentric and variable?" The answer is yes. Hydrodynamic simulations of mass flow in Algol-type binaries show that as an accretion disk builds up around the primary in a long-period system, it is eccentric. It's only after some time passes that the accretion structure becomes stable and starts to resemble a symmetric, circular disk (Richards & Ratliff, 1998). Because intermediate-period Algols, such as R Ara, oscillate between states of direct impact and indirect accretion, they likely undergo the rebuilding of their accretion structures fairly often and can therefore be regularly found with eccentric and variable accretion structures.

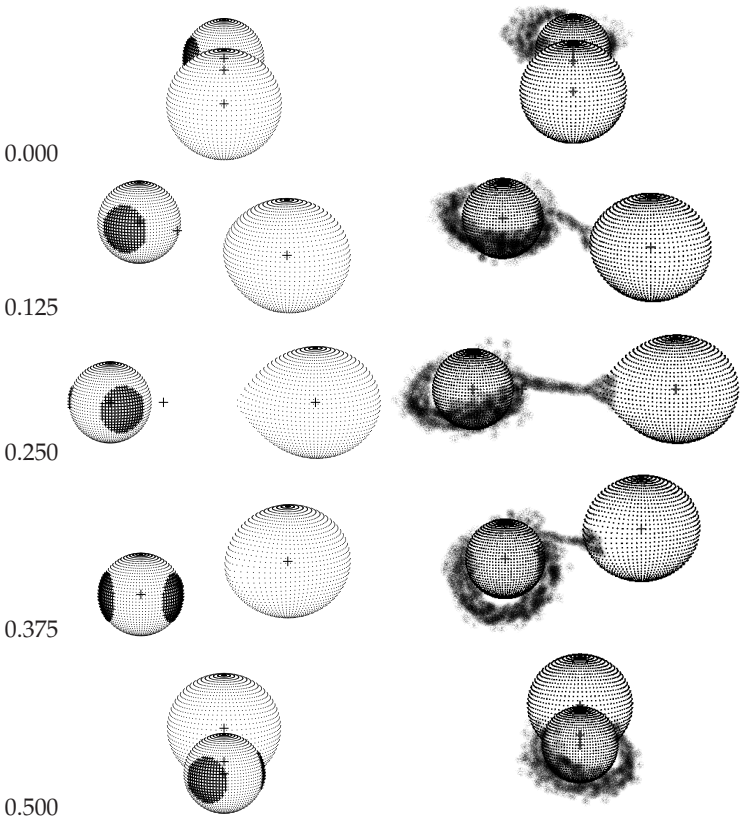

Fig. 9. These are 3-D views of the model for R Ara through the first half of its orbit. The left-hand column shows the W.D. model with the "cool clouds" (spots), and the right-hand column illustrates the corresponding proposed accretion structure. The orbital phase values for each view are listed to the left.

7. Future work

There are many neglected intermediate-period interacting binary star systems that deserve studying. Two examples are Y Piscium (orbital period = 3.7 days) and RV Ophiuchus (orbital period = 3.9 days), both of which show outside-of-eclipse variations in their latest light curves, which are more than 25 years old (Walter, 1973). Can the light curves of these star systems be modelled with eccentric accretion structures and orbital inclinations that lead to apparent eclipses of the primary star by the accretion cloud? If not, what else could explain the light curve variations? If something else can explain them, can it also explain the variations seen in R Ara?

On the theoretical side of the research, it is desirable to modify the W.D. code to account for eccentric accretion structures (disks or annuli). A limitation to the "cool cloud" method used in Section 6 is that the model does not account for the emission of light by the parts of the accretion structure not in the line of sight to the primary star. This condition is quite acceptable

for observations in UV light because, in that range of frequencies, the cool accretion structure emits very little light compared with the hot primary star. In visible, red, and infrared light, however, the accretion structure will emit more light than it does in the UV and the primary star will emit less light that is does in the UV, which makes the limitation of the "cool cloud" method more serious. Including the entire eccentric accretion structure in the light curve model will eliminate these limitations at all wavelengths are will provide a more accurate picture of the transfer of mass between these stars.

8. References

Nield K. M. (1991). Observations and Analysis of the Southern Binary R Arae, *Astrophysics and Space Science*, Vol. 180, 1991, 233-252

Reed P. (2011). A 116 Year Record of Mass Transfer in R Arae, *Information Bulletin on Variable Stars*, No. 5975, February 2011, 1-4, ISSN 0374-0676

Reed P. A., McCluskey Jr., G. E., Kondo, Y., Sahade, J., Guinan, E. F., Giménez, A., Caton, D. B., Reichart, D. E., Ivarsen, K. M., Nysewander, M. C. (2010). Ultraviolet Study of the Interacting Binary Star R Arae Using Archival IUE Data, *Monthly Notices of the Royal Astronomical Society*, Vol. 401, No. 2, January 2010, 913-923, ISSN 1365-2966

Richards, M. T., Sharova, O. I., Agafonov, M. I. (2010). Three-dimensional Doppler Tomography of the RS Vulpeculae Interacting Binary, *Astrophysical Journal*, Vol. 720, No.2, 2010, 996-1007, ISSN 0004-637X

Richards, M. T., & Ratliff, M. A. (1998). Hydrodynamic Simulations of Hα Emission in Algol-Type Binaries, *Astrophysical Journal*, Vol. 493, January 1998, 326-341, ISSN 0004-637X

Sahade, J. (1952). The Spectrum of the Eclipsing Variable R Arae, *Astrophysical Journal*, Vol. 116, 1952, 27-34, ISSN 0004-637X

Walter, K. (1973). Photometric Effects of Gas Streams in Algol Systems and Their Influence on the Light Curves Outside Of and Within Eclipses, *Astrophysics and Space Science*, Vol. 21, 1973, 289-305

Wilson, R. E. & Devinney, E. J. (1971). Realization of Accurate Close-Binary Light Curves: Application to MR Cygni, *Astrophysical Journal*, Vol. 166, June 1971, 605-619, ISSN 0004-637X

2

UV Emission and Spectral Synthesis of Accretion Disks in Non-Magnetic Cataclysmic Variables

Raul E. Puebla and Marcos P. Diaz
Departamento de Astronomia. IAG. Universidade de São Paulo. Brazil

1. Introduction

Accretion disks are present throughout the wide Universe at multiple scales. They are in the active galactic nuclei (AGN) with a disk radius ($r_{\rm disk}$) $\sim$ 0.1-1.0 parsecs (1.0 pc $\sim$ 206264 AU $\sim 3.1\times10^{18}$ cm), protostars (YSOs) ($r_{\rm disk}\sim$ 1000 AU), Debris disks ($r_{\rm disk}\sim$10-100 AU) and in close binary systems: Cataclysmic Variables (CVs), Low Mass X-Ray Binaries (LMXBs) and some symbiotic stars ($r_{\rm disk}\sim R_\odot\sim6.9\times10^{10}$ cm). Being a very common phenomenon in the Universe, the understanding of accretion disk behavior, time scales and evolution are crucial to have a clearer vision of most of the systems present in the Universe.
Among these systems, interacting binaries are the best laboratories to understand the accretion disk physics. This because of its abundance in the Galaxy, the amount of nearby systems, data availability and the existance of observational facilities to obtain them. Cataclysmic Variables present the best scenery to analyze accretion disk behavior due to the fact that its main emission region falls on ultraviolet (UV) and optical. In these wavelength bands, we have the tools with the spectral and the time resolution that allow us to see most of the disk with good detail. Also, due to the order of magnitude of CVs periods and luminosity, it is feasible to study the disk physics in a wide range of time scales, which facilities the understanding of its evolution in a multiplicity of cases.
Cataclysmic Variables are semidetached binary systems with orbital periods between 0.28 and 18 hours (Ritter & Kolb, 2003), where a Roche-lobe filling main sequence star (secondary) transfers mass onto a white dwarf (primary). Depending on the magnitude of the primary magnetic field, this mass transfer can be performed through an accretion disk (non-magnetic CVs), a truncated disk (intermediate polars) or funnels (polars). CVs can also be classified into several types depending on their erupting behavior. System that do not show any eruptions is called "$Nova-Like$" (NL), systems that show one or more thermonuclear eruptions are "$Novae$" (Ne) and "$RecurrentNovae$" (RN) respectively. Also, there exists systems with a kind of "weak" periodic eruption, caused by disk instabilities. These systems are known as "$DwarfNovae$" (DNe) (Warner, 1995). It is important to score that the types of CVs are not exclusive each other i.e. both magnetic or non-magnetic CVs can show novae eruptions.
The NL systems are non-magnetic CVs with a high mass accretion rate ($\dot{M}_a$). This fact bears a bright accretion disk, unlike DNe that show low $\dot{M}_a$ values and then weaker disks. For NL the disk emission greatly exceeds the emission of the other members of the binary system (primary plus secondary), and specially dominates the UV region of the spectrum. Also, it has

been set that high accretion rates through the disk guarantees its stability (see Lasota, 2001). Because of these reasons, NL are the best systems to study the emission, origin and physics of disk radiation as well as to limit the disk models. Furthermore, due to the strong dependence of the UV spectra on the accretion rate, white dwarf mass (M_{WD}) and disk radius (r_{disk}), UV spectroscopy is a crucial tool to establish the binary system parameters, and to find the correlation between them. Likewise, these correlations could help to constrain the evolution models for these kind of close binary systems (see Rappaport et al., 1982; 1983).
In this chapter we expose the different efforts made through the years to reproduce the UV spectral observations, using several methods of spectral synthesis. Also, we focus on different tests done on those different methods through UV data taken from the different satellites as *International Ultraviolet Explorer* (IUE), *Hubble Space Telescope* (HST), *Hopkins Ultraviolet Telescope* (HUT) and *Far Ultraviolet Spectroscopic Explorer* (FUSE). In recent years important advances have been done in the sense of building a consistent model of accretion disk plus wind (Noebauer et al., 2010; Puebla et al., 2011). Here we explore these efforts and point out the potential solutions to the problems found. Special attention is focused on the new methods for spectral synthesis and for structure calculation, comparing with the standard models.
The structure of this chapter is as follows: The following section describes the disk formation in CVs as well as the main spectral region of its radiative emission. Section 3 describes the main spectral characteristics in UV of the brightest non-magnetic CVs (NLs and DNe in outburst). Section 4 delineates the main spectral synthesis method currently used to describe the UV spectra of CVs disk, the *disk-atmosphere*. We make a special focus on works of Hubeny (1990); Kriz & Hubeny (1986); Wade & Hubeny (1998) and Puebla et al. (2007). In section 5 we describe disk wind models with a comparative analysis with UV data, specially focusing on works of Long & Knigge (2002); Noebauer et al. (2010) and Puebla et al. (2011). Finally in section 6 we present a brief view the current stage on the spectral synthesis methods and the challenges for the future, as well as possible solutions to the problems that still remain.

2. Disk formation and its spectrum

The VCs are formed from binary systems with an original orbital period between 1-10 years. After the system has lost sufficient angular momentum, the secondary star can fill its Roche lobe. At this point in the evolution the mass transfer starts through a stream that falls into the primary potential well. Due to the angular momentum conservation, the stream has a velocity perpendicular to the axis that joins the stars $v_\perp \sim b_1\omega$, where $\omega = 2\pi/P_{orb}$ and b_1 is the distance between the WD and the inner Lagrange point (L_1, see figure 1) (Frank et al., 2002; Warner, 1995). For typical values for P_{orb} of CVs, $v_\perp \sim 100$ km s^{-1}, which indicates a super-sonic flow, the streamline will orbit the WD in an elliptical trajectory. Due to its continuum flux, the stream will collide with itself. These shocks will cause energy dissipation and the circularization of the trajectory, thus forming a ring around the white dwarf. As matter accumulates within the ring, the internal friction becomes important, and viscosity processes begin to act. These processes convert the gravitational energy to internal energy, which is then radiated. This loss of energy makes the particles occupy trajectories closer to the WD. As the scale of time of this process is large when compared to radiation and dynamic time scales, the orbits of particles thus formed are almost circular. As the angular momentum is conserved, the angular momentum of the falling particles must be transported to external regions. Thus

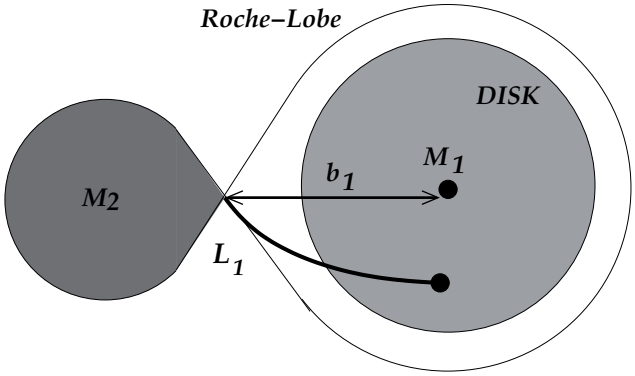

Fig. 1. Binary geometry. It shows the Roche-lobe filling secondary, accretion disk, WD (primary) and the streamline that leaves the secondary through the inner Lagrange point (L_1). It also shows the hot spot.

a small portion of gas is transported away from the white dwarf. The structure formed in this way is known as *accretion disk* (Frank et al., 2002).

As was mentioned above, the particle trajectories within the disk are almost circular and keplerian, balancing gravitational and centrifugal forces. Thus, the velocity will be given by:

$$v_K = \sqrt{\frac{GM_{WD}}{r}}, \tag{1}$$

where r is the distance to the WD center and G the gravitational constant. It is easy to estimate the accretion luminosity of the disk if we suppose that the falling matter reaches the WD surface with the corresponding keplerian velocity. From there the disk luminosity is given by:

$$L_d = \frac{GM_{WD}\dot{M}_a}{2R_{WD}} = \frac{1}{2}L_{ac}, \tag{2}$$

where $\dot{M}_a$ is the mass accretion rate through the disk and L_{ac} is the accretion luminosity. For typical values of $\dot{M}_a$ for bright CVs (10^{-10} - 10^{-8} $M_\odot$ yr^{-1} (Puebla et al., 2007)), the disk luminosity is between $\sim$1-100 solar luminosities ($L_\odot$).
One of the main problems of the accretion disk physics is to understand the origin of the viscosity that dissipates the energy and transports the angular momentum to the outer radii. Nowadays, it is accepted that the viscosity is driven by what is called *magnetohydrodymacis turbulence* (Balbus & Hawley, 1991). However, some properties of the disk can be studied by using the standard Shakura & Sunyaev (1973) α parametrization for kinematic viscosity $\overline{w}$:

$$\overline{w} = \alpha c_s H\,, \tag{3}$$

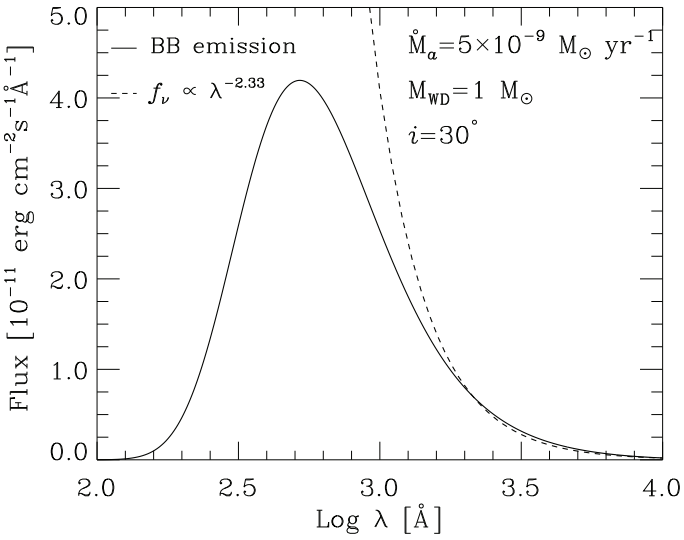

Fig. 2. The spectrum of an assemble of black bodies radiating concentric rings. The temperature of rings follows the steady model (eq.4). The parameters of system are shown in the figure. The dashed line shows the Lynden-Bell (1969) emission of an infinite disk: $f_\lambda \propto \lambda^{-2.33}$.

where c_s is the sound velocity and H is the hydrostatic vertical scale of the disk. In the case of a bright disk, its high mass accretion rate makes it stable (Lasota, 2001) and if we suppose that the keplerian orbits are maintained as far as a region close to the WD, the radial distribution of energy dissipated by a disk is independent of viscosity. Therefore, the effective temperature within the standard model for a steady accretion disk can be expressed by (Pringle, 1981; Shakura & Sunyaev, 1973):

$$T(r) = \left(\frac{3GM_{WD}\dot{M}_a}{8\pi\sigma {R_{WD}}^3}\right)^{1/4} \left(\frac{R_{WD}}{r}\right)^{3/4} \left[1 - \left(\frac{R_{WD}}{r}\right)^{1/2}\right]^{1/4}, \quad (4)$$

where σ is the Stefan-Boltzmann constant. If we call $T_* = \left(3GM_{WD}\dot{M}_a/8\pi\sigma {R_{WD}}^3\right)^{1/4}$, the temperature maximum is T_{max}=0.49T_* at r=(49/36)R_{WD}. Thus, for the typical physical parameters for luminous VCs, the accretion disk have temperatures between 50000 K and 10000 K. Therefore, the disk spectrum is mainly emitted in UV between 500-3000 Å, hence the importance of the spectroscopy in this spectral region to understand the accretion disk physics. For a disk formed by an assembling of infinite black body emitting rings, Lynden-Bell (1969) shows that the spectrum has the form: $f_\lambda \propto \lambda^{-2.33}$. Figure 2 shows the spectrum of a finite accretion disk, also as an assembling of blackbody emitting rings with an accretion mass rate $\dot{M}_a$=5×10^{-9} M$_\odot$ yr^{-1}, a M$_{WD}$=1 M$_\odot$ and an orbital inclination i=30°. The external radius of disk (r_{disk}) is set through the tidal forces that disrupt the disk to ∼0.8 b$_1$ (Osaki et al., 1993). Figure 2 also shows the disk spectrum from Lynden-Bell (1969) $f_\lambda \propto \lambda^{-2.33}$ (dashed line), which has a good similarity at low wavelengths (optical to middle ultraviolet, MUV), but a large discrepancy at short wavelengths (far, FUV, to extreme, EUV ultraviolet). It is clear that

for this kind of accretion disk, the emission peak falls on UV for typical parameters (M_{WD} and $\dot{M}_a$) found for CVs.

3. UV spectroscopy of non-magnetic CVs

For nearly 30 years the UV emission from CVs has been deeply studied through data taken form satellites (e.g. IUE, HST, HUT and FUSE). These studies have helped to constrain the main physical characteristics of disks. In general, the UV spectra of non-magnetic CVs show a strongly blue continuum and strong lines of high ionization as: C IV, N V, Si IV and He II. However, absorption and emission lines of an intermediately-to-low ionization state were also observed, as C III, C II, Si III, Si II and others. These features would show a strongly stratified temperature and density structure that would produce a complex ionization distribution. Here, we will focus on the spectral features of high state accretion disks, namely, NLs and DNe in outburst.

3.1 Continuum

For several decades a variety of models have been developed to reproduce the photometric and spectroscopic data. For the last case, the first efforts were made performing models with an arrange of concentric rings that radiate as black-bodies following the standard temperature radial distribution (eq. 4). This models bears a UV continuum that follows the $f_\lambda \propto \lambda^{-2.33}$ form for an infinite disk (Lynden-Bell, 1969) or for a finite disk as was shown in figure 2 (Lynden-Bell & Pringle, 1974; Pringle, 1981; Tylenda, 1977). The first attempts to incorporate line and continuum opacities in the calculus of UV emission was performed by La Dous (1989). In a parallel, a composite of concentric rings of Kurucz (1979) stellar atmospheres was calculated by Wade (1984). Although these models have managed to reproduce some spectral features, a crucial problem was found. Wade (1988) tried to fit these models with the UV data for nine NLs and pointed out that when the models match the flux level cannot match the spectrum slope. This problem is now know as the "*color-magnitude*" dichotomy or the "*color-magnitude*" problem. Few years later, these kinds of models were followed by more realistic ones. They calculate the whole vertical structure assuming that physical properties of the disk vary in the vertical sense faster than in the radial direction. Also, the models take into account the vertical dependence of gravity and an internal energy generation by viscosity (Kriz & Hubeny, 1986; Shaviv & Wehrse, 1986). The internal viscosity is parameterized through algebraic expressions compatible with the α models of disks (Shakura & Sunyaev, 1973). Besides, in these models, the following are taken into account: line blanketing, Doppler broadening and limb darkening (Diaz et al., 1996; Wade & Hubeny, 1998). These models are known as: "*disk atmospheres*". In the subsequent years, the WD's emission, orbital phase and disk rim influence on model spectrum were included (Linnell et al., 2007; Linnell & Hubeny, 1996).

This generation of models is capable to reproduce some photospheric spectral features as well as the broadening of lines due to disk rotation, however some problems still persist. The main of them is the color-magnitude dichotomy found in subsequent works that used this model to study the disk properties and to estimate systems parameters (Diaz & Hubeny, 1999; Engle & Sion, 2005; Linnell et al., 2008; Long et al., 1994; Nadalin & Sion, 2001). Recently, Puebla et al. (2007) used the model to fit the continuum UV for 33 CVs (NLs and old Ne) using a multi-parametric optimization method. They confirmed the same problem for the most of

Ion	λ(Å)	Ion	λ(Å)
Ly $_\beta$	1025.18	C II	1335.3
O IV	1031.6	O IV	1338.6
Si IV	1062.6	P III	1341.6
Si IV	1073.6	O V	1371
P IV	1117.8	Si IV	1393.8,1402.7
P V	1128.01	Ni IV]	1486
C III	1175	Si II	1526.7,1533.4
Si III	1201.3	C IV	1548.2,1550,7
Si III	1206.5	Mg V	1575.2
Ly $_\alpha$	1215.67	Fe II	1608
N V	1238.40,1242.78	He II	1640.4
Si II	1251	N IV	1718.5
Si II	1260,1264	Si II	1815
Si III	1298.9,1304.3	Al III	1860
[Mg V]	1324	Si III]	1896
C II	1323.9	C III]	1909

Table 1. Commonly observed lines in VC's UV spectra. The wavelengths are in the rest frame.

their sample. Also, they didn't find a strong correlation between the orbital period ($P_{\rm orb}$) and the mass accretion rate, as is predicted by the standard evolution models and as was found by Patterson (1984).

3.2 Lines

One of most important characteristic of the observed UV spectra of CVs are the behavior of the line profiles. The main lines that are found in the UV spectra of CVs are shown in the table 1 with their wavelengths in rest frame. In the case of non-magnetic CVs in high state, there exists line characteristics strongly defined. The emission line are strongly dependent on orbital inclination, namely, high inclination systems show strong emission lines. Unlike them, low inclination systems show spectra mainly in absorption (La Dous, 1991). Furthermore, Puebla et al. (2007) found that low accretion rate systems don't show strong emission lines. Also, intermediate-to-low inclination systems show P Cyg profiles and/or blueshifted deep absorptions. Some examples of these characteristics are shown in figure 3 where the UV spectra of three VCs are shown, the NLs V3885 Sgr and RW Sex, and the DN in outburst Z Cam ($i = 50^\circ$, 35° and 60° respectively). The spectra show strong P Cyg profiles in C IV $\lambda\lambda$1548,1551 and deep absorptions in the rest of the lines, which are shown blueshifted. In other systems lines Si IV $\lambda\lambda$1393,1402 and N V $\lambda\lambda$1238,1242 also show P Cyg profiles. The absorption component of these profiles commonly shows a blue wing between 3000 to 5000 km s^{-1} from the rest frame, and the red wing of the emission component could attain $\sim$1000 km s^{-1}.

These features couldn't be reproduced by any model using arrays of photospheres. Reproducing the line profiles has been a hard challenge in study of accretion disk through decades. Since models using optically thin layers (e.g. Tylenda, 1981; Williams & Ferguson, 1982) some physical frameworks have been suggested to explain the line profiles, at the present it is accepted that the these spectral structures are formed in a wind that escapes from the disk. This hypothesis is based on the correlations found between several geometrical and

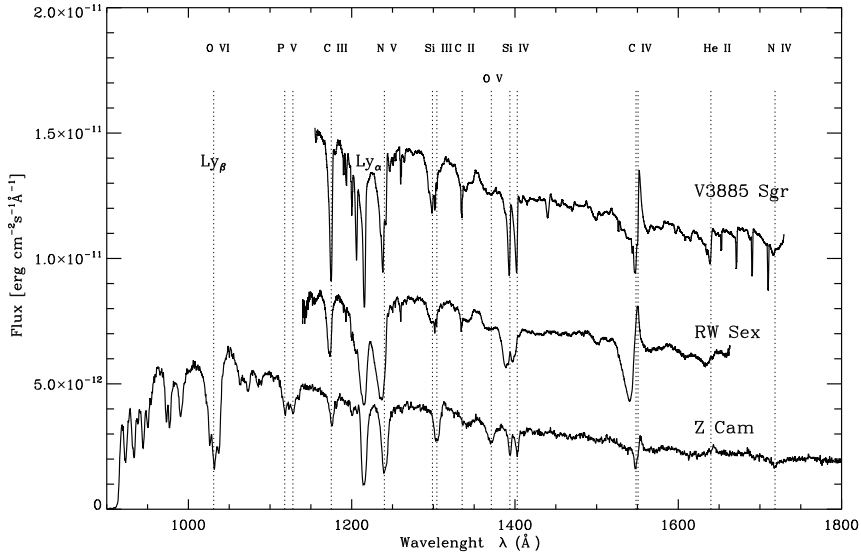

Fig. 3. UV observed spectra for three non-magnetic CVs: the NLs V3885 Sgr and RW Sex, observed by HST and the DN Z Cam observed by HUT.

physical parameters with line profiles (e.g. Shlosman & Vitello, 1993) and the resemblance of line profiles to those observed in radiative driven winds from OB stars (Cordova & Mason, 1982; 1985), specially the similarity of P Cyg profiles. However, there are characteristics of line profiles that are different from those ones of OB stars. For example, the minimum of flux in the absorption component of the P Cyg is close to the rest frame wavelength, unlike what happens in OB stars where it is close to the wind terminal velocity.

4. Accretion disk atmosphere

4.1 The model

In the last fifteen years, the most used method to study the UV emission of non-magnetic CVs has been the one developed by Hubeny et al. (Hubeny, 1990; Kriz & Hubeny, 1986; Wade & Hubeny, 1998). Here, we briefly describe the basis of this model, whose structure calculus is based on the method by Hubeny & Lanz (1995) and its spectral synthesis on the one by Hubeny et al. (1994).

The model separates the disk in concentric rings rotating with keplerian velocity. For each ring the internal structure is calculated taking into account the internal energy generation due to viscous friction between two regions with different rotational rate (eq. 1). For the structure calculus a plane-parallel geometry is adopted. The viscous mechanical energy generated per unit volume per unit time inside the disk can be described according to Lynden-Bell & Pringle (1974) (see also Frank et al., 2002) as:

$$d_{mec} = w_1 \rho \left(r \frac{\partial \Omega}{\partial r} \right)^2 \tag{5}$$

where w_l is the local kinematic viscosity, Ω is the angular velocity at radius r and ρ is the local mass density. The vertical coordinate z is changed through a new parametrization by:

$$m(z) = \int_z^\infty \rho dz' \tag{6}$$

Thus, $m(0)$=M and $m(\infty)$=0, where M=$\Sigma/2$, and $\Sigma(r)$ is the column mass density of disk at r in gr $\cdot$ cm^{-2}. In the model, the local viscosity w_l is parametrized through a power function of m by:

$$w_l = \overline{w}(\zeta + 1)\left(\frac{m}{M}\right)^\zeta \tag{7}$$

where $\overline{w}$ is the main kinetic viscosity defined in equation (3). This expression evaluates where, within the disc, the viscous energy is released. For the structure calculus, the condition of energy balance is imposed. This condition involves that the viscous dissipation energy is equal to the radiatively released energy:

$$d_{rad} = d_{mech} \tag{8}$$

$$\int_0^\infty (\chi_\nu S_\nu - \chi_\nu J_\nu)\, d\nu = \frac{9}{16\pi}\overline{w}(\zeta + 1)\left(\frac{m}{M}\right)^\zeta \rho \frac{GM_{WD}}{r^3}, \tag{9}$$

where χ_ν is the opacity, S_ν is the fource function and J_ν is the mean specific intensity for each frequency ν. This will cause the non-conservative of radiation flux through the disk atmosphere, thus:

$$\frac{dH}{dz} = 4\pi\frac{dF}{dz} = \frac{9}{16\pi}\overline{w}(\zeta + 1)\left(\frac{m}{M}\right)^\zeta \rho \frac{GM_{WD}}{r^3}. \tag{10}$$

This characteristic is different from the case of stellar atmospheres, where the radiative equilibrium bears a conservative flux through the structure ($dF/dz = 0$).
Another important difference with the stellar case is the gravity. In the stellar case the gravity is constant in the atmosphere, for disks the gravity is dependent on the depth. In this approximation it is not considered the self-gravity, so that gravity comes from the WD. The vertical component in this case is:

$$g_z = \frac{GM_{WD}}{(r^2 + z^2)^{3/2}} z \approx \frac{GM_{WD}}{r^3} z \quad \text{for } z \ll r. \tag{11}$$

With these conditions the equations for the structure are solved. These equations include the hydrostatic equilibrium, the equation of state taking into account the opacities of Hydrogen and Helium for radiation pressure, the radiative transfer equation, the radiative equilibrium equation and the statistical equilibrium equations for the level populations. The method used to solve this system of equations was developed by Hubeny (1988) and it is based on the complete linearization by Auer & Mihalas (1969). Once the convergence is attained, the specific intensities and the flux that are emited by each ring is calculated using the code SYNSPEC[1]. Then the emissions of all rings are corrected for disk rotation and integrated in the solid angle subtended by disk and the observer, taking into account the orbital inclination through (Wade & Hubeny, 1998):

[1] http://nova.astro.umd.edu

$$f_\nu = \frac{\mu}{d^2} \int_{r_{min}}^{r_{max}} \int_0^{2\pi} \int_0^{\infty} I_\nu(\lambda', r, \mu) \Delta dr d\phi d\lambda \,, \tag{12}$$

where:

$$\Delta = \delta \left\{ \lambda - \lambda' \left[1 + \frac{1}{c} \left(\frac{GM_{WD}}{r} \right)^{1/2} \sin i \sin \phi \right] \right\}. \tag{13}$$

4.2 Results

Having a reliable of accretion disk model is crucial for understanding not only the disk physics, but also the binary system evolution. The latter due to the dependency of disk emission mainly on M_{WD} and $\dot{M}_a$, orbital inclination (i) and distance (d). The M_{WD}, i and d can be measured through independent methods, specially for eclipsing systems. Thus, the accretion rate, determinant in evolution models, can be obtained from disk emission.

The Hubeny's models described above, have been widely used to estimate the binary parameters or to test the model itself. This was done using first the IUE data and then, with a better resolution and signal to noise ratio, using the HST and FUSE data for FUV. Recently, we have taken the UV IUE and HST data for a sample of 33 non-magnetic CVs (10 old Ne and 23 NLs). We seek both, to calculate the $\dot{M}_a$ for the sample usign the same method and to test the accretion disk emission model by Hubeny widely used now today. We used a multiparametric optimization method leaving three free parameters: M_{WD}, i and $\dot{M}_a$, and fixing the d. Thus, using this three-dimensional space of parameters we generated a set of models within it. The models were calculated between reliable ranges for free parameters. These ranges were obtained from the measured values that we found in literature. Also we collected from literature the values of d, the interstellar extinction parameter $E(B-V)$, and the orbital period P_{orb} (Puebla et al., 2007).

The optimization was done through the minimization of the reduced χ^2_{red} function:

$$\chi^2_{red} = \frac{1}{N-L} \sum_{i=1}^{N} \left(\frac{f_{obs}(\lambda_i) - f_{mod}(\lambda_i)}{\sigma_i} \right)^2 \,, \tag{14}$$

where N is the number of observed wavelengths, L is the number of free parameters of the model, f_{obs} and f_{mod} are the fluxes of spectra observed and modeled, respectively in the observed wavelength λ_i and σ_i is the error for each measured flux $f_{obs}(\lambda_i)$. For the χ^2_{red} calculus all the lines are masked, thereby, only the continuum is taken into account for the fit. The χ^2_{red} values for each model thus calculated, were fitted to a smooth surface and its minimum was searched within the three-dimensional parameter space. We used a surface like the one shown in figure 4, taking slices that cut the 3D surface of χ^2_{red} in some parameter. Also we calculated the influence that WD emission would have on UV. For this, we calculated the UV spectrum of a WD with the same mass and a effective temperature equal to 40000 K. We compared the UV integrated flux of this model with the flux from the disk model. We defined ξ as the ratio of these fluxes: $\xi = f_{WD}/f_{disk}$. If ξ<0.1 we called this models as *disk dominated* systems. For the system with ξ>0.1, we cannot conclude if the spectrum is disk dominated or not, because of the uncertainty of the real value of effective temperature. However, we found

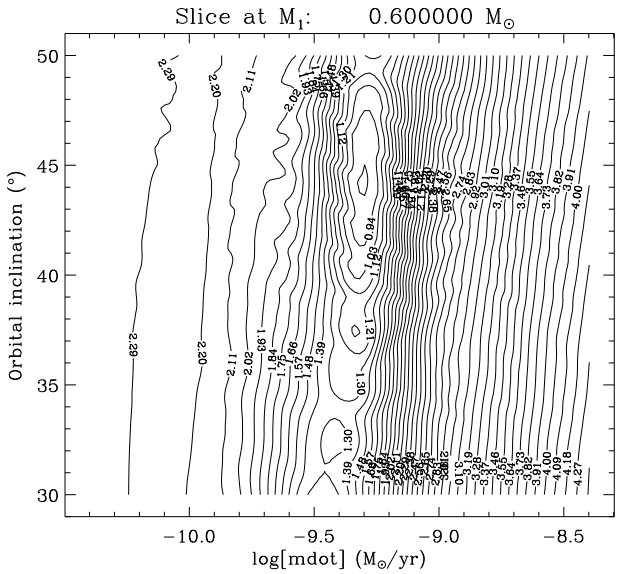

Fig. 4. Sample of a $\log \chi^2_{red}$ surface for disk spectrum fitting. This sample corresponds to the fitting of the UV spectrum of KR Aur. Figure taken from Puebla et al. (2007). Reproduced by permission of the AAS[1].

that the influence of the WD emission on UV spectrum would be less than 10% for most of the systems of our sample.

In figure 4 it is shown a cut at M_{WD}=0.6 $M_\odot$ slice in the plane ($\dot{M}_a$, i). This figure shows an important feature of the χ^2_{red} surfaces. It is no possible to find an absolute minimum. The surface shows a band of multiple relative minima slightly tilted towards higher $\dot{M}_a$ values. For higher inclination cases the slope of this band decreases due to the combined effect of aspect factor $\cos i$ and *limb darkening*. The same applies in the case of slices of constant $\dot{M}_a$ or i. The reason for this is when fitting only the continuum it is difficult to simultaneously constrain all the parameters. The UV continuum of CVs has not strong inflections, and the slope can be reproduced by a non-unique set of parameters. For the case shown in figure 4, a slight loss of flux caused by lower $\dot{M}_a$ can be balanced with a slight lower orbital inclination. The same happens with the other combinations of parameters. Also, for the case of the slope of spectrum, a change caused by one parameter can be compensated by altering another. This degeneracy between parameters makes the modeling of continuum insufficient to fully characterize the disk. It is also found that the base of the band of minima decreases towards cooler disks (lower M_{WD} and $\dot{M}_a$). It tells us that the models, in the most cases, are too blue in comparison with the observed data. This confirms the dichotomy color-magnitude problem pointed out by Wade (1988) using stellar atmosphere, now with this model of disk-atmosphere.

[1] American Astronomical Society

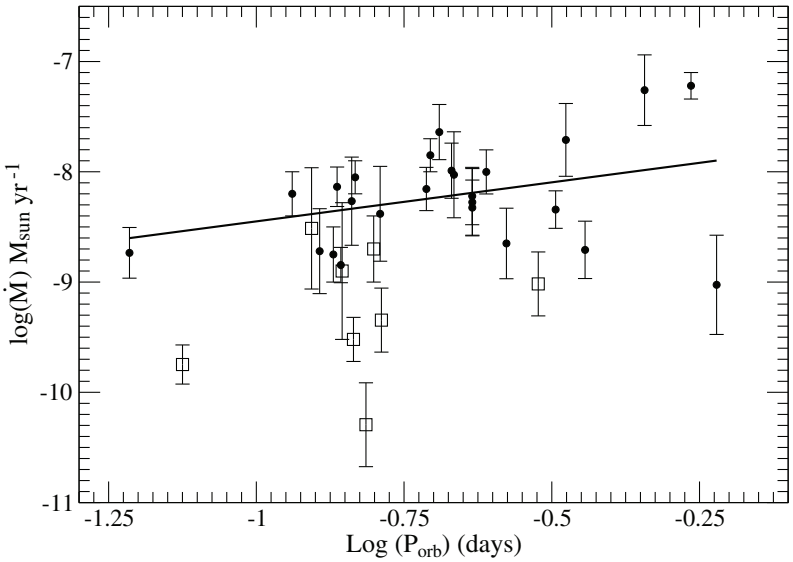

Fig. 5. Mass accretion rate $\dot{M}_a$ as a function of orbital period. The best linear fit is shown and is expressed by equation (15). The filled circles are disk dominated CV's while the squares represents the objects with an eventual contribution from the WD. The latter ones were not considered in the linear fit. Figure taken from Puebla et al. (2007). Reproduced by permission of the AAS.

Due to the arguments exposed above, to calculate the accretion mass rate through the UV continuum emission of non-magnetic CVs, the remaining parameters must be known through independent methods. Thus, using this model we calculated the $\dot{M}_a$ for our sample constraining the other parameters inside reliable intervals. With these values we seek correlations with others parameters of the binary aiming to find the ones predicted by evolution models.

Figure 5 shows the accretion rate as a function of the orbital period. Patterson (1984) found a strong correlation between these parameters that is predicted by the evolution models (Rappaport et al., 1983). We did not find such a strong correlation. Our values are systematically higher than Patterson's and show a higher dispersion in the $\dot{M}_a$-P_{orb} plane. Rutten et al. (1992) analyzed a sample of six eclipsing CVs with luminous disks through the eclipse-mapping method (Horne, 1985). They also found no correlation, and their values of $\dot{M}_a$ are more in agreement with our values (Puebla et al., 2007). The weak correlation can be expressed as shown in equation (15), where P_{orb} is in days. For the linear regretion the white squares from figure 5 were not taken into account, because these systems could be influenced by the WD.

$$\dot{M} = 1.82^{+1.64}_{-0.86} \times 10^{-8} P_{orb}^{0.7\pm0.40} \quad \mathrm{M}_\odot\ \mathrm{yr}^{-1} \tag{15}$$

$$\dot{M} = 1.69^{+1.26}_{-0.71} \times 10^{(-0.34\pm0.05)M_V - 7} \quad \mathrm{M}_\odot\ \mathrm{yr}^{-1} \tag{16}$$

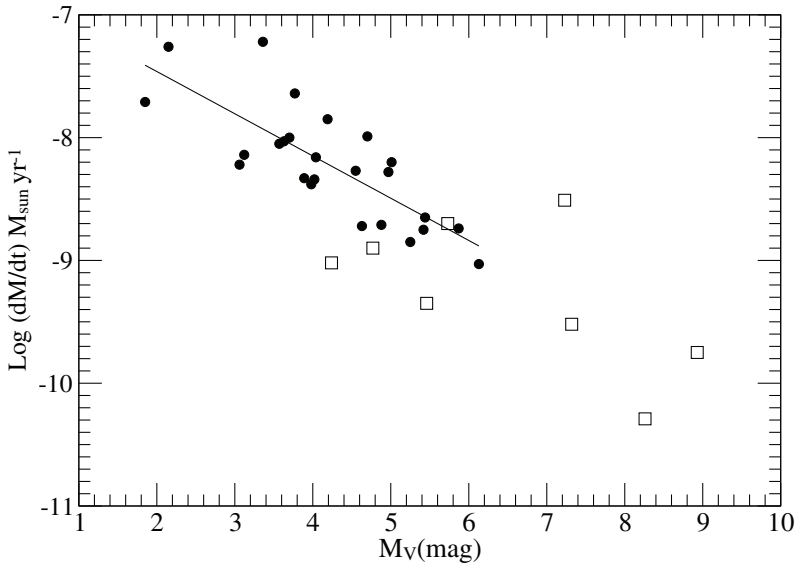

Fig. 6. Mass accretion rate $\dot{M}_a$ as a function of the absolute magnitude of disk M_V(disk) corrected for inclination effects. The best linear fit is shown and is given by equation (16). The squares were not considered in the linear fit. Figure taken from Puebla et al. (2007). Reproduced by permission of the AAS.

Another correlation that we tried was between the absolute magnitude (M_V) and accretion rate. The absolute magnitude was corrected for inclination and limb darkening effects and calculated using the approximation of Warner (1987). Figure 6 shows $\dot{M}_a$ as a function of M_V. The correlation is evident and stronger than with the P_{orb}.

We also tried our optimization method setting free the distance d. In this case we now have a four-dimensional space for trying to simultaneously constrain the set of parameters. To let free the distance we introduced a scaling factor in order to match the flux levels. In that case the method is trying to exclusively fit the spectrum shape or slope. In the most of cases this attempt was unsuccessful, because the χ^2_{red} did not attain any minimum, instead the χ^2_{red} surfaces fall towards the redder models until living the allowed space of parameters. In a few cases we can find such kind of minima, for systems: V592 Cas, V442 Oph and CM Del. This shows that, generally, this accretion disk atmosphere model bears too blue spectra when compared with the data.

4.3 Discussion

The problems of this model pointed out above, don't appear with the same intensity for all binaries. Actually, each case has its own particularities. Also, there exist some cases where even this model attain to describe the UV continuum with a set of parameters compatible with the literature.

Throughout the last twenty years, some hypotheses have been proposed to overcome the problems. A widely studied hypothesis is that the standard disk model, expressed by equation

(4), doesn't describe the real disks. Due to the fact that the model bears too blue spectra, the idea is to propose a new radial temperature structure that will yield a redder spectrum. The analysis of Rutten et al. (1992) shows that the temperature profiles of their six CVs deviate from the standard model. They show temperature profiles flatter than the steady disk. Several studies have been made to test different temperature profiles, for example Orosz & Wade (2003) tested different temperature laws than $T(r) \propto r^{-3/4}$, through the law $T(r) \propto r^{-\gamma}$, with $\gamma < 0.75$. They found that these profiles reduce the discrepancies between flux and color of the models. Before that, Long et al. (1994) made a detailed analysis of other possibilities in order to fit the IX Vel UV spectrum taken from HUT. They proposed three possibilities: 1) the truncation of disk at some inner disk radius, 2) setting a region of constant temperature for inner disk regions and 3) the inner disk radius could be greater than R_{WD}. The first possibility could be caused by a WD magnetic field disk disruption or due to inner disk evaporation (Linnell et al., 2007). In the former case, the necessary magnetic field intensity would bear a strong X-Ray emission or coherent pulsations due to the rotation of the spot of accretion, but neither of them were observed. In the case of evaporation that could be caused by the *boundary layer* (BL) radiation, that needs a value of mass loss that is four times higher than the predicted by the models (Linnell et al., 2007). Moreover, the BL radiation has been too hard to be detected in non-magnetic CVs. The other two possibilities can be related with assumptions made for obtaining the temperature profile (eq. 4). Specially the assumption that the keplerian disk rotation is maintained as far as the WD surface or boundary layer. This came from the presumption that $\partial\Omega/\partial r$=0 at the WD-star interface. If that condition is changed, the disk will not be keplerian everywhere and the temperature profile could be flatter. Disks without keplerian rotations appear when the complete momentum equation (including radial transport of energy) is solved, that bears a more extended boundary layer (Long et al., 1994). Another possibility is the energy that can be removed by a strong wind emerging from the inner disk regions (Linnell et al., 2007). But it is necessary too high mass loss rates to effectively act on the temperature profile (Knigge, 1999). It is almost certain that this kind of accretion disk is not totally described by the steady model (eq. 4), and new attempts are necessary to understand their structure and emission.

5. Disk winds

One of the most interesting challenges in the spectral synthesis of accretion disks is the UV line emission. In section 1 some spectral features were pointed that suggest that the nature of these emission profiles are a wind that is released from inner disk regions.

In the case of CVs with high accretion mass rates (NL's and DNe in eruption), the emission line profiles are strongly dependent on orbital inclination. Thus, the line strength grows with inclination (La Dous, 1991). The accretion mass rate seems to be correlated with the strength of lines. Systems with low accretion mass rate do not show strong emission lines. Figure 7 shows the strength of lines C IV $\lambda\lambda$1548,1551 and He II λ1640 as a function of $\dot{M}_a$ for a sample of 33 non-magnetic CVs. It is evident that strong lines appear preferably in systems with high mass accretion rate (Puebla, 2005). Furthermore, the velocities attained by the blue wing in the P Cyg profiles show that the winds are highly accelerated. Figure 8 shows the P Cyg profiles of line C IV $\lambda\lambda$1548,1551 for three CVs and for the O star ζ Pup. These figures show the similarity of profiles, but also some differences. For example, the minimum of depth of the blueshifted component, in the case of CVs is closer to the rest-frame wavelength, instead of O

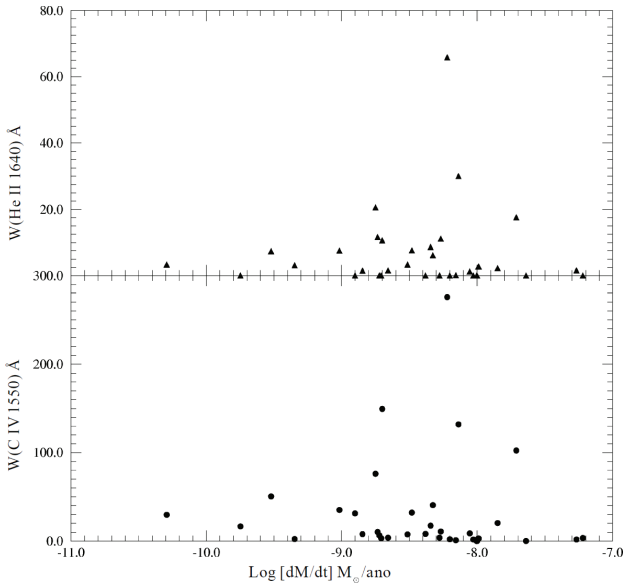

Fig. 7. Equivalent width for C IV $\lambda\lambda$1548,1551 and He II λ1640 as a function of accretion rate $\dot{M}_a$. Figure taken form Puebla (2005).

stars whose minimum is commonly observed close to the terminal velocity (Prinja & Rosen, 1995; Shlosman & Vitello, 1993). Emission lines behavior of eclipsing systems evidences an axi-symmetric wind geometry instead of a spherical one (Mason et al., 1995). Furthermore, the multiplicity of ionization states in observed lines indicates a highly stratified ionization structure where the lines are produced. Mason et al. (1995) show that, in eclipsing systems, the lines are less eclipsed than the continuum. This suggests that the lines are produced in an extended region when compared with the origin of the continuum (the disk). There exists a correlation of the inclination not only with the strength, but also with the line profile, thus, for low-to-intermediate inclination systems P Cyg profiles are observed (e.g. DI Lac, RW Sex and HR Del), on the other hand, for systems with high inclination emission lines are seen. However, Hartley et al. (2002), from HST UV data for V3885 Sgr and IX Vel, did not find the direct correlations between the UV brightness and the wind signals as predicted by accretion disk models (Pereyra et al., 1997; 2000).

With those observational evidences, it is accepted that the winds from accretion disks are driven by line radiation, like the winds of OB stars. Efforts have been made aiming to better understand the winds from disks. Some kinds of hidrodynamical models of radiation driven disk winds have been developed in the last decades. Among them, the models of Proga et al. (1998; 1999) and Pereyra & Kallman (2003); Pereyra et al. (1997; 2000) predict bi-polar collimated winds with high density (shock) regions and complex velocity fields. The main characteristic of such winds is that a strong stratified ionization structure is necessary in order to overcome the gravitational hill produced by the WD (eq. 11). This fact makes the disk wind notably different from the stellar winds. Specially in regard to the α and k constants. These constants evaluate the distribution of the radiative force with the optically

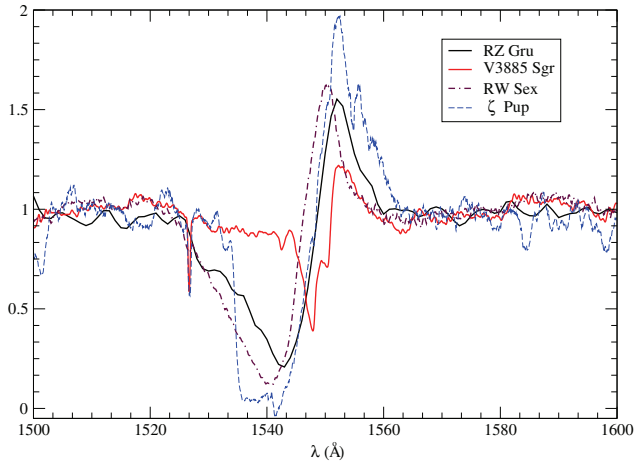

Fig. 8. Line profiles of resonant transition C IV $\lambda\lambda$1548,1551 for the CVs RZ Gru, V3885 Sgr and RW Sex. They are compared to the IUE data for the hot O star, ζ Pup.

thin and optically thick lines taken into account to evaluate that force (Abbott, 1980; 1982). For example, Pereyra et al. (1997) concluded that it is necessary a value of α>0.5 (many optically thick lines) to accomplish a wind from accretion disks of CVs.

Following these clues, many kinematic models and methods of spectral synthesis for disk winds have been developed. The kinematic model of Shlosman & Vitello (1993), achieved to reproduce the emission line C IV $\lambda\lambda$1548,1551 of RWTri, V Sge and the P Cyg profile of RW Sex. They used a stellar velocity profile and the Sobolev approximation to calculate the ionization structure. The next generation of models have used the Monte Carlo method to calculate the temperature structure consistent with the continuum emission of a steady disk (Long & Knigge, 2002). Their work is based on the method developed by Knigge et al. (1995), that take into account the contributions of the WD, disk and eventually a BL using the exact solution for radiative transfer. They also used a stellar wind velocity profile. Long & Knigge (2002) implemented the ionization and temperature calculus using the Sobolev approximation (Sobolev, 1957). This was the first effort to synthesize the UV spectra in a wide range of wavelengths, instead of a single line as in previous works. This method managed to reproduce well the phase behavior of the line C IV $\lambda\lambda$1548,1551 of UX UMa (Knigge & Drew, 1997) including a dense region in the disk-wind transition. Long (2006) pointed out how it is difficult to model all lines with the same wind parameters (collimation, temperature and ionization structure, etc.). Besides, they suggested a hybrid nature of disk wind based also on the results of Hartley et al. (2002).

Recently, we developed an alternative method to calculate the structure and spectral synthesis for accretion disk winds. In this work we tried to use a method widely employed in the study and analysis of stellar winds of hot stars. This method is based on the code CMFGEN[1] (Hillier, 2003; Hillier & Miller, 1998). We separate the disc in concentric rings and calculate a series of 1D models, each corresponding to a ring. For each model the inner disk, photosphere and a

[1] http://kookaburra.phyast.pitt.edu/hillier/web/CMFGEN

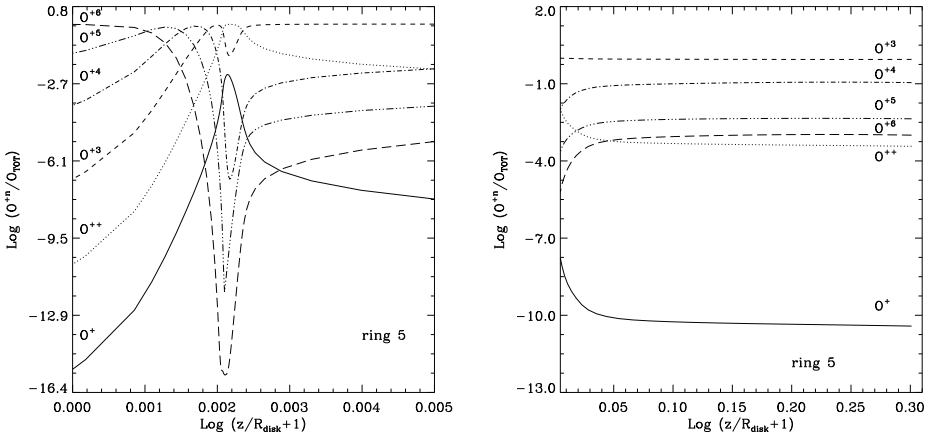

Fig. 9. Ionization structure for Oxygen of the ring 5 model (disk plus wind) with (T_{eff}(R)=38600 K). Left panel shows the inner disk and disk-wind interface. Right panel shows the extensive region of the wind.

vertical wind is calculated. The vertical density structure is calculated using a vertical velocity profile, which is computed exactly solving the Euler equation for a vertical disk wind in the context of Pereyra et al. (2004). The temperature and ionization structure is then calculated through CMFGEN in non-local thermodynamic equilibrium (NLTE) with the approximation plane-parallel. These structures show three regions: the inner and photosphere, disk-wind interface and extensive wind. Figure 9 shows the ionization structure for the oxygen for a vertical model of a ring disk with an effective temperature of 36000 K. It is clear the strong changes in the ionization state in the disk-wind interface region (left panel) and the almost uniform structure in the extensive wind region (right panel). This kind of structures proceed from the plane-parallel approximation and has a strong influence on line profiles (Puebla et al., 2011).

The synthesis spectra follow the trends observed in the UV data of CVs. The lines ratio show a dependence on the temperature of the wind, which also depends on the accretion rate and M_{WD}. We found a dependence of the depth of absorption profiles with the M_{WD}. In the context of the model, we found that the lower is M_{WD}, the deeper the absorption profile. Also, for low orbital inclination models we find emission profiles that are not observed, these features are caused by our simple approximation of a set of 1D plane-parallel models. However, we find that the model is capable to reproduce well the emission lines observed in high inclination systems. For RW Tri, a model with physical parameters close to those found in the literature was tested with the UV spectrum from the HST archive. Figure 10 shows two different synthetic spectra (red lines) and the HST UV data (black line). It is clear the lack of flux for the line C IV $\lambda\lambda$1548,1551. In order to increase the flux of this line, a region of enhanced density was included between rings 1 and 4 (continuous red line). Nevertheless, it was not possible to increment the line intensity to attain the observed intensity without influencing the other lines, taking them away from the observed profiles. This shows that improvements are still necessary to the models.

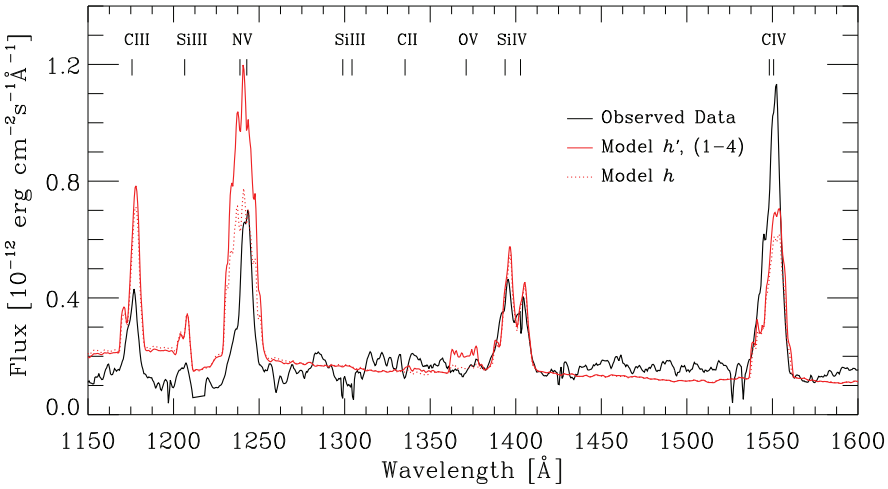

Fig. 10. Simulations for RW Tri UV (HST) data. The data are the mean of spectra taken out of eclipse. The numbers in the parentheses show the rings where a density enhancement was included. For details of h and h', see Puebla et al. (2011). Figure taken from Puebla et al. (2011). Reproduced by permission of the AAS.

An advantage of this approximation is the consistent treatment of the disk-wind interface. This region is strongly influenced by the local wind acceleration. Figure 11 shows the C II λ1335 line profile for two models with different velocity profiles (see Puebla et al., 2011, for details). The figure shows that for lines that are generated close to the disk surface the acceleration of the wind has influence on line structure as well as on line intensity. These models are still in evolution and more work is needed to improve it.

5.1 Discussion

The model developed by Puebla et al. (2011) has the advantage of treating consistently the disk-wind interface, but for that they sacrificed the necessary (at least) 2D treatment of the interaction between wind and disk radiation. However, they got reasonably good line profiles for high inclination models, when compared with data of the same kind of binary systems. A 2.5 dimensional (2 spacial plus rotation) treatment is necessary to improve the line profiles and to better understand the wind structure and the emission line regions in the wind.

Recently, Noebauer et al. (2010), using an improved method of Long & Knigge (2002) (Sim et al. (2005) included the treatment of recombination lines), got good line profiles for RW Tri HST UV data. The advantage of their Monte Carlo method is the possibility of 3D treatment of radiative transfer and radiative equilibrium with a bi-conical wind geometry. They show the strong effect of the inner disk radiation on the outer and higher wind regions structures (temperature and ionization). This has a special effect on lines that are produced far from the disk, as C IV $\lambda\lambda$1548,1551.

Data from FUSE of low inclination systems, commonly show bluehifted absorption profiles, but with low velocities ($\sim$100-500 km s^{-1}). These values contrast with the high velocities observed in the longward region of the spectrum. This could be a signal that a region of low accelerated wind could exist in the wind-disk interface, and that the wind could be

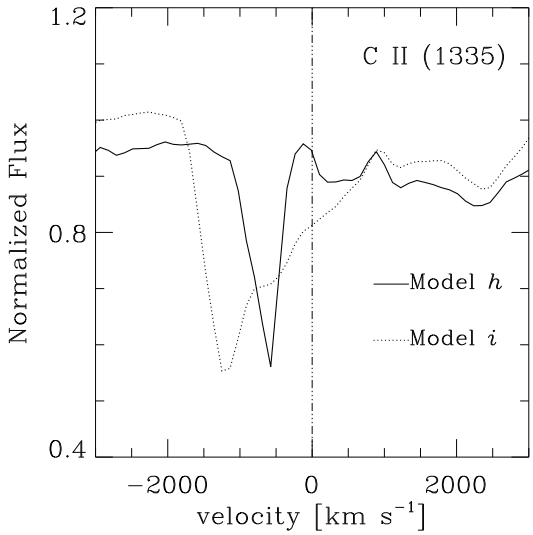

Fig. 11. C II λ1335 line profiles for two models with different acceleration law (for details see Puebla et al. (2011)). They show the effect of the different acceleration laws on the photosphere-wind interface region. Figure taken from Puebla et al. (2011). Reproduced by permission of the AAS.

strongly accelerated in regions farther from the disk. These facts agree with the high density region postulated by Knigge & Drew (1997) and would suggest the importance of an extended disk-wind interface. This possibility should be more explored.

6. Conclusion and future work

Modeling accretion disk emission is still a challenge for understanding the accretion physics. UV spectroscopy of CVs is crucial to understand the physical processes in accretion disks.
Many efforts have been done to develop models that can describe the spectroscopic data (continuum and lines). For the continuum, observational evidences show that the accretion disks don't follow the steady state disk model. This model cannot fit the color and flux at the same time using the known parameters of a system. Observational trends suggests a shallower temperature profile than the predicted by the steady model. Some alternatives to solve this problem have been raised through the years, among them: evaporation of inner disk regions, non-keplerian disks, influence of a WD magnetic field, the influence of a hot WD on the inner disk radius and accretion disk winds.
With respect to the emission line, observational clues suggest that they are formed in a wind that emerges from the disk. The complexity of the problem claims for an at least 2.5 D approximation calculus. Observational evidences point towards a strong influence of a disk-wind interface on spectral features. That interface was recently consistently modelated. These models show that the wind acceleration close to the disk surface strongly influences the line profile. Also, works using Monte Carlo methods have shown the importance of the inner regions on the whole wind structure, and therefore on the line profiles that are formed farther from the disk surface.

Work is being done to improve the models described here, it is necessary to know the actual structure of disk that bears its continuum emission and the nature of the wind and the emission lines. More consistent methods are under development aiming to establish more restrictions to the physical processes in the disk.

7. Acknowledgments

We thank FAPESP (process: 2010/16010-7) for financial support. MPD thanks support form CNPq under grant: 305725.

8. References

Abbott, D. C. (1980). The theory of radiatively driven stellar winds. I - A physical interpretation, *ApJ* 242: 1183–1207.

Abbott, D. C. (1982). The theory of radiatively driven stellar winds. II - The line acceleration, *ApJ* 259: 282–301.

Auer, L. H. & Mihalas, D. (1969). Non-Lte Model Atmospheres. I. Radiative Equilibrium Models with - Alpha, *ApJ* 156: 157–+.

Balbus, S. A. & Hawley, J. F. (1991). A powerful local shear instability in weakly magnetized disks. I - Linear analysis. II - Nonlinear evolution, *ApJ* 376: 214–233.

Cordova, F. A. & Mason, K. O. (1982). High-velocity winds from a dwarf nova during outburst, *ApJ* 260: 716–721.

Cordova, F. A. & Mason, K. O. (1985). High-velocity winds in close binaries with accretion disks. II - The view along the plane of the disk, *ApJ* 290: 671–682.

Diaz, M. P. & Hubeny, I. (1999). The Eclipsing Cataclysmic Variable V347 Puppis Revisited, *ApJ* 523: 786–796.

Diaz, M. P., Wade, R. A. & Hubeny, I. (1996). Ultraviolet Limb Darkening and Spectra for Accretion Disks in Cataclysmic Variables, *ApJ* 459: 236–+.

Engle, S. G. & Sion, E. M. (2005). A Far-Ultraviolet Study of the Old Nova V841 Ophiuchi, *PASP* 117: 1230–1235.

Frank, J., King, A. & Raine, D. J. (2002). *Accretion Power in Astrophysics: Third Edition*.

Hartley, L. E., Drew, J. E., Long, K. S., Knigge, C. & Proga, D. (2002). Testing the line-driven disc wind model: time-resolved ultraviolet spectroscopy of IX Vel and V3885Sgr, *MNRAS* 332: 127–143.

Hillier, D. J. (2003). On the Solution of the Statistical Equilibrium Equations, *in* I. Hubeny, D. Mihalas, & K. Werner (ed.), *Stellar Atmosphere Modeling*, Vol. 288 of *Astronomical Society of the Pacific Conference Series*, pp. 199–+.

Hillier, D. J. & Miller, D. L. (1998). The Treatment of Non-LTE Line Blanketing in Spherically Expanding Outflows, *ApJ* 496: 407–+.

Horne, K. (1985). Images of accretion discs. I - The eclipse mapping method, *MNRAS* 213: 129–141.

Hubeny, I. (1988). A computer program for calculating non-LTE model stellar atmospheres, *Computer Physics Communications* 52: 103–132.

Hubeny, I. (1990). Vertical structure of accretion disks - A simplified analytical model, *ApJ* 351: 632–641.

Hubeny, I. & Lanz, T. (1995). Non-LTE line-blanketed model atmospheres of hot stars. 1: Hybrid complete linearization/accelerated lambda iteration method, *ApJ* 439: 875–904.

Hubeny, I., Lanz, T. & Jeffery, C. (1994). , *St. Andrew Univ. Newsletter on Analysis of Astronomical Spectra* 20: 30.

Knigge, C. (1999). The effective temperature distribution of steady-state, mass-losing accretion discs, *MNRAS* 309: 409–420.

Knigge, C. & Drew, J. E. (1997). Eclipse Mapping of the Accretion Disk Wind in the Cataclysmic Variable UX Ursae Majoris, *ApJ* 486: 445–+.

Knigge, C., Woods, J. A. & Drew, J. E. (1995). The application of Monte Carlo methods to the synthesis of spectral line profiles arising from accretion disc winds, *MNRAS* 273: 225–248.

Kriz, S. & Hubeny, I. (1986). Models and theoretical spectra of accretion discs in dwarf novae, *Bulletin of the Astronomical Institutes of Czechoslovakia* 37: 129–142.

Kurucz, R. L. (1979). Model atmospheres for G, F, A, B, and O stars, *ApJS* 40: 1–340.

La Dous, C. (1989). Synthetic optical and ultraviolet spectra of stationary accretion disks, *A&A* 211: 131–155.

La Dous, C. (1991). New insights from a statistical analysis of IUE spectra of dwarf novae and nova-like stars. I - Inclination effects in lines and continua, *A&A* 252: 100–122.

Lasota, J. (2001). The disc instability model of dwarf novae and low-mass X-ray binary transients, *New A Rev.* 45: 449–508.

Linnell, A. P., Godon, P., Hubeny, I., Sion, E. M. & Szkody, P. (2007). A Synthetic Spectrum and Light-Curve Analysis of the Cataclysmic Variable IX Velorum, *ApJ* 662: 1204–1219.

Linnell, A. P., Godon, P., Hubeny, I., Sion, E. M. & Szkody, P. (2008). Modeling UX Ursae Majoris: An Abundance of Challenges, *ApJ* 688: 568–582.

Linnell, A. P. & Hubeny, I. (1996). A Spectrum Synthesis and Light Synthesis Program for Binary Stars with Optically Thick Accretion Disks, *ApJ* 471: 958–+.

Long, K. S. (2006). Far ultraviolet spectroscopy of (non-magnetic) cataclysmic variables, *Advances in Space Research* 38: 2827–2831.

Long, K. S. & Knigge, C. (2002). Modeling the Spectral Signatures of Accretion Disk Winds: A New Monte Carlo Approach, *ApJ* 579: 725–740.

Long, K. S., Wade, R. A., Blair, W. P., Davidsen, A. F. & Hubeny, I. (1994). Observations of the bright novalike variable IX Velorum with the Hopkins Ultraviolet Telescope, *ApJ* 426: 704–715.

Lynden-Bell, D. (1969). Galactic Nuclei as Collapsed Old Quasars, *Nature* 223: 690–694.

Lynden-Bell, D. & Pringle, J. E. (1974). The evolution of viscous discs and the origin of the nebular variables., *MNRAS* 168: 603–637.

Mason, K. O., Drew, J. E., Cordova, F. A., Horne, K., Hilditch, R., Knigge, C., Lanz, T. & Meylan, T. (1995). Eclipse observations of an accretion disc wind, *MNRAS* 274: 271–286.

Nadalin, I. & Sion, E. M. (2001). The Accretion Disk and White Dwarf in the Short-Period Dwarf Novae TY Piscium and V436 Centauri during Quiescence, *PASP* 113: 829–834.

Noebauer, U. M., Long, K. S., Sim, S. A. & Knigge, C. (2010). The Geometry and Ionization Structure of the Wind in the Eclipsing Nova-like Variables RW Tri and UX UMa, *ApJ* 719: 1932–1945.

Orosz, J. A. & Wade, R. A. (2003). Ultraviolet Spectra of Cataclysmic Variable Accretion Disks with Nonsteady T(r) Laws, *ApJ* 593: 1032–1039.

Osaki, Y., Hirose, M. & Ichikawa, S. (1993). *Tidal Effects on Accretion Disks in Close Binary Systems*, pp. 272–+.

Patterson, J. (1984). The evolution of cataclysmic and low-mass X-ray binaries, *ApJS* 54: 443–493.

Pereyra, N. A. & Kallman, T. R. (2003). Hydrodynamic Models of Line-driven Accretion Disk Winds. III. Local Ionization Equilibrium, *ApJ* 582: 984–1000.

Pereyra, N. A., Kallman, T. R. & Blondin, J. M. (1997). Hydrodynamical Models of Line-driven Accretion Disk Winds, *ApJ* 477: 368–+.

Pereyra, N. A., Kallman, T. R. & Blondin, J. M. (2000). Hydrodynamic Models of Line-driven Accretion Disk Winds. II. Adiabatic Winds from Nonisothermal Disks, *ApJ* 532: 563–580.

Pereyra, N. A., Owocki, S. P., Hillier, D. J. & Turnshek, D. A. (2004). On the Steady Nature of Line-Driven Disk Winds, *ApJ* 608: 454–469.

Pringle, J. E. (1981). Accretion discs in astrophysics, *ARA&A* 19: 137–162.

Prinja, R. K. & Rosen, R. (1995). High-resolution IUE spectroscopy of fast winds from cataclysmic variables, *MNRAS* 273: 461–474.

Proga, D., Stone, J. M. & Drew, J. E. (1998). Radiation-driven winds from luminous accretion discs, *MNRAS* 295: 595–+.

Proga, D., Stone, J. M. & Drew, J. E. (1999). Line-driven disc wind models with an improved line force, *MNRAS* 310: 476–482.

Puebla, R. E. (2005). *Sobre a Taxa de Transfèrencia de Massa em Variáveis Cataclísmicas Quiescentes*, Master's thesis, São Paulo: Universidade 1.

Puebla, R. E., Diaz, M. P., Hillier, D. J. & Hubeny, I. (2011). A Method for the Study of Accretion Disk Emission in Cataclysmic Variables I: The Model, *accepted in ApJ* .

Puebla, R. E., Diaz, M. P. & Hubeny, I. (2007). A Statistical Study of Accretion Disk Model Spectra for Cataclysmic Variables, *AJ* 134: 1923–1933.

Rappaport, S., Joss, P. C. & Webbink, R. F. (1982). The evolution of highly compact binary stellar systems, *ApJ* 254: 616–640.

Rappaport, S., Verbunt, F. & Joss, P. C. (1983). A new technique for calculations of binary stellar evolution, with application to magnetic braking, *ApJ* 275: 713–731.

Ritter, H. & Kolb, U. (2003). Catalogue of cataclysmic binaries, low-mass X-ray binaries and related objects (Seventh edition), *A&A* 404: 301–303.

Rutten, R. G. M., van Paradijs, J. & Tinbergen, J. (1992). Reconstruction of the accretion disk in six cataclysmic variable stars, *A&A* 260: 213–226.

Shakura, N. I. & Sunyaev, R. A. (1973). Black holes in binary systems. Observational appearance., *A&A* 24: 337–355.

Shaviv, G. & Wehrse, R. (1986). The vertical temperature stratification and corona formation of accretion disc atmospheres, *A&A* 159: L5–L7.

Shlosman, I. & Vitello, P. (1993). Winds from accretion disks - Ultraviolet line formation in cataclysmic variables, *ApJ* 409: 372–386.

Sim, S. A., Drew, J. E. & Long, K. S. (2005). Two-dimensional Monte Carlo simulations of HI line formation in massive young stellar object disc winds, *MNRAS* 363: 615–627.

Sobolev, V. V. (1957). The Diffusion of Lα Radiation in Nebulae and Stellar Envelopes., *Soviet Astronomy* 1: 678–+.

Tylenda, R. (1977). The continuous radiation emitted by accretion discs in cataclysmic binaries - The dwarf nova SS CYG during outburst and the old novae V 603 AQL and RR PIC, *Acta Astronomica* 27: 235–249.

Tylenda, R. (1981). Radiation from Optically Thin Accretion Discs, *Acta Astronomica* 31: 127–+.

Wade, R. A. (1984). A double grid of accretion disc model spectra for cataclysmic variable stars, *MNRAS* 208: 381–398.

Wade, R. A. (1988). A test of synthetic accretion disk spectra using ultraviolet flux distributions of novalike variables, *ApJ* 335: 394–405.

Wade, R. A. & Hubeny, I. (1998). Detailed Mid- and Far-Ultraviolet Model Spectra for Accretion Disks in Cataclysmic Binaries, *ApJ* 509: 350–361.

Warner, B. (1987). Absolute magnitudes of cataclysmic variables, *MNRAS* 227: 23–73.

Warner, B. (1995). *Cataclysmic variable stars*, Cambridge Astrophysics Series, Cambridge, New York: Cambridge University Press, |c1995.

Williams, R. E. & Ferguson, D. H. (1982). He I line emission and the helium abundance in cataclysmic variables, *ApJ* 257: 672–685.

3

On a Role of Viscosity in Phenomena of Mass Transfer Caused by Nonlinear Periodic Waves Propagating Over the Liquid Surface

Dmitry Belonozhko and Artem Ochirov
Yaroslavl State University/Physical Department
Russia

1. Introduction

In the 1847 G. Stokes pointed out in his work [G.G. Stokes, 1847] that the propagation of periodic gravitational waves on the horizontal surface of a liquid induces the total drift of liquid particles at a velocity lower than the phase velocity of waves, which became known as the Stokes drift. Stokes considered the problem of calculation of the velocity field in an infinitely deep inviscid incompressible liquid with a gravitational wave propagating over its surface, the wave amplitude being much smaller than the wavelength. The solution of the problem in the second order approximation in the wave amplitude showed that the periodic wave perturbation of the free surface induces not only a periodic motion of liquid particles about a certain mean position in the bulk of the liquid, but also a horizontal motion of the mean position in the direction of wave propagation.
Stokes derived the following expression for the absolute value of the velocity of this drift [G.G. Stokes, 1847, 1880]:

$$w_S = A^2 k\omega_0 \exp(-2kd). \tag{1}$$

Here, A is the wave amplitude, k is the wavenumber, ω_0 is the circular frequency of oscillatory motion, and d is the depth at which the drift velocity is calculated. Formula (1) was derived for the velocity of the drift induced by the gravitational wave is also valid for a capillary-gravitational wave if we use the following expression for circular frequency ω_0 [Le Blon & Mysak, 1978]:

$$\omega_0 = \sqrt{gk(1+\alpha^2 k^2)}\,;\ \alpha = \sqrt{\frac{\gamma}{\rho g}}\,. \tag{2}$$

Here, α is the capillary constant of the liquid, g is the free-fall acceleration, γ is the surface tension , and ρ is the density of the liquid.
The existence of the Stokes drift was confirmed by various observations and experiments [Le Blon & Mysak 1978; Longuet-Higgens 1953, 1986]. The drift phenomenon induced by a small-amplitude periodic traveling wave is second-order effect in wave amplitude. The rough analysis of the problem in the linear (first-order) approximation in the wave amplitude

reveals only a circulating of liquid particles in the vertical plane around a certain stationary position with period $T = 2\pi/\omega_0$. The radius of the circular trajectory of liquid particles relating to the free surface is estimated as the wave amplitude A. But second-order approximation shows that during the period T liquid particle draws trajectory which is not an exact circle but a disconnected loop. The lower part of the trajectory must be shorter than the upper one by a certain quantity much smaller than the amplitude, for particle motion decays with increasing depth. Consequently, after time T, the particle does not return to the initial position but is slightly shifted relative to this position in the direction of propagation of the wave. With each new period, this displacement is systematically accumulated and adds up into average drift with the velocity defined by formula (1). Liquid particles located not on the free surface but at a certain depth perform analogous movements. With increasing depth, the amplitude of periodic movements, as well as the mean drift velocity, decreases.

In various applications dealing with wave motion on the free surface of a liquid, it is important to take into account the drift flow emerging as a result of propagation of surface waves, which can be responsible for the transport of a surfactants or electric charge distributed on the liquid surface. It is important to note that in the general case, the dynamics of distribution of a certain substance over the free surface of a liquid is controlled by viscous shear stresses [Belonozhko & Grigor'ev, 2004; Belonozhko et. al, 2005] which are disregarded in the Stokes drift model.

In 1953 M.S. Longuet-Higgins supposed an improved model of the mass-transport induced by surface progressive waves propagating over the free surface of a low viscous liquid and currently this model is the main tool for making a various estimations concerning the drift phenomena in a viscous liquid [Longuet-Higgins, 1953]. The base of the model is several auxiliary assumptions corresponding to properties of viscous boundary layer located in the vicinity of the free surface. Thereby the supposed reasoning is suitable only for a low-viscosity limit. The practical employment of Longuet-Higgins's approach is essentially complicated, for the model has somewhat artificiality and a cumbersome structure.

Analytic description of the influence of arbitrary viscous forces on the structure of the drift flow caused by the propagation of waves has not been obtained for more than 150 years after the formulation of the problem because of the absence of an appropriated nonlinear solution to the problem of the arbitrary viscosity influence on the propagation of periodic capillary-gravitational wave. The suited solution was obtained in works [Belonozhko & Grigor'ev, 2003, 2004] only at beginning of XXI century and analytical analysis of the problem had become possible.

2. Determination of the mean drift caused by nonlinear periodic waves propagating over the surface of viscous liquid

We will consider analytic calculations of the velocity field in an infinitely deep and unbounded in horizontal direction incompressible viscous liquid with a periodic capillary-gravitational wave propagating over its free horizontal surface. The solution will be constructed in the second order of smallness in wave amplitude. The main attention will be paint to the details of the solution associated with the appearance of the drift terms. The notations used in the procedure of the solution permit to concentrate efforts only to definition of the drift part of the flow without calculating total expression for the velocity field. The suggested approach makes it possible to effectively analyze more complicated

questions concerning to a medium drift induced by the wave motion, for instance an analytic calculation of the mean surface drift of surfactant or redistributing surface electric charge.

2.1 Decomposition of the problem of the velocity field calculating on the problem of the first and second order of smallness in wave amplitude

Let us suppose that an incompressible Newtonian liquid of kinematic viscosity ν, density ρ, and surface tension γ in a Cartesian system of coordinates with the z axis directed vertically upwards fills the half-space $z < 0$ in the gravity field **g**. We disregard the physical properties of the medium above the liquid and consider a periodic capillary-gravitational wave propagating over the free surface of the liquid along the horizontal x axis, assuming that the wave amplitude is much smaller than the wavelength. We also assume for simplicity that the flow of the liquid is independent of horizontal coordinate y. Let us determine the mean velocity of the horizontal drift of the liquid, induced by the propagation of a periodic wave with known amplitude and wavenumber.

We denote by $u = u(t,x,z)$ and $v = v(t,x,z)$ the horizontal and vertical components of the velocity field of the liquid; $\mathbf{e}_x$ and $\mathbf{e}_z$ are the unit vectors along the x and z axis. The deviation of free surface $\xi = \xi(t,x)$ of the liquid from equilibrium state $z = 0$, which is associated with the wave motion, and velocity field $\mathbf{U} = u\mathbf{e}_x + v\mathbf{e}_z$ induced in the liquid satisfy the familiar set of hydrodynamic equations for an incompressible Newtonian liquid and the corresponding boundary conditions [Le Blon & Mysak, 1978; Le Méhauté, 1976]:

$$z < \xi: \quad \frac{\partial \mathbf{U}}{\partial t} + (\mathbf{U}\cdot\nabla)\mathbf{U} = -\frac{1}{\rho}\nabla p + \nu\nabla^2\mathbf{U}; \quad \nabla\cdot\mathbf{U} = 0;$$

$$z = \xi: \quad \frac{\partial \xi}{\partial t} + u\frac{\partial \xi}{\partial x} = v; \quad p - 2\rho\nu\,\mathbf{n}(\mathbf{n}\cdot\nabla)\mathbf{U} = -\gamma\frac{\partial^2\xi}{\partial x^2}\left(1+\left(\frac{\partial \xi}{\partial x}\right)^2\right)^{-3/2}; \tag{3}$$

$$\boldsymbol{\tau}\cdot\left((\mathbf{n}\cdot\nabla)\mathbf{U}\right) + \mathbf{n}\cdot\left((\boldsymbol{\tau}\cdot\nabla)\mathbf{U}\right) = 0;$$

$$z \to -\infty: \quad u \to 0; \quad v \to 0; \quad \nabla \equiv \frac{\partial}{\partial x}\mathbf{e}_x + \frac{\partial}{\partial z}\mathbf{e}_z.$$

Here, $p = p(t,x,z)$ is the pressure in the liquid; $\mathbf{n} = \mathbf{n}(t,x)$ is the unit vector of the outward normal to the free surface constructed from the point of the surface with horizontal coordinate x at instant t; $\boldsymbol{\tau} = \boldsymbol{\tau}(t,x)$ is the unit vector of the tangent to the free surface.

Instead of the initial conditions, which determine in the general case the spectrum of modes of the wave motion generated at the initial instant, we will follow the considerations of the simplest spectral composition of the sought solution. The appropriate approach is traditionally used in similar problems to obtain the least cumbersome solution fittest for analytic description and qualitative analysis [Le Blon & Mysak, 1978; Le Méhauté, 1976; Belonozhko & Grigor'ev 2003, 2004].

Following the standard procedure in the nonlinear theory of periodic waves of small but finite amplitude [Le Blon & Mysak, 1978; Le Méhauté, 1976], we will construct the solution to problem (3) in the form of power expansions of unknown quantities in the small parameter equal to the product of the wave amplitude and wavenumber $\varepsilon = kA$. We will

seek unknown quantities confining our analysis to the second approximation in parameter ε in the form of asymptotic expansions:

$$\begin{aligned} &\mathbf{U} = \mathbf{U}_1 + \mathbf{U}_2 + O\left(\varepsilon^3\right);\ \mathbf{U}_j = O\left(\varepsilon^j\right); \\ &p = p_0 + p_1 + p_2 + O\left(\varepsilon^3\right);\ p_j = O\left(\varepsilon^j\right);\quad j = 1,2\,. \\ &\xi = \xi_1 + \xi_2 + O\left(\varepsilon^3\right);\ \xi_j = O\left(\varepsilon^j\right); \end{aligned} \tag{4}$$

Here, O is the symbol of the order of magnitude. In expressions for the velocity vector, the order of magnitude is estimated for each vector component. In final expressions, we will disclose the definition of parameter $\varepsilon = kA$, $\varepsilon^2 = k^2A^2$ and, using the traditional terminology in the theory of waves with a small but finite amplitude on the surface of an liquid, refer to variables $\mathbf{U}_j$, p_j and ξ_j as j-th order quantities in the wave amplitude, bearing in mind that the small parameter is in fact the ratio of the wave amplitude to the wavelength, which is proportional to dimensionless parameter $\varepsilon = kA$.

Substitution of expansions (4) into relations (3) and transposition of the boundary conditions to unperturbed surface $z = 0$ allow separate the problem (3) into the zeroth-, first, and second-order problems in the wave amplitude. The procedure of the separation of problem (3) in accordance with the order of magnitude is described in detail in [Le Blon & Mysak, 1978; Le Méhauté, 1976].

The analytic formulation of the first-order problem in the wave amplitude has the form

$$z < 0:\quad \frac{\partial \mathbf{U}_1}{\partial t} + \frac{1}{\rho}\nabla p_1 - \nu\nabla^2\mathbf{U}_1 = 0;\ \ \nabla\cdot\mathbf{U}_1 = 0; \tag{5}$$

$$z = 0:\quad \frac{\partial \xi_1}{\partial t} - v_1 = 0;\quad -\rho g\xi_1 - p_1 - 2\rho\nu\frac{\partial v_1}{\partial z} + \gamma\frac{\partial^2\xi_1}{\partial x^2} = 0;\quad \frac{\partial u_1}{\partial z} + \frac{\partial v_1}{\partial x} = 0; \tag{6}$$

$$z \to -\infty:\quad u_1 \to 0;\quad v_1 \to 0\,.$$

The formulation of the second-order problem consists of relation:

$$z < 0:\quad \frac{\partial \mathbf{U}_2}{\partial t} + \frac{1}{\rho}\nabla p_2 - \nu\nabla^2\mathbf{U}_2 = -\left(\mathbf{U}_1\cdot\nabla\right)\mathbf{U}_1;\ \ \nabla\cdot\mathbf{U}_2 = 0; \tag{7}$$

$$\begin{aligned} z = 0:\quad &\frac{\partial \xi_2}{\partial t} - v_2 = \xi_1\frac{\partial v_1}{\partial z} - u_1\frac{\partial \xi_1}{\partial x};\quad -\rho g\xi_2 - p_2 - 2\rho\nu\frac{\partial v_2}{\partial z} + \gamma\frac{\partial^2\xi_2}{\partial x^2} = \xi_1\left(2\rho\nu\frac{\partial^2 v_1}{\partial z^2} - \frac{\partial p_1}{\partial z}\right); \\ &\frac{\partial u_2}{\partial z} + \frac{\partial v_2}{\partial x} = -4\frac{\partial v_1}{\partial z}\frac{\partial \xi_1}{\partial z} - \xi_1\frac{\partial}{\partial z}\left(\frac{\partial v_1}{\partial x} + \frac{\partial u_1}{\partial z}\right); \end{aligned} \tag{8}$$

$$z \to -\infty:\quad u_2 \to 0;\quad v_2 \to 0\,.$$

2.2 Solution of the first-order problem in wave amplitude

The solution to the first-order problem (5), (6) is well known and can be described by expressions of the type of a traveling wave [Belonozhko & Grigor'ev, 2003]:

$$\begin{pmatrix}\xi_1\\ u_1\\ v_1\\ p_1\end{pmatrix}=\frac{A}{2}\begin{pmatrix}1\\ -i\left(S+2\nu k^2\right)\exp(kz)+2\,i\,\nu kq\exp(qz)\\ \left(S+2\nu k^2\right)\exp(kz)-2\,i\,\nu k^2\exp(qz)\\ -\rho S\left(\frac{S}{k}+2\nu k\right)\exp(kz)\end{pmatrix}\exp(St-ikx)+c.c.; \qquad (9)$$

where

$$q=\sqrt{k^2+\frac{S}{\nu}}; \qquad (10)$$

or a superposition of the waves (9) with different wavenumbers k. For a fixed value of k, set of relations (9) is an individual mode of the wave motion. Abbreviation "c.c." means "complex-conjugate terms" and i is the imaginary unit. Parameter S is the complex frequency. It is connected with the wavenumber and other parameters of the problem via the dispersion relation :

$$\left(S+2\nu k^2\right)^2+\omega_0^2=4\nu^2k^3\sqrt{k^2+\frac{S}{\nu}}; \qquad (11)$$

where ω_0 is defined by (2). The physical meaning can be attached not to all values of complex frequency S satisfying the dispersion relation, but only to those for which the condition holds:

$$\left(S+2\nu k^2\right)^2+\omega_0^2>0.$$

In this case only, the vortex part of the velocity field, which is described in set (9) by the terms proportional to $\exp(qz)$, decays with increasing depth.
We will use in further analysis the following notation:

$$r=\mathrm{Re}(S);\quad \omega=\mathrm{Im}(S);\quad b=\mathrm{Re}(q);\quad \chi=\mathrm{Im}(q). \qquad (12)$$

The absolute value of real-valued parameter r characterizes the rate of variation of the amplitude of wave motion. The value of r is smaller than zero and for this reason $|r|$ is the damping decrement of the wave motion. Real-valued quantity ω has the meaning of the circular frequency of wave motion in the viscous liquid.
In accordance with the results of work [Belonozhko & Grigor'ev, 2004] in the limit of a low viscosity dispersion relation (11) reduces to the asymptotic expansions for quantities r and ω as well as for auxiliary parameters b and χ:

$$\frac{r}{\omega_0}=-2N^2+O\left(N^3\right)\approx-2\nu k^2;\quad \frac{\omega}{\omega_0}=1+O\left(N^3\right)\approx1;$$
$$\frac{b}{k}=\frac{1}{N\sqrt{2}}-\frac{1}{2\sqrt{2}}N+O\left(N^3\right)\approx\frac{1}{k}\sqrt{\frac{\omega_0}{2\nu}};\quad \frac{\chi}{k}=\frac{1}{N\sqrt{2}}+\frac{1}{2\sqrt{2}}N-N^2+O\left(N^3\right)\approx\frac{1}{k}\sqrt{\frac{\omega_0}{2\nu}}; \qquad (13)$$
$$N=k\sqrt{\frac{\nu}{\omega_0}}<<1.$$

In the right-hand sides of the relations (13) after the symbol "$\approx$" the expressions are written witch retain only the principal terms of the expansions in the viscosity.
Expressions (9) were deliberately written in complete form, although these expressions do not contain the drift terms explicitly, for the following two reasons. First, to solve the second-order problem in the wave amplitude, we must calculate the right-hand sides of first relation (7) and relations (8) containing quantities u_1 v_1, ξ_1 and p_1. Second, it will be shown below that the expressions for quantities u_1 v_1 play an important role in calculating the velocity of the mean drift flow.

2.3 Structure of expressions for the velocity field in the second order in wave amplitude

In contrast to first-order problem (5), (6), the solution to second-order problem (7), (8) contains the component describing the explicit drift of the liquid along the x axis. To simplify our analysis, we will confine ourselves to determining the form of this particular part of the solution. It will be shown below that the rest part of the solution is not used in constructing the expression for the velocity of total drift.
We assume that the solution to the starting problem (3) in the first approximation in the wave amplitude is described by only one mode of the wave motion, viz., a set of relations of type (9) with a specified wavenumber k. Using set (9), we can write the right-hand side of the first equation in system (7) in a more detailed form:

$$z<0: \quad \frac{\partial \mathbf{U}_2}{\partial t}+\frac{1}{\rho}\nabla p_2 - \nu\nabla^2\mathbf{U}_2 = V_x\mathbf{e}_x + V_z\mathbf{e}_z;$$

$$V_x = A^2\left(-2k^3\omega\nu\exp(2bz)+\left\{-\frac{ikS}{2}\left(S^*+2\nu k^2\right)\exp\left((k+q)z\right)+c.c.\right\}+\right.$$
$$\left.+\left\{\frac{ikS^*}{2}\left(S+2\nu k^2\right)\exp\left(\left(k+q^*\right)z\right)+c.c.\right\}\right)\exp(2rt)+A^2\Pi(2\theta)\exp(2rt);$$

$$V_z = A^2\left(-\left|S+2\nu k^2\right|^2 k\exp(2kz)-4\nu^2k^4 b\exp(2bz)+\right.$$
$$+\left\{\nu k^2(k+q)\left(S^*+2\nu k^2\right)\exp\left((k+q)z\right)+c.c.\right\}+$$
$$\left.+\left\{\nu k^2\left(k+q^*\right)\left(S+2\nu k^2\right)\exp\left(\left(k+q^*\right)z\right)+c.c.\right\}\right)\exp(2rt)+A^2\Pi(2\theta)\exp(2rt);$$

$$\theta = \omega t - kx. \tag{14}$$

The asterisk in the superscript indicates complex conjugation. Here and below, symbol $\Pi(\Theta)$ is used as the general notation for various sums consisting of terms proportional to $\cos(\Theta)$ and $\sin(\Theta)$ with constant coefficients of proportionality or with coefficients depending only on coordinate z. For the column of quantities each of which is the sum of this type will be denoted by bold symbol $\mathbf{\Pi}(\Theta)$.
The expressions obtained for V_x and V_z describe the right-hand side of the first equation in system (7) explicitly. This allows us to use the method of undetermined coefficients and find partial solution (7) u_2^a, v_2^a, p_2^a:

$$\begin{pmatrix} u_2^a \\ v_2^a \\ p_2^a \end{pmatrix} = A^2 \left(\begin{pmatrix} 0 \\ 0 \\ \dfrac{-\rho\left|S+2\nu k^2\right|}{2} \end{pmatrix} \exp(2kz) + \left(\begin{pmatrix} -\dfrac{2\nu k b\chi}{r-2\nu b^2} \\ 0 \\ -2\rho\nu^2 k^4 \end{pmatrix} \exp(2bz) + \right.\right.$$
$$\left.\left. + \left\{ \begin{pmatrix} \dfrac{ikS\left(S^*+2\nu k^2\right)}{2\left(2r-\nu(k+q)^2\right)} \\ 0 \\ \rho\nu k^2\left(S^*+2\nu k^2\right) \end{pmatrix} \exp\left((k+q)z\right) + c.c. \right\} \right) \exp(2rt) + A^2\Pi(2\theta)\exp(2rt). \tag{15}$$

The values u_2^a, v_2^a, p_2^a are auxiliary. They satisfy (7) and can therefore be used to construct the substitution:

$$\begin{pmatrix} u_2 \\ v_2 \\ p_2 \end{pmatrix} = \begin{pmatrix} u_2^a \\ v_2^a \\ p_2^a \end{pmatrix} + \begin{pmatrix} u_2^b \\ v_2^b \\ p_2^b \end{pmatrix}.$$

which reduces (7), (8) to the problem with homogeneous equations and nonhomogeneous boundary conditions

$z < 0$:

$$\begin{aligned} &\frac{\partial u_2^b}{\partial t} + \frac{1}{\rho}\frac{\partial p_2^b}{\partial x} - \nu\left(\frac{\partial^2 u_2^b}{\partial x^2} + \frac{\partial^2 v_2^b}{\partial z^2}\right) = 0; \\ &\frac{\partial v_2^b}{\partial t} + \frac{1}{\rho}\frac{\partial p_2^b}{\partial z} - \nu\left(\frac{\partial^2 v_2^b}{\partial x^2} + \frac{\partial^2 v_2^b}{\partial z^2}\right) = 0; \\ &\left(\frac{\partial u_2^b}{\partial x} + \frac{\partial v_2^b}{\partial z}\right) = 0; \end{aligned} \tag{16}$$

$z = 0$:

$$\frac{\partial \xi_2}{\partial t} - v_2^b = \xi_1\frac{\partial v_1}{\partial z} - u_1\frac{\partial \xi_1}{\partial x} + v_2^a; \tag{17}$$

$$p_2^b - 2\rho\nu\frac{\partial v_2^b}{\partial z} + \gamma\frac{\partial^2 \xi_2}{\partial x^2} = \xi_1\left(2\rho\nu\frac{\partial^2 v_1}{\partial z^2} - \frac{\partial p_1}{\partial z}\right) - p_2^a + 2\rho\nu\frac{\partial v_2^a}{\partial z}; \tag{18}$$

$$\frac{\partial u_2^b}{\partial z} + \frac{\partial v_2^b}{\partial x} = -4\frac{\partial v_1}{\partial z}\frac{\partial \xi_1}{\partial z} - \xi_1\frac{\partial}{\partial z}\left(\frac{\partial v_1}{\partial x} + \frac{\partial u_1}{\partial z}\right) - \frac{\partial u_2^a}{\partial z} - \frac{\partial v_2^a}{\partial x}; \tag{19}$$

$z \to -\infty$:

$$u_2^b \to 0; \quad v_2^b \to 0. \tag{20}$$

Taking into account the explicit expressions (9) for quantities ξ_1, u_1 v_1, p_1 and (15) for u_2^a, v_2^a, p_2^a, we can easily establish even without detailed calculations that the structure of the right-hand side of each boundary condition from (17)-(19) defined at the level of $z = 0$ can be described by the formula $A^2\left(F(t)+\Pi(2\theta)\exp(2rt)\right)$, where $F(t)$ is a certain function of time for each condition from (17)—(19). This means that the unknown quantities (in particular, $u_2^b = u_2^b(t,x,z)$ and $p_2^b = p_2^b(t,x,z)$ should be sought in the form of a term independent of coordinate x and a term proportional to $A^2\Pi(2\theta)\exp(2rt)$:

$$u_2^b = A^2\left(w(t,z)+\Pi(2\theta)\exp(2rt)\right);\quad p_2^b = A^2\left(h(t,z)+\Pi(2\theta)\exp(2rt)\right). \tag{21}$$

Here, $w(t,z)$ and $h(t,z)$ are the functions to be determined.
Using relations (9), (15) we can easily calculate the right-hand side of boundary condition (19):

$z = 0$:

$$\frac{\partial u_2^b}{\partial z}+\frac{\partial v_2^b}{\partial x} = A^2\Lambda\exp(2rt)+A^2\Pi(2\theta)\exp(2rt); \tag{22}$$

$$\begin{aligned}\Lambda = &-\frac{1}{2}ik\left(2i\omega k+6i\nu k^2\chi+\nu\left(q^3-\left(q^*\right)^3\right)\right)+\\ &+\frac{1}{2}\nu k\left(\frac{4k^2\omega b}{r+b^2}+\left\{\frac{i(q-k)(q+k)^2\left(S^*+\nu k^2\right)}{2r+(q+k)^2}+c.c.\right\}\right).\end{aligned} \tag{23}$$

Substituting relations (21) into the first equation of system (16) and conditions (20), (22) and noting that $\left(\partial p_2^b/\partial x\right)\sim\Pi(2\theta)$, we can easily separate the component independent of parameter θ in these expressions and obtain the individual problem for determining function $w = w(t,z)$:

$$\begin{aligned} &z<0: && \frac{\partial w}{\partial t}-\nu\frac{\partial^2 w}{\partial z^2}=0;\\ &z=0: && \frac{\partial w}{\partial x}=\Lambda\exp(2rt);\\ &z\to-\infty: && w\to 0.\end{aligned} \tag{24}$$

In accordance with relations (21), value $A^2w = A^2w(t,z)$ at fixed z is velocity of the horizontal drift for all liquid particles that reside on the level $z = \mathrm{const}\,t$.
The solution to problem (24) has the form [Polyanin, 2002]:

$$\begin{aligned}w = w(t,z) = &\Lambda\sqrt{\frac{\nu}{\pi}}\int_0^t\exp\left(-\frac{z^2}{4\nu(t-\eta)}\right)\frac{\exp(2r\eta)}{\sqrt{t-\eta}}d\eta+\\ &+\Lambda\sqrt{\frac{1}{\pi\nu t}}\int_0^\infty\left\{\exp\left(-\frac{(z-\zeta)^2}{4\nu t}\right)+\exp\left(-\frac{(z+\zeta)^2}{4\nu t}\right)\right\}\Psi(\zeta)d\zeta;\end{aligned} \tag{25}$$

$$\psi(z)\equiv w(0,z). \tag{26}$$

For the vertical component of the velocity field, we have, analogously to relations (21), $v_2^b = A^2\left(\beta(t,z) + \Pi(2\theta)\exp(2rt)\right)$ where $\beta(t,z)$ is the function to be determined. Substituting the expression for v_2^b and the second relation from (21) into last equation (16), we can easily see that $(\partial\beta/\partial z) = 0$ and hence $\beta(t,z) = F(t)$ is a function of time. We must set $F(t) \equiv 0$, for the liquid is not moves with time along the z axis as a "whole". Thereby $v_2^b = A^2\Pi(2\theta)\exp(2rt)$.
The above calculations show that when a periodic capillary-gravitational wave with wavenumber k propagates over the horizontal surface of an infinitely deep liquid, a velocity field emerging in the liquid has following structure of the components in the second approximation in wave amplitude:

$$u = u_1 + A^2 w(t,z) + U_2^a + A^2\Pi(2\theta)\exp(2rt); \tag{27}$$

$$v = v_1 + A^2\Pi(2\theta)\exp(2rt); \tag{28}$$

$$u_1 = \frac{A}{2}\left(-i\left(S + 2\nu k^2\right)\exp(kz) + 2\,i\,\nu kq\exp(qz)\right)\exp(St - ikx) + c.c.; \tag{29}$$

$$v_1 = \frac{A}{2}\left(\left(S + 2\nu k^2\right)\exp(kz) - 2\,i\,\nu k^2\exp(qz)\right)\exp(St - ikx) + c.c.; \tag{30}$$

$$U_2^a = A^2\left(-\frac{2\nu k b\chi}{r - 2\nu b^2}\exp(2bz) + \left\{\frac{ikS\left(S^* + 2\nu k^2\right)}{2\left(2r - \nu(k+q)^2\right)}\exp\left((k+q)z\right) + c.c.\right\}\right)\exp(2rt). \tag{31}$$

Here U_2^a is the part of the expression for u_2^a without the terms proportional to $\Pi(2\theta)$.
The function $w(t,z)$ is given by (25), (26) with parameter Λ defined by (23). In limit of low viscosity $r = \mathrm{Re}(S)$, $\omega = \mathrm{Im}(S)$, $b = \mathrm{Re}(q)$, $\chi = \mathrm{Im}(q)$ are described by asymptotic relations (13) and in this regard asymptotic expressions for Λ and U_2^a containing only the principle on the viscosity terms take on the form:

$$\Lambda \approx 2k^2\omega_0^2; \tag{32}$$

$$U_2^a \approx A^2\,k\omega_0\cos\left(\frac{z}{\delta}\right)\exp\left(\left(k + \delta^{-1}\right)z\right)\exp\left(-4\nu k^2 t\right); \tag{33}$$

$$\delta = \sqrt{\frac{2\nu}{\omega_0}}. \tag{34}$$

The value of parameter δ is rough estimation for the thickness of viscous boundary layer in vicinity of free surface. At the depth δ the amplitude of the vortex motion decreases in e time compare to value of the amplitude at the surface [Longuet-Higgins, 1953]. There is improving estimation 4δ for the boundary layer thickness [Belonozhko & Grigor'ev, 2008]. On this depth the amplitude of the vortex motion decreases to only several percent from value of the amplitude at the surface. The liquid flow is essentially rotational inside the boundary layer and can be considered as nearly irrotational outside the layer.

2.4 Construction of expression for the velocity of the mean horizontal drift taking viscosity into account

Expressions (27), (28) describe the velocity field of a liquid flow in the Euler representation [Longuet-Higgens, 1986)]. To calculate the velocity of an individual particle, we must pass from the description of the velocity field in the Euler variables

$$\mathbf{U} \equiv \mathbf{U}(t,\mathbf{r}) = U(t,x,z) = u(t,x,z)e_x + v(t,x,z)\mathbf{e}_z ;$$

to the description in the Lagrange form:

$$\mathbf{U}_L \equiv \mathbf{U}_L(t,\mathbf{r}) = U_L(t,x,z) = u_L(t,x,z)e_x + v_L(t,x,z)\mathbf{e}_z .$$

In both cases, the argument of the quantities considered here is the radius vector **r** of a point with coordinates x and z. In the Euler representation, **r** defines the position of a stationary point in space, through which various liquid particles pass in time t with velocity $\mathbf{U}(t,\mathbf{r})$. In the Lagrange representation, **r** fixes the position of an individual liquid particle at instant $t = 0$, while vector $\mathbf{U}_L(t,\mathbf{r})$ characterizes the time variation of the velocity of namely this liquid particle.

It was shown in [Le Blon & Mysak L, 1978; Lokenath, 1994] that in the problem of propagation of a periodic small-amplitude capillary-gravitational wave over the horizontal surface of a liquid in the second approximation in amplitude of the wave motion, the velocity vector in the Lagrange representation can be expressed via components of velocity vector in the Euler representation:

$$\mathbf{U}_L(t,\mathbf{r}) = \mathbf{U}(t,\mathbf{r}) + \left(\left(\int_0^t \mathbf{U}(\eta,\mathbf{r})d\eta\right)\nabla\right)\mathbf{U}(t,\mathbf{r}).$$

For the horizontal velocity component, we have

$$u_L(t,x,z) = u(t,x,z) + \left\{\left(\int_0^t u(\eta,x,z)d\eta\right)\frac{\partial u(t,x,z)}{\partial x}\right\} + \left\{\left(\int_0^t v(\eta,x,z)d\eta\right)\frac{\partial u(t,x,z)}{\partial z}\right\} \qquad (35)$$

Substituting relations (27), (28) into (35) and retaining the terms of the order not higher than second in wave amplitude we can easily derive the expression for the horizontal velocity of the individual liquid particle, which was at the point with coordinates x and z at $t = 0$:

$$\begin{aligned} u = {} & u_1 + A^2 w(t,z) + \\ & + U_2^a + \left\{\left(\int_0^t u_1(\eta,x,z)d\eta\right)\frac{\partial u_1(t,x,z)}{\partial x}\right\} + \left\{\left(\int_0^t v_1(\eta,x,z)d\eta\right)\frac{\partial u_1(t,x,z)}{\partial z}\right\} + \\ & + A^2\Pi(2\theta)\exp(2rt). \end{aligned} \qquad (36)$$

To derive the formula (36) we have taken into account that in the second approximation in wave amplitude the asymptotic relations hold:

$$\left(\int_0^t u(\eta,x,z)d\eta\right)\frac{\partial u(t,x,z)}{\partial x} \approx \left(\int_0^t u_1(\eta,x,z)d\eta\right)\frac{\partial u_1(t,x,z)}{\partial x} ;$$

$$\left(\int_0^t v(\eta,x,z)d\eta\right)\frac{\partial u(t,x,z)}{\partial z}\approx\left(\int_0^t v_1(\eta,x,z)d\eta\right)\frac{\partial u_1(t,x,z)}{\partial z}.$$

Expressions for u_1, w and U_2^a are known. The explicit form for part of expression (36) enclosed in braces is derived by substitution (29) (30) in the braces. But total form of the expression is not needed. A significant part of the terms on the right-hand side of expression (36) is sums consisting of terms proportional to $\cos(\theta)$ and $\sin(\theta)$ or $\cos(2\theta)$ and $\sin(2\theta)$ ($\theta = \omega t - kx$). Obviously they are responsible for an apptoximatly circular motion of liquid particle relative to a certain average position. Let call them the cyclic components of the velocity. According to (29) and definition of symbol Π the terms u_1, $A^2\Pi(2\theta)\exp(2rt)$ are cyclic components of the velocity. All cyclic terms in (36) must be drooped in order to write the expression for mean horizontal velocity of liquid particle. Specifically for the part (36) in braces it is sufficient to obtain an explicit expression only for noncyclic terms without making complete calculations. As result relation (36) is transformed to expression for velocity of mean drift caused by periodical capillary-gravitational wave propagating over the surface of a viscous liquid:

$$u_d = A^2 w(t,z) + u_S(t,z); \tag{37}$$

$$u_S(t,z) = U_B(t,z) + U_2^a(t,z). \tag{38}$$

Here U_B denotes the noncyclic part of relation enclosed in braces in the expression (36). Taking into account the explicit relations for u_1 and v_1 (see (9)) the expression for U_B may be written in the form:

$$\begin{aligned} U_B(t,z) = \frac{A^2}{|S|}\Big(& M\exp(2kz) + N\exp(2bz) + \\ & + \nu k\big(G\cos(\chi z) + H\sin(\chi z)\big)\exp\big((k+b)z\big)\Big)\exp(2rt); \end{aligned} \tag{39}$$

$$M = \omega k\left(\omega^2 + \left(r + 2\nu k^2\right)\right)^2;\quad N = 4\nu^2 k^3 b\left(b\omega + \chi r\right);$$

$$G = -2\Big(\omega(k+b)(\chi\omega + kr) + b\chi r^2 + \nu k^2\left(\omega\left((k+b)^2 - \chi^2\right) + 2b\chi r\right)\Big);$$

$$\begin{aligned} H = {} & 2k\omega\left(\chi r - b\omega\right) + \left(\chi^2 - b^2\right)|S|^2 + 2\nu k^3\left(2\chi\omega + kr\right) + \\ & + k^2\left(r\left(r + 2\nu\left(\chi^2 - b^2\right)\right) - \omega\left(\omega - 4\nu\chi b\right)\right). \end{aligned}$$

With help of asymptotic expression (13) we can proceed to the limit of low viscosity and write asymptotic expressions for U_B containing only the principle on the viscosity terms:

$$U_B \approx A^2 k\omega_0 \exp(2kz)\exp\left(-4\nu k^2 t\right)\left(1 - \exp\left(\frac{z}{\delta} - kz\right)\cos\left(\frac{z}{\delta}\right)\right). \tag{40}$$

The expression (40) follows from (39) on the basis of (13). The parameter δ is defined in (34).

In what follows one term $A^2 w(t,z)$ in the sum (37) will be called velocity of "Additional drift" and another term $u_S(t,z)$ will be referred to velocity of "Modified Stokes drift". Reasons for using the above terminology and individual notation $u_S(t,x)$ for sum of $U_B(t,x)$ and $U_2^a(t,x)$ will be clarified below.

2.5 Modified Stokes drift

The drift component (38) with $U_B(t,x)$ defined by (39) ((40) in limit of low viscosity) and $U_2^a(t,x)$ defined by (31) ((33) in limit of low viscosity) is called Modified Stokes drift due to closeness of its properties with features of the classical Stokes drift defined by (1). The best agreement of the properties is archived when one takes into account both terms $U_B(t,x)$ and $U_2^a(t,x)$ together.

The fig.1 show the behavior only term $U_B(t,x)$ calculated at different times (line 1-3) compare to the classical Stokes drift (line 4). For instance we assumed that the drift is caused by the propagation of a periodic wave with a length 5 sm over the surface of water ($\rho = 1\ kg/m^3$; $\gamma = 72 \cdot 10^{-3}\ N/m$; $\nu = 10^{-6}\ m^2/s$). It was thought that at initial time moment the wave amplitude is equal to 1 mm.

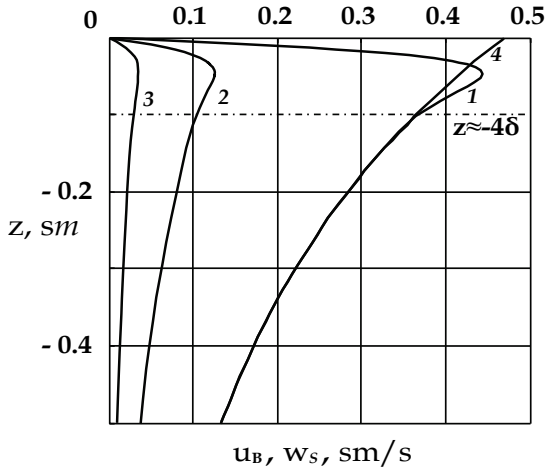

Fig. 1. The behavior of the drift velocity component $U_B(t,x)$ from (38) at different depth is plotted. Calculations are performed for the drift caused by periodic wave with wavelength 5 sm and amplitude 1 mm propagating over horizontal water surface. The curves 1,2,3 specify profile of $U_B(t,z)$ at moment times: t = 0 s; t = 20 s; t = 40 s. The curve 1 show behavior of the classical Stokes Drift (1). The horizontal dotted line held at the lower border of the surface boundary layer z = -4δ

In the course of time a monotonic profile of the classical Stokes drift is not changed since an approximation of inviscid liquid is working. Fig 1 show that the velocity of the component $U_B(t,x)$ at all depths decreases with a time proportionally to factor $\exp(2rt)$ where $r < 0$ (at low viscosity $r \approx -4\nu k^2$). The damping of the liquid motion in time is natural since the influence of viscous dissipation was taken into account. A characteristic shape of the profile $U_B(t,x)$ remains same for all time but horizontal extent of the profile shrinks with the course of time.

The characteristic shape of the profile $U_B(t,x)$ qualitative distinguishes from profile of the classical Stokes drift. In contrast to classical model the profile of velocity $U_B(t,x)$ is not monotonic near the liquid surface but one has a maximum on some level inside viscous boundary layer. Above the level corresponding to the maximum of velocity the values $U_B(t,x)$ dramatically decrease with decreasing a depth and tend to zero at the liquid surface. But it should be noted that pure classical drift (1) (see curve 4 at fig.1) rigorously monotonic on all depth and one reaches its maximum exactly at the liquid surface.

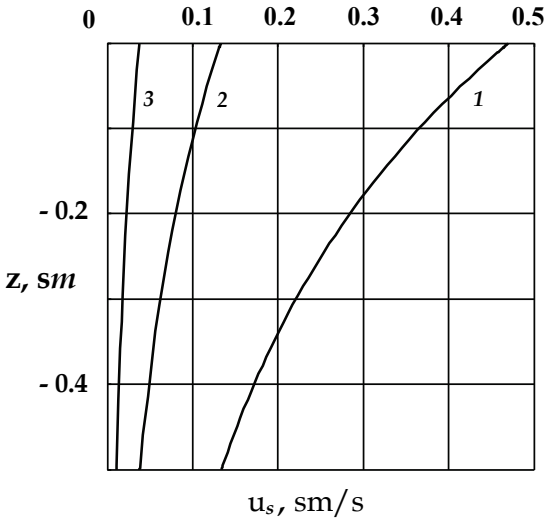

Fig. 2. The behavior of the Modified Stokes Drift $u_S(t,z)$ (see (38)) at different depth is plotted. The physical conditions are same that was used for plotting fig.1. The curves $1,2,3$ specify profile of $u_S(t,z)$ at moment times: $t = 0\,s$; $t = 20\,s$; $t = 40\,s$

Analysis of expression (40) presenting the limit values of $U_B(t,x)$ at a low viscosity show that the discovered difference between $U_B(t,x)$ and classical Stokes drift dos not vanish even for an arbitrary small viscosity. The decreases of viscosity leads only to a narrowing of the field near the liquid surface within which the deference between velocities (1) and (40) is essential. Directly on the surface the value of the difference at limit of zero viscosity tends to $A^2k\omega$ and not equal to zero. The observed discrepancy between behavior of $U_B(t,x)$ and drift (1) in vicinity of liquid surface suggests that the component $U_B(t,x)$ alone can not be regarded as naturally generalization of the classical Stokes drift.

We have combined the components $U_B(t,x)$ and $U_2^a(t,z)$ of drift velocity in sum (38) in order to produce expression for special part of drift velocity in viscous liquid $u_S(t,x)$ that is named by velocity of the Modified Stokes drift. Values $U_2^a(t,z)$ are essential only in vicinity of the surface and negligible in region below the viscous boundary layer. The component $U_2^a(t,z)$ is added to $U_B(t,x)$ in order to correct the properties of component $U_B(t,x)$ inside the viscous boundary layer. Profile of the sum in vicinity of liquid surface has no any drastic changes inherent in to the separate term $U_B(t,x)$. At least at low viscosity the shape of profile of the Modified Stokes drift $u_S(t,x)$ (sum $U_B(t,x)$ and $U_2^a(t,z)$) is rather close to profile of the Classical Stokes drift.

The fig. 2 is similar to fig.1 but the profiles of velocity $u_S(t,z) = U_B(t,x) + U_2^a(t,z)$ are depicted instead of the profiles related to the component $U_B(t,x)$. One can see that Modified Stokes drift at all depths behaves almost like the classical Stokes drift and it is only horizontal extent of the profile $u_S(t,x)$ that shrinks with time due to viscous dissipation.

2.6 Additional drift flow

Let consider the component $A^2w(t,z)$ of total mean drift (37) that was called the Additional drift flow. To find the reasons for the emergence of the Additional drift flow, let us consider an example of calculation of together evolution of horizontal velocity of the Modified Stokes drift $u_S(t,z)$ and the Additional drift velocity $A^2w(t,z)$ at a level of $z = 0$. To definiteness let suppose that initially velocity of the Additional drift equal to zero $A^2w(0,z) = 0$.
The time variation of velocities $u_S(t,z)$ and $A^2w(t,z)$ of the drift flows induced by a periodic capillary-gravitational wave having a wavelength of 5 cm and an amplitude of 1 mm and propagating on the surface of water are plotted in the fig 3.

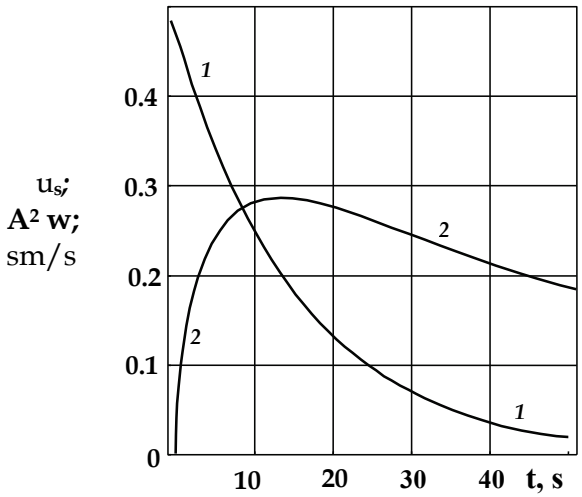

Fig. 3. The dependences of two velocity components of mean horizomtal drift on the water surface in the directions of propagation of the periodic capillary-gravitational wave. The values of all physical parameter same as used for plotting fig. 1 and fig. 2. Curve 1 - velocity $u_S(t,0)$ of the Modified Stokes drift (formula (37)); curve 2 – velocity $A^2w(t,0)$ of the Additional drift (formula (25) under condition $A^2w(0,z) = 0$)

It can be seen that at the initial stage of the flow, the Modified Stokes drift (curve 1) is the main part of the total horizontal drift. The drift flow almost follows the laws for an inviscid liquid, and it is only the magnitude of the drift velocity that weakly decreases with time due to viscous dissipation.
At the same time, owing to components of viscous forces associated with the drift component of the flow, other types of changes occur in the velocity field. Viscous stresses emerging in the liquid have components periodic in the horizontal coordinate as well as aperiodic components. The aperiodic horizontal component of viscous stresses appears due to the drift component of the flow. Since horizontal drift velocity $u_S(t,z)$ varies with the

depth (see fig. 2) and the inequality $(\partial u_S(t,z)/\partial z) < 0$ holds, horizontal viscous shear stresses $-\rho\nu(\partial u_S(t,z)/\partial z)$ appear between adjacent horizontal layers in accordance with the properties of a Newtonian liquid [Faber, 1997]. Under the action of these shear stresses, the liquid is involved into an additional horizontal drift flow with a velocity described by function $A^2w(t,z)$ (curve 2).

For chosen initial condition $A^2w(0,z) = 0$, the Additional drift velocity increases monotonically with time from zero at $t = 0$ to the velocity of the Modified Stokes drift. For values of physical parameters used for construction of the fig. 3, the velocities of both drifts become equal approximately 8.5 s after the beginning of the flow. The Modified Stokes drift entrains the liquid due to horizontal viscous stresses distributed from the surface to the deep layers. After leveling out the drift velocities, the velocity of the Modified Stokes drift continues to decrease exponentially and becomes smaller than the velocity of Additional drift. At now the Modified Stokes drift decelerates the Additional drift due to the same viscous stresses, which are acting now in the opposite direction. The deceleration of the Additional drift takes a certain time (about 3 s in the figure), after which its velocity attains the maximal value and then decreases together with the decreasing velocity of the Modified Stokes drift.

At fig. 4 the depths profiles of drift component $u_S(t,z)$ and $A^2w(t,z)$ are plotted at instant $t = 8.5$ s when velocities of the both component are equal (the physical conditions are same that used for plotting fig. 1-3). One can see the velocity of the Additional drift $A^2w(t,z)$ decreases with depth faster than velocity of the Modified Stokes drift. This means that Additional drift decreases with depth faster than on exponential law.

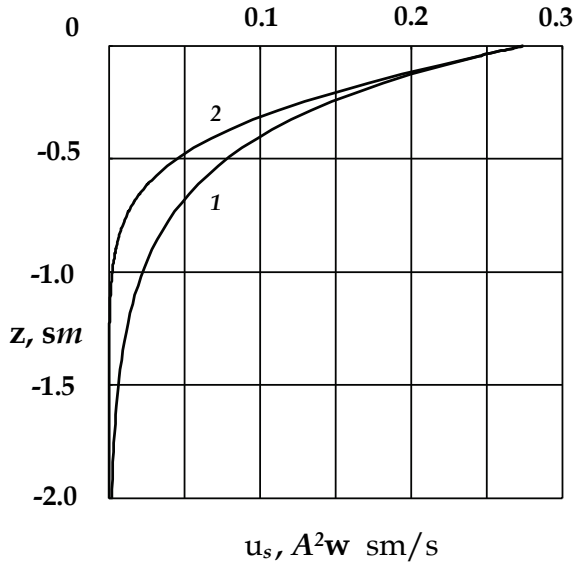

Fig. 4. The profiles of drift component $u_S(t,z)$ and $A^2w(t,z)$ are plotted at $t = 8.5$ s after launching of the Additional drift ($A^2w(0,z) = 0$). The values of all physical parameter are same as used for plotting fig.1-3. Curve 1 – the profile of the Modified Stokes drift (formula (37)); curve 2 – profile of the Additional drift (formula (25) under condition $A^2w(0,z) = 0$)

2.7 Example: qualitative investigation of influence of surface electric charge on the drift flow caused by periodic capillary-gravitational waves

Let consider the problem similar to what was discussed in paragraph 2.1-2.4, but with an electric charge distributed over the liquid surface. We suppose that liquid is an ideal conductor and the upper half-space is filled with a dielectric medium having a permittivity approximately equal to unit (like water and air). Let upper medium has a negligible density and not affects on the motion in the lower liquid. We assume that in the equilibrium state the electric charge uniformly distributes at the plane surface with surface density σ_0.

Now in order to calculate the liquid motion caused by capillary-gravitational wave we must take into account an effect of electric forces on the free surface. In electro-hydrodynamic approximation [Melcher, 1963] the formulation of the problem (3) should be supplemented by the equation for the electric potential φ in the field above liquid and appropriate conditions at the surface and at the infinity:

$$z > \xi: \ \Delta\varphi = 0; \ z = \xi: \ \varphi = \text{const}; \ z \to \infty: \ -\nabla\varphi = 4\pi\sigma_0^2 \mathbf{e}_z . \tag{41}$$

In addition the effect of the electric ponderomotive force $4\pi\sigma_0^2$ should be included in the condition for pressure:

$$z = \xi: \qquad p - 2\rho\nu\mathbf{n}(\mathbf{n}\cdot\nabla)\mathbf{U} + 4\pi\sigma_0^2 = -\gamma\frac{\partial^2\xi}{\partial x^2}\left(1+\left(\frac{\partial\xi}{\partial x}\right)^2\right)^{-3/2} . \tag{42}$$

We offer to draw attention on a one way of qualitative investigation of properties of the drift in depending on value of some parameter (in our case parameter is surface charge). In the introduction it was indicate on the physical mechanism responsible for the creation of the mean drift. A liquid particle makes approximately circular motion but returns not to initial position but is shifted a little in the direction of wave propagation. The shift is occurred due to that the lower part of the trajectory is shorter than upper since the motion decays with depth. In the viscous liquid these mechanism is responsible for initiating main drift or Modified Stokes drift (see 2.4). The Modified Stokes drift initiates Additional drift (see 2.6). Thereby the presence of cyclical movements of liquid particles is an important factor contributing to the formation of the mean drift. Of course in order to obtain the expressions for drift components we have omitted the cyclic component of velocity of a liquid particle. But it is important remember that the noncyclic particle's velocity components that have been saved previously had been expressed via cyclic components of the velocity field in the liquid. The key role of the cyclic motion manifests itself in fact that in the low viscosity approximation all drift components are proportional to the circular frequency of cyclic motion (see (32), (33), (40)). More detailed calculations showed that the marked regularity holds for arbitrary viscosity too. In general, a drift of a liquid can be created through a variety of circumstance but we emphasize that our conclusion relate to the mean drift generated by propagation of the capillary-gravitational wave along the surface of a liquid.

From the above we can conclude that qualitative investigation of the effect of a physical parameter on the drift is reduced to the question about influence of the parameter at the frequency of the cyclic motion. In other words it is necessary to study the behavior of the roots of a dispersion equation depending on value of the parameter.

The problem (3), (41), (42) easy reduce to the problem of the first order of smallness in wave amplitude and then dispersion equation is found by standard method. For considered

problem the dispersion equation has already obtained (see for example [Belonozhko & Grigor'ev (2004)]) and has same view as equation (11), only the parameter ω_0 is defined by the new formula:

$$\omega_0 = \sqrt{gk\left(1+\alpha^2k^2-\alpha kW\right)};\ W=\frac{4\pi\sigma_0^2}{\sqrt{\rho g\gamma}}. \tag{43}$$

Here α as before is the capillary constant of a liquid. The dimensionless parameter W can be regarded as the square of the dimensionless electric charge density in equilibrium state when a wave motion at the free surface is absent. On the other hand parameter W is proportional to ratio of electric and capillary forces at the crest of the wave with wave number $k=\alpha^{-1}$ propagating at the free surface.

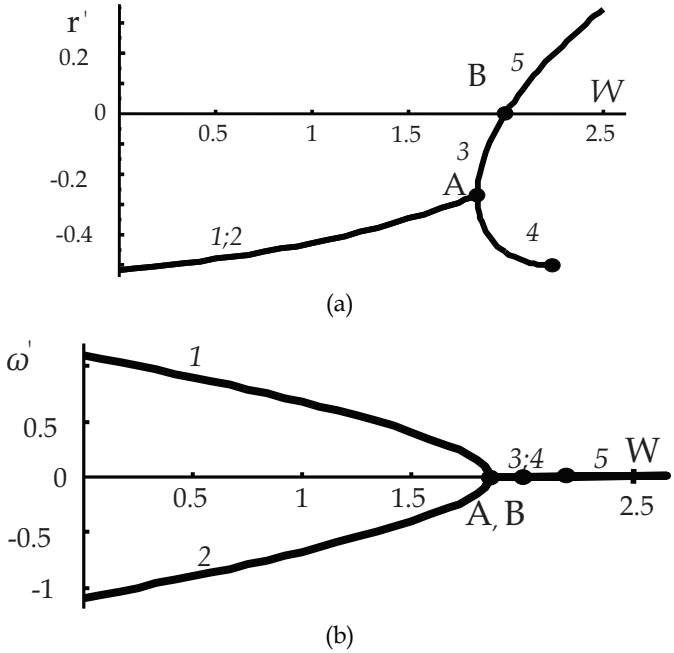

Fig. 5. Dependences of real (a) and imaginary (b) parts of dimensionless complex frequency on parameter W calculated at dimensionless values wave number $k'=1$ and at dimensionless viscosity $\nu'=0.5$

Typical dependencies of real and imaginary parts of the complex frequency on parameter W, calculated by the dispersion equation (11) with taking into account relation (43) are plotted at fig. 5a,b. We used dimensionless variable

$$r'=\frac{r}{r_*}=\frac{\mathrm{Re}(S)}{r_*};\ \omega'=\frac{\omega}{\omega_*}=\frac{\mathrm{Im}(S)}{\omega_*};\ k'=\frac{k}{k_*};\ \nu'=\frac{\nu}{\nu_*}.$$

with characteristic scale

$$r_* = \omega_* = \sqrt[4]{\frac{\rho g^3}{\gamma}};\ \ k_* = \frac{1}{\alpha} = \sqrt{\frac{\rho g}{\gamma}};\ \ \nu_* = \sqrt[4]{\frac{\gamma^3}{\rho^3 g}}.$$

According to work [Belonozhko & Grigor'ev, 2008] the position of the reference points W_A and W_B depicted at the fig. 5 are defined by formulas:

$$W_A \equiv W_A(k) = W_B - (\nu' k')^2 = W_B - \frac{(\nu k)^2}{g\alpha};\ \ W_B \equiv W_B(k) = \frac{1}{k'} + k' = \frac{1}{\alpha k} + \alpha k. \qquad (44)$$

The fig. 5 show that for every value of wave number k there is a critical value of the surface charge density corresponding to condition $W = W_B(k)$. If the surface charge density larger than the critical value ($W > W_B$), complex frequency is pure real and cyclic motion of liquid particle is absent (see curve 5: if $W > W_B$ then $r' > 0$ and $\omega' = 0$). The liquid motion under these conditions can not be a wave. The real part of the complex frequency describes increment of well-known instability of the charged liquid surface relative to excess of a surface charge [Taylor, 1965; Baily, 1974]. Aperiodic growth over time is only an initial stage of the instability appearing owing to what electric forces on the free surface dominate over capillary and gravity forces. The experiments have shown that the instability leads to what a strongly nonlinear conical projections (Taylor's cones) are formed on the charged liquid surface [Taylor & McEwan, 1965]. From the peak of the cones the emission of small strongly charged droplet is occurring. Analyses of expression for $W_B(k)$ shows that if condition $W > 2$ is valid, there is a range of values k for which $W > W_B(k)$ and appropriated small wave perturbations (for example thermal fluctuating) are involved in formation of the Taylor's cones. This phenomenon is well-known and underlies the work of different devices for electrodispersion of various liquid [Baily, 1974].

Thereby if $W > 2$, we can not speak about any drift flow caused by the propagation of the capillary gravitational waves.

If $W_A < W < W_B$, real and imaginary parts of roots of the dispersion equation described by curves 3,4. It can be see that under these conditions there are two modes of liquid motion. Both modes are aperiodic damping ($r' < 0$) and differ only in the damping rate. The cyclic motion of the liquid particle is absent ($\omega' < 0$). For both modes initially deformation of the liquid surface monotonically diminishes over time till complete disappearing. Liquid particles participate only in vertical motion and there is not any horizontal drift.

If $W < W_B(k)$, there are two modes of wave liquid motion with same damping rate and $\omega' \neq 0$ (see curves 1,2 at fig.5). One mode $\omega'_1 > 0$ (curve 1) correspond to wave that is propagating in direction Ox and another mode $\omega'_2 = -\omega'_1 < 0$ (curve 2) describes the wave that is traveling in the opposite direction. One can see that for the capillary-gravitational wave with wave number k the dimensionless circular frequency ω' (in absolute value) decreasing with increasing value of W and vanishes if $W \geq W_B(k)$. As was notice above the drift velocity is proportional to the frequency and consequently behaves as it.

Summarizing the above-said we can conclude that horizontal drift caused by propagation of the periodic capillary-gravitational wave with wave number k is possible only under conditions $W < 2$ and $W < W_B(k)$ where W and $W_B(k)$ is defined by (43) and (44). The first condition ensures that liquid surface is not subjected to instability with respect to an excess of surface electric charge. The second condition provides circumstances under which frequency of cyclical motion of the liquid is not zero. The velocity of the drift flow decreasing with increasing of surface charge density and vanishes if values of surface charge density is reached quantity so that $W = W_B(k)$.

We have demonstrated the possibilities of qualitative investigation of behavior of the mean drift caused by propagation of capillary-gravitational wave over surface of a viscous liquid in dependence on values of certain parameter responsible for supplementary physical effect. In any more complicated physical circumstance the qualitative investigation can be carried out by similarly.

3. Conclusion

Viscous forces play an important role in formation and evolution of the mean horizontal drift induced by periodic capillary-gravitational waves propagating over liquid surface. There are two components of the mean drift flow caused by the propagation of waves: main part that is called the Modified Stokes drift and supplementary part that is named the Additional flow or Additional drift.

At low but nonzero viscosity the Modified Stokes drift behaves almost like classical Stokes drift (model of drift phenomenon without a viscosity) at all depths there is only exponential decrease in the rate of flow over time due to viscous dissipation. The physical mechanism responsible for an appearance of the Modified Stokes drift is same as that of the classical Stokes drift. For period of the wave motion a liquid particle makes approximately circular motion but returns not to initial position but is shifted a little in the direction of wave propagation. The shift is occurred due to that the lower part of the trajectory is shorter than upper since the motion decays with depth.

A considerable contribution to the total drift flow comes from Additional drift into which the liquid is entrained by horizontal viscous stresses acting along the direction of propagation of the Modified Stokes drift. The horizontal viscous shear stresses appear between adjacent horizontal layers since velocity of Modified Stokes drift decreases with the depth. The phenomenon of the Additional drift appears exclusively in the model of a viscous liquid and is ruled out by the laws of an inviscid liquid flow.

Velocities of the Modified Stokes drift and the Additional drift are values of the second order of smallness in wave amplitude. In present work we have offered an analytical procedure of calculation of both drift components.

Expression for velocity of the Modified Stokes drift consists of two terms. The first term is calculated in the same way as in the case of the classical Stokes drift and it is a result of special manipulation with products of values of first order in wave amplitude. Thereby, first term of the Modified Stokes drift is expressed only via quantities that are found as result of calculating in the first order in wave amplitude velocity field caused by propagation of a capillary-gravitational wave over liquid surface.

The second term of the Modified Stokes drift is a special particular solution of the problem of calculating of second order in wave amplitude corrections for the velocity field caused by propagation of a capillary-gravitational wave over liquid surface. This term is essential only in vicinity of liquid surface in the narrow field of viscous boundary layer and negligible in deeper layers. In the limit of almost vanishing viscosity the thickness of the surface viscous boundary layer becomes nearly zero. At the upper bounder of this layer the first term tends to zero and the second term takes care of the correct description of the drift. The best agreement of the properties classical and Modified drifts is archived only when one takes into account both terms.

Expression for the Additional drift is derived as a special part of solution of the problem of calculating of second order in wave amplitude corrections for the velocity field caused by propagation of a capillary-gravitational wave over liquid surface.

The procedure developed here for calculating the drift is especially important for applications associated with phenomena on the free surface of a liquid with the participation of viscous stresses. In particular, the approach proposed here makes it possible to calculate analytically the velocity of surface drift caused by wave perturbation for various surface substances (surface charge, surface-active substances, etc.) distributed over the free surface. If there is a total motion of the upper liquid along the interface between liquids (like wind along surface of ocean) then is interesting to study influence of the total upper liquid velocity on the arising of drift flow in lower liquid. Especially interesting if total upper liquid velocity is sufficient to excite an oscillatory instability which in the case of ideal liquids is known as Kelvin-Helmholtz instability. For all cases the qualitative preliminary analysis is helpful which is based on what the velocity of drift caused by the wave propagation is proportional to frequency of the wave motion and hence supporting information about behavior of the drift is contained in dispersion equation of the analyzed problem.

4. References

Baily A.G. Electrostatic atomization of liquids (rev.)// Sci. Prog., Oxf. 1974. V.61. P. 555-581.

Belonozhko D.F. & Grigor'ev A.I. (2003) Finite-amplitude waves on the surface of a viscous deep liquid// *Tech. Phys.* Vol.48. N.4. pp.404-414.

Belonozhko D.F. & Grigor'ev A.I. (2004) Nonlinear periodic waves on the charged surface of a deep low-viscosity conducting liquid// *Tech. Phys.* Vol.49. N.3. pp.5-13.

Belonozhko D.F. & Grigor'ev A.I. (2004) Nonlinear periodic waves on the charged surfactant-covered surface of a viscous fluid//*Tech. Phys.* Vol.49. N.11. pp.1422-1430.

Belonozhko D.F. & Grigor'ev A.I. (2008) Thickness of a boundary layer attributed to the wave motion on the charged free surface of a viscous liquid // *Tech. Phys.* Vol.53. N.3. pp. 306-313.

Belonozhko D.F., Shiryaeva S.O. & Grigor'ev A.I. (2005) Nonlinear periodic waves on the charged surface of a viscous finite-conductivity fluid//*Tech. Phys.* Vol.50. N.2. pp.177-184.

Faber T. E. Fluid Dynamics for Physicists, Cambridge University Press, 1997. 440 p.

Le Blon P. H. & Mysak L. A. (1978) Waves in Ocean. *Amsterdam: Elsevier.* 602 p.

Le Méhauté B. (1976) An Introduction to Hydrodynamics and Water Waves, Springer - Verlag, 322 p.

Lokenath D. (1994.) Nonlinear water waves. San Diego. Academiv Press. Inc. 544 p.

Longuet-Higgens M.S. Mass transport in water waves//*Phil. Trans. Roy. Soc. London. Ser. A.* 1953. V.245. N 903. pp.535-581.

Longuet-Higgens M.S. *(1986)* Eulerian and Lagragian aspects of surface waves //*J. Fluid Mech.* Vol.173. pp.683-707.

Melcher J.R. Field-coupled surface waves. A comparative study of surface coupled electrohydrodynemics and magnetohydrodynemics systems. Cambridge. 1963. 190 p.

Polyanin A.D. (2002), HandBook of Linear Differential Equations for Engineers and Scientist.

Stokes G.G. (1847). On the theory of oscillatory waves *Transactions of the Cambridge Philosophical Society* Vol.8. pp. 441–455.

Stokes G.G. (1880). *Mathematical and Physical Papers*, Vol. I. Cambridge University Press. pp. 197–229.

Taylor G.I. & McEwan A.D. The stability of horizontal fluid interface in a vertical electric field//*J. Fluid Mech.* 1965. V.22. N 1. pp. 1-15

4

Macroscopic Gas-Liquid Interfacial Equation Based on Thermodynamic and Mathematical Approaches

Yukihiro Yonemoto[1] and Tomoaki Kunugi[2]
[1]*Japan Atomic Energy Agency*
[2]*Kyoto University*
Japan

1. Introduction

At a gas–liquid interface, many complicated phenomena such as evaporation, condensation, electrokinesis, and heat and mass transfer occur. These phenomena are widely seen in various industrial and chemical systems. In chemical or biochemical reactive operations, bubble columns are used for increasing the mass transfer through the interface and for enhancing the separation of mixtures by rectification and water purification (Hong and Brauer 1989; Álvarez et al. 2000). However, the interfacial phenomena have various time and space scales (multi-scale) that are interrelated at the interface. Therefore, modeling gas–liquid interfaces over a wide range of scales spanning molecular motion to vortical fluid motion is very difficult, and this has remained one of the key unresolved issues in multiphase flow science and engineering since a long time. In particular, the mechanism for bubble coalescence/repulsion behaviour is unknown, although it is a superficially simple behaviour and fundamental phenomena in bubbly flows. In order to evaluate the interfacial interactions such as bubble coalescence and repulsion quantitatively, we need a new gas–liquid interfacial model based on the multi-scale concept which is expressed mathematically and that takes into account physical and chemical phenomena and heat and mass transfer at the interface.

In the theoretical point of view, the interfacial equation for a macroscopic-scale gas–liquid interface is mainly characterized by a jump condition. The macroscopic interface is discontinuous, and its physical properties such as density, viscosity, and temperature have discontinuous values. The jump condition has been discussed in terms of the mechanical energy balance (Scriven, 1960; Delhaye, 1974) using Stokes' theorem, the Gauss divergence theorem, differential geometry and so on. In these theorems, a test volume is considered at the interface between two continuous phases. In the derivation, the surface force acting on the discontinuous interface is modeled using the Young–Laplace equation. However, in such a mechanical approach, the definition of the curvature is unclear at the interface, and the surface tension coefficient is treated as a macroscopic experimental value. The interfacial model, which is based only on the mechanical energy balance, cannot take into account detailed physical and chemical phenomena occurring at the interface. In particular, the contamination at the interface, which is related to electric charges, is important for an

interfacial interaction. Craig (2004) and Henry and Craig (2008) have discussed the effects of specific ions on bubble interactions. They have reported that bubble coalescence is affected by the ions adsorbed at the interface, combination of these ions, and the electrolyte concentration. Others have similarly reported the importance of electrolytes in bubble coalescence (Marčelja, 2004; Ribeiro & Mewes, 2007; Tsang et al., 2004; Lessaard & Zieminski, 1971). In our experimental research on microbubble flow (Yonemoto et al., 2008), some patterns have been observed with respect to microbubble coalescence. Microbubble coalescence has been estimated analytically using the film thinning theory. Results have shown that microbubble coalescence cannot be explained based only on hydrodynamics. That is to say, our results indicate the importance of mass transfer, which is related to contamination at the interface, for interfacial interaction.

Recently, the phase field theory (Cahn & Hilliard, 1958) and van der Waals theory (Rowlinson & Widom, 1984), wherein the interface is assumed to be a diffuse interface with a finite thickness, have been applied to perform numerical research on multiphase flow. The surface force is evaluated by the free energy defined at the interface and depends on both concentration (or density) and its gradient. Anderson et al. (1998) have reviewed the diffuse-interface models of hydrodynamics and their application to various interfacial phenomena. In their study, the diffuse-interface model was associated with the sharp-interface model (Delhaye, 1974). But the multi-scale concept was not expressed in concrete terms.

In a previous study (Yonemoto & Kunugi, 2010a), a thermodynamic and mathematical interfacial model that takes into account the multi-scale concept has been developed on the basis of the phase field theory (Cahn & Hilliard, 1958). In this model, we assumed that the interface has a finite thickness and that free energy is defined at the interface. In particular, the free energy is derived on a microscopic scale (Hamiltonian); this includes the electrostatic potential due to contamination at the interface. The free energy is incorporated into the Navier–Stokes (NS) equation by using the Chapman–Enskog expansion (Chapman & Cowling, 1970), which mathematically discriminates the time and space scales of the interfacial phenomena. Finally, a new equation governing the fluid motion, called the multi-scale multiphase flow equation, is derived. The multi-scale multiphase flow equation has been proven to have the potential to simulate interfacial interactions (Yonemoto & Kunugi, 2010b). In the simulation, microbubble interaction is simulated and a liquid film between them is observed when the bubbles interact with each other. In the present study, the multi-scale multiphase flow equation, which is the mesoscopic interfacial equation, was further discussed, and a macroscopic interfacial equation was derived based on our interfacial model. In particular, an interfacial jump condition treated by thermodynamics was derived from the multi-scale multiphase flow equation, and the thermodynamic interfacial jump condition was then compared with the conventional jump condition. In addition, we derived the Kelvin equation based on both the multi-scale multiphase flow equation (Yonemoto & Kunugi, 2010a) and the thermodynamic jump condition. The present results indicate that our interfacial model can theoretically support various interfacial phenomena characterized by thermodynamics from a multi-scale viewpoint (micro to macro).

2. Multi-scale multiphase flow equation

In a previous study (Yonemoto & Kunugi, 2010a), the multi-scale multiphase flow equation was derived based on the phase field theory (Cahn & Hilliard, 1958). In the derivation, we assumed that the interface has a finite thickness similar to that of a fluid membrane

(mesoscopic interface). The concept of the gas–liquid interface is shown in Fig. 1. Experimental observations of bubble interactions (Craig, 2004; Henry & Craig, 2008) revealed that contamination at the interface may be an important factor. With this in mind, the contamination at the interface was associated with an electrostatic potential due to an electric double layer at the gas–liquid interface, and the free-energy equation, including the electrostatic potential, was then derived from a lattice-gas model (Safran, 1994):

$$F = \int_V \left[f_0(\psi) + \frac{d}{2}(\nabla\psi)^2 \right] \mathrm{d}V \tag{1}$$

Here,

$$f_0(\psi) = -\frac{a}{2}\psi^2 + \frac{b}{4}\psi^4 - cz_i eV_e\psi \tag{2}$$

$$a = \frac{U_{sum} - 4k_B T}{l^3} \tag{3}$$

$$b = \frac{16k_B T}{3l^3} \tag{4}$$

$$c = \frac{1}{2l^3} \tag{5}$$

$$d = \frac{U_{sum}}{2l^3} \tag{6}$$

The first and the second terms on the right-hand side of Eq. (1) denote the free energy in homogeneous and inhomogeneous systems, respectively. Coefficients a [J/m^3], b [J/m^3], c [1/m^3], and d [J/m] in Eqs. (1) and (2) have constant values. In Eqs. (3) and (6), U_{sum} is related to an intermolecular potential. These values include microscopic physical information (Yonemoto & Kunugi, 2010a). The symbols of z_i [-], e [C], V_e [V], and ψ [-] are the charge number, elementary charge, electrostatic potential, and order parameter, respectively. The third term on the right-hand side of Eq. (2) is related to the contamination at the interface. In general, the surface tension is evaluated by the surface tension coefficient and the curvature characterizing the macroscopic shape of the interface. As mentioned earlier, in our model, the interface has a finite thickness similar to that of a fluid membrane (Fig. 1). For an interface with finite thickness, it is very difficult to determine the geometric shape of the interface. Therefore, the surface tension should be considered from the free energy at the interface rather than from the curvature (Fialkowski et at., 2000; Yonemoto et al., 2005). Moreover, there are many physical and chemical processes at the interface that are characterized by various time and space scales. Therefore, in order to consider the various scale interactions that may arise among interfacial phenomena, the Chapman–Enskog expansion (Chapman & Cowling, 1970) was applied to the NS equation. Here, the original NS equation is expressed as

$$\rho \frac{\mathrm{D}\,\boldsymbol{u}}{\mathrm{D}\,t} = -\nabla \cdot \boldsymbol{T} + \rho \boldsymbol{g} \tag{7}$$

where ρ [kg/m^3], $\boldsymbol{u}$ [m/s], $\boldsymbol{T}$ [N/m^2], $\boldsymbol{g}$ [m/s^2], and t [s] represent the fluid density, velocity, stress tensor, acceleration due to gravity, and time, respectively.

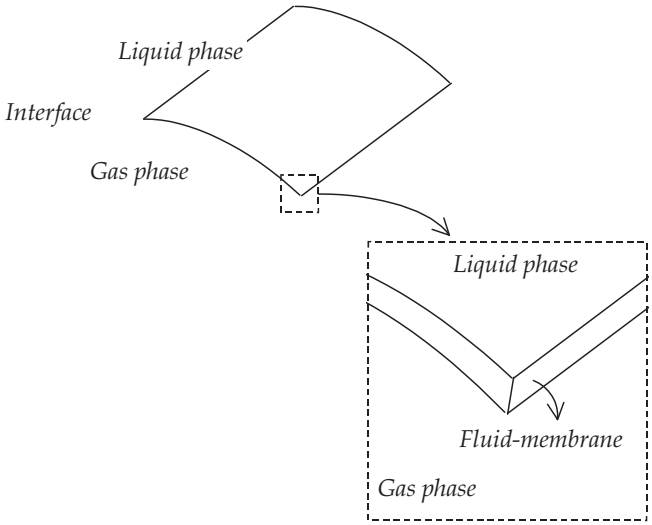

Fig. 1. Concept of a gas–liquid interface: macroscopic and mesoscopic image of the interface

Stress tensor $\boldsymbol{T}$ [N/m^3] is defined as $\boldsymbol{T} = P\boldsymbol{I} - \boldsymbol{\tau}$. The shear stress is τ [N/m^2]. Pressure P [N/m^2] is the mechanical pressure, hereafter represented by P_{mech}. At this point, the operators $\mathrm{D}/\mathrm{D}t$ and $\boldsymbol{\nabla}$ must include the various time and space scales (multi-scale concept). Therefore, in order to discriminate their scales, the Chapman–Enskog expansion was applied to $\mathrm{D}/\mathrm{D}t$ and $\boldsymbol{\nabla}$ in the NS equation. The operators $\mathrm{D}/\mathrm{D}t$ and $\boldsymbol{\nabla}$ were decomposed into the following expressions by using the small parameter ε:

$$\boldsymbol{\nabla} = \boldsymbol{\nabla}^{(0)} + \varepsilon\boldsymbol{\nabla}^{(1)} + \varepsilon^2\boldsymbol{\nabla}^{(2)} + \cdots + \varepsilon^k\boldsymbol{\nabla}^{(k)} + \cdots \tag{8}$$

$$\frac{\mathrm{D}}{\mathrm{D}\,t} = \frac{\mathrm{D}}{\mathrm{D}\,t^{(0)}} + \varepsilon\frac{\mathrm{D}}{\mathrm{D}\,t^{(1)}} + \varepsilon^2\frac{\mathrm{D}}{\mathrm{D}\,t^{(2)}} + \cdots + \varepsilon^k\frac{\mathrm{D}}{\mathrm{D}\,t^{(k)}} + \cdots \tag{9}$$

Here, superscript k (k = 0, 1, 2...) represents the scale of the phenomena, which becomes smaller as (k) increases. For example, the superscript (0) corresponds to the macroscopic scale. In Eqs. (8) and (9), the small parameter ε is defined as $\varepsilon = \delta / L$. The symbols of δ [m] and L [m] represent the characteristic lengths of the interface and the vortical fluid flow, respectively. After substituting Eqs. (8) and (9) into Eq. (7) and performing a simple tensor analysis, we obtain a new governing equation:

$$\rho\frac{\mathrm{D}\,\boldsymbol{u}}{\mathrm{D}\,t^{(0)}} + \varepsilon\rho\frac{\mathrm{D}\,\boldsymbol{u}'}{\mathrm{D}\,t^{(1)}} = -\boldsymbol{\nabla}^{(0)}\cdot\boldsymbol{T} + \varepsilon\boldsymbol{\nabla}^{(1)}\cdot\left(f_0(\psi)\boldsymbol{I}\right) - \varepsilon d\boldsymbol{\nabla}^{(1)}\psi\left(\boldsymbol{\nabla}^{(1)}\cdot\boldsymbol{\nabla}^{(1)}\psi\right) + \rho\boldsymbol{g} \tag{10}$$

In the derivation, the free energy (Eq. (1)) is associated with thermodynamic pressure using the Maxwell relation. This equation is the multi-scale multiphase flow equation (Yonemoto & Kunugi, 2010a).

3. Jump condition at gas–liquid interface

3.1 Momentum jump condition

An interfacial phenomenon is complex and interpreted as a discontinuous problem. The interface separates two continuous equilibrium phases. When the curvature radius is considerably larger than the thickness of the interface, the equilibrium force balance at the interface is given by the following equation based on the interfacial coordinates shown in Fig. 2:

$$\dot{\boldsymbol{M}}_{\mathrm{G}} + \dot{\boldsymbol{M}}_{\mathrm{L}} - \left\{(-P_{\mathrm{G}})\boldsymbol{n}_{\mathrm{G}} + \boldsymbol{\tau}_{\mathrm{G}} \cdot \boldsymbol{n}_{\mathrm{G}}\right\} - \left\{(-P_{\mathrm{L}})\boldsymbol{n}_{\mathrm{L}} + \boldsymbol{\tau}_{\mathrm{L}} \cdot \boldsymbol{n}_{\mathrm{L}}\right\} - 2H\sigma\boldsymbol{n}_{\mathrm{G}} - \frac{\mathrm{d}\sigma}{\mathrm{d}s}\boldsymbol{t} = 0 \tag{11}$$

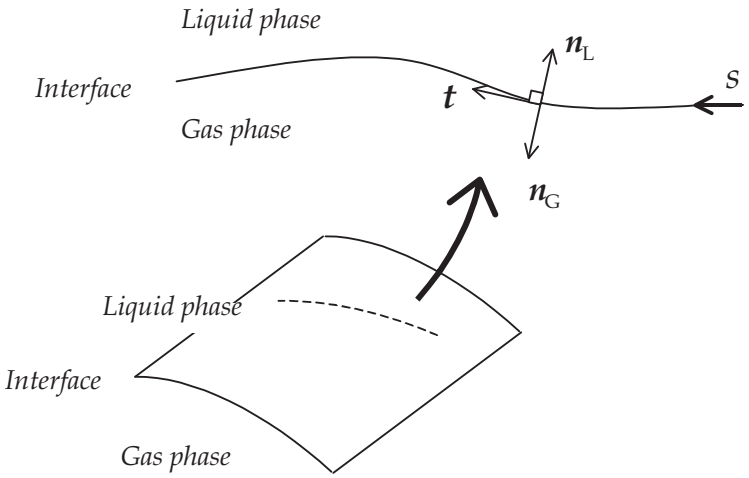

Fig. 2. Interfacial coordinates at the gas–liquid interface

where the subscripts L and G represent liquid and gas phases, respectively. This is called the momentum jump condition at the interface. The symbols σ [N/m], P_k (k = G, L) [N/m²], and s [m] are the surface tension coefficient, pressure, and coordinate along the interface, respectively. The mean curvature is denoted by the symbol H; here, $H = (\kappa_1 + \kappa_2)/2$, where κ_1 and κ_2 [1/m] are the principal curvatures. The bold symbols $\boldsymbol{n}_k$, $\boldsymbol{t}$, and $\boldsymbol{\tau}_k$ [N/m²] are the unit normal, unit tangential vector, and shear stress, respectively. $\boldsymbol{M}_k$ [kg/ms] ($\dot{\boldsymbol{M}}_k$ [N/m²] is the time derivative of $\boldsymbol{M}_k$) denotes the term related to mass transfer through the interface. In this paper, we call this equation the conventional jump condition. The jump condition at the interface is characterized by the curvature related to the shape of the interface, which means that the interface is a mathematical interface with zero thickness. Therefore, we consider the jump condition to be a macroscopic interfacial equation.

3.2 Derivation of thermodynamic jump condition

Here, the interfacial jump condition treated by thermodynamics is derived using the multi-scale multiphase flow equation (Eq. (10)). We call this derived condition the "thermodynamic jump condition" because Equation (10) is based on the thermodynamic concept (Yonemoto & Kunugi, 2010a).

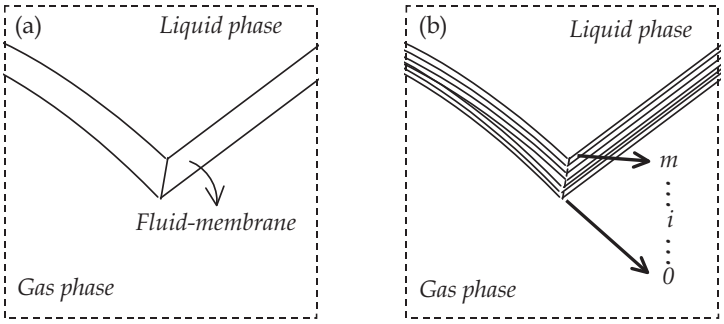

Fig. 3. Fluid membrane comprising elemental interfaces: (a) Fluid membrane, (b) Elemental interfaces. Interpretation of the fluid membrane based on interfacial coordinates

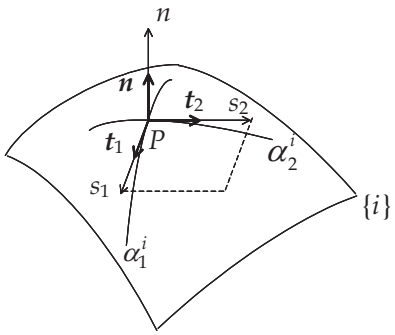

Fig. 4. Elemental interface {*i*} with interfacial coordinates in a fluid membrane

The interfacial jump condition is mainly considered in the moving coordinate system. This means that this jump condition is discussed under the condition that the relative velocity between the convected interface and fluid motion that convects the interface is neglected. In particular, assuming that the interface is in the steady state, the left-hand side of Eq. (10) (substantial derivative term) is neglected. In this study, phase changes such as evaporation and condensation and the effect of gravity on the interface are not considered. Therefore, Equation (10) reduces to

$$0 = -\boldsymbol{\nabla}^{(0)} \cdot \boldsymbol{T} + \varepsilon \boldsymbol{\nabla}^{(1)} \cdot \left(f_0(\psi) \boldsymbol{I} \right) - \varepsilon d \boldsymbol{\nabla}^{(1)} \psi \left(\boldsymbol{\nabla}^{(1)} \cdot \boldsymbol{\nabla}^{(1)} \psi \right). \tag{12}$$

Because Equation (11) is based on the interfacial coordinate system, Equation (12) is also transformed into an equation based on the interfacial coordinate system.

Before the concrete derivation of the thermodynamic jump condition, a mathematical operation is prepared. First, a test interface is defined as shown in Fig. 3. The test interface is divided into many elemental interfaces along the normal coordinate perpendicular to each elemental interface. We assume that the curvature is constant along the normal coordinate with respect to all elemental interfaces. Figure 4 shows representative interface {*i*} for a number of elemental interfaces. Next, the interfacial coordinate system is considered at point P on its interface. The tangential axes are represented by s_1 and s_2, and n is the normal

axis. Unit vectors $\boldsymbol{t}_1$, $\boldsymbol{t}_2$, and $\boldsymbol{n}_k$ (k = G or L) are defined on the s_1, s_2, and n axes, respectively. The unit vectors are orthogonal to each other. The direction of $\boldsymbol{n}_\mathrm{L}$ is upward, and $\boldsymbol{n}_\mathrm{G}$ is opposite to $\boldsymbol{n}_\mathrm{L}$ (i.e., $\boldsymbol{n}_\mathrm{L} = -\boldsymbol{n}_\mathrm{G} = \boldsymbol{t}_1 \times \boldsymbol{t}_2$). In the present study, we focused on the local interface; therefore, general covariance (Aris, 1962) such as the change in the tangential vector along the interface is not considered.

Because $u_i = (s_1, s_2, n)$ and $x_i = (x, y, z)$, the operator $\boldsymbol{\nabla}$ is transformed into the interfacial coordinate system, which leads to

$$\boldsymbol{\nabla} = \boldsymbol{t}_1 \frac{\partial}{\partial s_1} + \boldsymbol{t}_2 \frac{\partial}{\partial s_2} + \boldsymbol{n} \frac{\partial}{\partial n} \tag{13}$$

Thus, the operator $\boldsymbol{\nabla} \cdot \boldsymbol{\nabla}$ becomes

$$\boldsymbol{\nabla} \cdot \boldsymbol{\nabla} = (\kappa_1 + \kappa_2) \frac{\partial}{\partial n} + \frac{\partial^2}{\partial s_1^2} + \frac{\partial^2}{\partial s_2^2} + \frac{\partial^2}{\partial n^2} \tag{14}$$

where κ_1 and κ_2 are the principal curvatures at the interface. In what follows, for the sake of simplicity, only the s_1–n coordinate system is considered. Using Eqs. (13) and (14), we can rewrite Eq. (12) as

$$\begin{aligned} 0 = & -\boldsymbol{t}_1 \frac{\partial P_\mathrm{mech}}{\partial s_1^{(0)}} - \boldsymbol{n}_\mathrm{L} \frac{\partial P_\mathrm{mech}}{\partial n^{(0)}} \\ & + \boldsymbol{t}_1 \cdot \frac{\partial \boldsymbol{\tau}}{\partial s_1^{(0)}} + \boldsymbol{n}_\mathrm{L} \cdot \frac{\partial \boldsymbol{\tau}}{\partial n^{(0)}} + \varepsilon \boldsymbol{t}_1 \frac{\partial f_0}{\partial s_1^{(1)}} + \varepsilon \boldsymbol{n}_\mathrm{L} \frac{\partial f_0}{\partial n^{(1)}} \\ & - \varepsilon d \left(\boldsymbol{t}_1 \frac{\partial \psi}{\partial s_1^{(1)}} + \boldsymbol{n}_\mathrm{L} \frac{\partial \psi}{\partial n^{(1)}} \right) \left(\kappa_1 \frac{\partial \psi}{\partial n^{(1)}} + \frac{\partial^2 \psi}{\partial s_1^{(1)2}} + \frac{\partial^2 \psi}{\partial n^{(1)2}} \right) \end{aligned} \tag{15}$$

Here, we assume $\partial \boldsymbol{\tau} / \partial s_1^{(0)} = 0$ and $\partial P_\mathrm{mech} / \partial s_1^{(0)} = 0$ at the interface. Then, the integration of Eq. (15) from $-\infty$ to $+\infty$ along the n axis gives

$$\begin{aligned} 0 = & -\boldsymbol{n}_\mathrm{L} \int_{-\infty}^{+\infty} \frac{\partial P_\mathrm{mech}}{\partial n} \mathrm{d}n + \boldsymbol{n}_\mathrm{L} \cdot \int_{-\infty}^{+\infty} \frac{\partial \boldsymbol{\tau}}{\partial n} \mathrm{d}n \\ & - \varepsilon \boldsymbol{t}_1 \int_{-\infty}^{+\infty} \frac{\partial f_0}{\partial s_1} \mathrm{d}n + \varepsilon \boldsymbol{n}_\mathrm{L} \int_{-\infty}^{+\infty} \frac{\partial f_0}{\partial n} \mathrm{d}n \\ & - \boldsymbol{t}_1 \varepsilon d \int_{-\infty}^{+\infty} \kappa_1 \frac{\partial \psi}{\partial s_1} \frac{\partial \psi}{\partial n} \mathrm{d}n - \boldsymbol{t}_1 \frac{\varepsilon d}{2} \int_{-\infty}^{+\infty} \frac{\partial}{\partial s_1} \left(\frac{\partial \psi}{\partial s_1} \right)^2 \mathrm{d}n \\ & - \boldsymbol{t}_1 \varepsilon d \int_{-\infty}^{+\infty} \frac{\partial}{\partial n} \left(\frac{\partial \psi}{\partial s_1} \frac{\partial \psi}{\partial n} \right) \mathrm{d}n + \boldsymbol{t}_1 \frac{\varepsilon d}{2} \int_{-\infty}^{+\infty} \frac{\partial}{\partial s_1} \left(\frac{\partial \psi}{\partial n} \right)^2 \mathrm{d}n \\ & - \boldsymbol{n}_\mathrm{L} \varepsilon d \int_{-\infty}^{+\infty} \frac{\partial}{\partial s_1} \left(\frac{\partial \psi}{\partial n} \frac{\partial \psi}{\partial s_1} \right) \mathrm{d}n + \boldsymbol{n}_\mathrm{L} \frac{\varepsilon d}{2} \int_{-\infty}^{+\infty} \frac{\partial}{\partial n} \left(\frac{\partial \psi}{\partial s_1} \right)^2 \mathrm{d}n \\ & - \boldsymbol{n}_\mathrm{L} \varepsilon d \int_{-\infty}^{+\infty} \kappa_1 \left(\frac{\partial \psi}{\partial n} \right)^2 \mathrm{d}n + \boldsymbol{n}_\mathrm{L} \frac{\varepsilon d}{2} \int_{-\infty}^{+\infty} \frac{\partial}{\partial n} \left(\frac{\partial \psi}{\partial n} \right)^2 \mathrm{d}n \end{aligned} \tag{16}$$

The superscripts in terms $n^{(0)}$ and $n^{(1)}$ in Eq. (15) can be omitted in Eq. (16) because there is no difference between the normal directions $n^{(0)}$ and $n^{(1)}$ over the integration. The first term on the right-hand side of Eq. (16) is calculated as follows:

$$-\boldsymbol{n}_{\mathrm{L}}\int_{P_{\mathrm{G}}}^{P_{\mathrm{L}}}\mathrm{d}P_{\mathrm{mech}} = -\boldsymbol{n}_{\mathrm{L}}P_{\mathrm{L}} - \boldsymbol{n}_{\mathrm{G}}P_{\mathrm{G}}, \tag{17}$$

and the second term is

$$\boldsymbol{n}_{\mathrm{L}}\cdot\int_{\boldsymbol{\tau}_{\mathrm{G}}}^{\boldsymbol{\tau}_{\mathrm{L}}}\mathrm{d}\boldsymbol{\tau} = \boldsymbol{n}_{\mathrm{L}}\cdot\boldsymbol{\tau}_{\mathrm{L}} + \boldsymbol{n}_{\mathrm{G}}\cdot\boldsymbol{\tau}_{\mathrm{G}} \tag{18}$$

When $\partial\psi/\partial n = 0$ at $n = -\infty$ or $+\infty$, we obtain

$$\begin{aligned}
0 = &-\left[\left(-P_{\mathrm{G}} - \varepsilon\pi_{\mathrm{G}}\right)\boldsymbol{n}_{\mathrm{G}} + \boldsymbol{n}_{\mathrm{G}}\cdot\boldsymbol{\tau}_{\mathrm{G}}\right] - \left[\left(-P_{\mathrm{L}} - \varepsilon\pi_{\mathrm{L}}\right)\boldsymbol{n}_{\mathrm{L}} + \boldsymbol{n}_{\mathrm{L}}\cdot\boldsymbol{\tau}_{\mathrm{L}}\right] \\
&+\boldsymbol{n}_{\mathrm{L}}\varepsilon d\int_{-\infty}^{+\infty}\kappa_1\left(\frac{\partial\psi}{\partial n}\right)^2\mathrm{d}n - \boldsymbol{t}_1\frac{\varepsilon d}{2}\int_{-\infty}^{+\infty}\frac{\partial}{\partial s_1}\left(\frac{\partial\psi}{\partial n}\right)^2\mathrm{d}n \\
&+\boldsymbol{n}_{\mathrm{L}}\varepsilon d\int_{-\infty}^{+\infty}\frac{\partial}{\partial s_1}\left(\frac{\partial\psi}{\partial n}\frac{\partial\psi}{\partial s_1}\right)\mathrm{d}n - \boldsymbol{n}_{\mathrm{L}}\frac{\varepsilon d}{2}\int_{-\infty}^{+\infty}\frac{\partial}{\partial n}\left(\frac{\partial\psi}{\partial s_1}\right)^2\mathrm{d}n \\
&-\boldsymbol{t}_1\int_{-\infty}^{+\infty}\varepsilon\frac{\partial\psi}{\partial s_1}\left(-a\psi + b\psi^3\right)\mathrm{d}n + \boldsymbol{t}_1\int_{-\infty}^{+\infty}\varepsilon\frac{\partial\pi_{\mathrm{i}}}{\partial s_1}\mathrm{d}n \\
&+\boldsymbol{t}_1\frac{\varepsilon d}{2}\int_{-\infty}^{+\infty}\frac{\partial}{\partial s_1}\left(\frac{\partial\psi}{\partial s_1}\right)^2\mathrm{d}n + \boldsymbol{t}_1\varepsilon d\int_{-\infty}^{+\infty}\kappa_1\frac{\partial\psi}{\partial s_1}\frac{\partial\psi}{\partial n}\mathrm{d}n
\end{aligned} \tag{19}$$

where $\pi_i = cz_ieV_e\psi$ [N/m²]. The function π_i (i = L or G) represents contamination at the interface (liquid or gas phase). The surface tension coefficient under the flat surface is defined as follows (Rowlinson & Widom, 1984):

$$\sigma = d\int_{-\infty}^{\infty}\left(\frac{\partial\psi}{\partial n}\right)^2\mathrm{d}n \tag{20}$$

Equation (20) is substituted into Eq. (19) and is transformed in order to consider the relation between Eqs. (11) and (19).
Using Eq. (20), we can rewrite the third and fourth terms on the right-hand side of Eq. (19) as

$$\boldsymbol{n}_{\mathrm{L}}\varepsilon d\int_{-\infty}^{+\infty}\kappa_1\left(\frac{\partial\psi}{\partial n}\right)^2\mathrm{d}n = \boldsymbol{n}_{\mathrm{L}}\varepsilon\sigma\kappa_1 \tag{21}$$

$$\begin{aligned}
\boldsymbol{t}_1\frac{\varepsilon d}{2}\int_{-\infty}^{+\infty}\frac{\partial}{\partial s_1}\left(\frac{\partial\psi}{\partial n}\right)^2\mathrm{d}n &= \boldsymbol{t}_1\frac{\varepsilon}{2}\frac{\partial}{\partial s_1}\left[d\int_{-\infty}^{+\infty}\left(\frac{\partial\psi}{\partial n}\right)^2\mathrm{d}n\right] \\
&= \boldsymbol{t}_1\frac{\varepsilon}{2}\frac{\mathrm{d}\sigma}{\mathrm{d}s_1}
\end{aligned} \tag{22}$$

In Eq. (21), although the curvature depends not only on the s_1, s_2 directions but also on the n direction, as shown in Fig. 5, we do not consider the change in the curvature in the normal direction because the interface is very thin. In Eq. (22), the replacement of $\partial/\partial s_1 = 0$ by $\mathrm{d}/\mathrm{d}s_1 = 0$ means that the dependency of the surface tension coefficient on the s_2 coordinate is not considered. After substituting Eqs. (20), (21), and (22) into Eq. (19) and adding the terms with respect to the s_2 coordinate in Eq. (19), we derive the following equation:

$$
\begin{aligned}
0 = & \underbrace{-\left[\left(-P_{\mathrm{G}} - \varepsilon\pi_{\mathrm{G}}\right)\boldsymbol{n}_{\mathrm{G}} + \boldsymbol{n}_{\mathrm{G}}\cdot\boldsymbol{\tau}_{\mathrm{G}}\right]}_{(a)} \underbrace{-\left[\left(-P_{\mathrm{L}} - \varepsilon\pi_{\mathrm{L}}\right)\boldsymbol{n}_{\mathrm{L}} + \boldsymbol{n}_{\mathrm{L}}\cdot\boldsymbol{\tau}_{\mathrm{L}}\right]}_{(b)} \underbrace{-\boldsymbol{n}_{\mathrm{G}}\varepsilon\left(\kappa_1+\kappa_2\right)\sigma}_{(c)} \\
& \underbrace{-\varepsilon\left(\boldsymbol{t}_1\frac{1}{2}\frac{\partial\,\sigma}{\partial\,s_1} + \boldsymbol{t}_2\frac{1}{2}\frac{\partial\,\sigma}{\partial\,s_2}\right)}_{(d)} \underbrace{-\boldsymbol{n}_{\mathrm{G}}\varepsilon d\int_{-\infty}^{+\infty}\left[\frac{\partial}{\partial\,s_1}\left(\frac{\partial\,\psi}{\partial\,n}\frac{\partial\,\psi}{\partial\,s_1}\right) + \frac{\partial}{\partial\,s_2}\left(\frac{\partial\,\psi}{\partial\,n}\frac{\partial\,\psi}{\partial\,s_2}\right)\right]\mathrm{d}n}_{(e)} \\
& \underbrace{+\boldsymbol{n}_{\mathrm{G}}\varepsilon d\int_{-\infty}^{+\infty}\frac{1}{2}\frac{\partial}{\partial\,n}\left[\left(\frac{\partial\,\psi}{\partial\,s_1}\right)^2 + \left(\frac{\partial\,\psi}{\partial\,s_2}\right)^2\right]\mathrm{d}n}_{(f)} \underbrace{-\varepsilon\int_{-\infty}^{+\infty}\left(\boldsymbol{t}_1\frac{\partial\,\psi}{\partial\,s_1} + \boldsymbol{t}_2\frac{\partial\,\psi}{\partial\,s_2}\right)\left(-a\psi + b\psi^3\right)\mathrm{d}n}_{(g)} \\
& \underbrace{+\varepsilon\int_{-\infty}^{+\infty}\left(\boldsymbol{t}_1\frac{\partial\,\pi_{\mathrm{i}}}{\partial\,s_1} + \boldsymbol{t}_2\frac{\partial\,\pi_{\mathrm{i}}}{\partial\,s_2}\right)\mathrm{d}n}_{(h)} + \underbrace{\frac{\varepsilon d}{2}\int_{-\infty}^{+\infty}\left[\boldsymbol{t}_1\frac{\partial}{\partial\,s_1}\left(\frac{\partial\,\psi}{\partial\,s_1}\right)^2 + \boldsymbol{t}_2\frac{\partial}{\partial\,s_2}\left(\frac{\partial\,\psi}{\partial\,s_2}\right)^2\right]\mathrm{d}n}_{(i)} \\
& \underbrace{+\varepsilon d\left(\kappa_1+\kappa_2\right)\int_{-\infty}^{+\infty}\left(\boldsymbol{t}_1\frac{\partial\,\psi}{\partial\,s_1} + \boldsymbol{t}_2\frac{\partial\,\psi}{\partial\,s_2}\right)\left(\frac{\partial\,\psi}{\partial\,n}\right)\mathrm{d}n}_{(j)} \\
& \underbrace{+\varepsilon d\int_{-\infty}^{+\infty}\left[\boldsymbol{t}_1\frac{\partial}{\partial\,s_2}\left(\frac{\partial\,\psi}{\partial\,s_1}\frac{\partial\,\psi}{\partial\,s_2}\right) + \boldsymbol{t}_2\frac{\partial}{\partial\,s_1}\left(\frac{\partial\,\psi}{\partial\,s_1}\frac{\partial\,\psi}{\partial\,s_2}\right)\right]\mathrm{d}n}_{(k)} \\
& \underbrace{-\frac{\varepsilon d}{2}\int_{-\infty}^{+\infty}\left[\boldsymbol{t}_1\frac{\partial}{\partial\,s_1}\left(\frac{\partial\,\psi}{\partial\,s_2}\right)^2 + \boldsymbol{t}_2\frac{\partial}{\partial\,s_2}\left(\frac{\partial\,\psi}{\partial\,s_1}\right)^2\right]\mathrm{d}n}_{(l)}
\end{aligned}
\tag{23}
$$

This equation is the thermodynamic jump condition at the interface and is obtained by assuming that many elemental interfaces lie on the interface with a finite thickness and integrating it over the normal direction. The free energy is defined at the interface and is derived from the microscopic viewpoint (Hamiltonian) (Yonemoto & Kunugi, 2010a). Therefore, Equation (23) considers multiple scales from microscopic to macroscopic. In order of appearance, the physical meaning of each term in Eq. (23) is discussed as follows:

a. The effects of the pressure, contamination at the interface, and shear stress caused by the fluid motion (gas phase side) on the interface
b. The effects of the pressure, contamination at the interface, and shear stress caused by the fluid motion (liquid phase side) on the interface
c. The conventional surface tension, known as the Young–Laplace formula
d. The gradient of the surface tension in the tangential direction; this term differs from the conventional term in Eq. (11), and we discuss this difference in Section 3.4

e. The synergy effect of the change in ψ in the normal and tangential directions at the interface
f. The change in the normal direction with respect to the ψ gradient in the tangential direction; this term arises if the ψ gradient changes in the tangential direction at the interface of the gas or liquid phase
g. The Marangoni effect term, which depends on the temperature difference because of the temperature-dependent coefficients a and b
h. The effect of contamination in the tangential direction
i. The change in the tangential direction with respect to the ψ gradient in the tangential direction; this term may simply be the tensile force
j. The synergy effect, which is the same as term (e); however, this term is slightly different from term (e) because this term includes the curvature
k. The synergy effect of the change in the tangential direction with respect to the ψ gradient in the s_1 and s_2 tangential directions
l. The effect of the change in the tangential direction with respect to the ψ gradient in the tangential direction; this term may simply be the tensile force, and the tangential directions are different from term (i).

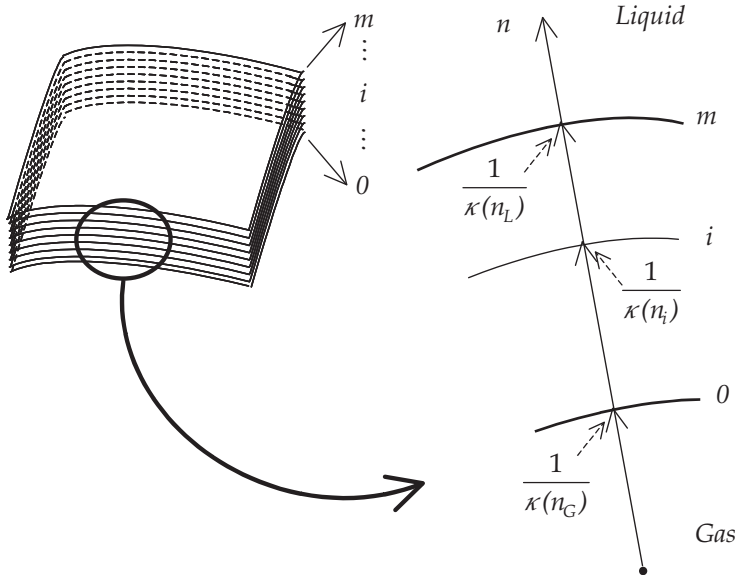

Fig. 5. Curvature through the interface

3.3 Order estimation of jump condition

We now consider the order estimation of the thermodynamic jump condition. The characteristic velocity, length, density, viscosity, interfacial thickness, surface tension coefficient, and electrostatic potential at the interface are U_0 [m/s], L[m], $\bar{\rho} = (\rho_l + \rho_g)/2$ [kg/m^3], μ_0 [kg/ms], δ [m], σ_0 [N/m], and V_0 [V], respectively. The characteristic pressure is $\bar{\rho}U_0^2$ or P_0 [N/m^2], and the interfacial wavelength is λ_1 (s_1 axis) or λ_2 (s_2 axis) [m].

First, Equation (23) is divided by $\bar{\rho}U_0^2$ and then normalized by other characteristic values. In particular, we normalize n, κ_1, and κ_2 by δ and s_1 and s_2 by λ_1 and λ_2, respectively. This normalization reduces Eq. (23) to

$$
\begin{aligned}
0 = &\underbrace{-\left[\left(-\frac{1}{\mathrm{E}}P_{\mathrm{G}}^{*}-\frac{1}{4\mathrm{N}}\pi_{\mathrm{G}}^{*}\right)\boldsymbol{n}_{\mathrm{G}}+\frac{1}{\mathrm{Re}}\boldsymbol{n}_{\mathrm{G}}\cdot\boldsymbol{\tau}_{\mathrm{G}}^{*}\right]}_{(a)'}\underbrace{-\left[\left(-\frac{1}{\mathrm{E}}P_{\mathrm{L}}^{*}-\frac{1}{4\mathrm{N}}\pi_{\mathrm{L}}^{*}\right)\boldsymbol{n}_{\mathrm{L}}+\frac{1}{\mathrm{Re}}\boldsymbol{n}_{\mathrm{L}}\cdot\boldsymbol{\tau}_{\mathrm{L}}^{*}\right]}_{(b)'}\\
&\underbrace{-\boldsymbol{n}_{\mathrm{G}}\frac{1}{\mathrm{We}}\left(\kappa_1^{*}+\kappa_2^{*}\right)\sigma^{*}}_{(c)'}\underbrace{-\varepsilon\left(\boldsymbol{t}_1\frac{1}{\mathrm{We}_1}\frac{1}{2}\frac{\partial\,\sigma^{*}}{\partial\,s_1^{*}}+\boldsymbol{t}_2\frac{1}{\mathrm{We}_2}\frac{1}{2}\frac{\partial\,\sigma^{*}}{\partial\,s_2^{*}}\right)}_{(d)'}\\
&\underbrace{-\boldsymbol{n}_{\mathrm{G}}\varepsilon d^{*}\int_{-\infty}^{+\infty}\left[\frac{\mathrm{Kn}_1}{\mathrm{We}_1}\frac{\partial}{\partial\,s_1^{*}}\left(\frac{\partial\,\psi}{\partial\,n^{*}}\frac{\partial\,\psi}{\partial\,s_1^{*}}\right)+\frac{\mathrm{Kn}_2}{\mathrm{We}_2}\frac{\partial}{\partial\,s_2^{*}}\left(\frac{\partial\,\psi}{\partial\,n^{*}}\frac{\partial\,\psi}{\partial\,s_2^{*}}\right)\right]\mathrm{d}n^{*}}_{(e)'}\\
&\underbrace{+\boldsymbol{n}_{\mathrm{G}}\varepsilon d^{*}\int_{-\infty}^{+\infty}\frac{1}{2}\frac{\partial}{\partial\,n^{*}}\left[\frac{\mathrm{Kn}_1}{\mathrm{We}_1}\left(\frac{\partial\,\psi}{\partial\,s_1^{*}}\right)^2+\frac{\mathrm{Kn}_2}{\mathrm{We}_2}\left(\frac{\partial\,\psi}{\partial\,s_2^{*}}\right)^2\right]\mathrm{d}n^{*}}_{(f)'}\\
&\underbrace{-\varepsilon\int_{-\infty}^{+\infty}\left(\boldsymbol{t}_1\frac{\mathrm{Kn}_1}{\mathrm{E}}\frac{\partial\,\psi}{\partial\,s_1^{*}}+\boldsymbol{t}_2\frac{\mathrm{Kn}_2}{\mathrm{E}}\frac{\partial\,\psi}{\partial\,s_2^{*}}\right)\left(-a^{*}\psi+b^{*}\psi^3\right)\mathrm{d}n^{*}}_{(g)'}\\
&\underbrace{+\int_{-\infty}^{+\infty}\left(\boldsymbol{t}_1\frac{\mathrm{Kn}_1}{4\mathrm{N}}\frac{\partial\,\pi_{\mathrm{i}}^{*}}{\partial\,s_1^{*}}+\boldsymbol{t}_2\frac{\mathrm{Kn}_2}{4\mathrm{N}}\frac{\partial\,\pi_{\mathrm{i}}^{*}}{\partial\,s_2^{*}}\right)\mathrm{d}n^{*}}_{(h)'}\\
&\underbrace{+\frac{\varepsilon d^{*}}{2}\int_{-\infty}^{+\infty}\left[\boldsymbol{t}_1\frac{\mathrm{Kn}_1}{\mathrm{We}_1}\frac{\partial}{\partial\,s_1^{*}}\left(\frac{\partial\,\psi}{\partial\,s_1^{*}}\right)^2+\boldsymbol{t}_2\frac{\mathrm{Kn}_2}{\mathrm{We}_2}\frac{\partial}{\partial\,s_2^{*}}\left(\frac{\partial\,\psi}{\partial\,s_2^{*}}\right)^2\right]\mathrm{d}n^{*}}_{(i)'}\\
&\underbrace{+\varepsilon d^{*}\left(\kappa_1^{*}+\kappa_2^{*}\right)\int_{-\infty}^{+\infty}\left(\boldsymbol{t}_1\frac{1}{\mathrm{We}_1}\frac{\partial\,\psi}{\partial\,s_1^{*}}+\boldsymbol{t}_2\frac{1}{\mathrm{We}_2}\frac{\partial\,\psi}{\partial\,s_2^{*}}\right)\left(\frac{\partial\,\psi}{\partial\,n^{*}}\right)\mathrm{d}n^{*}}_{(j)'}\\
&\underbrace{+\varepsilon d^{*}\int_{-\infty}^{+\infty}\left[\boldsymbol{t}_1\frac{\mathrm{Kn}_2^2}{\mathrm{We}_1}\frac{\partial}{\partial\,s_2^{*}}\left(\frac{\partial\,\psi}{\partial\,s_1^{*}}\frac{\partial\,\psi}{\partial\,s_2^{*}}\right)+\boldsymbol{t}_2\frac{\mathrm{Kn}_1^2}{\mathrm{We}_2}\frac{\partial}{\partial\,s_1^{*}}\left(\frac{\partial\,\psi}{\partial\,s_1^{*}}\frac{\partial\,\psi}{\partial\,s_2^{*}}\right)\right]\mathrm{d}n^{*}}_{(k)'}\\
&\underbrace{-\frac{\varepsilon d^{*}}{2}\int_{-\infty}^{+\infty}\left[\boldsymbol{t}_1\frac{\mathrm{Kn}_2^2}{\mathrm{We}_1}\frac{\partial}{\partial\,s_1^{*}}\left(\frac{\partial\,\psi}{\partial\,s_2^{*}}\right)^2+\boldsymbol{t}_2\frac{\mathrm{Kn}_1^2}{\mathrm{We}_2}\frac{\partial}{\partial\,s_2^{*}}\left(\frac{\partial\,\psi}{\partial\,s_1^{*}}\right)^2\right]\mathrm{d}n^{*}}_{(l)'}.
\end{aligned}
\tag{24}
$$

In Eq. (24), the dimensionless numbers are

$$\mathrm{E}=\frac{\bar{\rho}U_0^2}{P_0} \quad \mathrm{N}=\frac{L\delta^2\bar{\rho}U_0^2}{z_i e V_0} \quad \mathrm{Re}=\frac{\bar{\rho}U_0 L}{\mu_0} \quad \mathrm{We}=\frac{\bar{\rho}U_0^2\delta}{\sigma_0} \tag{25 a, b, c, d}$$

$$\mathrm{We}_1=\frac{\bar{\rho}U_0^2\lambda_1}{\sigma_0} \quad \mathrm{We}_2=\frac{\bar{\rho}U_0^2\lambda_2}{\sigma_0} \quad \mathrm{Kn}_1=\frac{\delta}{\lambda_1} \quad \mathrm{Kn}_2=\frac{\delta}{\lambda_2} \tag{26 a, b, c, d}$$

Of these equations, we especially focus on Eq. (25b).

Focusing on the electrical repulsive and hydrodynamic forces, we discuss a situation in which two bubbles either coalesce or bounce off each other. In terms (*a*)', (*b*)', and (*h*)' of Eq. (24), the dimensionless number N represents the relationship between the electrostatic force due to contamination at the interface and the hydrodynamic force. With respect to the dimensionless number N, we assume a situation in which bubbles A and B interact and there is a difference in the velocities of the bubbles, as shown in Fig. 6. Here, we simply take the interfacial electrostatic potential of an experimental value as the measured ζ potential of gas bubbles (Graciaa et al., 1995). The measured ζ potential is on the order of tens of millivolts. The density is 10^3 [kg/m^3], and δ is 10^{-9} [m]. The elementary charge is 10^{-19} [C]. If the characteristic length L corresponding to the bubble diameter is 1 [mm], and the characteristic velocity corresponding to the relative bubble velocity between bubbles A and B is 1 [m/s], then the order of the inverse of the dimensionless number N in terms (*a*)', (*b*)', and (*h*)' becomes 10^{-2}. This means that the electrostatic force due to contamination can be ignored when compared with the hydrodynamic force. However, if the characteristic velocity is 0.01 [m/s], the order of the inverse of the dimensionless number N becomes 10^2, and the electrostatic force due to contamination is significant when compared to the hydrodynamic force. This order estimation indicates that the dimensionless number N may be important for evaluating bubble coalescence and repulsion when focusing on both the electrostatic potential at the interface and the bubble velocity. In contrast, assume a situation where the relative bubble velocity between bubbles A and B is 0, as shown in Fig. 6 (i.e., the

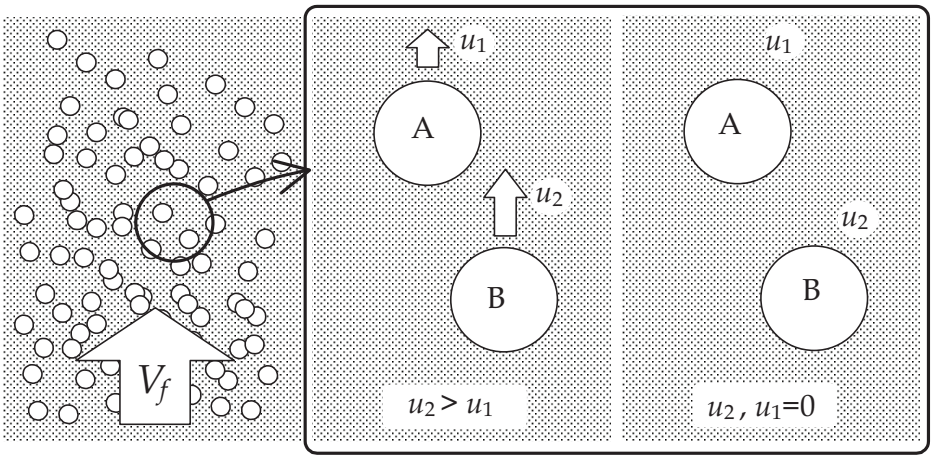

V_f: Fluid velocity $u_{1,2}$: Relative velocity $u_{1,2}$: Relative velocity

Fig. 6. Schematic of two microbubbles

characteristic velocity is the bubble velocity). If the bubble velocity approaches zero and the bubble diameter decreases, the inverse of the dimensionless number N increases. This indicates that the electrostatic force due to contamination at the interface is significant when compared to the hydrodynamic force, although it depends on the magnitude of the electrostatic potential at the interface. In other words, it is difficult to deform the bubble; it maintains a spherical shape except for the effect of the electrostatic force or mass transfer at the interface. In this situation, the dimensionless number N roughly explains that the breakup of a small bubble has difficult occurring if the bubble diameter is very small.

3.4 Consideration of surface tension gradient

The thermodynamic jump condition seems to be the same as the conventional jump condition when we focus on terms (a)–(d) in Eq. (23). However, the detailed formula of (d) differs from that of the conventional one. In this section, we discuss term (d).

The interfacial coordinate system shown in Fig. 7 is reconsidered using the same notations as in Section 3.2: n, s_1, and s_2. Vector $\boldsymbol{t}$ is defined on the l axis and consists of $\boldsymbol{t}_1$ and $\boldsymbol{t}_2$. Unit vectors $\boldsymbol{t}_1$ and $\boldsymbol{t}_2$ are the tangential vectors of the s_1 and s_2 axes, respectively. Here, $\boldsymbol{t} = \boldsymbol{t}_1 + \boldsymbol{t}_2$. However, the coordinate system in Fig. 7 has different implications from the implication in Fig. 4: the interface shown in Fig. 7 is a statistical interface obtained after integrating the elemental interfaces of Fig. 4. This means that the integrated interface is the macroscopic interface in which the interface can be recognized geometrically, such as a plane or spherical surface. Based on these concepts, we discuss term (d).

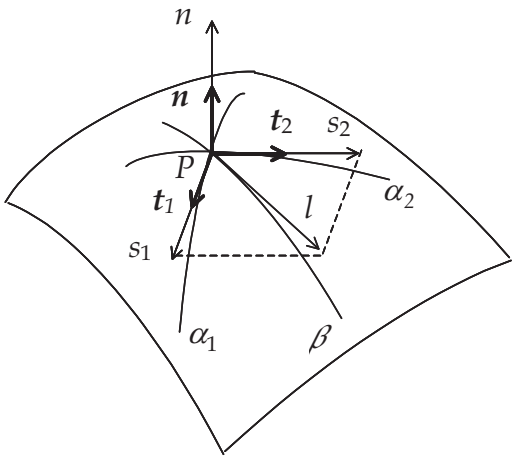

Fig. 7. Statistical local interface

Let $\boldsymbol{f}$ denote term (d) in Eq. (23). This term can be expressed as

$$\boldsymbol{f} = \boldsymbol{f}_1 + \boldsymbol{f}_2 \tag{27}$$

Equation (27) is a resultant force with respect to the gradient of surface tension in the tangential direction. In this equation, force $\boldsymbol{f}_1$ is the gradient of the surface tension defined on the s_1 axis, and force $\boldsymbol{f}_2$ is defined on the s_2 axis as follows:

$$\boldsymbol{f}_1 = \boldsymbol{t}_1 \frac{1}{2} \frac{\partial \sigma}{\partial s_1} \tag{28}$$

$$\boldsymbol{f}_2 = \boldsymbol{t}_2 \frac{1}{2} \frac{\partial \sigma}{\partial s_2} \tag{29}$$

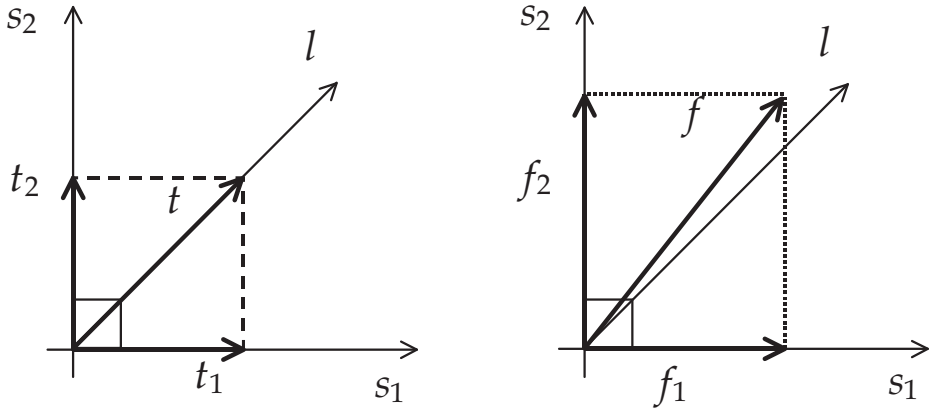

Fig. 8. Vector diagram in the s_1–s_2 tangential plane: (a) Unit base vector t_1, t_2 (t=t_1+t_2), (b) Surface force f_1, f_2(f=f_1+f_2)

Therefore, an image of Eq. (27) is represented by a vector diagram, as shown in Fig. 8. The direction of $\boldsymbol{f}$ is arbitrary in the s_1–s_2 plane, as shown in Fig. 8b, because the magnitude of $\boldsymbol{f}_1$ is not always equal to that of $\boldsymbol{f}_2$. However, if the magnitude of $\boldsymbol{f}_1$ is equal to that of $\boldsymbol{f}_2$, then

$$\frac{\partial \sigma}{\partial s_1} = \frac{\partial \sigma}{\partial s_2} \tag{30}$$

This equation indicates that the direction of $\boldsymbol{f}$ is parallel to that of the l axis. Therefore, the resultant force $\boldsymbol{f}$ is revaluated by using vector $\tilde{\boldsymbol{t}}$, which is a unit tangential vector of the l axis. Eventually, Equation (27) is transformed as follows:

$$\begin{aligned} \boldsymbol{f} &= \left(\boldsymbol{t}_1 \frac{1}{2} \frac{\partial \sigma}{\partial s_1} + \boldsymbol{t}_2 \frac{1}{2} \frac{\partial \sigma}{\partial s_2} \right) \\ &= \frac{1}{2} \frac{\mathrm{d} \sigma}{\mathrm{d} l} \left(\boldsymbol{t}_1 \frac{\partial l}{\partial s_1} + \boldsymbol{t}_2 \frac{\partial l}{\partial s_2} \right) \\ &= \frac{\sqrt{2}}{2} \frac{\mathrm{d} \sigma}{\mathrm{d} l} (\boldsymbol{t}_1 + \boldsymbol{t}_2) \\ &= \frac{\mathrm{d} \sigma}{\mathrm{d} l} \tilde{\boldsymbol{t}} \end{aligned} \tag{31}$$

In this equation, $\tilde{\boldsymbol{t}}$ is $\boldsymbol{t}/|\boldsymbol{t}|$. By replacing term (d) in Eq. (23) with Eq. (31), we establish that the thermodynamic jump condition agrees with the conventional condition except for terms (e)–(j) in Eq. (23). This result suggests that the conventional jump condition holds under the conditions of Eqs. (20) and (30). Therefore, the conventional jump condition is restricted to spherical bubbles or droplets and is inaccurate when the relationship between the surface tensions of the s_1 and s_2 directions is imbalanced.

4. Consideration of Kelvin equation

We consider the equilibrium state where the gas and liquid phases coexist and temperature is constant. The gas–liquid interface is a flat surface. In this situation, the amount of evaporated liquid from the gas phase to the liquid phase is determined by the relationship between the saturated vapor pressure and ambient pressure if the temperature is constant. The vapor in the gas phase condenses to the liquid phase when the ambient pressure is increased to greater than the saturated vapor pressure. On the other hand, the liquid evaporates to the gas phase when the ambient pressure is decreased to less than the saturated vapor pressure. This is formulated by considering the changes in chemical potential thermodynamically. The same discussion is applied to a bubble and droplet. However, a bubble or droplet has a curvature. The vapor pressure of a droplet takes a different value when the interface has a curvature. The concrete equation is as follows (Butt et al., 2003).

$$\ln\left(\frac{P_\kappa}{P^*}\right) = \frac{2H\sigma V_m}{\mathrm{R}T} \tag{32}$$

In this equation, P^* and P_κ represent the vapor pressures where the gas–liquid interface is flat and with a curvature, respectively. H [1/m^3], σ [N/m], V_m [m^3/kg], R [J/kg K], and T [K] are the mean curvature, surface tension coefficient, specific volume, gas constant, and temperature, respectively. Equation (32) is mainly derived based on both the Gibbs–Duhem equation and Young-Laplace equation from the thermodynamic point of view. In this section, we show that the Kelvin equation can be derived from the multi-scale multiphase flow equation.

4.1 Derivation of Kelvin equation from multi-scale multiphase flow equation

The Chapman–Enskog expansion is applied to the conventional Navier–Stokes equation to derive the multi-scale multiphase flow equation from which the thermodynamic interfacial jump condition is finally derived. In this section, the Kelvin equation is derived using the same procedure.

Figure 9 shows a schematic of a multi-scale concept around the interface. $O(1)$ represents the order of a macroscopic scale. ε and ε^2 represent mesoscopic scales: the scale of ε is smaller than that of ε^2. However, we assume that the continuum approximation holds in each scale. Based on this assumption, we consider the Kelvin equation.

By considering the Chapman–Enskog expansion in Eq. (7) and ε until the second order, the following equation is derived.

$$\rho\frac{\mathrm{D}\,\boldsymbol{u}}{\mathrm{D}\,t^{(0)}} + \varepsilon\rho\frac{\mathrm{D}\,\boldsymbol{u}'}{\mathrm{D}\,t^{(1)}} + \varepsilon^2\rho\frac{\mathrm{D}\,\boldsymbol{u}''}{\mathrm{D}\,t^{(2)}} = -\boldsymbol{\nabla}^{(0)}\cdot\boldsymbol{T} - \varepsilon\boldsymbol{\nabla}^{(1)}\cdot\boldsymbol{T}' - \varepsilon^2\boldsymbol{\nabla}^{(2)}\cdot\boldsymbol{T}'' + \rho\boldsymbol{g}, \tag{33}$$

Here, the diffusion process is proportional to the gradient of the chemical potential (Onsager, 1931a, 1931b), which yields the thermodynamic driving force as follows:

$$\begin{aligned} \boldsymbol{F}'' &= -\rho \boldsymbol{\nabla} \frac{\delta F}{\delta \tilde{\eta}} \\ &= -\rho \boldsymbol{\nabla} \mu \end{aligned} \tag{34}$$

The diffusion flux ($\boldsymbol{J}$) is then represented by

$$\boldsymbol{J} = -mC\boldsymbol{\nabla}\mu \tag{35}$$

where, m and C are the mobility [m·mol/N·s] and mol concentration[mol/m^3], respectively. In the present study, we assumed that the thermodynamic force (Eq. (34)) corresponds to T'' in Eq. (33) as follows:

$$-\varepsilon^2 \boldsymbol{\nabla}^{(2)} \cdot \boldsymbol{T}'' = \varepsilon^2 \boldsymbol{F}'' \tag{36}$$

In Eq. (33), the order of ε is smaller than that of $O(1)$. Thus, the order of ε^2 is smaller than that of ε. Therefore, an interfacial phenomena characterized by ε^2 can be negligible compared to that of $O(1)$.
However, the driving force (Eq. (34)) characterized by small scales such as ε^2 will affect phenomena at large scales such as $O(1)$ after enough time, even if there are differences between the scales in Eq. (33).
Considering Eqs. (33), (34), and (36) and performing a simple tensor analysis, such as the derivation of Eq. (10), gives

$$\begin{aligned} \rho \frac{\mathrm{D}\,\boldsymbol{u}}{\mathrm{D}\,t^{(0)}} + \varepsilon\rho \frac{\mathrm{D}\,\boldsymbol{u}'}{\mathrm{D}\,t^{(1)}} + \varepsilon^2 \rho \frac{\mathrm{D}\,\boldsymbol{u}''}{\mathrm{D}\,t^{(2)}} = &-\boldsymbol{\nabla}^{(0)} \cdot \boldsymbol{T} + \varepsilon \boldsymbol{\nabla}^{(1)} \cdot \left(f_0(\psi) \boldsymbol{I} \right) \\ &-\varepsilon d \boldsymbol{\nabla}^{(1)} \psi \left(\boldsymbol{\nabla}^{(1)} \cdot \boldsymbol{\nabla}^{(1)} \psi \right) - \varepsilon^2 \rho \boldsymbol{\nabla}^{(2)} \mu + \rho \boldsymbol{g}, \end{aligned} \tag{37}$$

Equation (37) is transformed into the interfacial coordinates system in a similar manner to that discussed in section 3.2. For the sake of simplicity, we show the transformation of the fourth term on the right-hand side of Eq. (37). Referring to Eq. (13) in section 3.2, the fourth term on the right-hand side of Eq. (37) is transformed as follows:

$$-\varepsilon^2 \rho \boldsymbol{\nabla}^{(2)} \mu \to -\varepsilon^2 \rho \left(\boldsymbol{t}_1 \frac{\partial \mu}{\partial s_1^{(2)}} + \boldsymbol{t}_2 \frac{\partial \mu}{\partial s_2^{(2)}} + \boldsymbol{n}_{\mathrm{L}} \frac{\partial \mu}{\partial n^{(2)}} \right) \tag{38}$$

Integration of this equation over the interface gives

$$-\varepsilon^2 \rho \int_{-\infty}^{\infty} \left(\boldsymbol{t}_1 \frac{\partial \mu}{\partial s_1^{(2)}} + \boldsymbol{t}_2 \frac{\partial \mu}{\partial s_2^{(2)}} \right) \mathrm{d}n - \varepsilon^2 \rho \boldsymbol{n}_{\mathrm{L}} \int_{-\infty}^{\infty} \frac{\partial \mu}{\partial n^{(2)}} \mathrm{d}n \tag{39}$$

In this calculation, chemical potential is assumed to be constant along the interface in tangential direction. Therefore, the first term in Eq. (39) is omitted. Thus, Equation (38) is calculated as follows:

$$-\varepsilon^2\rho\boldsymbol{\nabla}^{(2)}\mu=-\varepsilon^2\rho\boldsymbol{n}_{\mathrm{L}}\int_{-\infty}^{\infty}\frac{\partial\mu}{\partial n^{(2)}}\mathrm{d}n \tag{40}$$

Finally, Equation (37) is transformed into the interfacial coordinates system as follows:

$$\begin{aligned}0=&\underbrace{-\left[\left(-P_{\mathrm{G}}-\varepsilon\pi_{\mathrm{G}}\right)\boldsymbol{n}_{\mathrm{G}}+\boldsymbol{n}_{\mathrm{G}}\cdot\boldsymbol{\tau}_{\mathrm{G}}\right]}_{(a)}\underbrace{-\left[\left(-P_{\mathrm{L}}-\varepsilon\pi_{\mathrm{L}}\right)\boldsymbol{n}_{\mathrm{L}}+\boldsymbol{n}_{\mathrm{L}}\cdot\boldsymbol{\tau}_{\mathrm{L}}\right]}_{(b)}\underbrace{-\boldsymbol{n}_{\mathrm{G}}\varepsilon\left(\kappa_1+\kappa_2\right)\sigma}_{(c)}\\
&\underbrace{-\varepsilon\left(\boldsymbol{t}_1\frac{1}{2}\frac{\partial\,\sigma}{\partial\,s_1^{(1)}}+\boldsymbol{t}_2\frac{1}{2}\frac{\partial\,\sigma}{\partial\,s_2^{(1)}}\right)}_{(d)}\underbrace{-\boldsymbol{n}_{\mathrm{G}}\varepsilon d\int_{-\infty}^{+\infty}\left[\frac{\partial}{\partial\,s_1^{(1)}}\left(\frac{\partial\,\psi}{\partial\,n^{(1)}}\frac{\partial\,\psi}{\partial\,s_1^{(1)}}\right)+\frac{\partial}{\partial\,s_2^{(1)}}\left(\frac{\partial\,\psi}{\partial\,n^{(1)}}\frac{\partial\,\psi}{\partial\,s_2^{(1)}}\right)\right]\mathrm{d}n}_{(e)}\\
&\underbrace{+\boldsymbol{n}_{\mathrm{G}}\varepsilon d\int_{-\infty}^{+\infty}\frac{1}{2}\frac{\partial}{\partial\,n^{(1)}}\left[\left(\frac{\partial\,\psi}{\partial\,s_1^{(1)}}\right)^2+\left(\frac{\partial\,\psi}{\partial\,s_2^{(1)}}\right)^2\right]\mathrm{d}n}_{(f)}\underbrace{-\varepsilon\int_{-\infty}^{+\infty}\left(\boldsymbol{t}_1\frac{\partial\,\psi}{\partial\,s_1^{(1)}}+\boldsymbol{t}_2\frac{\partial\,\psi}{\partial\,s_2^{(1)}}\right)\left(-a\psi+b\psi^3\right)\mathrm{d}n}_{(g)}\\
&\underbrace{+\varepsilon\int_{-\infty}^{+\infty}\left(\boldsymbol{t}_1\frac{\partial\,\pi_{\mathrm{i}}}{\partial\,s_1^{(1)}}+\boldsymbol{t}_2\frac{\partial\,\pi_{\mathrm{i}}}{\partial\,s_2^{(1)}}\right)\mathrm{d}n}_{(h)}\underbrace{+\frac{\varepsilon d}{2}\int_{-\infty}^{+\infty}\left[\boldsymbol{t}_1\frac{\partial}{\partial\,s_1^{(1)}}\left(\frac{\partial\,\psi}{\partial\,s_1^{(1)}}\right)^2+\boldsymbol{t}_2\frac{\partial}{\partial\,s_2^{(1)}}\left(\frac{\partial\,\psi}{\partial\,s_2^{(1)}}\right)^2\right]\mathrm{d}n}_{(i)}\\
&\underbrace{+\varepsilon d\left(\kappa_1+\kappa_2\right)\int_{-\infty}^{+\infty}\left(\boldsymbol{t}_1\frac{\partial\,\psi}{\partial\,s_1^{(1)}}+\boldsymbol{t}_2\frac{\partial\,\psi}{\partial\,s_2^{(1)}}\right)\left(\frac{\partial\,\psi}{\partial\,n^{(1)}}\right)\mathrm{d}n}_{(j)}\\
&\underbrace{-\frac{\varepsilon d}{2}\int_{-\infty}^{+\infty}\left[\boldsymbol{t}_1\frac{\partial}{\partial\,s_1^{(1)}}\left(\frac{\partial\,\psi}{\partial\,s_2^{(1)}}\right)^2+\boldsymbol{t}_2\frac{\partial}{\partial\,s_2^{(1)}}\left(\frac{\partial\,\psi}{\partial\,s_1^{(1)}}\right)^2\right]\mathrm{d}n}_{(l)}\\
&\underbrace{-\varepsilon^2\rho\boldsymbol{n}_{\mathrm{G}}\int_{-\infty}^{\infty}\frac{\partial\mu}{\partial n^{(2)}}\mathrm{d}n}_{(m)}\underbrace{+\varepsilon d\int_{-\infty}^{+\infty}\left[\boldsymbol{t}_1\frac{\partial}{\partial\,s_2^{(1)}}\left(\frac{\partial\,\psi}{\partial\,s_1^{(1)}}\frac{\partial\,\psi}{\partial\,s_2^{(1)}}\right)+\boldsymbol{t}_2\frac{\partial}{\partial\,s_1^{(1)}}\left(\frac{\partial\,\psi}{\partial\,s_1^{(1)}}\frac{\partial\,\psi}{\partial\,s_2^{(1)}}\right)\right]\mathrm{d}n}_{(k)}\end{aligned} \tag{41}$$

Here, for the sake of simplicity, we focus on the terms (a), (b), (c), and (m) (this is new term.) as follows:

$$0=\left(P_{\mathrm{G}}-P_{\mathrm{L}}\right)\boldsymbol{n}_{\mathrm{G}}-\boldsymbol{n}_{\mathrm{G}}\varepsilon\left(\kappa_1+\kappa_2\right)\sigma-\varepsilon^2\rho\boldsymbol{n}_{\mathrm{G}}\int_{-\infty}^{\infty}\frac{\partial\mu}{\partial n^{(2)}}\mathrm{d}n \tag{42}$$

In this equation, the third term is transformed into

$$\int_{-\infty}^{\infty}\frac{\partial\mu}{\partial n^{(2)}}\mathrm{d}n=\int_{-\infty}^{\infty}\frac{\partial\mu}{\partial P}\frac{\partial P}{\partial n^{(2)}}\mathrm{d}n+\int_{-\infty}^{\infty}\frac{\partial\mu}{\partial T}\frac{\partial T}{\partial n^{(2)}}\mathrm{d}n \tag{43}$$

In the present discussion, change in temperature is not considered. Thus, the second term on the right-hand side of Eq. (43) is omitted. Here, the thermodynamic relation is considered as follows:

$$\mathrm{d}\mu_i=-\overline{s}_i\mathrm{d}T+\overline{V}_i\mathrm{d}P+\sum_j^{N_j}\mu_{ij}^c\mathrm{d}n_j \tag{44}$$

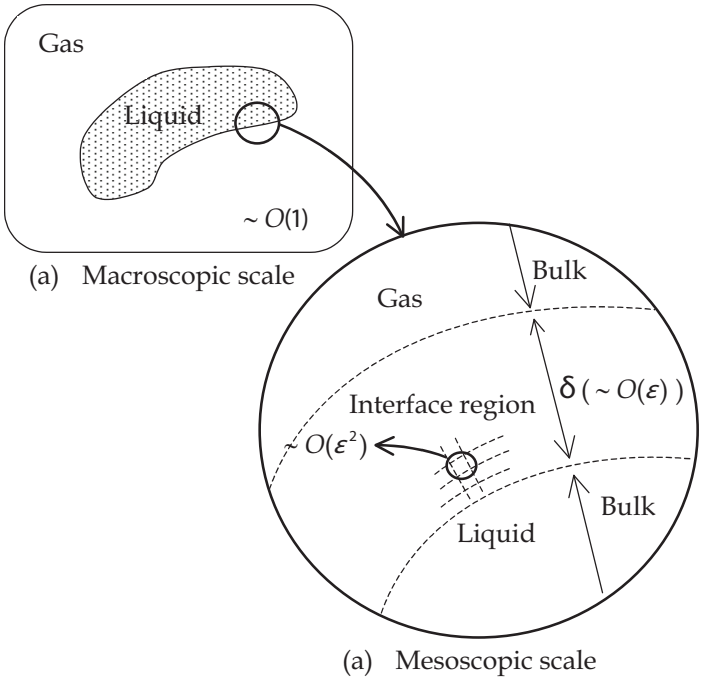

Fig. 9. Multi-scale schematic around the interface region

In this equation, $\overline{s}_i$ and $\overline{V}_i$ are the enthalpy and volume per unit mol of component *i*. In the derivation, adding or reducing new components from the external system is not considered. Thus, $\mathrm{d}n_j = 0$. The following equation is derived from Eq. (44) under constant temperature.

$$\begin{aligned}\left(\frac{\partial \mu_i}{\partial P}\right)_{T,n_j} &= \overline{V}_i \\ &= \frac{\mathrm{R}T}{P_i}\end{aligned} \tag{45}$$

Then, the substitution of Eq. (45) into the third term in Eq. (42) by considering Eq. (43) and transformation of the equation yields

$$\begin{aligned}\int_{-\infty}^{\infty} \frac{\partial \mu}{\partial n^{(2)}} \mathrm{d}n &= \int_{-\infty}^{\infty} \frac{\partial \mu}{\partial P} \frac{\partial P}{\partial n^{(2)}} \mathrm{d}n \\ &= \int_{-\infty}^{\infty} \frac{\partial \mu}{\partial P} \mathrm{d}P \\ &= \int_{P_{i\mathrm{G}}}^{P_{i\mathrm{L}}} \frac{\mathrm{R}T}{P_i} \mathrm{d}P \\ &= \mathrm{R}T \ln\left(\frac{P_{i\mathrm{L}}}{P_{i\mathrm{G}}}\right)\end{aligned} \tag{46}$$

Then, the following equation is obtained by considering Eqs. (46) and (42).

$$0 = \left(P_{\mathrm{G}} - P_{\mathrm{L}}\right)\boldsymbol{n}_{\mathrm{G}} - \boldsymbol{n}_{\mathrm{G}}\varepsilon\left(\kappa_1 + \kappa_2\right)\sigma - \varepsilon^2\rho\boldsymbol{n}_{\mathrm{G}}\mathrm{R}T\ln\left(\frac{P_{i\mathrm{L}}}{P_{i\mathrm{G}}}\right) \tag{47}$$

In this equation, P_{L} and P_{G} are the pressure in bulk phase. The Kelvin equation explains the difference in vapor pressure between the flat surface ($H = 0$) and curved surface ($H \neq 0$). The mean curvature $H = 0$ in Eq. (47) gives

$$0 = \left(P_{\mathrm{G}} - P_{\mathrm{L}}\right)\boldsymbol{n}_{\mathrm{G}} - \varepsilon^2\rho\boldsymbol{n}_{\mathrm{G}}\mathrm{R}T\ln\left(\frac{P_{i0\mathrm{L}}}{P_{i0\mathrm{G}}}\right) \tag{48}$$

Thus, the subtraction of Eq. (48) from Eq. (47) is

$$0 = \boldsymbol{n}_{\mathrm{G}}\varepsilon\left(\kappa_1 + \kappa_2\right)\sigma - \varepsilon^2\rho\boldsymbol{n}_{\mathrm{G}}\mathrm{R}T\ln\left(\frac{P_{i\mathrm{L}}}{P_{i\mathrm{G}}}\frac{P_{i0\mathrm{G}}}{P_{i0\mathrm{L}}}\right) \tag{49}$$

In Eq. (49), we assume $P_{i\mathrm{G}} \approx P_{i0\mathrm{G}}$ and focus on the liquid phase. Equation (49) becomes

$$0 = \boldsymbol{n}_{\mathrm{G}}\varepsilon\left(\kappa_1 + \kappa_2\right)\sigma - \varepsilon^2\rho\boldsymbol{n}_{\mathrm{G}}\mathrm{R}T\ln\left(\frac{P_{i\mathrm{L}}}{P_{i0\mathrm{L}}}\right) \tag{50}$$

Considering the equilibrium state in Eq. (50), the coefficient of the normal vector is set to zero. Finally, the following equation is obtained.

$$\frac{2H\sigma V_m}{\mathrm{R}T} = \varepsilon\ln\left(\frac{P_{i\mathrm{L}}}{P_{i0\mathrm{L}}}\right) \tag{51}$$

where $V_m = 1/\rho$. This equation is the Kelvin equation derived from the multi-scale multiphase flow equation.

5. Conclusion

In a previous study, a new interfacial model of the gas–liquid interface was developed based on thermodynamics, assuming that the interface has a finite thickness, similar to a thin fluid membrane. In particular, the free energy was derived based on a lattice-gas model that includes the electrostatic potential due to contamination. The free energy was incorporated into the NS equation by using the Chapman–Enskog expansion. Finally, a multi-scale multiphase flow equation was derived that characterizes the mesoscopic scale. The interfacial equation for a macroscopic-scale gas–liquid interface is characterized by a jump condition. In the present study, the jump condition at the gas–liquid interface treated by thermodynamics was derived by using the multi-scale multiphase flow equation and compared with the conventional jump condition. Finally, we developed the multi-scale gas–liquid interfacial model; this model supports the interfacial phenomena from the microscopic to macroscopic scale theoretically to give the following results:

1. The thermodynamic interfacial jump condition was derived by using the multi-scale multiphase flow equation. The present study indicated the relationship between the

mechanical and thermodynamic approaches with respect to the model of the gas–liquid interface.

2. The Marangoni-effect terms, which are related to temperature differences and contamination at the interface, were included in some additional terms derived under the thermodynamic jump condition.
3. From the normalized thermodynamic jump condition, we obtained a new dimensionless number N that represents the relationship between the electrostatic force due to contamination at the interface and the hydrodynamic force. The order estimation of N suggests that we may be able to specifically classify bubble coalescence or breakup.
4. Considering term (d) of Eq. (23), we concluded that the conventional jump condition holds true for Eqs. (20) and (30). Therefore, the conventional jump condition is restricted to the case of spherical bubbles or droplets and is inaccurate when the relationship between the surface tensions in the s_1 and s_2 tangential directions is imbalanced.
5. On the basis of the multi-scale multiphase flow equation, we derived the Kelvin equation. This result indicates that equation (37) contains the physics for the evaporation/condensation of a curved surface and will support other interfacial phenomena characterized by thermodynamics. However, more detailed discussion of Eq. (51) is needed because other terms in Eq. (41) are omitted in the derivation of Eq. (51).

In our recent study (Yonemoto & Kunugi, 2010c), the momentum jump condition was applied to a discussion on an equilibrium condition at a three-phase contact line of a sessile droplet on a smooth solid surface. Furthermore, the equilibrium condition of the sessile droplet was also considered by the thermodynamic approach (Yonemoto & Kunugi, 2009). Therefore, our new interfacial model may allow the development of a general multi-scale interfacial model that can treat two-phase and three-phase interfaces theoretically in the future.

6. References

Álvarez, E., Sanjurjo, B., Cancela, A. & Navaza, J. M. (2000). Mass transfer and influence of solutions in a bubbling column, *Chem. Eng. Res. Des.*, Vol. 78(6), September 2000, pp. 889-893

Anderson, D. M., McFadden, G. B. & Wheeler, A. A. (1998). Diffuse-interface methods in fluid mechanics, *Annu. Rev. Fluid Mech.*, Vol. 30, January 1998, pp. 139-165, ISSN 0066-4189

Aris, R. (1962). *Vectors, tensors and the basic equations of fluid mechanics*, ISBN 0486661105, Prentice-Hall

Butt, H-J, Graf, K. & Kappl, M. (2003). *Physics and chemistry of interfaces*, ISBN 3527404139, WILEY-VCH Verlag GmbH & Co. KgaA, Weinheim

Cahn, J. W., Hilliard, J. E. (1958). Free energy of a nonuniform system, I. Interfacial energy, *J. Chem. Phys.*, Vol. 28, No. 2, February 1958, pp. 258–267, ISSN 1089-7690

Chapman, S., Cowling, T. (1970). *The mathematical theory of non-uniform gases*, 3rd ed. ISBN 9780521408448, Cambridge University Press

Craig, V. S. J. (2004). Bubble coalescence and specific-ion effects, *Curr Opin Colloid Interface Sci.*, Vol. 9, August 2004, pp. 178-184, ISSN 1359-0294

Delhaye, J. M. (1974). Jump conditions and entropy surfaces in two-phase systems. Local instant formulation, *Int. J. Multiphase Flow*, Vol. 1, June 1974, pp. 395-409, ISSN 0301-9322

Fialkowski, M., Aksimentiev, A. & Holyst, R. (2001). Scaling of the euler characteristic, surface area, and curvatures in the phase separating or ordering systems, *Phys. Rev. Lett.*, Vol. 86, No. 2, January 2001, pp. 240-243, ISSN 1079-7114

Graciaa, A., Morel, G., Paulner, P., Lachaise, J. & Schechter, R. S. (1995). The ζ -potential of gas bubbles, *J. Colloid Interface Sci.*, Vol. 172, June 1995, pp. 131-136, ISSN 0021-9797

Henry, C. L., Craig, V. S. J. (2008). Ion-specific influence of electrolytes on bubble coalescence in nonaqueous solvents, *Langmuir*, Vol. 24, July 2008, pp. 7979-7985, ISSN 1520-5827

Hong, W. H. & Brauer, H. (1989). Gas-liquid mass transfer in bubble – column reactors, *Int. Chem. Eng.*, Vol. 29(3), July 1989, pp. 388-434

Lessaard, R. R. & Zieminski, S. A. (1971). Bubble coalescence and gas transfer in aqueous electrolytic solutions, *Ind. Eng. Chem. Fundam.*, Vol. 10, No. 2, May 1971, pp. 260-269, ISSN 0196-4313

Marčelja, S. (2004). Short-range forces in surface and bubble interaction, *Curr Opin Colloid Interface Sci.*, Vol. 9, August 2004, pp. 165-167, ISSN 1359-0294

Onsager, L. (1931a). Reciprocal relations in irreversible processes. I., *Phys. Rev.*, Vol. 37, February 1931a, pp. 405-426, ISSN 1536-6065

Onsager, L. (1931b). Reciprocal relations in irreversible processes. II., *Phys. Rev.*, Vol. 38, December 1931b, pp. 2265-2279, ISSN 1536-6065

Ribeiro Jr, C. P., Mewes, D. (2007). The influence of electrolytes on gas hold-up and regime transition in bubble columns, *Chem. Eng. Sci.*, Vol. 62, September 2007, pp. 4501-4509, ISSN 0009-2509

Rowlinson, J. S., Widom, B. (1984), *Molecular theory of capillarity*, Oxford University Press

Safran, S. A. (1994). *Statistical thermodynamics of surfaces, interfaces, and membranes*, ISBN 9780813340791, ADDISON-WESLEY PUBLISHING COMPANY

Scriven, L. E. (1960). Dynamics of a fluid interface: equation of motion for Newtonian surface fluids, *Chem. Eng. Sci.*, Vol. 12, May 1960, pp. 98-108, ISSN 0009-2509

Tsang, T. H., Koh, Y-H. & Koch, D. L. (2004). Bubble-size dependence of the critical electrolyte concentration for inhibition of coalescence, *J. Colloid Interface Sci.*, Vol. 275, July 2004, pp. 290-297, ISSN 0021-9797

Yonemoto, Y., Kunugi, T. & Serizawa, A. (2005). Study on bubble shape interacted with vortex motion via mathematical approach, 58th Annual Meeting of the Division of Fluid Dynamics, Vol. 50, No. 9, November 2005, p 250

Yonemoto, Y., Yanagisawa, H., Kawara, Z. & Kunugi, T. (2008). Coalescence of microbubble, *J. JSEM*, Vol. 8, No. 1, March 2008, pp. 38-44, ISSN 13464930

Yonemoto, Y., Kunugi, T. (2009). Discussion on a mechanical equilibrium condition of a sessile drop on a smooth solid surface, *J. Chem. Phys.*, Vol. 130, No. 14, April 2009, pp. 144106-1-144106-12, ISSN 1089-7690

Yonemoto. Y, Kunugi, T. (2010a). Multi-scale modeling of the gas-liquid interface based on mathematical and thermodynamic approaches, *Open transport phenom.J.*, Vol. 2, pp. 69-79

Yonemoto, Y., Kunugi, T. (2010b). Fundamental numerical simulation of microbubble interaction using multi-scale multiphase flow equation, *Microgravity Sci. Technol.*, Vol. 22, September 2010b, pp. 397-405, ISSN 1875-0494

Yonemoto, Y, Kunugi, T. (2010c). Macroscopic wettability based on an interfacial jump condition, *Phys. Rev. E.*, Vol. 81, May 2010c, pp. 056310-1-056310-8, ISSN 1550-2376

5

Heat and Mass Transfer from an Inverted Cone in a Porous Medium with Cross-Diffusion Effects

Faiz GA Awad, Precious Sibanda and Mahesha Narayana
School of Mathematical Sciences, University of KwaZulu-Natal
South Africa

1. Introduction

The study of double-diffusive convection has received considerable attention during the last several decades since this occurs in a wide range of natural settings. The origins of these studies can be traced to oceanography when hot salty water lies over cold fresh water of a higher density resulting in double-diffusive instabilities known as "salt-fingers," Stern (35; 36). Typical technological motivations for the study of double-diffusive convection range from such diverse fields as the migration of moisture through air contained in fibrous insulations, grain storage systems, the dispersion of contaminants through water-saturated soil, crystal growth and the underground disposal of nuclear wastes. Double-diffusive convection has also been cited as being of particular relevance in the modeling of solar ponds (Akbarzadeh and Manins (1)) and magma chambers (Fernando and Brandt (12)).

Double-diffusive convection problems have been investigated by, among others, Nield (28) Baines and Gill (3), Guo et al. (14), Khanafer and Vafai (17), Sunil et al. (37) and Gaikwad et al. (13). Studies have been carried out on horizontal, inclined and vertical surfaces in a porous medium by, among others, Cheng (9; 10), Nield and Bejan (29) and Ingham and Pop (32). Na and Chiou (24) presented the problem of laminar natural convection in Newtonian fluids over the frustum of a cone while Lai (18) investigated the heat and mass transfer by natural convection from a horizontal line source in saturated porous medium. Natural convection over a vertical wavy cone has been investigated by Pop and Na (33). Nakyam and Hussain (25) studied the combined heat and mass transfer by natural convection in a porous medium by integral methods.

Chamkha and Khaled (4) studied the hydromagnetic heat and mass transfer by mixed convection from a vertical plate embedded in a uniform porous medium. Chamkha (5) investigated the coupled heat and mass transfer by natural convection of Newtonian fluids about a truncated cone in the presence of magnetic field and radiation effects and Yih (38) examined the effect of radiation in convective flow over a cone. Cheng (6) used an integral approach to study the heat and mass transfer by natural convection from truncated cones in porous media with variable wall temperature and concentration. Khanafer and Vafai (17) studied the double-diffusive convection in a lid-driven enclosure filled with a fluid-saturated porous medium. Mortimer and Eyring (22) used an elementary transition state approach to obtain a simple model for Soret and Dufour effects in thermodynamically ideal mixtures of substances with molecules of nearly equal size. In their model the flow of heat in the Dufour effect was identified as the transport of the enthalpy change of activation as molecules diffuse.

The results were found to fit the Onsager reciprocal relationship (Onsager, (30)). Alam et al. (2) investigated the Dufour and Soret effects on steady combined free-forced convective and mass transfer flow past a semi-infinite vertical flat plate of hydrogen-air mixtures. They used the fourth order Runge-Kutta method to solve the governing equations of motion. Their study showed that the Dufour and Soret effects should not be neglected. Mansour et al. (21) studied the effects of a chemical reaction and thermal stratification on MHD free convective heat and mass transfer over a vertical stretching surface embedded in a porous media with Soret and Dufour effects. Narayana and Murthy (26) examined the Soret and Dufour effects on free convection heat and mass transfer from a horizontal flat plate in a Darcy porous medium.
The effects of the Soret and Dufour parameters on free convection along a vertical wavy surface in a Newtonian fluid saturated Darcy porous medium has been investigated by Narayana and Sibanda (27). Their study showed that in both the aiding and opposing buoyancy cases increasing the Soret parameter leads to a reduction in the axial mass transfer coefficient. They further showed that the effect of the Dufour parameter is to increase the heat transfer coefficient at the surface. On the other hand, the mass transfer coefficient increased with the Dufour parameter only up to a certain critical value of the Soret parameter. Beyond this critical value, the mass transfer coefficient decreased with increasing Dufour parameter values.
The thermophoresis effect on a vertical plate embedded in a non-Darcy porous medium with suction and injection and subject to Dufour and Soret effects was investigated by Partha (31). The findings in this study underlined the importance of the Dufour, Soret and dispersion parameters on heat and mass transfer. The results showed that the Soret effect is influential in increasing the concentration distribution in both aiding as well as opposing buoyancy cases.
Cheng (8) studied the Dufour and Soret effects on heat and mass transfer over a downward-pointing vertical cone embedded in a porous medium saturated with a Newtonian fluid and constant wall temperature and concentration.
In this work we investigate heat and mass transfer from an inverted smooth and a wavy cone in porous media. In the case of the smooth cone we extend the work of Murthy and Singh (23) and El-Amin (11) to include cross-diffusion effects.
As with most problems in science and engineering, the equations that describe double-diffusive convection from an inverted cone in a porous medium are highly nonlinear and do not have closed form solutions. For the smooth cone, the equations are solved used the successive linearisation method (see Makukula et al. (19; 20)) which combines a non-perturbation technique with the Chebyshev spectral collocation method to produce an algorithm that is numerically accurate. The accuracy and robustness of the linearisation method is proved by using the Matlab bvp4c numerical routine and a shooting method to solve the equations. For the wavy cone, the governing nonlinear partial differential equations are solved using the well known Keller-box method.

2. Flow over a smooth cone in porous medium

Consider the problem of double-diffusive convection flow over inverted cone with half-angle Ω, embedded in a saturated non-Darcy porous medium as shown in Figure 1. The origin of the coordinate system is at the vertex of the cone. The x-axis measures the distance along the surface of the cone and the y-axis measures the distance outward and normal to the surface of the cone. The surface of the cone is subject to a non-uniform temperature $T_w > T_\infty$ where T_∞ is the temperature far from the cone surface. The solute concentration varies from C_w on the surface of the inverted cone to a lower concentration C_∞ in the ambient fluid. The solid

and fluid phases are assumed to be in local thermal equilibrium. The governing equations for such a flow are (see Yih (38), Cheng (8), Murthy (23), El-Amin (11));

$$\frac{\partial}{\partial x}(ru) + \frac{\partial}{\partial y}(rv) = 0, \tag{1}$$

$$\frac{\partial u}{\partial y} + \frac{c\sqrt{K}}{\nu}\frac{\partial u^2}{\partial y} = \frac{Kg\beta\cos\Omega}{\nu}\left(\frac{\partial T}{\partial y} + \frac{\beta^*}{\beta}\frac{\partial C}{\partial y}\right), \tag{2}$$

$$u\frac{\partial T}{\partial x} + v\frac{\partial T}{\partial y} = \frac{\partial}{\partial y}\left(\alpha_y\frac{\partial T}{\partial y}\right) + \frac{Dk_T}{c_s c_p}\frac{\partial^2 C}{\partial y^2}, \tag{3}$$

$$u\frac{\partial C}{\partial x} + v\frac{\partial C}{\partial y} = \frac{\partial}{\partial y}\left(D_y\frac{\partial C}{\partial y}\right) + \frac{Dk_T}{c_s c_p}\frac{\partial^2 T}{\partial y^2}, \tag{4}$$

where for a thin boundary layer, $r = x\sin\Omega$, g is the acceleration due to gravity, c is an empirical constant, K is the permeability, ν is kinematic viscosity of the fluid, respectively, β and β^* are the thermal expansion and the concentration expansion coefficients, α_y and D_y are the effective thermal and mass diffusivities of the saturated porous medium defined by $\alpha_y = \alpha + \gamma du$ and $D_y = D + \xi du$, respectively, γ and ξ are coefficients of thermal and solutal dispersions, respectively, α and D are constant thermal and molecular diffusivities, k_T is the thermal diffusion ratio, c_s is concentration susceptibility and c_p is the specific heat at constant pressure. We assume a nonlinear power-law for temperature and concentration

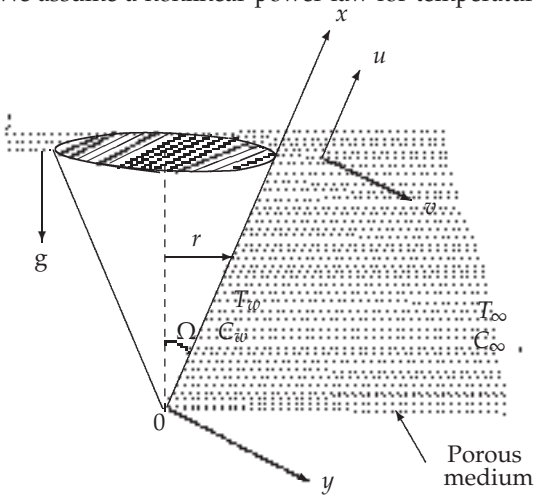

Fig. 1. Inverted smooth cone in a porous medium

variations within the fluid so that the boundary conditions are

$$v = 0,\ u = 0,\ T = T_w = T_\infty + Ax^n,\ C = C_w = C_\infty + Bx^n \quad \text{on} \quad y = 0,\ x \geq 0 \tag{5}$$

$$u = 0, \quad T = T_\infty, \quad C = C_\infty \quad \text{as} \quad y \to \infty, \tag{6}$$

where $A, B > 0$ are constants and n is the power-law index. The subscripts w, ∞ refer to the cone surface and ambient conditions respectively. We introduce the similarity variables

$$\eta = \frac{y}{x}Ra_x^{\frac{1}{2}}, \quad \psi = \alpha r Ra_x{}^{\frac{1}{2}} f(\eta), \quad \theta(\eta) = \frac{T - T_\infty}{T_w - T_\infty}, \quad \phi(\eta) = \frac{C - C_\infty}{C_w - C_\infty}, \tag{7}$$

where ψ is the stream function and Ra_x is the Rayleigh number defined by:

$$u = \frac{1}{r}\frac{\partial \psi}{\partial y}, \quad v = -\frac{1}{r}\frac{\partial \psi}{\partial x} \quad \text{and} \quad Ra_x = \frac{g\beta K \cos\Omega (T_w - T_\infty)x}{\alpha\nu}. \tag{8}$$

The dimensionless momentum, energy and concentration equations become

$$f'' + 2\lambda f' f'' - \theta' - N\phi' = 0, \tag{9}$$

$$\theta'' + \frac{n+3}{2} f\theta' - nf'\theta + Ra_\gamma (f''\theta' + f'\theta'') + D_f \phi'' = 0, \tag{10}$$

$$\frac{1}{Le}\phi'' + \frac{n+3}{2} f\phi' - nf'\phi + Ra_\xi (f''\phi' + f'\phi'') + S_r \theta'' = 0, \tag{11}$$

subject to the boundary conditions

$$\begin{aligned} &f = 0, \quad \theta = 1\,, \quad \phi = 1 \quad \text{on} \quad \eta = 0, \\ &f' = 0, \quad \theta = 0\,, \quad \phi = 0 \quad \text{on} \quad \eta \to \infty. \end{aligned} \tag{12}$$

where primes denote differentiation with respect to η. The important thermo-physical parameters are the buoyancy ratio N (where $N > 0$ represents aiding buoyancy and $N < 0$ represents the opposing buoyancy), the Dufour parameter D_f, the Soret parameter S_r, the pore depended Rayleigh number Ra_d and the Lewis number Le. These are defined as

$$N = \frac{\beta^*}{\beta}\frac{C_w - C_\infty}{T_w - T_\infty}, \; D_f = \frac{Dk_T}{c_s c_p}\frac{C_w - C_\infty}{\alpha(T_w - T_\infty)}, \; S_r = \frac{Dk_T}{c_s c_p}\frac{\alpha(T_w - T_\infty)}{C_w - C_\infty}, \tag{13}$$

$$Ra_d = \frac{g\beta K \cos(\Omega)(T_w - T_\infty)d}{\alpha\nu}, \; Le = \frac{\alpha}{D}, \; \hat{\sigma} = \frac{C\sqrt{K}\alpha}{\nu d}, \tag{14}$$

where $Ra_\gamma = \gamma Ra_d$, $Ra_\xi = \xi Ra_d$ represent the thermal and solutal dispersions respectively, $\lambda = \hat{\sigma} Ra_d$ and $\hat{\sigma}$ is an inertial parameter. The parameters of engineering interest in heat and mass problems are the local Nusselt number Nu_x and the local Sherwood number Sh_x. These parameters characterize the surface heat and mass transfer rates respectively. The local heat and mass transfer rates from the surface of the cone are characterized by the Nusselt and Sherwood numbers respectively where

$$Nu_x = -Ra_x^{\frac{1}{2}}\,[1 + Ra_\gamma f'(0)]\theta'(0) \quad \text{and} \quad Sh_x = -Ra_x^{\frac{1}{2}}\,[1 + Ra_\xi f'(0)]\phi'(0). \tag{15}$$

2.1 Method of solution

To solve equations (9) - (12), the successive linearisation method (see Makukula et al. (19; 20)) was used. This assumes that the functions $f(\eta)$, $\theta(\eta)$ and $\phi(\eta))$ may be expressed as

$$\begin{aligned} f(\eta) &= f_i(\eta) + \sum_{m=0}^{i-1} f_m(\eta), \\ \theta(\eta) &= \theta_i(\eta) + \sum_{m=0}^{i-1} \theta_m(\eta), \\ phi(\eta) &= \phi_i(\eta) + \sum_{m=0}^{i-1} \phi_m(\eta), \end{aligned} \tag{16}$$

where f_i, θ_i, ϕ_i $(i = 1, 2, 3, \ldots)$ are such that

$$\lim_{i\to\infty} f_i = \lim_{i\to\infty} \theta_i = \lim_{i\to\infty} \phi_i = 0. \tag{17}$$

The functions f_m, θ_m and ϕ_m $(m \geq 1)$ are approximations that are obtained by recursively solving the linear parts of the equations that result from substituting (16) in equations (9) - (11). Using the above assumptions, nonlinear terms in f_i, θ_i, ϕ_i and their corresponding derivatives are considered to be very small and therefore neglected.
Starting from the initial guesses

$$f_0(\eta) = 1 - e^{-\eta}, \quad \theta_0(\eta) = e^{-\eta} \quad \text{and} \quad \phi_0(\eta) = e^{-\eta}, \tag{18}$$

which are chosen to satisfy boundary conditions (12), the subsequent solutions for f_i, h_i, θ_i $i \geq 1$ are obtained by successively solving the linearized form of the governing equations.
The linearized equations to be solved are

$$a_{1,i-1}f_i''' + a_{2,i-1}f_i'' - \theta_i' - N\phi_i' = r_{1,i-1}, \tag{19}$$

$$b_{1,i-1}\theta_i'' + b_{2,i-1}\theta_i' + b_{3,i-1}\theta_i + b_{4,i-1}f_i''' + b_{5,i-1}f_i'' + b_{6,i-1}f_i + D_f\phi_i'' = r_{2,i-1}, \tag{20}$$

$$c_{1,i-1}\phi_i'' + c_{2,i-1}\phi_i' + c_{3,i-1}\phi_i + c_{4,i-1}f_i''' + c_{5,i-1}f_i'' + c_{6,i-1}f_i + Sr\theta_i'' = r_{3,i-1}, \tag{21}$$

subject to the boundary conditions

$$f_i(0) = f_i'(\infty) = 0, \;\; \theta_i(0) = \theta_i(\infty) = \phi_i(0) = \phi_i(\infty) = 0. \tag{22}$$

The coefficient parameters $a_{k,i-1}$, $b_{k,i-1}$, $c_{k,i-1}$ $(k = 1, 2, ..., 6)$, $r_{j,i-1}$ $(j = 1, 2, 3)$ are given by

$$a_{1,i-1} = 1 + 2\lambda \sum_{m=0}^{i-1} f_m', \quad a_{2,i-1} = 2\lambda \sum_{m=0}^{i-1} f_m'', \tag{23}$$

$$b_{1,i-1} = 1 + Ra_\gamma \sum_{m=0}^{i-1} f_m', \quad b_{2,i-1} = \frac{n+3}{2} \sum_{m=0}^{i-1} f_m + Ra_\gamma \sum_{m=0}^{i-1} f_m'',$$

$$b_{3,i-1} = -n \sum_{m=0}^{i-1} f_m', \quad b_{4,i-1} = Ra_\gamma \sum_{m=0}^{i-1} \theta_m', \quad b_{5,i-1} = Ra_\gamma \sum_{m=0}^{i-1} \theta_m'' - n \sum_{m=0}^{i-1} \theta_m',$$

$$b_{6,i-1} = \frac{n+3}{2} \sum_{m=0}^{i-1} \theta_m', \tag{24}$$

$$c_{1,i-1} = \frac{1}{Le} + Ra_\xi \sum_{m=0}^{i-1} f_m', \quad c_{2,i-1} = \frac{n+3}{2} \sum_{m=0}^{i-1} f_m + Ra_\xi \sum_{m=0}^{i-1} f_m'', \tag{25}$$

$$c_{3,i-1} = -n \sum_{m=0}^{i-1} f_m', \quad c_{4,i-1} = Ra_\xi \sum_{m=0}^{i-1} \phi_m', \quad c_{5,i-1} = Ra_\xi \sum_{m=0}^{i-1} \phi_m'' - n \sum_{m=0}^{i-1} \phi_m', \tag{26}$$

$$c_{6,i-1} = \frac{n+3}{2} \sum_{m=0}^{i-1} \phi_m', \tag{27}$$

$$r_{1,i-1} = -\left[\sum_{m=0}^{i-1} f_m'' + 2\lambda \sum_{m=0}^{i-1} f_m' \sum_{m=0}^{i-1} f_m'' - \sum_{m=0}^{i-1} h_m' - N \sum_{m=0}^{i-1} g_m'\right], \tag{28}$$

$$r_{2,i-1} = -\left[\sum_{m=0}^{i-1} \theta_m'' + D_f \sum_{m=0}^{i-1} \phi_m'' + \frac{n+3}{2} \sum_{n=0}^{i-1} f_m \sum_{n=0}^{i-1} \theta_n' - n \sum_{m=0}^{i-1} f_m' \sum_{m=0}^{i-1} \theta_m + Ra_\gamma \left(f_m'' \sum_{m=0}^{i-1} \theta_m' + f_m' \sum_{m=0}^{i-1} \theta_m''\right)\right],$$

$$r_{3,i-1} = -\left[\frac{1}{Le} \sum_{m=0}^{i-1} \phi_m'' + S_r \sum_{m=0}^{i-1} \phi_m'' + \frac{n+3}{2} \sum_{m=0}^{i-1} f_m \sum_{m=0}^{i-1} \phi_m' - n \sum_{m=0}^{i-1} f_m' \sum_{m=0}^{i-1} \phi_m \right. \tag{29}$$

$$\left. + Ra_\gamma \left(f_m'' \sum_{m=0}^{i-1} g_m' + f_m' \sum_{m=0}^{i-1} \phi_m''\right)\right]. \tag{30}$$

The functions f_i, θ_i, ϕ_i ($i \geq 1$) are obtained by iteratively solving equations (19) - (22). The approximate solutions for $f(\eta)$, $\theta(\eta)$ and $\phi(\eta)$ are then obtained as

$$f(\eta) \approx \sum_{m=0}^{\widehat{M}} f_m(\eta), \quad \theta(\eta) \approx \sum_{m=0}^{\widehat{M}} \theta_m(\eta), \quad \phi(\eta) \approx \sum_{m=0}^{\widehat{M}} \phi_m(\eta), \tag{31}$$

where $\widehat{M}$ is the order of the SLM approximation. Equations (19) - (22) were solved using the Chebyshev spectral collocation method where the unknown functions are approximated using Chebyshev interpolating polynomials at the Gauss-Lobatto points

$$\xi_j = \cos\frac{\pi j}{\widehat{N}}, \quad j = 0, 1, \ldots, \widehat{N}, \tag{32}$$

where $\widehat{N}$ is the number of collocation points. The physical region $[0, \infty)$ is first transformed into the region $[-1, 1]$ using the domain truncation technique in which the problem is solved on the interval $[0, L]$ instead of $[0, \infty)$. This is achieved by using the mapping

$$\frac{\eta}{L} = \frac{\xi + 1}{2}, \quad -1 \leq \xi \leq 1, \tag{33}$$

where L is the scaling parameter used to invoke the boundary condition at infinity. The unknown functions f_i, θ_i and ϕ_i are approximated at the collocation points by

$$f_i(\xi) \approx \sum_{k=0}^{N} f_i(\xi_k) T_k(\xi_j), \quad \theta_i(\xi) \approx \sum_{k=0}^{N} \theta_i(\xi_k) T_k(\xi_j), \quad \phi_i(\xi) \approx \sum_{k=0}^{N} \phi_i(\xi_k) T_k(\xi_j), \quad j = 0, 1, \ldots, \widehat{N}, \tag{34}$$

where T_k is the kth Chebyshev polynomial defined as

$$T_k(\xi) = \cos[k \cos^{-1}(\xi)]. \tag{35}$$

The derivatives at the collocation points are represented as

$$\frac{d^s f_i}{d\eta^s} = \sum_{k=0}^{\widehat{N}} \mathbf{D}_{kj}^s f_i(\xi_k), \quad \frac{d^s \theta_i}{d\eta^s} = \sum_{k=0}^{\widehat{N}} \mathbf{D}_{kj}^s \theta_i(\xi_k), \quad \frac{d^s \phi_i}{d\eta^s} = \sum_{k=0}^{\widehat{N}} \mathbf{D}_{kj}^s \phi_i(\xi_k), \quad j = 0, 1, \ldots, \widehat{N}, \tag{36}$$

where s is the order of differentiation and $\mathbf{D} = \frac{2}{L}\mathcal{D}$ with $\mathcal{D}$ being the Chebyshev spectral differentiation matrix. Substituting equations (34) - (36) in (19) - (22) leads to the matrix equation

$$\mathbf{A}_{i-1}\mathbf{X}_i = \mathbf{R}_{i-1}, \tag{37}$$

subject to the boundary conditions

$$f_i(\xi_{\widehat{N}}) = 0, \ \sum_{k=0}^{\widehat{N}} \mathbf{D}_{\widehat{N}k} f_i(\xi_k) = 0, \ \sum_{k=0}^{\widehat{N}} \mathbf{D}_{0k} f_i(\xi_k) = 0, \tag{38}$$

$$\theta_i(\xi_{\widehat{N}}) = \theta_i(\xi_0) = \phi_i(\xi_{\widehat{N}}) = \phi_i(\xi_0) = 0. \tag{39}$$

In equation (37), $\mathbf{A}_{i-1}$ is a $(3\widehat{N}+3)\times(3\widehat{N}+3)$ square matrix and $\mathbf{X}_i$ and $\mathbf{R}_i$ are $(3\widehat{N}+1)\times 1$ column vectors defined by

$$\mathbf{A}_{i-1} = \begin{bmatrix} A_{11} & A_{12} & A_{13} \\ A_{21} & A_{22} & A_{23} \\ A_{31} & A_{32} & A_{33} \end{bmatrix}, \quad \mathbf{X}_i = \begin{bmatrix} \mathbf{F}_i \\ \mathbf{\Theta}_i \\ \mathbf{\Phi}_i \end{bmatrix}, \quad \mathbf{R}_{i-1} = \begin{bmatrix} \mathbf{r}_{1,i-1} \\ \mathbf{r}_{2,i-1} \\ \mathbf{r}_{3,i-1} \end{bmatrix}, \tag{40}$$

where

$$\mathbf{F}_i = [f_i(\xi_0), f_i(\xi_1), \ldots, f_i(\xi_{\widehat{N}-1}), f_i(\xi_{\widehat{N}})]^T, \tag{41}$$

$$\mathbf{\Theta}_i = [\theta_i(\xi_0), \theta_i(\xi_1), \ldots, \theta_i(\xi_{\widehat{N}-1}), \theta_i(\xi_{\widehat{N}})]^T, \tag{42}$$

$$\mathbf{\Phi}_i = [\phi_i(\xi_0), \phi_i(\xi_1), \ldots, \phi_i(\xi_{\widehat{N}-1}), \phi_i(\xi_{\widehat{N}})]^T, \tag{43}$$

$$\mathbf{r}_{1,i-1} = [r_{1,i-1}(\xi_0), r_{1,i-1}(\xi_1), \ldots, r_{1,i-1}(\xi_{\widehat{N}-1}), r_{1,i-1}(\xi_{\widehat{N}})]^T, \tag{44}$$

$$\mathbf{r}_{2,i-1} = [r_{2,i-1}(\xi_0), r_{2,i-1}(\xi_1), \ldots, r_{2,i-1}(\xi_{\widehat{N}-1}), r_{2,i-1}(\xi_{\widehat{N}})]^T, \tag{45}$$

$$\mathbf{r}_{3,i-1} = [r_{3,i-1}(\xi_0), r_{3,i-1}(\xi_1), \ldots, r_{3,i-1}(\xi_{\widehat{N}-1}), r_{3,i-1}(\xi_{\widehat{N}})]^T, \tag{46}$$

$$A_{11} = \mathbf{a}_{1,i-1}\mathbf{D}^2 + \mathbf{a}_{2,i-1}\mathbf{D}, \quad A_{12} = -\mathbf{I}, \quad A_{13} = -N\mathbf{I} \tag{47}$$

$$A_{21} = \mathbf{b}_{4,i-1}\mathbf{D}^2 + \mathbf{b}_{5,i-1}\mathbf{D} + \mathbf{b}_{6,i-1}\mathbf{I}, A_{22} = \mathbf{b}_{1,i-1}\mathbf{D}^2 + \mathbf{b}_{2,i-1}\mathbf{D} + \mathbf{b}_{3,i-1}\mathbf{I}, \tag{48}$$

$$A_{23} = D_f\mathbf{D}^2, \ A_{31} = \mathbf{c}_{4,i-1}\mathbf{D}^2 + \mathbf{c}_{5,i-1}\mathbf{D} + \mathbf{c}_{6,i-1}\mathbf{I}, \tag{49}$$

$$A_{32} = \mathbf{c}_{1,i-1}\mathbf{D}^2 + \mathbf{c}_{2,i-1}\mathbf{D} + \mathbf{c}_{3,i-1}\mathbf{I}, \ A_{33} = S_r\mathbf{D}^2. \tag{50}$$

In the above definitions, $\mathbf{a}_{k,i-1}$, $\mathbf{b}_{k,i-1}$, $\mathbf{c}_{k,i-1}$ $(k = 1, 2, .., 6)$ are diagonal matrices of size $(\widehat{N}+1)\times(\widehat{N}+1)$ and $\mathbf{I}$ is an identity matrix of size $(\widehat{N}+1)\times(\widehat{N}+1)$. After modifying the matrix system (37) to incorporate boundary conditions (38) - (37), the solution is obtained as

$$\mathbf{X}_i = \mathbf{A}_{i-1}^{-1}\mathbf{R}_{i-1}. \tag{51}$$

Equations (9) - (12) were further solved numerically using the Matlab bvp4c routine and a shooting technique comprising the Runge-Kutta method of four slopes and the Newton-Raphson method. In solving the boundary value problem by the shooting method, the appropriate '∞' was determined through actual computations and differs for each set of parameter values.

2.2 Discussion of smooth cone results

In the absence of the inertia parameter λ, Soret and Dufour effects, the non-Darcy problem reduces to that considered by Yih (38) who solved the governing equations using the Keller-box scheme. The problem would also be a special case of the study by Cheng (8) who used a cubic spline collocation method to solve the governing equations. The results from these previous studies are used as a benchmark to test the accuracy of the linearisation method. The heat and mass transfer coefficients are given in Table 1 for different orders of the linearisation method, buoyancy and Lewis numbers. In general, the linearisation method has fully converged to the numerical results at the seventh order for all parameter values.

	N	Le	SLM			Yih (38)	Cheng (8)
			order 3	order 7	order 8		
$\frac{Nu_x}{\sqrt{Ra_x}}$	4	1	1.5990	1.7186	1.7186	1.7186	1.7186
	4	10	1.1886	1.1795	1.1795	1.1795	1.1794
	1	1	1.0869	1.0870	1.0870	1.0869	1.0870
	1	10	0.9031	0.9031	0.9031	0.9030	0.9032
	1	100	0.8141	0.8141	0.8141	0.8141	0.8143
	0	1	0.7686	0.7686	0.7686	0.7686	0.7685
	0	10	0.7686	0.7686	0.7686	0.7686	0.7685
$\frac{Sh_x}{\sqrt{Ra_x}}$	4	1	1.5990	1.7186	1.7186	1.7186	1.7186
	4	10	5.6790	5.6980	5.6980	5.6977	5.6949
	1	1	1.0869	1.0870	1.0870	1.0869	1.0870
	1	10	3.8141	3.8141	3.8141	3.8139	3.8134
	1	100	12.3653	12.3653	12.3653	12.3645	12.3377
	0	1	0.7686	0.7686	0.7686	0.7686	0.7685
	0	10	0.7686	0.7686	0.7686	0.7686	0.7686

Table 1. Benchmark results for $Nu_x/Ra_x^{\frac{1}{2}}$ and $Sh_x/Ra_x^{\frac{1}{2}}$ when $\lambda = 0.0$, $n = 0.0$, $Ra_\gamma = 0.0$, $Ra_\xi = 0.0$, $D_f = 0.0$ and $Sr = 0.0$

	Sr	D_f	SLM			bvp4c	Shooting method
			order 3	order 7	order 8		
$\frac{Nu_x}{\sqrt{Ra_x}}$	1.5	0.03	1.550183	1.550010	1.550010	1.550010	1.55001
	1.0	0.12	1.493268	1.493106	1.493106	1.493106	1.49311
	0.5	0.30	1.373266	1.373121	1.373121	1.373121	1.37312
	0.1	0.60	1.170132	1.169958	1.169958	1.169958	1.16996
$\frac{Sh_x}{\sqrt{Ra_x}}$	1.5	0.03	0.674035	0.675657	0.675657	0.675657	0.675658
	1.0	0.12	0.960995	0.962038	0.962038	0.962038	0.962039
	0.5	0.30	1.251253	1.251840	1.251840	1.251840	1.251840
	0.1	0.60	1.466009	1.466449	1.466449	1.466449	1.466450

Table 2. Comparison of values of $Nu_x/Ra_x^{\frac{1}{2}}$ and $Sh_x/Ra_x^{\frac{1}{2}}$ for $\lambda = 1.0$, $N = 1.0$, $n = 1.0$, $Ra_\gamma = 0.5$, $Ra_\xi = 0.5$ and $Le = 1.0$

Table 2 shows the effects of the Dufour and Soret parameters on the heat and mass transfer coefficients when the other parameters are held constant. The accuracy of the method is compared with the Matlab bvp4c solver and a shooting method. Again, the results demonstrate that the SLM is accurate and converges rapidly to the numerical approximations. Furthermore the results show that the heat transfer rate increases with the Soret effect but decreases with the Dufour parameter. On the other hand, mass transfer decreases with increasing Soret numbers while increasing with Dufour numbers. These findings are consistent with those of Narayana and Sibanda (26) where the heat transfer coefficient was observed to increase with increasing values of the Soret parameter while the mass transfer coefficient decreased with increasing values of the Soret parameter.

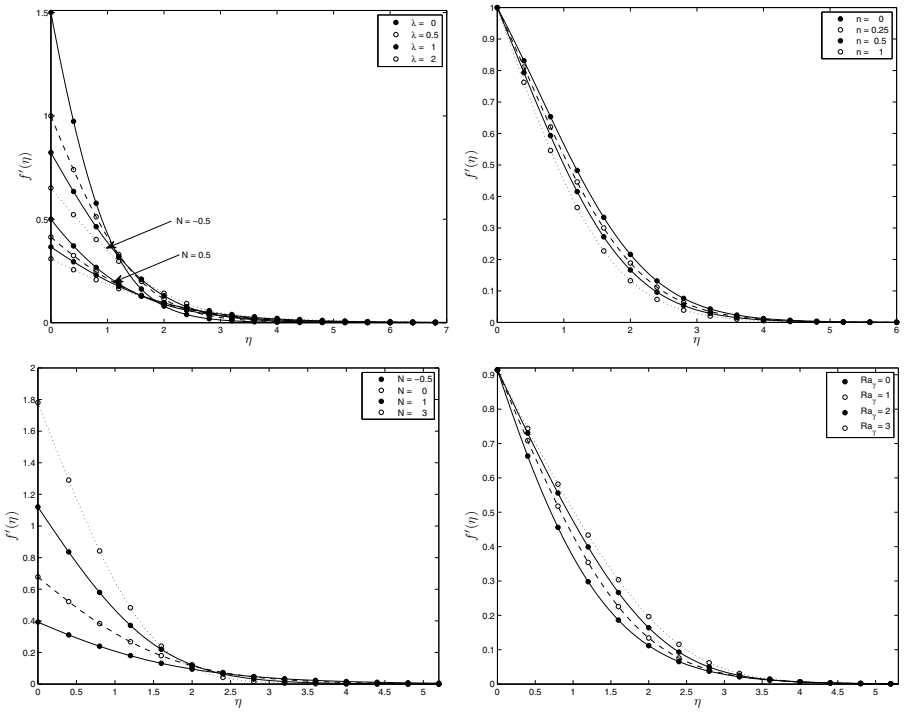

Fig. 2. Effect of (a) inertia parameter λ, (b) power-law index n, (c) buoyancy parameter N, and (d) the thermal dispersion parameter Ra_γ on the fluid velocity when $Le = 1$, $Sr = 0.3$ and $D_f = 0.2$

Figure 2 shows the effect of (a) the inertia parameter λ, (b) the power-law index n, (c) the buoyancy parameter N, and (d) the modified Rayleigh number Ra_γ on the fluid velocity for the inverted cone in a non-Darcy porous medium. Here $N < 1$ implies that the concentration buoyancy force is less than the thermal buoyancy force, $N = 1$ implies that the buoyancy forces are equal and the case $N > 1$ exists when the concentration buoyancy force exceeds the thermal buoyancy force. It is clear that the boundary layer thickness increases with λ, N and the Rayleigh number. However, the velocity decreases as the power-law index increases.

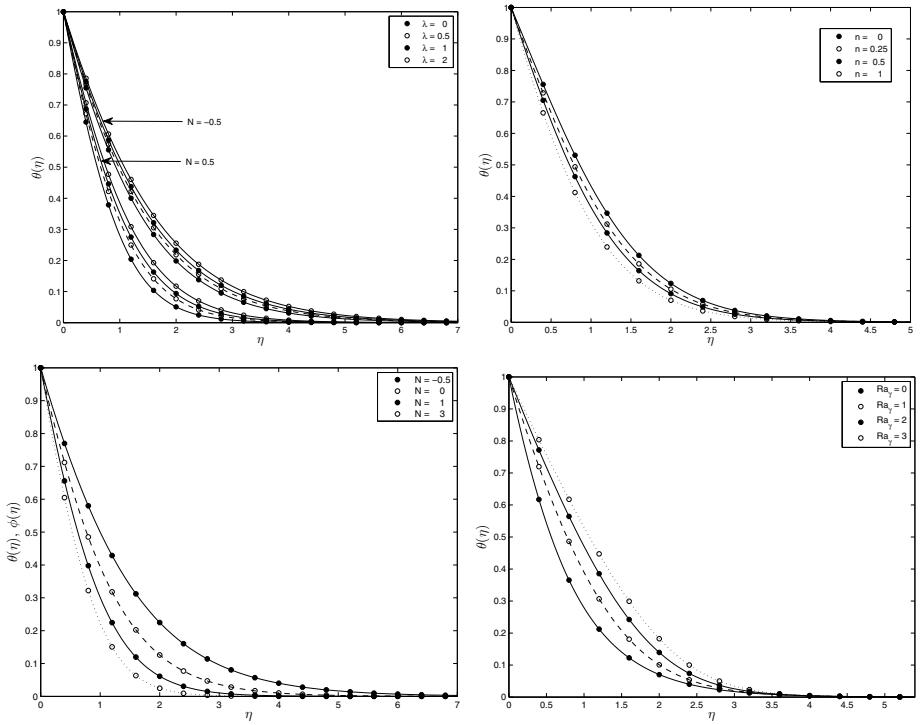

Fig. 3. Effect of (a) inertia parameter λ, (b) power-law index n, (c) the buoyancy parameter N, and (d) the thermal dispersion parameter Ra_γ on the temperature profile when $Le = 1$, $Sr = 0.3$ and $D_f = 0.2$

Figures 3 - 4 show the effects of (a) the inertia parameter λ, (b) the power-law index n, (c) the buoyancy parameter N, and (d) the thermal dispersion parameter Ra_γ on the temperature and solute concentration profiles. The temperature profiles decrease with increasing n. The concentration profiles increase whereas temperature profile decreases with increasing thermal dispersion parameter.

Figure 5 depicts the variation of the heat transfer rate $Nu_x Ra_x^{-1/2}$ and the mass transfer rate $Sh_x Ra_x^{-1/2}$ with Lewis numbers for different values of the Dufour and Soret parameters. For fixed Soret numbers, it is evident that as Le increases, the Nusselt number decreases for any particular value of D_f. The variation of the Sherwood number with Le for different values of D_f is shown in Figure 5(b). Increasing Le enhances the mass transfer rate for any particular value of D_f. It is also evident that as D_f increases the Sherwood number increases for all values of Le.

The variation of the Nusselt and Sherwood numbers with Le and Sr when the Dufour number is fixed is shown in Figures 5(c) - 5(d). Increasing Le reduces the Nusselt number for all values of Sr. Conversely, increasing the Soret parameter enhances the Nusselt number. Also, increasing Le contributes to enhancing the mass transfer rate for any particular value of Sr. On the other hand, increasing Sr reduces the Sherwood number.

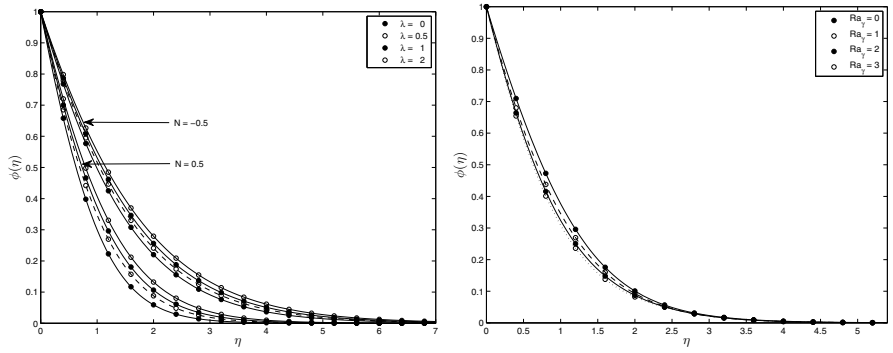

Fig. 4. Effect of (a) inertia parameter λ, and (b) the thermal dispersion parameter Ra_γ on the concentration profile when $Le = 1$, $Sr = 0.3$ and $D_f = 0.2$

3. Flow over a wavy cone in porous media

In this section we investigate the case of double-diffusive convection in a fluid around an inverted wavy cone. Figure 6 shows the model of the problem investigated. The wavy surface of the cone is described by

$$y = \sigma^*(x) = a^* \sin(\pi x/\ell), \tag{52}$$

where a^* is the amplitude of the wavy surface and 2ℓ is the characteristic length of the wave. The governing momentum, heat and solute concentration equations can be written in the form

$$\frac{\partial u}{\partial y} - \frac{\partial v}{\partial x} = \frac{gK}{\nu}\left(\beta_t \cos(\Omega)\frac{\partial T}{\partial y} + \beta_t \sin(\Omega)\frac{\partial T}{\partial x} + \beta_c \cos(\Omega)\frac{\partial C}{\partial y} + \beta_c \cos(\Omega)\frac{\partial C}{\partial x}\right), \tag{53}$$

$$u\frac{\partial T}{\partial x} + v\frac{\partial T}{\partial y} = \alpha\left(\frac{\partial^2 T}{\partial x^2} + \frac{\partial^2 T}{\partial y^2}\right) + \frac{Dk}{c_s c_p}\left(\frac{\partial^2 C}{\partial x^2} + \frac{\partial^2 C}{\partial y^2}\right), \tag{54}$$

$$u\frac{\partial C}{\partial x} + v\frac{\partial C}{\partial y} = D\left(\frac{\partial^2 C}{\partial x^2} + \frac{\partial^2 C}{\partial y^2}\right) + \frac{Dk}{c_s c_p}\left(\frac{\partial^2 T}{\partial x^2} + \frac{\partial^2 T}{\partial y^2}\right), \tag{55}$$

subject to boundary conditions

$$v = 0, \;\; T = T_w, \;\; C = C_w \quad \text{on} \quad y = \sigma^*(x) = a^* \sin(\pi x/\ell), \tag{56}$$

$$u = 0, \; T = T_\infty, \;\; C = C_\infty \quad \text{as} \quad y \to \infty. \tag{57}$$

Here the symbols have their usual meanings. We now use the following non-dimensional variables;

$$(X, Y, R, \sigma, a) = (x, y, r, \sigma^*, a^*)/\ell, \;\; (U, V) = (u, v)\,\ell/\alpha, \tag{58}$$

$$\Theta = (T - T_\infty)/(T_w - T_\infty) \quad \text{and} \quad \Phi = (C - C_\infty)/(C_w - C_\infty). \tag{59}$$

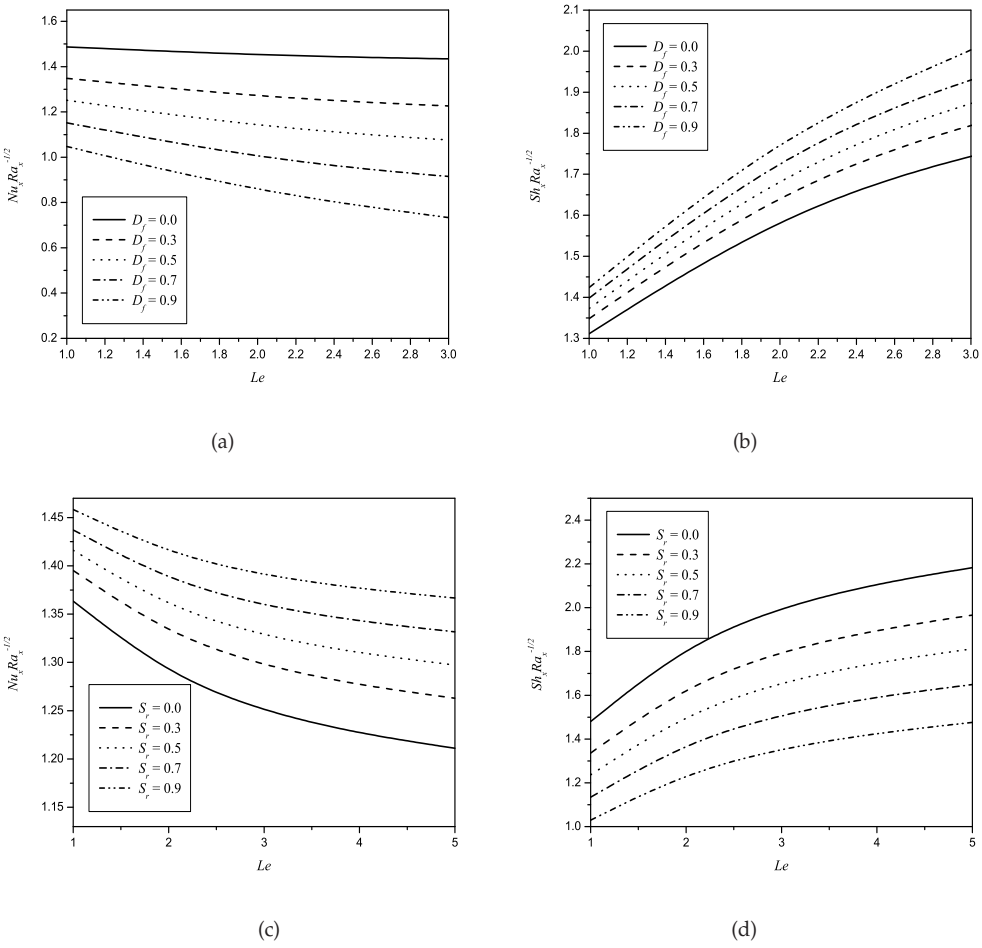

Fig. 5. The effect of the Dufour and Soret parameters on heat and mass transfers with $\lambda = 0.7$, $n = 1$, $Ra_\gamma = 0.5$, $Ra_\xi = 0.5$, $Le = 1$ (i) $Sr = 0.3$ and (ii) $D_f = 0.2$

The governing equations now become,

$$\frac{\partial U}{\partial Y} - \frac{\partial V}{\partial X} = Ra\left[\frac{\partial \Theta}{\partial Y} + N\frac{\partial \Phi}{\partial Y} + \tan(\Omega)\left(\frac{\partial \Theta}{\partial X} + N\frac{\partial \Phi}{\partial X}\right)\right], \tag{60}$$

$$U\frac{\partial \Theta}{\partial X} + V\frac{\partial \Theta}{\partial Y} = \left(\frac{\partial^2 \Theta}{\partial X^2} + \frac{\partial^2 \Theta}{\partial Y^2}\right) + D_f\left(\frac{\partial^2 \Phi}{\partial X^2} + \frac{\partial^2 \Phi}{\partial Y^2}\right), \tag{61}$$

$$U\frac{\partial \Phi}{\partial X} + V\frac{\partial \Phi}{\partial Y} = \frac{1}{Le}\left(\frac{\partial^2 \Phi}{\partial X^2} + \frac{\partial^2 \Phi}{\partial Y^2}\right) + S_r\left(\frac{\partial^2 \Theta}{\partial X^2} + \frac{\partial^2 \Theta}{\partial Y^2}\right). \tag{62}$$

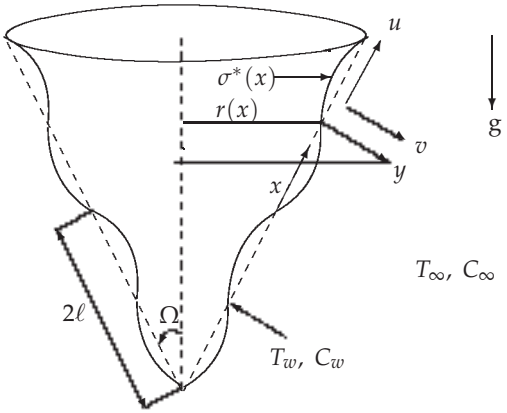

Fig. 6. Schematic sketch of the vertical wavy cone

The parameters appearing above are given by equations (13) - (14). Introducing the stream function $\psi(X,Y)$ defined such that

$$U = \frac{1}{R}\frac{\partial \psi}{\partial Y} \quad \text{and} \quad V = -\frac{1}{R}\frac{\partial \psi}{\partial X}, \tag{63}$$

equations (60) - (62) can be written in the following form

$$\frac{1}{R}\left(\frac{\partial^2\psi}{\partial X^2} + \frac{\partial^2\psi}{\partial Y^2} - \frac{R_X}{R}\frac{\partial \psi}{\partial X}\right) = Ra\left[\frac{\partial \Theta}{\partial Y} + N\frac{\partial \Phi}{\partial Y} + \tan(\Omega)\left(\frac{\partial \Theta}{\partial X} + N\frac{\partial \Phi}{\partial X}\right)\right], \tag{64}$$

$$\frac{1}{R}\left(\frac{\partial \psi}{\partial Y}\frac{\partial \Theta}{\partial X} - \frac{\partial \psi}{\partial X}\frac{\partial \Theta}{\partial Y}\right) = \left(\frac{\partial^2\Theta}{\partial X^2} + \frac{\partial^2\Theta}{\partial Y^2}\right) + D_f\left(\frac{\partial^2\Phi}{\partial X^2} + \frac{\partial^2\Phi}{\partial Y^2}\right), \tag{65}$$

$$\frac{1}{R}\left(\frac{\partial \psi}{\partial Y}\frac{\partial \Phi}{\partial X} - \frac{\partial \psi}{\partial X}\frac{\partial \Phi}{\partial Y}\right) = \frac{1}{Le}\left(\frac{\partial^2\Phi}{\partial X^2} + \frac{\partial^2\Phi}{\partial Y^2}\right) + S_r\left(\frac{\partial^2\Theta}{\partial X^2} + \frac{\partial^2\Theta}{\partial Y^2}\right), \tag{66}$$

where R is the non-dimensional radius of the cone. The appropriate boundary conditions are

$$\psi = 0, \;\; \Theta = 1, \;\; \Phi = 1 \quad \text{on} \quad Y = \sigma(X) = a\sin(\pi X), \tag{67}$$

$$\frac{\partial \psi}{\partial y} = 0, \;\; \Theta = 0, \;\; \Phi = 0 \quad \text{as} \quad Y \to \infty. \tag{68}$$

To transform the wavy surface of the cone to a smooth one we introduce the following transformation,

$$\begin{aligned} \bar{X} &= X, \\ \bar{Y}Ra^{-1/2} &= Y - \sigma(X), \\ \bar{\psi} &= Ra^{-1/2}\psi. \end{aligned} \tag{69}$$

Substituting the transformations (70) into equations (64) - (66) and letting $Ra \to \infty$, we obtain the following equations

$$\frac{1+\sigma_{\bar{X}}^2}{R}\frac{\partial^2\bar{\psi}}{\partial\bar{Y}^2} = [1-\sigma_{\bar{X}}\tan(\Omega)]\left(\frac{\partial\Theta}{\partial\bar{Y}} + N\frac{\partial\Phi}{\partial\bar{Y}}\right), \tag{70}$$

$$(1+\sigma_{\bar{X}}^2)\left(\frac{\partial^2\Theta}{\partial\bar{Y}^2} + D_f\frac{\partial^2\Phi}{\partial\bar{Y}^2}\right) = \frac{1}{R}\left(\frac{\partial\bar{\psi}}{\partial\bar{Y}}\frac{\partial\Theta}{\partial\bar{X}} - \frac{\partial\bar{\psi}}{\partial\bar{X}}\frac{\partial\Theta}{\partial\bar{Y}}\right), \tag{71}$$

$$(1+\sigma_{\bar{X}}^2)\left(\frac{1}{Le}\frac{\partial^2\Phi}{\partial\bar{Y}^2} + S_r\frac{\partial^2\Theta}{\partial\bar{Y}^2}\right) = \frac{1}{R}\left(\frac{\partial\bar{\psi}}{\partial\bar{Y}}\frac{\partial\Phi}{\partial\bar{X}} - \frac{\partial\bar{\psi}}{\partial\bar{X}}\frac{\partial\Phi}{\partial\bar{Y}}\right). \tag{72}$$

We may further simplify equations (70) - (72) by introducing the following transformation

$$\xi = \bar{X},\ \ \eta = \bar{Y}/[(1+\sigma_{\xi}^2)\xi^{1/2}],\ \ \bar{\psi} = R\xi^{1/2}f(\xi,\,\eta),\ \ \Theta = \theta(\xi,\,\eta),\ \ \Phi = \phi(\xi,\,\eta). \tag{73}$$

Substituting equation (73) into equations (70) - (72), gives the nonlinear system of differential equations;

$$f'' = [1-\sigma_{\xi}\tan(\Omega)](\theta' + N\phi'), \tag{74}$$

$$\theta'' + \frac{3}{2}f\theta' + D_f\phi'' = \xi(f'\theta_{\xi} - \theta' f_{\xi}), \tag{75}$$

$$\frac{1}{Le}\phi'' + \frac{3}{2}f\phi' + S_r\theta'' = \xi(f'\phi_{\xi} - \phi' f_{\xi}), \tag{76}$$

with boundary conditions

$$\begin{array}{lll} f(\xi,0) = 0, & \theta(\xi,0) = 1, & \phi(\xi,0) = 1, \\ f'(\xi,\infty) = 0, & \theta(\xi,\infty) = 0, & \phi(\xi,\infty) = 0. \end{array} \tag{77}$$

The associated local Nusselt and Sherwood numbers are given by

$$Nu_x = -Ra^{1/2}\,\frac{\xi^{1/2}\theta'(\xi,0)}{(1+\sigma_{\xi}^2)^{\frac{1}{2}}} \quad \text{and} \quad Sh_x = -Ra^{1/2}\,\frac{\xi^{1/2}\phi'(\xi,0)}{(1+\sigma_{\xi}^2)^{\frac{1}{2}}}. \tag{78}$$

The mean Nusselt and Sherwood numbers from the leading edge to streamwise position x are given by

$$\frac{Nu_m}{Ra^{1/2}} = -\frac{x}{\ell}\frac{\int_0^{\frac{x}{\ell}}\xi^{-1/2}\theta'(\xi,0)d\xi}{\int_0^{\frac{x}{\ell}}(1+\sigma_{\xi}^2)^{\frac{1}{2}}d\xi}, \quad \frac{Sh_m}{Ra^{1/2}} = -\frac{x}{\ell}\frac{\int_0^{\frac{x}{\ell}}\xi^{-1/2}\phi'(\xi,0)d\xi}{\int_0^{\frac{x}{\ell}}(1+\sigma_{\xi}^2)^{\frac{1}{2}}d\xi}. \tag{79}$$

3.1 Discussion of wavy cone results

The governing equations (74) - (76) along with the boundary conditions (77), were solved numerically using the Keller-box method (see Keller (16)) for various parameter combinations. Two hundred uniform grid points of step size 0.05 were used in the η- direction. A uniform grid with 120 nodes was used in the ξ direction. At every ξ grid line, the iteration process is carried out until an accuracy of 10^{-6} is achieved for all the variables. The computations carried out are given in Figures 7 to 14.

Figure 7 shows the effect of the Dufour number D_f on heat and mass transfer for two different values of the amplitude a. The effect of increasing the amplitude, on average, is to reduce the heat and mass transfer rates as compared with the limiting case of a smooth cone. Figures 7(c) and 7(d) highlight the same. Figures 7(a) and 7(b) show that for $a = 0$ (smooth cone) both $Nu_x Ra^{-1/2}$ and $Sh_x Ra^{-1/2}$ increase steadily with ξ whereas for the wavy cone (i.e., $a \neq 0$) we observe oscillations in $Nu_x Ra^{-1/2}$ and $Sh_x Ra^{-1/2}$ over the three complete cycles of undulations from $\xi = 0$ to $\xi = 6$ having length two. These results represent the nonlinear coupling of the change in fluid velocity and orientation of the gravitation. The results are in agreement with those reported by Cheng (6) and Pop and Na (34). The Dufour number D_f reduces $Nu_x Ra^{-1/2}$ and $Nu_m Ra^{-1/2}$. The opposite is true in the case of $Sh_x Ra^{-1/2}$ and $Sh_m Ra^{-1/2}$.

The effect of D_f on heat and mass transfer is depicted in Figure 8 for two different values of the cone half angle Ω. From 8(c) and 8(d) it is clear that increasing the half angle Ω, on average, reduces the heat and mass transfer rates. Figures 8(a) and 8(b) show that there is an increase in oscillations of $Nu_x Ra^{-1/2}$ and $Sh_x Ra^{-1/2}$ for higher values of Ω. In this case the Dufour number also reduces the heat transfer while enhancing mass transfer.

Figure 9 demonstrates the effect of D_f on heat and mass transfer for two different values of buoyancy ratio N. It is evident that the buoyancy ratio amplifies heat and mass transfer from the cone. Again, the Dufour number contributes to lowering heat transfer while enhancing mass transfer rates.

The effect of D_f on the heat and mass transfer is highlighted for two different values of Lewis numbers in Figure 10. We observe that Le reduces heat transfer whereas the opposite is true in the case of mass transfer. For large values of Le, higher values of D_f (≥ 0.5) produce negative heat transfer rates indicating that heat diffuses from fluid to the cone in such cases. Figures 10(a) and 10(c) confirm and reinforce the same fact. The effect of Soret number S_r on heat and mass transfer for two different values of amplitude a is projected in Figure 11. The decreasing effect of the amplitude a on heat and mass transfer rates observed in this situation also. The Soret number S_r contributes to increasing $Nu_x Ra^{-1/2}$ and $Nu_m Ra^{-1/2}$ while reducing $Sh_x Ra^{-1/2}$ $Sh_m Ra^{-1/2}$ as can be seen in Figures 11(a) - 11(d).

The effect of S_r on heat and mass transfer is shown in Figure 12 for two different values of cone half angle Ω. The fact that Ω reduces the heat and mass transfer rates is observed in plots 12(a) and 12(d). The Soret number S_r has the effect of increasing the heat transfer and reducing the mass transfer for all values of Ω.

Figure 13 shows the effect of S_r on heat and mass transfer rates for two different values of the buoyancy ratio N. From 13(a) - 13(d) we observe that the buoyancy ratio enhances both heat and mass transfer rates. For selected values of N, S_r contributes towards enhancing the heat transfer rate while reducing the mass transfer rate.

The effect of S_r on the heat and mass transfer rates is shown in Figure 14 for selected values of the Lewis number Le. It is evident that Le reduces the heat transfer whereas the opposite is true in case of mass transfer. At large values of Le there is a critical value of S_r up to which $Nu_x Ra^{-1/2}$ and $Nu_m Ra^{-1/2}$ increases and beyond this critical value, both $Nu_x Ra^{-1/2}$ and $Nu_m Ra^{-1/2}$ start to fall as can be more clearly seen in Figures 14(a) and 14(c). From Figures 14(b) - 14(d) we observe that the effect of S_r is to reduce the rate of mass transfer from the surface of the wavy cone.

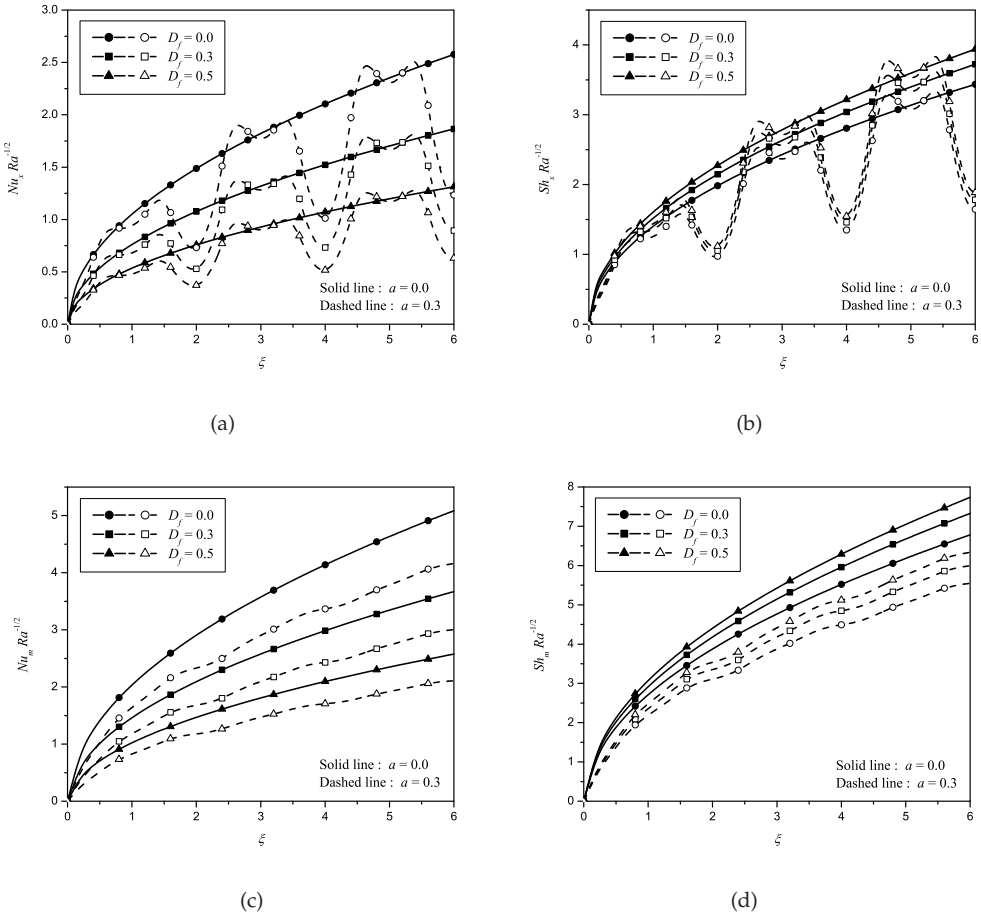

Fig. 7. Effect of D_f on heat and mass transfer with $\Omega = \pi/9$, $N = 1$, $Le = 2$ and $S_r = 0.2$

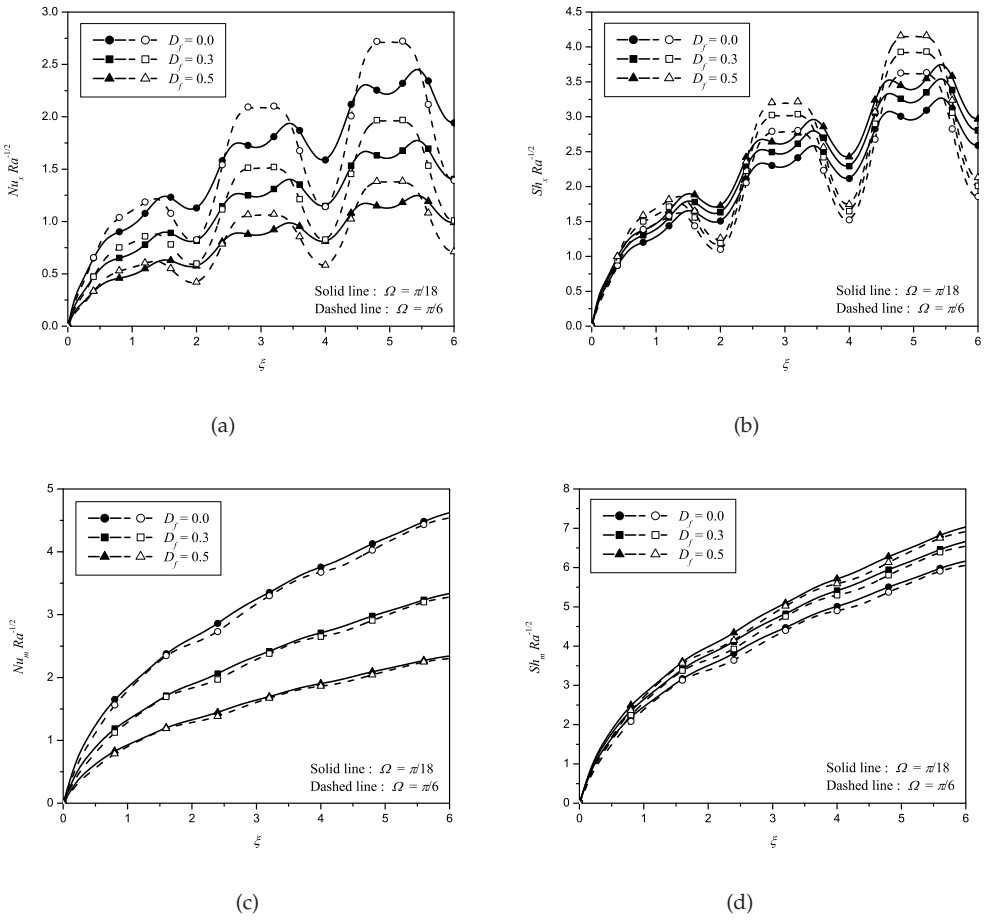

Fig. 8. Effect of D_f on heat and mass transfer with $a = 0.2$, $N = 1$, $Le = 2$and $S_r = 0.2$

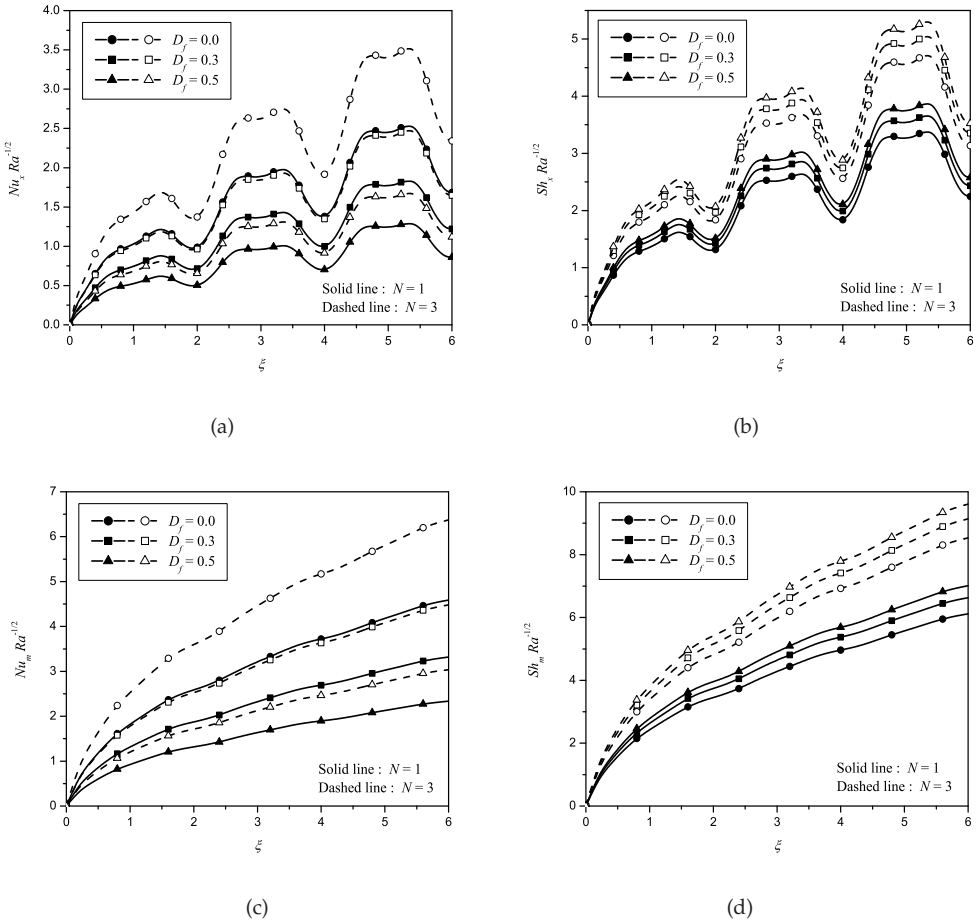

Fig. 9. Effect of D_f on heat and mass transfer with $a = 0.2$, $\Omega = \pi/9$, $Le = 2$ and $S_r = 0.2$

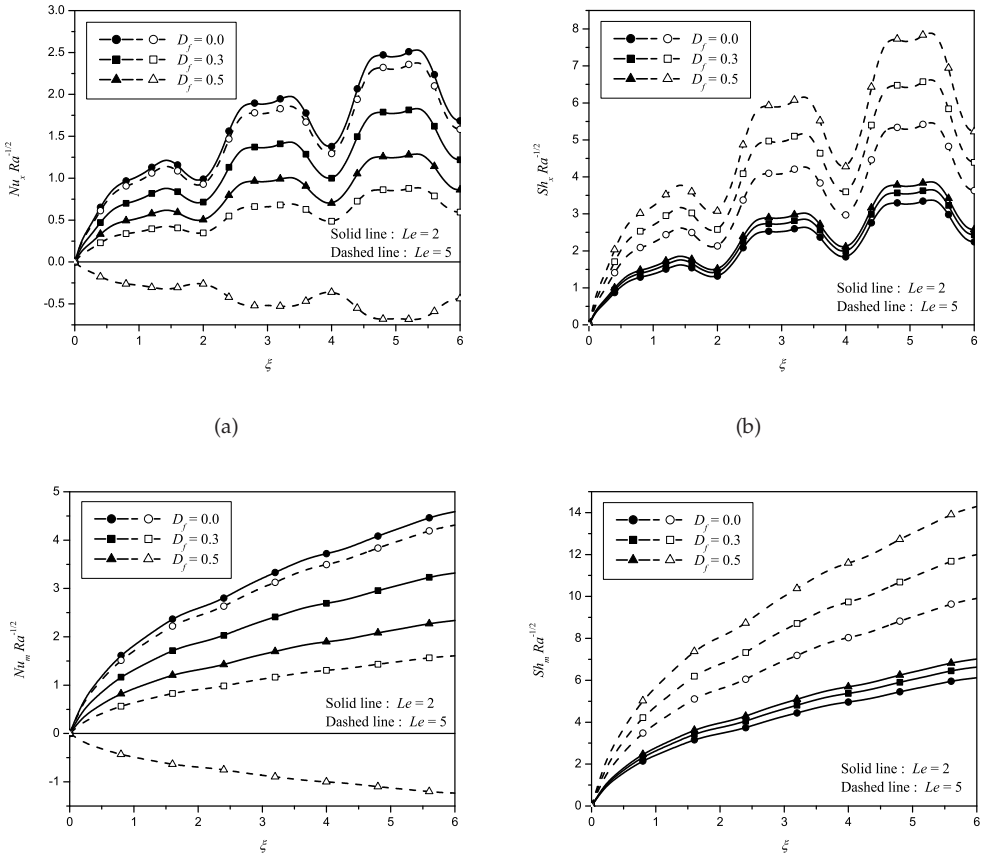

Fig. 10. Effect of D_f on heat and mass transfer with $a = 0.2$, $\Omega = \pi/9$, $N = 1$ and $S_r = 0.2$

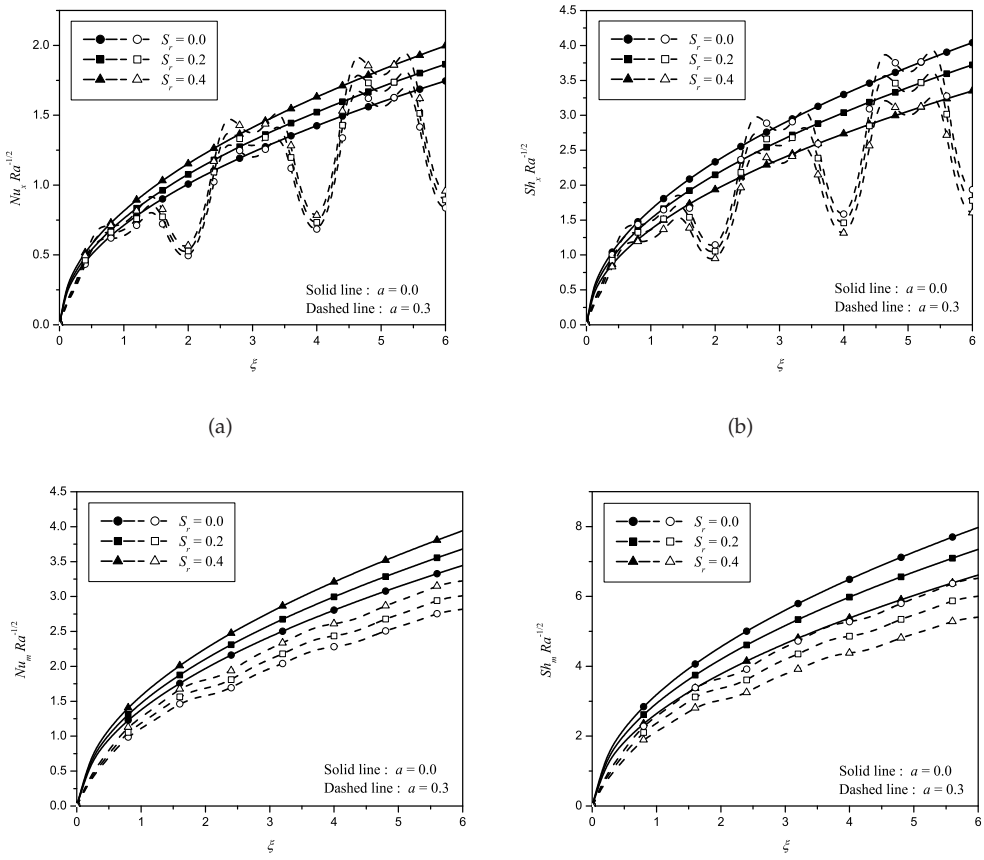

Fig. 11. Effect of S_r on heat and mass transfer with $\Omega = \pi/9$, $N = 1$, $Le = 2$ and $D_f = 0.3$

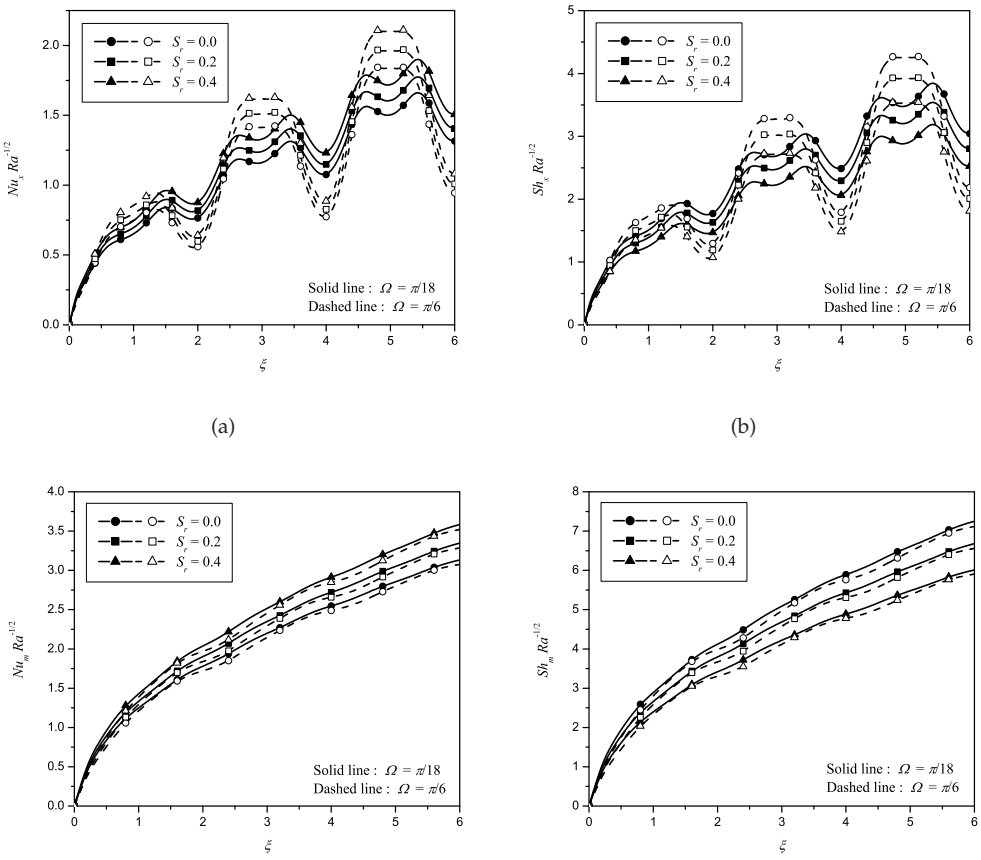

Fig. 12. Effect of S_r on heat and mass transfer with $a = 0.2$, $N = 1$, $Le = 2$and $D_f = 0.3$

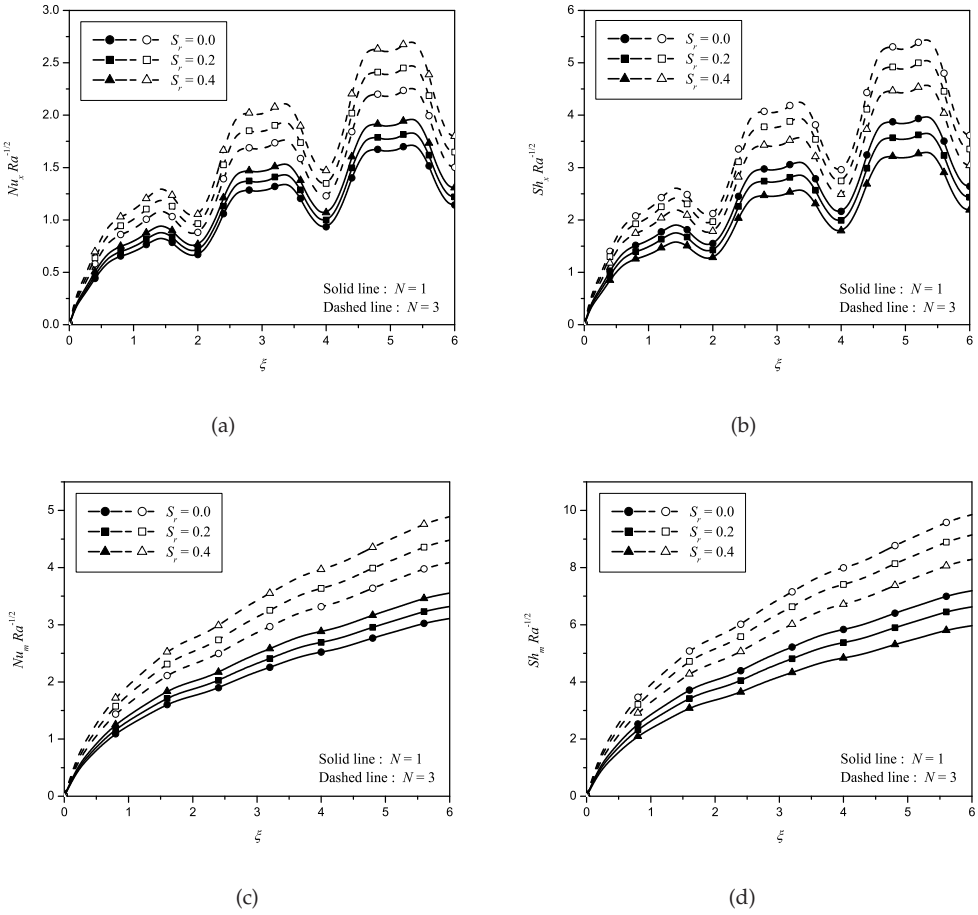

Fig. 13. Effect of S_r on heat and mass transfer with $a = 0.2$, $\Omega = \pi/9$, $Le = 2$ and $D_f = 0.3$

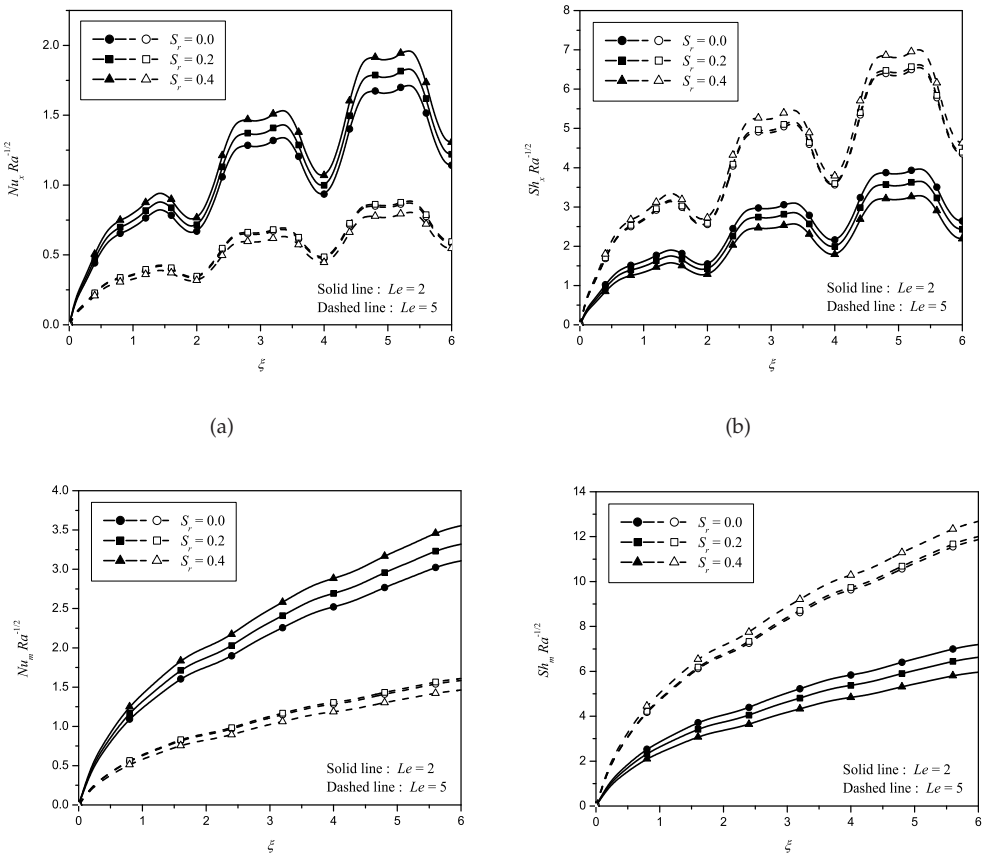

Fig. 14. Effect of S_r on heat and mass transfer with $a = 0.2$, $\Omega = \pi/9$, $N = 1$ and $D_f = 0.3$

4. Conclusions

Double-diffusive convection from inverted smooth and wavy cones in Darcy porous media has been investigated. A similarity analysis is performed to reduce the governing equations to coupled nonlinear differential equations that are solved by using the successive linearisation method (SLM), the Matlab bvp4c, a shooting technique and the Keller-box method.
For the smooth cone the effects of the governing parameters on the velocity, temperature and concentration profiles have been studied. The effects of Dufour and Soret effect on the rate of heat and mass transfer were determined. Comparison between our results and earlier results has been made. The findings suggest that the successive linearisation method is a reliable method for solving nonlinear ordinary differential equations.
In the case of the wavy cone we have studied the effects of cross-diffusion on the heat and the mass transfer rates. From the present study we can see that D_f reduces heat transfer and increases mass transfer. The effect of S_r is exactly the opposite except at high Lewis numbers when the heat transfer rate increases up to a critical value of S_r and then starts decreasing beyond that value.

5. References

[1] Akbarzadeh, A. & P. Manins, P. (1988). Convective layers generated by side walls in solar ponds. *Solar Energy*, 41(6), pp. 521 - 529.
[2] Alam, M. S.; Rahman, M. M.; Maleque A. & Ferdows, M. (2006). Dufour and Soret Effects on Steady MHD Combined Free-Forced Convective and Mass Transfer Flow Past a Semi-Infinite Vertical Plate. *Thammasat International Journal of Science and Technology*, 11, pp. 1 - 12.
[3] Baines, P.G. & Gill, A. E. (1969). On thermohaline convection with linear gradients, *Journal of Fluid Mechanics*, 37, pp. 289 - 306.
[4] Chamkha, A. J. & Khaled, A. A. (1999). Nonsimilar hydromagnetic simultaneous heat and mass transfer by mixed convection from a vertical plate embedded in a uniform porous medium. *Numerical Heat Transfer- Part A: Applications*, 36, pp. 327 - 344.
[5] Chamkha, A. J. (2001). Coupled heat and mass transfer by natrual convection about a truncated cone in the presence of magnetic field and radiation effects. *Numerical Heat Transfer- Part A: Applications*, 38, pp. 511 - 530.
[6] Cheng, C. Y. (2000a). Natural convection heat and mass transfer near a wavy cone with constant wall temperature and concentration in a porous medium. *Mechanics Research Communications*, 27, pp. 613 - 620.
[7] Cheng, C. Y. (2000b). An integral approach for heat and mass transfer by natural convection from truncated cones in porous media with variable wall temperature and concentration. *International Communications in Heat and Mass Transfer*, 27, pp. 437 - 548.
[8] Cheng, C. -Y. (2009). Soret and Dufour effects on natural convection heat and mass transfer from a vertical cone in a porous medium. *International Communications in Heat and Mass Transfer*, 36, pp. 1020-1024.
[9] Cheng, P. (1977). Similarity solutions for mixed convection from horizontal impermeable surfaces in saturated porous media. *International Journal of Heat Mass Transfer*, 20 (9), pp. 893 - 898.
[10] Cheng, P. (1985). Natural convection in a porous medium: external flow. *Proceedings of the NATO Advanced Study in Natural Convection*, Ezmir, Turkey, 1985.

[11] El-Amin, M.F. (2004). Double dispersion effects on natural convection heat and mass transfer in non-Darcy porous medium. *Applied Mathematics and Computation*, 156, pp. 1-17.
[12] Fernando, H. J. S. & Brandt, A. (1995). Recent advances in double-diffusive convection. *Applied Mechanics Reviews*, 47(9), pp. C1-C7.
[13] Gaikwad, S. N.; Malashetty, M. S. & Rama Prasad, K. (2009). An analytic study of linear and nonlinear double-diffusive convection in a fluid saturated anisotropic porous layer with Soret effect. *Applied Mathematical Modelling*, 33, pp. 3617 - 3635.
[14] Guo, J.; Qin, Y. & Kaloni, P. N. (1994). Nonlinear stability problem of a rotating doubly diffusive fluid layer. *Int. J. Eng. Sci*. 32, pp. 1207 - 1219.
[15] Ingham D. B. & Pop, I. (2002). *Transport Phenomenon in Porous Media*. Second Ed., Elsevier, Oxford.
[16] Keller, H. B. (1978). Numerical methods in boundary-layer theory. *Ann. Rev. Fluid Mech.*, 10, pp. 417 - 433.
[17] Khanafer, K. & Vafai, K. (2002). Double-diffusive mixed convection in a lid-driven enclosure filled with a fluid-saturated porous medium. *Numerical Heat Transfer. Part A : Applications*, 42, pp. 465 - 486.
[18] Lai, F. C. (1990). Coupled heat and mass transfer by natural convection from a horizontal line source in saturated porous medium. *International Communications in Heat and Mass Transfer*, 17, pp. 489 - 499.
[19] Makukula, Z. G.; Motsa, S. S. & Sibanda, P. (2010a). On a new solution for the viscoelastic squeezing flow between two parallel plates. *Journal of Advanced Research in Applied Mathematics*, vol. 2, no. 4, pp. 31-38.
[20] Makukula, Z. G.; Sibanda, P. & Motsa, S. S. (2010b). A novel numerical technique for two-dimensional laminar flow between two moving porous walls. *Mathematical Problems in Engineering*, Article ID 528956, 15 pages; doi:10.1155/2010/528-956.
[21] Mansour, M. A.; El-Anssary, N. F. & Aly, A. M. (2008). Effects of chemical reaction and thermal stratification on MHD free convective heat and mass transfer over a vertical stretching surface embedded in a porous media considering Soret and Dufour numbers. *Chemical Engineering Journal*, 145, pp. 340-345.
[22] Mortimer, R.G. & Eyring, H. (1980). Elementary transition state theory of the Soret and Dufour effects. *Proceedings of the National Academy of Sciences of the United States of America*, vol. 77, no. 4, pp. 1728 - 1731.
[23] Murthy, P. V. S. N. & Singh, P. (2000). Thermal Dispersion Effects on Non-Darcy Convection over a Cone. *International Journal of Computer and Mathematics with Applications*, 40, pp. 1433-1444.
[24] Na, T. Y. & Chiou, J. P. (1979). laminar natural convection over a frustum of a cone. *Applied Scientific Research*, 35, pp. 409 - 421.
[25] Nakayama, A. & Hossain, M. A. (1995). An integral treatment for combined heat and mass transfer by natural convection in a porous medium. *International Journal of Heat and Mass Transfer*, 38, pp. 761 - 765.
[26] Narayana, P.A.L. & Murthy, P.V.S.N. (2008). Soret and Dufour effects on free convection heat and mass transfer from a horizontal flat plate in a Darcy porous medium. *International Journal of Heat Tansfer and Mass Transfer*, 130, pp. 104504-1-104504-5.
[27] Narayana, P.A.L. & Sibanda, P. (2010). Soret and Dufour effects on free convection along a vertical wavy surface in a fluid saturated Darcy porous medium. *International Journal of Heat and Mass Transfer*, 53, pp. 3030-3034.

[28] Nield, D.A. (1968). Onset of thermohaline convection in a porous medium. *Water Resources Research*, 5, pp. 553 - 560.
[29] Nield, D.A. & Bejan, A. (1992). *Convection in Porous Media*, Springer-Verlag, New York.
[30] Onsager, L. (1931). Reciprocal Relations in Irreversible Processes. *Phys. Rev*, 37, pp. 405 - 426.
[31] Partha, M. K. (2009). Suction/injection effects on thermophoresis particle deposition in a non-Darcy porous meduim under the influence of Soret, Dufour effects. *International Journal of heat and mass transfer*, 52, pp. 1971-1979.
[32] Pop, I. & Ingham, D. B. (2001). *Convective Heat Transfer*, Elsevier.
[33] Pop, I. & Na, T. Y. (1994). Natural convection of a Darcian fluid about a cone. *International Communications in Heat and Mass Transfer*, 12, pp. 891 - 899.
[34] Pop, I. & Na, T. Y. (1995). Natural convection over a frustum of a wavy cone in a porous medium. *Mechanics Research Communications*, 22, pp. 181 - 190.
[35] Stern, M. E. (1960). The 'salt fountain' and thermohaline convection. *Tellus*, 12, pp. 172 - 175.
[36] Stern, M. E. (1969). Collective instability of salt fingers. *Journal of Fluid Mechanics*, 35, pp. 209 - 218.
[37] Sunil; Sharma, A. & Sharma, R. C. (2006). Effect of dust particles on ferrofluid heated and soluted from below. *Int. J. Therm. Sci*. 45, pp. 347 - 458.
[38] Yih, K. A. (1999). Coupled heat and mass transfer by free convection over a truncated cone in porous media: VWT/ VWC or VHF/VMF. *Acta Mechanica*, 137, pp. 83-97.

6

Mass Transfer Between Clusters Under Ostwald's Ripening

Roman Vengrenovich, Bohdan Ivanskii,
Anatolii Moskalyuk, Sergey Yarema and Miroslav Stasyk
Chernivtsi National University after Yu. Fed'kovich, Chernivtsi, Ukraine

1. Introduction

Decay of oversaturated solid solutions with forming a new phase includes three stages, *viz.* nucleation of centers (clusters, nucleation centers, extractions), independent growth of them and, at last, development of these centers interconnecting to each other. This last stage, so-called late stage of decay of oversaturated solid solution has been firstly revealed by Ostwald (Ostwald, 1900). Its peculiarity consists in the following. Diffusion mass transfer of a matter from clusters with larger magnitudes of surface curvature to ones with smaller magnitudes of surface curvature (owing to the Gibbs-Thomson effect) results in dissolving and disappearing small clusters that causes permanent growth of the mean size of extractions. In accordance with papers (Sagalovich, Slyozov, 1987; Kukushkin, Osipov, 1998), interaction between clusters is realized through the 'generalized self-consistent diffusion field'. This process, when large clusters grow for account of small ones is referred to as the Ostwald's ripening. Investigation of the Ostwald's ripening resulted in determination of the form of the size distribution function in respect of the mass transfer mechanisms. The first detailed theory of the Ostwald's ripening for the diffusion mass transfer mechanism has been developed by Lifshitz and Slyozov (Lifshitz and Slyozov, 1958, 1961). Under diffusion mass transfer mechanism, atoms of a solved matter reaching clusters by diffusion are then entirely absorbed by them, so that cluster growth is controlled by matrix diffusion and, in part, by the volume diffusion coefficient, D_v. In paper (Wagner, 1961), Wagner has firstly showed that it is possible, if the atoms crossing the interface 'cluster-matrix' and falling at a cluster surface in unit of time have a time to form chemical connections necessary for reproduction of cluster matter structure. If it is not so, solved atoms are accumulated near the interface 'cluster-matrix' with concentration C that is equal to the mean concentration of a solution, $\langle C \rangle$. For that, growing process is not controlled by the volume diffusion coefficient, D_v, but rather by kinetic coefficient, β. Thus, in his paper published three years later than the papers by Lifshitz and Slyozov, Wagner considered other mechanism of cluster growth controlled by the rate of formation of chemical connection at cluster surface. The quoted papers (Lifshitz, Slyozov, 1958, 1961; Wagner, 1961) form the base of the theory of the Ostwald's ripening that is conventionally referred to as the Lifshitz-Slyozov-Wagner (LSW) theory. Within the framework of this theory, several

other problems connected with the Ostwald's ripening for diffusion at grain boundaries (Slyozov, 1967; Kirchner, 1971), for surface diffusion (Chakraverty, 1967; Vengrenovich, 1977), for diffusion along dislocation pipes (Ardell, 1972; Kreye, 1970; Vengrenovich, 1975, 1982; Vengrenovich *et al.*, 2001a, 2002) etc. have been solved later. A new phase extracted during decay of oversaturated solid solution as specific matrices of particles (clusters) is the strengthening phase. Its extractions act as a stopper for traveling dislocations. Elastic strength fields arising around clusters and interacting with matrix dislocations, depending on their energy, can be fixed at cluster surfaces or cut of them. Cutting the extracted particles (clusters) by dislocations or fixing of them at particle surfaces leads to the pipe mechanism of diffusion along dislocations with diffusion coefficient D_d (Vengrenovich, 1980a, 1980b, 1983; Vengrenovich *et al.*, 1998).

For some time past, the LSW theory is successfully used for analysis of evolution of island structure resulting from self-organization in semiconductor heterosystems (Bartelt *et al.*, 1992, 1996; Goldfarb *et al.*, 1997a, 1997b; Joyce *et al.*, 1998; Kamins *et al.*, 1999; Vengrenovich *et al.*, 2001b, 2005, 2010; Pchelyakov *et al.*, 2000; Ledentsov *et al.*, 1998; Xiaosheng Fang *et al.*, 2011). It is also used for dscription of dissipative structures in non-equilibrium semiconductor systems (Gudyma, Vengrenovich, 2001c; Vengrenovich *et al.*, 2001d).

Mass transfer between clusters under the Ostwald's ripening depends on the kind of diffusion than, in its turn, determines the rate of growth of clusters and the size distribution function of them. As it has been noted above, the size distribution function of clusters for matrix diffusion mechanism has been for the first time obtained by Lifshitz and Slyozov within the framework of hydrodynamic approximation. So, this distribution is referred to as the Lifshitz-Slyozov distribution.

This chapter is devoted to the computing of the size distribution function of clusters under mass transfer corresponding to simultaneous (combined) action of various diffusion mechanisms. Topicality of this study follows from the fact that often in practice (due to various reasons) mass transfer between clusters is controlled in parallel, to say, by the kinetic diffusion coefficient, β, and by the matrix diffusion coefficient D_v, or, alternatively, by the coefficients D_v and D_d, simultaneously, ect. All following computations are carried out within the Lifshitz-Slyozov hydrodynamic approximation using the approach developed earlier by one of the authors of this chapter (Vengrenovich, 1982).

2. Cluster growth under diffusion and Wagner mechanisms of mass transfer. Generalized Lifshitz-Slyozov-Wagner distribution

Following to Wagner, the number of atoms crossing the interface 'cluster-matrix' and getting to the cluster surface in unite of time, j_1, is

$$j_1 = 4\pi r^2 \beta \langle C \rangle , \tag{1}$$

and the number of atoms leaving it in unite of time is

$$j_2 = 4\pi r^2 \beta C_r , \tag{2}$$

so that the resulting flux of atoms involving into formation of chemical connections is

$$j_i = j_1 - j_2 = 4\pi r^2 \beta \left(\langle C \rangle - C_r \right) , \tag{3}$$

where $C_r = C_\infty \exp\left(\frac{2\sigma\upsilon_m}{kTr}\right) \approx C_\infty\left(1+\frac{2\sigma\upsilon_m}{rkT}\right)$ – concentration of atoms of solved matter at the boundary of a cluster of radius r, C_∞ – equilibrium concentration for specified temperature T, σ – interface surface energy, υ_m – volume of an atom of solved matter, and k – the Boltzmann constant.

The flows j_1 (Eq. 1) (to the cluster) and j_2 (Eq. 2) (from the cluster) are caused by thermal motion of atoms. j_1 in Eq. 1 is proportional to the mean concentration of the solution, $\langle C\rangle$. j_2 in Eq. 2 is proportional to concentration C_r, that is set at the cluster boundary in accordance with the Gibbs-Thomson formula: ($C_r = C_\infty \exp\left(\frac{2\sigma\upsilon_m}{kTr}\right)$).

Both in j_1 (Eq. 1) and in j_2 (Eq. 2), the kinetic diffusion coefficient equals the flow density for the unit concentration. Thus, taking into account the nature of flows, the kinetic diffusion coefficients are regarded to be equal to each other in j_1 and in j_2.

Introducing the kinetic coefficient, β, determining the flow j_i is caused by non-equilibrium character of the processes occurring both at the cluster surfaces and at their interfaces with a matrix. On this reason, one can not write the flow j_i through the concentration gradient at the interface. Formally, it can be represented through concentration gradient:

$$j_i = 4\pi r^2\beta\left(\langle C\rangle - C_r\right) = 4\pi r^2\beta r\frac{\langle C\rangle - C_r}{r}, \tag{4}$$

where $\beta\cdot r$ has a dimension of the diffusion coefficient; however, such diffusion coefficient, $D^* = \beta r$, has no physical sense. That is why, one proceeds to the kinetics.

In equilibrium state one has:

$$j_i = j_v = j, \tag{5}$$

that is why the flow j of atoms to (from) a cluster can be determined as

$$j = \frac{1}{2}\left(j_i + j_v\right), \tag{6}$$

where j_v – the number of atoms reaching a cluster surface in unite of time through diffusion.

In general case, the flow j of atoms to (from) a cluster will be

$$j = j_i + j_v. \tag{7}$$

The flow j in Eq. (7) provides determination of the rate of cluster growth.

2.1 The rate of cluster growth

For determining the size distribution function of particles, $f(r,t)$, one must know the rate of particle's growth, $\dot{r} = \frac{dr}{dt}$, that is connected with the size distribution function of the continuity equation:

$$\frac{\partial f(r,t)}{\partial t}+\frac{\partial}{\partial r}\left(f(r,t)\dot{r}\right)=0\,. \tag{8}$$

The rate of cluster growth is determined from a condition:

$$\frac{d}{dt}\left(\frac{4}{3}\pi r^3\right)=j\upsilon_m\,, \tag{9}$$

where j is determined by Eq. (7). There is the diffusion part of a flow:

$$j_v=4\pi r^2 D_v\left(\frac{dC}{dr}\right)_{R=r}=4\pi r^2 D_v\frac{\langle C\rangle-C_r}{r}\,. \tag{10}$$

Taking into account Eqs. (3) and (10), one finds from Eq. (9):

$$\frac{dr}{dt}=\frac{\left(\langle C\rangle-C_r\right)\upsilon_m}{4\pi r^2}\left(4\pi r^2\beta+4\pi r^2 D_v\frac{1}{r}\right). \tag{11}$$

Let us denote the shares j_v and j_i in general flow j as x and $(1-x)$, respectively:

$$x=\frac{j_v}{j}\,,\ 1-x=\frac{j_i}{j}\,,\ \frac{j_v}{j_i}=\frac{x}{1-x} \tag{12}$$

To represent the rate of growth (11) through the share flows j_i and j_v, let us take out of the brackets the second term, $4\pi r^2 D_v\frac{1}{r}$, and multiply nominator and denominator of the firs term by $\left(\langle C\rangle-C_{r_g}\right)r_g^2$, where C_{r_g} is the concentration at the boundary with a cluster of maximal size r_g:

$$\frac{dr}{dt}=\left(\langle C\rangle-C_r\right)\frac{D_v\upsilon_m}{r}\left(\frac{4\pi r_g^2\beta\left(\langle C\rangle-C_{r_g}\right)}{4\pi r_g^2 D_v\dfrac{\left(\langle C\rangle-C_{r_g}\right)}{r_g}}\frac{r}{r_g}+1\right). \tag{13}$$

The ratio $\dfrac{4\pi r_g^2\beta\left(\langle C\rangle-C_{r_g}\right)}{4\pi r_g^2 D_v\dfrac{\left(\langle C\rangle-C_{r_g}\right)}{r_g}}$ equals the ratio of the flows $\frac{j_i}{j_v}$ for a particle of the maximal size, and, in accordance with Eq. (12), it can be replaced by $\left(\frac{1-x}{x}\right)$, while there are not any limitations on particle size in Eq. (12). Besides, taking into account that $\langle C\rangle-C_r=\frac{2C_\infty\sigma\upsilon_m}{kT}\left(\frac{1}{r_k}-\frac{1}{r}\right)$, the rate of growth (13) can be rewritten in the following form:

$$\frac{dr}{dt}=\frac{\sigma C_\infty \upsilon_m^2 D_v}{kT}\frac{1}{r^2}\left(\frac{1-x}{x}\frac{r}{r_g}+1\right)\left(\frac{r}{r_k}-1\right), \tag{14}$$

where r_k is the critical radius. Within the LSW theory, r_k coincides with a mean size of particles, $r_k=\langle r\rangle$.

Eq. (14) corresponds to the rate of cluster growth through matrix diffusion with the share contribution $(1-x)$ of the part of flow controlled by the kinetic coefficient β. For $x=1$, Eq. (14) coincides with the rate of growth Eq. (2.15) from the review paper (Sagalovich, Slyozov, 1987), *viz.* $\left(\frac{dR}{dt}=\frac{D_{n-1}a_{n-1}}{R^{n-1}}\left(\frac{R}{R_k}-1\right)\right.$, where $\left.\Delta=\frac{\alpha}{R_k}\right)$ for $n=3$, where $D_2=D_v$, $a_2=\frac{C_\infty\sigma\upsilon_m^2}{kT}$.

Repeating this procedure and taking out of the brackets $4\pi r^2\beta$, one obtains:

$$\frac{dr}{dt}=\frac{C_\infty\sigma\upsilon_m^2\beta}{kT}\frac{1}{r}\left(\frac{x}{1-x}\frac{r_g}{r}+1\right)\left(\frac{r}{r_k}-1\right). \tag{15}$$

Eq. (15) determines the rate of cluster growth under conditions controlled by the kinetic coefficient β with the share contribution x of matrix diffusion. If $x=0$, then growth is fully determined by the kinetic coefficient, and our Eq. (15) coincides with Eq. (2.15) form (Sagalovich, Slyozov, 1987) for $n=2$, where, $D_1=\beta$, $a_1=\frac{C_\infty\sigma\upsilon_m^2}{kT}$. In Eqs. (14) or (15) for the rate of growth that are the combinations of the Wagner and conventional diffusion mechanisms of cluster's enlargement, one assumes that no any term in the general flow j, Eq. (7), can be neglected. It means that the flows j_v and j_i must be commensurable. However, the intrigue consists in that formation of chemical connections is electron process, while the classical diffusion is the atomic activation process with considerably different temporal scale. Thus, the question arises: what are the conditions for two qualitatively different relaxation times, $\tau_{chem.con.}$ and $\tau_{diffus.}$, become comparable to each other? Thus the question on the ratio of flows j_v and j_i is reduced, in fact, to the ratio of the relaxation times $\tau_{chem.con.}$ and $\tau_{diffus.}$, and, as a result, to the question on the possibility to implement the proposed mechanism of cluster growth. To obtain answer on this question is, in general, too hardly.

To all appearance, the relaxation times $\tau_{chem.con.}$ and $\tau_{diffus.}$ are commensurable, if the electron process of formation of chemical connections is activation one, and if the activation energies for both processes (electron and diffusion) are comparable.

In paper (Wagner, 1961), the solution is obtained for the limiting cases: $x=0$, $\tau_{diffus.} << \tau_{chem.con.}$, (the Wagner mechanism of growth), and, $x=1$, $\tau_{chem.con.} << \tau_{difus.}$, (the diffusion mechanism of growth). Note, Wagner (Wagner, 1961) does not discuss the relaxation times.

In the case under consideration here, when the solution is found for arbitrary magnitude of x within the interval $0<x<1$, relaxation times must be comparable to each other at least for the systems whose histograms are represented by the computed curves. We provide this comparison below.

2.2 Temporal dependences of r_g and r_k

One of the main parameters of the LSW theory is the ratio r_g/r_k (in terms of the papers (Lifshitz and Slyozov, 1958, 1961), locking point u_0), whose magnitude together with the equation for the rate of growth (14) or (15) provides integration of Eq. (8) after separation of variables and determination of the analytical form of the size distribution function. This ratio can be determined from the dependence of the specific rate of growth $\dot{r}/r$ on r, that is schematically shown in Fig. 1, where $\dot{r}$ is determined by Eq. (14) or (15) (Vengrenovich, 1982).

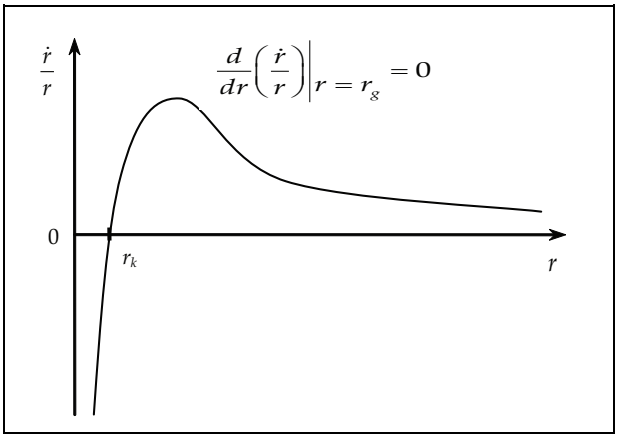

Fig. 1. Schematic dependence of the specific rate of growth $\frac{\dot{r}}{r}$ on r

At the point where the rate of growth on the unite length of cluster radius reaches its maximal magnitude, derivation equals zero:

$$\left.\frac{d}{dr}\left(\frac{\dot{r}}{r}\right)\right|_{r=r_g} = 0\,. \tag{16}$$

From the physical point of view, it means that the maximal size of r_g is reached for the particle, for which the rate of growth of the unit of length of its radius is maximal. Thus, one obtains from Eq. (16):

$$\frac{r_g}{r_k} = \frac{2+x}{1+x}\,. \tag{17}$$

Assuming in Eq. (14) $r = r_g$ and replacing the ratio $\frac{r_g}{r_k}$ by its magnitude from Eq. (17), one obtains by integration:

$$r_g^3 = A^* \frac{t}{x(1+x)}\,, \tag{18}$$

where, $A^* = \frac{3\sigma\upsilon_m^2 C_\infty D_v}{kT}$, or:

$$r_k^3 = A^* \frac{(1+x)^2}{x(2+x)^3} t \,. \tag{19}$$

For $x = 1$ particle growth is full controlled by the volume diffusion coefficient:

$$r_g^3 = \frac{1}{2} A^* t \,,\; r_k^3 = \frac{4}{27} A^* t \,,\; \frac{r_g}{r_k} = \frac{3}{2} \,. \tag{20}$$

By analogy, one obtains from Eq. (15):

$$r_g^2 = B^* \frac{t}{1-x^2} \,, \tag{21}$$

where $B^* = \frac{2\sigma\upsilon_m^2 C_\infty \beta}{kT}$, or:

$$r_k^2 = B^* \frac{1+x}{(1-x)(2+x)^2} t \,. \tag{22}$$

Eqs. (21) and (22) describe changing in time cluster sizes, when growth of them is controlled by the kinetic coefficient β, with the share contribution x of matrix diffusion. If $x = 0$, then the process of growth is fully controlled by kinetics of transition through the interface 'cluster-matrix':

$$r_g^2 = B^* t \,,\; r_k^2 = \frac{1}{4} B^* t \,,\; \frac{r_g}{r_k} = 2 \,. \tag{23}$$

2.3 Size distribution function

The size distribution function, $f(r,t)$, and the rate of growth, $\dot{r}$, are connected by the continuity equation (8). Knowing $\dot{r}$ (Eqs. (14) or (15)), one can find $f(r,t)$ from Eq. (8). Following to paper (Vengrenovich, 1982), $f(r,t)$ is found as the product:

$$f(r,t) = \varphi(r_g) g'(u) \,, \tag{24}$$

where $g'(u)$ is the relative size distribution function of clusters, $u = \frac{r}{r_g}$.

To determine the function $\varphi(r_g)$, let us apply the conservation law for mass of disperse phase:

$$M = \frac{4}{3}\pi\rho \int_0^{r_g} r^3 f(r,t)\, dr \,, \tag{25}$$

by substituting in it $f(r,t)$ from Eq. (24):

$$\varphi\left(r_g\right)=\frac{Q}{r_g^4}, \tag{26}$$

where $Q=\dfrac{M}{\dfrac{4}{3}\pi\rho\int_0^1 u^3 g'(u)\,du}$.

Substituting Eq. (26) in Eq. (24), one obtains:

$$f(r,t)=\frac{Q}{r_g^3}g'(u)=\frac{g(u)}{r_g^3}, \tag{27}$$

where:

$$g(u)=Q\cdot g'(u). \tag{28}$$

The relative size distribution function $g'(u)$ is determined from the continuity equation. For that, one substitutes in Eq. (8) the magnitude $f(r,t)$ from Eq. (24) and takes into account Eq. (26), as well as the magnitude of $\dot{r}$ from Eqs. (14) or (15). After the mentioned substitution and transition in Eq. (8) from differentiation on r and t to differentiation on $u=\dfrac{r}{r_g}$ ($\dfrac{\partial}{\partial r}=\dfrac{\partial}{\partial u}\dfrac{du}{dr}$, where $\dfrac{du}{dr}=\dfrac{1}{r_g}$; $\dfrac{\partial}{\partial t}=\dfrac{\partial}{\partial u}\dfrac{du}{dr_g}\dfrac{dr_g}{dt}$, where $\dfrac{\partial u}{\partial r_g}=-\dfrac{u}{r_g}$), the variables are separated, and Eq. (8) takes the form:

$$\frac{dg'(u)}{g'(u)}=-\frac{4\upsilon_g-\dfrac{1}{u^2}\dfrac{d\upsilon}{du}+2\dfrac{\upsilon}{u^3}}{u\upsilon_g-\dfrac{\upsilon}{u^2}}du, \tag{29}$$

where it is taken into account that:

$$\upsilon=\frac{r^2\dot{r}}{B^*}=\left(1+\frac{1-x}{x}u\right)\left(\frac{2+x}{1+x}u-1\right),\ \upsilon_g=\frac{r_g^2}{B^*}\frac{dr_g}{dt}=\upsilon\Big|_{u=1}=\frac{1}{x(1+x)}. \tag{30}$$

Substituting the magnitudes υ, υ_g and $\dfrac{d\upsilon}{du}$ into Eq. (29), after straightforward transformations one obtains:

$$\frac{dg'(u)}{g'(u)}=-\frac{4u^3+u\left(2x^2+2x-1\right)-2(1+x)x}{u(1-u)^2\left(u+x+x^2\right)}du. \tag{31}$$

Integration of Eq. (31) provides obtaining the analytical form of the generalized LSW distribution, which has been for the first time obtained by us (Vengrenovich *et al*., 2007b) :

$$g'(u)=u^2(1-u)^{-B}(u+x^2+x)^D\exp\left[\frac{C}{1-u}\right], \tag{32}$$

where

$$\begin{cases} B = \dfrac{2x^4 + 4x^3 + 12x^2 + 10x + 5}{A}, \quad C = -\dfrac{3x^2 + 3x + 3}{A}, \\ D = -\dfrac{4x^4 + 8x^3 + 6x^2 + 2x + 1}{A}, \; A = x^4 + 2x^3 + 3x^2 + 2x + 1. \end{cases} \tag{33}$$

For $x = 1$, $B = 11/3$, $C = -1$, $D = -7/3$ Eq. (32) corresponds to the Lifshitz-Slyozov distribution:

$$g'(u) = u^2 (1-u)^{-11/3} (u+2)^{-7/3} \exp\left(-\frac{1}{1-u}\right). \tag{34}$$

For $x = 0$, $B = 5$, $C = -3$, $D = -1$ Eq. (32) corresponds to the Wagner distribution:

$$g'(u) = u(1-u)^{-5} \exp\left(-\frac{3}{1-u}\right). \tag{35}$$

Within the interval $0 \le x \le 1$, the size distribution function is represented by the generalized LSW function. However, for graphic representation of the size distribution function one must compute following Eq. (28), where the conservation law for mass (volume) of a film is taken into account.

To obtain the distributions represented by Eqs. (34) and (35) in the form derived by Lifshitz and Slyozov (Lifshitz and Slyozov, 1958, 1961) and by Wagner (Wagner, 1961), one must go from the variable $u = \dfrac{r}{r_g}$ to the variable $\rho = \dfrac{r}{r_k}$: $u = \dfrac{r}{r_g} = \dfrac{r}{r_k}\dfrac{r_k}{r_g} = \dfrac{\rho}{u_0}$, where u_0 – the locking point ($u_0 = \dfrac{r_g}{r_k}$), and r_k – the critical radius.

2.4 Discussion

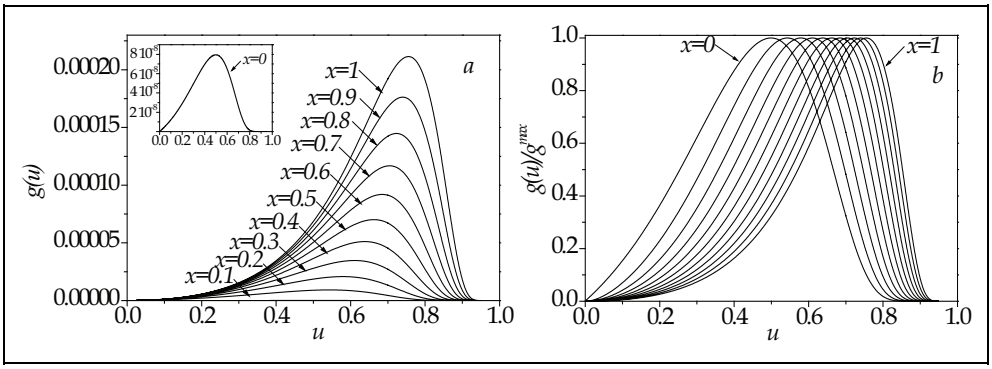

Fig. 2. The curves computed following Eq. (28): a – depending on *x*; b – normalized by maximal magnitudes

Fig. 2,a illustrates the curves corresponding to the distribution Eq. (28) computed for various magnitudes of the parameter x with interval $\Delta x = 0.1$. Inset shows the Wagner function $(x = 0)$, which is hardly to be shown in the main graph in its scale. One can see gradual

transition from the Lifshitz-Slyozov distribution, Eq. (34) ($x = 1$), to the Wagner distribution, Eq. (35). The same curves normalized by their maxima are shown in Fig. 2, b. In this form, these curves are suitable for comparison with the corresponding normalized experimentally obtained histograms.

Note, that computation of the theoretical curve under simultaneous (combined) action of two mass transfer mechanisms, *viz.* volume diffusion and chemical reaction at the interface 'extraction-matrix' has been performed earlier by using numerical techniques (Sagalovich, Slyozov, 1987).

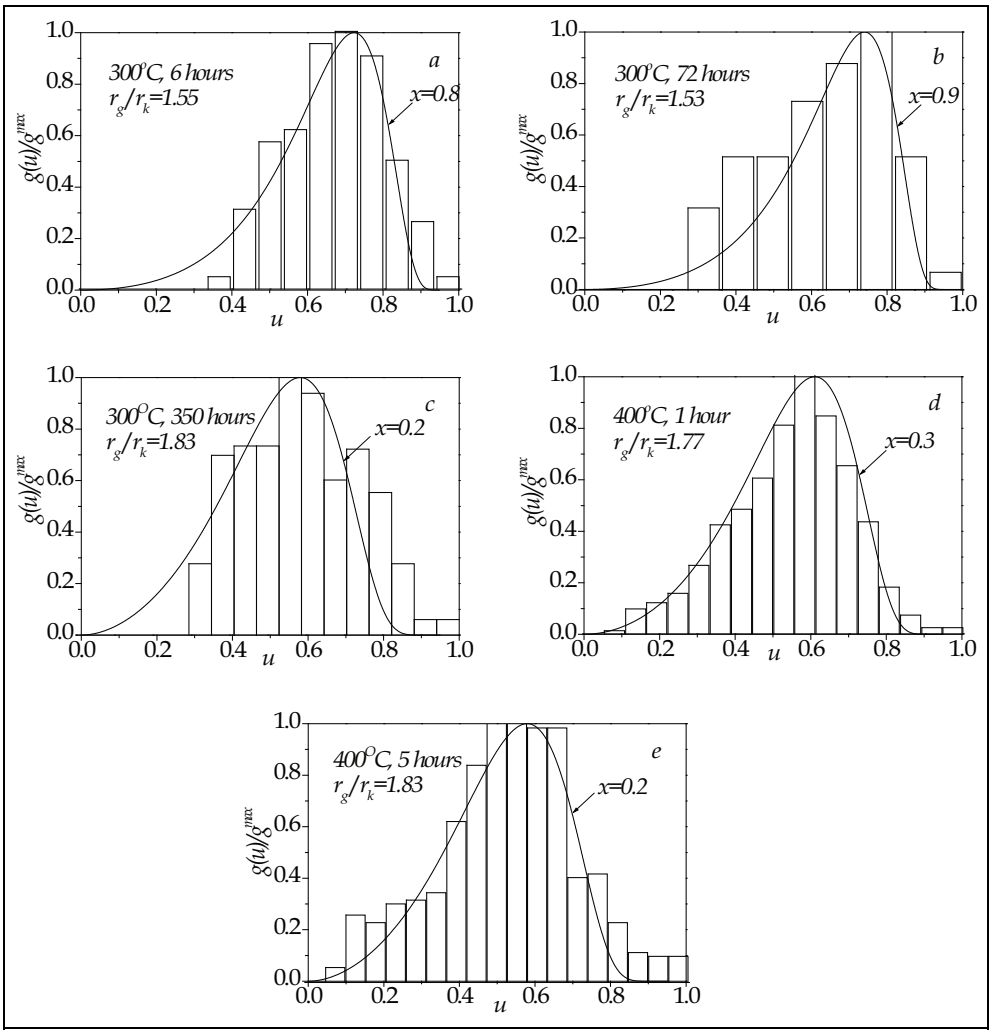

Fig. 3. Comparison of the dependence (28) with the experimentally obtained histograms of nano-scale particles Al_3Sc in alloys $Al-Sc$ (Marquis and Seidman, 2001) for various temperatures and exposure times shown in fragments a, b, c, d, and e

However, the distribution Eq. (28) computed for two mechanisms of mass transfer controlled by the volume diffusion coefficient and kinetics of transition of solved atoms through the interface 'cluster-martix', i.e. by the kinetic coefficient β, has been firstly obtained in analytic form by us. As the rate of forming the chemical connection is higher, as more simply solved atoms overcome potential barrier at the interface 'cluster-martix'. In this case, the rate of cluster growth is in less degree controlled by kinetics at the interface and in more degree by the diffusion processes of mass transfer. For that, the contribution of diffusion flow j_v in general flow of matter j to (from) a particle increases, and the size distribution function becomes more and more close to the Lifshitz-Slyozov distribution, Eq. (34).

Fig. 3 illustrates the results of comparison of the theoretical dependence, Eq. (28), with the experimentally obtained histograms of nano-scale particles Al_3Sc in alloys $Al-Sc$ (Marquis and Seidman, 2001) corresponding to temperature 300°C and exposure times *a* – 6, *в* – 72, *c* – 350 hours; to temperature 400°C and exposure times *d* – 1, *e* – 5 hours. Using the magnitudes of x from the results of comparison, one can determine percentage ratio between the flows $(x \cdot 100\%)$ and find, in this way, what mechanism is predominant.

Besides, knowing x, one can find the ratio $\frac{r_g}{r_k}$ that then may be used as the evaluation parameter for the choice of theoretical curve and comparison with desired histogram.

It follows from Fig. 3 that increasing of the exposure time for temperature 300°C up to 350 hours results in changing the mechanism of particle growth from one limited predominantly by diffusion processes of mass transfer, cf. fragments a – $x = 0.8$; b – $x = 0.9$, to one controlled predominantly by kinetics at the interface 'cluster-matrix', cf. fragment c – $x = 0.2$. Increasing the exposure temperature to 400°C leads to particle growth under conditions controlled predominantly by kinetics at the interface, cf. fragments d – $x = 0.3$; e – $x = 0.2$.

The possibility for implementation of the considered mechanism of particle growth controlled simultaneously both by the volume diffusion coefficient, D_v, and by the kinetic coefficient, β, is also proved by the experimentally obtained histograms for nano-crystals of aluminium obtained under crystallization of amorphous alloy $Al_{85}Ni_8Y_5Co_2$ (Nitsche *et al.*, 2005).

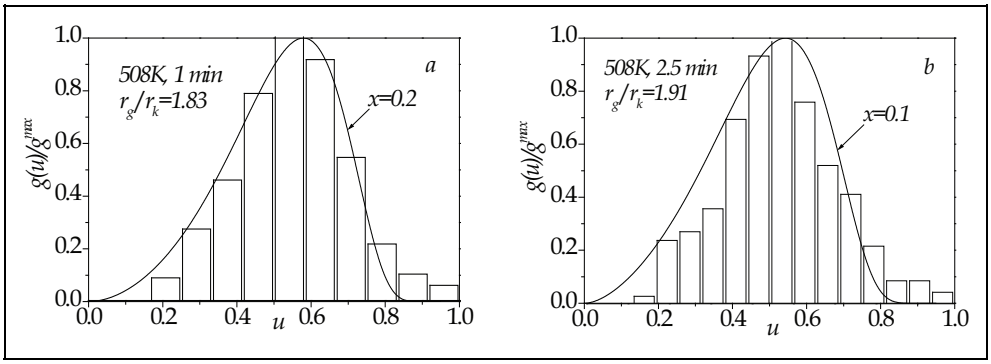

Fig. 4. Comparison with experimental histograms for nano-crystals Al, obtained under annealing of amorphous alloy $Al_{85}Ni_8Y_5Co_2$ (508°K) during: a – 1 min; b – 2.5 min (Nitsche *et al.*, 2005)

Fig. 4 shows comparison of the experimental histograms obtained under crystallization of amorphous alloy for temperature 508°K during 1 min and 2.5 min (fragments a and b, respectively) with the theoretical dependence, Eq. (28). One can see that theoretical dependences well fit the experimental histograms for $x = 0.2$ (fragment a) and $x = 0.1$ (fragment b).

Thus, the considered examples of comparison with the experimental data prove the conclusion that the distribution Eq. (28) is quite eligible for description of experimentally obtained histograms, if particle growth in the process of the Ostwald ripening is controlled simultaneously by two mechanisms of mass transfer, which earlier were considered separately by Lifshitz and Slyozov, and Wagner.

3. Cluster growth under dislocation-matrix diffusion. Size distribution function

The Ostwald's ripening of disperse phases in metallic alloys at the final stage of forming their structure reflecting the late stage of the development of nucleation centers of a new phase in time, when oversaturation between them decreases and their diffusion fields overlap.

In respect to metallic alloys strengthened by disperse extractions of the second phase, the Ostwald ripening is one of the causes of loss of strength of them. As large particles grow and small particles disappear (due to dissolution), distance between particles increases resulting in decreasing of tension necessary for pushing the dislocations between particles and, correspondingly, to decreasing of the creep strength.

For the dislocation mechanism of growth of particles that are coherent with a matrix, the flow along dislocations, j_d, much exceeds the flow of matrix diffusion, j_v:

$$D_d Z q \left(\frac{dC}{dR}\right)_{R=r} >> D_v 4\pi r^2 \left(\frac{dC}{dR}\right)_{R=r}, \tag{36}$$

where D_d, D_v – the coefficients of dislocation and matrix diffusion, respectively, Z – the number of dislocation lines that are fixed or crossing a particle of radius r, q – the square of dislocation pipe cross-section, $\left(\frac{dC}{dR}\right)_{R=r}$ – gradient of concentration at the boundary of a particle. Taking into account that for disturbed coherence (as a consequence of relaxation of elastic tensions (Kondratyev & Utyugow, 1987)) Z is not constant $(Z \neq const)$ being changed in inverse proportion to the particle radius, inequality (36) determines limitations on particle sizes for which the pipe mechanism of diffusion is yet possible (Vengrenovich *et al*., 2002):

$$r << \sqrt[3]{\frac{D_d Z_0 q^{3/2}}{4\pi^2 D_v}}, \tag{37}$$

where Z_0 is the initial number of dislocations fixed at particle surface. If the condition (37) is violated, it means that one can not neglect the component j_v caused by matrix diffusion in full flow of matter j to (from) a particle. In this case, particle growth takes place under diffusion of mixed type (dislocation-matrix one), when one can not neglect any of two components, j_d or j_v, in the resulting flow

$$j = j_d + j_v . \tag{38}$$

Below we represent the results of investigation of peculiarities of the Ostwald ripening of clusters under dislocation-matrix diffusion and, in part, computation of the size distribution function and temporal dependences for mean (critical) and maximal particle sizes as a function of the ratio of flows j_d and j_v .

3.1 The rate of growth and temporal dependences for the mean (critical) and maximal sizes of clusters

As in previous case, the rate of growth is determined from Eq. (9):

$$\frac{dr}{dt} = \frac{1}{4\pi r^2} j v_m , \tag{39}$$

where j is given by Eq. (38), and j_d and j_v take the magnitudes of left and right parts of inequality (36), respectively:

$$j = D_d \cdot 2\frac{Z_0 q^{1/2}}{2\pi r} q \left(\frac{dC}{dR}\right)_{R=r} + D_v 4\pi r^2 \left(\frac{dC}{dR}\right)_{R=r} , \tag{40}$$

where we take into account that, in a flow j_d, there is $Z = \frac{Z_0 q^{1/2}}{2\pi r}$ (Vengrenovich *et al.*, 2002).

Substituting Eq. (40) in Eq. (39) and taking into account that $\left(\frac{dC}{dR}\right)_{R=r}$ $= \frac{2\sigma v_m}{\mathrm{T}R^*} C_\infty \cdot \frac{1}{r^2}\left(\frac{r}{r_\kappa} - 1\right)$, where σ is the surface energy, C_∞ is the equilibrium concentration of solid solution, R^* is the gas constant, and T is a temperature, one obtains:

$$\frac{dr}{dt} = \frac{1}{4\pi r^4} \frac{2\sigma v_m^2 C_\infty}{R^* \mathrm{T}} \left(D_d 2 \cdot \frac{Z_0 q^{1/2}}{2\pi r} \cdot q + D_v 4\pi r^2 \right) \left(\frac{r}{r_\kappa} - 1\right). \tag{41}$$

Designating, as previously, the shares j_v and j_d in the general flow j as x and $(1-x)$, respectrively, one can represent the rate of growth, Eq. (41), in the form

$$\frac{dr}{dt} = \frac{1}{r^5} \frac{\sigma v_m^2 C_\infty Z_0 q^{3/2} D_d}{2\pi^2 R^* \mathrm{T}} \left(1 + \frac{x}{1-x}\frac{r^3}{r_g^3}\right)\left(\frac{r}{r_\kappa} - 1\right), \tag{42}$$

or:

$$\frac{dr}{dt} = \frac{1}{r^2} \frac{\sigma v_m^2 C_\infty Dv}{R^* \mathrm{T}} \left(\frac{1-x}{x}\frac{r_g^3}{r^3} + 1\right)\left(\frac{r}{r_\kappa} - 1\right). \tag{43}$$

Eq. (42) describes the rate of particle growth for predominant contribution in the general flow of the diffusion matter along dislocations, with the share contribution x of matrix

diffusion; and Eq. (43) describes the rate of growth under matrix diffusion, with the share contribution $(1-x)$ along dislocations.

Eqs. (42) or (43) provide determining the locking point $u_0 = \frac{r_g}{r_k}$, and one finds out from the continuity equation (8), after separation of variables, the specific size distribution function, $f(u)$, where $u = \frac{r}{r_g}$. The ratio $\frac{r_g}{r_\kappa}$, in accordance with (Vengrenovich, 1982), equals:

$$\frac{r_g}{r_\kappa} = \frac{6-3x}{5-3x}. \tag{44}$$

If we let $r = r_g$ in Eq. (42), and the ratio $\frac{r_g}{r_\kappa}$ is replaced by its magnitude from Eq. (44), then after integration one obtains the temporal dependence for maximal

$$r_g = \left(\frac{6A^*}{(5-3x)(1-x)} t \right)^{1/6}, \tag{45}$$

and critical

$$r_\kappa = \left(\frac{6A^*(5-3x)^5}{(6-3x)^6(1-x)} t \right)^{1/6}, \tag{46}$$

particle sizes, where $A^* = \frac{\sigma v_m^2 C_\infty Z_0 q^{3/2} D_d}{2R^* T}$.

Eqs. (45) and (46) describe changing in time the sizes of particles under dislocation-matrix diffusion for predominant contribution of matter diffusion along dislocations. For $x = 0$, that corresponds to the first limiting case, particle growth is limited by diffusion along dislocation:

$$r_g^6 = \frac{6}{5} A^* t, \; r_\kappa^6 = \left(\frac{5}{6} \right)^5 A^* t, \; \frac{r_g}{r_k} = \frac{6}{5}. \tag{47}$$

For that ($x = 0$), the specific size distribution function has a form (Vengrenovich *et al.*, 2002):

$$g'(u) = \frac{u^5 \exp\left(-\frac{0.2}{(1-u)} \right) \exp\left(-0.0287 \tan^{-1}\left(\frac{2u+a}{\sqrt{4b-a^2}} \right) \right) \exp\left(-0.1127 \tan^{-1}\left(\frac{2u+c}{\sqrt{4d-c^2}} \right) \right)}{(1-u)^\alpha \left(u^2 + au + b \right)^\beta \left(u^2 + cu + d \right)^\gamma}, \tag{48}$$

where $a \cong 2.576$, $b \cong 2.394$, $c \cong -0.576$, $d \cong 0.088$, $\alpha \cong 41/15$, $\beta \cong 1.562$, $\gamma \cong 1.572$.
Integrating for the same conditions Eq. (43), one obtains:

$$r_g = \left(\frac{6B^*}{x(5-3x)} t \right)^{1/3}, \tag{49}$$

$$r_{\kappa} = \left(\frac{6B^{*}(5-3x)^{2}}{x(6-3x)^{3}} t \right)^{1/3}, \tag{50}$$

where $B^{*} = \frac{2\sigma v_m C_{\infty} D_v}{R * \mathrm{T}}$.

Another limiting case corresponds to $x = 1$:

$$r_g^3 = \frac{3}{2} B^{*} t, \; r_{\kappa}^3 = \frac{4}{9} B^{*} t, \; \frac{r_g}{r_{\kappa}} = \frac{3}{2}, \tag{51}$$

and the size distribution function is described by the Lifshitz-Slyozov function, Eq. (34):

$$g'(u) = u^2 (1-u)^{-11/3} (u+2)^{-7/3} \exp\left(\frac{1}{1-u} \right).$$

3.2 Size distribution function of clusters

The size distribution function of clusters within the interval $0 \le x \le 1$ is represented, as previously, in the form Eq. (24) (Vengrenovich, 1982), where $g'(u)$ - relative size distribution function, and $u = \frac{r}{r_g}$. From the mass conservation law and disperse phase, Eq. (25), one finds $\varphi(r_g)$, Eq. (26), and, correspondingly,

$$g(u) = Q \cdot g'(u), \tag{52}$$

where $Q = \frac{\mathrm{M}}{\frac{4}{3}\pi\rho \int_0^1 u^3 g'(u) du}$, and ρ – particle density.

If one replaces in the continuity equation (8) $f(r,t)$ and $\dot{r}$ by their magnitudes from Eqs. (24) and (42) (or Eq. (43)) and differentiates u instead of on r and t, then variables in Eq. (8) are separated:

$$\frac{dg'(u)}{g'(u)} = -\frac{4\upsilon_g + 2\frac{\upsilon}{u^3} - \frac{1}{u^2}\frac{d\upsilon}{du}}{u\upsilon_g - \frac{\upsilon}{u^2}} du, \tag{53}$$

where we take into account that $\upsilon = \frac{\dot{r} r^3}{B^{*}}$, $\upsilon_g = \frac{\dot{r}_g r_g^3}{B^{*}}$, $\frac{du}{dr} = \frac{1}{r_g}$, and $\frac{du}{dr_g} = -\frac{u}{r_g}$.

Substituting in Eq. (53) the magnitudes $\upsilon = \left(\frac{1-x}{x}\frac{1}{u^3} + 1 \right)\left(\frac{6-3x}{5-3x} u - 1 \right)$ and $\upsilon_g = \frac{1}{x(5-3x)}$ and decomposing in denominator the second-order polynomial into prime factors, one gets the following form of Eq. (53):

$$\frac{dg'(u)}{g'(u)} = -\frac{4u^6 + u^4\left(6x - 3x^2\right) - 2u^3\left(5x - 3x^2\right) + 4u\left(3x^2 - 9x + 6\right) - 5\left(3x^2 - 8x + 5\right)}{u(1-u)^2\left(u^2 + au + d\right)\left(u^2 + bu + p\right)}du = \tag{54}$$

$$= A\frac{du}{u} + B\frac{du}{1-u} + C\frac{du}{(1-u)^2} + (Du + E)\frac{du}{u^2 + au + d} + (Fu + G)\frac{du}{u^2 + bu + p},$$

where $a = 2.575$; $b = -0.575$; $d = 2.398$; $p = 2.089$.

Integrating Eq. (54), one obtains the analytical form of the relative size distribution function for arbitrary $0 \le x \le 1$:

$$g'(u) = \frac{u^A\left(u^2 + au + d\right)^{\frac{D}{2}}\left(u^2 + bu + p\right)^{\frac{F}{2}}}{(1-u)^B}\exp\left(\frac{C}{1-u}\right)\exp\left(\frac{E - \frac{Da}{2}}{\sqrt{d - \frac{a^2}{4}}}\tan^{-1}\left(\frac{u + \frac{a}{2}}{\sqrt{d - \frac{a^2}{4}}}\right)\right) \times$$

$$\times \exp\left(\frac{G - \frac{Fb}{2}}{\sqrt{p - \frac{b^2}{4}}}\tan^{-1}\left(\frac{u + \frac{b}{2}}{\sqrt{p - \frac{b^2}{4}}}\right)\right), \tag{55}$$

where the coefficients A, B, C, D, E, F, G are found out by matrix solving (Gauss method) the system of seven equations obtained by integrating Eq. (54) ($A = 5; B = 2.731;\ C = -0.2;$ $D = -3.117; E = -4.037; F = -3.142;\ G = 0.747$) .

3.3 Discussion

Fig. 5 *a* shows the dependences corresponding to the size distribution function, Eq. (52), computed for various magnitudes of x . It is hardly to represent such dependence for $x = 1$ (the Lifshitz-Slyozov distribution) at the same scale; that is why this case is illustrated in other scale at inset.

It is clearly seen that the maxima of curves reached at point u' diminish, as x grows, taking the maximal magnitude for the curve $x = 1$. Magnitude u' itself is determined for the specified x from the following equation:

$$4u^6 + u^4\left(6x - 3x^2\right) - 2u^3\left(5x - 3x^2\right) + 4u\left(3x^2 - 9x + 6\right) - 5\left(3x^2 - 8x + 5\right)\Big|_{u=u'} = 0\,. \tag{56}$$

One can see from Fig. 5 *b*, showing the same dependences normalized by their maxima, that as x grows, as magnitudes u' are shifted to the left (diminish), cf. the inset.

Fig. 6 shows the results of comparison of experimentally obtained histogram with the Liwfitz-Slyozov distribution – (*a*), and the distribution (52) for $x = 0.7$ – (*b*). It is regularly *a priory* assumed (Gaponenko, 1996) that the experimentally obtained histogram shown in Fig. 6 and taken from the paper (Katsikas et al., 1990) that corresponds to the size distribution of nanoclusters of CdS is described by the Lifshitz-Slyozov distribution. However, as one can see from Fig. 6,*b*, the dependence computed by us is narrower, being better fitting a

histogram than the curve in Fig. 6,*a*. It means that formation of quantum dots of *CdS* in process of the Ostwald's ripening obtained by chemical evaporation is realized through mixed diffusion, with 70% share of matrix ($x = 0.7$) and 30% dislocation ($x = 0.3$) diffusion. For that, it is of importance that temporal growth of nanocrystals of *CdS* obeys the cubic law, $\langle r \rangle^3 \sim t$, cf. Eq. (50). It shows that, in first, that the size distribution is formed in process of the Ostwald's ripening, and, secondly, that growth of *CdS* nanocrystals is limited, mainly, by matrix diffusion with the mentioned above share contribution of dislocation diffusion.

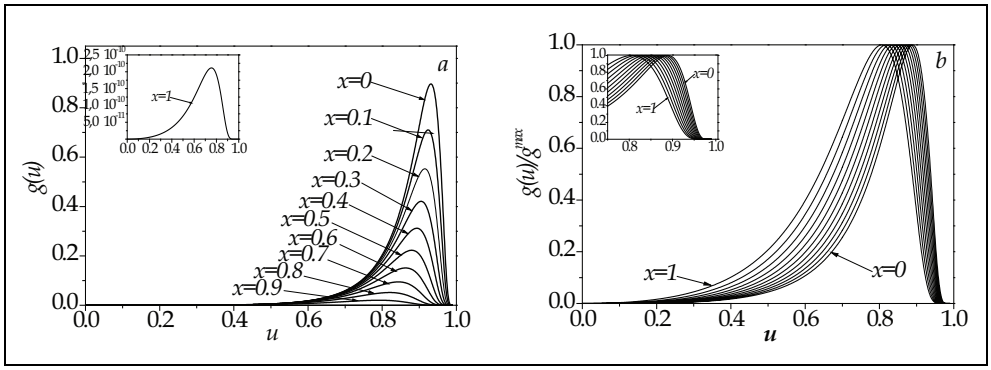

Fig. 5. Size distribution functions, Eq. (52), for various magnitudes of x - *a*; the same distributions normalized by their maxima - *b*

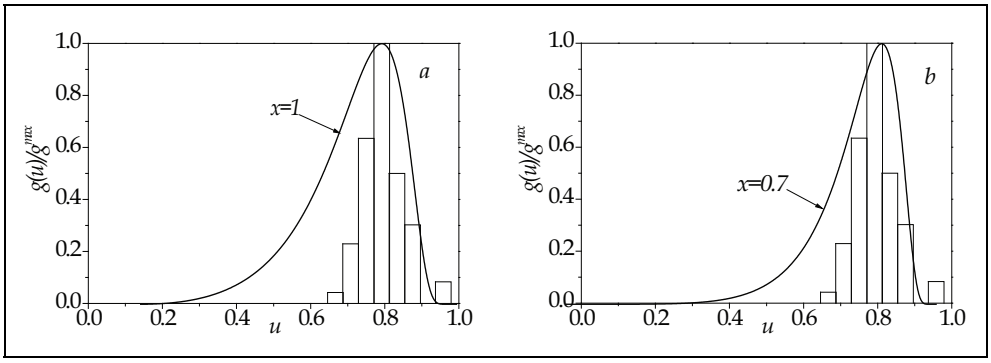

Fig. 6. Comparison with experimentally obtained histogram for nanocrystals of *CdS* (Katsikas *et. al*., 1990) with the theoretical dependence: *a* – the Lifshitz-Slyozov distribution, Eq. (34), *b* – distribution corresponding to Eq. (55) for $x = 0.7$

Let us note that there is the set of quantum dots in semiconductor compounds II-IV obtained by chemical evaporation techniques and having sizes from 1 to 5 nm (Gaponenko, 1996), for which the size distribution function occurs be narrower than one for the Lifshitz-Slyozov distribution.

Similarly to as crystalline gratings of numerous matters are controlled by simultaneous (combined) action of various connection types, the cluster growth goes on under mixed

diffusion, where only one of the types of diffusion can be predominant (matrix, surface, dislocation at the grain boundaries, etc.).

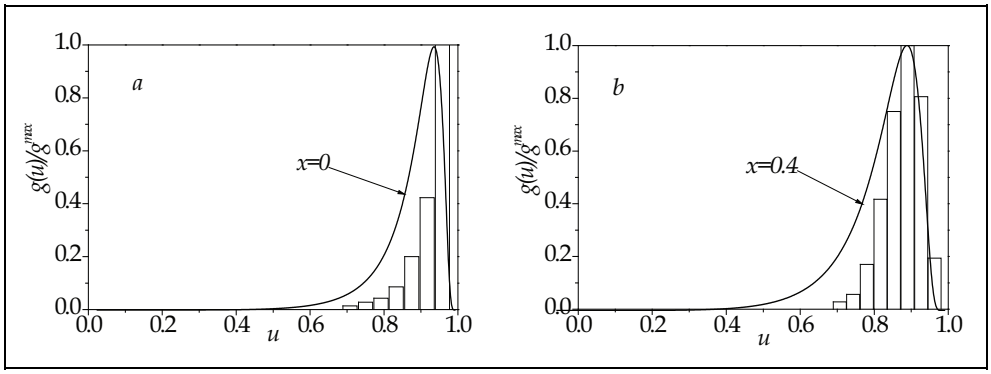

Fig. 7. Example of accidental concurrence of experimentally obtained histogram with the theoretical dependence, Eq. (55), for heterogeneous nucleation of aluminum nanoclusters (Aronin *et al.*, 2001), much earlier than the stage of the Ostwald's ripening comes: *a* – $x = 0$; *b* – $x = 0.4$

Note, the idea of combined action of several mechanisms of diffusion mass transfer has been formulated in several earlier papers (Slyzzov *et al.*, 1978; Sagalovich and Slyozov, 1987). However, the size distribution function for particles coherently connected with the matrix Eq. (55) for combined action of two mechanisms of mass transfer, i.e. diffusion along dislocations and matrix diffusion, has been firstly found by us (Vengrenovich *et al.*, 2007a).

Let us emphasize once more point connected with the study of particle growth under the Ostwald's ripening. It occurs that comparison of the experimentally obtained histograms with the theoretically found dependences does not provide an unambiguous answer the question: What is the mechanism of particle growth? and: is the stage of the Ostwald's ripening occurred? To elucidate these questions, the temporal dependences for a mean particle size, $\langle r \rangle$, are needed.

For example, Fig. 7 shows comparison of experimental histograms for nanoclusters of aluminum obtained by annealing of amorphous alloy $Al_{86}Ni_{11}Yb_3$ (Aronin *et al.*, 2001) with theoretical dependence, Eq. (55), for (*a*) – $x = 0$, and (*b*) – $x = 0.4$. Satisfactory concurrence, however, is accidental. As it is shown in paper (Aronin *et al.*, 2001), the LWS theory is not applicable to this case. Growth of aluminum nanocrystals obeys parabolic dependence $\langle r \rangle \sim t^{1/2}$, rather than to the dependence $\langle r \rangle \sim t^{1/6}$. Histograms in Fig. 7 correspond to heterogeneous nucleation of aluminium clusters that precedes the Ostwald's ripening, which follows much later.

Thus, for estimation of a share (percentage) of the each component, j_d and j_v, in the diffusion flow, one must compare both experimentally obtained histograms with the theoretical dependences and temporal dependences for mean (critical) particle sizes. In the case of metallic alloys strengthened by disperse particles, it enables establishing the mechanism of particle's enlargement, while for quasi-zero-dimension semiconductor structures it makes possible to study, under the Ostwald's ripening, nanoclusters (quantum dots) obtaining by chemical evaporation techniques.

4. Mass transfer between clusters in heterostructures. The generalized Chakraverty-Wagner distribution

The structure and phase dispersion (the particle size distribution function) at the late stages of decay of oversaturated solid solution, i.e. under the stage of the Ostwald's ripening, are determined by the mechanisms of mass transfer between the structure components.

If the particle growth is limited by the coefficient of volume or matrix diffusion D_υ, then a mean cluster size, $\langle r \rangle$, changes in time as $t^{1/3}$, and the particle size distribution is governed by the Lifshitz-Slyozov distribution function (Lifshits, Slyozov, 1958, 1961). But if the cluster growth is controlled by the processes at the boundary 'particle-matrix', being governed by the kinetic coefficient β, then $\langle r \rangle$ changes as $t^{1/2}$, and the size distribution function corresponds to the Wagner distribution (Wagner, 1961). In the case of simultaneous action of two mechanisms of growth, dispersion of extractions is described by the generalized LSW distribution (Vengrenovich *et al.,* 2007b).

Generalization of the LSW theory for surface disperse systems, in part, for island films, is of especial interest. This generalization becomes urgent now in connection with development of nanotechnologies and forming nanostructures (Alekhin, 2004; Alfimov *et al.*, 2004; Andrievskii, 2002; Dunaevskii *et al.*, 2003; Dmitriev, Reutov, 2002; Roko, 2002; Gerasimenko, 2002). In part, semiconductor heterostructures with quantum dots obtained under the Stranskii-Kastranov self-organizing process find out numerous practical applications (Bartelt, Evans, 1992; Bartelt *et al.,* 1996; Goldfarb *et al.,* 1997a, 1997b; Joyce *et al.,* 1998; Kamins *et al.,* 1999; Pchelyakov *et al.,* 2000; Ledentsov *et al.,* 1998; Vengrenovich *et al.,* 2001b, 2005, 2006a, 2006b, 2007a).

Chakraverty (Chakraverty, 1967) for the first time applied the LSW theory to describe evolution of structure of discrete films containing of separate islands (clusters) of the form of spherical segments, cf. Fig. 8. Within the Chakraverty model, a film consists of separate cupola-like islands, which are homogeneously (in statistics sense) distributed into oversaturated 'sea' (solution) of atoms absorbed by a substrate, so-called adatoms.

One can see from Fig. 8 that cupola-like clusters are the part of a sphere of radius R_C, with the boundary angle θ. That is why, the radius of base of island, r, length of its perimeter, l, its surface, S, and volume, V, can be expressed through R_C: $r = R_C \sin\theta$, $l = 2\pi R_C \sin\theta$, $S = 4\pi R_C^2 \alpha_2(\theta)$, $V = \frac{4}{3}\pi R_C^3 \alpha_1(\theta)$, where $\alpha_1(\theta) = \frac{2 - 3\cos\theta + \cos^2\theta}{4}$, $\alpha_2(\theta) = \frac{1 - \cos\theta}{2}$ (Hirth, Pound, 1963).

Concentration of adatoms at the cluster base, C_r, is given by the Gibbs-Thomson formula:

$$C_r = C_\infty \exp\left(\Delta P \frac{\upsilon_m}{kT}\right) \approx C_\infty \left(1 + \Delta P \frac{\upsilon_m}{kT}\right), \tag{57}$$

where C_∞ - equilibrium concentration at temperature T, υ_m - volume of adatoms, k - the Boltzmann's constant, ΔP - the Laplasian pressure caused by island surface's curvature. It can be determined by equaling the work necessary for diminishing of an island volume by $d\mathrm{V}$ to the caused by it free energy of island surface:

$$\Delta P d\mathrm{V} = \sigma dS \quad \text{or} \quad \Delta P = \sigma \frac{dS}{d\mathrm{V}} = 2\frac{\sigma}{R_C}\frac{\alpha_2(\theta)}{\alpha_1(\theta)}, \tag{58}$$

where σ - specific magnitude of surface energy.
Taking into account Eq. (58), Eq. (57) can be rewritten in the form:

$$C_r = C_\infty \exp\left(\frac{2\sigma}{R_C}\frac{\upsilon_m}{kT}\frac{\alpha_2(\theta)}{\alpha_1(\theta)}\right) = C_\infty \exp\left(\frac{2\sigma}{r}\frac{\upsilon_m \sin\theta}{kT}\frac{\alpha_2(\theta)}{\alpha_1(\theta)}\right) \approx C_\infty\left(1+\frac{2\sigma}{r}\frac{\upsilon_m \sin\theta}{kT}\frac{\alpha_2(\theta)}{\alpha_1(\theta)}\right). \quad (59)$$

Note, the Gibbs-Thomson formula in the form Eq. (59) has been written for the first time in paper (Vengrenovich *et. al.*, 2008a).

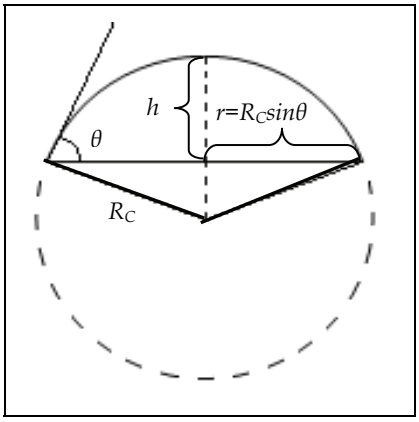

Fig. 8. An island (cluster) in the form of spherical segment as a part of the sphere of radius R_C

Thus, the concentration of adatroms at the boundary 'cluter-substarte' along the line of separation (along the cluster diameter) is determined by the curvature radius of cluster base, r, as it is expected for a plane problem. As the cluster radius diminishes, as the concentration of adatoms at the interface with the cluster must grow. And *vice versa*, as cluster size grows as C_r diminishes. For that, some mean concentration, $\langle C\rangle$, is set in at a substrate that is determined by the critical radius r_k:

$$\langle C\rangle = C_\infty \exp\left(\frac{2\sigma}{r_k}\frac{\upsilon_m \sin\theta}{kT}\frac{\alpha_2(\theta)}{\alpha_1(\theta)}\right) \approx C_\infty\left(1+\frac{2\sigma}{r_k}\frac{\upsilon_m \sin\theta}{kT}\frac{\alpha_2(\theta)}{\alpha_1(\theta)}\right) \quad (60)$$

The clusters for which $C_r > \langle C\rangle$ will dissolve. The clusters for which $C_r < \langle C\rangle$ will grow. So, the clusters of critical size r_k are in equilibrium with a solution of adatoms and radius of such adatoms is determined by Eq. (60):

$$r_k = \frac{\alpha}{\Delta}, \quad (61)$$

where oversaturation is $\Delta = \langle C\rangle - C_\infty$, and $\alpha = \frac{2\sigma C_\infty \upsilon_m}{kT}\sin\theta\frac{\alpha_2(\theta)}{\alpha_1(\theta)}$.

For the diffusion mechanism of growth of cupola-like clusters, the mass transfer between them is realized through surface diffusion under conditions of self-consistent diffusion field (Sagalovich, Slyozov, 1987; Kukushkin, Osipov, 1998) that is characterized by the surface

diffusion coefficient, D_S. Adatoms reaching island perimeters through surface diffusion and overcoming the potential barrier at the interface 'island-substrate', occur at their surfaces. Redistribution of adatoms at cluster surface is made by capillary forces, *viz*. surface tension forces.

In accordance with Wagner, the diffusion growth mechanism with maintenance of island form, i.e. with maintenance of the boundary angle θ is possible, if atoms crossing the interface 'island-substrate' and occurring at their surface in unite time have the time to form chemical connections necessary for reproduction of island matter structure. If it is not so, then adatoms are accumulated near the interface 'island-substrate' with concentration C, that is equal to mean concentration of a solution, $\langle C \rangle$. For that, the process of growth is no more controlled by the surface diffusion coefficient, D_S, but rather by the kinetic coefficient β.

Following to Wagner (Wagner, 1961), the number of adatoms crossing the boundary 'island-substrate' and occurring at the island surface at unite of time is determined as:

$$j_1 = 4\pi R_C^2 \alpha_2(\theta)\beta\langle C\rangle = 4\pi r^2 \frac{\alpha_2(\theta)}{\sin^2\theta}\beta\langle C\rangle, \tag{62}$$

and the number of atoms leaving it at unite of time equals:

$$j_2 = 4\pi r^2 \frac{\alpha_2(\theta)}{\sin^2\theta}\beta C_r, \tag{63}$$

so that the total flow of atoms involved into formation of chemical connection is:

$$j_i = j_1 - j_2 = 4\pi r^2 \frac{\alpha_2(\theta)}{\sin^2\theta}\beta\left(\langle C\rangle - C_r\right), \tag{64}$$

where C_r is determined by Eq. (59).

At the same time, the diffusion flow of adatoms, j_S, to (from) an island is determined by the concentration gradient, $\left(\frac{dC}{dR}\right)_{R=r}$, at the boundary 'island-substrate':

$$j_S = 2\pi r D_S \left(\frac{dC}{dR}\right)_{R=r}. \tag{65}$$

It can be determined by solving the Fick equation that describes concentration of adatoms in the vicinity of isolated island. This equation, within the conditions of stationarity and radial symmetry, takes the form:

$$\frac{1}{R}\frac{d}{dR}\left(RD_S\frac{dC}{dR}\right) = 0, \tag{66}$$

where R is changed within the interval $r \le R \le lr$, $l = 2;3$ (screening distance (Chakraverty, 1967)).

Solution of Eq. (66) can be represented in the form:

$$C(R) = C_1 \ln\frac{R}{r} + C_2, \tag{67}$$

where the constants C_1 and C_2 are determined form the boundary conditions:

$$C(R) = C_r \text{, if } R = r \text{,} \tag{68}$$

$$C(R) = \langle C \rangle \text{, if } R = lr \text{,} \tag{69}$$

from which one obtains:

$$C_1 = \frac{\langle C \rangle - C_r}{\ln l} \text{, } C_2 = C_r \text{.} \tag{70}$$

Thus, the solution of Eq. (67) takes the form:

$$C(R) = \frac{\langle C \rangle - C_r}{\ln l} \ln \frac{R}{r} + C_r \text{.} \tag{71}$$

Knowing $C(R)$, one can determine j_S:

$$j_S = \frac{2\pi D_S}{\ln l} \left(\langle C \rangle - C_r \right) \text{.} \tag{72}$$

At the equilibrium state:

$$j_i = j_S = j \text{.} \tag{73}$$

Thus, the flow j to (from) a cluster can be written as:

$$j = \frac{1}{2} \left(j_i + j_S \right) \text{.} \tag{74}$$

In general case, the flow j equals:

$$j = j_i + j_S \text{.} \tag{75}$$

Thus, the problem of determination of the cluster size distribution function is reduced to accounting the ratio between the flows j_i and j_S in the equation of cluster growth rate.

4.1 Island growth rate

The rate of growth of isolated island (cluster) is determined form the following condition:

$$\frac{d}{dt} \left(\frac{4}{3} \pi R_C^3 \alpha_1(\theta) \right) = \frac{d}{dt} \left(\frac{4}{3} \pi \frac{r^3}{\sin^3 \theta} \alpha_1(\theta) \right) = j \upsilon_m \text{,} \tag{76}$$

where j is given by Eq. (75). Taking into account Eqs. (64) and (72), one finds from Eq. (76) the rate of cluster growth:

$$\frac{dr}{dt} = \frac{1}{4\pi r^2} \frac{\sin^3 \theta}{\alpha_1(\theta)} \upsilon_m \left[4\pi r^2 \frac{\alpha_2(\theta)}{\sin^2(\theta)} \beta \left(\langle C \rangle - C_r \right) + \frac{2\pi D_S}{\ln l} \left(\langle C \rangle - C_r \right) \right] \text{.} \tag{77}$$

Designating the ratio of flows as:

$$\frac{j_S}{j_i} = \frac{x}{1-x}, \tag{78}$$

where $x = j_S / j$ is the contribution of the flow j_S in the total flow j and, correspondingly, $(1-x) = j_i / j$, the rate of growth of islands, Eq. (77), under surface diffusion with the share contribution $(1-x) = j_i / j$ of the part of flow controlled by the kinetic coefficient β, is rewritten in the form:

$$\frac{dr}{dt} = \frac{\sigma C_\infty \upsilon_m^2 D_S}{2kT} \frac{\sin^4 \theta \alpha_2(\theta)}{\alpha_1^2(\theta) \ln l} \frac{1}{r^3} \left(\frac{1-x}{x} \frac{r^2}{r_g^2} + 1 \right) \left(\frac{r}{r_k} - 1 \right) = \frac{A^*}{r^3} \left(\frac{1-x}{x} \frac{r^2}{r_g^2} + 1 \right) \left(\frac{r}{r_k} - 1 \right), \tag{79}$$

where $A^* = \frac{\sigma C_\infty \upsilon_m^2 D_S}{2kT} \frac{\sin^4 \theta \alpha_2(\theta)}{\alpha_1^2(\theta) \ln l}$.

For $x = 1$, Eq. (79) takes the following simplified form:

$$\frac{dr}{dt} = \frac{A^*}{r^3} \left(\frac{r}{r_k} - 1 \right), \tag{80}$$

coinciding with the diffusion rate of growth of islands (Chakraverty, 1967; Eq. (17)).
If the rate of island growth is controlled by the kinetic coefficient β with the share contribution of a flow due to surface diffusion, ($x = j_S / j$), then the rate of growth, Eq. (79), takes the form:

$$\frac{dr}{dt} = \frac{\sigma C_\infty \upsilon_m^2 \beta}{kT} \frac{\sin^2 \theta \alpha_2^2(\theta)}{\alpha_1(\theta)} \frac{1}{r} \left(\frac{x}{1-x} \cdot \frac{r_g^2}{r^2} + 1 \right) \left(\frac{r}{r_k} - 1 \right) = \frac{B^*}{r} \left(\frac{x}{1-x} \cdot \frac{r_g^2}{r^2} + 1 \right) \left(\frac{r}{r_k} - 1 \right), \tag{81}$$

where $B^* = \frac{\sigma C_\infty \upsilon_m^2 \beta}{kT} \frac{\sin^2 \theta \alpha_2^2(\theta)}{\alpha_1(\theta)}$.

For $x = 0$, Eq. (81) is rewritten as:

$$\frac{dr}{dt} = \frac{B^*}{r} \left(\frac{r}{r_k} - 1 \right), \tag{82}$$

that coincides with the equation for the rate of island growth controlled by the kinetic coefficient β (Chakraverty, 1967; Eq. (31)).

4.2 Temporal dependences for critical (r_k) and maximal (r_g) sizes of islands (clusters)

For integrating Eqs. (79) and (81) to determine the temporal dependences of r_k and r_g, it is necessary to determine the magnitudes of the locking point, $u_0 = r_g / r_k$. Its magnitude, in accordance with paper (Vengrenovich, 1982), is found from the condition:

$$\frac{d}{dr} \left(\frac{\dot{r}}{r} \right) \Bigg|_{r=r_g} = 0, \tag{83}$$

where, for example:

$$\frac{\dot{r}}{r}=\frac{A^*}{r^4}\left(\frac{1-x}{x}\frac{r^2}{r_g^2}+1\right)\left(\frac{r}{r_k}-1\right). \tag{84}$$

By differentiation, one finds:

$$u_0=\frac{r_g}{r_k}=\frac{2x+2}{2x+1}. \tag{85}$$

For $x=0$ (the Wagner mechanism of growth), $r_g/r_k=2$, and for $x=1$ (the diffusion mechanism of growth), $r_g/r_k=4/3$.

Using the magnitude u_o of the locking point, Eq. (85), one can express the specific rate of growth $\dot{r}/r$, Eq. (84), through dimensionless variable, $u=r/r_g$, that enables its representation not schematically, but in the form of a graph for various magnitudes of the parameter x:

$$\upsilon'=\frac{r_g^4}{A^*}\frac{dr}{dt}=\frac{1}{u^4}\left(\frac{1-x}{x}u^2+1\right)\left(\frac{2x+2}{2x+1}u-1\right), \tag{86}$$

where the dimensionless specific rate of growth is $\upsilon'=\frac{r_g^4}{A^*}\frac{dr}{dt}$.

Fig. 9 shows the dependence of υ' on u as a function of x. The role of the locking point consists in that within the LSW theory all solutions, including the size distribution function, are determined for magnitudes u_o alone. It means physically that under the Ostwald's ripening process, the relation between critical and maximal sizes of clusters is always the same, i.e. being constant one.

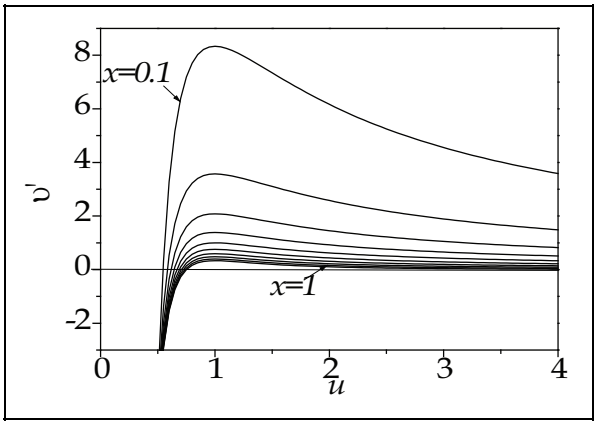

Fig. 9. Dependence of the dimensionless growth rate, υ', on u for various magnitudes of x

For determining r_g and r_k, we use Eqs. (79) and (81). Substituting in Eq. (79) $r=r_g$ and replacing the ratio r_g/r_k by its magnitude (85), one obtains after integrating:

$$r_g^4=4\frac{A^*}{x(2x+1)}t, \tag{87}$$

or:

$$r_k^4 = 4A^* \frac{(2x+1)^3}{x(2x+2)^4} t \,. \tag{88}$$

For $x = 1$, growth of islands is fully controlled by the surface diffusion coefficient (Chakraverty, 1967):

$$r_g^4 = \frac{4}{3} A^* t \,, \quad r_k^4 = \frac{27}{64} A^* t \,, \quad \frac{r_g}{r_k} = \frac{4}{3} \,. \tag{89}$$

In the same way, one obtains from Eq. (81):

$$r_g^2 = 2\frac{B^*}{(1-x)(2x+1)} t \,, \; r_k^2 = 2\frac{B^*(2x+1)}{(1-x)(2x+2)^2} t \,. \tag{90}$$

Eq. (90) describes of island growth under conditions controlled by the kinetic coefficient β, with the contribution x of surface diffusion. If $x = 0$, then the growth process is fully controlled by kinetics of crossing the interface 'island-substrate' (Wagner, 1961):

$$r_g^2 = 2B^* t \,, \; r_k^2 = \frac{1}{2} B^* t \,, \; \frac{r_g}{r_k} = 2 \,. \tag{91}$$

4.3 Generalized Chakraverty-Wagner distribution for the case of cupola-like islands (clusters)

As previously, the size distribution function of clusters (islands) within the interval $0 \le x \le 1$ is represented as the product $f(r,t) = \varphi(r_g) g'(u)$, where $g'(u)$ is the relative size distribution of clusters, $u = r/r_g$. The function $\varphi(r_g)$ is determined from the conservation law of disperse phase volume:

$$\Phi = \frac{4}{3}\pi\alpha_1(\theta)\frac{1}{\sin^3\theta}\int_0^{r_g} r^3 f(r,t)\,dr \,. \tag{92}$$

Using Eq. (92), one finds:

$$\varphi(r_g) = \frac{Q}{r_g^4} \,, \tag{93}$$

where:

$$Q = \frac{\Phi}{\frac{4}{3}\pi\alpha_1(\theta)\frac{1}{\sin^3\theta}\int_0^1 u^3 g'(u)\,du} \,. \tag{94}$$

Taking into account Eq. (93), the function $f(r,t)$ is rewritten as:

$$f(r,t) = \frac{1}{r_g^4} Q \cdot g'(u) = \frac{1}{r_g^4} g(u) \,, \tag{95}$$

where the relative size distribution function is:

$$g(u) = Q \cdot g'(u). \tag{96}$$

To determine $g'(u)$, we use the continuity equation (8), substituting in it, instead of $f(r,t)$ and $\dot{r}$, their magnitudes from Eqs. (95) and (81) (or 79)). Under preceding from differentiation on r and t to differentiation on u, the variables are separated, and Eq. (8) takes the form:

$$\frac{dg'(u)}{g'(u)} = -\frac{4\upsilon_g - \frac{1}{u}\frac{d\upsilon}{du} + \frac{\upsilon}{u^2}}{u\upsilon_g - \frac{\upsilon}{u}}du, \tag{97}$$

where $\upsilon = \frac{r\cdot\dot{r}}{B^*} = \left(1 + \frac{x}{1-x}\frac{1}{u^2}\right)\left(\frac{2x+2}{2x+1}u - 1\right)$, $\upsilon_g = \upsilon\big|_{u=1} = \frac{r_g}{B^*}\frac{dr_g}{dt} = \frac{1}{(1-x)(2x+1)}$, $\frac{du}{dr} = \frac{1}{r_g}$, $\frac{du}{dr_g} = -\frac{u}{r_g}$.

Substituting υ, υ_g and $d\upsilon/du$ in Eq. в (97), one obtains the expression:

$$\frac{dg'(u)}{g'(u)} = -\frac{4u^4 - u^2\left(1 + x - 2x^2\right) + 4u\left(x^2 + x\right) - 3x(2x+1)}{u(1-u)^2\left(u^2 + 2ux^2 + 2x^2 + x\right)}du, \tag{98}$$

after integration of which we find $g'(u)$, i.e. the generalized Chakraverty-Wagner distribution for islands of cupola-like form:

$$g'(u) = \frac{u^3\left(u^2 + 2ux^2 + 2x^2 + x\right)^{D/2}}{(1-u)^B}\exp\left(\frac{F - Dx^2}{\sqrt{2x^2 + x - x^4}}\tan^{-1}\left(\frac{u + x^2}{\sqrt{2x^2 + x - x^4}}\right)\right) \times \exp\left(\frac{C}{1-u}\right), \tag{99}$$

where:

$$\begin{cases} B = \dfrac{32x^4 + 16x^3 + 48x^2 + 13x + 5}{A}, \\ C = -\dfrac{12x^2 + 3x + 3}{A}, \\ D = -\dfrac{80x^4 + 40x^3 + 15x^2 + x + 2}{A}, \\ F = -\dfrac{32x^6 + 16x^5 + 54x^4 + 34x^3 + 8x^2}{A}, \\ A = 16x^4 + 8x^3 + 9x^2 + 2x + 1. \end{cases} \tag{100}$$

For $x = 0$: $B = 5$, $C = -3$, $D = -2$, $F = 0$, $A = 1$, and Eq. (99) is transformed into the Wagner distribution (Wagner, 1961):

$$g'(u) = u(1-u)^{-5} \exp\left(-\frac{3}{1-u}\right). \tag{101}$$

For $x = 1$: $A = 36$, $B = 19/6$, $C = -1/2$, $D = -23/6$, $F = -4$, and Eq. (99) corresponds to the Chakraverty distribution (Chakraverty, 1967):

$$g'(u) = \frac{u^3 \exp\left(-\frac{1}{2(1-u)}\right) \exp\left(-\frac{1}{6\sqrt{2}} \tan^{-1}\left(\frac{u+1}{\sqrt{2}}\right)\right)}{(1-u)^{19/6}\left(u^2+2u+3\right)^{23/12}}. \tag{102}$$

Taking into account the volume (mass) conservation law for island condensate, one can find the cluster's relative size distribution function $g(u)$ from Eq. (96).

4.4 Discussion

The dependences shown in Fig. 10 *a* correspond to the size distribution function computed using Eq. (96) for various magnitudes of x. The extreme curves for $x = 0$ and $x = 1$ determine the Chakraverty distribution and the Wagner distributions, respectively (Wagner, 1961; Chakraverty, 1967). All other curves, within interval $0 < x < 1$, describe the size distribution of islands for simultaneous action of the Wagner and diffusion mechanisms of cluster growth (the generalized Chakraverty-Wagner distribution.).

The same dependences normalized by their maxima are shown in Fig. 10 *b*. In such form, being normalized by unity along the coordinate axes, such dependences are easy-to-use for comparison with experimentally obtained histograms.

For the computed family of distributions, see Eq. (96), the magnitude of the locking point changes in accordance with Eq. (85) within the interval $4/3 \le u_0 \le 2$. For $x = 0.5$, one obtains $u_0 = 3/2$, what coincides with similar magnitude for the Lifshitz-Slyozov distribution. At the same time, the curve Eq. (96) for $x = 0.5$ is not the Lifshitz-Slyozov distribution:

$$g(u) = \frac{u^3 \exp\left[-1.084435 \tan^{-1}\left(1.032795u + 0.258199\right)\right] \cdot \exp\left(-\frac{1.2}{1-u}\right)}{(1-u)^{\frac{22}{5}}\left(u^2 + 0{,}5u + 1\right)^{\frac{4}{3}}}. \tag{103}$$

It means that one can not judge on the type of distribution proceeding from the locking point magnitude u_0. It must be considered only as evaluating parameter for choice of the theoretical curve from the family Eq. (96), for comparison with specific experimentally obtained histogram.

Once more important property of the found distribution, Eq. (96), consists in that it can be used not only for comparison with experimentally obtained histograms in the form of distribution of particles of radii r (or diameters d), but also for description of the particle height distribution, h. One can see in Fig. 8 that island height is equal to:

$$h = R_C(1 - \cos\theta) = r\frac{1-\cos\theta}{\sin\theta}, \tag{104}$$

so that $r/r_g = h/h_g = u$.

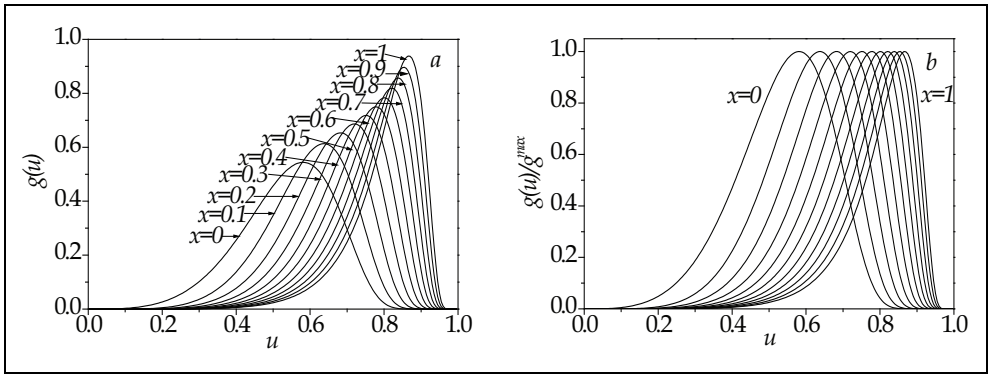

Fig. 10. The generalized Chakraverty-Wagner distribution: *a* – dependences computed for various magnitudes of *x* following Eq. (96); *b* – the same dependences normalized by their maxima

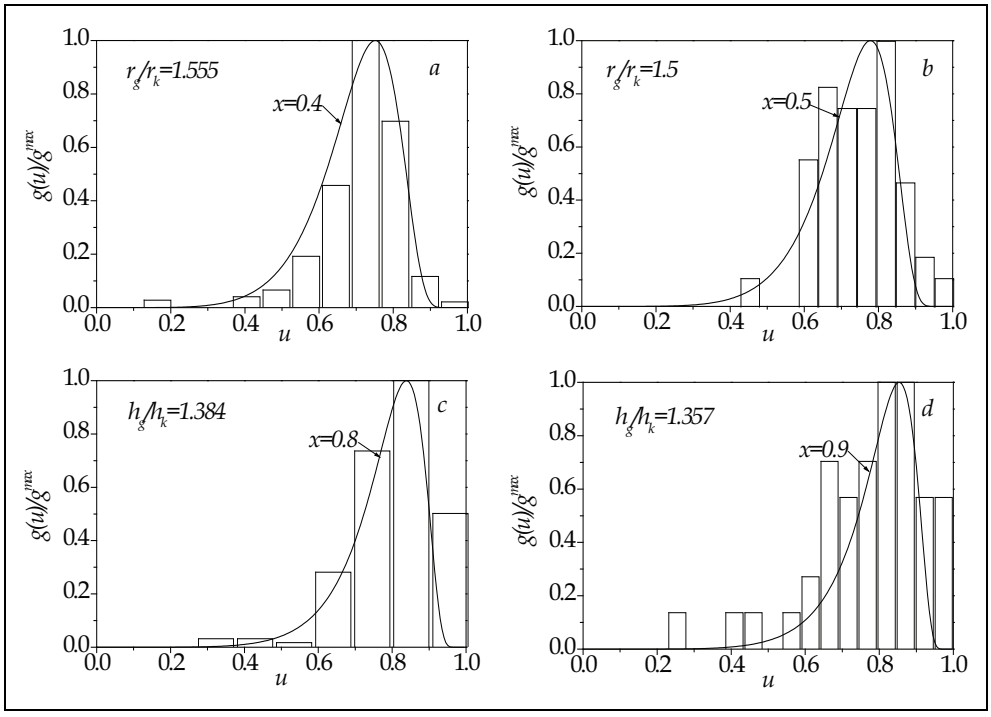

Fig. 11. Comparison of the dependence represented by Eq. (96) with experimentally obtained histograms on diameter, d, and height, h, of nanodots of Mn at various temperatures and thickness of monolayer of Mn : *a* - room temperature, Mn 0.21 ML, $r_g/r_k = 1.555$; *b* - temperature 180°C, $r_g/r_k = 1.5$; *c* - room temperature, Mn 0.21 ML, $h_g/h_k = 1.384$; *d* - temperature 180°C, $h_g/h_k = 1.357$

Fig. 11 shows comparison of experimental histograms of nanodots Mn at substrate Si on diameters, d, (*a* and *b*) and on heights, h, (*c* and *d*), obtained by the molecular beam epitaxy technique at various temperatures, *viz.* at room temperature (fragments *a* and *c*) and at 180˚C (fragments *b* and *d)*, as well as for various thickness of molecular layers of Mn (ML) (De-yong Wang *et. al.*, 2006), with theoretical dependence Eq. (96). It is seen from comparison that for experimental distributions on diameters, the contributions of the each of two mechanisms of growth, i.e. Wagner and diffusion ones, are approximately the same, cf. Fig. 11 *a*, $x = 0.4$, and Fig. 11 *b*, $x = 0.5$.

At the same time, the diffusion mechanism occurs to be predominant for the height distribution functions, cf. Fig. 11 *c*, $x = 0.8$, and Fig. 11 *d*, $x = 0.9$. It means that as nanodots of Mn grow, increasing of height leaves behind increasing lateral size d, so that $h/d > 1$. Probably, this circumstance just explains of the form of nanodots of Mn obtained by the authors of paper (De-yong Wang *et al.*, 2006).

Fig. 12 shows the results of comparison of the theoretical dependence, cf. Eq. (96), with experimentally obtained histograms of particles of gold obtained at temperature 525°C at silicon substrate $\left(Au / Si(111)\right)$ - (Fig. 12 *a*), and later, after 180-min isothermal exposure - (Fig. 12 *b*) (Werner *et al.*, 2006). Judging by the magnitude of x, particle growth is initially controlled by the kinetic coefficient β (Fig. 12 *a*). But later, the mechanism of growth changes, and after three-hour exposure it becomes predominantly diffusion one (Fig. 12 *b*).

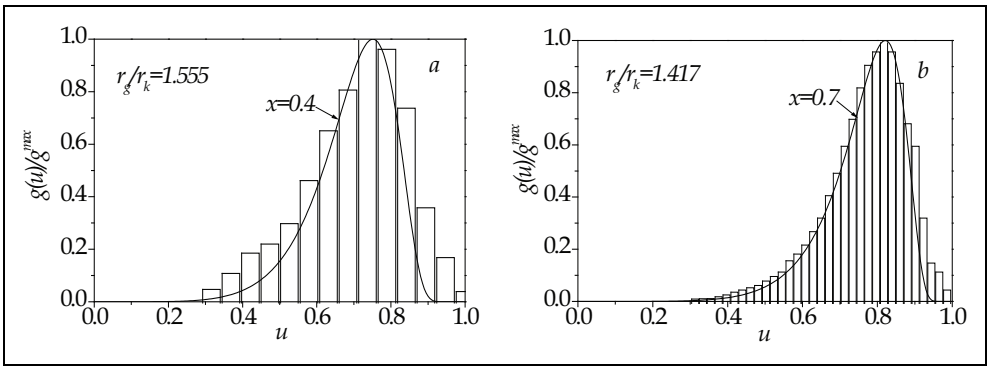

Fig. 12. Comparison of the dependence Eq. (96) with experimentally obtained histograms for particles of *Au* obtained by the molecular beam epitaxy technique for temperature 525°C (*a*) and 180 min later, after isothermal exposure (*b*)

The results of comparison of the theoretical dependence computed for $x = 0.3$ with the experimental histogram for nanoclusters of Ag obtained by the molecular beam epitaxy technique at room temperature at substrate $TiO_2(110)$ (Xiaofeng Lai *et al.*, 1999), cf. Fig. 13, also argue in favour of the proposed mechanism of growth.

Thus, the considered examples of comparison of computed and experimentally obtained data leads to the conclusion on the possibility to implement simultaneous action of both mechanisms of growth, i.e. Wagner and diffusion ones. What is more, the situation when both mechanisms of growth co-exist and act in parallel is, to all appearance, more general than separate manifestations of one of two mechanisms considered early by Wagner and Chakraverty.

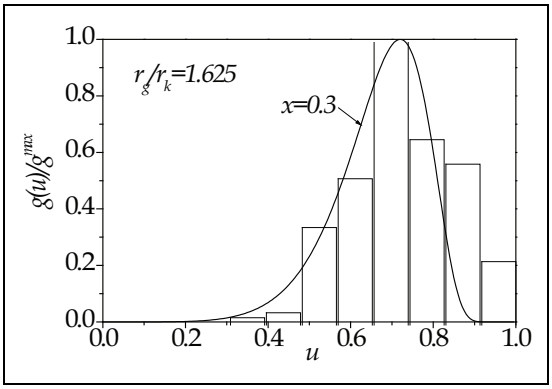

Fig. 13. Comparison of the dependence Eq. (96) with experimental histogram of nanoclusters Ag obtained by the molecular beam epitaxy technique at substrate $TiO_2(110)$ at room temperature

5. Influence of form of nanoclusters in heterostructures on the size distribution function

Obtaining the heterostructures containing quantum dots of specified concentration, form, sizes and homogeneity is connected with considerable experimental difficulties. However, if even such structure has been obtained, its properties can change under the Ostwald's ripening. For that, as it has been shown above, the character of the size distribution function of clusters changes not only as a result of transition from one growth mechanism to another one, but also due to simultaneous action of such mechanisms (Sagalovich & Slyozov, 1987; Vengrenovich *et al*., 2006a, 2007a, 2008a, 2008b). Below we represent the results of investigation of the influence of cluster form on the size distribution function in semiconductor heterosystems with quantum dots. A heterosystem is considered as island film consisting of disk-like islands of cylindrical form, with height h (Fig. 14).

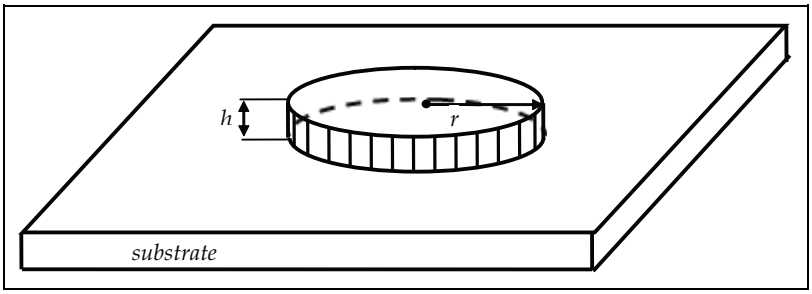

Fig. 14. Disc-like cluster of radius r and constant height h

5.1 Generalized Chakraverty-Wagner distribution for islands (clusters) of cylindrical form ($h = const$)

The problem of determination of the size distribution function is analogous to the above considered problem for clusters of cupola-like form. Modeling the island film by disk-like

islands corresponds to heterostructure with more stable form of hut-clusters (Safonov & Trushin, 2007).
The rate of change of volume of cluster with constant height h (Fig. 14) is determined by the flow j of adatoms to (from) a cluster:

$$\frac{d}{dt}(\pi r^2 h) = j\upsilon_m , \tag{105}$$

where υ_m – adatom volume. From Eq. (105) one obtains:

$$\frac{dr}{dt} = \frac{1}{2\pi rh} j\upsilon_m . \tag{106}$$

Following to (Vengrenovich *et al*., 2008a), the flow j consists of two parts:

$$j = j_S + j_i , \tag{107}$$

where j_S – the part of flow caused by surface diffusion, and j_i – the part of flow of adatoms, which due to overcoming the potential barrier at the interface 'cluster-substrate' fall at cluster surface and, then, take part in formation of chemical connections (the Wagner mechanism of growth).
By definition, the diffusion part of a flow equals:

$$j_S = 2\pi r D_S (\frac{dC}{dR})_{R=r} , \tag{108}$$

where D_S – the surface diffusion coefficient, $(\frac{dC}{dR})_{R=r}$ – concentration gradient at the interface 'cluster-substrate', which can be represented in the form (Chakraverty, 1967; Vengrenovich 1980a, 1980b; Vengrenovich *et al*., 2008a):

$$(\frac{dC}{dR})_{R=r} = \frac{\langle C\rangle - C_r}{\ln l} \cdot \frac{1}{r} , \tag{109}$$

where l determines the distance from an island, $(R = lr)$, at which a mean concentration of adatoms at a substrate, $\langle C\rangle$, is set around separate cluster of radius r ($l = 2, 3$). Taking into account Eq. (109), one can rewrite Eq. (108) in the form:

$$j_S = \frac{2\pi D_S}{\ln l}(\langle C\rangle - C_r) . \tag{110}$$

Concentration of adatoms at the cluster base, C_r, is determined by the Gibbs-Thomson equation:

$$C_r = C_\infty \exp\left(\Delta P \frac{\upsilon_m}{kT}\right) \approx C_\infty (1 + \Delta P \frac{\upsilon_m}{kT}) , \tag{111}$$

where C_∞ – the equilibrium concentration at temperature T, ΔP – the Laplacian pressure caused by island surface curvature, k – the Boltzmann constant. Pressure ΔP, in accordance with (Vengrenovich et al., 2008a), equals:

$$\Delta P = \sigma \frac{dS}{dV} = \sigma \frac{2\pi h dr}{2\pi r h dr} = \frac{\sigma}{r}. \tag{112}$$

Taking into account Eq. (112), C_r can be represented in the form:

$$C_r \approx C_\infty (1 + \frac{\sigma \upsilon_m}{kT} \cdot \frac{1}{r}), \tag{113}$$

where σ – the specific magnitude of surface energy.
A mean concentration of adatoms at surface, $\langle C \rangle$, is determined, by analogy with Eq. (113), by the mean (or critical) cluster size r_k:

$$\langle C \rangle \approx C_\infty (1 + \frac{\sigma \upsilon_m}{kT} \cdot \frac{1}{r_k}). \tag{114}$$

Thus:

$$j_S = \frac{2\pi D_S C_\infty \sigma \upsilon_m}{kT \ln l} (\frac{1}{r_k} - \frac{1}{r}) = \frac{2\pi D_S C_\infty \sigma \upsilon_m}{kT \ln l} \frac{1}{r} (\frac{r}{r_k} - 1). \tag{115}$$

In accordance with Wagner, the number of adatoms occurring in the unite of time at side surface of a cluster $(h = const)$ is determined as:

$$j_1 = 2\pi r h \beta \langle C \rangle, \tag{116}$$

and the number of adatoms leaving a cluster in the unite of time is:

$$j_2 = 2\pi r h \beta C_r, \tag{117}$$

so that the resulting flow of atoms involved into forming chemical connections equals:

$$j_i = j_1 - j_2 = 2\pi r h \beta (\langle C \rangle - C_r) = \frac{2\pi h \beta C_\infty \sigma \upsilon_m}{kT} (\frac{r}{r_k} - 1). \tag{118}$$

Substituting j_S and j_i in Eq. (107), one obtains:

$$j = \frac{2\pi D_S C_\infty \sigma \upsilon_m^2}{kT \ln l} \cdot \frac{1}{r} (\frac{r}{r_k} - 1) + \frac{2\pi h \beta C_\infty \sigma \upsilon_m}{kT} (\frac{r}{r_k} - 1). \tag{119}$$

Substituting Eq. (119) in Eq. (106), one finds out the rate of growth:

$$\frac{dr}{dt} = \frac{1}{2\pi r h} (\frac{2\pi D_S C_\infty \sigma \upsilon_m^2}{kT \ln l} \cdot \frac{1}{r} (\frac{r}{r_k} - 1) + \frac{2\pi h \beta C_\infty \sigma \upsilon_m}{kT} (\frac{r}{r_k} - 1)) \tag{120}$$

For the combined action of two mechanisms of growth, i.e. the diffusion and the Wagner ones, the rate of growth, $\dot{r}$, will be dependent on the ratio of the flows j_S and j_i. Designating, as previously, the shares of flows j_S and j_i in general flow j, as $x = j_S / j$ and $1 - x = j_i / j$, respectively, so that the ratio of them equals:

$$\frac{j_S}{j_i} = \frac{x}{1 - x}, \tag{121}$$

one obtains the formula for the rate of cluster growth under surface diffusion, with the share contribution $(1-x)$ of the flow j_i:

$$\frac{dr}{dt}=\frac{A^*}{r^2}[1+(\frac{1-x}{x})\frac{r}{r_g}](\frac{r}{r_k}-1), \tag{122}$$

or:

$$\frac{dr}{dt}=\frac{B^*}{r}[1+(\frac{x}{1-x})\frac{r_g}{r}](\frac{r}{r_k}-1), \tag{123}$$

that corresponds to the Wagner mechanism of cluster growth with the share contribution x of the diffusion flow j_S, where $A^*=\frac{D_S C_\infty \sigma \upsilon_m^2}{hkT\ln l}$, $B^*=\frac{\beta C_\infty \sigma \upsilon_m^2}{kT}$.

Solving jointly Eq. (122) (or Eq. (123)) and Eq.(8) and applying the method derived in paper (Vengrenovich, 1982), one finds out the generalized relative size distribution function, $g'(u)$, for disk-like clusters corresponding to the combined action of two mechanisms of growth, i.e. the Wagner and the diffusion ones (Vengrenovich *et al*., 2010):

$$g'(u)=u^2(1-u)^{-B}\left(u+x^2+x\right)^D\exp(\frac{C}{1-u}), \tag{124}$$

where:

$$\begin{cases} B=\dfrac{2x^4+4x^3+10x^2+8x+4}{A}, \\ C=-\dfrac{2x^2+2x+2}{A}, \\ D=-\dfrac{3x^4+6x^3+5x^2+2x+1}{A}, \\ A=x^4+2x^3+3x^2+2x+1. \end{cases}, \tag{125}$$

For $x=1$, $B=28/9$, $D=-17/9$, $C=-2/3$, and Eq. (124) corresponds to the distribution obtained in paper (Vengrenovich, 1980):

$$g(u)'=u^2(1-u)^{-28/9}(u+2)^{-17/9}\exp(-\frac{2/3}{1-u}). \tag{126}$$

For $x=0$, $B=4$, $D=-1$, $C=-2$, and Eq. (124) turns into the Wagner distribution (Chakraverty, 1967; Vengrenovich, 1980a, 1980b):

$$g'(u)=u(1-u)^{-4}\exp(-\frac{2}{1-u}). \tag{127}$$

However, for graphic representation of the size distribution function one must carry out computations following equation that is analogous to Eq. (28):

$$g(u)=Q\cdot g'(u), \tag{128}$$

where $Q = \dfrac{\Phi}{\pi h \int_0^1 u^2 g'(u)\,du}$, Φ – the volume (mass) of disperse phase in the form of clusters.

5.2 Discussion

The dependences shown in Fig. 15,*a* correspond to the size distribution function Eq. (128) computed for various magnitudes of x. The limiting curves, for $x = 0$ and $x = 1$, correspond to the Wagner distribution (Wagner, 1961) and to the distribution obtained in papers (Vengrenovich, 1980a, 1980b), respectively. All other distributions within the interval $0 \le x < 1$ describe the size distribution functions of clusters for the combined action of the Wagner and the diffusion mechanisms of growth. The same dependences normalized by their maxima are shown in Fig.15,*b*.

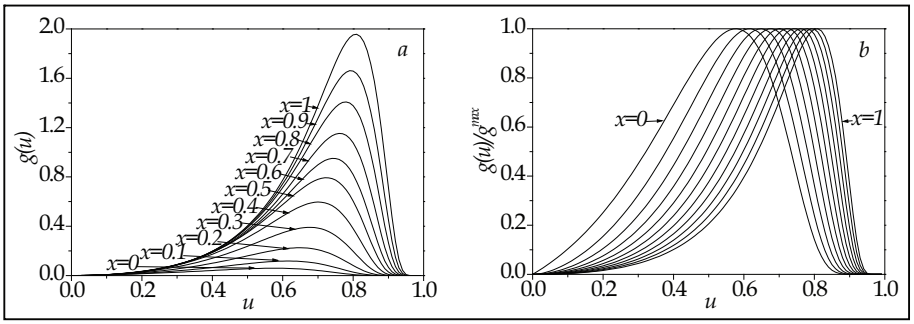

Fig. 15. Functions $g(u)$ (*a*) and $\left(g(u)/g^{\max}\right)$ (*b*) computed following Eq. (128)

Fig. 16 illustrates comparison of experimental histogram of nanodots Ge/SiO_2 (Kan *et al.*, 2005), obtained by evaporating technique with following thermal annealing, with the theoretical dependence, Eq. (128), for $x = 0.7$. A mean size of clusters is 5.6 nm. One can see satisfactory agreement of the theory and experimental data.

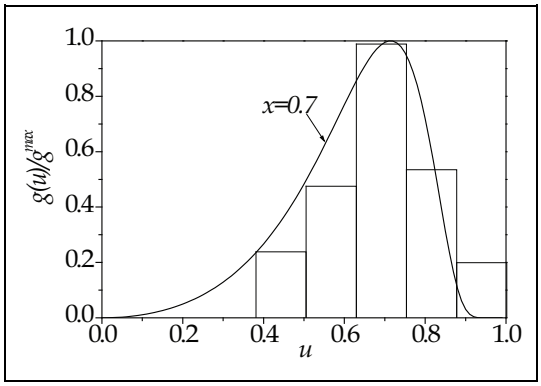

Fig. 16. Comparison of the dependence Eq. (128) with experimental histogram of nanodots Ge at substrate SiO2 obtained by evaporating with following thermal annealing (Kan et al., 2005)

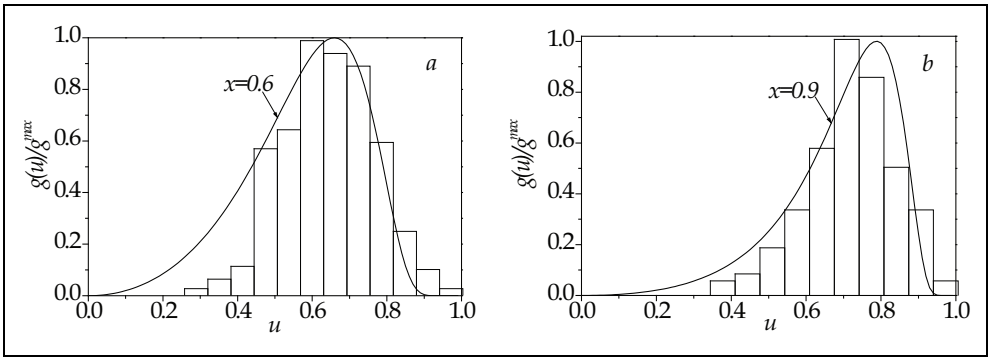

Fig. 17. Comparison of dependence (128) with experimental histograms Ge at substrate Si obtained by molecular beam epitaxy with one (*a*) and two (*b*) layers of nano-clusters Ge (Yakimov *et al*., 2007)

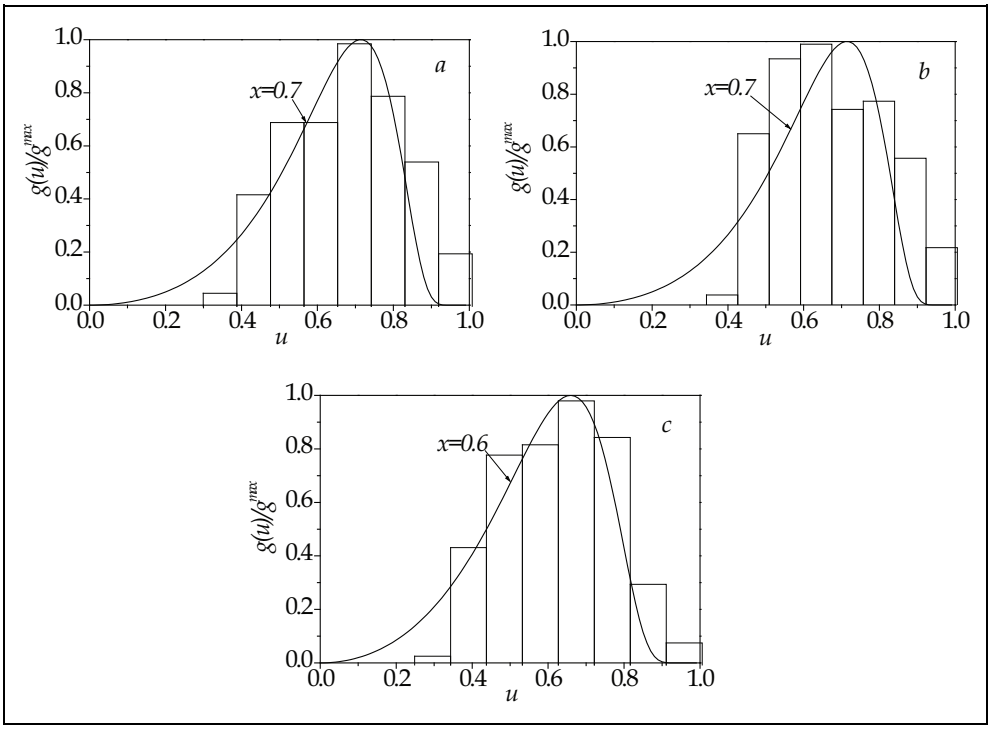

Fig. 18. Comparison of dependence (128) with experimental histograms Co at Si_3N_4 obtained by evaporating at room temperature: (*a*) 0.1 ML Co, (*b*) 0.17 ML Co, (*c*) 0.36 ML Co (Shangjr Gwo *et al*., 2003)

In other case that is illustrated in Fig. 17, the theoretical dependence Eq. (128) is compared with experimental histograms Ge/Si(001) obtained by the molecular-beam epitaxy

technique at temperature 500ºC (Yakimov *et al.*, 2007). The experimentally obtained histogram in Fig. 17,*a* corresponds to one layer of nanoclusters of Ge of a main size ~10.4 nm. One can see that for $x = 0.6$ theoretical results are well fitting the experimental data. For two layers of nanoclusters (with a mean size ~10.7 nm), cf. Fig. 17,*b*, ripening of nanoclusters is almost entirely determined by surface diffusion. The diffusion flow j_S constitutes about 90% of the total flow j $\left(j_S = 0.9j\right)$.

It is of especial interest from the theoretical point of view to compare the computed dependences and experimentally obtained histograms illustrated in Fig. 18 (Shangjr Gwo *et al.*, 2003). Nanoclusters of Co at Si_3N_4 substrate were obtained by applying the evaporation technique at room temperature with rate (0.3-1.2) ML/min. Histograms shown in Fig. 18 correspond to the following conditions: *a*) 0.1 ML Co; *b*) 0.17 ML Co; c) 0.36 ML Co.

As opposed to heterostructures Ge/Si (001) and Ge/ SiO_2 on the base of quantum dots of Ge, which are widely used in optoelectronics and microelectronics, Co is not semiconductor, and the system Co/Si_3N_4 is the model one for investigation of regularities of forming defect-free nanoclusters.

However, one can see from Figs. 16, 17, and 18 that the regularities of the Ostwald's ripening are the same both for the clusters of semiconductor, Ge, and for metallic clusters of Co. In both cases, irrespectively of metallic or semiconductor nature of clusters, ripening of them is governed by the combined mechanism of growth, i.e. the diffusion and the Wagner's ones, with predomination, in the resulting flow, of the flow j_S due to surface diffusion. It proves generality of the considered by us mechanism of cluster ripening, when the rate of growth of them is determined by the ratio of the diffusion flow, j_S, to the flow j_i through the interface 'cluster-substrate'.

6. Mass transfer between clusters under dislocation-surface diffusion. Size distribution function

Obtaining nanocrystals meeting the requirements raised to quantum dots by applying the conventional techniques, such as selective etching, growth at profiled substrate, chemical evaporation, condensation in glass matrices, crystallization under ultrahigh rate of cooling or annealing of amorphous matrices has not led to desirable results (Ledentsov *et al.*, 1998; Pchelyakov *et al.*, 2000). And only under the process of self-organization in semiconductor heteroepitaxial systems it occurs possible to form ideal heterostructures with quantum dots.

The technique of heteroepitaxial growing in the Stranski-Kastranov regime (Krastanow & Stranski, 1937) is the most widely used for obtaining quantum dots. In this case, layer-wise growth of a film is replaced, due to self-organization phenomena, by nucleation and following development of nanostructures in form of volume (3D) islands (Bimberg & Shchukin, 1999; Kern & Müller, 1998; Mo *et al.*, 1990). Islands with spatial limitation of charge carriers in all three directions are referred to as quantum dots. Quantum dots obtained in such a way have perfect crystalline structure, high quantum efficiency of radiation recombination and are characterized by enough high homogeneity in size (Aleksandrov *et al.*, 1974; Leonard *et al.*, 1993; Moison *et al.*, 1994; Ledentsov *et al.*, 1996a, 1996b). Sizes of quantum dots can vary from several nanometers to several hundred nanometers. For example, size of quantum dots in heteroystems Ge-Si and InAs-GaAs lies within the interval from 10 nm to 100 nm, with concentration $10^{10} \div 10^{11}$ cm $^{-2}$.

Much prominence is given in the literature to the size distribution function of islands, while this parameter of a system of quantum dots is of high importance in practical applications

(Bartelt *et al*., 1996; Goldfarb *et al*., 1997a, 1997b; Joyce *et al*., 1998; Kamins *et al*., 1999; Ivanov-Omski *et al*., 2004; Antonov *et al*., 2005). In part, changing the form and sizes of islands, one can control their energy spectrum that is of great importance for practical applications of them. As the size distribution function becomes more homogeneous, as (for other equivalent conditions) the system of quantum dots becomes more attractive from the practical point of view.

Homogeneity of the size distribution function can be conveniently characterized by root-mean-square (*rms*) deviation, $\sigma' = \sqrt{D}$, where D – dispersion. As the size distribution function becomes narrower, as σ' decreases. In this respect, the best size distribution functions have been obtained for island of germanium into heterosystem Ge/Si(001), where $\sigma' < 10\%$ (Jian-hong Zhu *et al*., 1998).

Theoretical distributions corresponding to such magnitudes of dispersion D (or associated magnitudes of *rms*) have been obtained in papers (Vengrenovich *et al*., 2001b, 2005) in assumption that the main factor determining the form of the size distribution function of island film at later stages is the Ostwald's ripening. Computations have been carried out within the LSW theory, in assumption that dislocation diffusion is the limiting factor of the Ostwald's ripening. For that, the dislocation mechanism of growth of islands under the Ostwald's ripening is possible, if the flow of matter due to dislocation diffusion much exceeds the flow due to surface diffusion, i.e.

$$D_s^{(d)} Zd \left(\frac{dC}{dR} \right)_{R=r} >> D_s 2\pi r \left(\frac{dC}{dR} \right)_{R=r} \tag{129}$$

where $D_s^{(d)}$ – the diffusion coefficient along dislocation grooves, D_s – the surface diffusion coefficient, $\left(\frac{dC}{dR} \right)_{R=r}$ – the concentration gradient at island surface, d – the width of dislocation groove, $d = 2\sqrt{2q/\pi}$, $b^2 \le q \le 60b^2$, where b – the Burgers vector, Z – the number of dislocation lines ending at the island base of radius r $(Z \equiv const)$. For simplifying the computations, islands are considered as disk-like ones, with constant height h (Vengrenovich *et al*., 2001b). General case, when both h and r are changed, is considered in paper (Vengrenovich *et al*., 2005).

Eq. (129) sets limitations on island sizes, which grow due to dislocation diffusion:

$$r << \frac{Zd}{2\pi} \frac{D_s^{(d)}}{D_s} . \tag{130}$$

If the condition Eq. (130) is violated, one must take into account in the resulting flow of matter, beside of the flow due to dislocation diffusion, the flow component caused by surface diffusion.

Under dislocation-surface diffusion one has:

$$j = j_d + j_s , \tag{131}$$

where j_d – the flow to a particle due to diffusion along dislocations, j_s – the flow due to surface diffusion, j_d and j_s are determined by the left and the right sides of Eq. (129), respectively.

The rate of growth of isolated island under condition $h = const$ is determined from equation:

$$\frac{d}{dt}\left(\pi r^2 h\right) = j v_m . \tag{132}$$

Substitution Eq. (131) in Eq. (132) and taking into account the magnitudes of j_d and j_s, as well as of the concentration gradient at the island boundary, one obtains:

$$\frac{dr}{dt} = \frac{\sigma\ v_m^2 C_\infty}{2\pi hkT \ln l}\frac{1}{r^2}\left(D_s^{(d)} Zd\frac{1}{r} + 2\pi D_s\right)\left(\frac{r}{r_k} - 1\right). \tag{133}$$

Taking into account the ratio of flows,

$$x = \frac{j_s}{j},\ 1 - x = \frac{j_d}{j},\ \frac{j_d}{j_s} = \frac{1-x}{x}, \tag{134}$$

one can write Eq. (133) in the form:

$$\frac{dr}{dt} = \frac{\sigma v_m^2 C_\infty D_s^{(d)} Zd}{\pi hkT \ln l}\frac{1}{r^3}\left(\frac{x}{1-x}\frac{r}{r_g} + 1\right)\left(\frac{r}{r_k} - 1\right), \tag{135}$$

or:

$$\frac{dr}{dt} = \frac{\sigma v_m^2 C_\infty D_s}{hkT \ln l}\frac{1}{r^2}\left(\frac{1-x}{x}\frac{r_g}{r} + 1\right)\left(\frac{r}{r_k} - 1\right). \tag{136}$$

Eqs. (135) and (136) describe the rate of growth of clusters under dislocation and surface diffusion with contributions (x) and ($1-x$) corresponding to the flows of them.
Taking into account Eqs. (135) and (136) for the rate of growth and performing computations following the algorithm introduced in paper (Vengrenovich, 1982), one can represent the relative size distribution function of clusters, under assumption that mass transfer between clusters is realized due to dislocation-surface diffusion, in the form:

$$g'(u) = \frac{u^3 (u^2 + bu + c)^{\frac{D}{2}}}{(u-1)^K}\exp\left(\frac{F}{u-1}\right) \times \exp\left(\frac{\frac{E - Db}{2}}{\sqrt{c - \frac{b^2}{4}}}\tan^{-1}\left(\frac{u + b/2}{\sqrt{c - b^2/4}}\right)\right), \tag{137}$$

Where

$$\begin{cases} D = \dfrac{3c^2 + \left(x^2 - 4x + 6b - 6\right)c + 6b^2 + \left(4x^2 - 16x + 14\right)b + 7x^2 - 28x + 19}{c^2 + (b+1)2c + b^2 + 2b + 1}, \\ E = \dfrac{(3-D)c + (D-3)b^2 + (2b+1)D + x^2 - 4x - 3}{2 + b}, \\ F = D(b+1) - 3b - E, \\ K = 6 - D. \end{cases} \tag{138}$$

6.1 Comparison with experimental data

Fig. 19 *a* illustrates the family of distributions computed following Eq. (137) with the step $\Delta x = 0.1$ for magnitudes of x between zero and unity. One can see that as magnitude of x increases, as the maxima of the distributions decreases, and the magnitudes of u' where $g(u')$ reaches maximum are shifted to the left, in direction of decreasing u. This shift is clearly observable in Fig. 19 *b*, where the same distributions normalized by their maxima are shown, so that $g^{\max} \equiv g(u')$. For that, the magnitudes of u' are determined from the following equation:

$$3u^4 - (x^2 - 4x)u^2 + (x^2 - 4x + 2)4u^2 - 3x^2 + 12x - 9\Big|_{u=u'} = 0 \,. \tag{139}$$

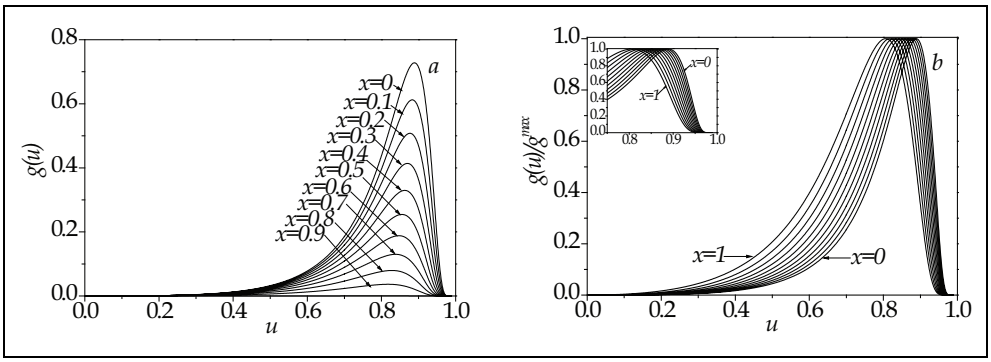

Fig. 19. Size distribution functions computed with the step $\Delta x = 0.1$ (*a*); the same distributions, normalized by their maxima (enlarged version is in the inset), where $g^{\max} \equiv g(u')$ (*b*).

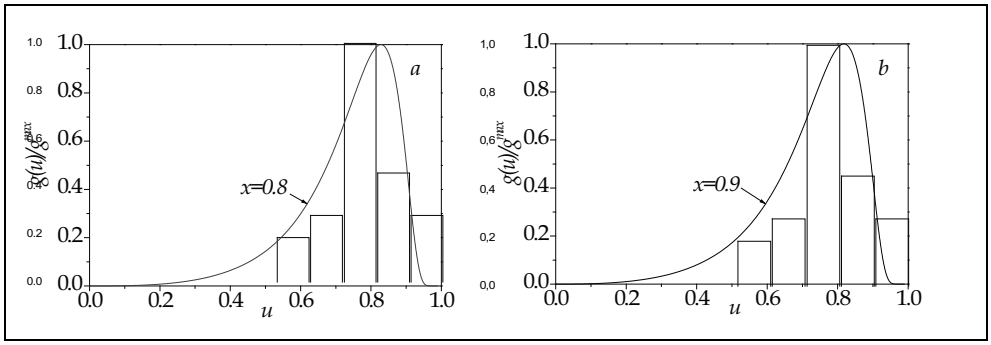

Fig. 20. Comparison with experiment (Neizvestnii *et al.*, 2001) $x = 0.8$ (*a*), $x = 0.9$ (*b*).

It must be noted that in the most cases experimental histograms are obtained as the dependences of the number of islands (share of islands) at the unit area on island's height, h. Theoretically, the choice of variable is arbitrary. For constant rate of change of island volume, it is of no importance, either r or h variable is constant. That is why, the

distributions shown in Fig. 19 can be used also for comparison with experimentally obtained histograms, when the island height, h, is constant.

One of such comparisons is illustrated in Fig. 20 (a – $x = 0.8$, b – $x = 0.9$). Experimentally obtained histogram normalized by unity on axes $u\left(h/h_g\right)$ and $g(u)/g^{\max}$ corresponds to the height (on h) distribution function in (Ge/ZnSe) (Neizvestnii *et al.*, 2001).

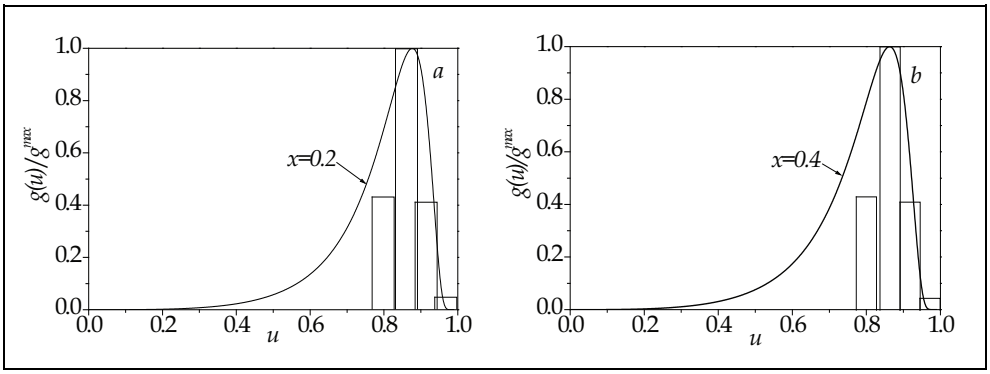

Fig. 21. Comparison of the experimentally obtained histograms with theoretically computed dependences (Vostokov *et al.*, 2000) $x = 0.2$ (*a*), $x = 0.4$ (*b*)

In Fig. 21, the experimentally obtained histogram normalized in the same manner as in previous case, corresponds to the height distribution of islands of germanium (Ge/Si (001)) for the quantity of fall out of germanium 5.5 monolayers ($d_{Ge} = 5.5ML$) (Vostokov *et al.*, 2000). Theoretical curves have been computed for a – $x = 0.2$, and b – $x = 0.4$. One can see that as x increases, as discrepancy between the experimentally obtained histogram and theoretically computed dependences increases also.

7. Conclusions

We have developed the theory of the Ostwald's ripening, taking into account not only mass transfer between clusters due to diffusion (volume, surface, dislocation), but also the kinetics of mass transfer through the interface 'cluster-matrix' ('cluster-substrate') determining the formation of chemical connections at cluster surface (the Wagner mechanism of cluster growth).

Within the developed by us theory, diffusion and kinetics of mass transfer through the interface 'cluster-matrix' are taken into account as the corresponding flows, $j_V\,(j_S)$ and j_i, in the resulting flow to (from) a cluster: $j = j_V\,(j_S) + j_i$. The contribution of the each mechanism of mass transfer in the resulting flow, j, is represented as the ratio of the partial flows: $x = \frac{j_V}{j}\left(\frac{j_S}{j}\right)$ and $1 - x = \frac{j_i}{j}$. Taking into account both diffusion and kinetics of mass transfer through interface of two structural components means that one can not neglect any of the components of flow j, both $j_V\,(j_S)$ and j_i. It corresponds to the model of cluster ripening, in accordance with which growth of them is governed by two mechanisms, i.e. by the Wagner and by the diffusion ones. Within the framework of this model, the size

distribution function of clusters is described by the generalized Lifshitz-Slyozov-Wagner distribution (alloys, nanocomposites as nc CdS / polimer (Savchuk *et al*., 2010a, 2010b, 2010c) or the generalized Chakraverty-Wagner distribution (island films, heterostructures with quantum dots, etc.)

If in the resulting flow j the component $j_i << j_V$, it can lead to new mechanism of cluster growth under dislocation-matrix or dislocation-surface diffusion, for the each of which the specific size distribution function and the corresponding temporal dependences of $\langle r \rangle$ and r_g are intrinsic.

Comparison of the theoretically computed size distribution functions with experimentally obtained histograms leads to the following two main conclusions.

1. The introduced model of cluster ripening under simultaneous (combined) action of both the diffuse mechanism and the Wagner one is proved experimentally. Other of the considered models is also finds out experimental proof, *viz.* the case when one neglects the Wagner mechanism of growth and cluster ripening results from mixed dislocation-matrix and dislocation-surface diffusion. Thus, it is the most likelihood that, in practice, cluster growth follows to not only one isolated of the considered early mechanisms of growth, i.e. the diffusion mechanism or the Wagner one, but rather to the mixed (combined) mechanism, when two mentioned limiting mechanisms act together.

It also follows from the results of comparison of the computed and experimental data, that cluster growth under mixed (combined) dislocation-matrix or dislocation-surface diffusion is most probable than cluster growth under any of two mentioned mechanisms, if isolated.

2. In connection with intense development of nanotechnologies and related techniques for generating of nanostructures, the problem arises: in what framework is the LSW theory applied to analysis of nanosystems containing nanoclusters. The final answer on this question is now absent. Also, the main question concerning stability of nanosystems in respect to the Ostwald's ripening leaves opened. Nevertheless, it follows from the represented by us results of comparison of theoretical and experimental data, that in many cases the experimentally obtained histograms built for nanoparticles (nanoclusters) by many authors for various nanosystems are quite satisfactory fitted by the computed by us theoretical distributions (the generalized Lifshitz-Slyozov-Wagner distribution, the generalized Chakraverty-Wagner distribution etc.). In means that the developed by us LSW theory can be, in principle, be used for analysis of phase and structural transformations in nanosystems with nanophases. Of course, derived by us approach requires further investigations, both theoretical and experimental.

8. Acknowledgement

This investigation has been carried out under supporting the Ministry of Education and Science of Ukraine, grant No0110 U000190.

9. References

Alechin A.P. (2004). Structural organization of a matter at surface in nanotechnology – a way to nanotechnology. *Russian Usp. Mod. Radioelectr.*, V. 5, (2004), pp. 118-122

Aleksandrov L.N., Lovyagin R.N., Pchelyakov O.P., Stenin S.I. (1974). Heteroepitaxy of germanium thin films on silicon by ion sputtering. *J. Cryst., Growth*, V. 24-25, (1974), pp. 298-301

Alfimov S.M., Bykov V.A., Grebennikov E.P., Zheludeva S.I., Malzev P.P., Petrunin V.F., Chapligin Yu.A. (2004). Development of R&D in nanotechnologies in Russia. *Microsystem Technique,* V. 8, (2004), pp. 2-8

Andrievskiy R.A. (2002). Nanomaterials: the concept and modern problems. *Russian Chem. J.*, V. 46, (2002), pp. (50-56)

Antonov A.V., Gaponova D.M., Danilzev V.M., Drozdov M.N., Moldavskaya L.D., Murel A.V., Tulovchikov V.S., Shashkin V.I. (2005). Heterostructures InGaAs/GaAs with quantum dots for IR photodetectors within the region 3-5 μm. *Russian Phys. Semicond.*, V.39, No. 1. pp. 96-99

Ardell A.J. (1972). On the coarsening of grain boundary precipitates. *Acta Metall*, Vol. 20, (1972), pp. 602-609

Aronin A.S., Abrosimova U.Ye., Kiryanov Yu.V. (2001). Formation and structure of nanocrystals in alloy $Al_{86}Ni_{11}Yb_3$. *Russian Phys. Solid State,* V. 43, No. 11, (2001), pp. 1925-1933

Bartelt M.C., Evans J.W. (1992). Scaling analysis of diffusion-mediated island growth in surface adsorption processes. *Phys. Rev. B,* V. 46, No. 19, (1992), pp. 12675-12687

Bartelt N.C., Theis W., Tromp R.M. (1996). Ostwald ripening of two-dimensional islands on Si(001). *Phys. Rev. B,* V. 54, No. 16, (1996), pp. 11741-11751

Chakraverty B.K. (1967). Grain size distribution in thin films. I. Conservative systems. *J. Phys. Chem. Solid.,* V. 28, (1967), pp. 2401-2412

De-yong Wang, Li-jun Chen, Wei He, Qing-feng Zhan and Zhao-hua Cheng. (2006). Preferential arrangement of uniform Mn nanodots on Si(111)-7 × 7 surface. *J. Physics. D, Applied Physics* V. 39, No. 2, (2006), pp. 347-350

Dunaevskiy M.S., Krasilnik Z.F., Lobanov D.N., Novikov A.V., Titkov A.N., Laiho R. (2003). Vizualization of tangled nanoislands of GeSi vi silocon structures by atom-force technique at knocks. *Russian Phys. Semicond.*, V. 37, (2003), pp. 692-699

Gaponenko S.V. (1996). Optical processes in semiconductor nanocrystals (quantum dots). Review. *Russian Phys. Semicond.*, V. 30, No. 4, (1996), pp. 577-619

Gerasimenko N.N. (2002). Nanoscale structures in implanted semiconductors. *Rusian Chem. J.*, V. 46, (2002), pp. 30-41

Goldfarb I., Hayden P.T., Owen J.H.G., Briggs G.A.D. (1997a) Nucleation of "Hut" Pits and Clusters during Gas-Source Molecular-Beam Epitaxy of Ge/Si(001) in *In Situ* Scanning Tunneling Microscopy. *Phys. Rev. Lett,* V. 78, No. 20, (1997), pp. 3959-3962

Goldfarb I., Hayden P.T., Owen J.H.G., Briggs G.A.D. (1997b). Competing growth mechanisms of Ge/Si(001) coherent clusters. *Phys. Rev. B,* V. 56, (1997), pp. 10459-10468

Hirth J. P., Pound G. M. (1963). Condensation and Evaporation, Nucleation und Growth Kinetics; Band 11 der Serie "Progress in Material Science", herausgegeben von Bruce Chalmers, Pergamon Press, Oxford-London-Paris-Frankfurt; 190 Seiten

Ivanov-Omsky V.I., Kolobov A.V., Lodygin A.B., Yastrebov S.G. (2004). Size distribution of clusters of cobalt in amorphous carbon matrix. *Russian Phys. Semicond.*, V. 38, No. 12 (2004), pp. 1463-1465

Jian-hong Zhu, Brunner K., Abstreiter G. (1998). Two-dimensional ordering of self-assembled Ge islands on vicinal Si(001) surfaces with regular ripples. *Appl. Phys. Lett*, V. 73, No. 5, (1998), pp. 620-622

Joyce B.A., Vvedensky D.D., Avery A.R., Belk J.G., Dobbs H.T., Jones T.S. (1998). Nucleation mechanisms during MBE growth of lattice-matched and strained III–V compound films. *Appl. Surf. Sci*, V. 130-132, (1998), pp. 357-366

Kamins T.I., Medeiros-Ribeiro G., Ohlberg D.A.A., Stanley Williams R. (1999). Evolution of Ge islands on Si(001) during annealing. *J. Appl. Phys,* V. 85, No. 2, (1999), pp. 1159-1171

Kan E. W. H., Koh B. H., Choi W. K., Chim W. K., Antoniadis D. A., Fitzgerald E. A. (2005). Nanocrystalline Ge Flash Memories: Electrical Characterization and Trap Engineering. *The 5th Singapore-MIT Alliance Annual Symposium*, Singapore, (January 2005), pp. 19-20

Katsikas L., Eychmuller A., Giersig M., Weller H. (1990). Discrete excitonic transitions in quantum-sized CdS particles. *Chem. Phys. Letters,* V.172, No. 3-4, (1990) pp. 201-204

Kirchner H.O.K. (1971). Coarsening of grain-boundary precipitates. *Metall. Trans,* No. 2, (1971), pp. 2861 – 2864

Kondratyev V.V., Ustyugov Yu.M. (1987). On kinetics of decay of oversaturated solid solution under partial relaxation of inner tensions. The model of partially coherent inter-phase boundaries. *Soviet Phys. Met. Metallogr.*, V. 64, No. 5, (1987), pp. 858-866

Kreye H. (1970). Einflus von Versetzungen auf die Umlosung von Teilchen. *Zs. Metallkunde,* V. 61, No. 2, (1970), pp. 108 – 113

Kukushkin S.A., Osipov A.V. (1998). Processes of condensation of thin films (Review of actual problems). *Russian Phys. Usp.*, V. 168, No. 10 (1998), pp. 1083-1116

Ledentsov N.N., Ustinov V.M., Ivanov S.V., Meltser B.Ya., Kopyev P.S., Bimberg D., Alferov J.I. (1996). Ordered arrays of quantum dots in semiconductor matrices. *Russian Phys. Usp.*, V. 166, No. 4, (1996), pp. 423-431

Ledentsov N.N., Shchukin V.A., Grundmann M., Kirstaedter N., Böhrer J., Schmidt O., Bimberg D., Zaitsev S.V., Ustinov V.M., Zhukov A.E., Kop'ev P.S., Alferov Zh.I., Kosogov A.O., Ruvimov S.S., Werner P., Gösele U., Heydenreich J. (1996b). Direct formation of vertically coupled quantum dots in Stranski-Krastanow growth. *Phys. Rev. B*, V. 54, No. 12, (1996), pp. 8743–8750

Ledentsov N.N., Ustinov V.M., Schukin V.A., Kopyev P.S., Alferov J.I., Bimberg D. (1998). Heterostructures with quantum dots: obtaining, properties, lasers. *Russian Phys. Semicond.*, V. 32, No. 4, (1998), pp. 385-410

Leonard D., Krishnamurthy M., Reaves C.M., Denbaars S.P., Petroff P.M. (1993). Direct formation of quantum-sized dots from uniform coherent islands of InGaAs on GaAs surfaces. *Appl. Phys. Lett*, V. 63, No. 23, (1993), pp. 3203-3205

Lifshitz I.M., Slyozov V.V. (1958). On kinetics of diffusion decay of oversaturated solid solutions. *JETP*, V. 35, No. 2 (1958), pp. 479-492

Lifshitz I.M., Slesov V.V. (1961). The kinetics of precipitation from supersaturated solid solution. *J. Phys. Chem. Solids*, V. 19, No.1/2, (1961), pp. 35-50

Marquis E.A., Seidman D.N. (2001). Error! Hyperlink reference not valid.. *Acta Materialia*, V. 49, No. 10, (2001), pp. 1909-1919

Mo Y.-W., Savage D.E., Swartzentruber B.S., Lagally M.G. (1990). Kinetic pathway in Stranski-Krastanov growth of Ge on Si(001). *Phys. Rev. Lett*, V. 65, No. 8, (1990), pp. 1020-1023

Moison J.M., Houzay F., Barthe F., Leprince L., Andre E., Vatel O. (1994). Self-organized growth of regular nanometer-scale InAs dots on GaAs. *Appl. Phys. Lett,* V. 64, No. 2, (1994), pp. 196-198

Müller P., Kern R. (1998). Equilibrium shape of epitaxially strained crystals (Volmer–Weber case). *J. Cryst. Growth*, V. 193, (1998), pp. 257-270

Neizvestny I.G., Suprun S.P., Talochkin A.B., Shumsky V.N., Efanov A.V. (2001). Quantum dots of Ge in non-strained heterosystem GaAs/ZnSe/Ge/ZnSe. *Russian PTS*, V. 35, No. 9, (2001), pp. 1135-1142

Nitsche H., Sommer F., and Mittemeijer E.J. (2005). The Al nano-crystallization process in amorphous Al, Ni,Y,Co. *J. Non Cryst. Solids*, V. 351, (2005), pp. 3760-3771

Ostwald W. (1900). Über die Vermeintliche Isometric des roten undgelben Quecksilberxyds und die Oberflachenspannung fester Körper. *Z. Phys. Chem,* Bd.34, (1900), pp. 495-503

Pchelyakov O.P., Bolkhovityanov Yu.B., Dvurechensky A.V., Sokolov L.V., Nikiforov A.I., Yakimov A.I., Voightlender B. (2000). Silicon-germanium nanostructures with quantum dots: mechanisms of formation and electrical properties. *Russian Phys. Semicond.*, V. 34, No. 11, (2000), pp. 1281-1299

Reutov V.F., Dmitriev S.N. (2002). Ion-track nanotehnology. *Russian Chem. J.*, V. 46, (2002), pp. 74-80

Roko M. (2002). Prospects of development of nanotehnology: National programs, and Educational problems. *Russian Chem. J.*, V. 46, (2002), pp. 90-95

Safonov K.L., Trushin Yu.V. (2007). Criteria of transition of nanoclusters of Ge at Si from pyramidal to cupola-like form. *JTP Lett.*, V. 33, (2007), pp. 7-12

Savchuk A.I., Rudko G.Yu., Fediv V.I., Voloshchuk A.G., Gule E.G., Ivanchak S.A., Makoviy V.V. (2010a). Evolution of $CdS:Mn$ nanoparticle properties caused by pH of colloid solution and ultrasound irradiation. *Phys. Stat. Sol. (c).* V. 7, No.6, (2010), pp. 1510-1512

Savchuk A.I., Makhniy V.P., Fediv V.I., Kleto G.I., Savchuk S.A., Perrone A., Cultrera L. (2010b). Effects of co-doping in ZnO-based semimagnetic semiconductor thin films. *J. Phys.: Conference Series,* V. 8, (2010), pp. 1-4

Savchuk A.I., Fediv V.I., Ivanchak S.A., Makoviy V.V., Smolinsky M.M., Savchuk O.A., Perrone A., Cultrera L. (2010c). Formation and transformation of II-VI semiconductor nanoparticles by laser radiation. *J. Optoelectron. Adv. Mater.,* V. 12, No. 3, (2010), pp. 561-564

Shangjr Gwo, Chung-Pin Chou, Chung-Lin Wu, Yi-Jen Ye, Shu-Ju Tsai,Wen-Chin Lin, Minn-Tsong Lin. (2003) Self-Limiting Size Distribution of Supported Cobalt Nanoclusters at Room Temperature. *Phys. Rev. Letters,* V. 90, (2003), pp. 185506-185510

Shchukin V.A. and Bimberg D. (1999). Spontaneous ordering of nanostructures on crystal surfaces. *Review of Modern Physics,* V. 71, No. 4, (1999) pp. 1125-1171

Slyozov V.V. (1967). Coalescence of oversaturated solid solution under diffusion along the boundaries of blocks and dislocation lines. *Soviet Phys. Solid Staste*, V. 9, (1967), pp. 1187-1191

Slyozov V.V., Sagalovich V.V., Tanatarov L.V. (1978). Theory of diffusive decomposition of supersaturated solid solution under the condition of simultaneous operating of several mass-transfer mechanisms. *J. Phys. Chem. Solids,* V. 10, (1978), pp. 705-709

Slyozov V.B., Sagalovich V.V. (1987). Diffusion decay of solid solutions. *Soviet Phys. Usp.*, V. 151, No. 1 (1987), pp. 67-103

Stranski I.N., Krastanow L. (1937). Sitzungsberichte d. Akad. d. Wissenscaften in Wien, Abt. lib. (1937), 146. P. 797

Vengrenovich R.D. (1975). On kinetics of coalescence of disperse extractions at dislocation network. *Soviet Phys. Met. Metallogr.,* V. 39, (1975), pp. 435-439

Vengrenovich R.D. (1977). On calculation of distribution in surface disperse systems. *Ukr. J. Phys,* V. 22, No. 2, (1977), pp. 219-223

Vengrenovitch R.D. (1980a). On the bimodal distribution in disperse systems. *Phys. Stat. Sol. (a),* V. 62, (1980a) pp. 39-44

Vengrenovitch R.D. (1980b). On kinetics of coalescence in thin films. *Ukr. J. Phys.*, V. 25, No. 3, (1980b), pp. 442-447

Vengrenovich R.D. (1982). On the Ostwald ripening theory. Overview 20. *Acta Metall,* V. 20, (1982), pp. 1079 – 1086

Vengrenovich R.D. (1983). On solution of the problem of kinetics of coalescence by Ostwald. *Rep. Ukr. Acad. Sc. A*, No. 7, (1983), pp. 28 – 33

Vengrenovich R.D., Polushina I.A. (1985). Influence of the volume part of disperse phase on kinetics of coalescence under dislocation diffusion. *Soviet Phys. Met. Metallogr.,* V. 59, No. 4, (1985), pp. 650-660

Vengrenovich R.D. (1998). The size distribution function under dislocation-matrix diffusion. *Rep. Ukr. Acad. Sc. A*, No. 1, (1998), pp. 112 – 120

Vengrenovich R.D., Kovalik F.L., Foglinsky S.V. (1998). Size distribution function under dislocation-matrix diffusion. *Russian Pysics Journ.,* No. 10, (1998), pp. 25-35

Vengrenovich R.D., Gudyma Yu.V. (2001). Kinetics of optical thermal breakdown of thin semiconductor film. *Russian Phys. Solid State,* V. 43, No. 7, (2001), pp. 1171-1175

Vengrenovich R.D., Gudyma Yu.V. and Yarema S.V. (2001a). Growth of Second-Phase Particles upon the Loss of Coherency. *Russian Phys. Met. Metallogr.,* V. 91, No. 3, (2001a), pp. 228-232

Vengrenovich R.D., Gudyma Yu.V., Yarema S.V. (2001b). Ostwald's ripening of nanostructures with nanodots. *Russian Phys. Semicond.,* V. 35, No. 12, (2001), pp. 1440-1444

Vengrenovich R.D., Gudyma Yu.V. and Nikirsa d.d. (2001c). Kinetics of the photoinduced phase transition at the surface of a semiconductor with renormalized bandgar. *J. Phys.: Condens. Matter,* V. 13, (Januar 2001), pp. (2947-2953)

Vengrenovich R.D., Gudyma Yu.V. and Yarema S.V. (2002) Ostwald Ripening under dislocation diffusion. *Scripta Materialia,* V.46, No. 5, (2002), pp. 363-367

Vengrenovitch R.D., Gudyma Yu. V., Yarema S.V. (2005). Quantum dot formation in heteroepitaxial structures. *Phys. Stat. Sol. (b),* V. 242, (2005), pp. 881-889

Vengrenovich R.D., Moskalyuk A.V., Yarema S.V. (2006a). Size distribution function of islands under dislocation-surface diffusion for semiconductor structures. *Rusian Phys. Semicond.*, V. 40, No. 3, (2006), pp. 276-280

Vengrenovich R.D., Moskalyuk A.V., Yarema S.V. (2006b). Ostwald's ripening of heterostructures with quantum dots under dislocation-surface diffusion. *Ukr. J. Phys.*, V. 51, No. 3, (2006), pp. 307-310

Vengrenovich R.D., Moskalyuk A.V., Yarema S.V. (2007a). Ostwald's ripening under mixed-type diffusion, *Russian Phys. Solid State*, V. 49, No. 1, (2007), pp. (13-18)

Vengrenovich R.D., Ivanskii B.V., Moskalyuk A.V. (2007b). Generalized Lifshitz-Slyozov-Wagner distribution. *JETP*, V. 131, No. 6, (2007). pp. 1040-1047

Vengrenovich R.D., Ivans'kyi B.V., Moskalyuk A.V. (2008a). Generalized Chakraverty-Wagner Distribution. *Ukr. J. Phys.*, Vol.53, No. 11, (2008), pp. 1101-1109

Vengrenovich R.D., Ivanskii B.V., Moskalyuk A.V. (2008b). Ostwald's ripening of quantum-sized crystals under mixed diffusion. *Metalooptics and Modern Technologies*, V. 30, No. 2, (2008), pp. 247-266

Vengrenovich R.D., Ivanskii B.V., Moskalyuk A.V. (2010). Ostwald ripening of nanoislands in semiconductor heterosystemsand its influence on optical properties. *Opto-electronics Review*, V. 18, No 2, (2010), pp. 168-176.

Vostokov N.V., Gusev S.A., Dolgov I.V., Drozdov Yu.N., Krasilnik Z.F., Lobanov D.N., Moldavskaya L.D., Novikov A.V., Postnikov V.V., Filatov D.O. (2000). Elastic strains and compound of self-organized nanoislands of GeSi at Si (001). *Russian Phys. Semicond.,* V. 34, No. 1. (2000), pp .8-12

Wagner C. (1961). Theorie der Alterung von Niderschlagen durch Umlösen (Ostwald Reifung). *Zs. Electrochem.,* Bd. 65, №7/8, (1961), pp. 581 – 591

Werner P., Zakharov N.D., Gerth G., Schubert L., Gösele U. (2006). On the formation of Si nanowires by molecular beam epitaxy. *Int. J. Mat. Res. (formelly Z. Metallkd.)* V. 97, No. 7, (2006). pp. 1008-1015

Xiaofeng Lai, Todd P. St.Clair and D. Wayne Goodma. (1999). Oxygen-induced morphological changes of Ag nanoclusters supported on TiO_2(110). *Faraday Discuss.* V. 114, (1999), pp. 279-284

Xiaosheng Fang, Tianyou Zhai, Ujjal K. Gautam, Liang Li, Limin Wu, Yoshio Bando, Dmitri Golberg. (2011). ZnS nanostructures: From synthesis to applications. *Progress in Materials Science,* V. 56, (2011), pp. 175-287

Yakimov A. I., Nikiforov A. I., and Dvurechenski A. V. (2007). Bonding State of a Hole in Ge/Si Double Quantum Dots. *JETP Letters*, V. 86. (2007), pp. 478-481

Part 2

Advances in Mechanical Engineering Aspects

7

Shock-Induced Turbulent Boundary Layer Separation in Over-Expanded Rocket Nozzles: Physics, Models, Random Side Loads, and the Diffusive Character of Stochastic Rocket Ascent

R. G. Keanini, T. D. Nortey, Karen Thorsett-Hill, N. Srivastava,
Sam Hellman, P. T. Tkacik and P. Douglas Knight
Department of Mechanical Engineering & Engineering Science
The University of North Carolina at Charlotte
USA

1. Introduction

Contrary to popular belief, and notwithstanding two hundred years of scientific study (Gruntman , 2004), the problem of accurately predicting rocket ascent remains largely unsolved. The difficulties trace to a variety of altitude-, speed-, and launch-site-dependent random forces that act during rocket ascent, including: i) aerodynamic forces (Sutton & Biblarz, 2001), ii) forces due to wind and atmospheric turbulence (Flemming et al., 1988; Justus & Johnson, 1999; Justus et al., 1990; Leahy, 2006), iii) forces produced by rocket construction imperfections (Schmucker, 1984), and iv) impacts with air-borne animals and debris (McNaughtan, 1964). Significantly, our physical understanding and ability to model the dynamical effects of each of these random features is fairly well-developed.

By contrast, understanding of the *physical origins,* as well as the *dynamical effects* of altitude-dependent, in-nozzle *random side loads,* has only recently begun to emerge (Keanini et al., 2011; Ostlund, 2002; Srivastava et al., 2010). Referring to figures 1 through 3, we find that side loads represent the end result of a chain of in-nozzle fluid dynamic processes. During low altitude flight, under over-expanded flight conditions, a pressure gradient can exist between the high pressure ambient air surrounding the rocket and nozzle, and the low pressures extant within the nozzle. This pressure gradient can force ambient air *upstream* along the nozzle wall; eventually, inertia of the ambient inflow is overcome by the pressure and inertial forces associated with the outflow, producing a near-wall recirculation region. To the supersonic flow outside the near-wall boundary layer, the recirculation zone functions as a virtual compression corner, producing an oblique shock (Keanini & Brown, 2007; Ostlund, 2002; Summerfield et al., 1954). See figures 1 through 3. Due to the altitude dependence of $P_a = P_a(H(t))$, where P_a is the ambient pressure and $H(t)$ is the rocket's time-dependent altitude, the nominal location of the oblique shock, $x_{shock} = x_{shock}(H(t))$, also varies with altitude.

Random side loads arise due to two coupled flow features: i) The oblique shock produces a sharp, adverse pressure rise within the near-wall outflow boundary layer, forcing the boundary layer to separate from the nozzle wall; see figure 1. ii) The *shape* of the boundary

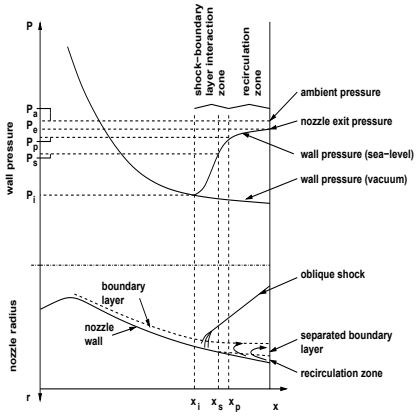

Fig. 1. Schematic of shock-induced boundary layer separation in rocket nozzles. The pressure variation shown is characteristic of free interaction separation problems. Adapted from Ostlund (2002).

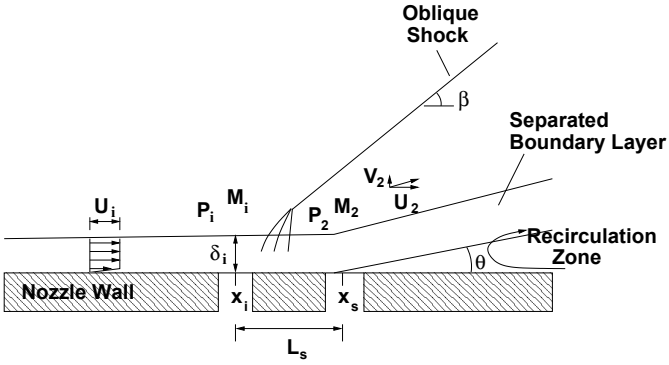

Fig. 2. Shock-induced boundary layer separation in overexpanded supersonic nozzle flow. The process typically occurs during low altitude flight when ambient pressure is high enough to force atmospheric air into the nozzle. The incoming air flows upstream along the low-inertia, near-wall region until downstream-directed boundary layer inertia turns it, forming a virtual compression corner. An oblique shock thus forms, and the combined action of shock-induced pressure rise and inertial pressurization produced by the inflow forces the down-flow boundary layer to separate. Pressures, mach numbers, and velocities are denoted, respectively, by P, M, and U and V. Axial positions where the boundary layer starts to thicken (i denotes *incipient*), and where it separates are denoted, respectively, as x_i and x_s; the nominal shock-boundary layer interaction zone is shown as L_s. Since the separation line position, x_s, and downstream conditions vary with the altitude-dependent ambient pressure, $P_a = P_a(H(t))$ (Keanini & Brown, 2007), all variables shown likewise vary with $H(t)$.

layer separation line, which at any instant, forms a closed curve along the nozzle periphery, varies randomly in space and time; see figure 3. Due to relatively uniform pressure distributions extant on the up- and downstream sides of the instantaneous separation line

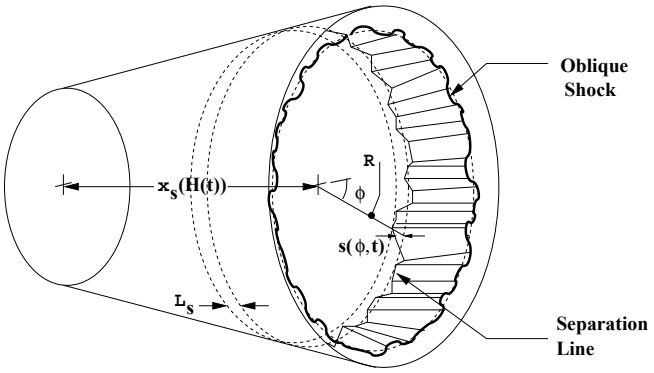

Fig. 3. Schematic of stochastic boundary layer separation line and associated, rippled, azimuthal oblique shock. The mean separation line position relative to the nozzle throat, x_s, varies with rocket altitude, $H(t)$; the corresponding nozzle radius is $R = R(H(t))$. The instantaneous separation line position relative to $x_s(t)$ is shown as $s(\phi, t)$. The separation line lies on the nozzle wall and, in a nominally symmetric nozzle, the shock forms an azimuthally independent, average angle which varies with $x_s(t)$. Adapted from (Keanini et al., 2011).

(Keanini et al., 2011; Srivastava et al., 2010) - where fore and aft pressures, determined by the shock, differ significantly - a net, time- dependent side force, or *side load*, $\mathbf{F_s}$, is produced.

1.1 Connection to mass transfer

From a mass transfer perspective, a deep and unanticipated connection exists between the stochastic ascent of rockets subjected to side loading and damped diffusion processes. In order to understand the complex physical origins of this connection, it is necessary to first consider the purely mechanical features that connect shock-induced boundary layer separation to stochastic rocket response. Thus, much of this Chapter describes recent work focused on understanding these connections (Keanini et al., 2011; Srivastava et al., 2010). From a technological standpoint, the importance of separation-induced side loads derives from their sometimes catastrophic effect on rocket ascent. Side loads have been implicated, for example, in the in-flight break-up of rockets (Sekita et al., 2001), and in the failure of various rocket engine components (Keanini & Brown, 2007).

1.2 Chapter objectives

The objectives of this Chapter are as follows:

I) Two stochastic models (Keanini et al., 2011; Srivastava et al., 2010) and two simple (deterministic) scaling models (Keanini & Brown, 2007) have recently been proposed to describe shock-induced boundary layer separation within over-expanded rocket nozzles (Keanini & Brown, 2007; Keanini et al., 2011; Srivastava et al., 2010). Earlier work, carried out in the 1950's and 60's and focused on time-averaged separation behavior, lead to development of the Free Interaction model of boundary layer separation (Carriere et al., 1968; Chapman et al., 1958; Erdos & Pallone, 1962; Keanini & Brown, 2007; Ostlund, 2002). Our first objective centers on describing the physical bases underlying these models, as well as highlighting experimental evidence that supports the validity of each.

II) The stochastic boundary layer separation models developed in (Keanini et al., 2011; Srivastava et al., 2010) allow construction of stochastic side load models that, on one hand, are physically self-consistent, and on the other, are imbued with statistical properties that are fully consistent with available experimental observations. Our second objective focuses on describing these new stochastic side load models.

III) Given physically consistent separation and side load models (Keanini et al., 2011; Srivastava et al., 2010), the effect of random nozzle side loads on rocket ascent can be computed. Our group recently developed (Keanini et al., 2011) a series of interconnected, analytical models describing: i) fast time-scale, altitude-dependent stochastic boundary layer separation, ii) associated short-time- and long(rocket-dynamics)-time-scale stochastic side load generation, and iii) stochastic, altitude-dependent rocket response. In addition, a high-fidelity numerical model which solved the full nonlinear, coupled equations of rocket rotational and translational motion, under the action of altitude-dependent random side loads, was also reported (Srivastava et al., 2010). Our third objective centers on outlining these analytical and numerical models, and on describing recent results.

IV) Our most recent work (Keanini et al., 2011) demonstrates that rocket pitch and yaw rates evolve as Ornstein-Uhlenbeck processes. Since stochastic pitch and yaw rate evolution determines not only the random evolution of pitch/yaw displacement, but also the stochastic evolution of the rocket's lateral velocity and displacement (Keanini et al., 2011), the rocket's rotational and translational dynamics, fundamentally, trace to a damped diffusion process. The last objective centers on highlighting the connection between stochastic side load-driven rocket response and Ornstein-Uhlenbeck diffusion.

2. Boundary layer separation models and mean separation location

Two physically-based models of shock-induced separation were developed in 2007 (Keanini & Brown, 2007). The models assume importance for two reasons. First, they provide verifiable insight into the physical processes underlying shock-separation of compressible turbulent boundary layers. Second, they allow prediction of the altitude-dependent mean separation line, crucial in determining both the location and magnitude of altitude-dependent random side loads (Keanini et al., 2011; Srivastava et al., 2010). This section describes the more refined of these two models, as well as Chapman's Free Interaction Model (Chapman et al., 1958). All three models rely on scaling analyses of the boundary layer and near-boundary flows, in and near the boundary layer separation zone.

2.1 Time-average separation

Two distinct separation processes have been identified in overexpanded rocket nozzles, *free shock separation*, in which the turbulent boundary layer separates without reattachment, and *restricted shock separation*, in which the separated boundary layer reattaches, forming a small, closed recirculation zone immediately downstream of the separation point; see, e.g., (Keanini & Brown, 2007; Ostlund, 2002) for recent reviews of this work. This Chapter focuses on free shock separation.

The time-average flow features associated with free shock separation in nozzles were first characterized by Summerfield et al. (Summerfield et al., 1954), and are depicted schematically in figures 1 and 2. As shown, the time average pressure along the nozzle wall increases from P_i at the incipient separation point, x_i, to a peak value of P_p at x_p. Depending on the nozzle and the shock location relative to the nozzle exit, P_p is typically on the order of 80 to 100 % of

the ambient pressure, P_a. The time-average separation point, x_s, lies immediately upstream of x_p.

Of central importance in nozzle design is determining both the conditions under which separation will occur and the approximate separation location. A number of criteria have been proposed for predicting the nominal free shock separation point, x_s; see, e.g., (Keanini & Brown, 2007; Ostlund, 2002) for reviews. Since the boundary layer pressure rise between x_i and x_s depends primarily on the inviscid flow Mach number, M_i, most criteria relate either a gross separation pressure ratio, P_i/P_a, or more recently, a refined ratio, P_i/P_p, to M_i (Ostlund, 2002). Given the separation pressure ratio, the separation location can then be determined using an appropriate model of flow upstream of separation.

Although the actual separation process is highly dynamic, the scaling model focuses on time average flow dynamics in the vicinity of the shock interaction zone. In order to provide physical context, we briefly review the dynamical features associated with free shock separation and note simplifying assumptions made. Shock motion over the shock interaction zone appears to be comprised of essentially two components: i) a low frequency, large scale motion produced by flow variations downstream of the separation point, and occurring over the length of the shock interaction zone, $l_p = x_p - x_i$, at characteristic frequencies, f_s [on the order of 300 to 2000 Hz in the case of compression ramp and backward facing step flows (Dolling & Brusniak, 1989)], and ii) a high frequency, low amplitude jitter produced by advection of vortical structures through the shock interaction zone (Dolling & Brusniak, 1989). The scaling models in (Keanini & Brown, 2007) limit attention to time scales that are long relative to f_s^{-1}. In addition, the model assumes that the flow is statistically stationary and that the separation process is two-dimensional.

The time average pressure gradient over the shock interaction zone $(x_i \leq x \leq x_p)$, given approximately by

$$\frac{\partial P}{\partial x} \sim \frac{P_p - P_i}{l_p} \tag{1}$$

in reality reflects the intermittent, random motion of the shock between x_i and x_p; see, e.g., (Dolling & Brusniak, 1989). As the shock-compression wave system oscillates randomly above (and partially within) the boundary layer, the associated pressure jump across the system is transmitted across the boundary layer on a time scale $\tau_s \sim \delta_i/\sqrt{kRT_i}$, where δ_i and T_i are the characteristic boundary layer thickness and temperature in the vicinity of x_i. Under typical experimental conditions, τ_s is much shorter than the slow time scale, f_s^{-1} (where $\tau_s \approx$ 1 to $10\mu s$); thus, the instantaneous separation point essentially tracks the random position of the shock-compression wave system, where the position of the separation point is described by a Gaussian distribution over the length of the interaction zone (Dolling & Brusniak, 1989).

2.2 Scale analysis of shock-induced separation

In the vicinity of the separation point,x_s, we recognize that a fluid particle's normal acceleration component within the separating boundary layer is determined by the normal component of the pressure gradient across the separating boundary layer. Thus, balancing these terms (in the Navier- Stokes equations) yields:

$$\rho \frac{V_s^2}{R} \sim \frac{\partial P}{\partial n} \tag{2}$$

where V_s is the particle speed in the streamwise (s-)direction, and R^{-1} is the local streamline curvature. The curvature can be evaluated by first defining the shape of the boundary layer's

outer-most streamline (i.e., a streamline in the vicinity of δ which is roughly parallel to the local displacement thickness) as $r(x) = f(x)$, where $r(x)$ is the radial distance from the nozzle centerline to the streamline, evaluated at axial position x. Thus, $R^{-1} = f''(\sqrt{1+(f')^2})^{-3}$. Expressing V_s^2 in terms of local cartesian velocity components, $V_s^2 = u_s^2 + v_s^2$, and estimating u_s and v_s by their approximate free stream magnitudes downstream of the oblique shock (since again, at axial position x_s, the boundary layer has passed through the compression system below the shock), we obtain $V_s^2 \approx U_2^2 + V_2^2$. Replacing terms in (2) by their approximate magnitudes then leads to

$$\rho_2 \frac{U_2^2 + V_2^2}{R} \sim \frac{P_p - P_2}{\delta_s} \tag{3}$$

where arguments given in (Keanini & Brown, 2007) lead to the necessary pressure gradient and density estimates.

2.3 Boundary layer thickness

In order to proceed, we must estimate the magnitude of the boundary layer thickness, δ_s, immediately upstream of the separation point, x_s. First, note that at the wall between x_i and x_s, the x-momentum equation yields the approximate balance

$$\mu \frac{\partial^2 u}{\partial y^2} \sim \frac{\partial P}{\partial x} \tag{4}$$

where μ is the dynamic viscosity. Estimating the magnitude of each term in this equation leads to

$$\frac{U_2}{\delta_s^2} \sim \frac{1}{\mu} \frac{(P_p - P_1)}{l_s} \tag{5}$$

where, since we are focusing on the neighborhood of x_s, u is approximated as U_2, and where it is recognized that the streamwise pressure increases from approximately P_1 near x_i to approximately P_p near x_s. [Although P equals P_s at x_s, due to the relatively small difference between P_s and P_p, for simplicity, we approximate $P(x_s)$ as P_p.] The x-length scale, $l_s = (x_s - x_i)$, is approximately equal to the length of the shock interaction zone, $l_p = x_p - x_i$. Considering the continuity equation near x_s, we recognize that since the boundary layer acquires a vertical velocity component as it travels toward and past x_s, and since associated mass advection and volumetric dilatation terms, $\rho^{-1}\mathbf{u} \cdot \nabla\rho$, and $\nabla \cdot \mathbf{u}$, respectively, are of the same order, then

$$\frac{\partial u}{\partial x} \approx \frac{\partial v}{\partial y} \tag{6}$$

or in terms of orders of magnitude,

$$\frac{U_2}{l_s} \sim \frac{V_2}{\delta_s} \tag{7}$$

where again the vertical velocity near x_s is on the order of V_2, the inviscid flow's vertical velocity component immediately downstream of the oblique shock. Thus, since $V_2/U_2 \sim \tan\,\theta$, we obtain the following estimate for δ_s/l_s :

$$\delta_s/l_s \sim \tan\,\theta \tag{8}$$

Note that this relationship is analogous to one of the key assumptions underlying Chapman's (Chapman et al., 1958) free interaction model, viz, the displacement of the external inviscid

flow is determined by the streamwise rate of boundary layer growth. Using (8) in (5) and solving for δ_s finally yields an estimate for the boundary layer thickness near x_s :

$$\delta_s \sim \frac{\mu M_2 a_2 \cos\,\theta}{(P_p - P_1) tan\theta} \tag{9}$$

where $U_2 = M_2 a_2 \cos\theta$ and a_2 is the sound speed.
Before proceeding, and as an aside, we rewrite the estimate in (9) as

$$\frac{\mu U_2/\delta_s}{P_p - P_1} \sim \frac{\tau_2}{\Delta P} \sim \tan\,\theta \tag{10}$$

Recognizing that the resultant stress on a fluid particle near x_s is approximately equal to the vector sum of the horizontally acting viscous shear stress, τ_2, and the vertically-acting net pressure, $\Delta P = P_p - P_1$, then (10) shows that the resultant acts in the direction of the separating boundary layer, θ, as it must. Since $\delta_s/l_s \sim \tan\theta$, then (10) is also consistent with Chapman's (Chapman et al., 1958) estimate for $\tau_2/\Delta P$. Likewise, Chapman et al. (Chapman et al., 1958) argued that $\delta^*/l_s \sim C_f = \tau_w/(\rho_1 u_1^2/2)$, where C_f is the friction factor; since $\tau_w \sim \Delta P$, then for nominally fixed θ (see Sec. II.D below), (10) is also consistent with Chapman's estimate for C_f.
Returning to Eqn. (3), inserting (9) and the expression for R^{-1} and rearranging leads to an expression of the following form:

$$(\frac{P_p}{P_1})^2 - (1+G)\frac{P_p}{P_1} + G(1+\epsilon) \sim 0 \tag{11}$$

where $G = P_2/P_1$, $\epsilon = kM_2^3 a_2 \cos\,\theta \mu_2 f''/(P_1 f')$, μ_2 is the gas viscosity near the separation point,and where the approximation $\tan\,\theta \approx -f'$ has been used. Under typical conditions, e.g., those extant in experiments described below [$M_i \approx 5$, $\theta \approx 16^o$, $T_o = 310$K, $P_o = 1.24$ Mpa], $\epsilon = O(10^{-3})$, i.e., $\epsilon << 1$ [where $f''|_{max} \approx (d\theta/dx)|_{max} = O(1)$]. Thus, solving (11) for P_p/P_1 and neglecting terms smaller than $O(\epsilon)$, we finally obtain

$$\frac{P_p}{P_1} \sim G - \epsilon\frac{2G}{G-1} \tag{12}$$

Importantly, this equation shows that $P_1/P_p \approx P_i/P_p \sim P_1/P_2$, *demonstrating that the separation pressure ratio essentially corresponds to the oblique shock pressure ratio.*

2.4 Shock and flow deflection angles

In order to close the approximate model embodied in (12), it is necessary to specify the shock angle, β, and the flow deflection angle, θ. Referring to earlier work, Summerfield et al. (Summerfield et al., 1954) used measured separation pressure ratios and Mach numbers in the oblique shock relations to infer θ; based on their data, they inferred a nominally fixed value, $\theta \approx 16^o$. By contrast, Ostlund (Ostlund, 2002), again using the same approach,argued that θ varies with M_i, albeit weakly; he fit his estimate with a linear relationship, $\theta = 1.678M_i + 9.347$, valid for $2.5 \leq M_i \leq 4.5$. For this range of M_i, however, the correlation indicates that θ only varies from 13.5^o and 16.9^o. Based on these indirect estimates, we assume that θ is constant; for simplicity, we will arbitrarily adopt the average value of θ indicated by Ostlund's correlation, $\theta \approx 15.2^o$, nearly equal to Summerfield's (Summerfield et al., 1954)

estimate. Second, we follow Summerfield (Summerfield et al., 1954) and assume that the oblique shock relation

$$\tan\theta = \frac{2\cot\beta(M_1^2\sin^2\beta - 1)}{(k+1)M_1^2 - 2(M_1^2\sin^2\beta - 1)} \tag{13}$$

applies to the inviscid flow outside the separating boundary layer.

2.5 Free interaction model

Chapman's (Chapman et al., 1958) original analysis posited that thickening of the boundary layer displacement thickness displaced the inviscid flow above the boundary layer according to

$$P(x) - P_i = \frac{\rho_i u_i^2}{\sqrt{M_i^2 - 1}} d\theta \tag{14}$$

where $d\delta^*/dx = d\theta$, and where the subscripts refer to conditions at x_i. He then estimated terms in the balance between the axial pressure gradient and cross-stream shear stress gradient as

$$\frac{P - P_i}{l_s} \sim \frac{\tau_{wi}}{\delta^*} \tag{15}$$

(where τ_{wi} is the wall shear stress near x_i), then estimated $d\delta^*/dx$ as δ^*/l_s (where $\delta^* \sim \delta_s$), and finally combined and linearized (for small $P - P_i$) to obtain

$$\frac{P - P_i}{q_i} \sim \frac{\sqrt{C_{fi}}}{(M_i^2 - 1)^{1/4}} \tag{16}$$

where $q_i = \rho_i u_i^2/2$ and $C_{fi} = \tau_{wi}/q_i$.
Dividing the left side of (16) by the right suggests that

$$\Big(\frac{P - P_i}{q_i}\Big)\Big(\frac{(M_i^2 - 1)^{1/4}}{\sqrt{C_{fi}}}\Big) \sim f(x - x_i) \tag{17}$$

i.e., that the term on the left depends only on position within the shock interaction zone. Erdos and Pallone (Erdos & Pallone, 1962) exploited this idea to develop a wall pressure correlation, $F(s)$, which describes the self-similar pressure variation over the shock interaction zone, where

$$F(s) = \Big(\frac{P - P_i}{q_i}\Big)\Big(\frac{(M_i^2 - 1)^{1/4}}{\sqrt{2C_{fi}}}\Big) \tag{18}$$

and where $s = (x - x_i)/(x_s - x_i)$. Carriere et al. (Carriere et al., 1968) extended this work by developing a generalized version of (18), suitable for the non- uniform flows in nozzles. In this case, the self-similar pressure variation over the separation zone is described by

$$F(s; p') = \sqrt{\Big(\frac{P - P_i}{q_i}\Big)\Big(\frac{\bar{\nu}(s) - \nu(s)}{\sqrt{C_{fi}}}\Big)} \tag{19}$$

where $p' = (\delta_i^*/q_i)(dP/dx)$ is the normalized inviscid flow pressure gradient immediately upstream of x_i, $\nu(s)$ is the Prandtl-Meyer function, and $\bar{\nu}(s)$ is the value of the function in the

absence of separation. For a range of pressure gradients observed in a number of different nozzles, the two correlations, $F(s)$ and $F(s;p')$, are nearly identical (Ostlund, 2002).
Given $F(s;p')$ (or $F(s)$), the predicted separation pressure ratio, P_i/P_p, can be determined from either (18) or (19); in the latter case, we follow Chapman (Chapman et al., 1958) and linearize (19) to obtain

$$\frac{P_i}{P_p} = \left[F(s_p;p')kM_i^2\left(\frac{\sqrt{C_{fi}}}{\sqrt{2}(M_i^2-1)^{1/4}}\right)+1\right]^{-1} \tag{20}$$

where $\bar{\nu}(s)$ is approximated as ν_i and where $F(s_p;p')$ [= 6.0; see (Ostlund, 2002)] is the value of $F(s;p')$ at the effective separation point, $s_p[=(x_p-x_i)/(x_s-x_i)]$. It is important to note that (Ostlund, 2002) has developed an alternative separation criterion which requires *a priori* specification of both the plateau pressure, P_p, and the friction coefficient, C_{fi} at x_i. The criterion in (20) by contrast only requires information on C_{fi}. Fortuitously, and as originally shown by Chapman (Chapman et al., 1958), for shock-induced separation of *turbulent* boundary layers, the dependence of P_i/P_p on C_{fi} (or equivalently, on $Re_{\delta*}$, the displacement thickness Reynolds number at x_i) is weak, at least over the range of Mach numbers investigated $(1.3 \leq M_i \leq 4.0)$, consistent with both the scale analysis above and previously developed correlations; see (Keanini & Brown, 2007) for further details.

2.6 Experimental measurements

A series of experiments were carried out in the Nozzle Test Facility at Marshall Space Flight Center (Keanini & Brown, 2007). The experiments were designed to investigate the role of boundary layer separation on nozzle side- loading and to examine fluid-solid interactions underlying oscillatory modes observed in side-loaded nozzles.
A sub-scale, ideal-contour nozzle, having an area ratio of approximately 30:1 (exit to throat area) was operated under a range of cold-flow, overexpanded conditions. The nozzle was outfitted with a series of pressure taps, where tap spacing in the axial direction was 0.0254 m. Two sets of azimuthally spaced taps were also used, placed at two axial locations, at 45^o intervals around the nozzle circumference. The axially-spaced taps allowed measurement of the instantaneous and time-average axial pressure distribution within the nozzle while the azimuthally distributed taps allowed examination of the instantaneous and time-average separation line (under conditions where the shock interaction zone coincides with either set of azimuthally distributed taps). The throat diameter was 0.0254 m and the design Mach number was 5.25. Pressures at all taps were sampled at 10 kHz, sufficiently high to allow study of the low-frequency, large-amplitude component of shock motion (Dolling & Brusniak, 1989; Keanini & Brown, 2007), but not sufficient to resolve small-scale, high frequency jitter.

2.7 Results

The scaling relationship in (12) was fit to available data on separation in overexpanded nozzles. Data on free shock separation was obtained from a number of sources (Keanini & Brown, 2007), and represents flow in a variety of nozzle geometries, in both full-scale and sub-scale models, under both cold flow and hot fire conditions. Although the working fluid in most experiments was air, Bloomer's (Bloomer et al., 1961) hot fire measurements, which used a mixture of JP-4 rocket fuel and liquid oxygen $(k = 1.2)$, are included in estimating best fit parameters. This approach is allowable due to the weak dependence between separation pressure ratio and k; see review in (Keanini & Brown, 2007). Since solutions for P_1/P_2 at a

turning angle of $\theta = 15.2^o$ do not exist for $M_i <\approx 1.7$, only data obtained at $M_i \geq 1.75$ are used in the fitting procedure. For comparative purposes, however, the limited data available at $M_i \leq 1.75$ are presented in the graphs below.

A comparison of separation pressure ratios predicted by the first scaling model (Keanini & Brown, 2007), model I in figures 4 and 5, with available data, shown in figure 4, indicates that the model provides reasonable predictions over the range $1.75 \leq M_i \leq 4.0$. The least square fitting constant is found to be 1.52 . A similar comparison using model II, Eq. (12), shown in figure 5, likewise indicates reasonable agreement over $1.75 \leq M_i \leq 4.5$, with significantly improved agreement for $M_i > 4.0$; the fitting constant in this case is 1.14. Comparing with Ostlund (Ostlund, 2002) and Frey's (Frey & Hagemann, 1998) correlations, which fit observed shock pressure ratios to the oblique shock pressure ratio (based on inferred shock and deflection angles), we note that their quoted ranges of validity were in both cases $2.5 \leq M_i \leq 4.5$. At higher Mach numbers $(M_i \geq 4)$, the data suggests that P_i/P_p becomes

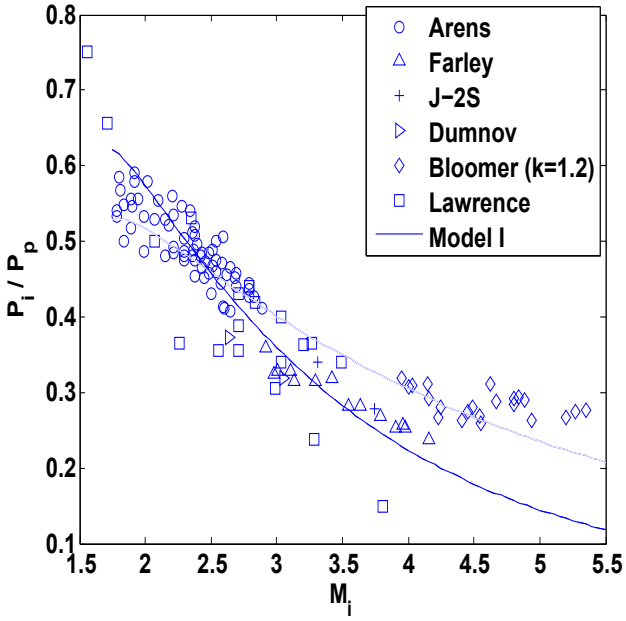

Fig. 4. Comparison of Model I in (Keanini & Brown, 2007) with separation measurements in rocket engine nozzles. The fitting constant equals 1.52.

largely independent of M_i. Although constancy of P_i/P_p is not inconsistent with separation remaining dominated by the oblique shock, since the asymptotic expression for P_i/P_p at large M_i is, from (12),

$$\frac{P_i}{P_p} \sim \frac{k+1}{2k \sin^2 \beta M_i^2}$$

then due to an 82 % variation in M_i^2 over $4.0 \leq M_i \leq 5.4$, the time-average deflection angle, θ, likely becomes moderately dependent on M_i.

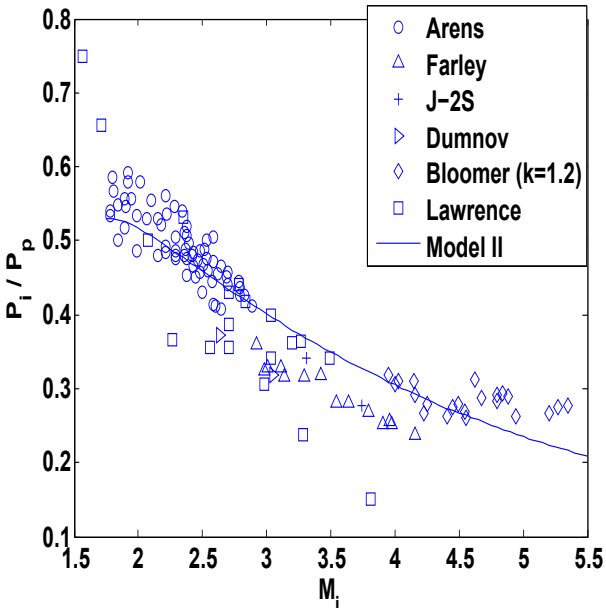

Fig. 5. Comparison of Model II (Keanini & Brown, 2007) with separation measurements in rocket engine nozzles. The fitting constant equals 1.14.

2.8 Separation pressure ratios via the free interaction model

In order to use the free interaction separation criterion in (20), C_{fi} must be specified. As noted, and based on Chapman's (Chapman et al., 1958) observation that P_i/P_p is weakly dependent on C_{fi}, we assume that C_{fi} is constant. The assumed magnitude, $C_{fi} = 0.00245$, represents the characteristic value obtained from fitting the free interaction model to observed time-average shock interaction zone pressure variations, as described in (Keanini & Brown, 2007). In addition, this value is used in fitting the generalized quasi-one-dimensional flow model, necessary for computing the flow upstream of the separation zone, to our experimental shock-free flow measurements; see (Keanini & Brown, 2007) for details.

As shown in figure 6, over $1.75 \leq M_i \leq 5.5$, predicted separation pressure ratios obtained via the free interaction model are quite similar to those obtained via the scaling analysis above. Given the reasonable agreement between model predictions and previous observations, this result simplifies Ostlund's (Ostlund, 2002) separation criterion by eliminating the need for *a priori* specification of P_p. Importantly, this result provides further evidence of the applicability of the free interaction model to separation in nozzles, and moreover, further indicates the physical consistency of the scale analyses presented in (Keanini & Brown, 2007).

3. Physically consistent models of random nozzle side loads

The models described in the previous section allow determination of the mean separation line position, $x_s(t) = x_s(H(t))$, within the nozzle, as a function of the instantaneous nozzle pressure ratio $NPR = NPR(H(t)) = P_o(t)/P_a(H(t))$ (Keanini & Brown, 2007; Keanini et al., 2011; Srivastava et al., 2010), where $P_o(t)$ is the time-dependent combustion chamber pressure

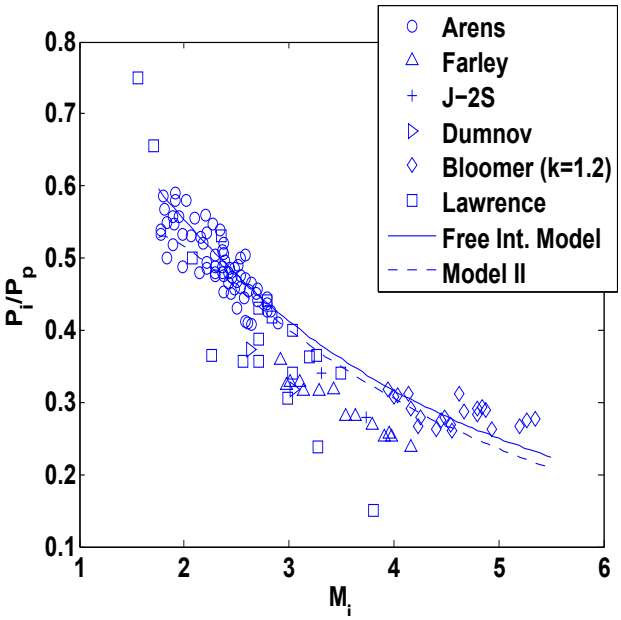

Fig. 6. Comparison of free interaction model and model II (Keanini & Brown, 2007) with separation measurements in rocket engine nozzles.

and $P_a(H(t))$ is the altitude- dependent ambient pressure. Given $x_s(t)$, physically consistent models that describe the stochastic evolution of the separation line *shape* relative to $x_s(t)$, can be developed. This section first highlights the essential elements of the stochastic side load models developed in (Keanini et al., 2011; Srivastava et al., 2010) and then briefly outlines a new, physically consistent model of stochastic separation line evolution (Keanini et al., 2011). As detailed in (Keanini et al., 2011; Srivastava et al., 2010), and in response to the decaying altitude-dependent ambient pressure, the mean position of boundary layer separation line, $x_s(t)$, travels down the nozzle axis toward the nozzle exit, with motion taking place on a relatively slow time scale, $\tau_a = \Delta x_a / V_R$, where Δx_a is the characteristic incremental altitude over which ambient pressure varies and V_R is the characteristic rocket speed. Superposed on this slow motion is a fast, random, azimuthally homogeneous stochastic motion. Following (Keanini et al., 2011; Srivastava et al., 2010), the joint probability density, p_s, associated with the instantaneous random separation line shape is given by

$$p_s(s_1, s_2, \ldots, s_N) = \prod_I p_I = \frac{1}{(2\pi\sigma_s)^{N/2}} \exp\left[- \frac{s_1^2 + s_2^2 + s_3^2 + \ldots + s_N^2}{2\sigma_s^2} \right] \tag{21}$$

where, as shown in figure 7, s_I is the random axial displacement of the separation line at azimuthal angle ϕ_I, and σ_s^2 is the (assumed) constant variance of local separation line displacements.

Constituent displacements in the set of N displacements are assumed independent, and based on experimental observations (Dolling & Brusniak, 1989), gaussian. Thus, each p_I is given by

$$p_I(s_I) = \frac{1}{\sqrt{2\pi\sigma_s^2}} \exp\Big[-\frac{s_I^2}{2\sigma_s^2}\Big] \tag{22}$$

In moving to a continuous description of the separation line, (Srivastava et al., 2010) assumes that

$$< s(\phi,t)s(\phi',t) >= \sigma_s^2\delta(\phi-\phi') \tag{23}$$

Considering next the side load, we express the instantaneous force vector produced by

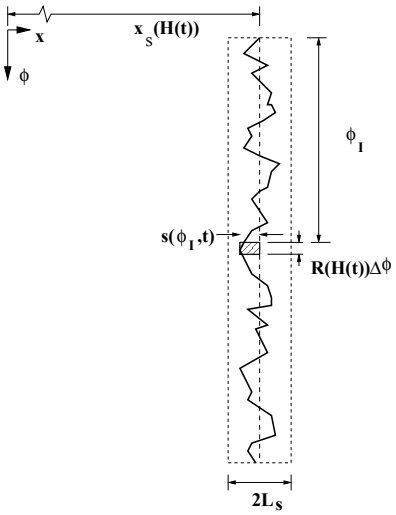

Fig. 7. Model I (Srivastava et al., 2010) separation line model. The mean separation line position, $x_s(H(t))$, moves down the nozzle axis, on the slow time scale associated with vertical rocket motion. By contrast, axial separation line motion about $x_s(H(t))$, at any angular position, ϕ_I, is random, and takes place on a much shorter time scale. Rapid axial motion, in addition, is confined to the nominal shock-boundary layer interaction zone, again denoted by L_s. Pressures upstream and downstream of the instantaneous separation line, $P_i = P_i(H(t))$ and $P_2 = P_2(H(t))$, respectively, are assumed to be spatially uniform within L_s. Adapted from (Srivastava et al., 2010).

asymmetric boundary layer separation, $\mathbf{F_s}(t)$, as a sum of radial and axial components

$$\mathbf{F_s}(t) = \mathbf{F_r}(t) + \mathbf{F_x}(t) \tag{24}$$

In (Srivastava et al., 2010), the following *ad hoc* side load model was assumed:

A) F_{sy} and F_{sz} are independent, gaussian random variables,

B) $< F_{sy} >= 0$ and $< F_{sz} >= 0$,

C) $\Big\langle \big(F_{sy} - < F_{sy} > \big)^2 \Big\rangle = \Big\langle \big(F_{sz} - < F_{sz} > \big)^2 \Big\rangle = \sigma^2$,

where, assuming ergodicity, $< \cdot >$ denotes either an ensemble or time average, and where the separation line model above is used to calculate the force variance σ^2. The side load components F_{sy} and F_{sz} are expressed with respect to rocket-fixed coordinates; see (Keanini et al., 2011; Srivastava et al., 2010).

In order to demonstrate the physical consistency of the model introduced in (Srivastava et al., 2010), (Keanini et al., 2011) first shows that the *assumed* properties, A) -C), can be *derived* from the simple *separation line model* developed in (Srivastava et al., 2010). Second, and as shown in the next subsection, the side load model in A) - C) then leads to *experimentally observed* side load amplitude and direction densities (Keanini et al., 2011).

3.1 Derivation of density functions for side load amplitude and direction

Two important experimental and numerical observations concerning the side load, $\mathbf{F_s}$ (within rigid, axisymmetric nozzles) are first noted:

a) the probability density of the random amplitude, $A = |\mathbf{F_s}|$, is a Rayleigh distribution (Deck & Nguyen, 2004; Deck et al., 2002), and

b) the random instantaneous direction, ϕ_s, of $\mathbf{F_s}$ is uniformly distributed over the periphery of the nozzle, or $p_{\phi_s}(\phi_s) = 1/2\pi$, where p_{ϕ_s} is the pdf of the side load direction (Deck & Nguyen, 2004; Deck et al., 2002).

Both observations can be *derived*, starting from the simple statistical model of random side loads, A) - C), immediately above. Thus, given A and ϕ_s, the instantaneous side load components in body-fixed y and z directions are given by

$$F_{sy} = A\cos\phi_s \qquad\qquad F_{sz} = A\sin\phi_s$$

Following (Srivastava et al., 2010), write F_{sy} and F_{sz} as $F_{sy} = \bar{Y} = A\cos\phi_s$ and $F_{sz} = \bar{Z} = A\sin\phi_s$; thus, the joint probability density associated with F_{sy} and F_{sz} can be expressed as

$$p_{\bar{Y}\bar{Z}}(\bar{Y},\bar{Z}) = p_{\bar{Y}}(\bar{Y})p_{\bar{Z}}(\bar{Z}) = \frac{1}{2\pi\sigma^2}\exp\left(-\frac{\bar{Y}^2+\bar{Z}^2}{2\sigma^2}\right) \tag{25}$$

Following (Srivastava et al., 2010), we restate $p_{\bar{Y}\bar{Z}}$ in terms of A and ϕ_s as,

$$p_{A\phi_s} = |J|p_{\bar{Y}\bar{Z}}(\bar{Y},\bar{Z}) \tag{26}$$

where $p_{A\phi_s}(A,\phi_s)$ is the joint pdf for the random amplitude and direction of $\mathbf{F_r}$, and where the jacobian determinant is given by

$$|J| = \begin{vmatrix} \frac{\partial\bar{Y}}{\partial A} & \frac{\partial\bar{Y}}{\partial\phi_s} \\ \frac{\partial\bar{Z}}{\partial A} & \frac{\partial\bar{Z}}{\partial\phi_s} \end{vmatrix} = A \tag{27}$$

Thus,

$$p_{A\phi_s}(A,\phi_s) = \frac{A}{2\pi\sigma^2}\exp\left(-\frac{A^2}{2\sigma^2}\right) = \left(\frac{1}{2\pi}\right)\left[\frac{A}{\sigma^2}\exp\left(-\frac{A^2}{2\sigma^2}\right)\right] = p_{\phi_s}(\phi_s)p_A(A) \tag{28}$$

where,

$$p_{\phi_s}(\phi_s) = \frac{1}{2\pi} \qquad\qquad 0 < \phi_s \leq 2\pi \tag{29}$$

is the uniform probability density underlying the random direction ϕ_s, and

$$p_A(A) = \frac{A}{\sigma^2} \exp\left(-\frac{A^2}{2\sigma^2}\right) \tag{30}$$

is the Rayleigh distribution for the amplitude A.

3.2 Ornstein-Uhlenbeck model of separation line dynamics

Theoretical determination of rocket response to side loads requires that the time correlation function for either side load component, $\langle F_{s\alpha}(t')F_{s\alpha}(t)\rangle$, be first determined. As detailed in (Keanini et al., 2011), $\langle F_{s\alpha}(t')F_{s\alpha}(t)\rangle$ is developed in two steps. First, and as detailed in this subsection, we propose(and physically justify) that local separation line dynamics can be modeled as an Ornstein-Uhlenbeck process. Once this assumption is made, then the second step rests on a rigorous argument showing that on the relatively long rocket dynamics time scale, the boundary layer separation line shape, and importantly, associated side load components, are all delta correlated in time. See (Keanini et al., 2011)for details.
The following simple, explicit stochastic model of separation line dynamics is proposed:

$$ds_i(t) = -ks_i(t) + \sqrt{D_s}dW(t) \tag{31}$$

where $s_i(t) = s(\phi_i, t)$ is the instantaneous separation line position at ϕ_i, k and D_s are damping and effective diffusion coefficients, and $dW(t)$ is a differential Weiner process. This equation, describing an Ornstein-Uhlenbeck process, allows straightforward, physically consistent calculation of statistical properties associated with separation line motion and, more importantly, serves as the first link in a chain that connects short-time-scale random separation line motion to short-time-scale random side loads, and in turn, to long-time-scale stochastic rotational rocket dynamics (Keanini et al., 2011).
The form of this equation is chosen based on the following experimental features, observed in shock-separated flows near compression corners and blunt fins:

a) Under statistically stationary conditions, the feet of separation-inducing shocks oscillate randomly, up- and downstream, over limited distances, about a fixed mean position; see, e.g., (Dolling & Brusniak, 1989).

b) As observed in (Dolling & Brusniak, 1989)the distribution of shock foot positions within the shock-boundary layer interaction zone is approximately gaussian.

c) The time correlation of shock foot positions, as indicated by wall pressure measurements within the shock-boundary layer interaction zone, decays rapidly for time intervals, $\triangle t$, larger than a short correlation time, τ_s, a feature that can be inferred, for example, from (Plotkin, 1975).

Physically, the damping term captures the fact that the shock sits within a pressure-potential energy well. Thus, downstream shock excursions incrementally decrease and increase, respectively, upstream and downstream shock face pressures; the resulting pressure imbalance forces the shock back upstream. A similar mechanism operates during upstream excursions. Introduction of a Weiner process models the combined random forcing produced by advection of turbulent boundary layer structures through the upstream side of the shock foot and pressure oscillations emanating from the downstream separated boundary layer and recirculation zone.
We note that the proposed model is qualitatively consistent with Plotkin's model of boundary layer-driven shock motion near compression corners and blunt fins (Plotkin, 1975). Plotkin's

model, which captures low frequency spectra of wall pressure fluctuations within these flows, corresponds to a generalized Ornstein-Uhlenbeck process in which a deterministic linear damping term is superposed with a non-Markovian random forcing term. We use an ordinary OU process model, incorporating a Weiner process, since again, it is consistent with the above observations and more particularly, since it allows much simpler calculation of statistical properties (Keanini et al., 2011).

4. Rocket response to random side loads

This section highlights recent results on numerical simulation of the stochastic ascent of a sounding-rocket-scale rocket, subjected to altitude dependent random nozzle side loads (Srivastava et al., 2010). The numerical simulations solve the full, coupled, nonlinear equations of rotational and translational rocket motion. The simulations include the effects of altitude-dependent aerodynamic drag forces, random nozzle side loads, associated random torques, mass flux damping torques (Keanini et al., 2011), and time-varying changes in rocket mass and longitudinal moment of inertia. In order to clearly isolate the effects of nozzle side loads on rocket translational and rotational dynamics, random wind loads are suppressed. A simple scaling argument (Keanini et al., 2011) indicates that random winds: i) under most conditions, do not excite rotational motion, and ii) simply function as an *additive* source of variance in the rocket's *translational* motion. In other words, wind appears to have minimal influence on the stochastic, altitude-dependent evolution of *rotational* dynamics. Rather, (launch-site-specific) mean and random winds simply produce whole-rocket, random, *lateral translational* motion, superposed on a deterministic translational drift.

Given side load direction and amplitude densities in Eqs. (29) and (30), respectively, altitude- dependent side loads are simulated using a Monte Carlo approach; the nonlinear, coupled equations of translational and rotational motion are then solved using fourth order Runge-Kutta integration (Srivastava et al., 2010). In estimating altitude-dependent means and variances in translational and rotational velocities and displacements, an ensemble of 100 simulated flights are used; it is found that estimated statistics do not vary significantly when using ensembles of 40 and 100 flights (Srivastava et al., 2010). The parameters employed in the simulations are characteristic of medium sized sounding rockets (Srivastava et al., 2010).

Characteristic results are presented in figures 8 through 13. The stochastic evolution of both lateral side load components, F_{sy} and F_{sz}, observed during a single simulated realization, is shown in figure 8. Initially, i.e., at launch, the pressure jump across the separation-inducing shock is relatively high (Srivastava et al., 2010), and is manifested by somewhat higher initial side load amplitudes. However, as the rocket gains altitude, ambient pressure decays, and the cross-shock pressure jump decreases - characteristic side load magnitudes become smaller. At the instant when the slowly traveling in-nozzle shock reaches the nozzle exit, the nozzle flow becomes shock free, boundary layer separation ceases, and side loading stops. For these simulations, this instant corresponds to a flight time of 10.85 seconds (Srivastava et al., 2010), or an altitude of approximately 3.75 km. Note that side load amplitudes are significant, on the order of 10 to 16 % of the rocket's initial weight.

Figure 9 shows a single realization of the rocket's trajectory, under the action of random side loads, and is compared against the trajectory taken when side loads are suppressed. [Here, and throughout, X_o and (Y_o, Z_o) denote, respectively, the vertical, and (mutually orthogonal) lateral displacements of the rocket center of mass, relative to the launch location.] It is clear, that absent active control, a rocket can exhibit significant lateral displacements relative to the predicted zero-side-load path. Scaling shows that the characteristic magnitudes of random

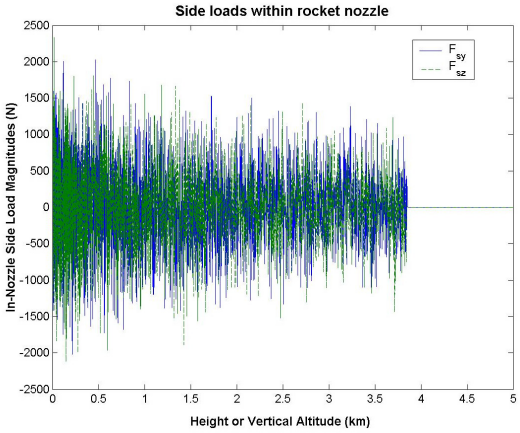

Fig. 8. In-nozzle stochastic side loads versus rocket altitude. Adapted from (Srivastava et al., 2010).

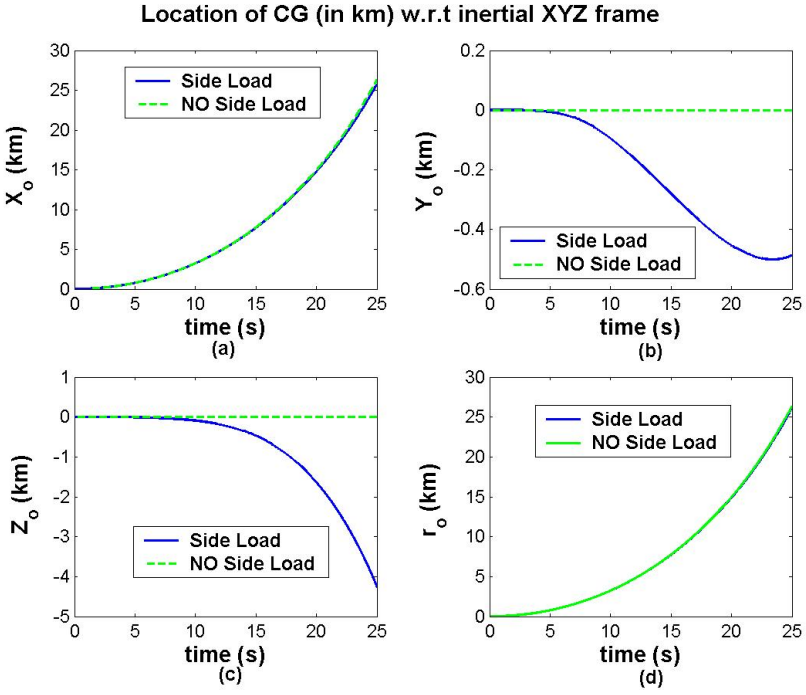

Fig. 9. Single realizations of rocket center of mass trajectory under random side loads and with side loads suppressed. X_o, and (Y_o, Z_o) denote, respectively, the vertical, and (mutually orthogonal) lateral displacements of the rocket center of mass, relative to the launch location. Adapted from (Srivastava et al., 2010).

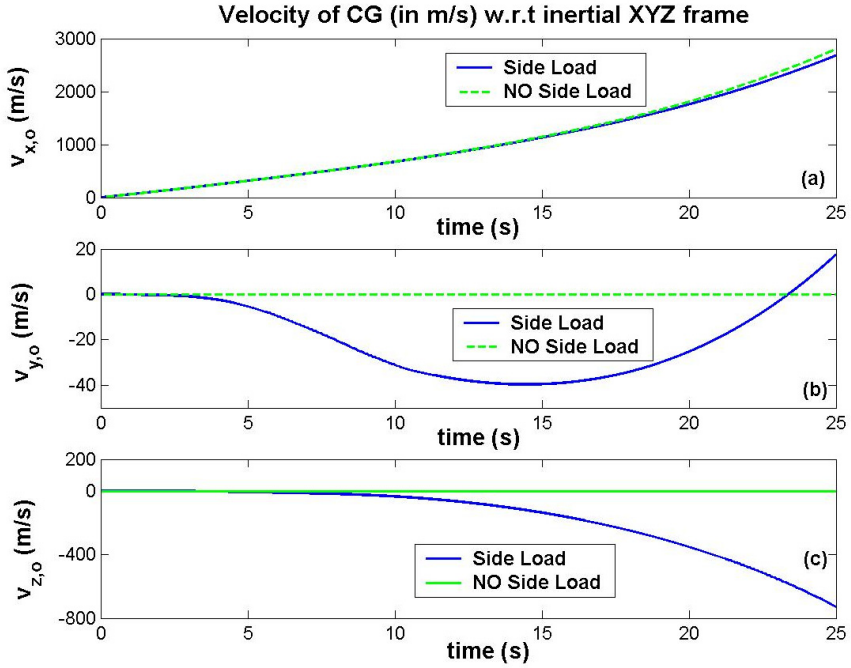

Fig. 10. Single realizations of rocket center of mass velocity under random side loads and with side loads suppressed. $v_{x,o}$ and $(v_{y,o}, v_{z,o})$, denote, respectively, the vertical, and (mutually orthogonal) lateral velocities of the rocket center of mass, relative to the launch location. Adapted from (Srivastava et al., 2010).

lateral displacements, which can be on the order of 1-4 kilometers over the simulated flight time of 25 seconds, are fully consistent with displacements estimated using characteristic side load magnitudes (Keanini et al., 2011; Srivastava et al., 2010). The several order of magnitude difference between (vertical) thrust forces and the small vertical component of $\mathbf{F_s}$ explains the result shown in figure 8a.

Random side loads produce significant excitation of pitch and yaw dynamics (Keanini et al., 2011; Srivastava et al., 2010). Thus, for example, once a rocket begins a random pitching and yawing motion, that motion continues, even after side loading stops (at $t = 10.85$ s). Random pitch and yaw, in turn, produce random lateral velocities. As indicated in figures 10 and 11, and as discussed in detail in (Keanini et al., 2011), a certain amount of time - an induction period - must pass before side-load-induced pitch and yaws grow large enough for significant lateral thrust components to appear. Once the induction period has passed, however, large lateral thrusts begin to act and the rocket begins to experience large lateral velocities and displacements. Figures 10 and 11 capture these essential dynamical features. The work in (Keanini et al., 2011) provides a detailed, physically-based analysis of the complex dynamics a rocket experiences during side loading.

As shown in (Keanini et al., 2011), and as indicated in figure 12, stochastic pitch and yaw rotational dynamics are characterized by two qualitatively distinct regimes. During the side load period, $t \leq 10.85$ s, the action of random side loads on pitch and yaw angular velocities

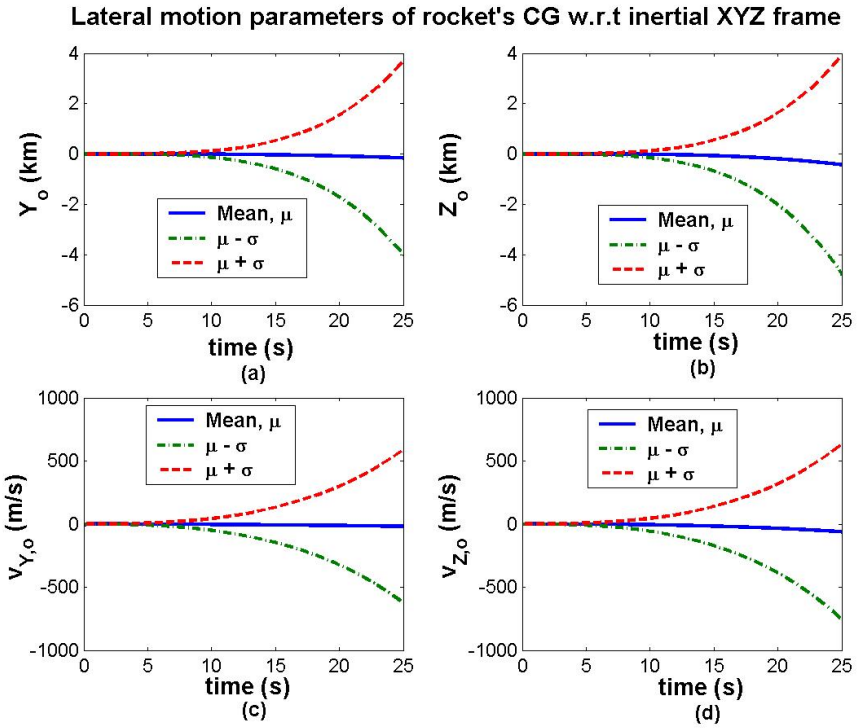

Fig. 11. Time-(altitude-)dependent means and variances of the rocket's lateral center of mass position (Y_o, Z_o) and lateral center of mass velocity (v_{yo}, v_{zo}). Adapted from (Srivastava et al., 2010).

can be modeled as an Ornstein-Uhlenbeck process, wherein side loads function, at least on the long rocket dynamics time scale, as Weiner processes. Simultaneous to stochastic pitch/yaw amplification, deterministic pitch/yaw damping, produced by incremental changes in the nozzle mass flux vector, i.e., mass flux damping (Keanini et al., 2011), counteract amplification. Thus, during the side load period, pitch/yaw velocities grow, but at an ever-decreasing rate. In the second regime, which begins when the separation-inducing shock exits the nozzle and side loads cease, mass-flux damping continues, driving pitch and yaw velocities toward zero (Keanini et al., 2011). These qualitative features are likewise apparent in plots of time-(altitude-)dependent pitch/yaw means and variances; see figure 13. As detailed in (Keanini et al., 2011), all of these features can be rigorously explained using, e.g., a course grained description of short-time-scale side load statistics, along with an asymptotic model of rocket translational and rotational motion.

5. Stochastic rocket ascent as a diffusion process

Starting with the nonlinear equations of rotational motion, (Keanini et al., 2011) use a rigorous argument to show that the equations governing evolution of pitch and yaw rates assume the

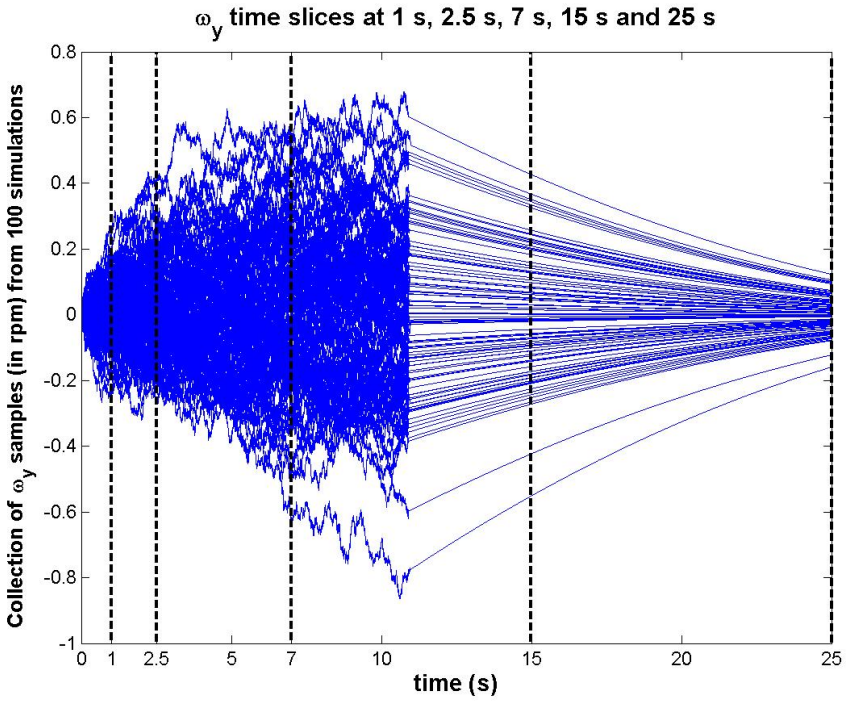

Fig. 12. Ensemble of 100 realizations of yaw angular velocity evolution. Side loads cease at $t = 10.85$ s. Adapted from (Srivastava et al., 2010).

form of an Ornstein-Uhlenbeck process:

$$d\omega_{\pm} = -A(t)\omega_{\pm} \pm \sqrt{D(t)}dW_{\pm} \tag{32}$$

where $\omega_{+} = \omega_y$ and $\omega_{-} = \omega_z$ correspond, respectively, to yaw and pitch rate, $A(t)$ and $D(t)$ are, respectively, the time-(altitude-)dependent effective damping and diffusion coefficients, and $W_{\pm}(t)$ are Weiner processes.

Fundamentally, and as detailed in (Keanini et al., 2011), equation (32) provides the key to analyzing both the rotational and translational rocket response to side loading. Physically, $A(t)$ is roughly proportional to both the squared moment arm from the rocket center of mass to the nozzle exit, L_{ce}^2, as well as the mass flux magnitude, and is inversely proportional to the lateral moment of inertia. Likewise, $D(t)$ is proportional L_{ce}^2, as well as the squared (altitude-dependent) pressure difference between the interior and exterior of the nozzle, and the squared altitude-dependent position of the separation-inducing shock.

Practically, the detailed formulas for $A(t)$ and $D(t)$ in (Keanini et al., 2011) are related to both rocket-specific design parameters, as well as universal, non-specific parameters characterizing in-nozzle, shock-boundary layer separation. Thus, as discussed in (Keanini et al., 2011), the formulas allow straightforward identification of design criteria for, e.g., enhancing pitch/yaw damping and/or suppressing diffusive, i.e., stochastic growth of random pitch and yaw.

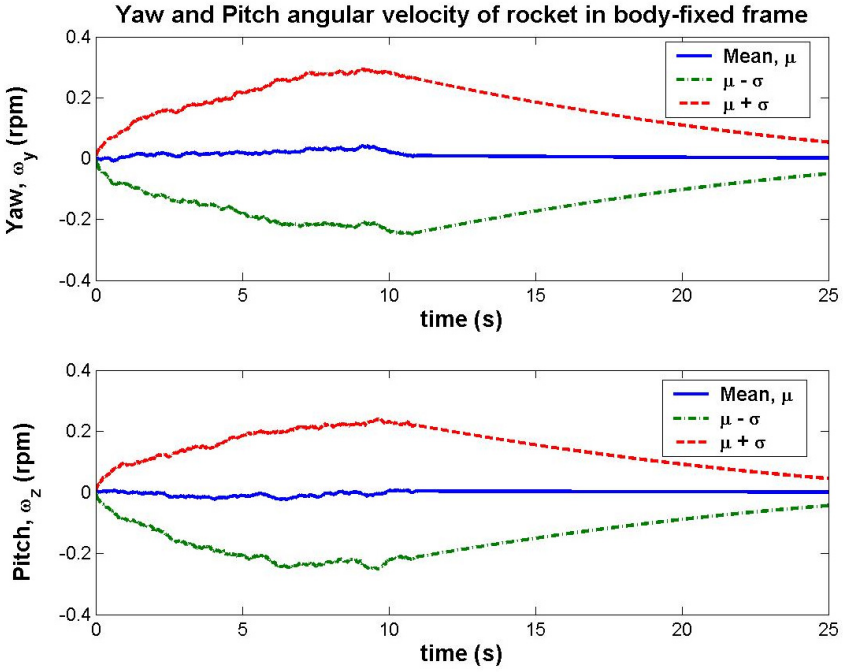

Fig. 13. Time-(altitude-)dependent means and variances of the rocket's pitch and yaw angular velocities. Adapted from (Srivastava et al., 2010).

6. References

Bloomer, H. E., Antl, R. J. & Renas, P. E. (1961). Experimental study of the effects of geometric variables on performance of conical rocket engine exhaust nozzles, NASA TN D-846.

Carriere, P., Sirieix, M. & Solignac, J. L. (1968). Properties de similitude des phenomenes de decollement laminaires ou turbulents en ecoulement supersonic nonuniforme, *12th Int. Congress of Applied Mech.*, Stanford Univ., Palo Alto, CA.

Chapman, D. R., Kuehn, H. K. & Larson, H. K. (1958). Investigation of separated flows in supersonic and subsonic streams with emphasis on the effect of transition, NACA Report 1356.

Deck, S. & Nguyen, A. T. (2004). Unsteady side loads in thrust-optimized contour nozzle at hysteresis regime, *AIAA J.*, Vol. 42, No. 9, pp. 1878-1888.

Deck, S., Garnier, E. & Guillen, P. (2002). Turbulence modeling applied to space launcher configurations, *J. Turbulence*, Vol. 3, No. 1, pp. 57-57(1).

Dolling, D. S. & Brusniak, L. (1989). Separation shock motion in fin, cylinder, and compression ramp-induced turbulent interactions, *AIAA J.*, Vol 27, No. 6, pp. 734-742.

Erdos, J. & Pallone, A. (1962). Shock-boundary layer interaction and flow separation, *Proc Heat Transfer and Fluid Mechanics Institute*, Stanford Univ. Press.

Flemming, E. L., Chandra, S., Schoeberl, M. R. & Barnett, J. J. (1988). Monthly Mean Global Climatology of Temperature, Wind, Geopotential Height, and Pressure for 0-120 km, NASA TM-100697.

Frey, M. & Hagemann, G. (1998). Status of flow separation prediction in rocket nozzles, AIAA Paper 98-3619.

Gruntman, M. (2004). *Blazing The Trail: The Early History Of Spacecraft and Rocketry,* AIAA, Reston, VA.

Justus, C. G. & Johnson, D. L. (1999). The NASA/MSFC Global Reference Atmospheric Model -1999 Version, NASA TM-1999-209630.

Justus, C. G., Campbell, C. W., Doubleday, M. J. & Johnson, D. L. (1990). New Atmospheric Turbulence Model for Shuttle Applications, NASA TM-4168.

Keanini, R. G. & Brown, A. (2007). Scale analysis and experimental observations of shock-induced turbulent boundary layer separation in nozzles, *European J. Mechanics B/Fluids,* Vol. 26, pp. 494-510.

Keanini, R. G., Srivastava, N. & Tkacik, P. T. (2011). Stochastic rocket dynamics under random nozzle side loads: Ornstein-Uhlenbeck boundary layer separation and its course grained connection to side loading and rocket response, in press *Annalen der Physik.*

Leahy, F. B. (2008). Discrete gust model for launch vehicle assessements, 12^{th} *Conf. on Aviation, Range and Aerospace Metrology,* Atlanta, GA, Jan. 2006, American Meteorology Society..

McNaughtan, I. I. (1993). The resistance of transparencies to bird impact at high speeds, *Aircraft Engrg. Aerospace Tech.,* Vol. 36, No. 12, pp. 409-413.

Ostlund, J. (2002). Supersonic flow separation with application to rocket engine nozzles, Doctoral Thesis, Department of Mechanics, Royal Institute of Technology, Stockholm, Sweden.

Plotkin, K. J. (1975). Shock wave oscillation driven by turbulent boundary-layer fluctuations, *AIAA J.,* Vol. 13, No. 8, pp. 1036-1040.

Schmucker, R. H. (1984). Flow Processes in Overexpanded Chemical Rocket Nozzles - Part I, NASA Rep. 77396.

Sekita, R., Watanabe, A., Hirata, K. & Imoto, T. (2001). Lessons learned from H-2 failure and enhancement of H-2A project, *Acta Astronautica,* Vol. 48, No. 5-12, pp. 431-438.

Srivastava, N., Tkacik, P. T. & Keanini, R. G. (2010). Influence of nozzle random side loads on launch vehicle dynamics, *J. Applied Physics,* Vol. 108, pp. 044911-044926.

Summerfield, M., Foster, C. R. & Swan, W. C. (1954). Flow separation in overexpanded supersonic exhaaust nozzles, *Jet Propulsion,* Vol. 24, No. 9, pp. 319-321.

Sutton, G. P. & Biblarz, O. (2001). *Rocket Propulsion Elements, 7th ed,* Wiley, New York.

8

Numerical and Experimental Study of Mass Transfer Through Cavitation in Turbomachinery

Rafael Campos-Amezcua[1], Sofiane Khelladi[2],
Zdzislaw Mazur-Czerwiec[1], Farid Bakir[2],
Alfonso Campos-Amezcua[1] and Robert Rey[2]
[1] *Electrical Research Institute, Department of Turbomachinery, Cuernavaca,*
[2] *Arts et Métiers ParisTech, DynFluid Laboratory, Paris,*
[1]*Mexico*
[2]*France*

1. Introduction

The vapour generation in a liquid can be caused by two different mechanisms: following a heat input, thus an increase in temperature at constant pressure, which is well known as the boiling phenomenon, or, at constant temperature, a decrease of pressure, which corresponds to the cavitation phenomenon.
When the liquid pressure decreases below the saturation pressure, some liquid undergoes a phase change, from liquid to vapour. The saturation pressure, p_v, is a fluid property which depends strongly on the fluid temperature. The cavitation phenomenon is manifested, in the fluid flow, by the formation of bubbles, regions of vapour or vapour eddies.
The cavitation phenomenon frequently occurs in hydraulic machines operating under low pressure conditions. The cavitation phenomenon causes several undesirable effects on this type of machines, for example: the noise generated by the mass transfer between the phases, the efficiency loss of the hydraulic machines, and the erosion of certain elements caused by the vapour bubbles collapses near walls. Additionally, it should be mentioned the flow instabilities caused by the vapour appearance, such as alternate blade cavitation and rotating blade cavitation (Campos-Amezcua et al., 2009).
The formation of cavitating structures in the hydraulic machines, their geometry and more generally, their static and dynamic properties, depend on several parameters (Bakir et al., 2003), such as:

- Geometrical conditions: profile, camber, thickness, incidence, and leading edge shape of the blades, as well as the walls roughness.
- Local flow conditions: pressure, velocities, turbulence, the existence of gas micro-bubbles dissolved in the flow.
- Fluid properties: saturation pressure, density, dynamic viscosity and surface tension.

This chapter presents an analysis of the cavitating flows on three axial inducers. These studies include numerical analyses at a range of flow rates and cavitation numbers, which were validated with experimental tests (Campos-Amezcua et al., 2009; Mejri et al., 2006). The obtained results can be summarized of the following way:

1. Experimental results concerning:
   a. Steady state performances: pressure head coefficient and efficiency versus flow rates.
   b. Steady state cavitating behaviour of the studied inducers.
2. Numerical results concerning:
   a. Steady and unsteady states performances: pressure head coefficient and efficiency versus flow rates.
   b. Steady and unsteady states cavitating behaviour of the studied inducers.
   c. Vapour distributions and other numerical results, which enable to explain the cavitating behaviour for these inducers.
   d. The fluid flow instabilities generated by the presence of vapour.

The numerical simulations were performed using the commercial code *Fluent*, which is based on a cell-centred finite-volume method. The cavitation model used for the calculations assumes a thermal equilibrium between the phases. It is based on the classical conservation equations of the vapour phase and a mixture phase, with mass transfer due to the cavitation, which appears as a source term and a sink term in the vapour mass fraction equation. The mass transfer rate is derived from a simplified Rayleigh–Plesset model for bubble dynamics. The experimental tests were carried out at the DynFluid Laboratory of Arts et Métiers ParisTech.

Next, the different cases studied in this work, to understand the cavitating behaviour of the inducers, are described:

a. Cavitating flow through venturi geometry.
   This part presents the numerical validation of the cavitating flow through a 2D simple geometry. On the one hand, the numerical results demonstrate the influence of the turbulence model to predict instabilities in non-homogeneous flows. On the other hand, the intrinsic instabilities were detected and compared to experimental data.
b. Analysis of cavitating flow in two-dimensional inducers – blades cascades.
   This part presents the steady and unsteady numerical study carried out on two blades cascades: first, on a two-blade aircraft inducer, and then, on a three-blade industrial inducer, see Fig. 1. This analysis confirms the influence of blades number and the solidity on the behaviour of the instabilities of cavitating flow. Various forms and behaviours of vapour have been observed in the blades cascades, such as: stable blade cavitation, alternate blade cavitation and rotating blade cavitation.
c. Experimental study and numerical analysis of the cavitating flow in three-dimensional inducers.
   This part presents the steady and unsteady numerical simulations, and experimental investigations in steady state of the cavitating flow through of the three inducers presented in the Fig. 1. The flow behaviour in the inducers is modified by the appearance of the cavitation on the leading edge. These cavitating behaviours change with respect to the operating conditions of the inducer: flow rates and cavitation levels.

Fig. 1 shows the three inducers used for the numerical and experimental study in cavitating regime, and the Table 1 presents the main characteristics of these inducers.

2. Numerical method

The commercial code used for all simulations was *Fluent*. This code employs a cell–centred finite–volume method that allows the use of computational elements with arbitrary

(a) (b) (c)

Fig. 1. Inducers used for the numerical and experimental study in cavitating regime.
(a) Three-blade industrial inducer with β=16° (b) Three-blade industrial inducer with β=8°
(c) Two-blade aircraft inducer with β=4°

Parameters	**Industrial inducer** ***β=16°***	**Industrial inducer** ***β=8°***	**Aircraft inducer** ***β=4°***
Maximal efficiency	57%	54.1%	15.5%
Nominal flow rate coeff.	0.159	0.076	0.014
Nominal head coeff.	0.310	0.228	0.188
Blade number	3	3	2
Blade tip angle	16°	8°	4°
Tip solidity	2.95	2.45	3
Rotational velocity	1,450 RPM	1,450 RPM	8,000 RPM

Table 1. Principal characteristics of inducers used for the cavitating analyses

Nomenclature

D	diameter
f_{cav}	detachment frequency
l	blade chord length
l_{cav}	cavitation length
p	pressure
P_v	saturation pressure
Q	flow rate
R	radius
St	Strouhal number
T	cycle period
t	time
U	tangential velocity
v	velocity magnitude

Greek

a	vapour volume fraction
β	blade tip angle
η	efficiency
γ	vapour mass fraction
Φ	flow coefficient
Ψ	head coefficient
ω	rotational speed
ρ	density
σ	cavitation number
σ_s	surface tension

Subscript

1, 2	inlet, outlet
a	axial direction
B	bubble
c	condensation
cav	cavitation
e	vaporization
g	gas
l	liquid
nom	nominal
t	blade tip
v	vapour

polyhedral shape. Convective terms were discretized using the second–order upwind scheme. The velocity–pressure coupling and overall solution procedure were based on a SIMPLE type segregated algorithm adapted to unstructured grids. The discretized equations were solved using point-wise Gauss–Seidel iterations, and an algebraic multi–grid method accelerates the solution convergence. A more detailed description of the numerical method is available in Kim et al. (1998).
The convergence criteria in the present numerical analysis were at least of three orders of magnitude, for the mass conservation imbalance and momentum equation residuals, which are deemed sufficient for most steady flow solutions. On the other hand, the residual values were defined at least of six orders of magnitude, for the unsteady flow solutions.

2.1 Cavitation model

The cavitation model used for this study was developed by Singhal et al. (2002). It takes into account all first–order effects (i.e., the phase change, the bubble dynamics, the turbulent pressure fluctuations, and the non–condensable gases). The influence of slip velocity between the liquid and the vapour phases was not considering.
For the multi–phase flow solution, the single–fluid mixture model was employed. The mixture model solves the continuity and momentum equations for the mixture, and the volume fraction equation for the secondary phases. The cavitation model consists of solving the standard incompressible Reynolds–Average Navier–Stokes equations (RANS) using a conventional turbulence model (e.g., κ–ε turbulence model).
The working fluid is assumed to be a mixture of liquid, vapour and non-condensable gas (NCG). The mixture density is a function of vapour and NCG mass fractions, γ_v and γ_g, which is computed by solving a transport equation, coupled with the mass and momentum conservation equations. The mixture density is defined by:

$$\frac{1}{\rho} = \frac{\gamma_v}{\rho_v} + \frac{\gamma_g}{\rho_g} + \frac{1-\gamma_v-\gamma_g}{\rho_l} \tag{1}$$

With

$$\gamma_v = \frac{\alpha_v \rho_v}{\rho}, \quad \gamma_g = \frac{\alpha_g \rho_g}{\rho}, \quad and \quad \gamma_l = \frac{\alpha_l \rho_l}{\rho} = 1 - \gamma_v - \gamma_g \tag{2}$$

where a_g, a_l and a_v are the non–condensable gas, liquid and local vapour volume fraction, respectively; and $a = a_g + a_v$ is the global vapour volume fraction.
The vapour mass fraction is governed by the transport equation given by:

$$\frac{\partial}{\partial t}(\rho\gamma) + \nabla \cdot (\rho \boldsymbol{v}\gamma) = \nabla \cdot (\Gamma \nabla \gamma) + R_e - R_c \tag{3}$$

where $\boldsymbol{v}$ is the velocity vector of the vapour phase; Γ is the effective exchange coefficient, and R_e and R_c are the vapour generation and condensation rate terms. The above formulation employs a homogenous flow approach.
In a flowing liquid, with null slip velocity between the phases, the bubble dynamics equation can be derived from the generalized Rayleigh–Plesset equation as:

$$R_B \frac{D^2 R_B}{Dt^2} + \frac{2}{3}\left(\frac{DR_B}{Dt}\right)^2 = \frac{P_B - P}{\rho_l} - \frac{4\nu_l}{R_B}\dot{R_B} - \frac{2\sigma_s}{\rho_l R_B} \tag{4}$$

This equation provides a physical approach to introduce the effects of bubble dynamics into the cavitation model. In fact, it can be considered to be an equation for vapour propagation and, hence, mixture density.
Using the Rayleigh–Plesset equation without the viscous damping and surface tension terms and coupling with the two-phase continuity equations (liquid phase, vapour phase and mixture), the expression for the net phase change rate, R, is finally obtained as:

$$R = (n4\pi)^{1/3} \frac{\rho_v \rho_l}{\rho} \left[\frac{2}{3} \left(\frac{P_B - P}{\rho_l} \right) - \frac{2}{3} R_B \frac{D^2 R_B}{Dt^2} \right]^{1/2} \tag{5}$$

Using this equation and ignoring the second–order derivative of R_B, the simplified equation for vapour transport is obtained as:

$$\frac{\partial}{\partial t}(\rho\gamma) + \nabla \cdot (\rho\gamma\vec{v}) = (n4\pi)^{1/3} (3\alpha)^{2/3} \frac{\rho_v \rho_l}{\rho} \left[\frac{2}{3} \left(\frac{P_B - P}{\rho_l} \right) \right]^{1/2} \tag{6}$$

The global vapour volume fraction, a, can be related to the bubble number density, n, and radius of bubble R_B as:

$$\alpha_v = n \cdot (4/3) \cdot \pi \cdot R_B^3 \tag{7}$$

Turbulent effects are considered using a simply raising of the phase change threshold pressure value as:

$$P_v = P_{sat} + 0.195 \cdot \rho \cdot \kappa \tag{8}$$

Finally, with the consideration of the NCG effect, and the turbulent effects, the phase change rate expressions are derived from the reduced form of Rayleigh–Plesset equation of bubble dynamics as:

$$R_e = C_e \frac{\sqrt{\kappa}}{\sigma_s} \rho_v \rho_l \left[\frac{2}{3} \frac{P_v - P}{\rho_l} \right]^{1/2} \left(1 - \gamma_v - \gamma_g \right) \tag{9}$$

$$R_c = C_c \frac{\sqrt{\kappa}}{\sigma_s} \rho_l \rho_l \left[\frac{2}{3} \frac{P - P_v}{\rho} \right]^{1/2} \gamma_v \tag{10}$$

where: C_e=*0.02* and C_c=*0.01* are empirical coefficients and κ is the local turbulent kinetic energy. A more detailed description of the cavitation model is available in Singhal et al. (2002).

2.2 RNG κ–ε model

This model was developed by Yakhot & Orszag (1986). It uses the Re–Normalisation Group (RNG) methods to renormalize the Navier–Stokes equations, and take into account the effects of smaller scales of motion. The RNG κ–ε model is derived from the standard κ–ε model. The main difference is the form of the dissipation of the kinetic turbulent energy equation.
The turbulence kinetic energy, κ, and its rate of dissipation, ε, are obtained from the following transport equations:

$$\frac{\partial}{\partial t}(\rho\kappa)+\frac{\partial}{\partial x_i}(\rho\kappa u_i)=\frac{\partial}{\partial x_j}\left[\left(\mu+\frac{\mu_t}{\sigma_\kappa}\right)\frac{\partial\kappa}{\partial x_j}\right]+P_\kappa-\rho\varepsilon \tag{11}$$

$$\frac{\partial}{\partial t}(\rho\varepsilon)+\frac{\partial}{\partial x_i}(\rho\varepsilon u_i)=\frac{\partial}{\partial x_j}\left[\left(\mu+\frac{\mu_t}{\sigma_\varepsilon}\right)\frac{\partial\varepsilon}{\partial x_j}\right]+C_{1\varepsilon}^{*}\frac{\varepsilon}{\kappa}P_\kappa-C_{2\varepsilon}\rho\frac{\varepsilon^2}{\kappa} \tag{12}$$

where

$$C_{1\varepsilon}^{*}=C_{1\varepsilon}-\frac{C_\kappa\eta^3(1-\eta/\eta_0)}{1+\beta\eta^3},\quad \eta=\frac{S\kappa}{\varepsilon},\quad \text{and}\quad S=\left(2S_{ij}S_{ij}\right)^{1/2}$$

P_κ represents the production of turbulence kinetic energy and is defined as:

$$P_\kappa=-\rho\overline{u_i'u_j'}\frac{\partial u_j}{\partial u_i} \tag{13}$$

The turbulent viscosity, μ_t, is given by:

$$\mu_t=\rho C_\mu\frac{\kappa^2}{\varepsilon} \tag{14}$$

The constants of the model are: $C_\mu=0.0845$, $C_{1\varepsilon}=1.42$, $C_{2\varepsilon}=1.68$, $\sigma_\mu=\sigma_\varepsilon=0.7194$, $\eta_0=4.38$, $\beta=0.012$.

2.3 RNG κ–ε modified model

This turbulent model is an adaptation from the RNG κ–ε model. The modification concerns the reduction, in the high vapour volume fraction regions, of the effective viscosity, $\mu_{eff}=\mu_{flow}+\mu_t$. For this purpose, the mixture turbulent viscosity is given by:

$$\mu_t=f(\rho)C_\mu\frac{\kappa^2}{\varepsilon} \tag{15}$$

where mixture density function, $f(\rho)$, is given by:

$$f(\rho)=\rho_v+\left(\frac{\rho_v-\rho}{\rho_v-\rho_l}\right)^n(\rho_l-\rho_v)\quad where\quad n>1 \tag{16}$$

This model was proposed by Reboud et al. (1998). This one allows the formation of the re-entrant jet which causes the vapour fluctuations of the cavitating flow in a venturi. The RNG κ–ε modified model has been implemented using a User's Defined Function supplied by *Fluent*.

3. Cases of study

To understand the cavitation phenomenon and calibrate the numerical code used for the analysis of the cavitating flows; first, the numerical analysis was performed on a simplified geometry. The numerical results were compared with experimental data available in references.

After that, the analysis was extended to cavitating flows in two blades cascades with different blades number and solidities. The main purpose of this study was to detect the instabilities of cavitating flow, such as: alternate blade cavitation and rotating blade cavitation.

Finally, the experimental and numerical analyses of cavitating flow were realized in three dimensions. The numerical simulations were developed in steady and unsteady states, and experimental investigations were realized only in steady state.

All the numerical simulations have used water at 300 *K* as the working fluid. The liquid density and the vapour density are ρ_l=1,000 *kg/m*^{3} and ρ_v=0.5542 *kg/m*^{3}, respectively. The liquid viscosity and the vapour viscosity are μ_l=1E-3 *Pa·s* and μ_l=1.34E-5 *Pa·s*, respectively. The saturation pressure is p_v=2,340 *Pa* and surface tension is σ_s=0.0717 *N/m*. Finally, the non-condensable gas was defined as γ_g= 15 *ppm*.

3.1 Numerical analysis of the cavitating flow through venturi type duct

This section presents the calibration of numerical code and the validation of obtained results for a cavitating flow in a venturi duct with convergence and divergence angles of 18° and 8°, respectively, see Fig. 2(a). The experimental study on this geometry was conducted by (Stutz & Reboud, 2000), who used double optical probes to measure the vapour fraction and the velocity. They have observed that the cavitating flow has an unsteady behaviour with cyclic fluctuations caused by the detachment of the cavitation.

Fig. 2(b) shows the computational grid, which is a structured mesh of 400 X 100 cells. A special refinement was used near the venturi throat and the lower wall, where it is assumed that cavitation will occur.

All simulations were carried out for a constant flow rate, the inlet velocity was fixed to u_1=*7.9 m/s*. The pressure outlet, p_2, was varied to have different cavitation conditions.

Two turbulence models were tested: first, the RNG κ–ε model, and then, the RNG κ–ε modified model. In both cases, the near-wall regions were treated by the wall function method.

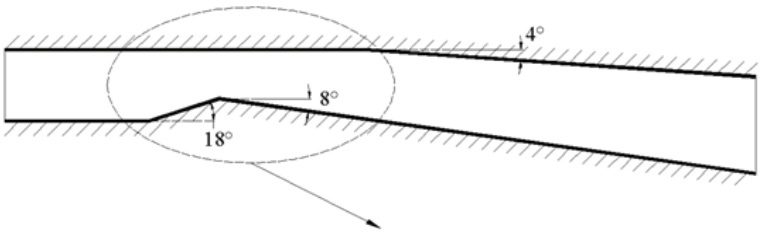

(a)

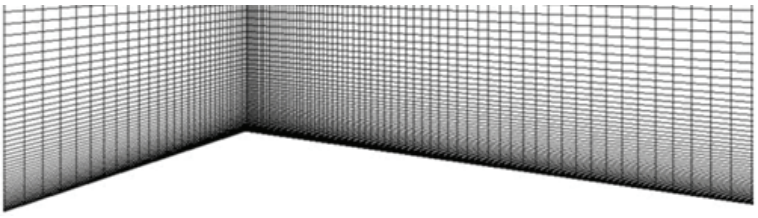

(b)

Fig. 2. Venturi type duct: (a) Computational domain, and (b) Grid distribution near venturi throat

3.1.1 Numerical results

The cavitating flow in the venturi type duct was characterized using the pressure coefficient, C_p, the cavitation number, σ, and the Strouhal number, St, defined as:

$$C_p = \frac{p - p_{ref}}{1/2 \cdot \rho_l \cdot v_1^2}, \quad \sigma = \frac{p_1 - p_v}{1/2 \cdot \rho_l \cdot v_1^2} \quad and \quad St = \frac{f_{cav} \cdot \overline{l_{cav}}}{v_1} \tag{17}$$

where $\overline{l_{cav}}$ is the time average of l_{cav}.

Preliminary 2D computations suggest a strong interaction of the turbulence and the unsteady cavitation at the venturi throat.

3.1.1.1 RNG κ–ε turbulence model

The first unsteady simulations were carried out using the classical RNG $\kappa - \varepsilon$ model. These numerical results did not reproduce the well-known instabilities of this configuration. The results show, after an unsteady numerical behaviour, a steady cavitation with l_{cav} constant for all the times. This cavity remains attached on the lower wall downstream of the venturi throat. This vapour region grows when σ is reduced, but it remains stable.

The cavitation detachment could not be modelled appropriately. The reason is that RNG $\kappa - \varepsilon$ model overestimates the turbulent viscosity in the cavitation region. Hence, the re-entrant jet is stopped at cavitation sheet closure and then, it could not incite the cavitation break off.

The RNG $\kappa - \varepsilon$ model was originally conceived to fully incompressible fluids, and no particular correction was applied in the case of the highly compressible two-phase mixture. Therefore, the fluid compressibility is only taken into account in the turbulence equations through the mixture density changes (Wilcox, 1998).

3.1.1.2 RNG κ–ε modified turbulence model

On the other hand, other calculations were performed using the RNG $\kappa - \varepsilon$ modified model. The results show an unstable flow due to the vapour detachment, as it was observed experimentally. The modification of turbulent viscosity allows the detachment of the cavitation caused by a re-entrant jet, which appears on the lower divergent wall. The re-entrant jet goes from cavitation sheet closure toward the venturi throat in the opposite direction to the main flow, which lets the detachment of the cavitation from the wall, see Fig. 3. Thus, the cavitation can be convected in the main flow, where it will be collapsed downstream.

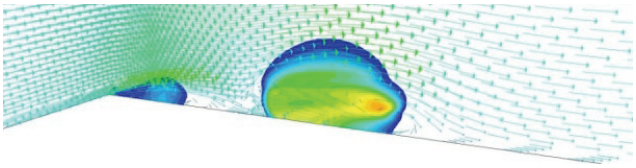

Fig. 3. Contours of vapour fraction ($\alpha \geq 10\%$) and velocity vectors near to venturi throat at $t=0.273 \cdot t_{ref}$ and $\sigma=2.45$. Calculations using RNG $\kappa - \varepsilon$ modified model

The cavitation detachment cycles can be observed, for σ values of 2.45, 2.34, and 2.30, in Fig. 4. This figure shows that the cavitation length, l_{cav}, increases while the cavitation number, σ, and the detachment frequency, f_{cav}, decrease. Generally, the cavitation detachment cycle is composed of the following steps, see the cycle of σ=2.45 in Fig. 4:

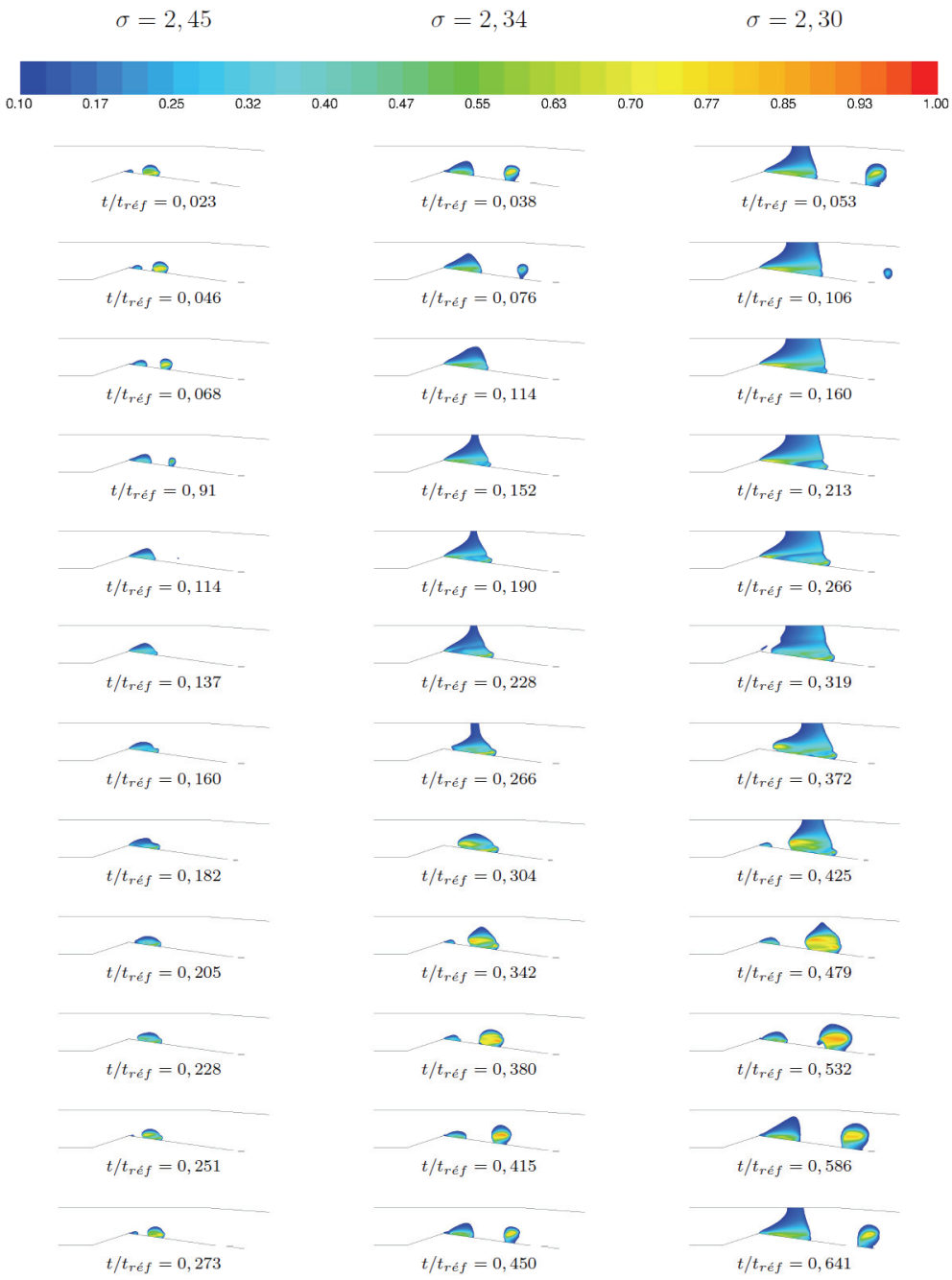

Fig. 4. Contours of vapour volume fraction (a≥10%). Vapour detachment cycle calculated for three cavitation numbers. Calculations using RNG κ–ε modified model, t_{ref}=*65.8E-3 s*

1. A very small vapour region appears at the venturi throat (from t=0.023·t_{ref} to t=0.046·t_{ref}).
2. The attached vapour region grows at the downstream venturi throat (from t=0.068·t_{ref} to t=0.137·t_{ref}).
3. A jet flow is generated along the lower wall in the vapour region and goes from cavitation closure towards the venturi throat. The interaction between this re-entrant jet and the interface liquid-vapour causes the detachment of the cavitation (from t=0.160·t_{ref} to t=0.228·t_{ref}).
4. The generated vapour region is convected in the main flow (from t=0.251·t_{ref} to t=0.273·t_{ref}) and (from t=0.023·t_{ref} to t=0.068·t_{ref}).
5. The cavitation collapses downstream (from t=0.091·t_{ref} to t=0.114·t_{ref}).

Fig. 5(a) shows the spectral analysis of the upstream static pressure behaviour (σ=2.45) which is disturbed by the cavitation detachment. The cavitating flow has a cyclic behaviour with a frequency of cavitation detachment of about f_{cav}=60 Hz. The numerical results were compared with the experimental data obtained for the same geometry. Although the vapour volume fraction obtained numerically is higher than the reference data, there is a good agreement if the vapour detachment frequencies are compared, see Fig. 4(b).

Table 2 summarizes the main characteristics of the vapour detachment cycles. According to the experimental data, the detachment frequencies are inversely proportional to the cavitation lengths, and so the Strouhal number remains constant for all the cavitation numbers, St=0.27. The cavitation length was measured at twelve instants of the cavitating period and so, the average value was obtained.

3.2 Numerical analysis of the unsteady cavitating flow in two blades cascades

This part presents the numerical study carried out on two blades cascades: first, on a two-blade aircraft inducer with a blade tip angle of 4°, and then, on a three-blade industrial inducer with a blade tip angle of 8°, see Fig. 1.

3.2.1 Geometrical model and grid generation

The numerical domain, for both cases, has been divided into three sub-domains in order to impose moving mesh conditions. Fig. 6(a) shows the three computational sub-domains of whole numerical model, defined as: upstream region (A), inter-blades region (B), and downstream region (C). Tangential velocity was imposed in the moving region (B) using a sliding mesh technique, whereas (A) and (C) regions were defined as static.

Boundary conditions at the domain inlet and outlet were imposed far enough (15·l), from the leading and trailing edges, respectively, in order to avoid influencing the final results. The used boundary conditions are the following:

a. Constant velocity at the inlet. The nominal flow corresponds to a null incidence angle.
b. Constant static pressure at the outlet. This value has been modified for to get diverse cavitation conditions.
c. Non-slip conditions at the blades boundaries.
d. Sliding conditions at the interfaces (A)–(B) and (B)–(C).
e. Cyclic conditions were applied at two or three successive blades, depending of the analyzed inducer.

By way of example, the Fig. 6(b) shows the computational grid of two-blade inducer. The mesh was generated with a rectangle–like structured grid. An independence grid study was

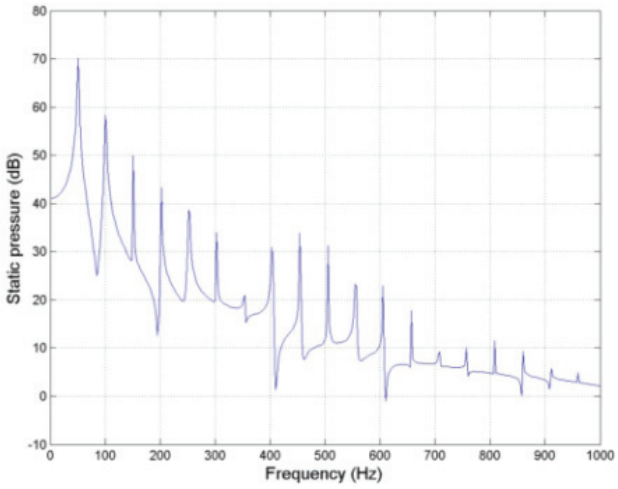

(a)

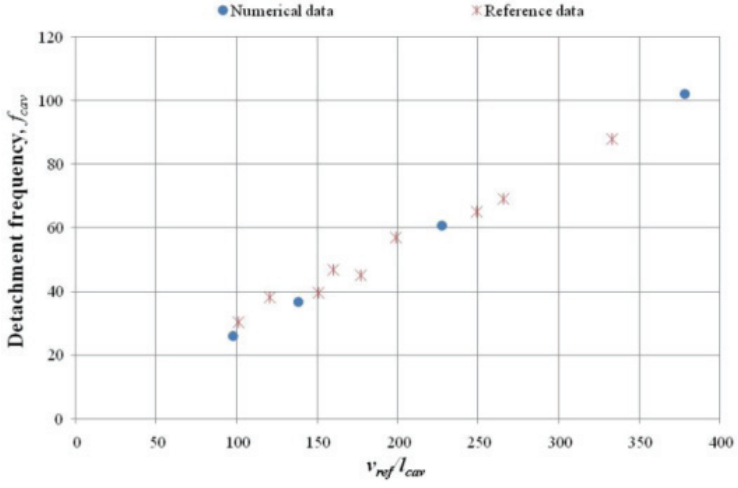

(b)

Fig. 5. (a) Spectral analysis of the upstream static pressure (σ=2.45). (b) Comparison of numerical results and experimental data (Stutz & Reboud, 2000)

σ	T_{cav} (s)	f_{cav} (Hz)	l_{cav}	St
2.61	*9.8e-3*	*102.0*	*20.90*	*0.27*
2.45	*16.5e-3*	*60.6*	*34.77*	*0.27*
2.34	*27.3e-3*	*36.6*	*57.20*	*0.27*
2.30	*38.6e-3*	*25.9*	*81.02*	*0.27*

Table 2. Characteristics of the cycles of vapour detachment

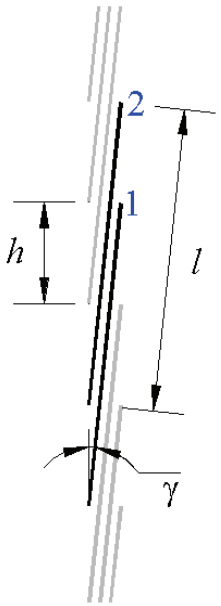

(a) Two-blade cascade

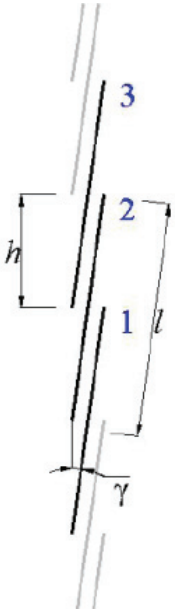

(b) Three-blade cascade

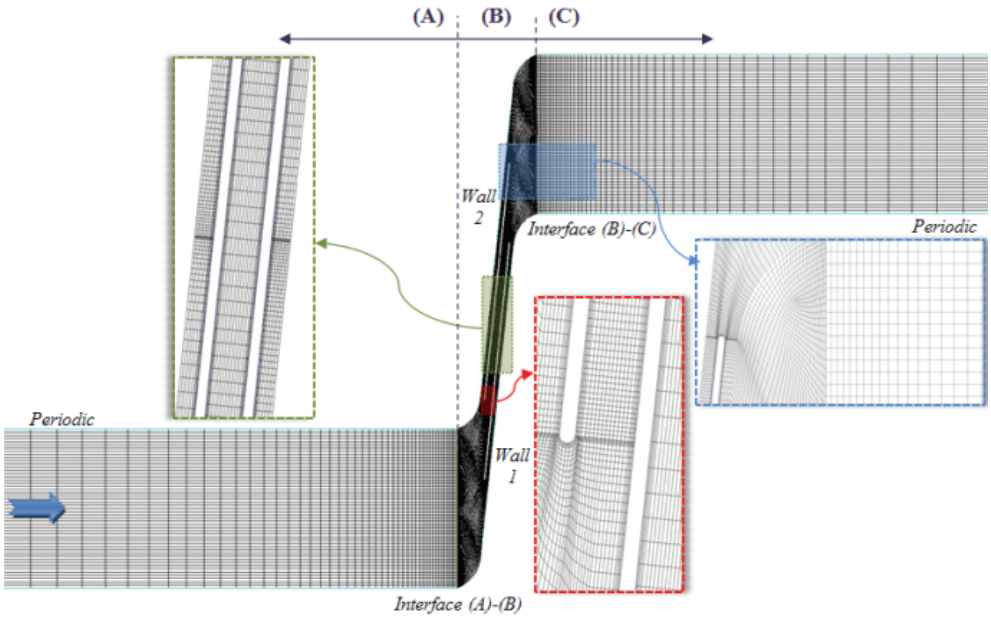

(c) Boundary condition and near-wall mesh resolution

Fig. 6. Blades cascades corresponding to the inducers studied, see Fig. 1

carried out on non-cavitating flow. Three meshes were tested: a coarse mesh (300X50), a fine mesh (500X50), and a refined mesh (650X50). The first coarse mesh presented the backflow at outlet domain because of very important aspect ratio upstream and downstream regions. The fine and refined meshes presented similar results, but the fine mesh reaches the solution faster than the refined mesh; for this reason, the fine mesh was selected for realize all calculations. Boundary layer meshing was used to ensure sufficient refinement near the walls and thus a small dimensionless factor y^+. First cell distance was imposed to 1 *mm*, with a growth rate of 1.2 which allowed values of y^+ between 6 and 51.

3.2.2 Numerical results

The unsteady cavitating flow was characterized by the cavitation number, σ, and the Strouhal number, *St*, defined in (17); and by the head coefficient, Ψ, and the flow coefficient, Φ, given by:

$$\Psi = \frac{P_2 - P_1}{1/2 \cdot \rho_l \cdot v_1^2} \quad and \quad \Phi = \frac{(C_a)_1}{C_t} \tag{18}$$

3.2.2.1 Stable blade cavitation

Calculations of unsteady cavitating flow were carried out for four flow rates over the blades cascade of a two–blade inducer and for three flow rates over the blades cascade of a three–blade inducer, see Fig. 7. En general, the results present two small regions of vapour, at high values of σ, on the leading edge of suction side. The regions of vapour are symmetric, for all the time and all the values of σ. The vapour region increases as σ decreases, until these regions of vapour become large enough to block the flow channel, resulting in the performance drop of inducer, see Fig. 7.

Fig. 8 presents, for Φ=*0.056*, the regions of vapour corresponding to diverse values of σ. This figure shows that the cavitation begins with very small regions of vapour which appear on the leading edge of the blade, on the suction side. The regions of vapour have a steady behaviour, for values of σ between σ=*0.723* and σ=*0.219*. This stable behaviour is characterized by a symmetrical cavitation attached to each blade. The cavitation length grows gradually as σ decreases. When σ decreases even more, the regions of vapour increase and it obstruct the flow channel. So, at σ=*0.219*, the cavitation length containing α≥*10%* of vapour takes, approximately, *50%* of the blade spacing, *h*. Consequently, the alternate blade cavitation appears when the cavitation number decreases to σ=*0.174* and this asymmetrical cavitation continue to σ=*0.140*. After that, for σ=*0.114*, the cavitation becomes symmetrical on both blades and large enough to produce the performances drop of inducer.

Alternate blade cavitation is a phenomenon in which the cavitation length on the blades changes alternately from blade to blade. According to (Tsujimoto, 2005) the alternate blade cavitation starts to develop when the cavitation length exceeds about *65%* of the blade spacing: $(l_{cav}/h) \geq 65\%$. So, the incidence angle to the neighbouring blade decreases and, hence the cavitation length on the neighbouring blade decreases also. Then the incidence angle of the original blade increases and the cavitation length on it also increases.

The cavitation behaviour for Φ=*0.042* presents the same patron of cavitation than for Φ=0.056; after a symmetrical blade cavitation, the alternate blade cavitation starts as soon as the l_{cav}/h ratio is higher than 65%, i.e. to σ=*0.156*.

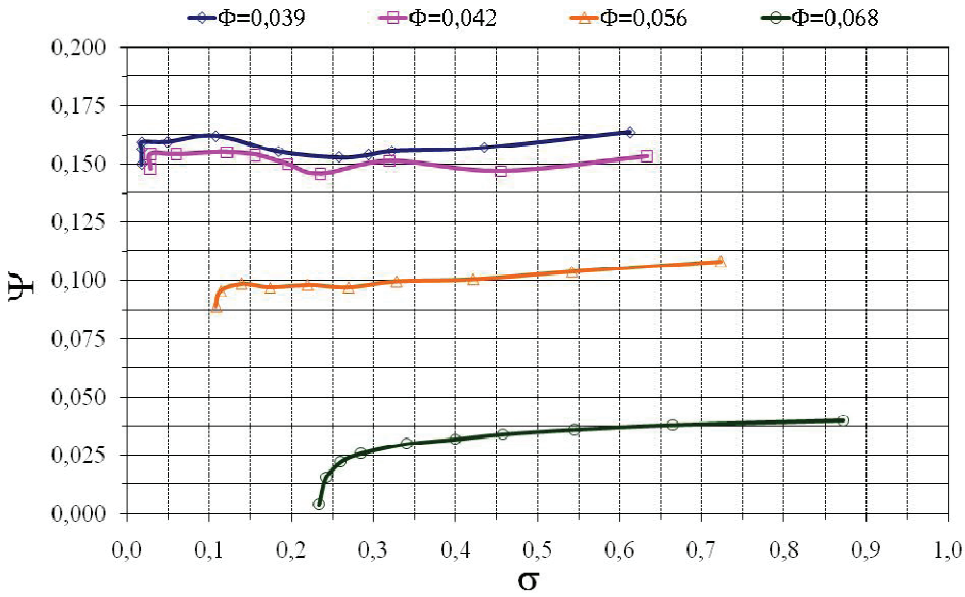

(a) Two-blade inducer

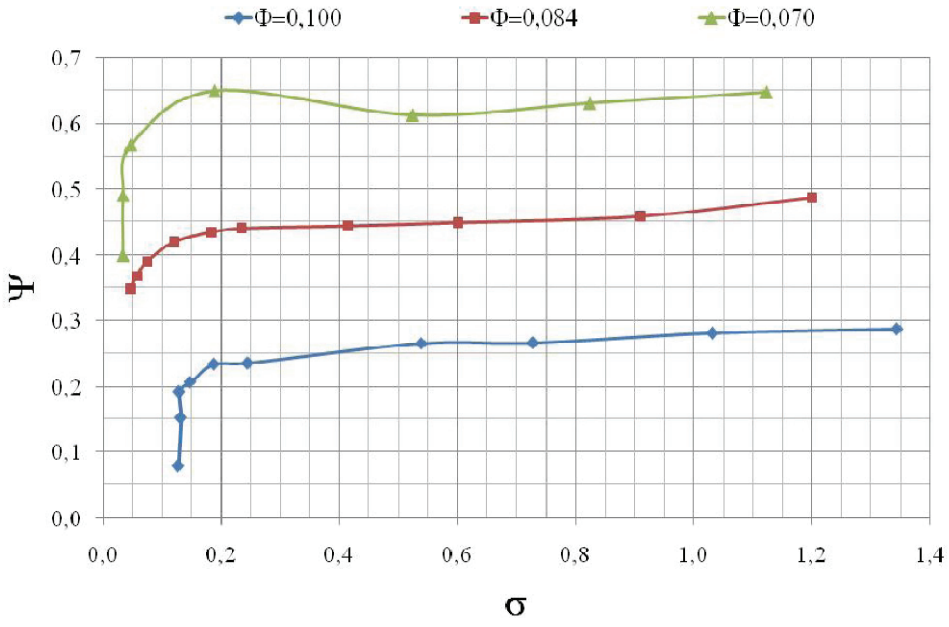

(b) Three-blade inducer

Fig. 7. Curves of the performance drop inducer

However, the alternate blade cavitation was not detected in the three-blade inducer, this agrees with experimental observations which have noted this instability only on inducers with pair blades number.

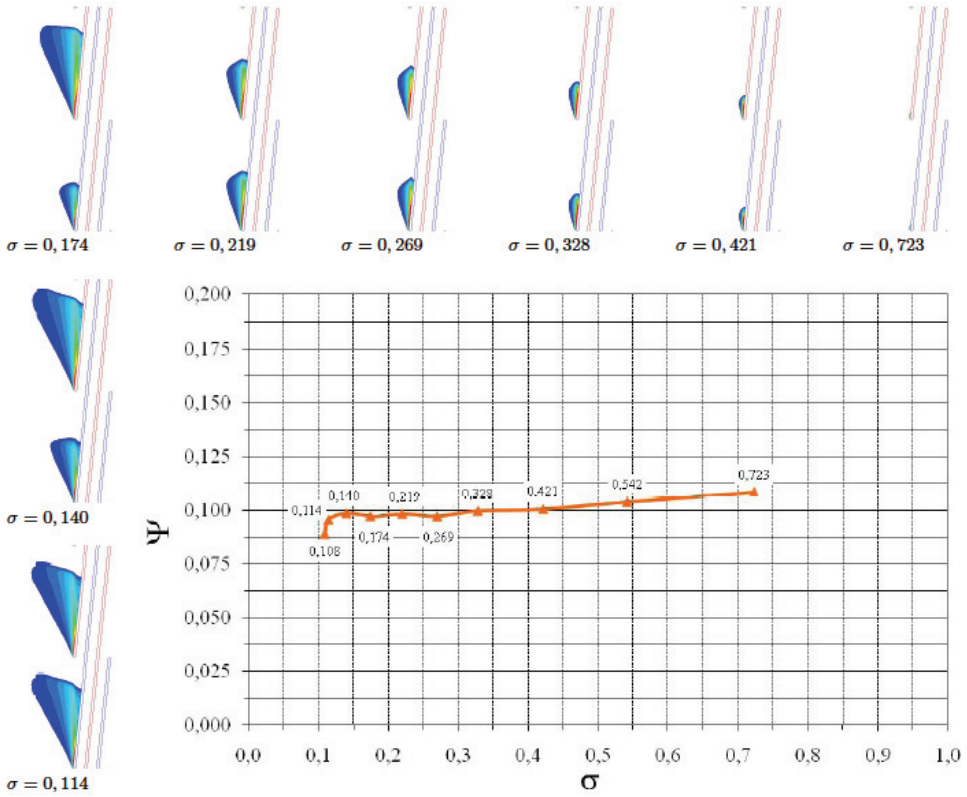

Fig. 8. Curve of the performance drop (Φ=*0.056*) and pictures of the regions of vapour (a≥*10%*) corresponding to diverse values of σ. Calculations using RNG κ–ε model

3.2.2.2 Unstable blade cavitation

The numerical results show the appearance of the rotating blade cavitation to a low flow rate (Φ=*0.039*). As it was observed for the flow rates analysed previously, the cavitation has diverse forms which vary as σ; e.g., for Φ=*0.039*, symmetrical cavitations were observed for high values of the cavitation number (σ≥*0.294*). However, as soon as the cavitation number was decreased to σ=*0.258*, the rotating blade cavitation was occurred. After that, the cavitation became symmetrical on both blades, for cavitation numbers lower than σ<*0.185*.
Fig. 9 shows the contours of vapour fraction (a=*10%* and σ=*0.258*) at different times, with the purpose of observing a cycle of the rotating blade cavitation, T_{cav}. In monitoring the evolution of the cavitation on blade **1**, it is observed that the cavitation length is the same on both blades at t=*0.5*·T_{cav} and t=*1.0*·T_{cav}. In the beginning of the cycle, the cavitation length on the blade **1**, $l_{cav\text{-}b1}$, decreases with the time. So, at t=*0.267*·T_{cav}, the size of $l_{cav\text{-}b1}$ is the smallest on the blade **1**, while the size of $l_{cav\text{-}b2}$ becomes the largest on the blade **2**. The cavitation

length on the blade **2** is inversed to the one on the blade **1**. So, $l_{cav\text{-}b2}$ decreases from $t=0.267 \cdot T_{cav}$ to $t=0.777 \cdot T_{cav}$, where $l_{cav\text{-}b2}$ is the smallest on the blade **2** and $l_{cav\text{-}b1}$ is the largest on blade **1**.

Blade cascade	Φ	σ	f_{cav}	f_{cav}/f_{ω}	T_{cav}
Two-blade	0.039	0.258	9.1 *Hz*	0.068	0.110 *s*
Three-blade	0.070	0.189	1 *Hz*	0.041	1.000 *s*
	0.084	0.184	1.59 *Hz*	0.066	0.630 *s*

Table 3. Comparison of frequencies of vapour detachment in the studied blades cascades

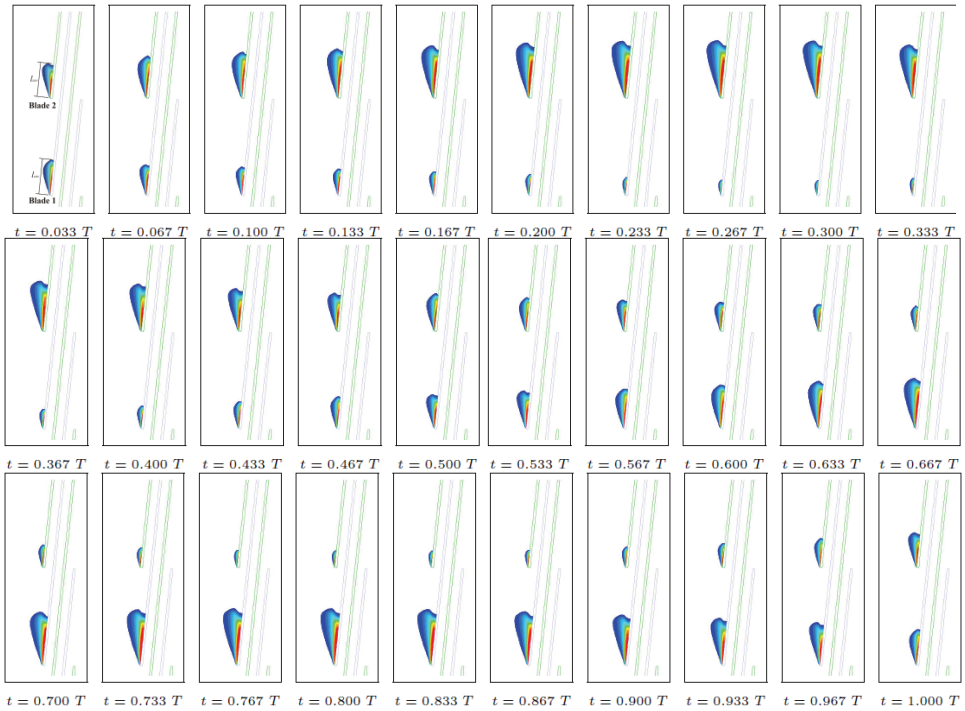

Fig. 9. Rotating blade cavitation on a two-blade inducer (σ=0.258 and Φ=0.039). Calculations using RNG κ-ε turbulence model

The vapour fluctuation has an unsteady cyclic behaviour, with a low frequency equal to $f_{cav}=0.07 \cdot f_{\omega}$ on one blade, see Fig. 10(a). The unsteady behaviour of the cavitation modifies the flow patterns which cause a pressure fluctuation upstream. The frequency analysis on the absolute frame gives a cavitating frequency of $f_{cav}=0.14 \cdot f_{\omega}$, because of the cavitation fluctuation on the two blades.

Fig. 10 shows the pressure coefficients measured on the two blades for the aircraft inducer and on the three blades for the industrial inducer. These ones were measured by virtual probes on the suction side of the blades inducers. These pressure fluctuations have been caused by the variation of the cavitation size attached to each blade. Rotating blade

cavitation was observed for two flow rate coefficients in the three-blade inducer. In these cases it was observed, at a certain time, two cavitations with the same size and another cavitation with a smaller size. This smaller cavitation moved in the same translational direction than the blade cascade, i.e. in the same rotational direction of the inducer; see Fig. 10(b). These cavitating fluctuations are cyclic with specific frequency. Table 3 resumes the frequencies of the rotating blade cavitation captured numerically for different flow rates and on different configurations.

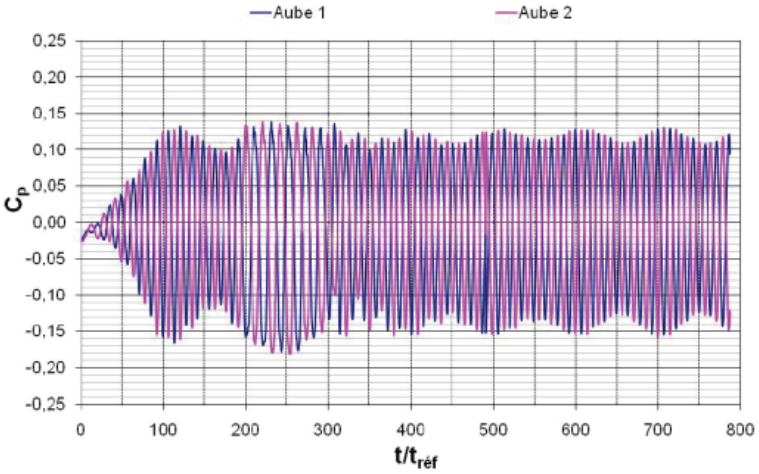

(a) Two-blade cascade

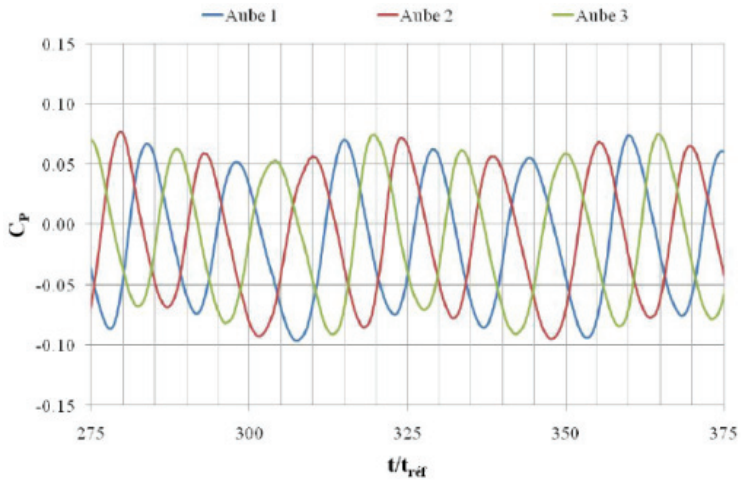

(b) Three blade cascade

Fig. 10. Pressure fluctuation on suction side of the blades caused by the variation of the length cavitation

3.2.2.3 Coupling of the intrinsic instabilities and the system instabilities

Numerical simulations were complemented using the RNG κ–ε modified turbulence model for $\sigma=0.258$ and $\Phi=0.039$. This modification allows the interaction between the system unsteadiness and the self–oscillation of the vapour region.

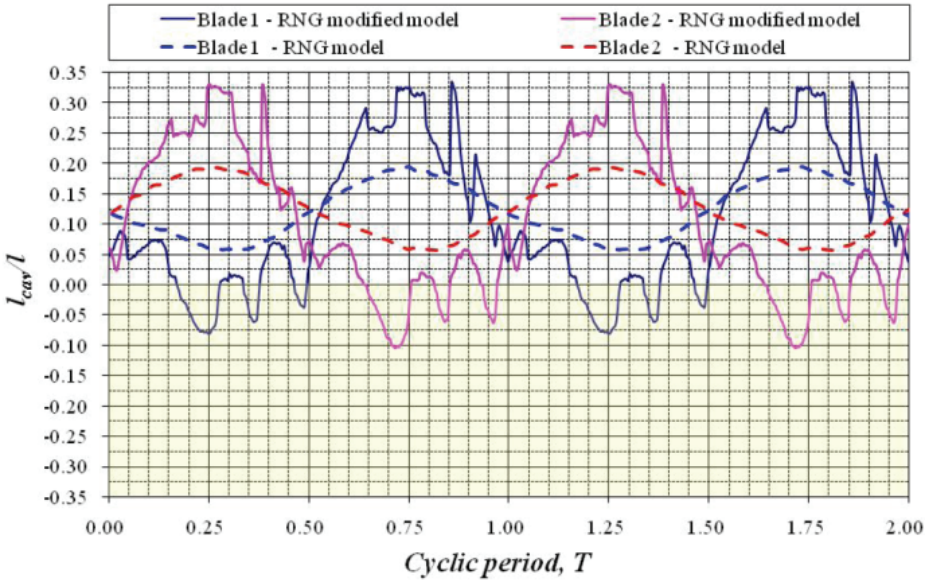

Fig. 11. Temporal evolution of the cavitation length. Calculations using RNG κ-ε and RNG κ-ε modified models

Fig. 12 presents the contours of vapour fraction at different times on a blades cascade. The cavitation shows a quasi–cyclical unsteady behaviour with a cavitation detachment frequency equal to $f_{cav}=0.06 \cdot f_{\omega}$ on relative frame and $f_{cav}=0.12 \cdot f_{\omega}$ on absolute frame.
The cavity has a similar cyclical unsteady behaviour than in the analysis using RNG κ–ε model, but now, the results show the vapour detachment ($t=0.833 \cdot T$ to $t=0.867 \cdot T_{cav}$, see Fig. 12, blade **1**), followed by its convection downstream ($t=0.900 \cdot T_{cav}$ to $t=0.933 \cdot T_{cav}$, see Fig. 12, blade **1**) and then, the cavitation passing from blade **1** to blade **2** at blades cascade throat ($t=0.967 \cdot T_{cav}$ to $t=1.0 \cdot T_{cav}$, see Fig. 12, blade **1** and blade **2**).
The curves of Fig. 11 show the temporal evolution of the cavitation length ($a \geq 10\%$) measured on each blade (e.g., $t=0.033 \cdot T_{cav}$ on Fig. 9), for both results calculations using RNG κ-ε and RNG κ-ε modified models. A negative cavitation length, for calculations using RNG κ-ε modified model, means that vapour region is attached to the pressure side of the neighbour blade. This phenomenon appears when the cavitation length of neighbour blade is large enough which produces the blockage of the channel flow. Thus, the fluid flow passes only through the other channel. All curves have a similar behaviour but the cavitation length is larger with the RNG κ–ε modified model than the RNG κ–ε model. The local length fluctuations observed on modified turbulence model are caused by the self–oscillation of the vapour region.

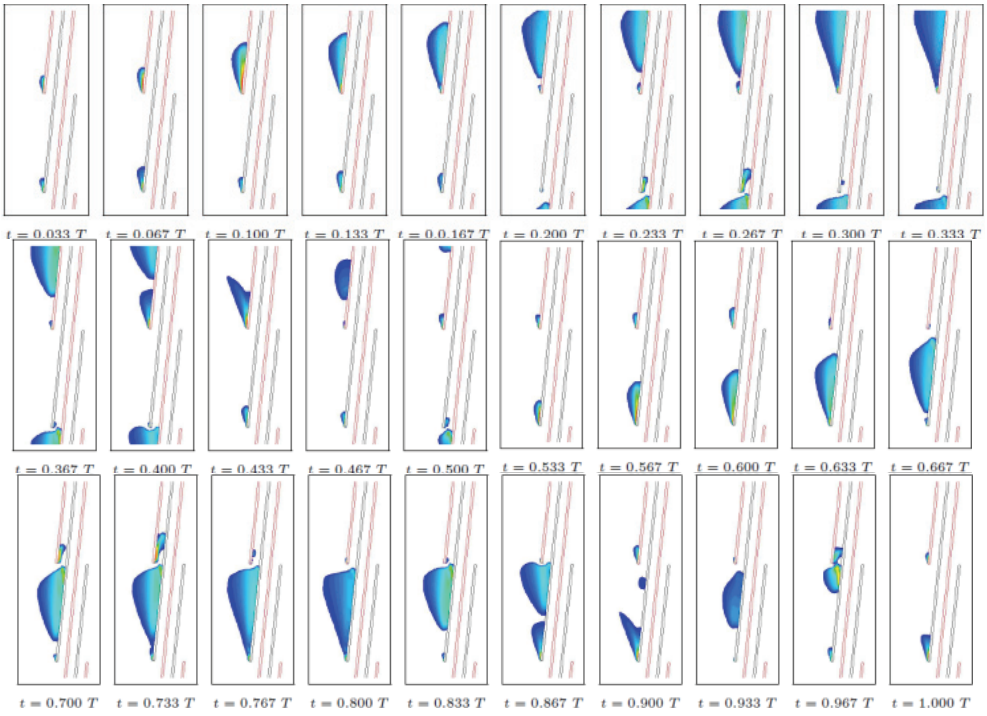

Fig. 12. Rotating blade cavitation on a two-blade inducer (σ=*0.258* and Φ=*0.039*). Calculations using RNG κ-ε modified turbulence model

3.3 Experimental study and numerical analysis of cavitating flows in three inducers

3.3.1 Experimental tests

Fig. 13. Bank of experimental tests from DynFluid laboratory (Arts et Métiers ParisTech), loop of the industrial inducers

The hydrodynamic bank used for the experimental tests consists of three independent closed loops. The first loop is adapted for test on the industrial inducers, see Fig. 13. The second loop is used for experimental tests of centrifugal pumps alone or coupled to an inducer. The third loop is adapted for aircraft-type inducers.

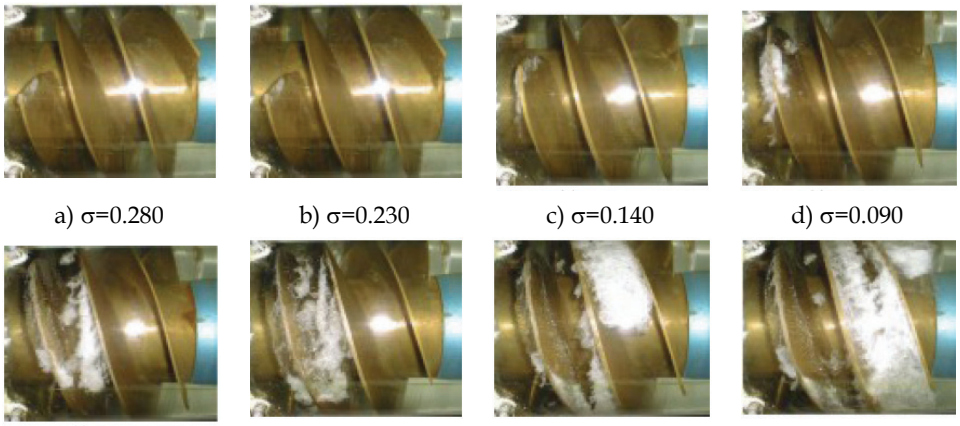

a) σ=0.280 b) σ=0.230 c) σ=0.140 d) σ=0.090

e) σ=0.060 f) σ=0.055 g) σ=0.050 h) σ=0.045

Fig. 14. Diverse cavitation forms obtained experimentally on a three-blade inducer with β=16° (Φ=0.164)

The industrial inducers loop consists mainly of the follow elements:

- Two tanks with a capacity of *4* m^3, connected by pipes of diameter of *350 mm*.
- A vacuum pump adjusts the pressure at the free surface tank.
- A *22 kW* motor controls the rotational velocity. It is measured using a tachometer.
- A motorized valve is used to vary the fluid flow of the inducer.
- The inducer has a transparent casing allowing the observation of vapour structures (transparent cover).
- A temperature sensor. The average temperature during the tests was about *20* °C.

To capture the experimental structures of vapour through the transparent cover, it was used a digital camera under strobe lighting.

Fig. 14 shows the vapour formation at leading edge of a three blade inducer. The regions of vapour were mainly manifested in the form of three identical regions attached to each blade (σ=0.280). As the inlet pressure decreases, the cavitating structures suffer a growth phase, principally at tip leading edge of the blade (from σ=0.230 to σ=0.090), which move to down to the hub until they block the flow channel (σ=0.060 and σ=0.055). When the passage inter-blade is blocked by the vapour, the performance drop of the inducer occurs suddenly (σ=0.050 and σ=0.045). The gradual vapour apparition generates noise and vibrations. In this figure, each image corresponds to a value of σ for a flow rate constant.

The pictures obtained during the cavitation tests are typical cavitation forms and, in general, they are consistent with those reported by (Offtinger et al., 1996), see Fig. 14. Representative pictures were obtained from different experimental tests on the three studied inducers at partial flow rate, nominal flow rate and over-flow rate. As an example, some pictures obtained on a three-blade industrial inducer with blade tip angle of 16° are commented:

- The inception of the cavitation at leading edge of the tip blade, see Fig. 14(a-b).
- The formation of a tip tourbillon which captures the vapour, see Fig. 14(c).
- The cavitation grows in forms of vapour pockets which remain attached to the tip blade, see Fig. 14(d).

- The formation of a recirculation zone (backflow) which captures the vapour bubbles and becomes, with the low pressure, in the siege of a vapour region located on the leading edge of the tip blade. This cavitation tends to move in the opposite direction of the main flow, see Fig. 14(e-f).
- Blockage of the flow channel by the vapour which causes the performance drop of the inducer, see Fig. 14(g-h).

The formation of various type of cavitation is caused by the kinematics of the flow in the inducer. The numerical and experimental analyses suggest that the high velocity regions (favourable zone to cavitation inception) are localized to the inlet at partial flow rates, and toward the outlet at high flow rates.

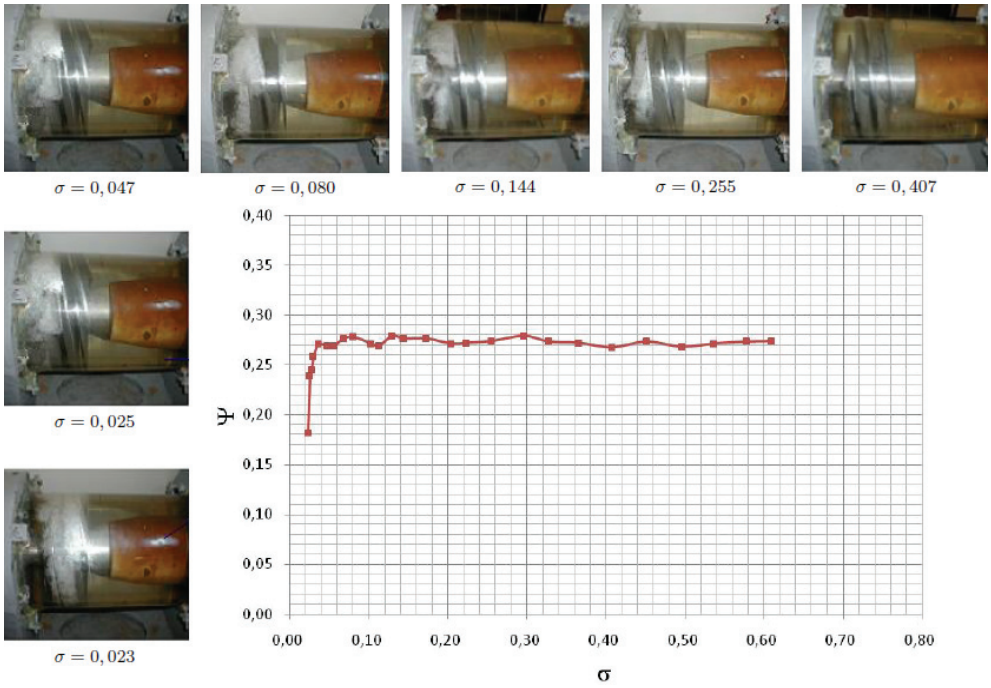

Fig. 15. Vapour behaviour for various cavitation conditions and its corresponding performance drop curve obtained experimentally on a three-blade inducer with β=8° (Φ=0.057)

3.3.2 Numerical analysis

3.3.2.1 Domain de control and grid generation

The numerical simulations, in steady and unsteady regime, were carried out on a two-blade aircraft inducer with a blade tip angle of 4°. In order of accelerate the calculation time, for the steady numerical simulations, only one third of the inducer was modelled. By contrast, this simplification could not be considered for the unsteady calculations because the instabilities of the cavitating flow are influencing by the neighbour blades (system instabilities).

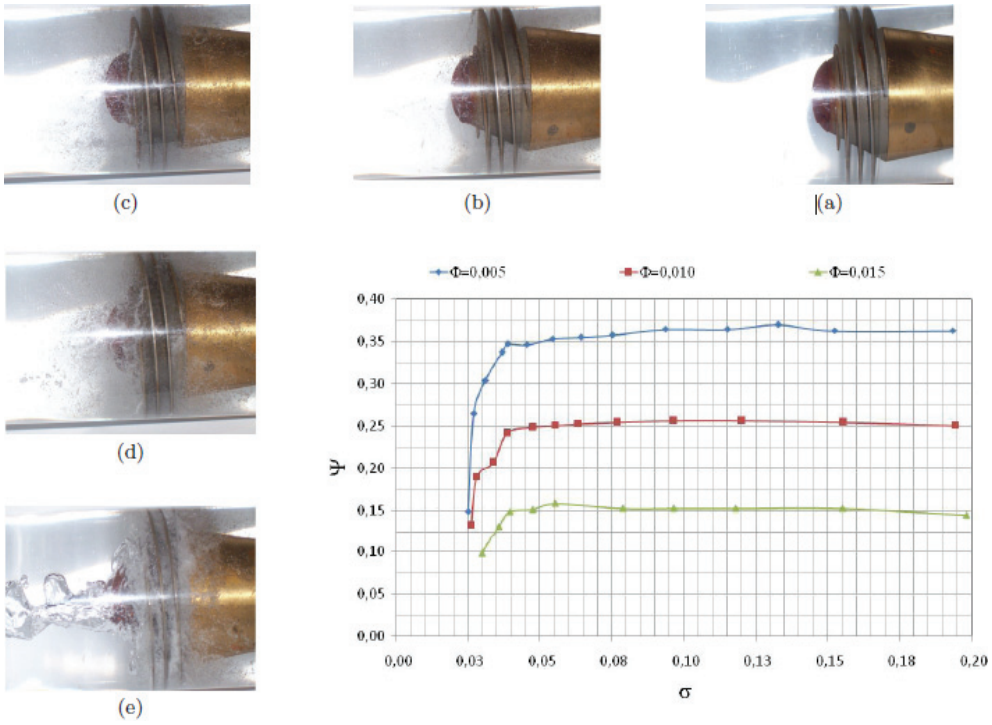

Fig. 16. Vapour behaviour for different cavitation conditions and its corresponding performance drop curve obtained experimentally on a two-blade inducer (Φ=*0.005*)

Many three-dimensional hybrid grids were generated using the pre-processor *Gambit*. The computational domain was divided into four sub–blocks in order to facilitate the grid generation. The sub–blocks are located as follow, see Fig. 17:

- **Inlet region**, lengthened *2.6* D_t upstream of the blade leading edge;
- **Blade to blade region**, which includes the flow channels formed by the blades;
- **Outlet region**, extended *2.4* D_t downstream of trailing edge; and
- **Tip clearance region**, modelled by a ring of thickness δ_t and an axial length l_{rotor}.

The grid process starts by meshing, with 2D triangular type cells, the blades surfaces. Then, the blade to blade region was meshed with 3D tetrahedral type cells. The tip clearance and blade to blade regions were meshed using smaller size cells than inlet and outlet regions, which were meshed with prism type cells, see Fig. 18. One conformal grid interfaces were used at the boundary of the regions "blade to blade – tip clearance". Two non–conformal grid interfaces were used at the boundary of the regions "upstream – blade to blade" and "blade to blade – downstream", see Fig. 17. Fig. 18 shows the surface grid on the rotor and the meridional view which is noticed the tip clearance grid.

For the grid independence study, four computational grids were tested. All these were generated with the same meshing strategy, but they are different in the cells number. The grid sizes are: (a) 480,185; (b) 1, 050,154; (c) 1,528,668; and (d) 1,996,418. The numerical results in steady state were compared to the experimental data. The first two grids show

variations on the numerical results because of a poor grid used. The last two grids give approximately the same than the experimental data but the grid (d) makes a lot of computational time to find the solution. For this reason, the grid (c) was selected for carried out the numerical results.

Finally, a grid dependence study to model the radial tip clearance was made. Fist, different grid types were tested, see Fig. 19. The first two grids were generated automatically on only one region which merges the blade to blade region and the tip clearance region. In this type of grids is very difficult to control the mesh near to wall, particularly the space formed between the tip blade and the carter, so the grid (d) on Fig. 19 was selected because it uses two blocks to defines the blade to blade and tip clearance regions and a conformal grid interfaces between both regions. Second, the grid density was varied from 5, 15, 25 and 30 equidistant cells in radial direction.

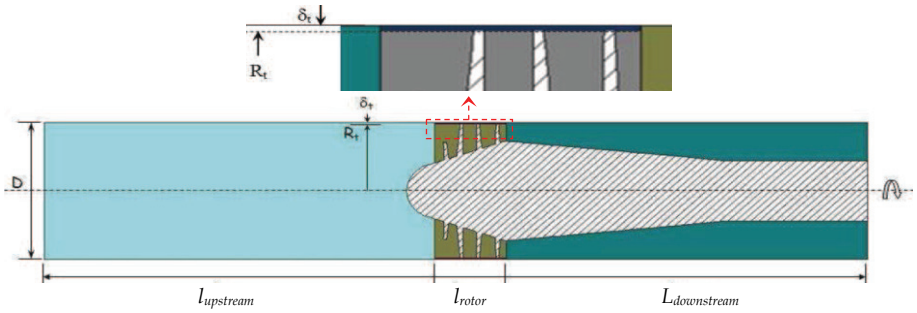

Fig. 17. Different blocks which form whole of the computational domain

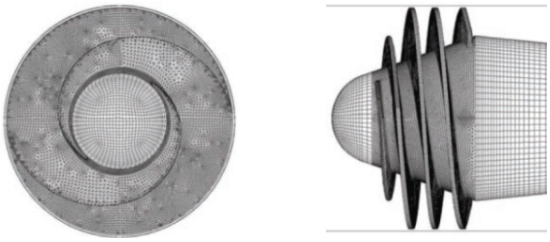

(a) Front view (b) Lateral view

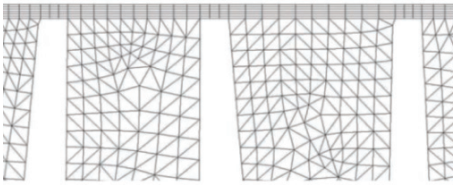

(c) Meridional view

Fig. 18. Computational grid used for the numerical simulations

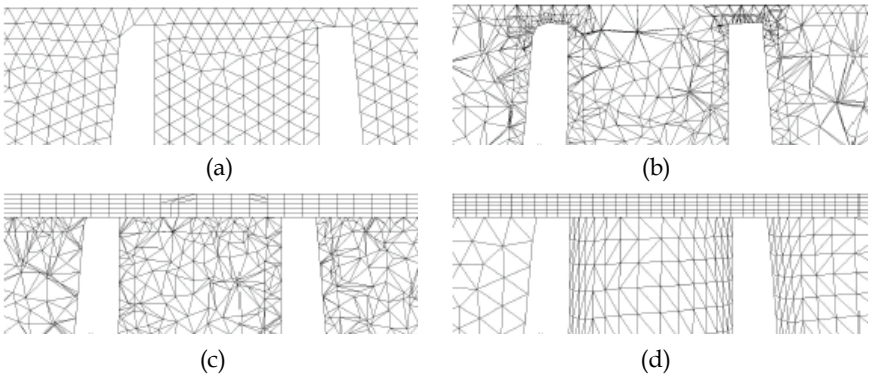

Fig. 19. Tip clearance grids tested

3.3.2.2 Numerical results in steady state

The numerical simulations in steady state were carried out for the three inducers presented on the Fig. 1. The cavitating calculations were realized on one flow channel of the inducers using periodical conditions for different flow rates (partial flow rates, nominal flow rates and over-flows), and for various cavitation conditions (σ). By way of example, the Fig. 20 shows the diverse cavitation forms which rise as the cavitation number decreases. It is

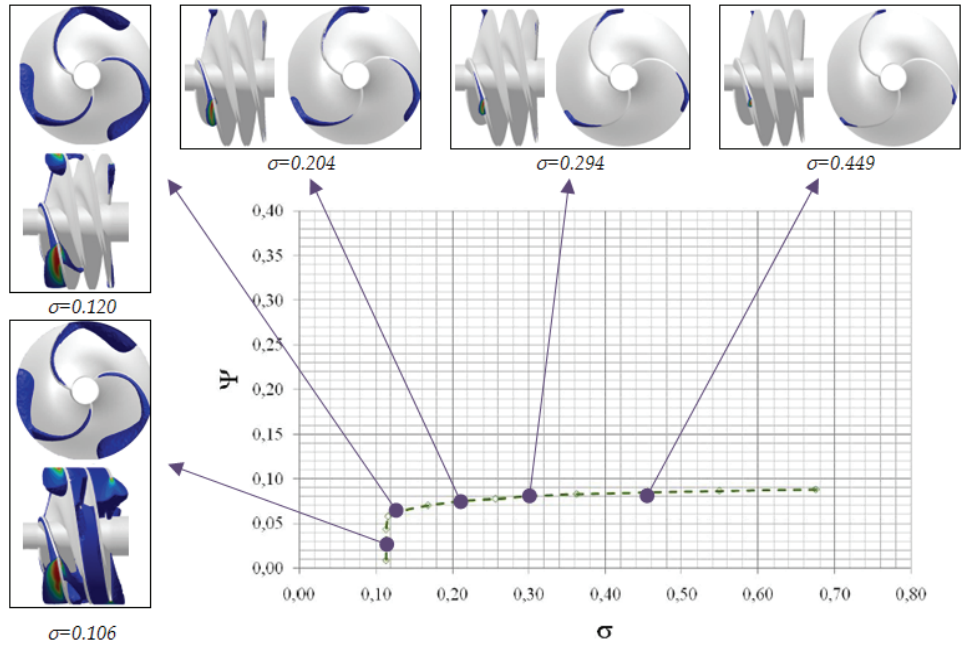

Fig. 20. Vapour behaviour for different cavitation conditions and its corresponding performance drop curve obtained numerically on a three-blade inducer with β=8° (a≥15 and Φ=0.112)

possible to observe that, as numerical as experimentally, at the inception of cavitation, the vapour appears in form of triangle at leading edge, and it is extended at tip blade as far as to cause the flow channel blockage.

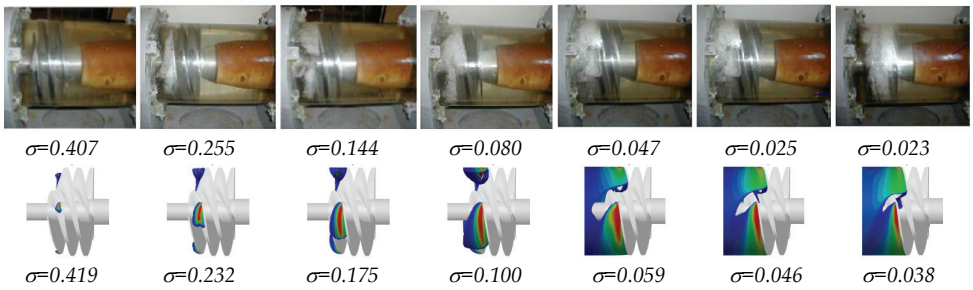

Fig. 21. Qualitative comparison of cavitation between experimental tests and numerical results on a three-blade inducer with β=8° (a≥15% and Φ=0.079)

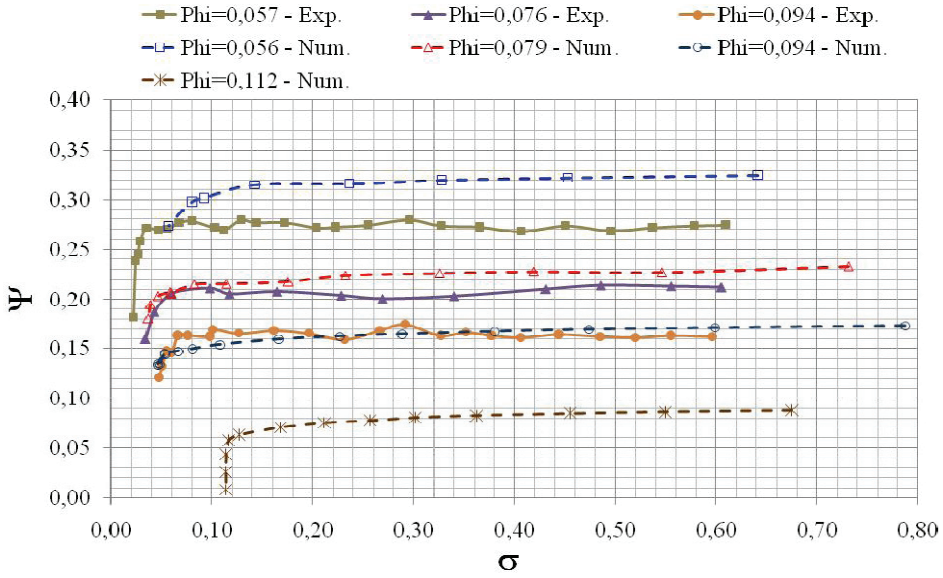

Fig. 22. Quantitative comparison of cavitation between experimental tests and numerical results on a three-blade inducer with β=8°

The numerical results obtained in steady state were compared as much qualitatively as qualitatively to the experimental tests. Fig. 21 shows a qualitative comparison of cavitation behaviour on a three-blade inducer with blade tip angle of 8°.

The cavitating analyse find a fluid flow more instable, during the numerical simulations and experimental tests, in the partial flow rates than in the over-flows. In the Fig. 20 is possible to note that, when the performance drop arrives, the flow channel is filled by the vapour for an over-flow (Φ=0.112) unlike a partial flow rate (Φ=0.079) in the Fig. 21. On the other hand,

the main difference found on the curves of the Fig. 22 was to the partial flow rate where the performance drop was predicted faster by the calculation than the experimental tests.
Fig. 22 shows a comparison of the performance drop curves obtained numerical and experimentally where is possible to observer a good coherence of the results. The differences found between numerical results and experimental data are, amongst others, attributing to that:

- The numerical simulations were carried out on only one flow channel using cyclical conditions; consequently, the fluid flow is perfectly identical on the three flow channels. This configuration does not consider the interaction between the flow channels.
- The numerical simulations suppose that the inducer has parfait geometry, without manufacturing defects and composed of identical blades.
- The experimental back elements located upstream and downstream were negligee.
- The numerical model does not consider the radial tip clearance.

3.3.2.3 Numerical results in unsteady state

The numerical simulations in unsteady state were carried out from the results obtained in steady state for a two-blade inducer with tip blade angle of 4° described in the Fig. 1. The calculations were realized to partial flow rates, where more instability problems were detected in the previous experimental and numerical cavitating analyse.

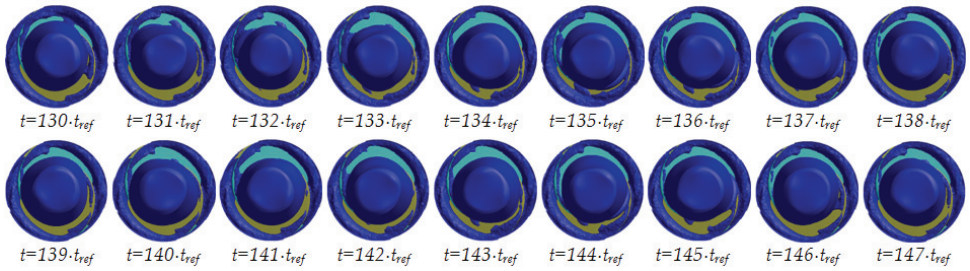

Fig. 23. Temporal evolution of the vapour (α=20%) in the two-blade inducer (Φ=0.0050 and σ=0.064), front view

The reference time was defined as the inducer rotating period, $t_{ref}=T_{\omega}=7.5E\text{-}3$ *s*. The time step, used for all numerical simulations, was calculated, after a temporal independence study, for an angular moving of 3.6°; then, the time step was defined as $\Delta t=t_{ref}/100=7.5E\text{-}5$ *s*.
It is important to underline that the unsteady calculations needed about 80 iterations by time step, resulting in 8,000 iterations by one inducer turn. The numerical stability was noted after 50 inducer turns, i.e. it was necessary at least 400,000 iterations to start to observe the instabilities caused by the cavitating flow in the inducer… if these ones exist at these flow conditions (Φ and σ). In considering that, the calculations were developed on an 8 processors cluster, with a calculation time of about 10 *s/iteration*, the unsteady calculations can take more than two months (time of machine) for a constant flow rate and a specific cavitation number. The very long calculating time, combined with the high capacity of storage, necessary for the post-processing stage, make very difficult to realize successfully the numerical calculations in unsteady state. Moreover, the analysis of the results requires a hard work to find the instabilities.

Knowingly the hard work needed to detect the instabilities by 3D numerical simulations; the results obtained to Φ=0.0050 and σ=0.064 are presented, in different views, on the Fig. 23, Fig. 24 and Fig. 25. The pictures were obtained when all flow parameters were stabilized (after $t=130 \cdot t_{ref}$). This figure shows the temporal evolution of the vapour ($\alpha \geq 20\%$) in the two-blade aircraft inducer with blade tip angle of 4°. Eighteen instants can be observed between $t=130 \cdot t_{ref}$ and $t=147 \cdot t_{ref}$, each picture corresponds to one inducer turn (t_{ref}).

These three figures show the cavitation has a crown form located at the periphery of the inducer. Another vapour region, with shape of the torch is located upstream, see Fig. 24 and Fig. 25. In certain instants, both cavitations, this one located at the periphery and the other one in form of torch, are connected by a narrow vapour region formed along the leading edge, from the tip blade to the inducer hub.

The cavitation develops gradually on the leading edge of the blade **2** (green blade), and it becomes bigger than on the blade **1** (blue blade) at $t=135 \cdot t_{ref}$. Later, the cavitation decreases gradually on the blade **2** until $t=140 \cdot t_{ref}$. In contrast, at this instant, the cavitation on the leading edge of the blade **1** is the biggest. Finally, the size cavitation increases again on the blade **2** and it decreases on the blade **1** at $t=144 \cdot t_{ref}$.

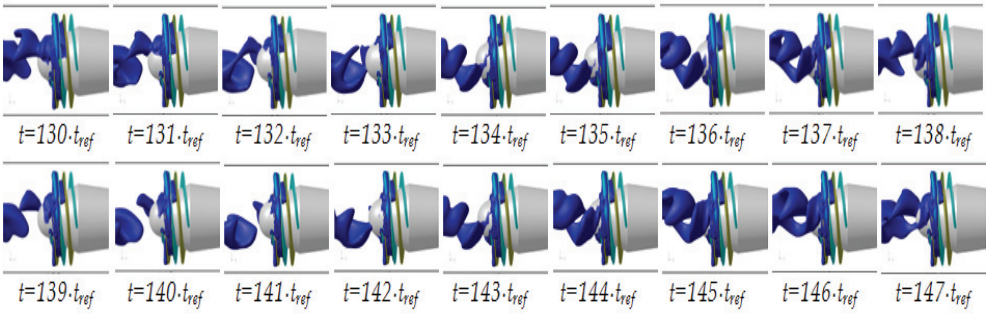

Fig. 24. Temporal evolution of the vapour ($\alpha=20\%$) in the two-blade inducer ($\Phi=0.0050$ and $\sigma=0.064$), lateral view

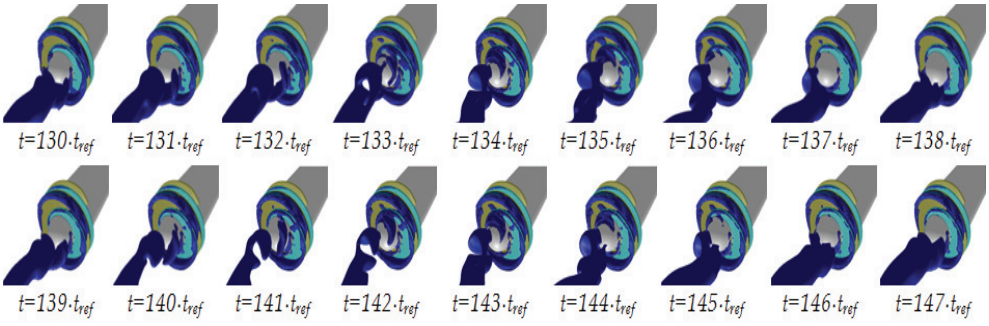

Fig. 25. Temporal evolution of the vapour ($\alpha=20\%$) in the two-blade inducer ($\Phi=0.0050$ and $\sigma=0.064$), isometric view

In conclusion, this fluctuation of cavitation size is almost cyclic, as observed previously in the analysis of the 2D unsteady cavitating flow. As can be seen in the figure, the cavitation length is maximal at the instants $t=135 \cdot t_{ref}$ and $t=144 \cdot t_{ref}$ on the blade **2** and at the instants $t=131 \cdot t_{ref}$ and $t=140 \cdot t_{ref}$, and $t=149 \cdot t_{ref}$ on the blade **1**.
The period of the cavitation fluctuation is $T_{cav}=0.0675\ s$ and its frequency $f_{cav}=14.8\ Hz$. The fluctuations can be driven by the cavitation torch formed upstream of the inducer. The torch turns in the same direction, but with a lower rotational velocity of the inducer. So, the torch turns 1 time while the inducer turns 9 times, as can be observed on the Fig. 23. The unsteady cavitating calculations were performed, in the first place, for $\sigma=0.064$. Then, from this unsteady results, the calculations were realized for $\sigma=0.051$, and then, for $\sigma=0.043$. This last calculation corresponds about *10%* of the inducer performance drop curve. In this case, one cavitation fluctuation occurs each 22 inducer turns. Thus, the cavitation fluctuation period is $T_{cav}=0.0600\ s$ and its frequency $f_{cav}=16.7\ Hz$, for $\sigma=0.043$.

4. Conclusion

Steady and unsteady numerical simulations were carried out in many configurations: first, in a venturi duct, next in two blades cascades with different characteristics, and then, in three axial inducers.
In order to understand the cavitation behaviour in the inducers and to validate the steady results obtained numerically, many experimental tests were developed, in steady state, for the three studied inducers.
In general, a good agreement between experimental and predicted results was found for a range of flow rates and cavitation behaviour, i.e., overall performances, cavities sizes and cavities location, etc. This study shows that the optimal inducer design depends mainly on three criterions to choose the best design for the three studied inducers: The critical cavitation coefficients corresponding to 5% and 15% of head drop, the head and efficiency produced in cavitating and non-cavitating conditions, and the vibrations generated by the inducers operations.
The numerical results, in a simple geometry, suggest a strong interaction of the turbulence and the unsteady cavitation.
Cavitating flow in the blades cascades, for various values of σ and flow rates, predicted three types of cavitation behaviour on the blades cascade:

a. Stable behaviour with symmetrical cavitation length,
b. Stable behaviour with non–symmetrical cavitation length, observed only for a two-blade inducer, according experimental observations (Tsujimoto, 2001)
c. Cyclical unstable behaviour with non–symmetrical cavitation length.

Symmetrical cavitations on all the blades were observed for high values of σ and high flow rates. Alternate blade cavitation was observed numerically for partial flow rates, when the *l/h* ratio was higher than about *65%*. This phenomenon was observed only on the two-blade inducer. Finally, the rotating cavitation was observed for lower flow rates, on both studied blades cascades. The calculations were carried out using RNG κ–ε model and RNG κ–ε modified model which provide different results.
Unsteady numerical results showed three different mechanisms of cavitation instabilities:

- Self–oscillation of the cavitation due to the interaction between the recirculation flow and the cavity surface (intrinsic instability).

- Rotating cavitation due to the interaction of one cavitation attached to a blade with the leading edge of the neighbouring blade (system instability).
- Coupling of the rotating cavitation and the self–oscillating of the cavitation (combination of intrinsic and system instabilities).

Finally, the unsteady cavitating calculations realized in three-dimensions for a two-blade inducer demonstrate the complexity to obtain and analyze the flow instabilities caused by the cavitation in these machines. The obtained results show that rotating cavitation appears for a partial flow rate, but it is less obvious in the inducer than in the blades cascade. It was noted that the shape and behaviour of cavitation is greatly disturbed by the tip radial clearance, which also modifies the torch which is formed upstream.

5. References

Bakir, F., Kouidri, S., Noguera, R. & Rey, R. (2003). *Experimental analysis of an axial inducer influence of the shape of the blade leading edge on the performances in cavitating regime*, Journal of Fluids Engineering, Transactions of the ASME, Vol. 125(2), pp. 293-301.

Campos-Amezcua, R., Khelladi, S., Bakir, F., Mazur-Czerwiec, Z., Sarraf, C., & Rey, R. (2010) *Numerical analysis of unsteady cavitating flow in an axial inducer*, Proceedings of the Institution of Mechanical Engineers, Part A: Journal of Power and Energy, Vol. 224(2), pp. 223-238.

Campos-Amezcua, R. (2009). *Analyse des écoulements cavitants stationnaires et instationnaires dans les turbomachines*, PhD thesis. Arts et Métiers ParisTech - Laboratoire d'Energétique et Mécanique des Fluides Interne, Paris, France.

Mejri, I., Bakir, F., Rey, R. & Belamri, T. (2006). *Comparison of computational results obtained from a homogeneous cavitation model with experimental investigations of three inducers*, Journal of Fluids Engineering, Transactions of the ASME, Vol. 128(6), pp. 1308-1323.

Kim, S.E., Mathur, S.R., Murthy, J.Y. & Chouhury, D. (1998). *A Reynolds–Average Navier–Stokes solver using unstructured mesh based finite–volume scheme,* 36th Aerospace Sciences Meeting and Exhibit, Reno, NV.

Offtinger, C. Henry, C. & Morel, R. (1996). *Instabilité de fonctionnement en débit partiel d'un inducteur fretté and comparaison avec le cas non fretté,* 3ème journée on cavitation, SHF. pp. 31–38. Grenoble, France.

Reboud, J., Stutz, B. & Coutier-Delgosha, O. (1998). *Two-phase flow structure of cavitation: Experiment and modelling of unsteady effects,* 3rd Int. Symp. Cavitation. April 7-10, Grenoble, France.

Singhal, A.K., Athavale, M.M., Li, H.Y. & Jiang, Y. (2002). *Mathematical basis and validation of the full cavitation model*, J. Fluids Eng. Vol. 124(3), pp. 617–624.

Stutz, B. & Reboud, J. L. (2000). *Measurements within unsteady cavitation,* Exp. in Fluids. Vol. 29, pp. 245–552.

Tsujimoto, Y., Horiguchi, H. & Qiao, X. (2005). *Backflow from inducer and its dynamics*, 5th Pumping Machinery Symp., June 19–23, Houston, Texas.

Tsujimoto, Y., Kamijo, K., & Brennen, C. (2001). *Unified treatment of flow instabilities of turbomachines,* J. propulsion and power. Vol. 17(3), pp. 636-643.

Yakhot, V. & Orszag, A.S. (1986). *Renormalization group analysis of turbulence–Basic theory,* J. Scientific Computing. Vol. 1(1), pp. 3–51.

Wilcox, D.C. (1998). *Turbulence Modeling for CFD*, DCW industries. La Canada, California.

9

Mass Transfer Within the Location Where Micro Electroplating Takes Place

Jing-Chie Lin[1], Ting-Kang Chang[2],
Jen-Horn Yang[2], Yean-Ren Hwang[3] and Chuan Li[4]
[1]*Institute of Materials Science and Engineering, National Central University,*
[2,3,4]*Department of Mechanical Engineering, National Central University,*
Taiwan

1. Introduction

Electroplating and electroforming are the two electrochemical processes extensively used in metal fabrication. Electroplating provides a thin metal film to bestow the surface with desired property such as abrasion and wear resistance, corrosion protection, lubricity and aesthetic qualities; electroforming leads to a deposition of metal skin onto a mandrel which is then removed and then the metal deposit was thickened to obtain precise fabrication of molds. Both the electrochemical processes are carried out in the bath where sufficient concentration of metal salt is supplied in presence of an electric field. The electrochemical kinetics is determined not only by the strength of electric field but also by the mass transport phenomenon of the electrochemical active ions. The electric field employed in the electroplating is relatively lower and the field distribution is homogeneous. In contrast, the electrical field exerted in electroforming seems to be much stronger and the field distribution becomes less homogeneous.

In 1995, a novel localized electrochemical deposition (LECD) process was pioneered by Hunter [1] to fabricate three-dimensional (3D) metal microstructures. The LECD brings the electrochemical process to a new era. However, in the LECD process, the electrical field exerted at the electroplating site is super high and the distribution of field strength is ultra heterogeneous. The phenomenon of mass transport in such a strong field distributed in extremely heterogeneous is the case which we have never encountered in doing usual electrodeposition. In the process of micro electroplating, the site where LECD taking place was experimentally controlled to along the track guided with a microanode. Accordingly, the micro metallic features could be fabricated electrochemically along the motional track guided by the microanode [2]. Due to this fact, LECD was also named as microanode guided electroplating (MAGE) process. The schematic diagram of MAGE is shown in Fig. 1.

A platinum wire (diameter in the range from 25 to 125 μm) was fixed coaxially, and cold mounted with epoxy resin in polymethylmethacrylate (PMMA) tube (inner and outer diameters are 3 and 5 mm, respectively) to expose a disk (25 ~ 125 μm in diameter) acting as the microanode. The micranode was driven to move by a stepping motor in an electroplating bath thus guiding the micro electroplating way according to the program built in the micro-CPU. The micoanode assembly and microanode was driven to move by a

stepping motor under precise control, as shown in Fig. 1. In Fig. 1, the cathode was placed horizontally in the electrolytic cell (F) and connected with the negative pole of the dc power supply (V). The microanode assembly (H), connected with the positive pole of the power supply (V), was vertically fixed on a one-dimensional moving table. A servo micro-stepping motor (M) was used to drive the table through a micro-CPU (C) via the D/A converter (D) and driver (E). A relay (G) was connected with the anode assembly. Through control with dedicated software, the microanode was moved vertically with a resolution of 20 nm per step. Prior to electroplating, intimate contact between the microanode and the cathode was assured through a measurement of null electrical resistance. The microanode was then lifted from the cathode to a variety of gaps (in the range from 1 to 100 μm) to start the MAGE. In this study, a variety of dc-voltage biases (in the range from 3 to 6 V) were employed to conduct MAGE and their corresponding current was monitored with the current sensor (A).

So far we have publish a few papers [2-11] to discuss the electrochemical kinetics with respect to MAGE process. The heterogeneous distribution of very intensive electric field in local sites was determined significantly by experimental parameters such as motion modes of the microanode, applied electric voltage, initial gap between the cathode and microanode, and etc. In the present work, we concentrate ourselves on mass balance of electrochemical active ions those which supplied via mass transport from the bulk solution and to be consumed to turn into metallic micro feature. In terms of various models, we applied the commercial software ANSYS 8.0 to simulate the systems so as to understand the electrochemical mechanism of the MAGE process.

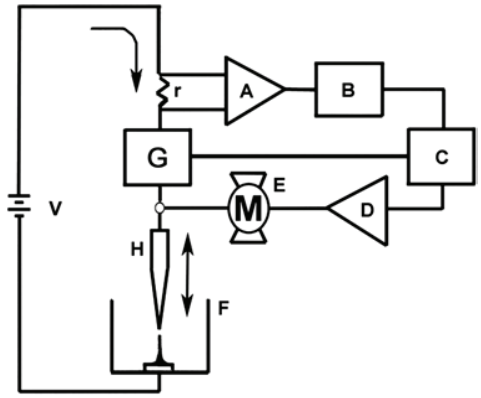

Fig. 1. Schematic diagram of the microanode-guide electroplating system in which the capital letters denote the following. (A) Current sensor, (B) A/D converter, (C) micro-CPU, (D) D/A converter, (E) driver, (F) cell, (G) relay, (H) anode,(M) micro-stepping motor and (V) voltage source

2. Surface morphology of micrometer columns influenced by motion modes of the micro anode

At first, the morphology of micrometer columns fabricated in nickel sulfate bath by MAGE was of concern interest. Optical microscopy (OM) and scanning electron microscopy (SEM,

S3500, Hitachi Co.) were employed to observe their surface morphology. Figure 2 depicts the OM of the micro columns fabricated under certain conditions with different motion modes of the micro anode. As the micro anode was driven to ascend continuously at a constant rate of 1.8 μm s^{-1} to perform MAGE at 5.0 V, a column appearing in dendrite was formed (Fig. 2(a)). In contrast, if the micro anode was driven to ascend intermittently (with an initial gap of 10 μm within each intermittent cycle) at the same voltage (i.e., 5.0 V) until reaching certain heights, a column revealing periodical nodes (Fig. 2(b)) was established. Comparing with both the columns, we found that they showed a similar diameter (roughly 50 μm), the dendrite tended to decrease the diameter with increasing its height, as shown in Fig. 2(a); however, the nodal one, depicted in Fig. 2(b), tended to vary the diameter periodically with the height. If we conducted the intermittent MAGE under a lower bias (i.e., at 3.5 V), we obtain a micrometer nickel column in uniform diameter (50 μm) with smooth morphology (as shown in Fig. 2(c)).

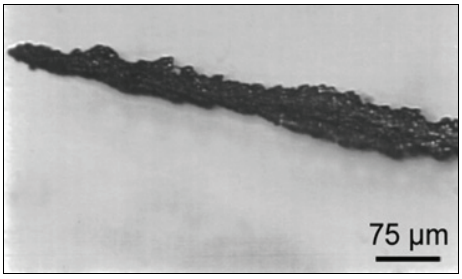

(a)

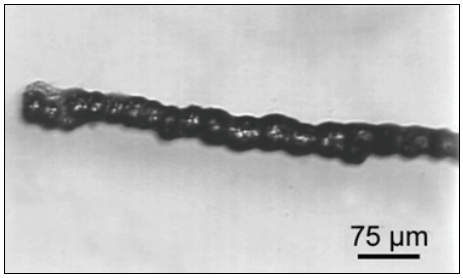

(b)

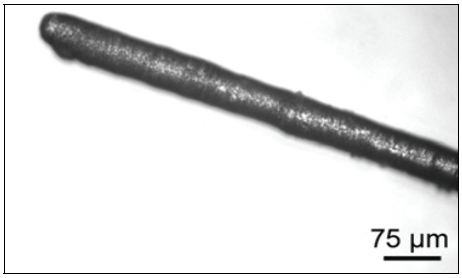

(c)

Fig. 2. Optical micrographs (OM) of the nickel micrometer columns fabricated by the MAGE process in a sulfate bath where the initial gap between the electrodes was the same (at 10 μm) but their dc-voltage bias and the motion mode of the microanode changed as follows: (a) bias at 5.0 V and the microanode moved continuously at a rate of 1.8 μm s^{-1}, (b) bias at 5.0 V and the microanode moved intermittently and (c) bias at 3.5 V and the microanode moved intermittently

Figure 3(a) exhibits SEM morphologies of a nickel column consisting of two segments due to change of voltages in the intermittent MAGE. With respect to fabricating the lower segment (i.e., 3(b) in Fig. 3(a)), we conducted MAGE at 3.2 V until reaching a height of 500 μm. Then we switched the voltage to 4.0 V to continue the MAGE process to grow the upper segment

(i.e., 3(c) in Fig. 3(a)) up to 1000 μm. In higher magnification, we are able to distinguish between Fig. 3(b) and (c). The upper segment is covered by greater (65 μm in diameter) nodular particles but the lower one is covered by finer particles (44 μm in diameter). The deviation of particle sizes is higher for the upper (±3.5 μm) than the lower (±0.5 μm).

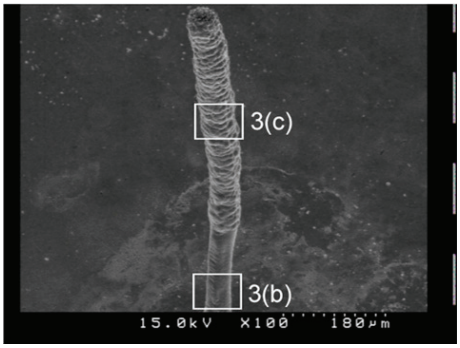

(a)

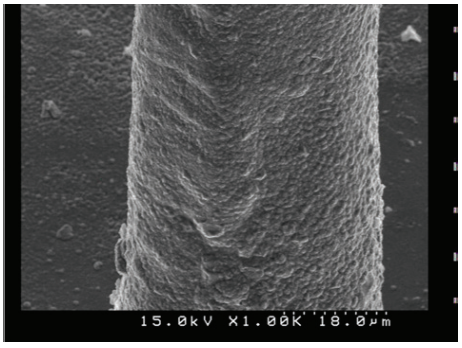

(b)

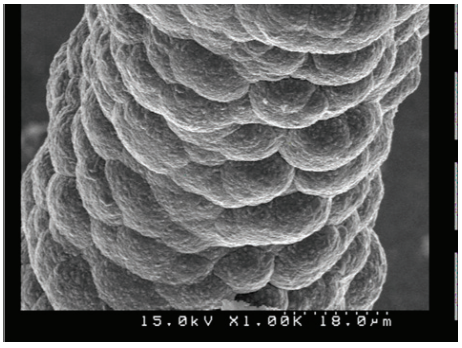

(c)

Fig. 3. (a) SEM morphology of the nickel microcolumn resulted from intermittent MAGE under two different biases in a sulfate bath where the microanode was kept at a separation of 10 μm from the cathode to start electroplating in each step. The microcolumn was deposited at a bias of 3.2 V on the copper surface to a height of 500 μm, then the bias was switched to 4.0 V to continue the deposition from 500 to 1000 μm. (b) Magnified morphology of the lower portion (formed at a bias of 3.2 V) and (c) Magnified morphology of the upper portion (formed at a bias of 4.0 V) for the micrometer nickel column

3. Current measured in the continuous MAGE

Figure 4 exhibits the variation of electroplating current against time in MAGE process where the microanode was ascended continuously at a constant rate of 2.0 μm s^{-1}. In Fig. 4, we found that continuous MAGE could only possibly be performed in the voltage range from 3.0 to 5.0 V. Otherwise, as the continuous MAGE is conducted at voltages less than 2 V, the current responsible for growing the column is too tiny (in a range from 325 to 25 μA) to be

used in practice. To the contrary, as the continuous MAGE is performed at voltages higher than 6.0 V, the current rose rapidly (in 18 s) to reach a critical value (i.e., 20mA), then the circuit is shut off on the purpose to protect the apparatus. As shown in Fig. 4, the current rises fast and it fluctuates profoundly with the continuous MAGE conducted at higher voltages (e.g., 4 and 5 V) than at lower voltages (e.g., 3 V). Higher current may result from abundant reduction of nickel ions and hydrogen ions; current fluctuation especially happened at higher voltages is ascribed to gas –bubbling (evolution of oxygen and hydrogen gas) from both electrodes.

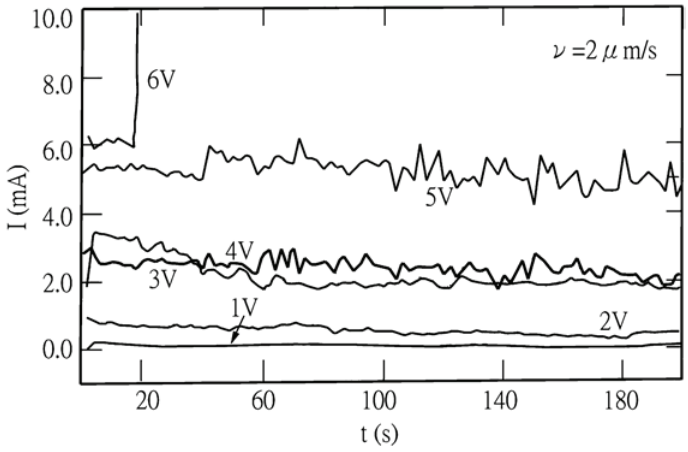

Fig. 4. A plot of current against the electroplating time for the MAGE process conducted at various biases and the microanode moved continuously at a constant rate (e.g., 2.0 μm s^{-1}). The initial gap between the microanode and the Cu-substrate was 20 μm

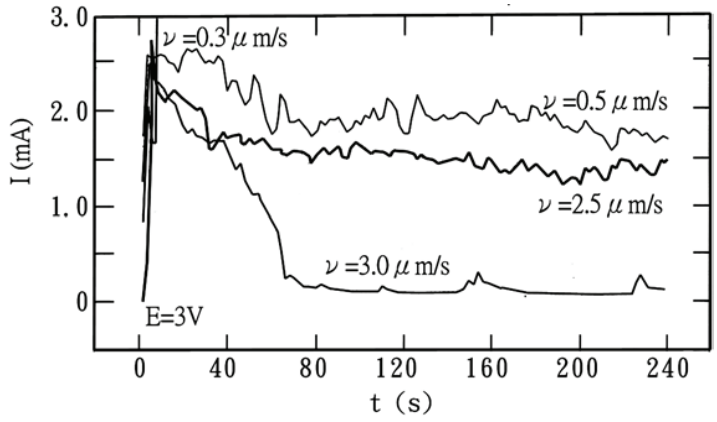

Fig. 5. Current against the electroplating time in the process of continuous MAGE at a bias of 3.0 V with the motion rate of the microanode varying in the range from 0.3 to 3.0 μm s^{-1}. The initial gap between the microanode and the Cu-substrate was 20 μm

Another plot is given in Fig. 5 to show the current variation against time for MAGE conducted at 3.0 V by controlling the microanode to ascend continuously at a variety of rates from 0.3 to 3.0 μm s^{-1}. In Fig. 5, on the curve responsible for continuous MAGE with ascending rate at 3.0 μm s^{-1}, the current rises abruptly to 2.5 mA, drops to 0.25 mA in 60 s and levels off subsequently. This implies that the nickel column grows very fast in the initial period (less than 60 s) but the growth rate in the subsequent stages decays to very slow. Even the duration of this process lasted for 240 s, the column grew rapidly to a height of 25.1 μm almost within the initial 60 s. In contrast to the case where the microanode ascended continuously at 0.3μm s^{-1}, the current led to a sudden rise in 10 s. The growth rate of the column is much faster than the ascending rate of the microanode. As a result, the column grows so swiftly that facilitates its top to contact the microanode. This short-circuit contact may ruin the apparatus. Therefore, on purpose to protect the apparatus, we designed an automatic switch into the system. Once the current exceeding 20 mA the power of the system is shut off. According to Fig. 5, the ascending rate of the microanode is better controlled in the range from 0.5 to 2.0 μm s^{-1} to ensure longer duration for column growth.

4. Current measured in the intermittent MAGE

Figure 6 demonstrates the current variation with time for the intermittent MAGE conducted at 3.2 and 4.2 V, respectively. The initiate gap between the electrodes was set at 10 μm in each intermittent cycle. Two different time-intervals are concerned: within the initial 20 s, the current profile is displayed in Fig. 6(a); at the final stage to grow a column up to 500 μm, the current profile is shown in Fig. 6 (b). The current exhibits different profiles in Fig. 6(a) depending upon the voltages employed. The current level responsible for on-time intermittent MAGE conducting at 4.2 V is higher than that conducting at 3.2 V (i.e., −3.70 ± 0.19 mA as compared to −2.26 ± 0.07 mA); however, the time period at 4.2 V is shorter than that at 3.2 V (i.e., 0.24–0.95 s against 6.19–8.81 s). Greater current variation is also found at 4.2 V than 3.2 V.

Analysis of the current profile in the initial 20 s indicates that intermittent MAGE conducted at 4.2 V almost completing 10 cycles (each cycle including one on-time half cycle and off-time half cycle) but that conducted at 3.2 V only accomplishing 2.3 cycles. Total height of the micrometer column could be estimated from multiplication of the intermittent gap (i.e., 10 μm per cycle) with the number of off-time cycles (i.e., the height roughly at 100 μm for 4.2 V compared to 23 μm for 3.2 V). Checking with SEM examination, the columns fabricated by intermittent MAGE at 4.2 and 3.2 V revealed their heights at 93 and 22 μm, respectively. Obviously, the intermittent MAGE conducted at 3.2 V revealed better consistency for the column height coming from calculated and observed results.

It is possible to evaluate the time needed to grow a nickel microcolumn up to 500 μm. Fig. 6 (b) displays a few final cycles in the cases of intermittent MAGE conducted at 4.2V (on the left-hand side) and at 3.2V (on the right-hand side), respectively. It takes 107.18 s (overall *t*-on = 35.78 s; overall *t*-off = 71.40 s) at 4.2 V, and 510.03 s (overall *t*-on=438.63; overall *t*-off=71.40 s) at 3.2 V, respectively. If time-consumption for ascending the microanode is ignored, the average growth rates are estimated at 13.97 and 1.14 μm s^{-1} for the columns fabricated by intermittent MAGE conducted at 4.2 and 3.2 V, respectively. A close examination in Figs 6(a) and (b) indicated that the off-time period is a constant (1.4 s) but the on-time period varies with voltages employed.

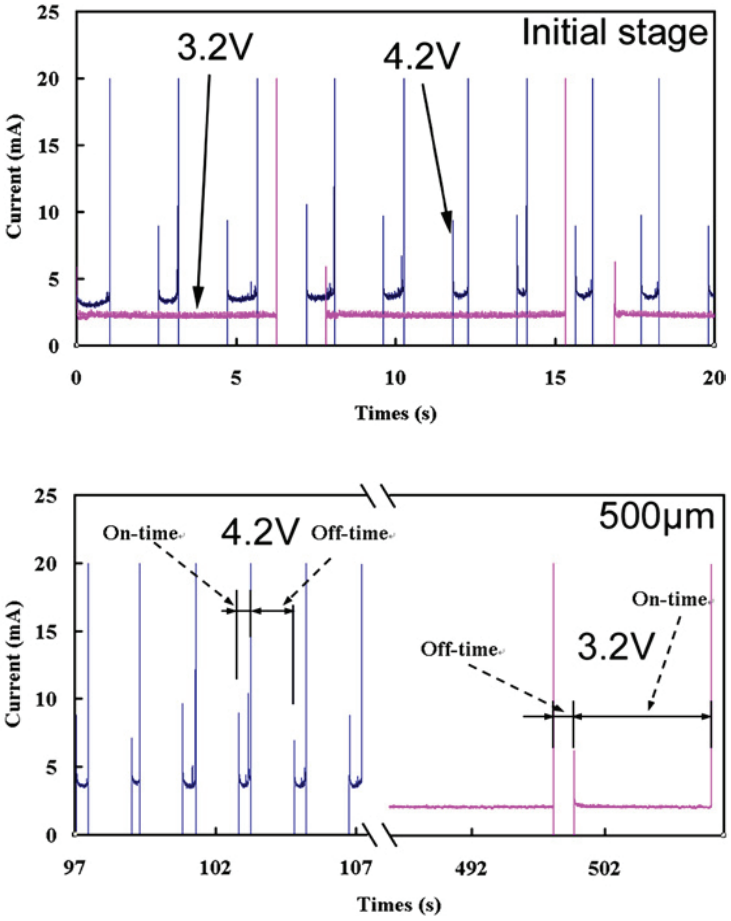

Fig. 6. Variation of current with the electroplating time for the micrometer nickel column fabricated via intermittent MAGE at 3.2 and 4.2 V during (a) the initial stage (in 20 s) and (b) the final stage to reach a column height of 500 μm. The initial gap is at 10 μm in each intermittent cycle

5. Models for column growth in continuous MAGE

A schematic model is demonstrated in Fig. 7(a) to illustrate the growth of the column fabricated by continuous MAGE. Prior to electrochemical reaction, the microanode was ascended to keep an initial gap of 20 μm from the cathode. As soon as the electrochemical deposition started, the microanode was driven to ascend at a constant rate (V). In response to stages 1, 2, ... and n, as shown in Fig. 7(a1), (a2) and (a3), the micrometer column was growing to various heights (i.e., at h_1, h_2, ... and h_n) with the separation between the microanode and microcolumn at d_1, d_2, ... and d_n, respectively. The dashed region in Fig. 7(a3) was re-plotted in Fig. 7(an) for detailed investigation. Supposedly a column established continuously from the (n-1)th stage to nth. The top surface of the column

established at the (n-1)th stage was covered by new deposit coming from the nth stage. It is well known that both deposition rate and surface coverage are determined by the strength of electric field exerted. Accordingly, at the instance of (n-1) stage, the strength at the center top of the column is the strongest, this strength decreases from the center to periphery at the column transverse. Under the condition where the strength of $E_{(n-1)}$ is small enough, no contribution of deposition leads to a confinement of maximal radius at $R_{(n-1)}$ for the column. In the continuous MAGE process, the variation of strength may depend upon the ascending rate of the microanode. Under higher ascending rates, the microanode moves further away from the column in shorter durations. The separation between the microanode and the microcolumn tends to increase in the sequence 20μm < d1< d2 < dn, so that the electric field strength reduces rapidly with time. A field gradient between E_n and $E_{(n-1)}$ caused by this quick strength change will be intensified and the strength of $E_{(n-1)}$ is soon reduced to an insignificant magnitude. Further proceeding to the process at the nth stage, the deposition would undergo mainly on the top rather than on the periphery of the column. As a result, the columns fabricated by continuous MAGE tended to reduce their radius gradually thus exhibiting the dendrite morphology as shown in Fig 2 (a). The strength difference between the (n-1)th and nth stages may offer an indication of radius uniformity for the column. It is defined by ΔE^c in Eq (5.1)

$$\Delta E^c = E_n - E_{(n-1)} \tag{5.1}$$

Where $E_{(n-1)}$ and E_n denote the strength at the (n-1) and nth stages, respectively. Moreover, the mean strength (E_m^c) defined in Eq (5.2), also based on the strengths arisen from the (n-1)th and nth stages

$$E_m^c = [E_{(n-1)} + E_n]/2 \tag{5.2}$$

Both the ΔE^c and E_m^c provide with a criterion to judge whether the microcolumn is possible to grow.

In the case of continuous MAGE conducted at higher voltages under lower ascending rate of the microanode, the strength gets stronger resultant from the growth of the column to diminish the gap between the electrodes. If the growth rate on the column is much higher than the ascending rate of the microanode, the separation between the microanode and the microcolumn will deduce in the order 20 μm > d1 > d2 > dn. Increasing with the elapsed time, this gap is soon reduced so that the field strength and the current responsible for electrochemical deposition are both intensified. Once the current measured exceeding 20 mA, the power of this system is shut off to interrupt MAGE for protection. Theoretically, fabrication of a micrometer column to any height is possible by continuous MAGE via optimal controlling the experimental conditions to balance the growth rate of the microcolumn with the ascending rate of the microanode. It may be accomplished by controlling a constant gap between the microanode and the microcolumn (e.g., 20 μm = d1 = d2 = dn) at any time. However, it is not easy to manipulate in practice. The microcolumn exhibited in figure 2(a) is the longest one we had via continuous MAGE.

Figure 7(b) shows a simulated diagram to elucidate the strength distribution for the electric field strength exerted in the continuous MAGE conducted at 5 V for 240 s, under an initial gap of 20 μm, with ascending rate of the microanode at 2 μm s^{-1}. This simulation is accomplished using the commercial software ANSYS 8.0 by input the data of electrical conductivity of electrolyte with 42.02 mS cm^{-1}. According to the same procedure, we also

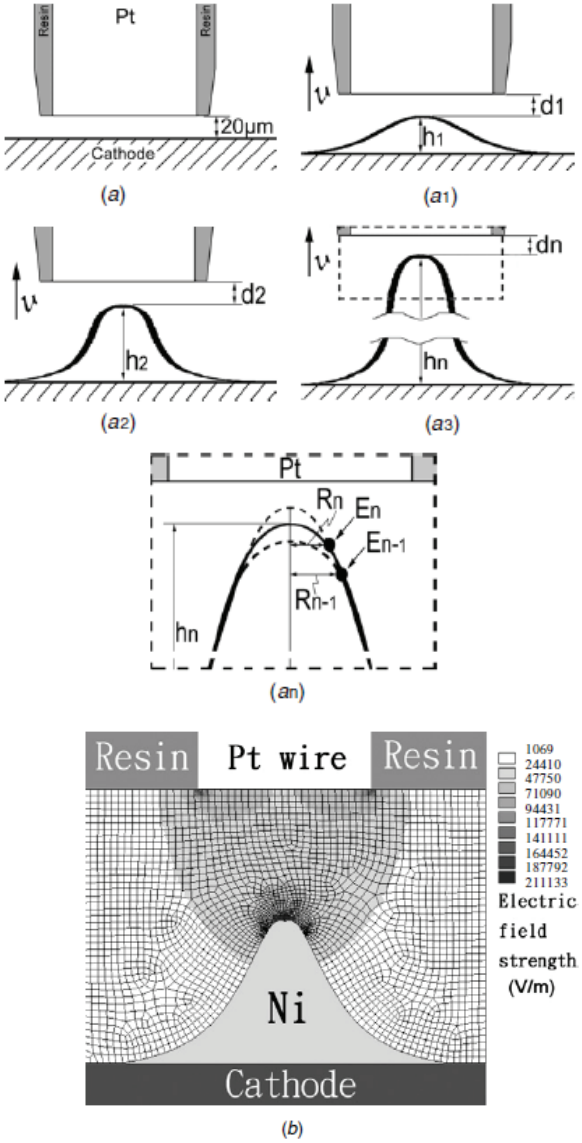

Fig. 7. (a) A scheme of sequential models for the continuous MAGE process initiated with a gap of 20 μm between the microanode and the Cu-substrate. In the diagrams, h_1, h_2, ..., h_n and R_1, R_2, ..., R_n represent the column height and column radius at a variety of duration t_1, t_2...and t_n, respectively. The eventual gaps in response to different duration are d_1, d_2 ... and d_n. The strength of electric-field strength at $t_n{-}_1$ and t_n is represented by $E_n{-}_1$ and E_n. (b) Distribution map of the electric-field strength simulated with the software ANSYS 8.0 for the system conducted by the continuous MAGE at the final stage. The bias is 5.0 V and the conductivity of the electrolyte is 42.02 mS cm^{-1}

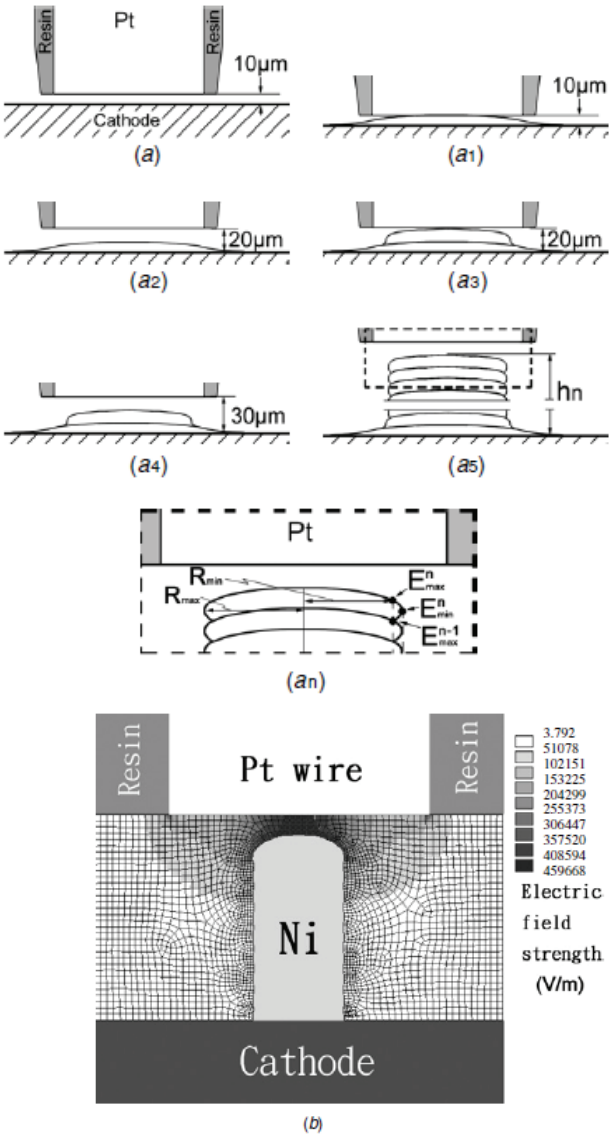

Fig. 8. (a) A scheme of sequential models for the intermittent MAGE process with each cycle initiated with a gap of 10 μm between the microanode and the column top. In the diagrams, h_n is the column height after n-cycles of intermittent MAGE; 1, 2, ..., n and 1′, 2′, ..., n' correspond to the on- and off-cycles, respectively, in each complete cycle; R_{max} and R_{min} represent the maximal and minimal radii of the column corresponding to the points with the highest (E_{max}) and the lowest strength (E_{min}) in each intermittent cycle. (b) Distribution map of the electric-field strength simulated with the software ANSYS 8.0 for the system conducted by intermittent MAGE at the final stage. The bias is 3.2 V and the conductivity of the electrolyte is 42.02 mS cm^{-1}

simulate the continuous MAGE conducted in different conditions. Diagrams were constructed and the data of ΔE^c and E_m^c were evaluated and compared. In a system where the microanode ascended at 2 μm s^{-1}, the profile of the microcolumn is determined by the electric voltage. The relationship between the surface morphology of the microcolumns and the voltage is discussed later in terms of ΔE^c and E_m^c.

6. Models for column growth in intermittent MAGE

Figure 8(a) shows the schematic models for the intermittent MAGE process. The microanode was first ascended to keep an initial separation of 10 μm from the substrate, and the power was turned on to proceed electrochemical reaction at a certain voltage. This electroplating process was carried out until the microcolumn growing up to almost in contact with the microanode, as shown at stage 1. The power was switched off to interrupt the electrochemical reaction, the microanode was ascended to another gap (at 10 μm), as depicted in stage 1′. Monitoring of the current would provide with a criterion for this on/off decision-making. The power would keep on as the current measured is less than 20 mA; however, it would turn to off as the current is higher than 20 mA. Another gap of 10 μm-gap was set and the second cycle would succeeded to undergo stages 2 and 2′, and so on until the nth cycles (via stages n and n′) to accomplish a microcolumn with an overall height of hn. It is apparent that microcolumn revealed a periodic variation in radius (from R_{min} to R_{max} and R_{min} again) in response to periodic performance of the intermittent MAGE through positions $E_{\max}^{(n-1)}$ to $E_{\min}^n$ and $E_{\max}^n$ again. It is worth noting that the mean strength of electric field (i.e., E_m^i) can be calculated from two different positions (i.e., $E_{\max}^n$ and $E_{\min}^n$) in Eq. (6.1) as follows

$$E_m^i = \left[E_{\min}^n + E_{\max}^n \right] / 2 \tag{6.1}$$

$E^i{}_m$ may offer a criterion to predict whether the microcolumn keeps on growing. In addition, the strength difference (i.e., ΔE^i) of the electric field between positions $E_{\max}^n$ and $E_{\min}^n$ can be estimated in Eq. (6.2) in the following

$$\Delta E^i = E_{\max}^n - E_{\min}^n \tag{6.2}$$

ΔE^i may offer an estimation of the diameter uniformity for the column fabricated from intermittent MAGE.

Figure 8(b) shows a schematic diagram to elucidate the distribution of the electric field in the intermittent MAGE conducted at an electric bias of 3.2 V, with the initial gap of each intermittent cycle at 10 μm. This diagram was also established via simulation by using commercial software ANSYS 8.0 through input the data of electrical conductivity for the electrolyte. A number of diagrams were constructed depending upon various experimental parameters and the corresponding data of E_m^i and ΔE^i were evaluated. The relationship between the surface morphology and the electric voltage employed in the intermittent MAGE is discussed later on basis of E_m^i and ΔE^i data.

7. Effect of electric voltages on the surface morphology and radius of the microcolumns

Figure 9 shows the effect of the electric voltages on the average radius (to the left ordinate) of the microcolumns fabricated from continuous MAGE. The radius of the columns was

evaluated from the SEM micrographs. The average radius was calculated from arithmetic average of three microcolumns fabricated under the same conditions. Standard deviation of the data was concerned in the plot. The average radius of the microcolumns tended to increase gradually from 2.59 to 10.34 μm with increasing the voltage from 1 to 5 V; however, it increases suddenly from 10.34 to 26.77 μm with increasing the voltage form 5 to 6 V. The standard deviation of the radius increases from 1.54 to 3.11 μm in the range from 1.0 to 4.0 V but decreases from 3.11 to 0.77 μm in the range from 4.0 to 6.0 V. At voltages below 5 V, a short vertebra-like structure was slowly formed to reveal a smaller radius at the top. When the continuous MAGE conducted in the range from 5 to 6 V, the growth rate of the micro-feature seemed to be similar to the ascending rate of the microanode. This led to a longer microcolumn appearing in uniform diameter.

Figure 9 also depicts the dependence of the mean strength (E_m^c , to the right ordinate) on the electric voltages. The magnitude of E_m^c almost increases one order of magnitude with increasing the voltage from 1.0 to 5.0V, and roughly 50 times with an increase of voltage from 5.0 to 6.0 V. A sudden rise in E_m^c within the range from 5.0 to 6.0 V is ascribed to much higher growth rate of the column compared to the ascending rate of the microanode. In practice, the huge change in E_m^c may lead to a problem to balance the growth rate and the ascending rate between the microcolumn and microanode.

Variation of ΔE^c with the voltages applied in continuous MAGE is also of concern. It reveals gradual increase (from 37 to 1238 V m^{-1}) with increasing the voltage from 1 to 5 V; however, a sudden increase (from 1238 to 140 000 V m^{-1}) within 5 –6V. The gradual increase of ΔE^c results in a radius discrepancy of the cylinder-like column with the voltages within 1 – 5 V. The sudden rise of ΔE^c tends to a momentary growth of the micro feature thus leading to rapid touch with the microanode. Thus, conducting continuous MAGE within 5–6 V to fabricate microcolumns is impractical.

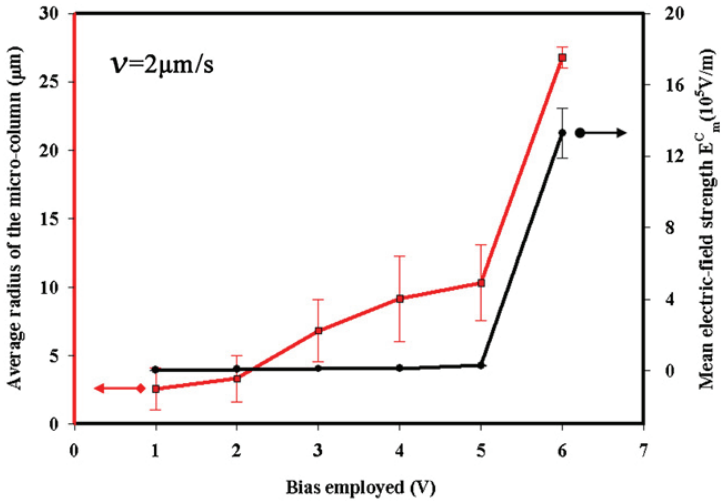

Fig. 9. Variation of the average radius for the micrometer columns (left ordinate) and the mean strength of the electric field (right ordinate) with the bias employed in the process of continuous MAGE with various ascending rates of the microanode in 240 s. The initial separation between the microanode and the Cu-substrate was 20 μm

Figure 10 depicts the dependence of the column radius (to the left ordinate) upon the voltages employed in the intermittent MAGE. The radius increases gradually (from 22.20 to 31.23 μm) with increasing the voltages from 3.2 to 4.2 V, and so does the corresponding standard deviation (from 0.25 to 1.75 μm.)

Regarding the dependence of the mean strength (E_m^i) of electric field (to the right ordinate) upon the voltages applied in the intermittent MAGE. The mean strength displays a gradual increase from 194 324 to 268 163 V m^{-1} (roughly 1.4 times) in the range from 3.2 to 4.2 V. The gradual change of E_m^i reflects the availability to manipulate experimental conditions in fabrication of the columns. The microcolumns fabricated at higher voltages depict greater standard deviation. This result reflects high degree of non-uniformity for the columns fabricated at higher voltages. Checking the data of ΔE^i (increase from 9909 to 37 391 V m^{-1}), the result is consistent. A comparison is made for fabricating microcolumns by means of intermittent MAGE (in the range from 3.2 to 4.2 V) and continuous MAGE (in the range from 5.0 to 6.0 V). Strength change in the electric field and standard deviation from the mean strength is much higher in the continuous MAGE than in the intermittent MAGE. Due to this fact, intermittent MAGE is better than continuous MAGE to fabricate microcolumn with a uniform diameter at expected length.

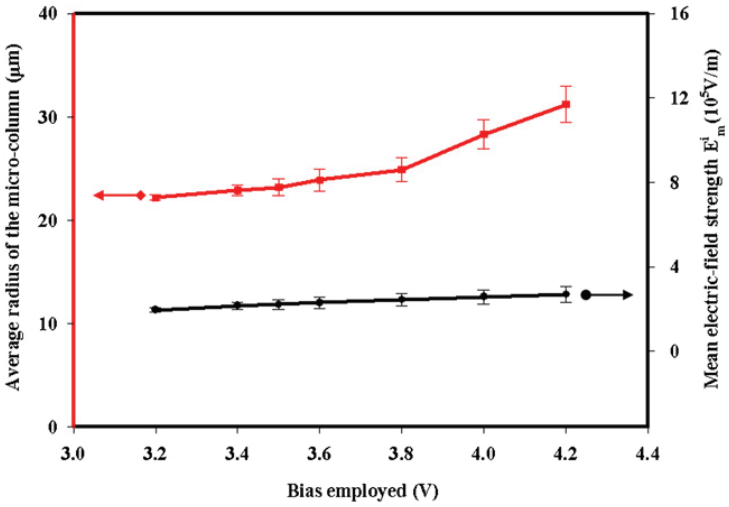

Fig. 10. Variation of the average radius for the micrometer columns (left coordinate) and the mean strength of the electric field (right coordinate) with the bias employed in the process of intermittent MAGE to a height of 500 μm. In each intermittent cycle, a gap of 10 μm is set between the microanode and the top of the column.

8. Surface and transverse morphology of micrometer columns influenced by electrical voltages

Micrometer nickel columns obtained from intermittent MAGE were treated in the following procedures to observe their cross section. They were first mounted in an epoxy resin. The mounted columns were ground in a plane perpendicular to the longitudinal direction to expose their cross-sections. A series of carbide paper (in the grade of 400, 600, 800, 1000,

1200, 2000) were used in the wet grinding, and subsequently slurries with fine powders of Al_2O_3 (1.0 and 0.3 μm in diameter, respectively) were employed to polish the cross-sectional surface to a mirror. The mirror surface was pickled in a 0.1% HF solution for 30 s, rinsed with water and dried ready for the SEM examination. Figure 11 displays the SEM morphologies and their transverse section at the position marked with a line across the micrometer. Ni columns deposited at 3.2V (Fig. 11(a)), 3.4V (Fig. 11(b)), 3.6 V (Fig. 11(c)), 4.4 V (Fig. 11(d)) and 4.6 V (Fig. 11(e)). Obviously, the surface morphology and transverse structure of the columns revealed a big difference depending on the biases. The micrometer columns deposited at 3.2 V depicted a smooth surface and a regular circular transverse (Fig. 11(a)). Checking the micrographs shown in Fig. 11 (from 11(a)–(e)),we found that by increasing the electrical voltages, the columns grew into shapes with higher irregularity and less smoothness on their surface. The columns deposited at higher voltages (e.g., 4.4 V) displayed an uneven circular profile around the transverse with the surface in nodular morphology. The columns deposited at much higher voltages (e.g., 4.6 V) appeared to have a branched coral with irregular transverses shape. We were concerned with the internal compactness of the columns, which could be estimated by examining their transverse using the SEM. The compactness was found to vary to different extents, depending on the electrical biases employed. Full compactness was observed in the transverse of the columns deposited at 3.2 V (Fig. 11(a)). Less compact were the columns, with porosity in the center of their transverse (Fig. 11(c)), deposited at little higher voltages (e.g., 3.6 V). The compactness was much less for the columns (Fig. 11(c)) deposited at much higher voltages (e.g., 4.4 V), because of radial expansion of the porosity from the transverse center resulting from coarsening and combination of the voids. The interior of the transverse was almost empty and remained a coral shell for the columns fabricated at an extremely high voltage (i.e. 4.6V). The deposit looked like a branched coral with a hollow interior.

9. Local potential measurement

Figure 12 depicts the scheme of an experimental setup for conducting LECD by a MAGE system. The microanode was driven to move by a step motor through an interface controlled by a computer, and the electroplating current was measured using a galvanometer. In addition, we set up a microelectrode, coupled with the saturated calomel electrode in connection with a potentiostat (Princeton EG&G Model 273 A), to oversee the potential at the location where the LECD proceeded. At least three runs had been carried out, and the standard deviation was presented in the error bar. Before setting out the deposition, the open-circuit potential was recorded (i.e. at -491.0 mV versus the SCE). The microanode was descended to touch the cathode, then drawn back to keep an initial gap at 10 μm to start the intermittent MAGE process as mentioned earlier. Once the power switched on, the potential decreased suddenly within several tenths of a second and level off to different levels depending on the electric voltages applied. This potential drop implies the occurrence of electroplating and the deposition rate could be estimated from the magnitude of current. Variation of the current with time has been discussed so we concentrate on the local potential in this section.

Figure 13 depicts the variation of local potential in the intermittent MAGE process against the voltages. Prior to electrochemical deposition, the open circuit potential (OCP) was stabilized at -491.0 mV. It dropped suddenly to a variety of levels in few tenths of a second once the electroplating setting out. The potential level decreased (in the range from -550.0 to -635.0 mV) with increasing the voltages from 3.2 to 4.6 V. The difference between the OCP

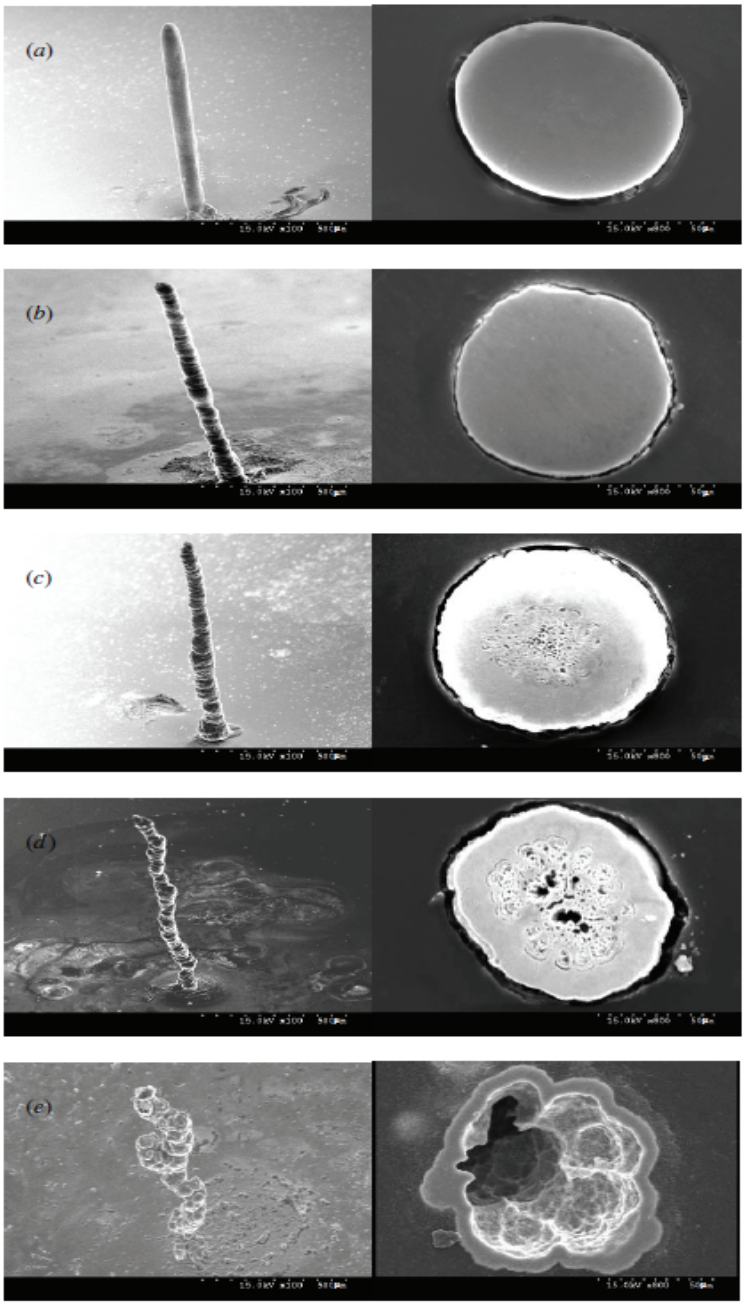

Fig. 11. SEM morphologies for the micrometer Ni columns deposited at various voltages and their corresponding transverse section. The columns were deposited at (a) 3.2V,(b) 3.4 V, (c) 3.6 V, (d) 4.4V and (e) 4.6 V with the gap between the electrodes initially set at 10 μm

and local potential measured under various voltages was of concern. The difference is much greater (i.e. 144.0 ± 1.0 mV) for the MAGE conducted at 4.6 V than that (59.0 ± 1.0 mV) conducted at 3.2 V.

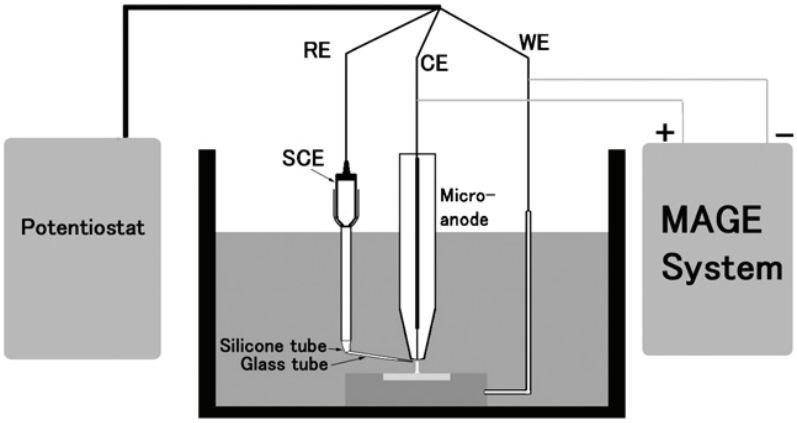

Fig. 12. Schematic diagram of the experimental setup for LECD conducted with the MAGE system and the local potential at the location near the top of the micrometer column measured by a microelectrode coupled with the SCE connected with a potentiostat

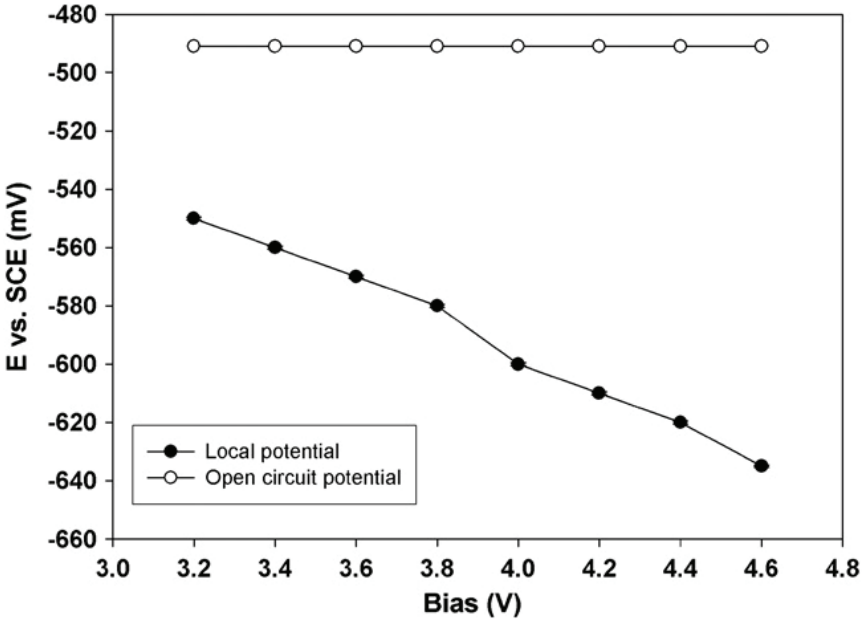

Fig. 13. A plot of open-circuit potential and local potentials against the voltages employed in the MAGE with the initial gap at 10 μm between the electrodes

10. Average growth rate for the columns with a height of 1000 μm

Figure 14 shows the dependence of the average growth rate (in the right ordinate) on the voltages employed to grow a micrometer Ni column, 1000 ± 10 μm in height. The average growth rate was calculated by dividing the height of the columns (i.e. 1000 ± 10 μm) by the growth duration. The time taken by the step motor should be deducted from the total duration of the process. From Fig. 14, the growth rate at 3.2 V is 0.114 μm s^{-1} and it increases from 0.114 ± 0.004 to 1.76 ± 0.06 μm s^{-1} with increasing the voltages from 3.2 to 4.6 V. The standard deviation increases with an increase of voltages. Voltages less than 3.2 V or higher than 4.6 V were ignored because of impractical tiny rate in the former and unsatisfactory appearance for the deposits obtained in the latter. In Fig. 14, the average current responsible for LECD was also measured and plotted (in the left ordinate) against the voltages. It increases from 0.225 ± 0.021 to 1.881 ± 0.046 mA with increasing the voltage from 3.2 to 4.6 V. The current is almost nine fold for the MAGE conducted at 4.6 V in comparison to that at 3.2 V. With respect to error bars in Fig. 14, the standard deviation increases with voltages. The growth rate estimated from the data of average current is consistent with that evaluated from column height divided by the electroplating duration.

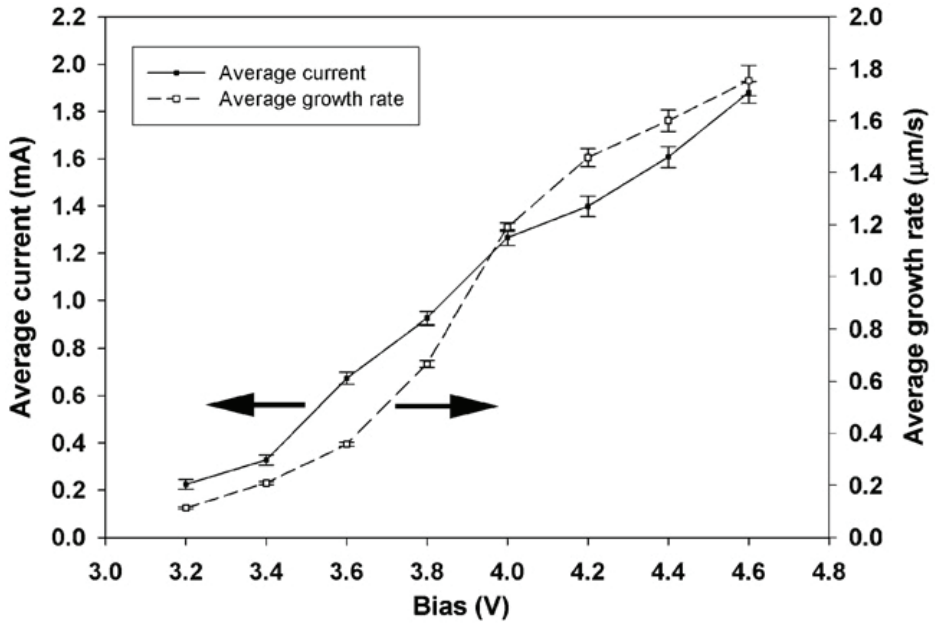

Fig. 14. A plot of the average current and average growth rate for the columns against the electrical bias employed in the MAGE

11. Concentration of nickel ions in the location proceeding LECD

As shown in Fig. 14, the stabilized local potential was in the range from -550 to -635 mV for the intermittent MAGE conducted at voltages ranging from 3.2 to 4.6V (vs. SCE). The

concentration of nickel ions at the local site taking place LECD could be estimated by the Nernst equation as shown in the following.

$$E = E^0 + \frac{RT}{\nu_e F}\ln\{c_{ox} / c_{Red}\} \tag{11-1}$$

Where E^0 is the standard potential of the electrode, R is gas constant, T is absolute temperature, ν_e is the valence number of the metal and F is Faraday's constant. C_{ox} and C_{Red} are the concentrations of oxidation species and reduction species.
By substituting E^0 with -0.25V (i.e. the standard EMF for 1.0 M nickel ions [12]), T with 328 K (55°C), R with 8.3144 joules/degree-mole (gas constant), F with 96487 Coulomb/mole and ν_e = 2, we gained the equation against SHE as follows.

$$E = -0.491 + \frac{0.065}{2}\log\left\{Ni^{2+}\right\} \quad \text{VS.} \quad \text{SHE} \tag{11-2}$$

In place of E in equation (11-2) with the data of local potentials measured under various voltages, the steady-state concentration of nickel ions remained at the location after LECD can be calculated. The concentration of nickel ions is plotted against the voltages employed in intermittent MAGE, as shown in Fig. 15. It reveals nickel ions remaining in the LECD vicinity decrease suddenly when increasing the voltages from 3.2 to 4.6 V.

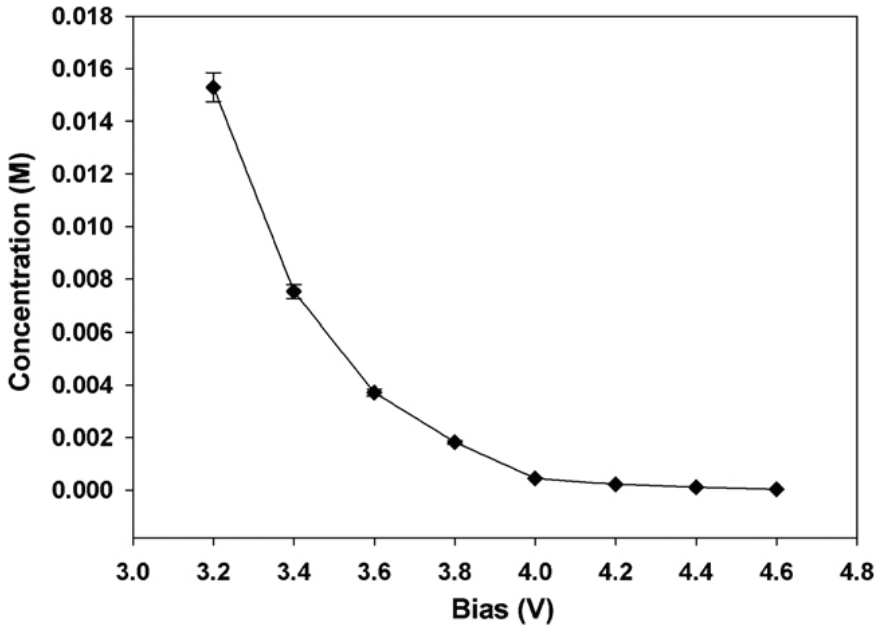

Fig. 15. The concentration of nickel ions calculated from stabilized local potentials at the location where the LECD takes place

A blank test was carried out to verify the correspondence between the electric potential and the concentration of nickel ions present in the solution. The bath conditions were set

unchanged except the concentration of nickel ions. The potential was measured using the same reference microelectrode depicted in Fig. 12. The relationship between the potential measured and the concentration of nickel ions prepared was plotted in Fig. 13. The curve representing the dependence of potential on the concentration of nickel ions obeyed equation (11-2) is in good agreement with that based on experimental measurements.

12. Supply of nickel ions from bulk solution to the LECD location

Mass transport of nickel ions in the electroplating process is theoretically governed by the Nernst-Planck equation [13]. According to the Nernst-Planck equation, the flux (in mol s^{-1} m^{-2}) for the specific ions transported and to be deposited (assigned as J_i) is represented as

$$J_i = -D_i \nabla C_i - \frac{Z_i F}{RT} D_i C_i \nabla \phi + C_i v \tag{12-1}$$

Where D_i is the diffusion coefficient (in m^2 s^{-1}), ∇C_i is the concentration gradient, $\nabla \phi$ is the potential gradient, Z_i and C_i are the charge (dimensionless) and concentration (in mol m^{-3}) of species i, respectively, and v stands for the velocity (in m s^{-1}) of the solution flow under stirring. In equation (12-1) the flux is expressed in detail with three terms on the right-hand side to describe the contribution of diffusion, migration, and convection, respectively. The diffusion coefficient (D_i) of nickel ions in the solution is 8.157×10^{-10} m^2 s^{-1} [14]. The concentration of nickel ions in the bulk solution of watts bath is 1.445×10^{3} mol m^{-3}. The convection term in Equation (12-1) could be ignored in the LECD process without stirring.

In an attempt to calculate the flux of nickel ions transported in the LECD process, the geometric transport in a specific electric field should be considered. As soon as the voltages are applied, nickel ions nearby the electrodes migrate to the cathode surface to discharge and are consumed. Reduction of nickel ions into metallic nickel within the local region leads to depletion of the nickel ions. This depletion causes a concentration gradient as compared this location to the around surroundings. The gradient offers a driving force for diffusion of nickel ions from the bulk solution to the depletion zone. Neglecting the initial stage in LECD, the micrometer columns are steadily deposited in an egg-head on their top [15]. We presume the nickel ions migrate into a boundary of semi-sphere rather than egg-head for simplifying the calculation. The semi-spherical boundary responsible for migration is illustrated in Fig. 16a. The nickel ions discharge and are consumed in the electric field surrounded with a cone. The boundary of the cone responsible for further supply of nickel ions by diffusion is illustrated in Fig. 16b. In Fig. 16, r is the average radius (in m) of the microcolumn, g marks the gap (also in m) between the microanode and the top of the column deposited. The area for the semi-sphere (A_{mig}, in m^2) and for the cone (A_{diff}, in m^2) can be estimated in the following:

$$A_{mig} = 2\pi r^2 \tag{12-2}$$

$$A_{dif} = 2\pi(r+g)\left(\frac{125\times10^{-6}/2 + r}{2}\right) \tag{12-3}$$

The figure 125 x 10^{-6} in equation (12-3) is the diameter of the tip-end disk of the microanode. The extent of r can be evaluated through examining the columns with SEM, and g is replaced by 10^{-5} m in this work because of its initial setting.

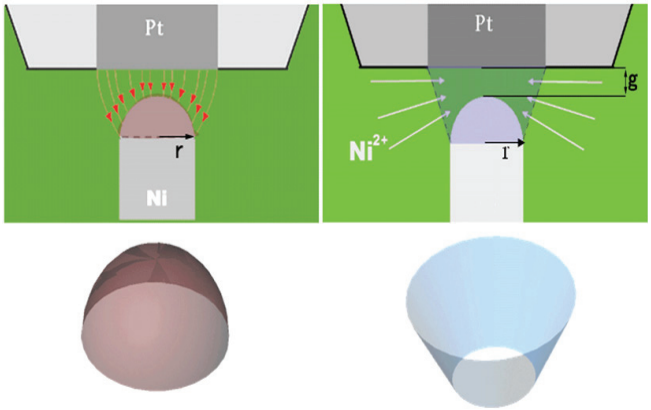

Fig. 16. Schematic models to illustrate the region involving mass transportation of nickel ions caused by (a) migration and (b) diffusion

The transport rate of nickel ions to the location exerted LECD can be arrived at from a product between the flux and the area of the plane perpendicular to the transport direction.

$$Transport\ rate(mol/s) = J(mol/s \cdot m^2) \times A(m^2) \tag{12-4}$$

An instance is given to explain calculating the fluxes for the transport of nickel ions by migration and diffusion, respectively, in the process performed at 3.2 V.

$$J_{mig} = -\frac{2 \times 96487}{8.314 \times 328} \times 8.157 \times 10^{-10} \times C_{local} / 10^{-3} \times \frac{voltage}{10 \times 10^{-6}} \tag{12-5}$$

$$J_{dif} = -8.157 \times 10^{-10} \times \frac{(1.445 - C_{local}) / 10^{-3}}{r \times 10^{-6}} \tag{12-6}$$

Replacing the voltage in equation (12-5) with 3.2 V, C_{local} in equation (12-6) with the value read from Fig. 15 (i.e., 0.01530 M), and r with the radius (that is, 36.1μm) of columns measured in the SEM micrograph, we obtain the fluxes of nickel ions contributed by migration and diffusion separately as follows.

$$J_{3.2Vmig} = -\frac{2 \times 96487}{8.314 \times 328K} \times 8.157 \times 10^{-6} \times 0.01530 mol/L \times 3.2V / 10\mu m \tag{12-7}$$

$$J_{3.2Vdif} = -8.157 \times 10^{-6} cm^2/s \times \frac{(1.445 - 0.01530) mol/L}{36.1\mu m} \tag{12-8}$$

From equation (12-4), we can estimate the total transport using equation (12-9)

$$Transport\ rate_{total} = J_{dif} \cdot A_{dif} + J_{mig} \cdot A_{mig} = 2.77 \times 10^{-9} mol/s \tag{12-9}$$

The same treatment can be used to calculate the corresponding transport rate for the LECD performed under other voltages. The average supplying rate calculated from equation (12-9) is plotted with the voltages, as shown in Fig. 17.

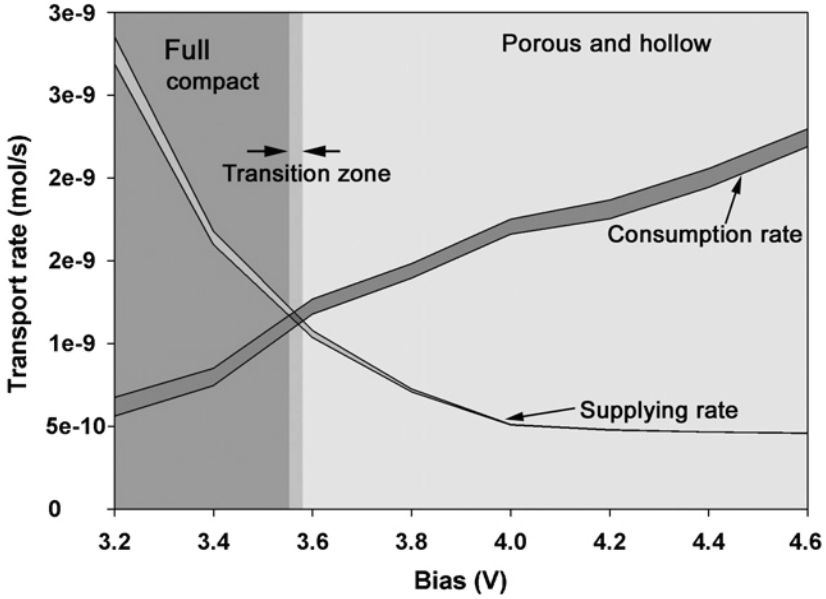

Fig. 17. Transport rate as a function of voltages adopted in the intermittent MAGE to display the balance between the supply and consumption rate of the nickel ions within the localization taking place LECD

13. Consumption of nickel ions in the LECD location

Figure 18 displays the plot of average current measured at steady state in the LECD and the current efficiency against the voltages employed. It is seen in Fig. 18 the average current increases from 0.2 to 1.8 mA, whereas the current efficiency decreases from 53 to 23 % with increasing the biases in the range from 3.2 to 4.6 V. The standard deviation of the average current also increases with the electrical biases. Observation suggested the increase in average current is proportional to the augmenting in the growing rate of columns. The decrease in the current efficiency responds to the phenomenon that bubbles evolve much more generously when increasing the biases. This enlargement in bubbles evolution implies reducing hydrogen ions contributes much more than nickel ions. The higher standard deviation in the average current at higher corresponding biases reflects the greater variation in the diameter of the columns and in the roughness of their surface morphology.

The weight of a single micrometer column is so slight and beyond the detection limit of a usual balance. Three columns fabricated at the same conditions were gathered to overcome this difficulty, thus an average weight for a single column could be estimated ($W_{estimated\ by\ weighing}$). The current efficiency (η) for the LECD conducted under specific conditions can be estimated by equation (13-1)

$$\eta = \frac{W_{estimated\ by\ weighing}}{W_{calculated\ from\ current}} \tag{13-1}$$

In which the numerator ($W_{estimated\ by\ weighing}$) is the average weight obtained by the aforementioned for a single micrometer column and the denominator ($W_{estimated\ by\ weighing}$) was

calculated from the data of electroplating current consumed to grow the column within the duration. The theoretical weight of the column ($W_{estimated\ by\ weighing}$) estimated by the data of current and duration measured is believed to obey the following equation (13-2).

$$W_{calculated\ from\ current} = \frac{ItA}{zF} \tag{13-2}$$

Where I is the average current; t is the duration to grow a 1000 μm-height column; A is the atomic weight of nickel; z is the valence; and F is the Faraday constant. The average consumption rate of the nickel ions in the local region taking place by LECD could be estimated by the equation (13-3)

$$\text{Consumption } rate = \frac{W}{t \times A} = \frac{I\eta}{zF} \tag{13-3}$$

The average consumption rates calculated from equation (13-3) are plotted with the voltages, as shown in Fig. 17

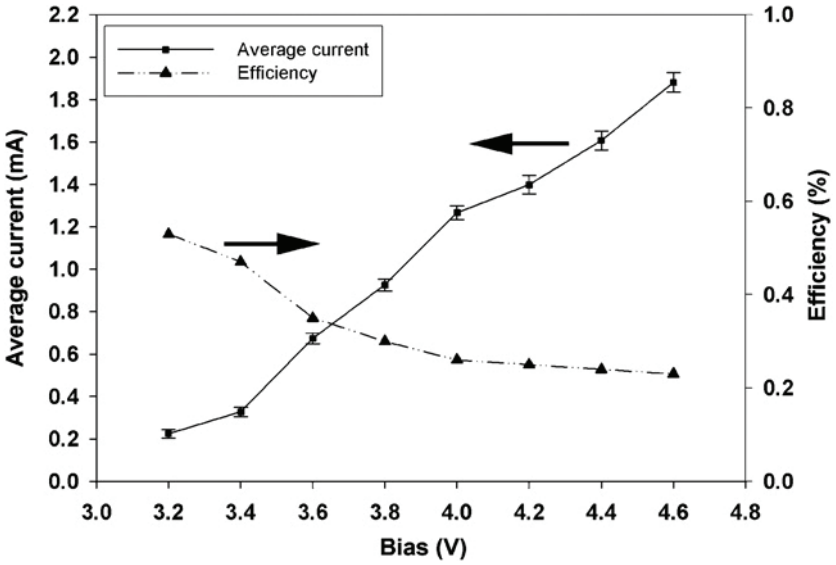

Fig. 18. The average current measured in the LECD and the current efficiency plotted against the electrical bias (voltage) employed

14. Balance between the supply and consumption of nickel ions within the location taking place LECD

Figure 17 summarizes the variation of supply rate and consumption rate within the location where taking place LECD with the voltage employed in the intermittent MAGE. The increase in the consumption rate and the decrease in the supply rate when increasing the electrical biases tend to meet at a point which reaches a balance. At the balance point the consumption rate of nickel ions in the local region could be compensated by the supply rate. Therefore, this point defines a critical voltage to separate the columns with internal

transverse in compact from those with porous transverse internal. At voltages less than the critical, the columns will lead to a compact transverse, whereas at voltages higher than the critical the columns will lead to a porous one. Considering the LECD performed at 3.2V the supplying rate of nickel ions (that is, 2.77 $x10^{-9}$ mol s^{-1}) is much higher than the consumption rate (that is, 6.19 $x10^{-10}$ mol s^{-1}). Nickel ions supplied to the location are more than consumed within the LECD region. Surplus supply of nickel ions leads to a complete filling of internal transverse of the columns. Stable current results in smooth morphology of the columns. On the other hand, as the LECD performed at 4.6V, the supply rate (4.58 $x10^{-10}$ mol s^{-1}) is much less than the consumption rate (2.24 $x10^{-9}$ mol s^{-1}). Shortage of nickel ions resultant from a lower rate of supply rate than the consumption leads to formation of internal pores thus resulting in porous transverse in the center of the columns. Greater variation in the deposition current results in rough morphology of the columns. The higher the biases employed in the LECD, the more severe the porous transverse in the columns, and the rougher their surface, as shown in Fig. 11.

There exists a transition zone in a narrow range of the electric bias (from 3.55 to 3.57 V) in Fig. 17. This transition zone arises from the deviation of accuracy in calculating of nickel concentrations and measuring local potentials. Apparently, the accuracy deviation is so small (at 0.02 V) that 3.56 ± 0.01 V is the critical voltage for conducting the intermittent MAGE to separate the micrometer columns with a smooth surface and full compact internal from those with rough surface and porous (or even hollow) internal. At any voltage less than this critical, the nickel ions consumed by electrochemical deposition in the depletion region could be completely compensated by the diffusion of nickel ions from nearby surroundings. This ensures sufficient supply for the need in the electrochemical consumption thus resulting in a full compact internal transverse of the columns. On the contrary, at the overages higher than this critical, the consumption of nickel ions is faster than their supply within the electroplating location. Insufficient supply of nickel ions leads to a porous (and even empty) internal transverse of the columns. Lower current density arising from the cases conducted at lower voltages results in a finely grained smooth surface; higher current density arising from the cases conducted at higher voltage results in an irregularly nodular rough surface.

15. Conclusions

The kinetics of electrochemical processes is determined not only by the strength of electric field but also by the mass transport phenomenon of the electrochemical active ions. In the cases of ordinary electrochemical deposition, the electric field employed is relatively low and the field distribution is homogeneous. Localized electrochemical deposition (LECD) process provides a new concept to fabricate three-dimensional (3D) metal microstructures. However, a super high electrical field is exerted at the electroplating site in the LECD, and the distribution of field strength is ultra heterogeneous. The site chosen to conduct LECD is controlled experimentally to follow the track guided with a microanode. Consequently, LECD is also named as microanode guided electroplating (MAGE) process.

Through discussion on the phenomenon of mass transport in such a strong field distributed in extremely heterogeneous manner, balance between the supply rate and consumption rate of nickel ions in the region where LECD taking place plays a role on the surface morphology and the transverse internal structure. This balance is determined significantly by experimental parameters such as motion modes of the microanode, applied electric voltage, initial gap between the cathode and microanode. In terms of models, we simulate the system with commercial software ANSYS 8.0 to realize the electrochemical mechanism satisfactory.

16. Acknowledgments

The authors are grateful to the National Science Council of the Republic of China (Taiwan) for the financial support of the project under contract No. NSC 97-2221-E-008-009-MY3.

17. References

[1] J. D. Madden and I. W. Hunter, "Three-dimensional micro fabrication by localized electrochemical deposition", *J. Micromech. Microeng*., 1996, 5, 24–32.

[2] J. C. Lin, S. B. Jiang, D. L. Lee, C. C. Chen, P. C. Yeh, T. K. Chang, J. H. Yang, "Fabrication of micrometer Ni columns by continuous and intermittent microanode guided electroplating", *J. Micromech. Microeng*. , 2005, 15, 2405–2413.

[3] D. L. Lee, J. C. Lin, P. F. Kao, S. B. Jiang, "Micro-anode Guided Electroplating (MAGE) control system", *Materials Science Forum*, 2006, 505~507, 115-120.

[4] T. K. Chang, J. C. Lin, J. H. Yang, P. C. Yeh, D. L. Lee and S. B. Jiang, " Surface and transverse morphology of micrometer nickel columns fabricated by localized electrochemical deposition", *J. Micromech. Microeng*. 2007, 17, 2336–2343.

[5] J. H. Yang, J. C. Lin, T. K Chang, G. Y. Lai and S. B. Jiang, "Assessing the degree of localization in localized electrochemical deposition of copper", *J. Micromech. Microeng*., 2008, 18, 055023 -005030.

[6] J. C. Lin, T. K. Chang, J. H. Yang, J. H. Jeng, D. L. Lee and S. B. Jiang, "Fabrication of a micrometer Ni–Cu alloy column coupled with a Cu micro-column for thermal measurement", *J. Micromech. Microeng*., 2008, 19, 015030-015039.

[7] J. H. Yang, J. C. Lin, T. K. Chang, X. B. You and S. B. Jiang, "Localized Ni deposition improved by saccharin sodium in the intermittent MAGE process", *J. Micromech. Microeng*., 2009, 19, 025015-25026.

[8] J. C. Lin, J. H. Yang, T. K. Chang, H. B. Jiang, "On the Structure of Micrometer Copper Features Fabricated by Intermittent Microanode-guided Electroplating", *Electrochim. Acta*, 2009, 54, 5703-5708.

[9] J. C. Lin, T. K. Chang, J. H. Yang, Y. S. Chen, and C. L. Chuang, " Localized Electrochemical Deposition of Micrometer Copper Columns by Pulse Plating", *Electrochim. Acta*, 2010, 55 , 1888-1894.

[10] Ting-Chao Chen, Yean-Ren Hwang, Jing-Chie Lin, Yong-Jie Ciou, "The Development of a Real-Time Image Guided Micro Electroplating System", *Int. J. Electrochem. Sci.,* 2010, 5, 1810 - 1820.

[11] Y. S. Chen, J. C. Lin, Z. H. Lin, C. Li, and J. K. Chang, "Effect of Solvent on the Morphology of Nickel Localized Electrochemical Deposition", *J. Electrochem. Soc.,* 2011, 158 (5) D264-D268.

[12] D. A. Jones, "Principles and Prevention of Corrosion", 2nd Edn. Englewood Cliff, NJ: *Prentice Hall*. 1996, 44

[13] A. J. Bard and L. R. Faulkner, "Electrochemical Methods Fundamentals and Applications", 2nd Edn., New York: *Wiley,* 2000, 29

[14] D. R. Lide, 2001–2002 CRC, "Handbook of Chemistry and Physics", 82nd Edn., Boca Raton, FL: CRC Press.

[15] K. Ikuta, S. Maruo and S. Kojima, " New micro stereo lithography for freely movable 3D micro structures", *J. Microelectromech. S*. 1998, 290–2955

Part 3

Advances in Energy and Environmental Engineering Aspects

10

Dissolution Trapping of Carbon Dioxide in Reservoir Formation Brine – A Carbon Storage Mechanism

Stefan Iglauer
Curtin University, Department of Petroleum Engineering, ARRC Building, Australia

1. Introduction

Carbon Capture and Storage (CCS) is a method to reduce anthropogenic greenhouse gas emissions thereby mitigating global warming. In CCS, carbon dioxide (CO_2) is captured from fossil fuel-fired power plants or other large point-source emitters, purified, compressed and injected deep underground into subsurface formations at depths of or greater than 800m. At such depths CO_2 is in a supercritical (sc) state increasing storage capacity (IPCC 2005).

In CCS, there are four main mechanisms which keep the buoyant CO_2 underground:

1. Structural/stratigraphic trapping – here an impermeable caprock prevents the CO_2 from flowing upwards,
2. Capillary trapping, where micrometer-sized disconnected CO_2 bubbles are formed and held in place by local capillary forces in the rock pore-network,
3. Dissolution trapping, where CO_2 dissolves in the formation brine and sinks in the reservoir as the CO_2-enriched brine has an increased density,
4. Mineral trapping, where the dissolved CO_2 reacts with the formation brine, forms carbonic acid which dissociates generating protons, HCO_3^- and CO_3^{2-} ions; these species subsequently react with the formation brine and/or host rock to form solid minerals which trap the CO_2 very safely.

The focus of this text is on dissolution trapping; how much CO_2 dissolves under which geothermal conditions and what happens to the CO_2-enriched brine, which is slightly denser than the original formation brine, in the formation.

Important open questions in this context are: How fast are these mass transfer processes in real geological porous media under realistic CCS conditions? Are there means of accelerating CO_2 dissolution? How do separate gas and/or oil phases (oil and/or gas reservoirs) in the reservoir affect CO_2 dissolution processes and reservoir fluid dynamics? How does the pressure drop due to CO_2 dissolution affect injectivity and storage capacity of CO_2?

2. Geological background of dissolution trapping

The International Panel on Climate Change (IPCC) (2005) has suggested several possible geological storage media, including deep saline aquifers, oil or gas reservoirs and unmineable

coal seams. In case of CO_2 storage in coal, a benefit is that additional methane is produced which is adsorbed on the coal surface and displaced by CO_2 (so-called enhanced coal-bed methane (ECBM) production). However, CO_2 injection leads to the highly detrimental effect of coal swelling which strongly deteriorates injectivity as observed from laboratory and pilot field studies (Reeves and Oudinot, 2005). This text focuses on aquifers and oil/gas reservoirs and will not discuss ECBM any further as low permeability and swelling characteristics limit the scale of exploitation of coalbeds as potential CO_2 storage sinks.
In terms of CO_2 storage, deep saline aquifers – too saline for drinking water or agricultural usage – are most promising, because they are geographically widespread and have large potential storage capacities. Published storage capacity estimates especially for aquifers vary widely based on the assumptions made. This is an active area of research with the objective to provide accurate basic information so that effective CCS schemes can be planned in order to store the large quantities of anthopogenic CO_2 emitted (circa 30 Gt CO_2/a, IPCC 2007).
To focus on dissolution trapping, the topic of this chapter, the main problem associated with it is addressed straight away: it is the slow speed of CO_2 dissolution and the two-phase (CO_2 and brine) reservoir flow dynamics – as long as the CO_2 is in a separate supercritical state it tends to flow upwards because of buoyancy forces, and it can potentially leak to the surface. Mass transfer of CO_2 from the supercritical phase into the aqueous phase is the time-determining step in dissolution trapping which therefore also determines leakage risk. In fact CO_2 is only stored safely once it is dissolved in the aqueous phase (or precipitated as a solid). Hence the study of CO_2 dissolution is an essential aspect of CCS risk assessment. Mass transfer and solubilities of CO_2 into brine are functions of pressure, temperature, salinity, local CO_2 concentration and subsequent chemical reactions (formation and dissociation of carbonic acid and following rock dissolution/precipitation). Moreover interfacial areas $scCO_2$-brine play a vital role in the mass transfer kinetics, and they are closely related to the two-phase flow dynamics in the reservoir. All these aspects will be discussed in this chapter. In addition several reservoir scale computer simulations will be presented which analyze fluid flow and CO_2 storage in CCS schemes.
In this context it is worth noting that CO_2 is a naturally abundant species in the subsurface. Rumble et al. (1982) suggested two possible chemical reactions between calcite and quartz which formed this naturally occuring CO_2 over geological times. A result of this is that CO_2 content in oil or gas reservoirs can be very high. In gas reservoirs CO_2 content can reach concentrations larger than 90 mol% and in oil reservoirs CO_2 content can be as high as 70-80 mol% (Badessich et al. 2005). As an example Ballentine et al. (2001) state that the CO_2 concentration in gas fields in Texas varies from 3% to 97% depending on the geographical location.
In summary dissolution trapping is a feasible mechanism to store large quantities of CO_2, and if a route could be found to quickly dissolve $scCO_2$ into brine CO_2 emissions could be dramatically, rapidly and economically reduced this way, maybe even solving the climate change problem caused by CO_2 gas emitted from large point-sources. However, although CO_2 contributes the largest chunk to greenhouse gas emissions, other gases such as CH_4, CO, N_2O, halogenated carbons, etc., also need to be eliminated to completely stop global warming. One route for disposing these gases may also be dissolution into formation brines.

3. Reservoir fluid dynamics

In actual ongoing CCS projects large quantities of CO_2 are injected deep underground. The largest injection time for a pure CCS project has been achieved in Norway in the Sleipner

project, where 1 Mt CO_2/a are injected into the Utsira sandstone formation in the Norwegian sector of the North Sea at 800m depth (Iglauer 2011). This project started in 1996, and reservoir CO_2 monitors confirm reservoir simulations which predict that the CO_2 rises upwards and accumulates beneath the caprock (Hesse et al. 2008).
CO_2 from this rising CO_2-plume dissolves in brine as it migrates upwards (Pruess and Garcia 2002, Bachu and Adams 2003). The CO_2-enriched brine has a slightly higher density than the original brine (Ennis-King and Paterson 2005, Moortgat et al. 2011). This leads to gravitational flow instabilities in the reservoir (Riaz et al. 2006, Pau et al. 2010), and it is believed that the CO_2-rich brine sinks in the reservoir over hundreds to millions of years (Bachu 2000, Ennis-King and Paterson 2005, Lindeberg and Wessel-Berg 1997) in the form of thick and thin fingers (cp. Figures 1 and 2), however this is an active area of research and it has been suggested that this mechanism is considerably faster (Moortgat et al. 2011).
Again, this storage mechanism is very safe, but if the dissolution process is a very slow process then that means that the leakage risk is high in the short term (= initial several hundreds of years) since the CO_2 may escape before it can dissolve.

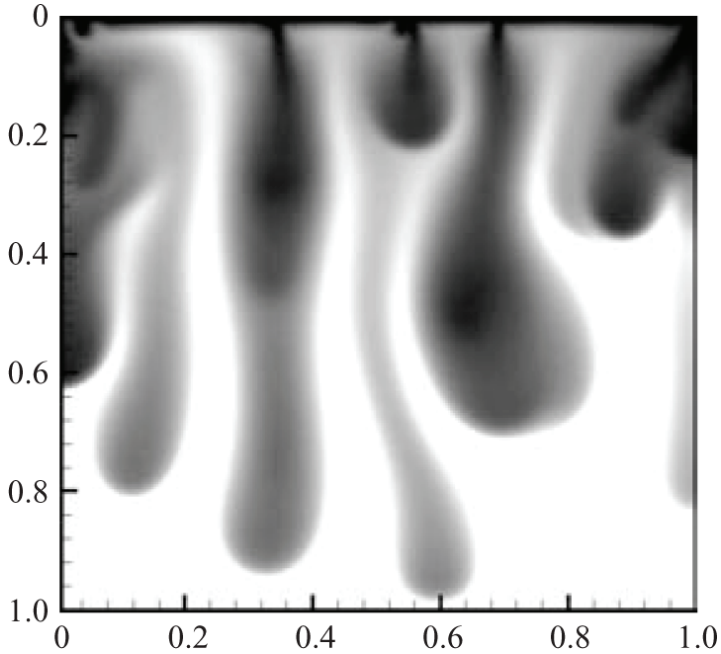

Fig. 1. CO_2-enriched brine sinks in a normalized simulated reservoir over hundreds to thousands of years (from Riaz et al. 2006 with permission from Cambridge University Press). The CO_2-concentration contours are shown in greyscales. The x- and y-axis are normalized lengths, the corresponding absolute values are in the kilometer range

4. Thermodynamics of CO_2 dissolution into formation brine

It has been reported that 0.9-3.6 mol% of CO_2 can be dissolved in brine, depending on pressure, temperature and brine composition (Rumpf et al. 1994, Koschel et al. 2006, Bando et al.

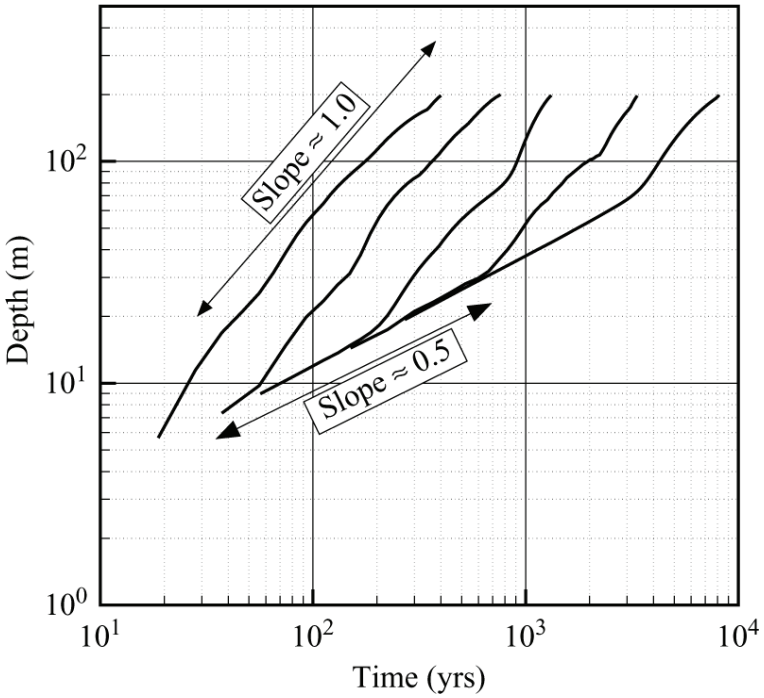

Fig. 2. The advance of the fastest finger front is shown for different permeabilities (represented by different lines) (from Riaz et al. 2006 with permission from Cambridge University Press)

2003, Kiepe et al. 2002). Before analyzing these relationships in more depth, it should be pointed out that CO_2 and brine are a reactive system, CO_2 reacts with water to form carbonic acid which subsequently dissociates (scheme 1) through a proton-relay mechanism that is catalyzed by several water molecules (Adamczyk et al. 2009) lowering the pH value of the brine.

$$CO_2(sc) + 3H_2O \rightleftharpoons CO_2(aq) + 3H_2O \quad (a)$$

$$H_2O + CO_2(aq) \rightleftharpoons H_2CO_3 \quad (b)$$

$$H_2CO_3 \rightleftharpoons HCO_3^- + H^+ \quad (c)$$

$$HCO_3^- \rightleftharpoons CO_3^{2-} + H^+ \quad (d)$$

Scheme 1. Formation and dissociation of carbonic acid. Reaction scheme (a) assumes that $scCO_2$ is dissolved in an analogous way to gaseous CO_2 (Adamczyk et al. 2009)

Adamczyk et al. (2009) studied these reactions at atmospheric pressure and found that the slowest step in scheme 1 is the forward reaction of (b), the hydration of $CO_2(aq)$ resulting in

H_2CO_3. The dehydration of H_2CO_3 is also relatively slow, with a dehydration rate constant of $k_{de} = 18\ s^{-1}$ (Pocker and Bjorkquist 1977). The deprotonation rate in scheme (c) is $k_{off} = 10^7\ s^{-1}$ (Pocker and Bjorkquist 1977) and the associated pK_a value is 3.45. Note that this pK_a value published by Adamczyk et al. (2009) is considerably different from the normally assumed $pK_a = 6.35$ for the $CO_2(aq)/H_2O$ system at atmospheric pressure conditions. The protonation rate of scheme (c) then results in $k_{on} = k_{off}/K_a$. The K value at 50.66 MPa for the reaction in scheme (d) is 5.13×10^{-11} (Hirai et al. 1997)

In addition, one consequence of an increase in CO_2 solubility with increasing pressure (or decreasing temperature or salinity) is that the aqueous phase increasingly acidifies because more CO_2 is present in the aqueous phase and reaction (b) is shifted to the right side according to Le-Chatelier's principle. It can therefore be expected that the pK_a value of scheme (c) drops further at increased CO_2 pressure.

In laboratory measurements pH values between 3.2-3.6 were observed within a temperature range between 300-343 K, a pressure range between 4-11 MPa and a salinity range 1-4 M NaCl solutions (Schaeff and McGrail 2004). In siliclastic and carbonate gas fields however pH values between 5-5.8 have been observed (Gilfillan et al. 2009); the discrepancy between lab and field data is most likely caused by complex geochemical buffering reactions, e.g. with carbonate host rock or carbonate based cements.

The increased proton concentration in the brine has significant implications for geochemical reactions (Stumm and Morgan 1996, Gauss 2010) generally leading to more rock dissolution and higher dissolution rates. When the pH value has increased again to sufficiently high levels CO_2 can be trapped as a solid phase – so-called mineral trapping (IPCC 2005, Gauss 2010). This could in principle also be engineered in the future although the physical and chemical phenomena associated with this process are highly complex and coupled.

Such reactions bring a range of problems and advantages with them:

- It is possible that too much rock is dissolved and high permeability channels are formed; this is especially a problem in carbonates (Egermann et al. 2005, Luquot and Gouze 2009). Injected CO_2 will preferentially flow through such channels, which are also termed "wormholes". This reduces reservoir sweep efficiency which again decreases capillary trapping as only low initial CO_2 saturations are achieved. Low initial CO_2 saturations however result in low residual CO_2 saturations (Pentland 2010 and 2011a,b; Al-Mansoori et al. 2010; Iglauer 2009). In addition such high permeability flow paths increase the risk of CO_2 leakage, especially if caprock material is affected.
- Should so much host rock be dissolved that the mechanical rock integrity is affected, then this can result in wellbore instability or even landmass subsidence.
- In case of precipitation of solid minerals due to geochemical reactions (when the pH value has increased again) rock permeability can be significantly reduced, e.g. by blockage of small pore throats (which determine the permeability value). This can result in serious injectivity problems, e.g. injection rates may have to be reduced dramatically which may render CCS schemes ineffective.
- Rock dissolution increases permeability and enhances injectivity rendering CCS schemes more economical.
- Precipitation of CO_2 in solid minerals (after chemical reactions) is the safest form of CO_2 storage in CCS as the CO_2 cannot escape to the surface anymore. This trapping mechanism is believed to take between thousands to billions of years (IPCC 2005, Xu et al. 2003).

In light of the new results published by Adamczyk et al. (2009) it is important to note that carbonic acid has a considerable acidity as it acts like a carboxylic acid on nanosecond timescales; this may have significant implications for geochemical reactions, rock surface alterations and associated possible rock wettability changes. Rock wettability strongly influences multi-phase fluid dynamics and capillary trapping.
On an important side issue these chemical reactions also happen in the oceans when CO_2 gas in the atmosphere dissolves in seawater thereby reducing its pH value. With the increasing CO_2 concentration in the atmosphere (from 190 ppm in 1750 to 380 ppm in 2005, IPCC 2005) more carbonic acid is formed in the oceans and the seawater pH value decreases with possible massive effects on sea life, starting with the sensitive but all important sea plankton. Therefore disposing anthropogenic CO_2 by dissolving it into the ocean seems to be a risky enterprise, as the pH value would drop further and locally reach substantially lower numbers.

4.1 Effect of pressure on CO_2 solubility in brine

CO_2 solubility (mole fraction of CO_2 per mass unit of brine) in formation brine is a strong function of pressure as shown in Figure 3. The data curve (open diamonds) in Figure 3 was computed with Duan and Sun (2003) and Duan et al. (2006)'s online CO_2 solubility calculator. The temperature was held constant at 323 K and brine salinity was 1 mol NaCl/kg brine. CO_2 solubility rapidly increases when pressure is raised from 0.1 MPa to 10 MPa, then the increase flattens out although a slight solubility increase follows. Three experimentally measured points at CCS pressure conditions are also added to the graph.

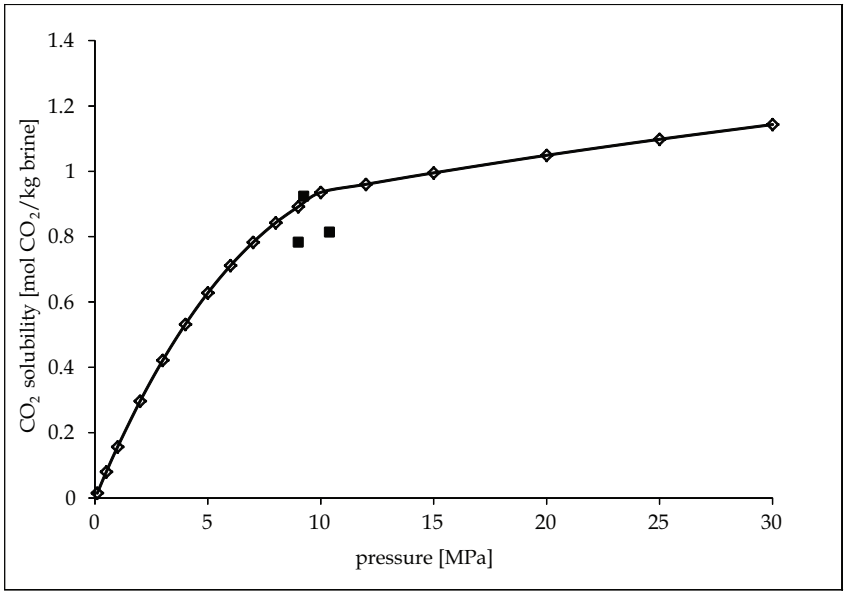

Fig. 3. CO_2 solubility increases with pressure increase. The data shown was computed with Duan and Sun (2003) and Duan et al. (2006)'s CO_2 solubility calculator. The black squares show experimental data points measured by Nighswander et al. (1989), Li et al. (2004) and Kiepe et al. (2002)

4.2 Effect of temperature on CO_2 solubility in brine

CO_2 solubility decreases with increasing temperature as shown in Figure 4. Experimental data relevant for CCS and simulated data are displayed. The computational data curve (open diamonds) was calculated with Duan et al. (2003+2006)'s solubility calculator setting the pressure to 10 MPa and salinity to 1 mole NaCl/kg.

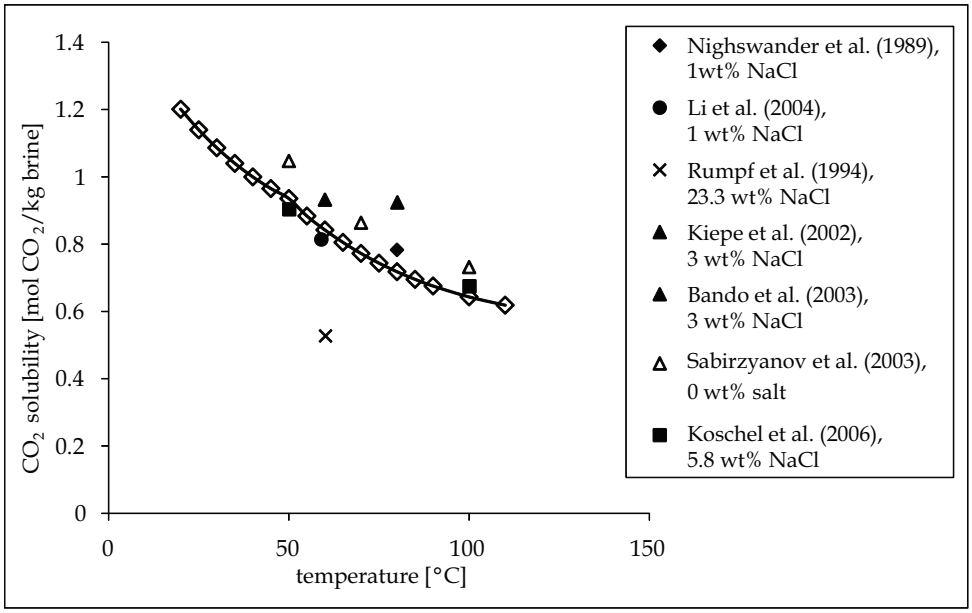

Fig. 4. CO_2 solubility versus temperature at high pressures. The substantially lower value measured by Rumpf et al. (1994) is caused by the high brine salinity (cp. section 4.3). Duan et al.'s (2003+2006) data is simulation data (open diamonds); the other points are experimentally measured values

4.3 Effect of brine salinity on CO_2 solubility in brines

CO_2 solubility decreases with increasing salinity as show in Figure 5. The open diamonds show simulated data calculated with Duan et al.'s (2003+2006) CO_2 solubility calculator setting the temperature to 323 K and the pressure to 10 MPa. It appears that Duan et al's. (2003+2006) model slightly over predicts CO_2 solubilities. The other points shown are experimentally determined values.

Moreover, the type of dissolved salt has an influence on CO_2 solubility. Yasunishi and Yoshda (1979) studied CO_2 solubilites at atmospheric pressure in a wide variety of salt solutions, these salts included NaCl, KCl, Na_2SO_4, $MgCl_2$, $CaCl_2$, K_2SO_4, $MgSO_4$, $BaCl_2$, $AlCl_3$, $Al_2(SO_4)_3$ among others. They found that for the same electrolyte concentration, KCl solutions can absorb more CO_2 than NaCl solutions, while $CaCl_2$ and $MgCl_2$ solutions absorb approximately the same amount of CO_2. Monovalent NaCl or KCl solutions with the same salt concentration absorb more CO_2 than their divalent $CaCl_2$ or $MgCl_2$ counterparts. For example Yasunishi and Yoshda (1979) measured at atmospheric pressure and 298 K that a 4.216 mol/L NaCl solution absorbs L = 0.3144 (L is the Ostwald coefficient, $L = V_g/V_l$ with

V_g = volume of CO_2 absorbed and V_l = volume of absorbing brine) while a 4.131 mol/L KCl solution absorbed L = 0.4703. For a 3.955 mol/L $MgCl_2$ solution they measured L = 0.1648. Chloride salt solutions absorbed more CO_2 than the corresponding sulphate solutions (that was tested for Na^+, K^+, Al^{3+} and Mg^{2+}).

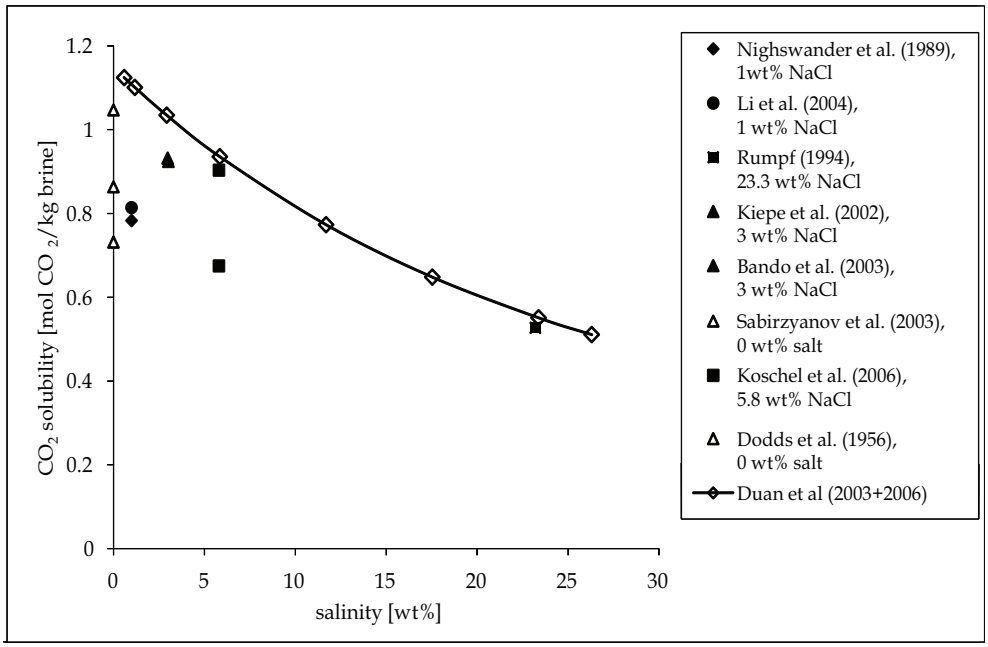

Fig. 5. CO_2 solubility as a function of brine salinity. The open diamonds represent data calculated with Duan et al. (2003+2006)'s CO_2 solubility calculator; the other points are experimentally measured values

Enick and Klara (1990) tested the influence of dissolved solids on CO_2 solubility in the temperature and pressure ranges 298-523 K and 3.40-72.41 MPa. Based on their results they developed an empirical equation for estimating salinity effects on CO_2 solubility (equation 1).

$$Y_{CO_2,brine} = Y_{CO_2,pureH_2O}\left(1 - 0.04893414 \cdot S + 0.001302838 \cdot S^2 - 0.00001871199 \cdot S^3\right) \quad (1)$$

where

$Y_{CO2,brine}$ = CO_2 solubility in brine (mass fraction)
$Y_{CO2,pureH2O}$ = CO_2 solubility in pure water (mass fraction)
S = salinity of brine (weight percent)

4.4 Theoretical model for computing CO_2 solubilities

Duan and Sun (2003, 2006) developed an equation (equation 2) which can predict CO_2 solubilites in brine as a function of temperature (range 273-533 K), pressure (range 0-20 MPa) and salinity (different salts/ions can be considered: Na^+, K^+, Mg^{2+}, Ca^{2+}, Cl^-, SO_4^{2-}).

$$\begin{aligned}\ln m_{CO_2} &= \ln y_{CO_2} F_{CO_2} p - \mu_{CO_2}^{l(0)} / RT \\ &-2\lambda_{CO_2-Na}\left(m_{Na} + m_K + 2m_{Ca} + 2m_{Mg}\right) \\ &-\zeta_{CO_2-Na-Cl} m_{Cl}\left(m_{Na} + m_K + m_{Mg} + m_{Ca}\right) + 0.07 m_{SO_4}\end{aligned} \tag{2}$$

Here T is the temperature, p the pressure, R is the universal gas constant, m is the molality of components dissolved in water, y_{CO2} is the mole fraction of CO_2 in the vapour phase, F_{CO2} is the fugacity coefficient of CO_2, $\mu_{CO_2}^{l(0)}$ is the standard chemical potential of CO_2 in the liquid phase, $\lambda_{CO2\text{-}Na}$ is the interaction parameter between CO_2 and Na^+ and $\zeta_{CO2\text{-}Na\text{-}Cl}$ is the interaction parameter between CO_2 and Na^+, Cl^-.
The fugacity F_{CO2} can be calculated via a fifth-order virial equation of state (equation 3). The coefficients c_i are stored in a look-up table (Duan et al. 2006) and they vary with the pressure and temperature regime.

$$\begin{aligned}F_{CO_2} &= c_1 + \left[c_2 + c_3 T + c_4 / T + c_5 / (T - 150)\right] p + \left[c_6 + c_7 T + c_8 / T\right] p^2 \\ &+\left[c_9 + c_{10} T + c_{11} / T\right] \ln p + \left[c_{12} + c_{13} T\right] / p + c_{14} / T + c_{15} T^2\end{aligned} \tag{3}$$

For the pressure and temperature regime most relevant to CCS, i.e. for a pressure below 100 MPa and a temperature range 273-340 K, the coefficients are inserted and shown in equation (3b).

$$\begin{aligned}F_{CO_2} &= -0.71734882 + \left[0.00015985379 - 4.9286471 \cdot 10^{-7} T\right] p \\ &+\left[-2.7855285 \cdot 10^{-7} + 1.1877015 \cdot 10^{-9} T\right] p^2 \\ &+\left[-96.539512 + 0.44774938 \cdot T\right] / p \\ &+101.81078 / T + 5.3783879 \cdot 10^{-6} T^2\end{aligned} \tag{3b}$$

The mole fraction of CO_2 in the vapour phase y_{CO2} can be computed with equation (4)

$$y_{CO_2} = \left(p - p_{H_2O}\right) / p \tag{4}$$

where p_{H2O} is the water vapour pressure which can be estimated with the empirical equation (5) (Duan and Sun 2003).

$$p_{H_2O} = \left(\frac{p_c T}{T_c}\right)\left[\begin{array}{l}1 - 38.640844(-t)^{1.9} + 5.8948420 \cdot t + 59.876516 \cdot t^2 \\ +26.654627 \cdot t^3 + 10.637097 \cdot t^4\end{array}\right] \tag{5}$$

where $t = (T\text{-}T_c)/T_c$ and T_c and p_c are the critical temperature and critical pressure of water (T_c = 647.29 K, p_c = 22.085 MPa).
The parameters $\mu_{CO_2}^{l(0)}$, $\lambda_{CO2\text{-}Na}$ and $\zeta_{CO2\text{-}Na\text{-}Cl}$ are estimated with equation (6) and Table 1 (Duan and Sun 2003).

$$\begin{aligned}Par(T,p) &= a_1 + a_2 \cdot T + a_3 / T + a_4 \cdot T^2 + a_5 / (630 - T) + a_6 \cdot p + a_7 \cdot p \cdot \ln T \\ &+a_8 \cdot p / T + a_9 \cdot p / (630 - T) + a_{10} \cdot p^2 / (630 - T)^2 + a_{11} \cdot T \cdot \ln p\end{aligned} \tag{6}$$

T-p coefficient	$\mu_{CO_2}^{I(0)} / RT$	$\lambda_{CO2\text{-}Na}$	$\zeta_{CO2\text{-}Na\text{-}Cl}$
a_1	28.9447706	-0.411370585	3.36389723E-4
a_2	-0.0354581768	6.07632013E-4	-1.98298980E-5
a_3	-4770.67077	97.5347708	
a_4	1.02782768E-5		
a_5	33.8126098		
a_6	9.04037140E-3		
a_7	-1.14934031E-3		
a_8	-0.307405726	-0.0237622469	2.12220830E-3
a_9	-0.0907301486	0.0170656236	-5.24873303E-3
a_{10}	9.32713393E-4		
a_{11}		1.41335834E-5	

Table 1. CO_2 solubility interactions parameters (Duan et al. 2003, 2006)

4.5 Effect of injection depth on CO_2 solubilities

In a deep saline aquifer or oil reservoir high pressures and elevated temperatures are found. The pore pressure at depth is usually assumed to be equal to the hydrostatic pressure; a typical hydrostatic pressure gradient is 10.35 MPa/1000m (Dake 2007). In addition a geothermal gradient exists, the reservoir temperature increases with depth. Average typical geothermal gradients are 25-30 K/1000 m (Fridleifsson et al. 2008). Average temperatures and pressures at depth are listed in Table 2, they were calculated assuming typical pressure and temperature gradients and a surface temperature of 293 K. The surface temperature needs to be adjusted for each specific geographical location, e.g. average temperature is low in Norway (average temperature throughout the year is around 281 K) while average yearly temperature is high in Saudi Arabia (298 K).

As stated above CO_2 solubility decreases with increase in temperature, but increases with increase in pressure. In Table 2 CO_2 solubilities calculated with Duan's web based CO_2-solubility calculator (Duan et al. 2003, 2006) are shown. The pressure effect over compensates the temperature effect so that CO_2 solubility increases with reservoir depth up to a depth of approximately 900m when it reaches a plateau.

With regard to storage of CO_2 in a supercritical phase optimal CCS conditions are conditions where the CO_2 density ρ_{CO2} is maximal, because then a maximum mass of CO_2 can be stored in the same rock pore space. Thermodynamically ρ_{CO2} increases with pressure but decreases with temperature. ρ_{CO2} as a function of depth increases monotonically as the pressure effect also over compensates the temperature effect (Table 2).

4.6 Effect of presence of oil (CCS in oil reservoirs)

CO_2 can also be injected into depleted oil reservoirs although storage capacities are much smaller than in aquifers (IPCC 2005). It is estimated that 50 Gt of CO_2 can be stored in this way worldwide (Firoozabadi and Cheng 2010) which is roughly 1.5 times of what is emitted per year. So this is clearly not the solution to mitigate global warming, however CO_2 solubility in oil is very high, up to 60-80 mol% of CO_2 can be dissolved (De Ruiter et al. 1994, Kokal and Sayegh 1993, Emera and Sarma 2006, Firoozabadi and Cheng 2010).

CO_2 solubility generally increases with pressure and it is higher at lower temperatures. If the temperature is below the critical CO_2 temperature (T_c = 304.13 K), then CO_2 solubility increases until the CO_2 liquefaction pressure is reached (circa 5.88 MPa), then it levels off

with further pressure increase. CO_2 solubility also depends on oil composition and for light oils CO_2 can be completely miscible. For example De Ruiters et al. (1994) measured a strong increase of CO_2 solubility with pressure in two crude oils, at low pressures (0.69 MPa) the gas-oil ratio (GOR) was approximately 5.3 m^3/m^3, and GOR increased rapidly up to the CO_2 liquefaction pressure when it reached 71 m^3/m^3 and 102 m^3/m^3, respectively. With a further pressure increase GOR stayed approximately constant. The experimental temperature in De Ruiters et al. experiments was low (290 K). If the temperature is above T_c as expected for CCS conditions, then CO_2 solubility monotonically increases; but it is nominally lower as compared to lower temperatures (Kokal and Sayegh 1993).

Depth [m]	**Temperature [K]**	**Pressure [MPa]**	**ρ_{CO2} [kg/m³]***	**CO_2 solubility [mol/kg]****
0	293	0.1	1.8	0.0307
100	296	1.135	21.8	0.3036
200	299	2.17	43.7	0.5037
300	302	3.205	68.3	0.6496
400	305	4.24	96.5	0.7542
500	308	5.275	130	0.8274
600	311	6.31	171.7	0.8769
700	314	7.345	221.8	0.9082
800	317	8.38	311.8	0.9260
900	320	9.415	391.9	0.9338
1000	323	10.45	412.8	0.9353
1100	326	11.485	449.6	0.9344
1200	329	12.52	486.3	0.9334
1300	332	13.555	522.7	0.9330
1400	335	14.59	561.3	0.9335
1500	338	15.625	576.1	0.9348

* estimated from Span and Wagner (1996).
** 1 mol/kg NaCl brine, calculated with Duan et al.'s (2003, 2006) calculator.

Table 2. Variation of temperature, pressure, CO_2 solubility and CO_2 density with depth

In case of heavy oils CO_2 dissolves into the oil phase while some light oil fractions are extracted into the CO_2 phase. Depending on the oil and thermophysical condition, vapour-liquid, liquid-liquid, liquid-supercritical fluid, liquid-liquid-vapour phase behaviours are observed. The densities of CO_2-saturated oil increase at lower temperature (294 K) while they decrease at higher temperature (e.g. 413 K) (Kokal and Sayegh 1993).
This makes CO_2 a very efficient solvent for crude oil extraction in tertiary oil recovery processes (Green and Willhite 1998, Blunt et al. 1993). The dissolved CO_2 reduces oil viscosity significantly which improves the mobility ratio oil-injected fluid (for improving production) and results in a much better reservoir sweep efficiency. The flow of oil in the reservoir is improved by the improved oil relative permeability, which leads to increased oil production. In addition, CO_2 which dissolves into the oil causes oil swelling (up to 50-60%, Firoozabadi and Cheng 2010) which also leads to enhanced oil production. One side effect of CO_2 addition to crude oil is that large asphaltene molecules precipitate (crude oil is a very complex fluid (cp. Table 3) with a multitude of components including such large asphaltene

components which are dissolved in the oleic phase under reservoir conditions, Dandekar 2006) which renders the rock surface more oil-wet which again changes multi-phase fluid dynamics in the reservoir. According to contact angle studies (Dickson et al. 2006, Espinoza and Santamaria 2010) this can result in CO_2-wet surfaces which would eliminate the possibility of capillary trapping of CO_2. Also the surface area CO_2-brine would most likely be affected by such wettability effects, which in turn would affect CO_2 dissolution kinetics (cp. section 5.1 and equations 12 and 17).

Component	**mole %***	**mole %****
Methane, CH_4	45.93	36.47
Ethane, C_2H_6	7.32	9.67
Propane, C_3H_8	6.42	6.95
n-Butane, C_4H_{10}	3.87	3.93
i-Butane, C_4H_{10}	1.42	1.44
n-Pentane C_5H_{12}	2.05	1.41
i-Pentane C_5H_{12}	1.68	1.44
Hexanes	2.93	4.33
C_7	2.30	C_{7+} 33.29
C_8	2.21	
C_9	1.66	
C_{10}	1.97	
C_{11}	1.61	
C_{12}	1.39	
C_{13}	1.36	
C_{14}	1.28	
C_{15}	1.22	
C_{16}	1.09	
C_{17}	1.04	
C_{18}	0.98	
C_{19}	0.77	
C_{20+}	6.63	
Hydrogen sulphide, H_2S	0.60	0
Carbon dioxide, CO_2	1.47	0.91
Nitrogen, N_2	0.81	0.16

Table 3. Typical composition of black crude oil (*Dandekar 2006, **McCain 1990). Of course the exact compositions of crude oils are extremely complex and vary widely depending on the exact geographical location. The C fractions C_{6+} upwards contain many isomers and also hydrocarbons with additional functional groups (e.g. alcohol, ester, carbonyl, amine, etc. pp.). Crude oil also contains metal cations (e.g. Vanadium)

Moreover there is a very important reservoir engineering aspect associated with depleted oil reservoirs; reservoir pressure is low (because of oil production) and CO_2 can be injected at fairly high rates and comparatively large quantities of CO_2 can be stored. It is important not to exceed the fracture pressure of the caprock which would result in catastrophic leakage of

CO_2. Exceeding the capillary entry pressure of CO_2 into the caprock should also be avoided (then CO_2 will also flow through the caprock although very slowly because of the very low permeability of the caprock shale) resulting in potential CO_2 leakage to the surface.
Estimates suggest that many millions of tons of crude oil are produced yearly via enhanced oil recovery with CO_2 (CO_2-EOR) (Firoozabadi and Cheng (2010)). Crude oil production could be further increased if more CO_2 would be used but such CO_2-EOR schemes should have a CO_2 storage element.
In principle oil would be a very good storage medium for CO_2 (provided that the oil does not migrate upwards after CO_2-takeup, so ideally the process would be designed in such a way that oil density increases), but of course oil is an economically valuable commodity and will be produced, so oil production schemes need to be combined with CCS schemes and optimized, essentially as much oil as possible needs to be recovered while storing as much CO_2 as possible.
Reservoir simulations can calculate such CO_2-EOR recovery/injection schemes over several years (Qi et al. 2008, Firoozabadi 2011), one complication here is the three-phase flow and the associated complex fluid thermodynamics occurring in the reservoir. This includes mass transfer of CO_2 into the oil and aqueous phases.
In summary, most of the current CCS schemes which are online are actually EOR processes because of profitability. Example projects are the Weyburn-Midale project in Canada, which started in the year 2000. 1.8 Mt/a of CO_2 are injected into a depth of 1500m into a depleted oil reservoir (PTRC 2011, Pentland 2011). 225 m^3 of CO_2 produce 0.12 m^3 extra crude oil there. Another CO_2-EOR project is underway in the Salt Creek field in Wyoming, USA; here 2.09 Mt of CO_2 are injected yearly and more than 1.2×10^6 m^3 of incremental crude oil have been recovered so far and it is planned to store 50 Mt of CO_2 in total (Andarko 2010, Pentland 2011).

4.7 Effect of presence of gas (gas reservoirs or oil reservoirs with a gas cap)

CO_2 can also be injected into depleted gas reservoirs in order to produce additional gas, this is called enhanced gas recovery (EGR). The injected CO_2 increases reservoir pressure which supports gas production. As in the case of oil reservoirs or indeed aquifers the caprock failure stress must not be exceeded. Natural gas is a mixture of various components (cp. Table 4); the exact composition varies with the location of the gas fields and it is determined by the original hydrocarbon generation (Dandekar 2006).
In the reservoir, the CO_2 flood front mixes with the natural gas by dispersion and diffusion. In parallel to the CO_2 – gas mixing process, CO_2 also equilibrates with the formation brine, similar to the mixing processes occurring in deep saline aquifers. The main advantage of CO_2-EGR is profitability as in CO_2-EOR, and an optimum between additional gas production and CO_2 sequestration needs to be found. There are several CO_2-EGR pilot units where these processes are tested, e.g. in the Lacq demonstration project in southwest France, 10^5 t of CO_2 will be injected and stored in a depleted gas field at a depth of 4500m (Total 2011).
A thorough study of nine natural gas fields (including sandstone and carbonate reservoirs) concludes that the main trapping mechanism over millennial timescales is dissolution trapping. At most 18% of injected CO_2 is stored as a solid mineral phase (Gilfillan et al. 2009) and mineral trapping is predicted to happen only for siliclastic reservoirs.
In the case of oil reservoirs with a gas cap, the mixing thermodynamics are a combination of CO_2-gas mixing, CO_2 dissolution in oil and CO_2 dissolution in brine. These complex

processes are topic of current research (DaVega 2011). These mixing processes result in three-phase flow in the reservoir (oil, gas and water flow as separated phases); in addition it is possible that additional phases are formed (e.g. a second immiscible oil phase or a solid asphaltene phase) which can further complicate fluid dynamics at the pore-scale and in the whole reservoir. Depending on rock surface wettabilities CO_2 dissolution into brine can be slowed down, e.g. in case of a water-wet surface water covers the rock surface, and an oil layer may separate the brine from the CO_2 (Piri and Blunt 2005). This oil layer then essentially acts as a barrier through which the CO_2 has to pass in order to reach the brine and to be stored there safely by the dissolution trapping mechanism.

Component	**mole %**
Methane, CH_4	70-98
Ethane, C_2H_6	1-10
Propane, C_3H_8	trace - 5
Butanes, C_4H_{10}	trace - 2
Pentanes, C_5H_{12}	trace - 1
Hexanes C_6H_{14}	trace – 0.5
Heptanes C_7H_{16}	trace – 0.5
Carbon dioxide, CO_2	trace – 5
Nitrogen, N_2	trace - 15
Hydrogen sulphide, H_2S	trace – 3
Helium, He	0 - 5

Table 4. Typical composition of natural gas (McCain 1990). Apart from methane and ethane traces of medium sized hydrocarbons can be found. In addition, natural gas can contain significant amounts of H_2S, CO_2 or N_2 – up to 90 mol% (Firoozabadi and Cheng 2010). Such non-hydrocarbon gases usually need to be separated out of the production stream in order to achieve sellable gas quality

5. Kinetics of CO_2 dissolution into formation brines

Dissolution kinetics of CO_2 into brine in a reservoir are driven by four main factors, namely molecular diffusion of CO_2 into brine, dispersion during flow, convection of CO_2-saturated (heavier) brine in the reservoir and flow of the $scCO_2$ phase in the reservoir. These mechanisms are described in more detail in the following paragraphs.

5.1 Molecular CO_2 diffusion into reservoir brines.

Molecular diffusion in natural groundwater systems is usually a time-dependent unsteady-state process. This is described by Fick's second law (equation 7). The driving force behind molecular diffusion is the concentration gradient, essentially the entropy of the system is increased by molecular diffusion.

$$D\frac{\partial^2 c}{\partial z^2} = \frac{\partial c}{\partial t} \tag{7}$$

where
D = diffusion coefficient
c = concentration
t = time
z = depth

A limited number of measurements of the CO_2 diffusion coefficient in water $D_{CO2\text{-}H2O}$ at high pressure have been conducted. Renner (1988) measured $D_{CO2\text{-}H2O}$ for 0.25 N NaCl brine at 311 K for a pressure range 1.54-5.86 MPa and recorded $D_{CO2\text{-}H2O}$ values in the range 3.07-7.35 x 10^{-9} m²/s. More measurements at atmospheric pressure were conducted and $D_{CO2\text{-}H2O}$ values between 1.8 x 10^{-9} – 8 x 10^{-9} m²/s (Mazarei and Sandall 1980, Unver and Himmelblau 1964) were reported. Based on these datasets, Renner (1988) developed an empirical-statistical expression (equation 8).

$$D_{CO_2-H_2O} = 6391\ \mu_{CO_2}^{-0.1584}\mu_{H_2O}^{6.911} \tag{8}$$

where
μ_{CO2} = CO_2 viscosity
μ_{H2O} = H_2O viscosity

Renner's analysis (1988) indicated that water viscosity and CO_2 viscosity were highly correlated with the diffusion coefficient, but molecular weight of CO_2, molar volume of CO_2, pressure or temperature were not statistically significant. However Renner states in his paper and Renner's data show that $D_{CO2\text{-}H2O}$ increases with an increase in pressure. Therefore it can be expected that CO_2 diffusion processes under CCS conditions are faster than at atmospheric pressure conditions – which is positive news for dissolution trapping as it minimizes leakage risks by absorbing the mobile CO_2 faster in the aqueous phase.

Hirai et al. (1997) measured $D_{CO2\text{-}H2O}$ via laser-induced fluorescence at 286 K and 29.4 and 39.3 MPa ($D_{CO2\text{-}H2O}$ = 1.3 x 10^{-9} and 1.5 x 10^{-9} m²/s). Their results fit perfectly with the empirical equation (9) suggested by Wilke and Chang (1955). ι is an association parameter equal to 2.26 for water. The experimental data measured by Shimizu et al. (1995) ($D_{CO2\text{-}H2O}$ is approximately 1.8 x 10^{-9} m²/s at 286 K and 9-13 MPa) is however 40% larger than predicted by equation (9). Hirai's data and the Wilke-Chang equation both indicate that $D_{CO2\text{-}H2O}$ increases slightly with pressure.

$$D_{CO_2-H_2O} = 7.4\cdot 10^{-8}\left(\iota M_{H_2O}\right)^{0.5} T / \left(\mu_{CO_2} V_{CO_2}^{0.6}\right) \tag{9}$$

More recently, Mutoru et al. (2010) developed a semi-empirical model for calculating diffusion coefficients for infinitely diluted CO_2 and water mixtures (equation 10) based on 187 experimental data points. The subscript 1 denotes CO_2 and the subscript 2 denotes water. However, in case of water diffusing into the CO_2 phase, subscript 1 denotes water and subscript 2 CO_2.

$$D_{CO_2-H_2O} = \frac{k_1\left(M_{12}\varepsilon_{12}\right)^{k_2} T_{r,2}^{k_3}}{p_{r,2}^{k_4}\left(\mu_2 c_2\right)^{k_5}} \tag{10}$$

where

$$M_{12} = \left(\frac{1}{M_{H_2O}} + \frac{1}{M_{CO_2}} \right)^{-1} \tag{11}$$

M = molecular mass
ε_1 = dipole moment
ε_{12} = ratio of dipole moments, $\varepsilon_1 / \varepsilon_2$
k_1 = $10^{-7.23389}$
k_2 = 0.135607
k_3 = 1.84220
k_4 = 2.41943 x 10^{-3}
k_5 = 0.858204
$T_{r,2}$ = reduced temperature
$p_{r,2}$ = reduced pressure
μ = viscosity
c_2 = solvent molar density (the solvent is defined here as the dominant component)

The advantage of Mutoru et al.'s (2010) model is that it incorporates the temperature and pressure effects on the total dipole moment of water and the induced dipole moment of CO_2. In addition, it can predict $D_{CO2\text{-}H2O}$ over the complete range from infinitely diluted CO_2 to infinitely diluted H_2O. From equation (10) it is clear that temperature has a stronger influence on $D_{CO2\text{-}H2O}$ than pressure. This is due to the strong dependence of the viscosity and the solvent molar density on the temperature. However, pressure influences are also strong as pressure determines equilibrium compositions (Mutoru et al. 2010).

An interesting perspective on CO_2 dissolution into brine is the consideration of the CO_2 droplet diameter (Hirai et al. 1997). Especially in the context of residual trapping; here the rising CO_2 plume is split into a large number of small disconnected CO_2 clusters at the trailing edge of the plume due to natural water influx or chase brine injection (Iglauer et al. 2010).

The drop diameter is expected to have a highly significant effect on CO_2 dissolution speed. A strong enhancement of CO_2 dissolution is expected for such small CO_2 bubbles as their CO_2-brine surface area is significantly increased compared with that of a single-cluster CO_2 plume.

The dissolution rate of CO_2 can be described by equation (12) (Hirai et al. 1997).

$$d\left(\rho_{CO_2} V\right) / dt = -kA\left(C_0 - C_\infty\right) \tag{12}$$

where

V = volume of the $scCO_2$ droplet,
A = surface area of the $scCO_2$ droplet
k = mass transfer coefficient
C_0 = surface concentration of the droplet
C_∞ = concentration at infinity

The mass transfer coefficient k is expressed in equation (13) for high Schmidt (Sc) numbers

$$Sh = 1 + \left(Sc + 1 / \mathrm{Re}\right)^{1/3} 0.752\,\mathrm{Re}^{0.472} \tag{13}$$

where

Sh = Sherwood number (= $k \cdot d_{CO_2} / D_{CO_2-H_2O}$)

Sc = Schmidt number (= $\nu / D_{CO_2-H_2O}$)

Re = Reynolds number (= $u \cdot d_{CO_2} / \nu$)

d_{CO_2} = CO_2 droplet diameter

ν = kinematic viscosity

u = flow velocity

According to equation (13) small CO_2 droplets dissolve faster than large ones (assuming that $D_{CO2-H2O}$ is a constant). Essentially this is a formal description of how residual trapping enhances dissolution trapping. More research in this area would certainly improve understanding of the relation between residual and dissolution trapping.

Suekane et al. (2006) studied such mass transfer processes of $scCO_2$ dissolution into pure water in packed glass beads (measurement conditions were 313 K, 8.3 MPa, 70 µm bead diameter) and developed relation (14)

$$Sh' = 0.029 \mathrm{Re}^{0.92} \tag{14}$$

with the modified Sherwood number Sh'. Sh' can be calculated with equations (15) and (16).

$$Sh' = \frac{\hat{k} d^2}{D} \tag{15}$$

$$\hat{k} = \frac{u}{L} \ln\left(1 - \frac{C}{C_\infty}\right) \tag{16}$$

where $\hat{k}$ is the total mass transfer rate (= kA) and L is the length of the glass bead pack. Equation (16) is the solution of the one-dimensional steady state mass balance equation (17) with the boundary conditions C = 0 at x = 0.

$$u \frac{dC}{dx} = -kA\left(C - C_\infty\right) = \hat{k}\left(C - C_\infty\right) \tag{17}$$

Another interesting suggested correlation for $D_{CO2-H2O}$ has been put forward by Bahar and Liu (2008); they measured $D_{CO2-H2O}$ at 17.8 MPa and 356 K in 2 wt% NaCl brines and developed an empirical correlation between $D_{CO2-H2O}$ and the pressure p, temperature T, molecular weight MW, volume V and viscosity µ of the liquid (equation 18).

$$D_{CO_2} = 1.3678 \cdot 10^{-7} \frac{T^{1.47} MW^{2.2}}{V^{0.5} p \mu} \tag{18}$$

Bahar and Liu (2008) found that $D_{CO2-H2O}$ is higher for unsteady-state systems, and that the duration of the unsteady-state system strongly depends on the pressure and temperature.

5.1.1 Effect of temperature on CO_2 diffusion in water

As stated in equation (10), temperature has a clear effect on $D_{CO2-H2O}$. Unver and Himmelblau (1964) developed an empirial equation (19) for the dependence of $D_{CO2-H2O}$ on

temperature for atmospheric pressure within a temperature range between 279-338 K. D increases monotonically with temperature T (equation 19).

$$D = \left(A + BT + CT^2\right) \cdot 10^{-9} \tag{19}$$

A = 0.95893, B = 0.024161, C = 0.00039813 are constants for CO_2, A, B and C adopt different values for other gases. D is given in m^2/s. Again, diffusion-dominated CO_2 dissolution is more effective at higher temperatures.

5.1.2 Effect of pressure on CO_2 diffusion in water

According to measurements conducted by Wilke-Chang (1955), Shimizu et al. (1995) and Hirai et al. (1997) $D_{CO2\text{-}H2O}$ (approximately 1.5 x 10^{-9} m^2/s) is quasi independent of pressure in the tested range of circa 9-40 MPa. Their measurements were all performed at 286 K. However, Renner's (1988) measurements show that $D_{CO2\text{-}H2O}$ increases with pressure, this is supported by Mutora et al.'s (2010) analysis.

5.2 CO_2 diffusion into oil

Renner (1988) measured diffusion coefficients of CO_2 in decane $D_{CO2\text{-}C10}$ at a temperature of 311 K and in a pressure range 1.54-5.86 MPa. The results for $D_{CO2\text{-}C10}$ ranged from 1.97-11.8 x 10^{-9} m^2/s. An increase in pressure led to an increase in $D_{CO2\text{-}C10}$ and measured diffusion coefficients in a vertical sandstone core were significantly higher than in a horizontal core; this might have been due to convective forces in the vertical core. Renner developed the empirical-statistical equation (20) for $D_{CO2\text{-}HC}$ estimates.

$$D_{CO_2-HC} = 10^{-9} \mu_{CO_2}^{-0.4562} M_{CO_2}^{-0.6898} V_{CO_2}^{-1.706} p^{-1.831} T^{4.524} \tag{20}$$

where V_{CO2} is the molar volume of CO_2.

Model equation (10) can also estimate the diffusion coefficients of CO_2-hydrocarbon (HC) systems $D_{CO2\text{-}HC}$; predictions can be made for small alkane molecules (e.g. methane, ethane, butane) and polar H_2S.

5.3 Water diffusion into $scCO_2$ phase

Although not essential for CO_2 storage, it is noted for completeness that water diffuses and dissolves into the $scCO_2$ phase. Water solubility in $scCO_2$ is low, it increases with pressure. For a pressure range from 8.31-20.54 MPa at 313 K water mole fractions between 0.00053-0.00596 were measured, for a pressure range between 2.51-10.20 MPa at 323 K the water mole fraction measured ranged between 0.00251-0.0120 (Sabirzyanov et al. 2002).

Measured diffusion coefficients of water in CO_2 $D_{H2O\text{-}CO2}$ are reported to be much higher than diffusion coefficients of CO_2 into water. Values between 1.5 x 10^{-8} to 1.8 x 10^{-9} m^2/s were published for a pressure range between 7-20 MPa and a temperature of 298 K (Espinoza and Santamaria 2010). However the investigated temperature was lower than the expected temperature at CCS storage depths. The cited numbers could therefore be slightly different for actual CCS conditions. In addition, the semi-empirical model equation (10) can also estimate $D_{H2O\text{-}CO2}$ diffusion coefficients.

5.4 Dispersion of dissolved CO_2 due to flow through a porous medium

In addition to diffusion, dispersion occurs when a solute flows through a porous medium. This can essentially be understood as an unsteady irreversible mixing process of two miscible fluids which have different solute concentrations (e.g. brine saturated with CO_2 = fluid 1, and brine undersaturated with CO_2 = fluid 2). Dispersion can therefore influence CO_2 mass transfer as it changes the CO_2 concentration gradient. Dispersion is caused by several effects (Bear 1972, Özgür 2006, 2010):

1. The flow velocity profile in a pore (the flow velocity has a maximum in the middle of a pore).
2. Different flow velocities in different pores (the pores in a geological rock have a pore size distribution and therefore different flow resistances to fluids according to their size; faster flow happens in the pores with a larger diameter).
3. The complex tortuosity of the pores in the rock; some pores are longer and fluid flow takes longer.
4. Interactions of the solute with the rock matrix/rock surface.
5. Chemical reactions, e.g. ion exchange, of the solute with species in the brine or on the rock surface.

Bear (1972) distinguishes between mechanical dispersion and hydrodynamic dispersion. He defined hydrodynamical dispersion as the sum of mechanical dispersion plus molecular diffusion. The dispersion described above - and all dispersion mentioned in this text – is the same as Bear's mechanical dispersion.

At reservoir scale dispersion can be described by equation (21) where D_{dis} is the dispersion coefficient, u is the average pore flow velocity and α the dispersivity (Bear, 1972; Özgür, 2006).

$$D_{dis} = u\alpha \tag{21}$$

The dispersivity α is a property of the reservoir and it depends on the heterogeneity of the porous medium and the length of flow. Schulze-Makuch (2005) reviewed 307 datasets and suggested $\alpha_L = c\ L^{0.5}$ (where α_L is the longitudinal dispersivity, L is flow distance and c varies between 0.01 m for sandstones and unconsolidated material and 0.8 m for carbonates). A detailed discussion of dispersion and dispersivities is given by Bear (1972).

5.5 Convection of CO_2-enriched brine in the reservoir

Convection – here defined as flow at the reservoir scale induced by gradients in density, concentration or heat – can potentially move large quantities of dissolved CO_2 through the formation. A resistance threshold has to be overcome for convection to commence, this threshold can be assessed with the Rayleigh number Ra (equation 22) (Riaz et al. 2006).

$$Ra = \frac{K\Delta\rho g H}{\phi D \mu} \tag{22}$$

where

K = permeability
$\Delta\rho$ = density difference (between brine with high CO_2 concentration and brine with low CO_2 concentration)
g = gravitational constant
H = reservoir depth

D = diffusion coefficient
μ = brine viscosity
ϕ = porosity

Above a critical Rayleigh number Ra_c convection will occur; Ra_c is a function of the boundary conditions of the system (Weatherill et al. 2004), e.g. for a homogenous reservoir where the horizontal boundaries are impermeable and perfect heat conductors $Ra_c = 4\pi^2$ (Lindeberg and Wessel-Berg 1997).

One mechanism which can trigger convective flow is dissolution of CO_2 into brine, which can increase brine density by 1% under CCS conditions (Ennis-King and Paterson 2005).

Based on an expression suggested by Garcia (2001) Özgür (2006) developed an equation (23) with which the effect of aqueous CO_2 concentration on brine density can be estimated.

$$\rho_{CO_2,brine} = \frac{\rho_{brine}}{1 - Y_{CO_2}\left(1 - \frac{V_{m,brine}}{M}\rho_{brine}\right)} \tag{23}$$

where

$\rho_{CO2,brine}$ = density of CO_2-enriched brine
ρ_{brine} = original brine density
Y_{CO2} = dissolved CO_2 mass fraction
$V_{m,brine}$ = apparent molar volume of CO_2 in brine
M = molecular weight of CO_2

6. Reservoir scale dissolution trapping

In the context of reservoir flow where dissolved CO_2 molecules are transported, convection, dispersion, diffusion and maximum CO_2 solubilities can all play a significant role. This is an active field of research, and three literature examples are presented where CO_2 solute transport was modelled at reservoir scale.

Interesting conclusions extracted from these computations are that dissolution trapping is favourably done in a high permeability reservoir. Moreover CO_2 dissolution can significantly reduce reservoir pressure (the pressure is increased by CO_2 injection, but only a maximum reservoir pressure is tolerable, the fracture pressure), improving injectivity, i.e. CO_2 can be injected at a faster rate, and more CO_2 can be stored in total – provided that CO_2 dissolves at an adequate rate or CO_2 injection is slow enough.

6.1 Özgür model (2006)

Özgür (2006, 2010) modelled diffusion and convection in an aquifer with the diffusion-convection equation (24). $D\frac{\partial^2 c}{\partial z^2}$ is the diffusion term and $\frac{u}{\phi}\frac{\partial c}{\partial z}$ is the convection term.

$$D\frac{\partial^2 c}{\partial z^2} - \frac{u}{\phi}\frac{\partial c}{\partial z} = \frac{\partial c}{\partial t} \tag{24}$$

This model considers one-dimensional vertical flow in an aquifer, temperature and CO_2 gas cap pressure are assumed to be constant; chemical reactions are ignored and the porous

medium is considered to be isotropic and homogenous. The aquifer thickness is set to 100m, porosity to 20%, temperature to 323 K, pressure to 7.6 MPa and $D_{CO2\text{-}H2O}$ to 3 x 10^{-9} m²/s. Equation 24 can be re-written in dimensionless form

$$\frac{1}{Pe}\frac{\partial^2 C_D^2}{\partial Z_D^2} - \frac{\partial C_D}{\partial Z_D} = \frac{\partial C_D}{\partial t_D} \tag{25}$$

with

$C_D = \frac{C_{CO_2}}{C_{CO_2,saturated}}$, normalized concentration of CO_2 in brine at CCS conditions

$Z_D = \frac{z}{H}$, normalized reservoir height, H is the total thickness of the aquifer

$t_D = \frac{ut}{\phi H}$, dimensionless time

$Pe = \frac{uH}{\phi D}$, Peclet number = ratio between transport by convection/transport by molecular diffusion (Bear 1972)

Özgür (2006, 2010) solved the diffusion-convection equation (25) for one set of initial and boundary conditions:

Initial conditions:

$C_D = 0$ for $t_D = 0$ and all Z_D

Boundary conditions:

at $Z_D = 0$: $C_D = 1$ for $t_D > 0$

at $Z_D = 1$: $\frac{\partial C_D}{\partial Z_D} = 0$

The solution for equation (25) is then (Lake 1989)

$$C_D = \frac{1}{2} erfc\left(\frac{Z_D - t_D}{2\sqrt{\frac{t_D}{Pe}}}\right) + \frac{e^{Z_D Pe}}{2} erfc\left(\frac{Z_D - t_D}{2\sqrt{\frac{t_D}{Pe}}}\right) \tag{26}$$

where

$erf(\beta) = \frac{2}{\sqrt{\pi}}\int_0^z e^{-t^2} dt$ is the error function

and $erfc(\beta) = 1 - erf(\beta)$ is the complementary error function.

Özgür (2006, 2010) also conducted numerical modelling studies, and found that convection rate strongly increases with increasing permeability and dissolution trapping is strongly accelerated thereby. In diffusion dominated systems the dissolution rate is very slow, however, and only after 10^7 years the considered aquifer was completely saturated with CO_2. Higher dispersivity generally supports dissolution trapping.

It is moreover interesting to note that the mixing zone length Δz_D (which is defined as the distance between the points $C_D = 0.1$ and $C_D = 0.9$ in the reservoir, Lake 1989) reaches a value of 0.9 in diffusion dominated systems only after 10^5 years in Özgür's model. Increased porosity slightly increases Δz_D, and Δz_D strongly increases with permeability once

a threshold (when convection sets in) is reached. In convection dominated systems, porosity decreases Δz_D, while dispersivity slightly increases Δz_D.

6.2 The Lindeberg/Wessel-Berg model (1997)

Lindeberg and Wessel-Berg (1997) modelled the onset of convection in aquifers into which CO_2 has been injected. The water column in such aquifers can be unstable because of the density gradient introduced by molecular CO_2 diffusion into the brine.
In their simulation they solved the Darcy equation, heat conduction equation, equation of continuity and energy equation (details are described very thoroughly by Bear (1972)). They also included the equation of diffusion (27) so that diffusive mass transfer was considered.

$$\frac{\partial \rho}{\partial t} + \frac{j}{\phi}\nabla\rho = \nabla \cdot \left(\frac{D}{\phi}\nabla\rho \right) \tag{27}$$

where j is the volume flux.
They calculated the Rayleigh numbers for an array of model reservoirs, spanning a temperature range from 303-363 K, a pressure range from 10-30 MPa, a permeability range from 100-2000 mD, while the porosity was a constant 30%. Variations in pressure and temperature resulted in brine density variations between 1013.5-1036 kg/m^3 and molecular diffusion coefficients between 2.2-6.3 x 10^{-9} m^2/s. The brine density difference $\Delta\rho$ was 14.42 kg/m^3 due to difference in dissolved CO_2 concentration, while $\Delta\rho$ was only 2.847-2.910 kg/m^3 due to differences in temperature.
In Lindeberg and Wessel-Berg's model the water column is stable if only thermal gradients are considered, Ra lies then in the range 3.53-29.3 and no convection occurs (Ra_c = 39.5 in this case). However, if molecular CO_2 diffusion is considered (resulting in a significantly higher $\Delta\rho$), convection is predicted to occur. Lindeberg and Wessel-Berg define a stability criterion S which is the sum of the temperature and concentration effect on convective stability. S is analogous to Ra, and for infinite CO_2 dilution or an infinite molecular diffusion coefficient S becomes equal to Ra. The computed S values range from 1046-24204, and they are much higher than Ra_c. This means that convection will occur in aquifers under CCS conditions, which strongly enhances dissolution trapping and storage security. This convection is caused by the concentration gradient, not the temperature gradient. Lindeberg and Wessel-Berg (1997) suggest improvements for their model, especially a more sophisticated description of the concentration gradient should be implemented (they used a linearized concentration gradient). Moreover the Soret effect should be considered.

6.3 The Riaz model (2006)

Riaz et al. (2006) conducted a linear analysis and numerical simulations of the stability of the diffusive boundary layer (i.e. the brine layer adjacent to the $scCO_2$ phase into which the CO_2 diffuses) in a semi-infinite domain. Their calculations are based on Boussinesq-flow in a horizontal porous layer. The model neglects dispersion and geochemical reactions and assumes a homogenous and isotropic porous medium. Riaz et al. (2006) describe a critical time t_c (equation 28) which is a criterion for the onset of gravitational instability. For times larger than t_c convection will occur.

$$t_c = 146\frac{\phi\mu^2 D}{\left(K\Delta\rho g\right)^2} \tag{28}$$

t_c influences the penetration depth of the diffusive boundary layer δ(t), which again influences $Ra_c = Ra(\delta(t))$. t_c can vary over several magnitudes, mainly because permeability can span several magnitudes in a geological formation. For a permeability increase from 1 mD to 3 Darcy Riaz et al. (2006) calculated a t_c decrease from 2000 years to below 10 days, and associated with that δ(t) changed from 55 m (for 1 mD permeability) to 0.07 m.
The model also demonstrates that Ra has a strong influence on the finger-like flow in the reservoir, including finger thickness and shape. In terms of the numerical model they found that grid size plays an important role and a fine grid is required to resolve disturbances at small times. Correct identification of such early disturbances is necessary to obtain reliable results.
One important conclusion they make is that dissolution trapping is strongly enhanced in high permeability reservoirs. They estimate that the onset of gravitational instabilities - essentially induced by molecular diffusion mass transfer processes – occurs after several hundreds of years for typical aquifers with average permeability. It should be noted that these estimates are quite rough because of the assumptions made.

6.4 Summary of reservoir models

There are other reservoir models described in the literature, e.g. Ennis-King and Paterson (2005) conclude that anisotropy of the reservoir has a strong effect on dissolution trapping, but this is beyond the scope of this book chapter and the reader is encouraged to check current research; this is an active area of research.
The simulation results are very important for CCS assessments and project planning, but it must be emphasized that more experimental research should be conducted, in the laboratory and especially at field scale to evaluate the quality of the model predictions. In addition, it is important to stress the approximative character of these models, real field situations are much more complex, e.g. it is not clear whether Fick's law can describe diffusion in the field or whether very heterogeneous pore structures (for instance in carbonate reservoirs) enhance convection or slow it down.

7. Multiphase flow in the reservoir – flow of the $scCO_2$ phase

The flow of the $scCO_2$ phase affects the dissolution process as it determines interfacial areas and overall position of the CO_2 in the reservoir. Reservoir models predict that the injected CO_2 phase rises upwards and is stopped by the caprock (Qi et al. 2009, Juanes 2006, Hesse 2008). This behaviour has been confirmed experimentally in the Sleipner formation by seismic imaging (Iglauer 2011).
Small residual CO_2 clusters at the trailing edge of the rising CO_2 plume - trapped by capillary forces (Iglauer et al. 2010, Juanes et al. 2006) - strongly increase CO_2-brine interfacial areas. Hence CO_2 dissolution speed is predicted to be accelerated, especially if combined with convective flow of saturated/undersaturated brine. However experimental reservoir monitoring data is needed to confirm these predictions. Optimal conditions would be to bring undersaturated brine continuously into contact with residual micrometer-sized CO_2 bubbles while removing saturated or highly CO_2-enriched brine simultaneously. Engineering this dissolution phenomenon can be a promising topic for future research.
Moreover, and most likely even more significant in the short term - thereby strongly affecting the economics of CCS schemes are the fluid dynamics associated with CO_2 injection. CO_2 injectivity and CO_2-wellbore effects can strongly impact CCS schemes. For

example, flow in the reservoir is strongly influenced by changes in rock morphology and wettability, which can result in changes of relative permeabilites and capillary pressures of CO_2 and brine. Relative permeability and capillary pressures however strongly influence multi-phase fluid flow in the reservoir. As an example, there is evidence that wettability (Espinoza and Santamaria 2010, Chiquet et al. 2007) and rock pore morphology – especially carbonates (Luquot and Gouze 2009) are changed by $scCO_2$. More research work is required in this area to completely understand these changes and improve CCS risk assessment.

8. Conclusions

In summary it is clear that dissolution trapping is a potential solution for storing large quantities of anthropogenic CO_2 thereby reducing carbon emissions. More research is required, especially field testing with integrated monitoring to check how the CO_2 behaves under realistic injection and reservoir conditions in the medium-to-long term. The major advantages of dissolution trapping are that very substantial amounts of CO_2 can be stored very safely. The risk is that CO_2 dissolves too slowly so that a significant part of CO_2 is still in a mobile separate supercritical phase (separated from the brine phase) which is buoyant and could escape to the surface. There are however two other CCS mechanisms, structural and residual trapping which prevent or at least reduce the CO_2 leakage risk. It must also be guaranteed that no drinkable-water aquifers are contaminated with CO_2 or any harmful species mobilized by CO_2 injection (e.g. dissolution of heavy metal ions by the acidic brine generated), which may then be transported into drinking water reservoirs.

9. Acknowledgements

I would like to thank Prof. Martin Blunt, Prof. Tetsuya Suekane, Dr. Amer Syed and Prof. Abbas Firoozabadi for reviewing this book chapter and helpful comments. Many thanks go to Prof. Zhenhao Duan for supplying the CO_2 solubility calculator software.

10. Nomenclature

CCS	carbon capture and storage (of carbon dioxide)
CO_2	carbon dioxide
HCO_3^-	hydrogen carbonate anion
CO_3^{2-}	carbonate anion
H^+	proton
HC	hydrocarbon
a	year
Gt	Gigatons = 10^9 tons
ϕ	porosity [-]
K	permeability [m^2]
M	molar mass [g/mol]
μ	viscosity [Pa.s]
ρ_{CO2}	CO_2 density [kg/m^3]
GOR	gas-oil ratio [m^3/m^3]
H	domain depth; reservoir height [m]
D	diffusion coefficient [m^2/s]

$D_{CO2-H2O}$	diffusion coefficient of CO_2 into brine [m^2/s]
$D_{H2O-CO2}$	diffusion coefficient of H_2O into $scCO_2$ [m^2/s]
D_{CO2-HC}	diffusion coefficient of CO_2 into hydrocarbon [m^2/s]
$D_{CO2-C10}$	diffusion coefficient of CO_2 into n-decane [m^2/s]
p	pressure [Pa]
T	temperature [K]
μ	viscosity [Pa.s]
μ_{CO2}	viscosity of CO_2 [Pa.s]
μ_{H2O}	viscosity of water [Pa.s]
ρ	density [kg/m^3]
ρ_{brine}	density of brine [kg/m^3]
$\rho_{CO2,brine}$	density of CO_2-enriched brine [kg/m^3]
$\Delta\rho$	density difference [kg/m^3]
g	gravitational constant [m/s^2]
y	molality [mol/kg]
R	universal gas constant [J/mol.K]
$\mu_{CO_2}^{1(0)}$	standard chemical potential of CO_2 [J/mol]
F	fugacity coefficient [-]
$\zeta_{CO2-Na-Cl}$	interaction parameter between CO_2 and Na^+ and Cl^-
λ_{CO2-Na}	interaction parameter between CO_2 and Na^+
H	reservoir height [m]
Z_D	normalized reservoir height [-]
$V_{m,brine}$	apparent molar volume of CO_2 in brine [m^3/mol]
V_{CO2}	molar volume of CO_2 [m^3/mol]
Y_{CO2}	dissolved CO_2 mass fraction [-]
t_D	dimensionless time [-]
t	time [s]
u	interstitial or pore flow velocity [m/s]
Ra	Rayleigh number [-]
Re	Reynolds number [-]
Sh	Sherwood number [-]
Sc	Schmidt number [-]
z	depth [m]
α	dispersivity [m]
α_L	longitudinal dispersivity [m]
D_{dis}	dispersion coefficient [m^2/s]
C_0	surface concentration of droplet [mol/L]
C_∞	concentration at infinity [mol/L]
A	surface area of CO_2 droplet [m^2]
k	mass transfer coefficient [m/s]
j	volumetric flux [m/s]

11. References

Adamczyk, K., Premont-Schwarz, M., Pines, D., Pines, E., Nibbering, E.T.J. (2009). Real-time observation of carbonic acid formation in aqueous solution", *Science*, 326, 1690-1694.

Andarko (2010). *Wyoming Fact Sheet*.

Al-Mansoori, S.K., Itsekiri, E., Iglauer, S., Pentland, C.H., Bijeljic, B., Blunt, M.J. (2010). Measurements of non-wetting phase trapping applied to carbon dioxide storage, *International Journal of Greenhouse Gas Control*, 4, 283-288.

Bachu, S. (2000). Sequestration of CO_2 in geological media: criteria and approach for site selection in response to climate change, *Energy Conversion and Management*, 41,953-970.

Bachu, S., Adams, J.J. (2003). Sequestration of CO_2 in geological media in response to climate change: capacity of deep saline aquifers to sequester CO_2 in solution, *Energy Conversion and Management*, 44, 3151-3175.

Badessich, M.F., Gait, M., Carbone, C., Dzelalija, F., Giampaoli, P. (2005). Integrated reservoir characterization for the redevelopment of a highly complex field, SPE 93797, *Proceedings of the SPE Europec/EAGE Annual Conference*, Madrid, Spain, 13-16 June.

Bahar, M., Liu, K. (2008). Measurement of the diffusion coefficient of CO_2 in formation water under reservoir conditions: implications for CO_2 storage, SPE 116513, *Proceedings of the SPE Asia Pacific Oil & Gas Conference and Exhibition*, Perth, Australia, 20-22 October.

Ballentine, C.J., Schoell, M., Coleman, D., Cain, B.A. (2001). 300-Myr-old magmatic CO_2 in natural gas reservoirs of the west Texas Permian basin, *Nature*, 409, 327-331.

Bando, S., Takemura, F., Nishio, M., Hihara, E., Akai, M. (2003). Solubility of CO_2 in aqueous solutions of NaCl at (30 to 60) ^oC and (10 to 20) MPa, *Journal of Chemical & Engineering Data*, 48, 576-579.

Bear, J. (1972). *Dynamics of fluids in porous media*, New York: Dover Publications.

Blunt, M.J., Fayers, F.J., Orr, F.M. (1993) Carbon dioxide in enhanced oil recovery *Energy Conversion and Management*, 34, 9-11, 1197- 1204.

Chiquet, P., Broseta, D., Thibeau, S. (2007). Wettability alteration of caprock minerals by carbon dioxide, *Geofluids*, 7, 112-122.

Dake, L.P. (2007). *Fundamentals of reservoir engineering*, Elsevier: Amsterdam.

Dandekar, A.Y. (2006). *Petroleum reservoir rock and fluid properties*, Boca Raton: Taylor & Francis.

Vega Maza, D. (2011). *Private communication*.

De Ruiter, R.A., Nash, L.J., Singletary, M.S. (1994). Solubility and displacement behavior of a viscous crude with CO_2 and hydrocarbon gas, *SPE Reservoir Engineering*, 101-106.

Dickson, J.L., Gupta, G., Horozov, T.S., Binks, B.P., Johnston, K.P. (2006). Wetting phenomena at the CO_2/water/glass interface, *Langmuir*, 22, 2161-2170.

Duan, Z., Sun, R. (2003). An improved model calculating CO_2 solubility in pure water and aqueous NaCl solutions from 273 to 533 K and from 0 to 2000 bar, *Chemical Geology*, 193, 257-271.

Duan, Z., Sun, R., Zhu, C., Chou, I.-M. (2006). An improved model for the calculation of CO_2 solubilites in aqueous solutions containing Na^+, K^+, Ca^{2+}, Mg^{2+}, Cl^- and SO_4^{2-}, *Marine Chemistry*, 98, 131-139.

Egermann, P., Bazin, B., Vizika, O. (2005). An experimental investigation of reaction-transport phenomena during CO_2 injection, SPE 93674, P*roceedings of the 14th Middle East Oil & Gas Show*, Bahrain.

Enick, R.M., Klara, S.M. (1990). CO_2 solubility in water and brine under reservoir conditions, *Chem. Eng. Comm.*, 90, 23-22.

Ennis-King J., Paterson, L. (2005). Role of convective mixing in the long-term storage of carbon dioxide in deep saline formations, *SPE Journal*, 10, 3, 349-356.

Espinoza, D.N., Santamarina, J.C. (2010). Water-CO_2-mineral systems: interfacial tension, contact angle, and diffusion-implications to CO_2 geological storage, *Water Resources Research*, 46, W07537.

Firoozabadi, A., Cheng, P. (2010). Prospects for subsurface CO_2 sequestration, *AIChE Journal*, 56, 6, 1398-1405.

Fridleifsson, I.B., Bertani, R., Huenges, E., Lund, J.W., Ragnarsson, A., Rybach, L. (2008). The possible role and contribution of geothermal energy to the mitigation of climate change. In: O. Hohmeyer and T. Trittin (Eds.) IPCC Scoping Meeting on Renewable Energy Sources, Luebeck, Germany.

Garcia, J. E. (2001). Density of aqueous solutions of CO_2, *Report LBNL-49023*, Lawrence Berkeley National Laboratory, CA.

Gaus, I. (2010). Role and impact of CO_2-rock interactions during CO_2 storage in sedimentary rocks, *International Journal of Greenhouse Gas Control*, 4, 73-89.

Gilfillan, S.M.V., Sherwood Lollar, B., Holland, G., Blagburn, D., Stevens, S., Schoell, M., Cassidy, M., Ding, Z., Zhou, Z., Lacrampe-Couloume, G., Ballentine, C.J. (2009). Solubility trapping in formation water as dominant CO_2 sink in natural gas fields, *Nature*, 458, 2, 614-618.

Green, D.W., Willhite, G.P. (1998). *Enhanced oil recovery*, Richardson: SPE Publications.

Hesse, M.A., Orr, F.M., Tchelepi, H.A. (2008). Gravity currents with residual trapping, *Journal of Fluid Mechanics*, 611, 35-60.

Hirai, S., Okazaki, K., Yazawa, H., Ito, H., Tabe, Y., Hijikata, K. (1997). Measurement of CO_2 diffusion coefficient and application of LIF in pressurized water, *Energy*, 22, 2-3, 363-367.

Iglauer, S. (2011). *Carbon capture and storage with a focus on capillary trapping as a mechanism to store carbon dioxide in geological porous media*, in Advances in Multiphase Flow and Heat Transfer, volume 3, chapter 4, 177-197 (eds. L. Cheng and D. Mewes) [in press]

Iglauer, S., Favretto, S, Spinelli, G., Schena, G., Blunt, M.J. (2010). X-ray tomography measurements of power-law cluster size distributions for the nonwetting phase in sandstones, *Physical Review E*, 82, 056315.

Iglauer, S., Wülling, W., Pentland, C.H., Al Mansoori, S.K., Blunt, M.J. (2009). Capillary trapping capacity of rocks and sandpacks. SPE 120960, *Proceedings of the SPE EUROPEC/EAGE Annual Conference and Exhibition*, Amsterdam, The Netherlands.

Intergovernmental Panel on Climate Change (IPCC), (2005). *IPCC Special Report on Carbon Dioxide Capture and Storage. Prepared by Working Group III of the Intergovernmental Panel on Climate Change*, Cambridge University Press.

Intergovernmental Panel on Climate Change (IPCC) (2007). *Climate Change 2007: The Physical Science Basis. Working Group I Contribution to the Fourth Assessment Report of the Intergovernmental Panel on Climate Change*, Cambridge University Press.

Juanes, R., Spiteri, E.J., Orr, F.M., Blunt, M.J. (2006). Impact of relative permeability hysteresis on geological CO_2 storage, *Water Resources Research*, 42, W12418.

Kiepe, J., Horstmann, S., Fischer, K., Gmehling, J. (2002). Experimental determination and prediction of gas solubility data for CO_2 + H_2O mixtures containing NaCl or KCl at temperatures between 313 and 393 K and pressures up to 10 MPa, *Industrial and Engineering Chemistry Research*, 41, 4393-4398.

Kokal, S.L., Sayegh, S.G. (1993). Phase behavior and physical properties of CO_2-saturated heavy oil and its constitutive fractions: experimental data and correlations, *Journal of Petroleum Science and Engineering*, 9, 289-302.

Koschel, D., Coxam, J.-Y., Rodier, L., Majer, V. (2006). Enthalpy and solubility data of CO_2 in water and $NaCl_{(aq)}$ at conditions of interest for geological sequestration, *Fluid Phase Equilibria*, 247, 107-120.

Lake, L. W. (1989). *Enhanced oil recovery*, New Jersey: Prentice-Hall.

Li, Z., Dong, M., Li, S., Dai, L. (2004). Densities and solubilities for binary systems of carbon dioxide + water and carbon dioxide + brine at 59°C and pressures to 29 MPa, *J. Chem. Eng. Data*, 49, 4, 1026-1031.

Li, Z., Firoozabadi, A. (2009). Cubic-plus-association equation of state for water-containing mixtures: is cross association necessary?, *AIChEJ*, 55, 1803.

Lindeberg, E., Wessel-Berg, D. (1997). Vertical convection in an aquifer column under a gas cap of CO_2, *Energy Conversion Management*, 38, 1, 229-234.

Luquot, L., Gouze, P. (2009). Experimental determination of porosity and permeability changes induced by injection of CO_2 into carbonate rocks, *Chemical Geology*, 265, 148-159.

Mazarei, A.F., Sandall, O.C. (1980). Diffusion coefficients for helium, hydrogen and carbon dioxide in water at 25°C, *AIChE Journal*, 26, 1, 154-157.

McCain, W.D. (1990). *The properties of petroleum fluids*, Tulsa: Penn Well Corporation.

McCain, W.D. (1991). Reservoir fluid property correlations-state of the art, *SPE Reservoir Engineering*, 6, 266-272.

Moortgat, J., Sun, S., Firoozabadi, A. (2011). Compositional modeling of three-phase flow with gravity using higher-order finite element methods, *Water Resources Research*, 47, W05511.

Mutoru, J.W., Leahy-Dios, A., Firoozabadi, A. (2011). Modeling infinite dilution and Fickian diffusion coefficients of carbon dioxide in water, *AIChE Journal*, 57, 6, 1617-1627.

Nighswander, J.A., Kalogerakis, N., Mehrotra, K. (1989). Solubilities of carbon dioxide in water and 1 wt% NaCl solution at pressures up to 10 MPa and temperatures from 80 to 200° C, *J. Chem. Eng. Data*, 34, 355-360.

Özgür, E. (2006). *Assessment of diffusive and convective mechanisms during carbon dioxide sequestration into deep saline aquifers*, PhD thesis, Middle East Technical University, Ankara, Turkey.

Özgür, E., Gümrah, F. (2010). Analytical and numerical modeling of CO_2 sequestration in deep saline aquifers. *Energy Sources*, Part A, 32, 674-687.

Pau, G.S.H., Bell, J.B., Pruess, K., Almgren, A.S., Lijewski, M.J., Zhang, K. (2010). High-resolution simulation and characterisation of density-driven flow in CO_2 storage in saline aquifers, *Advances in Water Resources*, 33, 443-455.

Pentland, C.H., Itsekiri, E., Al-Mansoori, S.K., Iglauer, S., Bijeljic, B., Blunt, M.J. (2010). Measurements of nonwetting-phase trapping in sandpacks, *SPE Journal*, 38, 274-281.

Pentland, C.H. (2011a). *Measurements of non-wetting phase trapping in porous media*, PhD thesis, Imperial College London, UK.

Pentland, C.H., El-Maghraby, R., Iglauer, S., Blunt, M.J. (2011b). Measurements of the capillary trapping of supercritical carbon dioxide in Berea sandstone, *Geophysical Research Letters,* 38, L06401.

Piri, M., Blunt, M.J. (2005). Three-dimensional mixed-wet random pore-scale network modeling of two- and three-phase flow in porous media. I. Model description, *Physical Review E*, 71, 026301.

Pocker, Y., Bjorkquist, D.W. (1977). Stopped-flow studies of carbon dioxide hydration and bicarbonate dehydration in H_2O and D_2O. Acid-base and metal ion catalysis, *Journal of the Americal Chemical Society*, 99, 20, 6537-6543.

Pruess, K., Garcia, J. (2002). Multiphase flow dynamics during CO_2 disposal into saline aquifers, *Environmental Geology*, 42, 282-295.

PTRC, Petroleum Technology Research Center, 6 Research Drive Regina, SK, Canada [online]. Available: http://www.ptrc.ca/weyburn_overview.php. [accessed: 22.3.2011].

Qi, R., LaForce, T.C., Blunt, M.J. (2009). Design of carbon dioxide storage in aquifers, *International Journal of Greenhouse Gas Control*, 3, 195-205.

Reeves, S., Oudinot, A. (2005). The Allison CO_2 ECBM pilot: A reservoir and economic analysis, *Proceedings of the International Coalbed Methane Symposium, Tuscaloosa, USA, May 17-19,* Paper 0522.

Rumble, D., Ferry, J.M., Hoering, T.C., Boucot, A.J. (1982). Fluid flow during metamorphism at the Beaver Brook fossil locality, New Hampshire, *American Journal of Science*, 282, 886-919.

Rumpf, B., Nicolaisen, H., Őcal, C., Maurer, G. (1994). Solubility of carbon dioxide in aqueous solutions and sodium chloride: experimental results and correlation, *Journal of Solution Chemistry*, 23, 3, 431-448.

Reamer, H.H., Sage, B.H. (1963). Phase equilibria in hydrocarbon systems. Volumetric and phase behavior of the n-decane-CO_2 system, *J. Chem. Eng. Data*, 8, 508.

Renner, T.A. (1988). Measurement and correlation of diffusion coefficients for CO_2 and rich-gas applications, *SPE Reservoir Engineering*, 3, 2, 517-523.

Riaz, A., Hesse, M., Tchelepi, H.A., Orr, F.M. (2006). Onset of convection in a gravitationally unstable diffusive boundary layer in porous media, *Journal of Fluid Mechanics*, 548, 87-111.

Sabirzyanov, A.N., Il'in, A.P., Akhunov, A.R., Gumerov, F.M. (2002). Solubility of water in supercritical carbon dioxide, *High Temperature*, 40, 2, 203-206.

Sabirzyanov, A.N., Shagiakhmetov, R.A., Gabitov, F.R., Tarzimanov, A.A., Gumerov, F.M. (2003). Water solubility of carbon dioxide under supercritical and subcritical conditions, *Theoretical Foundations of Chemical Engineering*, 37, 1, 51-53.

Schaeff, H.T., McGrail, B.P. (2004). Direct measurements of pH in H_2O-CO_2 brine mixtures to supercritical conditions, *Proceedings of the 7th International Conference on Greenhouse Gas Control Technologies (GHGT-7)*, Vancouver, Canada.

Schulze-Makuch, D. (2005). Longitudinal dispersivity data and implications for scaling behavior, *Groundwater*, 43, 3, 443-456.

Shimizu, K., Kikkawa, N., Nagashima, A. (1995). *Proceedings of the 4th Asian Thermophysical Properties Conference*, 3, 771.

Span, R., Wagner, W. (1996). A new equation of state for carbon dioxide covering the fluid region from the triple-point temperature to 1100 K at pressures up to 800 MPa. *Journal of Physical and Chemical Reference Data*, 25, 6, 1509-1596.

Stumm, W., Morgan, J.J. (1996). *Aquatic chemistry: chemical equilibria and rates in natural waters*, New York: John Wiley and Sons.

Suekane, T., Mizumoto, A., Nobuso, T., Yamazaki, M., Tsushima, S., Hirai, S. (2006). Solubility and residual gas trapping of CO_2 in geological storage, *Proceedings of the 8th International Conference on Greenhouse Gas Control Technologies GHGT-8* (CD-ROM).

Tang, Y.P., Himmelblau, D.M. (1965). Effect of solute concentration on the diffusivity of carbon dioxide in water, *Chemcial Engineering Sciences*, 20, 7-14.

Total, [online], available: http://www.total.com/en/special-reports/capture-and-geological-storage-of-co2/capture-and-geological-storage-of-co2-the-lacq-demonstration-200969.html, [accessed: 22.3.2011].

Unver, A.A, Himmelblau, D.M. (1964). Diffusion coefficients of CO_2, C_2H_4, C_3H_6, and C_4H_8 in water from 6°C to 65°C, *Journal of Chemical and Engineering Data*, 9, 3, 428-431.

Weatherill, D., Simmons, C. T., Voss, C. I., and Robinson, N. I. (2004). Testing density-dependent groundwater models: two-dimensional steady state unstable convection in infinite, finite and inclined porous layers, *Advances in Water Resources*, 27, 547-562.

Wilke, C.R., Chang, P. (1955). Correlation of diffusion coefficients in dilute solutions. *Am. Inst. Chem. Eng. J.*, 1, 264-270.

Xu, T.F., Apps, J.A., Pruess, K. (2003). Reactive geochemical transport simulation to study mineral trapping for CO_2 disposal in deep arenaceous formations", *Journal of Geophysical Research*, 108, B2, 2071.

Yasunishi, A., Yoshida, F. (1979). Solubility of carbon dioxide in aqueous electrolyte solutions, *J. Chem. Eng. Data,* 24, 1, 11-14.

11

Electrochemistry of Tm(III) and Yb(III) in Molten Salts

Alena Novoselova[1], Valeri Smolenski[1],
Alexander Osipenko[2] and Michael Kormilitsyn[2]
[1]*Institute of High-Temperature Electrochemistry, Ural Division, Russian Academy of Science,*
[2]*Research Institute of Atomic Reactors, Russia*

1. Introduction

Pyrochemical processes appeared today gives an interesting option for future nuclear fuel cycles in several aspects. These latter will have to provide high recovery yields for actinides elements, (taking into account the sustainability requirement) to be safe, resistant versus proliferation risks, and cost-effective. This lead to a rather prolific research today, with many innovative concepts for future reactors, future fuels, and obviously future processes. Pyrochemical processes seems in this context to offer significant-established or presumed-advantages: (i) low radiolytical effects versus solvent processes (which increases the ability to process high burn-up, short-time cooled hot fuels); (ii) ability to dissolve new ceramic or dense fuel compounds; (iii) presumed compactness of technology (low number of transformation steps, small size of unit operations) [Uozumi, 2004; Willit, 2005].

Partitioning and transmutation (P&T) concept is nowadays considered as one of the strategies to reduce the long-term radiotoxicity of the nuclear wastes [Kinoshita et al., 2000]. To achieve this, the efficient recovery and multi-recycling of actinides (An), especially TRU elements, in advanced dedicated reactors is essential. Fuels proposed to transmute the actinides into short-lived or even stable radionuclides will contain significant amounts of Pu and minor actinides (Np, Am, Cm), possibly dissolved in inert matrices (U free), and will reach high burn-ups. Pyrochemical separation techniques offer some potential advantages compared to the hydrometallurgical processes to separate actinides from fission products (FP) contained in the irradiated fuel. The high radiation stability of the salt or metallic solvents used, resulting in shorter fuel cooling times stands out.

The aim of the separation techniques which are currently being investigated, both hydrometallurgical and pyrometallurgical ones, is to optimize the recovery efficiency of minor actinides minimizing at the same time the fission products (FP) content in the final product. Special attention is devoted to rare earth elements (REE) mainly due to its neutronic poison effect and the high content into the spend fuel. In addition, REE have similar chemical properties [Bermejo et al., 2006, 2007, 2008a, 2008b; Castrillejo et al., 2005a, 2005b, 2005c, 2009; De Cordoba et al., 2004, 2008; Kuznetsov et al., 2006; Novoselova &

Smolenski, 2010; Smolenski et al., 2008a, 2008b, 2009] to those of actinides [Fusselman et al., 1999; Morss, 2008; Osipenko et al., 2010, 2011; Roy et al., 1996; Sakamura et al., 1998; Serp et al., 2004, 2005a, 2005b, 2006; Serrano & Taxil, 1999; Shirai et al., 2000] hence separation between these groups of elements is very difficult. For this reason, a good knowledge of the basic properties of REE in the proposed separation media is very important.
The goal of these investigations is to determine the electrochemical and thermodynamic properties of some fission products (Tm and Yb), their mass transfer, and behavior in different fused solvents using transient electrochemical techniques, and potentiometric method (*emf*).

2. Experimental

2.1 Preparation of starting materials

The solvents LiCl (Aldrich, 99.9%), NaCl (Aldrich, 99.9%), KCl (Aldrich, 99.9%), and CsCl(Aldrich, 99.9%) were purified under vacuum in the temperatures range 293-773 K. Then the reagents were fused under dry argon atmosphere. Afterwards these reagents were purified by the operation of the direct crystallization [Shishkin & Mityaev, 1982]. The calculated amounts of prepared solvents were melted in the cell before any experiment [Korshunov et al., 1979].
Dry lanthanide trichlorides ($LnCl_3$) were obtained by the way of well-known method [Revzin, 1967] in two steps:

- First, the crystalline hydrate ($LnCl_3 \cdot nH_2O$, where n is 4.5-5.0) was prepared by direct interaction of Ln_2O_3 (Tm_2O_3 OST 46-205-81 TuO-1 and Yb_2O_3 IbO-L TU 48-4-524-90) with HCl acid solution.
- Second, dry $LnCl_3$ was prepared by using the operation of carbochlorination of crystalline hydrate during heating in CCl_4 stream vapor in horizontal furnace.

The obtained lanthanide chlorides ($LnCl_3$) were kept into glass ampoules under atmosphere of dry argon in inert glove box. Ln^{3+} ions were prepared by direct addition of anhydrous $LnCl_3$ to the fused electrolytic bath.

2.2 Transient electrochemical technique

The experiments were carried out under inert argon atmosphere using a standard electrochemical quartz sealed cell using a three electrodes setup. Different transient electrochemical techniques were used such as linear sweep, cyclic, square wave and semi-integral voltammetry, as well as potentiometry at zero current. The electrochemical measurements were carried out using an Autolab PGSTAT30 potentiostat-galvanostat (Eco-Chimie) with specific GPES electrochemical software (version 4.9).
The inert working electrode was prepared using a 1mm metallic W wire (Goodfellow, 99.9%). It was immersed into the molten bath between 3 - 10 mm. The active surface area was determined after each experiment by measuring the immersion depth of the electrode. The counter electrode consisted of a 3 mm vitreous carbon rod (SU - 2000). The Cl^-/Cl_2 electrode is the most convenient reference electrode because it can be used for the direct thermodynamic calculations. It standard construction is the following. The quartz tube with porous membrane in the bottom and molten solvent in it has the graphite tube for chlorine gas introduction into the system. The chlorine gas is bubbling through the melt during the experiment [Smirnov, 1973].

The lanthanide concentrations were determined by taking samples from the melt which were dissolved in nitric acid solutions and then analyzed by ICP-MS.

2.3 Direct potentiometric method

The potentiometric study was carried out using an Autolab PGSTAT30 potentiostat-galvanostat (Eco-Chimie) with specific GPES electrochemical software (version 4.9). The electrochemical techniques were used such as potentiometry (zero current) and coulometry methods.

The electrochemical set-up for potentiometric investigations is shown in Fig. 1. The inert working electrode was prepared using a 5 mm vitreous carbon rod (SU - 2000) which was located in BeO crucible with the investigated melt. It was immersed into the molten bath between 3 - 5 mm. During the experiments Ln^{3+} ions were electrochemically reduced to Ln^{2+} ions up to ratio Ln^{3+}/Ln^{2+} equals one. The counter electrode consisted of a 3 mm vitreous carbon rod (SU - 2000) which was placed in quartz tube with porous membrane in the bottom with solvent melt and located in vitreous carbon crucible (SU - 2000) with pure solvent without lanthanide chlorides. The Cl^-/Cl_2 electrode was used as reference electrode.

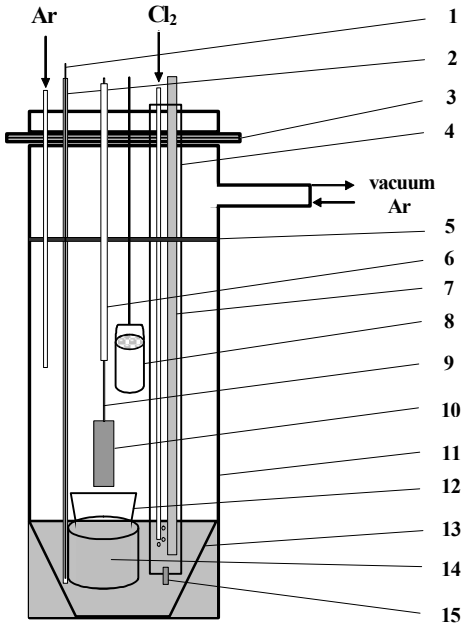

1 – Pt/Pt-Rh thermocouple; 2- Cover of thermocouple; 3- Section; 4- Capsule of chlorine electrode; 5- Nickel screen; 6- Alumina tube; 7- Cl^-/Cl_2 reference electrode/counter electrode; 8- Getter of zirconium; 9- Current contact; 10- Vitreous carbon working electrode; 11- Quartz test-tube with cover; 12- Beryllium oxide crucible; 13- Vitreous carbon crucible; 14- Investigated salt system; 15- Asbestos diaphragm.

Fig. 1. Experimental set-up for potentiometric study

The total lanthanide concentrations were determined by taking samples from the melt which were dissolved in nitric acid solutions and then analysed by ICP-MS. The concentration of the reduced form of lanthanides was determined by volumetric method.

3. Results and discussion

3.1 Transient electrochemical technique

3.1.1 Voltammetric studies on inert electrodes

Cyclic voltammetry was carried out on inert tungsten electrodes for all melts tested: eutectic LiCl-KCl, equimolar NaCl-KCl, eutectic NaCl-KCl-CsCl and individual CsCl, at several temperatures (723-1073 K). Fig. 2 (red solid line) shows the electrochemical window obtained in LiCl-KCl at 723 K. The cathodic and anodic limits of the electrochemical window correspond to the reduction of the solvent alkali metal ions and to the oxidation of chloride ions into chlorine gas, respectively.

Fig. 2 also plots the cyclic voltammogram of a LiCl-KCl-$YbCl_3$ solution on W at 723K (blue solid line). It shows a single cathodic peak at a potential of -1.762V vs. Cl^-/Cl_2 and its corresponding anodic peak at -1.566V vs. the Cl^-/Cl_2. Similar behaviour for the reduction of Yb(III) ions has been observed in the fused equimolar NaCl-KCl mixture (Fig. 3), NaCl-KCl-CsCl eutectic (Fig. 4) and CsCl (Fig. 5). These figures show the linear sweep and the cyclic voltammograms obtained in the above systems with $YbCl_3$ at several scan rates, respectively.

The square wave voltammetry technique was used to determine the number of electrons exchanged in the reduction of Yb(III) ions in different molten compositions. Fig. 6 shows the bell-shaped symmetric cathodic wave obtained in the LiCl-KCl-$YbCl_3$ melt at 723 K. The number of electrons exchanged is determined by measuring the width at half height of the reduction peak, $W_{1/2}$ (V), registered at different frequencies (6– 80 Hz). $W_{1/2}$ is given by the following equation, valid for reversible systems:

$$W_{1/2} = 3.52\frac{RT}{nF} \tag{1}$$

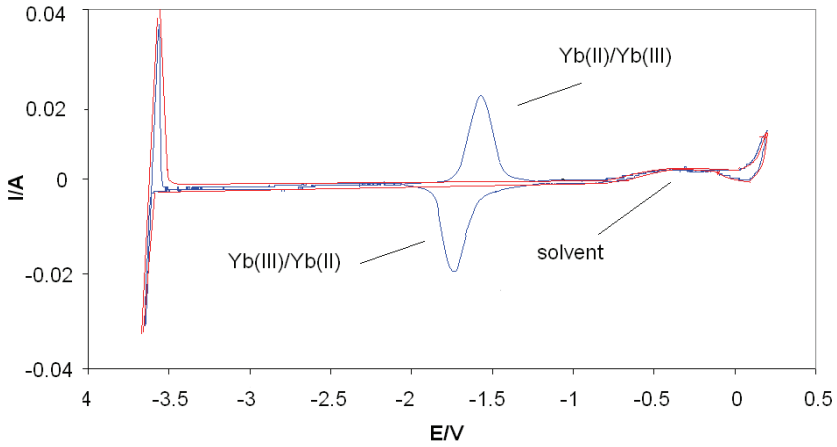

Fig. 2. Cyclic voltammograms of pure LiCl-KCl eutectic melt (red solid line). Cyclic voltammograms of LiCl-KCl-$YbCl_3$ ($9.41\cdot10^{-2}$ mol/kg) melt (blue solid line) corresponding to the reduction reaction $Yb(III) + e^- \Leftrightarrow Yb(II)$ at 723 K. Working electrode: W (surface area = 0.25 cm^2). Scan rate = 0.1 V s^{-1}

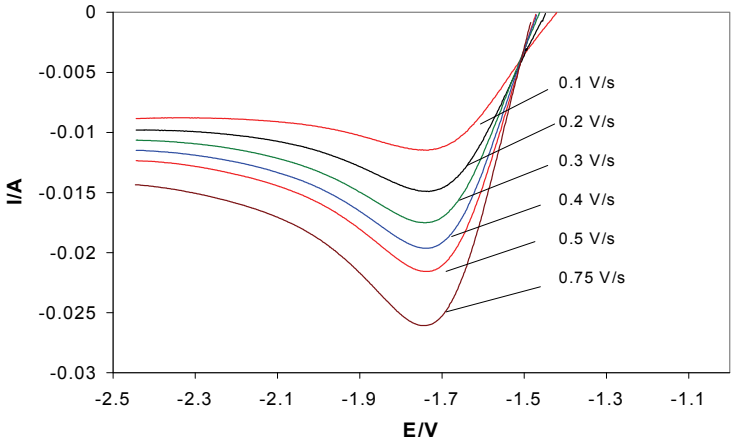

Fig. 3. Linear sweep voltammograms of fused NaCl-KCl-$YbCl_3$ ($3.79 \cdot 10^{-2}$ mol/kg) for the reduction of Yb(III) to Yb(II) ions at different sweep potential rates at 973 K. Working electrode: W (surface area = 0.27 cm^2)

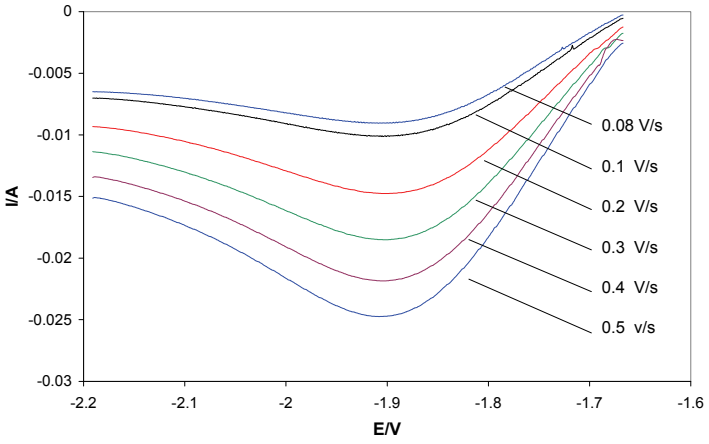

Fig. 4. Linear sweep voltammograms of fused NaCl-KCl-CsCl-$YbCl_3$ salt at different sweep rates at 873 K. [Yb(III)] = $7.45 \cdot 10^{-2}$ mol kg^{-1}. Working electrode: W (S = 0.36 cm^2)

At low frequencies a linear relationship between the cathodic peak current and the square root of the frequency was found. Under these conditions the system can be considered as reversible and equation 1 can be applied [Bard & Faulkner, 1980]. The number of electrons exchanged was close to 1. The same results were obtained in NaCl-KCl, NaCl-KCl-CsCl and CsCl media.

Potentiostatic electrolysis at potentials of the cathodic peaks for all systems studied did not show the formation of the solid phase of tungsten surface after polarization. There is no plateau on the dependences potential – time. Also the working electrode did not undergo any visual change. X-ray analysis of the surface of the working electrodes after experiments also show an absence of formation of solid phase.

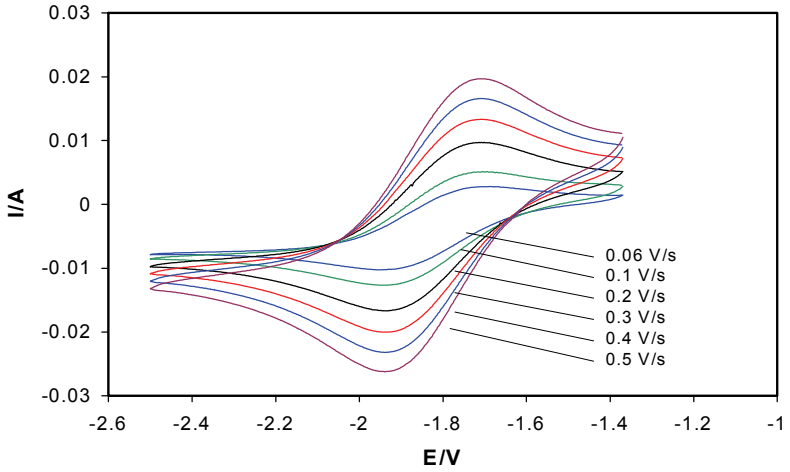

Fig. 5. Cyclic voltammograms of a CsCl-$YbCl_3$ ($3.70 \cdot 10^{-2}$ mol/kg) solution for the reaction $Yb(III) + e^- \Leftrightarrow Yb(II)$ at different potential sweep rates at 973 K. Working electrode: W (surface area = 0.31 cm^2)

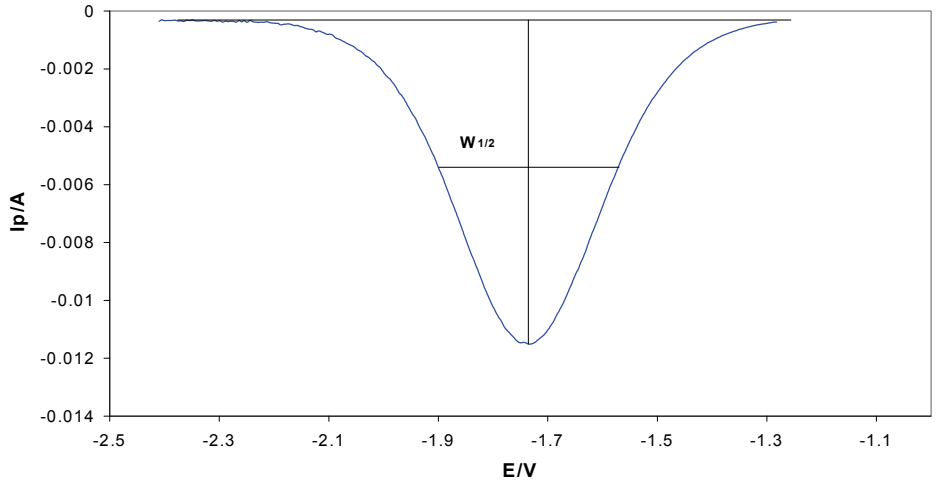

Fig. 6. Square wave voltammogram of LiCl-KCl-$YbCl_3$ ($9.41 \cdot 10^{-2}$ mol/kg) at 12 Hz at 723 K. Working electrode: W (surface area = 0.25 cm^2)

The results obtained allow concluding that the reduction of Yb(III) ions takes place in a single step with the exchange of one electron and the formation of a soluble product, according to the following reaction:

$$Yb(III) + \bar{e} \Leftrightarrow Yb(II) \quad (2)$$

The reaction mechanism of the soluble-soluble Yb(III)/Yb(II) redox system was investigated by analyzing the voltammetric curves obtained at several scan rates. It shows that the

cathodic and anodic peak potential (E_p) is constant and independent of the potential sweep rate (Fig. 7). On the other hand the cathodic and anodic peak current (I_p) is directly proportional to the square root of the polarization rate (υ) (Fig. 8). A linear relationship between the cathodic peak current density and the concentration of $YbCl_3$ ions in the melt was observed (Fig. 9). From these results and according to the theory of linear sweep voltammetry technique [Bard & Faulkner, 1980] it is concluded that the redox system Yb(III)/Yb(II) is a reversible and controlled by the rate of the mass transfer.

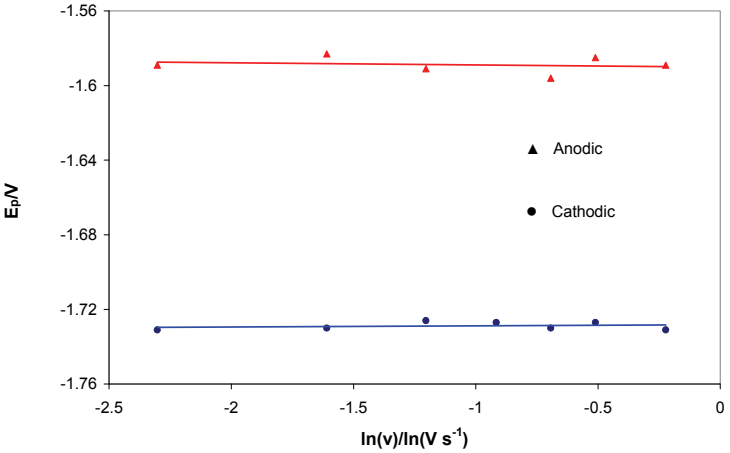

Fig. 7. Variation of the cathodic and anodic peak potential as a function of the sweep rate in fused LiCl-KCl-$YbCl_3$ ($9.41 \cdot 10^{-2}$ mol/kg) at 723K. Working electrode: W (surface area = 0.25 cm^2)

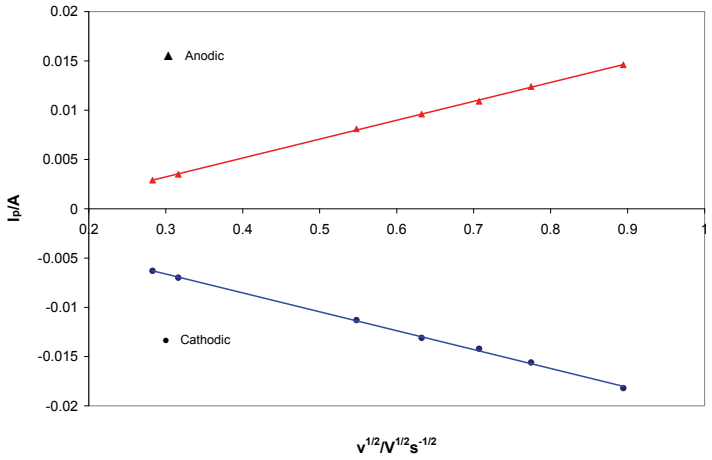

Fig. 8. Variation of the cathodic and anodic peak current as a function of the square root of the potential scan rate in fused LiCl-KCl-$YbCl_3$ ($9.41 \cdot 10^{-2}$ mol/kg) at 723K. Working electrode: W (surface area = 0.25 cm^2)

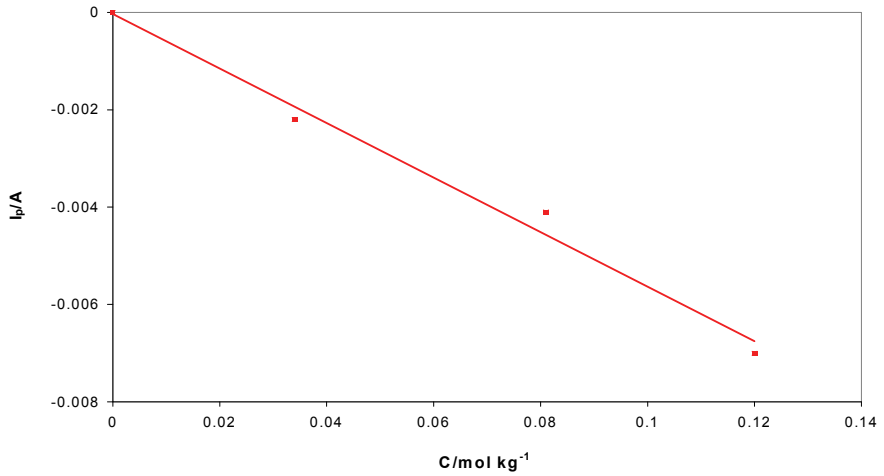

Fig. 9. Variation of the cathodic peak current as a function of the concentration of $YbCl_3$ in LiCl-KCl-$YbCl_3$ at 723 K. Working electrode: W (S = 0.25 cm^2). Scan rate = 0.1 V s^{-1}

From the transient electrochemical techniques applied we concluded that the potential of the system [Yb(II)/Yb(0)] can not be observed in the molten alkali chlorides media because it is more negative than the potential of the solvent Me(I)/Me(0), being Me: Li, Na, K and Cs, (Fig. 1).

3.1.2 Diffusion coefficient of Yb (III) ions

The diffusion coefficient of Yb(III) ions in molten chloride media was determined using the cyclic voltammetry technique and applying the Randles-Sevčik equation, valid for reversible soluble-soluble system [Bard & Faulkner, 1980]:

$$I_p = 0.446(nF)^{3/2} C_0 S \left(\frac{D\nu}{RT} \right)^{1/2} \tag{3}$$

where S is the electrode surface area (in cm^2), C_0 is the solute concentration (in mol cm^{-3}), D is the diffusion coefficient (in cm^2 s^{-1}), F is the Faraday constant (in 96500 C mol^{-1}), R is the ideal gas constant (in J K^{-1} mol^{-1}), n is the number of exchanged electrons, v is the potential sweep rate (in V s^{-1}) and T is the absolute temperature (in K).

The values obtained for the different molten chlorides tested at several temperatures are quoted in Table 1.

The diffusion coefficient values have been used to calculate the activation energy for the diffusion process. The influence of the temperature on the diffusion coefficient obeys the Arrhenius's law through the following equation:

$$D = D_o \exp\left(-\frac{E_A}{RT} \right) \pm \Delta \tag{4}$$

where E_A is the activation energy for the diffusion process (in kJ mol^{-1}), D_o is the pre-exponential term (in cm^2 s^{-1}) and Δ is the experimental error.

From this expression, the value of the activation energy for the Yb(III) ions diffusion process was calculated in the different melts tested (Table 1).
The diffusion coefficient of ytterbium (III) ions becomes smaller with the increase of the radius of the cation of alkali metal in the line from Li to Cs (Table 1). Such behaviour takes place due to an increasing on the strength of complex ions and the decrease in contribution of D to the "hopping" mechanism. The increase of temperature leads to the increase of the diffusion coefficients in all the solvents.

Solvent	T/K	$D \cdot 10^5/cm^2 \cdot s^{-1}$	$-E_A/kJ \cdot mol^{-1}$
LiCl-KCl	723	1.0 ± 0.1	38.3
	848	2.7 ± 0.1	
	973	5.4 ± 0.1	
NaCl-KCl	973	2.8 ± 0.2	45.4
	1023	3.2 ± 0.2	
	1073	4.1 ± 0.2	
NaCl-KCl-CsCl	873	0.66± 0.1	51.3
	973	1.38± 0.1	
	1073	2.45± 0.1	
CsCl	973	0.9 ± 0.1	54.4
	1023	1.2 ± 0.1	
	1073	1.7 ± 0.1	

Table 1. Diffusion coefficient of Yb(III) ions in molten alkali metal chlorides at several temperatures. Activation energy for the ytterbium ions diffusion process

The variation of the logarithm of the diffusion coefficient as a function of the reverse radius of the solvent cation (r) and reverse temperatures is given by the following expression:

$$\log D_{Yb(III)} = -2.38 - \frac{3596}{T} + \frac{\left(0.0071 + \frac{158}{T}\right)}{r} \pm 0.02 \quad (5)$$

The average value of the radius of molten mixtures $\left(r_{R^+}\right)$ was calculated by using the following equation [Lebedev, 1993]:

$$r_{R^+} = \sum_{i=1}^{N} c_i r_i \quad (6)$$

where c_i is the mole fraction of i cations; r_i is the radius of i cations in molten mixture, consist of N different alkali chlorides, nm.

3.1.3 Apparent standard potentials of the redox couple Yb(III)/Yb(II)

The apparent standard potential of the Yb(III)/Yb(II) system was determined from the cyclic voltammograms registered in $YbCl_3$ solutions in the different alkali metal chlorides tested at several temperatures.
According to the theory of linear sweep voltammetry the following expressions, including the anodic and cathodic peak potentials and the half-wave potential, can be applied in the case of a soluble-soluble reversible system [Bard & Faulkner, 1980]:

$$E_P^C = E_{1/2} - 1.11\frac{RT}{F} \tag{6}$$

$$E_P^A = E_{1/2} + 1.11\frac{RT}{F} \tag{7}$$

$$\frac{\left(E_P^C + E_P^A\right)}{2} = E_{1/2} \tag{8}$$

where the half-wave potential is given by:

$$E_{1/2} = E^0_{Yb(III)/Yb(II)} + \frac{RT}{F}\ln\left(\frac{D_{Yb(II)}}{D_{Yb(III)}}\right)^{1/2} + \frac{RT}{F}\ln\left(\frac{\gamma_{Yb(III)}}{\gamma_{Yb(II)}}\right) \tag{9}$$

It is known that for concentrations of electroactive species lower than 3 to $5{\cdot}10^{-2}$ in mole fraction scale, their activity coefficient is almost constant. In these conditions, it is more convenient using the apparent standard redox potential concept ($E^*_{Yb(III)/Yb(II)}$) expressed as follows [Smirnov, 1973]:

$$E^*_{Yb(III)/Yb(II)} = E^0_{Yb(III)/Yb(II)} + \frac{RT}{F}\ln\left(\frac{\gamma_{Vb(III)}}{\gamma_{Yb(II)}}\right) \tag{10}$$

The formal standard redox potentials of $E^*_{Yb(III)/Yb(II)}$ were calculated from the following equations:

$$E^*_{Yb(III)/Yb(II)} = E_P^C + 1.11\frac{RT}{F} + \frac{RT}{F}\ln\left(\frac{D_{ox}}{D_{red}}\right)^{1/2} \tag{11}$$

$$E^*_{Yb(III)/Yb(II)} = E_P^A - 1.11\frac{RT}{F} + \frac{RT}{F}\ln\left(\frac{D_{ox}}{D_{red}}\right)^{1/2} \tag{12}$$

$$E^*_{Yb(III)/Yb(II)} = \frac{\left(E_P^C + E_P^A\right)}{2} + \frac{RT}{F}\ln\left(\frac{D_{ox}}{D_{red}}\right)^{1/2} \tag{13}$$

From the peak potential values measured in the cyclic voltammograms and the diffusion coefficients of Yb(III) and Yb(II) the following empirical equation for the apparent standard redox potentials versus the Cl^-/Cl_2 reference electrode in different solvents were obtained.

$$E^*_{Yb(III)/Yb(II)} = -(1.915 \pm 0.005) + (3.5 \pm 0.2)\times 10^{-4}T, \quad V \quad \text{[723-973 K]} \quad \text{LiCl-KCl} \tag{14}$$

$$E^*_{Yb(III)/Yb(II)} = -(2.031 \pm 0.005) + (3.7 \pm 0.2)\times 10^{-4}T, \quad V \quad \text{[973-1075 K]} \quad \text{NaCl-KCl} \tag{15}$$

$$E^*_{Yb(III)/Yb(II)} = -(2.192 \pm 0.016) + (4.3 \pm 0.2)\times 10^{-4}T, \quad V \quad \text{[723-1073 K]} \quad \text{NaCl-KCl-CsCl} \tag{16}$$

$$E^*_{Yb(III)/Yb(II)} = -(2.262 \pm 0.004) + (4.2 \pm 0.2)\times 10^{-4}T, \quad V \quad \text{[973-1079 K]} \quad \text{CsCl} \tag{17}$$

The variation of the apparent standard potential of the redox couple Yb(III)/Yb(II) as a function of the reverse radius of the solvent cation (r) and the temperature was calculated. The relation obtained is:

$$E^*_{Yb(III)/Yb(II)} = -3.031 + 8 \cdot 10^{-4} T + \frac{(0.104 - 4 \cdot 10^{-5} T)}{r} \quad (18)$$

Normally, lanthanide chlorides dissolved in alkali chloride melts are solvated by the chloride ions forming different complex ions like $\left[LnCl_6\right]^{3-}$ and $\left[LnCl_4\right]^{2-}$ [Barbanel, 1985; Papatheodorou & Kleppa, 1974; Yamana et al., 2003]. In the case of ytterbium, $\left[YbCl_6\right]^{3-}$ complex ions are present in the melts [Novoselova et al., 2004]. Their relative stability increases with the increase of the solvent cation radius, and the apparent standard redox potential shifts to more negative values. Our results are in a good agreement with the literature ones [Smirnov, 1973].

3.1.4 Thermodynamics properties

Using the values of the apparent standard redox potentials the formal free Gibbs energy changes of the redox reaction

$$YbCl_{2(l)} + ½\ Cl_{2(g)} \Leftrightarrow YbCl_{3(l)} \quad (19)$$

was calculated according to following expression:

$$\Delta G^* = -nFE^*_{Yb(III)/Yb(II)} \quad (20)$$

Its temperature dependence allows calculating the enthalpy and entropy of the $YbCl_3$ formation by means of the relation [Bard & Faulkner, 1980]:

$$\Delta G^* = \Delta H^* - T\Delta S^* \quad (21)$$

The apparent standard Gibbs energy of formation of $YbCl_3$ in the different solvents tested can be expressed as:

$$\Delta G^*_{YbCl_3} = -184.80 + 0.033 \cdot T \pm 2.46\ \text{kJ/mol} \quad [723\text{-}973\ \text{K}] \quad \text{LiCl-KCl} \quad (22)$$

$$\Delta G^*_{YbCl_3} = -195.96 + 0.036 \cdot T \pm 2.46\ \text{kJ/mol} \quad [973\text{-}1075\ \text{K}] \quad \text{NaCl-KCl} \quad (23)$$

$$\Delta G^*_{YbCl_3} = -211.52 + 0.041 \cdot T \pm 2.43\ \text{kJ/mol} \quad [723\text{-}1073\ \text{K}] \quad \text{NaCl-KCl-CsCl} \quad (24)$$

$$\Delta G^*_{YbCl_3} = -218.25 + 0.041 \cdot T \pm 2.46\ \text{kJ/mol} \quad [973\text{-}1079\ \text{K}] \quad \text{CsCl} \quad (25)$$

The changes of the thermodynamic parameters of the redox reaction (19) versus the radius of the solvent cation show the increasing in strength of the Yb-Cl bond in the complex ions $\left[YbCl_6\right]^{3-}$ in the line from LiCl to CsCl.

3.1.5 Voltammetric studies on active electrodes

Linear sweep voltammograms for the reduction of Yb(III) solution at inert tungsten (1) and active aluminum (2) electrodes at 873 K are presented in Fig. 10. The voltammogram on

aluminum working electrode show the existence of two cathodic peaks at the potentials approximately –1.92 V and –2.92 V vs. Cl^-/Cl_2 instead of one on tungsten electrode. Potentiostatic electrolysis at potential –1.92 V did not show the formation of solid phase on tungsten and aluminum surfaces after polarization. So we can suppose passing the reaction (2) at this potential on inert and active electrodes.

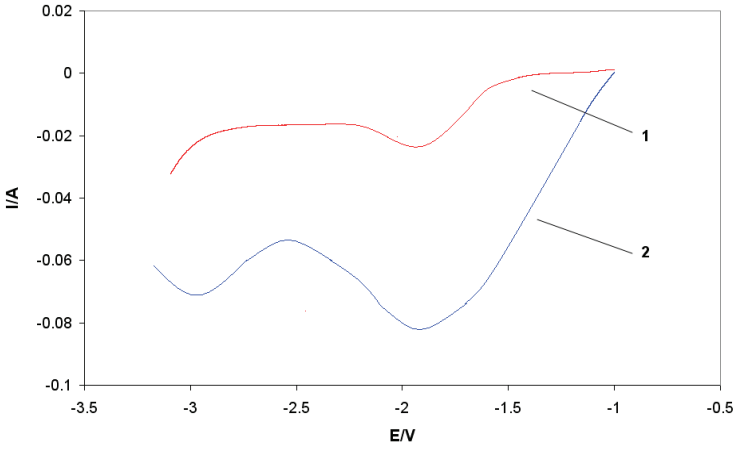

Fig.10. Linear sweep voltammograms of fused NaCl-KCl-CsCl-$YbCl_3$ salt on inert W electrode (1) and active Al electrode (2) at 873 K. [Yb(III)] = $8.26 \cdot 10^{-2}$ mol kg^{-1}. Working electrode: W (S = 0.23 cm^2); Al (S = 0.47 cm^2)

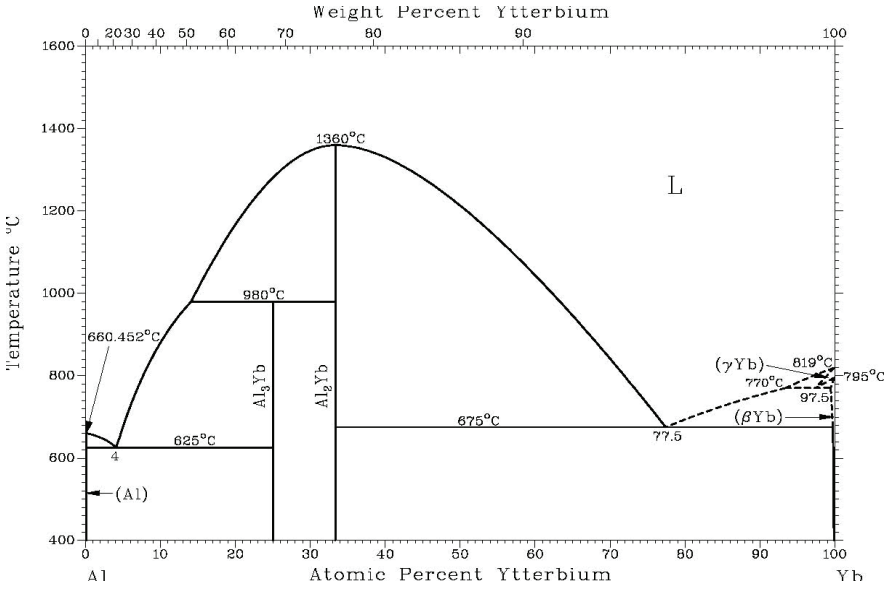

Fig. 11. Phase diagram of Yb-Al system

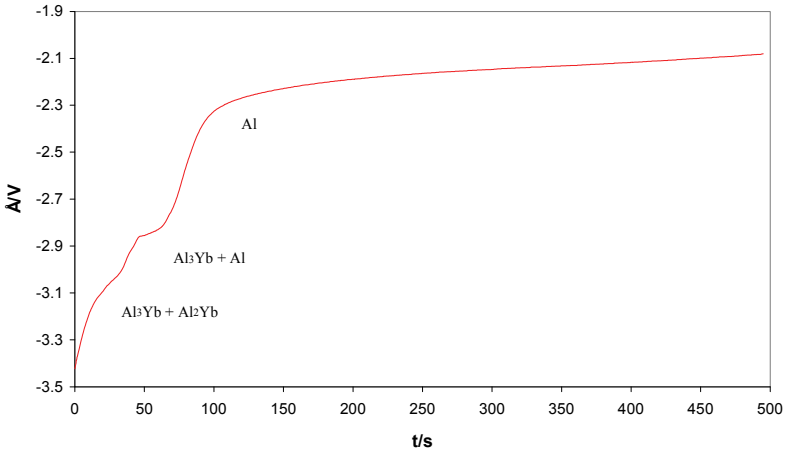

Fig. 12. The dependence of potential – time, obtained after short polarization of Al electrode in NaCl-KCl-CsCl-$YbCl_3$ melt at 873 K. [Yb(III)] = $3.17 \cdot 10^{-2}$ mol kg^{-1}. $E_{dep.}$ = –3.4 V; $t_{dep.}$ = 9 s

Potentiostatic electrolysis at the potential –2.92 V shows the formation of solid cathodic product on a surface of Al electrode. Phase diagram of the system Al-Yb, Fig. 11, show the formation of two intermetallic compounds Al_3Yb and Al_2Yb.

The dependence potential – time, obtained after shot polarization of aluminum working electrode, show the existence of two waves at potentials average –2.88 V and –3.04 V vs. Cl^-/Cl_2, Fig. 12. It can be combined with the formation of two intermetallic compounds Al_3Yb and Al_2Yb. The X-ray analysis of the deposits, obtained after potentiostatic electrolysis at the potential –2.88 V show the existence of Al_3Yb alloy on the surface of aluminum electrode and at potential –3.04 V show the existence of the mixture of Al_3Yb and Al_2Yb alloys.

Analyzing the results of investigations it can be concluded that the mechanism of the reduction of Yb(III) ions in fused NaCl-KCl-CsCl eutectic on active electrode occurs in two steps with the formation of Al_3Yb and Al_2Yb alloys:

$$Yb(III) + \bar{e} = Yb(II) \quad (26)$$

$$Yb(II) + nAl + 2\,\bar{e} = Al_nYb, \quad (27)$$

where *n* is equal 2, 3.

Potentiostatic electrolysis allow to deposit Al_3Yb or the mixture of Al_2Tm and Al_3Tm alloys as a thin films on the aluminum surface.

3.2 Electromotive force method

3.2.1 Apparent standard potentials of the redox couple Ln(III)/Ln(II)

The typical dependences of the redox potential of the couple Yb^{3+}/Yb^{2+} with different ratio Yb(III)/Yb(II) versus the duration at the temperature 818 K in NaCl-KCl-CsCl-$YbCl_3$ melt are presented in Fig. 13.

The same type of the pictures was obtained for Tm^{3+}/Tm^{2+} and Yb^{3+}/Yb^{2+} systems in all investigations solvents. The equilibrium potential were fixed after 30-90 minutes after finishing of the electrolysis and depends from the conditions of the experiment. If the value

of potential is constant during 30-40 minutes within the limits of ± 0.001 V then it is possible to say that the investigation system is in equilibrium conditions.
The value of the apparent redox potential is determined by:

$$E_{Ln^{3+}/Ln^{2+}} = E^{*}_{Ln^{3+}/Ln^{2+}} + \frac{RT}{nF}\ln\left(\frac{[Ln^{3+}]}{[Ln^{2+}]}\right) \quad (28)$$

where $E_{Ln^{3+}/Ln^{2+}}$ is the equilibrium potential of the system, V; $E^{*}_{Ln^{3+}/Ln^{2+}}$ is the apparent standard redox potential of the system, V; n is the number of exchange electrons; $[Ln^{3+}]$ and $[Ln^{2+}]$ are the concentrations of lanthanide ions in mole fraction.
Variation of the equilibrium potential of the couple Ln^{3+}/Ln^{2+} as a function of the napierian logarithm ratio of concentrations $[Ln^{3+}]$ and $[Ln^{2+}]$ in fused $LnCl_3$ solutions on vitreous carbon indicated electrode at 818 K (NaCl-KCl-CsCl eutectic) and at 973 K (CsCl) is shown

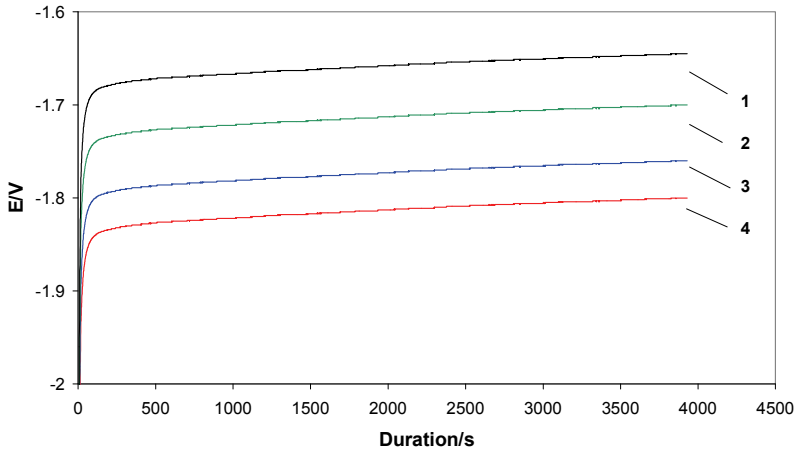

Fig. 13. The typical dependences of the redox potential of the couple Yb^{3+}/Yb^{2+} versus the duration in NaCl-KCl-CsCl-$YbCl_3$ melt. Temperature – 818 K. Initial concentration of $[Yb^{3+}]$ = 3.96 mol%. Working electrode – GC. **1** – $\ln[Yb^{3+}]/[Yb^{2+}]$ = 1.96; **2** – $\ln[Yb^{3+}]/[Yb^{2+}]$ = 1.58; **3** – $\ln[Yb^{3+}]/[Yb^{2+}]$ = 0.54; **4** – $\ln[Yb^{3+}]/[Yb^{2+}]$ = 0

In Fig. 14. Linear dependences of $E_{Ln^{3+}/Ln^{2+}}$ *vs.* $\ln([Ln^{3+}]/[Ln^{2+}])$ obeys the Nernst's law by the following equations using Software Origin Pro version 7.5:

$$E_{Tm^{3+}/Tm^{2+}} = -(2.827 \pm 0.005) + (0.083 \pm 0.005)\ln([Tm^{3+}]/[Tm^{2+}]) \pm 0.007 \ / \ V \quad \text{CsCl} \quad (29)$$

$$E_{Tm^{3+}/Tm^{2+}} = -(2.906 \pm 0.001) + (0.070 \pm 0.001)\ln([Tm^{3+}]/[Tm^{2+}]) \pm 0.002 \ / \ V \quad \text{(Na-K-Cs)Cl} \quad (30)$$

$$E_{Yb^{3+}/Yb^{2+}} = -(1.809 \pm 0.001) + (0.086 \pm 0.001)\ln([Yb^{3+}]/[Yb^{2+}]) \pm 0.002 \ / \ V \quad \text{CsCl} \quad (31)$$

$$E_{Yb^{3+}/Yb^{2+}} = -(1.805 \pm 0.005) + (0.071 \pm 0.004)\ln([Yb^{3+}]/[Yb^{2+}]) \pm 0.006 \ / \ V \quad \text{(Na-K-Cs)Cl} \quad (32)$$

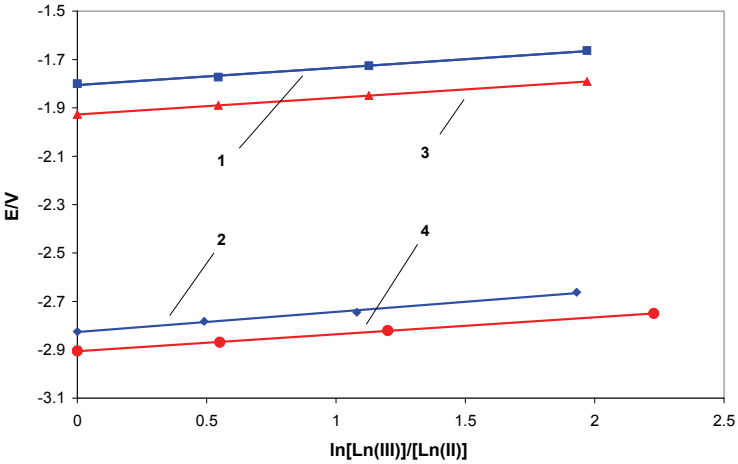

Fig. 14. Variation of the equilibrium potential of the couple Ln^{3+}/Ln^{2+} as a function of the napierian logarithm ratio of concentrations $[Ln^{3+}]$ and $[Ln^{2+}]$ in fused NaCl-KCl-CsCl eutectic (1 - Yb; 2 – Tm) at 818 K and in fused CsCl (3 – Yb; 4 – Tm) at 973 K on vitreous carbon indicated electrode. $[Yb^{3+}] = 3.96$ mol%. $[Tm^{3+}] = 4.28$ mol%

The number of exchange electrons (n) taking part in the process of electrochemical reduction of rare-earth trichlorides was determined from the slopes of the straight lines. From equations (29-32) the number of exchange electrons for the reaction (33):

$$Ln^{3+} + e = Ln^{2+} \tag{33}$$

was 0.99 ± 0.01 for Tm and 0.99 ± 0.02 for Yb.

The chemical analysis of the solidified thulium or ytterbium chloride melts performed after experiments confirmed the results of the electrochemical measurements. The difference in concentrations of $LnCl_2$ determined by coulometry (i.e., calculated from the amount of electric charge passed through the melt for the reduction of Ln^{3+} ions) and analytically did not exceed 2.5 %.

The temperature dependences of apparent standard redox potentials of Ln^{3+}/Ln^{2+} systems on vitreous carbon indicated electrode were linear in the whole temperature range studied, Fig. 15. The experiment data were fitted to the following equations using Software Origin Pro version 7.5:

$$E^*_{Tm^{3+}/Tm^{2+}} = -(3.742 \pm 0.006) + (105.0 \pm 0.6) \cdot 10^{-5} T \pm 0.001 \,/\, V \quad [823\text{-}973\ K]\ (Na\text{-}K\text{-}Cs)Cl \tag{34}$$

$$E^*_{Yb^{3+}/Yb^{2+}} = -(2.580 \pm 0.013) + (80.6 \pm 1.5) \cdot 10^{-5} T \pm 0.003 \,/\, V \quad [823\text{-}973\ K]\ (Na\text{-}K\text{-}Cs)Cl \tag{35}$$

$$E^*_{Tm^{3+}/Tm^{2+}} = -(4.029 \pm 0.03) + (124.0 \pm 2.7) \cdot 10^{-5} T \pm 0.005 \,/\, V \quad [973\text{-}1123\ K]\ CsCl \tag{36}$$

$$E^*_{Yb^{3+}/Yb^{2+}} = -(2.464 \pm 0.008) + (65.0 \pm 0.7) \cdot 10^{-5} T \pm 0.001 \,/\, V \quad [973\text{-}1123\ K]\ CsCl \tag{37}$$

The results of our investigations show that at equal temperatures the apparent redox potentials of thulium $\left(E^{*}_{Tm^{3+}/Tm^{2+}}\right)$ are more negative than ytterbium $\left(E^{*}_{Yt^{3+}/Yb^{2+}}\right)$. The comparison of data for apparent standard redox potentials of thulium (-2.822 V) and ytterbium (-1.831 V) in molten *CsCl* ($r_{Cs^{+}} = 0.165\,nm$) with data in fused NaCl-KCl-CsCl eutectic ($r_{eut.^{+}} = 0.137\,nm$) [Lebedev, 1993] for thulium (-2.720 V) and ytterbium (-1.796 V) at 973 K show the natural shift of the potential values to more negative region in line LiCl-CsCl.

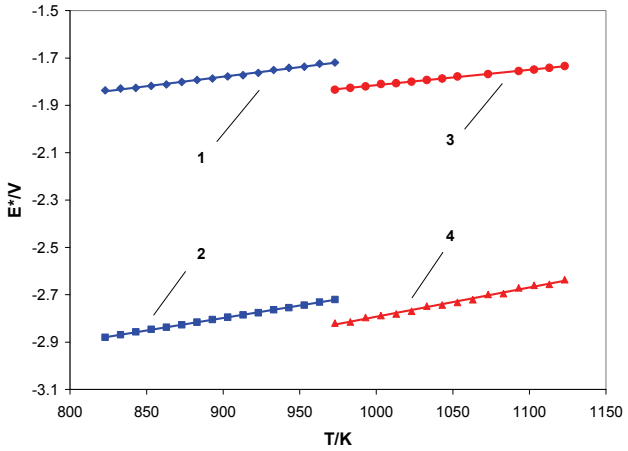

Fig. 15. Apparent standard redox potentials of the Ln^{3+}/Ln^{2+} system as a function of the temperature on vitreous carbon indicated electrode. 1 – System $YbCl_3$-$YbCl_2$-NaCl-KCl-CsCl. 2 – System $TmCl_3$-$TmCl_2$-NaCl-KCl-CsCl. 3 – System $YbCl_3$-$YbCl_2$-CsCl. 4 – System $TmCl_3$-$TmCl_2$-CsCl

Typical complexes of dilute solution of lanthanide chlorides in alkali chloride melts are $LnCl_6^{3-}$ and $LnCl_4^{2-}$ [Papatheodorou & Kleppa, 1974; Yamana et al., 2003]. Their relative stability increases with increasing of solvent cation radius from Li^{+} to Cs^{+} and the apparent standard redox potentials are shifted to more negative values. These results are in good agreement with literature data concerning the second coordination sphere influence on apparent standard redox potentials.

3.2.2 Thermodynamics properties

Using the values of the apparent standard redox potentials the formal free Gibbs energy changes and the apparent equilibrium constants of the redox reaction (38):

$$LnCl_{2(l)} + \tfrac{1}{2}\,Cl_{2(g)} \Leftrightarrow LnCl_{3(l)} \tag{38}$$

can be calculated using the well-known expressions:

$$\Delta G^{*} = nFE^{*}_{Ln^{3+}/Ln^{2+}} \tag{39}$$

and

$$\Delta G^* = -RT \ln K^*_{eq.} \tag{40}$$

The temperature dependence of the Gibbs energy change can be described by the following equation:

$$\Delta G^* = \Delta H^* - T\Delta S^* \tag{41}$$

The experiment data were fitted to the following equations using Software Origin Pro version 7.5:

$$\Delta G^* = -(354.1 \pm 0.6) + (94.5 \pm 0.6) \cdot 10^{-3} T \pm 0.1 \quad kJ / mol \quad TmCl_3\text{-NaCl-KCl-CsCl} \tag{42}$$

$$\Delta G^* = -(249.0 \pm 1.3) + (77.8 \pm 0.1) \cdot 10^{-3} T \pm 0.3 \quad kJ / mol \quad YbCl_3\text{-NaCl-KCl-CsCl} \tag{43}$$

$$\Delta G^* = -(388.8 \pm 0.9) + (119.7 \pm 0.9) \cdot 10^{-3} T \pm 0.2 \quad kJ / mol \quad TmCl_3\text{-CsCl} \tag{44}$$

$$\Delta G^* = -(237.8 \pm 0.8) + (62.7 \pm 0.7) \cdot 10^{-3} T \pm 0.1 \quad kJ / mol \quad YbCl_3\text{-CsCl} \tag{45}$$

By the expression (40) one can calculate the apparent equilibrium constants for the redox reaction (38) in fused salts. The temperature dependences are the following:

$$\ln K^*_{eq.} - 13.78 + \frac{44997}{T} \pm 0.01 \quad TmCl_3\text{-NaCl-KCl-CsCl} \tag{46}$$

$$\ln K^*_{eq.} - 10.56 + \frac{31114}{T} \pm 0.01 \quad YbCl_3\text{-NaCl-KCl-CsCl} \tag{47}$$

$$\ln K^*_{eq.} - 14.40 + \frac{46787}{T} \pm 0.02 \quad TmCl_3\text{-CsCl} \tag{48}$$

$$\ln K^*_{eq.} = -7.54 + \frac{28602}{T} \pm 0.01 \quad YbCl_3\text{-CsCl} \tag{49}$$

The activity coefficients of $YbCl_3$ in fused salts was determined from the difference between the apparent Gibbs free energy derived from the experimental measurements and the standard Gibbs free energy for pure compounds obtained in the literature [Barin, 1994]:

$$\log \gamma_{YbCl_3} = -1.23 - \frac{4436}{T} \pm 0.02 \quad YbCl_3\text{-NaCl-KCl-CsCl} \tag{50}$$

$$\log \gamma_{YbCl_3} = -2.09 - \frac{3761}{T} \pm 0.02 \quad YbCl_3\text{-CsCl} \tag{51}$$

The dependence of the activity coefficient of $YbCl_3$ versus the reverse temperature is given by the expressions (50, 51). Database for thulium compounds is absent in the literature [Barin, 1994].

It is also possible to estimate the equilibrium chlorine gas pressure above an alkali metal chloride melts containing hulium or ytterbium tri- and dichlorides for the reaction (52) by

$$LnCl_{3(l)} \Leftrightarrow LnCl_{2(l)} + \tfrac{1}{2}\, Cl_{2(g)} \tag{52}$$

well-known equation (53) [Smirnov, 1973]. Such kind of calculations were done for the concentration ratio of $[Ln^{3+}]/Ln^{2+}]$ equals one in fused NaCl-KCl-CsCl eutectic and individual CsCl.

$$\frac{RT}{2F}\ln P_{Cl_2} = E_{Ln^{3+}/Ln^{2+}} + \frac{RT}{F}\ln\frac{[Ln^{3+}]}{[Ln^{2+}]} \tag{53}$$

The calculated values are summarized in Table 2. The average value of the radius of these molten mixtures in this line, *pro tanto*, is 0.137; 0.165 nm [Lebedev, 1993]. From the data given in Table 2 one can see that the relative stability of lanthanides(III) complexes ions is naturally increased in the line $(NaCl\text{-}KCl\text{-}CsCl)_{eut.}$ – CsCl.

Thermodynamic properties	Tm		Yb	
	NaCl-KCl-CsCl	CsCl	NaCl-KCl-CsCl	CsCl
E*/V	–2.721	–2.822	–1.796	–1.846
ΔG*/(kJ·mol-1)	–262.6	–272.3	–173.3	–178.2
ΔH*/(kJ·mol-1)	–354.1	–388.8	–249.0	–258.7
ΔS*/(J·K-1·mol-1)	94.5	119.7	77.8	82.8
γ	–	–	1.6·10-6	9.0·10-7
$K^*_{eq.}$	1.31·1014	4.40·1014	2.08·109	3.80·109
p_{Cl_2} / Pa	5.86·10-29	1.05·10-24	2.31·10-19	6.92·10-20

Table 2. The comparison of the base thermodynamic properties of Tm and Yb in molten alkali metal chlorides at 973 K. Apparent standard redox potentials are given in the molar fraction scale

4. Conclusion

The electrochemical behaviour of $[YbCl_6]^{3-}$ ions in fused alkali metal chlorides was investigated. It was found that the reduction of Yb(III) to Yb(II) ions is a reversible process being controlled by the rate of the mass transfer. The diffusion coefficient of $[YbCl_6]^{3-}$ ions was determined at different temperatures in all investigation systems. The apparent standard electrode potential of the redox couple Yb^{3+}/Yb^{2+} was calculated from the analysis of the cyclic voltammograms registered at different temperatures. The apparent standard redox potentials of $E^*_{Tm^{3+}/Tm^{2+}}$ and $E^*_{Yb^{3+}/Yb^{2+}}$ in molten alkali metal chlorides were also determined by *emf* method. The basic thermodynamic properties of the reactions $TmCl_{2(l)} + \tfrac{1}{2}\, Cl_{2(g)} \Leftrightarrow TmCl_{3(l)}$ and $YbCl_{2(l)} + \tfrac{1}{2}\, Cl_{2(g)} \Leftrightarrow YbCl_{3(l)}$ were calculated.
The influence of the nature of the solvent (ionic radius) on the thermodynamic properties of thulium and ytterbium compounds was assessed. It was found that the strength of the Ln–Cl bonds increases in the line from Li to Cs cation.

5. References

Barbanel, Ya.A. (1985). *Coordination Chemistry of f-elements in Melts*, Energoatomizdat, Moscow, Russia.

Bard, A.J. & Faulkner, L.R. (1980). *Electrochemical Methods. Fundamentals and Applications*, John Wiley & Sons Inc., ISBN 0-471-05542-5, USA.

Barin, I. (1994). *Thermochemical Data of Pure Substances*, Third Edition, Wiley-VCH, ISBN 3-527-30993-4, USA.

Bermejo, M.R., Gomez, J., Medina, J., Martinez, A.M. & Castrillejo, Y. (2006). The electrochemistry of gadolinium in the eutectic LiCl-KCl on W and Al electrodes, In: *Journal of Electroanalitical Chemistry,* Vol. 588, No. 2, (March 2006), pp. 253-266, ISSN 0022-0728.

Bermejo, M.R., de la Rosa, F., Barrado, E. & Castrillejo, Y. (2007). Cathodic behaviour of europium(III) on glassy carbon, electrochemical formation of Al_4Eu, and oxoacidity reactions in the eutectic LiCl-KCl, In: *Journal of Electroanalitical Chemistry,* Vol. 603, No. 1, (May 2007), pp. 81- 95, ISSN 0022-0728.

Bermejo, M.R., Gomez, J., Martinez, A.M., Barrado, E. & Castrillejo, Y. (2008). Electrochemistry of terbium in the eutectic LiCl-KCl, In: *Electrochimica Acta,* Vol. 53, No. 16, (June 2008), pp. 5106-5112, ISSN 0013-4686.

Bermejo, M.R., Barrado, E., Martinez, A.M. & Castrillejo, Y. (2008). Electrodeposition of Lu on W and Al electrodes: Electrochemical formation of Lu-Al alloys and oxoacidity reactions of Lu(III) in eutectic LiCl-KCl, In: *Journal of Electroanalitical Chemistry,* Vol. 617, No. 1, (June 2008), pp. 85- 100, ISSN 0022-0728.

Castrillejo, Y., Bermejo, M.R., Diaz Arocas, P., Martinez, A.M. & Barrado, E. (2005). The electrochemical behavior of praseodymium(III) in molten chlorides, In: *Journal of Electroanalitical Chemistry,* Vol. 575, No. 1, (January 1995), pp. 61- 74, ISSN 0022-0728.

Castrillejo, Y., Bermejo, M.R., Diaz Arocas, P., Martinez, A.M. & Barrado, E. (2005). The electrochemical behavior of the Pr(III)/Pr redox system at Bi and Cd liquid electrodes in the molten eutectic LiCl-KCl, In: *Journal of Electroanalitical Chemistry,* Vol. 579, No. 1, (January 2005), pp. 343-358, ISSN 0022-0728.

Castrillejo, Y., Bermejo, M.R., Barrado, A.I., Pardo, R., Barrado, E. & Martinez, A.M. (2005). Electrochemical behavior of dysprosium in the eutectic LiCl-KCl at W and Al electrodes, In: *Electrochimica Acta,* Vol. 50, No. 10, (March 2005), pp. 2047- 2057, ISSN 0013-4686.

Castrillejo, Y., Fernandes, P., Bermejo, M.R., Barrado, A.I. & Martinez, A.M. (2009). Electrochemistry of thulium on inert electrodes and electrochemical formation of a Tm-Al alloy from molten chlorides, In: *Electrochimica Acta,* Vol. 54, No. 26, (November 2009), pp. 6212-6222, ISSN 0013-4686.

De Cordoba, G. & Caravaca, C. (2004). An electrochemical study of samarium ions in the molten eutectic LiCl+KCl, In: *Journal of Electroanalitical Chemistry,* Vol. 572, No. 1, (October 2004), pp. 145-151, ISSN 0022-0728.

De Cordoba, G., Laplace, A., Conocar, O., Lacquement, G. & Caravaca, C. (2008). Determination of the activity coefficients of neodymium in liquid aluminum by potentiometric methords, In: *Electrochimica Acta,* Vol. 54, No. 2, (December 2008), pp. 280-288, ISSN 0013-4686.

Fusselman, S.P., Roy, J.J., Grimmett, D.L., Grantham, L.F., Krueger, C.L., Nabelek, C.R., Storvick, T.S., Inoue, T., Hijikata, T., Kinoshita, K., Sakamura, Y., Uozumi, K., Kawai, T. & Takahashi, N. (1999). Thermodynamic properties for rare earths and

americium in pyropartitioning process solvents, In: *Journal of The Electrochemical Society,* Vol. 146, No. 7, (July 1999), pp. 2573-2580, ISSN 0013-4651.

Kinoshita, K., Kurata, M. & Inoue, T. (2000). Estimation of material balance in pyrometallurgical partitioning process of transuranic elements from high-level liquid waste, In: *Journal of Nuclear Science and Technology*, Vol. 37, No. 1, (January 2000), pp. 75-83, ISSN 0022-3131.

Korshunov, B.G., Safonov, V.V. & Drobot, D.V. (1979). *Phase equilibriums in halide systems*, Metallurgiya, Moscow, USSR.

Kuznetsov, S.A., Hayashi, H., Minato, K. & Gaune-Escard, M. (2006). Electrochemical transient techniques for determination of uranium and rare-earth metal separation coefficients in molten salts, In: *Electrochimica Acta,* Vol. 51, No. 12 (February 2006), pp. 2463-2470, ISSN 0013-4686.

Lebedev, V.A. (1993). *Selectivity of Liquid Metal Electrodes in Molten Halide*, Metallurgiya, ISBN 5-229-00962-4, Russia.

Morss, L.R., Edelstein, N.M., Fuger, J. & Katz, J.J. (2008). *The chemistry of the actinide and transactinide elements,* Springer, ISBN-13 978-1-4020-3555-5, Netherlands.

Novoselova, A.V., Potapov, A.M. & Khokhlov, V.A. (2004). Empirical Estimation of the Thulium and Ytterbium Redox Potentials in Molten Alkali Metal Chlorides, *Proceeding of Euchem 2004 Molten Salts Conference,* Piechowice, Poland, June 2004.

Novoselova, A. & Smolenski, V. (2010). Thermodynamic properties of thulium and ytterbium in molten caesium chloride, In: *Journal of Chemical Thermodynamics,* Vol. 42, No. 8, (August 2010), pp. 973-977, ISSN 0021- 9614.

Osipenko, A., Maershin, A., Smolenski, V., Novoselova, A., Kormilitsyn, M. & Bychkov, A. (2010). Electrochemistry of oxygen-free curium compounds in fused NaCl-2CsCl eutectic, In: *Journal of Nuclear Materials,* Vol. 396, No. 1, (January 2010), pp. 102-1067, ISSN 0022-3115.

Osipenko, A., Maershin, A., Smolenski, V., Novoselova, A., Kormilitsyn, M. & Bychkov, A. (2011). Electrochemical behaviour of curium (III) ions in fused 3LiCl-2KCl eutectic, In: *Journal of Electroanalitical Chemistry,* Vol. 651, No. 1, (January 2011), pp. 67-71, ISSN 0022-0728.

Papatheodorou, G.N. & Kleppa, O.J. (1974). Thermodynamic studies of binary charge unsymmetrical fused salt systems. Cerium(III) chloride-alkali chloride mixtures, In: *Journal of Physical Chemistry,* Vol. 78, No. 2, (January 1974), pp. 178-181, ISSN 0144-235X.

Revzin, G.E. (1967). No. 16. Waterless Chlorides of Rare-Earth Elements and Scandium. In: *Methods of Preparation of Chemical Reagents and Compounds,* pp. 124-129, IREA, Moscow, USSR.

Roy, J.J., Grantham, L.F., Grimmett, D.L., Fusselman, S.P., Krueger, C.L., Storvick, T.S., Inoue, T., Sakamura, Y. & Takahashi, N. (1996). Thermodynamic properties of U, Np, Pu, and Am in molten LiCl-KCl eutectic and liquid cadmium, In: *Journal of The Electrochemical Society,* Vol. 143, No. 8, (August 1996), pp. 2487-2492, ISSN 0013-4651.

Sakamura, Y., Hijikata, T., Kinoshita, K., Inoue, T., Storvick, T.S., Krueger, C.L., Roy, J.J., Grimmett, D.L., Fusselman, S.P. & Gay, R.L. (1998). Measurement of standard

potentials of actinides (U, Np, Pu, Am) in LiCl-KCl eutectic salt and separation of actinides from rare earths by electrorefining, In: *Journal of Alloys and Compounds,* Vol. 271-273, (June 1998), pp. 592-596, ISSN 0925-8388.

Serp, J., Konings, R.J.M., Malmbeck, R., Rebizant, J., Scheppler, C. & Glatz, J-P. (2004). Electrochemical of plutonium ion in LiCl-KCl eutectic melts, In: *Journal of Electroanalitical Chemistry,* Vol. 561, (January 2004), pp. 143-148, ISSN 0022-0728.

Serp, J., Allibert, M., Terrier, A.L., Malmbeck, R., Ougier, M., Rebizant, J. & Glatz, J-P. (2005). Electroseparation of actinides from lanthanides on solid aluminum electrode in LiCl-KCl eutectic melts, In: *Journal of The Electrochemical Society,* Vol. 152, No. 3, (March 2005), pp. C167-C172, ISSN 0013-4651.

Serp, J., Lefebvre, P., Malmbeck, R., Rebizant, J., Vallet, P. & Glatz, J-P. (2005). Separation of plutonium from lanthanum by electrolysis in LiCl-KCl onto molten bismuth electrode, In: *Journal of Nuclear Materials,* Vol. 340, No. 2-3, (April 2005), pp. 266-270, ISSN 0022-3115.

Serp, J., Chamelot, P., Fourcaudot, S., Konings, R.J.M., Malmbeck, R., Pernel, C., Poignet, J.C., Rebizant, J. & Glatz, J.P. (2006). Electrochemical behavior of americium ions in LiCl-KCl eutectic melt, In: *Electrochimica Acta,* Vol. 51, No. 19, (May 2006), pp. 4024-4032, ISSN 0013-4686.

Serrano, K. & Taxil, P. (1999). Electrochemical nucleation of uranium in molten chlorides, In: *Journal of Applied Electrochemistry,* Vol. 29, No. 4, (April 1999), pp. 505-510, ISSN 0021-891X.

Shishkin, V.Yu. & Mityaev, V.S. (1982). Purification of alkali chloride metals by direct crystallization. In: Proceedings of the Academy of Sciences. *Journal of Inorganic materials*, Vol. 18, No. 11 (November 1982), pp. 1917-1918, ISSN 0002-337X.

Shirai, O., Iizuka, M., Iwai, T., Suzuki, Y. & Arai, Y. (2000). Electrode reaction of plutonium at liquid cadmium in LiCl-KCl eutectic melts, In: *Journal of Electroanalitical Chemistry,* Vol. 490, No. 1-2, (August 2000), pp. 31-36, ISSN 0022-0728.

Smirnov M.V. (1973). *Electrode Potentials in Molten Chlorides*, Nauka, Moscow, USSR.

Smolenski, V., Novoselova, A., Osipenko, A., Caravaca, C. & de Cordoda, G. (2008). Electrochemistry of ytterbium(III) in molten alkali chlorides, In: *Electrochimica Acta*, Vol. 54, No. 2, (December 2008), pp. 382-387, ISSN 0013-4686.

Smolenski, V., Novoselova, A., Bovet, A., Osipenko, A. & Kormilitsyn, M. (2009). Electrochemical and thermodynamic properties if ytterbium trichloride in molten caesium chloride, In: *Journal of Nuclear Materials,* Vol. 385, No. 1, (March 2009), pp. 184-185, ISSN 0022-3115.

Smolenski, V., Novoselova, A., Osipenko, A. & Kormilitsyn, M. (2009). The influence of electrode material nature on the mechanism of cathodic reduction of ytterbium (III) ions in fused NaCl-KCl-CsCl eutectic, In: *Journal of Electroanalitical Chemistry,* Vol. 633, No. 2, (August 2009), pp. 291-296, ISSN 0022-0728.

Uozumi, K., Iizuka, M., Kato, T., Inoue, T., Shirai, O., Iwai, T. & Arai, Y. (2004). Electrochemical behaviors of uranium and plutonium at simultaneous recoveries into liquid cadmium cathodes, In: *Journal of Nuclear Materials,* Vol. 325, No. 1, (February 2004), pp. 34-43, ISSN 0022-3115.

Willit J. (2005). 7th International Symposium on Molten Salts Chemistry & Technology, *Proceeding of Overview and Status of Pyroprocessing Development at Argonne National Laboratory,* Toulouse, France, August 2005.

Yamana, H., Fujii, T. & Shirai, O. (2003). UV/Vis Adsorption Spectrophotometry of some f-elements in Chloride Melt, *Proceeding of International Symposium on Ionic Liquids on Honor of Marcelle Gaune-Escard,* Carry le Rouet, France, June 2003.

12

Electrochemical Impedance Spectroscopy Study of the Mass Transfer in an Anode-Supported Microtubular Solid Oxide Fuel Cell

Hironori Nakajima
Kyushu University
Japan

1. Introduction

Solid oxide fuel cell (SOFC) has advantages including high efficiency power generation by operation at 500-1000 °C, which results in a low environmental load. Moreover, SOFCs provide high quality waste heat, and the use of hydrocarbon fuels such as city gas, liquefied petroleum gas, and alcohol is relatively easy. However, for practical use, optimization of the electrode and electrolyte materials and the structure of the cell are required to improve the performance. In addition, optimization of the operation conditions and improvement of cell durability need to be addressed.

Mass transfers of the fuel and oxygen at the anode and cathode, respectively, greatly affect the cell performance by giving rise to the concentration overpotentials which result in the voltage loss of the cell. The concentration overpotentials including the Nernst loss by the fuel and oxygen depletions in the cell (Li, 2007; Morita et al., 2002) also affect the cell durability since they cause current distribution which leads to temperature distribution in the cell and anode oxidation. The current distribution also prevents effective use of whole electrode areas in a cell geometry.

This chapter describes the concentration overpotentials and current distribution in an intermediate temperature anode-supported microtubular SOFC which can be operated in the temperature range of 500-800 °C (IT-SOFC) with an analysis by electrochemical impedance spectroscopy (EIS) and cell surface temperature measurements.

EIS has been widely employed for the analysis of fuel cells. In particular, the author's group has developed diagnosis methods of operating status of the polymer electrolyte fuel cell (PEFC) by analyzing the variation of resistances and capacitances of equivalent circuit models of the PEFC (Konomi & Saho, 2006; Nakajima et al., 2008).

For the SOFC, a number of EIS analyses have been reported (Barsoukov & Macdonald, 2005; Esquirol et al., 2004; Horita et al., 2001; Huang et al., 2007; Ishihara et al., 2000; Jiang, 2002; Leonide et al., 2010; McIntosh et al., 2003). Although many of those reports focused on the characterization of developed materials, there were very few reports (Barfod et al., 2007) that analyze each impedance of the anode and cathode in the full cell impedance of a practical cell simultaneously and separately by applying EIS under operation.

EIS with two-electrode set-up on the practical microtubular IT-SOFC was thus carried out. To evaluate the impedance variation of each part of the cell under operation, gas feeding conditions for the anode and cathode were varied.
In addition, very few experimental studies on current distributions in a cell that lead to temperature distributions have been reported to date, although a number of computational analyses have been reported (Campanari & Iora, 2004; Costamagna & Honegger, 1998; Kanamura & Takehara, 1993; Nishino et al., 2006; Suzuki et al., 2008). Thus the current distributions are estimated by using the overpotentials evaluated with EIS.

2. Experimental

2.1 EIS measurements

All measurements were performed using an anode-supported microtubular SOFC(Kawakami et al., 2006) with an outer and an inner diameters of 5 mm and 3 mm, respectively. The thickness of the electrolyte was 30 μm(Ueno, 2005). Anode substrate tube was made of $NiO/(ZrO_2)_{0.9}$
$(Y_2O_3)_{0.1}$ (NiO/YSZ). Anode interlayer of $NiO/(Ce_{0.9}Gd_{0.1})O_{1.95}$ (NiO/GDC10) for low temperature operation was coated onto the anode substrate. Electrolyte was $La_{0.8}Sr_{0.2}Ga_{0.8}Mg_{0.2}O_{2.8}$ (LSGM). A layer of $(Ce_{0.6}La_{0.4})O_{1.8}$ (LDC40) was inserted between the anode interlayer and electrolyte to prevent undesirable nickel diffusion during cell preparation at high temperature. Cathode made of $(La_{0.6}Sr_{0.4})(Co_{0.2}Fe_{0.8})O_3$ (LSCF), whose length in the axial direction was 3.8 cm, was coated on the electrolyte. Geometrical electrode area was 5.9 cm^2.
Figure 1 illustrates the configuration of the experimental set-up. Temperature of the quartz tube having an inner diameter of 4.6 cm was maintained at 700 °C with an electric furnace. Anode and cathode gas lines were supplied with mixtures of H_2/N_2 and O_2/N_2 at constant flow rates, respectively. The anode NiO was reduced to Ni by feeding H_2/N_2 mixture gas for two hours prior to measurements. The anode and cathode were electrically connected with the four-terminal method.
Current-voltage (I-V) curves were measured with a potentio/galvanostat (HA-320, Hokuto Denko Co., Ltd) and mass flow controllers (SEC-40, Horiba STEC) controlled by LabView 8.5 (National Instruments Inc.) on a personal computer through a data acquisition board (NI USB-6008, National Instruments Inc.). ElS measurements were carried out using a frequency response analyzer (FRA) (DS-2100/DS-266/DS-273, Ono Sokki Co Ltd.) combined with the potentio/galvanostat. EIS was carried out with two-electrode set-up without the reference electrode. An equivalent circuit presented in Fig. 2 (Barsoukov & Macdonald, 2005; McIntosh et al., 2003) is used for the complex nonlinear least square (CNLS) fitting (Barsoukov & Macdonald, 2005) of obtained impedance spectra with excluding inductive part.
Each resistance and capacitance is evaluated with a CNLS fitting program, Z-View (Scribner Inc.). In this circuit, R_{hf} and C_{hf} denote resistance and associated capacitance corresponding to the high frequency arc in the complex-plane plot of the impedance, respectively, R_{Ohm} is the Ohmic resistance of the cell, R_{lf} and C_{lf} are resistance and associated capacitance for the low frequency arc, respectively.
Each one of the R-C branches dominantly represents the charge transfer process in low current density region, and mass transfer process in high current density region. In the

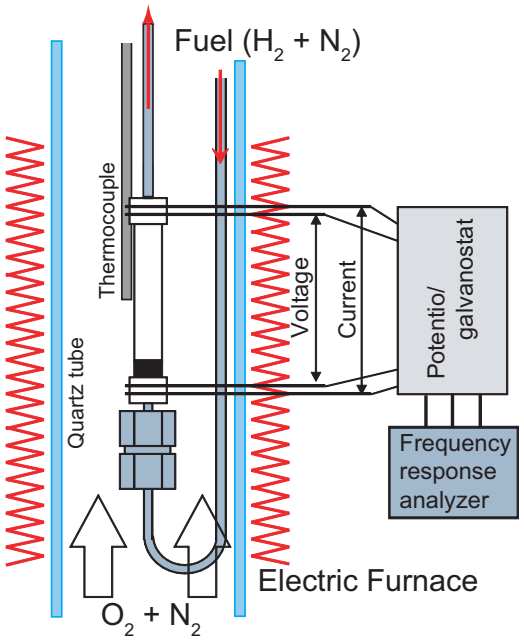

Fig. 1. Experimental set-up of the microtubular SOFC.

present chapter, the equivalent circuit is not separated into the charge and mass transfer processes since the complex plane plots exhibited only two arcs, whose behavior should be analyzed with simple one R-C branch prior to appropriate separations of overlapping arcs and equivalent circuit.

The Nernst loss by the partial pressure gradient of hydrogen and oxygen ascribed to their consumption leads to current distribution in the axial direction. Ohmic resistance in the anode and cathode electrodes is also attributed to this current distribution. However, the author use the above equivalent circuit for uniform current distribution to obtain average behavior over the axial direction of the cell.

As a result, the variations in these circuit parameters are obtained in accordance with current densities, and anode and cathode gas-feed conditions. In addition, the impedance of the mass transfer process can be analyzed as that of the finite length diffusion (Nakajima et al., 2010).

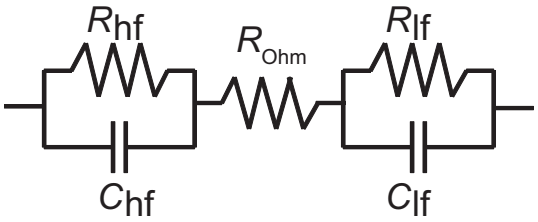

Fig. 2. Equivalent circuit of an SOFC.

2.2 Temperature measurements

During the measurements, anode and cathode were fed upward with mixtures of H_2/N_2 and dried air at constant flow rates with current density, respectively. Temperatures at the upper, middle, and lower parts in the axial direction of the anode and cathode surfaces were measured by thermocouples. The cathode side thermocouple tip was fixed with silver paste and wire to retain contact and to minimize radiation heat transfer at the thermocouple with their low emissivity. The changes of the cell voltages by the installation of the thermocouples were less than 3%.

3. Results and discussion

3.1 Evaluation of overpotentials from EIS spectra

Figure 3 shows the I-V curves for the different anode fed gas flow rates and gas compositions. The performance of this type of the cell significantly depends on the fuel utilization and the partial pressure, indicating the effect of the fuel mass transfer.

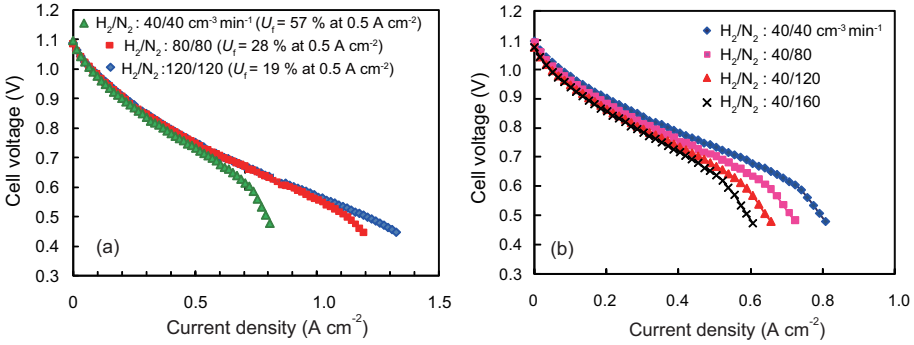

Fig. 3. I-V curves of the SOFC under different (a) anode gas flow rates and (b) partial pressures. Cathode: Dried air of 1000 $cm^3 min^{-1}$. $U_{ox} = 5.7\%$ at 0.5 A cm^{-2}.

The resistances in the equivalent circuit can be written as the derivatives of the anode, Ohmic, and cathode overpotentials because EIS measures voltage drops in an infinitesimal interval of the current (Konomi & Saho, 2006; Nakajima et al., 2005). The resistances are non-Ohmic resistance and depend on current density (Nakajima et al., 2006). Overpotentials are hence calculated by integrating each resistance with respect to current as follows.

$$R_x(I) = \frac{\partial \eta_x}{\partial I} \tag{1}$$

where x = hf, Ohm, lf. Each overpotential is then evaluated by integration of those resistances as follows.

$$\eta_x = \int R_x(I) dI \tag{2}$$

Figure 4 shows the complex plane plots by EIS, where low frequency arc becomes large according to a decrease in hydrogen partial pressure by variation of the anode gas flow rate from H_2/N_2 = 40/40 cm^3 min^{-1} (1atm, 25 °C) to 40/160 cm^3 min^{-1}. Change of high

frequency arc is small. In the previous study, the high and low frequency arcs have been found to be attributed to the cathode and anode reactions, respectively, in the low and medium current regions, from the variation of the arcs with anode and cathode gas feeding conditions (Nakajima et al., 2010). Hence anode and cathode impedances can be separated for a cell with two electrode set-up (without the reference electrode) by frequency domain when the time constant (relaxation time) sufficiently differs between the anode and cathode as the present cell.

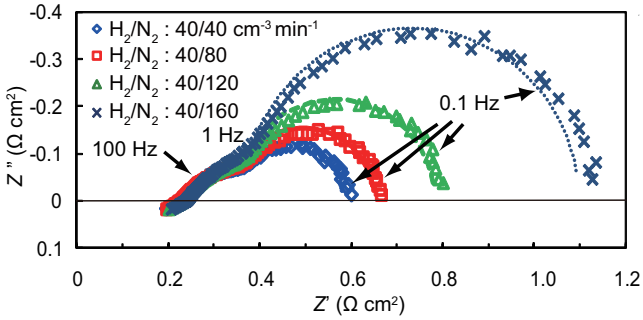

Fig. 4. Complex-plane plots of the SOFC at 0.51 A cm^{-2} under different H_2 partial pressures. Cathode: Dried air of 1000 $cm^3 min^{-1}$. $U_f = 58\%$ and $U_{ox} = 5.8\%$.

The resistances obtained by the CNLS fitting are numerically integrated according to Eq. 2. Then overpotential at each part is averagely obtained as illustrated in Fig. 5 with I-V curves. In this case, η_{hf} is the cathode overpotential, η_c, η_{Ohm} is the Ohmic overpotential, and η_{lf} is the anode overpotential, η_a. The I-V curves and voltages evaluated by subtracting the sum of the overpotentials from the open circuit voltage are in good agreement. Each overpotential is presented in Figs. 6 and 7.

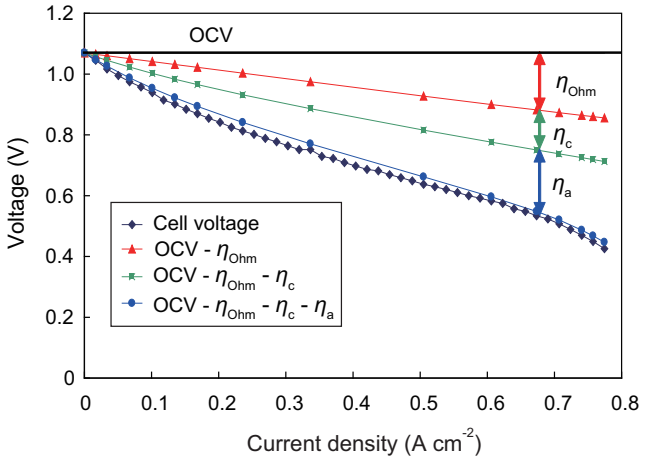

Fig. 5. Cell voltage and overpotential map of the SOFC. Cathode: Dried air of 1000 $cm^3 min^{-1}$. Anode: H_2/N_2 = 40/40 $cm^3 min^{-1}$. U_f = 57% and U_{ox} = 5.7% at 0.5 A cm^{-2}.

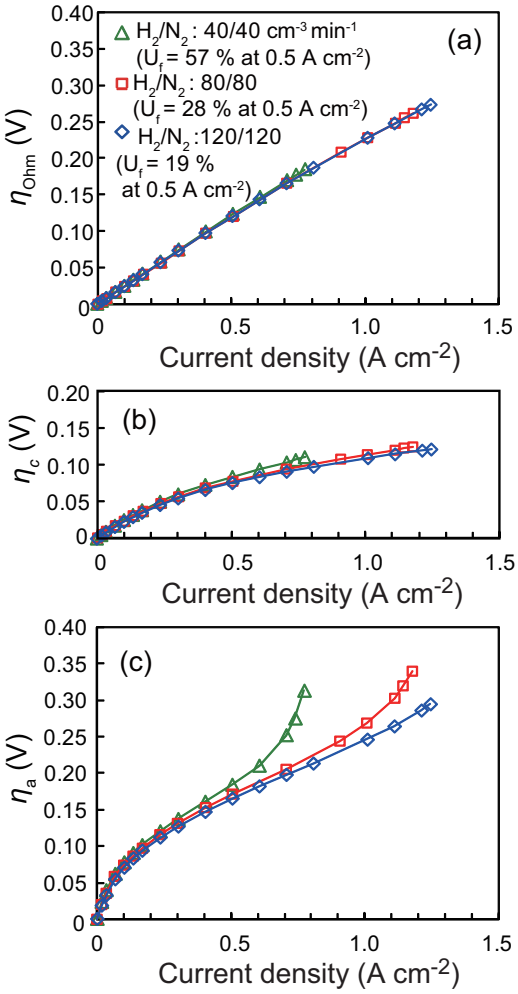

Fig. 6. (a) Ohmic, (b) cathode, and (c) anode overpotentials of the SOFC for different anode gas flow rates. U_{ox} = 5.7% at 0.5 A cm^{-2}.

3.2 Anode overpotentials

The anode and cathode activation overpotentials, η_{aa}, and η_{ca}, respectively, are then separated using the Butler-Volmer (BV) equation as illustrated in Fig. 8. Thereby the concentration overpotential of the anode, η_{ac}, is also separated by subtracting the anode activation overpotentials from the anode overpotentials as presented in Figs. 9 and 10. It should be noted that the overpotential described by the BV type equation is controversial in terms of the electron transfer rate limiting (the activation overpotential) or chemical reaction rate limiting process.

The separation of the overpotentials is successfully confirmed by the observation of the overpotential variation in conjunction with the variation of the anode gas flow rate and

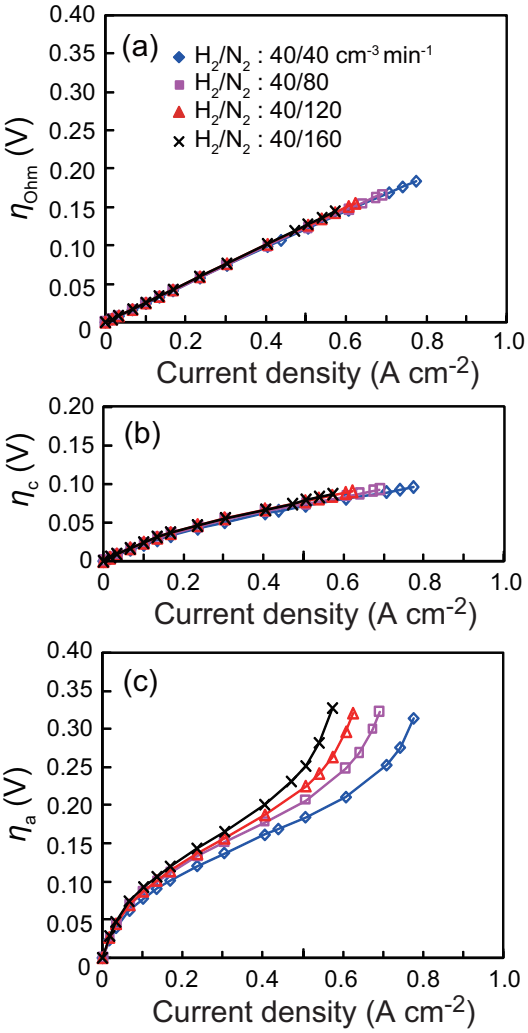

Fig. 7. (a) Ohmic, (b) cathode, and (c) anode overpotentials of the SOFC for different H_2 partial pressures. U_f = 57% and U_{ox} = 5.7% at 0.5 A cm^{-2}.

composition. When hydrogen partial pressure in the fed gas is decreased, the activation overpotential also increases owing to the decrease in the exchange current density. In this way, EIS can be used to diagnose the cell status under operation.

The Nernst loss due to the fuel partial pressure gradient along the axis by the fuel consumption contributes the large anode concentration overpotential as indicated from the diffusion impedance in the previous report (Nakajima et al., 2010). This Nernst loss results in current distribution along the axis as described in later section.

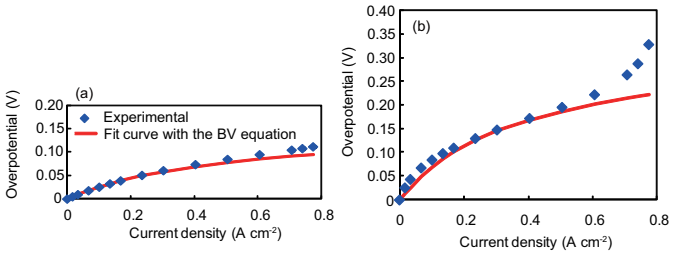

Fig. 8. (a) Activation and (b) concentration overpotentials at the anode of the SOFC for different anode gas flow rates.

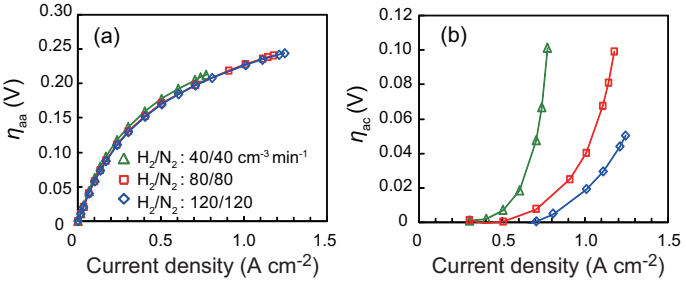

Fig. 9. (a) Activation and (b) concentration overpotentials at the anode of the SOFC for different anode gas flow rates.

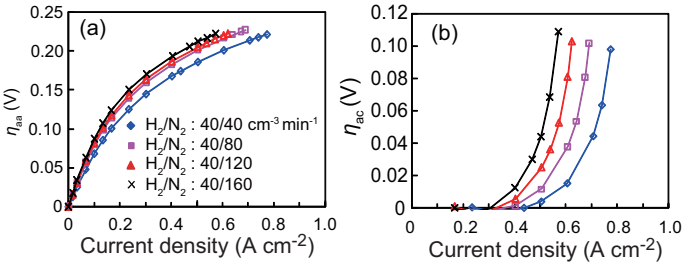

Fig. 10. (a) Activation and (b) concentration overpotentials at the anode of the SOFC for different anode gas flow rates.

3.3 Cathode overpotentials

At the cathode, the oxygen utilization was rather smaller than fuel utilization according to practical operation conditions. So, the Nernst loss from the oxygen concentration gradient along the axis is small in contrast to the anode. In the low and medium current regions, the concentration overpotential at the cathode is almost negligible and the activation overpotential is observed as shown in Figs. 6 and 7. However, the large current region in the case of large hydrogen flow rate, decrease in the oxygen partial pressure of the fed gas in the cathode side leads to an increase in the diameter of the low frequency arc of the complex plane plot, that is R_{lf}, as seen in Fig. 11. Thus the oxygen mass transfer impedance is included in the low frequency arc. Hence η_{lf} increases with a decrease in the oxygen partial pressure in the fed gas as shown in Fig. 12(a).

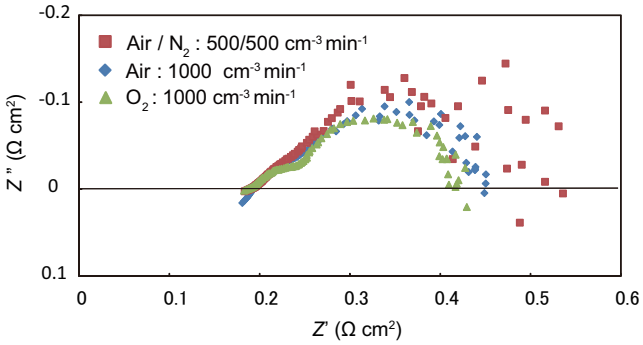

Fig. 11. Complex-plane plots of the SOFC for different oxygen partial pressures.

Assuming that the cathode concentration overpotential is zero when oxygen gas is fed, it can be separated by subtracting η_{lf} for oxygen gas from η_{lf} for other oxygen gas partial pressures as presented in Fig. 12(b). This is so-called O_2 gain with reference to the case of oxygen gas.

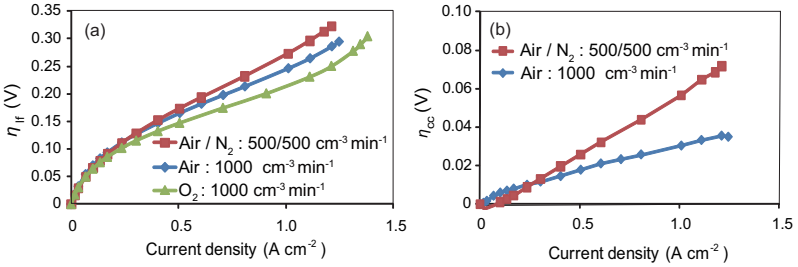

Fig. 12. (a) Overpotential for the low frequency arc and (b) cathode concentration overpotentials of the SOFC for different oxygen partial pressures.

Then the concentration overpotential at the cathode is analyzed in the light of the oxygen transfer at the cathode surface boundary layer. The author calculates the concentration overpotentials from the convective mass transfer using the Sherwood numbers for forced and natural convections for the cells having two different diameters in the cylindrical quartz tube. Then the calculated overpotential is compared with that derived from the EIS measurements. In analogy with the Nusselt number, Nu, for the circular-tube annulus (Kays & Perkins, 1985), the Sherwood number, Sh, is

$$Sh = \frac{h_{O_2} D_e}{D_{O_2}} \tag{3}$$

where h_{O_2} and D_{O_2} represent the mass transfer coefficient and the binary molecular diffusivity of O_2, respectively. D_{O_2} can be calculated from reported values at low temperatures on the basis of the Chapman-Enskog model (Bird et al., 2007). D_e is the hydraulic diameter, $D_o - D_i$, difference between the outer and inner diameters of the circular-tube annulus. In the present case, D_o and D_i are the diameters of the quartz tube and the cell, respectively.
In the case of forced convection, known Nu for fully developed laminar flow (Kays & Perkins, 1985) is used as Sh.

In the case of natural convection with laminar flow, in analogy with Nu for vertical fluid layer (Churchill, 1983),

$$Sh = \frac{h_{O_2}(r_o - r_i)}{D_{O_2}} = 0.28Ra^{1/4}\left(\frac{l}{r_o - r_i}\right)^{-1/4} \tag{4}$$

where

$$Ra = GrSc \tag{5}$$

$$= \frac{g(\rho^* - \rho^{el})(r_o - r_i)^3}{\rho^* \nu D_{O_2}} \tag{6}$$

l is the cathode axial length. ρ^* and ρ^{el} are the densities of the fed and cathode surface gas, respectively, r_o and r_i are the radii of the quartz tube and the cell, respectively. ν is the kinematic viscosity of air. In the present chapter, h_{O_2} at ρ^{el} of fed nitrogen density is used for simplification.

Oxygen flux, J_{O_2} is expressed as

$$J_{O_2} = h_{O_2}(C^b_{O_2} - C^{el}_{O_2}) \tag{7}$$

where C^b and $C^{el}_{O_2}$ are oxygen concentrations in the fed gas and at the cathode surface, respectively. In the case of natural convection, the mass transfer coefficient is compensated with the average radius, r_m, by multiplying $r_m/r_i = (r_o - r_i)/r_i ln(r_o/r_i)$ (Churchill, 1983) to correlate the current density. Since J_{O_2} can be calculated from current, and h_{O_2} and $C^b_{O_2}$ are known, $C^{el}_{O_2}$ is yielded.

The cathode concentration overpotential, η_{cc}, is given by substituting $C^{el}_{O_2}$ into the following equation.

$$\eta_{cc} = \frac{RT}{\alpha nF}\left(\ln\frac{C^b_{O_2}}{C^{el}_{O_2}} - \ln\frac{C^{*b}_{O_2}}{C^{*el}_{O_2}}\right) \tag{8}$$

Here, η_{cc} is derived as the O_2 gain with the second term in the right-hand side for O_2 gas having negligibly small value.

As presented in Fig. 13, the concentration overpotentials measured from EIS are larger than that calculated for forced convection and smaller than that for natural convection. Despite that h_{O_2} for natural convection is overestimated for simplification, the concentration overpotentials measured are smaller than those for natural convection. The cathode concentration overpotentials in the present experimental set-up are thus determined by the mass transfer in the transition region between forced and natural convections.

Figure 14 shows the measured and calculated cathode concentration overpotentials for the cell having twice the diameter (Ishihara et al., 2009; Watanabe et al., 2010). The concentration overpotential is larger as predicted from the Sherwood numbers of Eq. 3. The concentration overpotentials measured from the EIS are also between those calculated for forced and natural convections.

In this way, the cathode concentration overpotential can be related with the Sherwood number. This is useful for actual SOFC systems because the Sherwood number can be determined for the structure of a cell, alignment of the cells in a stack, and gas feed conditions in the actual systems.

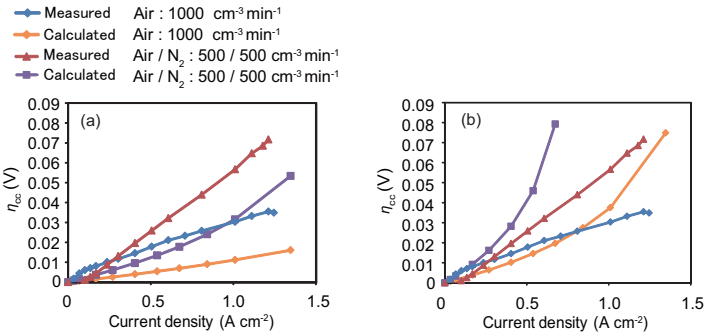

Fig. 13. Comparison of the cathode concentration overpotentials between those from EIS and those calculated for (a) forced convection and (b) natural convection.

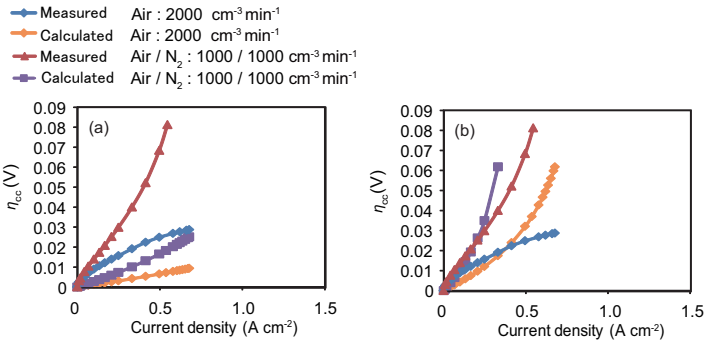

Fig. 14. Comparison of the cathode concentration overpotentials for the cell with twice the diameter between those from EIS and those calculated for (a) forced convection and (b) natural convection.

3.4 Current distribution in the cell derived from surface temperature measurements

In this section, current distribution in the axial direction of the cell by the fuel consumption is estimated by comparing the measured and calculated cell surface temperatures on the basis of the derivation of the relation between current (heat production rate) and cell temperature. This relation is derived using the anode, Ohmic, and cathode overpotentials evaluated in the previous section.

3.4.1 Heat production rates at the anode and cathode

Rates of irreversible heat production ascribed to the overpotentials are calculated by the product of the overpotentials and current as follows.

$$q_{\mathrm{op},x} = I\eta_{\mathrm{x}} \tag{9}$$

The author regards the heat production associated with the Ohmic overpotential as that originating in the electrolyte.

Figure 15(a) presents the irreversible heat production rates at the respective parts of the cell calculated from the overpotentials.

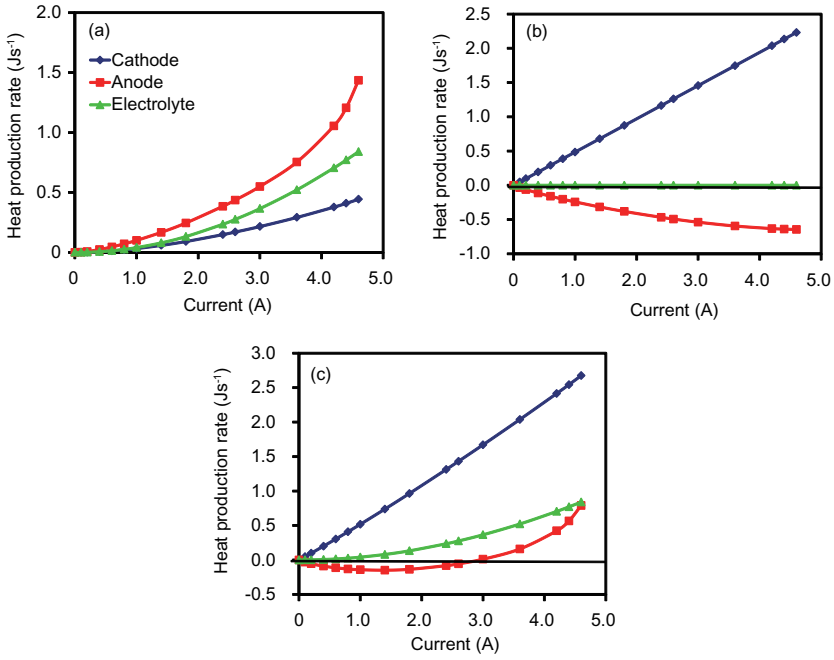

Fig. 15. Heat production rates of the SOFC with (a) the overpotentials, (b) the single electrode Peltier heats, and (c) the sum of them. $H_2/N_2 = 40/40$ cm^{-3} min^{-1}. Cathode: Dried air of 1000 cm^{-3} min^{-1}. $U_f = 57\%$ and $U_{ox} = 5.7\%$ at 3.0 A.

Reversible heat production with the entropy received reversibly by the anode, the electrochemical Peltier heat at the anode, is then derived from the entropy balance at the anode. The entropy balance for the anode reaction

$$\frac{1}{2}H_2 + O^{2-} \rightharpoonup \frac{1}{2}H_2O + e^- \tag{10}$$

is expressed as follows on the basis of the local equilibrium hypothesis(Kjelstrup & Bedeaux, 1997; Nakajima et al., 2004).

$$\frac{\pi_a}{T} + \frac{1}{2}S_{O^{2-}} + \frac{1}{2}S_{H_2} = S_{H_2O} \tag{11}$$

where π_a/T and $S_{O^{2-}}$ denote the entropies reversibly received by the anode and transported by O^{2-} in the electrolyte, respectively. π_a corresponds to the single electrode Peltier heat. S_{H_2}, S_{H_2O} are the entropies consumed by the formations of H_2 and H_2O, respectively.
Here the entropy transported by electrons at the electrode is neglected since its value in metal is negligibly small compared with the other terms in general (Moore & Graves, 1973; Vedernikov, 1969). In this section, T and F have their common meanings. Because $S_{O^{2-}}$ in the LSGM has not been reported, that in $(ZrO_2)_{0.92}(Y_2O_3)_{0.08}$(YSZ) obtained by thermoelectric power measurement (Ahlgren & Willy Poulsen, 1994) is applied.
Then S_{H_2} and S_{H_2O} are obtained from those at 1 atm in thermodynamic data. Here, partial pressures of H_2 and H_2O are calculated from the ratio of molar flow rate of the product water

to that of fed gases. For this calculation, 50 - 75 % of total current is assumed between the inlet and midpoint of the anode tube according to hydrogen utilization to estimate the amounts of the product water and remaining hydrogen at the midpoint, considering current distribution along the axial direction owing to the Nernst loss. Strictly speaking, this partial pressure terms should be excluded for the calculation of total heat production since those terms are included in the measured overpotential as the Nernst loss.
The entropy received by the cathode is also derived from the entropy balance between the formation of O_2 and transport of O^{2-}.

$$\frac{\pi_c}{T} + \frac{1}{2}S_{O^{2-}} + \frac{1}{2}S_{H_2} = S_{H_2O} \tag{12}$$

The relation between current and reversible heat production rates of the anode and cathode are given from the product of the Peltier heats and current as presented in Fig. 15(b).
Since the total heat production rates at the anode, q_a, and cathode, q_c, are expressed as the sum of the heat production rates associated with the overpotentials and the single electrode Peltier heats as follows,

$$q_a = q_{op,a} - \frac{I\pi_a}{F} \tag{13}$$

$$q_c = q_{op,c} + \frac{I\pi_c}{F} \tag{14}$$

the total heat production rates at the respective parts of the cell are shown in Fig. 15(c). These heat production rates seem to represent those in the middle part of the cell (Nakajima et al., 2009). The heat production rate at the cathode is significantly large compared with those at the anode and electrolyte. The heat absorption by the single electrode Peltier heat associated with current can be seen at the anode.
By substituting the total heat production rates per unit volume into the heat conduction (energy balance) equations for the constitutive layers and integrating the differential equations with boundary conditions between the layers and at the surfaces, temperatures at the anode and cathode surfaces can be evaluated.

3.4.2 Relation between the surface temperature and local current

Assuming uniform heat flux in the axial direction and temperature in the circumferential direction, the energy balance (the heat conduction) equation at steady state of the anode, electrolyte and cathode layers reduces to

$$0 = \frac{1}{r}\frac{d}{dr}\left(\lambda_x r \frac{dT_x(r)}{dr}\right) + \frac{q_x}{V_x} \tag{15}$$

Here, r, T, λ, and V are the radial coordinate, temperature, thermal conductivity, and volume of each layer, respectively. The subscripts, x = a, el (Ohm), c represent the anode, electrolyte and cathode layers. The radiation heat transfer is also assumed to be negligible owing to metallic cathode current collector layer (Nakajima et al., 2009). Integration of this simplified

equation yields the relation between the local current density and temperature in the anode and cathode (Nakajima et al., 2009).
The heat fluxes at the boundaries give the following boundary conditions.

$$-\lambda_{\mathrm{el}}\left(\frac{dT_{\mathrm{el}}(r)}{dr}\right)_{r=r_{\mathrm{a-el}}} = -\lambda_{\mathrm{a}}\left(\frac{dT_{\mathrm{a}}(r)}{dr}\right)_{r=r_{\mathrm{a-el}}} \tag{16}$$

$$-\lambda_{\mathrm{el}}\left(\frac{dT_{\mathrm{el}}(r)}{dr}\right)_{r=r_{\mathrm{c-el}}} = -\lambda_{\mathrm{c}}\left(\frac{dT_{\mathrm{c}}(r)}{dr}\right)_{r=r_{\mathrm{c-el}}} \tag{17}$$

$$-\lambda_{\mathrm{a}}\left(\frac{dT_{\mathrm{a}}(r)}{dr}\right)_{r=r_{\mathrm{a,s}}} = h_{\mathrm{fu}}(T_{\mathrm{fu}} - T_{\mathrm{a,s}}) \tag{18}$$

$$-\lambda_{\mathrm{c}}\left(\frac{dT_{\mathrm{c}}(r)}{dr}\right)_{r=r_{\mathrm{c,s}}} = h_{\mathrm{air}}(T_{\mathrm{c,s}} - T_{\mathrm{air}}) \tag{19}$$

where the subscripts, "c,s" and "c-el" represent the cathode surface and cathode-electrolyte boundary, respectively. h_{fu} and h_{air} denote the heat transfer coefficients at the anode and cathode surfaces, respectively. T_{fu} and T_{air} are temperatures of fed gases in the anode and cathode sides, respectively, which equal to the cell surface temperature at zero current. The thermal conductivities of the anode and cathode layers are effective values obtained from those of gas phase and materials with the common mixture law in porous media.
The above heat transfer coefficients are calculated by the Nusselt numbers for fully developed laminar flow of forced convection in a circular tube annulus (Kays & Perkins, 1985). The Nusselt numbers on the anode and cathode are 3.66 and 11.3, respectively for the present experimental set-up. Here, the thermal conductivity of the anode gas, λ_{fu}, is estimated from a partial-pressure-weighted average of individual thermal conductivities of fed gases and the product water. Thus λ_{fu} varies with current according to the amounts of the product water and remaining hydrogen.
Substituting these heat production rates into Eq. 15, the author derives the relation between the local current density and temperatures at the surfaces of the anode and cathode using thermal conductivities presented in Table 1.

Materials and gases	λ (W m^{-1} K^{-1})
Anode (Effective value)(Wang et al., 2009)	1.4
Electrolyte (Yasuda et al., 2000)	2.08
Cathode (Effective value)(Campanari & Iora, 2004)	2.0
Hydrogen (1 atm, 700°C)(PROPATH-group, 2008)	0.438
Nitrogen (1 atm, 700°C)(PROPATH-group, 2008)	0.064
Water vapor (1 atm, 700°C)(PROPATH-group, 2008)	0.094
Air (1 atm, 700°C)(PROPATH-group, 2008)	0.066

Table 1. Thermal conductivities of the materials and gases in the SOFC.

Thereby the current density at each part can be determined so that the surface temperature calculated at each part of the anode and cathode is identical with the measured temperature.

In the present study, overpotentials are regarded as uniform in the axis direction because the voltage between the upper and lower ends of the cathode was smaller than 50 mV.
In the above analysis, the sensitivity of the derived temperatures to the heat transfer coefficient at the anode surface is rather larger than that to the heat transfer coefficient at the cathode surface and the other thermal conductivities. That is, the contributions of hydrogen partial pressure due to the large thermal conductivity and of anode-supported tube design are significant.

3.4.3 Local current densities

Figure 16 shows the surface temperatures of the cell measured at anode gas flow rates of H_2/N_2 = 40/40, 40/160 cm^{-3} min^{-1} and a cathode flow rate of dried air of 1000 cm^{-3} min^{-1}. In this case, the cathode concentration overpotential is not significant. The temperatures increase with an increase in the cell average current density. The increase in the temperature at the lower parts (upstream) of the anode and cathode are largest.

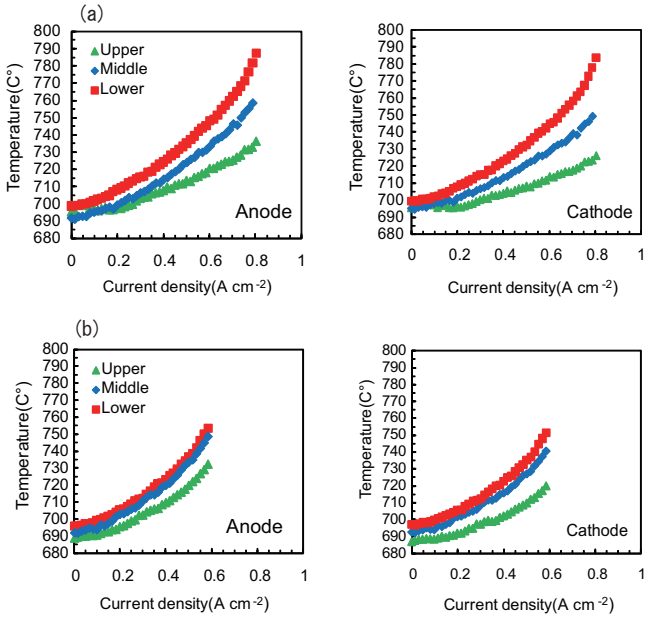

Fig. 16. Surface temperatures against the average current density of the SOFC for (a) H_2/N_2 = 40/40 cm^{-3} min^{-1} and (b) H_2/N_2 = 40/160 cm^{-3} min^{-1}. Cathode: Dried air of 1000 cm^{-3} min^{-1}. U_f = 57% and U_{ox} = 5.7% at 0.5 A cm^{-2}.

The temperature distributions represent the current density distributions. With an increase in the cell current, the surface temperature of the anode becomes higher than that of the cathode, especially at the upper part (downstream). This is probably ascribed to the temperature rise of the anode gas from the upstream to the downstream along the axis. Thus the cathode surface temperatures calculated and measured are compared to determine the local current densities at the upper part. In the author's previous report, this anode gas temperature effect was

overestimated, so that the current densities derived at the upper part were extremely small (Nakajima & Kitahara, 2011).

The local current densities determined are plotted against the total current in Fig. 17. The current density decreases with the decrease in the hydrogen partial pressure in the fed fuel in accordance with an increase in the average anode activation and concentration overpotentials in the previous section. Hence the current distributions exhibited in the cell are probably ascribed to the hydrogen consumption in upstream. In particular, the current density at the upper part is small in both cases, which shows that the upper part does not effectively take part in the power generation. The higher hydrogen partial pressure results in significantly larger current in the lower part with increasing the temperature and decreasing the overpotentials there. Thus the current distribution is enhanced although the cell power output is increased.

Figure 18 shows the local I-V characteristics. The current distribution seems to be attributed mainly to the concentration overpotential, which also indicates the Nernst loss by the hydrogen consumption in the upstream. The higher temperatures at the lower part also would decrease the Ohmic and activation overpotentials. Total currents calculated by the integration of linearly interpolated local current densities along the axis agree well with the measured current as shown in Fig. 19. Hence the local current densities obtained in the present study are reasonable.

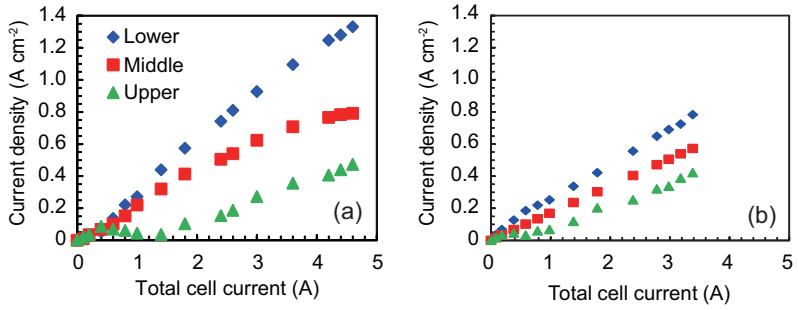

Fig. 17. Local current densities against the total cell current of the SOFC for (a) H_2/N_2 = 40/40 cm^{-3} min^{-1} and (b) H_2/N_2 = 40/160 cm^{-3} min^{-1}. Cathode: Dried air of 1000 cm^{-3} min^{-1}. U_f = 57% and U_{ox} = 5.7% at 3.0 A.

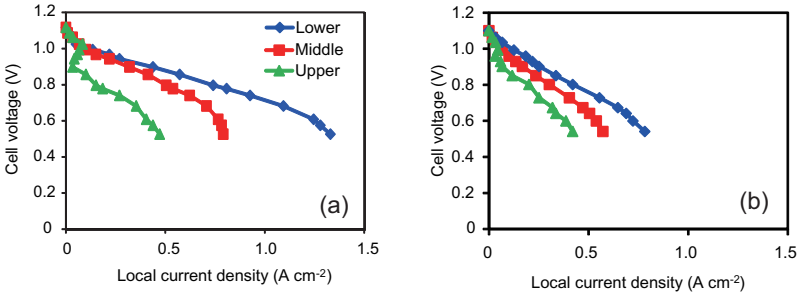

Fig. 18. Local I-V characteristics of the SOFC for (a) H_2/N_2 = 40/40 cm^{-3} min^{-1} and (b) H_2/N_2 = 40/160 cm^{-3} min^{-1}. Cathode: Dried air of 1000 cm^{-3} min^{-1}.

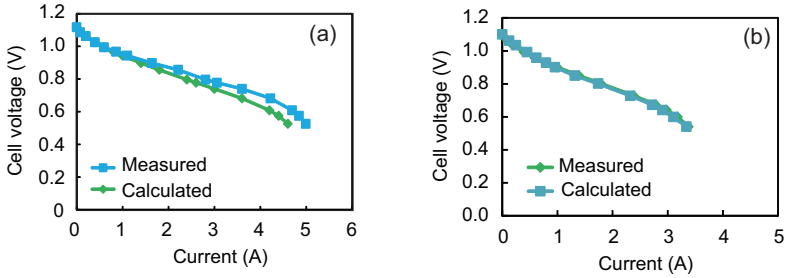

Fig. 19. Comparison of the calculated and measured I-V characteristics of the SOFC for (a) H_2/N_2 = 40/40 cm^{-3} min^{-1} and (b) H_2/N_2 = 40/160 cm^{-3} min^{-1}. Cathode: Dried air of 1000 cm^{-3} min^{-1}.

4. Conclusion

In this chapter, EIS analysis clarifies the concentration overpotentials determined by the fuel and oxygen transfers in an intermediate temperature anode-supported microtubular SOFC. Current distribution in the cell by the Nernst loss due to the fuel partial pressure gradient along the axis of the cell is also described from surface temperature measurements. These results give the information for the optimization of the cell structure, cell alignment in the stack and operation conditions to decrease the anode concentration overpotential including the Nernst loss, for effective use of the whole electrodes in the cell, and to improve the durability of the cell by more uniform current and temperature distributions.

5. Acknowledgments

This work was supported by a grant of the Fukuoka Strategy Conference for Hydrogen Energy in the Fukuoka prefectural government, Japan. The author is also grateful to graduate students, Satoshi IGAUE, Atsushi OKAZAKI, Ryota MATSUMOTO, and Ken-ichi KIYAMA for assistance with the measurements and calculations.

6. References

Ahlgren, E. & Willy Poulsen, F. (1994). Thermoelectric power of YSZ, *Solid State Ionics* 70-71(PART 1): 528–532.

Barfod, R., Mogensen, M., Klemensø, T., Hagen, A., Liu, Y. L. & Hendriksen, P. V. (2007). Detailed characterization of anode-supported SOFCs by impedance spectroscopy, *Journal of the Electrochemical Society* 154(4): B371–B378.

Barsoukov, E. & Macdonald, J. R. (eds) (2005). *Impedance Spectroscopy: Theory, Experiment, and Applications*, 2nd edn, John Wiley & Sons, New York.

Bird, R. B., Stewart, W. E. & Lightfoot, E. N. (2007). *Transport Phenomenon*, 2nd edn, John Wiley & Sons, New York.

Campanari, S. & Iora, P. (2004). Definition and sensitivity analysis of a finite volume SOFC model for a tubular cell geometry, *Journal of Power Sources* 132(1-2): 113–126.

Churchill, S. W. (1983). *in* E. U. Schlunder (ed.), *Heat exchanger design handbook*, Hemisphere.

Costamagna, P. & Honegger, K. (1998). Modeling of solid oxide heat exchanger integrated stacks and simulation at high fuel utilization, *Journal of the Electrochemical Society* 145(11): 3995–4007.

Esquirol, A., Brandon, N. P., Kilner, J. A. & Mogensen, M. (2004). Electrochemical characterization of $La_{0.6}Sr_{0.4}Co_{0.2}Fe_{0.8}O_3$ cathodes for intermediate- temperature SOFCs, *Journal of the Electrochemical Society* 151(11): A1847–A1855.

Horita, T., Yamaji, K., Sakai, N., Yokokawa, H., Weber, A. & Ivers-Tiffée, E. (2001). Oxygen reduction mechanism at porous $La_{1-x}Sr_xCoO_{3-d}$ cathodes/$La_{0.8}Sr_{0.2}Ga_{0.8}Mg_{0.2}O_{2.8}$ electrolyte interface for solid oxide fuel cells, *Electrochimica Acta* 46(12): 1837–1845.

Huang, Q. A., Hui, R., Wang, B. & Zhang, J. (2007). A review of ac impedance modeling and validation in SOFC diagnosis, *Electrochimica Acta* 52(28): 8144–8164.

Ishihara, T., Eto, H., Zhong, H. & Matsumoto, H. (2009). Intermediate temperature solid oxide fuel cells using $LaGaO_3$ based perovskite oxide for electrolyte, *Electrochemistry* 77(2): 115–122.

Ishihara, T., Shibayama, T., Nishiguchi, H. & Takita, Y. (2000). Nickel-Gd-doped CeO_2 cermet anode for intermediate temperature operating solid oxide fuel cells using $LaGaO_3$-based perovskite electrolyte, *Solid State Ionics* 132: 209–216.

Jiang, S. P. (2002). A comparison of O_2 reduction reactions on porous (La,Sr)MnO_3 and (La,Sr)(Co,Fe)O_3 electrodes, *Solid State Ionics* 146(1-2): 1–22.

Kanamura, K. & Takehara, Z. (1993). Temperature and thermal stress distributions in a tubular solid oxide fuel cell, *Bulletin of the Chemical Society of Japan* 66(10): 2797–2803.

Kawakami, A., Matsuoka, S., Watanabe, N., Saito, T., Ueno, A., Ishihara, T., Sakai, N. & Yokokawa, H. (2006). Development of two types of tubular SOFCs at TOTO, *Ceram. Eng. Sci. Proc.* 27(4)(3): 3–13.

Kays, W. M. & Perkins, H. C. (1985). Forced convection, internal flow in ducts, *in* W. M. Rohsenow, J. P. Hartnett & E. N. Ganic (eds), *Handbook of Heat Transfer*, 2nd edn, McGraw-Hill, New York.

Kjelstrup, S. & Bedeaux, D. (1997). Jumps in electric potential and in temperature at the electrode surfaces of the solid oxide fuel cell, *Physica A: Statistical Mechanics and its Applications* 244(1-4): 213–226.

Konomi, T. & Saho, I. (2006). Research of diagnosis technique on PEFC running condition (overvoltage analysis and diagnosis of PEFC by FFT), *Transactions of the Japan Society of Mechanical Engineers, Series B* 72(2): 455–462.

Leonide, A., Rüger, B., Weber, A., Meulenberg, W. A. & Ivers-Tiffée, E. (2010). Impedance study of alternative (La,Sr) $FeO_{3-\delta}$ and (La,Sr) (Co,Fe) $O_{3-\delta}$ MIEC cathode compositions, *Journal of the Electrochemical Society* 157(2): B234–B239.

Li, X. (2007). Thermodynamic performance of fuel cells and comparison with heat engines, *in* T. S. Zhao, K.-D. Kreuer & T. V. Nguyen (eds), *Advances in Fuel Cells*, Vol. 1, Elsevier, Amsterdam.

McIntosh, S., Vohs, J. M. & Gorte, R. J. (2003). Impedance spectroscopy for the characterization of Cu-ceria-YSZ anodes for SOFCs, *Journal of the Electrochemical Society* 150(10): A1305–A1312.

Moore, J. P. & Graves, R. S. (1973). Absolute seebeck coefficient of platinum from 80 to 340 K and the thermal and electrical conductivities of lead from 80 to 400 K, *Journal of Applied Physics* 44(3): 1174–1178.

Morita, H., Komoda, M., Mugikura, Y., Izaki, Y., Watanabe, T., Masuda, Y. & Matsuyama, T. (2002). Performance analysis of molten carbonate fuel cell using a Li/Na electrolyte, *Journal of Power Sources* 112(2): 509–518.

Nakajima, H. & Kitahara, T. (2011). Current distribution analysis of a microtubular solid oxide fuel cell with surface temperature measurements, *ECS Transactions* 35(1): 1087-1096.

Nakajima, H., Kitahara, T. & Konomi, T. (2010). Electrochemical impedance spectroscopy analysis of an anode-supported microtubular solid oxide fuel cell, *Journal of the Electrochemical Society* 157(11): B1686–B1692.

Nakajima, H., Konomi, T. & Kitahara, T. (2009). Thermal analysis of a microtubular solid oxide fuel cell using electrochemical impedance spectroscopy, *ECS Transactions* 25(2): 359–368.

Nakajima, H., Konomi, T., Kitahara, T. & Tachibana, H. (2008). Electrochemical impedance parameters for the diagnosis of a polymer electrolyte fuel cell poisoned by carbon monoxide in reformed hydrogen fuel, *Journal of Fuel Cell Science and Technology* 5: 041013.

Nakajima, H., Nohira, T. & Ito, Y. (2004). The single electrode peltier heats of Li^+/Li, H_2/H^- and Li^+/Pd-Li couples in molten LiCl-KCl systems, *Electrochimica Acta* 49(27): 4987–4991.

Nakajima, H., Nohira, T. & Ito, Y. (2005). Electrochemical impedance spectroscopy study of a hydrogen electrode reaction at a Zn electrode in a molten LiCl-KCl-LiH system, *Journal of Physical Chemistry B* 109(19): 9645–9650.

Nakajima, H., Nohira, T., Ito, Y., Kjelstrup, S. & Bedeaux, D. (2006). The surface adsorption of hydride ions and hydrogen atoms on Zn studied by electrochemical impedance spectroscopy with a non-equilibrium thermodynamic formulation, *Journal of Non-Equilibrium Thermodynamics* 31(3): 231–255.

Nishino, T., Iwai, H. & Suzuki, K. (2006). Comprehensive numerical modeling and analysis of a cell-based indirect internal reforming tubular SOFC, *Journal of Fuel Cell Science and Technology* 3(1): 33–44.

PROPATH-group (2008). A program package for thermophysical properties of fluids, PROPATH, ver. 13.1.
URL: *http://gibbs.mech.kyushu-u.ac.jp/ akasaka/propath_man/*

Suzuki, M., Shikazono, N., Fukagata, K. & Kasagi, N. (2008). Numerical analysis of coupled transport and reaction phenomena in an anode-supported flat-tube solid oxide fuel cell, *Journal of Power Sources* 180(1): 29–40.

Ueno, A. (2005). Manufacturing and applications of a tubular fuel cell stack fabricated by wet process (in Japanese), *in* K. Eguchi (ed.), *Development of Solid Oxide Fuel Cell*, CMC Publishing, Tokyo.

Vedernikov, M. V. (1969). Thermoelectric powers of transition metals at high temperatures, *Advan Phys* 18(74): 337–369.

Wang, Y., Yoshiba, F., Kawase, M. & Watanabe, T. (2009). Performance and effective kinetic models of methane steam reforming over Ni/YSZ anode of planar SOFC, *International Journal of Hydrogen Energy* 34(9): 3885–3893.

Watanabe, N., Kawakami, A., Oe, T. & Ishihara, T. (2010). Research of current collect property in micro tubular solid oxide fuel cell (1st report, evaluation of current collecting of single terminal in anode), *Transactions of the Japan Society of Mechanical Engineers, Series B* 76(768): 1224–1231.

Yasuda, I., Matsuzaki, Y., Yamakawa, T. & Koyama, T. (2000). Electrical conductivity and mechanical properties of alumina-dispersed doped lanthanum gallates, *Solid State Ionics* 135(1-4): 381–388.

13

Mass Transport Limitations in Proton Exchange Membrane Fuel Cells and Electrolyzers

Elise B. Fox and Héctor R. Colón-Mercado
Savannah River National Laboratory; Aiken, SC 29808
USA

1. Introduction

The performance of Proton Exchange Membrane Fuel Cells (PEMFC) and Electrolyzers (PEME) is subject to mass transport limitations. Within this chapter we will discuss the origination of those limitations and the current research efforts for mitigation. Hydrogen powered fuel cells operate based on the reaction of hydrogen and oxygen, (Figure 1) where the anode reaction is found in Eq. 1, the cathode reaction in Eq. 2 and the overall reaction in Eq. 3. The reverse of this reaction (Eq. 4) is electrolysis. Where, in the electrolyzer the anode reaction is Eq. 5 and the cathode reaction is Eq. 6.

$$H_2 \rightarrow 2H^+ + 2e \qquad E= 0V \tag{1}$$

$$\tfrac{1}{2}\, O_2 + 2H+ +2e- \rightarrow H_2O \qquad E= 1.229V \tag{2}$$

$$H_2 + \tfrac{1}{2}O_2 \rightarrow H_2O \qquad E= 1.229V \tag{3}$$

$$H_2O \rightarrow H_2 + \tfrac{1}{2}\, O_2 \qquad E= -1.229V \tag{4}$$

$$H_2O \rightarrow \tfrac{1}{2}\, O_2 + 2H^+ + 2e^- \qquad E= -1.229V \tag{5}$$

$$2H^+ + 2e^- \rightarrow H_2 \qquad E= 0V \tag{6}$$

Basic cell construction is very similar for both PEMFC and PEME. During electrolysis a voltage is applied to the cell while an ion conductor with electrocatalyst layers, such as Pt black on Nafion®, is used to split water into hydrogen and oxygen, as in Figure 2. As water is split into hydrogen and oxygen ions at the anode, the hydrogen ions travel across the PEM and oxygen is collected and exhausted at the bipolar plate. At the cathode, hydrogen ions recombine to create diatomic hydrogen, which can be then be stored for later use. The cell components are similar to those used in a PEM fuel cell, but different bipolar plates must be used due to the corrosive environment. PEMFCs typically use graphite bipolar plates that will degrade under the conditions used in a PEME. Corrosion resistant bipolar plates are substituted for graphite. Titanium plates are typically used, but are very expensive. Stainless steel bipolar plates have also been used, but there is a risk of leaching iron into the water, which would affect the performance of the catalysts and the membrane.

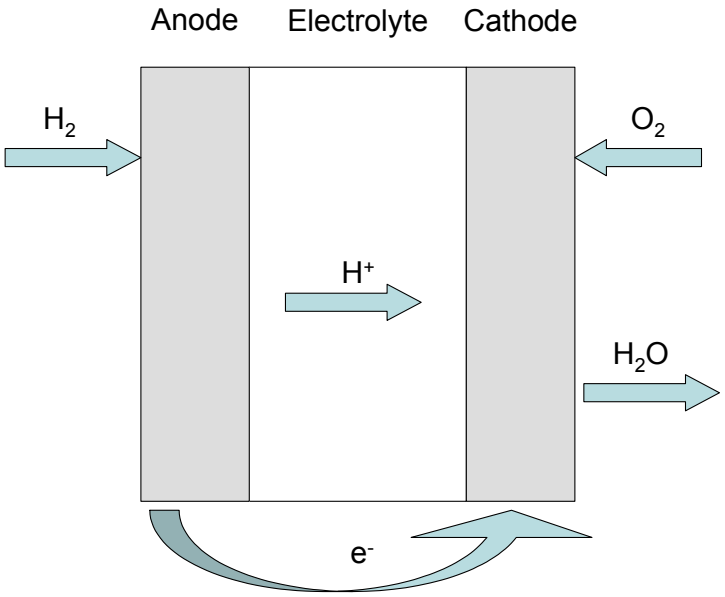

Fig. 1. Schematic of a PEM fuel cell

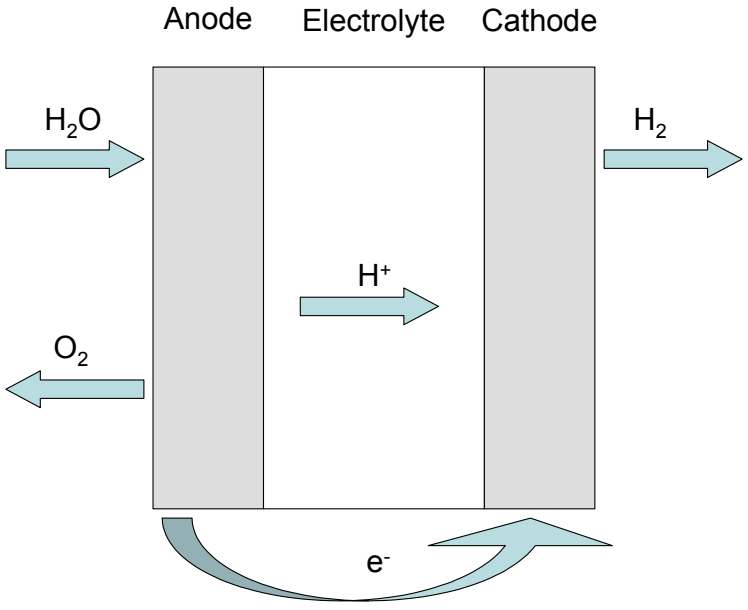

Fig. 2. Schematic of a PEM electrolyzer

Typically, the electrolyte is a solid polymer electrolyte, such as Nafion®, a sulfonated polytetrafluoroethylene based ionomer. One of the most widely sited structures in found in

Figure 3 (Yeager and Steck 1981). In this model, the structure of Nafion® is represented in three separate regions. Zone A is the fluorocarbon based backbone of the polymer. Zone C represents the ionic clusters, where ion transport occurs via either a vehicular motion or through the Grothaus mechanism. Zone B is representative of the interfacial region between A and C, consisting mostly of sulfonated ether side chains of the fluorocarbon backbone.

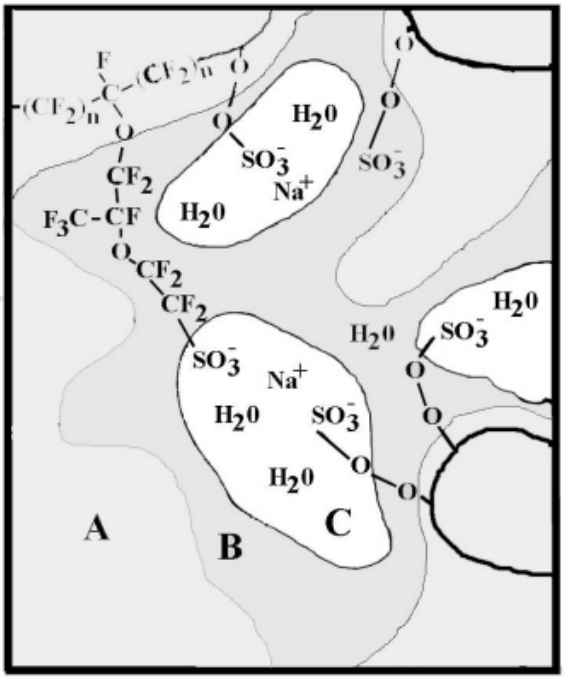

Fig. 3. Structure of Nafion®. Reproduced from (Yeager and Steck 1981)

The solid polymer electrolyte is in contact with the catalyst layer. Typically, the catalyst layer consists of a carbon supported Pt based catalyst mixed with ionomer (typically similar materials as the polymer electrolyte). The catalyst electrode must provide channels for the transport of reactants and products, and electrically conductive path for the transport of electrodes from the electrochemical reaction and an ion conductive path for the transport of protons from the electrode to the membrane. As it is shown in Figure 4, the electrode must have a balance in order to avoid performance losses and maximize the utilization of the Pt base catalyst.

The theoretical open circuit voltage for a PEMFC with a pure hydrogen feed is 1.23V. However, actual performance of the fuel cell is considerably lower due to cell resistances, slow reaction kinetics and gas transport limitations. At potentials above 0.9V, losses are attributed slow reaction kinetics at the cathode. Between 0.9 and 0.5V, internal cell resistances govern the incurred losses, while below 0.5V losses can be attributed to gas transport, or the availability of fuel supply for the reaction.

PEME are operated at higher potentials in order to drive the electrolysis reaction of water. During operation of a PEME in the voltage range below approximately 1.4 V the cell is

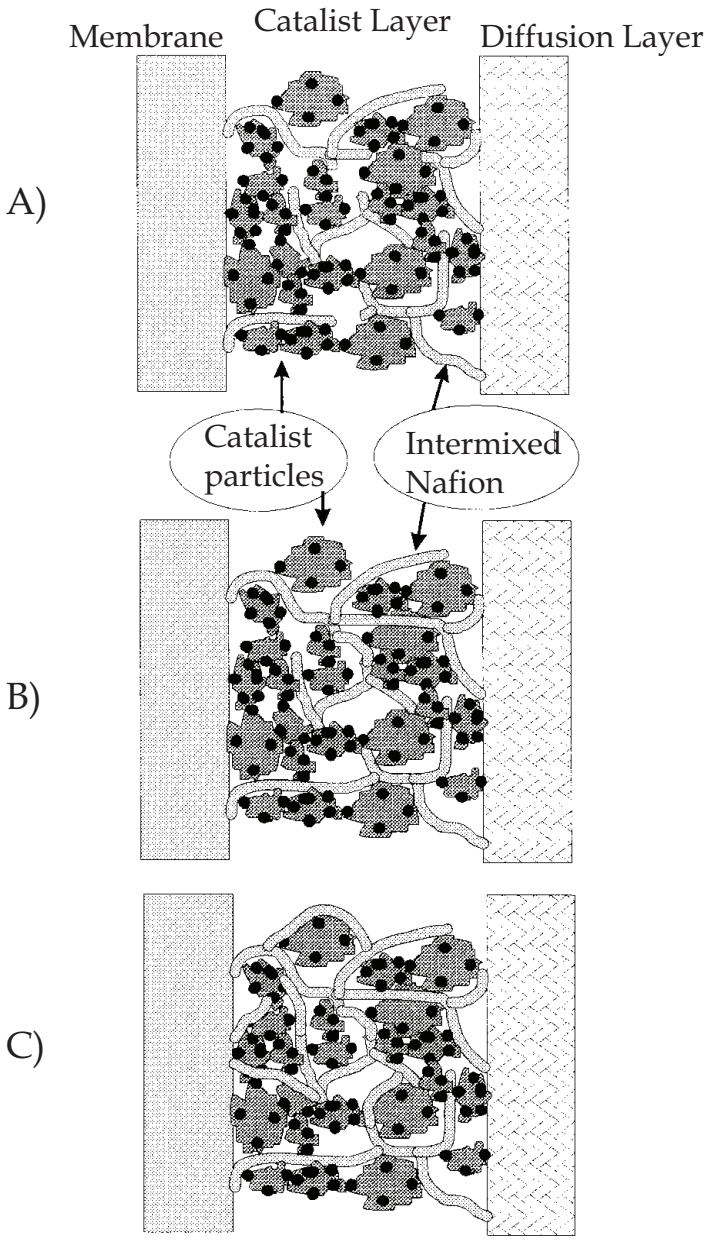

Fig. 4. Schematic representation of the catalytic layer. (A) where at low Nafion content not all the catalyst particles are connected to the membrane for ionic conduction (B) the optimal Nafion contentwhere there is good ionic and electronic conduction for all the catalyst particles. (C) When there is too much Nafion and not all of the catalyst particles are electronically connected to the diffusion layer. Reproduced from (Passalacqua, Lufrano et al. 2001)

kinetically limited and the current increases exponentially with the cell potential. Between 1.4 V and 1.7 V the cell is transitioning to a mass transfer limited mode of operation. Above 1.7 V, the cell current is completely limited by the diffusion rate of water across the membrane and further increases in the cell voltage do not result in higher cell current. The steady state current that is reached above 1.7 V is known as the mass transfer limited current density. At the mass transfer limiting current density, the rate of water diffusion across the membrane minus the rate of electroosmotic drag is equal to the reaction rate of water at the anode.

In general, the net water flux occurs from the anode to the cathode and higher water content is related to higher performance (Falcao, Rangel et al. 2009). Thus, the influence of water content at the cathode has a higher impact than the water content at the anode. At lower humidification levels, the hydrophilic fraction of the membrane, where the water travels, decreases and overall membrane permeation becomes limited by water diffusion (Majsztrik, Bocarsly et al. 2008).

Figure 4 and 5 shows the representative fuel cell performance outlining the different losses arising from the different components. At low current densities the losses are dominated by the the activation polarization, which occur at the cathode under operation with clean hydrogen. The losses are followed by the ohmic resistance, which is mostly attributed to the solid electrolyte. Finally at high current densities, the performance is limited by the mass transport of reactancts and products. Semi-empirical approaches have been used to predict and analyze the fuel cell performance. Such an approach is the one by (Pisani, Murgia et al. 2002). where the performance curve can be represented by:

$$V_{cell} \approx E_0 - R_{cell} I - b\ln(I) + a\ln\left(1 - \frac{I}{I_l} S^{-\mu\left(1-\frac{I}{I_l}\right)}\right)$$

with

$$E_0 = E(I=0) + K \qquad b = \frac{1 + N_d^0}{\alpha_c \beta_F} \qquad a = \frac{\gamma + N_d^l}{\alpha_c \beta_F}$$

where V_{cell} is the cell potential, E_0 is the standard cell potential, R_{cell} cell resistance, I is the current density, b is the Tafel slope, I_l cell current density at the limiting current density, S flooding parameter, μ is an empirical constant, E is the potential, K is the proportionality constant, N_d^0 is the diffusion mechanism parameter at the zero current density, α_c is the cathode transfer coefficient, β_F is the Faraday constant, γ is the kinetic exponent of the species in the Butler-Volmer equation, N_d^l is the diffusion mechanism parameter at the limiting current density.

In real life operation, the use of pure fuel and oxidant gases results in an impractical system. A more realistic and cost efficient approach is the use of air as an oxidant gas and hydrogen from hydrogen carrier molecules (i.e., ammonia, hydrocarbons, hydrides). The short and long term effect of impurities in these gases may have an overriding effect on the fuel cell performance. Common atmospheric impurities in the cathode gas stream that have an effect on the performance of the fuel cell include SO_2, NO_2, H_2S, O_3 (Veldhuis, deBrujin et al. 1998). Even though the hydrogen oxidation reaction occurs at higher rates than the oxygen reduction reaction at the cathode (Sukkee, Wang et al. 2000), the effect of hydrogen

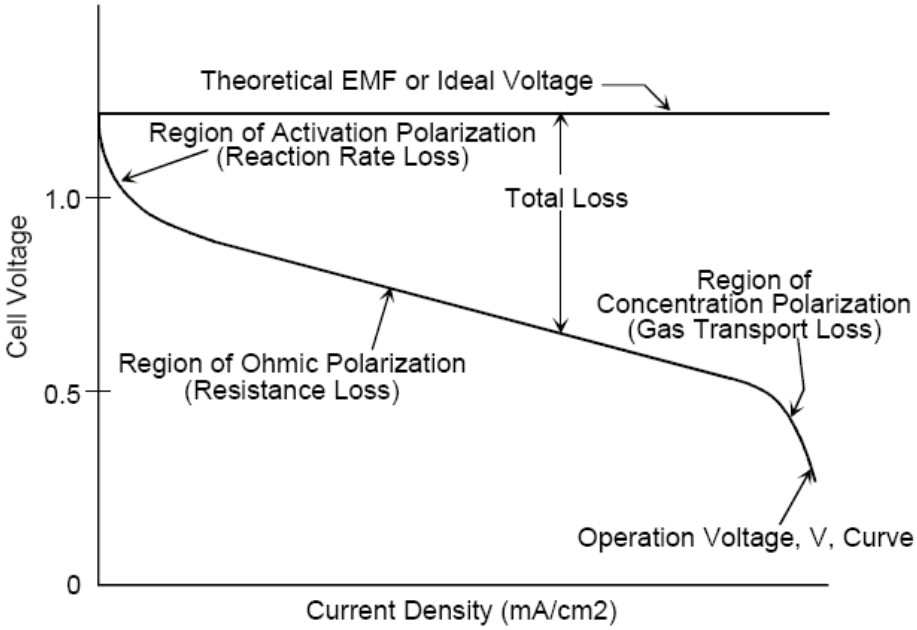

Fig. 5. Performance curve of a PEMFC. Reproduced from the DOE Fuel Cell Handbook (2004)

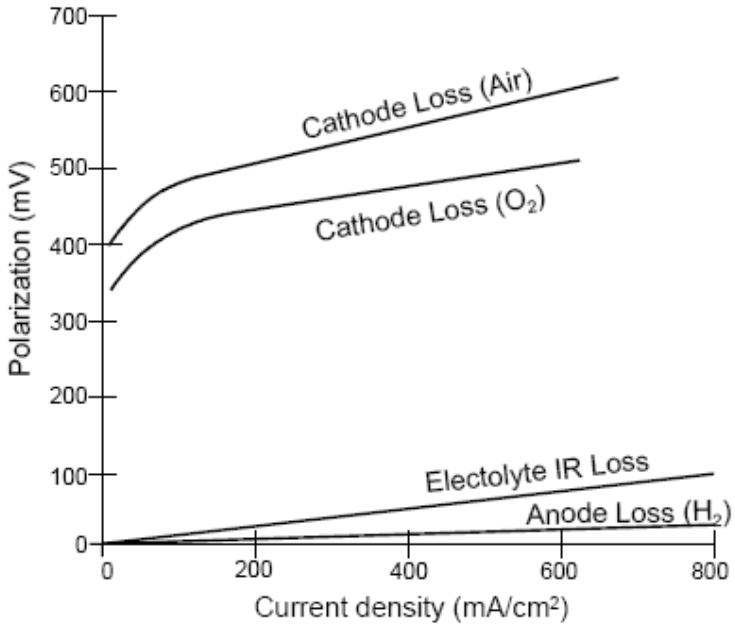

Fig. 6. Cell loses due to feed. Reproduced from the DOE Fuel Cell Handbook (2004)

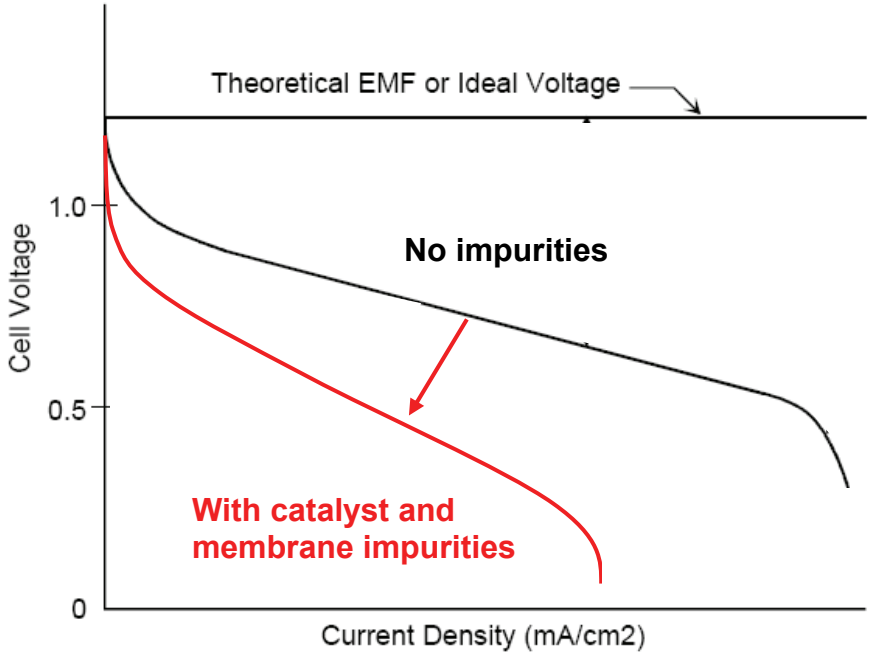

Fig. 7. Modified cell performance curve to include losses from impurities in cell feed

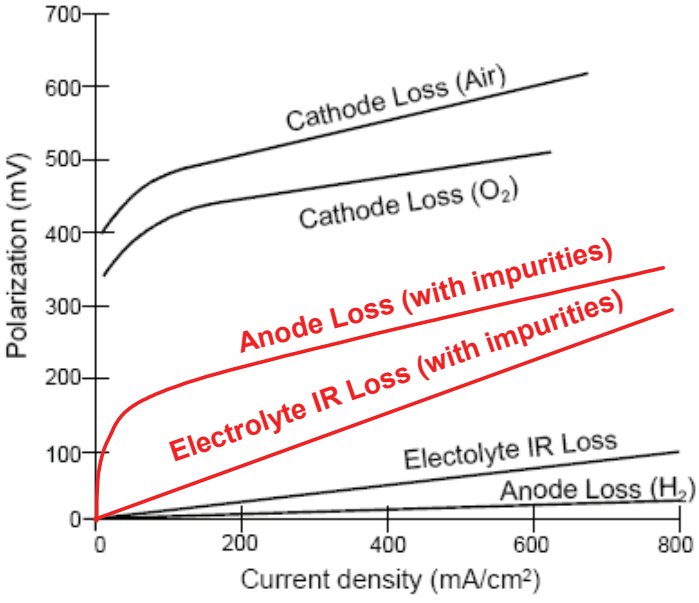

Fig. 8. Modified cell loss curves to include feed impurities

impurities on fuel cell performance can be devastating. Trace impurities arising from different hydrogen production processes include carbon monoxide, carbon dioxide, ammonia, water, sulfur, hydrocarbons, oxygen, helium, nitrogen, argon, formaldehyde, formic acid and halogenates. The effect of the impurities can alter the catalytic activity of the catalyst, the ohmic resistance due to poisoning on the solid electrolyte and changes in the hydrophobicity of the pores affecting the water management in the system, which in turn affects the mass transport. Figures 7 and 8 shows a simplified schematic of the losses on the performance.

2. Cell feed contributions to mass transport losses

2.1.1 Fuel cells

It has been determined that when a PEMFC is operating under dilute hydrogen feed streams (as low as 40% H_2 and a high utilization up to 90%) stack power losses should not exceed 10% of the power achieved with neat hydrogen (Springer, Rockward et al. 2001). When carbon monoxide was present in the dilute feed stream, the power losses were amplified significantly over the neat hydrogen feed stream. The authors suggest this problem may not be solved alone by changing anode catalysts and that a method such as air bleeding may need to be employed to achieve necessary power limits.

This work has been confirmed both experimentally and theoretically (Bhatia and Wang 2004) by other groups. The feed gases tested contained hydrogen contents as low as 40% and as high as 100%. The authors noted that the poisoning of CO was a quick process, taking less than 10 minutes for effects to be seen on the polarization curves for the fuel cell, taking two hours to reach steady state conditions. Yet, the poisoning process was reversible by feeding the cell with pure hydrogen for 2 hours. It was noted that CO preferentially adsorbs on the catalyst surface and when hydrogen is present in a dilute feed stream CO slows hydrogen adsorption even further, resulting in polarization losses. The hydrogen purity standard of the gas will depend dramatically on the dilution level of hydrogen.

The influence of ammonia on PEMFCs as been analyzed by only a few groups (Uribe, Gottesfeld et al. 2002; Soto, Lee et al. 2003; Halseid, Vie et al. 2006). In general, it was found that ammonia exposure has detrimental effects on the fuel cell performance. There was a steady loss of performance associated with the increase in current density and an overall increase in cell resistance. When the exposure was studied exposure from 1-30ppm NH_3, it was found that the poisoning process was slow, up to 24 hours (Halseid, Vie et al. 2006). This poisoning was also reversible in most cases, but only after exposure to neat hydrogen for several days, while exposure to as low as 1ppm was found to have had detrimental effects on the fuel cell system performance. Ammonia was highly soluble in the membrane, but had no significant adsorption on the gas diffusion layer. This adsorption on the membrane by ammonia impurity was determined to have the largest effect on the oxygen reduction reaction, requiring an increase in power to drive the reaction to occur. The authors suggest that all ammonia must be removed from the feed stream before hydrogen can be used as a fuel and that the nitrogen content is closely monitored to prevent formation by metal-hydride alloys for hydrogen storage. The effects of ammonia at ppm and sub-ppm concentrations have been studied by (Martinez-Rodriguez, Fox et al. 2011) In their testing it was demonstrated during hydrogen pump experiments and electrochemical impedance spectroscopy that at concentrations of 10 ppm the effects of ammonia not only affect the solid electrolyte membrane, but at high current densities the resistance by the ionomer in the

electrode is significantly higher than on the membrane. On the other hand during fuel cell testing, at 0.1 ppm the performance is unaffected by the ammonia.
An investigation on the effects of slightly higher concentrations of ammonia on PEMFC performance (Uribe, Gottesfeld et al. 2002), found the damage to the fuel cell to be irreversible, unlike previous results (Halseid, Vie et al. 2006). Even at 30ppm levels it was found the cell performance to drop considerably after several hours of exposure. The authors were able to successfully trap the ammonia using an ion exchange resin and continue use of the fuel cell without further damage.
Fuel cell systems are even more sensitive to sulfur containing compounds, yet few systematic studies have been completed on the phenomenon. Mohtadi et al. found that exposure to 5ppm of H_2S would cause a 96% performance loss in a Pt catalyst based PEMFC (Mohtadi, Lee et al. 2005). This rate of poisoning was approximately 69% lower at 50°C than at 90°C. There was also evidence that sulfur crossed over at the cathode and affected the oxygen reduction reaction.
Recent research by Ballard Power Systems on a commercial stack suggests that not only is the source of a hydrogen impurity important, but it's point of induction also (Knights, Jia et al.). The following impurities were found to effect cell performance in decreasing order: H_2S in fuel >SO_2 in air > NO_2 in air > NH_3 in air > CO in fuel > NH_3 in fuel. This suggests that the control of environmental air pollutants is as important for PEMFC operation as a high purity hydrogen standard. The changes in air quality could result in up to 30mV performance loss, which was most noticeable on cold, clear days. In order to address problems such as performance loss due to impurity effects, new catalysts or membranes are being developed.
Recent studies have been investigating the effect of trace halide contaminants on performance (Martínez-Rodríguez, Fox et al. 2011). The study of tetrachloroethylene, a common cleaning and degreasing agent, found that even at levels equal to the current ISO standards for hydrogen purity (ISO under development) detrimental impacts on fuel cell performance occur. At overpotentials above 0.2V, cell performance was fully recoverable. Poisoning that occurred at lower potentials was recoverable either by purging the cell or by changing the operating voltage.

2.1.2 Electrolyzers

PEM electrolyzers have a thermoneutral voltage of 1.48V, below which H_2 or O_2 cannot be generated. Testing of single cell PEM electrolyzers, operated at 75°C, have produced cell efficiencies of 82% at 1 A/cm² and 69% at 2 A/cm² (Badwal, Giddey et al. 2006). Results indicate that the voltage losses experienced are ohmic in nature, or the voltage drop is the resistance of electron flow across the electrodes and interconnects of the cell. The cell was found to have better performance with thinner membranes, but these membranes have a shorter lifetime and are more fragile. The optimal operating current density of a water electrolyzer is between 0.5-1 A/cm² , where resistances are minimized (Wendt and Imarisio 1988). Minimizing the ohmic resistance of the cell is important due to the high internal resistance and overvoltages experienced during operation. Cell efficiency will increase with decreasing resistance. Cell voltages will decrease with increasing cell temperature due to the decrease in overpotential and resistive losses (Onda, Murakami et al. 2002). If the individual cell is upgraded to small stacks of approximately fourteen cells, enough heat is generated due to internal resistive losses to make the cell thermally self-sustaining (Badwal, Giddey et al. 2006).

Uniform current density is an important factor to the lifetime of the membrane. A uniform current density is important to prevent the formation of hotspots, which can further decrease the performance of the electrodes and membranes. If the electrolyzer ratio (flow rate of electrolyzed water divided by the flow rate of the feed water) is less than 10%, the current density distribution in the cell is uniform in the cell (Onda, Murakami et al. 2002). At higher ratios, the current density will increase upstream where there is sufficient water and the current density will decrease downstream where there is insufficient water for the reaction.
The performance of PEM electrodes has been found to be sensitive to differential pressures as low as 20 mbar between the cathode and anode sides of the cell (Millet, Andolfatto et al. 1996). If high operating pressures are used, the differential pressure must be controlled. Stainless steel pipes in contact with deionized water can cause a steady decrease in cell voltage. Low concentrations of Fe, Ni and Cr from the stainless steel became concentrated in the membrane, limiting cell performance. On-line deionizers were found to give a more stable performance, but can impose limitations when used with high operating pressures and temperatures.
Demonstration electrolyzer plants, rated at 100kW, have been successfully run for up to 15,000 hours (Stucki, Scherer et al. 1998). One plant was shut down after 15,000 hours due to hydrogen concentrations in the oxygen off-gas of higher than 3 percent. A second demonstration plant, run for only 2300 hours with 50,000 hours of standby operation, was shut down for the same reason. During the standby period, a protective polarization current of 0.34 mA/cm^2 was applied in order to prevent corrosion of the current collectors at the cathode. Post mortem analyses of membranes from both plants indicate that stack failure was due to thinning of the Nafion® 117 membrane. The non-uniform membrane thinning coincided with an observed decrease in cell voltage. The ion exchange capacity of the membranes remained consistent throughout operation.

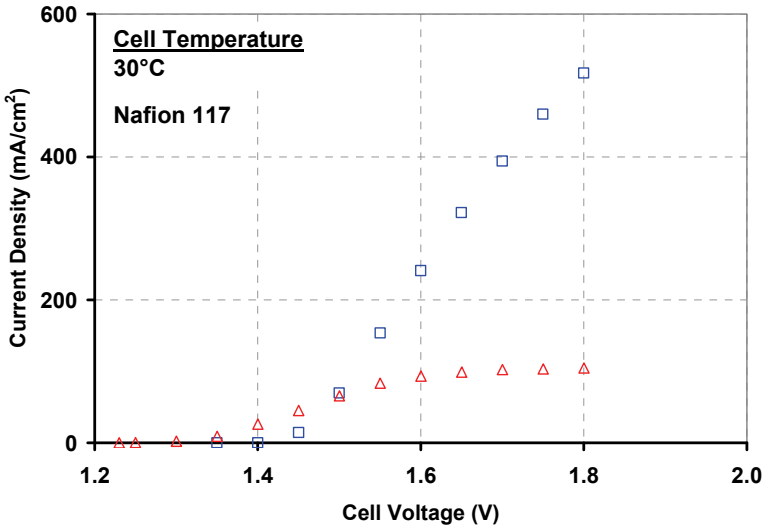

Fig. 9. Cell polarization comparison for anode liquid feed and cathode vapor feed PEM electrolyzer cells at 30°C. (□) Anode liquid feed (△) Cathode vapor feed. Reproduced from (Greenway, Fox et al. 2009)

The efficiency of PEME are greatly affected by the water content of the feed. The mass transfer model presented in previous work (Fox, Greenway et al. 2008) predicted that the current for an anode liquid water feed electrolyzer would be around 8 times larger than the limiting current in a cathode water vapor feed electrolyzer. The difference in the cell polarization between these two feed configurations is shown in Figure 9. The mass transfer limiting current density for the cathode water vapor feed system is around 92 mA/cm^2 while the current for the cathode water vapor feed system is near 475 mA/cm^2 at 1.8V at 30°C. This current density could most likely be increased to 1000-1400 mA/cm^2 if the a higher current density is desired and if it was determined that the higher voltage did not significantly affect the lifetime of the MEAs. Therefore, the cell current density produced by the anode liquid water feed system and thus the water reaction rate could be between 5-8 times larger than a similarly sized cathode water vapor feed system. To get an equivalent water processing rate between the two systems, either the reaction area of the cathode water vapor feed system or the number of cells used for processing the water would need to be increased proportionally to the difference in current density.

3. Mitigation of mass transport losses

Membrane development is of particular interest due to the limitations of current Nafion® membranes such as temperature restrictions due to dehydration and subsequent loss of conductivity. In order to meet these demands researchers have attempted to improve the membrane by doping or by investigating new polymer membranes. These alternate routes may also be used to increase fuel cell performance in the presence of gas impurities such as carbon monoxide.

For example, the effects of carbon monoxide on alternative membranes such as poly(2,5-benzimidazole) have been investigated (Krishnan, Park et al. 2006). These polymers, doped with phosphoric acid, had the ability to be operated at temperatures up to 210°C with 1% CO without performance losses, which are higher temperatures and higher carbon monoxide concentrations than conventional MEA configurations are tolerant. Other investigations involve using alternatives such as glass papers to support organic membranes (Tezuka, Tadanaga et al. 2005). The membranes cast from 3-glycidoxypropyltrimethoxysilane and tetraalkoxysilane would otherwise be too thick and have to high of a resistance for viable fuel cell use. These membranes were able to achieve a maximum power density of 80mW/cm^2 at 130°C and 7% relative humidity.

Other methods of development include (Jalani, Dunn et al. 2005) impregnating Nafion® to create more stable composite materials. The authors found that when Nafion® was impregnated with ZrO_2, SiO_2 and TiO_2 the composite membranes has better water retention and thermal stability than Nafion® alone. ZrO_2 impregnated Nafion® had the best performance overall and this is believed to be due to the increased acidity and surface area of the membrane. ZrO_2 impregnated Nafion® was the only modified membrane that showed increased conductivity over Nafion®. Leading the authors to conclude that the distribution of water between the surface and bulk of a system is as important as the amount of water absorbed.

Other than membrane development, an alternative method of improving the MEA is through catalyst development. A current area of interest is the use of non-precious metals or new binary catalysts for the oxygen reduction reaction at the cathode. Presently Pt and Pt alloys are widely used as anode and cathode materials in Proton Exchange Membrane

(PEM) Fuel Cells. Despite a cathodic over potential loss of 20%, Pt and Pt alloys are still preferred for their resistance towards corrosion in acidic media. Pt however, being an expensive metal of low abundance, it is of interest for researchers to develop a corrosion resistant non noble metal substitutes. These non-noble metal catalysts can range from metalloporphyins and bimetallic transition metals to heat treated metal catalyst (Wang 2005; Colón-Mercado and Popov 2006; Li, Qiao et al. 2009). The main advantage of the use of non-noble metal catalysts is the reduction in cost and ease of availability, although the precious metal based catalysts consistently have higher activity for the reaction, the results are promising.

4. Conclusion

Mass transport limitations in PEME and PEMFC may be due to several factors. Poor control of humidification levels within the cell can result in substantial losses in potential. In addition, good electrical and ionic conduction must be achieved between the electro catalyst layer and the membrane and diffusion layers. This will enable better utilization of the catalyst and limit cell losses through mass transport.

In addition, the feed provided to the PEMFC or PEME can greatly attribute to cell losses. If there are impurities present in the feed, it may affect the electrocatalyst performance or conductivity of the electrolyte. In both cases, substantial potential losses may be achieved, which may or may not be reversible, depending on the impurity present. In order to mitigate these effects, there is an on going effort to develop more tolerant electrocatalyst and membranes for these systems.

5. Acknowledgment

Savannah River National Laboratory is operated by Savannah River Nuclear Solutions. This document was prepared in conjunction with work accomplished under Contract No. DE-AC09-08SR22470 with the U.S. Department of Energy.

6. References

(2004). Fuel Cell Handbook. Morgantown, WV, Department of Energy, Office of Fossil Energy, National Energy Technology Laboratory.

Badwal, S. P. S., S. Giddey, et al. (2006). "Hydrogen and oxygen generation with polymer electrolyte membrane (PEM)-based electrolytic technology." Ionics 12: 7-14.

Bhatia, K. K. and C.-Y. Wang (2004). "Transient carbon monoxide poisoning of a polymer electrolyte fuel cell operating on diluted hydrogen feed." Electrochimica Acta 49: 2333-2341.

Colón-Mercado, H. R. and B. N. Popov (2006). "Stability of platinum based alloy cathode catalysts in PEM fuel cells." Journal of Power Sources 155(2): 253-263.

Falcao, D. S., C. M. Rangel, et al. (2009). "Water transport through a proton-exchange membrane (PEM) fuel cell operating near ambient conditions: experimental and modeling studies." Energy & Fuels 23: 397-402.

Fox, E. B., S. D. Greenway, et al. (2008). "Hydrogen isotope recovery using a cathode water vapor PEM electrolyzer." Fusion Science and Technology 54(2): 483-486.

Greenway, S. D., E. B. Fox, et al. (2009). "Proton exchange membrane (PEM) electrolyzer operation under anode liquid and cathode vapor feed configurations." International Journal of Hydrogen Energy 34: 6603-6608.

Halseid, R., P. J. S. Vie, et al. (2006). "Effect of ammonia on the performance of polymer electrolyte membrane fuel cells." Journal of Power Sources 154(2): 343-350.

ISO (under development). Hydrogen fuel- product specification- Part 2: proton exchange membrane (PEM) fuel cell applications for road vehicles. ISO/CD 14687-2. ISO TC 197 WG 12.

Jalani, N. H., K. Dunn, et al. (2005). "Synthesis and characterization of Nafion-MO_2 (M=Zr,Si,Ti) nanocomposite membranes for higher temperature PEM fuel cells." Electrochimica Acta 51: 553-560.

Knights, S., N. Jia, et al. Fuel cell reactant supply- Effects of reactant contaminants. Fuel Cell Seminar, Palm Springs, CA.

Krishnan, P., J.-S. Park, et al. (2006). "Performance of a poly(,5-benzimidazole) membrane based high temperature PEM fuel cell in the presence of carbon monoxide." J. Power Sources 159(2): 817-823.

Li, B., J. Qiao, et al. (2009). "Carbon-supported Ir-V nanoparticle as novel platinum-free anodic catalysts in proton exchange membrane fuel cell." International Journal of Hydrogen Energy 34: 5144-5151.

Majsztrik, P., A. Bocarsly, et al. (2008). "Water permeation through Nafion membranes: the role of water activity." J. Phys. Chem. B 112: 16280-16289.

Martínez-Rodríguez, M. J., E. B. Fox, et al. (2011). "The effect of low concentrations of tetrachloroethylene on the performance of PEM fuel cells." J. Electrochem. Soc. accepted.

Martinez-Rodriguez, M. J., E. B. Fox, et al. (2011). "The effect of low concentrations of ammonia on the performance of PEM fuel cells." J. Electorchem. Soc. under preparation.

Millet, P., F. Andolfatto, et al. (1996). "Design and performance of a solid polymer electrolyte water electrolyzer." Int. J. Hydrogen Energy 21(2): 87-93.

Mohtadi, R., W. K. Lee, et al. (2005). "The effect of temperature on the adsorption rate of hydrogen sulfide on Pt anodes in a PEMFC." Applied Catalysis B: Environmental 56: 37-42.

Onda, K., T. Murakami, et al. (2002). "Performance analysis of polymer-electrolyte water electrolysis cell at a small-unit test cell and performance prediction of large stacked cell." Journal of the Electrochemical Society 149(1): A1069-A1078.

Passalacqua, E., F. Lufrano, et al. (2001). "Nafion content in the catalyst layer of polymer electrolyte fuel cells: effects on structure and performance." Electrochimica Acta 46(6): 799-805.

Pisani, L., G. Murgia, et al. (2002). "A new semi-empirical approach to performance curves of polymer electrolyte fuel cells." Journal of Power Sources 108(1-2): 192-203.

Soto, H. J., W.-K. Lee, et al. (2003). "Effect of transient ammonia concentration on proton exchange membrane fuel cell performance." Electrochem. Solid-State Lett. 6(7): A133.

Springer, T. E., T. Rockward, et al. (2001). "Model for polymer electrolyte fuel cell operation on reformate feed: Effects of CO, H_2 dilution and high fuel utilization." J. Electrochem. Soc. 148(1): A11-A23.

Stucki, S., G. G. Scherer, et al. (1998). "PEM electrolyzers: evidence for membrane failure in 100kW demonstration plants." Journal of Applied Electrochemistry 28: 1041-1049.

Sukkee, U., C. Y. Wang, et al. (2000). "Computational Fluid Dynamics Modeling of Proton Exchange Membrane Fuel Cells." Journal of the Electrochemical Society 147(12): 4485-4493.

Tezuka, T., K. Tadanaga, et al. (2005). "Utilization of glass papers as a support for proton conducting inorganic-organic hybrid membranes from 3-glycidoxypropylmethoxysilane, tetraalkoxysilane and orthophosphoric acid." Solid State Ionics 176: 3001-3004.

Uribe, F. A., S. Gottesfeld, et al. (2002). "Effect of ammonia as potential fuel impurity on proton exchange membrane fuel cell performance." J. Electrochem. Soc. 149(3): A293-A296.

Veldhuis, J. B. J., F. A. deBrujin, et al. (1998). Air pollution: a problem for the SPFC cathode? Proceedings of the Seminar on Fuel Cell.

Wang, B. (2005). "Recent development of non-platinum catalysts for oxygen reduction reaction." J. Power Sources 152: 1-15.

Wendt, H. and G. Imarisio (1988). "Nine years of research and development on advanced water electrolysis: A review of the research programme of the Commision of European Communities." Journal of Applied Electrochemistry 18: 1-14.

Yeager, H. L. and A. Steck (1981). "Cation and water diffusion in Nafion ion exchange membranes: Influence of polymer structure." J. Electrochem. Soc. 128: 1880-1884.

14

Moisture Transport Through a Porous Plate with Micro Pores

Shixue Wang[1] and Yoshio Utaka[2]
[1]*State Key Laboratory of Engine, Tianjin University*
[2]*Division of Systems Research, Faculty of Engineering, Yokohama National University*
[1]*China*
[2]*Japan*

1. Introduction

Considering the variety of environment problems, including global warming, that call for a reduction in emission gases, increasing the fuel efficiency and reducing exhaust gases from automobiles has become an important issue for the automobile industry. Compared to traditional automobiles, fuel cell vehicles have many advantages, including high efficiency, low emissions, and diversification of fuel supply. Therefore, fuel cell vehicles are expected to become a viable means of transportation in the 21st century. Consequently, extensive research is being conducted to develop fuel cell vehicles that use polymer electrolyte membrane fuel cells as a power source.

Fuel cell systems for vehicles are composed primarily of a fuel and air supply unit, a humidifier, a cooling device, and the polymer electrolyte membrane fuel cell (PEMFC). Since the degree of ion conduction in an electrolyte film in the fuel cell is determined by the water content of the film, some water content is necessary in order to maintain ion conduction in the film. Generally, the film is humidified through gas diffusion layer (GDL) using high humidity work gases. The research on the humidifying methods and the influence of the humidity of work gases on the performance of fuel cells have been reported by Nguyen & White (1993) and Yoshikawa et al. (2000), respectively. Buchi & Scherer (2001) investigated the effects of the water content and the membrane thickness on the resistance of Nafion membranes in PEMFC.

From the point of view of saving space, it is desirable to recover and reuse the humidity in the exhaust gas using the supply air. In the present study, a method involving a thin porous plate for air dehumidification(Asaeda et al., 1984, 1986),in which direct recovery of the moisture of the exhaust gas to the supply air through a thin porous plate or membrane, is considered. In this case, the following phenomena may occur: 1) mass and heat transport and an accompanying phase change inside the porous plate, 2) water evaporation from the surface of the porous plate and moisture diffusion around the surface of the plate on the supply air side, and 3) condensation of moisture on the porous plate surface on the exhaust gas side. Analysis is difficult because of the complex interaction between these phenomena. Therefore, in order to simplify our investigation, as a first step, we focus on the heat and mass transport characteristics on the supply gas side and inside the porous plate. In order to fix the heat and mass transfer characteristics of the exhaust side, we assume that the

moisture supply capacity of the exhaust side is sufficiently high so that constant-temperature water can be used rather than the exhaust gas. Thus, the subject of the examination becomes the heat and mass transport between dry air and constant-temperature water through a porous plate.

A number of studies have examined the heat and mass transport accompanied by a phase change in porous media. For example, the gas-liquid two-phase flow, driven by capillary force in the porous media and accompanied by the evaporation of water has been experimentally and theoretically investigated by Udell (1983, 1985) and Zhao & Liao (2000). The sizes of the porous media used in these studies were ϕ54×254 mm and 40×99×29 mm, respectively. In addition, the diameter of the particles that composed the porous media were 0.1 ~ 0.8 mm and 1.09 mm, respectively, and the corresponding pore diameters were 0.05 ~0.3 mm and 0.46 mm, respectively. Wang et al. (1993a, 1993b, 1996) introduced a multiphase mixture model for the heat and mass transport of multiphase and multi-component mixtures, including the phase change in the porous media, based on a separated flow model in which various phases are regarded as distinct fluids. Simulations were performed employing this multiphase mixture flow model. The infiltration and transport of non-aqueous phase liquids in the unsaturated subsurface were investigated by Cheng & Wang (1996), and the mass transport in the cathode of a PEMFC under isothermal conditions was investigated by You & Liu (2002). Vafai & Whitaker (1986) applied a volume averaging technology to analyze the accumulation and migration of moisture in an insulation material, and, based on a previous study (Vafai & Whitaker, 1986), Vafai & Tien (1989) reduced the number of assumptions and simulated the same problem. Using the network method, Prat (1993) presented a model to investigate drying in porous media under the condition whereby the media was initially saturated with water. Plourde & Prat (2003) studied the influence of a surface tension gradient induced by thermal gradients on the phase distribution within a capillary porous media by developing the model described in Reference (Prat, 1993). Furthermore, Usami et al. (2000, 2001) conducted a quantitative evaluation of the controlling factors, both experimentally and via numerical analysis, for the heat and mass transport in the reforming catalyst bed of a steam reforming fuel cell using methane.

In summarizing the above studies, we observed the following. 1) Several theoretical studies have been performed. 2) The dimensions of the porous media used as an experimental object in previous studies (e.g., the size of the porous media and the diameter of the particles that comprise the porous media) were relatively large. 3) Few studies have examined the influencing factors or mechanism of heat and mass transport in porous media. Therefore, it is difficult to apply the results of the above-mentioned studies in the present study. In particular, research regarding the moisture transport through porous media plate depends of the heat and mass transport inside the porous media and the conditions of heat and mass transfer on the surface of the porous media plate are not reported.

In order to clarify the characteristics of moisture recovery from the exhaust gas of fuel cell vehicles with a porous plate, it is necessary to determine experimentally both the mechanism of heat and mass transport in a thin porous plate having very small pores and the influence of various factors on heat and mass transport in this process. As a first step towards this goal, we evaluate the factors that influence heat and mass transfer from constant-temperature water to dry air through a porous plate. The present authors have investigated moisture transport through a porous plate having a thermal conductivity of 1.7W/(mK) to dry air from constant-temperature water (Wang et al., 2005, 2006). And the

present authors have also investigated the effect of thermal conductivity of the porous plate on the moisture transport (Wang et al., 2009). Here,we will summarize the work done in these previous investigations.

2. Experimental apparatus and method

Figure 1 shows a schematic diagram of the experimental apparatus, which is composed of a constant-temperature water circulation system and an airflow loop. The constant-temperature water system consists of a circulation water tank, a water transport pump, a water filter, and ion-exchange equipment. The water used in the experiment is generally maintained in a pure state, using both a water filter that removes particles larger than 0.1 μm and the ion-exchange equipment. Air is pumped to the flow loop and is dehumidified by cooling with water at approximately 0°C. The dehumidified air is heated to an established temperature and absorbs moisture from the constant-temperature water that is in contact with the bottom of the porous plate when supplied to the test device. High-humidity air is discharged to the atmosphere from the test device. The flow rate of air is adjusted by a valve installed at the exit of the air pump and is measured by a flow meter installed after the valve. Thermo-hygrometers are installed at the entrance and exit of the test device to measure the temperature and humidity of the air. In order to prevent the formation of dew at the thermo-hygrometer, a heater was installed around the duct, including the thermo-hygrometer. The heater was also used to control the air temperature in the duct and to maintain the temperature to be consistent with the air temperature in the channel outlet. The temperature of the water was measured by a thermocouple installed on the undersurface of the porous plate in contact with the constant-temperature water. All measurement signals, for example, temperature, humidity, and flow rate, were converted to digital signals by an A/D converter and were recorded by a personal computer.

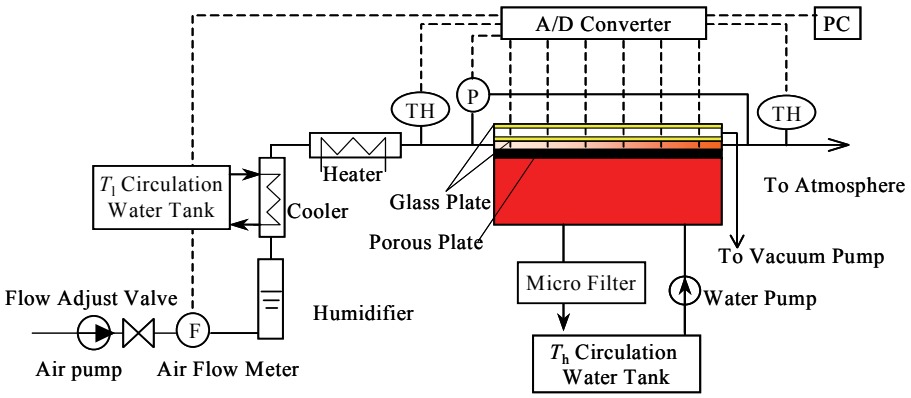

Fig. 1. Experimental system

Figure 2 shows a cross-section of the test device. The surface of the porous plate is 100×28 mm. To observe the surface state of the porous plate, the top of the test device is constructed of a transparent material. A space for vacuum thermal insulation exists at the top of the test device, and insulation is accomplished by the drawing of a vacuum pump. In addition, 1-mm Teflon sheets were installed as insulating material on two sides of the channel in

order to prevent heat loss from the sides of the metal frame. The air temperature in the channel above the porous plate and the temperature in the upper surface of the porous plate were measured by ten K-type thermocouples (±0.1°C) of 0.25 mm in diameter that were installed in the channel and the plate along the path of the airflow, respectively. Holes in the porous plate for the insertion of the thermocouples were 0.3 mm in diameter and 15 mm in depth. In Figure 2, the symbols ○ and ● represent the thermocouples, which measure the temperatures of the air in the channel and the upper surface of porous plate, respectively. The temperature of the porous media plate measured here is used as the air-side plate temperature. In addition, the temperature of the plate measured by the thermocouples attached to the bottom of the plate contacting the liquid is used as the liquid-side plate temperature. In the present study, since the temperature of the constant-temperature-water is adjusted to have a small range, the experiments were carried out under an approximately constant liquid-side plate temperature.

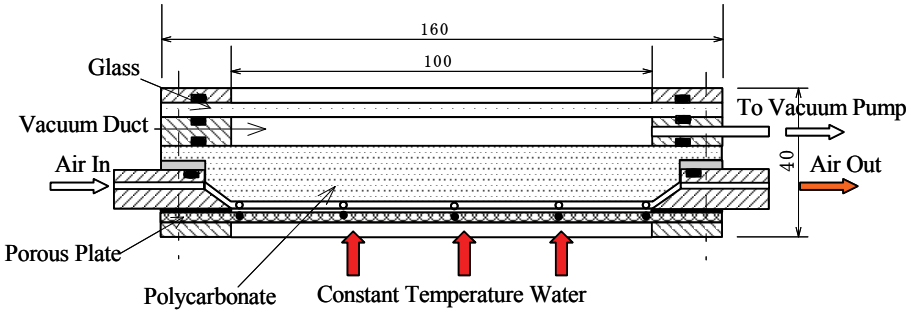

Fig. 2. Schematic diagram of the test section

Alternatively, in present study, in order to remove the effect of the air that is trapped in the porous plate on the experiment result, the porous plate, as a specimen, was impregnated by a vacuum impregnation method before beginning the experiments. In other words, air was evacuated from a closed vessel containing the porous plate in water in order to remove the air contained within the porous plate. Figures 3(a) ~ 3(c) show the variation in the mass flux of the moisture transport through the porous media plate with respect to the air volumetric flow under the conditions of both vacuum impregnation and non-vacuum impregnation. This graph indicates that the variation of the mass flux caused by the vacuum impregnation depends on the thickness and the pore diameter of the porous plate. In other words, the effect of vacuum impregnation appears to be more remarkable for porous plates having smaller pore diameter and greater thickness. The reason for this is thought to be that almost all of the air inside the pores of the porous plate was removed by the impregnation, so that the water transposition in the porous plate driven by capillary forces becomes easier. Therefore, the vacuum impregnation was carried out for the porous plate used in the present study before the experiments.

3. Experimental results and discussion

Since there are many factors that affect moisture transport from the constant-temperature water to the dry air through the porous plate, in the present study, we first examine the

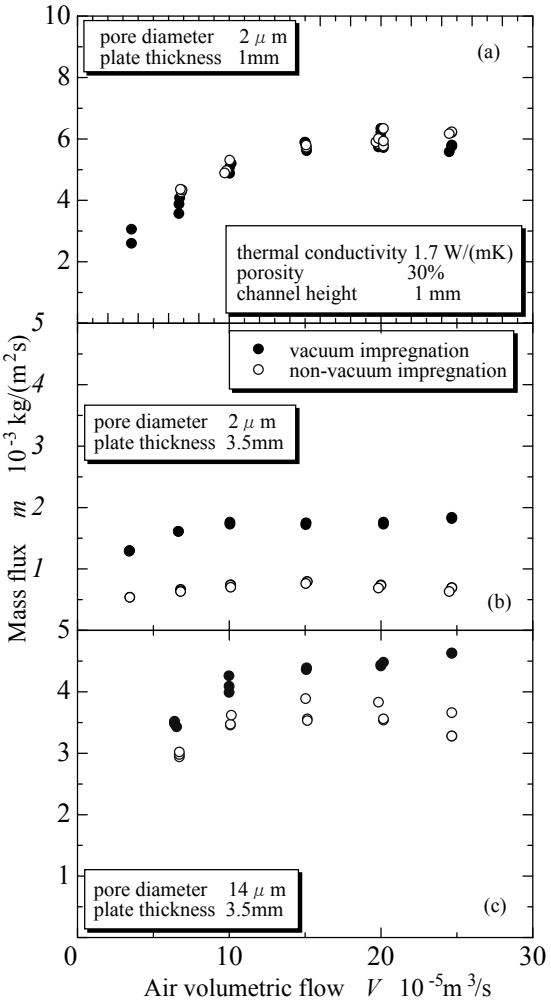

Fig. 3. Effect of impregnation on mass flux

effects of the flow condition of air, the physical properties of the porous plate, and the geometrical size of the channel on the moisture transport. Considering the conditions of practical use, experiments were performed under an air volumetric flow of 3.3 ~ 24.7×10^{-5} m^3/s. To examine the effect of the heat conductivity of the porous plate on the moisture transport, in present study, we used porous media having heat conductivities of 1.7 W/(mK) and 20.2 W/(mK). For reasons related to material manufacture, the experiment to investigate the effect of pore diameter was performed using the porous media with low heat conductivity (1.7 W/(mK))and three average pore diameters D of 2, 5, and 14 μm, and the experiment regarding the effect of porosity was performed mainly using the porous media with high heat conductivity (20.2 W/(mK))and average porosities of 12%, 20%, and 30%. The condition of detail is shown Table 1.

Heat conductivity λ_p W/(mK)	Porosityε	Pore diameter D μm	Plate thickness Δx mm	Channel height h mm
1.7	20%	2.0	1.0	1.0
			2.0	
	30%		1.0	
			2.0	
			3.5	
		5.0	1.0	0.5
				1.0
				1.5
			2.0	1.0
			3.5	
		14.0	1.0	
			2.0	
			3.5	
20.2	12%	2.0	0.5	
	20%		0.5	
			1.0	0.5
				1.0
				1.5
			2.0	1.0
	30%		0.5	
			2.0	

Air volumetric flow: 3.3-24.7×10^{-5} m^3/s, temperature of air at the inlet: 32^{o}C, relative humidity of air at the inlet: 15%, temperature of constant-temperature water: 69^{o}C.

Table 1. Specifications of the porous plate and experimental conditions

3.1 Basic characteristics of moisture transport through the porous plate

Figures 4(a) ~ 4(d) show the variations of parameters that represent the basic characteristics of the moisture transport from water to air flowing the channel through theporous plate, such as the mass flux, the heat flux, the temperature, and the relative humidity of the outlet air, with respect to the air volumetric flow. The experimental conditions are a plate thickness of 1 mm, a channel height of 1 mm, a heat conductivity in the plate of 1.7 W/(mK), a pore diameter of 5 μm, and a plate porosity of 30%. From this graph, it is first understood that the mass flux increases with respect to the increase in the air volumetric flow and varies little when the air volumetric flow exceeds approximately 10×10^{-5} m^3/s. This is thought to be because, even though the moisture absorption ability of the air increases with respect to the increase in the amount of air flowing through the channel, when the air volumetric flow exceeds approximately 10×10^{-5} m^3/s, the moisture transport through the porous plate or the heat transport required by the water vaporization were limited by the properties of the porous plate, e.g., the permeability of liquid or the thermal conductivity. In addition, the heat flux was determined from the heat transfer quantity in the heat and mass transport

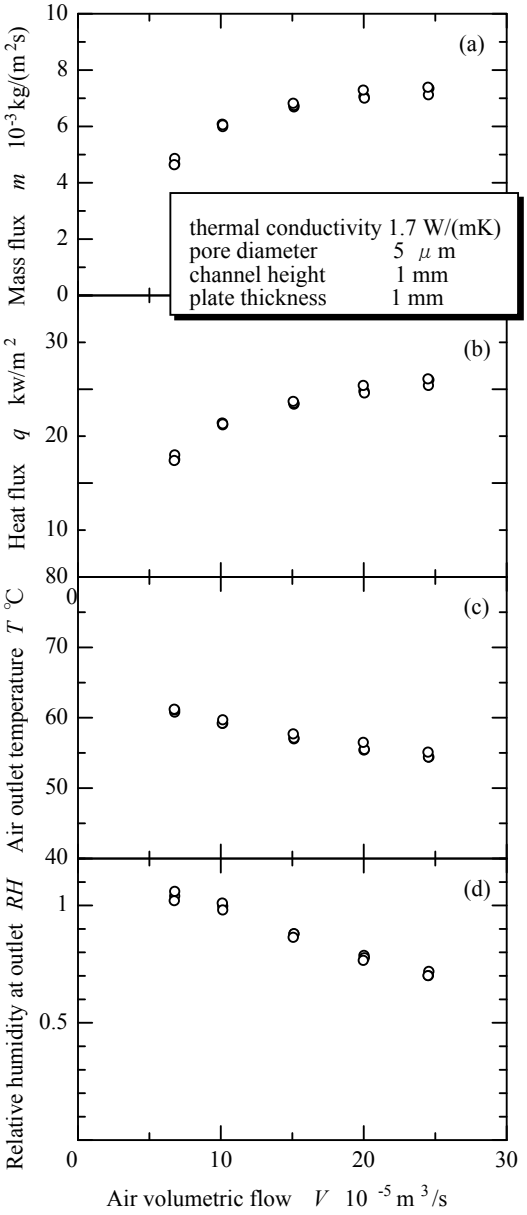

Fig. 4. Basic characteristics of moisture transport from water to air through a porous plate

process calculated from the airflow and the change in enthalpy of the air between the entrance and exit of the channel. The variation in the heat flux showed the same tendency as that for the above mass flux, because the heat flux is primarily caused by the transport of latent heat accompanying the mass transport in this process.

Furthermore, Fig. 4(d) shows that for the case in which the air volumetric flow is less than approximately 10×10^{-5} m^3/s, the relative humidity of the air in the channel exit is approximately 100%. This also explains the tendency of the mass flux variation shown in Fig. 4(a).That is, for the case of the small air volumetric flow, since the moisture absorption capacity of the air is comparatively small, the heat and moisture applied to the air through the porous plate is sufficient.

Figure 5 shows the distribution of temperature in the air flowing through the channel and porous plate. This graph indicates that the temperature of the air and the porous plate increase as the exit of the channel is approached. In the case of a water temperature of 69°C, in the flow direction, the liquid-side porous plate temperature changed from 62°C to 64.4°C due to the water evaporation to the air side. Since the temperature difference between the liquid side and air side of the porous plate decreases in the direction of the air flow, the heat flux, and the moisture transport accompanying it become small as the channel exit is approached. In addition, the temperature difference is found to be greater than that between the air and the porous plate. In particular, this tendency is clearly observed in the vicinity of the channel inlet. Compared to the thickness of 1 mm and thermal conductivity of approximately 1.7 W/(mK) for the porous plate, the heat transfer coefficient of the single-phase air flow in the channel is only a few tens of $W/(m^2K)$. This means that the heat transport by the heat conduction passing through the porous plate is far greater than that by the heat transfer of sensible heat on the porous plate surface. This can explain why the heat transport is approximately equal to the latent heat transport accompanying the moisture transport in this moisture transport process, as mentioned above, and indicates that the heat flux and mass flux are bigger in the vicinity of the channel inlet.

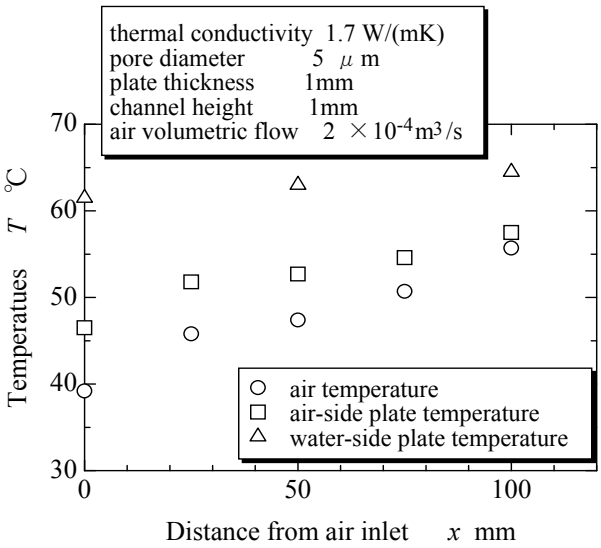

Fig. 5. Distributions of temperature in an air channel and a porous plate with flow direction

Figure 6 shows the distribution of the heat flux to the air from the constant-temperature water for the experimental conditions shown in Figure 5. This graph shows that, in the heat

transport to the air from the constant-temperature water through the porous plate, 77% of the heat transport is by the heat conduction in the porous plate, 15% is by the heat conduction in the water including in the porous plate, and 8% is by the transport of the sensible heat accompanying the water transportation through the porous plate. Thus, 85% of the heat transport is used for the evaporation of the water to the air and 7% of the heat transport is used for the temperature increase of the air. That is, the heat transfer between the porous plate and the air is mainly the transport of the latent heat accompanying the water transportation.

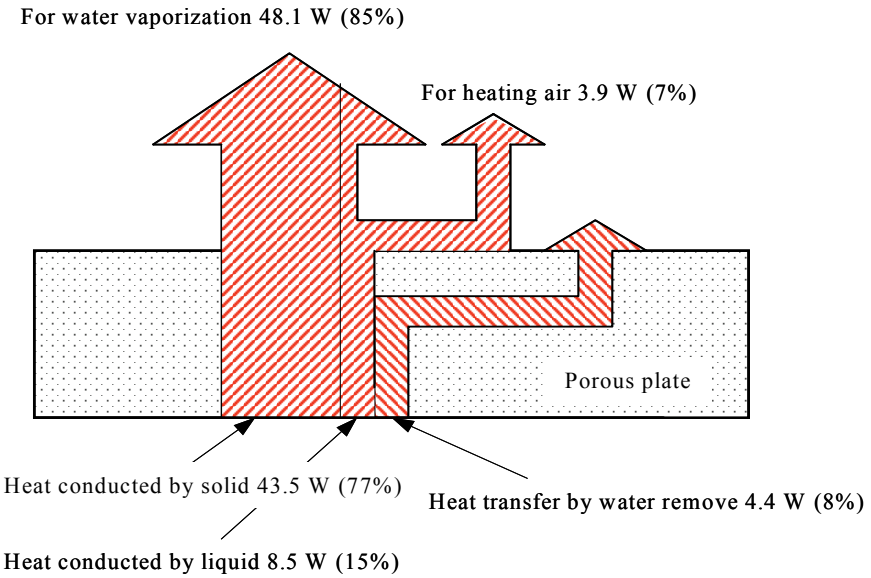

Fig. 6. Distribution of heat flux in the process of moisture transport through a porous plate

As described above, in the process of moisture transport through the porous plate, there are several factors controlling the phenomenon, e.g., the water flow resistance R_{fp} and heat transfer resistance R_{tp} inside the plate, and the mass transfer resistance R_{ms} and heat transfer resistance R_{ts} on the surface of the porous plate. Considering the influence of each factor involved and based on the one-dimensional system, the resistances of the mass transfer and heat transfer in the porous plate are defined and their influence on the performance of the moisture transport is discussed. Here, R_{fp} depends on the material structure, such as the size and distribution of the pore, and the surface properties of the plate, such as the wettability. Thus, based on the Darcy law, the maximum flux of the liquid water through the porous plate, in which the surface tension, as the driving force, can be determined as follows:

$$m^{f}_{\max} = \frac{4\sigma\cos\theta}{D} \cdot \frac{1}{\mu R_{fp}} \tag{1}$$

$$R_{fp} = \Delta x \,/\, K(\varepsilon, D) \tag{2}$$

$$K(\varepsilon, D) = C(\varepsilon)D^2 \tag{3}$$

where σ is the surface tension of the water, D is the characteristic pore diameter of the porous plate, $K(\varepsilon,D)$ is the permeability of the plate, Δx is the thickness of the plate, and $C(\varepsilon)$ is a coefficient depending on the porosity of the plate. In addition, as mentioned above, most of the heat from the constant-temperature water to the air through the porous plate is used for the water evaporation at the air-side of the plate. Therefore, the maximum evaporation of the liquid water at the air side can be determined by the heat transfer resistance of the porous plate:

$$m^t{}_{\max} = \frac{1}{R_{tp}} \cdot \frac{t_c - t_s}{h_{gl}} \tag{4}$$

$$R_{tp} = \Delta x / \lambda_p \tag{5}$$

where t_c is the temperature of the plate surface at the constant-temperature water side, t_s is the temperature of the plate surface at the air-side, h_{gl} is the latent heat of the vaporization of the water and λ_p is the thermal conductivity of the plate.

3.2 Effect of thermal conductivity

Figure 7 shows the variations in mass flux, temperature and relative humidity of the outlet air with respect to the air volumetric flow for porous plates having different thermal conductivities. The plate thickness and the height of the channel are 2 mm and 1 mm, respectively. In either high or low thermal conductivities of the porous plate, the mass flux first increases with the increase of the air volumetric flow, and then changes slightly when the air volumetric flow exceeds a threshold. This indicates that, as mentioned above, for the range in the low air volumetric flow, the factors controlling the moisture transport process are the moisture absorption capacity of the air and the resistances of the heat and mass transfer between the porous plate surface and the air, and those for the range in the high air volumetric flow are the thermal resistance and mass transport resistance inside the plate. In particular, in the range of the high air volumetric flow, the relative humidity and temperature in the outlet air are less remarkable than the saturation state or the temperature of the constant-temperature water, respectively. Therefore, for this range, it is remarkable that the moisture transport is controlled by the resistance of the heat and mass transfer inside the porous plate. Moreover, (1) the increase of the mass flux caused by the increase of the thermal conductivity of the porous plate is remarkable, and (2) although the thermal conductivity in the high-thermal-conductivity plate is approximately 11 times that in the low-thermal-conductivity plate, the mass flux in the former case less than twice that in the latter case. Therefore, it is thought that, the moisture transport is controlled by the mass transfer resistance inside the plate in the former case and by the thermal resistance inside the plate in the latter case. That is, for the former case, the maximum mass flux is limited to the maximum flux $m^t{}_{\max}$ of the liquid water through the porous plate determined by the mass transfer resistance inside the porous plate defined by equation (1), and, for the latter case, the maximum mass flux is limited to the maximum flux $m^t{}_{\max}$ of the water vaporization at the plate surface determined by the thermal resistance inside the porous plate defined by equation (4).

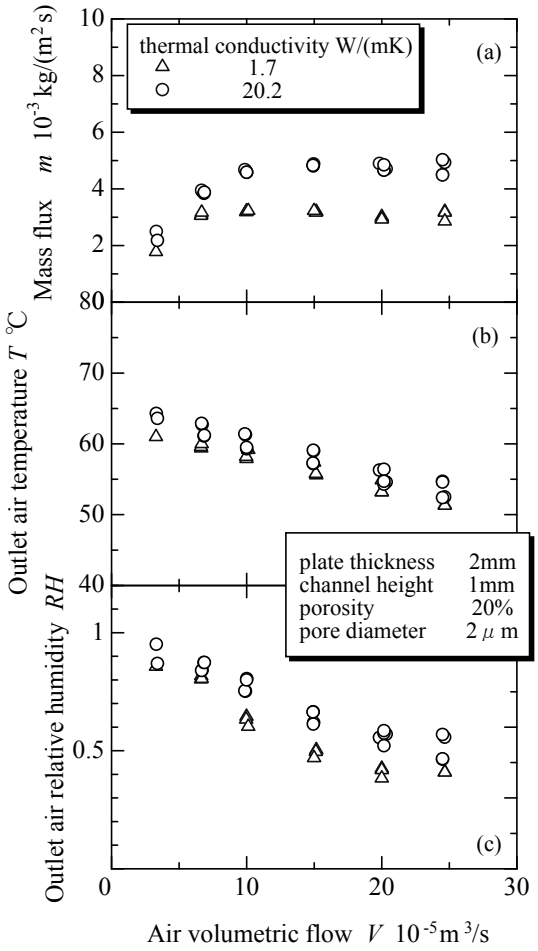

Fig. 7. Effect of thermal conductivity of a porous plate on moisture transport (plate thickness: 2 mm)

Figure 8 shows the variations in mass flux, temperature and relative humidity of the outlet air with respect to the air volumetric flow for porous plates having different thermal conductivities and thickness of 1 mm. In the case of the low-thermal-conductivity plate, the mass flux increases with respect to the increase of the air volumetric flow when the air volumetric flow is less than 1.0×10^{-4}m^3/s, and the relative humidity in the outlet air is approximately 100%. However, the mass flux changes slightly when the air volumetric flow exceeds 1.0×10^{-4}m^3/s. The reason is as mentioned above. Moreover, as shown in Figure 8(a), for the case of the high-thermal-conductivity porous plate with a thickness of 1 mm, there is no range in which the mass flux changes slightly with the air volumetric flow. Furthermore, the temperature in the outlet air is less than the temperature of the constant-temperature water, and the difference exceeds 7 K. At the same time, the relative humidity in the outlet air is approximately 100% with the air volumetric flow. Therefore, it is thought that, in this

case, the factor controlling the moisture transport is the heat transfer at the plate surface. That is, in the case in which the thin porous plate having a high thermal conductivity is used, it is best to promote the moisture transport that enhances the heat transfer at the plate surface facing the channel side.

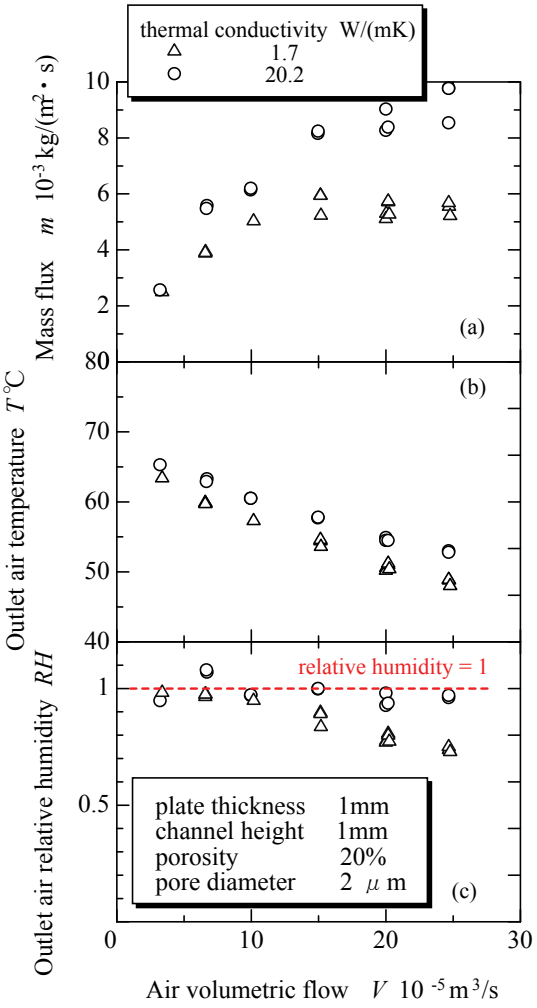

Fig. 8. Effect of thermal conductivity of a porous plate on moisture transport (plate thickness: 1 mm)

Moreover, comparing the results shown in Figures 7 and 8, in the range of the large air volumetric flow in which the moisture absorption capacity is sufficient, the mass flux, which is almost constant at approximately 3×10^{-5} kg/(m²s) for the case of the low-thermal-conductivity porous plate with a thickness of 2mm, and is approximately 5×10^{-5} kg/(m²s) for the case of the high-thermal-conductivity porous plate with a thickness of 2mm. In

contrast, the value is approximately 6×10^{-5} kg/(m²s) for the case of the low-thermal-conductivity porous plate with a thickness of 1mm. That is, when the thermal resistance and the mass transfer resistance inside the plate are the controlling factors, the mass flux doubled by halving the plate thickness. Furthermore, comparing the experimental results for the high-thermal-conductivity plate with a thickness of 2mm and the low-thermal-conductivity plate with a thickness of 1 mm reveals that although the mass transfer resistance inside the plate for the latter is half that for the former, the mass flux in the latter is only 1.2 times the mass flux in the former. Therefore, as in the case for a low-thermal-conductivity plate with a thickness of 2mm, for the case of the low-thermal-conductivity porous plate with a thickness of 1 mm, the mass flux is also controlled by the thermal resistance inside the plate, and the maximum mass flux is limited to m^{t}_{max}, as defined in Equation (5). This is also understood by that fact that the relative humidity in the outlet air is approximately 100% for the case of the high-thermal-conductivity porous plate with a thickness of 1 mm.

3.3 Effect of porosity

Figures 9 and 10 show the effect of the porosity in the porous plate on the mass flux for plate thicknesses of 0.5mm and 2mm, respectively. The thermal conductivity of the plate is 20.2W/(mK). For the plate thickness of 0.5mm, under the condition of the present study, although the porosity varied from 12% to 30% and the variation range is more than one time, no difference was observed to be caused by the porosity. As mentioned above, since, in this case, the mass transport is controlled by the heat transfer between air and the plate surface, it is ineffective to the moisture transport by changing the mass transport resistance inside the plate. However, for the plate thickness of 2mm, since the mass transport is controlled by the mass transport resistance inside the plate, the mass flux increases with the increase of the porosity. The increase is remarkable in the range of the large air volumetric flow.

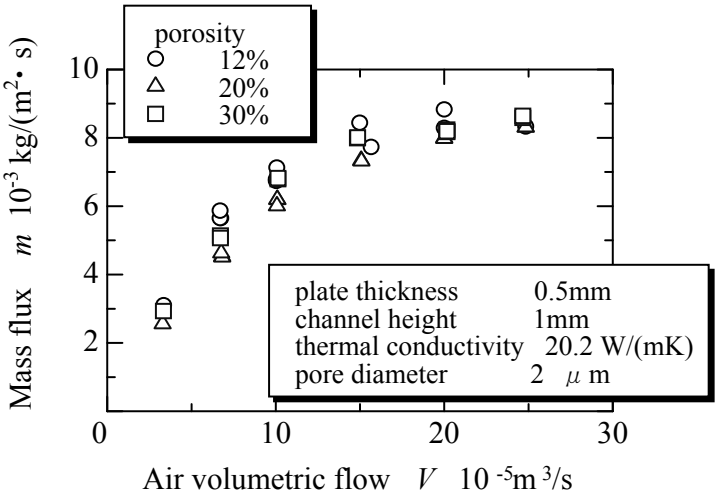

Fig. 9. Effect of porosity on mass flux (plate thickness: 0.5 mm)

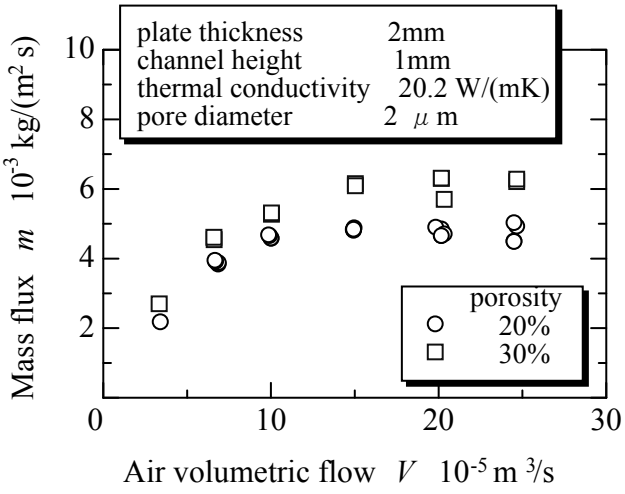

Fig. 10. Effect of porosity on mass flux (plate thickness: 2 mm)

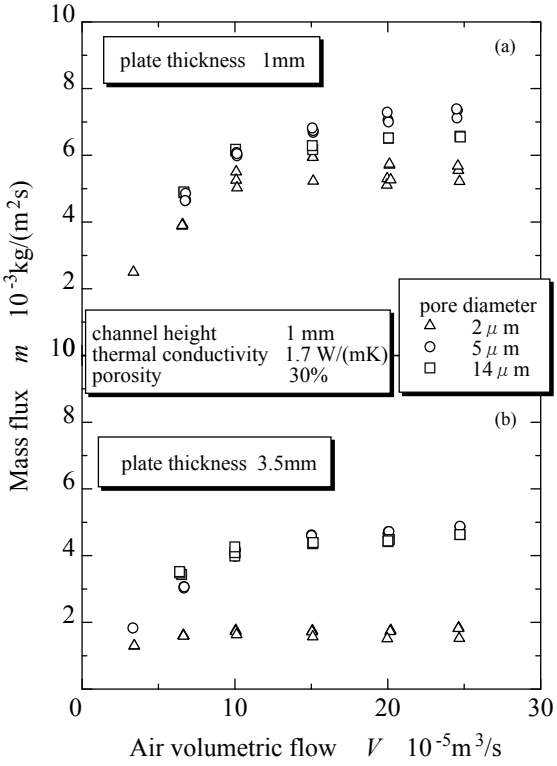

Fig. 11. Effect of pore diameter on mass flux for porous plates of different thickness

3.4 Effect of pore diameter

Figure 11 presents the variation of the mass flux for different pore diameters in plates having thicknesses of 1 mm and 3.5 mm. The thermal conductivity of the plate is 1.7 W/(mK). Similar values were observed for pore diameters of 5 μm and 14 μm. However, a comparatively low value was observed for a pore diameter of 2 μm. The difference increases with the increase in air volumetric flow, and the largest differences are approximately 25% and 60% for the plate thicknesses of 1 mm and 3.5 mm, respectively. This is thought to be caused by the remarkable resistance to the flow within the porous media for small pore diameters or thick plates. That is, in this moisture transport process, we suppose that the mass transfer resistance at the surface of a porous plate became small and the influence of flowing resistance inside the plate became strong.

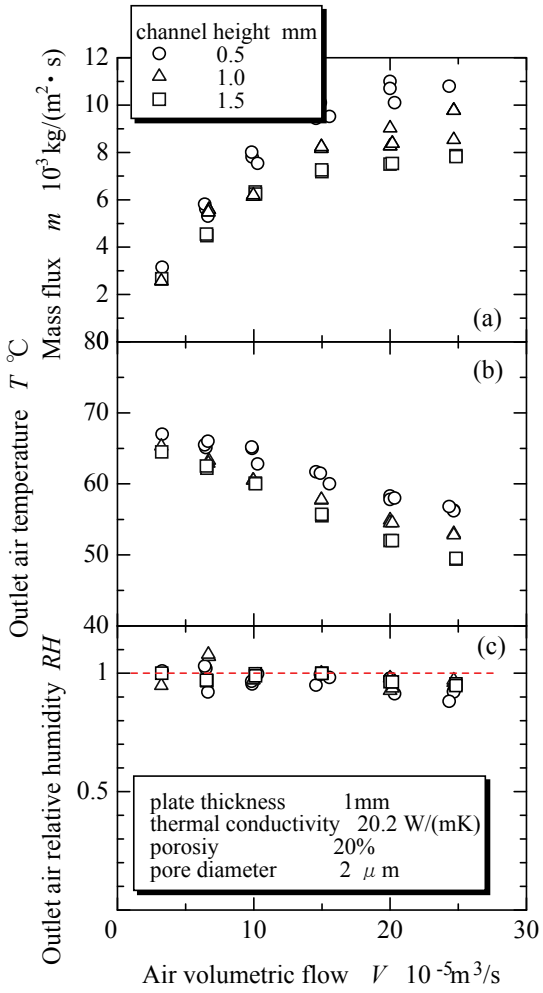

Fig. 12. Effect of channel height on moisture transport for a plate of high thermal conductivity

3.5 Effect of channel height

As mentioned above, the heat transfer and the mass transfer at the plate surface strongly affect the moisture transport through the porous plate. Consequently, the variations of the heat and mass transfer at the plate surface and the moisture absorption capacity of air caused by the variation in the quantity or the velocity of the airflow channel are projected. However, the variation of the mass flux cannot be easily predicted.

Figure 12 shows the variation in mass flux, temperature, and relative humidity in the outlet air with respect to the air volumetric flow using the high-thermal-conductivity plate for channel heights of 0.5, 1.0, and 1.5 mm. The mass flux increased when the channel height was varied from 1.5 mm to 1.0 mm and from 1.0 mm to 0.5 mm. As shown in Figure 12(b), over the entire range of the air volumetric flow, when the channel height was reduced, the heat transfer at the porous plate surface was promoted, resulting in an increase in the air temperature in the outlet air. This means that the moisture absorption capacity of air increased when the channel height was reduced. In addition, from Figure 12(c), the relative humidity of the air in the outlet air was approximately 100%, irrespective of the channel height and the air volumetric flow. This result has two implications. One is that there was sufficient water supplied from the constant-temperature water to the plate surface next to the air. The other implication is that mass transfer due to gas convection or diffusion at the plate surface has not hampered moisture transport under the experimental conditions. In other words, the results shown in Figure 12 confirmed that the controlling factor for the moisture transport through the porous plate under the experimental conditions is the heat transfer at the plate surface near the air channel and is not the thermal resistance or the mass transport resistance inside the plate. This result agrees with the discussion in Section 3.2. that is, in the case of the thin porous plate with high thermal conductivity, the factor controlling the moisture transport is the heat transfer resistance at the plate surface next to the channel.

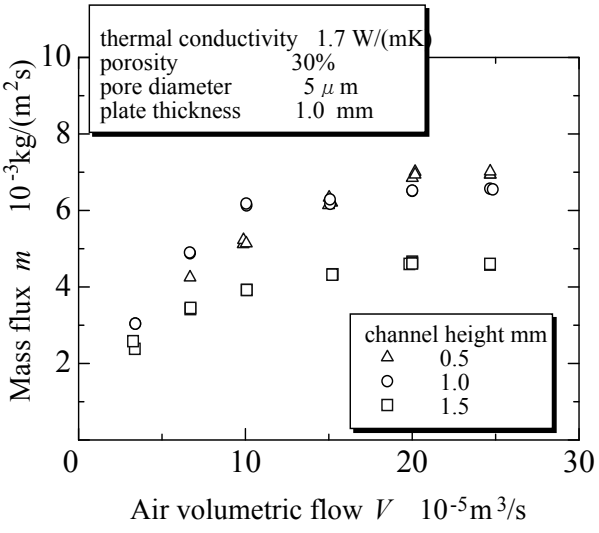

Fig. 13. Effect of channel height on moisture transport for a plate of low thermal conductivity

Figure 13 shows the variation in the mass flux with respect to the air volumetric flow using the low-thermal-conductivity plate for channel heights of 0.5, 1.0, and 1.5 mm. In contrast to the case for the high-thermal-conductivity plate, the mass flux increased when the channel height was varied from 1.5 mm to 1.0 mm, but it did not change much with air volumetric flow for channel heights between 1.0 mm and 0.5 mm. This is thought to be caused by that the main factors controlling the moisture transport are the thermal resistance inside the plate and the resistances of the heat and mass transfer at the plate surface next to the channel for a channel height of 1.5mm, and, the controlling factor just is the thermal resistance inside the plate for the channel height of less than 1mm.
Based on these results, to increase the moisture transport, a smaller apparatus would be used under the condition in which the pressure drop is less than a limited range.
Figure 14 shows the variation of pressure drop in air with respect to the air volumetric flow for the experimental conditions shown in Figure 13. The solid line represents the air pressure drop in the tube for a laminar flow obtained using the Hagen-Poiseuille equation (Welty et al., 1976), as follows:

$$\Delta P = \frac{32}{\mathrm{Re}} \cdot \frac{L}{D_e} v^2 \rho \tag{6}$$

where L is the channel length, D_e is the equivalent diameter of the channel, v is the air velocity, and ρ is the density of the air. The pressure drop increases rapidly when the channel height decreases, and the experimental results are higher than the calculation results for any channel height. This is thought to be due to the effect of the roughness of the porous plate surface and the water vaporization at the plate surface. In addition, the existence of the air volumetric flow that the mass flux varies only slightly with the air flow, as shown in Figure 13, indicates that a proper air volumetric flow (when the air volumetric flow exceeds the value the mass flux increases only slightly but the pressure drop increases. For example, approximately 10×10^{-5} m^3/s for channel heights of 1 mm) is favorable to

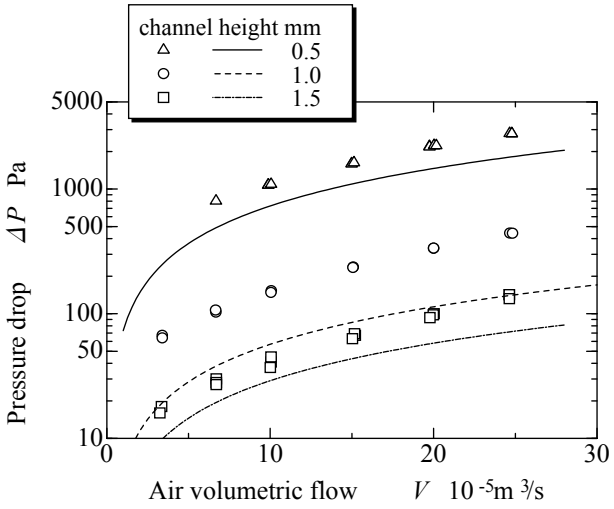

Fig. 14. Variation of pressure decrease with air volumetric flow for different channel heights

moisture recovery for the channel height is fixed. As same, the fact that the increase in the pressure drop with respect to the increasing air flow and decreasing channel height, as shown in Figure 14, shows that a proper channel height (the mass flux increase hardly if even the channel height is decreased further. For example, approximately 1.0 mm for the conditions of the channel length 100 mm and the pressure drop 200 Pa) is favorable to moisture recovery for the pressure drop is limited.

3.6 Moisture absorption rate

In order to evaluate the utilization degree of the moisture absorption capacity of the air, the moisture absorption rate η, which is the ratio of the increase in the absolute humidity to the maximum moisture absorption of the air, is introduced and is given by

$$\eta = (d_{out} - d_{in})/(d_w - d_{in}) \tag{7}$$

where d_{out} and d_{in} are the absolute humidities of the air at the exit and entrance, respectively, of the channel in which the air is flowing, and d_w is the absolute humidity of saturated air at the temperature of the constant-temperature water.

Figure 15 shows the variations in moisture absorption rate with respect to the air volumetric flow for porous plates having different thermal conductivities. This figure shows that the moisture absorption rate decreases as the air volumetric flow increases, and the values for both the high- and low-thermal-conductivity plates were approximately the same and exceeded 80% at an air volumetric flow of 3.3×10^{-5} m^3/s. However, as the air volumetric flow increases, the moisture absorption rates of the high- and low-thermal-conductivity plates gradually diverge, and at a volumetric flow rate of 24.7×10^{-5} m^3/s, the moisture absorption rate for the low-thermal-conductivity plate is 26%, while that for the high-thermal-conductivity plate is 40%, approximately 1.5 times that for the low-thermal-conductivity plate. That is, from the standpoint of the moisture recovery, it is effective to use the high-thermal-conductivity plate for the case of the large air volumetric flow.

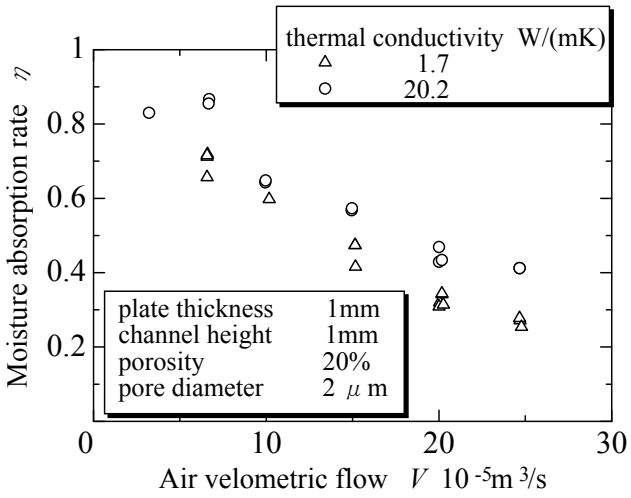

Fig. 15. Effect of thermal conductivity of the porous plate on moisture absorption rate

Figure 16 shows the variations in the moisture absorption rate with respect to the air volumetric flow using the high-thermal-conductivity plate for channel heights of 0.5, 1.0, and 1.5 mm. As mentioned in Section 3.5, the moisture transport increased with decreasing channel height because the heat transfer at the plate surface next the channel is promoted, so that the moisture absorption rate increased with the decrease of the channel height. In particular, the moisture absorption rate shows a high value that exceeds 90% for the case of an air volumetric flow of less than 6.7×10^{-5} m^3/sand a channel height of 0.5mm. That is, a high moisture recovery rate can be expected for a suitable working condition for the device design.

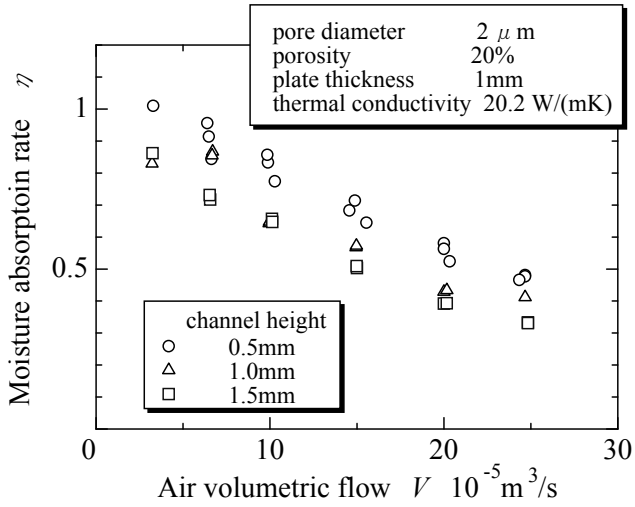

Fig. 16. Effect of channel height on moisture absorption rate

4. Conclusion

The present study attempted to clarify the characteristics of the heat and moisture transport in the process of moisture recovery from the exhaust gas of fuel cell vehicles using a porous plate having extremely small pores. As a first step, the moisture transport from constant-temperature water to dry air through the porous plate was measured. The general characteristics of moisture and the effects of the thermal conductivity, porosity and pore diameter in the porous plate, and the height of the channel of flowing air on the performance of moisture transport were examined experimentally. The results are summarized as follows:

1. For the process of moisture transport from constant-temperature water to dry air through a porous media plate, the mass flux increases with the increase of air volumetric flow, and the heat transport in this process is caused primarily by the transport of latent heat accompanying the mass transport.
2. The thermal conductivity of the porous plate is a very important factor and the controlling factor for moisture transport is different for the high- and low-thermal-conductivity plates. That is, for a plate thickness of 1 mm, the controlling factor is the

thermal resistance inside the porous plate for the low-thermal-conductivity plate; whereas, for the high-thermal-conductivity plate the controlling factor is the heat transfer at the surface of porous plate.

3. Under the experimental conditions of the present study, the effect of the porosity of the porous plate on the performance of moisture transport was not significant.
4. The effect of pore diameter on the moisture transport depends on the pore diameter and the plate thickness. That is, the smaller the pore diameter and the thicker the plate, the greater the effect.
5. The effect of the channel height on the moisture transport depends on the thermal conductivity of the porous plate. For the low-thermal-conductivity plate, the moisture transport increased when channel height varied from 1.5 mm to 1.0 mm, and the moisture transport varied little when the channel height varied from 1.0 mm to 0.5 mm. However, for the high-thermal-conductivity plate, the moisture transport increased when the channel height varied from 1.5 mm to 1.0 mm and from 1.0 mm to 0.5 mm. Thus, for highly efficient moisture recovery, a compact device is preferable, provided that the pressure drop ends in a limited range.

5. Acknowledgements

This project supported by the National Natural Science Foundation of China (Grant No. 50876076) and Nissan Motor Co. Ltd.

6. Nomenclature

d	absolute humidity (g/kg′)
D	pore diameter (μm)
D_e	equivalent diameter (m)
h_{gl}	latent heat (kJ/kg)
$K(\varepsilon,D)$	permeability (m²)
L	channel length (m)
M	mass flux (kg/(m²s))
ΔP	pressure drop (Pa)
q	heat flux (W/m²)
R_{fp}	moisture transport resistance (1/m)
R_{tp}	thermal resistance (m²K/W)
RH	relative humidity
v	air velocity (m/s)
V	air volumetric flow (m³/s)
Δx	thickness of porous plate (m)

Greek symbols

ε	porosity
η	moisture absorption rate
λ_p	thermal conductivity (W/(mK))
μ	viscosity (Pa.s)
θ	contact angle

ρ air density (kg/m^3)
σ surface tension of water (N/m)

Subscripts

c plate surface, water side
in inlet of the channel
out outlet of the channel
s plate surface, air side
w constant-temperature water

7. References

Asaeda, M.; Du, L. D.& Ushijima, M. (1984).Feasibility study on dehumidification of air by thin porous alumina gel membrane, *Proc. of 4th Int. Drying Symposium*, pp. 712-718.

Asaeda, M.; Du, L. D. & Ikeda, K. (1986).Experimental Studies of Dehumidification of Air by an Improved Ceramic Membrane, *Journal of Chemical Engineering of Japan*, Vol.19, pp. 238-240, ISSN 0021-9591.

Buchi, F. N.& Scherer, G. S. (2001).Investigation of the Transversal Water Profile in Nafion Membrane in Polymer Electrolyte Fuel Cells, *Journal of Electrochemical Society*, Vol.148, No.3, pp.183-188, ISSN 0013-4651.

Cheng, P. & Wang, C. Y. (1996).A Multiphase Mixture Model for Multiphase, Multi-component Transport in Capillary Porous Media-II. Numerical Simulation of the Transport of Organic Compounds in the Subsurface, *Int. J. Heat Mass Transfer*, Vol. 39, No 17, pp. 3619-3632, ISSN 0017-9310 .

Nguyen, V. T. &White, E. R. (1993).A Water and Heat Management Model for Proton-Exchange- Membrane Fuel Cells, *J. Electro. Chem. Soc.*, Vol.140, No.8,pp.2178-2186, ISSN 0013-4651.

Plourde, F. & Prat, M. (2003). Pore Network Simulations of Drying of Capillary Porous Media Influence of Thermal Gradients, *Int. J. Heat Mass Transfer*, Vol.46, No.7, pp.1293-1307, ISSN 0017-9310.

Prat, M. (1993).Percolation Model of Drying under Isothermal Conditions in Porous Media, *Int. J. Multiphase Flow*, Vol.19, No.4, pp. 691-704, ISSN 0301-9322.

Udell, K. S. (1983). Heat Transfer in Porous Media Heated From Above with Evaporation, Condensation and Capillary Effects, *Journal of Heat Transfer AMSE*, Vol.105, No.3, pp.485-492, ISSN 0022-1481.

Udell, K. S. (1985).Heat Transfer in Porous Media Considering Phase Change and Capillarity –the Heat pipe Effect, *Int. J. Heat Mass Transfer*, Vol. 28, No.2, pp.485-495, ISSN 0017-9310.

Usami, Y.; Fukusako, S. & Yamada,M. (2000).Heat and Mass Transfer in a Reforming Catalyst Bed (Analytical Prediction of Distributions in the Catalyst Bed),*Trans. JSME (B)*, Vol.66, No.641, pp.203-210, ISSN 0387-5016.

Usami, Y.; Fukusako, S. & Yamada, M. (2001).Heat and Mass Transfer in a Reforming Catalyst Bed (Quantitative Evaluation of the Controlling Factor by Experiment),*Trans. JSME (B)*, Vol.67, No.659, pp.1801-1808, ISSN 0387-5016.

Vafai, K. & Whitaker,S. (1986). Simultaneous Heat and Mass Transfer Accompanied by Phase Change in Porous Insulation, *Trans. ASME*, Vol.108, No.1,pp.132-140, ISSN 0022-1481.

Vafai, K. & Tien, C. (1989).A Numerical Investigation of Phase Change Effects in Porous Materials, *Int. J. Heat Mass Transfer*, Vol.32, No.7, pp.1261-1277, ISSN 0017-9310.

Wang, C. Y. & Cheng,P. (1996).A Multiphase Mixture Model for Multiphase, Multi-Component Transport in Capillary Porous Media-I. Formulation, *Int. J. Heat Mass Transfer*, Vol.39, No.17, pp.3607-3618, ISSN 0017-9310.

Wang, C. Y. & Beckermann, C. (1993).A Two-Phase Mixture Model of Liquid-Gas Flow and Heat Transfer in Capillary Porous Media-I. Formulation, *Int. J. Heat Transfer*, Vol.36, No.11, pp.2747-2758, ISSN 0017-9310.

Wang, C. Y. & Beckermann, C. (1993).A Two-Phase Mixture Model of Liquid-Gas Flow and Heat Transfer in Capillary Porous Media-II. Application to Pressure-Driven Boiling Flow Adjacent to a Vertical Heated Plate, *Int. J. Heat Transfer*, Vol.36, No.11, pp.2759-2768, ISSN 0017-9310.

Wang, S. X.; Utaka, Y. & Tasaki,Y. (2005). A Basic Study on Humidity Recovery by Using Micro-Porous Media (General Characteristics and Effect of Property of Materials on Transport Performance), *Trans. JSME (B)*, Vol.71, No.706, pp.1647-1654, ISSN 0387-5016 .

Wang, S. X.; Utaka, Y. & Tasaki,Y. (2006). A Basic Study on Humidity Recovery by Using Micro-Porous Media (Effects of Thermal Condition of fluids and geometrical Condition of Apparatus on Transport Performance), *Heat Transfer-Asian Research*, Vol.35, No.8, pp.568-581, ISSN 1523-1496 .

Wang, S. X.; Utaka, Y. & Tasaki,Y. (2009). An Experimental Study on Moisture Transport through a Porous Plate with Micro Pores, *Int. J. Heat Transfer*, Vol.52, No.19-20, pp.4386-4389, ISSN 0017-9310 .

Welty, J. R.; Wicks, C. E. & Wilson,R. E. (1976). *Fundamentals of Momentum, Heat, and Mass Transfer*, Wiley, ISBN 0471933546, New York, USA.

Yoshikawa, H.; Hishinuma, Y. & Chikahisa, T. (2000).Performance of a Polymer Electrolyte Fuel Cell for Automotive Applications, *1st ReportEffects of water Humidified Anode and Cathode Gases*, Trans. JSME (B), Vol.66, No.652, pp.3218-3225, ISSN 0387-5016.

You, L. & Liu,H. (2002).A Two-Phase Flow and Transport Model for the Cathode of PEM Fuel Cells, *Int. J. Heat Mass Transfer*, Vol.45, No.11, pp.2277-2287, ISSN 0017-9310.

Zhao,T. S.&Liao,Q. (2000).On Capillary-Driven Flow and Phase-Change Heat Transfer in a Porous Structure Heated By a Finned Surface: Measurement and Modeling, *Int. J. Heat Mass Transfer*, Vol.43, No.7, pp.1141-1155, ISSN 0017-9310.

15

Improvement of Oxygen Transfer Efficiency in Diffused Aeration Systems Using Liquid-Film-Forming Apparatus

Tsuyoshi Imai and Hua Zhu
Division of Environmental Science and Engineering,
Graduate School of Science and Engineering,
Yamaguchi University
Japan

1. Introduction

Currently, aerobic bio-treatment processes, in which activated sludge system is at the center of the attention, are extensively applied in sewage treatment plants around the world. For activated sludge process, the diffused aeration has been thought to be one of the most important and indispensable operational units. However, a major concern of this operational methodology is that a large amount of compressed air has to be consumed in a diffused aeration system owing to the low oxygen transfer efficiency in water. It has been previously demonstrated that more than 40 % of the total power consumption in sewage treatment plants in Japan is related to power consumption associated with aeration alone. Therefore, the development of highly efficient aeration strategies has presently emerged as an intriguing research topic in the field of energy savings.

The oxygen transfer in diffused aeration systems can be divided into two processes: bubble oxygen transfer and surface oxygen transfer. Bubble oxygen transfers into the water across the bubble-water interface as the bubbles rise from the diffuser to the water surface. Surface oxygen transfer exclusively occurs at the air-water interface situating on the water surface, originating from vigorous turbulence induced by bubble-plume motion and water circulation. Wilhelms and Martin's findings indicated that approximately one-third of the total volumetric mass transfer coefficient (k_La_t) is responsible for the volumetric mass transfer coefficient for surface transfer (k_La_s) [1]. McWhirter and Hutter determined that a representative k_La_s is 25-33 % of the k_La_t in a fine bubble diffuser system and 11-17 % of the k_La_t in a coarse bubble diffuser system [2]. DeMoyer *et al.* ever reported that the k_La_s is 59-85 % of the volumetric mass transfer coefficient for bubble surface (k_La_b) [3].

Bubble transfer and surface transfer both contribute remarkably to the total oxygen transfer in the submerged aeration system. However, bubble transfer is the predominant means of oxygen transfer. So far, considerable research interests have been focused on the enhancement of the bubble transfer efficiency by developing a wide variety of new aeration techniques, including the utilization of high-purity-oxygen aeration system [4-10], deep aeration system [11-13] and fine bubble diffuser [14-17], *etc.* Nevertheless, only a little effort has been devoted to the research on the improvement of surface transfer efficiency.

The improvement of oxygen transfer capability across water surface is pursued in this study. The objective is fulfilled with a liquid-film-forming apparatus (LFFA) by pre-forming an aggregative entity in the atmosphere near water surface. This entity is constructed of a large quantity of air-filled gas bubbles with the periphery of each gas bubble surrounded by an ultrathin layer of liquid film, thereby enlarging notably the effective interfacial contact area between air and water. Consequently, energy consumption problem can be solved by reducing the aeration depth down to 1 m or less without trading off the ideal aeration efficacy in a diffused aeration system. Based on the concept above, lab-scale experimental apparatus is designed in this study and the efficiency of oxygen transfer in this novel apparatus is determined either numerically or experimentally. Furthermore, a number of factors affecting the efficiency of oxygen transfer are also examined in detail, and the feasibility is preliminarily explored for the application in wastewater treatment plants.

2. Novel idea: Liquid-film aeration system (LFAS)

Liquid-film aeration system (LFAS) which means that LFFA developed in this study is installed on the water surface of existing aeration tanks. Under no extra energy consumption circumstances, water body is wholly membranized into a liquid film (i.e., a thin water film located at the water surface-air interface) by LFFA, thus realizing the oxygen supply towards liquid-film-formed water body simultaneously from the interior and exterior of the liquid film. The efficiency of atmospheric oxygen enrichment is improved as a consequence of dual-fold oxygen provisions. Namely, in addition to the existing oxygen supply efficiency of an aeration tank, the oxygen supply efficiency of LFAS is increased by one more term from the LFFA. As a result, the oxygen supply efficiency of the entire aeration system is enhanced.

Schematic drawings of the LFFA are illustrated in Fig. 1. The LFFA, made of plastics here, has a simple configuration constituting three sections: (1) trumpet-shaped capture part as a gas collector for converging the released gas bubbles; (2) airlift part, mainly made up of some pipes orienting parallel to each other, aiming to facilitate the relevant liquid film formation near the water surface and (3) effluent part which alternately reserves and discharges the treated water involving higher-concentration dissolved oxygen (DO).

Optionally, the LFFA can be compatibly installed in an existing aeration system. The whole set of equipment is denoted as liquid-film aeration system (Fig. 2). The joint interface between the capture and airlift parts of this LFFA is flush with the water surface with the former just submerged in water and the latter completely exposed to air. During the operating process, the gas bubbles released from a diffuser first rise to the airlift part through the capture part and then self-assemble into a macroscopic aggregated system of gas bubbles over the airlift part. This macroscopic ensemble of gas bubbles floating in the atmosphere in close proximity to the water surface are microscopically comprised of the combination of numerous agglomerated gas bubbles and a fraction of the bulk water (serving as liquid-film boundary layer surrounding each individual bubble herein) entrained by the ascending bubbles. In this case, air fills both the exterior and interior of these bubbles as well as the thin liquid film, as described above. Hence, oxygen transfer can take place both across the inner interface (gas bubble and liquid film) and the outer interface (atmosphere and liquid film) of the thin liquid film, which means that the available interfacial contact area between oxygen and water can be greatly multiplied, thereby promoting effectively oxygen transfer efficiency. Subsequently, oxygenic water is

discharged downstream from the effluent part. Furthermore, LFAS can supply oxygen either in a once-through mode in the case of which the effluent part is directly connected to another water reservoir, or in a recycle mode in the case of which the effluent part is directly connected to the original water tank itself.

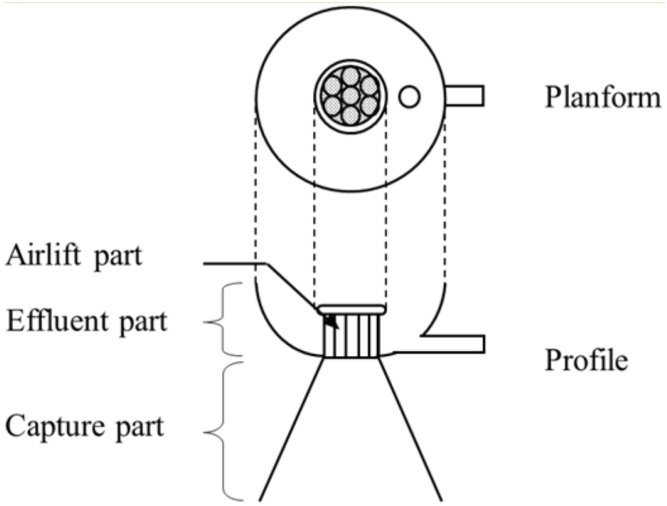

Fig. 1. Schematic diagram of the LFFA

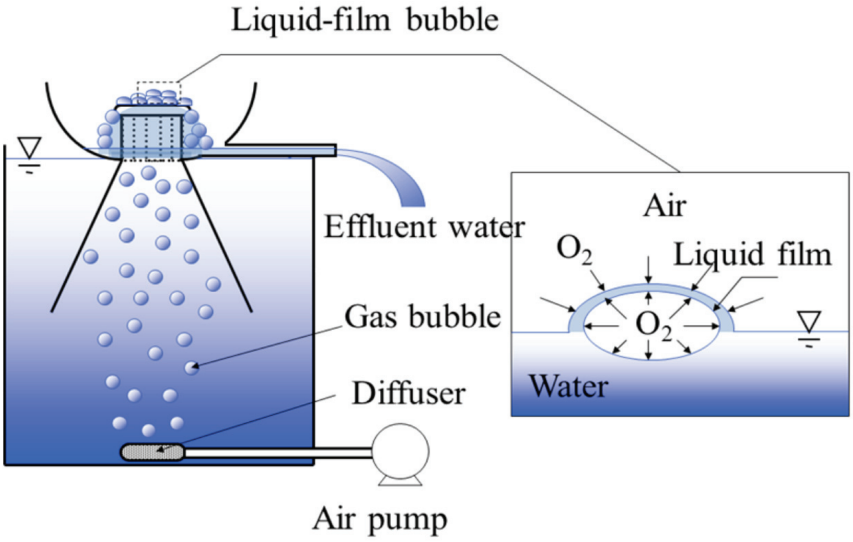

Fig. 2. Liquid-film aeration system (LFAS)

The picture of the actual experimental apparatus is shown in Fig. 3. Fig. 4 reveals the form of a liquid film.

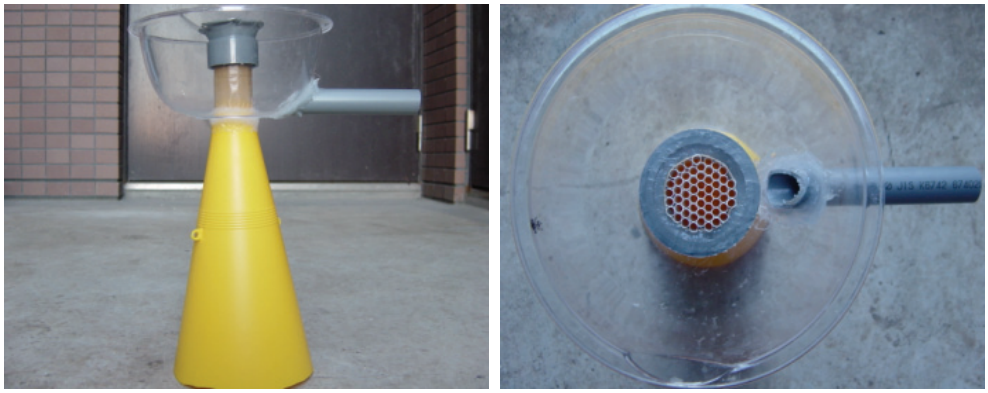

Profile Planform

Fig. 3. Lab-scale LFFA

Fig. 4. The picture of forming liquid film

LFAS possesses the following characteristics.
Due to the superior oxygen supply efficiency, even if the aeration depth is as low as less than 1 m, a sufficient amount of oxygen can still be provided. In contrast, the conventional aeration tank necessitates a depth of 4-5 m to achieve a commensurate oxygen supply. Therefore, LFAS is a very energy-saving aeration system.
Although some energy is consumed as a consequence of the friction between the airlift tube wall of LFFA and surrounding water body, we suggest that this portion of energy consumption is far below the wasted energy in the conventional aeration system. Moreover, the energy wasted in the traditional aeration system can be re-used for the oxygen supply. Therefore, this novel LFAS-based method definitely opens an energy-efficient pathway to improve the oxygen transfer efficiency.

LFFA has a very simple structure, and its production cost is very low. Optionally, it can be made from recycled plastics. As another advantage, this apparatus itself does not consume any power, and can be easily installed on the water surface of existing aeration tank without large-scale retrofitting. Thus this very cheap setup is well suited for the application in the recycle-type society.

3. Pre-experiment on the LFFA

3.1 Introduction

In order to evaluate the oxygen transfer performance of the LFFA, under the experimental conditions of different bubble diameters and different aeration amounts, comparative experiments are conducted on a liquid-film aeration system and conventional aeration system by respectively using de-oxygenated water and activated sludge.

3.2 Experimental methods

The diffuser is set in a 28.5 cm deep and 15 L capacity cylindrical water tank with a surface area of 526.3 cm^2. Its location is at the middle of the experimental water tank bottom with an aeration depth of 26 cm. The liquid-film apparatus with a pipe diameter of 1 cm, effective height of 10 cm and cross-sectional area of 12.56 cm^2 is mounted on the surface of a water tank. During the operational period, single-pass fashion is employed for this apparatus. After measurement of DO concentration and temperature in the initially de-oxygenated water, a given amount of aeration is provided and the aeration lasts for 4 min. The DO concentration in the discharged water from the effluent part is periodically measured at a sampling interval of 30 s. The amount of the effluent water is calculated before the aeration is suspended. To prevent the water surface in the water tank from going downwards, the volume of the de-oxygenated water equivalents to that of the treated water is periodically poured into the water tank to maintain the water surface's balance throughout the experiment. As a control, the conventional aeration experiment is also conducted at the same water disposal volume, aeration depth and aeration duration as the liquid-film aeration experiment. The experimental setup is demonstrated in Fig. 5.

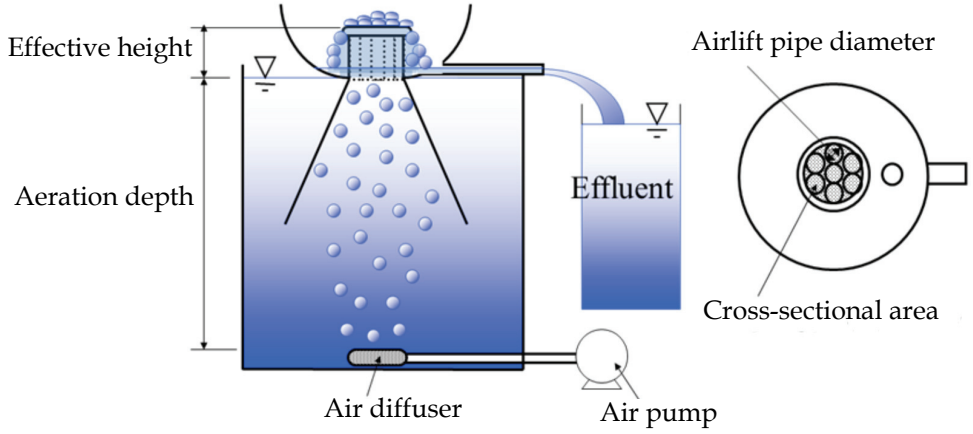

Fig. 5. Single-pass LFFA apparatus

A 0.08 g/L sodium sulfite solution is used to chemically de-oxygenate the tank water to around 0 mg/L at the start of each test. The activated sludge is taken from Ube Eastern Water Cleanup Center. DO concentrations are determined by YSI Model DO meter. Two types of air pumps (Iwaki APN-215CV-1 Model and Secoh DF-406 Model) are used herein. Two kinds of air diffusers are selected providing average gas bubble diameters of 3 and 6 mm, respectively. A series of the combinations of diffuser and air pump give rise to different aeration amounts, as shown in Table 1. The average bubble diameter is determined by averaging the diameters of several digital-camera-taken gas bubbles just released from the diffuser.

Average bubble diameter of a diffuser	Air pump type	Air flow rate
3 mm	APN-215CV-1	12.8 L/min
3 mm	DF-406	18.6 L/min
6 mm	APN-215CV-1	13.5 L/min
6 mm	DF-406	19.2 L/min

* Adjusting aeration amounts contingent on different experimental conditions.

Table 1. The air flow rate as a function of diffuser and air pump types*

The experimental results are compared in terms of DO saturation rate and oxygen transfer rate, both of which are calculated by the following Equations (1) and (2),

$$\text{DO saturation rate (\%)} = \frac{DO_{act}}{DO_{sat}} \times 100\% \tag{1}$$

$$\text{Oxygen mass transfer rate (mg-O}_2\text{/min)} = \left(DO_{act} - DO_0\right) \times Q_L \tag{2}$$

where $DO_{act.}$ is the measured DO average value in mg/L, $DO_{sat.}$ is the saturated DO concentration in water at 1 atm in mg/L, DO_o is the initial DO concentration in mg/L, and Q_L is the flow rate of the effluent water in L/min.

3.3 Results and discussion

3.3.1 DO saturation rate

Fig. 6 and Fig. 7 respectively show the experimental data using de-oxygenated water and DO saturation rate using activated sludge.

As shown in Figs. 6 and 7, independently of air flow rate and aerated bubble diameter, it is suggested from both de-oxygenated water and activated sludge experiments that the effluent DO concentration associated with liquid-film aeration is always higher than that by conventional aeration. While de-oxygenated water is in service, conventional aeration yields a DO saturation rate of 80%, in contrast to up to ca. 95% by way of liquid-film aeration. Even in the case of activated sludge, the corresponding value of over 90% is achieved via liquid-film aeration. It is found that in comparison with the conventional aeration by using continuously recirculated aeration to enhance DO concentration, for the liquid-film aeration, the DO content in the effluent can be raised up to the saturation state by only aerating once the effluent, thereby indicating strong oxygen supply capability of the latter.

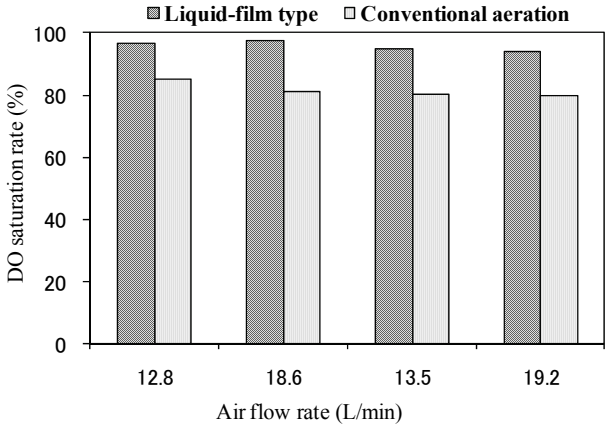

Fig. 6. The comparison of DO saturation rate (de-oxygenated water)

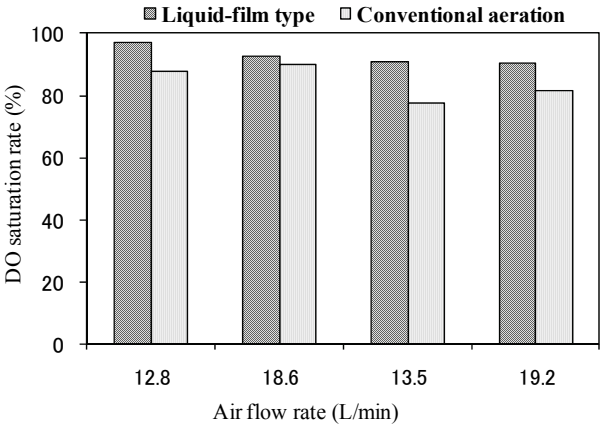

Fig. 7. The comparison of DO saturation rate (activated sludge)

3.3.2 Oxygen mass transfer rate

Figs. 8 and 9 show the oxygen mass transfer rates for the de-oxygenated water and activated sludge, respectively. As shown in these experimental findings, whether for de-oxygenated water or activated sludge, the smaller the gas bubble diameter or the higher the aeration amount at the same gas bubble diameter is, the faster the oxygen transfer rate is. While the de-oxygenated water is in use, oxygen transfer rate of liquid-film aeration increases by 30% in regard to conventional aeration. In the case of activated sludge, an increase of 10% is correspondingly observed.

As indicated in Figs. 8 and 9, liquid-film apparatus only needs an aeration depth of a few tens of centimeters to provide adequate amount of oxygen. However, 4-5 m in aeration depth is required for the conventional aeration apparatus to supply comparable oxygen content. Hence, liquid-film apparatus is regarded as a very energy-efficient setup.

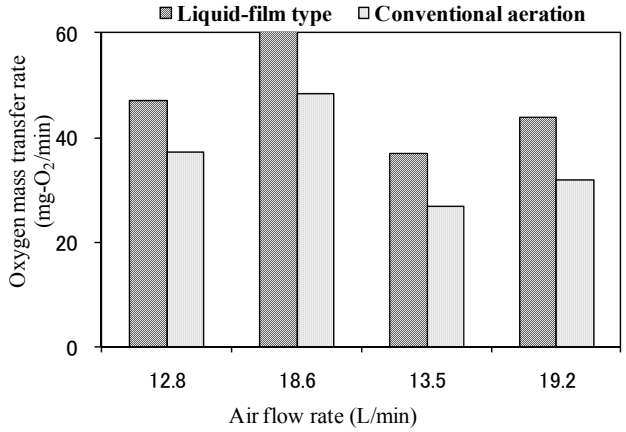

Fig. 8. The comparison of oxygen mass transfer rate (de-oxygenated water)

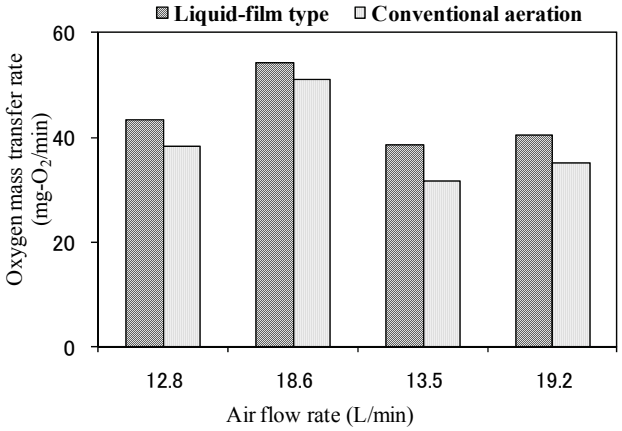

Fig. 9. The comparison of oxygen mass transfer rate (activated sludge)

4. Effect of the structural parameters of the LFFA

4.1 Introduction

According to the preceding pre-experiment on the LFFA, the basic factors influencing liquid film formation involve airlift pipe diameter, cross-sectional area, effective height, air flow rate, gas bubble diameter and aeration depth, etc. This section will discuss experimentally the effect of every factor on liquid film formation in detail, and the optimal design parameter of LFFA will then be identified.

Fig. 10 demonstrates a variety of factors impacting the liquid film formation. Each factor is defined as follows. Effective height refers to the length of airlift, and +/- symbols represent the lengths above/below the water surface, respectively. Aeration depth represents the distance from the diffuser to water surface, and cross-sectional area means the cross-sectional area of the airlift part.

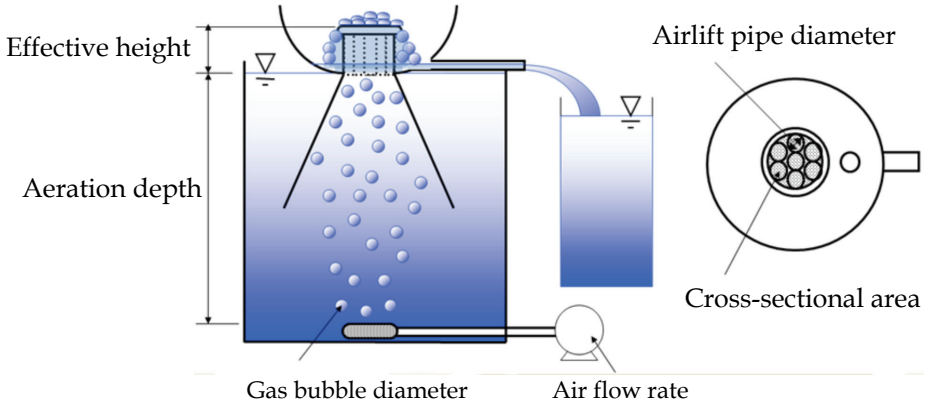

Fig. 10. The factors affecting the liquid film formation

4.2 Effect of altering gas bubble diameter on oxygen supply efficiency

4.2.1 Experimental conditions

In this trial, gas bubble diameter is varied by changing the type of diffuser. Diffuser can offer 2 kinds of gas bubbles with a diameter of 3 and 6 mm, respectively. The various combinations of diffuser and air pump as well as air flow rate are listed in Table 1. The average gas bubble diameter is determined by averaging the diameters of many digital-camera-taken gas bubbles located near the diffuser.

The parameter of the single-pass LFFA apparatus is listed as follows: 4, 6 and 10 mm in pipe diameter, 10 cm in effective height, and 12.56 cm^2 in cross-sectional area. The rig of experimental apparatus and experimental conditions are respectively shown in Fig. 11 and Table 1.

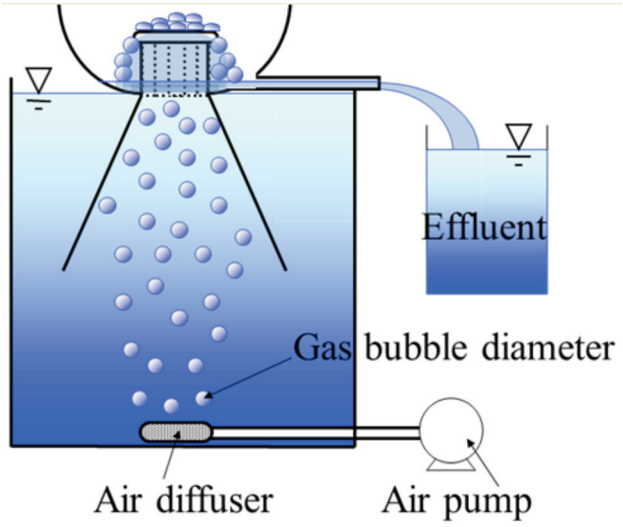

Fig. 11. Experimental apparatus relating to the variation in gas bubble diameter

4.2.2 Experimental methods

The LFFA operating in a single-pass manner is set in a 28.5 cm deep and 15 L cylindrical tank with a surface area of 526.3 cm^2. After measurement of DO concentration and temperature in the initially deoxygenated water, a given amount of aeration is provided and lasts for 4 min. The DO concentration in the discharged water from the effluent part is periodically measured at an interval of 30 s. The amount of the effluent water is calculated before aeration is stopped. To prevent the water surface in the water tank from going downwards, the volume of the de-oxygenated water equivalent to that of the treated water is periodically poured into the water tank to maintain the water surface's balance throughout the experiment.

DO concentrations are determined with YSI Model DO meter. Air pump includes Iwaki APN-215CV-1 Model and Secoh DF-406 Model.

4.2.3 Calculation methods

The parameters such as DO saturation rate, oxygen transfer rate and oxygen transfer mass per unit air aeration volume are used for evaluating the experimental results in this experiment. The calculation is based on Equations (1), (2) and (3).

$$E_O = \frac{(DO_{act} - DO_0) \times Q_L}{Q_G} \tag{3}$$

Herein, E_0 stands for oxygen transfer mass per unit air aeration volume in mg-O_2/L-air, $DO_{act.}$ is the actually measured average DO concentration in mg/L, DO_o is the initial DO concentration in mg/L, Q_L is the effluent flow rate in L/min, Q_G is air flow rate in L/min.

4.2.4 Results and discussion

The experimental results of the DO saturation rate, effluent flow rate, oxygen mass transfer rate and oxygen transfer mass per unit air aeration volume are respectively shown in Figs. 12, 13, 14 and 15.

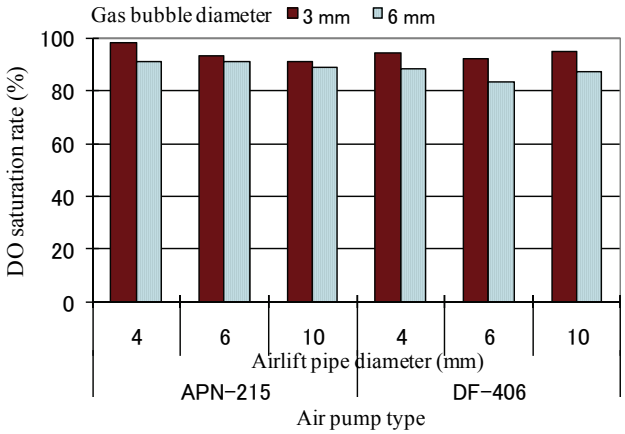

Fig. 12. Effect of gas bubble diameter on the DO saturation rate

As indicated in Fig. 12, DO saturation rates always maintain higher than 80% in all experiments, suggesting the superior oxygen transport ability of this novel setup. In Fig. 12, when the same air pump is used, the aeration amount of the diffuser providing a gas bubble diameter of 3 mm is less than that of the diffuser with a bubble diameter of 6 mm. However, it is found from the experiment results of 4 mm pipe diameter that though the aeration amount is comparatively small for the 3 mm diameter bubbles, DO saturation rate is still higher than that of 6 mm diameter bubbles. Likewise, the same trend is observed for the 6 and 10 mm diameter pipes. This is attributed to the fact that the finely divided gas bubbles allow for the enlarged contact area between water and gas bubbles in the aeration system, thereby enhancing the oxygen transport ability.

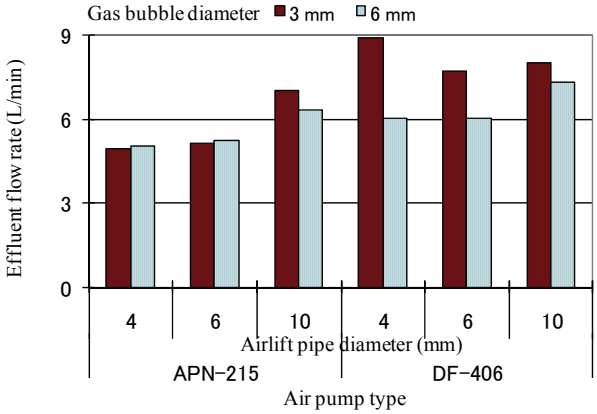

Fig. 13. Effect of gas bubble diameter on the effluent flow rate

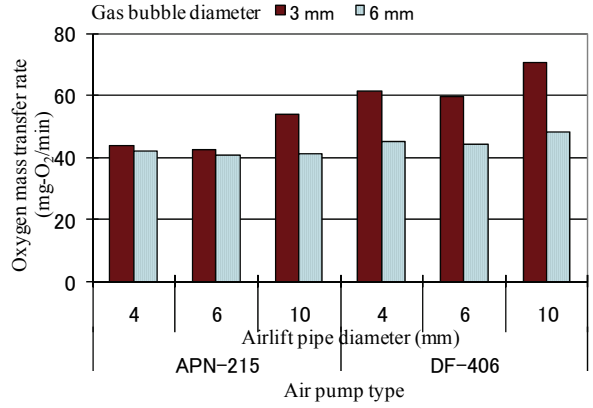

Fig. 14. Effect of gas bubble diameter on oxygen mass transfer rate

As shown in Figs. 13 and 14, both effluent flow rate and oxygen transfer rate exhibit a tendency same as DO saturation rate. However, as a result of the different aeration amounts applied, it is very hard to make a credible judgement.

Therefore, the parameter E_0 (DO amount per unit oxygen supply amount) is introduced herein. Its experimental result is shown in Fig. 15. As shown in this figure, when the pipe diameters are 4, 6 and 10 mm, the same trends are all manifested. That is, E_0 of 3 mm diameter gas bubble is greater than that of 6 mm.

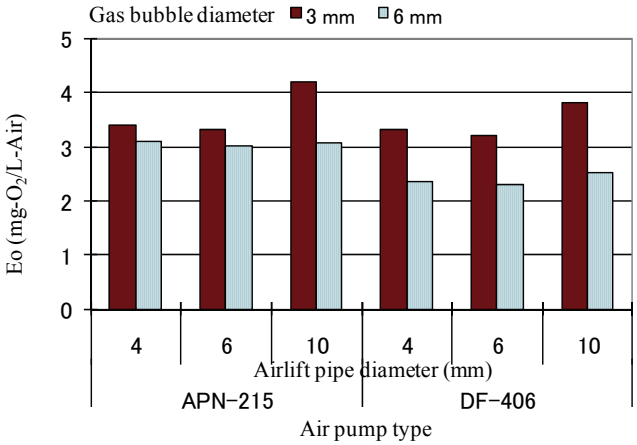

Fig. 15. Effect of gas bubble diameter on E_0

Similarly, while the other air pump is used, the similar evolving trends are observed for DO saturation rate, effluent flow rate, oxygen transfer rate and oxygen transfer efficiency. Namely, the smaller the gas bubble diameter is, the higher the result is. It is shown that the LFFA is likewise subjected to the effect of the interfacial contact area between air and water.

4.3 Effect of aeration depth on oxygen supply efficiency

4.3.1 Experimental conditions and methods

At an air flow rate of 13.5 L/min, aeration depth is respectively set at 26 and 63 cm. LFFA adopts a single-pass apparatus with a pipe diameter of 6 mm, effective height of 10 cm and cross-sectional area of 12.56 cm^2. The diffuser in connection with an Iwaki APN-215CV-1 Model air pump can release gas bubbles with an average diameter of 3 mm. The experimental apparatus relating to the differing aeration depths is shown in Fig. 16.
Experimental methods refer to Section 4.2.2.
The experimental results are evaluated in terms of DO saturation rate (*cf.* Equation 1) and oxygen transfer rate (*cf.* Equation 2).

4.3.2 Results and discussion

The experimental results are shown in Table 2. The larger the aeration depth is, the higher the DO saturation rate, effluent flow rate and oxygen transfer rate are. Thus, the oxygen supply ability of LFFA also obeys the oxygen diffusion regime at the gas-liquid interface.
At an aeration depth of 63 cm, the DO concentration in the effluent stream approximately approaches the saturation value, thereby determining the feasible aeration depth located at roughly 60 cm for the LFAS.

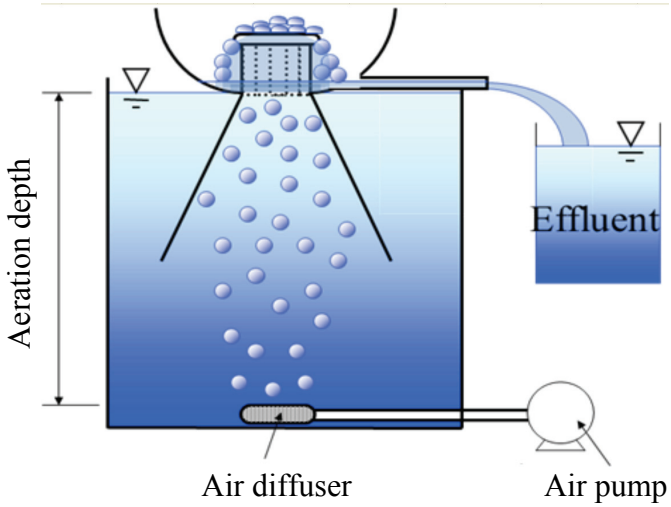

Fig. 16. Experimental apparatus relevant to the change in aeration depth

Aeration depth (cm)	Effluent flow rate (L/min)	DO saturation rate (%)	Oxygen mass transfer rate (mg-O_2/min)
26	5.36	83.7	37.4
63	5.60	98.5	44.1

Table 2. Experimental results pertaining to the variation in aeration depth

4.4 Effect of pipe diameter on oxygen transfer efficiency

4.4.1 Experimental conditions and methods

Three series of experiments are carried out with pipe diameters of 0.6, 1, 2, 4 and 5 cm, and effective heights of 1, 5 and 10 cm. At the pipe diameter of 0.6, 1, 2 and 4 cm, the diameter of the airlift part is set at 4 cm to attain the same cross-sectional area. By contrast, at a pipe diameter of 5 cm, setting the airlift part diameter at 5 cm leads to the altered cross-sectional area. In order to maintain the same aeration flux, the air flow rate is correspondingly increased when conducting this series of experiments involving 5 cm diameter pipes.
Experimental conditions and experimental apparatus diagram are respectively shown in Table 3 and Fig. 17.

Pipe diameter (cm)	Air flow rate (L/min)	Cross-sectional area (cm^2)	Aeration flux* [L/(min· cm^2)]	Effective height (cm)
0.6, 1, 2, 4	12.8	12.5	1.0	1, 5, 10
5	20.0	19.6	1.0	

* aeration flux：air flow rate per unit cross-sectional area.

Table 3. Experimental conditions relating to various pipe diameters

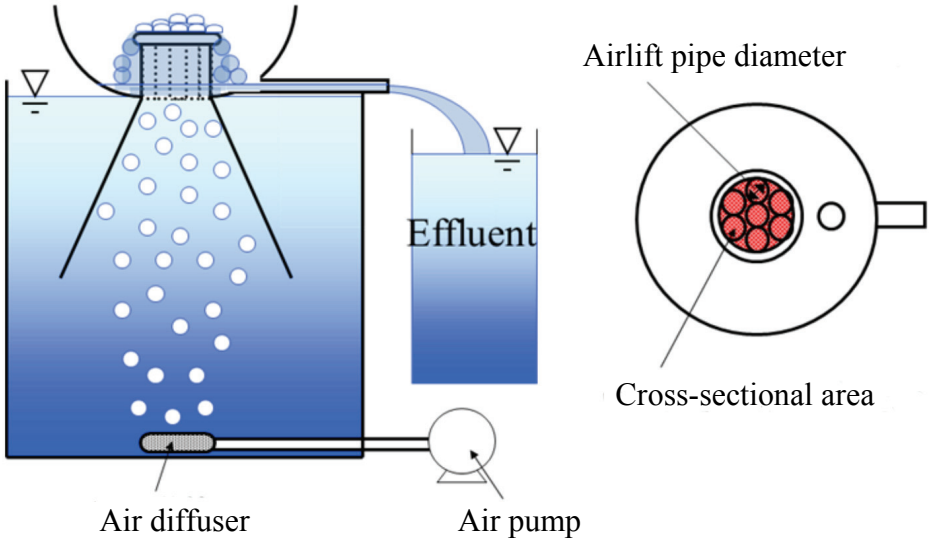

Fig. 17. Experimental apparatus relevant to various pipe diameters

The evaluation criteria include DO saturation rate (*cf.* Equation 1), liquid/gas ratio and E_0 (*cf.* Equation 3). The calculation of liquid/gas ratio is given by Equation 4.

$$\text{Liquid/gas ratio} = Q_L/Q_G \tag{4}$$

where Q_L refers to the effluent flow rate (L/min) and Q_G is air flow rate (L/min).

4.4.2 Results and discussion

The effect of pipe diameter on DO saturation rate, liquid/gas ratio, and E_0 is shown in Fig. 18.

Irrespectively of effective height, DO saturation rate, liquid/gas ratio and E_0 all exhibit similar trends. DO saturation rate tends to become large with decreasing pipe diameter. This is due to the fact that when the gas bubbles are passing through the LFFA setup, they are finely split, thereby enlarging dramatically the surface area of liquid film and consequently accelerating oxygen transport speed.

Liquid/gas ratio slowly increases with increasing pipe diameter and reaches the maximum value at 4 cm in pipe diameter. Because finely splitting of gas bubbles in the airlift part consumes some energy, the larger the pipe diameter, the smaller the hydraulic head loss in the airlift part, which thus increases the water flow rate there. However, if pipe diameter is over-sized, the airlift effect will be weakened, resulting in the reduced water flow rate through the airlift part. A direct outcome of interacting the 2 factors above with each other is the occurrence of an optimal parameter under a certain condition.

As shown by Equation 3, both DO concentration and liquid/gas ratio in the effluent water have an effect on oxygen transfer amount per unit air aeration volume, and 3 optimal conditions arise. They are listed as follows: (1) 4 cm in pipe diameter and 1 cm in effective height; (2) 4 cm in pipe diameter and 5 cm in effective height, and (3) 0.6 in pipe diameter

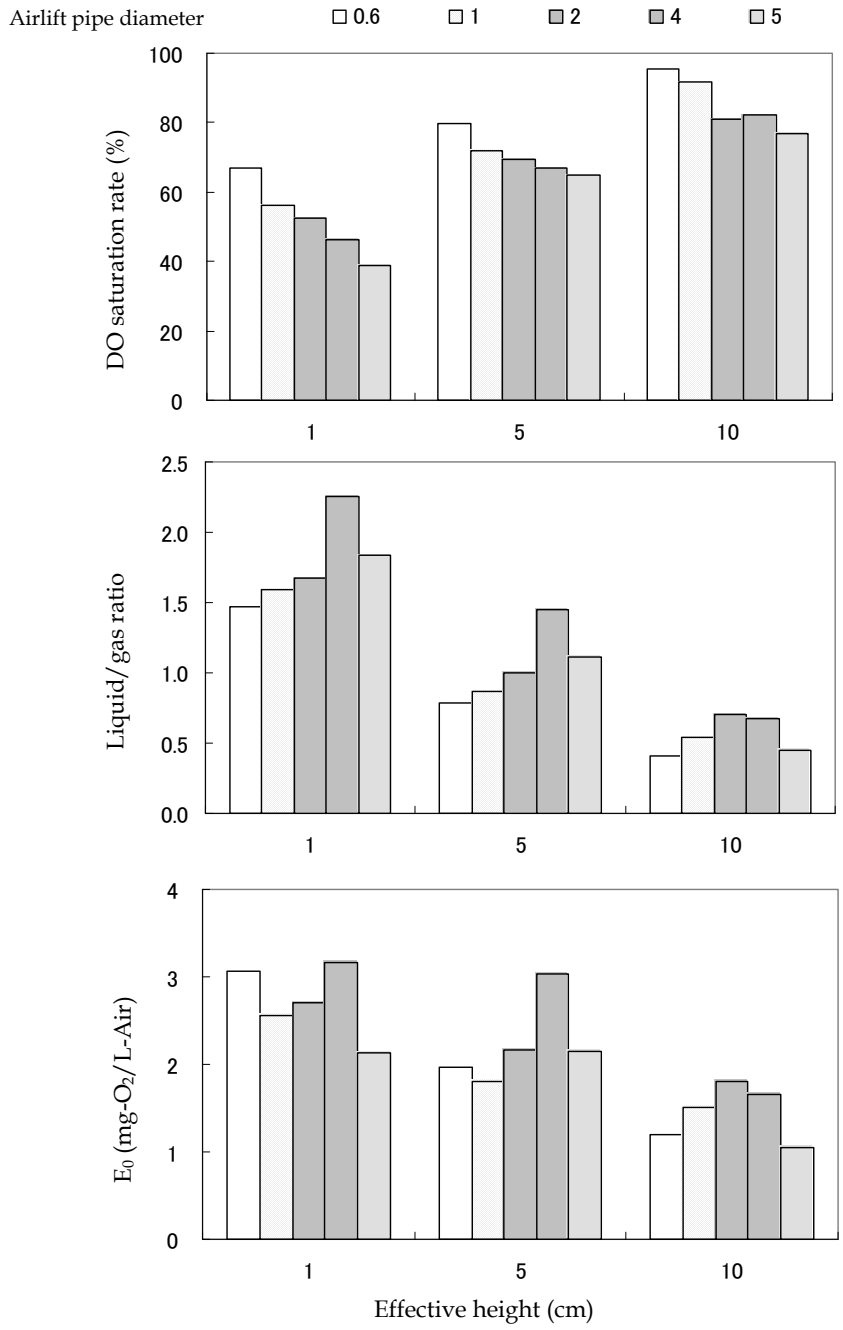

Fig. 18. Effect of airlift pipe diameter

and 1 cm in effective height. Meanwhile, as shown in Fig. 18, under the first condition, DO concentration relatively significantly affects oxygen transfer amount per unit air aeration volume. In contrast, liquid/gas ratio in the effluent plays a comparatively pronounced role under the third condition.

4.5 Effect of effective height on oxygen supply efficiency

4.5.1 Experimental conditions and methods

Effective height stands for airlift height. In this trial, the effective height is set at 1, 5 and 10 cm. Herein, the other structural parameters of the single-pass LFFA are 1, 2 and 4 cm in pipe diameter and 12.56 cm^2 in cross-sectional area. Air flow rate is 12.8 L/min.

Experimental conditions and experimental data are shown in Table 4 and Fig. 19, respectively.

DO saturation rate, liquid/gas ratio (*cf.* Equation 4) and E_0 (*cf.* Equation 3) are used as the evaluation criteria.

Effective height (cm)	Pipe diameter (cm)	Air flow rate (L/min)
1, 5, 10	1, 2, 4	12.8

Table 4. Experimental conditions linked to various effective heights

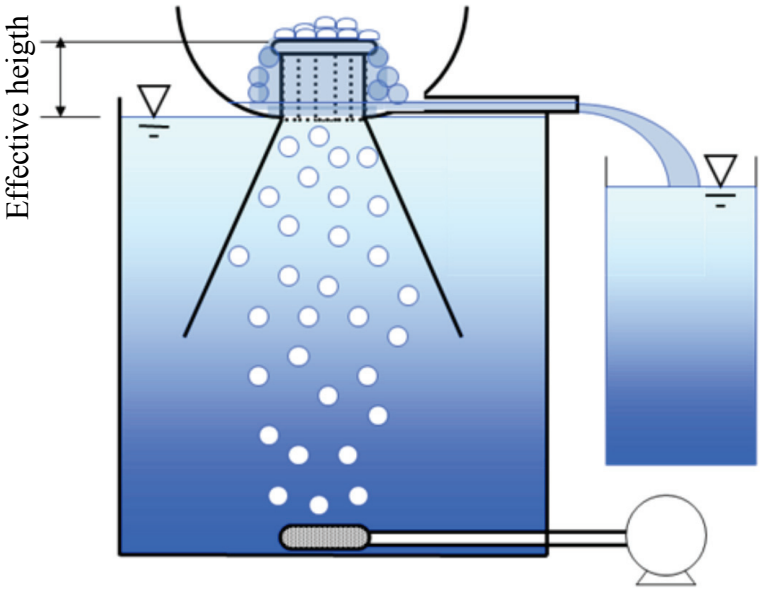

Fig. 19. Experimental apparatus relating to various effective heights

4.5.2 Results and discussion

Fig. 20 shows the effect of effective height on DO saturation rate, liquid/gas ratio and E_0.

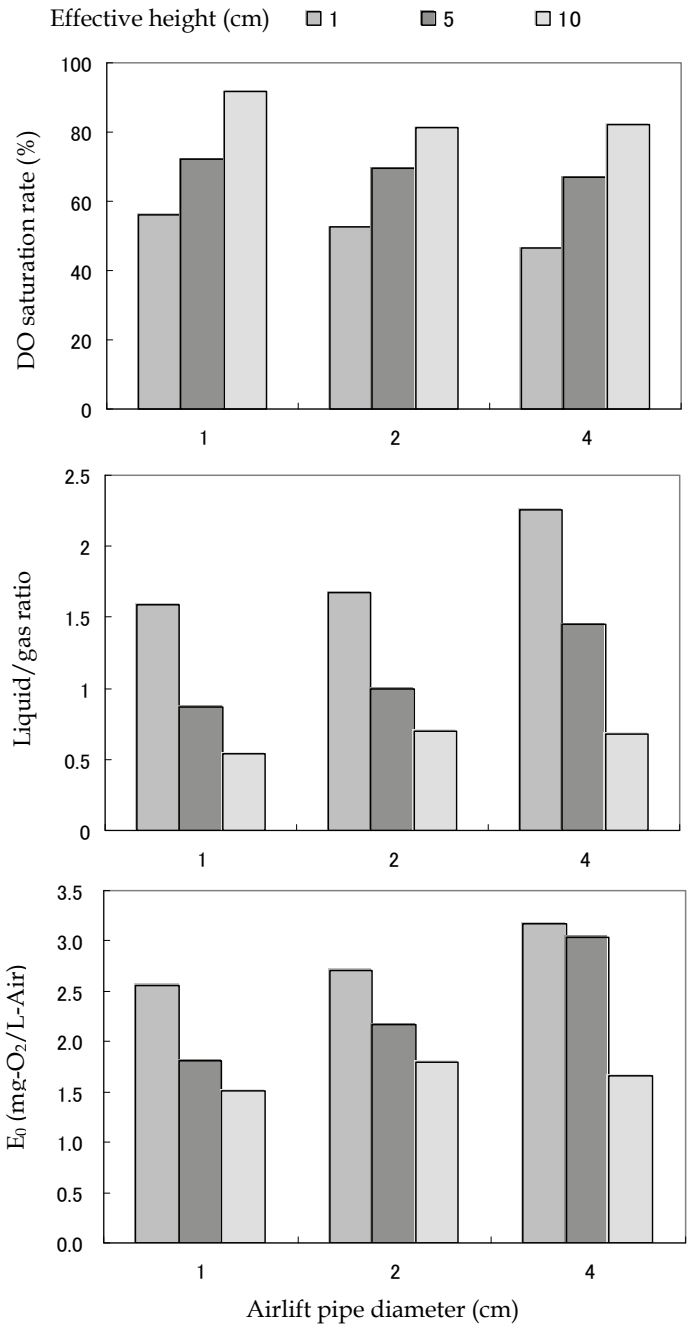

Fig. 20. Experimental findings as a function of effective height

The effluent flow rate displays a decreasing trend with increasing effective height. This can be explained by the fact that the higher the effective height in the atmosphere is, the larger the hydraulic head loss and the weaker the airlift effect are. DO saturation rate shows a propensity of going up of an increase in effective height. It can be easily understood that increased effective height leads to the prolonged contact time between the effluent water and air. Furthermore, in the case where the amount of the effluent water through the airlift pipes is reduced, a thinner liquid film can be formed, which can enhance the oxygen dissolution efficiency.
As a result, the oxygen transfer amount per unit air aeration volume approaches its maximum value under the experimental conditions of 1 and 5 cm in effective height, and 4 cm in pipe diameter.

4.6 Effect of the distribution of airlift pipes on oxygen supply efficiency

4.6.1 Experimental conditions and methods

Using highly oxygen-transfer-efficient airlift part with a pipe diameter of 4 cm and effective height of 1 cm, as shown in Fig. 21, we examine the effect of airlift part configuration by arranging 1, 2 and 3 pipes inside. To keep aeration flux constant, air flow rate normalized to each piece of airlift pipe is set at 6 L/min. The detailed experimental conditions are tabulated in Table 5.

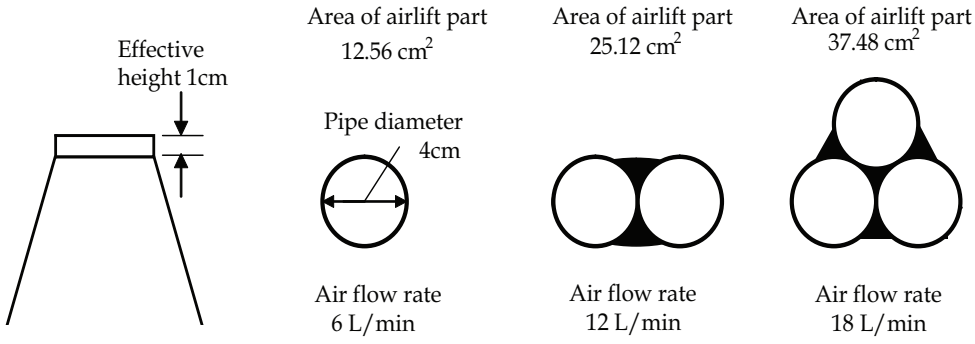

Fig. 21. The configuration of airlift part

Pipe diameter (cm)	Effective height (cm)	No. of airlift pipe	Cross-sectional area (cm^2)	Air flow rate per unit airlift pipe number (L/min)
4	1	1	12.56	6
		2	25.12	12
		3	37.48	18

Table 5. Experimental conditions relating to the configuration of the airlift part

4.6.2 Results and discussion

Figs. 22, 23, 24 and 25 respectively illustrate the effect of No. of airlift pipe on the effluent water flow rate per unit airlift pipe number, DO saturation rate in the effluent water, oxygen mass flow rate per unit airlift pipe number and oxygen transfer amount per unit cross-sectional area (cm^2) of airlift part.

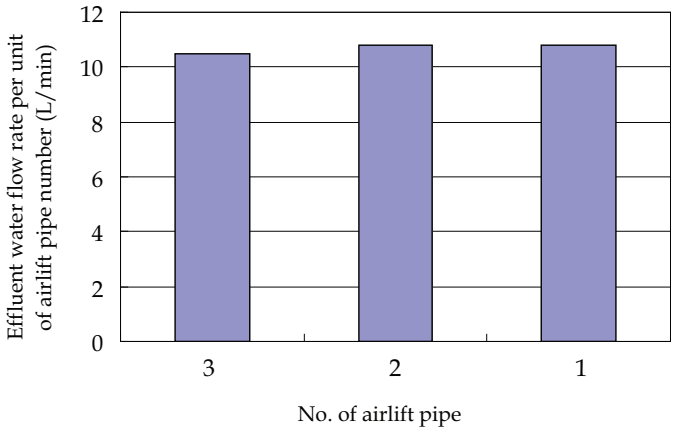

Fig. 22. Effect of airlift pipe No. on the effluent water flow rate per unit airlift pipe number

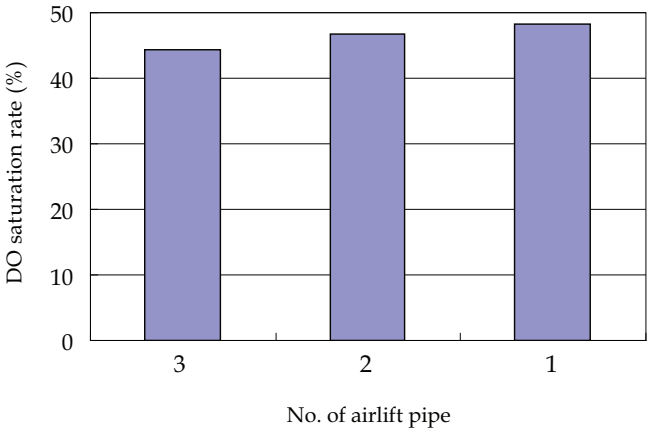

Fig. 23. Effect of airlift pipe No. on the DO saturation rate

As shown in Fig. 23, the lower the airlift pipe number is, the higher the DO saturation rate is. As revealed in Fig. 22, the effluent water flow rate per unit airlift pipe number does not change notably. Thus it appears that the aeration is evenly distributed among the airlift pipes. Namely, the air flow rate is the same through every airlift pipe. As revealed in Figs. 24 and 25, respectively, the oxygen transfer amount per unit airlift pipe number and oxygen transfer amount per unit airlift part cross-sectional area both exhibit a decreasing trend with increasing pieces of airlift pipes. If the air flow rate of every airlift pipe was same

(6 L/min), the same result is supposed to be obtained. On the contrary, the experimental data from Figs. 24 and 25 both tend to decay. This is due to the fact that for 1 piece of airlift pipe, the effluent can completely overflow through the periphery of the pipe. However, for 2 or 3 pieces of airlift pipes, a fraction of effluent overflowing from a certain airlift pipe can flow back into another airlift pipe, or 2 streams of effluents overflowing from 2 airlift pipes can hinder with each other, and thus flow back into the respective airlift pipes again, thereby causing the reduced effluent flow rate. Otherwise, with increasing airlift pipe number, the coverage area of the capture part is also increased. However, since only one diffuser is serving, it is impossible for aeration to uniformly distribute towards every airlift pipe. As a consequence, when designing the system, every airlift pipe should be separately installed. In the meanwhile, the design of the capture part should take into consideration that the gas bubbles can be well captured, and subsequently uniformly distributed to every airlift pipe.

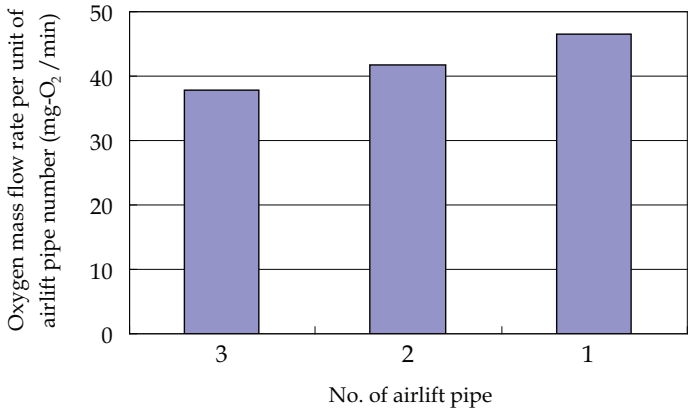

Fig. 24. Effect of airlift pipe No. on the oxygen mass flow rate per unit airlift pipe number

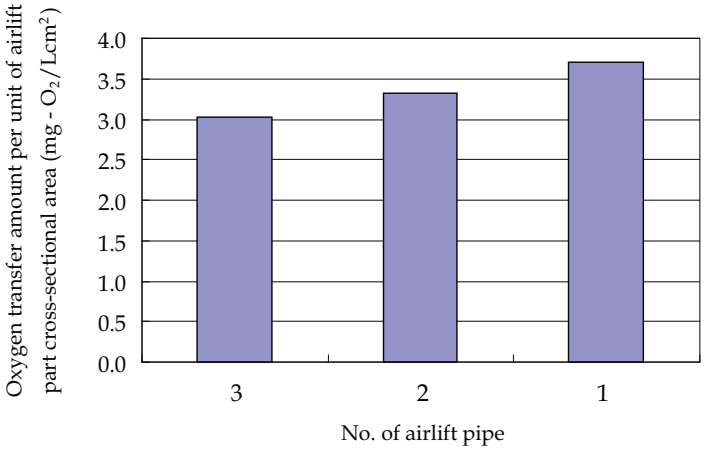

Fig. 25. Effect of airlift pipe No. on the oxygen transfer amount per unit airlift part cross-sectional area (cm^2)

4.7 Effect of air flow rate on oxygen supply efficiency

4.7.1 Experimental conditions and methods

At a cross-sectional area of 12.56 cm^2, the impact of air flow rate on oxygen supply efficiency is studied experimentally. The experimental conditions include the air flow rate ranging from 6 to 18 L/min with an increment of 2 L/min. The pipe diameter of 4 cm and effective height of 1 cm are chosen for the LFFA. The experimental conditions in detail are presented in Table 6.

Pipe diameter (cm)	Effective height (cm)	Cross-sectional area (cm^2)	Air flow rate (L/min)
4	1	12.56	6, 8, 10, 12, 14, 16, 18

Table 6. Experimental conditions focusing on the variation in air flow rate

4.7.2 Results and discussion

Figs. 26, 27 and 28 respectively present the effects of air flow rate on the liquid/gas ratio, DO saturation rate and oxygen transfer amount normalized to 1 L of air (E_0).

As indicated in Fig. 26, at all air flow rates except for that of 6 L/min, any liquid/gas ratio does not change too much. It is thus deduced that the energy loss is very low in the airlift part. The findings of DO saturation rate are shown in Fig. 27. Below 12 L/min, it does not make a difference. In contrast, beyond 14 L/min, DO saturation rate exhibits an attenuating tendency. Thus, the excess air flow rate brings about the energy waste. As revealed in Fig. 28, oxygen transfer amount normalized to 1 L of aeration air is gradually increasing in the 6-12 L/min range. However, below 14 L/min, it tends to decrease gradually. Owing to nearly unchanged liquid/gas ratio shown in Fig. 26, the dominant factor affecting oxygen transfer rate is DO concentration. The reason lies in that with air flow rate increasing, it will lead to increasing effluent flow rate, rendering too much effluent water flowing through the airlift part in relation to gas bubble number, thereby inhibiting the liquid-film formation. In summary, under the present experimental conditions, the optimal air flow rate normalized to 1 cm^2 of cross-sectional area is 1.1 L/min.

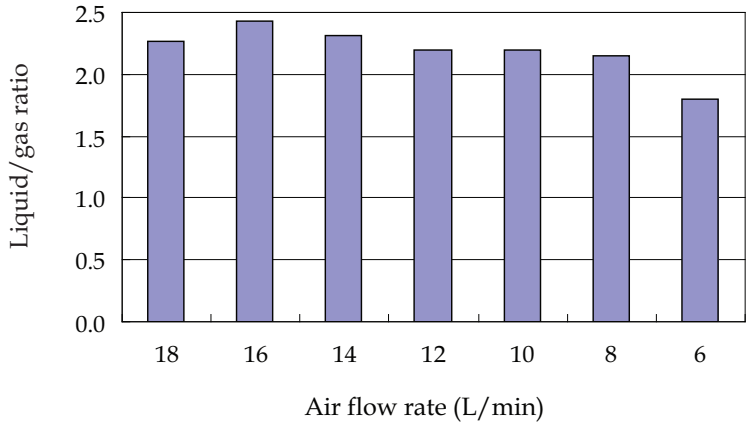

Fig. 26. Effect of air flow rate on the liquid/gas ratio

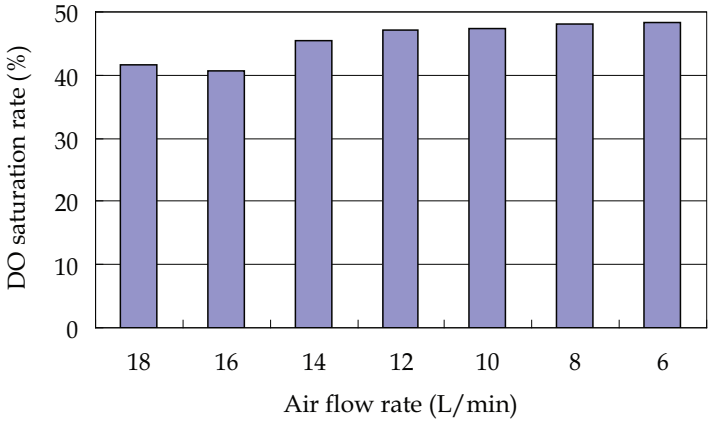

Fig. 27. DO saturation rate as a function of air flow rate

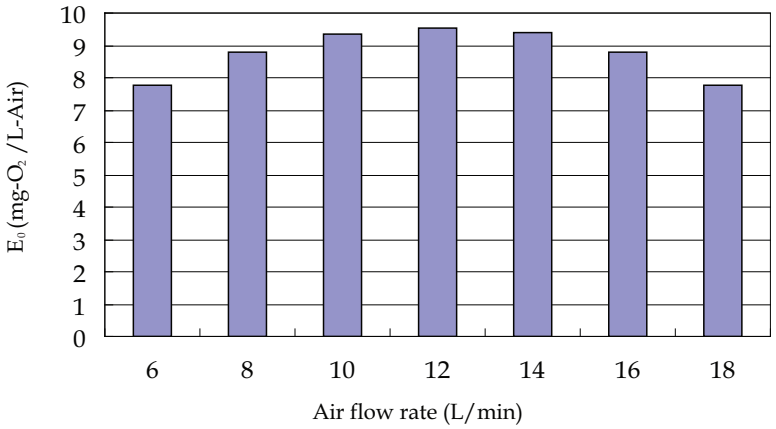

Fig. 28. E_0 as a function of air flow rate

5. Comparison of liquid film and conventional aeration systems in regard to k_La

5.1 Introduction

The performance of aeration apparatus is compared in terms of the k_La values of the liquid film and conventional aeration systems. Meanwhile, the effectiveness of LFFA is corroborated by calculating an important energy-saving index-oxygen transfer efficiency E_A, which is defined as the ratio of DO content to aeration-supplying oxygen amount.

5.2 Experimental conditions and methods

By means of a recycling liquid-film apparatus (4 cm in each individual airlift pipe diameter, 1 cm in effective height, 12.56 cm^2 in cross-sectional area of the airlift part), liquid film aeration tests in a 53 cm deep, 80 L water tank with a surface area of 1510 cm^2 are carried out

by applying air flow rates of 6, 8, 12 and 12.8 L/min. As a control, under the otherwise identical experimental conditions, the conventional aeration test is also investigated in this study. The experimental apparatus is shown in Fig. 29.

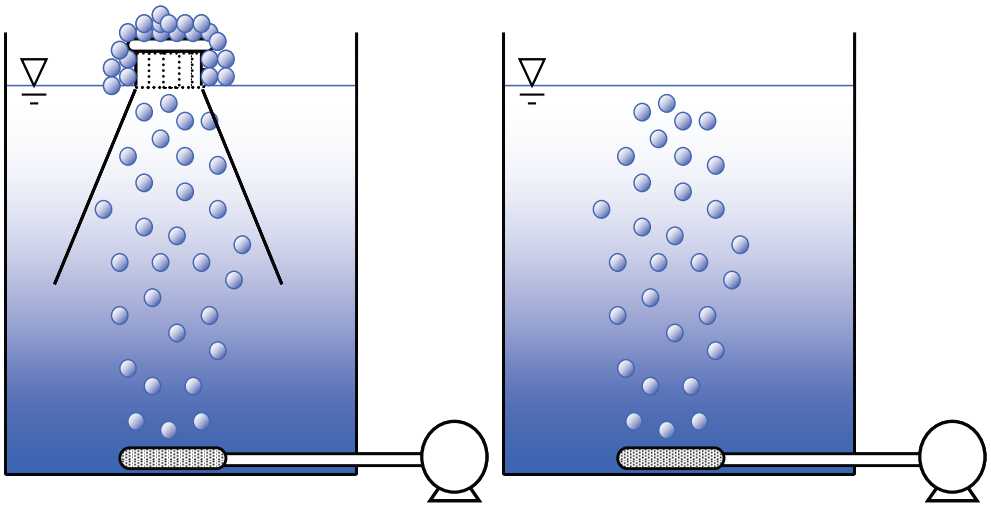

Liquid-film-type aeration experiment Conventional aeration experiment

Fig. 29. The experimental apparatus diagrams of liquid-film aeration system and conventional aeration system

5.3 Calculation methods

The calculation method for total volumetric mass transfer coefficient (k_La) follows the ASCE Standard for Measurement of Oxygen Transfer in Clean Water [18]. Then the obtained k_La_t is calibrated to a standard reference temperature of 20 °C by using Equation (5) [16, 18],

$$k_La(20) = 1/\gamma \times k_La(T) \times 1.024^{(20-T)} \tag{5}$$

where k_La (20) and k_La (T) (hr^{-1}) are k_La at 20 °C and the actual water temperature of T °C, respectively, γ is the activity coefficient of salt concentration and $\gamma = 8.8\times10^{-6}\times C_z+1$, C_z (mg l^{-1}) represents the concentration of sodium sulfite solution.

The performance of oxygen mass transfer is assessed in terms of oxygen mass transfer efficiency, which is calculated based upon Equation (6) [19],

$$E_A(20) = \frac{DO_S(20)\bullet k_La(20)\bullet V\times10^{-3}}{G_S(20)\bullet\rho\bullet O_w}\times100 \tag{6}$$

where E_A (20) refers to oxygen transfer efficiency at 20 °C, $k_La(20)$ (l/hr) is k_La at 20 °C, $DO_S(20)$ (mg/L) is liquid-phase saturated DO concentration at 20 °C, $G_S(20)$ (m^3/hr) is air flow rate at 20 °C and 1 atm, V (m^3) is effective capacity of water tank, ρ is air density at 20°C and 1 atm ($\rho = 1.204$ kg/m^3), and O_w (-) is oxygen content in air ($O_w = 0.233$ O_2-kg/air-kg).

5.4 Results and discussion

As shown in Table 7 and Fig. 30, $k_La(20)$ of liquid film aeration system displays an evolving trend same as that of conventional aeration system. That is, in the air flow rate range of 6-12 L/min, it gradually increases with increasing air flow rate. Beyond the upper limit, it will decrease slowly. However, as shown in Table 7 and Fig. 31. The $E_A(20)$ values of both liquid film aeration system and conventional aeration system decrease with increasing air flow rate.

Air flow rate(L/min)	$k_La(20)$.(1/hr)		$E_A(20)$ (%)	
	Liquid film aeration system	Conventional aeration system	Liquid film aeration system	Conventional aeration system
6	9.6	8.4	6.64	5.81
8	12.4	11.2	6.39	5.78
12	14.9	14.0	5.12	4.81
12.8	12.2	13.2	4.02	4.33

Table 7. Comparison of liquid film aeration system with conventional aeration system

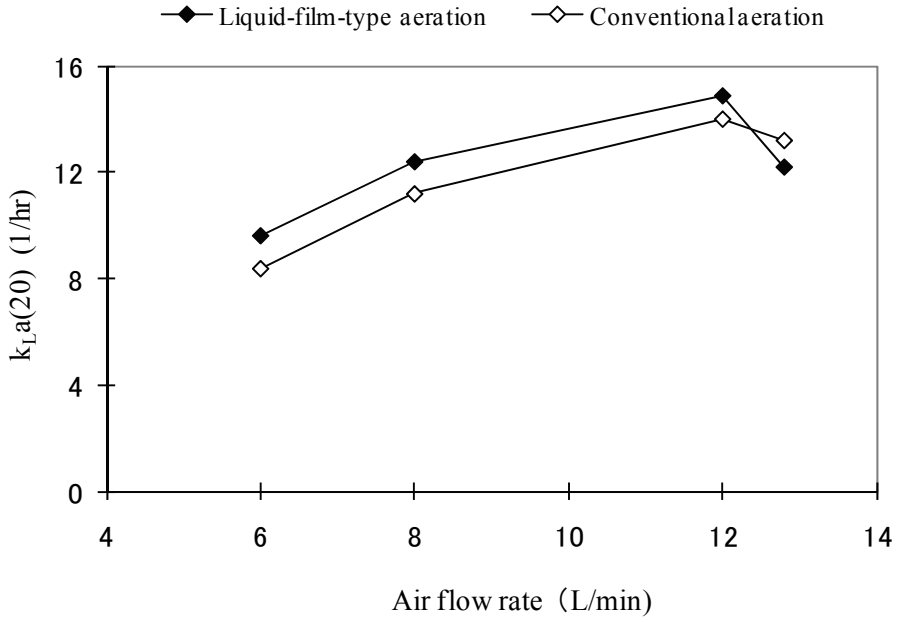

Fig. 30. The comparative data of $k_La(20)$ of liquid film and conventional aeration systems

As compared with $k_La(20)$ and $E_A(20)$ of both aeration systems, at the air flow rate ranging from 6 to 12 L/min, the aeration efficiency of liquid film aeration system increases by 6.3-14.3%. Particularly at the air flow rate of 6 L/min, $E_A(20)$ is still up to 6.64% even utilizing a very shallow aeration depth of 0.5 m. The efficiency of liquid-film aeration is enhanced by 14.3% relative to the conventional aeration system under the identical conditions.

As indicated above, water body can form a liquid film in the atmosphere. The LFFA can remarkably improve oxygen supply efficiency by simultaneously contacting the interior and exterior of the resulting liquid film with the air.

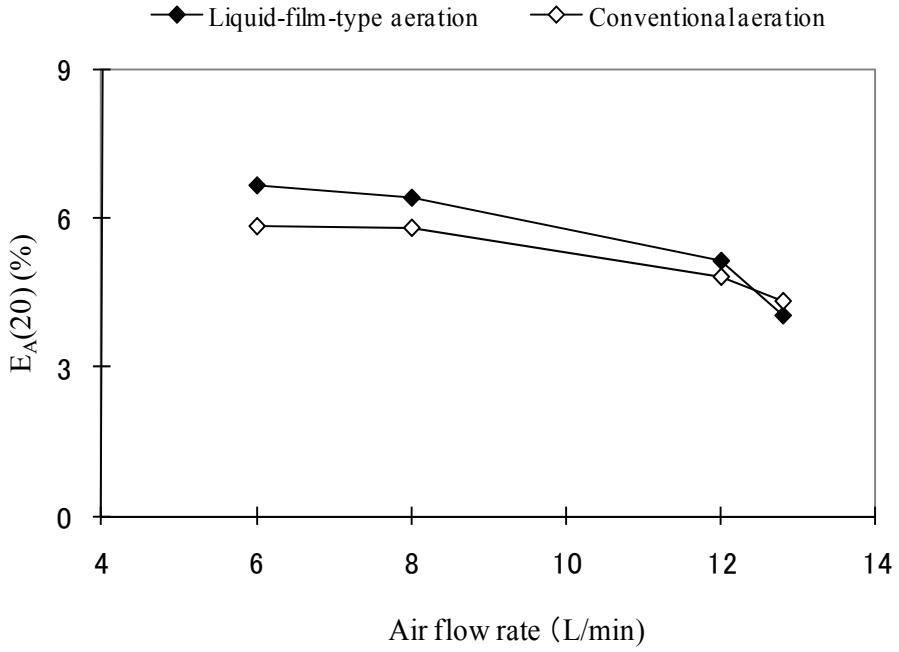

Fig. 31. The comparison data of $E_A(20)$ of liquid film and conventional aeration systems

6. Analysis of the performance of LFFA

6.1 Introduction

In order to evaluate the oxygen transfer performance of the LFFA, in this section, the overall oxygen transfer process is divided into two-step oxygen transfer. That is, in the conventional aeration system, oxygen transport process is split into bubble transfer and surface transfer. In contrast, in the liquid film aeration system, it is divided into bubble transfer and liquid film transfer. Oxygen transfer efficiency of every step is separately derived from the experiment. The performance of the LFFA is thus evaluated.

6.2 Experimental conditions and methods

By means of a recycling liquid film apparatus (4 cm in each individual airlift pipe diameter, 1 cm in effective height, 12.56 cm^2 in cross-sectional area of the airlift part), liquid film aeration tests in a 53 cm deep, 80 L water tank with a surface area of 1510 cm^2 are carried out applying an air flow rate of 6 L/min. As a control, under the otherwise identical experimental conditions, the conventional aeration test with air and diffused test with nitrogen are both investigated in this study. Their experimental apparatuses are shown in Fig. 32.

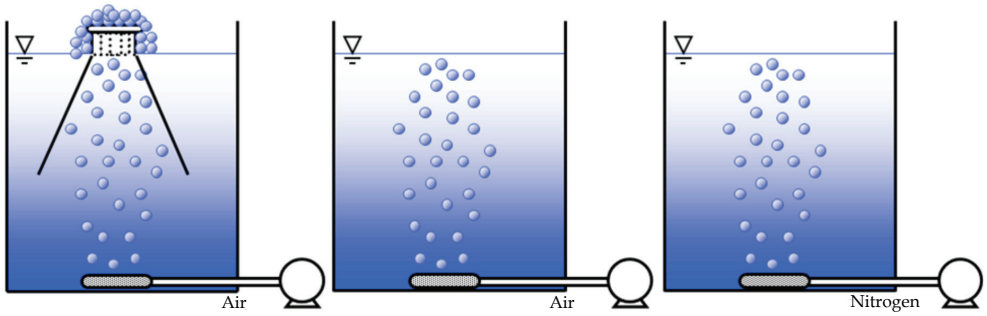

Fig. 32. Experimental apparatuses of testing liquid film aeration with air, and conventional aerations with air and nitrogen, respectively

6.3 Calculation methods

The calculation method for total volumetric mass transfer coefficient (k_La) follows the ASCE Standard for Measurement of Oxygen Transfer in Clean Water [18]. Then the obtained k_La is calibrated to a standard reference temperature of 20 °C by using Equation (5) [16, 18].

When a submerged diffuser is operating, there are two main interfaces through which oxygen transfer occurs, *i.e.*, bubble-water interface and air-water interface, as reflected in Equation (7) [2, 3],

$$\frac{dC}{dt} = \frac{k_L a_b}{h_d}\int_z \left(C_o^* - C\right)dz + k_L a_s \left(C_{sat} - C\right) \tag{7}$$

where k_La_b (l/hr) is the volumetric mass transfer coefficient for bubble surface, k_La_s (l/hr) is the volumetric mass transfer coefficient for water surface, h_d (m) is the depth from diffuser to water surface, z (m) is a variable distance from the diffuser, $C_{sat.}$ (mg/L) is the saturation oxygen concentration in water at atmospheric pressure, C (mg/L) is the actual DO concentration in water body and C_o^* (mg/L) is the liquid-phase equilibrium oxygen concentration of a bubble. C_o^* is not only a function of temperature and atmospheric pressure, but also hydrostatic pressure and gas-phase oxygen composition. Over depth, the bubble transfer of all gases affects the gas-phase oxygen composition and the equilibrium oxygen concentration.

Wilhelms and Martin developed an approach to split surface and bubble transfer by releasing nitrogen gas from a diffuser rather than air [1]. Herein, it is assumed that no oxygen is initially present in the bubbles, thereby eliminating the estimation of a value for concentration inside the bubbles. Additionally, as a result of utilizing the complete and shallow-depth aeration approach in this set of experiments, the contribution of water depth to DO concentration distribution is thus negligible. That is because the DO concentration is considered to be approximately constant over space in the whole water tank. Under such assumptions, Equation (7) can be rewritten as Equation (8),

$$\frac{dC}{dt} = k_L a_b (0 - C) + k_L a_s (C_{sat} - C) \tag{8}$$

Steady state is reached between the absorption of oxygen through surface transfer and the stripping of oxygen from the water by nitrogen bubbles, *i.e.*, dC/dt = 0. The formula can be hence deduced as follow,

$$\frac{k_L a_b}{k_L a_s} = \frac{C_{sat} - C_n}{C_n} \tag{9}$$

where C_n (mg/L) is the steady-state DO concentration in the diffused tests with nitrogen. $k_L a_b$ and $k_L a_s$ are calculated based upon Equation (9).

6.4 Results and discussion

DO concentration versus time curves for liquid film and conventional aeration tests as well as diffused test with nitrogen are illustrated in Fig. 33. The ultimate steady-state DO concentrations are 8.39 mg/L for the conventional aeration trial, 8.72 mg/L for the liquid film aeration trial and 0.94 mg/L for the diffused test with nitrogen.

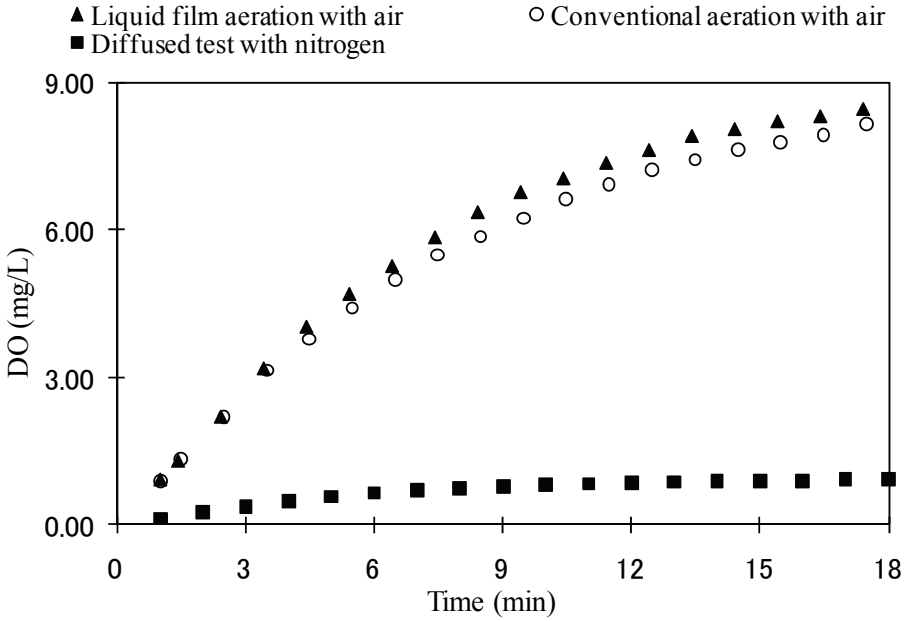

Fig. 33. DO concentration vs. time curves for liquid film aeration and conventional aeration tests as well as diffused test with nitrogen ($C_{sat.}$ = 8.84 mg/L)

Table 8 presents the calculation data derived from the experimental results shown in Fig. 33. Under the operating conditions of 80 L in water capacity, 53 cm in aeration depth, 1510 cm^2 in surface area and 6 L/min in air flow rate, a $k_L a(20)$ value of 8.4 hr^{-1} for the conventional aeration system is calculated. In contrast, the level of $k_L a(20)$ for the liquid film aeration system with the relevant LFFA installed simply on the water surface is 9.6 hr^{-1} (*cf.* Table 8). As compared with these data, the $k_L a(20)$ is increased by about 14% as a consequence of the substantial oxygen transfer contribution from the LFFA.

The k_La_b and k_La_s of conventional aeration testings are shown in Table 8 (i.e., k_La_b = 7.5 hr^{-1} and k_La_s = 0.9 hr^{-1}). That is, in a water tank with a water loading of 80 L, aeration depth of 53 cm, and surface area of 1510 cm^2, while aerating at an air flow rate of 6 L/min, oxygen transfer amount through water surface has a share of roughly 11% of the overall oxygen transfer quantity.

The oxygen transfer of liquid film aeration involves oxygen transfers through gas bubbles, water surface and liquid film. Because the experimental conditions such as aeration depth, aeration amount and gas bubble diameter are identical between the conventional aeration and liquid film aeration, it is reasonable to consider that gas bubble based oxygen transfer capabilities are same in both cases. For the water surface based oxygen transfer ability, liquid film aeration apparatus only occupies a water surface area of 12.56 cm^2 out of the total surface area of 1510 cm^2, taking up roughly 0.83% of the whole water surface area. Hence, the coverage area from the liquid film apparatus is completely negligible. However, because the disturbance effect of the liquid film apparatus on the water surface can not be estimated (either positive or negative action), in this discussion, water surface based oxygen transfer capacity is hard to be regarded as same in both cases. Accordingly, the liquid film based oxygen transfer capacity can not be accurately quantified. For the liquid-film aeration experiment, the oxygen transfers through the water surface and liquid film are thus summed up as an overall entity.

Based upon the reason above, the k_La_b and k_La_s of a liquid-film aeration system are derived as 7.5 and 2.1 hr^{-1}, respectively. Namely, the oxygen transfer amount via water surface accounts for 22% of overall oxygen transfer capacity.

As shown in Table 8, water surface based oxygen transfer efficiency by means of liquid film aeration apparatus is enhanced to 2.3 times in relation to that by the conventional aeration setup.

k_La (hr^{-1})	Conventional aeration system	Liquid-film aeration system
k_La_t	8.4	9.6
k_La_b	7.5	7.5
k_La_s	0.9	2.1

k_La_t: total volumetric mass transfer coefficient.
k_La_b: volumetric mass transfer coefficient for bubble surface.
k_La_s: volumetric mass transfer coefficient for water surface.

Table 8. Comparative results for k_La between the conventional aeration and liquid-film aeration systems.

7. Summary

Through a series of experiments, it is proven that the oxygen transfer rate of liquid-film aeration system is higher than that of conventional aeration system. Furthermore, the former can transiently produce the water with a high DO concentration. Obviously, this efficient aeration process is considered as a less energy-intensive alternative to current aeration methods.

By exploring a range of design factors affecting oxygen transfer efficiency of the LFFA, various design parameters of the LFFA are basically determined. The optimal structural parameters of the LFFA are identified to be 4 cm in airlift pipe diameter, ca. 1 cm in effective height and 1.1 L/min in air flow rate per unit cross-sectional area of an airlift part.

By forming a liquid film in the LFFA, the water surface based oxygen transfer efficiency increases by a factor of approximately 2.3 in comparison to the conventional aeration system. The overall oxygen transfer efficiency is raised to 14%. Especially, even at a very shallow aeration depth of 0.5 m, its $E_A(20)$ still reaches up to 6.64%. These data convincingly suggest that LFFA developed here has an effective oxygen transfer capacity.

Meanwhile, as a result of forming a liquid film by LFFA, the effluent water of high DO concentration can be produced even at an aeration depth of about 0.5 m. Therefore, the conventional aeration depth can be reduced down to a very shallow extent by installing LFFA. A direct outcome is that the energy consumption from the air supply devices such as the blower is supposed to be greatly lowered, therefore saving the costs of both aeration-related equipment and operation.

8. References

[1] Wilhelms, S. C. and Martin, S. K., Gas transfer in diffused bubble plumes, In Jenning S. M. and Bhowmilk N. G., Eds. *Hydraulic Engineering*: *saving a threatened resource-in search of solutions*. ASCE, New York, p.317-322, 1992.

[2] McWhirter, J. R. and Hutter, J. C., Improved oxygen mass transfer modelling for diffused/subsurface aeration systems. *AIChE J.*, 35, p.1527-1534, 1989.

[3] DeMoyer, C. D., Schierholz, L. E., Gulliver, J. S. and Wilhelms, S. C., Impact of bubble and free surface oxygen transfer on diffused aeration systems. *Water Res.*, 37, p.1890-1904 , 2003.

[4] Peterson, R. R., Design criteria for high purity oxygen treatment of kraft mill effluent. *J. Water Pollut. Control Fed.*, 47, p.2317-2329, 1975.

[5] Nelson, J. K. and Puntenney, J. L., Performance comparison of the air and high purity oxygen activated sludge systems. *J. Water Pollut. Control Fed.*, 55, p.336-340, 1983.

[6] Stenstrom, M. K., Kido, W., Shanks, R. F. and Mulkerin, M., Estimating oxygen transfer capacity of a full-scale pure oxygen activated sludge plant. *J. Water Pollut. Control Fed.*, 61, p.208-220, 1989.

[7] Yuan, W., Okrent, D. and Stenstrom, M. K., Model calibration for the high-purity oxygen activated sludge process-algorithm development and evaluation. *Water Sci. Technol.*, 28, p.163-171, 1993.

[8] Kuo, J. F., Dodd, K. M., Chen, C. L., Horvath, R. W. and Stahl, J. F. Evaluation of tertiary filtration and disinfection systems for upgrading high-purity oxygen-activated sludge plant effluent. *Water Environ. Res.*, 69, p.34-43, 1997.

[9] Tzeng, C. J., Iranpour, R. and Stenstrom, M. K., Modelling and control of oxygen transfer in high purity oxygen activated sludge process. *J. Environ. Eng.-ASCE*, 129, p.402-411, 2003.

[10] Jang, A. and Kim, I. S., Effect of high oxygen concentrations on nitrification and performance of high-purity oxygen A/O bio-film process. *Environ. Eng. Sci.*, 21, p.273-281, 2004.

[11] Moore, T. L., Basic criteria and design aspects for deep aeration tanks. *Water Res.*, 6, p.407-412, 1972.

[12] Polprasert, C. and Raghunandana, H. S., Wastewater treatment in a deep aeration tank. *Water Res.*, 19, p.257-264, 1985.

[13] Gnirss, R. and Peter-Frölich, A., Biological treatment of municipal wastewater with deep tanks and flotation for secondary clarification. *Water Sci. Technol.*, 34, p.257-265, 1991.

[14] Asselin, C., Comeau, Y. and Ton-That, Q. A., Alpha correction factors for static aerators and fine bubble diffusers used in municipal facultative aerated lagoons. *Water Sci. Technol.*, 38, p.79-85, 1998.

[15] Gillot, S. and Héduit, A., Effect of air flow rate on oxygen transfer in an oxidation ditch equipped with fine bubble diffusers and slow speed mixers. *Water Res.*, 34, p.1756-1762, 2000.

[16] Omatsu, R., Energy-saving efficiency of fine bubble diffuser in actual operation. *Kurimoto Research*, 48, p.2-7, 2003. (In Japanese).

[17] Gillot, S., Capela-Marsal, S., Roustan, M. and Héduit, A., Predicting oxygen transfer of fine bubble diffused aeration systems-model issued from dimensional analysis. *Water Res.*, 39, p.1379-1387, 2005.

[18] ASCE, Standard for the measurement of oxygen transfer in clean water, 2nd ed. ASCE, New York, 1993.

[19] Sewerage Facilities Planning and Design Manual (Volume 2), Japan Sewage Works Association, Tokyo, 1994. (Japanese)

16

Microcontaminant Sorption and Biodegradation in Wastewater Modeled as a Two-Phase System

Karl J. Ottmar
Ottmar Environmental Science and Engineering
United States

1. Introduction

It has only been within the past 15 years that concern about the presence of pharmaceutical compounds and other emerging contaminants in water and wastewater has garnered the attention of the scientific community. Although earlier research can be documented, it was not until the publication of the overarching analysis by Daughton and Ternes (1999) that scientific investigations began to take off, as evidenced by being cited over 900 times (As of March 2011). One of the key contributions of their research was to highlight the ubiquitous nature of those compounds in the environment and to highlight that their potential impact on human and environmental health was unknown. This work helped to spur one of the largest studies conducted, to date, the 1999 National Reconnaissance conducted by the U.S. Geological Survey (USGS 2003, Kolpin et al. 2003). As part of that study, investigators sampled 139 streams in 30 states and tested for 149 emerging compounds of interest to include hormones, steroids, prescription pharmaceuticals, insecticides, and pesticides. Perhaps the key finding from that survey was that every compound that was tested for was found to be present in the environment. Subsequent studies (Richardson and Ternes 2005, Daughton 2009, Bartelt-Hunt et al. 2009) have reinforced the need for continued research, both in regards to occurrence in surface water systems, as well as wastewater treatment plants.

As the research on the origination of these microcontaminants has progressed, it has become more apparent that wastewater treatment plants play a critical role (Lietz and Meyer 2004, Glassmeyer et al. 2005, Vanderford and Snyder 2006, Yu et al. 2006). These facilities are located at the nexus connecting the anthropogenic with the ecological and, as such, have become a focal point for environmental research, especially in regards to the fate, transport, and occurrence of emerging contaminants. A closer examination of the wastewater treatment process reveals two key fundamental processes: sorption and biodegradation (Joss et al. 2006, Ottmar et al. 2010a). These two processes are intrinsically linked as, in almost all instances, the rate of biodegradation will be related to the concentration of compound present in the aqueous phase, which, itself, is linked to the concentration in the solid phase by the process of sorption. It is this linkage that provides the motivation behind the development of a two-phase model that will account for both of these processes.

2. Model development

The examination of concurrent sorption and biodegradation in environmental systems is not actually a recent development. The method of volume averaging described by Hassanizadeh and Gray (1979) has frequently been used to examine contaminant transport in porous media. These analyses proceed by defining the groundwater system as containing two phases, the aqueous phase (groundwater) and the solid phase (soils). Of note, in some cases a more elaborate system could be defined with the solid phase actually consisting of multiple phases (i.e. an organic phase along with an inorganic phase), however it is the corollary with the two-phase system that will be used here. In the groundwater systems, the solid phase is stationary with the aqueous phase moving through it, as indicated below in Figure 1.

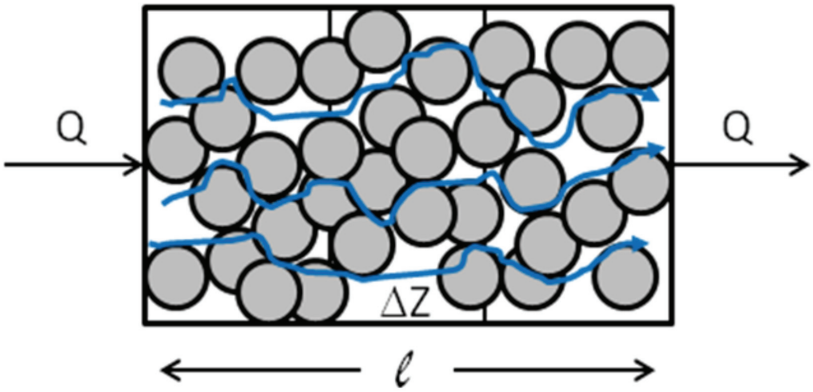

Fig. 1. Representation of porous media characteristic of groundwater systems

The analysis begins with a microscopic differential volume that is then expanded through volume averaging, with the ultimate result being the series of advection-dispersion-reaction (ADR) equations that are frequently encountered in groundwater research. This underlying methodology will now be applied to an activated sludge basin, with the key difference being that the solid phase will move in conjunction with the aqueous phase, rather than being stationary.

2.1 Modeling of the activated sludge basin

In broad terms, the wastewater treatment plant's activated sludge basin will be modeled as a plug flow reactor, with the key underlying assumption being that while there will be longitudinal variances along the length of the reactor, there will not be any vertical or latitudinal variances (i.e. for a given differential volume, it will be assumed to be completely mixed).

As seen in the folowing figures, the activated sludge basins are modeled as being a plug flow reactor (PFR) with a specified length, l, cross-sectional area, A, and volumetric flow rate, Q.

This process is defined as being a two-phase system, consisting of the solids phase and the aqueous phase. Inherent to this definition is the presumption that mass transfer of the target compounds to/from the gas phase due to deposition/volatilization is negligible based on their chemical properties (primarily pKa and Henry's Law coefficient).

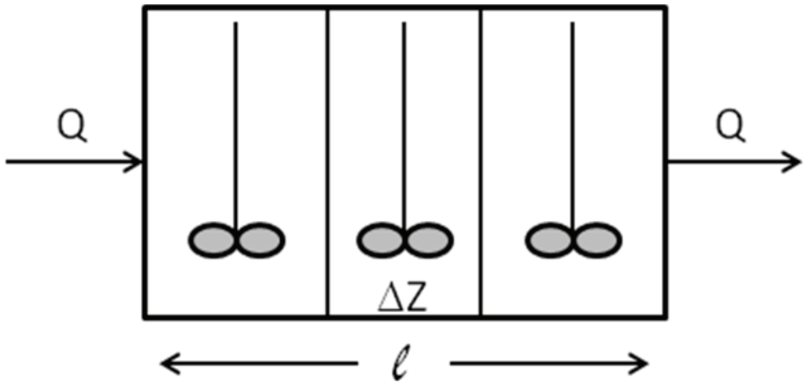

Fig. 2. Schematic of a plug flow reactor (PFR)

Having defined it as a two-phase system, the initial focus will be on the differential volume indicated by the ΔZ (and multiplied by A) in Figure 3. This differential volume is shown more clearly in the following figure.

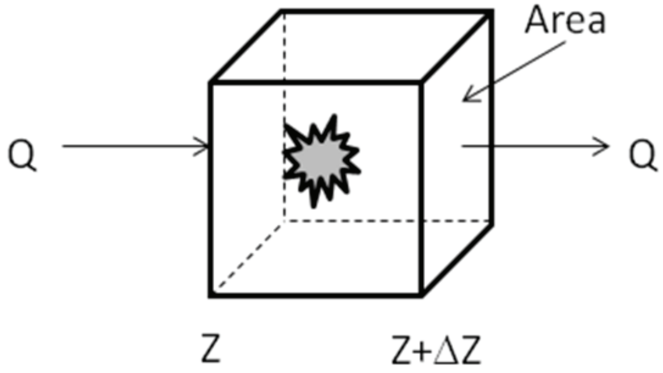

Fig. 3. Close-up of the differential volume

For this volume, a mass balance on the target compound in both phases is performed. First, as a word formulation and then as the mathematical representation of that phase:

2.1.1 Compound mass in the aqueous phase in the differential volume

(Change) = (Flow in with aqueous phase) – (Flow out with aqueous phase) + (flux from aqueous phase to solid phase) – (biodegradation in aqueous phase)

$$\frac{dm}{dt} = \dot{m}_{in} - \dot{m}_{out} + \dot{m}_{sorb\_flux} - \dot{m}_{bio} \tag{1}$$

Because the differential volume is extremely small, it is assumed to be at steady state, and so the overall change is mass is zero.

$$0 = QC\big|_{Z} - QC\big|_{Z+\Delta Z} + V_{aq} j_{sl} - V_{aq} r_{bio} \tag{2}$$

Where C is the concentration in the aqueous phase (µg/L), V_{aq} is the aqueous phase volume, j_{sl} is the mass flux to the solid phase (µg/L-time) and r_{bio} is the biodegradation rate expression (µg/L-time)
At this point, it is important to highlight the differences in the volumes presented so far. V is the total differential volume and V_{aq} is the volume of the aqueous phase within that differential volume, and V_s is the volume of the solid phase.

$$V = V_{aq} + V_s \Rightarrow A\Delta Z = V_{aq} + V_s \tag{3}$$

A further examination of the activated sludge system allows for a simplifying assumption in regards to the aqueous phase volume. The average solids concentration in an activated sludge tank is 3,250 mg/L for completely mixed tanks (Metcalf and Eddy 1991). These solids have a specific gravity of 1.25, meaning that in one liter of activated sludge, the 3,250 mg of solids will have a volume of 2.6 milliliters. Consequently, the aqueous volume (997.4 milliliters) is almost equal to the total volume (1,000 milliliters).
Returning to equation 2, by dividing both sides by Q and V results in:

$$\frac{C|_{Z+\Delta Z} - C|_Z}{\Delta Z} = \frac{A}{Q} j_{sl} - \frac{A}{Q} r_{bio} \tag{4}$$

Taking the limit as the differential length approaches zero yields:

$$\lim_{\Delta Z \to 0} \frac{C|_{Z+\Delta Z} - C|_Z}{\Delta Z} = \frac{A}{Q} j_{sl} - \frac{A}{Q} r_{bio} \Rightarrow \frac{dC}{dz} = \frac{A}{Q} j_{sl} - \frac{A}{Q} r_{bio} \tag{5}$$

Which is the PFR governing equation for the aqueous phase. The process is repeated for the solid phase.

2.1.2 Compound mass in the solid phase in the differential volume

(Change) = (Flow in with solid phase) – (Flow out with solid phase) + (flux from solid phase to aqueous phase)

$$\frac{dm}{dt} = \dot{m}_{in} - \dot{m}_{out} + \dot{m}_{sorb\_flux} \tag{6}$$

Again, because the differential volume is extremely small, it is assumed to be at steady state, and so the overall change in mass is zero.

$$0 = Q\,X|_Z\,S|_Z - Q\,X|_{Z+\Delta Z}\,S|_{Z+\Delta Z} + V\,X|_{Z+\Delta Z}\,j_{ls} \tag{7}$$

Where X is the solids concentration (kg/L), S is the compound concentration in the solid phase (µg/kg solids), and j_{ls} is the mass flux to the aqueous phase (µg/kg solids-time). Dividing both sides by Q and V results in:

$$\frac{X|_{Z+\Delta Z}\,S|_{Z+\Delta Z} - X|_Z\,S|_Z}{\Delta Z} = \frac{A}{Q} X|_{Z+\Delta Z}\,j_{ls} \tag{8}$$

Again, taking the limit as the differential length approaches zero yields:

$$\lim_{\Delta Z \to 0} \frac{X\big|_{Z+\Delta Z} S\big|_{Z+\Delta Z} - X\big|_{Z} S\big|_{Z}}{\Delta Z} = \frac{A}{Q} X\big|_{Z+\Delta Z} j_{ls} \Rightarrow \frac{d(XS)}{dz} = \frac{A}{Q} X\big|_{Z+\Delta Z} j_{ls} \tag{9}$$

Because the solids concentration varies minimally throughout the reactor (varying by less than 3% from one end to the other), it can effectively be treated as a constant, resulting in:

$$X \frac{dS}{dz} = \frac{A}{Q} X j_{ls} \tag{10}$$

At this point it can be seen that there are two governing equations for a target compound in the two different phases present in the PFR.

$$\frac{dC}{dz} = \frac{A}{Q} j_{sl} - \frac{A}{Q} r_{bio} \tag{5}$$

$$X \frac{dS}{dz} = \frac{A}{Q} X j_{ls} \tag{10}$$

At this point, two additional assertions can be made to simplify the governing equations and provide a unified theory encompassing transport in both phases. First, it should be noted that mass is conserved throughout the inter-phase mass transfer flux. Because of this, the following equation holds:

$$0 = \frac{V_{aq}}{V} j_{sl} + X j_{ls} \Rightarrow j_{sl} = -X j_{ls} \tag{11}$$

Equation 11 can then be combined with equation 10 to yield:

$$X \frac{dS}{dz} = -\frac{A}{Q} j_{sl} \tag{12}$$

Adding equation 12 to equation 5 gives:

$$\frac{dC}{dz} + X \frac{dS}{dz} = -\frac{A}{Q} r_{bio} \tag{13}$$

The second assertion to be made is in regards to the sorption mechanism occurring. If the assumption is made that sorption occurs very rapidly, is linear, and is essentially at equilibrium (as shown in Ottmar et al. 2010), then the following relation holds:

$$S = K_d C \tag{14}$$

Taking the derivative with respect to movement through the reactor yields:

$$\frac{dS}{dz} = K_d \frac{dC}{dz} \tag{15}$$

This can then be substituted into equation 13, giving:

$$\frac{dC}{dz} + K_d X \frac{dC}{dz} = -\frac{A}{Q} r_{bio} \Rightarrow (1 + K_d X) \frac{dC}{dz} = -\frac{A}{Q} r_{bio} \tag{16}$$

Then by defining that $(1 + K_d X) = R$, where R is the retardation factor, equation 16 ultimately reduces to:

$$R\frac{dC}{dz} = -\frac{A}{Q}r_{bio} \Rightarrow \frac{dC}{dz} = -\frac{1}{vR}r_{bio} \tag{17}$$

Where v is the linear velocity along the length of the reactor as defined by Q/A. At this point, the next step is to further examine r_{bio}, the biodegradation rate term. One of the most common approaches is to model biodegradation under a first-order process. This is manifested by:

$$r_{bio} = k_1 C(z) \tag{18}$$

Adding equation 18 back into equation 17 gives:

$$\frac{dC}{dz} = -\frac{k_1}{vR}C(z) \tag{19}$$

This expression can then be integrated:

$$\int \frac{dC}{C(z)} = -\frac{k_1}{vR}\int dz \Rightarrow \ln|C| = -\frac{k_1}{vR}z + Const_{Integration} \Rightarrow C = Be^{-\frac{k_1}{vR}z} \tag{20}$$

By applying the initial conditions that when $z = 0$, $C = C_0$, the equation can then be defined:

$$C_0 = B \Rightarrow C = C_0 e^{-\frac{k_1}{vR}z} \tag{21}$$

For the final step, the concentration at the end of the basin can be calculated by setting $z = l$.

$$C = C_0 e^{-\frac{k_1}{vR}l} \Rightarrow C_0 e^{-\frac{k_1\theta}{R}} \tag{22}$$

Where θ is the hydraulic retention time, which is equal to the length divided by the linear fluid velocity.

As has been observed experimentally, however, biodegradation sometimes does not quite appear to follow true first-order kinetics, but rather, a sort of substrate-enhanced process. One of the challenges with this is developing a relevant mathematic model that is grounded in physical principles and observations. To this end, the following expression is proposed for the biodegradation rate:

$$r_{bio} = k_1 X C(z)\left(1 + \frac{L(z)}{K_L}\right) \tag{23}$$

Where $L(z)$ is the concentration of substrate (BOD or COD) present and K_L is the Monod half saturation coefficient. Substituting this equation into equation 17 gives:

$$\frac{dC}{dz} = -\frac{k_1 X}{vR}C(z)\left(1 + \frac{L(z)}{K_L}\right) \tag{24}$$

Rearranging equation 24 and configuring it for integration yields:

$$\frac{dC}{C(z)} = -\frac{k_1 X}{vR}\left(1 + \frac{L(z)}{K_L}\right)dz \tag{25}$$

At this point, the challenge is in finding the appropriate mathematical expression for how the concentration of substrate (BOD or COD) changes as it moves through the reactor. The simplest model is that of a linear decrease from the concentration entering the reactor, L_0, to the concentration leaving the reactor, L_f:

$$L(z) = L_0 - \frac{1}{l}\left(L_0 - L_f\right) \tag{26}$$

Substituting this back into equation 25 gives:

$$\begin{aligned} &\frac{dC}{C(z)} = -\frac{k_1 X}{vR}\left(1 + \frac{L_0 - \frac{1}{l}\left(L_0 - L_f\right)z}{K_L}\right)dz \\ &\Rightarrow \frac{dC}{C(z)} = -\frac{k_1 X}{vRK_L}\left(K_L + L_0 - \frac{1}{l}\left(L_0 - L_f\right)z\right)dz \end{aligned} \tag{27}$$

This equation can then be integrated, giving:

$$\begin{aligned} &\ln|C| = -\frac{k_1 X}{vRK_L}\left[\left(K_L + L_0\right)z - \frac{1}{2l}\left(L_0 - L_f\right)z^2\right] + Const_{Integration} \\ &\Rightarrow C = Be^{-\frac{k_1 X}{K_L vR}\left[\left(K_L + L_0\right)z - \frac{1}{2l}\left(L_0 - L_f\right)z^2\right]} \end{aligned} \tag{28}$$

Applying the initial condition that at the beginning of the reactor, when $z = 0$, $C = C_0$, it can be seen that $B = C_0$, which results in the following governing equation for the aerobic basins:

$$C = C_0 e^{-\frac{k_1 X}{K_L vR}\left[\left(K_L + L_0\right)z - \frac{1}{2l}\left(L_0 - L_f\right)z^2\right]} \tag{29}$$

From this, the concentration at the end of the PFR can be calculated by setting $z = l$, and:

$$\begin{aligned} &C = C_0 e^{-\frac{k_1 X}{K_L vR}\left[\left(K_L + L_0\right)l - \frac{1}{2l}\left(L_0 - L_f\right)l^2\right]} \\ &\Rightarrow C = C_0 e^{-\frac{k_1 Xl}{K_L vR}\left[\left(K_L + L_0\right) - \frac{1}{2}\left(L_0 - L_f\right)\right]} \\ &\Rightarrow C = C_0 e^{-\frac{k_1 X\theta}{K_L R}\left(K_L + \frac{1}{2}L_0 + \frac{1}{2}L_f\right)} \end{aligned} \tag{30}$$

From this governing equation, the aqueous drug concentration at the end of the reactor, can then be determined. The mass of drug compound in the sorbed phase is calculated from the equilibrium sorption condition by means of the following equations:

$$Mass_{drug,total} = Mass_{drug,aq} + Mass_{drug,sorbed}$$
$$Mass_{drug,sorbed} = f_{sorbed} Mass_{drug,total}$$
$$\Rightarrow \frac{Mass_{drug,sorbed}}{f_{sorbed}} = Mass_{drug,aq} + Mass_{drug,sorbed}$$
$$\Rightarrow Mass_{drug,sorbed} - f_{sorbed} Mass_{drug,sorbed} = f_{sorbed} Mass_{drug,aq}$$
$$\Rightarrow Mass_{drug,sorbed} = \frac{f_{sorbed} Mass_{drug,aq}}{1 - f_{sorbed}}$$

The reduction in COD and the change in solids masses are based on the treatment plants operating characteristics.

2.2 Overall approach for wastewater treatment processes

Having developed a governing equation for simultaneous sorption and biodegradation, the model could then be applied to a wastewater treatment, as a single entity. Each wastewater treatment plant process is characterized by a set of ten parameters, each of which has been assigned to a specific cell in a table with five rows and two columns, as shown in Figure 4.

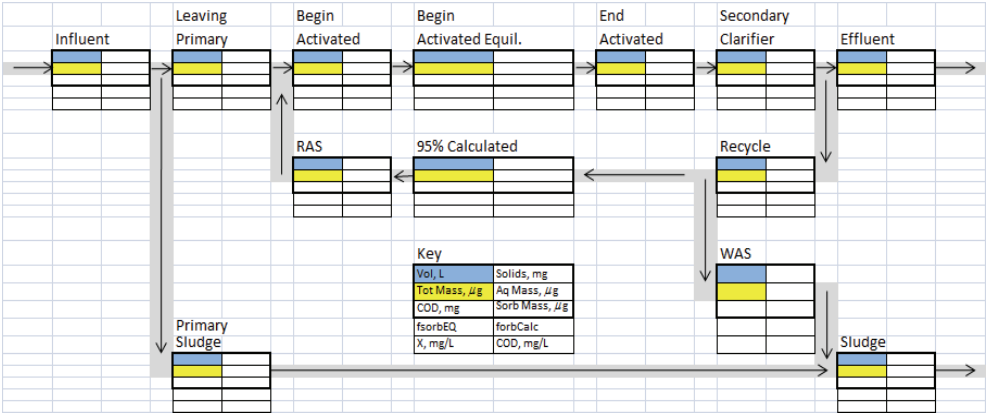

Fig. 4. Overall model schematic of a wastewater treatment plant. Note the key for the definition of individual cell values

The first row of each box contains the aqueous volume (V) of each compartment, as scaled to one liter, and the known mass of solids in that compartment. The second row contains the total mass of drug within each compartment (at left) and the mass of drug that exists in the aqueous phase within each compartment (at right). These drug masses are in units of μg. The third row contains the mass of COD substrate within each compartment (at left) and the mass of each drug that exists as sorbed phase (at right). COD mass is in mg, and drug mass is in μg. The total mass of drug compound (second row, first column) will always be equal to the sum of the mass in the aqueous phase (second row, second column) and the mass in the sorbed phase (third row, second column). The left-hand side of the fourth row contains the estimated fraction of each drug that exists in the sorbed phase assuming equilibrium conditions. This is based on the K_d value for each drug, as measured previously, and the

solids concentration in each compartment. The right-hand side of the fourth row contains the estimated fraction of each drug that exists in the sorbed phase, as calculated using mass in the aqueous phase and the mass in the sorbed phase. The equilibrium sorbed fraction and computed sorbed fraction are only different from each other when two streams with markedly different solids concentrations mix. For our model, this happens at the beginning of the aerobic basin, where effluent from the primary clarifiers mixes with return activated (RAS) sludge from underneath the secondary clarifiers. The fifth row contains two concentrations calculated from the aforementioned parameters: the biosolids concentration (X) at left and COD concentration (L) at right, both in mg/L.

2.2.1 Influent

The first modeled location corresponds to WWTP influent. The aqueous volume for this compartment is set to 1L, but this could be scaled based on actual flow rates. Masses and concentrations for COD and solids are set to match the characteristics of any specific WWTP. The total suspended solids (TSS) in the raw influent and the COD concentration (L) can be based on information from a treatment plant or from various references. Influent total drug masses can be taken from projection calculations by Ottmar et al. (2010b) for a plant with P/Q (service population over daily flow) equal to the target plant. Aqueous-phase and sorbed-phase drug masses can then be calculated assuming equilibrium conditions, using K_d values previously determined and the presumed TSS concentration in influent wastewater. Equation 31, below, can be re-arranged to solve for this:

$$K_d = \frac{1}{X_{ss}}\left(\frac{1}{1-f_{sorbed}} - 1\right) \Rightarrow K_d X_{ss} + 1 = \frac{1}{1-f_{sorbed}} \Rightarrow f_{sorbed} = 1 - \frac{1}{1+K_d X_{ss}} \tag{31}$$

From this, the mass in the sorbed phase is equal to the total mass multiplied by the sorbed fraction. The mass in the aqueous phase is equal to the total mass minus the mass in the sorbed phase.

2.2.2 Primary clarification

The second modeled location corresponds to the exit of the primary (1°) clarifiers. It was assumed that the overall flow splits into two smaller flows at this location, namely: primary sludge and primary effluent. For an example, it can be said that 60% of TSS and 40% of COD are removed into the primary sludge stream. The remaining TSS and COD flow from the primary clarifier into the activated sludge basin with the primary effluent. Based on these parameters and an assumed solids concentration of 45,000 mg/L for the primary sludge, a mass balance on the solids can be used to calculate the mass of solids (first row, second column) and the aqueous volume (first row, first column) leaving the primary clarifier as effluent or primary sludge. The following two equations are used, with the first being the mass balance equation and the second being the balance equation for a non-compressible aqueous fluid:

$$Mass_{solids\_in} = Mass_{solids\_primaryeff} + Mass_{solids\_primarysludge}$$
$$\Rightarrow X_{in}Q_{in} = X_{primaryeff}Q_{primaryeff} + X_{primarysludge}Q_{primarysludge}$$

$$Q_{in} = Q_{primaryeff} + Q_{primarysludge}$$

X_{in} is the solids concentration in the influent, Q_{in} is the aqueous flow rate (unit volume), $X_{primaryeff}$ is the solids concentration in the primary effluent, $Q_{primaryeff}$ is the flow rate leaving the primary clarifier, $X_{primarysludge}$ is the solids concentration in the primary sludge, and $Q_{primarysludge}$ is the sludge flow rate. Of these six, only $Q_{primaryeff}$ and $Q_{primarysludge}$ are unknown, but with two equations, they can be determined.
Concerning the transport of COD, a similar mass balance approach was used:

$$Mass_{COD\_in} = Mass_{COD\_primaryeff} + Mass_{COD\_primarysludge}$$
$$\Rightarrow L_{in}Q_{in} = L_{primaryeff}Q_{primaryeff} + L_{primarysludge}Q_{primarysludge}$$

The flow rates have already been determined (previously with the solids mass balance), and the amount of COD leaving the primary clarifier is set as part of this plant's operating characteristics (40% removal). Consequently, the masses of COD (third row, first column) and the concentrations (fifth row, second column) can be calculated.
For evaluation of drug compound transport, each phase is treated as a separate process. Beginning with the aqueous phase, we begin with the familiar mass balance. Here, we assume that substantial biodegradation does not occur in the primary clarifier due to the short hydraulic retention time and anoxic conditions:

$$Mass_{drug,aq,In} = Mass_{drug,aq,primaryeff} + Mass_{drug,aq,primarysludge}$$
$$\Rightarrow C_{in}Q_{in} = C_{primaryeff}Q_{primaryeff} + C_{primarysludge}Q_{primarysludge}$$

Because the drug compound will be dissolved in the aqueous phase, the concentrations (in μg/L) will not change, so C_{in} will be equal to $C_{primaryeff}$ and $C_{primarysludge}$. Consequently, the transport of drug mass in the aqueous phase will be proportional to the transport of the aqueous phase itself. For example, if the aqueous phase flow rate (first row, first column) leaving the primary clarifier as the primary sludge is equal to 0.4% of the volume in the influent, then the mass of drug compound in the aqueous phase of the primary sludge (second row, second column, Primary Sludge) will be equal to 0.4% of the mass of drug compound in the aqueous phase of the influent (second row, second column, Influent).
The transport of drug compound in the sorbed phase will be similarly governed, with the basis being a mass-balance approach, as outlined in the following equation:

$$Mass_{drug,sorb,in} = Mass_{drug,sorb,primaryeff} + Mass_{drug,sorb,primarysludge}$$
$$\Rightarrow S_{in}X_{in}Q_{in} = S_{primaryeff}X_{primaryeff}Q_{primaryeff} + S_{primarysludge}X_{primarysludge}Q_{primarysludge}$$

Because the only transport process occurring is a physical separation of the sludge, the sorbed concentration (in mg/kg sludge) will not change, so S_{in} will be equal to $S_{primaryeff}$ and $S_{primarysludge}$. For example, if 60% of the solids from the influent (first row, second column, influent) go to the primary sludge (first row, second column, primary sludge), then 60% of the total drug mass in the sorbed phase from the influent (third row, second column, influent) will go with the primary sludge (third row, second column, primary sludge).

2.2.3 Preliminary activated sludge treatment

Entrance into secondary (2°) treatment, "Start A.S. Basin," marks the third modeled location, in particular inlet to the activated sludge basins. Here, the effluent from the primary clarifier

is merged with recycled activated sludge (R.A.S.). Modeling at this location requires a two-step mathematical process. The first step comprises arithmetic addition of the physical properties from the two feeder streams:

$$Q_{StartASba\sin} = Q_{leaving1^o\,clarifier} + Q_{R.A.S.}(1stRow, 1stColumn)$$

$$Mass_{Solids,StartASba\sin} = Mass_{Solids,Leaving1^0\,Clarifier} + Mass_{Solids,R.A.S.}(1stRow, 2ndColumn)$$

$$Mass_{drug,aq,StartASba\sin} = Mass_{drug,aq,Leaving1^0\,Clarifier} + Mass_{drug,aq,R.A.S.}(2ndRow, 2ndColumn)$$

$$Mass_{drug,sorb,StartASba\sin} = Mass_{drug,sorb,Leaving1^0\,Clarifier} + Mass_{drug,sorb,R.A.S.}(3rdRow, 2ndColumn)$$

$$Mass_{COD,StartASba\sin} = Mass_{COD,Leaving1^0\,Clarifier} + Mass_{COD,R.A.S.}(3rdRow, 1stColumn)$$

As mentioned previously, the addition of the masses of drug compound in the solids phases and in the aqueous phases produces a condition whereby the equilibrium sorption conditions are not satisfied, owing to the marked increase in solids concentration (a jump from 120 mg/L to 3000 mg/L). This can be seen by re-visiting equation 31 and by the fact that the fraction of drug compound sorbed that is calculated based the masses in the aqueous phase and in the solids phase is not the same as the fraction sorbed calculated based on the solids concentration and the distribution coefficient. Because laboratory batch tests have shown that sorption happens quite rapidly and can be assumed be essentially at equilibrium, a subsequent series of data cells is used to make the conversion to an equilibrium condition. This is done by setting the mass of drug in the sorbed phase (3rd row, 2nd column) of the "Start A.S. EQM" data set equal to the total mass (2nd row, 1st column) in the "Start A.S. Basin" data set multiplied by the fraction sorbed at equilibrium (4th row, 1st column). The mass of drug in the aqueous phase (2nd row, 2nd column) of the "Start A.S. EQM data set is then calculated by subtracting the aforementioned calculated mass in the sorbed phase from the total mass.

2.2.4 Aerobic activated sludge treatment

The fourth modeled process is the activated sludge basin. This compartment is modeled as a plug flow reactor, which makes it possible to compute extent of pharmaceutical biodegradation and sorption as a function of travel time. A more rigorous, first-principles-based approach is needed for this process because both sorption and biodegradation are occurring and need to be accounted for simultaneously. The use of a plug-flow model allows for the appropriate formulation of the fate and transport of the compounds and phases (aqueous and solid).

2.2.5 Secondary clarification

The fifth modeled location comprises the secondary clarifier. Secondary clarification, like the equilibrium portion of the activated sludge basin, is modeled assuming plug flow conditions with equilibrium sorption. Extent of pharmaceutical biodegradation in this compartment is once again computed as a function of time in the reactor and the biodegradation rate coefficient, in this case, $k_1/2$. A decreased rate constant is used to account for the lack of aeration during secondary clarification and the presumption that the biomass are less actively degrading COD and drugs in the clarifiers relative to the activated sludge basins. After the secondary clarifier, the process stream splits into two streams: the effluent stream and the sludge recycle stream. The volume (first row, first column), the

solids mass (first row, second column), and the COD mass (third row, first column) in the effluent are set to match the plant operating characteristics (and also effluent regulatory requirements, 5 mg/L solids and 3 mg/L COD). The volume, solids mass, and the COD mass for the sludge recycle are calculated by subtracting the effluent values from the secondary clarifier values:

$$Q_{\mathrm{Re}cycle} = Q_{Leaving\,2^0\,Clarifier} - Q_{Effluent.}(1stRow, 1stColumn)$$
$$Mass_{Solids,\mathrm{Re}cycle} = Mass_{Solids,Leaving\,2^0\,Clarifier} - Mass_{Solids,Effluent.}(1stRow, 2ndColumn)$$
$$Mass_{COD,StartASba\mathrm{sin}} = Mass_{COD,Leaving\,2^0\,Clarifier} - Mass_{COD,Effluent}(3rdRow, 1stColumn)$$

As with separation after the primary clarifier, the transport of drug compound is modeled to mirror the transport of the phase containing the drug compound (i.e. inter-phase flux, or *j*, is assumed to not be significant owing to equilibrium conditions). If 66% of the aqueous phase goes into the effluent stream (first row, first column, Effluent), then 66% of the drug mass present in the aqueous phase leaving the secondary clarifier will go into the effluent stream (second row, second column, Effluent). The drug masses in the sludge recycle stream are the calculated by subtracting the effluent masses from the masses leaving the secondary clarifier.

2.2.6 Sludge recycle

After separation following the secondary clarifier, the next modeled process is the sludge recycle stream. As mentioned above, the values for the aqueous volume (first row, first column), the solids mass (first row, second column), the mass of COD (third row, first column), the aqueous drug mass (second row, second column), and the sorbed drug mass (third row, second column) for the recycle stream are calculated by subtracting the effluent values from the values leaving the secondary clarifier. The recycle stream is then split into two separate streams, the return activated sludge (RAS), which is pumped back to the beginning of the activated sludge basins, and the waste activated sludge (WAS), which is merged with the primary sludge stream and pumped to the anaerobic digesters (not modeled here). In this case, the treatment plant's operating characteristics define the separation between these two streams, specifically, the RAS is 95% of the recycle stream, whereas the WAS is 5% of the stream. Both the aqueous phase (first row, first column) and the solids phase (first row, second column) are split proportionately with 95% moving to the RAS and 5% moving to the WAS. Additionally, the COD mass dissolved in the aqueous phase (third row, first column) and the drug mass in the aqueous phase (second row, second column) are split proportionately to the phase (95% to RAS, 5% to WAS), as is the mass of drug in the sorbed phase (third row, second column).

The final component of the model is the iterative step that is part of the RAS stream. This two-step process was necessary to eliminate circular calculation errors that arise due to the recycle stream which otherwise would have produced an indeterminate system. This error can be highlighted by looking at just the aqueous phase drug mass. The mass at Start A.S. Basin is calculated from the mass leaving the primary clarifier and the mass in the RAS stream. The mass at Start A.S. EQM is calculated from the mass at Start A.S. Basin. The mass at Leaving A.S. Basin is calculated from the mass at Start A.S. Basin. The mass Leaving 2° Clarifier is calculated from the mass at Leaving A.S. Basin. The mass at Recycle is calculated from the Effluent and the mass at Leaving 2° Clarifier. Finally, the mass in the RAS stream is

calculated from the Recycle stream. This value then would be fed into the calculation for Start A.S. Basin, resulting in a circular calculation error. This error is resolved by essentially creating two separate entries in the model for the same process. The first, RAS, provided the values that feed into the Start A.S. Basin process. The second, 95% Calculated, is calculated from the Recycle stream, as described previously. Initially, two arbitrary values are inputted for the mass of drug compound in the aqueous phase (second row, second column) and the in the sorbed phase (third row, second column) for the RAS process. An optimization routine is then executed to minimize the sum of the squared residuals between the drug masses in the RAS line that feed into the activated sludge basin and the RAS line that is calculated as being 95% of the recycle line. By minimizing the difference between the two processes, the recycle loop is effectively closed, allowing for a complete modeling of the wastewater treatment process.

3. Conclusions

Modeling the simultaneous sorption and biodegradation in wastewater systems has proven to be a challenging problem for researchers. Because the two processes are intrinsically linked, a novel approach was needed to develop a comprehensive mathematical expression to be used in modelling analyses. To that end, the volume averaging methodology commonly employed in groundwater systems was used with one key difference: rather than the having the solid phase be stationary, it was mobile. This paradigm shift allowed for fate and transport modelling throughout a wastewater treatment plant. This new model is sufficiently robust that it can have applications with many different types of compounds in different treatment plants with varying operational characteristics.

4. References

Bartelt-Hunt, S., Snow, D., Damon, T., Shockley, J. & Hoagland, K. (2009). The occurrence of illicit and therapeutic pharmaceuticals in wastewater effluent and surface waters in Nebraska. *Environmental Pollution*, Vol. 157, No. 8, (August 2009), pp. 786-791, ISSN

Daughton, C & Ternes, T. (1999). Pharmaceuticals and personal care products in the environment: Agents of subtle change? *Environmental Health Perspectives*, Vol. 23, No. 2, (December 1999), pp. 123-123, ISSN

Daughton, C. (2009). Chemicals from the practice of healthcare: Challenges and unknowns posed by residues in the environment. *Environmental Toxicology and Chemistry*, Vol. 28, No. 3, (December 2009), pp. 2490-2494, ISSN

Glassmeyer, S., Furlong, E., Kolpin, D., Cahill, J., Zaugg, S., Werner, S., Meyer, M. & Kryak, D. (2005). Transport of chemical and microbial compounds from known wastewater discharges: A potential for use as indicators of human fecal contamination. *Environmental Science and Technology*, Vol. 39, No. 3, (November 2005), pp. 5157-5169, ISSN

Hassanizadeh, M. & Gray, W. (1979). General conservation equations for multi-phase systems: 1. Averaging procedure. Advances in Water Resources, Vol. 2, No. 3, (March 1979), pp. 131-144, ISSN

Joss, A., Zabczynski, S., Gobel, A., Hoffmann, B., Loffler, D., McArdell, C., Ternes, T., Thomsen, A. & Siegrist, H. (2006). Biological degradation of pharmaceuticals in

municipal wastewater treatment: Proposing a classification scheme. *Water Research*, Vol. 40, No. 5, (May 2006), pp. 1686-1696, ISSN

Kolpin, D., Furlong, E., Meyer, M., Thurman, E., Zaugg, S. & Barber, L. (2002). Pharmaceuticals, hormones, and other organic wastewater contaminants in U.S. streams, 1999-2000: A national reconnaissance. *Environmental Science and Technology*, Vol. 36, No. 6, (June 2002), pp. 1202-1211, ISSN

Lietz, A. & Meyer, M. (2006). Evaluation of emerging contaminants of concern at the South District Wastewater Treatment Plant based on seasonal sampling events, Miami-Dade County, Florida, 2004. *U.S. Geological Survey, Scientific Investigations Report* 2006-5240. Reston, Virginia.

Ottmar, K., Colosi, L. & Smith, J. (2010a). Sorption of statin pharmaceuticals to wastewater treatment biosolids, terrestrial soils, and freshwater sediment. *Journal of Environmental Engineering*, Vol. 136, No. 2, (February 2010), pp. 256-264, ISSN

Ottmar, K., Colosi, L. & Smith, J. (2010b). Development and application of a model to estimate wastewater treatment plant prescription pharmaceutical influent loadings and concentrations. Bulletin of Environmental Contamination, Vol. 84, No. 5, (May 2010), pp. 507-512, ISSN

Richardson, S & Ternes, T. (2005). Water analysis: Emerging contaminants and current issues. *Analytical Chemistry*, Vol. 77, No. 12, (December 2005), pp. 3807-3838, ISSN

Vanderford, B. & Snyder, S. (2006). Analysis of pharmaceuticals in water by isotope dilution liquid chromatography/tandem mass spectrometry. *Environmental Science and Technology*, Vol. 40, No. 23, (December 2006), pp. 7312-7320, ISSN

Yu, C. & Chu, K. (2009). Occurrence of pharmaceuticals and personal care products along the West Prong Little Pigeon River in east Tennessee, USA. *Chemosphere*, Vol. 75, No. 5, (May 2009), pp. 1281-1286, ISSN

Yu, J.; Bouwer, E. & Coelhan, M. (2006). Occurrence and biodegradability studies of selected pharmaceuticals and personal care products in sewage effluent. *Agricultural Water Management*, Vol. 86, No. 1-2, (January/February 2006), pp. 72-80, ISSN

17

Winery Wastewater Treatment - Evaluation of the Air Micro-Bubble Bioreactor Performance

Margarida Oliveira[1,2] and Elizabeth Duarte[2]
[1]*Instituto Superior Politécnico de Santarém, Escola Superior Agrária de Santarém*
[2]*Technical University of Lisbon, Instituto Superior de Agronomia*
Portugal

1. Introduction

The wine sector has faced increasing pressure in order to fulfill the legal environmental requirements, maintaining a competitive position in a global market. The rising costs associated have stimulated the sector to seek sustainable management's strategies, focussing on controlling the demand for water and improving its supply. These can be accomplished by defining the best practical techniques, using technological means (Best Available Technologies) (Duarte *et al*., 2004). Some EU Directives were implemented concerning water protection and management. These included in particular the Framework Directive in the field of water policy and environmental legislation about specific uses of water and discharges of substances. The disposal of the untreated waste from the wine sector is considered an environmental risk, causing salination and eutrophication of water resources; waterlogging and anaerobiosis and loss of soil structure with increased vulnerability to erosion (Schoor, 2005). The winery wastewater is seasonally produced and is generated mainly as the result of cleaning practices in winery, such as washing operations during crushing and pressing grapes, rinsing of fermentations tanks, barrels washing, bottling and purges from the cooling process. As a consequence of the working period and the winemaking technologies, volumes and pollution loads greatly vary over the year. Each winery is also unique in wastewater generation, highly variable, 0.8 to 14 L per litre of wine (Schoor, 2005; Moletta, 2009). Consequently, the treatment system must be versatile to face the loading regimen and stream fluctuation. During the peak season (vintage), the winery wastewater has a very high loading of solids and soluble organic contaminant, but after this period, contaminant load decreases substantially. The high concentration of ethanol and sugars in winery wastewater justifies often the choice of a biological treatment (Bolzonella & Rosso, 2007). But the different wine processing method of each winery generates wastewater with specific properties, causing the impossibility to meet a general agreement on the most suitable cost-effective alternative for biological treatment of this wastewater.

Several winery wastewater treatments are available, but the development of alternative technologies is essential to increase their efficiency and to decrease the investment and exploration costs (Coetzee *et al.*, 2004). So criteria should be considered in the selection of the adequate technology, such as maximization of removal efficiency, flexibility in order to deal with variable concentration and loads, moderate capital cost, easy to operate and maintain, small footprint, ability to meet discharge requirements for winery wastewater and also low sludge production. On the other hand, small producer with relatively modest financial

capacity are interested in simple treatment systems with low maintenance and manpower requirements (Andreottola *et al*., 2009).
Most treatment systems have been designed with large oxidation tanks and oversizing the aeration system to deal with the peak load with a very high oxygen demand, during the vintage period. As a result, wastewater treatment plants are quite large and difficult to manage. One of the most promising technologies appears to be the vertical reactors characterised by high oxygen mass transfer improving the biological conversion capacity. To optimise the mass transfer, a highly efficient Venturi injector coupled with multiplier nozzles were developed (AirJection®), in order to increase the treatment efficiency.
The main goals of the present paper are the comparison of different biological treatment systems, in particular fixed and suspended biomass, operating under aerobic conditions. Since the accurate design of the bioreactor is dependent on many operational parameters, aspects related to hydraulic retention time; oxygen mass transfer and contact time, energetic costs; sludge settling and production; response time during startup, flexibility and treated wastewater reuse, in crop irrigation, with the aim of closing the water cycle in the wine sector, will be addressed. A new treatment system will be presented as a case study, an air micro-bubble bioreactor (AMBB), that will highlight the advantages and constraints on its performance at bench-scale and full-scale, in order to fulfill the gaps associated with the implemented winery wastewater treatment systems. The data presented was collected during four years monitoring plan and used to develop a tool to support the selection of the best available technology. The present study will also contribute to the implementation of an integrated strategy for sustainable production in the wine sector, based on a modular and flexible technology that will facilitate compliance with environmental regulations and potential reuse for crop irrigation. This approach will contribute to the development of a bio-based economy in the wine sector that should be integrated in a Green Innovation Economy Cycle.

2. Comparison of different biological treatment systems

2.1 Biological treatments in winery wastewater

Several treatment systems, both physico-chemical and biological, have been assayed to reduce the organic load of the winery wastewater. Some of these technologies are based on membrane bioreactors (MBRs), sequencing batch reactor (SBR), upflow anaerobic sludge blanket (UASB), anaerobic sequencing batch reactor (ASBR) and jet loop reactors (JLR). However, most of these methods have some characteristics in common: they are relatively expensive, they are not applicable in all situations, and they are not always able to deal with fluctuations in the hydraulic and pollution load. In order to overcome some of these problems, research efforts have been made towards the development of novel bioreactors as alternatives or to improve, the above-mentioned conventional methods. Although the high organic load of this wastewater would recommend the application of an anaerobic treatment for removing its polluting content, several problems have been found in the application of anaerobic processes due to its seasonal nature, its variable volumes and compositions and the difficulties in the monitoring and process control by specialized personnel (Malandra *et al*., 2003). The anaerobic treatments such as UASB and ASBR have successfully been used to treat a variety of effluents including those from wineries. The chemical oxygen demand (COD) removal efficiency is greater than 90%, but a specific microbial community is required. However, normally after this reactor there is an aerobic

post-treatment, to return the treated water to environment (Moletta 2005) in addition, the process control needs specialized personnel (Malandra *et al*., 2003).

The MBRs are very compact systems and offer an alternative to conventional activated sludge processes. The COD efficiency achieved is above 97%. The electricity consumption and the operating life of the membranes are higher than those associated with traditional activated sludge systems (Artiga et al., 2005), what may constitute a constraint to its application.

The subsurface-flow constructed wetland is described as suitable for treating these wastewaters, but frequently wineries do not have available area for setting up such plants (Grismer *et al*., 2003). However, phytotoxicity bioassays carried out with *Phragmites, Juncus and Schoenoplectus* at different wastewater dilutions showed that at greater than 25% wastewater concentration all the macrophytes died (Arienzo *et al*., 2009a). Nevertheless, the same authors showed that this system when combined with a previously sedimentation/aerobic process could be used for small wineries located in rural areas, achieving 72% of COD removal rate (Arienzo *et al*., 2009b).

The wastewater treatment of small wineries (less than 15,000 hL of wine per year) can be also performed using a SBR, fed once a day. The SBR system is a modified design of conventional activated sludge process and it has been widely used in industrial wastewater treatment. The COD removal efficiency is between 86-99% (Torrijos & Moletta, 1997). The on-line monitoring of dissolved oxygen concentration appeared as a good indicator of the progress in the COD biodegradation (Andreottola *et al*., 2002). Some modifications have been done in order to improve the reactor performance. The opportunity of combining the advantages of the SBR with fixed biomass was investigated (Andreottola & *et al*., 2002). This system permits the treatment of high organic loads, 6.3 kg COD m^{-3} d^{-1} with high biofilm grown (4-5 kg TSS m^{-3}), allowing the reduction of the required volume for biological treatment and avoiding bulking problems. However, the degradation of organic matter present in a winery wastewater sometimes require the addition of extra nutrients, to balance the C/N/P ratio and some oxygen efficiency transfer problems were detected when higher organic loads were applied (Lopez-Palau & Mata-Alvarez, 2009).

The fixed bed biofilm reactor or the air-bubble column bioreactor using self-adapted microbial population either free or immobilized can achieve 90% of COD removal (Petruccioli *et al*., 2000). In order to overcome the energetic costs associated with the aeration systems, a Venturi injector was used in the JLRs. This system achieves COD removal efficiency near 90%. Though, the high shear stress applied on the Venturi influence the composition of the microbial population (Petruccioli *et al*., 2000; Eusébio *et al*., 2005) leading to settling sludge problems. A similar technology that utilizes also a Venturi injector is the AMBB. This technology is very promising because it consists in a vertical reactor with good oxygen transfer and high biological conversion capacity. To optimise the mass transfer, a highly efficient Venturi injector coupled with multiplier nozzles was patented (AirJection®) and was applied in a lagoon system (Meyer *et al*., 2004) and in a vertical reactor (Oliveira *et al*., 2009), at pilot scale, to treat winery wastewater with a treatment efficiency of 90 %.

The maintenance and enhancement of a biological reactor is highly dependent on the microbial population that changes with time and winery activity (Jourjon *et al*., 2005). A deep understanding on the microbial population involved in the process is crucial to address any strategy for treatment system management (Tandoi *et al*., 2006). Although some researchers have been developed (Eusébio *et al*., 2004; Eusébio *et al*., 2005; Jourjon *et al*.,

2005), the understanding of the microflora dynamics inside the bioreactor will be of utmost importance for the treatment system optimisation. Moreover, in the aerobic bioreactors the microorganisms are dependent on aeration oxygen supply. Knowledge of mass transfer coefficients between the different phases together with reaction dynamics is utmost importance to design gas-liquid-solid reactor and to predict the microbial metabolism pathway.

2.2 Optimization of operational parameters in aerobic reactors

The optimization of operational parameters in bioprocesses is based essentially on reducing the volume and footprint, oxygen mass transfer and contact time, energetic costs, sludge settling and production and response time during start-up, while maintain a high removal efficiency of organic matter.

The SBR system has been widely applied to organic carbon removal in municipal and industrial wastewater treatments, as this system presents different advantages such as space reduction and the ability to make operational changes, during the treatment cycle.

In the SBR system the sludge settlement occur in the same tank as oxidation, so in order to optimize the sludge settling time, the formation of granules could be performed based on feast-famine periods (Lopez-Palau *et al.*, 2009). The start-up were performed with the increasing of the COD loading (2.7-20 kg COD. m^{-3} day^{-1}) in order to reach the feast period. After ten days of operation, the first aggregates were observed. But, the use of a high organic load promotes microbial growth and the reactor reached solids concentration of around 6 g VSS L^{-1}. Consequently, some problems of aeration appeared, and the air supply had to be increased from 13.5 L min^{-1} to 20 L min^{-1}. This study showed that is possible to cultivate aerobic granular sludge in SBR, improving the sludge settleability. Nevertheless, the aeration must be proportional to the COD load.

The combination of the SBR with fixed biomass SBBR (Sequencing Batch Biofilm Reactor) to treat winery wastewater was studied by Andreottola *et al.* (2002) and revealed the possibility of treating higher organic loads without increasing the required treatment volume, as the biomass grown on plastic media. However, this type of reactor needs a separated settler, as the biomass settlement worsens in the presence of the plastic material. In order to optimize the energetic costs and the SBBR performance, a strategy based on dissolved oxygen (DO) monitoring was developed.

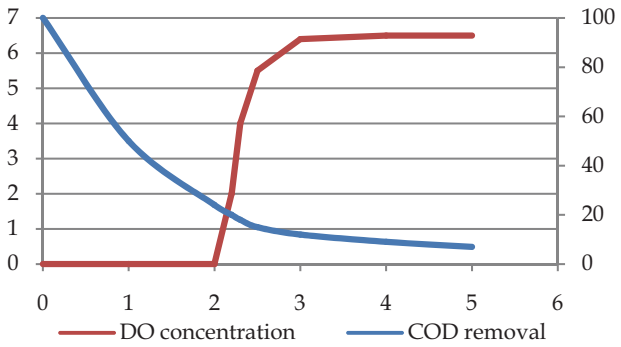

Adapted from Andreottola *et al.* (2002)

Fig. 1. DO concentration and COD dynamic during a typical SBBR cycle

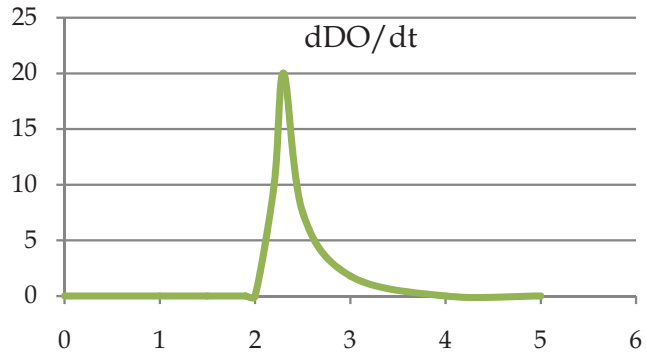

Fig. 2. Time derivative of DO concentration

During the assays the DO control was the key to the COD removal, because this treatment was carried out with constant aeration (up to 4.5 hours). When the treatment started the COD decreases as the DO concentration is maintained at low levels (Figure 1). Once the microbial activity decreases by diminishing the organic load, the DO concentration begins to rise until reaching a plateau. At this stage, the process is complete and the cycle can be stopped. The end of each cycle can be calculated based on the first derivative function of the DO concentration *vs* time (Figure 2). With this strategy it was possible to reduce the hydraulic retention time in about three times, which has allowed the treatment of a higher flow with a similar effluent quality.

Another approach based on dissolved oxygen control was carried out to optimize a SBR cycle for total organic carbon and ammonia removal (Puig *et al.*, 2006). In this treatment the aerobic phases of the SBR cycle were initially operated using an On/Off dissolved oxygen control strategy.

The cycle was divided in reaction phase, under aerobic and anoxic conditions, settling and discharge.

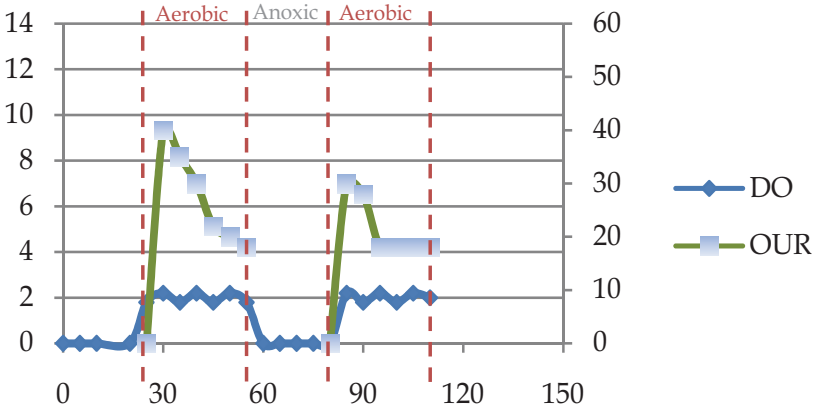

Adapted from Puig *et al.* (2006).

Fig. 3. DO and OUR evolution during aerobic and anoxic phases

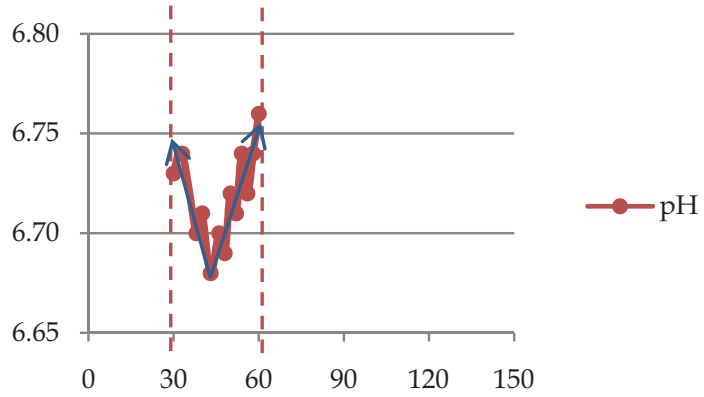

Adapted from Puig *et al.* (2006).

Fig. 4. Detection of the ammonia valley in the pH evolution during aerobic phase

During the aerobic phase a fixed DO set-point of 2.0 mg DO L^{-1} was applied, as a simple On/Off control. The system optimization was based on pH, DO and OUR evolution. This strategy allows the detection of the ammonia valley in the pH profile and also the end of nitrification, through the OUR outline (Figure 3 and Figure 4). The analysis of the OUR profile shows a plateau in the OUR value, in the end of the aerobic phase, which may indicate that the microbial populations are under endogenous conditions and that organic matter and ammonia has been completed degraded.

In fact, one of the most important aspects in many biological systems is the aeration supply. The wastewater treatment is one of these processes that require proper aeration to maintain the growth of the microorganisms responsible for the biodegradation of the organic matter. Most wastewater treatments are aerobic and are carried out in aqueous medium containing inorganic salts and organic substances which can give viscosity to the broth, showing a non-Newtonian behavior. In bioprocessing it is very important to ensure an adequate oxygen distribution to the gas stream and to the fermentation broth. Some of the systems used to supply the oxygen are sparging, free-jet flow and bubbling column, among others. Also the different nozzle geometry, the liquid phase properties, the jet length and diameter influences the oxygen distribution to the system that in many cases is a limiting factor to the success of the treatment process. In this sense, it is important to estimate the mass transfer characteristics in order to predict the kinetic growth reaction constant, and control and optimize the aerobic fermentation processes (Choi *et al.*, 1996; Fakeeha *et al.*, 1999; Tojabas & Garcia-Calvo, 2000; Garcia-Ochoa & Gomez, 2009). The volumetric mass transfer coefficient, k_La, is the parameter that characterizes the gas-liquid mass transfer in bioreactors. However, this value can vary substantially from those obtained for the oxygen absorption in water or in simple aqueous solutions, and in static systems with invariable composition of the liquid media along time. The transfer rate is very influenced by the nature of pollutants present in the wastewater, for example glucose increases the medium viscosity causing a decrease in the k_La value while the low foam surfactants enhances this value (Fakeeha *et al.*, 1999; Tojabas & Garcia-Calvo, 2000). Thus, it is necessary to know the composition of the fermentative broth, at least some of the major compounds, to understand the effect of combination of different pollutants for proper design and operation of aerobic process. Many strategies have been proposed to determine the volumetric mass transfer coefficient,

empirical equations and also theoretical prediction, most of them developed for bubble columns and airlifts (Garcia-Ochoa & Gomez, 2009).
The bioprocesses involves simultaneous transport and biochemical reactions, the oxygen is transferred from a rising gas bubble to the liquid phase and then to the place of oxidative phosphorylation within the cell, considered as a solid particle. The steps related to this mass transfer processes can be represented according to the film theory model for mass transfer, which describes the flux through the film based on a driving force (Figure 5).

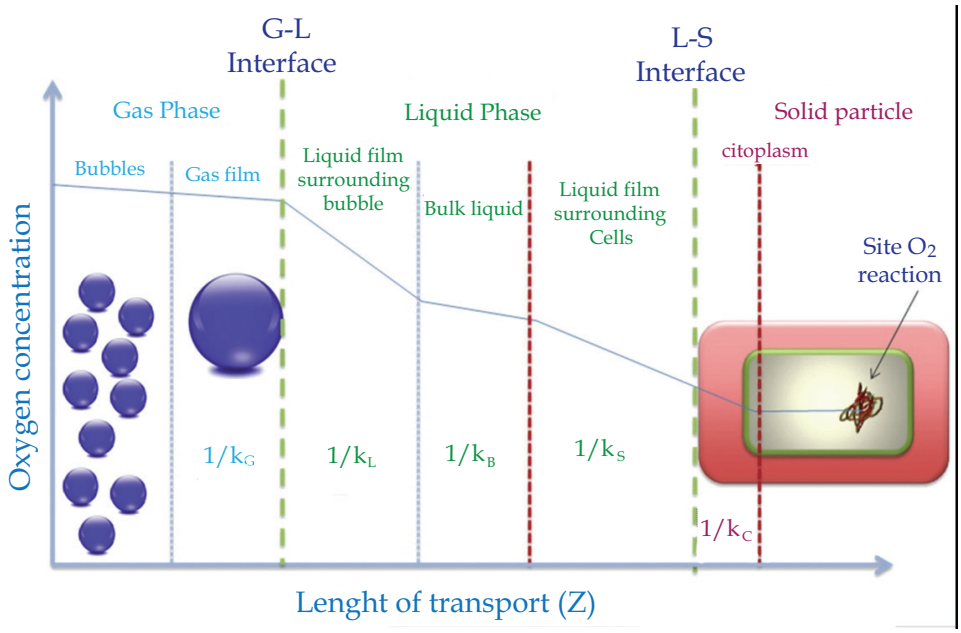

Adapted from Garcia-Ochoa & Gomez (2009)

Fig. 5. Steps and resistances for oxygen transfer from gas bubble to cell, in three phases reactors

The oxygen mass transfer rate per unit of reactor volume is obtained by a solute mass balance for the liquid phase (Fakeeha *et al.*, 1999):

$$OTR = k_L a \times (C^* - C_L) \quad (1)$$

As k_L and a are difficult to measure separately, usually the k_La is evaluated together and this parameter is identified as the volumetric mass transfer coefficient that characterizes the gas-liquid mass transfer. The driving force is the gradient between the oxygen concentration at the interface and in the bulk liquid. This gradient varies with the solubility and microbial activity. Also, the gas solubility depends on temperature, pressure, concentration and type of salts present in the system.
In bioreactors it is essential to determine the experimental k_La to set the aeration efficiency and to quantify the effects of the operating variables on the dissolved oxygen supply. To select the appropriated method, some factors should be taken into account, such as aeration

system; bioreactor type and its mechanical design; the composition of the fermentation broth and the possible effect of the microorganisms (Xu *et al*., 2010).
The mass balance for the dissolved oxygen in the well-mixed liquid phase can be established as (Garcia-Ochoa & Gomez, 2009; Irizar *et al*., 2009):

$$\frac{dC}{dt} = OTR - OUR \tag{2}$$

Where dC/dt is the accumulation oxygen rate in the liquid phase, OTR is the oxygen transfer rate from the gas to the liquid phase, described by equation (1) and OUR is the oxygen uptake rate by microorganisms. The methods that can be applied for the oxygen transfer rate measures can be classified depending on whether the measurement is done in the absence of microorganisms or with dead cells or in the presence of biomass that consumes oxygen at the time of measurement. When biochemical reactions do not take place, OUR=0, then the equation (2) can be simplified to:

$$\frac{dC}{dt} = k_L a \times (C^* - C_L) \tag{3}$$

The dynamic method used to measure the k_La value is based on the dissolved oxygen consumption and supply. In this method the change in the dissolved oxygen concentration is analyzed supplying air until the oxygen saturation concentration in the liquid phase is reached. The oxygen decreasing is then recorded as a function of time. Under these conditions the equation (2) can be expressed as equation (4), but, after the decreasing phase, the oxygen is again supplied and the equation (2) can be written as equation (5). In these cases the k_La values can be determined from the slope of the *ln f(C_L) vs* time.

$$ln\left(\frac{C_{L0}}{C_L}\right) = -k_L a \times t \tag{4}$$

$$ln\left(1 - \frac{C_L}{C^*}\right) = -k_L a \times t \tag{5}$$

Furthermore k_La is usually expressed at standard conditions of temperature and pressure, 20ºC, 1atm (equation 6).

$$k_L a_{20} = k_L a_T \times 1.024^{20-T} \tag{6}$$

The determination of the oxygen uptake rate OUR can also be carried out using a dynamic method which measures the respiratory activity of microorganisms that grow in the bioreactor. When the air supply is switching off, the dissolved oxygen concentration will decrease at a rate equal to oxygen consumption due to the microorganisms respiration rate. In this situation the OUR is determined from the slope of the plot of dissolved oxygen concentration *vs* time. The biomass concentration should be known in order to determined the specific oxygen uptake rate (SOUR).
Another important parameter in the aerobic reactors optimization is the sludge settling and production. The large amount of excess sludge generated during activated sludge process is estimated to cost about 40-60 % of the operating cost (Chen *et al*., 2001). This sludge contains volatile solids and retains about 95% of water resulting in a large volume of residual solids produced. The biological sludge production in conventional wastewater treatment plants

can be minimized using different strategies (Pérez-Elvira *et al.* 2006), such as endogenous metabolism and maintenance metabolism. In this last approach part of energy source is used for maintaining living functions, in this phase the substrate consumption is not used for cellular synthesis. In the endogenous metabolism part of cellular components is oxidized to produce the required energy for maintenance functions, which leads to a decrease in the biomass production. The objective is to reach a natural balance between biomass growth and decay rates. The oxic-settling-anoxic activated sludge process, considered as a sludge feast/famine treatment, is based on alternating exposure of sludge to oxic and anoxic environments. This working principle stimulate catabolic activity and make catabolism dissociate from anabolism. The sludge famine is related to an exposure of the settled sludge to anoxic conditions where the substrate concentration is low. Under these stressful conditions microorganisms are starving which may lead to a depletion of cell energy or nutrients storage. The sludge feasting means that fasted microorganisms return to an oxic environment with enough nutrients. As a consequence, the microorganisms growth may be limited by energy uncoupling (Chen *et al.*, 2001).

2.3 Diagnosis process

The selection of the most appropriate technology for the winery wastewater treatment is a difficult step that should be done after a diagnosis process. A proper diagnosis should conduct a survey report that includes all the information required for decision-makers. Regarding the production process, it should address all activities associated with it: vintage, racking and bottling (Figure 6). The knowledge of materials and supplies, as well as by-products generated during the process is essential in diagnosis. The water uses and water consumption are critical, both in terms of quantity or quality. The survey of sewers in the farm unit, particularly if the drainage system is separated or combined, and the points of wastewater discharge should also be covered. The wastewater flows should be evaluated through the installation of flow meters. The different streams of wastewater generated must be quantified in order to make an assessment, as rigorous as possible.

Fig. 6. Winery activities

The water consumption in two Portuguese wineries, one small and one medium size are quite different, with regard to quantity. However, the distribution of water consumption has a similar behavior throughout the year (Figure 7 and Figure 8). The data presented show that most water (60%-80%) is consumed in the vintage period that last about a month. So, the collection of water consumption associated with the physicochemical characterization of the wastewater is essential for the proper sizing of any treatment system. In addition, it is

possible to understand the need for flexibility of the treatment system, because the system should allow good removal yields, during the vintage period, but has also to remain in operation during the rest of the year even at low loads. In small wineries often there is a minor stream of wastewater during several months, which may lead to bioreactor inefficient performance. To overcome this situation a feast/famine strategy may be a challenge for future research at a full-scale.

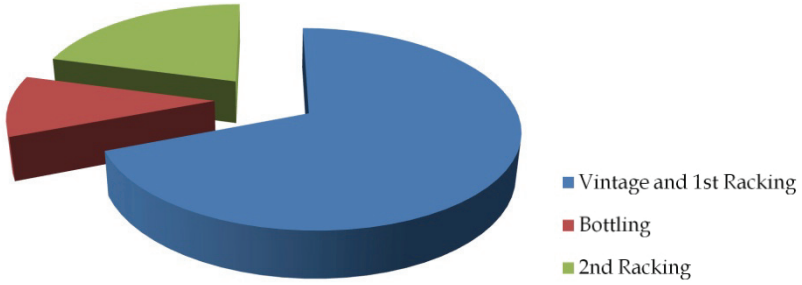

Adapted from Duarte *et al*. (2004).

Fig. 7. Distribution of water consumption during the global period of processing at a medium dimension winery

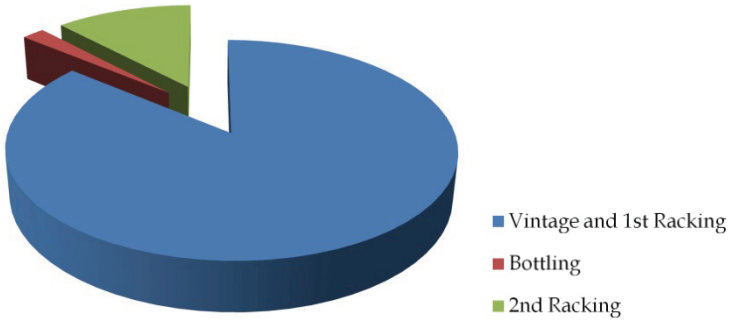

Fig. 8. Distribution of water consumption during the global period of processing at a small dimension winery

The physicochemical characterization assessment is carried out by determining specific parameters such as pH, electrical conductivity, dissolved oxygen, chemical oxygen demand, biochemical oxygen demand, total phosphorus, total nitrogen, total solids, suspended solids, total polyphenol compounds, anionic surfactants. In order to evaluate the fate of treated wastewater, it is also important to know the winery surroundings, in particular the existence of a sewage, the irrigation area, the type of structures and available areas, among others.
In wineries that intend to reuse the treated wastewater for irrigation, other concerns should be considered. The domestic wastewater flow containing high concentration of pathogenic microorganisms should not be mixed with the industrial wastewater stream. This flow should be treated separately or discharged in the sewage. This decision is extremely important, since the wastewater from winery operations does not contain pathogenic

microorganisms. Thus, this separation reduces the costs of wastewater treatment and monitoring, which are associated with the disinfection process.

3. Winery wastewater treatment in the Air Micro-Bubble Bioreactor

3.1 Wastewater characterization

The winery wastewater was collected, during four years, from three wineries of different sizes and characteristics and located in different Regions of Portugal. The Casa Agrícola Quinta da Casa Boa, located at Runa, Lisboa Region, producing only red wines, has a small/medium dimension with a production capacity of 200,000 L. The Catapereiro, located at Alcochete, Tejo Region, produces both white and red wines, has a medium dimension with a production capacity of 1 000,000 L of wine. The Herdade da Mingorra, located at Beja, Alentejo Region, has a medium dimension with a production capacity of 1 000,000 L of wine (Figure 9 to Figure 14).

Composite samples of the winery wastewater, representative of each phase of the process, were taken and maintained at 4ºC. A set of major key parameters were defined and analysed, according to *Standard Methods for the Examination of Water and Wastewater* (1998), in order to assess the winery wastewater pollutant charge: pH, conductivity, chemical oxygen demand (COD), biochemical oxygen demand (BOD), total suspended solids (TSS), volatile suspended solids (VSS), polyphenols, anionic surfactants, Na, K, Mg and Ca. The winery wastewater flows were evaluated from water consumption. With this propose the wineries installed general water counters to be daily read and register.

3.2 Bioreactor set-up

The Air Micro-Bubble Bioreactor (AMBB) with a total volume of 15 dm^3 consists of a cylindrical bioreactor, equipped with a circulated pump and a settler (Figure 15). The aeration was conducted during the wastewater recirculation by a high efficiency Venturi injector (HEVI) in conjunction with mass transfer multiplier nozzles (MTM). The MTM nozzles discharge the air/water mixture from the HEVI into the bottom of the bioreactor (Figure 14). The AMBB is equipped with an air flow meter and a monitoring probe (HANNA Instruments) able to on-line monitor pH, DO and temperature. Figure 16 shows a schematic overview of the bioreactor.

3.3 Bioreactor start-up and operating conditions

Several trails performed with the AMBB, under batch conditions were carried out during 15 days. The reactor was inoculated with 15 dm^3 of fresh winery wastewater, from the vintage period and with 0.15 dm^3 of acclimated biomass, obtained during the treatment of winery wastewater, in the previously year. Samples from the mixed liquor were daily taken for physico-chemical characterisation. The aerated flow was 2 $dm^3\,min^{-1}$. The operating temperature was 20-30ºC. The recirculation of the mixed liquor started with 20 min $hour^{-1}$, with a flow of 40 $dm^3\,min^{-1}$ and then was changed to 5 min $hour^{-1}$.

3.4 Seed germination bioassays

Germination bioassays were performed following Fuentes *et al.* (2004), by using cress *Lepidium sativum L.* seeds, to evaluate the suitability of the treated wastewater in relation to crop irrigation and expressed as Germination Index. The treated wastewater and two dilutions in distilled water (25%, 50% v/v) were tested (Oliveira *et al*., 2009).

Fig. 9. Global view at Mingorra winery

Fig. 10. Mingorra winery unit

Fig. 11. Vintage at Quinta da Casa Boa

Fig. 12. 1st Racking at Quinta da Casa Boa

Fig. 13. Wastewater treatment system at Catapereiro

Fig. 14. Wastewater treatment system at Mingorra

Fig. 15. The air micro-bubble bioreactor filled with clean water

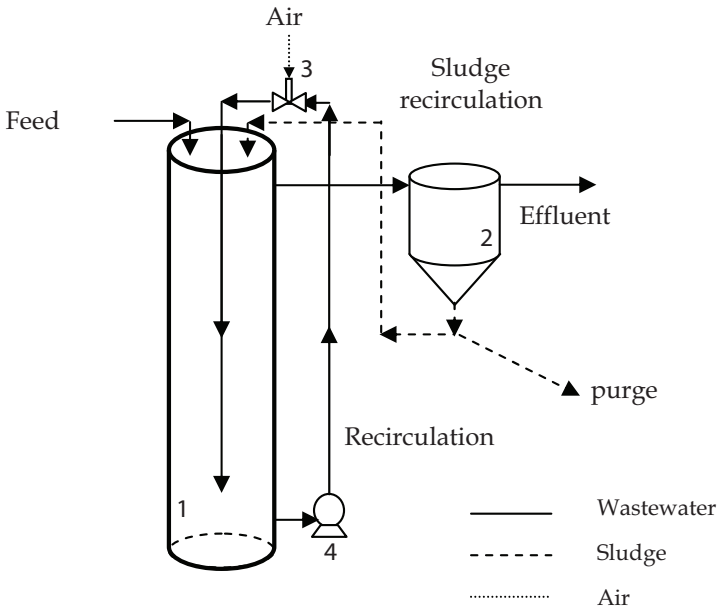

Fig. 16. Flow diagram of the air micro-bubble bioreactor. 1- Bioreactor; 2- Settler; 3- *Venturi* injector; 4- Recirculation pump

4. Results and discussion

4.1 Wastewater assessment

During the studying period, samples of winery wastewater were taken for laboratory characterization to evaluate their pollutant charge (Table 1). The values of pH ranged from 4 to 8, being this variation mostly dependent on the labor period. The electric conductivity of the wastewater showed no relevant variation in the different sampling periods and the range of registered values is not considered as inhibiting biomass growth.

The highest values of COD were reached during the vintage period, followed by the first racking. These results are in accordance to those previously reported by other authors (Petruccioli *et al.*, 2002). As expected, the highest values of biodegradability (BOD_5/COD) were achieved during the vintage period, due to the high concentration of simple molecules, easily metabolized (sugars and ethanol) by microorganisms (Duarte *et al.*, 2004).

Concerning TS and TSS parameters, the results reveal a high variability during the vinification period. Moreover, the TS are significantly higher than TSS, which means that these wastewaters contain, mostly, dissolved organic pollutant charge. However, during 2nd racking the TSS concentration reach the maximum value derived from the presence of tartrate. These solids are often problematic due to the high phenolic load adsorbed.

Although polyphenols and anionic surfactants are important pollutants, it is not expected that they could influence the organic load, since they are present in low concentration. Nevertheless, after the wastewater treatment some compounds known as recalcitrant may remain in the treated effluent, such as the polyphenols that are responsible for colour and the residual COD, this can also be observed by the low biodegradability ratio presented in Figure 17.

Moreover, this type of wastewater has very low levels of nutrients that are essential to microbial growth. For this reason, it is often required the addition of nutrients to guarantee the process of cellular synthesis. Alternatively, it is possible to change some practices at the winery in order to balance this ratio (Oliveira & Duarte, 2010).

The assessment of the water consumption is another key parameter for the successful of the winery wastewater treatment. In one of the monitored wineries the water consumption was evaluated throughout the operation period for two consecutive years. Internal management strategies were implemented to increase efficient water use, such as cleaning methods that aim the water reuse (closed-loop) pressure washing machines, among others. These simple changes showed a saving in water consumption of about 40%.

4.2 AMBB treatment

In this type of seasonal industry, the treatment system must be able to treat the wastewater produced in the vintage period. For this reason, many reactors have an appropriate volume for this stage but over dimensioned during the rest of the year. On the other hand, the high organic load of these wastewaters may promote the excessive growth of biomass, that requires an increase in the air supply (López-Palau *et al.*, 2009) and creates problems of sludge generation and disposal.

The adopted strategy in this study is based on sludge reduction, as the production of excess sludge from the wastewater treatment plant is considered one of the serious problems encountered in the aerobic treatments (Liu & Tay, 2001). In this study, an aerobic step alternated with an anoxic one was adopted as a strategy.

	Vintage			1st Racking			2nd Racking			Bottling
pH	5.88	±	0.92	5.92	±	1.95	5.23	±	2.15	8.42
Conductivity (µS cm^{-1})	1714	±	279	2036	±	618	3260	±	1666	1265
COD ($mg.L^{-1}$)	8942	±	5310	8025	±	4220	5993	±	4444	1805
BOD_5 ($mg.L^{-1}$)	4107	±	2900	3104	±	817	1395	±	1447	580
BOD_5/COD	0.66	±	0.32	0.47	±	0.26	0.23	±	0.09	0.32
Oxidized matter ($mg.L^{-1}$)*	5988	±	2448	4461	±	842	1640	±	1341	988
TS ($mg.L^{-1}$)	6268	±	4274	3034	±	248	8313	±	8725	2200
TSS ($mg.L^{-1}$)	523	±	190	866	±	199	3739	±	4654	185
NH_4^+ ($mg.L^{-1}$)	0.73	±	0.68	4.5	±	2.6		-		nd
Kjeldahl nitrogen ($mg.L^{-1}$)	16	±	8	26	±	19	135	±	71	3.5
P ($mg.L^{-1}$)	12	±	8	27	±	22	93	±	82	1.1
Na ($mg.L^{-1}$)	347	±	46	218	±	305	234	±	45	nd
K ($mg.L^{-1}$)	117	±	8	71	±	72	264	±	34	nd
Mg ($mg.L^{-1}$)	12	±	1	9.4	±	3.0	10	±	1	nd
Ca ($mg.L^{-1}$)	39	±	15	27	±	31	18	±	5	nd
Cu ($mg.L^{-1}$)	0.13	±	0.01	0.21	±	0.13	0.09	±	0.01	nd
Turbidity	209	±	138	635	±	214	3628	±	4225	3.1
Total Phenols ($mg.L^{-1}$)	28	±	11	32	±	15	30	±	14	2
SO_4^{2-} ($mg.L^{-1}$)	191	±	38	160	±	129	177	±	176	160
Cl^- ($mg.L^{-1}$)	130	±	62	185	±	129	113	±	56	nd
Anionic surfactants ($mgMBAS.L^{-1}$)	15	±	13	7	±	8	4.2	±	3.0	2

Table 1. Physico-chemical characterization of winery wastewater

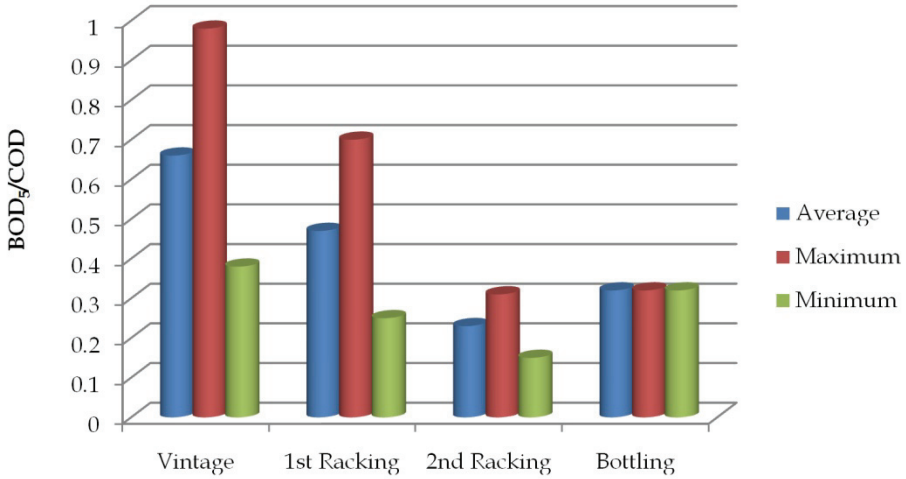

Fig. 17. Biodegradability indicators of the winery wastewater, in different labour periods

The bioreactor AMBB was tested in different phases of the wine process and it started in the vintage period (Figure 18-19). The biomass inoculated in this assay was already acclimated to winery wastewater and was maintained in aerobic/anoxic conditions, with insufficient substract. During the AMBB operation the microorganisms grow as suspended biomass but also as biofilm adsorbed to the reactor walls.

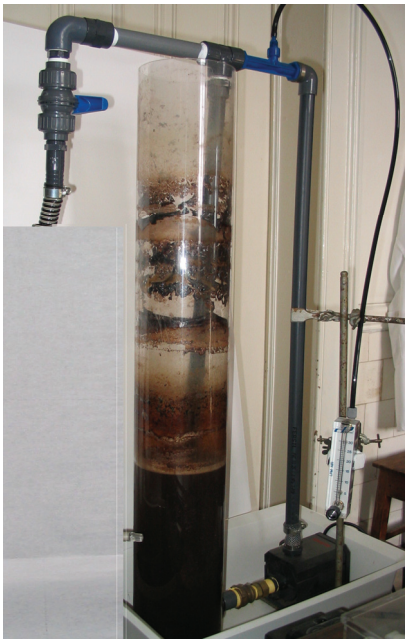

Fig. 18. Inoculation of the AMBB with fresh winery wastewater

Fig. 19. AMBB in the beginning of the treatment

The evolution of COD concentration, biomass and dissolved oxygen was followed. Regarding the biomass evolution, a typical growth curve for batch cultivation was achieved (Figure 20). This curve does not show a lag phase, since biomass was already adapted. The recirculation of the mixed liquor was 20 min hour^{-1}.

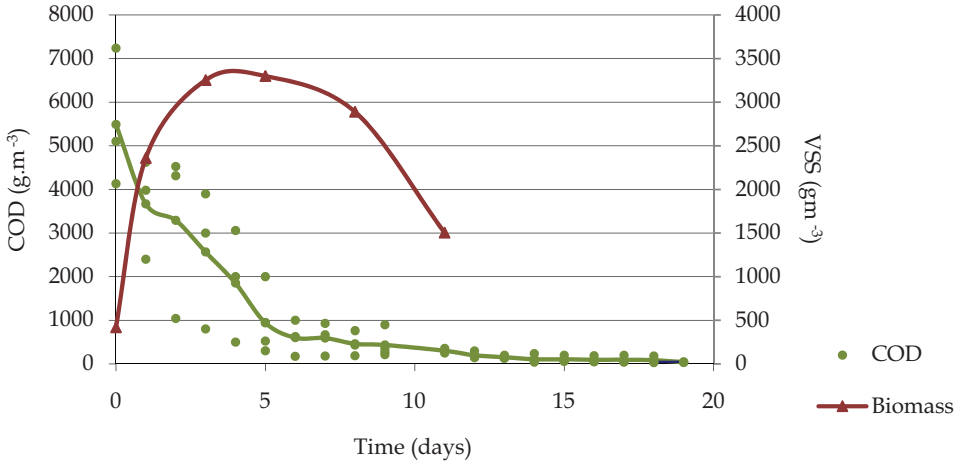

Fig. 20. Evolution on COD and biomass concentration in the AMBB

The COD of the winery wastewater ranged between 4.0-8.0 kg COD m^{-3} but the efficiency was similar for each batch, about 90.0±4.3%, after 6 days of operation. This period is related

to the biomass exponential phase. The maximum efficiency obtained (98.6±0.4%) was achieved after 15 days of treatment. These results are comparable with those reported by Beltran de Herédia *et al*. (2005), where they achieve 75% of COD reduction, after 3 days of treatment.

In order to minimize the sludge production and the energetic costs during the recirculation of the mixed liquor, the aeration time was reduced. During this assay dissolved oxygen, pH, COD and biomass was evaluated.

Concerning the DO concentration the Figure 21 illustrate the dynamic change of this parameter in the AMBB. During the air supplying, the DO increases until it reaches saturation. The period of time required to reach saturation is directly related to the oxygen transfer rate. The estimation of OTR under different operational conditions has a relevant role to predict the metabolic pathway for microbial growth in aerobic treatments. So, this approach could be interesting for studying the influence of operational conditions on volumetric mass transfer coefficient.

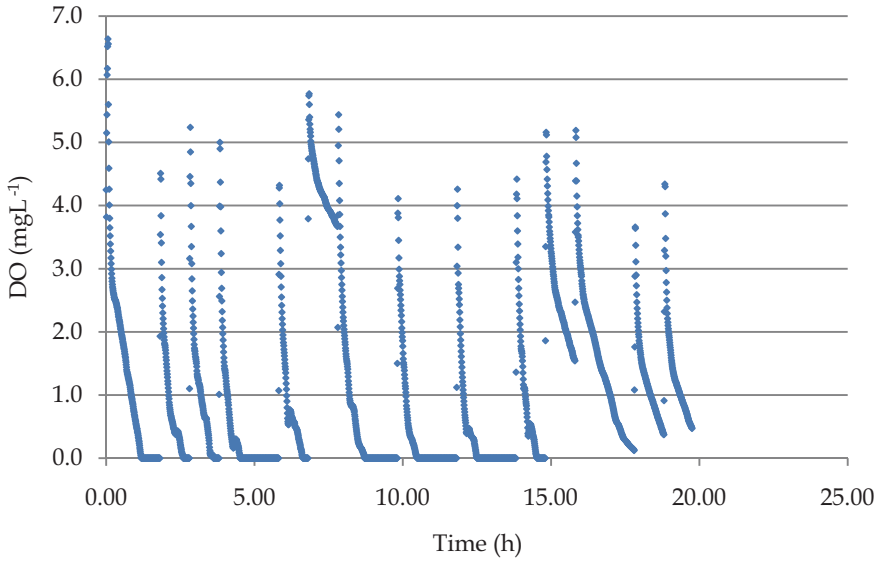

Fig. 21. Evolution on pH and DO concentration in the AMBB

A dynamic method was used to determine the volumetric mass transfer coefficient, k_La (Table 2). The k_La values were calculated by solving the Equation 2, during the aeration phase and considering that the gas flow and OUR were both constant. In these cases the slope of the *ln* f(DO) *vs* time allows the determination of the oxygen transfer parameter (Figure 22). The k_La values were corrected to 20 ° C, according to equation 6.

The results show a decrease in the k_La value during the treatment period (Figure 23). Many factors could influence k_La, including air flow rate, air pressure, temperature, vessel geometry and fluid characteristics. All parameters were kept constant throughout the treatment, except the wastewater composition that varies during the treatment period. More readily biodegradable compounds such as sugars and ethanol are firstly assimilated by microorganisms; the more complex substrates are only degraded at a later stage. Previous

studies indicate that the composition of the fermentation broth influences the oxygen mass transfer, such as glucose that can decrease the k_La, by increasing the viscosity of the medium but on the other surfactants increases this value (Fakeeha *et al.*, 1999). In fact, is practically impossible to determine the exact composition of wastewater, but the compounds mentioned above are always present in this type of wastewater. This decrease in k_La value means that some of the existing compounds in wastewater optimize the oxygen mass transfer during the initial phase of treatment. Indeed, even without being quantified, in all

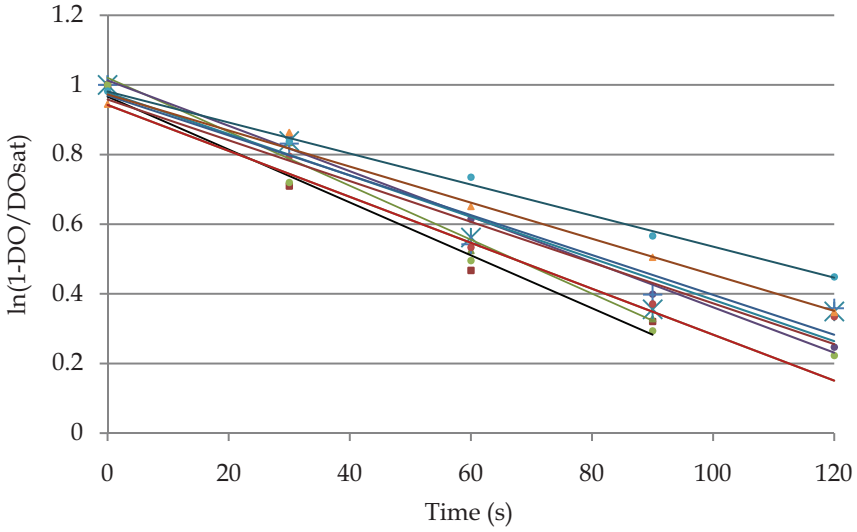

Fig. 22. Experimental determination of k_La based on DO concentration in the AMBB

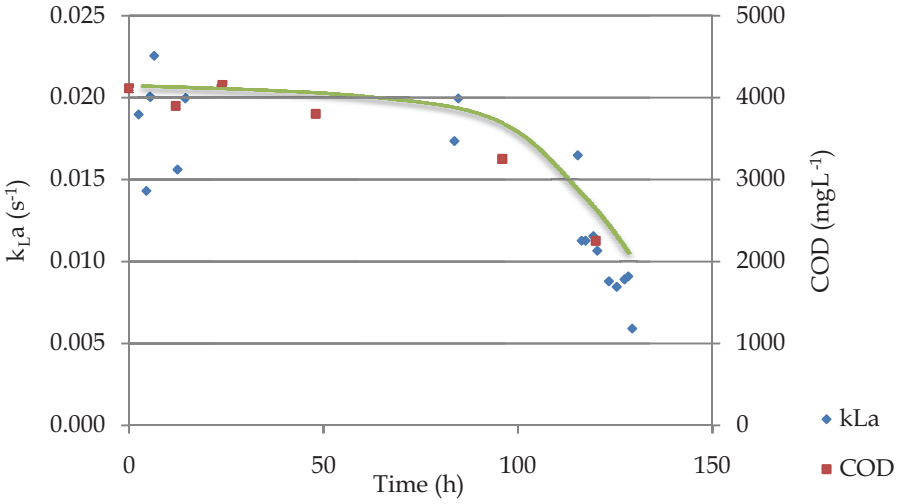

Fig. 23. k_La and COD dynamics during wastewater treatment in the AMBB

trials it was found that the size of the bubble formed, increased throughout the treatment period, which is in agreement with the obtained results. Moreover, it is interesting to observe that the k_La decline follows the degradation kinetics of organic matter, expressed as COD, which corroborate the obtained results. The k_La values obtained in these assays are in the same range that of values achieved by other authors in full-scale aeration tank equipped with fine bubble diffusers and jet loop reactor (Fakeeha *et al.*, 1999; Fayolle *et al.*, 2010).
In addition, the respirometric activity of microorganisms which are actively growing in the bioreactor can also be measured based on this dynamic method. When the gas supply to the bioreactor is turned off, the DO concentration decreases at a rate equal to oxygen consumption by the respiration process. In this situation the OUR can be calculated from the slope of the DO *vs* time (Figure 24).

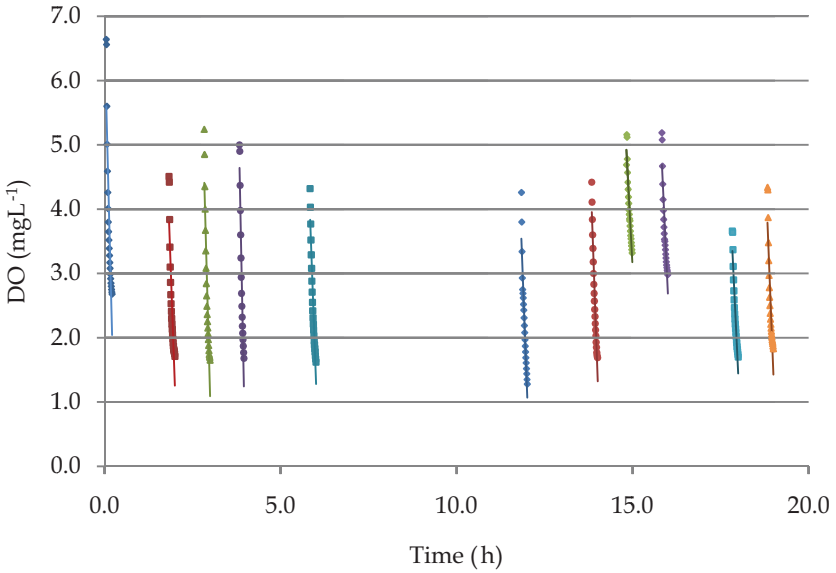

Fig. 24. Trendlines adjustment on DO concentration depletion to determine OUR in the AMBB

The specific oxygen uptake rate (SOUR) or respiration rate is expressed as milligrams of oxygen consumed per gram of volatile suspended solids per hour. The high SOUR values obtained (Table 2), indicate a high organic load to the existing suspended solids in the mixed liquor (MLSS).
The SOUR measurements throughout the wastewater treatment showed an initial increase in the SOUR values until reaching a plateau. The Figure 25 shows that after an adaptation period to the treatment system there is a removal of the organic load, expressed as COD rate corresponding to the increment of SOUR rate. This high SOUR rate is due to the high activity of the microbial population to oxidise substrates. These values may be induced by an increased energy requirement stimulated by a famine period, during sludge acclimatisation. The feast/famine phenomenon has been reported by several authors as a strategy on sludge production (Chen *et al.*, 2001; Ramakrishna & Viraraghavan, 2005; López-Palau *et al.*, 2009). A similar behaviour was found by Chen *et al.* (2001) during the study of

feast/famine growth on activated sludge cultures previously subjected to a famine treatment. This study also indicates that the COD removal ability of the fasted culture is higher than the non-fasted culture.

	OUR ($mg\ O_2\ (L.h)^{-1}$)	SOUR ($mg\ O_2\ (g\ MLSS.\ h)^{-1}$)	$k_La.10^3$ (20°C) (s^{-1})
	16.6	19.5	11.7
	19.8	23.3	19.0
	19.5	22.9	14.3
	17.6	20.7	20.0
Initial values	20.5	24.1	22.6
	20.2	23.8	13.0
	18.9	22.2	13.0
	19.5	22.9	15.6
	19.6	23.1	26.0
	21.4	25.2	19.9
	20.4	24.0	19.9
Maximum values	28.9	34.0	17.3
	32.8	38.6	19.9
	32.6	38.4	18.2
	31.8	37.4	16.5
	29.5	34.7	11.3
	32.8	37.4	11.3
	14.2	25.1	11.5
	21.4	17.9	10.7
Final values	15.2	23.4	8.9
	19.9	18.0	8.8
	15.3	17.4	8.5
	14.8	18.6	8.9
	15.8	12.4	9.1
	10.5	14.1	5.9
	12.0	13.4	7.7
	11.4	16.7	6.2

Table 2. Evolution of the mass transfer parameters OUR, SOUR and k_La values, throughout the treatment

In winery wastewater treatments systems the period prior to vintage is a non-productive period, without wastewater generation. In this sense, the existing biomass in the treatment system is subjected to a famine treatment. Moreover, during harvest the wastewater production has the highest flow rates and organic loadings. According to Chen *et al.*, 2001

after a famine period the microorganisms are starved and the substrate utilization rate increases. A treatment system based on this management model seems to be a good approach for winery wastewaters, with the additional advantage of keeping the low amount of sludge. The cause of sludge reduction in this process is not clearly known but the absence of oxygen reduces the growth of strictly aerobic populations and stimulates the facultative bacteria (unpublished results), which have lower specific growth rates. In this sense, as the dominant population is constituted of slow growers that may explain the low sludge yield production. Furthermore, the produced sludge shows low SVI values indicative of easy sludge settling.

The strategy based on low aeration time alternating with anoxic periods allows the treatment of the winery wastewater with lower sludge production but with lower efficiency. In fact, the MLSS achieved in this batch treatment, 1.2 g/L was lower compared with the initial assay. In the management of a wastewater treatment of this nature is necessary to establish a compromise between operating costs and final quality of the treated wastewater, taking into account the final destination and the legal requirements.

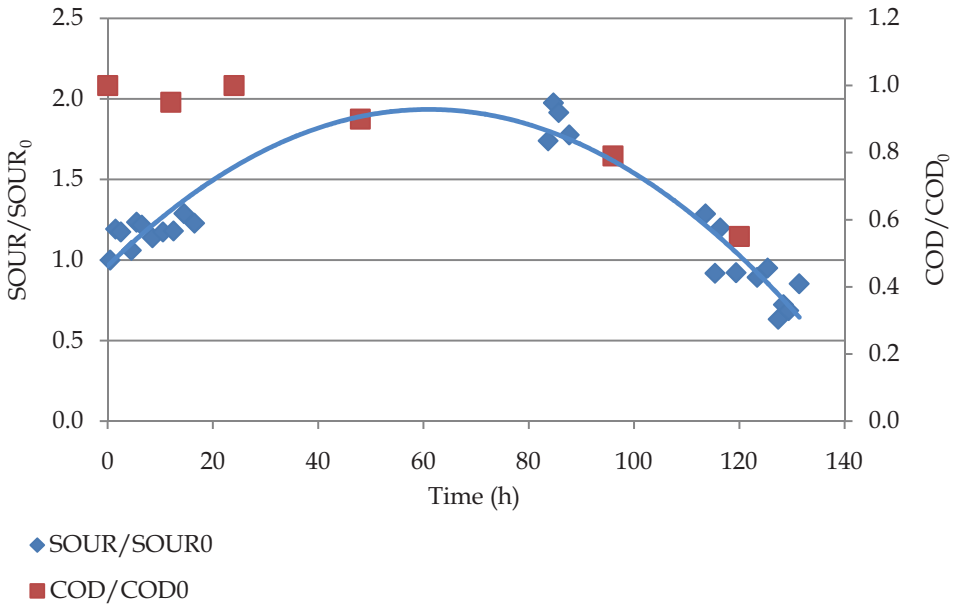

Fig. 25. Evolution of SOUR and COD rates during the batch treatment

In order to evaluate its suitability to be used in crop irrigation the treated wastewater from the AMBB batch assays was physico-chemical characterized. All the analyzed parameters except one were in agreement with EU and Portuguese Legislation (Directive 2000/60/EC, DL n° 236/98) for irrigation use (Table 3). Of particular concern was the sodium adsorption ratio (SAR), the proportion of sodium to calcium and magnesium, which was higher than the permitted parametric value. Probably, some strategies can be applied in winery in order to reduce the problem. Nevertheless, the treated wastewater, normally, is used in irrigation systems to supplement the irrigation water, as an economic additional water supply. Also,

seed germination assays carried out with *Lepidium sativum* were developed for evaluating the effects of water contaminants on germination and seedling growth. The adequacy of the treated wastewater for crop irrigation was evaluated with direct toxicity bioassays, by using cress seeds as indicator No significant differences (P=0.05) between batch experiments were registered on germination index (GI). As the cress bioassay is a standard procedure to evaluate the behaviour of crops to water contaminants, data (previously published) evidence the suitability of treated wastewater in relation to crop irrigation, thus minimizing water consumption (Oliveira *et al.*, 2009).

Parameter	**Treated wastewater**	**DL nº236/98**
pH	8.0	4.5-9.0
Conductivity (μS cm^{-1})	920	-
COD (mg L^{-1})	140	-
N total (mg L^{-1})	2.0	-
P total (mg L^{-1})	0.6	-
Phenolic compounds (mg L^{-1})	0.5	-
TSS (mg L^{-1})	30	60
Cl^- (mg L^{-1})	60	70
SO_4^{2-} (mg L^{-1})	50	575
SAR	27	8

Table 3. Physical and chemical characterization of the treated wastewater and standard parameter

5. Conclusion

In this type of seasonal industry, the treatment system must be able to treat the wastewater produced in all labour period. A vertical reactor coupled with highly efficient Venturi injector and multiplier nozzles was used for winery wastewater treatment. Regarding mass transfer parameters, the estimation of OTR could be interesting for studying the influence of operational conditions on volumetric mass transfer coefficient. The results showed a decrease in the k_La value during the treatment period. This decrease in k_La value may evidence that some of the existing compounds in wastewater optimize the oxygen mass transfer during the initial phase of treatment.

The SOUR measurements throughout the wastewater treatment showed high values, which could indicate a high organic load to the existing suspended solids in the mixed liquor. This high SOUR rate is due to the high activity of the microbial population to oxidise substrates, in the begging of the treatment.

The implemented strategy, where an aerobic step alternated with an anoxic one was adopted, showed to be a good approach to minimize the sludge production and to reduce energetic.

However, further studies should be conducted in order to better understand the effect of winery wastewater composition in mass transfer coefficients. The use of two consecutive

stages of treatment might improve the performance of this technology because it allows higher flexibility. The result of feast / famine treatment in sludge should also be exploited, as it is of interest in this type of seasonal industries.

Moreover, the treated wastewater revealed its suitability to be integrated in the irrigation systems as confirmed by direct toxicity bioassays. This study is expected to contribute to the implementation of an efficient wastewater treatment, intending the preservation of the water resource, the reduction of the wastewater sludge production and the energy safe.

6. Acknowledgment

Fundação para a Ciência e a Tecnologia (FCT) – PhD grant SFRH/BD/31653/2006, by finantial support and Quinta da Casaboa, Catapereiro and Herdade da Mingorra where the studies were conducted.

7. References

Andreottola, G., Foladori P., Ragazzi, M. & Villa, R. (2002). Treatment of winery wastewater in sequencing batch bofilm reactor. *Water Science and Technology* Vol. 45, No.12, pp. 347–354, ISSN 0273-1223.

Andreottola, G., Foladori P. & Ziglio, G. (2009). Biological treatment of winery wastewater: an overview. *Water Science and Technology* Vol. 60, No.5, pp. 1117–1125, ISSN 0273-1223.

A.P.H.A., A.W.W.A., W.E.F. (1998) *Standard methods for the examination of water and wastewater*, 20ª Ed., USA.

Arienzo, M., Christen, E.W., Quayle, W (2009a). Phytotoxicity testing of winery wastewater for constructed wetland treatment. *Journal of Hazardous Materials*, Vol. 169, No. 1, pp. 94-99, ISSN 0304-3894.

Arienzo, M., Christen, E.W., Quayle, W, Di Stefano, N. (2009b) Development of a Low-Cost Wastewater Treatment System for Small-Scale Wineries. *Water Environment Research*, Vol. 81, No. 3, pp. 233-241, ISSN 1061-4303.

Artiga,P.,Ficara,E.,Malpei,F.,Garrido,J.M. & Méndez,R.,2005. Treatment of two industrial wastewaters in a submerged membrane bioreactor. *Desalination*, Vol. 179, pp. 161-169, ISSN 0011-9164.

Beltran de Herédia J., Torregrosa J., Dominguez J.R. and Partido E. (2005). Degradation of wine distillery wastewaters by the combination of aerobic biological treatment with chemical by Fenton's reagent. *Water Science and Technology*, Vol. 51, No. 1, pp. 167-174, ISSN 0273-1223.

Bolzonella, D. & Rosso, D. (2007). Winery wastewater characterisation and biological treatment options. *Water Science and Technology*, Vol. 56, No. 2, pp. 79–87, ISSN 0273-1223.

Chen, G., Yip, W., Mo, H., Liu, Y. (2001). Effect of sludge fasting/feasting on growth of activated sludge cultures. *Water Research*. Vol. 35, No. 4, pp.1029-1037, ISSN: 0043-1354.

Choi, K.H., Christi, Y., Moo-Young, M. (1996). Comparative evaluation of hydrodynamic and gas-liquid mass transfer characteristics in bubble column and airlift slurry reactors. *The Chemical Engineering Journal,* Vol. 62, pp. 223-229. ISSN 0923-0467.

Coetzee G., Malandra, L., Wolfaardt, G.M. & Viljoen-Bloom, M., (2004). Dynamics of microbial biofilm in a rotating biological contactor for the treatment of winery effluent. *Water SA*, Vol. 30, No. 3, pp. 407-412.

Duarte E., Reis I.B., Martins M.O. (2004). *Proceedings of 3rd Internat. Special. Conf. Sustainable Vitic. Winery Wastes Management*, Barcelona 23-30.

Eusébio A., Mateus M., Baeta-Hall L., Almeida-Vara E., Duarte J.C. (2004). Microbial characterization of activated sludge in Jet-loop bioreactor treating winery wastewater. *Journal of Industrial Microbiology and Biothechonogy*. Vol. 31, 29-34, ISSN 1476-5535.

Eusébio A., Mateus M., Baeta-Hall L., Almeida-Vara E., Duarte J.C. (2005). Microflora evaluation of two agro-industrial effluents treated by the JACTO jet-loop type reactor system, *Water Science and Technology*. Vol. 51, 107-112, ISSN 0273-1223.

Fakeeha, A.H., Jibril, B.Y., Ibrahim, G., Abasaeed, A.E. (1999). Medium effects on oxygen mass transfer in plunging jet loop reactor with a downcomer. *Chemical Engineering and Processing,* Vol. 38, pp. 259-265, ISSN: 0255-2701.

Fayolle, Y., Gillot, S., Cockx, A., Bensimhon, L., Roustan, M., Heduit, A. (2010). *In situ* characterization of local hydrodynamic parameters in closed-loop aeration tanks. *Chemical Engineering Journal*, Vol. 158, pp. 207-212, ISSN: 1385-8947

Fuentes A., Lloréns M., Sáez J., Aguilar M.I., Ortuño J.F. and Meseguer V.F. (2004). Phytotoxicity and heavy metals speciation of stabilized sewage sludges. *Journal of Hazardous Materials*, Vol. 108 No. 3, pp. 161–169, ISSN: 0304-3894.

Garcia-Ochoa, F. & Gomez,E. (2009). Bioreactor scale-up and oxygen transfer rate in microbial processes: An overview. *Biotechnology Advances*, Vol. 27, pp.153-176, ISSN: 0734-9750.

Grismer M.E., Carr M.A., Shepherd H.L. (2003). Evaluation and constructed wetland treatment performance for winery wastewater. *Water Environment Research*, Vol. 75, pp. 412-421, ISSN 1061-4303.

Irizar, I., Zambrano, J.A., Montoya, D., Gracia, M., Garcia, R. (2009). Online monitoring of OUR, KLa and OTE indicators: pratical implementation in full-sacele industial WWTPs. *Water Science and Technology* Vol. 60, No. 2, pp. 459-466, ISSN 0273-1223.

Jourjon, F., Khaldi, S., Reveillere, M., Thibault, C., Poulard, A., Chretien, P., Bednar, J. (2005). Microbiological characterization of winery effluents: an inventory of the sites for different treatment systems , *Water Science and Technology*. Vol. 51, 19-26, ISSN 0273-1223.

Liu, Y. & Tay, J.H. (2001). Strategy for minimization of excess sludge production from activated sludge process. *Biotechnology Advances*, 19, 97-107, ISSN: 0734-9750.

López-Palau, S. Dosta, J. & Mata-Alvarez, J. (2009). Start-up of aerobic granular sequencing batch reactor for the treatment of winery wastewater. . *Water Science and Technology* Vol. 60, No. 4, pp. 1089-1095, ISSN 0273-1223.

Malandra, L. Wolfaardt, G., Zietsman, A., Viljoen-Bloom, (2003). Microbiology of biological contactor for winery wastewater treatment. *Water Research*, Vol. 37, pp. 4125-4134, ISSN: 0043-1354.

Meyer R.M., Mazzei A.L. and Mullin J.R. (2004). Aerobic treatment of winery wastewater utilizing new aeration technology. In: *Proceedings of the 3rd International Specialised Conference on Sustainable Viticulture and Winery Wastes Management,* Barcelona, 353-355.

Moletta, R. (2009). Biological treatment of wineries and distillery wastewater. *Proceedings of 5th International Specialized Conference on Sustainable Viticulture Winery Wastes and Ecological Impact Management*. pp. 389-398, ISBN 978-88-8443-284-1, Trento and Verona, 30 Mar-3 Apr.

Moletta R. (2005). Winery and distillery wastewater treatment by anaerobic digestion. *Water Science and Technology* Vol. 51, No.1, pp. 137–144, ISSN 0273-1223.

Oliveira, M., Queda, C., Duarte, E. (2009). Aerobic treatment of winery wastewater aiming the water reuse. *Water Science and Technology* Vol.Vol. 60, No. 5, pp.1217-1223. ISSN 0273-1223.

Oliveira, M. & Duarte, E. (2010). Guidelines for the management of winery wastewaters. *Proceedings of 14th Ramiran International Conference on Treatment and Use of Organic Residues in Agriculture: Challenges and Opportunities Towards Sustainable Management*, Lisboa, 12-15 Sept.

Pérez-Elvira, S. I., Diez, P.N., Fdz-Polanco, F. (2006). Sludge minimisation technologies. *Reviews in Environmental Science and Biotechnology*, Vol. 5, pp. 375-398, ISSN: 1569-1705.

Petruccioli M., Duarte J.C., Eusébio A. and Federici F. (2002). Aerobic treatment of winery wastewater using a jet-loop activated sludge reactor. *Process Biochemistry*, Vol. 37, No. 8, pp. 821-829, ISSN: 1359-5113.

Petruccioli M., Duarte J.C. and Federici F. (2000). High-rate aerobic treatment of winery wastewater using bioreactors with free and immobilized activated sludge. *Journal of Bioscience and Bioengineering* ,Vol. 90, No. 4, 381-386, ISSN: 1389-1723.

Puig, S., Corominas, L., Traore, A., Colomer, J., Balaguer, M.D., Colprim, J. (2006). An on-line optimization of a SBR cycle for carbon and nitrogen removal based on on-line pH and OUR: the role of dissolved oxygen control. . *Water Science and Technology* Vol. 53, No.4-5, pp. 171–178, ISSN 0273-1223.

Racault Y. and Stricker A.E.(2004). Combining membrane filtration and aerated storage: assessment of two full scale processes treating winery effluents. In: *Proceedings of the 3rd International Specialised Conference on Sustainable Viticulture and Winery Wastes Management,* Barcelona, 105-112.

Ramakrishna, D.M. & Viraraghavan, T. 2005. Strategies for sludge minimization in activated sludge process – a review. Fresenius Environmental Bulletin, Vo. 14, No.1, pp. 2-12, ISSN: 1018-4619.

Tojabas, M., Garcia-Calvo, E. (2000). Comparison of experimental methods for determination of the volumetric mass transfer coefficient in fermentation processes. *Heat and Mass Transfer*, Vol. 36, pp. 201-207.

Tandoi, V., Jenjins, D., Wanner, J. (2006). Activated sludge separation problems. *Scientific Technical Report 16*, 216 pp., ISBN: 1900222841.

Torrijos, M. & Moletta, R. (1997). Winery wastewater depollution by sequencing batch reactor. *Water Science and Technology* Vol. 35, No.1, pp. 249–257, ISSN 0273-1223.

van Schoor, L.H. (2005). Guidelines for the management of wastewater and solid waste at existing wineries. *Winetech*, 35 pp.

Xu, Y. Zhou, J., Qu, Y., Yang, H., Liu, Z. (2010). Dynamics and oxygen transfer of a noval vertical tubular biological reactor for wastewater treatment. *Chemical Engineering Journal* Vol. 156, pp. 92–97, ISSN 0273-1223.

Part 4

Advances in Materials Engineering Aspects

18

Light-Induced Surface Diffusion

Tigran Vartanyan, Sergey Przhibel'skii,
Valerii Khromov and Nikita Leonov
St. Petersburg State University of Information Technologies, Mechanics and Optics
Russian Federation

1. Introduction

Surface diffusion of indigenous and/or foreign atoms plays a key role in a number of physical and chemical processes. To name a few, it is important in crystal growth and epitaxy, heterogeneous catalysis, nucleation and growth of supported nanoparticles, and so on. Finding a reliable tool to control the surface diffusion processes is an attractive goal for many modern technologies.

Optical photons being absorbed by the surface or by the species adsorbed onto it can alter the surface diffusion considerably. At lager intensities of illumination these alternations are mainly due to the temperature rise, while at the lower intensities non-thermal mechanisms of light-induced surface diffusion are operative. The latter are the subjects of this chapter.

The electronic excitation follows after the photon absorption and changes the forces exerted by the surface onto the adsorbed atoms. After a short period of time the energy of the photon is partitioned between the surface and the adsorbed atom. The excess energy obtained by the adsorbed atom results in the increased desorption rates from as well as diffusion rates over the surface.

An inhomogeneous illumination of the surface leads to the inhomogeneous steady state distribution of the adsorbed atoms over the surface. The situation is similar to the Soret effect but require a special theoretical consideration that is presented in this chapter. An unexpected result of the theoretical analysis is that the spatial distribution of the surface number density of the adsorbed atoms is non monotone. There is a pronounced maximum of the surface number density of the adsorbed atoms at the boundary between the illuminated and the dark regions.

The shapes of the supported metal nanoparticles obtained via Volmer-Weber growth mode are metastable. Heating is known to speed up the equilibration of the particles shapes. In our experiments with silver and sodium nanoparticles supported on dielectric surfaces we found evidences of the reversible changes of the particle shapes. Hence, the temperature of the substrate determines the equilibrium shape of the nanoparticles. In the case of sodium, illumination speeds up the particles reshaping. This process is rationalized in terms of the light-induced diffusion of the indigenous atoms over the metal nanoparticle surface, while the main step of the process is identified as the photo-induced detachment of an atom from the terraces. The latter is found to be the rate limiting step in the nanoparticle reshaping process.

2. Nature of the photo-induced surface diffusion process

The effect of surface photodiffusion is closely related to the well-known process of photodesorption, because both processes begin with the resonance absorption of a light quantum by an atom adsorbed on the surface of a transparent substrate. From the theoretical point of view, the existence of photostimulated diffusion is justified by analysis of the previously established mechanism of photodesorption of resonantly absorbing atoms adsorbed on a transparent substrate (Bonch-Bruevich et al., 1990). Upon the resonant optical excitation of the electronic subsystem of an adsorbed atom, the energy of the photon is converted, rapidly and virtually completely, into vibrational degrees of freedom of the adsorbed atom and its nearest environment on the surface. Only in rare cases is the portion of energy gained by the adsorbed atom sufficient for it to overcome the adsorption potential and be desorbed. It is much more likely that this energy is insufficient for the atom to be desorbed. On the other hand, if we take into account that the activation energy of the surface diffusion is several times smaller than the adsorption energy, it becomes evident that photoexcitation should substantially affect the frequency of hopping of adsorbed atoms between neighboring minima of the adsorption potential even at low intensities of illumination, when the photodesorption rate is still not sufficient to significantly change the surface density of adsorbed atoms. Under nonuniform illumination, this gives rise to a surface flow of particles, which, in the first order in the light intensity, is proportional to the irradiance gradient. Note that photodiffusion does not remove the adsorbed atoms from the surface but rather redistributes them, so that a decrease in the surface density in some places is accompanied by an increase in the density of adsorbed atoms in other locations.

3. Case study: Cesium on sapphire

As the object of study, a system of cesium atoms adsorbed on the surface of a single-crystal sapphire was used. This system has been thoroughly studied previously (Bonch-Bruevich et al., 1985, 1990, 1997). The advantages of this system are the chemical inertness of sapphire and its transparency in a wide spectral range, covering the entire visible and near-IR regions, in which the adsorbed cesium atoms exhibit strong optical absorption. This allows one, using convenient laser sources, to selectively excite cesium atoms leaving the substrate unexcited. Saturated vapors of cesium atoms were placed into a sealed glass cell with sapphire windows. The volume density of the atoms at room temperature was 10^{10} cm^{-3}. The experiments were performed under conditions of dynamic equilibrium between the volume phase and the phase adsorbed on the surface. According to (Bonch-Bruevich et al., 1985, 1997) the energy of adsorption of the atoms on the sapphire surface is 0.6 eV, which provides, at room temperature, a surface density of the adsorbed atoms $n_0 = 10^{13} cm^{-2}$. Thus, the surface density of the adsorbed atoms appears to be fairly high, though still much lower than a monolayer.
Variations of the surface density of the adsorbed atoms induced by high-power radiation were detected by measuring the transmission of a relatively weak probe light of a cw semiconductor laser. Using the value of the absorption cross section of the adsorbed atom (Bonch-Bruevich et al., 1985, 1997) $\sigma = 3 \times 10^{-16} cm^2$, we find that the absorption in the adsorbed layer makes up $n_0\sigma = 3 \times 10^{-3}$ of the total intensity of the light passing through the layer. Thus, absorption of this kind can be reliably measured using low-noise high-intensity semiconductor lasers.

Among the important advantages of the chosen system is a relatively low quantum yield of the photodesorption process. According to (Bonch-Bruevich et al., 1985, 1997), it is as low as 10^{-5}. This allowed us to hope that the main mechanism for light-induced changes in the surface density of the atoms would be the photoinduced diffusion rather than photodesorption. As shown below, these expectations were fulfilled. Since the excitation of an adsorption system by high-power optical radiation induces both the photodesorption of atoms from the surface and their photodiffusion over the surface and, in addition, is accompanied by dark desorption and diffusion, we performed experiments of two types.

In the experiments of the first type, we studied the processes of photodesorption and dark desorption. For this purpose, the cesium atoms adsorbed on the sapphire surface were desorbed by single pulses of a ruby laser generating at a wavelength of 694 nm. The diameter of the irradiated spot varied from 1 to 4 mm. After the end of the strong desorbing pulse, the surface density of the adsorbed atoms gradually recovered. The kinetics of the recovery of the surface density was detected by measuring the intensity of a semiconductor laser beam transmitted through the irradiated area of the sapphire window of the cell. The intensity of the transmitted light at the wavelength 840 nm was measured by an FD-7K photodiode and was monitored by an S8-17 storage oscilloscope. At room temperature, the characteristic time of recovery of the surface density was 25 s. It was verified that this time did not depend on the radius of the irradiated spot within the limits indicated above. This allowed us to assign it exclusively to the process of deposition of atoms from the gas phase, rather than to their surface diffusion from dark regions, because in the latter case the recovery time would be dependent on the radius of the irradiated spot. From these experimental data, we determined the rate of thermal desorption to be $\tau=0.04\ s^{-1}$.

The photostimulated diffusion was studied by irradiating the surface with a cw beam of an argon laser at the wavelength 514.5 nm and a power of 1 W. The focused probe beam of a semiconductor laser ($20\times30\ \mu m^2$ in size) was scanned in such a way that it could repeatedly pass both regions of the surface subjected and regions not subjected to the optical treatment. The scanning was implemented using a lightweight mirror glued to the diaphragm of a high-power loudspeaker. The loudspeaker was fed by a sine voltage from a low frequency oscillator. The scanning range of the probe beam exceeded by approximately an order of magnitude the diameter of the exciting beam, which varied within the range 30–130 μm. After passing through the cell, the probe beam was detected by a photodiode. The signal thus obtained was amplified by a selective amplifier at a scanning frequency of 30 Hz and was detected by a lock-in amplifier with an XY recorder at the output. The time resolution of the setup was 0.5 s.

Because of different absorption in regions with higher and lower surface densities of adsorbed atoms, the intensity of the transmitted beam was modulated at the beam scanning frequency. Under the conditions described above, when the changes in the transmittance are concentrated within a region that is small compared to the whole scanning length, the amplitude of the first modulation harmonic in the transmitted beam, detected in the experiment, is proportional to the integral of variation of the surface density of the adsorbed atoms along the beam scanning path. In the experiment, we measured the kinetics of changes in the surface density of atoms after the argon laser beam was rapidly switched on and off. It was found that, as in the first experiments, for large spots of the exciting beam (~0.5 mm), this kinetics was exponential, with a rise and decay time of 25 s, and did not depend on the exciting beam power. It was verified that the amplitudes of the observed

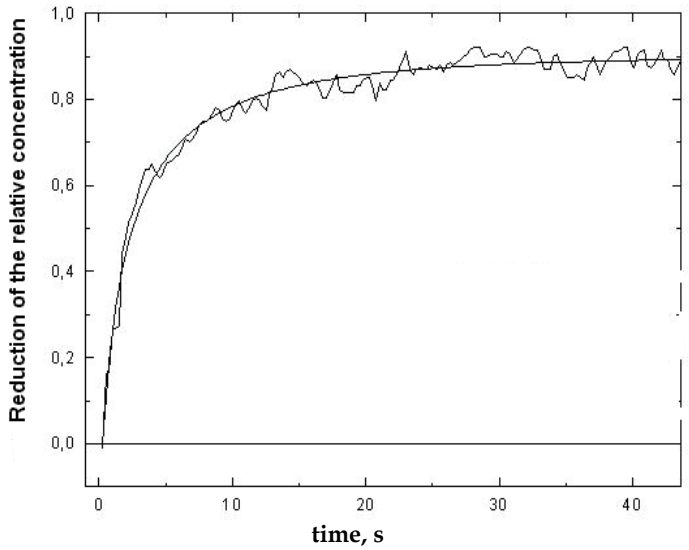

Fig. 1. Decrease of the surface concentration under illumination

signals varied linearly with the exciting beam power, while the changes in the surface density of the atoms did not exceed 20% of the equilibrium value. Upon a decrease in the diameter of the pump beam to 110 μm, the kinetics of the variation of the surface density of atoms changed sharply (Fig. 1). It is seen that, for such a small size of the irradiated area, the steady-state surface density of the particles is established during times substantially shorter

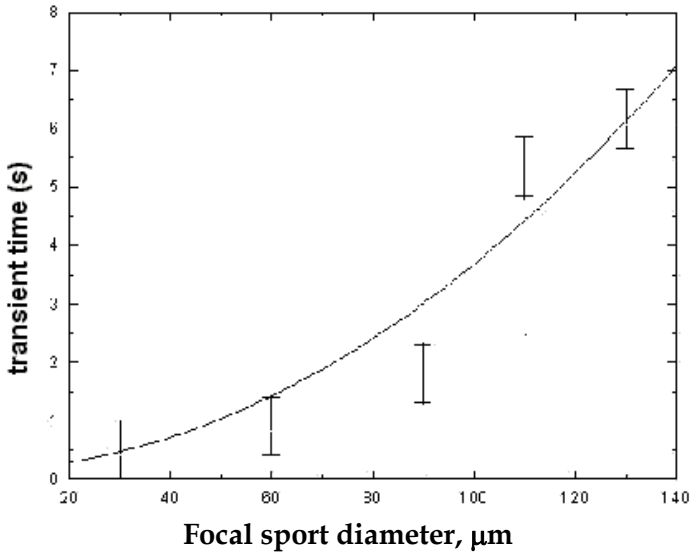

Fig. 2. Dependence of the transient time on the focal spot diameter

than the characteristic time for establishment of equilibrium with the volume phase, measured in the previous experiment. Since this time, as before, did not depend on the beam power but decreased quadratically with a decrease in the diameter of the pump beam from 130 to 30 μm (Fig. 2), we concluded that the time of transition to the steady state was governed by the rate of dark diffusion of the atoms over the surface. In addition, it can be concluded that the main contribution to the decrease in the surface density of atoms is made by photodiffusion rather than by photodesorption. Indeed, if the decrease in the surface density were related to the photodesorption, such a decrease of the density would occur until the surface was totally depleted. Moreover, recovery of the steady-state value of the surface density after the exciting radiation has been turned off could occur only from the gas phase with a characteristic time of 25 s.

From the fact that the times of transition to the steady-state value of the surface density of atoms when the pump beam was turned on and off were approximately the same, while the signal amplitudes varied linearly with the pump beam intensity, we concluded that the photodiffusion process is substantially slower than the dark diffusion and can be described in the linear approximation..

4. Theoretical description of the photo-induced surface transport

To derive the equation describing photodiffusion, we will use the standard scheme of the diffusion approximation (Lifshitz & Pitaevskii 1981). Let $n(r)$ be the surface density of particles at the point $r= (x,y)$ and $\nu(r,a)$ be the probability of hopping of an atom from the point r to the point $r–a$. Then the change in the surface density of the particles at the point r is determined by the difference between the numbers of particles arriving at this point from neighboring positions and leaving this point

$$\partial n(t,\mathbf{r}) / \partial t = \int \{ \mathrm{v}(\mathbf{r}+\boldsymbol{a},\boldsymbol{a}) n(t,\mathbf{r}+\boldsymbol{a}) - \mathrm{v}(\mathbf{r},\boldsymbol{a}) n(t,\mathbf{r}) \} \, d^2 a \tag{1}$$

Because the photoinduced inhomogeneities of the surface density and the photoinduced changes in the hopping frequency are characterized by a spatial scale of the order of the light wavelength, while the length of the hops of the adsorbed atoms is much smaller than this value, the integrand can be represented as a series expansion, using the hop length as a small parameter. By retaining the first two terms in the expansion, we may rewrite (1) in the form

$$\partial n / \partial t = \partial_j (\mathrm{A}_j n) + \partial_j \partial_l (\mathrm{B}_{jl} n) \,, \tag{2}$$

where

$$\mathrm{A}_j(\mathbf{r}) = \int a_j \mathrm{v}(\mathbf{r},\boldsymbol{a}) \mathrm{d}^2 \boldsymbol{a} \,, \;\; \mathrm{B}_{jl}(\mathbf{r}) = \frac{1}{2} \int a_j a_l \mathrm{v}(\mathbf{r},\boldsymbol{a}) \mathrm{d}^2 \boldsymbol{a} \tag{3}$$

and the sum over j and l that attain the values of x and y is assumed.

Since the surface is, by itself, homogeneous and isotropic and its irradiation affects only the hopping rate and does not break this isotropy, among all the quantities presented above, only the B_{xx} and B_{yy}, equal to each other, are nonzero. Their common value may be naturally denoted by $D(r)$,

$$B_{xx}(\mathbf{r}) = B_{yy}(\mathbf{r}) = D(\mathbf{r}) = \frac{1}{2}\int a_j a_l \nu(\mathbf{r}, \boldsymbol{a}) d^2\boldsymbol{a} \quad (4)$$

since, in the absence of irradiation, D(r) is reduced to D_0, i.e., to the coefficient of the dark surface diffusion, which does not depend on the surface coordinates.

According to Eq. (4), the diffusion coefficient can be interpreted as a product of the hop frequency and the mean square of the displacement per hop. In the absence of irradiation, the frequency of hops can be estimated as a product of the vibration frequency of an adsorbed atom and the Boltzmann factor, which controls the probability of the atom overcoming the diffusion barrier at a given temperature of the surface. In this case, the displacement per hop coincides, in order of magnitude, with the distance between neighboring minima of the adsorption potential. In the case of photostimulated diffusion, the frequency of hops is determined by the probability of a photon being absorbed by an adsorbed atom. The displacement per hop may be, generally speaking, larger than in conventional diffusion, because the energy received by an adsorbed atom upon absorption of a photon substantially exceeds the mean thermal energy and, probably, the height of the diffusion barrier. Note that, in the approximation linear with respect to the pump power, the frequency of the photoinduced hops is directly proportional to the intensity, while their length is intensity-independent.

By separating, in Eq. (4), the contributions of thermal and photostimulated hops, we may represent D(r) in the form

$$D(r) = D_0 + D_*(r) \quad (5)$$

where $D_*(r)$ is the photodiffusion coefficient, proportional to the intensity of irradiation at point r. With these notations, Eq. (2) becomes

$$\partial n/\partial t = \Delta\left[D(r)n(r)\right] \quad (6)$$

where Δ is the two-dimensional Laplace operator. Equation (6) allows us to describe the photodiffusion effect completely. In the next section, we will complement its right-hand side with the terms necessary to describe a number of concomitant processes important under our experimental conditions. The right-hand side of Eq. (6) differs from the conventional form of the diffusion equation with the coordinate-dependent diffusion coefficient div[D(r)gradn(r)] by the additional term div[n(r)gradD(r)]. This important distinction results from the fact that the conventional diffusion equation describes the transition to equilibrium, whereas Eq. (6) describes the transition to an established but not completely equilibrium state, caused by the nonuniform irradiation of the surface. Under these conditions, the diffusion flow is a sum of two terms, namely, the conventional contribution, proportional to the density gradient, and the photoinduced contribution, proportional to the illuminance gradient.

Various forms of the diffusion equation were discussed in (van Kampen, 1992; Zangwill 1988). An expression for the right-hand side of the diffusion equation having a similar structure is obtained for the case of thermodiffusion (Lifshitz & Pitaevskii, 1981), where the incompleteness of the equilibrium results from a specified inhomogeneity in the temperature distribution of the gas mixture.

Equation (6) fully describes the photodiffusion effect. However, to experimentally prove its existence, the theoretical model should be extended to include photodesorption, which

inevitably accompanies photodiffusion, as well as the usual thermal desorption and deposition of atoms from the gas phase onto the surface. These processes will be taken into account in the next section. This will allow us to unambiguously separate out the contribution of photodiffusion to the experimentally observed phenomena.

4.1 Influence of the surface - Gas phase exchange

Under conditions of direct contact between the surface and the gas phase, Eq. (6) should include terms describing the deposition of atoms onto the surface from the gas phase and their thermal desorption from the surface. In addition, the right-hand side of Eq. (6) should be complemented with terms describing the photodesorption, whose rate, along with the photodiffusion coefficient, is proportional to the illuminance. The most complete equation may be written in the form

$$\partial n/\partial t = \Delta\left[D(r)n(r)\right] - \Gamma(r)n + J - n\tau \ , \tag{7}$$

where J is the flow of atoms to the surface from the gas phase, τ is the thermal desorption rate, and Γ(r) is the rate of photodesorption. In the absence of light, the surface density is the same at any point and is equal to

$$n_0 = J/\tau \tag{8}$$

Let us separate out the relative change in the surface density p due to illumination according to the formula

$$n = n_0\left(1 + p\right) \tag{9}$$

Assuming p to be small compared with unity, we may neglect the terms containing the product of p and the rates of the photoinduced processes. Then Eq. (7) will acquire the form

$$\partial p/\partial t - D_0\Delta p + p\tau = \Delta D_* - \Gamma(r)n \tag{10}$$

The entire subsequent theoretical analysis is based on Eq. (10).

4.2 Surface density wells and humps due to photodiffusion

By introducing the new sought-for function

$$q\left(t,r\right) = \left[p(t,r)\right] + D_*\left(r\right)/D_0\ \Big]\exp(\tau t) \tag{11}$$

we transform Eq. (10) into a standard form of the inhomogeneous diffusion equation

$$\partial q/\partial t - D_0\,\Delta q = f\left(t,r\right) \tag{12}$$

where

$$f\left(t,r\right) = \left[\,\tau D_*\left(r\right)/D_0 - \Gamma\left(r\right)\right]\exp\left(\tau t\right) \tag{13}$$

Equation (12) may be solved using conventional methods (Vladimirov, 1971) for arbitrary initial conditions and an arbitrary form of the right-hand side, which is determined by the distribution of the illumination intensity.

Turning back to the function $p(t, r)$, let us write out the solution of Eq. (10) corresponding to instantaneous switching on, at t=0, of a normally incident axisymmetric Gaussian beam. By denoting the effective radius of the beam by a, the intensity-dependent photodesorption rate and photodiffusion coefficient may be represented in the form

$$\Gamma(r) = \gamma \exp\left(-r^2/a^2\right), \quad D_*(r) = D_*(0)\exp\left(-r^2/a^2\right). \tag{14}$$

Assume that the surface density of the adsorbed atoms at t=0 was equilibrium $p(t$=0, $r)$=0. Then, for $t > 0$, we have

$$\begin{aligned} \mathrm{p}(t,r) = {} & \frac{D_*(0)}{D_0}\left[\exp\left(-\frac{r^2}{a^2}\right) - \frac{a^2}{a^2+4D_0t}\exp\left(-\frac{r^2}{a^2+4D_0t} - t\tau\right)\right] - \\ & \frac{a^2}{D_0}\left[\gamma - \tau\frac{D_*(0)}{D_0}\right]\int_0^{D_0t/a^2} (1+4u)^{-1}\exp\left[-\frac{r^2}{a^2(1+4u)} - \frac{a^2\tau}{D_0}u\right]du \end{aligned} \tag{15}$$

Consider, first, the photostimulated diffusion effect in its pure form, when one may neglect not only the photodesorption, but also the processes of adsorption of atoms from the gas phase and their thermal desorption. For this purpose, we suppose that, in Eq. (15), $\gamma = \tau = 0$.

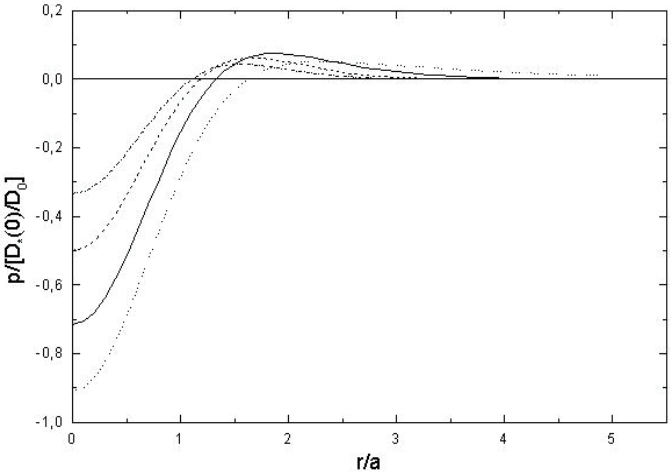

Fig. 3. A well and a hump in the surface number density due to the photodiffusion out of the illuminated region

The dependence of the surface density of the adsorbed atoms on the distance from the center of the light beam at different time moments is shown in Fig. 3. It is seen that, as a result of the photodiffusion, the surface density at the beam center decreases while increasing at the periphery. The boundary between the regions of increasing and decreasing density, r_1, shifts in time according to the equation

$$r_1 = a[(1 + a^2 / 4D_0t)\ln(1 + 4D_0t / a^2)] \tag{16}$$

and the greatest increase in the density is located at the distance $r_2 = r_1\sqrt{2}$. At t much smaller than $a^2/4D_0$, the value r_1 is close to a at t much larger than $a^2/4D_0$, the value of r_1 slowly increases.

The density minimum, attained at large times at the beam center, corresponds to $p(t=\infty, r=0)=-D_*(0)/D_0$, while the maximum increase in the relative density, attained at $t=2.513a^2/D_0$ at the distance $r=1.87a$, equals 7.5% of $D_*(0)/D_0$.

When all processes except for the photostimulated diffusion are neglected, the number of adsorbed particles does not change, so that, for any moment of time, the integral of $p(t, r)$ over the whole surface is zero.

The results obtained above should be compared with those that would have been obtained in the absence of the photostimulated diffusion, when the effect of light is reduced only to photodesorption. By setting $D_*(0)=0$ in Eq. (15), we have

$$\mathrm{p}(t,r) = \frac{a^2}{D_0}\int_0^{D_0 t/a^2} (1+4u)^{-1}\exp[-\frac{r^2}{a^2(1+4u)} - \frac{a^2\tau}{D_0}u]du \tag{17}$$

It is evident from the form of the integrand that the relative role of the processes of thermal desorption and thermal diffusion depends on the radius of the light beam a. If a^2 is much larger than D_0/τ, the main contribution to the integral is made by the region $u<<1$, and we may approximately write

$$\mathrm{p(t},r) = \frac{\gamma}{\tau}[1-\exp(-t\tau)]\exp(-r^2/a^2) \tag{18}$$

In this case, the surface density of the adsorbed atoms decreases in exact correspondence with the local illuminance, and the kinetics of this decrease is controlled only by the rate of thermal desorption. If $a^2>>D_0/\tau$, the change in the density at the center of the illuminated region, for times $t<1/\tau$, is described by the function

$$\mathrm{p}(t,r) = -(a^2\gamma/4D_0)\ln(1+4D_0t/a^2) \tag{19}$$

This equation shows that thermal diffusion cannot stabilize a surface density perturbed by the photodesorption process. The surface density, in this case, decreases infinitely until the process of deposition from the gas phase becomes noticeable or until the conditions for applicability of the linear approximation in the pump beam intensity are violated. When Eq. (17) is valid, the radial dependence of the surface density is monotonic. No increase in the surface density is possible in the absence of photodiffusion.

In the experimental study of the photostimulated diffusion, a Gaussian beam with the effective radius b was scanned through the center of a region with the modified surface density. As shown in the next section, at $b<<a$, the experimentally measured quantity can be represented in the form of an integral $S(t)$ of the surface density variation over the straight line passing through the center of the illuminated region,

$$S(t) = n_0 b\sqrt{\pi}\int_{-\infty}^{\infty} \mathrm{p(x}=0,y,t)dy \tag{20}$$

When b is comparable with a, then Eq. (20) should be replaced by an integral of variation of the surface density over the whole surface with a weight proportional to the probe beam intensity along the scanning path. In this case, Eq. (20) should be replaced by

$$S(t) = n_0 \iint p(t,x,y) e(-x^2 / a^2) dxdy \tag{21}$$

By substituting the solution (15) found above into Eq. (21), we have

$$S(t) = -n_0 ab\sqrt{\pi} \left\{ \begin{array}{l} \dfrac{a^2\gamma}{D_0} \displaystyle\int_0^{D_0 t/a^2} \dfrac{\exp(-a^2\tau u / D_0)du}{(1+4u+b^2/a^2)^{1/2}} \\ +2(D_*(0)/D_0) \displaystyle\int_0^{D_0 t/a^2} \dfrac{\exp(-a^2\tau u / D_0)du}{(1+4u+b^2/a^2)^{3/2}} \end{array} \right\} \tag{22}$$

Equation (22) describes the process that occurs after the pump beam is turned on. After the pump beam is turned off, the surface density recovers to its equilibrium value. In the approximations adopted here, the kinetics of recovery of the equilibrium concentration does not differ from that of its perturbation, because the rates of the photoinduced processes are assumed to be low compared with those of the processes leading to recovery of the equilibrium. This condition is well satisfied in the experiment.

5. Theory of the photo-induced surface diffusion versus experimental findings

Let us compare the kinetics of the surface density of adsorbed atoms measured in the experiments (Fig. 2) with the results of theoretical analysis. If the process of adsorption from the gas phase, whose rate is equal to that of the thermal desorption τ, is neglected, then the first integral in Eq. (22), corresponding to the photodesorption process, is reduced to the simple square-root dependence

$$\left(1+4t/T\right)^{-1/2} - 1 \tag{23}$$

infinitely growing with time, which contradicts the experimental data. Here,

$$T = \left(a^2 + b^2\right) \Big/ D_0 \tag{24}$$

is the characteristic time of the signal variation, related only to the diffusion processes. Under these conditions, the second integral in Eq. (22), corresponding to the photodiffusion process, is also simplified and yields a time dependence gradually approaching the steady-state value,

$$1 - \left[1 + 4t/T\right] \tag{25}$$

Equation (25) adequately describes the experimental nonexponential kinetics of variation of the surface density of the adsorbed particles, excluding long times, when the effect of adsorption from the gas phase becomes noticeable. In Fig. 1, the results of the measurements for the laser beam diameter of 110 μm are compared with the theoretical curve constructed by using the exact formula (22). By comparing the theoretical and experimental dependences, we can find the characteristic diffusion time T. Fig. 2 shows the dependence of T on the pump beam diameter, which, according to (23), should be quadratic. The best agreement with the experimental data is obtained for D_0=7×10^{-6} cm^{2}s^{-1}. If we assume that

the diffusion is of activation nature, with the length of an elementary hop being equal to a few tenths of a nanometer and with attempts to overcome the barrier occurring at the frequency of vibrational motion of the adsorbed atom, i.e., every several tenths of a picosecond, then the activation barrier for the diffusion can be estimated to be about 0.1 eV. This value agrees with the empirical "one sixth" rule (George et al., 1985) for the ratio of diffusion barrier height to adsorption energy. Since the photodiffusion coefficient $D_*(0)$ is proportional to the pump intensity $I(0)$, it may be naturally written in the form $D_*(0) = \kappa I(0)$, where the value of κ equals, according to the results of the measurements, 2×10^{-10} cm^{4}J^{-1}. If we compare this value with the absorption cross section for the adsorbed atoms, which controls the frequency of the photoinduced hops, we come to the conclusion that the mean square of displacement of an adsorbed atom per absorbed photon is of the order of 100 nm^2.

The above findings mean, first, that the photoinduced diffusion does not require overcoming any energy barrier and, second, that the rate of relaxation of the excess atomic energy is rather low (of the order of 10^{10}–10^{11} s^{-1}). The first assertion agrees fairly well with the mechanism of the photoinduced diffusion discussed above, because the effective temperature of an adsorbed atom that has absorbed a photon is comparable with the value of the diffusion barrier. The low rate of the energy relaxation of an adsorbed atom upon its interaction with the surface of sapphire was already noted by us previously, both in measuring the accommodation coefficients of atoms upon their impact on the surface (Bonch-Bruevich et al., 1990) and in studying the quasi-thermal regime of photodesorption of sodium atoms from the sapphire surface (Bonch-Bruevich et al., 1999), where the energy relaxation rate was also estimated to be of the order of 10^{10} s^{-1}. The role of long free paths in surface diffusion, for other mechanisms of transfer of excess energy to an adsorbed atom, has been discussed in the literature (Brune et al., 1992; Tully et al., 1979).

6. Novel aspects of the photoinduced surface transport

As a result of these studies, we have found a new light-induced effect in the processes of transfer on a solid surface—the effect of surface photodiffusion. The physical basis of the effect is the conversion of the energy of radiation into the energy of motion of an adsorbed atom over a surface. At the first stage, the system of the atom passes into an excited state. Then, the electronic excitation is quenched and its energy is distributed over the vibrational degrees of freedom of the substrate and the adsorbed atom. A fraction of adsorbed atoms acquire an energy sufficient to overcome the diffusion barrier and gain the probability to shift to another adsorption site. The frequency of the light-induced hops is proportional to the surface illuminance, while the length of the hops measures tens of the substrate lattice constants. Photoinduced desorption insignificantly affects the photoinduced diffusion, because the desorption is associated with overcoming of a much higher energy barrier, equal to the surface adsorption energy of the atom, and thus its probability is much lower.

It is shown that, under nonuniform illumination of a surface, the adsorbed atoms move away from the illuminated area and, on the boundary between the light and the shadow, the density of the adsorbed atoms exceeds the equilibrium density. Thus, we have discovered and studied a new phenomenon, which makes it possible to efficiently control, by light, the diffusion processes on a surface. Unlike the known process of photoinduced desorption, which removes adsorbed particles from the surface, in the process of photoinduced diffusion, the total number of adsorbed particles on the surface does not change. An important feature of photodiffusion is the possibility to control, by means of light, the

density of adsorbed particles on a surface (i.e., both to increase and to decrease it). Since the processes of origination of a new phase on a surface essentially depend on diffusion processes the use of photodiffusion is promising for controlling processes of nucleation and growth of surface nanostructures.

7. Self-diffusion of atoms over the surfaces of metal nanoparticles

The diffusion of atoms over the surfaces of small metal particles is of great scientific and practical interest. This interest is related to searching for ways to create nanostructures with the necessary properties controlled by the dimensions and shape of the structure's elements. Studies of self-diffusion of atoms over the surfaces of metal nanoparticles, which form island films, have already been started. These studies have shown, however, that the long-standing previous investigations of atomic diffusion over the surfaces of macroscopic bodies have proven to be inappropriate for the explanation of the mass transfer over the surfaces of nanoparticles. The same proved to be true with regard to standard methods of studying the surface diffusion based on electron and autoionization microscopy.

In recent years, optical methods for studying the reshaping of metal nanoparticles have entered into practice. In these methods, the optical characteristics of islands of films and, in particular, the extinction spectra, were connected with the morphology of film-forming particles. In (Warmack & Humphrey, 1986) it was found that changes in the extinction spectrum of a heated thin golden film whose nanoparticles were 5–100 nm in size are directly related to changes in the nanoparticle shape. Similar studies were performed with a silver film (Wenzel et al., 1999). In what follows the results obtained by the application of the optical technique for monitoring the processes that redistribute positions of atoms in solid silver particles ~10 nm in size are presented. The idea of the method is based on the relation between positions of plasma resonances of islands and the island shapes. The changes in the shapes of islands were induced by heating of a film and were revealed as a result of the modification of the extinction spectrum of the film. These changes were attributed to self-diffusion of atoms over the surfaces of nanoparticles. Spontaneous reshaping of isolated islands is related to the method of their creation in a non-equilibrium state when the metal is deposited onto the substrate. Transition from non-equilibrium shapes to equilibrium ones, referred to as the shape relaxation, is of thermal nature. It was found that the duration of the observed shape relaxation was determined not by the rate of the surface self-diffusion, but rather by the time of restructuring of the nanoparticles' facets.

7.1 Optical monitoring of silver nanoparticle annealing and aging

Granular silver films were obtained in a deep vacuum by deposition of silver atoms onto a quartz or sapphire substrate. Immediately after the deposition the extinction spectrum of the as-grown film was recorded in air. Then, the film was placed into the vacuum chamber and heated for a certain time. After that the spectrum was recorded again. This cycle of actions was repeated several times.

Fig. 4 shows extinction spectra of silver films after their heating at two fixed temperatures T= 473 and 553 K during different time intervals. The spectra are seen, first, to exhibit substantial changes for a short time; then, the rate of changes decreased. It should be emphasized that the detected changes in the extinction spectrum are not connected with the evaporation of the silver heated in a vacuum. The estimates have shown that no more than 10^{-3} of the total amount of the substance of the island film can be evaporated during this

time at T= 553 K. A certain decrease in the area under the curves of the extinction spectra (this quantity characterizes the total amount of substance in the film) is connected, as shown by numerical estimates, with the type of the frequency dispersion (differing from that of Drude–Lorenz) of the silver complex permittivity in the region of 2–4 eV.

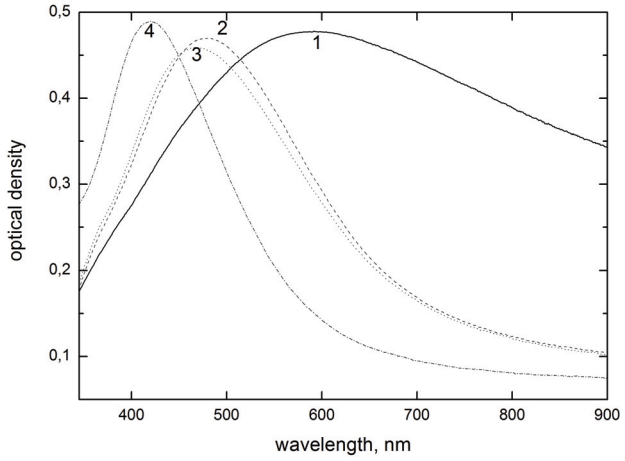

a)

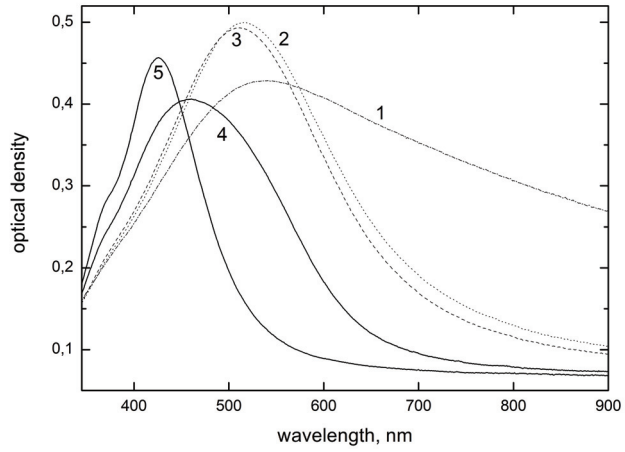

b)

Fig. 4. Annealing kinetics of the granular silver films (a) 1 – as prepared, 2 to 4 - after annealing at 473 K for 8, 16 and 56 minutes. (b) 1 – as prepared, 2 to 5 - after annealing at 553 K for 2, 4, 8 and 20 minutes

Fig. 5 shows the transmission electron microscopy images of (a) an as-grown film and (b) of the film annealed during 30 minutes at T= 553 K. One can see that agglomerates formed on the as-grown film (except for the smallest ones) are diverse in shape. As a result, the

extinction spectrum acquires a strong inhomogeneous broadening, which decreases under heating because islands are getting apart and more uniform in shape. It is likely that, at the initial stage of heating, the links between islands in agglomerates are being rapidly destroyed or separate islands are being formed due to merging of the smallest ones. Then, separate islands are being rounded (Fig. 5b). At the final stage, this transformation occurs at T= 553 K only by a factor of 3. 3 faster than at T= 473 K.

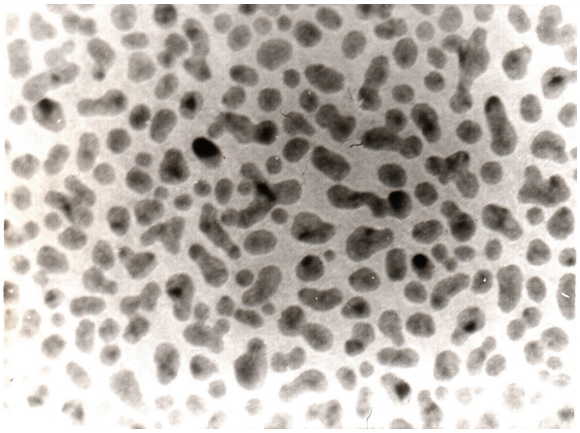

a)

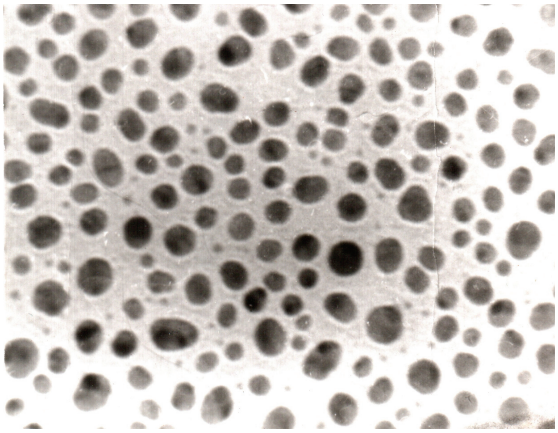

b)

Fig. 5. TEM micrographs of the granular silver films, a – as grown, b – after annealing

If the rounding of the islands at the final stage is related to the surface diffusion, then the above acceleration in the shape relaxation is provided by the activation energy E=0.36 eV. This agrees with the experimental (0.4 and 0.33 eV) and theoretical (from 0.5 to 0.25 eV) data (Brune, 1998).

In this case, according to (Mullins, 1957; Nichols & Mullins, 1965) the shape relaxation time τ_T can be estimated by the formula

$$\tau_T = N^{4/3}\kappa T/\gamma\nu_T . \quad (26)$$

Here, N is the number of atoms in a granule and γ is the surface tension coefficient (the energy of a single bond of an atom in the crystal equal, by the order of magnitude, to the fusion heat per atom). The frequency of jumps ν_T that determines the surface diffusion coefficient at the temperature T is given by the relationship

$$\nu_T = \nu_\bullet \exp(-E/kT), \quad (27)$$

where E is the activation energy of the surface diffusion, k is the Boltzmann constant, and $\nu_\bullet$ is the Debye frequency.

For the size of granules of about 10±2 nm and the cell size of 0.5 nm an estimate of N, yields $N \approx 10^4$. Assuming that E= 0.36 eV, $v_\bullet = 10^{13}$ c^{-1}, γ = 0.1 eV и kT = 0.04 eV we obtain from the above relationship that $\tau \approx 10^{-3}$, which is by six orders of magnitude smaller than the observed quantity. This, a large discrepancy cannot be substantially corrected by either taking into account the dependence of the relaxation time on the initial particle shape or by varying numerical values of the quantities entering this equation.

7.2 Theoretical estimates

In conformity with the commonly accepted ideas (Ehrlich, 1974; Naumovets & Zhang, 2002), atoms are heat transferred over surfaces from places with a higher chemical potential to those with a lower chemical potential. At temperatures much lower than the melting point, most atoms of the surface are located in terraces, i.e., facets with small indices. The atoms transferred over the terraces, torn away from the steps (boundaries of terraces) reach other steps and get stuck there. Thus, the sources of the transferred atoms are considered to be steps whose density characterizes facets of bulk crystals.

The shape of microcrystals (granules) also changes upon variation of temperature due to the surface selfdiffusion. In small rounded granules (smaller than 100 nm in size), the facets are rather small (smaller than the surface area of the granule by a factor of 10–20). The facets with the area of ~100 surface cells are separated from the neighboring facets by transition regions, i.e., by rough imperfect facets [8] referred to as atomic rough. The structure of surfaces of rounded crystal nanoparticles is mosaic, i.e., each facet borders several other with different structures. As the temperature changes, the free energies of the facets change differently and, as a result, the shape of the granules noticeably changes with no changes in their volumes.

With increasing temperature, the granules are getting rounder and their surface area decreases. Indeed, the increasing temperature of the granules leads to their melting, i.e., to total elimination of their flat terraces. For this reason, it is natural to assume that the area of the terraces, in the process of rounding, decreases, and the rough regions become wider. This process is possible when the chemical potential of atoms on the terraces (μ_f) is greater than the potential (μ_r) of atoms in the roughed regions. Changes in the shape of the granule shape stop when the potentials become equal.

In the continuum model of the crystal shape relaxation (Mullins, 1957; Nichols & Mullins, 1965), the shape of granules is characterized by the curvature of the surface. The curvature in the places where the roughed facets are localized is considered to be higher than in the places with flat facets. This simplification makes it possible to describe the mass transfer as a frictional flow of atoms over the surface induced by the capillary forces of surface tension.

This model provides the relationship (26), which we used to estimate the shape relaxation time.

The continuum model is evidently too rough to describe the phenomenon under study. This is obvious from the fact that the difference between flat facets cannot be characterized by the curvature. Fundamental reason for inapplicability of the continuum model to the description of the shape relaxation of crystalline atomic clusters has been revealed in (Combe et al,. 2000). Using the methods of computer simulation, it was established that, at temperatures far away from the melting point (more precisely, below the temperature of roughening), the shape relaxation rate is limited by the stage of attachment of transferred atoms to flat facets, which, in this process, are being rounded. Since the presence of steps on small flat facets is extremely unlikely, the attachment of transferred atoms to these facets is hampered. The stage of the rounding of facets starts with the appearance of critical nuclei on flat facets. At low temperatures, the appearance of critical nuclei is unlikely and, for this reason, the shape relaxation of facets is retarded.

In the same paper (Combe et al,. 2000), it was established that the law $\tau_T \sim N^{4/3}$ of the continuum model is obtained in the model under consideration at elevated temperatures, when granules practically have no flat facets. With decreasing temperature, the relation between τ_T and $\sim N$ changes and can be well approximated by the relationship $\tau \sim N^m$, where $m(T)$ monotonically increases from 4/3 to 5 with decreasing T.

The parameters of the model considered in (Combe et al,. 2000) regretfully are more appropriate for the description of aluminum, rather than silver, clusters. However, the qualitative results obtained for $N \leq 10^4$, in our opinion, allow one to apply them to the system under study.

For the values of $\tau \approx 10^2$s and $N \approx 10^4$, close to ours, from the data of (Combe et al,. 2000), we have $m \approx 4.2$ and, correspondingly, T= 450 K. As the temperature decreases by 50 K, the shape relaxation time increases by a factor of three. These data are close to those obtained in our experiments.

The model contains a single energy parameter, 0.4 eV, which, by its meaning, is the activation energy of the surface diffusion over the [100] facet of a cubic body-centered crystal. With allowance made for a slight difference between this energy and the appropriate quantity for silver (0.33–0.34 eV) and the difference between the surfaces of the body-centered lattice of the model and face-centered lattice of silver, the proximity of the model shape relaxation time to the observed value allows us to conclude that our observations can be qualitatively explained by the model of (Combe et al,. 2000). Thus, we believe that, in the above experiments, we observed a delay of the self-diffusion mass transfer over the surfaces of nanoparticles at the stage of roughening of their facets.

7.3 Mechanism of the shape relaxation of metal nanoparticles

The agreement between our experimental data and the model proposed in (Combe et al,. 2000) is only a qualitative result. For the strong dependence of the shape relaxation time of granules on their sizes, the order-of-magnitude errors are inevitable in experimental determination of the rate of changes of the islands' morphology and other characteristics of islands. At the same time, it is evident that, in spite of the inhomogeneity in the films of nanoparticles, their surfaces, and the parameters of self-diffusion of atoms over them, the temperature dependence of the mass transfer rate is characterized by the activation energies of various processes providing shape relaxation of granules. Due to the mosaic structure of

the granule surfaces, the self-diffusion depends not only on their material, but also on their shape. This results, in particular, in the characteristic nonexponential kinetics of the shape relaxation demonstrated by long intervals of absence of any changes (Combe et al,. 2000). The proposed optical method makes it possible to reveal these features.

It follows from the proposed mechanism of the shape relaxation of nanometer-sized granules that the time of relaxation to the equilibrium shape is determined not only by the temperature at which the relaxation occurs, but also by the state from which they relax. In particular, a non-equilibrium granule obtained by cooling a hot equilibrium granule to a certain temperature will relax faster than a granule obtained by heating an equilibrium cold granule to the same temperature. The difference between the two relaxation times results from the fact that, in the first case, the initial surface of the granule is disordered, and the facets on the surface will form faster than in the second case when a slow stage of formation of the critical nuclei is needed for roughening of the initial flat facets. The proposed reason for slowing down the shape relaxation of granular particles with flat facets presents new opportunities for controlling their shape by external perturbations of particles at the stage of their relaxation.

8. Illumination-stimulated reshaping of metal nanoparticles

At present, metal nanoparticles are used in various fields of science and engineering. Their optical properties associated with collective electronic excitations are of particular interest. In most cases, ensembles of nanoparticles obtained on dielectric surfaces by means of the self-organization of atoms adsorbed from a vapor phase are investigated and used. The shapes of the particles thus obtained are often nonequilibrium and vary with the time. The shapes vary more rapidly when the substrate is heated (Ivlev et al., 1988). These facts are well known and reported in detail in papers devoted to electron microscopy investigations, atomic force microscopy data, and the optical extinction spectra of metal island films (Warmack & Humphrey, 1986).

Although it is clear that the equilibrium shape of nanoparticles should depend on the temperature (Combe et al., 2000, as far as we know, this dependence has not yet been studied systematically. A change in the shapes of the particles is usually treated as an irreversible transition to the equilibrium state, and heating accelerates the transition process. We observed reversible changes in the optical extinction spectra of silver and sodium films on dielectric substrates under repeated cyclic variations of their temperatures. Moreover, it was found that the illumination of sodium films noticeably accelerates the transition of their spectra to a stable state corresponding to room temperature with the negligibly small heating of nanoparticles by light. The nonthermal photoevaporation of atoms from nanoparticles, i.e., photoatomic emission (Abramova et al., 1984; Bonch-Bruevich et al., 1998; Hoheisel 1988; Burchianti et al. 2009) was also insignificant owing to the choice of the wavelength of light near the threshold of this relatively low probable process. Light-induced changes in the shapes of metal nanoparticles are actively investigated at present. The most well-known works in this field are separated into two groups. In the first group(Huang et al., 2005; Stietz, 2000; Habenicht et al., 2005), the effect of light is reduced to the thermal effect, owing to which individual nanoparticles are either rounded or displaced on the substrate and coagulate when meeting each other. In the second group (Sun et al., 2003; Jin et al., 2001; Kim et al., 2009), light induces physicochemical processes in colloids of metal nanoparticles, which result first in their transformation usually from spheres to prisms and,

then, in the formation of complex aggregates of the latter. The nature of the effect of light on the formation of metal nanocrystals in liquids remains unclear. Note that in all of the mentioned works, irradiation induced significant irreversible changes in the nanoparticles, which were manifested as a substantial change in their optical spectra.

Here, we consider the observation of the effect of light on the formation of nanocrystals of absolutely different nature than that mentioned above. The observed light-induced acceleration of the relaxation process is due to the nonthermal photostimulation of the diffusion of metal atoms on the surface of metal nanoparticles. The light-induced acceleration of the relaxation of the shapes of nanoparticles is due to the same processes as photoatomic emission (Abramova et al. 1984). An attempt to observe photostimulated surface mass transport was reported in (Vartanyan et al., 2009a).

8.1 Observation of the illumination accelerated nanoparticle reshaping

The experiments were performed with silver and sodium films. The sodium films were obtained in sealed off evacuated cells with quartz, sapphire, or glass windows. The probing and illumination of the films were performed through the transparent windows of the cells. The silver films were obtained by thermal sputtering in a vacuum. The substrates were maintained at room temperature during the growth of the films. The optical probing of the silver films was the films from the vacuum setup.

The films formed under the indicated conditions are metastable. The kinetics of their morphology, which can be seen, e.g., in a change in the optical extinction spectra, is complex and long¬ term. The annealing of the films accelerated the processes resulting in the stabilization of their structure. The sodium and silver films were annealed at temperatures of 50 and 200°C for 10 and 30 min in a vacuum, respectively. Annealing was followed by the fast cooling of the films. Further, variations in the temperature induced small, but regular and reversible changes in the extinction spectra.

The changes in the spectrum of the annealed sodium film were investigated at room temperature. Fig. 6 shows (1) the optical extinction spectrum of two separated regions of the film immediately after annealing. Then, the film was aged for an hour at room temperature and one of the regions was illuminated by a cw laser with a power density of 4 mW/cm^2 (10^{16} photons per centimeter squared per second) and a wavelength of 810 nm (hv=1.53 eV), whereas the other region remained unilluminated. The spectrum of the unilluminated region changed very slightly and almost coincided with initial spectrum 1. The spectrum of the illuminated region changes noticeably (spectrum 2 in Fig. 1).

Fig. 7 shows the differences between the spectra of the unilluminated and illuminated regions after and before illumination. It is seen that the integral of the difference extinction spectrum is much smaller than a change in extinction. For this reason, it can be assumed that the light-induced change in the volume of nanoparticles is insignificant and the observed effect is attributed to a change in their shape. Note that an increase in the irradiation intensity, which did not noticeably heat the particles, was accompanied by an increase in photoatomic emission and a noticeable decrease in the size of the illuminated particles. This effect is not considered below.

A reversible change in the extinction spectra upon a variation of the temperature of the substrate was also observed in annealed silver films. Changes in the spectra were detected immediately after the cooling of the film and lasted for 40–60 min; after that, the extinction spectrum was stabilized. Fig. 8 shows the extinction spectra (1) immediately after deposition, (2) after annealing and fast cooling to room temperature, and (3) after aging at room

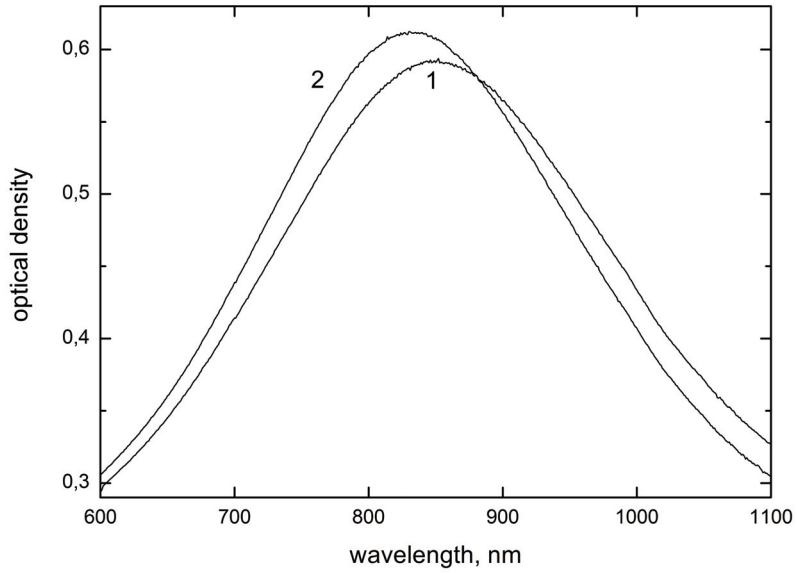

Fig. 6. Optical density of the annealed sodium film (1) and the same after an hour of illumination

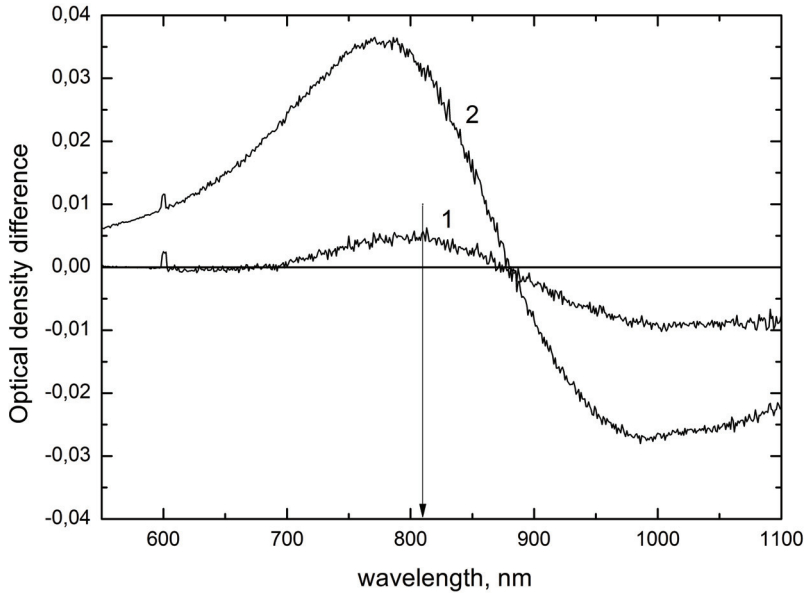

Fig. 7. Reshaping of sodium nanoparticles under laser illumination. Optical density differences in the dark region (1) and in the illuminated region (2). The laser wavelength is indicated by an arrow

temperature for an hour. Note that the extinction maximum at the last stage was shifted toward the opposite side with respect to the annealing induced shift. A change in the spectrally integrated absorption in the case under consideration is due not to the evaporation of nanoparticles, which is insignificant at the indicated heating. The change is caused by the interband¬ transition¬ induced difference of the dispersion of the relative permittivity of silver from that accepted in the Drude model. This is confirmed by the fact that the repeated annealing at 200°C in a vacuum for 5 min or a slightly longer time returned the extinction spectrum to the initial position (spectrum 2 in Fig. 8). The cycles of changes in the shape of the spectrum under the heating and cooling of the film were repeated many times. In this case, the almost complete reversibility of the changes in the extinction spectrum was observed, indicating a direct relation of the shapes of the islands with the temperature of the substrate. The illumination of silver films by available laser sources did not noticeably accelerate the relaxation processes.

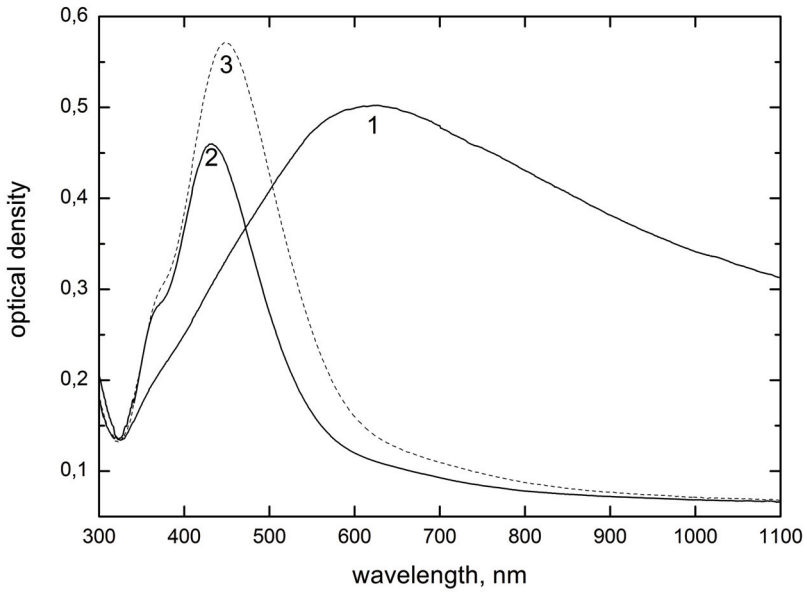

Fig. 8. Reshaping of silver nanoparticles in the dark

8.2 Sodium versus silver nanoparticles reshaping

The optical extinction spectra of metal nanoparticles are determined primarily by their shapes. The dependence of the shape of the spectrum on the size of the nanoparticles is not very noticeable. The extinction spectra of ensembles of particles are determined by the shape distribution of the particles. For this reason, the revealed reversible changes in the extinction spectra of silver and sodium films with the variation of their temperature can be attributed to changes in the shapes of individual islands, i.e., autocoalescence (Ivlev et al. 1988).

Other possible mechanisms of a change in the shapes of the particles, which are associated with the displacement of the material between the particles or the motion of particles themselves on the substrate, can berejected in view of the transmission electron microscopy

data. It is seen on the microphotographs (Vartanyan et al., 2009a) of our annealed silver films that the nanoparticles with a mean diameter of 14 nm are separated at large distances. Moreover, all of the changes associated with the mass transport on the substrate should be irreversible and manifested in the deviation of the spectra from the stable shapes, which increases in time; these features were not observed in our experiments.

We do not know any consistent theoretical description of the shape of nanoparticles. The numerical simulation (Combe et al., 2000) indicates that the rate of the relaxation of the shapes of the crystal nanoparticles owing to surface mass transport is limited not by the displacement of atoms through terraces, which is a very fast process, but by the escape of atoms from relatively stable positions near the steps and the attachment of diffusing atoms at the positions corresponding to the final equilibrium shapes. The activation energy of the escape of the atoms from the positions attached to the steps to a terrace is obviously lower than the evaporation heat, but can be comparable with the latter. The activation energy of the incorporation of atoms into stable positions can be low, but the incorporation process can be very long owing to the complexity of the path of the assembly of the stable final shapes of the nanoparticles.

In the light of the above discussion, the observed light-induced acceleration of the relaxation of the shapes of sodium nanoparticles is explained by the fact that photons trigger the mechanism of surface diffusion by separating atoms from the steps and their transfer to terraces. It is assumed that light excites electrons quasilocalized near the atoms situated on the surface at irregular positions, and the energy of the excitations is converted into the energy of the displacement of atoms on the surface. A similar, but low probable process results in the separation of atoms from the surface, which is manifested as the photoatomic emission (Bonch-Bruevich et al., 1998).

In the absence of illumination, the attachment of atoms diffusing on the terraces to the steps decelerates the relaxation of the shape, and nanoparticles are "frozen" in metastable shapes, so that the mean thermal energy is much lower than the energy of the separation of an atom from a step. In the presence of the illumination of sodium nanoparticles, the energy of a photon is sufficient for initiating separation. The efficiency of the light effect can be estimated as follows. In particular, if the cross section for the absorption of photons by atoms attached to the steps is taken to be a molecular value of 10^{-16} cm^{-2} and the quantum efficiency of the separation of the atom from the step is taken to be 0.01, the frequency of the photostimulated acts of the separation of the atom from the step for the radiation intensity corresponding to a photon flux of 10^{16} cm^{-2} s^{-1} is 0.01 s^{-1}. This is the frequency of the thermal activation of the separation at room temperature and at an activation energy of 0.8 eV (a sodium evaporation heat of 1.14 eV) of the transfer of the attached sodium atom from the step to the terrace. According to these estimates, light can noticeably affect the rate of the relaxation of the shape of the sodium nanoparticles. The evaporation heat of silver is larger than that for sodium. For this reason, high energies of photons are required to transfer attached silver atoms from steps to terraces. This circumstance can explain why illumination did not accelerate the relaxation of the shapes of the silver nanoparticles in our experiments.

9. Conclusion

Photostimulated mass transport over the solid surfaces is a wide and promising area of research in which only the very first steps are already made (Leonov et al. 2010) . Several directions of the future development may be identified right now. First, the electronic

excited states of the atoms adsorbed onto the surface and interacting with their neighbours are to be investigated thoroughly (Vartanyan et al. 2009b). Of prime interest here are such questions as the localization of the electronic excitation on the metal and semiconductor surfaces, their decay times, the pathways and probabilities of the transformation of the electron energy into atomic displacements. Second, photo-induced surface transport is to be studied on a wider range of objects, in particular, those with a metastable structure because in the case the one can expect more pronounced changes (Vartanyan et al. 2010). Finally, practical implementations of photo-induced surface transport may find their way into industry for non-thermal modification of the surfaces at low temperatures (Vartanyan et al., 2011).

10. Acknowledgment

This work was supported by the Russian Ministry of Science and Education and Russian Foundation for Basic Research.

11. References

Abramova, I.N., Aleksandrov, E.B., Bonch-Bruevich, A.M., & Khromov, V.V. (1984). Photostimulated desorption of metal atoms from surfaces of transparent insulators. *JETP Lett.*, Vol.39, No.4, (February 1984), pp. 203-205, ISSN 0370-274X

Bonch-Bruevich A.M., Vartanyan T.A., Maksimov Yu.N., & Khromov V.V. (1985). Spectral-kinetic investigations of Na -molecule triplet states. *Opt. Spectrosc. (USSR)*, Vol. 58, No.3, (March 1985) pp. 331 - 334. ISSN 0030-400X

Bonch-Bruevich, A.M., Vartanyan, T.A., Gorlanov, A.V., Maksimov Yu.N., Przhibel'skii S.G. & Khromov, V.V. (1990). Photodesorption of sodium from the surface of sapphire. *Sov. Phys. JETP*, Vol. 70, pp. 604 – 608, ISSN 1063-7761

Bonch-Bruevich, A. M., Vartanyan T. A., Maksimov Yu. N., Przhibel'skii S. G. & Khromov V.V. (1997). Adsorption of cesium atoms at stuctural defects on sapphire surfaces. *Journal of Experimental &Theoretical Physics*, Vol. 85, No.1, (January 1997), pp. 200-204, ISSN 1063-7761

Bonch-Bruevich, A.M., Vartanyan, T.A., Przhibel'skii, S.G., & Khromov V.V. (1998). Photodetachment of surface atoms of metals. *Physics - Uspekhi*, Vol. 41, No. 8, (August 1998), pp. 831-837, ISSN 1063-7869

Bonch-Bruevich A.M., Vartanyan T.A., Przhibel'skii S. G., & Khromov V.V. (1999). Photodesorption from the surface of a dielectric material: transition from a nonthermal to pseudothermal regime. *Bull. Russian Acad. Sciences, Physics,* Vol. 63, No.4, (April 1999), pp. 801-809. ISSN 1062-8738

Brune H., Wintterlin J., Behm R.J., & Ertl G. (1992). Surface migration of ''hot'' adatoms in the course of dissociative chemisorption of oxygen on Al(111). *Phys. Rev. Lett.*, Vol. 68, No.5, (May 1992), pp. 624-626, ISSN 0031-9007

Brune H. (1998). Microscopic view of epitaxial metal growth: nucleation and aggregation. *Surf. Sci. Rep.* Vol.31, No.4-6, (April 1998), pp. 125-229. ISSN 0167-5729

Burchianti A., Bogi A., Marinelli C., Mariotti E, & Moi L, (2009). *Phys. Scr.* Light-induced atomic desorption and related phenomena. Vol. 135 (July 2009), pp.014012-1-014012-5, ISSN 0031-8949

Combe N., Jensen P., & Pimpinelli A. (2000). Changing Shapes in the Nanoworld. *Phys. Rev. Lett*., Vol. 85, No.1, (January 2000), pp.110 – 113, ISSN 0031-9007

Ehrlich G. (1974). Surface self-diffusion. *CRC Crit. Rev. Solid State Sci.*. (1974). Vol. 4, No.2, (February 1974), pp. 205-219, ISSN: 0011-085X

George S.M., DeSantolo A.M. & Hall R.B.. (1985). Surface diffusion of hydrogen on Ni(100) studied using laser-induced thermal desorption. *Surf. Sci.* Vol. 159, No.1, (August 1985), pp. L425-L432, ISSN 0039-6028

Habenicht A., Olapinski M., Burmeister F., Leiderer P., & Boneberg J., (2005). Jumping Nanodroplets. *Science*, Vol. 309, No. 5743, (September 2005), pp. 2043-2045, ISSN 0036-8075

Hoheisel W., Jungmann K., Vollmer M., Weidenauer R., & Träger F. (1988). Desorption stimulated by laser-induced surface-plasmon excitation. *Phys. Rev. Lett.* Vol. 60, No.16, (April 1988), pp. 1649-1652, ISSN 0031-9007

Honigman B. (1958). *Gleichgewichts-und Wachstumsformen von Kristallen*. Steinkopff Verlag, Darmstadt

Huang W., Qian W., & El-Sayed M.A. (2005). Photothermal reshaping of prismatic Au nanoparticles in periodic monolayer arrays by femtosecond laser pulses. *J. Appl. Phys*., Vol. 98, No.11, (December 2005), pp. 114301-1-114301-8, ISSN 0021-8979

Ivlev V.M., Trusov L.I. & Kholmyanskii V.A. (1988). *Structural Transformations in Thin Films*, Metallurgiya, Moscow, [in Russian].

Jin R., Cao Y.W., Mirkin C.A., Kelly, K.L., Schatz G.C., Zhenget J.G. (2001). Photoinduced Conversion of Silver Nanospheres to Nanoprisms, *Science* , (2001). Vol. 294, pp. 1901 -1903, ISSN 0036-8075

Kim S.J., Ah C.S., &. Jang D.J. (2009). Laser-induced growth and reformation of gold and silver nanoparticles. *J. Nanopart. Res.,* Vol. 11, No.8, (August 2009), pp. 2023 -2030, ISSN 1388-0764

Leonov N.B., Przhibel'skii S.G. & Vartanyan T.A. (2010)Reversible Relaxation of the Shape of Metal Nanoparticles and Its Light-Induced Acceleration. *JETP Letters,* (March 2010), Vol. 91, No. 3, pp. 125–128. ISSN 0021-3640.

Lifshitz E.M. & Pitaevskii L.P.(1981). *Physical Kinetics,* Pergamon Press, Oxford.

Mullins, W.W. (1957). Theory of Thermal Grooving *J. Appl. Phys.* Vol. 28 , No. 3, (March 1957), pp. 333-339, ISSN 0021-8979

Naumovets A.G. & Zhang Zh. (2002). Fidgety particles on surfaces: how do they jump, walk, group, and settle in virgin areas? *Surface Science*, Vol. 500, No. 1-3, (March 2002), pp. 414–436, ISSN 00396028

Nichols F.A. & Mullins W.W. (1965). Morphological Changes of a Surface of Revolution due to Capillary Induced Surface Diffusion. *J. Appl. Phys.,* Vol. 36, No.6, (June 1965), pp. 1826 -1835, ISSN 0021-8979

Stietz F., Bosbach J., Wenzel T., Vartanyan, T., Goldmann A., & Träger F. (2000). Decay Times of Surface Plasmon Excitation in Metal Nanoparticles by Persistent Spectral Hole Burning. *Phys. Rev. Lett*. Vol. 84, No.24, (June 2000), pp. 5644-5647 ISSN 0031-9007

Sun Y., Mayers B., & Xia Y. (2003). Transformation of Silver Nanospheres into Nanobelts and Triangular Nanoplates through a Thermal Process. *Nano Lett.,* Vol. 3, No.5, (March 2003), pp. 675- 679, ISSN 1530-6984

Tully J.C., Gilmer C.H. & Shugart M. (1979) Molecular dynamics of surface diffusion. I. The motion of adatoms and clusters. *J.Chem.Phys*. Vol. 71. No. 4, (April 1979), pp. 1630 - 1642, ISSN 0021-9606

van Kampen N.G. (1992). *Stochastic Processes in Physics anid Chemistry*, North-Holland, Amsterdam

Vartanyan T.A., Leonov N.B., Przhibel'skii S.G., & Khromov V.V. (2009a) Optical Manifestations of Self-Diffusion of Atoms over the Surfaces of Silver Nanoparticles. *Opt. Spectrosc*. Vol.106, No.5, (May 2009), pp. 697-700, ISSN 0030-400X

Vartanyan T.A., Przhibelskii S.G., Khromov V.V. (2009b). Photoexcitation and photoregistration of atomic motion on the surfaces of solid materials. In: "New trends in quantum coherence and nonlinear optics", (Horizons in World Physics, Volume 263)Ed.: R. Drampyan. 2009. P. 245 – 263. Nova Science Publishers, N.Y. ISBN: 978-1-60741-025-6

Vartanyan T.A., Leonov N.B. & Przhibel'skii S.G. (2010). Application of localized surface plasmons to study morphological changes in metal nanoparticles. In: "Plasmons: Theory and Applications". Ed.: K.N. Helsey. Nova Science Publishers, N.Y., 2010. ISBN: 978-1-61761-306-7

Vartanyan T.A., Khromov V.V., Leonov N.B. & Przhibel'skii S.G. (2011). Shaping of surface nanostructures via non-thermal light-induced processes. *Proceedings SPIE*. 2011. Vol. 7996, pp. 79960H-1 - 79960H-7.

Vladimirov V.S. (1971). *Equations of Mathematical Physics*, Marcel Dekker, New York.

Warmack R.J. & Humphrey S.L. (1986). Observation of two surface plasmon modes on gold particles. *Phys. Rev*. B Vol.34, No.4, (August 1986). pp. 2246 -2252, ISSN 1098-0121

Wenzel T., Boshbach J., Steitz F., & Trager F. (1999) In situ determination of the shape of supported silver clusters during growth. *Surf. Sci.*. Vol. 432, No.3, (July 1999) , pp. 257-264, ISSN 0039-6028

Zangwill A. (1988). *Physics at Surfaces*. Cambridge Univ. Press, Cambridge.

19

Silver Recovery from Acidic Solutions by Formation of Nanoparticles and Submicroparticles of Ag on Microfiltration Membranes

Pilar González[1], F. Javier Recio[2], Dario Ribera[1], Oswaldo González[1], Pilar DaSilva[2], Pilar Herrasti[2] and Mario Avila-Rodriguez[1]
[1]*Universidad de Guanajuato, Guanajuato*
[2]*Universidad Autónoma de Madrid, Madrid*
[1]*México*
[2]*España*

1. Introduction

Despite environmental regulations, wastewaters generated by some industries are in some cases discharged into lakes, rivers or reservoirs after inefficient treatments or without any pretreatment for the elimination or reduction of certain pollutants. Effluents may sometimes contain valuable elements with significant commercial value such as precious metals. Recovery of these metals is important because they could be harmful to aquatic life in lakes and rivers and because of its economic value.

There are legal provisions regarding the composition of an effluent: in the case of liquids containing silver, it is a maximum of 5 ppm. It is known, however, that the silver ion could create a complex especially with thiosulfate, which has little effect on health.

Even if silver would not affect health and there were no restrictions to its discharge, there is an important reason to recover it: its value and scarcity. Annual global demand for silver is currently of 24,500 metric tons, used in a vast array of industrial and consumer products. For example, silver is widely used in industrial electroplating as a protective coating or as adornment. Silver reflects light very well, so it is used in car headlights and mirrors.

A laboratory that uses silver in its production could discharge monthly, a value of 150 to 1,800 dollars in silver.

Worldwide, approximately 57% of the silver present in discarded products is recovered. It has the highest rates of recovery among the most commonly used metals, but much of it is still lost in the various emissions to the environment.

Silver recovery

Various methodologies have been reported for the recovery of this metal ion, with efficiencies that vary depending on the experimental conditions.

Among the most common methods for silver recovery are: 1) Metal Replacement; 2) Electrolytic Recovery; 3) Precipitation; 4) Distillation; 5) Ion Exchange and 6) The use of

new compounds to precipitate silver (soil, silica, clays, etc.). The main features of the first five are:

1. Metal Replacement. It is one of the most popular and economical methods. It consists of a cartridge containing iron, wool and wooden chips or spirals. A solution circulates with a constant flux through the cartridge. As the silver is removed, iron is depleted, producing sediment. Finally the sediment is refined to recover the silver. One cartridge recovers 90% of silver, two in a series, 95%. Although the cost of implementation is low, the cost of refining is higher than the value of the recovered silver.
2. Electrolytic recovery. This technology was introduced in the year 1930. It uses a cell with two electrodes immersed in a solution, to which a constant current is applied. The silver is reduced to pure metal on the cathode (usually stainless steel). There are two basic types of this technic: one where the cathode rotates in a solution and another where the solution flows around the cathode. The recovery is around 96% (20 to 60 grams/hour of high purity) and it is easy to operate.
3. Precipitation. It was the first practical method for silver recovery. It has been used for over 50 years, so it is highly developed. It also precipitates copper, cadmium, mercury, lead, nickel and tin, amongst other metals. It uses a precipitant together with a flocculating agent to increase the size of the particles. Silver is recovered by filtration and then refined, with a yield of 99%. However, the equipment and the precipitant are expensive.
4. Distillation. It is normally used together with the external management of effluents. It reduces the amount of liquid to be transported:80 to 100% of water could be removed, leaving thick or solid silver. With this method 99% of silver could be recovered. The cost is high and it is recommended almost exclusively for industrial laboratories.
5. Ion Exchange. This technology can be used in solutions that have low percentages of silver, like stabilizers or wash water. In this process the metallic silver is obtained through a reversible process in which ions are exchanged between a solid (resin) and water with ionized salts. With a single column more than 90% of the silver could be recovered. With two columns in a series, about 99% could be recovered.

None of these methods gives any importance to the size or shape of the recovered metallic silver particles. Their main interest is on the efficiency of the recovery process. The recovery of the silver in specific shapes and sizes (nano and submicrometric), is an added value of the recovery processes.

1.1 Nanoparticles

Although nanomaterials have always existed in nature, our understanding of their properties and how they influence their environment has been limited. Many of these materials are currently under study and their applications have been developed over the last two decades.

Their manufacturing has gained importance because of their unusual properties compared to bulk materials. Examples include aluminium nanoparticles of 20 to 30 nm which can spontaneously combust while bulk aluminium is stable (Gromov & Vereshchagin, 2004) and calcium carbonate that forms either a fragile chalk or tough abalone shells, depending on the structural arrangement of the molecules (Tong-Xiang et al., 2009).

The applications of this relatively new technology are large and include: conductive plastics (Aravind et al., 2003), anticorrosive coatings (Gangopadhyay & De, 2000), fuel cells and batteries (González-Rodriguez, 2007; Ponce de León, 2006), solar energy generation

(Granqvist, 2007; Bavykin & Walsh, 2010), electricity carriers (Conte et al., 2004), fire resistant materials (Hamdani et al., 2010), computing and data storage (Jimenez & Jana, 2007), sensors (Yun et al., 2008; Rivas et al. 2009), water treatment (Thavasi et al., 2008), catalysis (Cheng et al., 2010) and early identification of cancer cells (Nanomedicine, 2007). Although many of these applications still remain untested, the investment over the last few years has been large: the USA allocated more than a billion dollars in 2005 (Pedreño A., 2005), and more recently Japan and the European Union invested 770 and 1400 million euros, respectively in scientific programs involving nanomaterials (EU Official Website, 2010).
Among the metallic nanomaterials, silver has been intensively studied because of its wide applications including catalysis, electronics, photonics, and photography (Maillard et al., 2010). Furthermore, low-dimensional silver materials may be utilized as interconnectors or as active components in the manufacture of micro/nanodevices (Sun et al., 2002).

1.1.1 Synthesis of silver nanomaterials

Many reports have focused on the synthesis of shape controlled Ag nanostructures, including quasi-spheres, decahedrons, cubes, prisms, rods, wires, tubes, branches, sheets or plates, and belts (Yin et al., 2001; Du et al., 2007; Cobley et al., 2009). Generally, size-controlled Ag particles can be realized adjusting the reaction parameters. Evanoff and Chumanov synthesized Ag particles with diameters between 15 and 200 nm, through variations in the reaction time (Evanoff & Chumanov, 2004). By varying the concentration of sodium borohydride ($NaBH_4$) employed in the reaction, Metraux and Mirkin have provided a straight forward and rapid route to Ag nanoprisms withover prism thickness control (Metraux & Mirkin, 2005). By adjusting intensity and spectral properties of the irradiating light, Pietrobon and Kitaev synthesized decahedral Ag nanoparticles with controllable regrowth to larger sizes (Pietrobon & Kitaev, 2008). Also, Yin's laboratory has recently demonstrated that the aspect ratio and optical properties of Ag nanoplates can be tuned with precision, over a wide range through a UV-light-induced reconstruction process (Zhang et al., 2009). However, in these examples of qualitative size control, the results can only be roughly speculated before the experiment (e.g., size-decrease or increase, but with no precise measurement). Quantitative size-control, where the product is size-designed by adjusting the reaction conditions to produce the desired particle sizes predictably and accurately, has not yet been established. Actually, it is well-known that the chemical synthesis of metal nanocrystals is influenced by several thermodynamic and kinetic factors, and much difficulty remains in capturing the distinct stages of nucleation and growth of nanocrystals (Burda et al., 2005). Also, it is very hard to establish a quantitative function to describe the relationship between the synthesis conditions and the size of the product. Therefore, carrying out qualitative and especially quantitative synthesis of size-controlled Ag particles is still a great challenge.
The synthesis of silver nanoparticles has been studied searching for an easy control over kinetics. The preparation of the conditions for each of the methods mentioned above, play an important role on the composition, structure and size of nanoparticles, and have a direct impact on their properties. The development of a methodology to provide adequate control of particle size in a simple way is an important contribution to the synthesis.
This paper presents a novel approach to recovering silver from aqueous solutions in its most valuable form: the metallic and the formation of particles with different size depending on the experimental conditions. This includes the reduction of silver ions with a reducing agent such as ascorbic acid in a microfiltration system. During reduction of the silver ions, the membrane is used as a support for the metallic silver formed. The size and shape of the

nanoparticles depends on different parameters such as, silver, nitric and ascorbic acids concentrations and the stirring rate of the solutions. Considering the extensive applications of nano and submicrometer Ag particles as catalysts, conductive adhesives, display devices, passive components, inkjet printing, photon emission, and higher order multiples resonances substrates (Dai et al., 2011; Hu et al., 2010; Xu et al. 2008; Sung et al., 2010; Gloskowskii et al., 2008), this methodology could be used in a wide range of industrial applications.

2. Experimental

2.1 Methodology for the transference of Ag (I)

All products used had analytical grade and were used as received. The device used for this work is shown in Figure 1 and comprises a two-compartment cell, divided by a microfiltration membrane.

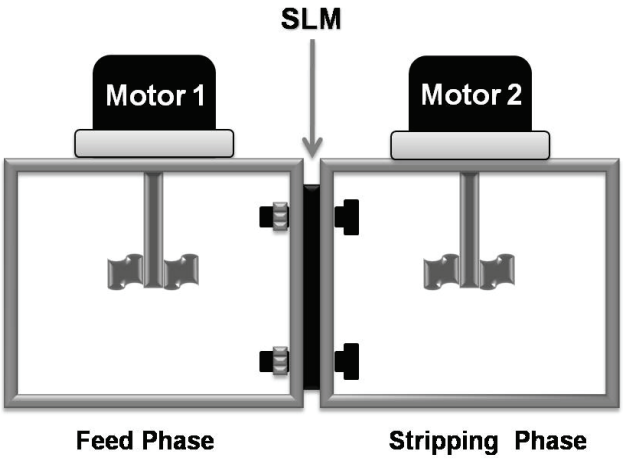

Fig. 1. Cell used for the recovering of silver, the membrane is located in between the two compartments

The feed phase was composed by different concentrations of $AgNO_3$ (from 25 to 100 mg L^{-1}) at various HNO_3 concentrations (from 0.1 to 1 mol L^{-1}). The stripping phase was composed by a solution of ascorbic acid and its concentrations were changed from 0.2 to 1.5 mol L^{-1}. The feed and stripping solutions were added to compartments 1 and 2, respectively. The cell was then covered and the system was stirred. Aliquots were taken from both sides at several different times and, finally; Ag (I) content was analyzed by atomic flame absorption using a Perkin-Elmer Analyst 200 flame atomic absorption spectrometer. The pH of both the feed and stripping solutions was measured with the help of a combined glass electrode using a Methrom potentiometer (Titrino 716). The ascorbic acid's quantitative determination in both compartments was performed by Iodometry using a standard solution of iodine and starch as an indicator of endpoint.

The microporous membrane used, was a polyvinylidene difluoride (PVDF) hydrophilic membrane with 75% porosity, 125 μm thickness and average pore size of 0.22 μm (Millipore). During reduction of the silver ions, the membrane is used as a support for the metallic silver formations.

After every experiment, the membrane was removed from the system and the water was eliminated by evaporation. Subsequently, the membrane was weighed to determine the variation with respect to its initial weight.
The characterization of the metallic silver particles was carried out with a SEM (Scanning Electronic Microscope) Hitachi S-3000N coupled to an EDAX InCAx-sight analyzer. Contact angle of the microporous membrane with ascorbic acid solutions and Ag (I) in HNO_3 solutions was measured using the CAM 200 from KSV Instruments Ltd. This unit has a measuring range of 0° to 180°, with an uncertainty of ± 0.1°.

3. Results and discussion

3.1 Silver nanoparticles formation on the microfiltration membranes

The recovery of Ag (I) was carried out using Ag^+ 100 mg L^{-1} and HNO_3 0.25 mol L^{-1} as the feed solution, and a solution of ascorbic acid (HA) 1 mol L^{-1} as the stripping solution. The contact time of the membrane with the feed and stripping solutions was 30 minutes, with a stirring speed of 600 rpm at both compartments.
After 30 minutes, the membrane was removed from the cell. The side of the membrane in contact with the feed solution showed a deposit, while any deposits were observed on the face in contact with the stripping solution. Figure 2a shows a part of the microfiltration membrane that was in contact with the feed solution. Figure 2b corresponds to an image obtained with the optical microscope.

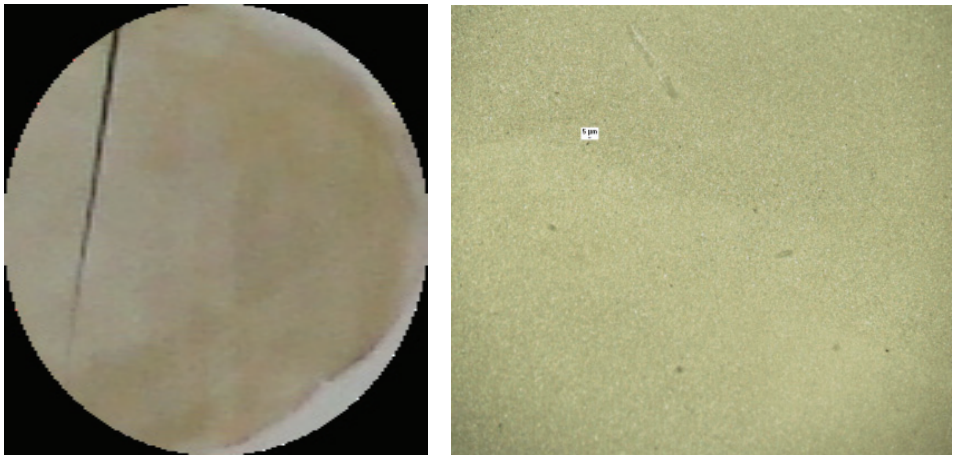

(a) (b)

Fig. 2. Images of (a) microfiltration membrane after contact with the feed (Ag (I)) and stripping (HA) solutions; and (b) small part of the membrane through an optical microscope

This deposit may have been caused by the formation of metallic silver by the reduction of Ag (I) with ascorbic acid. The deposit seems uniform both to the naked eye and through the optical microscope. In addition, the formation of silver on the membrane is consistent with the decrease concentration of Ag^+ ions in the feed solution (see Figure 3). No concentration of Ag^+ was detected in the stripping solution.

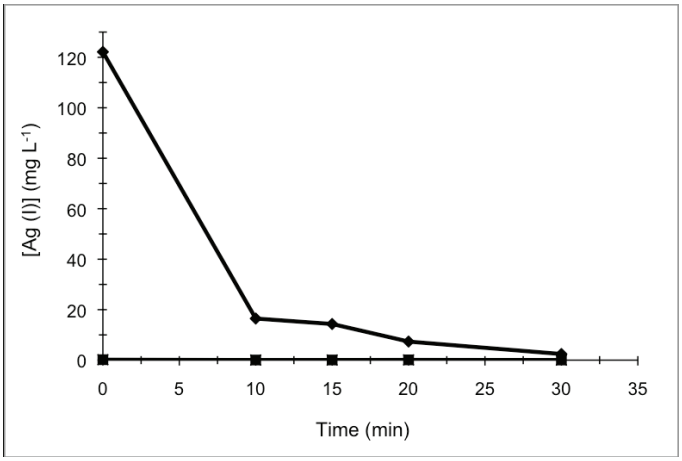

Fig. 3. Variation of Ag (I) concentration as a function of time. (◆)Feed solution: [Ag(I)] = 100 mg L^{-1}; [HNO_3] = 0.25 mol L^{-1}. (■) Stripping solution: [HA] = 0.25 mol L^{-1}

Comparing the weight of the membrane before (m1 = 0.1447 g) and after the experiment (m2=0.1739 g), we found that the difference in weigh was 29.2 mg. While the initial concentration of Ag+ ions in the feed solution was 122 mg L^{-1} and the volume of both solutions was 250 mL, for each trial, the amount of metallic silver that could be deposited on the membrane is of 30.5 mg. This value is very close to the mass in excess of the membrane and it corresponds to the metallic silver deposited on the membrane. The yield of silver recovery in these conditions is around 96%. To confirm the presence of metallic silver on the membrane, an EDAX analysis was performed. Figure 4 shows the spectrum which indicates the peaks that correspond to metallic silver.

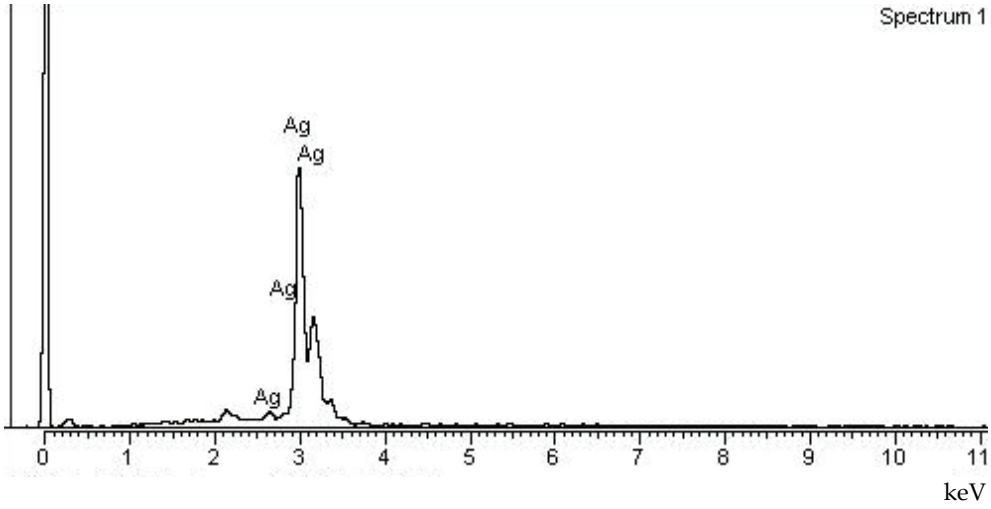

Fig. 4. EDAX spectrum of the membrane after contac twith the feed (Ag (I)) and stripping (HA) solutions

A deeper more detailed analysis on the morphology of the deposits was carried out using Scanning Electron Microscopy (SEM). The micrographs of different membranes are shown in Figure 5. The silver particles formed, are distributed over the membrane and in its pores. The shape acquired by the metallic silver depends on the synthesis conditions. We observe a non-homogeneous 3D growth, with a hexagonal shape resemblance and a broad size distribution. A similar result was recently reported by Masaharu et al., 2010.

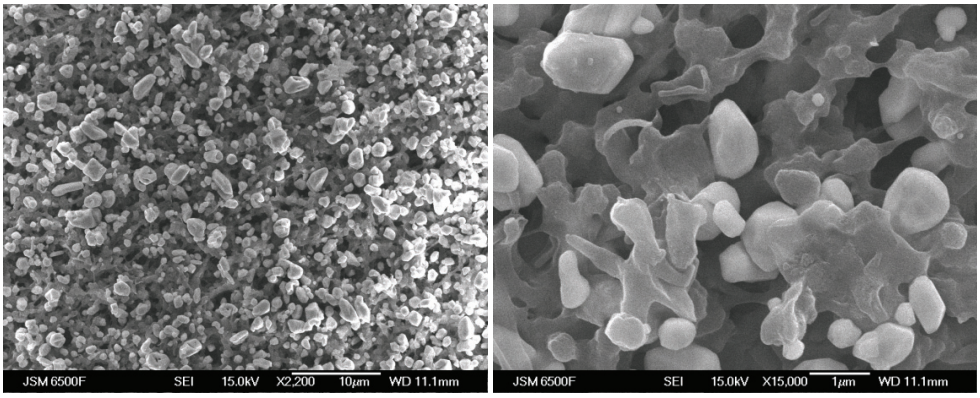

(a) (b)

Fig. 5. Micrograph of the silver particles on the membrane. Feed solution: 100 mg L^{-1} of Ag (I). Stripping solution: [HA] = 1 mol L^{-1}. Stirring speed: 600 rpm at both compartments. (a) and (b) are the same sample with different magnification

It is also evident, that the stirring speed has an impact on the size and location of the particles (on the surface or in the pores of the membrane). Figure 6 shows the micrographs of silver particles deposited on the microfiltration membrane at different stirring speeds.

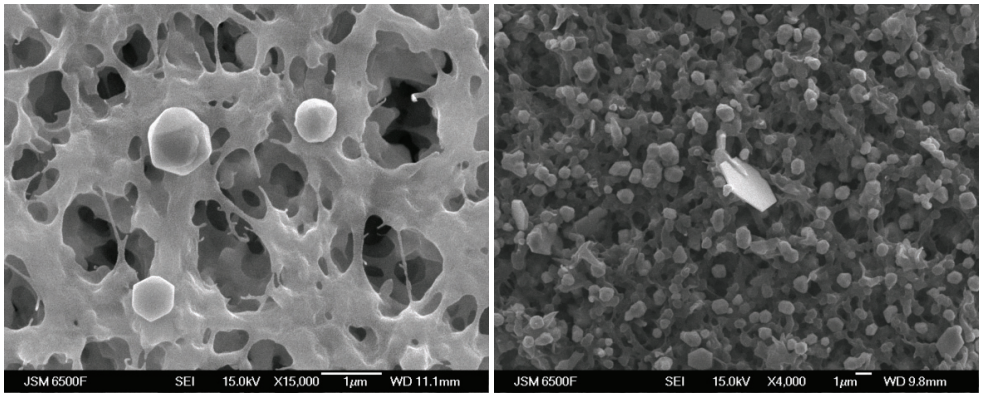

(a) (b)

Fig. 6. Micrograph of silver particles on the membrane, same solution that in figure 5.
(a) stirring speed 300 rpm, at both compartments. (b) stirring speed 1200 in the feed solution and 800 rpm in the stripping solution

As in the previous conditions, the silver particles are distributed over the membrane. For a stirring speed of 350 rpm at both phases, the silver particles shape is well defined, showing a hexagonal 3D growth (figure 6a and 6b). For a higher stirring speed (Figure 6c and 6d), the shape of the silver particles is less homogeneous. As we will show later in this paper, the crystalline shapes of the silver particles are highly dependent on the nucleation speed and are based on hydrodynamic and chemical aspects. The hexagonal crystal plate shape has been reported earlier in the literature (Jixiang et al., 2007; Masaharu et al. 2010).

Figure 7 shows the micrographs of silver particles deposited on the microfiltration membranes when a low stirring speed (350 rpm) or no agitation is applied to the stripping solution and different stirring speeds applied to the feed solution. From this, it is clear that every stirring speed causes significant changes in the shape and size distribution of the silver particles. For a 350 rpm stirring speed in the stripping solution (to 600 rpm in the feed

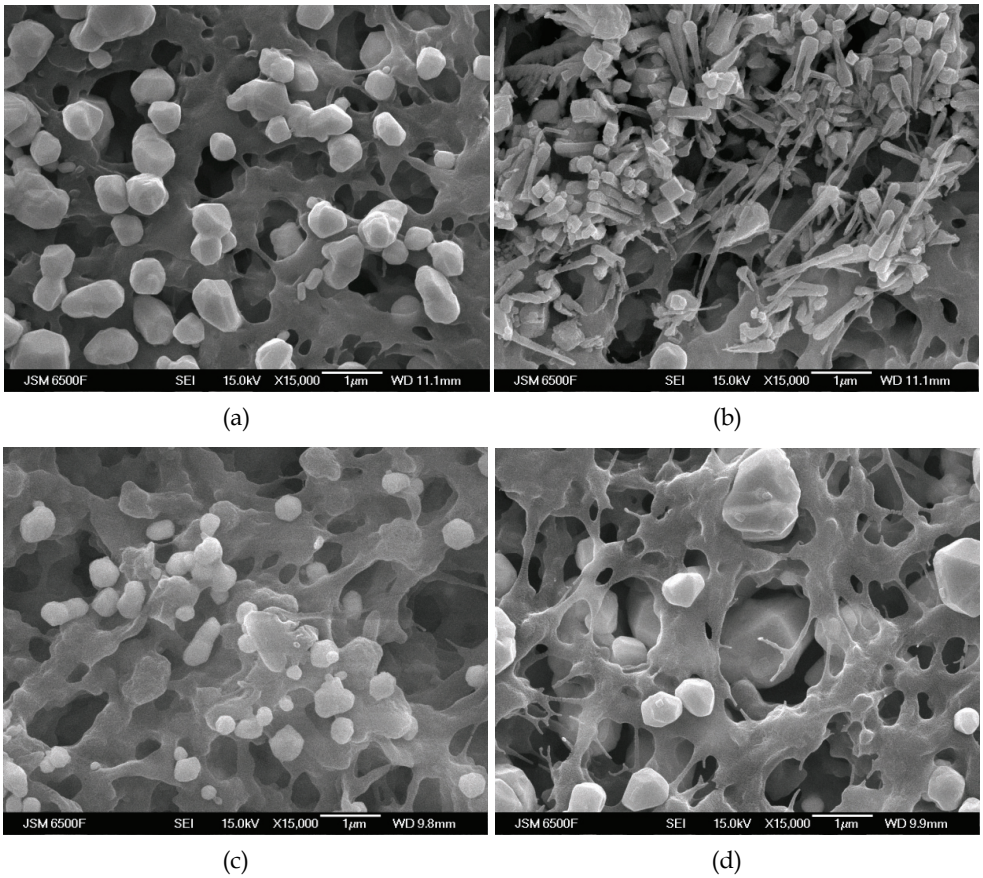

Fig. 7. Micrograph of silver particles on the membrane obtained with different stirring speeds in the two compartments. (a) Stirring speed 350 rpm in the stripping solution and 600 rpm in the feed solution. (b), (c) and (d) No agitation of the stripping solution. To the feed solution a stirring speed of 1000, 600 and 300 rpm, is applied respectively

solution), the particles maintain a certain homogeneity. A decahedron shape is observed in figure 7a. On the other hand, when the stripping solution was not stirred and the stirring speed on the feed solution was reduced (1000, 600, 300 rpm) the shape of the silver crystals gets very different. In the case of a stirring speed of 1000 rpm, the metallic silver takes crystal morphology in the shapes of cubes and rods. If the stirring speed is decreased to 600 rpm, the silver particles appear as rounded shapes but with traces of nucleation that form a cubic shape (figure 7b, 7c). At 300 rpm on the feed solution, the silver particles take decahedron shapes with an average particle size greater than in other cases. Also in this case, the large silver particles are occluded in the pores of the microfiltration membrane. It is important to observe that the proposed methodology is very suitable for obtaining metallic silver particles of different shapes and sizes. In fact, in the literature, in order to obtain different shape and size silver nanoparticles, more controlled and drastic conditions are required than those proposed here.
Finally, in the absence of stirring at both phases, the silver particles obtained on the membrane surface, clearly show the formation of hexagonal plates (Figure 8). These hexagonal plates come from the formation of dendrites on the surface, which is the first stage in the process of crystallization of silver on the microfiltration membrane.

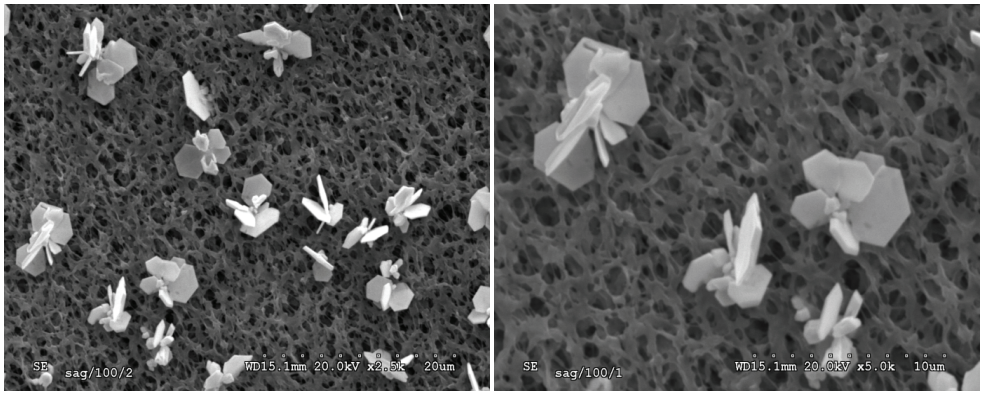

(a) (b)

Fig. 8. Micrograph of the silver particles on the membrane when no stirring is applied to the solutions. (b) Higher magnification of the same sample

We can conclude that hydrodynamics play an important role in the morphology and size of silver particles.
In the next section we will discuss the chemical aspects that affect the process of reducing Ag^+ ions by ascorbic acid. Additionally, we will analyze the conditions for efficient recovery of silver so we will have a better understanding of the mechanism under which the process is under mass transfer of Ag^+ ions.

3.2 Effect of Ag (I)'s concentration on the recovery efficiency

In order to evaluate the influence of Ag(I)'s concentration on the efficiency recovery of the proposed separation system, two tests with different concentrations of Ag(I) (25 and 100 mg L^{-1}), were performed. For the first test we used a 0.25 mol L^{-1} of HNO_3 as the feed solution

and 1 mol L^{-1} of ascorbic acid as the stripping solution. Figure 9 shows the variation of C_t/C_o with the Ag (I) in the feed solution as a function of time (being C_o the initial concentration of Ag (I) and C_t the concentration at time t).

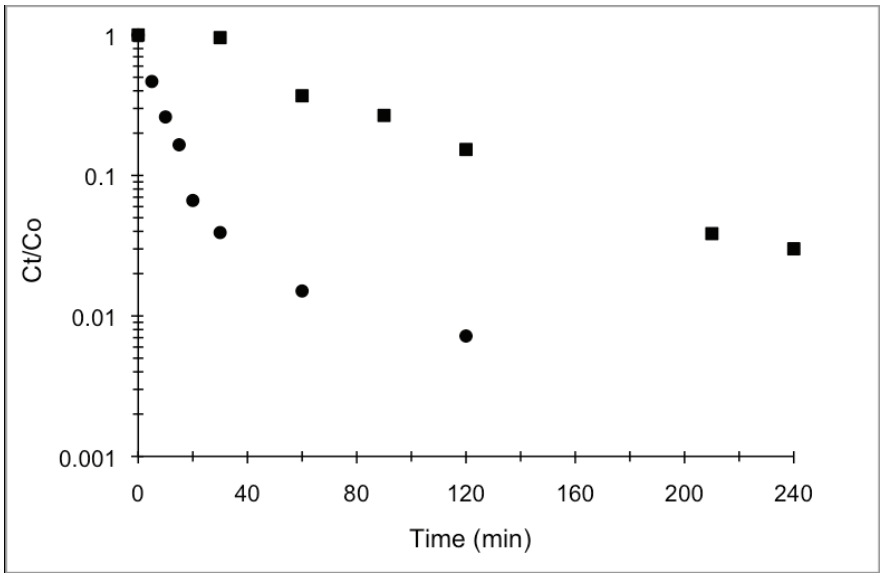

Fig. 9. Silver's C_t/C_o variation in the feed solution as a function of time. (■) [Ag (I)] = 25 mg L^{-1};(●)[Ag (I)] = 100 mg L^{-1}. Stripping solution [HA] = 1 mol L^{-1}

Silver C_t/C_o values decrease as function of time, in the feed solution in both tests. Silver recovery efficiency is near 95%. For initial silver's concentration of 25 and 100 mg L^{-1}, the recovery efficiency is 99%. Silver's concentrations decrease faster when the initial concentration is 100 mg L^{-1}. The concentration of Ag (I) in the stripping solution was practically negligible after 120 minutes of contact (no more than 0.2 mg L^{-1}). Therefore, we can consider that the transfer of Ag (I) from the feed solution to the stripping solution is negligible. In both cases the membrane has a silver deposit on the surface in contact with the feed solution, so that the absence of silver ions in the feed solution is due to its reduction induced by the ascorbic acid.

When a 25 mg L^{-1} concentration of silver is used in the feed solution, the quantity of silver particles on the surface of the membrane, are scarce and show a less uniform distribution (data not shown). Nevertheless, the silver particles morphology is quiet similar to the observed previously, namely in decahedra shapes.

3.3 Effect of the H^+ ions' and the ascorbic acid's concentrations

The effect of H^+'s concentration in the reduction of silver by ascorbic acid and its deposition on the microfiltration membrane, was performed by varying the HNO_3 concentration between 0 (pH 5) to 1 mol L^{-1} into the feed phase, while the ascorbic acid concentration was 1 mol L^{-1} into the stripping phase. The stirring speed was kept constant, in both compartments, at 600 rpm. In all cases the experimental time was 120 minutes. The recovery efficiency was evaluated by analyzing the amount of Ag (I) in the feed and in stripping

solutions as a function of time. Figure 10 shows the micrographs obtained in each condition. Figure 10a shows a dendritic shape of the silver particles when no HNO_3 is added to the solution. When HNO_3 is added to the feed solution, the particles have a decahedral structure (figures 9b, 9c, 9d); like those obtained earlier. Another important observation is that when the nitric acid's concentration increases, the number and size of silver particles on the membrane decreases. The shape in all cases does not change very much. In the absence of HNO_3 acid, the feed solution becomes cloudy after 5 minutes, suggesting that the Ag (I) reduction process takes place not only in the feed solution membrane interface but also in the bulk of the feed solution. By increasing the H^+'s concentration in the feed solution, the solution does not become cloudy and the silver is reduced on the membrane. The size distribution and dispersion of these particles is higher at 0.5 mol L^{-1} (Figure 9c) than at 0.1 mol L^{-1} (Figure 9b) of nitric acid. When the concentration of H^+ is increased to 1 mol L^{-1} (Figure 9d), there are few particles left on the membrane, indicating that a decrease in pH acts negatively on the Ag(I) reduction process, decreasing the reduction rate and generating fewer and smaller particles on the membrane.

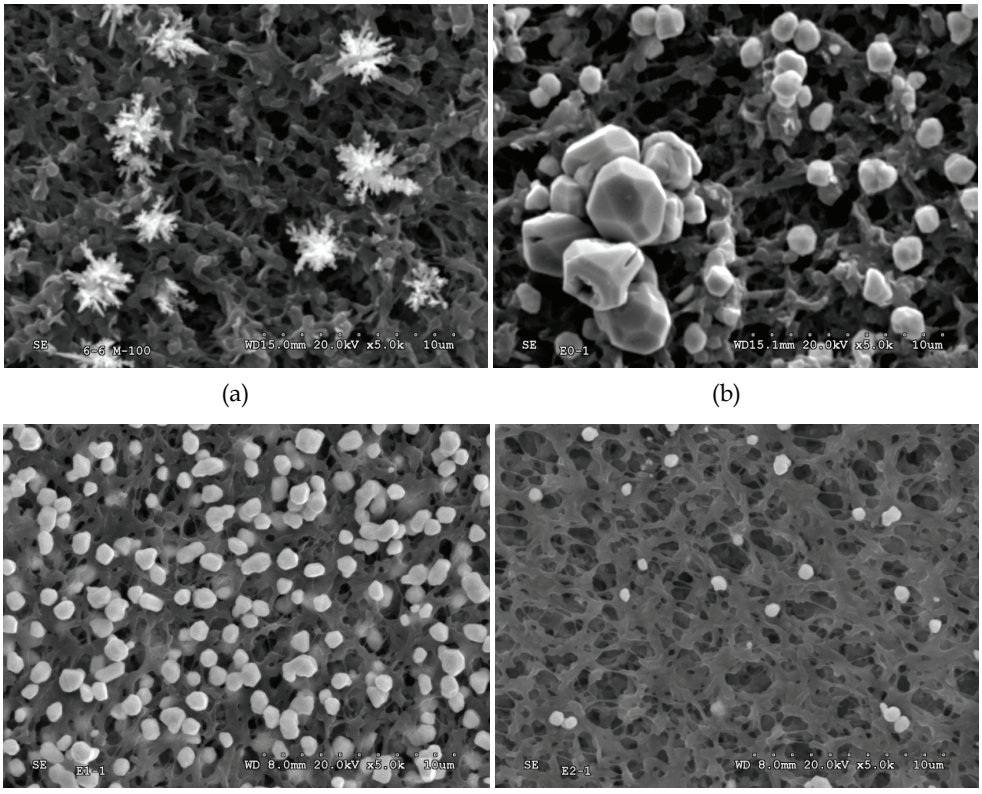

Fig. 10. Micrographs of the membrane after 120 minutes of contact. Feed solution: [Ag(I)] = 100 mg L^{-1}, [HNO_3]: a) without, pH 5.4, b) 0.1 mol L^{-1}, c) 0.5 mol L^{-1} and d) 1 mol L^{-1}. Stripping solution: [HA] =1 mol L^{-1}

Figure 11 shows the morphology of the silver nanoparticles at different HNO_3's concentration in the feed solution when the ascorbic acid concentration is reduced from 1 mol L^{-1} to 0.5 mol L^{-1} in the stripping solution. The silver deposits obtained, show a similar morphology that in Figure 10. The only difference is the amount of reduced silver; in this case the amount is less. In the absence of HNO_3, the morphology of the particles is dendritic (Figure 11a), but in the presence of HNO_3 acid a decahedra structure was obtained (Figure 11b, 11c and 11d). A more uniform particle size and better distribution occurs at low concentrations of acid in the feed compartment.

From this study it was found that a greater amount of ascorbic acid increases the reduction of Ag (I) on the membrane. The increase of H^+'s concentration results in a reduced amount of silver but on a more uniform shape and size.

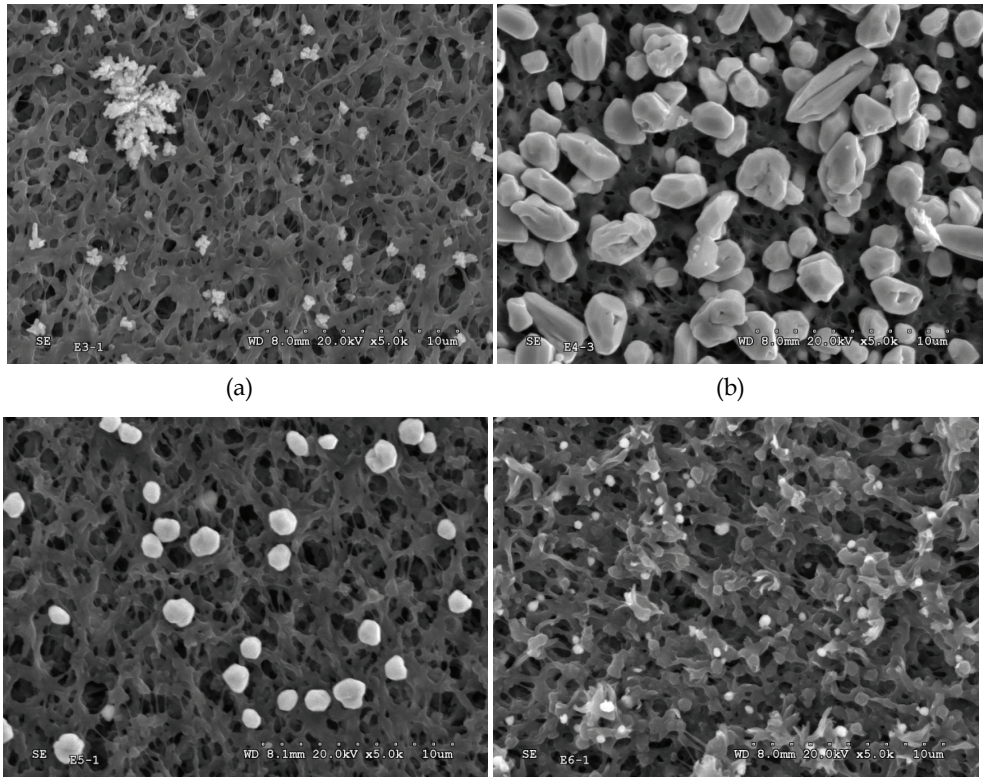

(a) (b)

(c) (d)

Fig. 11. Micrographs of the membranes after 120 minutes of contact. Feed solution: $[Ag^+]$ = 100 mg L^{-1}; $[HNO_3]$: a) without, pH 5.4, b) 0.1 mol L^{-1}, c) 0.5 mol L^{-1} and d) 1 mol L^{-1}. Stripping solution: [HA] = 0.5 mol L^{-1}

3.4 Analysis of the mass transfer process of Ag (I)

The morphology of Ag particles obtained is directly related to the hydrodynamic and chemical conditions of the system proposed. But also, the morphology is connected with the

mass transfer process of Ag^+ ions from the feed solution towards the specific zone where the redox process takes place with the ascorbic acid (which is also transported from the stripping solution).

The analysis of the concentration profiles of [Ag^+] at different concentrations of HNO_3 in the feed phase and with a two different ascorbic acid's concentrations in the stripping phase, allows to see that the rate of decrease of [Ag^+] in the feed solution as a function of time (figures 12a and 12b), strongly depends on the conditions of the feed phase as much as those of the stripping phase.

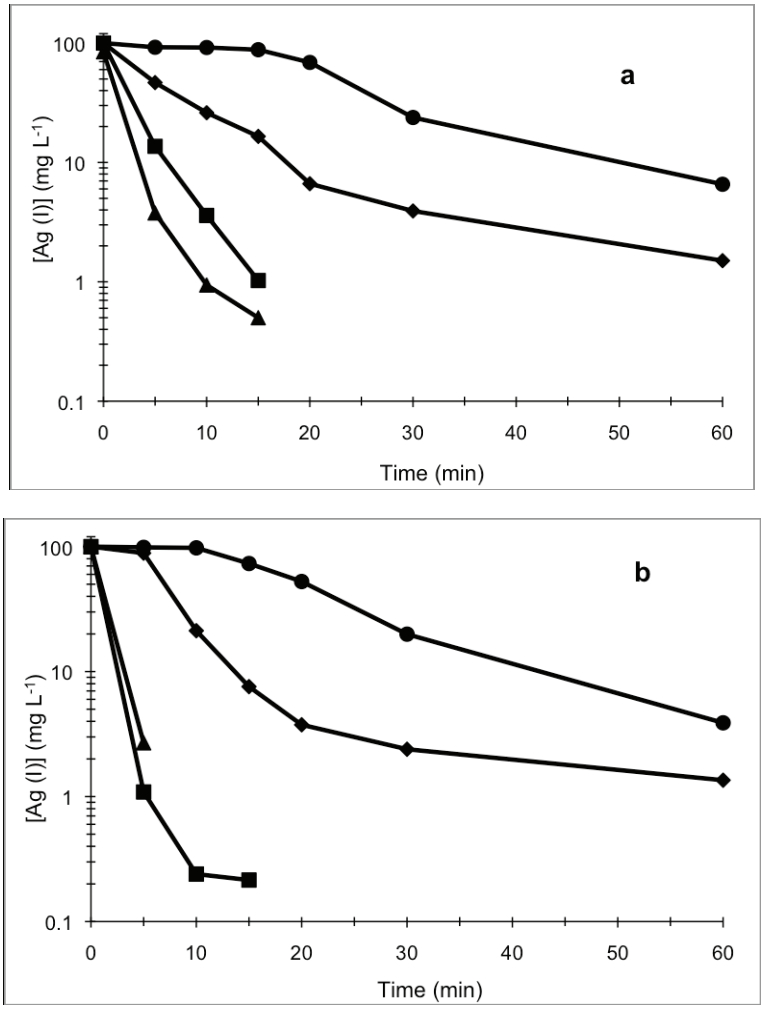

Fig. 12. Variation of Ag (I) concentration as a function of time in the feed compartment for different nitric acid's concentrations. (▲) In the absence of HNO_3, pH = 5.4; (■) [HNO_3] = 0.1 mol L^{-1}; (◆) [HNO_3] = 0.5 mol L^{-1}; (●) [HNO3] = 1 mol L^{-1}. Stripping solution: (A) [HA] = 1 mol L^{-1}, (B) [HA] = 0.5 mol L^{-1}

With a higher pH (without a HNO_3 addition) at the feed phase, we reach the highest Ag reduction rate, as shown in figure 12A. Due to the low Ag^+ concentration found at the stripping phase after the test, the Ag^+ mass transfer through the microfiltration membrane cannot be considered during the reduction process, indicating that the redox process takes place inside of the microfiltration membrane. Final Ag^+ concentrations in the feed solutions are close to 2% of the initial value, indicating a high yield process.

When the pH in the feed phase is 5, the $[Ag^+]$ in the feed solution diminishes to less than 1%, and a precipitate becomes apparent in the feed solution. This one can be associated to the saturation of Ag precipitate in the membrane and due to the stirring process the Ag particles come to the feed solution. However, when pH is reduced in the feed solution, the Ag precipitated in the feed solution does not appear anymore and all the Ag particles are retained in the membrane. When the HNO_3 concentrations are higher than 0.5 mol $L^{-1,}$ the reduction rates are slow and the curves trends of $[Ag^+]$ remain constant during the first 30 minutes of the experiment.

To explain the results obtained it is necessary to analyse the various phenomena that take place at the membrane. There are two important aspects: 1) Ag^+ and HA mass transfer process, and 2) the redox process of both compounds connected with the formation of silver particles.

In analysing the mass transfer process of Ag^+ and HA, it is necessary to consider the different zones existing in the system. Close to the membrane, a non-stirring zone exists. In non-stirring areas Ag^+ and HA movements are controlled by a diffusion process because the convection process is negligible. Figure 13 shows the several areas formed due to the stirring process. Zones named *a)* and *e)* correspond to non-stirring areas (diffusion region) in feed and stripping phases. Zones named *b)* and *d)* represent the interphases feed-membrane phase and stripping-membrane phase respectively, and *c)* is the membrane phase. The thickness of the diffusion regions are represented by d_a and d_e, corresponding to the thickness of feed and stripping diffusion areas respectively and d_o is the membrane thickness.

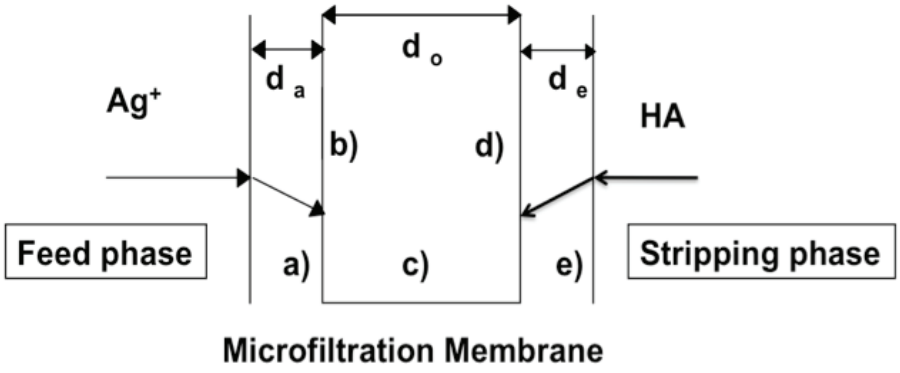

Fig. 13. Scheme of the mass transfer of Ag (I) and ascorbic acid (HA)

In order to correctly define the mass transfer process, it is necessary to determine the areas where the redox process could take place. The experimental results show that the redox process takes place mainly at the feed-membrane interface and Ag particles are formed on the feed side of the membrane. Based on this result, the Ag^+ and HA mass transfers were studied in the absence of one of the two compounds, alternately Ag^+ mass transfer studies

were performed by replacing HA by different concentrations of HNO_3 at the stripping phase (pH from 0 to 5), and a feed solution of Ag (I) 100 mg L^{-1} and HNO_3 0.5 mol L^{-1}. The Ag^+ concentration in the stripping phase after all the experiments, shows values around 10%, indicating that Ag^+ diffusion through the stripping phase is very low in all tests performed. A pH decrease in the stripping phase is also detected and this effect is more pronounced when the initial pH in the stripping phase is higher. Figure 14 shows Ag^+ concentrations in both phases.

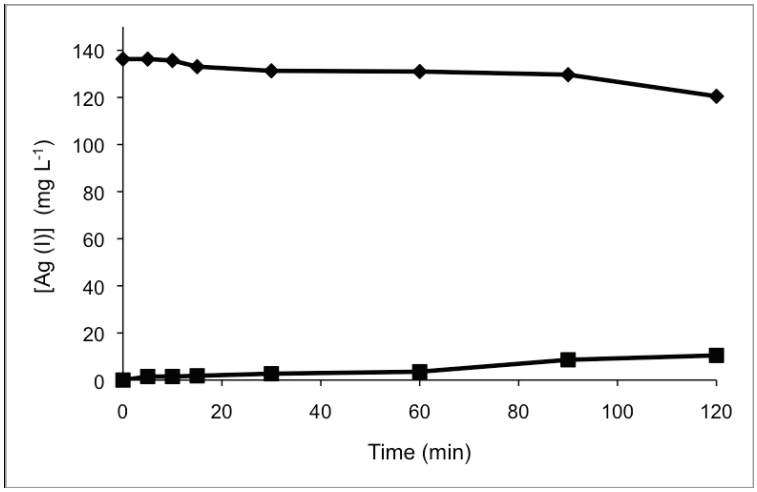

Fig. 14. Variation of Ag (I) concentration as a function of time in absence of HA. (◆) Feed solution: [Ag (I)] = 100 mg L^{-1}; [HNO_3] = 0.5 mol L^{-1}. (■) Stripping solution: [HNO_3] = 1 mol L^{-1}

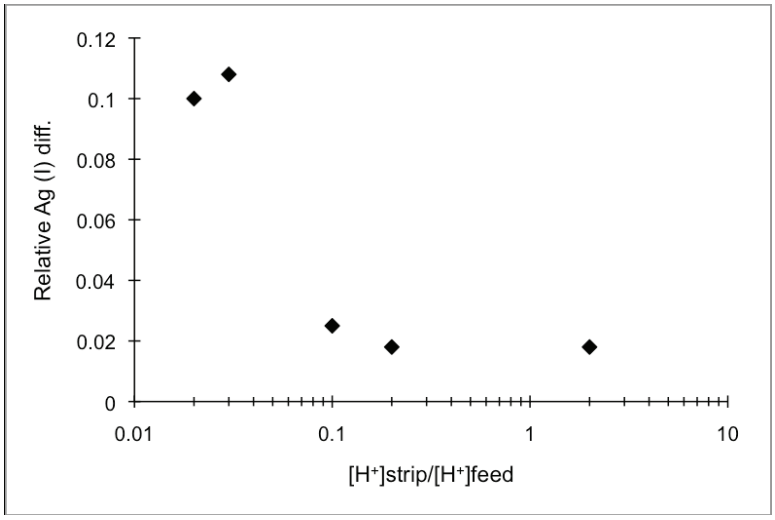

Fig. 15. Relative Ag^+ (I)'s concentration as a function of $[H^+]strip/[H^+]feed$

Analyzing the value of H^+'s concentration in the feed and in the stripping solutions, we found that there is a proton transfer from the feed solution to the stripping solution due to a concentration gradient. The silver ions diffused to the stripping compartment are related with the H^+ transfer. The diffusion of Ag^+ increases with the increasing of the H^+'s concentration in the feed solution. This effect can be observed in Figure 15.

The transference of ascorbic acid trough the membrane has been studied using a feed solution containing HNO_3 at different concentrations (0.1, 0.25 y 0.5 mol L^{-1}) and a HA's concentration of 1 mol L^{-1} in the stripping solution. The results show that the concentration of ascorbic acid in the feed phase after 120 minutes is minimal for each of the conditions studied. Figure 16 shows the results of the transfer of HA through the microfiltration membrane when HNO_3 in the feed solution was 0.5 mol L^{-1}.

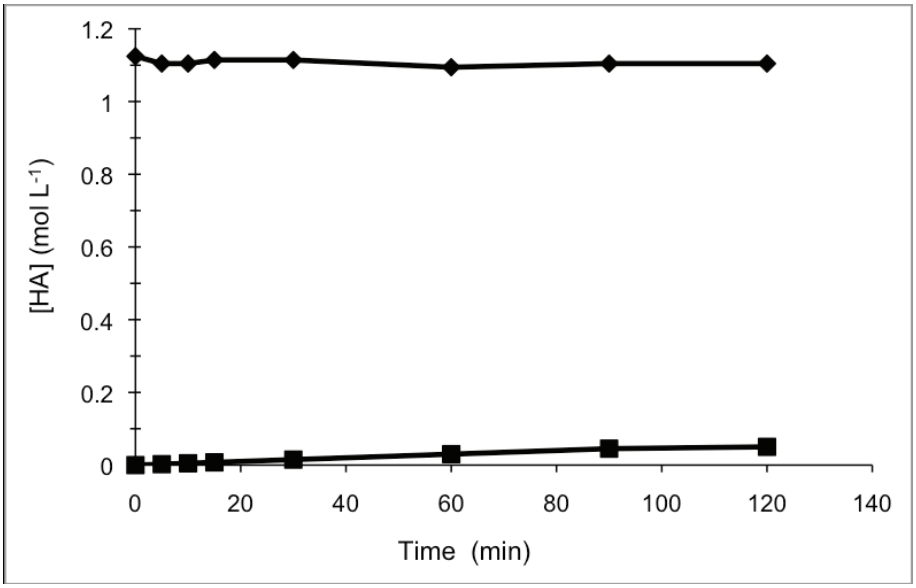

Fig. 16. Variation of the ascorbic acid's concentrations in the stripping (◆) and feed (■) phases as a function of time

In summary both Ag^+ and HA have a minimum transfer through the microfiltration membrane. This behavior can be explained considering that the membrane is made of a polyvinylidene fluoride polymer whose surface has been modified to increase the hydrophilicity. This modification produces electrical charges on the membrane surface. These charges could be positive or negative depending on the nature of aqueous solutions that are in contact with the membrane. Thus, there may be a rejection of the membrane to the charged species present in the interface membrane/feed or membrane/stripping solution. Although no transfer occurs of any of both species through the membrane, we have shown that the oxireduction reaction takes place in the interface (feed solution/membrane) generating silver nanoparticles on the membrane.

In order to determine the degree of rejection of the microfiltration membrane to Ag^+ and ascorbic acid, contact angle measurements were performed. Table 1 shows the contact angle

for a PVDF hydrophilic membrane and as means of comparison we included a PVDF hydrophobic membrane.

	PVDF Hydrophobic /H_2O	PVDF Hydrophilic/ H_2O	PVDF Hydrophilic/ $AgNO_3$ /HNO_3 0.1 mol L^{-1}	PVDF Hydrophilic/ $AgNO_3$ /HNO_3 0.5 mol L^{-1}	PVDF Hydrophilic/ HA
Contact angle (°)	143.1	72.9	115.2	114.58	58.47

Table 1. Contact angle values of the microfiltration membrane in contact with water and solutions containing $AgNO_3$ (100 mg L^{-1})/HNO_3 and ascorbic acid 1 mol L^{-1}

It can be seen that the values of water contact angles on a hydrophobic PVDF membrane are higher than those obtained with a hydrophilic PVDF membrane. When the polarities are very close, the contact angles are smaller. Also the analysis of Table 1 shows that the contact angle values of the solutions of Ag^+ are higher than those obtained with solutions of HA and water, and are similar to the contact angle values of a hydrophobic membrane with water (large difference in polarity). This clearly indicates that there is a rejection of the membrane to the $AgNO_3$/HNO_3 solutions.
Analyzing the variation of the contact angle as a function of time (see Table 2), we found that in the case of solutions $AgNO_3$/HNO_3 the value of the contact angle after 6 seconds, remained around 114°. In the case of ascorbic acid, the value of the contact angle ranged from 50.48° to 58.47°, which is a considerable variation. The decrease in the contact angle value indicates that the membrane gets impregnated by the ascorbic acid. Thus, the HA is transported into the membrane to reach the interfacial membrane area, where the oxireduction reaction is carried out.

Time (s)	$AgNO_3$ 100 mg L^{-1} HNO_3 0.5 mol L^{-1} Contact angle (°) (Average)	HA 1 mol L^{-1} Contact angle (°) (Average)
1.00	114.58	58.47
2.00	113.29	55.17
3.00	114.09	53.66
4.00	114.29	52.41
5.00	114.64	51.51
6.00	114.11	50.48

Table 2. Contact angle values of a microfiltration membrane in contact with water and solutions containing $AgNO_3$ (100 mg L^{-1})/HNO_3 and ascorbic acid 1 mol L^{-1} as a function of time

According to the above, the formation process speed of silver nanoparticles depends on the diffusion speed of Ag^+ ions to the membrane. If this speed is lower than the oxidation-

reduction speed, the diffusion process takes place and it is possible to calculate the overall mass transfer coefficient of the Ag^+ using the equation (1).

$$Ln\frac{[Ag^+]_t}{[Ag^+]_0} = -K\frac{Q}{V}t \quad (1)$$

Where:
K = overall mass transfer coefficient
t = time (sec)
Q = effective area of the membrane (11.34 cm^2)
V = volume (250 cm^3)
The overall mass transfer coefficient depends on the diffusion rate as well as on the chemical reaction between silver ions and ascorbic acid.
The variation of Ln $[Ag^+]_t/[Ag^+]_0$ as a function of t*Q/V, is a straight line with a slope equal to –K. Figure 17 shows the results obtained in the case of a system containing a feed solution of Ag(I) 100 mg L^{-1} with different HNO_3 concentrations and 1 mol L^{-1} of HA in the stripping solution.

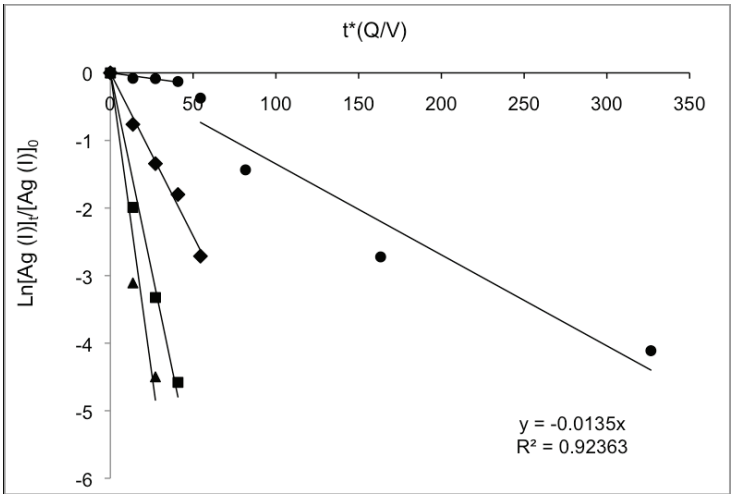

Fig. 17. Variation of de Ln$[Ag^+]_t/[Ag^+]_0$ as function of t*Q/V in the feed compartment for different nitric acid's concentrations. (▲) Without HNO_3, pH = 5.4; (■) $[HNO_3]$ = 0.1 mol L^{-1}; (♦) $[HNO_3]$ = 0.5 mol L^{-1}; (●) $[HNO_3]$ = 1 mol L^{-1}. Stripping solution: [HA] = 1 mol L^{-1}

The value of K (slope) obtained for the system in absence of HNO_3 is 0.1779 cm s^{-1},with a R^2 value of 0.94. For a HNO_3 concentration of 0.1 mol L^{-1}, in the feed solution, the value of K (0.1175 cm s^{-1}) is very close to the former. In these two cases the K values are high for a system with a diffusion control. It is important to note that under these conditions, the formation of silver nanoparticles not only occurs in the feed phase-membrane interface but also in the bulk of the feed solution, then the process is controlled by the redox reaction. On the other hand, when the concentration of HNO_3 is 0.5 mol L^{-1}, the value of the overall mass transfer coefficient is 0.0483 cm s^{-1}. When the HNO_3's concentration is 1 mol L^{-1}, there are

two well-defined zones, one with a value for K of 0.0033 cm s^{-1} and another with an overall mass transfer coefficient of 0.0135 cm s^{-1}. It is clear that an increase of the HNO_3's concentration, has a negative effect on the speed of the oxireduction reaction between Ag^+ ions and HA. Moreover, to understand better the results shown in Figure 17, it is necessary to consider the rate of impregnation of the membrane by HA. In the absence of HNO_3, the rate of impregnation of the membrane by the HA, appears to be faster than in the acidic media. This is why the K value diminishes with the increase of HNO_3's concentration and at 1 mol L^{-1} of HNO_3, the variation of $[Ag^+]$ remains almost constant during the first 30 minutes of contact between the phases and the membrane (Figure 12a and 12b).

It is possible to correlate the values of the global mass transfer coefficient with the morphology of silver particles deposited in the microfiltration membrane under each of the studied conditions. When the ascorbic acid rapidly permeates the microfiltration membrane (low concentration of HNO_3 in the feed solution) the value of K is high (0.1779 cm s^{-1}). The silver particles obtained in this case, have a dendritic shape (figure 10a and 11a). If the value of K decreases, the silver crystals grow as decahedra (Figures 10b and 11b). Finally, the no agitation of the feed and stripping phases make transference process very slow, and under these conditions the crystallization time is sufficient for the formation of metallic silver hexagonal plates (figure 8). These observations agree with those reported in the literature regarding the process of crystallization of metallic silver, which in a first stage involves the formation of dendrites trees that slowly form decahedra shaped particles leading to the formation of hexagonal plates (Jixiang et al. 2007).

The methodology proposed is suitable for obtaining silver nanoparticles and submicroparticles on microfiltration membranes with different shapes and sizes. The control of mass transference can be carried out by changes in the stirring solutions, the pH, and the concentrations of Ag^+ and ascorbic acid. The conditions used in this methodology are not drastic being an advantage over other methods reported.

4. Conclusions

We have developed a methodology for the recovery of silver (I) from aqueous solutions on a microfiltration membrane using ascorbic acid as a reducing agent. Under certain conditions, it is possible to recover about 99% of the silver contained in the aqueous solutions. The silver particles are deposited in nanometric and submicron sizes. The shape of these particles depends on the hydrodynamic and chemical conditions of the system. Silver particles can be obtained as dendrites, decahedra and hexagonal plates. We have analyzed the mass transfer process of the species involved in the system in order to explain the observed phenomena and to correlate the morphology of the particles obtained, with the mass transfer process. We can conclude that the reaction between silver and ascorbic acid occurs at the interface membrane-feed solution. The permeation rate of ascorbic acid into the membrane is linked to the Ag^+ mass transfer process. Finally, the global coefficient of mass transfer is related to the morphology of the particles obtained. At high K values, silver dendrites nanoparticles are obtained; whereas if the value of K decreases the deposit of silver particles corresponds to a slow crystallization process. The methodology proposed allows the efficient recovery of Ag (I) ions and allows the obtaining of microfiltration membranes modified by Ag particles, which can be used as filters for the removal of microorganisms contained in water.

5. Acknowledgments

The authors gratefully acknowledge the financial support of the Universidad de Guanajuato, Mexico and Spanish Ministry through the project MAT2009-14741-C02-02. Oswaldo Gonzalez would like to thank CONACYT for financial support.

6. References

Aravind D., Zhong-Zhen Y., Yiu-Wing M. (2009). Electrically conductive and super-tough polyamide-based nanocomposites. *Polymer*, 50, 4112-4121. ISSN: 0032-3861.

Bavykin D.V., Walsh F.C. (2010). Titanate and Titania Nanotubes; Synthesis, Properties and Applications. RSC Publishing, Cambridge, UK. *Nanoscience & Nanotechnology*. ISSN: 1550-7033.

Burda C., Chen X., Narayanan R.,. El-Sayed M.A, (2005). Chemistry and properties of nanocrystals of different shapes. *Chem. Rev* 105, 1025-1102. ISSN: 0009-2665.

Cheng F., Su Y., Liang J., Tao Z., Chen J. (2010). MnO_2-based nanostructures as catalysts for electrochemical oxygen reduction in alkaline media. *Chem. Mater*. 22 (3) 898-905. ISSN: 0897-4756.

Cobley C., Rycenga M., Zhou F., Li Z., Xia Y., (2009) Etching and growth: An intertwined pathway to silver nanocrystals with exotic shapes. *Angew. Chem., Int. Ed*. 48, 4824-4827 ISSN: 1521-3773.

Conte M., Prosini P.P,Passerini S (2004). Overview of energy/hydrogen storage: state-of-the-art of technologies and prospects for nanomaterials. *Mat. Sci. Eng. B-Solid* 108, 2-8. ISSN: 0921-5107.

Dai Y.M., Pan T.C., Liu W.J., Lehng J.M. (2011). Highly dispersed Ag nanoparticles on modified carbon nanotubes for low-temperature CO oxidations. *Applied catalysis B-Environmental.* 103, 221-225. ISSN: 0926-3373.

Du J., Han B., Liu Z., Liu Y., Kang D., (2007). Control synthesis of silver nansheets, chainlike sheets and microwires via a simple solvent-thermal method. *Cryst. Growth Des*. 7, 900-904. ISSN: 1528-7505.

Evanoff D.D, Chumanov G., (2004) Size-controlled synthesis of nanoparticles. 1. "silver only" aqueous suspensions via hydrogen reduction. *J. Phys. Chem. B* 108, 13948-13956 ISSN: 1089-5647.

Gangopadhyay R., De A. (2000). Conducting polymer nanocomposites: A Brief Overview. *Chem. Mater*. 12, 608-622. ISSN: 0897-4756.

Gloskowskii A., Valdaitsev D.A., Cinchetti M., Nepijko, S.A., Lange J., Aeschlimann M., Bauer M., Klimenkow M., Viduta L.V., Tomchuk P.M., Schonhense G. (2008). Electron emission from films of Ag and Au nanoparticles excited by a fentosecond punm-probe laser. *Physical Review B*. 77, Article number: 195427. ISSN: 1095-3795.

Gonzalez-Rodriguez J.G., Lucio-Garcıa M.A., Nicho M.E., Cruz-Silva R., Casales M., Valenzuela E. (2007). Improvement on the corrosion protection of conductive polymers in pemfc environments by adhesives. *J. Power Sources* 168, 184-190. ISSN: 0378-7753.

Granqvist C.G. (2007). Transparent conductors as solar energy materials: A panoramic review. *Sol. Energ. Mat. Sol. Cells*. 91, 1529-1598. ISSN: 0927-0248.

Gromov A., Vereshchagin V. (2004). Study of aluminum nitride formation by superfine aluminum powder combustion in air. *J. Eur. Ceram. Soc*, 24 2879-2884. ISSN: 0955-2219.

Hamdani S., Longuet C., Perrin D., Lopez-Cuesta J.M, Ganachaud F. (2009). Flame retardancy of silicone-based materials. *Polymer Degrad. Stab.* 94, 465-495. ISSN: 0141-3910.

Hu A., Guo J.Y., Alariji H., Patane G., Zhou Y., Compagnini G., Xu C.X. (2010). Low temperature sintering of Ag nanoparticles for flexible electronics packaging. *Applied Physics Letters*. 97, Article number: 153117. ISSN: 1077-3118.

Jimenez G.A, Jana S.C. (2007). Electrically conductive polymer nanocomposites of polymethylmethacrylate and carbon nanofibers prepared by chaotic mixing. *Composites Part A: Applied Science and Manufacturing*, Volume 38, Issue 3, March 2007, Pages 983-993. ISSN: 1359-835X.

Jin R., Cao Y., Mirkin C.A., Kelly K.L., Schatz G.C., J. Zheng, (2001). Photoinduced conversion of silver nanospheres to nanoprisms. *Science*, 294, 1901-1903. ISSN: 1095-9203.

Jixiang F., Hongjun Y., Peng K., Yan Y., Xiaoping S., Bingjun D. (2007). Silver Dendritic Nanostructure Growth and Evolution in Replacement Reaction. *Crystal Growth & Design*, Vol 7, No. 5, 864. ISSN: 1528-7505.

Maillard M., Giorgio S., Pileni M.P, (2003) Tuning the size of silver nanodisks with similar aspect ratios: synthesis optical properties. *J. Phys. Chem.*, 107, 2466-2470. ISSN: 0022-3654.

Masaharu Tsuji, Masatoshi Ogino, Ryoichi Matsuo, Hisayo Kumagae Sachie, Hikino, Taegon Kim, Seong-Ho Yoon (2010). Stepwise Growth of Silver Nanocrystals *Crystal Growth & Design*, Vol 10, No. 1, 296. ISSN: 1528-7505.

Metraux G.S., Mirkin C. A., (2005). Rapid thermal synthesis of silver nanoprisms with chemically tailorable thickness. *Adv. Mater* 17, 412. ISSN: 1521-4095.

Nanomedicine. National Horizon Scanning Unit Emerging Technology Bulletin. Published by HealthPACT Secretariat Department of Health and Ageing, (February 2007). Available at http://www.horizonscanning.gov.au [accessed September 2010].

Official website of the United States National Nanotechnology Initiative http://www.nano.gov [accessed September 2010].

Pedreño A. Nanotecnología y nanociencia: Aspectos económicos. http://iei.ua.es/nanotecnologia [accessed September 2010].

Pietrobon B., Kitaev V., (2008). Photochemcial synthesis of monodisperse size-controlled silver decahedral nanoparticles and their remarkable optical properties *Chem. Mater*. 20, 5186-5190 ISSN: 0897-4756.

Ponce de León C., Bavykin D.V., Walsh F.C. (2006). The oxidation of borohydride ion at titanate nanotube supported gold electrodes. *Electrochem. Comm*. 8, 1655-1660. ISSN: 1388-2481.

Rivas G.A., Rubianes M.D., Pedano M.L., Ferreyra N.F., Luque G., Miscoria S. A. (2009). Carbon Nanotubes: A New Alternative for Electrochemical Sensors. *Nova Science Publishers*. 978-1-60741-314-1. ISSN: 1535-6698.

Sun Y., Gates B., Mayers B., Xia Y.. Crystalline silver nanowires by soft solution processing (2002). *Nano Lett.* 2, 165-168. ISSN: 1530-6984.

Sung D., Vornbrock A.D., Subramanian V. (2010). Scaling and optimization of gravure-printed silver nanoparticle lines for pinted electronics. *IEEE Transaction of components and packaging technologies*. 33, 105-114. ISSN: 1521–3331.

Thavasi V., Singh G., Ramakrishna S. (2008). Electrospun nanofibers in energy and environmental applications. *Energ. Environ. Sci*. 1, 205-221. ISSN: 1754-5692.

Tong-Xiang F., Suk-Kwun Ch., Di Z. (2009). Biomorphic Mineralization: From Biology to Materials, *Progress in Materials Science*, 54(5): 542-659. ISSN: 0079-6425.

Xu J., Fu C., Li Y.C. (2008). Self-bank metal conductor fabricated with silver nanoparticles. *Journal of the Society for information display*. 16, 599-602. ISSN: 1071-0922.

Yun Y., Dong Z., Shanov V.N, Doepke A., Heineman W.R, Halsall H.B., Bhattacharya A, Wong D.K.Y, Schulz M.J. (2008). Fabrication and characterization of carbon nanotube array electrodes with gold nanoparticles tips. *Sensors and Actuators B: Chemical*, Volume 133, Issue 1, July 2008, Pages 208-212. ISSN: 0925-4005.

Zhang Q., Ge J., Pham T., Goebl J., Hu Y., Lu Z., Yin Y., (2009) Reconstruction of Ag Nanoplates by UV Irradiation: Tailored Optical Property and Enhanced Stability. *Angew. Chem., Int. Ed*. 48, 3516-3519 ISSN: 1521-3773.

20

Particles Formation Using Supercritical Fluids

A. Montes, M. D. Gordillo, C. Pereyra and E. J. Martinez de la Ossa
Department of Chemical Engineering and Food Technology, Faculty of Science, UCA
Spain

1. Introduction

The particle precipitation into micro and nanoparticles has been an active research field for decades (Chattopadhyay & Gupta, 2001; Kalogiannis et al., 2005; Rehman et al., 2001; Reverchon, 1999; Velaga et al., 2002; Yeo&Lee, 2004). The greatest requirement in the application of nanomaterials is its size and morphology control which determine the potential application of the nanoparticles, as their properties vary significantly with size. Micro and nanoparticles can be obtained by different techniques. Conventional techniques (spray drying, solute recrystallization, coacervation, freeze-drying, interfacial polymerization) present drawbacks such as excessive use of solvent, thermal and chemical solute degradation, structural changes, high residual solvent concentration, and mainly, difficulty of controlling the particle size (PS) and particle size distribution (PSD) during processing (He et al., 2004), so these techniques for particle formation may not be advisable.

However, the application of supercritical fluids (SCFs) is an attractive alternative for this particle formation because remove these drawbacks. These supercritical fluids have larger diffusivities than those of typical liquids, resulting in higher mass-transfer rates. Moreover its solvent power and selectivity can be tuned altering the experimental conditions.

There are two main ways of precipitating micro and nanoparticles using supercritical fluid as solvent, the RESS technique (Rapid Expansion of Supercritical Solutions); or using it as antisolvent, the SAS technique (Supercritical AntiSolvent); the choice between one or another depends on the active substance high or low solubility in the supercritical fluid.

The RESS process consists of solubilising the active ingredient of interest in the supercritical fluid and then rapidly depressurising this solution through a nozzle, thus causing the precipitation, extremely fast, of this compound. In other words, the process is based on the transition of active compound from soluble to insoluble state when the carbon dioxide passes from the supercritical to the gaseous phase. This technique has been applied on the particle precipitation and co-precipitation of many active ingredients/polymers (Kongsombut et al., 2009; Sane & Limtrakul, 2009; Turk et al., 2006; Vemavarapu et al., 2009; Wen et al., 2010).

The SAS technique, in all its variants, generally consists of spraying a solution of the solute to be precipitated into the supercritical fluid. The mass transfer behavior of the droplets is thought to be a key factor affecting particle morphology (Werling & Debenedetti, 1999). The volumetric expansion of the solvent reduces the solvation capacity of the solvent, causing the supersaturation of the liquid phase and the consequent generation of the particles. The SAS process has been carried out for many particles precipitation and polymeric encapsulation of particles of active ingredients (Ai-Zheng et al., 2009; Chong et al., 2009a;

Franceschi et al., 2008; Heyang et al., 2009; Kalogiannis et al., 2006; Kang et al., 2008; Thote & Gupta, 2005; Reverchon et al., 2008a; Ron et al., 2010; Tozuka et al., 2010).
The application of SAS processing has until now been explored in a wide range of fields including: explosives (Teipel et al., 2001), polymers (Garay et al., 2010), pharmaceutical compounds (Chen et al., 2010; Park et al., 2010), colouring matter (Reverchon et al., 2005), superconductors (Reverchon et al., 2002), catalysts and inorganic compounds (Lam et al., 2008). SAS exhibits the capacity of producing free-flowing particles in a single step at moderate pressure and temperature. In the pharmaceutical field, products with a high level of purity, suitable dimensional characteristics such as PS in the micrometer and sub-micrometer ranges, narrow PSD and spherical morphologies, have been obtained for use in developing delivery systems for drug targeting and controlled release.
In the facilities of University of Cádiz, amoxicillin (AMC) and ampicillin (AMP) micronization and polymer-drug co-precipitation have been carried out by SAS process. Several designs of experiments to evaluate the operating conditions influences on the PS and PSD have been made. In SAS, supercritical CO_2, is used as an antisolvent. The solution, containing solute, is shape as tiny droplets, produced by a nozzle through which the solution is sprayed into a high pressure vessel. When the droplets contact the supercritical CO_2 a very rapid diffusion takes place, including phase separation and precipitation of the solute (Chong et al., 2009b).
In the particle precipitation, mass transfer occurs between a droplet of organic solvent and a compressed antisolvent. In miscible conditions, above mixture critical point, there is no obvious way to define the interface between the two fluids. Dukhin et al. has evidenced the transient existence of droplets at conditions slightly above the mixture critical point, due to the existence of a dynamic interfacial tension, so a description of mass transfer from a droplet even in miscible conditions seems reasonable (Dukhin et al., 2003).
Two ways diffusion process, between a solvent droplet and its antisolvent environment at supercritical conditions, take place. There are evidences that antisolvent–solvent mass transfer is more important than jet break-up and droplet formation in determining particle size and morphology (Heater & Tomasko, 1998; Randolph et al., 1993).
However, the complexity of SAS process, which involves the interaction of thermodynamics, mass transfer, jet hydrodynamics and nucleation kinetics, makes it difficult to isolate one phenomenon as being responsible for a given trend in particle characteristics (Werling & Debenedetti, 2000).

2. Supercritical fluids

A supercritical fluid can be defined as a substance above its critical temperature and pressure. At this condition the fluid has unique properties, where it does not condense or evaporate to form a liquid or gas. A typical pressure-temperature phase diagram is shown in Figure 1. These supercritical fluids have diffusivities that are two orders of magnitude larger than those of typical liquids, resulting in higher mass-transfer rates. Properties of SCFs (solvent power and selectivity) can also be adjusted continuously by altering the experimental conditions (temperature and pressure). Supercritical fluids show many exceptional characteristics, such as singularities in compressibility and viscosity, diminishing difference in vapor and liquid phases and so on. Although a number of substances are useful as supercritical fluids, like water, carbon dioxide has been the most widely used. Supercritical CO_2 avoids water discharge; it is low in cost, non-toxic and non-flammable. It has low critical parameters (304 K, 73.8 bar) and the carbon dioxide can also be recycled (Özcan et al., 1998).

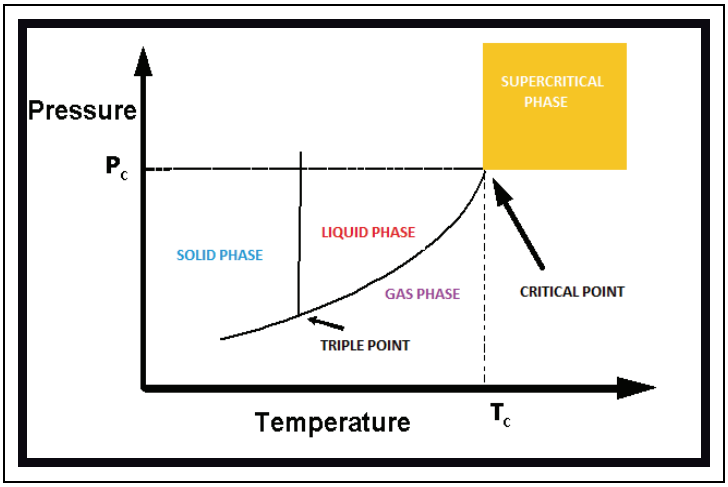

Fig. 1. Pressure-temperature phase diagram

3. Precipitation using supercritical fluids

In order to design a supercritical precipitation process several aspects must be taken into account. First, the solubility of the solute to micronize in supercritical fluids must be known in order to choose RESS or SAS process. Then, a solvent able to turn the solute soluble must be chosen, and elucidate the ternary phase equilibrium diagram solvent-solute-CO_2 or the binary phase equilibrium solvent-CO_2 when the solubility of the solute into CO_2 is neglected. Volumetric expansion curves and volumetric equilibrium data are required. Not only the thermodynamic data but also the hydrodynamic of the process should be investigated.

3.1 Solubility

Over the last few decades, the solubilities of solids and liquids in supercritical fluids (SCF) have been measured extensively. For instance, in the facilities of University of Cádiz, the solubility of solid dyes like 1,4-dimethylaminoanthraquinone (Disperse Blue 14) in supercritical carbon dioxide has been determined in the pressure range of 100-350 bar and in the temperature range of 313-353 K and correlated with empirical and semi empirical equations based model and models based on thermodynamic aspects and the use of equations of state (Gordillo et al., 2003). The solubility of palmitic acid in supercritical carbon dioxide was determined experimentally in the pressure range, 100 to 350 bar, and the temperature range, 308 to 323 K. A cubic equation of state and an empirical equation were used to correlate the solubility of this fatty acid in supercritical carbon dioxide (Gordillo et al., 2004). Such information takes an important part of establishing the technical and economic feasibility of any supercritical fluid process. Most of the investigations on solubility have been concerned about binary systems consisting of a single solute in contact with a single SCF. The solubility of solutes in supercritical fluids is related to its physical and chemical properties such as polarity, molecular structure, and nature of the material particles, and it is also related to the operating conditions such as temperature, pressure, density of solvent and co-solvents, and solvent flow rate in the supercritical region. From the 90s to now, many

articles about solubility of drugs in supercritical fluids were published. At the University of Cádiz, the solubility of the antibiotic Penicillin G in supercritical carbon dioxide was measured at pressures from 100 to 350 bar and temperatures from 313.15 to 333.15 K using a dynamic flow apparatus. Moreover a new empiric equation was proposed to improve the correlation with experimental data relating neperian logarithm with pressure and temperature (Gordillo et al., 1999). The model has been applied on several systems and the obtained results allow affirm that the thermodynamic model applied to fluid–solid equilibrium calculations is useful to predict the behaviour of this system.

Kikic et al developed an estimation method based on the Peng–Robinson´s equation of state in order to calculate the solubility of drugs such as acetaminophen, acyclovir, atenolol, Carbamazepine, ibuprofen, naproxen, nimesulide, and sotalol hydrochloride in mixtures of CO_2 and common organic solvents at a constant temperature but at variable pressure (Kikic et al., 2010). Wubbolts et al studied the systems p-acetamido phenol + ethanol + CO_2 (Wubbolts et al., 2004). In this way, Muntó et al measured the solubility of the two non-steroidal anti-inflammatory drugs ibuprofen and naproxen in CO_2-expanded ethanol and CO_2-expanded acetone. The obtained data reflected that naproxen solubility behavior was strongly dependent on the protic or aprotic nature of the organic solvent whereas for ibuprofen this solvent characteristic seemed to be less important (Munto et al., 2008). Tomasko et al. carried out a detailed review of solubilities of CO_2 into polymers as well as of other thermodynamic and transport properties of CO_2-polymer systems (Tomasko et al., 2003). Ugaonkar et al examined the rate of dissolution of carbamazepine, a hydrophobic drug for treating epilepsy, in supercritical CO_2 and its partitioning into polyvinylpyrrolidone and concluded that partitioning occurs by surface adsorption and impregnation within the polymer matrix (Ugaonkar et al., 2011).

The choice of RESS or SAS process depends on the active substance high or low solubility in the supercritical fluid. The very low solubility of solids in carbon dioxide makes the RESS process unattractive, since a very small amount of material is processed. A solvent mixture composed of carbon dioxide and a co- solvent (Bush et al., 2007; Hosseini et al., 2010) could be an alternative, since more material could be processed at high supersaturation rates in the RESS process. It is also possible to overcome the limitation of low solubility in CO_2 by employing alternative organic supercritical solvents such as trifluoromethane or clorodifluoromethane.

However, the very low solubility of solids in carbon dioxide makes the SAS process very attractive because in this process the solute must not be soluble in this fluid. So, understanding the phase behavior of solvent-supercritical fluid system can therefore provide important information regarding the role of this supercritical fluid as a solvent or reaction medium in diverse applications.

The miscibility of a dense gas with a liquid solvent is a fundamental requirement of a lot of precipitation techniques which use a gaseous or supercritical antisolvent. Vapour–liquid equilibria and volumetric expansion data for the CO_2-solvent binary system are a good starting point in order to design every supercritical process. While the vapour–liquid equilibrium data of solvents and CO_2 are usually available, the solubility of solids in a mixture of a common solvent and CO_2 are not. Gordillo et al developed and applied a thermodynamic model to several systems and the results obtained let affirm that the thermodynamic model applied to fluid–solid equilibrium calculations was useful to predict the behaviour of this system (Gordillo et al., 2005a). These authors proved that depending on the group contribution methods chosen to estimate the parameter critical the agreement

between measured and calculated solubility data varied (Gordillo et al., 2005b). Moreover, the results obtained in another work about the dye solubility correlation showed that the choice of group contribution method was more important than the choice of the equation of state used, Redlich-Kwong, Soave-Redlich-Kwong and Peng-Robinson (Gordillo et al., 2005c)

However in SAS process, according to usual practice in the ternary systems, it has been considered that the presence of non soluble drugs does not affect the solvent–CO_2 equilibrium, therefore to represent the ternary equilibrium of drug–solvent–CO_2, the solvent–CO_2 pseudo-binary diagram is used. Volumetric expansion curves provide a mean to determine an allowed range of pressure for solubility measurements at a given temperature and for a given solvent. Thus it is possible to know prior to the analysis whether the operating conditions are above, near or below the mixture critical point (MCP). The mass transfer between CO_2 and solution depends on the situation in this diagram. In Figure 2 it is shown a phase equilibrium diagram of the binary system NMP–CO_2, at two temperatures, estimated using the equation of state of Peng–Robinson, for the system NMP-CO_2. The data corresponding to this equilibrium diagram were obtained from the development of a computer program in Matllab 7.0 (Tenorio et al., 2008).

On the other hand, the presence of the solute can induce changes in the phase diagrams of the binary solvent–SC-CO_2 systems. These changes have been rarely measured and they are difficult to evaluate. However, when the solute has small interactions and a very low solubility in SC-CO_2, its influence on the phase diagrams should be small (Kikic et al., 2006). In systems with strong interactions between CO_2 and solute a drastic alteration of the phase diagrams is possible.

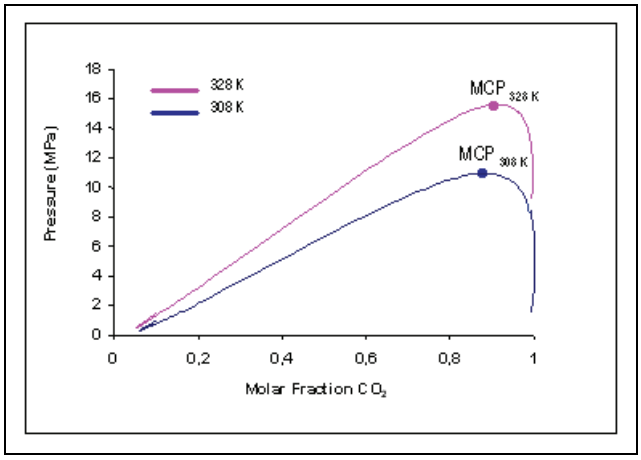

Fig. 2. P–x–y diagram of the CO_2–NMP system (Tenorio et al., 2008)

3.2 Precipitation

As it has been argued, the supercritical fluid technology has emerged as an important alternative to traditional processes of generation of micro and nanoparticles, offering opportunities and advantages such as higher product quality in terms of purity, more uniform dimensional characteristics, a variety of compounds to process and a substantial improvement on environmental considerations, among others.

Previously, it was discussed that the different particle formation processes using SCF are classified depending on how this SCF behaves, i.e., the supercritical CO_2 can play the role as antisolvent (AntiSolvent Supercritical process, SAS) or solvent (RESS process).
The SAS process (Figure 3) uses both the high power of supercritical fluids to dissolve the organic solvents and the low solubility of the compounds in supercritical fluids (Shekunov and York, 2000) to cause the precipitation of such compounds once they are dissolved in the organic phase. The dissolution of the supercritical fluid into the organic solvent goes along with a large volume expansion and, consequently, a reduction of the liquid density, and therefore, of its solvent power, causing a sharp rise in the supersaturation within the liquid mixture. Because of the high and uniform degree of supersaturation, small particles with a narrow particle size distribution are expected (Dukhin et al., 2005).

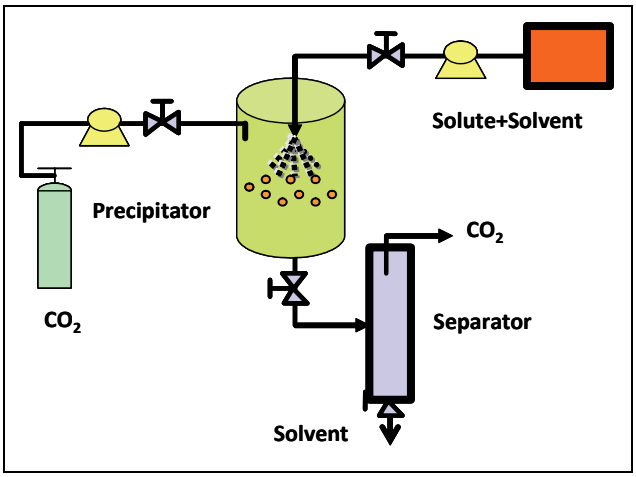

Fig. 3. SAS process diagram

In the RESS method, the sudden expansion of supercritical solution (solute dissolved in supercritical carbon dioxide) via nozzle and the rapid phase change at the exit of the nozzle cause a high super-saturation, thus causing very rapid nucleation of the substrate in the form of very small particles that are collected from the gas stream (Figure 4). Hence, the conditions inside the expansion chamber are one key factor to control particle size and the particles grow inside the expansion chamber to their final size. This result clarifies the influence of two important process parameters on particle size. Both, a shorter residence time and, hence, less time available for particle growth as well as a higher dilution of the particles in the expansion chamber result in smaller particles.
Harrison et al. performed RESS studies on benzoic acid, cholesterol and aspirin, in which the influence of several expansion parameters on the particle size were studied: the variation of the pre-expansion pressure and temperature, distance from the nozzle, and on the amount and type of co-solvent added. To characterize the supercritical CO_2 expansion, a modelling to calculate pressure, temperature, density and velocity, along the nozzle was developed. The average particle diameter decreased with increasing pre-expansion pressure, and increased with increasing pre-expansion temperature. This is probably due to a lower mass flow rate, which is associated to a lower pre-expansion pressure or higher pre-expansion temperature (Harrison et al., 2007).

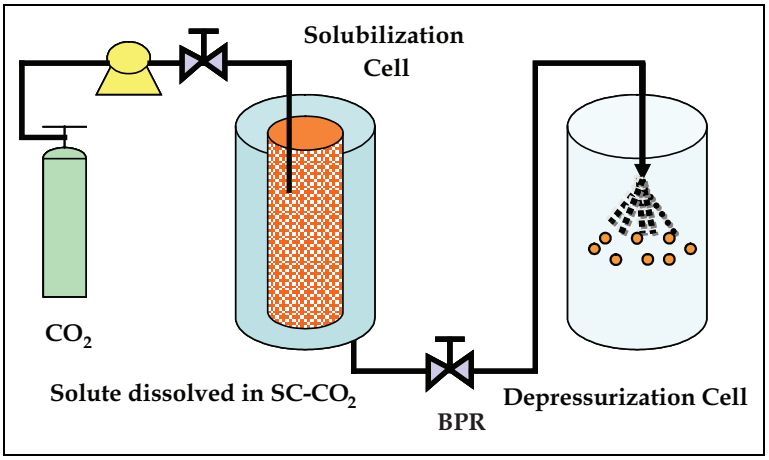

Fig. 4. RESS process diagram

In this way, Corazza et al. carried out an analysis of supersaturation of the system during expansion of the supercritical solution. For that the phase equilibrium problem was solved at system temperature and pressure for each specific position. Supersaturation values were very high in the free-jet expansion region, but depending on the preexpansion conditions, the supersaturation profile in the free jet region was quite different. These observations suggest that pre and post expansion conditions can have a remarkable effect on the characteristics of precipitated particles (Corazza et al., 2006). The results presented in this work indicate that the fluid residence time in the capillary region was very low, and thus the mechanism for microparticle formation could also be affected by mass transfer phenomena in addition to thermodynamic equilibrium. One more time, mass transfer must be studied from thermodynamic and hydrodynamic point of view.

4. SAS process

4.1 Mass transfer

In SAS process, mass transfer occurs between a droplet of organic solvent and a compressed antisolvent. In miscible conditions, above mixture critical point, there is no obvious way to define the interface between the two fluids. Dukhin et al. has evidenced the transient existence of droplets at conditions slightly above the mixture critical point, due to the existence of a dynamic interfacial tension, so a description of mass transfer from a droplet even in miscible conditions seems reasonable (Dukhin et al., 2003).

On the other hand, in the SAS process the solution is generally dilute and the equilibrium compositions of the binary and ternary mixtures are not significantly different. Accordingly to this, the solid present in the solution is not likely to affect the rates of mass transfer of CO_2 and solvent to and from the droplet respectively.

Mass transfer depend on the densities differences between solvent and antisolvent, viscosity, diffusivity, droplet or particle diameter and solvent flow rate. Chong et al. developed a mathematical model form mass transfer between a droplet of organic solvent and a compressed antisolvent in complete miscibility in SAS process. Calculations using Peng-Robinson equation of state showed that droplets swell upon interdiffusion when the

solvent is denser than the antisolvent and shrink when the antisolvent is denser (Chong et al., 2009b).

Some authors have modelled the behavior of an organic solvent droplet, considering different local mass transfer both at subcritical (Werling & Debenedetti, 1999) and supercritical (Werling & Debenedetti, 2000) conditions. In this case, the droplet is considered to be stagnant. Therefore, the only convective motion considered is that induced by the diffusion. At subcritical conditions, calculations showed that there is an initial period of droplet swelling, due to the diffusion of CO_2 into the organic solvent. Droplet lifetime decreases as the pressure increases, and increases sharply at near-critical conditions, because diffusivities tend to zero near the critical point. At miscible conditions, mass transfer is much faster than at subcritical conditions. Droplet diameter increases if the density of the organic solvent is higher than that of the CO_2, and vice versa. However, this ideal and local approach is often not enough to interpret the results. Elvassore et al. developed a model based on the mass transfer simulations of Werling and Debenedetti. This model included the solute in mass transfer calculations (Elvassore et al., 2004).

Pérez de Diego et al. and Martin et al. developed both models for the evaporation of dichloromethane (Pérez de Diego et al., 2006) and ethanol (Martín et al., 2007) droplets respectively which accounted for the higher mass transfer coefficients due to the convective motion of CO_2, explaining the change in particle morphology.

Shekunov et al proposed a simplified approach based on the calculation of different characteristic times (diffusion, jet break up...). They studied the phenomena of turbulent dispersion and micromixing in supercritical carbon dioxide using paracetamol as a model drug compound. They tried to describe the effect of mass-transfer on the particle size and morphology and suggested that particle growth is the time-limiting step (Shekunov et al., 1999).

Then, in order to describe the mass transfer, the drop size distribution, nucleation and particle growth during the drying of the drops as well as the fluid dynamics of the dispersed liquid must be known. Other works also carried out a complete modelling. In these cases, the overall process is modelled, taking into account thermodynamic, hydrodynamic, crystallization and mass transfer aspects (Cardoso et al., 2008; Martin & Cocero, 2004; Lora et al., 2000; Reverchon et al., 2010).

At the University of Cádiz, Tenorio et al, by determining the thermodynamic properties of the phases involved in the process, and applying empirical equations (operations with dimensionless numbers), have estimated the different disintegration regimes of the jet when an N-methyl-pyrrolidone (NMP)-ampicillin solution was injected into the CO_2-pressurized chamber. The application of the empirical hydrodynamics model proved the existence of significant mechanisms that stabilize the liquid jet, and it showed that there were limiting hydrodynamic conditions that had to be overcome to drive the process toward the formation of uniform spherical nanoparticles and the achievement of higher yields (Tenorio et al., 2009)

Reverchon et al., in some recent papers (Reverchon et al., 2007, 2008b, 2008c, 2011) studied the link between SAS morphologies and the relative position of the SAS operating point with respect the mixture critical point of the solvent-CO_2 mixtures. It was proposed several mechanisms and their interactions to elucidate the different morphologies and dimensions of precipitates. From a practical point of view, the knowledge of the competing mechanisms allows to select the dimensions of the precipitated particles. If nanoparticles are the objective of the process, low concentrations of the liquid solution are preferable and SAS operation

should be performed at completely developed supercritical conditions (when surface tension vanishes before jet break up occurs). If spherical microparticles are the target, the process conditions in which jet break-up produces micrometric droplets are the right ones; the increase in concentration of the starting solution will increase the average diameter of the particles, but, also their polydispersity.

4.2 Polymer and biopolymers

Among organic and inorganic compounds that have been processed with SAS process, polymers have remarkable interest and significance. Yeo and Kiran (Yeo & Kiran, 2005) and Tomasko et al. (Tomasko et al., 2003) presented extensive reviews of the supercritical processing of polymers. Because most of polymers are not soluble in supercritical fluids, this antisolvent process is especially suitable for their recrystallization or precipitation in form of microparticles. The polymer is firstly dissolved in a liquid organic solvent and a supercritical fluid is employed as an antisolvent for the polymer. Polymers in form of small particles are useful for several applications like stationary phases in chromatography, adsorbents and catalyst supports, as well as drug delivery systems (Dixon et al., 1993). The polymers must fulfil several requisites: its biocompatibility, non toxicity, providing a suitable medium for preserving the properties and activity of the active substance and easy to process with the selected precipitation technique.

It is particularly important for polymer processing with supercritical processes is the glass transition and the melting point temperature depressions induced by the supercritical fluid. In particular, the dissolution of SC-CO_2 into the polymer can reduce the glass transition temperature of amorphous polymers (Tomasko et al., 2003), an effect that is caused by intermolecular interactions between the dissolved CO_2 and the polymer. The melting point depression caused by the dissolution of CO_2 is less noticeable in magnitude.

A number of RESS processes for the encapsulation of particles with polymer (polylactic acid (PLA), polyethylene glycol (PEG), Eudragit) or composite particle formation for the controlled release of drugs have been reported as it was referenced before.

However, the potential application of RESS for particle coating or encapsulation is limited because the solubility of polymers in SC-CO_2 is generally very poor (O'Neill et al., 1998)

Compared to RESS, the SAS process offers much more flexibility in terms of choosing suitable solvents. Furthermore, SAS has advantages over RESS because SAS is usually operated under mild conditions compared with those of RESS, which is associated to relatively high temperature and high pressure. Therefore RESS is also less attractive from the perspectives of safety and cost. The SAS process has been carried out for many particles precipitation and polymeric encapsulation of particles of active ingredients.

In order to obtain polymer-drug composites several researches have been carried out at our laboratory. Ethyl cellulose (EC) is a biocompatible and non biodegradable polymer. Ethyl cellulose is commonly used as drug carrier in controlled delivery systems. For instance, ethyl cellulose microcapsules has been used as a drug-delivery device for protecting folic acid from release and degradation in the undesirable environmental conditions of the stomach, whilst allowing its release in the intestinal tract to make it available for absorption. In the same way, ethyl cellulose and antibiotic microcapsules have been developed to use as drug delivery protecting antibiotic of conditions of the stomach.

At University of Cádiz, ethyl cellulose microparticles were successfully precipitated from dichloromethane (DCM) by SAS process (Gordillo et al., 2008) and particles were reduced from 50-100 to 3-5 μm (Figure 5). The concentration was the factor that had the greatest

influence on the PS and PSD. An increase in the initial concentration of the solution led to larger particles sizes with a wider distribution.

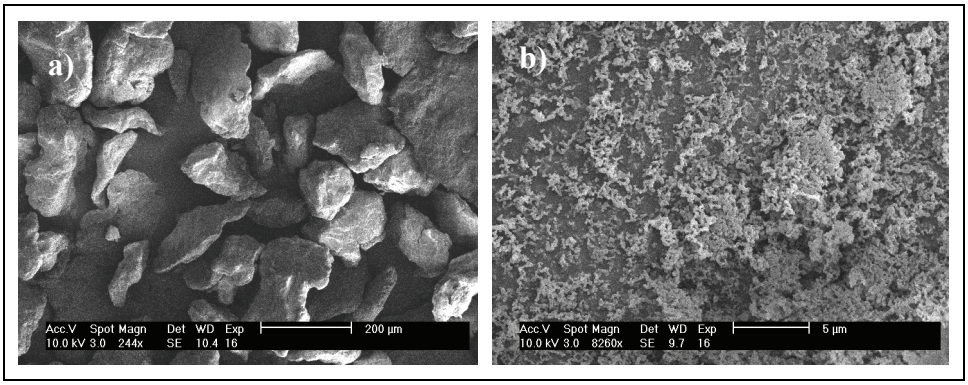

Fig. 5. SEM images of a) raw ethyl cellulose and b) precipitated ethyl cellulose

A pilot plant, developed by Thar Technologies® (model SAS 200) was used to carry out all the experiments. A schematic diagram of this plant is shown in Figure 6. The SAS 200 system comprises the following components: two high-pressure pumps, one for the CO_2 (P1) and the other for the solution (P2), which incorporate a low-dead-volume head and check valves to provide efficient pumping of CO_2 and many solvents; a stainless steel precipitator vessel (V1) with a 2-L volume consisting of two parts, the main body and the frit, all surrounded by an electrical heating jacket (V1-HJ1); an automated back-pressure regulator (ABPR1) of high precision, attached to a motor controller with a position indicator; and a jacketed (CS1-HJ1) stainless steel cyclone separator (CS1) with 0.5-L volume, to separate the solvent and CO_2 once the pressure was released by the manual back-pressure regulator (MBPR1).The following auxiliary elements were also necessary: a low pressure heat exchanger (HE1), cooling lines, and a cooling bath (CWB1) to keep the CO_2 inlet pump cold and to chill the pump heads; an electric high-pressure heat exchanger (HE2) to preheat the CO_2 in the precipitator vessel to the required temperature quickly; safety devices (rupture discs and safety valve MV2); pressure gauges for measuring the pump outlet pressure (P1, PG1), the precipitator vessel pressure (V1, PG1), and the cyclone separator pressure (CS1, PG1); thermocouples placed inside (V1-TS2) and outside (V1-TS1) the precipitator vessel, inside the cyclone separator (CS1-TS1), and on the electric high pressure heat exchanger to obtain continuous temperature measurements; and a FlexCOR coriolis mass flowmeter (FM1) to measure the CO_2 mass flow rate and another parameters such as total mass, density, temperature, volumetric flow rate, and total volume.

4.3 Pharmaceuticals

Pharmaceutical preparations are the final product of a technological process that gives the drugs the characteristics appropriate for easy administration, proper dosage and enhancement of the therapeutic efficacy. Among several kinds of development of modified release preparation, the design of pharmaceutical preparations in nanoparticulate form has emerged as a new strategy for drug delivery (Pasquali et al., 2006). Particle size and particle size distribution are critical parameters that determine the rate of dissolution of the drug in

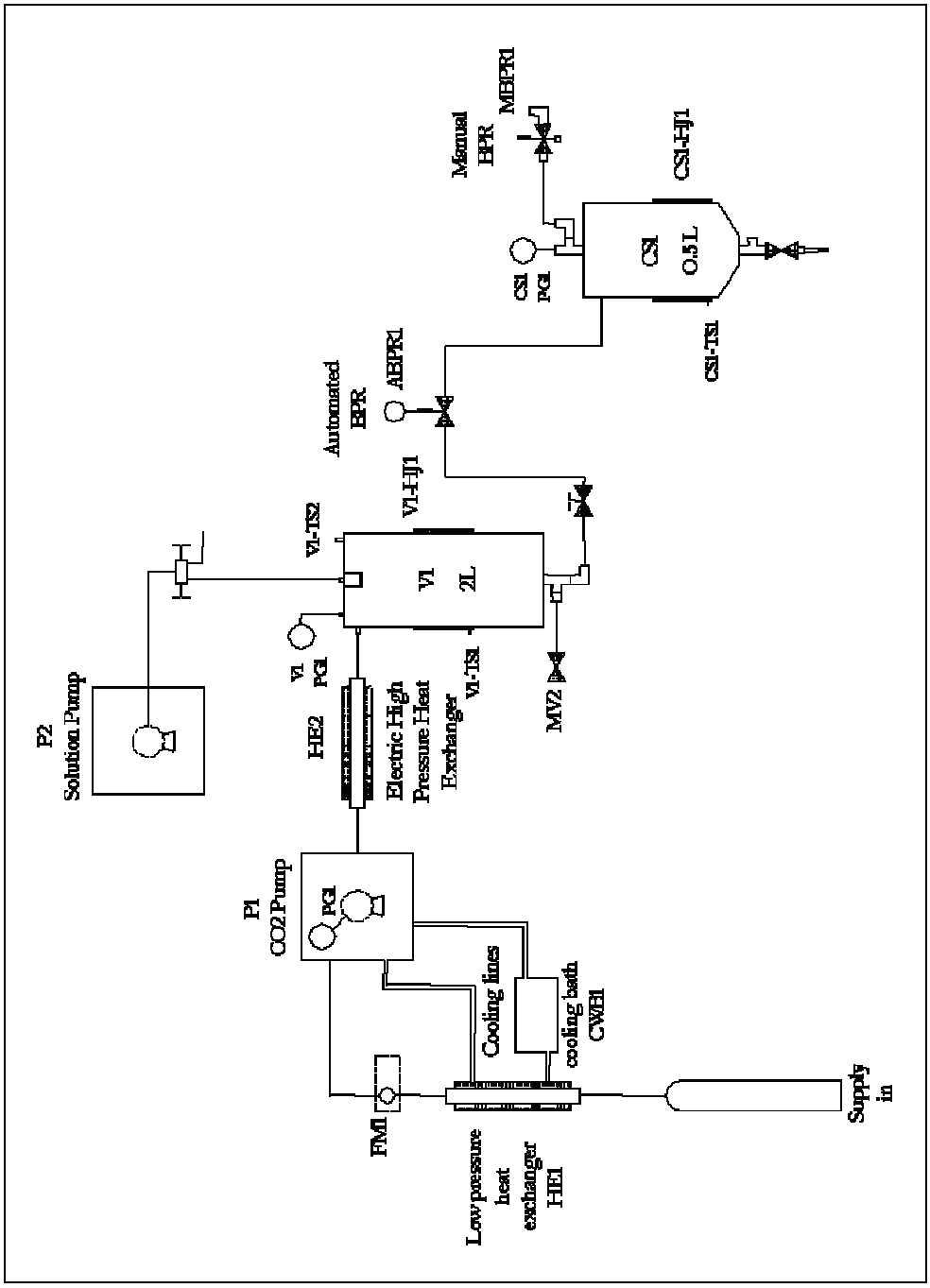

Fig. 6. Schematic diagram of the pilot plant

the biological fluids and, hence, have a significant effect on the bioavailability of those drugs (Perrut et al., 2005; Van Nijlen et al., 2003).

Methods used in the past for the manufacture of drug nanoparticles usually do not allow very accurate control of the particle size, and so broad particle size distributions are obtained. Supercritical antisolvent (SAS) processes have been widely used for the last ten years to precipitate Active Pharmaceutical Ingredients (APIs) (Chattopadhyay& Gupta, 2001; Rehman et al., 2001; Velaga et al., 2002; Yeo & Lee, 2004).

Supercritical antisolvent techniques overcome the main drawbacks of conventional techniques, such as the degradation of the active ingredients because of the high profiles of temperatures and tensile stresses reached and the large amount of organic solvent used, resulting in the need to remove the solvent from the final product.

Amoxicillin and ampicillin micronization have been carried out by SAS process in our laboratory (Montes et al., 2010, 2011; Tenorio et al., 2007a, 2007b, 2008). Several experiments designs to evaluate the operating conditions influences on the PS and PSD have been made. Pressures till 275 bar and temperatures till 338K have been used and antibiotic particle sizes have been reduced from 5-60 μm (raw material) to 200-500 nm (precipitated particles) (Figure 7).

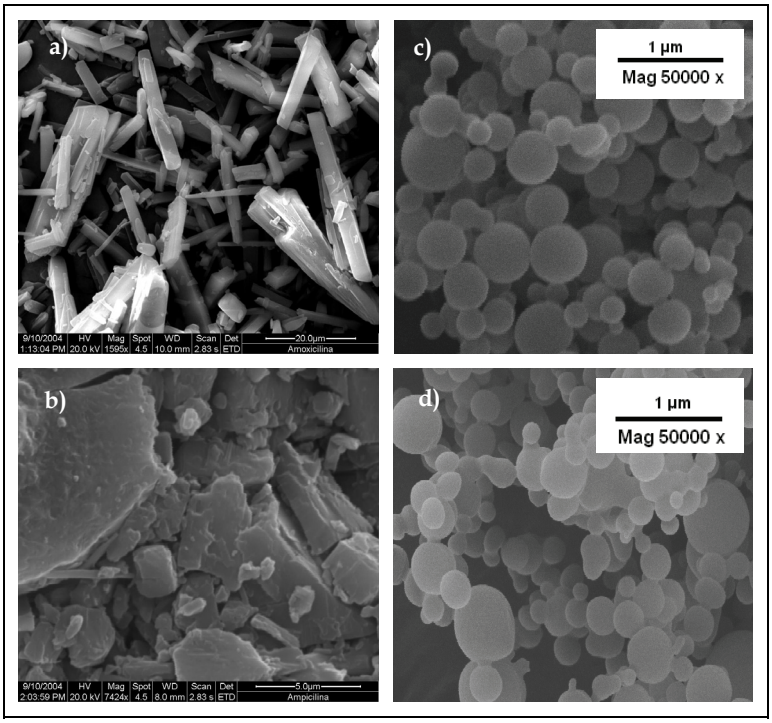

Fig. 7. SEM images of commercial a) amoxicillin and b) ampicillin, c)precipitated amoxicillin and d) ampicillin

The initial concentration of the drug solution pumped into the vessel, is the factor that has the greatest influence on both PS and PSD. Therefore, both PS and the PSD required for the

final formulation of drug could be adjusted well by a change in the initial concentration of the solution. An increase in initial concentration of the solution has two opposite effects: On one hand, with a higher concentration, it is possible to achieve higher supersaturations, which tends to diminish the particle size. On the other hand, condensation is directly proportional to the concentration of solute, and the increase of the condensation rate at higher concentrations tends to increase the particle size (Martin & Cocero, 2004). In our case, an increase in the initial concentration of the solution led to larger particles sizes with a wider distribution.

Thus, the second effect (condensation rate) prevailed under the operating conditions used in this work; that is, the higher the initial concentration of the solution, the higher the condensation rate, and thus, the greater the particle sizes produced. This result is consistent with those obtained by Reverchon et al., which were also explained in terms of competition between nucleation and growth processes (Reverchon et al., 2000).

4.4 Composites and encapsulates

The ability to tune polymer and drug simultaneously can be used to control the nature and extent of drug loading. In order to obtain polymer-drug composites several researches have been carried out. Composites are frequently produced by the simultaneous precipitation of the core and coating materials, leading to a dispersion of particles of the core material into a matrix of coating material while encapsulates are produced when the coating material is precipitated as a thin shell over a previously existing core material particle. These systems let achieve a controlled delivery of the active ingredients into its targeted media. In addition to oral administration, these particulate carriers can also be injected intramuscularly or intravenously as long as their particle size is within physiologically acceptable range to achieve a controlled dissolution of the active substance (Cocero et al., 2009).

In the pharmaceutical compounds encapsulation, the coating material must be biocompatible and non toxic, providing a suitable medium for preserving the properties and the activity of the active substance and easy to process with the precipitation technique.

In our research group, ethyl cellulose amoxicillin and ampicillin co-precipitation has been carried out. For that, commercials EC and AMC and AMP have been dissolved in a mixture of DCM and dimethylsulfoxide DMSO and this solution has been pumped by the high pressure pump of the SAS equipment. A temperature increase from 308 to 328 K, independently of pressure, is traduced to particle size increase but an agglomeration of particles formed by irregular block is observed when the temperature is increased to 333 K. However, at three temperatures, an increase of pressure leads to a smaller particle size. This fact can also be explained on the basis of the numerical modelling of mass transfer proposed by Werling and Debenedetti (Werling& Debenedetti, 2000). An increase of pressure brings the system to miscible conditions. These conditions result in faster mass transfer, causing a higher degree of supersaturation that results in higher nucleation rates, thus producing smaller particle size.

To study the ability of ethyl cellulose to encapsulate amoxicillin, a suspension of AMC microparticles in a solution of EC in DCM has been used. This suspension is sprayed by a nozzle using a KD410 Syringe Pump instead of the solvent pump of the SAS equipment to avoid blocking the pump. The supercritical CO_2 acts as an antisolvent for the DCM. A rapid mutual diffusion between the supercritical CO_2 and the organic solvent causes supersaturation of the polymer solution, leading to nucleation and precipitation of the

polymer to encapsulate the AMC particles. In the precipitation over a suspension of particles, the particles behave as nuclei for the precipitation of the polymer, and a polymer matrix of encapsulated particles is produced by agglomeration (Cocero et al., 2009).
SEM images of these microparticles are shown in Figure 8. SEM images are not accurate enough to observe the distribution of both compounds because all the active substance could be situated on the surface of these microspheres and/or into the core. Thus, X-ray photoelectron spectroscopy (XPS) is one of the main techniques used to determine the success of the encapsulation process by the chemical analysis of the particles on the precipitated surface (Morales et al, 2006). In this case, the elements that differentiate amoxicillin from ethyl cellulose are sulphur (S) and nitrogen (N) atoms. Therefore, these elements can indicate the location of the drug in the precipitated powders. In the co-precipitated the sulphur peak can be identified but there is an absence of this peak in the encapsulate. Moreover, an elemental analysis of the encapsulate is needed to confirm that the drug was situated into the core.

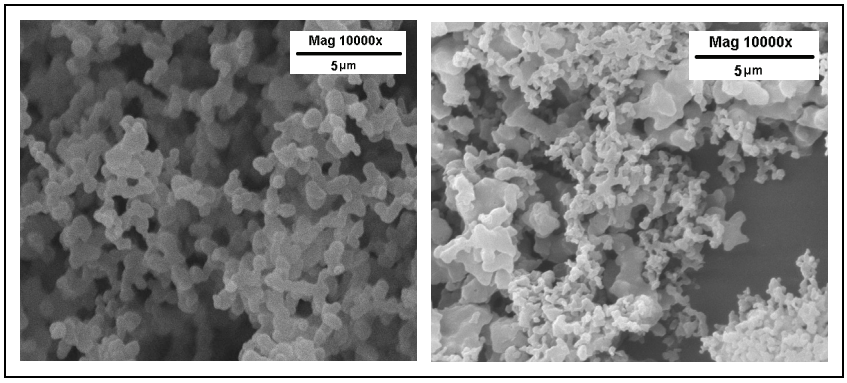

Fig. 8. SEM images of amoxicillin ethyl cellulose a) encapsulates and b) co-precipitated

5. Conclusions

Supercritical Fluid process can be an excellent alternative to conventional precipitation and encapsulation processes. RESS and SAS processes have been applied on the particle precipitation and co-precipitation of many active ingredient/polymer. Furthermore, SAS has advantages over RESS because SAS is usually operated under mild conditions compared with those of RESS, which is associated to relatively high temperature and high pressure. Anyway, the technical viability of the SAS process requires knowledge of the phase equilibrium of the system; its hydrodynamics (the disintegration regimes of the jet); the mass transfer between the jet generated and the continuous phase; and the mechanisms and kinetics of nucleation and crystal growth. Above MCP the surface tension vanishes before jet break up occurs and the jet evolves as gaseous plume producing nanoparticle. However near MCP the jets atomize into droplets producing spherical microparticles.
At the University of Cádiz, amoxicillin, ampicillin and ethyl cellulose have been sucessfully precipitated by SAS process. The concentration was the factor that had the greatest influence on the PS and PSD. An increase in the initial concentration of the solution led to larger particles sizes with a wider distribution. Moreover, ethyl cellulose- amoxicillin and ethyl

cellulose-ampicillin systems have been obtained successfully in our laboratory. A temperature increase of the experiments is traduced to particle size increase. An agglomeration of particles formed by irregular block is observed when the temperature is increased to 333 K. However, an increase of pressure leads to a smaller particle size.

6. Acknowledgment

We are grateful to the Spanish Ministry of Education and Science (Project No. CTQ2007-67622) for financial support.

7. References

Ai-Zheng C. , Yi, L. , Foo-Tim, C. , Tsui-Yan, L. , Jun-Yan, H., Zheng, Z. ,Daniel Kam-wah, M. (2009). Microencapsulation of puerarin nanoparticles by poly(L-lactide) in a supercritical CO_2 process. *Acta Biomaterialia* , 5, pp. 2913-2919.

Bush, J. R., Akgerman, A., Hall, K. R. (2007). Synthesis of controlled release device with supercritical CO_2 and co-solvent. *J. Supercrit. Fluids*, 41, pp. 311–316.

Cardoso, M. A. T.; Monteiro, G. A.; Cardoso, J. P.; Prazeres, T. J. V.; Figueiredo, J.M. F.; Martinho, J. M. G.; Cabral, J. M. S.; Palavra, A. M. F. (2008). Supercritical antisolvent micronization of minocycline hydrochloride. *J. Supercrit. Fluids*, 44, pp. 238–244.

Chattopadhyay, P., Gupta, R. B. (2001). Production of antibiotic nanoparticles using supercritical CO_2 as antisolvent with enhanced mass transfer, *Ind. Eng. Chem. Res.*, 40, pp. 3530-3539.

Chen, Y.-M., Tang, M., Chen. Y.-P. (2010). Recrystallization and micronization of sulfathiazole by applying the supercritical antisolvent technology. *Chem. Eng. J.*, 165, pp. 358–364.

Chong, G.H., Spotar, S.Y., Yunus, R. (2009). Numerical Modeling of Mass Transfer for Solvent-Carbon Dioxide System at Supercritical (Miscible) Conditions. *J. Appl. Sci.*, 9(17), pp. 3055-3061.

Chong, G.H., Yunus, R., Abdullah, N., Choong, T.S.Y., Spotar, S. (2009). Coating and Encapsulation of Nanoparticles using Supercritical Antisolvent. *Am. J. Appl. Sci.*, 6 (7), pp. 1352-1358.

Cocero, M. J., Martin, A., Mattea, F., Varona, S. (2009). Encapsulation and co-precipitation processes with supercritical fluids: Fundamentals and applications. *J. Supercrit. Fluids*, 47, pp. 546-555.

Corazza, M. L., Filho, C. L., Dariva, C. (2006). Modeling and simulation of rapid expansion of supercritical solutions. *Brazilian J. of Chem. Eng.*, 23(3), pp. 417-425.

Dixon, D.J., Johnston, K.P., Bodmeier, R.A. (1993).Polymeric materials formed by precipitation with a compressed fluid antisolvent, *AIChE J.*, 39 (1), pp. 127–139.

Dukhin, S.S., Zhu, C., Pfeffer, R., Luo, J.J., Chavez, F., Shen, Y. (2003). Dynamic interfacial tension near critical point of a solvent–antisolvent mixture and laminar jet stabilization, *Physicochem. Eng. Aspects*, 229, pp. 181-199.

Dukhin, S. S., Shen, Y., Dave, R., Pfeffer, R. (2005). Droplet mass transfer, intradroplet nucleation and submicron particle production in two-phase flow of solvent-supercritical antisolvent emulsion. *Colloids Surf. A*, 261, pp. 163-176.

Elvassore, N., Cozzi, F., Bertucco, A. (2004). Mass transport modeling in a gas antisolvent process, *Ind. Eng. Chem. Res.*, 43, pp. 4935–4943.

Franceschi, E., De Cesaro, A. M., Feiten, M., Ferreira, S. R.S., Darivac, C., Kunita, M.H., Rubira, A. F., Muniz, E. C., Corazza, M. L., Oliveira, J. V. (2008). Precipitation of β-carotene and PHBV and co-precipitation from SEDS technique using supercritical CO_2. *J. Supercrit.Fluids*, 47, pp. 259-269.

Garay, I., Pocheville, A., Madariaga, L. (2010). Polymeric microparticles prepared by supercritical antisolvent precipitation. *Powder Technology*, 197, pp. 211–217.

Gordillo, M.D., Blanco, M.A., Molero, A., Martinez De La Ossa, E. (1999). Solubility of the antibiotic Penicillin G in supercritical carbon dioxide, *J.Supercrit. Fluids*, 15 (3), pp. 183-190.

Gordillo, M.D., Pereyra, C., Martinez de la Ossa, E.J. (2003). Measurement and correlation of solubility of Disperse Blue 14 in supercritical carbon dioxide, *J. Supercrit. Fluids*, 27 (1), pp. 31-37.

Gordillo, D., Pereyra, C., De La Ossa, E.J.M. (2004). Supercritical fluid-solid phase equilibria calculations by cubic equations of state and empirical equations: Application to the palmitic acid + carbon dioxide system. J. *Chem. Eng. Data*, 49 (3), pp. 435-438.

Gordillo, M.D., Blanco, M.A., Pereyra, C., Martínez De La Ossa, E.J. (2005) .Thermodynamic modelling of supercritical fluid-solid phase equilibrium data, *Computers and Chemical Engineering*, 29 (9), pp. 1885-1890.

Gordillo, M.D., Sánchez-Oneto, J., Pereyra, C., De La Ossa, E.J.M. (2005). Review of the main methods of critical parameter estimation: Application to the correlation of palmitic acid / supercritical carbon dioxide phase equilibrium data. *Reviews in Chemical Engineering*, 21 (2), pp. 71-94.

Gordillo, M.D., Pereyra, C., Martínez de la Ossa, E.J. (2005) Solubility estimations for Disperse Blue 14 in supercritical carbon dioxide. *Dyes and Pigments*, 67 (3), pp. 167-173.

Gordillo, M.D., Di Giacomo, G., Schindhelm, S., Pereyra, C.M., Martínez de la Ossa, E.J. (2008). 11th Mediterranean Congress of Chemical Engeenering, Barcelona.

Harrison, J. J., Lee, C., Lenzer, T., Oum, K. (2007). On-line in-situ characterization of CO_2 RESS processes for benzoic acid, cholesterol and aspirin. *Green Chem.*, 9, pp. 351–356.

He, W.Z., Suo, Q.L., Jiang, Z.H., Shan, A., Hong, H.L. (2004). Precipitation of ephedrine by SEDS process using a specially designed prefilming atomizer, *J. Supercrit. Fluids*, 31, pp. 101-110.

Heater, K.J., Tomasko, D.L. (1998). Processing of epoxy resins using carbon dioxide as an antisolvent, *J. Supercrit. Fluids*, 14, pp. 55-65.

Heyang , J., Fei, X., Cuilan , J., Yaping, Z., Lin, H. (2009). Nanoencapsulation of Lutein with Hydroxypropylmethyl Cellulose Phthalate by Supercritical Antisolvent. *Chin. J. Chem. Eng.*, 17(4), pp. 672-677.

Hosseini, M. H., Alizadeh, N., A.R. Khanchi. (2010). Effect of menthol as solid cosolvent on the solubility enhancement of clozapine and lamorigine in supercritical CO_2. *J. Supercrit. Fluids*, 55, pp. 14–22.

Kalogiannis, C. G., Pavlidou, E., Panayiotou, C. G. (2005). Production of Amoxicillin Microparticles by Supercritical Antisolvent Precipitation. *Ind. Eng. Chem. Res.*, 44, pp. 9339-9346.

Kalogiannis, C. G., Michailof, C. M., Panayiotou. C. G. (2006). Microencapsulation of Amoxicillin in Poly(L-lactic acid) by Supercritical Antisolvent Precipitation. *Ind. Eng. Chem. Res.*, 45, pp. 8738-8743.

Kang, Y., Wu, J., Yin, G., Huang, Z., Liao, X., Yao, Y., Ouyang, P., Wang, H., Yang, Q. (2008). Characterization and Biological Evaluation of Paclitaxel-Loaded Poly(L-lactic acid) Microparticles Prepared by Supercritical CO_2, *Langmuir*, 24, pp. 7432-7441.

Kikic, I., Alessi, P., Eva, F., Moneghini, M., Perissutti, B. (2006). Supercritical antisolvent precipitation of atenolol: the influence of the organic solvent and of the processing approach, *J. Supercrit. Fluids*, 38 (3), pp. 434–441.

Kikic, I., De Zordi, N., Moneghini M., Solinas, D. (2010). Solubility estimation of drugs in ternary systems of interest for the antisolvent precipitation processes *J. Supercrit. Fluids*, 55, pp. 616–622.

Kongsombut, B., Tsutsumi, A., Suankaew, N., Charinpanitkul, T. (2009). Encapsulation of SiO2 and TiO2 Fine Powders with Poly(DL-lactic-co-glycolic acid) by Rapid Expansion of Supercritical CO_2 Incorporated with Ethanol Cosolvent. *Ind. Eng. Chem. Res.*, 48, pp. 11230-11235.

Lam, U. T., Mammucari, R., Suzuki, K., Foster, N. R. (2008). Processing of Iron Oxide Nanoparticles by Supercritical Fluids. *Ind. Eng. Chem. Res.*, 47, pp.599-614

Lora, M., Bertucco, A., Kikic, I. (2000). Simulation of the Semicontinuous Supercritical Antisolvent Recrystallization Process. *Ind. Eng. Chem. Res.*, 39, pp. 1487-1496.

Martín, A., Cocero, M.J. (2004). Numerical modeling of jet hydrodynamics, mass transfer, and crystallization kinetics in the supercritical antisolvent (SAS) process *J. Supercrit. Fluids*, 32, pp. 203–219.

Martín, A., Bouchard, A., Hofland, G.W., Witkamp, G.-J., Cocero, M.J. (2007) .Mathematical modeling of the mass transfer from aqueous solutions in a supercritical fluid during particle formation, *J. Supercrit. Fluids*, 41 (1), pp. 126–137.

Montes, A., Tenorio, A., Gordillo, M.D., Pereyra, C., Martínez de la Ossa, E. (2010). Screening design of experiment applied to supercritical antisolvent precipitation of amoxicillin: exploring new miscible conditions. *J. Supercrit. Fluids*, 51, pp. 399-403

Montes, A., Tenorio, A., Gordillo, M.D., Pereyra, C., Martínez de la Ossa, E. (2011). Supercritical Antisolvent Precipitation of Ampicillin in Complete Miscibility Conditions. *Ind. Eng. Chem. Res.*, 50, pp. 2343–2347.

Morales, M. E., Ruiz, M. A., Oliva, I., Oliva, M., Gallardo, V. (2007). Chemical characterization with XPS of the surface of polymer microparticles loaded with morphine. *Int. J. Pharm.*, 333, pp. 162-166.

Muntó, M., Ventosa, N., Sala, S., Veciana, J. (2008). Solubility behaviors of ibuprofen and naproxen drugs in liquid "CO_2–organic solvent" mixtures. *J. Supercrit. Fluids*, 47, pp. 147–153.

O'Neill, M.L, Cao, Q., Fang, M., Johnston, K.P., Wilkinson, S.P., Smith, C., Kerschner, J.L., Jureller, S.H. (1998). Solubility of homopolymers and copolymers in carbon dioxide. *Ind. Eng. Chem. Res.*, 37, pp. 3067-3079.

Park, J., Park, H.J., Cho, W., Cha, K.-H., Kang, Y.-S., Hwang, S.-J. (2010). Preparation and pharmaceutical characterization of amorphous cefdinir using spray-drying and SAS-process. *Int.l J. Pharm.*, 396, pp. 239–245.

Pasquali, I., Bettini, R., Giordano, F. (2006). Solid-state chemistry and particle engineeringwith supercritical fluids in pharmaceutics, *Eur. J. Pharm. Sci.*, 27, pp. 299-310.

Pérez de Diego, Y., Wubbolts, F.E., Jansens, P.J. (2006). Modelling mass transfer in the PCA process using the Maxwell–Stefan approach, *J. Supercrit. Fluids*, 37, pp. 53–62.

Perrut, M., Jung, J., Leboeuf, F. (2005). Enhancement of dissolution rate of poorly-soluble active ingredients by supercritical fluid processes. Part I. Micronization of neat particles, *Int. J. Pharm*., 288, pp. 3-10.

Randolph, T.W., Randolph, A.D., Mebes, M., Yeung, S. (1993). Sub-micrometer sized biodegradable particles of poly(L-lactic acid) via the gas antisolvent spray precipitation process, *Biotechnol. Prog*., 9,pp. 429-435.

Rehman, M., Shekunov, B. Y., York, P., Colthorpe, P. (2001). Solubility and precipitation of nicotinic acid in supercritical carbon dioxide, *J. Pharm. Sci*., 90, pp. 1570-1582.

Reverchon, E. (1999). Supercritical antisolvent precipitation of micro- and nanoparticles. *J. Supercrit. Fluids*, 15, pp. 1-21.

Reverchon, E.; Della Porta, G.; Falivene, M. G. (2000). Process parameters and morphology in amoxicillin micro and submicro particle generation by supercritical antisolvent precipitation. *J. Supercrit. Fluids*, 17, pp. 239- 248.

Reverchon , E. De Marco, I., Della Porta, G. (2002). Tailoring of nano- and micro-particles of some superconductor precursors by supercritical antisolvent precipitation. *J. Supercrit. Fluids*, 23, pp. 81–87.

Reverchon, E., Adami, R., De Marco, I., Laudani, C.G., Spada, A. (2005). Pigment Red 60 micronization using supercritical fluids based techniques. *J. Supercrit. Fluids*, 35, pp. 76–82.

Reverchon, E., DeMarco, I., Torino, E. (2007). Nanoparticles production by supercritical antisolvent precipitation: a general interpretation. *J. Supercrit. Fluids*, 43(1), pp.126–138.

Reverchon, E., Adami, R., Caputo, G., De Marco, I. (2008). Spherical microparticles production by supercritical antisolvent precipitation: interpretation of results. *J. Supercrit. Fluids*, 47(1), pp. 70–84.

Reverchon, E., Adami, R., Caputo, G., De Marco, I. (2008).Expanded microparticles by supercritical antisolvent precipitation: interpretation of results. *J. Supercrit.Fluids*, 44(1), pp. 98–108.

Reverchon, E., Lamberti, G., Antonacci, A. (2008). Supercritical fluid assisted production of HPMC composite microparticles. J. *Supercrit. Fluids*, 46, pp. 185-196.

Reverchon, E.; Torino, E.; Dowy, S.; Braeuer, A.; Leipertz, A. (2010). Interactions of phase equilibria, jet dynamics and mass transfer during supercritical antisolvent micronization. *Chem. Eng. J.*, 156, pp. 446-458.

Reverchon, E., DeMarco, I. (2011). Mechanisms controlling supercritical antisolvent precipitate morphology. *Chem. Eng. J.* In press.

Ron Tau Yee Lima, Wai Kiong Nga, Reginald B.H. Tan. (2010). Amorphization of pharmaceutical compound by co-precipitation using supercritical anti-solvent (SAS) process (Part I). *J. Supercrit. Fluids*, 53, pp. 179-183.

Sane, A., Limtrakul, J. (2009). Formation of retinyl palmitate-loaded poly(l-lactide) nanoparticles using rapid expansion of supercritical solutions into liquid solvents (RESOLV). *J. Supercrit. Fluids*, 51, pp. 230-237.

Shekunov, B.Yu., Hanna, M., York, P. (1999). Crystallization process in turbulent supercritical flows .*J. Cryst. Growth* ,198/199, pp. 1345-1351.

Shekunov, B. Y., York, P. (2000). Crystallization processes in pharmaceutical technology and drug delivery design, *J. Cryst. Growth.*, 211,pp.122-136.

Thote, A. J., Gupta, R. B. (2005). Formation of nanoparticles of a hydrophilic drug using supercritical carbon dioxide and microencapsulation for sustained release. *Nanomedicine: Nanotechnology, Biology, and Medicine*, 1, pp. 85-90.

Teipel, U., Kröber, H., Krause, H. (2001). Formation of Energetic Materials Using Supercritical Fluids. *Propellants, Explosives, Pyrothecnics*, 26, pp. 168-173.

Tenorio, A., Gordillo, M. D., Pereyra, C.M., Martínez de la Ossa, E.J. (2007a). Controlled submicro particle formation of ampicillin by supercritical antisolvent precipitation, *J. Supercrit. Fluids*, 40, pp. 308-316.

Tenorio, A.; Gordillo, M. D.; Pereyra, C. M.; Martínez de la Ossa, E. M. (2007b). Relative importance of the operating conditions involved in the formation of nanoparticles of ampicillin by supercritical antisolvent precipitation. *Ind. Eng. Chem. Res.*, 46, pp. 114-123.

Tenorio, A., Gordillo, M. D., Pereyra, C.M., Martínez de la Ossa, E.J. (2008). Screening design of experiment applied to supercritical antisolvent precipitation of amoxicillin, *J. Supercrit. Fluids*, 44, pp. 230-237.

Tenorio, A., Jaeger, P., Gordillo, M.D., Pereyra, C.M., Martínez de la Ossa, E.J. (2009). On the selection of limiting hydrodynamic conditions for the SAS process, *Ind. Eng. Chem. Res.*,48 (20), pp. 9224–9232.

Tomasko, D.L., Li, H., Lui, D., Han, X., Wingert, M.J. Lee, L.J., Koelling, K.W. (2003).A Review of CO_2 applications in the processing of polymers, *Ind. Eng. Chem. Res.*, 42, pp. 6431–6456.

Tozuka, Y., Miyazaki, Y., Takeuchi, H. (2010) .A combinational supercritical CO_2 system for nanoparticle preparation of indomethacin. *Int. J. Pharm.*, 386, pp. 243-248.

Turk , M., Upper , G., Hils, P. (2006). Formation of composite drug–polymer particles by co-precipitation during the rapid expansion of supercritical fluids. *J. Supercrit. Fluids*, 39, pp. 253-263.

Ugaonkara, S., Needhama, T. E., Bothun, G. D. (2011). Solubility and partitioning of carbamazepine in a two-phase supercritical carbon dioxide/poly vinylpyrrolidone system. *Int. J. Pharm.*, 403, pp. 96–100.

Van Nijlen, T., Van Den Mooter, G., Kinget, R., Augustijns, P., Blaton, N., Brennan, K. (2003). Improvement of the dissolution rate of artemisinin by means of supercritical fluid technology and solid dispersions, *Int. J. Pharm.*, 254, 173-181.

Velaga, S. P., Ghaderi, R., Carlfors, J. (2002). Preparation and characterisation of hydrocortisone particles using a supercritical fluids extraction process, *Int. J. Pharm.*, 231, pp. 155-166.

Vemavarapu, C., Mollan , M. J., Needham, T.E. (2009). Coprecipitation of pharmaceutical actives and their structurally related additives by the RESS process. *Powder Technology*, 189, pp. 444-453.

Wen, Z., Liu, B., Zheng, Z., You, X., Pua, Y., Li, Q. (2010). Preparation of liposomes entrapping essential oil from Atractylodes macrocephala Koidz by modified RESS technique. *Chem. Eng. Res. Des.*, 88, pp. 1102-1107.

Werling, J. O., Debenedetti, P. G. (2000). Numerical modeling of mass transfer in the supercritical antisolvent process: miscible conditions. *J. Supercrit. Fluids*, 18, pp. 11-24.

Werling, J. O., Debenedetti, P. G. (1999). Numerical modeling of mass transfer in the supercritical antisolvent process. *J. Supercrit. Fluids*, 16, pp. 167–181

Wubbolts, F.E., Bruinsma, O.S.L., Van Rosmalen, G.M. (2004). Measurement and modelling of the solubility of solids in mixtures of common solvents and compressed gases. *J. Supercrit. Fluids*, 32, pp. 79–87.

Yeo, S. D., Lee, J. C. (2004). Crystallization of sulfamethizole using the supercritical and liquid antisolvent processes, *J. Supercrit. Fluids*, 30, pp. 315-323.

Yeo, S.-D., Kiran, E. (2005). Formation of polymer particles with supercritical fluids: A review, J. *Supercrit. Fluids*, 34, pp. 287–308.

21

Electrospark Deposition: Mass Transfer

Orhan Sahin and Alexandre V. Ribalko
Gebze Institute of Technology
Turkey

1. Introduction

Electrospark alloying (ESA) is one of the surface modification methods to change physical and chemical properties of metal surfaces. It was developed by the Soviet scientists, B.R. Lazarenko and N.I. Lazarenko. The core of this method is the phenomenon of material erosion of both electrodes as a result of the electric discharge between them in a gaseous environment and subsequent mass transfer from one of them to the other, basically from anode to the cathode (Lazarenko, 1951; Lazarenko, 1976).
The anode (treating electrode) usually is a rod with several mm square cross sectional area. Comparing with treating electrode, the cathode (substrate) has significantly larger size and surface area. Both of them are electrically conductive. After the application of a current pulse, a spark discharge takes place between treating electrode and substrate. Following spark discharge, part of the tip of treating electrode and a corresponding spot on substrate melt. Molten spot on the substrate forms a swallow molten pool. Some of the molten tip of treating electrode material transfers to the substrate in the form of molten droplets, mixes with its molten pool and usually solidifies as in the form of splash. By scanning substrate surface, so many splashes could be deposited on it. As a Consequence of single or multiple scanning of substrate surface, a deposit having chemical composition same as treating electrode forms on the substrate.
According to Lazarenko (1951), the size and sign of electrical erosion at the electrodes, consequently, the mass transfer from the treating electrode to the substrate depends on chemical composition of electrode materials, environment between electrodes and parameters of the electrical pulse. It is obvious that for ESA in air, size of erosion depends basically on chemical composition of electrodes and pulse energy, in turn pulse parameters, pulse amplitude and pulse duration. Therefore, for a given pair of electrodes, mass transfer depends only on electrical parameters of pulses. It was experimentally shown that, the mass gain of substrate is limited, i.e. it is impossible to obtain thick electrospark coating. According to the author (Lazarenko, 1976), the limitation of mass gain of substrate depends on several factors. Lazarenko named them as: change in chemical properties of molten droplet during its transfer to the substrate; change in chemical properties of substrate surface due to mixing with molten droplet ejected from treating electrode and oxidation in air; radical changes arising in alloyed substrate surface - occurrence and accumulation of defects in crystal lattice preventing diffusion; occurrence of residual stress etc. She has also reported that even under the non-oxidizing gas environment–such as argon, helium, hydrogen, there was still limitation on coating thickness. In this case, the processing time till limitation was slightly longer than that of the processing in air.

Many years past since then; however, published scientific studies on ESA shows that, breakthrough in technology to form thick coating has not been achieved yet. This problem could partially be solved by using pulses providing maximum erosion (mass loss) of the treating electrode and maximum mass gain by the substrate. The process of mass transfer must be completed before any one of the factors described above could have sufficient time to be fully effective (Lazarenko, 1976).

Thus, in order to determine the condition of maximum mass transfer from treating electrode to substrate, it is necessary to study mass transfer characteristics of electrodes as a function of pulse durations. The literature review on this question shows that, the range of pulse durations is from 10^{-5} sec (short durations), to 10^{-3} – 10^{-2} sec (long durations). The pulse duration was limited by possibility of generating current pulses with amplitude of 100 A and voltage of 100 V at lower side of pulse duration range and change in polarity of mass transfer and increase in heat content of the substrate at upper side of pulse duration range. Thus, the possible interval of pulse durations for ESA is from 10 μs to 10000 μs.

Lazarenko (1957) investigated mass transfer characteristics of ESA process only in the range of 50 μs to 300 μs. For alloying, she used sinusoidal pulses generated by the discharge of capacitor on spark loading. According to the Lazarenko (1957), the optimal pulse duration for ESA is between 50 μs to 300 μs. The following years and practically at present, same pulse durations have been used for ESA, because above pulse range was considered as a base to fabricate ESA installations.

Zolotih (1957) investigated the dependence of erosion of treating electrode to pulse duration with reference to the electrospark dimensional machining (EDM) of metals. The range of sinusoidal pulse duration was 100 μs -1100 μs. It is interesting to notice that in EDM case the mass loss of treating electrode versus processing time curve has a maximum. The emergence of the maximum depends on pulse duration and physico-chemical properties of electrodes.

Dependence of erosion of treating electrode to the pulse shape (Rybalko et al., 2003a) revealed that, ESA with application of square pulses was more productive. Therefore, to form square pulses, an ESA installation has been developed (Rybalko et al., 2003b, 2003c) (see, Fig 1a and 1b). The current pulse shaper was executed on the basis of single-cycle electric generator with a transistor switchboard. It is capable to form a pulse with desired parameters by a method of pulse-duration modulation. Such approach allows producing a current pulse with various amplitude, duration and shape without changing the parameters of pulse forming circuit, U, C, L and R. The master generator of the pulse shaper regulate the duration of its pulses and pauses in steps of 200 nanoseconds. The pulse amplitude could be increased in the order of 3 A. For the case of forming more complicated pulse shape, the approach of pulse-duration modulation was used.

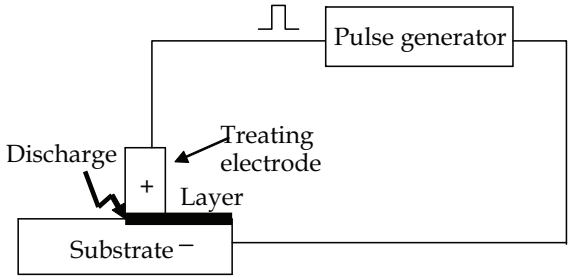

Fig. 1a. The diagram of the ESA installation

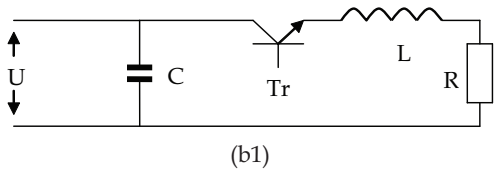

(b1)

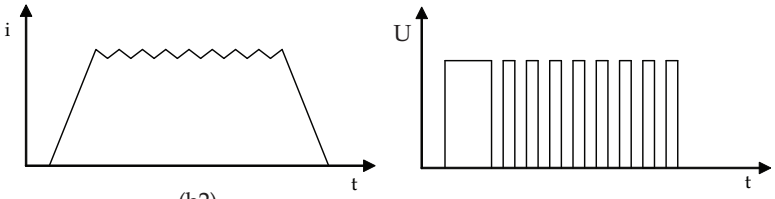

(b2) (b3)

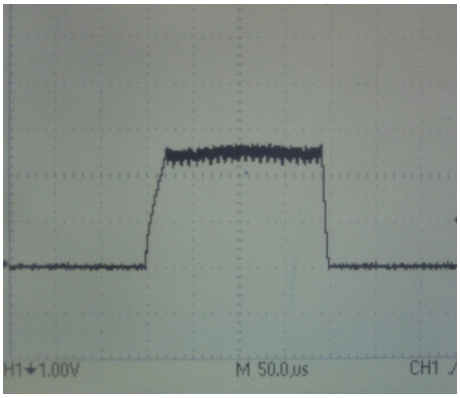

(b4)

Fig. 1b. Generating of a pulse by pulse-width modulation. The electrical discharge circuit (Tr is the transistor, U is the voltage of power supply, C, L and R are the capacitance, inductance and resistance (including the load) of the discharge circuit, respectively) (b1). A representative current pulse oscillogram (b2) could be formed by on-off switching of the transistor (b3). t and i are the time and current, respectively. The on-off switching of transistor was operated by programmed voltage pulses from pulse oscillator. A real current pulse oscillogram, pulse amplitude is 300 A and pulse duration is 200 µs (b4)

The present installation is capable of forming pulse groups with various parameters. Power consumption of the installation is 1000 W. The stabilized output voltage of the converter is 40 V. Range of energy and duration of pulse is $0{,}25 \times 10^{-3}$-15 J and 2-8000 µs respectively. Range of pulse frequency is 2-120000 Hz. The upper boundary of frequencies is used for minimum pulse amplitude of 15 A.

For a chosen voltage, taking into account the full resistance of discharge circuit, the average rate of increase of pulse first front (first slope of pulse) is 14,4 A/µs till to the amplitude of 1000 A. Continuous sliding of the processing electrode on the substrate surface back and forth, provided the possibility of discharge initiation with explosion of contacting micro roughness and formation of plasma channel at any moment of time (Rybalko et al., 2000).

The total electricity through the inter-electrode gap was kept constant at 3 Coulomb as a base for comparison of experimental results.

2. Experimental results of electrospark alloying

The following sets of experiments were carried out in order to have a broad idea about the mass transfer behavior from the treating electrode to the substrate. Pulse amplitudes ranging from 100 A to 1000 A and pulse duration ranging from 25 μs to 4000 μs were used (Rybalko et al., 2003d, 2004a, 2004b). The aim is to maximize mass gain of substrate at the initial stage of ESA, i.e. first layer of deposition, by increasing pulse energy. Because, as explained by Lazarenko (1976), when chemical composition of substrate surface becomes same as treating electrode after a single or multiple layer of deposition, mass transfer ceases down. Therefore, erosion of treating electrode should be as high as possible for the first layer of deposition. Experimental results revealed that one of the reasons limiting the thickness of deposit is the destruction of the layer already deposited during processing (Rybalko et al., 2003e). This was due to local evaporation of material underneath the outer surface of deposit. Evaporation was caused by the heat provided locally by spark discharges during second layer of deposition. Upon further processing evaporation intensifies and even cavities form. The point is to find out a common criterion for coating destruction during processing.

The mass loss of the treating electrode, the mass gain of the substrate, the calculation of mass transfer coefficient, the measurement of thickness and roughness (parameter Ra) of deposited layers, and some characteristics of the ESA process were studied for every 30 seconds for a total 3 minutes of processing. The amount of mass loss of the treating electrode and the amount of mass gain of the substrate at each time interval of 30 seconds for various pulse parameters (amplitude and duration) as a function of processing time were given in Figs 2-7. Usually in this type of ESA studies, not the mass difference between two successive measurements, but the cumulative mass change of the treating electrode and substrate versus processing time has been used to describe the change in the mass of the electrodes. The treating electrode and substrate were WC92-Co8 with cross section of 8 mm^2 and steel 35 with an area of 1 cm^2, respectively.

Mass loss curves of treating electrode and mass gain curves of substrate were not linear from the very beginning of alloying, for all investigated range of pulse parameters. Nonlinearity of the mass loss curves of treating electrode at the initial stage of the electrospark alloying was attributed to the nature of ESA method itself. After approximately 2 minutes of processing, mass loss of treating electrode leveled off and became stationary for the deposition with pulse amplitudes of 100 A, 200 A and 400 A. In case of deposition with pulse amplitude of 600 A, 800 A and 1000 A, this happened after approximately 1 minute of processing. Any increase in pulse duration caused: an increase in erosion of treating electrode at the initial stage of alloying, i.e. the first layer of deposition, an increase in the amount of stationary mass loss of the treating electrode, stationary level to emerge in shorter processing time.

Substrate mass gain curves were not linear either. After gradually decreasing they eventually became asymptotic to the horizontal axis. When substrate mass gain curves became asymptotic, mass loss of treating electrode became stationary. Upon further alloying the mass increment of substrate became negative. That is, instead of gaining mass, substrate started to lose mass. This is a sign for the beginning of destruction of deposit already formed. Moreover, for pulse amplitudes of 600 A, 800 A and 1000 A, mass gain of substrate sharply decreased down from the very beginning of processing, (Fig. 5-7), and almost for all experimental conditions, they were negative. These curves were indicated by dotted lines.

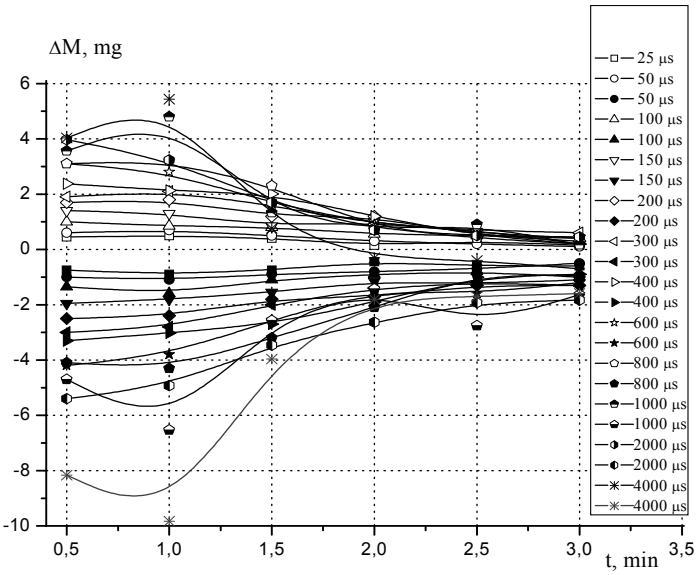

Fig. 2. Mass loss of treating electrode and mass gain of substrate (solid dots) as a function of pulse energy for a period of 3 minutes of processing. Pulse amplitude was 100 A. Pulse duration was variable

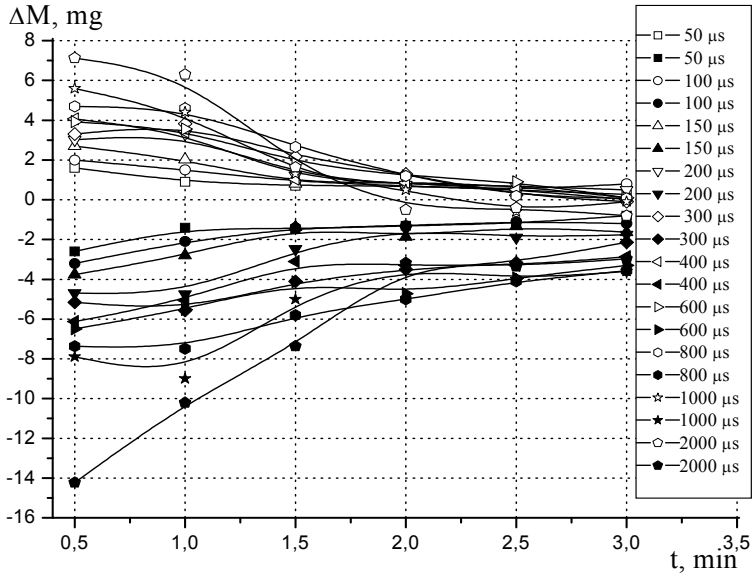

Fig. 3. Mass loss of treating electrode and mass gain of substrate (solid dots) as a function of pulse energy for a period of 3 minutes of processing. Pulse amplitude was 200 A. Pulse duration was variable

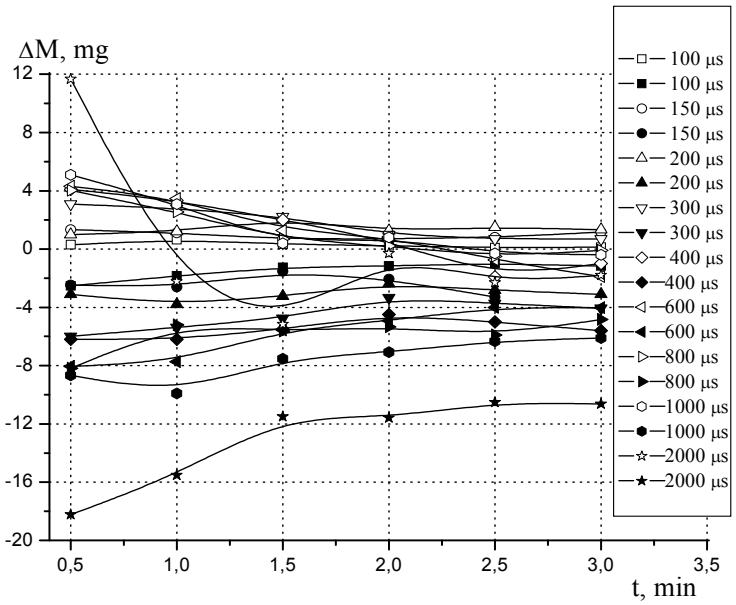

Fig. 4. Mass loss of treating electrode and mass gain of substrate (solid dots) as a function of pulse energy for a period of 3 minutes of processing. Pulse amplitude was 400 A. Pulse duration was variable

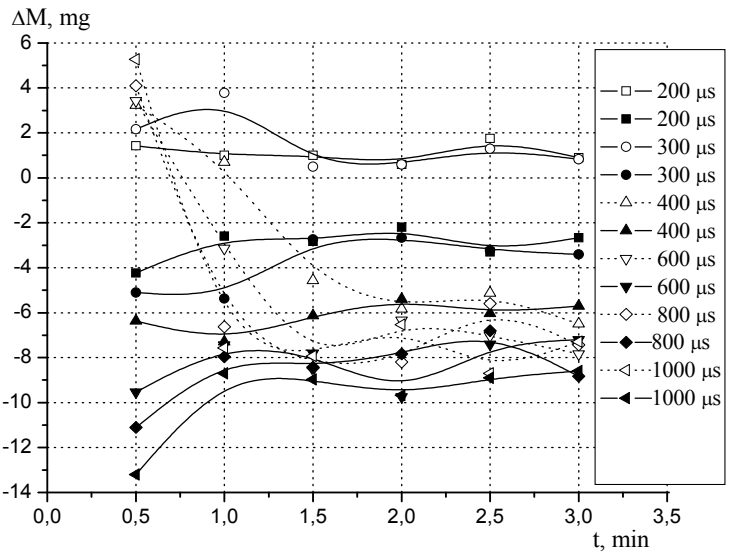

Fig. 5. Mass loss of treating electrode and mass gain of substrate (solid dots) as a function of pulse energy for a period of 3 minutes of processing. Pulse amplitude was 600 A. Pulse duration was variable

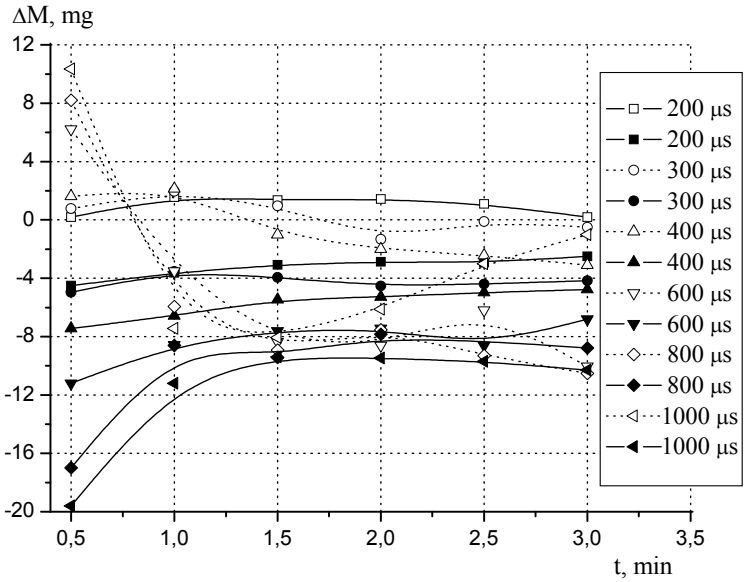

Fig. 6. Mass loss of treating electrode and mass gain of substrate (solid dots) as a function of pulse energy for a period of 3 minutes of processing. Pulse amplitude was 800 A. Pulse duration was variable

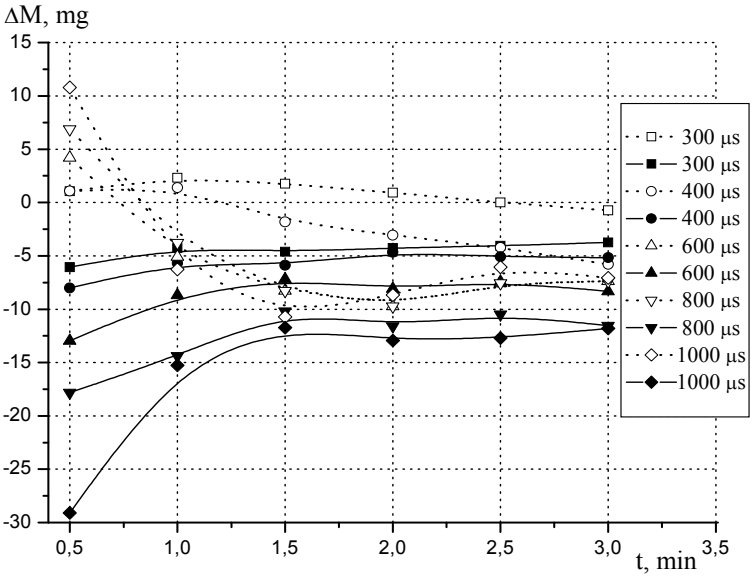

Fig. 7. Mass loss of treating electrode and mass gain of substrate (solid dots) as a function of pulse energy for a period of 3 minutes of processing. Pulse amplitude was 1000 A. Pulse duration was variable

Longer pulse durations caused higher mass gain of substrate at the first layer of deposition and shorter processing time till to the beginning of mass loss by these substrates. Higher pulse amplitude also was accompanied by an increase in substrate mass gain at the initial stage of alloying. The only exceptional data is that, in case of ESA with pulse amplitude of 1000 A, comparing to the case of 800 A, any significant increase in mass gain of substrate was not obtained.

Since, environment and initial condition of electrode materials were same for all experiments, the difference in experimental results was due to the difference in pulse parameters (pulse energy) for only the processing time of 30 seconds (first layer of deposition). This is not true for second and third layers of deposition. The mass gain of substrates, in turn surface properties of substrates, after first layer of deposition was all different from each other. Therefore, only the experimental results of first layer of deposition including some characteristic of processing were used to form a base, Tables 1-6, in order to find out the effect of pulse energy on mass transfer. Mass transfer coefficients were calculated from the data of mass transfer during the first 30 seconds of alloying.

Pulse duration (μs)	25	50	100	150	200	300	400	600	800	1000	2000	4000
Pulse energy (J)	0,032	0,08	0,17	0,233	0,297	0,529	0,72	1,08	1,44	1,7	3,4	6,79
Frequency (Hz)	1613	645	309	219	178	99	71	47	36	30	15	8
Processing electricity (C)	3,00	3,03	2,99	3,00	3,11	3,08	3,01	2,99	3,05	3	3	3,2
Time t_1 to scan 1cm^2 (sec)	50	50	50	45	45	45	55	50	55	55	70	60
Mass loss of anode (mg)	1,25	1,67	2,25	2,92	3,75	4,5	6,05	7	7,52	10,3	12,1	17,99
Mass gain of cathode (mg)	0,75	1,00	1,66	2,1	2,55	2,85	4,35	5,17	5,68	7,66	8,4	9,46
Mass transfer coefficient	0,6	0,6	0,74	0,68	0,68	0,63	0,72	0,74	0,75	0,74	0,69	0,76
Surface roughness (μm)	2,65	2,77	3,0	3,25	3,35	3,71	4,35	4,9	5,36	7,2	8,97	12,03
Recommended number of layers	3	3	3	2-3	2-3	2-3	2	2	1-2	1	1	1
Coating thickness till to failure (μm)	10±4	13±7	13±5	16±6	17±5	20±6	22±6	23±6	35±10	35±20	45±35	60±50

Table 1. Some parameters of processing. Pulse amplitude is 100 A

Pulse duration (μs)	50	100	150	200	300	400	600	800	1000	2000
Pulse energy (J)	0,097	0,257	0,427	0,602	0,927	1,28	1,9	2,72	3,31	6,74
Frequency (Hz)	528	198	119	92	55	39	26	19	16	8
Processing electricity (C)	2,99	2,997	2,99	3,25	3	2,95	2,91	3,04	3,12	3,17
Time t_1 to scan 1cm² (sec)	50	40	40	40	40	50	60	65	65	60
Mass loss of anode (mg)	2,33	3,47	4,27	5,03	5,59	8,6	11,2	13,0	16,1	16,9
Mass gain of cathode (mg)	1,33	2,13	2,66	3,6	4,02	5,5	7,46	8,11	10,1	10
Mass transfer coefficient	0,57	0,61	0,62	0,72	0,72	0,64	0,67	0,62	0,63	059
Surface roughness (μm)	3,07	3,12	4,1	4,61	5,01	6,8	7,42	8,83	9,98	11,67
Recommended number of layers	3	3	3-2	2	2	2-1	1	1	1	1
Coating thickness till to failure (μm)	12±7	17±5	32±5	37±10	41±10	50±20	55±20	55±20	55±25	60±25

Table 2. Some parameters of processing. Pulse amplitude is 200 A

Pulse duration (μs)	100	150	200	300	400	600	800	1000	2000
Pulse energy (J)	0,342	0,639	1,02	1,68	2,39	3,77	5,12	6,48	13,3
Frequency (Hz)	158	80	50	31	23	13	10	8	4
Processing electricity (C)	3,002	3,008	3,009	3,066	3,23	3,108	3,01	3,048	3,13
Time t_1 to scan 1cm² (sec)	35	50	50	50	50	50	40	40	28
Mass loss of anode (mg)	2,96	4,2	5,17	10	11,5	13,15	10,92	11,56	17,01
Mass gain of cathode (mg)	0,35	2,27	1,67	5,17	5,52	6,47	5,38	6,8	10,9
Mass transfer coefficient	0,12	0,54	0,32	0,52	0,48	0,49	0,59	0,59	0,64
Surface roughness (μm)	3,79	4,42	6,32	10,1	11,7	12,48	13,62	15,45	14,69
Recommended number of layers	3	2	2-1	2-1	1	1	1	1	1
Coating thickness till to failure (μm)	16±5	35±5	50±20	60±30	65±30	65±30	75±40	65±40	100±80

Table 3. Some parameters of processing. Pulse amplitude is 400 A

Pulse duration (μs)	200	300	400	600	800	1000
Pulse energy (J)	1,13	2,19	3,35	5,34	7,31	9,39
Frequency (Hz)	45	23	15	10	7	5
Processing electricity (C)	2,997	2,967	2,955	3,14	3,01	2,763
Time t_1 to scan 1cm² (sec)	35	35	35	35	30	25
Mass loss of anode (mg)	4,9	5,95	7,43	11,12	11,1	11
Mass gain of cathode (mg)	1,67	2,53	3,77	4	4,1	4,39
Mass transfer coefficient	0,34	0,43	0,51	0,36	0,37	0,4
Surface roughness (μm)	5,14	7,05	10,14	14,20	15,82	17,72
Recommended number of layers	3	2	1	1	1	1
Coating thickness till to failure (μm)	35±15	55±30	65±40	40±15	70±50	75±50

Table 4. Some parameters of processing. Pulse amplitude is 600 A

Pulse duration (μs)	200	300	400	600	800	1000
Pulse energy (J)	1,47	2,78	3,96	6,82	9,47	12,45
Frequency (Hz)	35	18	13	8	5	4
Processing electricity (C)	3,02	2,95	3,03	3,21	2,78	2,93
Time t_1 to scan 1cm² (sec)	35	35	35	25	25	25
Mass loss of anode (mg)	5,25	5,77	8,67	9,32	14,7	16,33
Mass gain of cathode (mg)	0,23	0,91	1,95	5,21	6,83	8,63
Mass transfer coefficient	0,04	0,16	0,22	0,56	0,48	0,53
Surface roughness (μm)	4,63	9,59	10,31	13,59	17,7	17,75
Recommended number of layers	3	2	2-1	1	1	1
Coating thickness till to failure (μm)	50±20	50±40	60±40	65±45	100±80	110±105

Table 5. Some parameters of processing. Pulse amplitude is 800 A

Pulse duration (μs)	300	400	600	800	1000
Pulse energy (J)	3,02	4,54	7,87	11,33	14,52
Frequency (Hz)	17	11	6	4	3
Processing electricity (C)	3,009	2,937	2,772	2,668	2,562
Time t_1 to scan 1cm² (sec)	25	20	20	20	20
Mass loss of anode (mg)	5,06	5,33	8,65	11,87	19,41
Mass gain of cathode (mg)	0,88	0,73	2,8	4,6	7,2
Mass transfer coefficient	0,17	0,14	0,32	0,39	0,37
Surface roughness (μm)	5,49	8,28	14,84	16,38	17,62
Recommended number of layers	3	2-1	1	1	1
Coating thickness till to failure (μm)	55±45	60±45	65±50	100±85	100±100

Table 6. Some parameters of processing. Pulse amplitude is 1000 A

The experimental results obtained under the condition of constant pulse amplitude and increasing pulse duration were given in Tables 1-6. As mentioned previously, processing electricity was kept constant at 3 Coulomb for all experiments. Since pulse amplitude was constant, pulse energy was increased by increasing pulse duration. Main objective of this investigation was to increase both mass loss of treating electrode and mass gain of the substrate, in turn coating thickness, especially for the first layer of deposition. Higher pulse energy causes higher mass gain of substrate and shorter processing time till to the beginning of mass loss (destruction of deposit already formed). Despite the mass gained from treating electrode, a decrease in weight of the substrate was observed for pulse duration of 4000 μs in case of 100 A pulse amplitude after 1.5 minutes of processing (Fig. 2), for pulse duration of 2000 μs in case of 200 A pulse amplitude after 1.5 minute processing (Fig. 3) and for pulse duration of 400 μs in case of 400 A pulse amplitude after 2.0 minute processing (Fig. 4). Further increase of pulse duration caused substrate to start to lose mass in shorter processing time.

Upon further alloying, the mass loss, in other words, the destruction of layer already formed intensifies and the destruction could reach substrate by removing already formed layer totally. In Fig. 8, cross-sectional micrograph of a coating was given as an example in order to show the beginning of destruction. Part of the specimen was not purposely alloyed (see the upper part of micrograph) in order to be able to compare the level of coating thickness and depth of destruction with the original level of the surface.

In case of 100 A pulse amplitude, during alloying with pulse duration longer than 200 μs, erosion of molten pool on substrate was observed from the very beginning of alloying due to the presence intensive gas dynamics phenomena in plasma channel. This type of erosion was named "washing away" which is the mass lost by substrate (Rybalko et al., 2008).

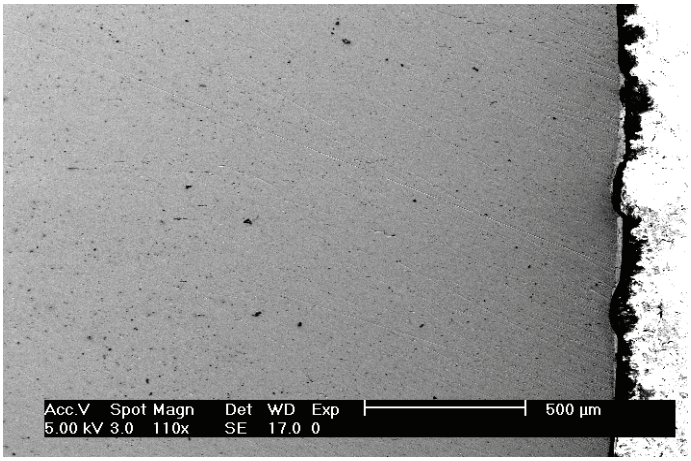

Fig. 8. Cross-sectional micrograph of a coating showing the locations of failure

Therefore, the change in weight of the substrate is the difference between the liquid mass received from treating electrode and the liquid mass loss due to washing away of its molten pool at the beginning of a spark discharge. Intensive washing away was observed with pulse durations of 400 µs in case of 100 A pulse amplitude, 200 µs in case 200 A pulse amplitude, and 200 µs in case of 400 A pulse amplitude. The micrograph (Fig. 9) shows that, the liquid material ejected from treating electrode filled up the substrate pool after washing away was completed.

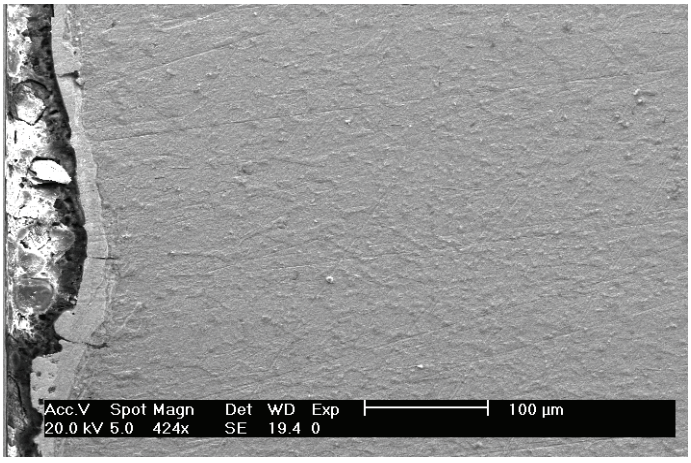

Fig. 9. Cross-sectional micrograph of a coating showing the location of pool on substrate

For the pulse duration of 1000 µs in case 100 A pulse amplitude, the morphology of coating changed essentially. There were pores at the upper part of the layer that were formed by superficial boiling of the transferred material. Pulse durations more than 1000 µs caused the formation of large pores not only at the surface, but also inside the deposited layer. Boiling was caused by significant amount of heat transferred to the substrate from overheated

liquid material of the treating electrode. It is obvious that such a large volume of mass transfer warms up the substrate. For pulse duration of 4000 μs, superficial boiling in deposited layer was all over and pores were close to the substrate (Fig. 10). As in the case of pulse duration of 1000 μs, the essential role in forming a layer was determined by gas dynamics in plasma channel.

Alloying in case of 200 A pulse amplitude was similar to the alloying in case of 100 A. Examination of the morphology and cross-section of deposited layer showed that high quality deposit was limited by pulse duration of less than 400 μs.

It is noticed that in case of 400 A pulse amplitude, alloying till pulse duration of 300 μs could be carried out without any destruction. However, mass transfer was low. The alloying by pulse duration above 300 μs was already characterized by a decrease in mass transfer that marks the beginning of destruction of layer formed already. Further increase in pulse durations leads to the evaporation of substrate through cavities in coating.

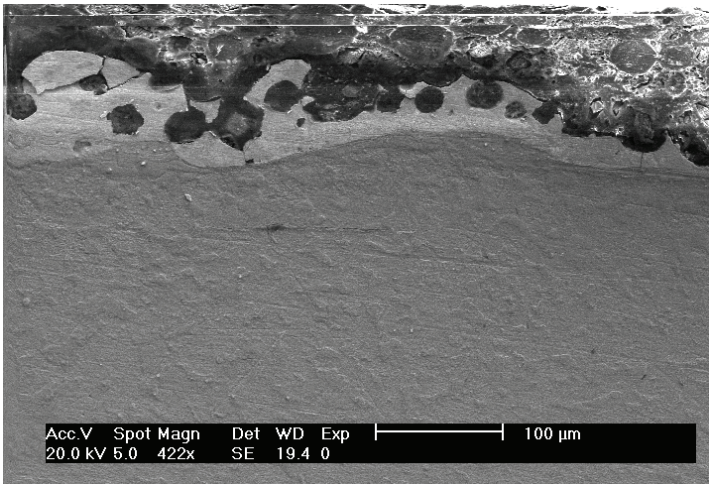

Fig. 10. Cross-sectional micrograph of a coating. Pulse duration is 4000 μs. Pulse energy is 6.8 J

Morphology of the deposited layer was different than that of alloying by pulse amplitudes of 200 A and 100 A. This is due to the overheating of substrate at the interface of plasma channel and substrate. The longer the pulse durations, the higher the overheating. Concerning deposition under these conditions, the following could be assumed. The plasma channel of the discharge overheats the deposited layer. Its melting temperature is already higher than that of substrate and, as a results, molten zones of substrate form under deposited layer. Molten zones flow out through cavities in coating. After reaching the surface the molten substrate material covers and mixes with the erosive mass transferred from the treating electrode. The mixed mass solidifies on the surface of coating formed earlier. This would probably explain the presence of low microhardness at the coating surface, and also increase its surface roughness. In case of ESA with pulse durations more than 600 μs (pulse amplitude is 400 A), the process was characterized by an increase in the area of splash. Thus, rate of the first layer deposition increases, but the rate of thickness build up of this layer decreases.

In case of alloying with pulse amplitudes of 100 A, 200 A and 400 A, if pulse duration is above 1000 μs, porous foam-like coatings were obtained. Since the amounts of pulse energies were significantly different for these three cases, one could conclude that the length of pulse duration is the reason of this kind of coating.

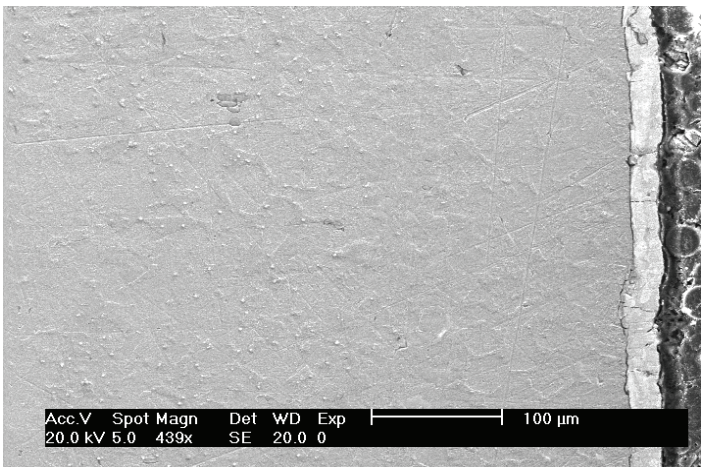

Fig. 11. Cross-sectional micrograph of a coating. Pulse duration is 600 μs. Pulse energy is 1.1 J

Alloying with the pulse amplitude of 100 A leads to high quality coatings with an average thickness of 10-35 μs for the pulse duration up to 1000 μs (Fig. 11). Increasing pulse duration was accompanied by an increase in non-uniformity of thickness. For manual alloying with pulse amplitudes of 200 A and 400 A, pulse duration more than 400 μs would not be recommended. Below 400 μs, it is possible to obtain a high quality coating with an average thickness of 50 microns (200 A) and 65 microns (400 A) till the beginning of destruction (Fig 12). ESA with longer pulse durations allows only one layer of scanning without destruction. The thickness of a spot due to an individual discharge could be as much as 120 microns at the center and lower at the edges. In this condition, in order to obtain high coating thickness the thinner edges of the neighboring splashes should be overlapped during the deposition process. Therefore, it is necessary to carry out process with use of an automated installation. Scanning rate of automated installation could be adjusted to provide partial overlapping of subsequent splashes.

In case of alloying with 600 A pulse amplitude, if the pulse durations were more than 300 μs, intensive substrate overheating occurred at the plasma channel-substrate interface. When the pulse durations were above 400 μs, substrate evaporated during deposition of the second layer. ESA process was accompanied by unusually big plasma flame escaping from the interelectrode zone during spark discharge. The size of plasma flame was essentially wider than the cross-sectional area of treating electrode. Layer formation by spark discharges with pulse durations of 1000 μs, was characterized by the occurrence of large pores including open pores at the surface. Alloying with pulse duration of 2000 μs (pulse energy is 18,78 J) was tried. However, due to sticking of electrodes, alloying was not possible.

In case of processing with pulse amplitude of 800 A and pulse duration of 600 μs, electrodes stuck to each other. Moreover, during processing with pulse duration of 800 μs, strong

radiation due to intensive evaporation in substrate was present (after scanning of the first layer), and use of pulse duration of 1000 μs formed a deposition with large pores. Alloying with pulse durations higher than 1000 μs could not been achieved due to strong sticking during the deposition of first layer.

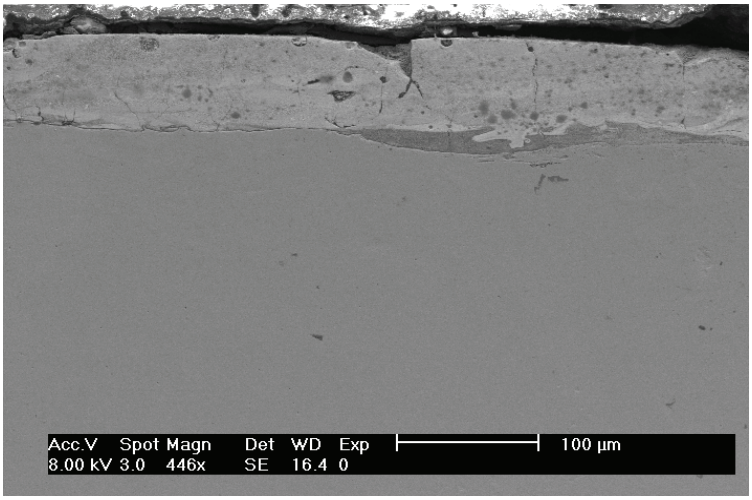

Fig. 12. Cross-sectional micrograph of a coating. Pulse duration is 400 μs. Pulse amplitude is 400 A. Pulse energy is 2.39 J

In case of alloying with 1000 A pulse amplitude, when the pulse duration was 300 μs, erosive mass of electrodes was scattered all over because of intensive gas dynamics phenomena in plasma channel. Therefore, as same as the processing with long pulse duration, the coefficient of mass transfer was low and roughness of deposition was high because of the big differences in thickness in an individual spot. The average thickness of deposit was 55 ± 40 micron. Alloying was carried out without sticking of electrodes and oxidation of surface.

When the pulse duration was more than 300 μs, substrate evaporation began right after coating of the first layer and an oxide film formed on the surface of deposit. Above 800 μs electrodes stuck to each other and above 1000 μs formation of large pores was all over. Coating thickness varied between 5 μs and 200 μs.

In case of alloying with pulse amplitudes of 600 A, 800 A and 1000 A, a porous deposition like foam was obtained by the application of 1000 μs pulse duration. Since, pulse energies were significantly different from each other for these three cases, pulse duration could be responsible for the formation of similar kind of porous formation.

The analysis of the experimental results shows that, the occurrence of destruction correlates with the time of decrease in mass transfer coefficient, calculated from data, given in Tables 4, 5 and 6. Proceeding from the data of the beginning of decrease in mass transfer coefficient, number of probable deposited layers (number of scanning), at which coating destruction will not be observed, was determined and recommended in these tables. Investigation shows that under the experimental conditions given above, it is possible to deposit only one layer above the pulse duration of 400 μs.

In Tables 4, 5 and 6, average coating thickness obtained under recommended number of scanning is given. The analysis of this data shows that if pulse duration increases, the average thickness increases, in spite of the fact, that the number of recommended layers for alloying decreases.
In case, if it is necessary to deposit only one layer, irregular coating (non uniform thickness) is inevitable. For example, ESA with pulse duration of 800 μs and pulse amplitude of 1000 A, the minimum thickness of the deposited spot due to a single spark discharge was 10 microns at the edge and 200 microns at the center. Thus, a layer of 1 cm^2 area could be formed by only 60 spark discharges: 3 pulses per second for a total processing of 20 seconds (Table 6). Morphology of coating is similar to the one illustrated in Fig. 13 (cross-sectional micrograph)

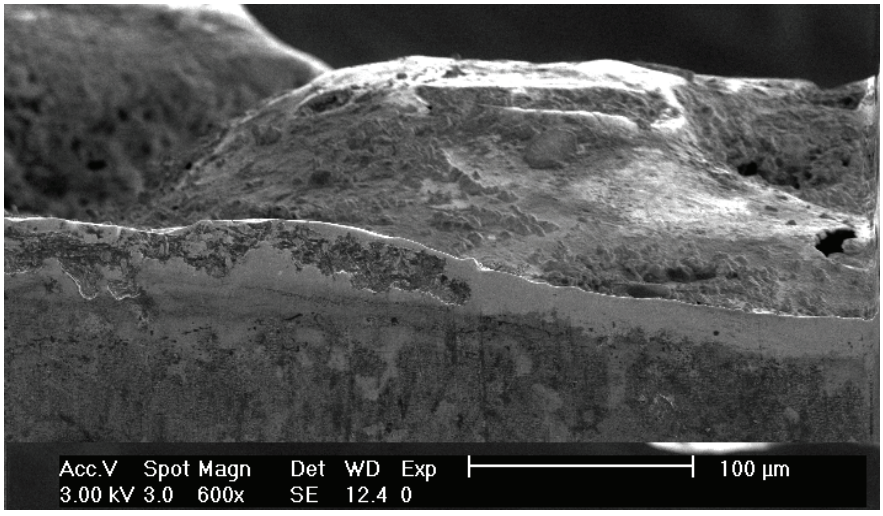

Fig. 13. A typical view of cross-section and surface of a coating could be obtained with high energy pulses. Pulse amplitudes and pulse durations could be from 600 A to 1000 A and 400 to 1000 μs respectively

3. General results of electrospark alloying

Regarding the experimental results, following generalizations could be made, which essentially could change the approach to the ESA technology (Ribalko et al., 2005; Ribalko & Sahin, 2006). Nonlinear decrease in erosion of treating electrode during alloying of steel specimens after the first layer deposition was a fact. Thus, it is possible to ascertain that an additivity principle observed by B.R. Lazarenko in case of electroerosive dimensional machining, is not true in case of ESA after first layer of deposition (Ribalko et al., 2004b). The additivity principle is the stationary anodic erosion when the discharge energy between electrodes is constant. The observed decrease in anodic mass change in case of ESA was due to the decrease in power of cathodic stream, in turn, due to the change in surface properties of the substrate after alloying of its surface with treating electrode. The cathodic stream conduces to the anodic erosion.

As it was shown experimentally, the phenomenon of coating destruction by its evaporation occurred during alloying in all ranges of pulse parameters investigated. Thus, to obtain high quality depositions, it is necessary to limit the processing time by the moment of the signs, indicating destruction of the deposited layer. The beginning of coating destruction could be determined by some features of ESA, namely: when mass loss of treating electrode ceases down to a minimum stable level, when mass gain of substrate becomes zero or even negative and the moment of a sharp decrease in mass transfer coefficient

Most precisely, the beginning of coating destruction could be defined as the moment of sharp decrease in mass transfer coefficient, which is the ratio between the mass gain of substrate to the corresponding mass loss of treating electrode between two successive measurements. The decision could be considered as a criterion to end the process.

The analysis of experimental results indicates that the number of superimposed layers prior to the beginning of coating failure, for the investigated range of pulse energies, depends on pulse energy and it could be between 1 and 3 (the latest one is for low pulse energy) (Fig. 14). A single-valued dependence of the number of these layers to the amount of pulse energy was not observed. The same number of layers could be obtained by the employment of different pulse energies which depend on pulse amplitude and pulse duration. As an example, for 3 layers of deposition, either a pulse amplitude of 400 A (pulse energy not more than 0.3 J), or a pulse amplitude of 800 A (pulse energy not more than 1.5 J) or pulse amplitude of 1000 A (pulse energy not more than 3 J) could be employed. It should be noticed that, although there is a ten fold increase in pulse energy, the maximum number of deposited layers prior to fracture does not change. This behavior was explained as follows.

Despite of the constant amount of electricity for the ESA processing (3 Coulomb), deposition time of the first layer strongly varies, and it was, for example, 20 seconds for a high pulse energy case and 70 seconds for a low pulse energy case. Examination of the surface morphology of coatings shows that size, e.g. average diameter, of the solidified splashes due to mass transferred by a single pulse for the each energy significantly varies. For the low pulse energy of 0.032 J (100 A, 25 μs) the time to scan the substrate area of 1 cm^2 requires 80650 pulses (then the average splash area as a result of each spark discharge is roughly 0.00124 mm^2) and for the high pulse energy of 9.47 J (800 A, 800 μs), the same area was totally scanned by the application of only 125 pulses (thus the average splash area is nearly 0.8 mm^2 per pulse). That is, although pulse energy was increased 259 times, the average splash area was increased 645 times. Therefore, the growth of splash size is not directly proportional to the increase in pulse energy.

The erosive processes on treating electrode and substrate are determined not only by the electrical parameters of discharge and the chemical properties of the electrodes, but also, substantially by the rate of heat flow received by the electrodes (Namitokov, 1978; Butkevich et al., 1978). The amount of heat which could cause evaporation of substrate under the first layer of coating is not reached by the employment of long duration pulses, as in the case of pulses which have same energy but shorter duration. To reach dense heat flow in electrodes high enough to cause same kind of fracture, it is necessary to raise the energy of a long duration pulse by increasing its amplitude.

Since the number of superimposed layers prior to beginning the fracture of coating is limited, the amount of mass loss of the treating electrode and mass gain of the substrate are also limited. It is of interest to determine the amount of mass transfer, in turn coating thickness, quantitatively till fracture. As mentioned previously, it is a fact that the

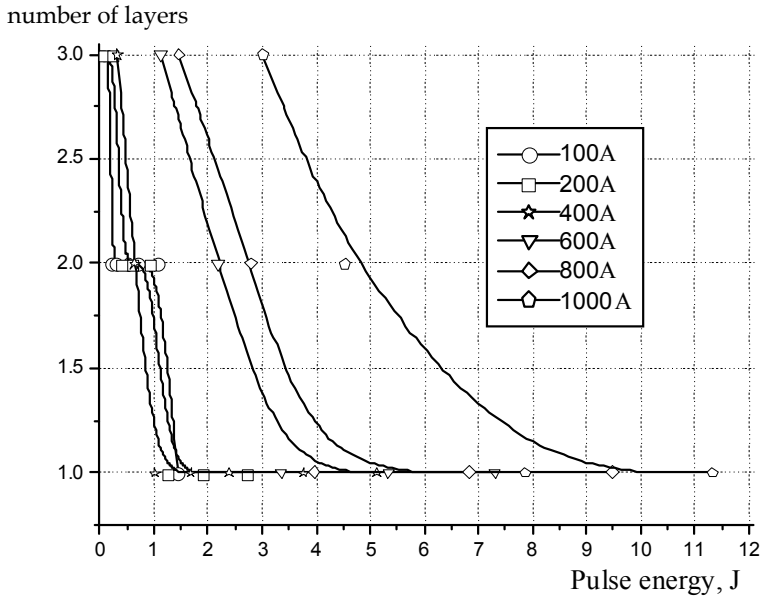

Fig. 14. The relationship between pulse energy and number of layers which could be superimposed without fracture of coating

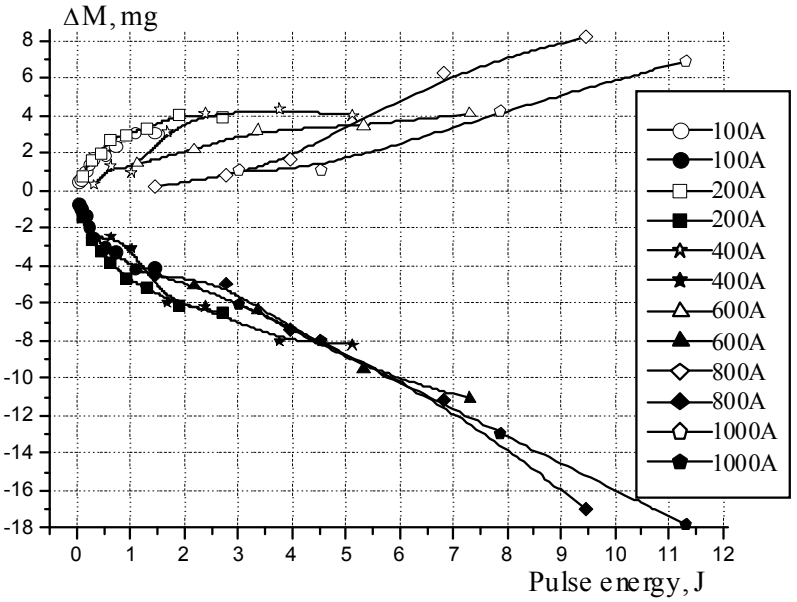

Fig. 15. Mass loss of treating electrode (solid dots) and mass gain of substrate as a function of pulse energy. Processing time is 30 s

experimental conditions of ESA (processing parameters e.g. properties of electrodes, medium and electrical pulse parameters), are the same only for the deposition of first layer. Therefore, the experimental data could be compared for the first layer of depositions only.
For alloying time of 30 seconds, i.e. first layer of deposition, the change in mass of electrodes as a function of pulse energy was given in Fig. 15. Amplitudes of pulses were marked on the figure as well. The data were taken from Tables 1-6. As it is seen, the relation between the mass loss of treating electrode and pulse energy is not linear. For example, the mass loss of treating electrode to the pulse energy ratio is about 10.0 -12.0 mg/J for pulse energy of 0.25 J. This ratio is only 1.42 mg/J for the pulse energy of 1.0 J and it does not practically vary further with increasing energy. The nonlinearity of the treating electrode mass loss is originated from the decreasing rate of heat flow density in electrodes.
Apparently, the difference between these two ratios is significant. This result could be interpreted as; on the one hand, to use energy effectively, pulses with low energy should be used for processing, on the other hand, to obtain considerably thick coating, i.e. high erosion of treating electrode, it is necessary to use pulses with high energy under the condition of single layer scanning.
Various combinations of pulse energy components, pulse amplitude and pulse duration did not produce a wide scatter in the values of mass loss of the treating electrode (Fig. 15). The voltage drop at the moment of spark discharge which is a requirement of ESA was constant at around 17 V for the present electrode couple (WC92-Co8 - steel 35). Using the experimental data about mass loss of treating electrode versus pulse energy till 5 J, an empirical relation given below was derived. For a given energy, the corresponding values of mass loss of treating electrode taken from Fig. 15, were averaged.

$$\Delta M_a = (\Delta M_{a,sp} \cdot C \cdot t) \text{ mg} \quad (1)$$

where, $\Delta M_{a,sp.} = (0.0089+0.0555\ W - 0.0243\ W^2 + 0.0054\ W^3 - 0.0004\ W^4)$ is the specific value of the mass loss of treating electrode for 1 Coulomb of electricity spent during 1 second alloying (mg/C · s); C is the amount of electricity of ESA processing (Coulomb); t is the time for the first layer deposition (s); W is the amount of pulse energy (J). The calculated curve and experimental average curve (solid dots) of the mass loss of the treating electrode are given in Fig. 16 for a 30 seconds of alloying by spending 3 Coulomb of electricity.
However, for a given pulse energy, the mass gain of the substrate shows a wide scattering depending on the pulse amplitude (Fig. 15). For example, for a pulse energy of 1.5 J which could be obtained by the application of pulse amplitudes of 200 A, 400 A, 600 A and 800 A, the mass gains of substrate were 3.5 mg, 2.5 mg, 1.7 mg and 0.25 mg, respectively. The difference in mass gained by substrate is because of two concurrent mass actions. These are the mass transferred from treating electrode and the mass loss due to washing away of molten pool of substrate spot caused by the intensive gas dynamics phenomena in plasma channel at the beginning of each spark discharge. In the case of processing with high pulse amplitude, due to larger material washed away, the mass loss of substrate would be expected to be more. However, cross sectional thickness measurements show that the thicknesses of coatings were close to each other despite the large differences in the amount of mass gain (14 times). This shows that the mass gained by substrates were almost the same despite the differences in pulse amplitudes. So, the amount of mass gained by substrate could be calculated by a simple relation, if the effect of washing away is negligible:

$$\Delta M_c = (k_{tf} \cdot \Delta M_a)\ mg \quad (2)$$

where, the mass transfer coefficient, k_{tf}, is equal to 0.74-0.60 (less for higher pulse amplitude). The mass transfer coefficients given in Fig. 28 for the pulse amplitude beyond 200 A could not be used in Eq. 2, because the amount of mass loss of substrate due to washing away was not taken into account for the calculation of k_{tf}.

Under this circumstance, the mass transfer coefficient should carefully be used to estimate the efficiency of mass transfer from treating electrodes to substrates. The following is an attempt to explain this point in detail.

The mass transfer coefficients as a function of pulse energy for the first layer of deposition were given in Fig. 17. The mass transfer coefficients corresponding to the short pulse durations were minimum for all pulse amplitudes ranging from 100 A to 1000 A. Since the substrate material was washed away due to the gas dynamics process at the beginning of a pulse, among these, the highest mass transfer coefficient belongs to smallest pulse amplitude which could not wash away molten substrate material.

The increase in pulse energy by means of increasing pulse duration which increases the mass transfer coefficient, because the mass gained by substrate from treating electrode is probably higher than the mass loss of original substrate as a result of washing away that occurs mainly at the beginning of the pulse. The amount of mass washed away during deposition of the first layer is not simple to measure, therefore the procedure to estimate the efficiency of mass transfer from treating electrode to substrate with the help of mass transfer coefficients is not quite correct.

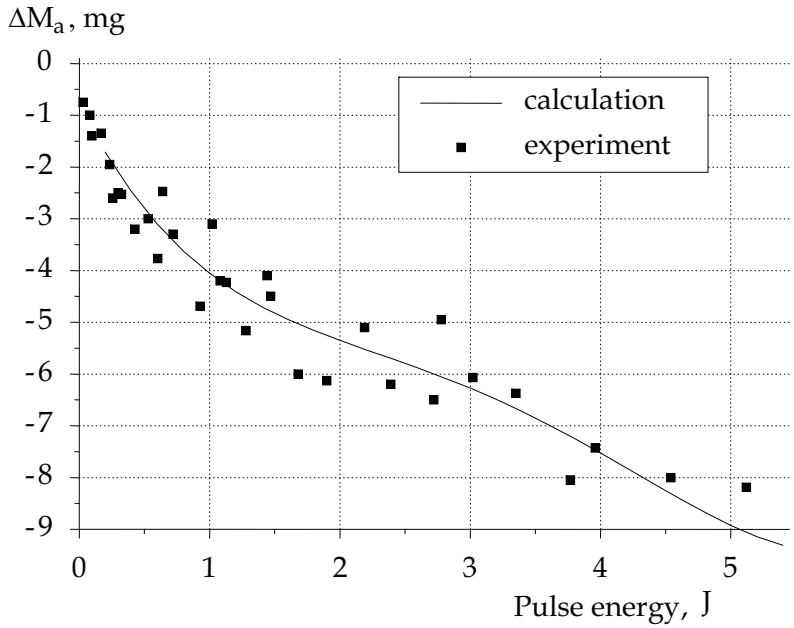

Fig. 16. Calculated curve and experimental data of mass loss of treating electrode as a function of pulse energy

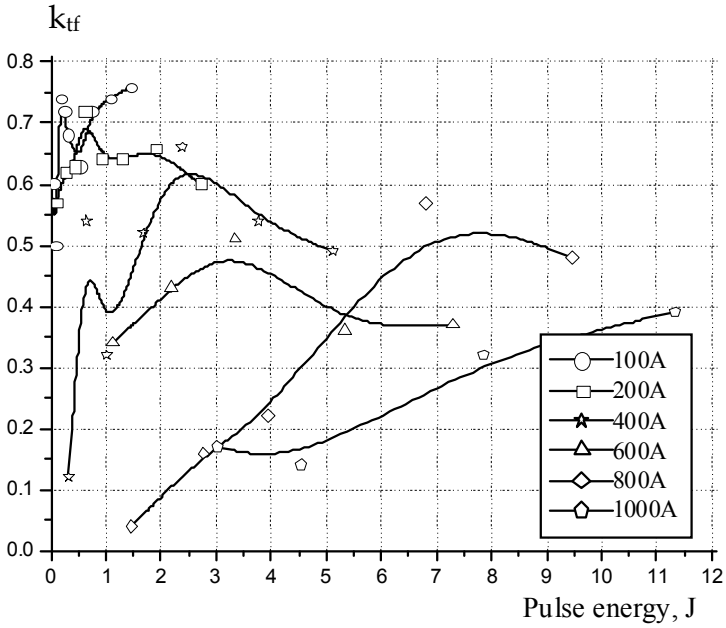

Fig. 17. Mass transfer coefficient as a function of pulse energy. Processing time is 30 s

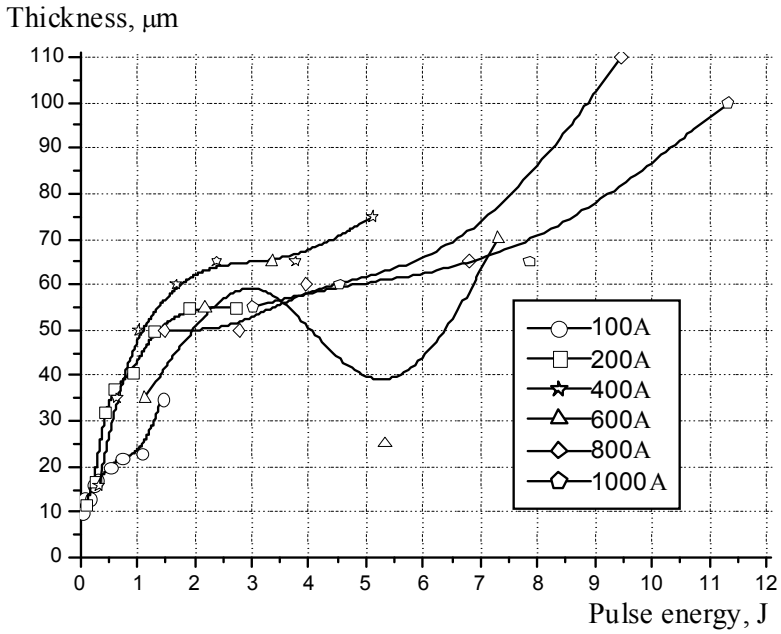

Fig. 18. Average coating thickness as a function of pulses energy

One might estimate the range of coating thicknesses that could be obtained under the necessary restrictions for the number of superimposed layers. That is, substrates should be alloyed according to the condition given in Fig. 14. The average thickness of coating as a function of pulse energy was given in Fig. 18. For any chosen pulse amplitude, the coating thickness increases with increasing pulse energy, especially, for the low pulse energy range the rate of increase was the highest. Upon further increase of pulse energy, above 1 J, the growth of coating thickness levels off, that correlates in the course of mass loss of treating electrode as shown in Fig. 15.

4. General conclusion

The failure of coating during processing was observed for the entire range of pulse parameters that were employed. In order to save already deposited layer, it is necessary to limit the processing time by the beginning of its failure.

As mentioned previously, when chemical composition of the substrate surface becomes as same as that of treating electrode after some deposition, the mass transfer from treating electrode to substrate ceases down. This is a limitation on coating thickness in ESA technology. Therefore, pulse energy was increased in order to increase the mass loss of treating electrode and its transfer to the substrate. However, it was experimentally found out that the other limitation of mass transfer, in turn limitation on layer thickness is the destruction of already deposited layer during processing. This was due to local evaporation of materials underneath the outer surface of deposit. Evaporation was due to the heat provided locally by spark discharges of high energy pulses.

Most of the molten material at the tip of the treating electrode could not be ejected out. Part of the ejected molten mass could be transferred to substrate and the rest is wasted. The ejected mass, so the transferred mass, could be increased by the employment of pulse groups instead of employing individual pulses (Rybalko et al., 1998; Ribalko et al., 2006, 2008). Mass transferred to the substrate could also be increased by the choice of an optimum scanning rate of the treating electrode. Because cross-section of a single deposit has very big difference in thickness (if the mass transfer time is long), the spot has higher thickness in center. For a continuous coating, the subsequent spot should partially overlap with previous spot. But, continuity of coating essentially depends on the experience of the operator. Thus, a continuous coating with uniform thickness demands compulsory automated spot deposition system with pre-determined rate of speed to provide necessary level of spot overlapping. Consequently, the non uniformity in coating thickness could be lowered and average coating thickness, that is mass transfer, would essentially be increased.

5. References

Butkevich, G.V.; Belkin, G.S.; Vedeshenkov, N.A. & Javoronkov, M.A. (1978). *Electrical erosion of heavy-current contacts, Energy*. Moscow, 256 p. (in Russian)

Lazarenko, B.R. (1951). *Method of metal surfaces deposition*. The USSR Patent №89933. Unveil in Bulletin of Invention in USSR (in Russian)

Lazarenko, N.I. (1976). Electrospark alloying of metal surfaces. In: *Mechanical Engineering*, Vanity press, Moscow (in Russian)

Lazarenko, N.I. (1957). Change of initial properties of a cathode surface under the electric pulses, proceeding in the gas environment. In: *Electrospark Processing of Current-Carrying Materials, Publication 1*. Vanity Press, Academy of Science of the USSR, Moscow, pp. 70-94 (in Russian)

Namitokov, K.K. (1978). *Electroerosion phenomenon, Energy.* Moscow, 456p. (in Russian).

Ribalko, A.V.; Siminel, A.V. & Sahin, O. (2004a). Electrospark processing by hard-alloy treating electrode under the conditions of unconventional pulse parameters. 2. Range of pulse duration (50-4000) μs at amplitude of current 200 and 400A. *Metal working*, Vol.2, No.20, pp. 6-11 (in Russian)

Ribalko, A.V.; Siminel, A.V. & Sahin, O. (2004b). Electrospark processing by hard-alloy treating electrode under the conditions of unconventional pulse parameters. 3. Range of pulse duration (200-1000) μs at amplitude of current 600-1000A. *Metal working*, Vol.4, No.22, pp. 10-15 (in Russian)

Ribalko, A.V.; Siminel, A.V. & Sahin, O. (2005). Electrospark processing by hard-alloy treating electrode under the conditions of unconventional pulse parameters. 4. Generalization of results. *Metal working*, Vol.3, No.27, pp. 21-28 (in Russian)

Ribalko, A.V. & Sahin, O. (2006). A modern representation of the behavior of electrospark alloying of steel by hard alloy. *Surface and Coatings Technology*, Vol.201, No.3-4, pp.1724-1730.

Ribalko, A.V.; Korkmaz, K. & Sahin, O. (2008). Intensification of the anodic erosion in electrospark alloying by the emploument of pulse group. *Surface and Coatings Technology*. Vol.202, No.15, pp. 3591-3599

Ribalko, A.V.; Siminel, A.V.; Sahin, O. & Korkmaz, K. (2006). About possibility of anode erosion increase in electrospark alloying by pulses of invariable electric parameters. *Metal working*, Vol.6, No.36, pp. 45-52 (in Russian)

Rybalko, A.V.; Grichuk, D.; Ermilov, V.V. & Mindru, D. (1998). The patent of Moldova №997. Procedeu de aliere prin electrorodare, *Method of an electrospark alloying*, Vol.7 (in Moldovian)

Rybalko, A.V.; Siminel, A.V. & Sahin, O. (2003a). The Electrospark alloying by isopower current pulses with various form. *Metal working*, Vol.1, No.13, pp. 18-22 (in Russian)

Rybalko, A.V.; Siminel, A.V. & Sahin, O. (2003b). Installation for an electrospark alloying of new generation. *International Symposium on Electroerosive processing of materials*. Moscow, Russia, April 2003 (in Russian)

Rybalko, A.V.; Siminel, A.V. & Sahin, O. (2003c). Modern installation for an electrospark alloying. *Metal working*, Vol.6, No.18, pp. 38-40 (in Russian)

Rybalco, A.V.; Grichuc, D.M.; Ermilov, V.V. & Sahin, O. (2000). Procedeu de aplicare an acoperirilor prin electrorodare (the Method of electrospark processing). Pat. №1414. Moldova (in Moldovian)

Rybalko, A.V.; Siminel, A.V. & Sahin, O. (2003e). Dynamic of formation and destruction carbide of tungsten coverings in the course of an electrospark alloying. *Metal working*, Vol.4, No.16, pp. 7-10 (in Russian)

Rybalko, A.V.; Siminel A.V. & Sahin, O. (2003d). An electrospark alloying by hardfacing treating electrode in the conditions of application of nonconventional of pulse electric parameters. 1. Change of pulse duration in a range (25-4000)μs at the fixed current amplitude 100A. *Metal working*, Vol.5, No.17, pp. 10-15

Zolotih, B.N. (1957). About the physical nature of electrospark metal processing. In: *Electrospark processing of current-carrying materials*, *Publication 1*. Vanity Press Academy of Science of the USSR, Moscow, pp.38-69 (in Russian)

22

Mass Transfer in the Electro-Dissolution of 90% Copper-10% Nickel Alloy in a Solution of Lithium Bromide

Martínez-Meza E., Uruchurtu Chavarín J. and Genescá Llongueras J.
Universidad Nacional Autónoma de México
México

1. Introduction

Copper is considered to be among the most important structural elements, just below iron and aluminum. Usually, the properties of this metal improve when combined with other elements (Kear et al., 2004b); the 90% Cu-10% Ni alloy has excellent physical, chemical and mechanical properties that allow it to adapt to different operating conditions (Kutz, 2002; Othmer, 2004). This metal is relatively inexpensive, as a structural element it is aesthetically attractive. It shows good thermal conductivity and a lower electrical resistivity than that observed both in the 70% Cu-30% Ni alloy and in steel; these characteristics make the 90% Cu-10% Ni alloy an efficient and competitive structural element in heat transfer processes (Copper-Nickel Alloys in Marine Environment).
In the last few decades, while trying to establish the dissolution mechanism in the presence of chlorides (Cl^-), this alloy has been the subject of numerous studies (Lee & Nobe, 1984; Crundwell, 1991; Milosev & Metikos, 1997; Kear et al., 2004b), usually at low concentrations and operating conditions close to those in the environment. However, its behavior in the presence of other agents such as bromides (Br^-), has received little attention (Itzhak & Greenberg, 1999; Muñoz-Portero et al., 2005), especially under operating conditions similar to those found in a heat pump that uses the H_2O-LiBr pair as a working fluid, which is very attractive because of its thermodynamic properties, however, it is very aggressive to the structural elements of the equipment (Muñoz-Portero et al., 2006).

1.2 Dissolution mechanism

The kinetics of dissolution of the 90% Cu-10% Ni alloy, in the presence of halides, shows marked similarities to the reaction mechanism of copper (Lee & Nobe, 1984; Crundwell, 1991; Kear et al., 2004a, 2004b).
In the Tafel region, in the vicinity of corrosion potential, three dissolution mechanisms have been proposed. Some researchers (Taylor 1971; Wagner et al., 1998; Kear et al., 2000, cited in Kear et al., 2004a) propose a two step mechanism; the first step consists in an electrochemical reaction, in which the cuprous ion (Cu^+) is produced due to the anodic dissolution of metallic copper (Cu). Then, in a chemical process, this species is combined with two chloride ions (Cl^-) to form the cuprous chloride complex ion ($CuCl_2^-$). However, due to thermodynamic matters, this is the least viable of the proposed mechanisms.

In studies carried out by (Walton & Brook, 1977, cited in Dhar et al., 1985) the same mechanism is proposed, concluding that the dissolution of the alloy takes place due to the degradation of a single component: copper. Meanwhile, (Beccaria & Crousier, 1989) speak of a simultaneous dissolution of both components, observing that copper is redeposited in the alloy.

The mechanism proposed by (Lee & Nobe, 1984; Crundwell, 1991; Deslouis et al., 1988a, 1988b) mentions that the alloy is dissolved through a process that takes place in two stages. It begins with the formation of cuprous chloride (CuCl) through an electrochemical reaction between Cu and the Cl^- ion. Later, in a chemical reaction between CuCl and the Cl^- ion, the $CuCl_2^-$ ion is formed. This reaction, according to (Kear et al., 2004b, 2007) is partly controlled by a mass transfer process.

Direct dissolution between Cu and two Cl^- ions through an electrochemical process to produce the $CuCl_2^-$ ion, has been adopted by other researchers (Kato et al., 1980a; Dhar et al., 1985; Muñoz-Portero et al., 2004; Kear et al., 2004b, 2007).

2. Results

2.1 Polarization curves

In the absence of oxygen, copper behaves according to the diagrams shown in (Figure 1(a)). In these circumstances, the metal reaches the E_{corr} at –437.4 $mV_{Ag/AgCl}$ at 25 °C; 28 mV, in more oxidizing conditions, it is reached at 55 °C.

Anodic polarization develops a slope of 75 mV/decade. This segment at 25 °C shows the turning point at -206.74 $mV_{Ag/AgCl}$ and generates a current of 3 mA/cm^2. As temperature increases, the active segment of the curve increases, developing at 55 °C a current of 9.5 mA/cm^2 to a potential of -219.1 $mV_{Ag/AgCl}$. The behavior of the curves after the inflection point is similar, however, the range widens, having the most unfavorable conditions at the upper temperature level with a current of 171.64 mA/cm^2 in the noblest part.

The range in the cathodic fraction opens in a significant way showing on the whole level, the establishment of limit currents. This current reaches a maximum value at the upper temperature level, developing at -870.18 $mV_{Ag/AgCl}$ a current of 0.195 mA/cm^2.

In the absence of oxygen, the 90% Cu-10% Ni alloy behaves as shown in the graphs (Figure 1(b)). In such circumstances, the development of a corrosive process controlled by activation can be observed across the anodic fraction only at 25°C. The curve in these circumstances reaches a slope of approximately 63 mV/decade. At -361 $mV_{Ag/AgCl}$ a slope change occurs, narrowing the activation process.

As temperature increases there is a turning point indicating an active-passive transition. At 35 °C, this change takes place at -347.51 $mV_{Ag/AgCl}$, generating a i_{crit} of 36 $\mu A/cm^2$; then, the current drops to -298 $mV_{Ag/AgCl}$. When the slope increases again after this point, the curve displays a value of 72 mV/decade.

At the upper temperature level, the passive region is manifested in a wider range. "The passive primary potential" is established at -415.1 $mV_{Ag/AgCl}$, generating a i_{crit} of 34.18 $\mu A/cm^2$; it is observed a reduction in the current until an inflexión point at –307.1 $mV_{Ag/AgCl}$. In such circumstances, a current of 8.5 $\mu A/cm^2$ is generated. From this point on, the current increases again. In this segment it develops a slope of approximately 50 mV/decade until a new inflexión point at –109.28 $mV_{Ag/AgCl}$, from this point on the current is stabilized in a value of 107.34 mA/cm^2.

The system's E_{corr} is set in a 72 mV range, reaching at -458 $mV_{Ag/AgCl}$ the most oxidizing conditions at 35 °C. The cathodic part of the curve at the analyzed temperature level shows the development of limit currents, reaching its maximum value at 55 °C at -752.25 $mV_{Ag/AgCl}$.

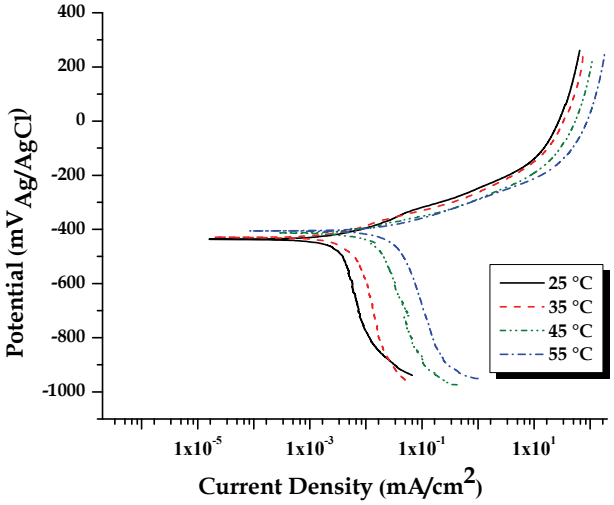

(a)

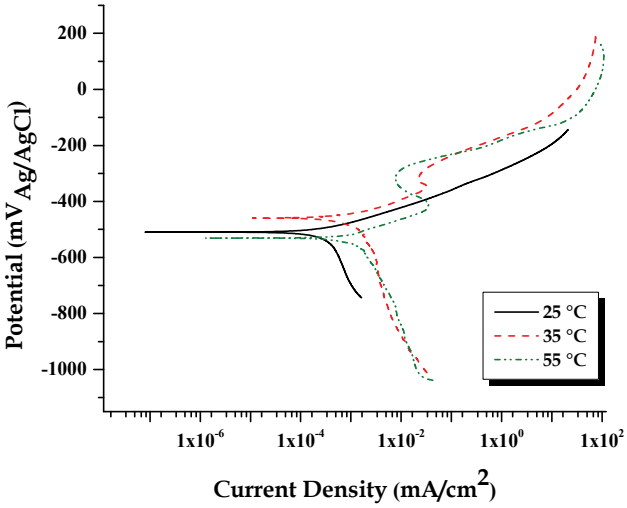

(b)

Fig. 1. Polarization diagrams the absence of oxygen and static conditions in 53% LiBr solution: (a) Copper, (b) 90% Cu-10% Ni

2.2 Impedance

Impedance spectroscopy is an appropriate technique to determine the electrical behavior of an electrochemical system, in which the system's general behavior is determined by a number of tightly coupled processes, each proceeding at a different speed (J. R. Macdonald). The diagrams in (Figure 2) show the behavior in the impedance spectrum of the 90% copper-10% nickel alloy in the 50% solution of LiBr, in the absence of oxygen, under static conditions at 25 °C.

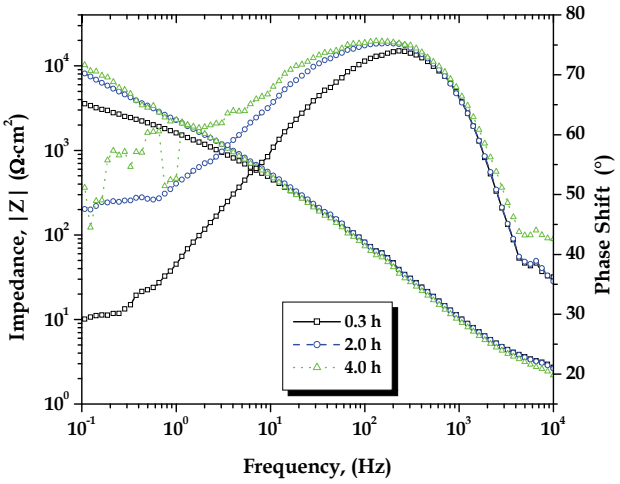

(a)

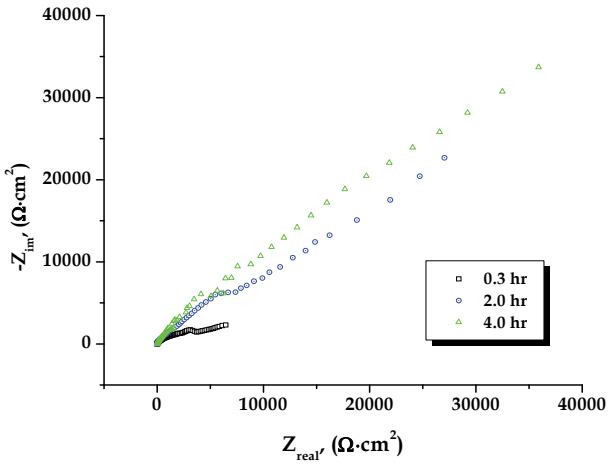

(b)

Fig. 2. Impedance spectrum of the 90% Copper-10% Ni-50% LiBr system, (a) Bode diagrams (b) diagrams in the complex plane

According to the Bode diagram, the system behaves similarly in the three periods of exposure up to a frequency of approximately 400 Hz. As this factor decreases, a mass transport phenomenon is manifested. This behavior is best seen in the complex plane, (Figure 2(b)). When the exposure period exceeds two hours, the development of a pure diffusion process is observed, which, due to its magnitude, dominates the metal dissolution process.

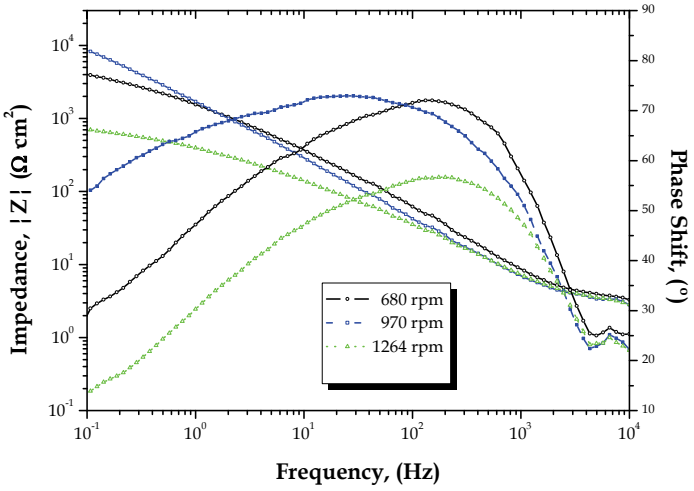

(a)

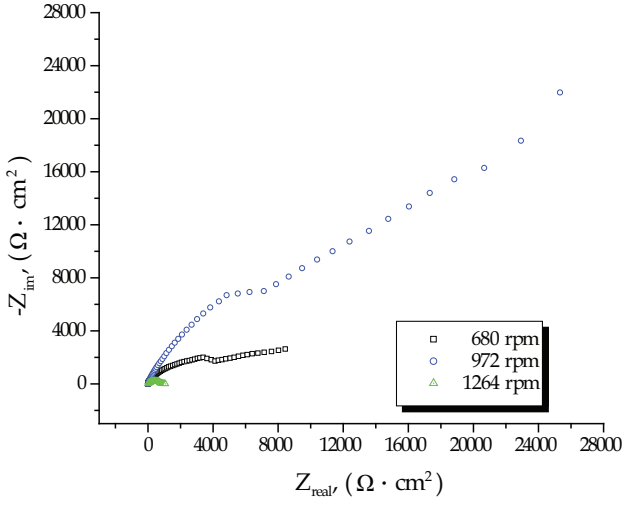

(b)

Fig. 3. Impedance spectrum for the 90% Copper-10% Nickel-50% LiBr system. Dynamic conditions at 25°C, at different rotation velocities, (a) Bode diagrams, (b) diagrams in the complex plane

The system behavior under dynamic conditions in the absence of oxygen is shown in the diagrams (Figure 3). In these circumstances the system behaves differently in the three rotation levels and only at 972 rpm, the development of a pure diffusion process can be observed, (Figure 3 (b)). As the rotation speed increases, the effect caused by this phenomenon decreases significantly. The behavior of the cell in the analyzed temperature range is synthesized in the values reported in Table 1. These parameters form the equivalent circuit (Figure 4), which acceptably describes the system behavior.

Temp. (°C)	Time (h)	rpm	E_{corr} ($mV_{Ag/AgCl}$)	R_Ω (Ω)	C_{dl} (μF/cm²)	R_{ct} (Ω·cm²)	Z_w (Ω·cm²)	Z_f (Ω·cm²)	|Z| (Ω·cm²)	θ (°)	$w_{(\theta=max)}$ (Hz)
25	0.3		-373.1	2.8	14.6	861	3,761	4,412	3,014	50	12.67
	2	0	-434.9	2.67	13.9	854	33,392	34,002	18,026	31.65	13.4
	4		-472.1	2.3	14.29	1,014	15,717	16,450	9,984	38.99	10.98
	-	680	-363.6	3.745	18.39	201	7,238	7,382	4,767	41	43
	-	972	-458.3	3.18	25.2	71	29,868	29,918	13,787	25.85	89
	-	1,264	-280.4	3.329	21.23	45	848.8	881	430	62.87	166.6
45	0.3		-387.3	3.2	15.8	255	5,993	6,176	4,090	42.86	39.5
	2	0	-420.9	3.35	19.4	230	21,059	21,222	11,626	32.61	35.6
	4		-435.7	3.37	20.7	234	22,825	22,991	12,167	31.16	32.9
	-	476	-402.9	3.15	18.2	147	17,305	17,409	10,060	34.89	59.5
	-	680	-355.8	2.86	23	198	1,225	1,372	957	49.48	35
	-	884	-344.5	2.91	21.4	170	972	1,099	772	50.24	43.8
60	0.3		-381.9	2	28.45	123.6	5,200	5,288	3,382	40.35	45.3
	2	0	-469.2	2.043	39.66	494.4	62,940	63,291	16,130	12.47	8.12
	4		-495.5	2.084	46.96	529.4	28,355	28,732	10,400	19.28	6.4
	-	380	-361	2.72	49.8	79	4,053	4,109	2,541	38.46	40.5
	-	543	-501.7	2.48	55.2	142	9,567	9,668	4,966	30.08	20.3
	-	706	-534.5	2.563	61.89	223.5	5,367	5,527	3,151	35.25	11.5

Table 1. Equivalent Circuit Parameters for System 90% Copper-10%Nickel-50% LiBr. Under Static and Dynamic Conditions

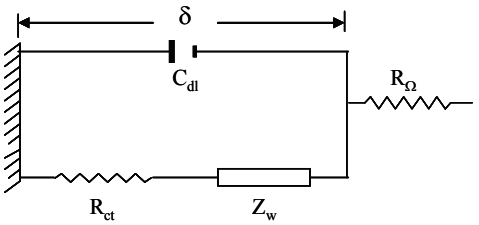

Fig. 4. Randles equivalent circuit, which describes the response of a system with a charge transfer process in one step coupled to a diffusion process at the interface

2.3 Electrochemical noise

The presence of noise processes in an electrochemical system is characterized by fluctuations in current and potential generated at random on the interface. This signal is a rich source of

information of a corrosive process; however, the signal as such masks phenomena occurring outside the charge transfer process (Hassibi et al., 2004).
The diagrams (Figure 5) show the behavior of the noise signal in current and potential in the time domain of copper-nickel alloy in the LiBr solution at different periods of exposure under static conditions at 25 °C.

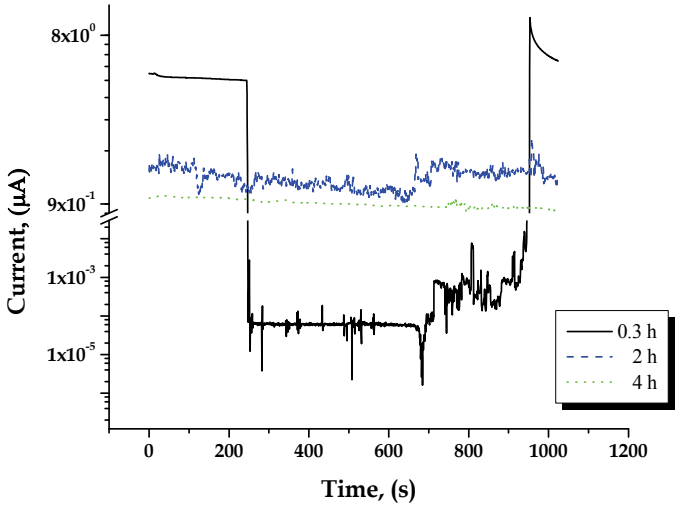

(a)

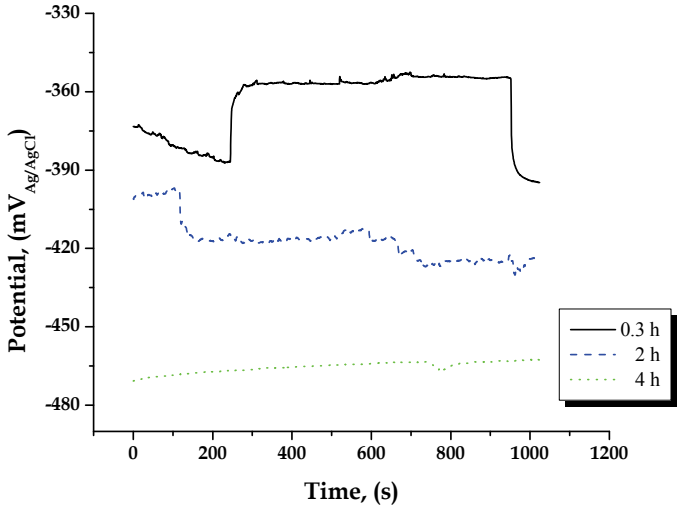

(b)

Fig. 5. Record in the time domain of noise signal in (a) current and (b) 90% Cu-10% Ni-50% LiBr system potential in static conditions at 25°C

The current and potential values in the time domain were obtained simultaneously. In the initial moments, in the test done at the 0.3 h, the current showed a very stable behavior. However, 250 s after the test started the current abruptly decreased about 5 logarithmic units until it reached a value of 5×10^{-5} μA. From that moment on, the development of transitional currents of a relative magnitude and frequency in the signal could be observed. However, it didn´t show a defined behavior pattern which suggests that this is the typical behavior of a pitting corrosion process. This phenomenon can be observed for a period of 700 s. Subsequently, the current increases again near the end of the registry, reaching a maximum value of 9.5 μA, and then decreases slightly. The current's behavior in the registry after two hours of exposure shows a more stable behavior over time, however, the development of a high frequency and low amplitude metastable process can also be observed, which reveals the origin of the signal, as this is caused by a more severe pitting corrosion process.

The current signal in the last period of exposure, after 4 hours, shows a fairly stable behavior over time, and due to the processes developed in the interface, the current generated in the system is lower compared to the previous test. Besides, judging by the shape of the graph, the development of a uniform corrosion process can be predicted.

As for the potential, the signal at 0.3 h of exposure showed the following behavior. In the first 250 s the potential moves in an active direction approximately 14 mV, and then suddenly shifts towards a noble direction 30 mV, remaining virtually unchanged during the next 700 s. Later, near the end of the test, the signal registered again a major shift toward an active direction. After two hours of exposure, the signal record is irregular, suggesting that its origin is a random pitting corrosion process; the signal is developed in a more active region, also showing a very small dc trend. As for the last test, in these conditions the signal seems to be fairly stable in all directions moving further into an active region.

In flow conditions, the records for both current and potential noise generated by the system at 45°C in the absence of oxygen are shown in the diagrams (Figure 6). In contrast to the behavior shown by the system at a lower temperature level, the current generated in the cell at 45°C decreases significantly as the electrode velocity increases. At a velocity of 680 and 884 rpm the current signal reaches during the initial moments a stationary state, maintaining this condition during the development of the test. Under these conditions the signal gives the impression of having been filtered, however, it is the original signal.

The behavior of the potential noise signal can be considered normal because as the electrode velocity increases, the signal shifts to a nobler region. Despite the fact that the potential noise signal at 884 rpm seems a bit irregular during its registry, it shows a trend of only 3 mV. At 476 rpm the trend in the signal was 35 mV, and during the record of this period, the signal did not reach the stationary state.

Table 2 shows the resistance value for each experimental condition determined by different electrochemical techniques used for that purpose. Also, a comparison of the values obtained by filtering the signal is shown in it. The difference is significant and is almost constant throughout the experimental range. This was the main reason for deciding to work with the original signal from the current and potential records over time.

1. Resistance in noise measured before and after removing the dc component of the signal,
2. Resistance in noise measured after removing the dc component with the average removal method, MAR (Tan et al., 1996).

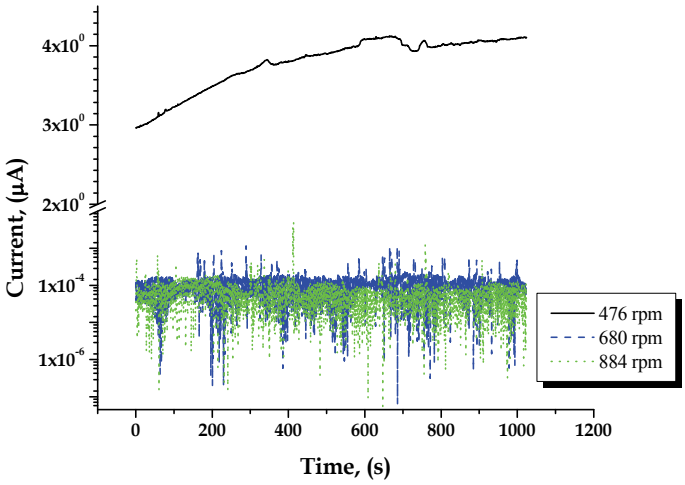

(a)

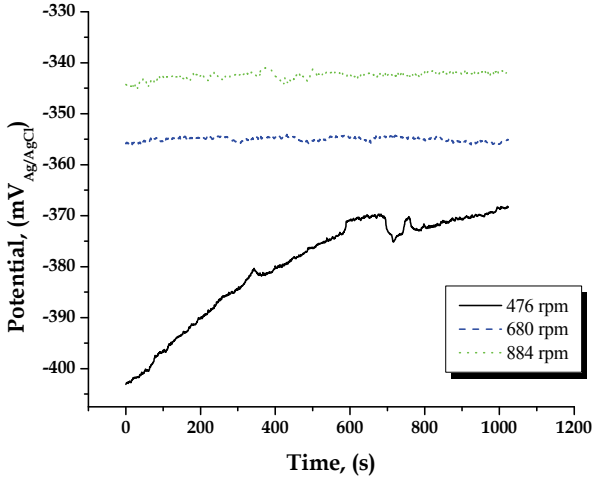

(b)

Fig. 6. Record in the time domain of noise signal (a) current and (b) potential, 90% Cu-10% Ni-50% LiBr system potential under flow conditions at 45°C

For this reason it is assumed that the signal is due solely to charge transfer processes. When the velocity is increased, due to the generation of transitory currents of high frequency and relative amplitude, the development of a pitting corrosion process could be considered. However, this phenomenon is not reflected in the potential noise signal, either because there is no such process or because the current generated in these conditions is very small. Statistically, the average current value at 884 rpm is 4.47×10^{-8} μA. At 476 rpm the oscillatory phenomenon in the current is not seen, on the contrary, a fairly stable signal is shown, with a tendency of just 1 μA.

Temperature (°C)	Time (h)	Velocity (rpm)	$Rn_{(1)}$ ($\Omega \cdot cm^2$)	LPR ($\Omega \cdot cm^2$)	Z_f ($\Omega \cdot cm^2$)	$Rn_{(2)}$ ($\Omega \cdot cm^2$)
25	0.3	-	4,283	7,366	4,412	1,853
	2	-	37,244	24,977	34,002	4,759
	4	-	32,637	113,789	16,450	5,068
	-	680	13,905	9,375	7,382	90,859
	-	972	20,527	18,092	29,918	40,556
	-	1,264	6,613	649	881	11,315
45	0.3	-	3,273	7,704	6,176	1,412
	2	-	25,205	18,413	21,222	1,553
	4	-	28,247	30,306	22,991	1,549
	-	476	24,527	17,974	17,409	26,683
	-	680	2,699,167	3,377	1,372	491,550
	-	884	3,219,963	2,383	1,099	303,667
60	0.3	-	8,810	8,352	5,288	1,063
	2	-	50,941	40,317	63,291	1,489
	4	-	146,872	61,506	28,732	35,449
	-	380	5,408	1,800	4,109	803
	-	543	20,942	14,130	9,668	3,905
	-	706	22,938	12,565	5,527	6,650

Table 2. Resistance determined using different electrochemical techniques Static and dynamic conditions for the 90% Cu-10% Ni-50% Lithium Bromide System

The corrosion rate i_{corr} of the system is obtained using the Tafel slopes and polarization resistance Rp, along with the Stern-Geary relationship, equation 1, (Stern & Geary, 1957; Mansfeld F., 1973a, 1973b)

$$i_{corr} = \frac{\beta_a \beta_c}{2.3(\beta_a + \beta_c)} \frac{1}{R_p} = \frac{B}{R_p} \tag{1}$$

Where β_a and β_c are the anodic and cathodic Tafel slopes, respectively.

Temp. (°C)	Time (h)	Velocity (rpm)	E_{corr} ($mV_{Ag/AgCl}$)	R_n ($\Omega \cdot cm^2$)	LPR ($\Omega \cdot cm^2$)	Z_f ($\Omega \cdot cm^2$)	i_{corr} (B=0.026)		
							($\mu A/cm^2$)$_{(Rn)}$	($\mu A/cm^2$)$_{(LPR)}$	($\mu A/cm^2$)$_{(Zf)}$
25	0.3	-	-373.1	4,283	7,366	4,412	6.07	3.528	5.893
	2	-	-434.9	37,244	24,977	34,002	0.698	1.04	0.765
	4	-	-472.1	32,637	113,789	16,450	0.796	0.228	1.58
	-	680	-363.6	13,905	9,375	7,382	1.869	2.77	3.522
	-	972	-458.3	20,527	18,092	29,918	1.266	1.44	0.869
	-	1,264	-280.4	6,613	649	881	3.931	40	29.5

Table 3. Corrosion Rate in Static and Dynamic Conditions of the 90% Cu -10% Ni Alloy in a 50% Lithium Bromide solution at 25°C

2.4 Kinetic parameters

According to the values reported in Table 1 and the proposed equivalent circuit (Figure 4), the dissolution of the alloy is under mixed kinetic control, by activation and diffusion. However, the mass transport resistance under all experimental conditions is higher than that observed for charge transfer. On the other hand, as both elements are in series, the one representing the mass transport process shows more resistance to current flow. Therefore, the diffusion phenomenon should be the process that controls the dissolution of the alloy.

For the dissolution process to be maintained, the reacting species must match on the interface in an electrochemical process. Transport to the electrode surface is given by a combination of two phenomena. First, by a convective process from the bulk of the solution to the outside of the film. Subsequently, the reagent must diffuse through this layer to reach the electrode surface (Brossard & Raynaud, 1985).

According to the values in Table 1, mass transfer controls the kinetics of the system; however, it didn´t always follow the Levich relation. The oxygen diffusion coefficient was determined for those conditions that apply to this relation according to the following equation (Bard & Faulkner, 1980; Barsoukov & Macdonald, 2005).

$$D_{o_2} = \left[\frac{R\,T}{\sigma\, n^2\, F^2\, \sqrt{2}\, C_{o_2}} \right]^2 \tag{2}$$

Where:

σ, Warburg coefficient, Ω $s^{1/2}$; R, gas constant, 8.314 J mol^{-1} K^{-1}; F, Faraday constant, 96,485.309 C mol^{-1}; T, temperature, K; C_{O_2}, Oxygen concentration, mol cm^{-3}; D_{O_2}, Diffusion coefficient, cm^2 s^{-1}; n, number of electrons transferred in reaction

The film thickness δ under static conditions was determined according to the following equation (Bard & Faulkner, 1980).

$$\delta = \frac{n\, F\, D_{o_2}\, C^*_{o_2}}{i_L} \tag{3}$$

Where:

i_L, cathodic limit current density, A cm^{-2}; $C^*_{O_2}$, Oxygen concentration within the solution, mol cm^{-3}

Under flow conditions, the thickness was determined by the following equation

$$\delta = 1.61\, D_{o_2}^{1/3}\, w^{-1/2}\, \gamma^{1/6} \tag{4}$$

Where:

w, angular velocity, radians s^{-1}; γ, kinematic viscosity, cm^2 s^{-1}

The exchange current density i_o and the rate constant k_o were determined according to the following equations

$$i_o = \frac{RT}{nFR_{ct}} \tag{5}$$

Where:

R_{ct}, Resistance to charge transfer, Ω·cm^2

$$k_o = \frac{RT}{n^2 F^2 R_{ct} C_{CuBr}} \quad (6)$$

Where:
C_{CuBr} Solution concentration, mol cm^{-3}
The results in Table 4 show the diffusion coefficient and the thickness of the film only on those system conditions where the Levich relation was followed.

Temperature (°C)	Time (h)	Velocity (rpm)	E_{corr} ($mV_{Ag/AgCl}$)	$i_0 \times 10^5$ (A/cm^2)	$D_{O_2} \times 10^5$ (cm^2/s)	$k_0 \times 10^8$ (cm/s)	δ (μm)
25	0.3	-	-373.1	2.98	-	3.5	
	2	-	-434.9	1.2	0.149	0.5	1.14
	4	-	-472.1	1	0.123	0.4	1.89
	-	680	-363.6	12.79	-	15	
	-	972	-458.3	14.5	0.218	6.8	10.9
	-	1,264	-280.4	57.17	-	67.3	
45	0.3	-	-387.3	10.75	-	12.6	
	2	-	-420.9	4.8	1.53	2.2	3.44
	4	-	-435.7	4.7	0.675	2.2	2.33
	-	476	-402.9	18.65	65.8	21.9	98.1
	-	680	-355.8	13.84	-	16.3	
	-	884	-344.5	16.13	-	18.9	
60	0.3	-	-381.9	23.22	611.2	27.3	1,284.20
	2	-	-469.2	2.32	-	1	
	4	-	-495.5	2.17	-	1	
	-	380	-361	36.34	-	42.7	
	-	543	-501.7	8.1	1.83	3.8	26.9
	-	706	-534.5	5.14	-	2.4	

Table 4. Kinetic Parameters for System 90% Copper-10% Níkel-50% Lithium Bromide Under Static and Dynamic Conditions

3. Discussion

According to the Pourbaix diagram for the Cu-Br – H_2O system at 25°C (Muñoz-Portero et al., 2004), the only products of metal corrosion in the Tafel region and acidic conditions are: cuprous bromide, CuBr, and the complex ion $CuBr_2^-$. These species are formed according to the following reactions:

$$Cu + Br^- \rightarrow CuBr + 1\,e^- \quad (7)$$

With an equilibrium potential at 25°C defined by the following equation

$$E_{(Cu/CuBr)} = 0.031 + 0.0591 \log\left[\frac{1}{Br^-}\right]; V_{(SHE)} \quad (8)$$

The complex ion formation requires the participation of two units of bromide ion producing tha same amount of charge

$$Cu + 2\,Br^- \rightarrow CuBr_2^- + 1\,e^- \tag{9}$$

With an equilibrium potential at 25ºC defined by the following equation

$$E_{\left(Cu/CuBr_2^-\right)} = 0.195 + 0.0591 \log\left[\frac{\left(CuBr_2^-\right)}{\left(Br^-\right)^2}\right]; V_{(SHE)} \tag{10}$$

Anodic polarization of the cell in the Tafel region develops slopes in a range of 60 to 75 mV/decade, Figure 1. (Lee & Nobe, 1984) determine the slope in a chloride solution at approximately 60 mV/decade. This fact implies that the dissolution of the electrode is accomplished by activation. However, these researchers argue that the electro-dissolution of metal is controlled by a mass transport process. The value of this parameter (Pérez-Herranz et al., 2001) is in a range of 70 to 80 mV /decade, for a velocity range of 265 < Re <3,120. This range is close to slopes of 60 mV/decade, typical of a metal dissolution process controlled by diffusion of products from the metal surface to the bulk of the solution. The active dissolution region observed at potentials nobler than E_{corr}, the author goes on, is consistent with the formation and dissemination of the complex ion, and when this phenomenon increases, it alters the anodic Tafel slopes. (Kear et al., 2004b) provides a summary of several research papers on chlorides determining the anodic slope at different operating conditions.
The electrochemical reaction rate is limited by environmental factors, both physical and chemical, so that the reaction is polarized or delayed due to these factors. Activation polarization refers to an electrochemical process controlled by the slowest step in a reaction sequence on the interface. Polarization can be defined as the displacement of the electrode potential due to a net current flow and its magnitude is overpotential η, which is a polarization measure with respect to the equilibrium potential of the electrode (Fontana & Greene, 1978)
The relationship between reaction rate and η due to activation polarization is

$$\eta_a = \pm \beta_a \log \frac{i}{i_o} \tag{11}$$

Above is the Tafel equation, where β is frecuently known as the Tafel slope or constant and I_o has been defined before

$$\beta_a = \frac{2.303\,RT}{\alpha n F} \tag{12}$$

α is the transfer coefficient, the constants R, T, F and n were defined before.
The Tafel law (Bockris et al., 2000) shows the exponential relationship between reaction rate and the η. This approach can be seen clearly in the dissolution of copper and in the 90/10 alloy, Fig. 1. (Lee & Nobe, 1984, Fig 2, 4-5) claim that the anodic behavior in this region is an "apparent" Tafel behavior, since it doesn´t represent an activation controlled process. This idea is shared by other researchers, however, (Kato & Pickering, 1984; Pérez-Herranz et al., 2001) despite stating that for a slope of 60 mV/decade the anodic process is controlled by diffusion, determine the i_{corr} by the Tafel extrapolation method (Fontana & Greene, 1978;

Flitt & Schweinsberg, 2005), which is well known and often poorly implemented. Researchers often forget that the metal needs to corrode evenly, and in the corrosion potential the anodic and/or cathodic reactions must be under complete control by activation. Furthermore, in order to estimate the i_{corr} correctly, the linear portion identified in the curves should extend at least a decade on the current's logarithmic scale. The i_{corr} is calculated by (Deslouis et al., 1988a) assuming a pure activation mechanism for both fractions, which is contrary to their approach.

As the potential shifts in noble direction the curve develops a gradual change of slope. At about -200 $mV_{Ag/AgCl}$, this change takes place virtually under the same conditions (Cooper & Bartlett, 1958; Brossard, 1984a, 1984b; Wood et al., 1990; Muñoz-Portero et al., 2005) thus indicating that the dissolution mechanism is changing. The end of the apparent Tafel region is associated with the formation of CuBr (Brossard, 1984b; Valero-Gómez et al., 2006). A similar pattern was seen in the work of (Pérez-Herranz et al., 2001) at a Re = 263. This behavior was attributed by (Aben & Tromans, 1995 cited in Pérez-Herranz et al., 2001) to the CuBr formation, and the stationary current observed at nobler potentials was attributed to the presence of a CuBr passive film. This behavior was also observed (Lal & Thirsk, 1953, quoted in Kear et al., 2004a; Deslouis et al., 1988a) in a solution of Cl-, however, when $[Cl^-] \geq 2$ mol/l , the development of critical current density is not observed due to a faster dissolution of the CuCl layer, which is why they take on a film-free surface.

However, Deslouis attributes this behavior to the fact that the reaction equilibrium, equation 13, changes, favoring the formation of the complex ion.

The relationship between species CuBr, Br^- and $CuBr_2^-$ helps define some significant differences in the approach given to this system's dissolution process. The equilibrium between these species is defined through the following reaction

$$CuBr + Br^- = CuBr_2^- \tag{13}$$

At 25°C equilibrium is defined according to the following equation

$$\log\left(CuBr_2^-\right) = \log\left(Br^-\right) - 2.778 \tag{14}$$

In the active state, reactions, equations 7 and 9, properly describe the behavior of the system, since both proceed on the same energy level, having the same equilibrium potential, which suggests that they are thermodynamically equivalent. This is contrary to the dissolution mechanism proposed by (Kato et al., 1980a; Brossard, 1984a, 1984b; Dhar et al., 1985; Muñoz-Portero et al., 2004; Kear et al., 2004b, 2007).

Table 5 shows the equilibrium potential for equation 8 in function of the Br^- ion activity and temperature (Appendixes A-C). Values in parentheses show the equilibrium potential for equation 10.

According to the information in Table 5, the $E_{Cu/CuBr}$, consistently moves an average of 98 mV in an active direction due to the $[Br^-]$ and 17 mV due to the effect of temperature. The analysis would seem trivial and out of context if not for the fact that this behavior and the linear relation of the potential and the logarithm of current density, E vs log i, equation 11, with a slope close to 60 mV/decade were taken as a basis for claiming that the dissolution rate of copper in a solution of Cl^- in a potential close to E_{corr}, goes on under the influence of a combined process of diffusion and activation. The first to demonstrate such behavior were (Lal & Thirst, 1953, quoted in Kear et al., 2004a, Fig. 4), in these circumstances (Crundwell, 1991) falls into contradiction.

Temperature	$E_{CuBr/Cu}$ ($mV_{Ag/AgCl}$)			
(°C)	**40%**	**50%**	**53%**	**60%**
25	-355.6	-400.1	-415.6	-453.9
	(-355.7)	*(-400.9)*	*(-415.9)*	*(-454.22)*
35	-358.8		-418.8	-457.2
45	-363.1	-408.2	-423.1	-461.4
55	-368.7		-428.4	-466.5
60	-373.1	-418	-432.7	-470.7

Table 5. Copper-X% Lithium Bromide System, Equilibrium Potentials

If the system proceeds according to equation 7, as the potential moves in a positive direction to the inflection point, the CuBr formation will increase significantly. The CuCl formation on the electrode surface is observed at η = 16 mV and the covered area increases as the potential becomes nobler (Brossard, 1984a, 1984b). On the other hand (Bjorndahl & Nobe, 1984 and Dhar et al., 1985, cited in Deslouis et al., 1988a), they take on an oxide-free surface.
In the electrochemical process, the atoms on the surface react with the Br^- ion of the solution by generating a charge unit and the CuBr compound, which is poorly soluble, $k_{ps} = 6.27 \times 10^{-9}$, (Weast, 1984), which is why it precipitates and adheres to the electrode surface. In a second step, through a chemical process, the substance continues to react with the Br^- ion in the solution, dissolving at a constant rate, equation 13, even after polarization is interrupted (Crundwell, 1991). The dissolution rate of the precipitate is constant until dissolution is complete (Brossard & Raynaud, 1985), finally producing the complex species, which is soluble and diffuses into the bulk of the solution. (Lal & Thirsk, 1953 cited in Kear et al., 2004a) found that the formation of $CuCl_2^-$ is consistent with increases in the potential for a given $[Cl^-]$.
The anodic behavior of the system can be described in a fairly acceptable way with the combination of equations 7 and 13. Thus, the dissolution mechanism takes place due to a simultaneous process in two stages. The mathematical model that best describes the dissolution of this metal corresponds to this mechanism (Deslouis et al., 1988a). A common mechanism may explain the process in acidic and neutral environments (Deslouis et al., 1993), however, this assertion is not possible due to thermodynamic matters.
Typically, the corrosion potential of the cell was established in the stability region of water. In a nobler region compared to the hydrogen electrode, but well below the oxygen electrode potential, which ultimately controls the cathodic portion of the system. Under flow conditions, this behavior can be seen more clearly as shown in (Pérez-Herranz et al., 2001, Fig. 2). By increasing the flow rate, the current value in the cathodic fraction increases significantly; however, the response of the anodic branch is more discreet to these changes.
A similar behavior suggests that the partial anodic fraction is more affected than the cathodic fraction by mass transfer (Deslouis et al., 1988a). According to Pérez-Herranz, the limit current observed in the cathodic fraction is attributed to hydrogen evolution. During the dissolution process, protons (H^+) diffuse to the metal surface, so if the dissolution rate is controlled by this current, the diffusion of protons could be seen as the step that determines the metal's rate of dissolution. The displacement of E_{corr} in a noble direction as velocity increases could be attributed to the control of the cathodic reaction due to the detachment of clusters of hydrogen molecules from the metal surface, which improves as velocity increases

(Brown et al., 1992, cited in Pérez-Herranz et al., 2001; Montañés et al., 2006). According to (Muñoz-Portero et al., 2005), pH causes the current to increase and the potential to shift to a nobler zone, restricting the passive zone. The electro-dissolution of copper is essentially independent from pH (Brossard, 1984a).

3.1 90% Copper-10% Nickel-X% Lithium Bromide System

As an average, in the range 40% ≤ [Br-] ≤ 60% and 25°C ≤ T ≤ 60°C, the alloy E_{corr} moves, compared to the copper E_{corr}, 57 mV in a negative direction. This is due only the presence of nickel and is crucial to establish a significant difference in the behavior of both materials. (Kato et al., 1980a) report that the alloy E_{corr} is 10 mV nobler.

The nickel in the LiBr solution, under the conditions of this investigation, dissolves according to the Ni-H_2O-Br system (Muñoz-Portero et al., 2007) as follows:

$$NiH_{0.5} + 2\,Br^- \rightarrow NiBr_{2(s)} + 0.5\,H^+ + 2.5\,e^- \tag{15}$$

With an equilibrium potential at 25°C according to the following equation

$$E = -0.04543 + 0.02365 \log\left[\frac{1}{(Br^-)^2}\right] - 0.011827\ pH \tag{16}$$

Generally, under the conditions in which the alloy E_{corr} is established, copper is found in a condition of immunity (Tables 1 and 5).

For example, in the 40% LiBr solution at 25°C, the alloy E_{corr} -393.22 $mV_{Ag/AgCl}$ is found 37.62 mV in a more active region compared to the copper equilibrium potential $E_{CuBr/Cu}$, -355.6 $mV_{Ag/AgCl,}$ and is polarized compared to the nickel equilibrium potential $E_{NiH_{0.5}/NiBr_{2(S)}}$, with an η_a of 78.2 mV, (Martínez-Meza E, 2011).

(Brossard, 1984a) observed a surface free of corrosion products at more active potentials than $E_{Cu/CuCl}$.

Under these conditions, in the E_{corr} vicinity, the anodic fraction of the system is due to nickel dissolution, according to the above reaction, equation 15. This could be the reason why (Lee & Nobe, 1984) observed a selective nickel electro-dissolution.

The composition of the reaction products depends heavily on the potential. At more active potentials nickel dissolution is favored; therefore the reaction products contain higher nickel concentrations than the alloy (Milosev & Metikos, 1997). (Cahan & Haynes, 1969, cited in Lee & Nobe, 1984) conclude that the overall reaction is controlled by nickel dissolution. However, as explained below this behavior is not possible in the alloy, otherwise it wouldn´t passivate. (Kato & Pickering, 1984) claim that the selective dissolution of copper doesn't take place when significant concentrations of nickel are found in the layers of corrosion products. (Dhar et al., 1985) state that the role of nickel in the corrosion process is not evident. In this sense (Crundwell, 1991) obtained contradictory results.

When the system is anodically polarized due to the kinetics of copper in the 53% solution and to a temperature of 25°C with the presence of oxygen, for example, $i_o = 7.3 \times 10^{-6}$ A cm^{-2}, this metal dissolves more rapidly than nickel, $i_o = 0.523 \times 10^{-6}$ A cm^{-2}. Thus, this element has a main role in the dissolution of the alloy (Martinez-Meza E, 2011). As the potential increases, the selective electro-dissolution of nickel gradually decreases and the electro-dissolution of copper increases (Lee & Nobe, 1984). For this reason the polarization diagrams of both copper and the 90/10 alloy are similar. The polarization and E_{corr}

characteristics of the 90/10 alloy show a marked similarity to those of copper (Crundwell, 1991; Kear et al., 2004b). (Kear 2001 cited in Kear et al., 2004b) found in dynamic conditions 200 < rpm < 9.500 that the morphology of the anodic fraction of the alloy was similar to that determined independently for copper. On the other hand (Milosev & Metikos, 1997) support the similarity of the two systems using cyclic voltammetry. However, an E_{corr} in more active areas and a smaller i_{corr} in the 90/10 alloy show significant differences between these materials. When the CuNi-90/10 polarization exceeds copper $E_{Cu/CuBr}$, the alloy corrodes due to the dissolution of both elements according to equation 7, 13 and 15. The alloy in the 53% solution at 35 and 55°C (Figure 1 (b)) shows an active-passive behavior. This behavior is observed in the work of (Kato et al., 1980a; Lee & Nobe, 1984) and (Walton & Brook, 1977 cited in Lee & Nobe, 1984), unfortunately, this behavior was not understood.

According to Lee, the dissolution of the CuCl film is the dominant process in this region, and is under mass transfer control, the diffusion of the complex ion to the bulk of the solution.

This behavior according to the Pourbaix diagrams for the Cu-H_2O-Br and Ni-H_2O-Br systems, (Muñoz-Portero et al., 2004, 2007) is not explained by the presence of an oxidized compound which could passivate the electrode. This behavior is due to a very aggressive copper dissolution, causing the electrode surface to be enriched in nickel.

By increasing the concentration of nickel, the 90/10 ratio is modified in such a way that the alloy passivates due to the characteristics of nickel. Under these conditions, it is likely that a Cu/Ni relation between 1.9 and 2.2 will be established. When the relation is established on the upper level the probable concentration of nickel on the electrode surface is 31.25% by weight. There is a critical composition of nickel in the alloy (Mansfeld & Uhlig, 1970) over which the polarization curves exhibit a passive current density similar to that shown by nickel, and under which passive current density disappears, causing the alloy to behave like copper.

According to the theory of electronic configuration, metals with orbital vacancies in "d", also known as transition metals are known to favor the chemisorption of oxygen. Therefore, passivity in the alloy is only observed when the vacancies in these orbitals are present. When such vacancies have been occupied by electrons of the alloy components, the necessary chemisorption of oxygen required to cause passivation does not occur.

This behavior is typical of an adsorption process as the one observed in stainless steel. For this reason it is not uncommon to assume that under these circumstances, a passivation process occurs, similar to that observed in these materials.

The standard Flade potential E_F^0 for nickel is 0.2 V_{SHE} (Uhlig & Revie, 1985); therefore, the Flade potential, passivation potential, for the alloy in the 53% LiBr solution is given in correspondence to the equation.

$$E_F = 0.2 - 0.059\,pH;\ V_{(SHE)} \tag{17}$$

Under these conditions the system presents a passivation potential of -301.85 $mV_{Ag/AgCl}$. In the charts this potential is observed at -298 and -307.1 $mV_{Ag/AgCl}$ for the system at 35 and 55°C, (Figure 1(b)).

For this reason, it can be said that under these conditions the alloy passivates due to an oxygen chemisorption process, and not because of the formation of a CuBr film, which is why the complex species does not spread in this region. However, due to the instability of the film and the Br^- ion concentration, the film dissolves quickly.

The 90% Cu-10% Ni-50% LiBr system during the first period, 0.3 h, invariably reaching the E_{corr}, Table 1, in nobler conditions respect to $E_{Cu/CuBr}$, Table 5. In the impedance spectrum at 25°C, a resistance of 3.01 kΩ·cm² is developed. As the exposure time goes by, the value of this parameter increases, reaching its maximum value after two hours, at 25 and 60°C. The cell at 45°C, in the last two periods, develops a similar value close to 12 kΩ·cm².

The cell reaches the E_{corr} in nobler conditions due to increased oxygen presence in the solution. In these circumstances a segment of the cathodic fraction, close to E_{corr} develops a Tafelian behavior (Figure 7) before reaching a limit current status, and for this reason, the diffusion phenomenon shows less presence.

At 60°C the contribution of this factor is 5.2 kΩ·cm². As time of exposure goes by, E_{corr} is reached at more reducing conditions. Apparently this behavior is generated by the system itself, either because of a lower oxygen concentration in the interface due to the same process of dissolution, or by an enrichment of nickel on the electrode surface due to copper dissolution.

Under these conditions, oxygen diffusion turns relevant, becoming the step that controls the dissolution rate. At 25°C, the i_L goes from 13.58 μA/cm² in the first period to 1.9 μA/cm² after 4 hours. At 60°C, i_L goes from 5.74 μA/cm² at 0.3 h to 2.6 μA/cm² in the last period (Figure 7(a)). After two hours of exposure, the system at 60°C develops the highest mass transport resistance, 62.9 kΩ·cm², Table 1.

The film causes a substantial decrease in the oxygen reduction rate. This reaction near E_{corr} potentials is more affected by corrosion products than the anodic reaction. In the Tafel region, the formation of the layer significantly affects the cathodic fraction, only mildly affecting the anodic fraction, which indicates a cathodically controlled corrosive process (Hack & Pickering, 1991). Thus, oxygen reduction can be regarded as the most important reaction to determinate the general corrosion rate in the presence of a protective film (Kato et al., 1980b).

(Kear et al., 2004a) present a list of equations developed by different researchers, which describe copper dissolution in a chloride solution in the apparent Tafel región. Almost all of them regard the process as reversible and dependent on a combined charge transfer and mass transport process. The diffusion of $CuCl_2^-$ complex ion from the electrode surface to the bulk of the solution, takes control in mass transport.

As mentioned before, during the first period of exposure 0.3 h, the cell E_{corr} invariably moves towards a noble direction respect to $E_{Cu/CuBr}$, reflecting an anodic polarization at 25°C of 27.58 mV. This behavior indicates that the system is not in equilibrium. (Deslouis et al., 1988b, 1993) consider the electro-dissolution to be in pseudo-equilibrium, in such a way that can not be considered reversible. The establishment of a reversible state applies for a half-cell reaction, but is not appropriate to describe a corrosive system.

In dynamic conditions, especially at 45°C, the effect of velocity on the system is clearly shown, because as it increases the E_{corr} moves towards a noble direction and the i_L is increased (Figure 7(b)). This effect of velocity is typical of a diffusion-controlled cathodic process (Fontana & Greene, 1978).

(Kear et al., 2004a) mention that in the three copper dissolution mechanisms in a chloride solution proposed to date, it is generally assumed that the anodic reactions are reversible, and it is universally accepted that they are all under a mixed kinetic control near the corrosion potential.

According to Figure 5, in static conditions a few seconds are needed to appreciate the formation of corrosion products on metal surface. 40 seconds of oxidation are sufficient to form a layer of corrosion products that fully cover the electrode (Brossard & Raynaud, 1985).

In this regard, the system's response depends on the operating conditions thereof, as the diffusive barrier morphology varies according to temperature as shown the images (Figure 8) (Brossard & Raynaud, 1985).

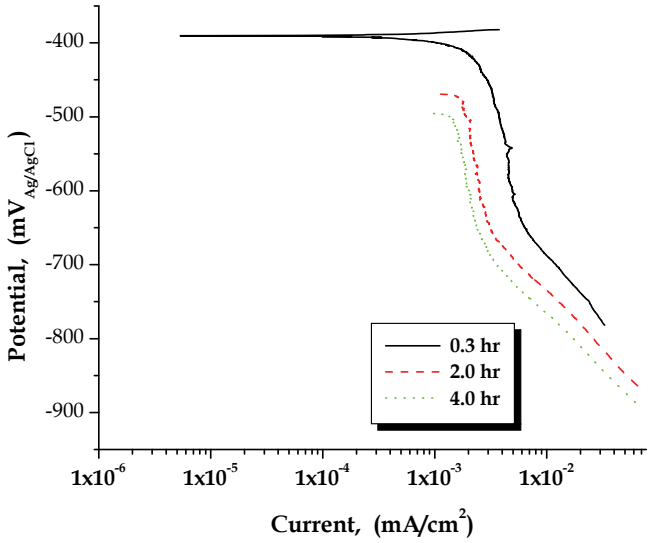

(a)

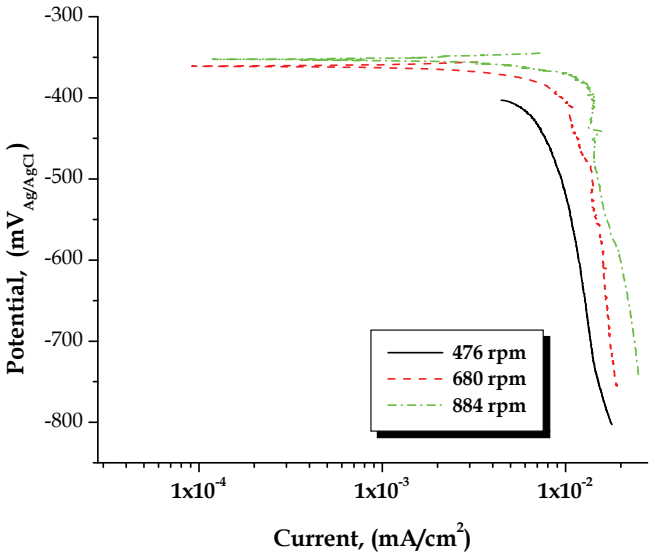

(b)

Fig. 7. Cathodic polarization of the 90 % Cu-10% Ni-50% LiBr system, (a) in static conditions at 60°C (b) in dynamic conditions at 45°C

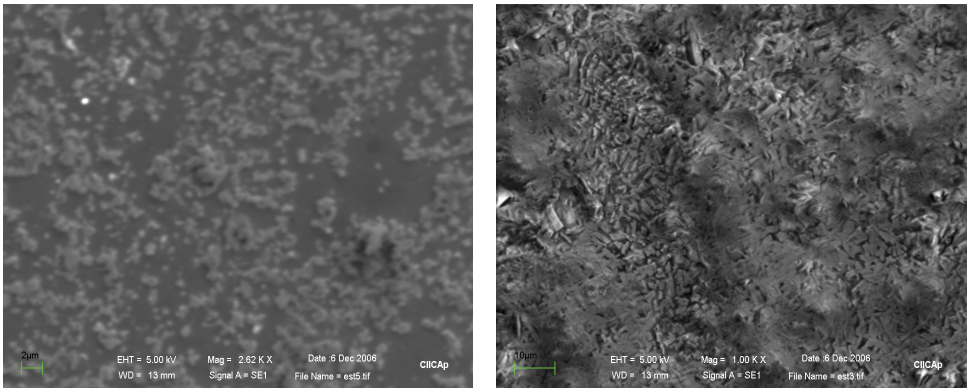

(a) (b)

Fig. 8. Images taken with scanning electronic microscope, showing the electrode surface after the tests made in static conditions in the absence of oxygen (a) 25°C and (b) 60°C

The morphology of the film formed at 25°C is characteristic of a uniform corrosion process, noting in the first period of exposure an important amount of particles adhered to the electrode surface. The film formed at 60°C (Figure 8(b)) shows a rather compact morphology, very different from the response of the system at 25°C.

This difference can be seen in the response of the system, Tables 1 and 4. Despite the morphological differences in the diffusive barriers, the film shows good protective capacity. (Muñoz-Portero et al., 2006) indicate that the morphology of the corrosion products depend on the Br^- concentration in the solution. According to their results, the diffusive barrier developed in the conditions of this project should show an amorphous and gelatinous morphology associated with a mixture of CuBr y $CuBr_2 \cdot 3Cu(OH)_2$.

The records of current and potential noise, show other system characteristics. At 25°C, during the first period, a greater presence of an oxidizing agent in the interface causes an increase in copper dissolution which accelerates the production of CuBr. This substance accumulates on the electrode surface promoting the formation of a protective coating that inhibits the activity at the interface, due to its permeable nature, a pitting corrosion process takes place (Figure 5).

Under flow conditions at 45°C, as the solution velocity increases, the mass transport by diffusion contributes less to the dissolution process, Table 1. At higher velocities, the E_{corr} develops at nobler conditions due to increased oxygen presence in the interface. The system behavior under these conditions clearly reflects the importance of oxygen and the diffusion phenomenon of this element in the dissolution process of the alloy.

Given the conditions that occur at higher levels of velocity, greater involvement of an activation process of the cathodic fraction would be expected. A Tafelian behavior does not occur in these conditions. On the other hand, the behavior at higher levels is very similar giving the impression of having reached the same level at the stationary state.

According to the records of the noise signal in current and potential (Figure 6), at 680 and 884 rpm the potential noise signal reaches the stationary state almost from the start of the test, showing no trend in both levels. Despite the difference in potential, ≈ 12 mV, the current noise signal at both levels is practically the same. This suggests that under these conditions the system is in a passive state. As mentioned above, the increase in the electrode

velocity suggests a greater dissolution of copper, leading to greater nickel presence on the electrode surface.
The system E_{corr}, Table 1, under these conditions is very close to the Flade potential, equation 17, with a difference of 37.4 mV at 680 rpm and only 25.6 mV at 884 rpm, which is why it is not unreasonable to suppose that under these conditions a passive process by chemisorption is developed.

4. Appendices

4.1 Appendix A

Calculation of Gibbs free energy
Calculation of heat capacity C_p^o (Heng & Johnston, 1952; Dean, 1989) in function of absolute temperature for pure substances CuBr.

$$C_p^o = 49.898 + 0.0169\ T - 1.769 \times 10^{-6}\ T^{-2} \tag{A1}$$

The method for determination the heat capacity C_p^o of ionic species, Br^- is that proposed by (Criss & Cobble, 1964; Taylor, 1978) for T< 200ºC, values of absolute entropy and the value of the parameters: a = -0.37 and b = 0.0055 (Roberge, 2000).

$$C_p^o = \left[\left(4.186\ a + b\ S_{(298\ K)}^o\right)\left(T_2 - 298.16\right)\right] \Big/ \ln\left(T_2/298.16\right) \tag{A2}$$

Calculation of Gibbs free energy in the temperature range

$$G_{(T)}^o = G_{(298\ K)}^o + \left(C_p^o - S_{(298\ K)}^o\right)\left(T_2 - 298.16\right) - C_p^o\ T_2 \ln\left(\frac{T_2}{298.16}\right) \tag{A3}$$

Calculation of equilibrium potential E^o for the reaction of copper dissolution

$$Cu + Br^- \Leftrightarrow CuBr + 1\ e^- \tag{A4}$$

$$E_{(T)}^o = \frac{-\Delta G^o}{n\ F}\ ;\ \left(V_{(SHE)}\right) \tag{A5}$$

Calculation of the potential of equation A4

$$E_{(T)} = E_{(T)}^o + 0.0591 \log\left(\frac{1}{Br^-}\right) \tag{A6}$$

Where Br^- is the activity of bromide ion

4.2 Appendix B

Physicochemical properties of the LiBr-H_2O pair (Torres Merino, 1997)
Calculation of the LiBr solution density based on the density of water, d `Alefeld equation

$$\rho_{(X_{sol},T_{sol})} = \frac{\rho_{H_2O(T_{sol})}}{2}\left[\exp\left(0.012 X_{sol}\right) + \exp\left(\left(0.842 + 1.6414 \times 10^{-3}\ T_{sol}\right)\left(\frac{X_{sol}}{100}\right)^2\right)\right] \tag{B1}$$

Where:

$\rho_{H_2O}(T_{sol})$, water density at the solution temperature, kg m^{-3}; $\rho_{(X_{sol},\,T_{sol})}$, solution density, kg m^{-3}; X_{sol}, (mass% LiBr)
Domain range: $40\% \le X_{sol} \le 75\%$; $0^oC \le T_{sol} \le 190\ ^oC$
Calculation of dynamic viscosity μ d'Alefeld equation

$$\mu = \exp\left[A_1 + \frac{A_2}{T_{sol}} + A_3 \cdot \ln T_{sol}\right] \tag{B2}$$

Where:
$A_1 = -494.122 + 16.3967\ X_{sol} - 0.14511\ (X_{sol})^2$; $A_2 = 28606.4 - 934.568\ X_{sol} + 8.52755\ (X_{sol})^2$; $A_3 = 70.3848 - 2.35014\ X_{sol} + 0.0207809\ (X_{sol})^2$; μ = dynamic viscosity, cp; T_{sol} = Temperature solution, K; X_{sol} = mass %, LiBr
Domain: $45\% \le X_{sol} \le 65\%$; $30^oC \le T_{sol} \le 210^oC$

4.3 Appendix C

Calculation of the activity of LiBr-H_2O solution.
The model for calculating the activity of strong electrolytes in aqueous solution is proposed by (Meissner et al., 1972; Meissner & Tester, 1972). The calculation of the activity coefficient for a strong electrolyte solution at 25°C is as follows

$$\Gamma^o = \left[1 + B\,(1 + 0.1\,I)^q - B\right]\Gamma^* \tag{C1}$$

With:

$$B = 0.75 - 0.065\,q \tag{C2}$$

$$\log \Gamma^* = \left(-5107\sqrt{I}\right)\Big/\left(1 + C\sqrt{I}\right) \tag{C3}$$

$$C = 1 + 0.055\,q \exp\left(-0.023\,I^3\right) \tag{C4}$$

where Γ^o is the reduced activity coefficient of the pure solution at 25°C, q is the Meissner parameter (q = 7.27 for LiBr) I is the ionic strength of electrolyte

$$I = \frac{\sum m_i\,Z_i^2}{2} = m_{LiBr} \tag{C5}$$

Z is the number of charges on the cation or anion (Z = 1 for LiBr)
The average ionic activity coefficient for LiBr-H_2O solution

$$\gamma_{\pm} = \left(\Gamma^o\right)^{Z_+\,Z_-} = \Gamma^o \tag{C6}$$

Finally, the activity of the LiBr solution is given by the expression

$$a_{(LiBr)} = \frac{m_{LiBr}}{m^o}\,\gamma_{\pm} \tag{C7}$$

Where m^o is the standard solution molality (1 mol LiBr/kg H_2O)

The calculation of the Kusik-Meissner parameter (Kusik & Meissner, 1978) for temperature t in ^{o}C is given by the following equation

$$q_t = \left(a\, q_{(25)} + b^*\right)(t - 25) + q_{(25)} \quad \text{(C8)}$$

Where:
$a = -0.005$ and $b^* = 0.0085$

5. Conclusions

Both the 90% Cu-10% Ni alloy and copper are dissolved, in the Tafel region, by a mechanism consisting of two steps that occur simultaneously. However, the kinetics of copper dissolution results in significant changes in the dissolution process of the alloy.
Corrosion potential in more active regions and smaller corrosion rates due to the presence of nickel in the alloy, generate significant differences between these metals.
Due to the fact that the 90% Cu-10% Ni-X% LiBr system always polarized in comparison to the nickel equilibrium potential, and only sometimes compared to the copper equilibrium potential, the anodic reaction can not be considered reversible, and according to the dissolution mechanism, is under activation control.
According to the proposed equivalent circuit, the dissolution process of the alloy is in fact under a mixed kinetic control, by activation and diffusion. However, the mass transport resistance under all experimental conditions is higher than that observed for charge transfer. On the other hand, as both elements are part of a series, the one representing the mass transport process is the one that shows a greater resistance to current flow. Thus, the diffusion phenomenon must be the process that controls the dissolution of the alloy.
For the dissolution process to be maintained, the reacting species must match at the interface in an electrochemical process. In this sense the complex ion is generated at the interface of the film (equation 13) and spreads to the bulk of the solution. Therefore, oxygen is responsible for the diffusion phenomenon, and does not always follow the Levich relationship.

6. Acknowledgment

The authors acknowledge Consejo Nacional de Ciencia y Tecnología (CONACyT) for financial assistance for the realization of this work. Berenice Adame for her assistance in the translation of this document.

7. References

Bard A. J. & Faulkner L. R. (1980). *Electrochemical Methods Fundamentals and Applications*, ISBN 0-471-04372-9 John Wiley & Sons, Inc., Published in the United States of America simultaneously in Canada

Barsoukov E. & Macdonald J. Ross. (2005). *Impedance Spectroscopy Theory, Experiment, and Applicatons*, second edition. Wiley-Interscience. A John Wiley & Sons, Inc., Publication. 0-471-64749-7, Hoboken, New Jersey. Published simultaneously in Canada.

Beccaria A. M. & Crousier J. (1989). Dealloying of Cu-Ni alloys in natural sea water. *Br. Corros. J.*, Vol. 24, No. 1, (march 1988), pp. 49-52

Bockris J. O`M, Reddy A. K. N. & Gamboa-Aldeco M. (2000). *Modern Electrochemistry Fundamentals of Electrodics*, *Vol. 2A (second edition),* Kluwer Academic/Plenum

Publishers, New York, 0-306-46166-8 (Hardbound), 0-306-46167-6 (paperbound), Printed in the United States of America

Brossard L. (1984). Potentiodynamic Investigation of Copper in LiCl Solutions. *Corrosion,* Vol. 40, No. 8, (august 1984), pp. 420-425

Brossard L. (1984). Potentiodynamic Investigation of Copper in the Presence of Bromide Ions. *J. Electrochem. Soc.*, Vol. 131, No. 8, (1984), pp. 1847-1849

Brossard R. L. & Raynaud G. M. (1985). Influence of Temperature on copper bromide formation and dissolution. *Can. J. Chem*., Vol. 63, (april 1984), pp. 720-724

Cooper R. S. & Bartlett J. H. (1958). Convection and Film Instability, Copper anodes in Hydrochloric Acid. *Journal of the Electrochemical Society*, Vol. 105, No. 5, (march 1958), pp. 109-116

Copper-Nickel Alloys in Marine Environments, available from, http:/www.copper.org/applications/cuni/visual_overview/full-text.htm

Criss C. M. & Cobble J. W. (1964). The Thermodynamic Properties of High Temperature Aqueous Solutions. IV. Entropies of the ions up to 200^{o}C and the Correspondence Principle. *J. Am. Chem Soc.,* Vol. 86, (december 1964), pp. 5385-5401

Crundwell F. K. (1991). The Anodic Dissolution of 90% Copper-10% Nickel alloy in Hydrochloric Acid Solution. *Electrochimica Acta*, Vol. 36, No. 14, (february 1991), pp. 2135-2141

Dean John A. (1989). Manual de Química Lange, Decimotercera Edición McGraw-Hill, 13^{a} edición, 968-422-087-1 (obra completa) Tomo IV, paginas, 9-20, 9-106, 9-107, 9-118 Impreso en México

Deslouis C., Tribollet B., Mengoli G. & Musiani M. M. (1988). Electrochemical behaviour of copper in neutral aereated chloride solution. I Steady-State investigation. *Journal of Applied Electrochemistry*, Vol. 18, (october 1987), pp. 374-383

Deslouis C., Tribollet B., Mengoli G. & Musiani M. M. (1988). Electrochemical behaviour of copper in neutral aereated chloride solution. II Impedance investigation. *Journal of Applied Electrochemistry*, Vol. 18, (october 1987), pp. 384-393

Deslouis C., Mattos O. R., Musiani M. M. & Tribollet B. (1993). Comments on Mechanism of copper electrodissolution in chloride media. *Electrochimica Acta*, Vol. 38, No. 18, (july 1993), pp. 2781-2783

Dhar H. P., White R. E., Darby R., Cornwell L. R., Griffin R. B. & Burnell G. (1985). Corrosion Behavior of 70Cu-30Ni Alloy in 0.5 NaCl and in Synthetic Seawater. *Corrosion*, Vol. 41, pp. 193-196

Flitt H. J. & Schweinsberg D. P. (2005). A Guide to Polarisation curve interpretation: deconstruction of experimental curves typical of the $Fe/H_2O/H^+/O_2$ corrosion system. *Corros. Sci*., 47, (february 2005), pp. 2125-2156

Fontana M. G. & Greene N. D. (1978). *Corrosion Engineering (second edition)* McGraw-Hill Book Company, 0-07-021461-1, Printed in the United States of America

Hack H. P. & Pickering H. W. (1991). AC Impedance Study of Cu and Cu-Ni Alloys in Aerated Salt Water. I. Pd Coating and Corrosion Product Stripping. *J. Electrochem*. Soc., Vol. 138, No. 3, (March 1991), pp. 690 – 695

Hassibi A., Navid R., Dutton R. W. & Lee T. H. (2004). Comprehensive study of noise processes in electrode electrolyte interfaces. *Journal of Applied Physics,* Vol. 96, No. 2, (April 2004), pp. 1074 – 1082

Heng J. & Johnston H. L. (1952). Low Temperature Heat Capacity of Inorganic Solids XII. Heat Capacity and Thermodynamic Properties of Cuprous Bromide from 16 to 300 K. *The Journal of the American Chemical Society*, Vol. 74, (october 1952), pp. 4771-472

Itzhak D. & Greenberg T. (1999). Galvanic Corrosion of a Copper Alloy in Lithium Bromide Heavy Brine Environments. *Corrosion*, Vol. 55, No. 8, (august 1999), pp. 795-799

Kato C., Ateya B. G., Castle J. E. & Pickering H. W. (1980). On the Mechanism of Corrosion of Cu-9.4Ni-1.7Fe Alloy in air Saturated Aqueous NaCl Solution. I Kinetic Investigations. *J. Electrochem. Soc.*, Vol. 127, No. 9, (september 1980), pp. 1890-1896

Kato C., Castle J. E., Ateya B. G. & Pickering H. W. (1980). On the Mechanism of Corrosion of Cu-9.4Ni-1.7Fe Alloy in air Saturated Aqueous NaCl Solution. II Composition of the Protective Surface Layer. *J. Electrochem. Soc.*, Vol. 127, No. 9, (september 1980), pp. 1897-1903

Kato C. & Pickering H. W. (1984). A Rotating Disk Study of the Corrosion Behavior of Cu-9.4Ni-1.7Fe Alloy in Air-Saturated Aqueous NaCl Solution, *J. Electrochem. Soc.*, Vol. 131, No. 6, (june 1984), pp. 1219-1224

Kear G., Barker B. D. & Walsh F. C. (2004). Electrochemical corrosion of unalloyed copper in chloride media – a critical review. *Corrosion Science*, Vol. 46, (december 2002), pp. 109-135

Kear G., Barker B. D., Stokes K. & Walsh F. C. (2004). Electrochemical corrosion behaviour of 90-10Cu-Ni alloy in chloride media – based electrolytes. *Journal of Applied Electrochemistry*, Vol. 34, No. 55, (january 2004), pp. 659-669

Kear G., Barker B. D., Stokes K. R. & Walsh F. C. (2007). Electrochemistry of non-aged 90-10 copper-nickel alloy (UNS C70610) as a function of fluid flow Part 1: Cathodic and anodic characteristics. *Electrochimica Acta*, Vol. 52, (july 2006), pp. 1889-1898

Kusik C. L. & Meissner H. P. (1978). Electrolyte Activity Coefficients in Inorganic Processing. Fundamentals Aspects of Hydrometallurgical Processes, *AIChE* Symposium Series, Vol. 74, No.173, (1978), pp. 14-20

Kutz M. (2002). *Handbook of Materials Selection*, John Wiley & Sons, Inc., New York United States of America

Lee H. P. & Nobe K. (1984). Rotating Ring-Electrode Studies of Cu-Ni Alloy Electrodissolution in Acidic Chloride Solution, A Commercial Cu-Ni (90/10) Alloy. *J. Electrochem. Soc.*, Vol. 131, No. 6, (june 1984), pp. 1236-1243

Mansfeld F. & Uhlig H. H. (1970). Effect of Electron Donor and Acceptor Elements an Passivity of Copper-Nickel Alloys. *J. Electrochem. Soc.*, Vol. 117, No. 4, (april 1970), pp. 427-432

Mansfeld F. (1973). Simultaneous Determination of Instantaneous Corrosion Rates and Tafel Slopes from Polarization Resistance Measurements. *J. Electrochemical Soc.*: ELECTROCHEMICAL SCIENCE AND TECHNOLOGY. Vol. 120, (april 1973), pp. 515-518

Mansfeld F. (1973). Tafel Slopes and Corrosion Rates from Polarization Resistance Measurements, *Corrosion*, Vol. 29, No. 10, (october 1973), pp. 397-402

Martínez-Meza E. (2011). Corrosión e Inhibición Sobre Acero, Cobre y Aleaciones en Solución Refrigerante de Bromuro de Litio, Empleada en Bombas de Calor. *Ph. D Tesis*. Universidad Nacional Autónoma de México, México D.F.

Meissner H. P. & Tester J. W. (1972). Activity Coefficients of Strong Electrolytes in Aqueous Solutions. *Ind. Eng. Chem. Process Des. Develop.*, Vol. 11, No. 1, pp. 128-133

Meissner H. P., Kusik C. L. & Tester J. W. (1972). Activity Coefficients of Strong Electrolytes in Aqueous Solutions-Effect of Temperature. *AIChE Journal*, Vol. 18, No. 3, (may 1972), pp. 661-662

Milosev I. & Metikos H. M. (1997). The behaviour of Cu-$_x$Ni (x = 10 to 40 %) alloys in alkaline solutions containing chloride ions. *Electrochimica Acta*, Vol. 42, No. 10, (september 1996), pp. 1537-1548

Montañés M. T., Pérez-Herranz V., García-Antón J. & Guiñon J. L. (2006). Evolution with Exposure Time of Copper Corrosion in a Concentrated Lithium Bromide Solution Characterization of Corrosion Products by Energy-Dispersive X-Ray Analysis and X-Ray Diffraction. *Corrosion*, Vol. 62, No. 1, (january 2006), pp. 64-73

Muñoz-Portero M. J., García-Antón J., Guiñon J. L. & Pérez-Herranz V. (2006). Corrosion of Copper in Aqueous Lithium Bromide Concentrated Solutions by Immersion Testing. *Corrosion,* Vol. 62, No. 11, (november 2006), pp. 1018-1027

Muñoz-Portero M. J., García-Antón J., Guiñon J. L. & Pérez-Herranz V. (2005). Anodic Polarization Behavior of Copper in Concentrated Aqueous Lithium Bromide Solutions and Comparison with Pourbaix Diagrams. *Corrosion*, Vol. 61, No. 5, (may 2005), pp. 464-472

Muñoz-Portero M. J., García-Antón J., Guiñòn J. L. & Pérez-Herranz V. (2007). Pourbaix Diagrams for Níckel in Concentrated Aqueous Lithium Bromide Solutions at 25 ^{o}C. *Corrosion*, Vol. 63, No. 7, (july 2007), pp. 625-634

Muñoz-Portero M. J., García-Antón J., Guiñòn J. L. & Pérez-Herranz V. (2004). Pourbaix Diagrams for Copper in Aqueous Lithium Bromide Concentrated Solutions. *Corrosion*, Vol. 60, No. 8, (august 2004), pp. 749-756

Othmer K. (2004). *Encyclopedia of Chemical Technology 5th edition*, John Wiley & Sons, Inc., New York, NY United States of America, pp. 679

Pérez-Herranz V., Montañés M. T., García-Antón J. & Guiñon J. L. (2001). Effect of Fluid Velocity and Exposure Time on Copper Corrosion in a Concentrated Lithium Bromide Solution. *Corrosion*, Vol. 57, No. 10, (october 2001), pp. 835-842

Roberge P. R. (2000). *Handbook of Corrosion Engineering*. McGraw Hill. 0-07-076516-2 Appendix D, Electrochemistry Basics, pp. 1011-1059. United States of America.

Stern M. & Geary A. L. (1957). Electrochemical Polarization. I. A Theoretical Analysis of the Shape of Polarization Curves, *J. Electrochem. Soc.,* Vol. 104, No. 1, (january 1957), pp. 56-63

Tan Y. J., Bayley S. & Kinsella B. (1996). The Monitoring of the Formation and Destruction of Corrosion Inhibitor Films Using Electrochemical Noise Analysis (ENA). *Corrosion Science*, Vol. 38, No. 10, (Fefruary 1996), pp. 1681 – 1695

Taylor D. F. (1978). Thermodynamic Properties of Metal-Water Systems at Elevated Temperatures. *J. Electrochem. Soc.*, Solid State Science and Technology, Vol. 125, No. 5, (may 1978), pp. 808-812

Torres Merino J. (1997). Ècole Nationale Superieure des Industries Chimiques Laboratoire des Sciences du Genie Chimique, Thèse. Prèsentee a. L'Institut Nacional Polytechnique de Lorraine pour l'obtention du Titre de Docteur de I'Inpl Spècialite Genie des Procedes par Jesús Torres Merino. Ingenier en Genie Chimique UNAM. Sujet: "Contacteurs Gaz-Liquide pour Pompes a Chaleur a Absortion Multi-Ètages", Fèvrier 1997

Uhlig H. H. & Revie R. W. (1985). *Corrosion and Corrosion Control, An Introduction to Corrosion Science and Engineering, Third Edition*. John Wily & Sons. A Wiley Interscience Publication, 0-471-07818-2, United States of America, Published simultaneously in Canada.

Valero-Gómez A., Igual-Muñoz A. & García-Antón J. (2006). Corrosion and Galvanic Behavior of Copper and Copper-Brazed Joints in Heavy Brine Lithium Bromide Solutions. *Corrosion*, Vol. 62, No. 12, (december 2006), pp. 1117-1131

Weast R. C. (1984). *Handbook of Chemistry and Physics* (65th ed). CRC Press, Inc. 0-8493-0465-2. Boca Raton FL. United States of America

Wood R. J. K., Hutton S. P. & Schiffrin D. J. (1990). Mass Transfer Effects of Non-Cavitating Seawater on the Corrosion of Cu and 70Cu-30Ni. *Corrosion Science*, Vol. 30, No. 12, (december 1989), pp. 1177-1201

23

Interfacial Mass Transfer and Morphological Instability of Oxide Crystal Growth

Xiuhong Pan, Weiqing Jin and Yan Liu
State Key Laboratory of High Performance Ceramics and Superfine Microstructure, Shanghai Institute of Ceramics, Chinese Academy of Sciences, Shanghai 200050, China

1. Introduction

Mass transfer near the solid-liquid interface is a fundamental problem in crystal growth and it is also a prerequisite for producing high-quality homogeneous crystals. It is desired that the mass transport phenomenon in the liquid phase can be visualized simultaneously with the growing interface. Such information is very helpful for the understanding of crystal growth mechanism. But little is known about the direct connection between mass transport and interfacial morphology in oxide crystal growth, mainly because it is technically difficult to visualize interface growth with mass flow in the high-temperature environment.

In the present chapter of the book, we take high-temperature melt (or solution) growth of oxide crystal as an example, to study the interfacial mass transport and its effect on the interfacial morphology. Most of the results are based on the experiments performed in a high-temperature in situ observation system developed by the authors (W. Q. Jin, et al., 1993), which will be firstly introduced in the following. This system is designed specially for visualizing and recording the mass transport as well as the growth process under the condition of high temperature. After that we will show the typical buoyancy and Marangoni convections in-situ observed in high temperature oxide melt in a loop-like heater. The effect of convection on the thickness of interfacial boundary layer will also be demonstrated. Then, we will discuss the diffusion-induced microconvection near the solid-liquid interface and the mass transport in the boundary layer.

The next section is devoted to deriving the correlation between the mass transfer and the interfacial morphology. After that, we shall see how external forces, such as magnetic field and mechanical vibration, stabilize the unsteady convection. Coupled with the help of external forces, effect of mass transfer near solid-liquid interface is optimized and then bulk oxide crystals with high quality are obtained by vertical zone-melting technique or vertical Bridgman growth technique. Finally, we will give a short summary and express our acknowledgments.

2. High-temperature in situ observation system

Crystal growth is a dynamic process which is composed of the mass and heat transport and interface kinetics. In this part, a high temperature in situ observation method coupling differential interference microscope and the Schlieren techniques will be introduced. The

kinetic and morphological behaviour of the growing crystals can be observed by the differential interference microscope, and Schlieren technique is applied here to visualize simultaneously convective flow in the liquid phase. Melting and growing of oxide crystal taking place in high temperature up to 1400 °C can be observed and recorded by this system.
Fig. 1 shows the photograph of the in situ observation system. The system consists of a crystal growth part, a differential interference microscope coupling with Schlieren system, and the controlling part.

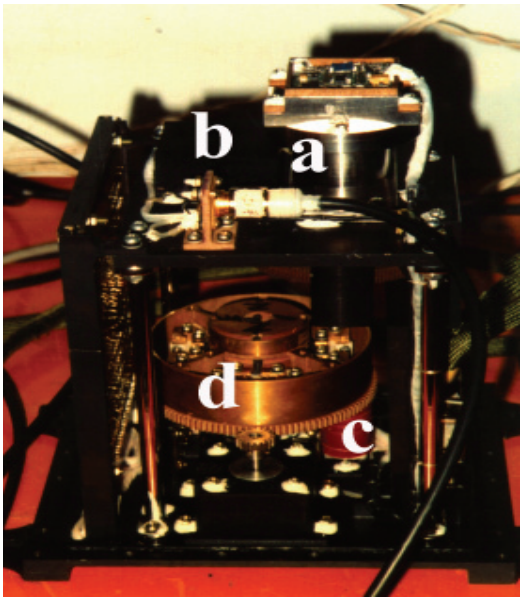

Fig. 1. The photograph of the optical in situ observation system. a: differential interference microscope coupling with Schlieren system; b: crystal growth part; c: optical light source; d: mechanical controlling part

The crystal growth part consists of a growth cell, a digital volt meter and a stabilized DC power supply. Fig. 2 shows the photo of the micro-floating-zone growth cell. A loop-like Pt wire (ϕ0.2-0.5 mm) is employed to heat and suspend the oxide melt/solution. The temperature of the loop is measured by a Pt-10%Rh thermocouple (ϕ0.08 mm). Temperature fluctuations of less than ±1 °C are obtained for high temperature melts. Two V-typed electrodes are used to prevent the loop from deformation at high temperature. For crystal growth experiment, oxide material is firstly heated and suspended horizontally on the loop heater to form a melt/solution film. The amount of the melt should be precisely adjusted so that the upper and lower planes of the thin film of the liquid are parallel to each other. Moreover, to avoid the contamination of the volatile materials, the top window in the growth cell should be eccentrically placed and rotatable. Then nucleation and crystal growth in two-dimensions are performed by decreasing the temperature of the loop heater.
A differential interference microscope is applied to visualize the crystal growth processes from the melt/solution. Schlieren technique is coupled into the microscrope for visualization

of mass flow. Fig. 3 shows the schematic of the Schlieren optical system includes two lens. The fore lens L_1 is used to form parallel rays, and a knife edge is placed at the rear focal point of lens L_2. Similarly, these parallel lights are also used to pass through the objective of the optical system of differential interference microscope. If a knife edge is installed at the rear focal point of the objective of the microscope, part of the light which has passed through the ununiform region of the object will be refracted and shielded, and the Schlieren effect can be obtained, i.e., the mass flow can be observed. So with this method, the growth pattern and the mass transportation phenomenon can be visualized simultaneously. The video from the microscope (through CCD) is recorded and visualized by the monitor. The video signal can also be transferred digitally into a computer directly for further analysis.

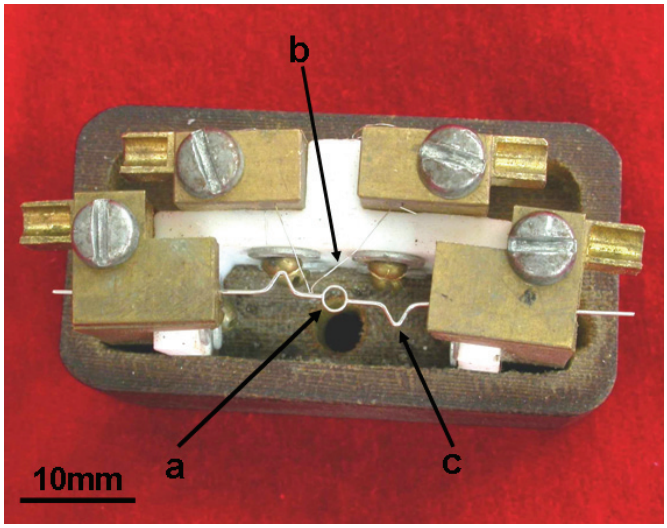

Fig. 2. The photograph of the crystal growth cell. a: loop-shaped Pt wire heater; b: Pt-10%Rh thermocouple; c: V-typed electrode

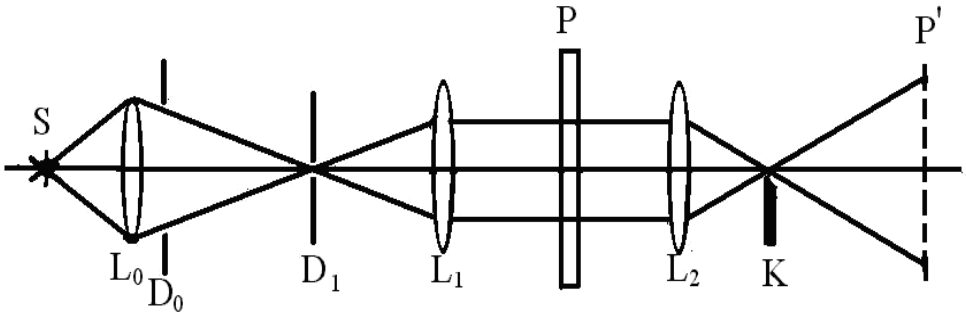

Fig. 3. Schematic figure of the Schlieren optical system. S: light source; L_0, L_1, L_2: lens; D_0,D_1: diaphragms; P: specimen; K: knife edge; P': image of P

3. Buoyancy and Marangoni convection in oxide melt

Buoyancy and thermal capillary convections (namely Marangoni convection) are the main styles of mass transfer in melt especially for high temperature condition. In this section, the typical steady buoyancy and Marangoni convections in the oxide melt/solution suspended on the loop heater will be shown. The unsteady convective flows will be illustrated in the section 6 of this chapter.

3.1 Buoyancy driven convection

Generally, buoyancy driven convection is in close correlation to the temperature distribution in the liquid phase. Fig. 4 shows the typical temperature distribution in the horizontal direction of the thin liquid film suspended by Pt loop. In the central portion of the loop, the melt temperature gradient can be negligible. This region is called pure diffusion region as indicated by sign A in Fig. 4. The situation has an advantage for studying interfacial kinetics process with pure diffusion transport. But in the marginal portion of the heater, the horizontal thermal gradient is significant, and this portion is called diffusion-convective region as hinted by the sign B in Fig. 4. In this region, the growth may be controlled by the buoyancy driven convection due to the higher temperature gradient. The width of diffusion-convective region depends on the loop diameter as well as on the thermophysical parameters of oxide melt, such as the density, thermal diffusivity and viscosity.

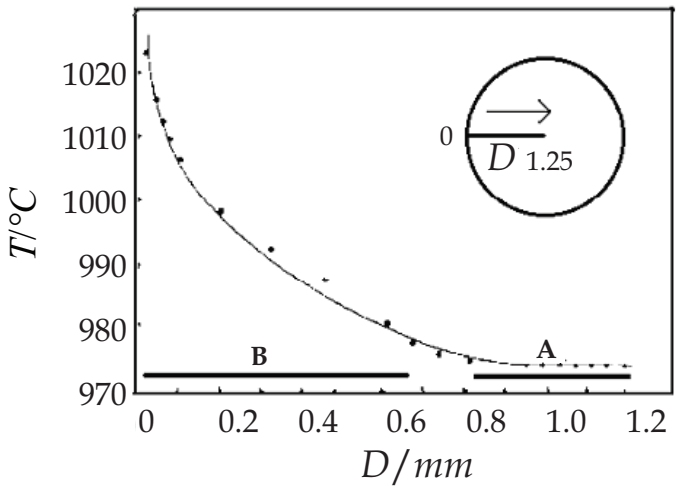

Fig. 4. Typical radial temperature distribution in the horizontal direction of the thin liquid film suspended by Pt loop. D is the distance from the loop margin. Here the temperature distribution profile is supplied for $KNbO_3$ melt

Buoyancy driven convection can be visualized since Schlieren technique has been introduced. However, quantitative measurement of flow velocity needs the help of some tracing particles. Since some tiny crystals can be nucleated when the melt becomes undercooled, the buoyancy driven convection can be indicated by observing the movement of tiny crystals as described in the reference (W. Q. Jin, et al., 1993). As shown in Fig. 5, the tiny crystals move from the margin to the center of the heater. This is typical buoyancy

driven flow caused by the melt rising along the hot wall and descending in the center of vessel which is heated from the side and cooled from the top surface. Fluid flow velocity measurement shows that the momentum profile in the melt is similar to the thermal one. In the central portion of the loop, the flow is steady because of low value of the applied temperature gradient.

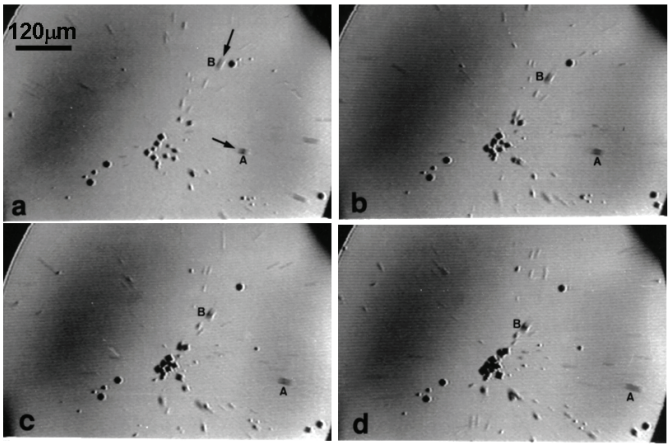

Fig. 5. The buoyancy driven convection indicated by the movement of tiny $KNbO_3$ crystals

3.2 Marangoni convection

Marangoni convection is driven by the variation of surface tension along the free surface. The temperature distribution along the azimuthal coordinate of the loop-like heater is measured by our developed non-contact method (X. A. Liang et al., 2000), which is based on the fact that dissolvability is one-valued function of the temperature. The result is shown in Fig. 6. Here $\Delta T_x=T_B-T_A$. Clearly, the temperature along the free surface is not uniform, which is caused by existence of thermocouple and other attachment. The side with thermocouple on has a lower temperature.

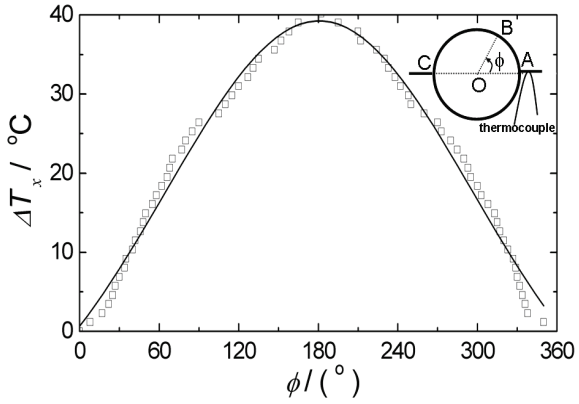

Fig. 6. Temperature difference along the azimuthal coordinate of the heater

Fig. 7 shows the streamlines of the steady Marangoni convection in the BaB_2O_4- $Li_2B_4O_7$ melt-solution. Compared with the buoyancy driven flow in the oxide melt (Fig.5), the type of Marangoni streamlines is quite different. The streamlines in Fig. 7 are concentrated at the surface. This is observed by changing the focus plane of the object lens. As one can see, the flow structure of Marangoni convection is of two symmetrical vortices, with one in the one half of the loop and its mirror image in the other half. The flow direction is from the hot point C to the cooler point A as shown in the inset of Fig.6. This is a typical pattern for Marangoni flow induced by surface tension driven convection. Such convective pattern has also been observed in $KNbO_3$ melt film (W. Q. Jin et al., 1999). It should be mentioned that if the temperature difference between the hot point C and the cooler point A exceeds some critical value, the Marangoni convection may become unsteady, which has been proved in our previous work (Y. Hong et al., 2004, 2005). Those cases are always undesired in crystal growth because growth rate fluctuation as well as microscopic defects may occur, and consequently the quality of the as-grown crystal is deteriorated.

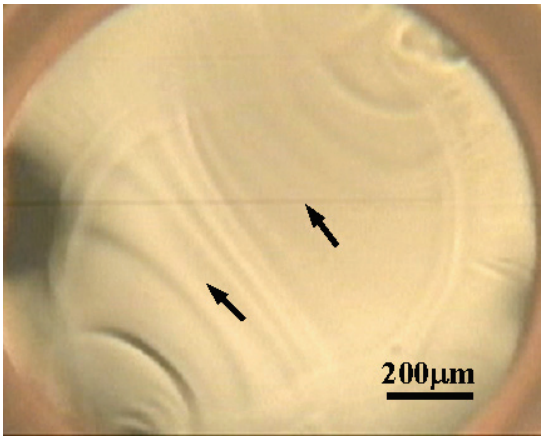

Fig. 7. Steady Marangoni convection in the BaB_2O_4- $Li_2B_4O_7$ melt-solution. The arrows indicate the flow direction

3.3 Coupling of buoyancy and Marangoni convection

The relation between buoyancy and surface tension convection is investigated in the convective region of the loop melt, since only within this region both convections exist simultaneously. In this region, a typical helix flow can be observed as shown in Fig. 8(a) and its schematic figure is drawn in Fig. 8(b). The velocities of the flow are divided into the cross section through the diameter of the loop heater (V_d) and azimuthal direction along the loop heater (V_θ), as shown in Fig. 8(c).

The flow velocity V_θ along the azimuthal direction of the loop due to the surface tension effect may be estimated by balancing the surface tension force with viscous force (F. Ai et al., 2009). This gives

$$V_\theta = C\Delta T\left(\frac{\sigma}{T} - C_\sigma\right)\exp\left(-\frac{b}{RT}\right) \tag{1}$$

where C is a geometry-dependent factor, σ is the surface tension,C_σ is specific heat at constant surface tension, b is a constant independent of temperature, and R is the gas constant.

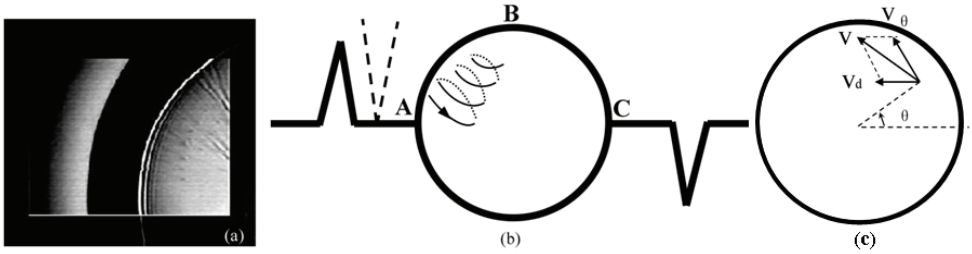

Fig. 8. Helix flow in the loop (a), the corresponding schematic figure (b) and schematic figure of the coordinates (c)

For oxide melt, by using typical values such as σ ~ 0.2 g/s² , C_σ = 1.73×10⁹ g·cm/s²·K and the experimental data, the constants can be determined as C = 2.5×10⁻⁵ cm·s/g and b/R = 1/K. Thus, from the temperature data measured, one can get the theoretical velocity along the azimuthal loop direction ($V_{s\theta}$) profile as shown in Fig. 9(a), which agrees with the experimental data ($V_{e\theta}$). This means that the flow along the azimuthal loop is mainly driven by Marangoni convection.

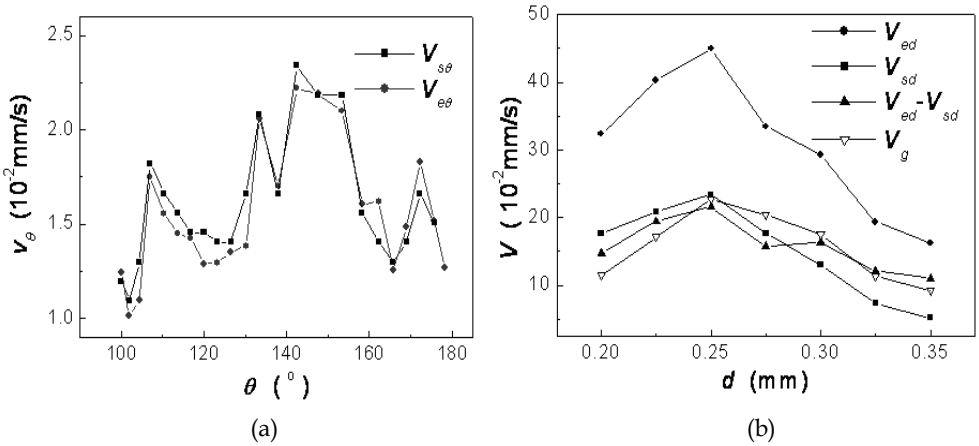

Fig. 9. (a) Comparison between experimental data $V_{e\theta}$ and theoretical calculation $V_{s\theta}$ of surface tension convection along the azimuthal direction of the loop-shaped heater; (b) The velocities of buoyancy and surface tension convection along the radial direction of the loop-shaped heater (• V_{ed} , ■ V_{sd} , ▲ (V_{ed}-V_{sd}) , ∇ V_g)

By the similar calculation process mentioned above, the convection velocity V_d, which results from the temperature difference along radial direction, can be calculated and profiled in Fig. 9(b). It is obvious that the calculated surface tension flow velocity V_{sd} is less than V_{ed} obtained by experimental data. Based on an axial symmetry solution of Navier-Stokes equation, the flow velocity V_g that is driven by buoyancy convection has also theoretically

calculated and is also illustrated in Fig. 9(b). For comparison, the profile of (V_{ed}-V_{sd}) is simultaneously illustrated. Obviously, V_g agrees well with the profile of (V_{ed}-V_{sd}). That is, the difference between V_{ed} and V_{sd} indeed results from buoyancy convection effect in present system.

4. Interfacial boundary layer and microconvection during oxide crystal growth

In crystal growth, interfacial gradients in velocity, concentration or temperature are often summarily referred to as boundary layers. The concept of interfacial boundary layer concerning of crystal growth has been thoroughly expounded by Franz Rosenberger (F. Rosenberger, 1993). The domain of liquid can be subdivided into two regions. Inside the boundary layer, the gradient is high, while out side the boundary layer, the gradient is negligible.

4.1 Calculation of interfacial boundary layer thickness

One important and effective method for calculation of interfacial boundary layer thickness is developed by the help of crystal rotation. In present high temperature in situ observation system, the rotating growth of oxide crystal has been realized (W. Q. Jin et al., 1998; X. H. Pan et al., 2008). Fig. 10 shows a typical process of BaB_2O_4 crystal growth with rotation in the center of one toroidal Marangoni flow as depicted in Fig. 7. During the growth, the Marangoni flow may be as a forced convection to rotate the tiny crystal.

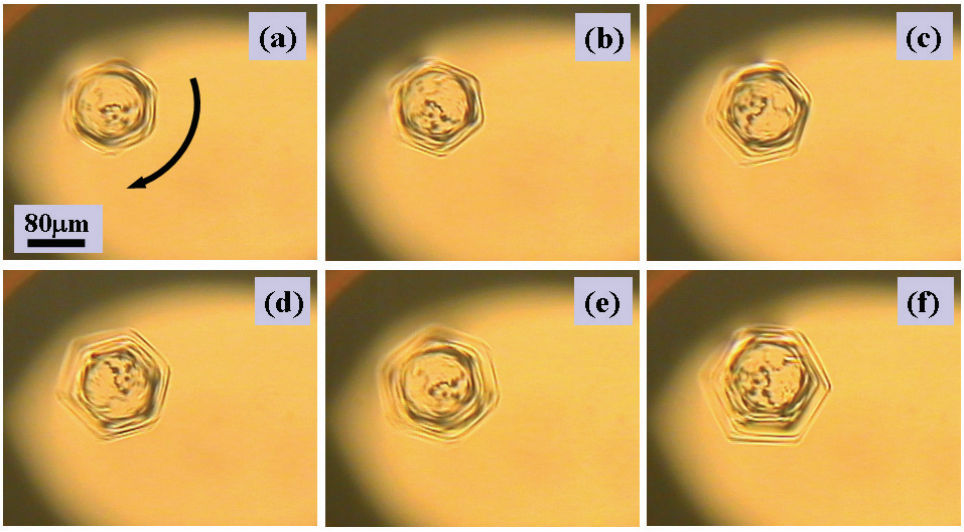

Fig. 10. BaB_2O_4 single crystal growth process with rotation. The dark arrow shows the direction of rotation and rotating velocity ω is 6 rad/s

The arrow in Fig. 10(a) illustrates the rotation direction, and the angular velocity ω is 6 rad/s. The widths of the interfacial momentum, heat and concentration boundary layer are given by following equations respectively. Where ν is the kinematic viscosity, κ is the thermal

diffusivity, D is the mass diffusivity, P is the Prantdl number and S is the Schmidt number. With $\nu = 40$ mm^2/s , $\omega = 6$ rad/s, and the estimation of $\kappa = 10^{-2}$cm^2/s and $D = 10^{-5}$cm^2/s for oxide melt (W. Q. Jin, 1997), one then obtain $\delta_\upsilon = 9.2$ mm, $\delta_T = 1.25$ mm and $\delta_C = 0.12$mm, respectively.

$$\delta_\upsilon = 3.6\left(\frac{\nu}{\omega}\right)^{1/2} \tag{2}$$

$$\delta_T = 1.61\left(\frac{\nu}{\omega}\right)^{1/2} P^{-1/3} = 1.61\kappa^{1/3}\nu^{1/6}\omega^{-1/2} \tag{3}$$

$$\delta_C = 1.61\left(\frac{\nu}{\omega}\right)^{1/2} S^{-1/3} = 1.61D^{1/3}\nu^{1/6}\omega^{-1/2} \tag{4}$$

Fig. 11 shows the schematic comparison among concentration, velocity and temperature distribution at solid-liquid interface of oxide crystal growth. It is obvious that there is a big difference between the diffusivities for momentum, heat and species in the solution. The magnitudes of δ_T and δ_υ are at least one order larger than that of δ_C. This indicates that the thermal and momentum transition zone extends further into the fluid than the concentration transitional region. Thus, in the concentration boundary layer, the flow velocity and conductive heat flux are reduced to relatively small values and it is obviously meaningless to discuss interfacial heat and velocity transport in oxide crystal growth.

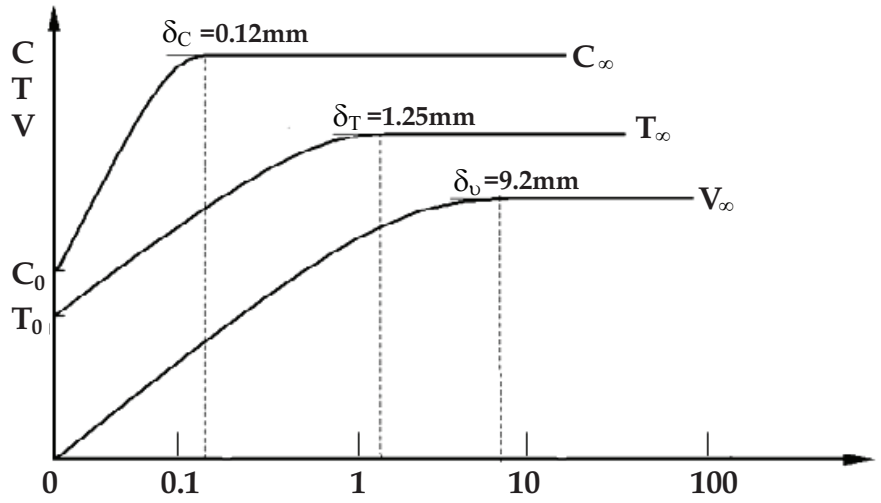

Fig. 11. Schematic comparison between δ_υ , δ_T and δ_C for BaB_2O_4 crystal rotated at 6 rad/s

One important parameter determining the thickness of interfacial boundary layer is the rotating rate ω as indicates from equations (2) to (4). Since the driving force of crystal rotation is the surface tension-driven flow caused by the horizontal temperature difference ΔT along the heater, the value of ω is consequently correlated with the strength of the Marangoni convection. Here, ΔT is the temperature difference between the hottest point C

and the coolest point A across the heater. The values of ω with various ΔT have been experimentally measured as shown in Fig. 12(a). With a larger value of ΔT, the crystal rotates faster and then a smaller width of concentration boundary layer is obtained. It should be noted that present calculating method for boundary layer thickness is unsuitable for the cases with too large or too small values of ΔT. In the former case the rotation is unsteady, while in the latter case no obvious convection is visible due to the viscous force of the melt.

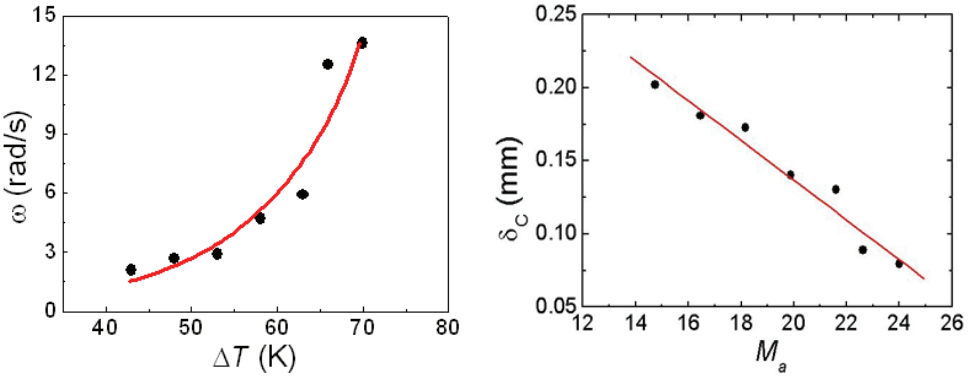

(a) (b)

Fig. 12. The dependence of rotating angular velocity on temperature (a) and the variation of concentration boundary layer thickness δ_C versus Marangoni number M_a (b)

In general, the strength of Marangoni convection can be characterized by dimensionless Marangoni number $M_a = \sigma_T \Delta T d / \eta\kappa$. Where $\sigma_T = d\sigma / dT$ is the temperature coefficient of surface tension σ, d is the characteristic length of the liquid, η is dynamic viscosity and κ is the thermal diffusivity. By taking d = 0.8 mm, σ_T = -0.06 dyn/cm•K, η = 0.16 Pa•s, and $\kappa = 10^{-2}$cm²/s, then the calculated concentration boundary layer thickness δ_C versus M_a is plotted in Fig. 12(b). The thickness of concentration boundary layer is in inverse proportion to the value of Marangoni number. It suggests that the concentration boundary layer is suppressed by the enhancement of Marangoni convection. This is due to the fact that heat and mass transfer is enhanced and therefore the interfacial diffusion field is weakened.

4.2 Microconvection within the boundary layer

Since in the central portion of the loop, the melt/solution temperature gradient along the radial direction can be negligible, this has an advantage for studying the "pure diffusive" mass flow. Fig. 13 shows the $KNbO_3$ grains and the surrounding flow structure during growth in the center of $KNbO_3/Li_2B_4O_7$ solution. One significant flow cell is observed around each grain. Since such flow is usually restricted only in a narrow region of several tens of microns near the solid-liquid interface, that is the size scale of grain, cell or dendrite, it can be called the microconvection as described by Sahm and Tensi (P. R. Sahm and H. M. Tensi, 1981).

The growth of the grains is restricted to each other. As a result, the growing rate of the grains is much low which is helpful for velocity measurement of microconvection. The

velocity of mass flow parallel to the solid-liquid interface (transversal flow) and that of flow perpendicular to the interface (normal flow) are depicted as the solid lines in Fig. 14. Here, the origin of coordinate axes is at the center of $KNbO_3$ grain face as indicated in Fig. 13. Since the growth of the grains is restricted to each other, the quenched solution retains their situation in high temperature. And thus the solute concentration near the grain can be examined microscopically by the electron-microprobe analyses.

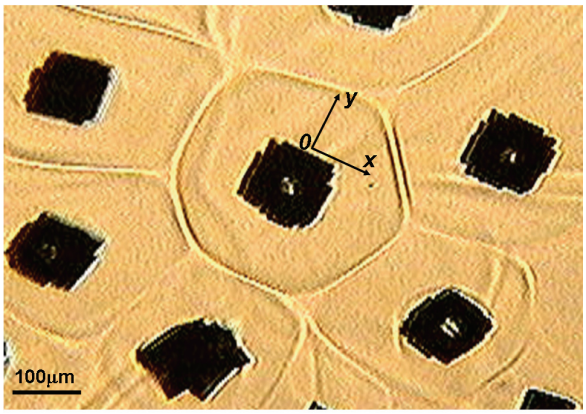

Fig. 13. Growth pattern of $KNbO_3$ solute grains in $KNbO_3/Li_2B_4O_7$ solution, showing the existence of microconvection near the solid-liquid interface

In the absence of temperature gradient for a binary system in the solution growth, it is rational to assume that the solvent is quantitatively rejected at the interface and the velocity of solvent flow is zero (W. Q. Jin et al., 2005, 2006). Then the mass transport is mainly by diffusive flux. Diffusion is in general understood as the component flux with respect to an average velocity of the system. The total mass flux of solute $KNbO_3$ in the binary system can be expressed as

$$n_K = \rho_K \upsilon_K = \rho_K \upsilon + \rho D \nabla W_K \tag{5}$$

where ρ_K is component mass density of the $KNbO_3$ solute, ρ is the total mass density, D is binary diffusivity, $W_K=\rho_K/\rho$ is the mass fraction of component $KNbO_3$, and υ is the mass average velocity

$$\upsilon = \frac{1}{\rho}\sum \rho_i \upsilon_i \tag{6}$$

For the binary system in the solution growth, the solvent is quantitatively rejected at the interface and the velocity of solvent flow is zero. So one obtain

$$\upsilon \approx \rho_K \upsilon_K / \rho = W_K \upsilon_K \tag{7}$$

So the "convective" term in (5) is

$$\rho_K \upsilon = \rho_K W_K \upsilon_K = n_K W_K \tag{8}$$

The flow in (8) is the so-called diffusion-induced bulk flow as described by Franz Rosenberger (F. Rosenberger, 1983). Substitution of (8) in to (5) yields for the "purely diffusive" component mass flux towards the growing crystal

$$n_K = \frac{\rho D}{1 - W_K} \bullet \nabla W_K \tag{9}$$

rather than the widely used

$$n_K = \rho D \bullet \nabla W_K \tag{10}$$

Furthermore, substitution of $\upsilon_K = \upsilon / W_K$ into (9), one obtains

$$\upsilon = \frac{D}{1 - W_K} \bullet \nabla W_K \tag{11}$$

Then the mass average velocity of present system in two-dimensional treatment is

$$\begin{aligned} \vec{\upsilon}(x,y) &= \frac{D}{1 - W_K(x,y)} \left(\frac{\partial}{\partial x} W_K(x,y)\vec{i} + \frac{\partial}{\partial y} W_K(x,y)\vec{j} \right) \\ &\equiv \upsilon_1(x,y)\vec{i} + \upsilon_2(x,y)\vec{j} \end{aligned} \tag{12}$$

By the experimentally measured $KNbO_3$ concentration W_K along the growing interface and normal to the interface, respectively, the authors have got the calculated profiles of velocities both along and normal to the solid-liquid interface during oxide crystal growth (W. Q. Jin et al., 2006). This is indicated by the dotted line as $\upsilon_1^t(x,0)$ and $\upsilon_2^t(0,y)$ in Fig. 14, which agrees with the experimental profile data $\upsilon_1^e(x,0)$ and $\upsilon_2^e(0,y)$, respectively. It means that on segregation at the interface, the solute diffusion-induced bulk flow is exactly nonzero and can be detected experimentally.

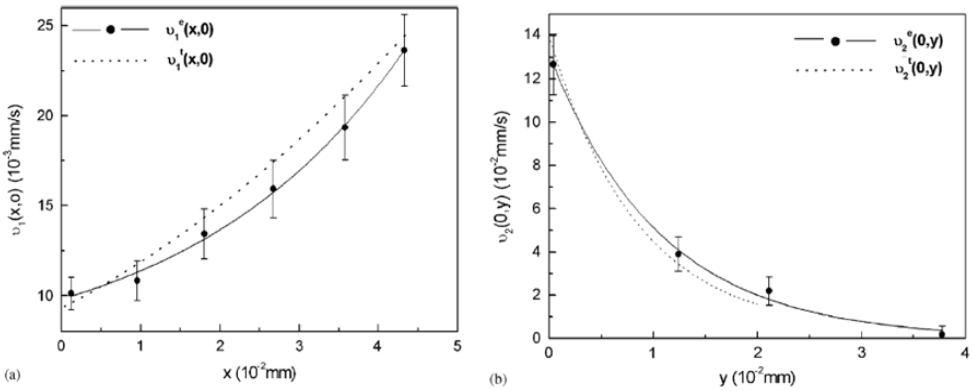

Fig. 14. Comparison between experimental velocities of $KNbO_3$ microconvection flow (solid line) and theoretical calculation velocities of $KNbO_3$ diffusion-induced bulk flow (dotted lines): (a) parallel flow to the interface $\upsilon_1(x,0)$; (b) normal flow to the interface $\upsilon_2(0,y)$

5. Effect of mass transport on interfacial kinetics and morphological instability

If only one single seed crystal is formed in the centre of the loop, it can grow larger because no surrounding grains restrain its growth. At the initial stage of growth, the crystal size is comparatively small. In this case, the growing solid-liquid interface is in the "pure" diffusion region and the interfacial mass transport visualized by Schlieren technique is shown in Fig. 15(a). However, the interfacial mass transport becomes different when the solid-liquid interface enters the diffusion-convective region near the melt margin as indicated in Fig. 15 (b). Here the mass transport is governed by the diffusive-convective flow due to the significant temperature gradient.

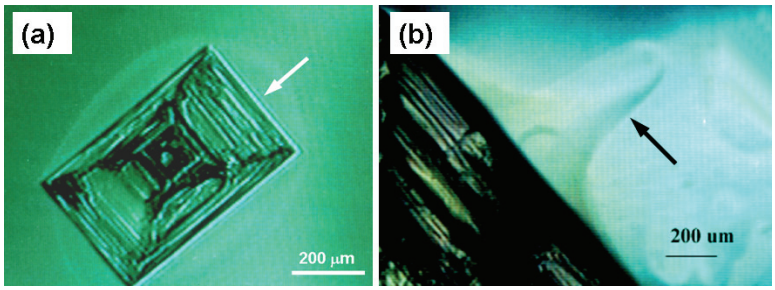

Fig. 15. Morphology of the interfacial fluid flow for one single crystal growth

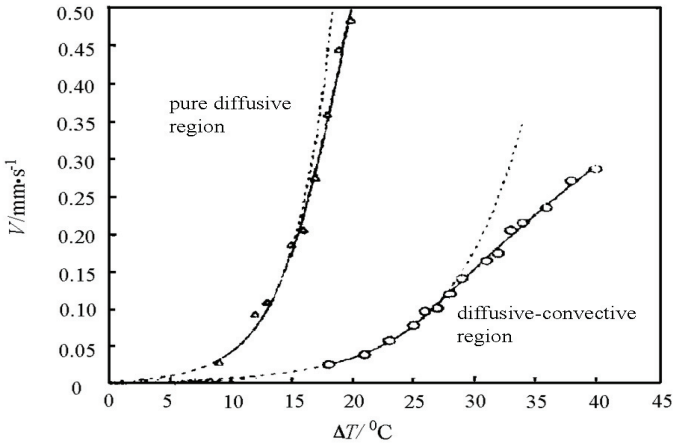

Fig. 16. The data plotted as V~ΔT for (100) face of $KNbO_3$ in the pure diffusive region and in the diffusive-convective region, respectively

To examine the influence of the mass transport on the interface growth kinetics, the growing rate data plotted as V~ΔT are shown in Fig. 16 for two different flow states. The growing rate in pure diffusive region can be described as $V=1.1\exp(-4.5\times10^4/T\Delta T)$, while that in the diffusive-convective region is expressed as $V=0.59\exp(-8.4\times10^4/T\Delta T)$. These exponential

functions indicate a growth mechanism by two-dimension nucleation. The experimental data coincide well with the dotted curves predicted by the theory of two-dimension nucleation. It can be seen that, at the lower supercoolings two-dimensional nucleation growth has been obtained irrespective of the state of mass transport in the melt. However, at the same supercooling, the discrepancy between the growth rates for two different states of convection may be assigned to the buoyancy driven convection of the interfacial mass flow.
The best model to describe the growth kinetics of two-dimensional nucleation is the birth and spread model (J. W. Cahn et al., 1964). According to this model, many nuclei occur on a flat crystal surface, and the steps annihilate when they spread and impinge. The growth rate V is given by

$$V = V_{\infty}\left(\frac{L\Delta T}{RT_m^{\,2}}\right)^{1/6} e^{\Delta G^*/3KT} \tag{13}$$

where V_{∞} is the velocity of a straight step, L is the latent heat of fusion per mole, T_m is the melting temperature, and ΔG^* is the thermodynamic potential barrier for two dimensional nucleation.
The energy barrier ΔG^* for this is given by the following equation (W. Q. Jin, 1983)

$$\Delta G^* = \frac{\pi\varepsilon^2 T_m}{L\Delta T^*} \tag{14}$$

in which ε is the free energy per unit length of a step and ΔT^* is the threshold supercooling for the growth of a flat surface. The values of ε and ΔG^* have been calculated from the experimental data for two different states of mass transport. The various results are summarized in Table.1. On comparing these experimental results with the theoretical kinetic equations (13) and (14), it is implicated that the growth kinetics is dependent upon the convection flow through the two quantities ε and V_{∞}.

mass transport state	ΔT^* (°C)	ε(J/m)	ΔG^* (J)
pure diffusive	3.0	1.2×10^{-11}	6.3×10^{-19}
diffusive-convective	5.0	1.6×10^{-11}	7.0×10^{-19}

Table 1. Data of ε and ΔG^* of $KNbO_3$ crystal growth for the (001) face in different mass transport state

The mass transport in the melt may also have great effect on the morphological stability of the growing crystal. In general, the solid-liquid interface during oxide crystal growth from high temperature melt-solution is flat and smooth for its high melting entropy, and the shape of single crystal is usually polygonal in two dimensions. However, the instability of solid-liquid interface may occur when the mass transport becomes unsteady. This is especially for the case of unsteady convection or rapid growth. Fig. 17 shows a typical unsteady growth of BaB_2O_4 melt where significant cellular shape is observed for the solid-liquid interface. Cellular growth and the resulted striations are usually found accompanied with appearance of oscillatory or turbulent flows.
In case of high cooling rate the morphology of solid-liquid interface may also become unsteady. The interfacial morphology instability has been in situ observed in the rapid

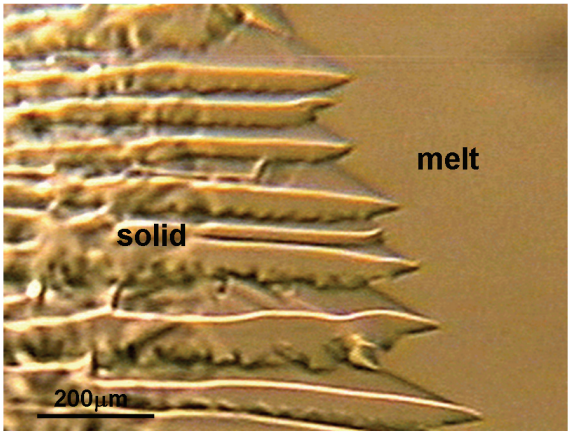

Fig. 17. Cellular interface during BaB_2O_4 crystal growth indicating the occurence of morphological instability

growth of BaB_2O_4 single crystal from high-temperature solutions (X. H. Pan et al., 2006, 2007, 2009), where skeletal shape of growing interface is obtained due to the reduction of convective regime by rapid growth. Fig. 18 shows a typical microscopic morphology of BaB_2O_4 single crystal. It is obvious that the interface is deformed and the crystal presents a shape of snowflake. This kind of interface with the centre region depressed is the so called skeletal shape. The formation of skeletal shape is the result of the extremely non-uniform supersaturation in front of the interface owing to reduction of convective effect. The concentration of solute can be examined by element detection with electro-microprobe analysis when the solution is quenched as described in section 4.2. Unfortunately, the quantitative data about interfacial concentration of BaB_2O_4 in the solution is impossible primarily due to the existence of light element boron that can not be examined effectively even by electro-microprobe technique.

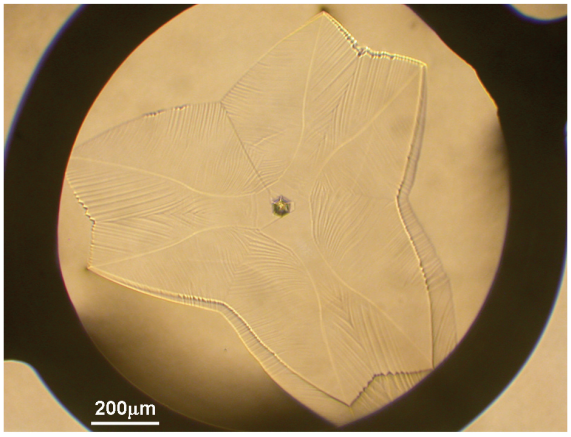

Fig. 18. Skeletal morphology of BaB_2O_4 single crystal with high growth rate

Morphological instability has also been obtained for $KNbO_3$ grains (X. H. Pan et al., 2009). Fig. 19 shows the microscopic morphologies of quenched $KNbO_3$ grains observed by electro-microprobe, which are achieved under the condition of rapid solidification. Dendrite grows in the central region of the melt indicating the appearance of morphological instability, whereas crystal with smooth surface is observed in the quenched melt adjacent to the periphery of the loop heater.

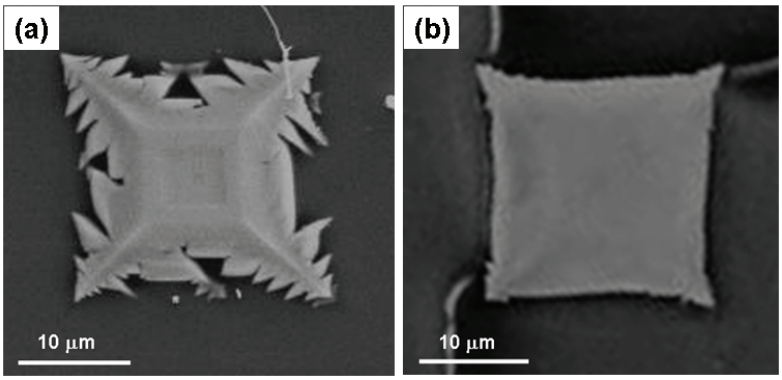

Fig. 19. Morphologies of $KNbO_3$ grains in (a) the central region and (b) the marginal region of the melt-solution observed by electron-microprobe

The instability of interfacial morphology is close by related to the solute distribution in front of the solid-liquid interface. Fig.20 shows the concentrations of solute $KNbO_3$ in the quenched melt–solution near $KNbO_3$ grains examined by electron-microprobe analysis. Here, W_{KN} is the experimentally measured mass fraction of the solute distribution in the solution and r refers to the distance in the direction parallel to the interface with origin of x-coordinate axe being at the face centre. The point "▲" is for the grain obtained in the central region while point "●" is for the grain obtained in the marginal region of the melt.

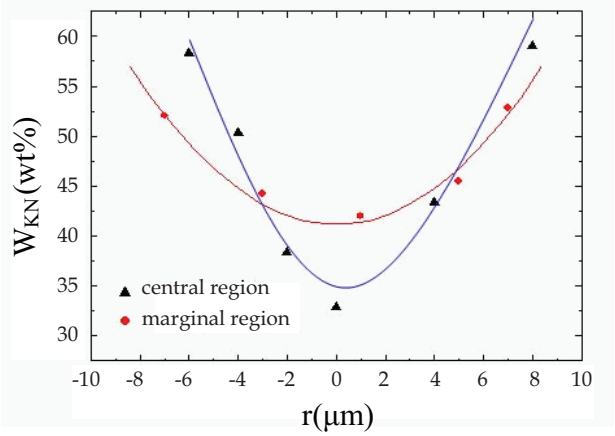

Fig. 20. Solute distribution along the solid-liquid interface of $KNbO_3$ grains in solution

It is obvious that the solute concentration along the interface is uneven both for pure diffusive and diffusive-convective regions which is in related with the specie supplies. In terms of the Berg effect, the apexes of a polyhedral crystal are the best supplied regions and the concentration along the crystal surface varies, being the lowest at the face centre. This is the shape destabilizing factor. The shape stabilizing factor is connected with the anisotropy in the surface growth kinetics. If the kinetic coefficient with its anisotropy is not sufficient to compensate for the inhomogeneity in the concentration distribution over the growing crystal face, the appearance of morphological instability in the crystal faces takes place. The curves in Fig.20 indicate that not only the concentration difference between the centre and corner of a $KNbO_3$ grain face but also the concentration gradient along the face in the convective region are lower than that in the diffusive region. This is attributed to the enhanced mass transport and thus the improved homogeneity of solute concentration by convection. As a result, morphological instability occurs more easily in the diffusive region where dendrites are found whereas crystal in the convective region conserves a polyhedral shape. This result indicates that, even underlying a very high cooling rate, flat interface may still keep its shape in case of the existence of certain convection.
It should be emphasized from above results that, only steady convection is helpful for the maintaining of flat interface during oxide crystal growth. Mass transfer governed by pure diffusion or unsteady convection may leads to morphological instability of growing interface, and thus deteriorate the crystal quality.

6. Mass transfer with external forces in oxide crystal growth

In crystal growth, steady convection is always desired because it is helpful for mass transfer and thus provides an enhanced renewal of the melt/solution in the region near the crystallization interface. However, when the temperature gradient gets larger enough, the convective flow may become oscillatory or even turbulent, which inevitably gives rise to generation of striations. In some cases, the unsteady flow may be suppressed by external force such as rotation, vibration or magnetic field. In this part, some experimental results will be given about the effect of external forces on mass transport during oxide crystal growth.

6.1 Suppression of oscillatory flow by transverse magnetic field in $NaBi(WO_4)_2$ melt

For oxide melt, oscillatory convection can be observed if the temperature gradient along the loop heater gets large enough. Fig. 21(a) shows a typical unsteady flow pattern of $NaBi(WO_4)_2$ melt. This pattern comprises one main trunk and the branches. The main trunk oscillates with time, and the arrows I, II represent the range of oscillation. Fig. 21(b) shows the schematic diagram of oscillatory pattern. The main trunk oscillates around the position A with the amplitude as shown by the bi-directional arrow 1. The oscillatory frequency reached about 10 Hz, and the amplitude was about 500 μm. Similar convective oscillations have also been observed in $KNbO_3$, BaB_2O_4 and $Bi_{12}SiO_{20}$ melts or solutions suspended on a loop heater (Z. H. Liu et al., 1998; W. Q. Jin et al., 2004; Y. Hong et al., 2006).
When a 60 mT transverse static magnetic field is applied, the distinct attenuation of the oscillation is observed and arrows III, IV represent the range of oscillation as shown in Fig. 22(a). The main trunk oscillates around the position A with the amplitude (~200 μm) as shown by the bi-directional arrow 2 in Fig. 22(b), which is smaller than that as shown by arrow 1. So the oscillatory amplitude of main trunk decreased when the magnetic field is applied. The frequency of oscillation is measured to be about 4 Hz. This means that the instability of convective flow has been effectively reduced.

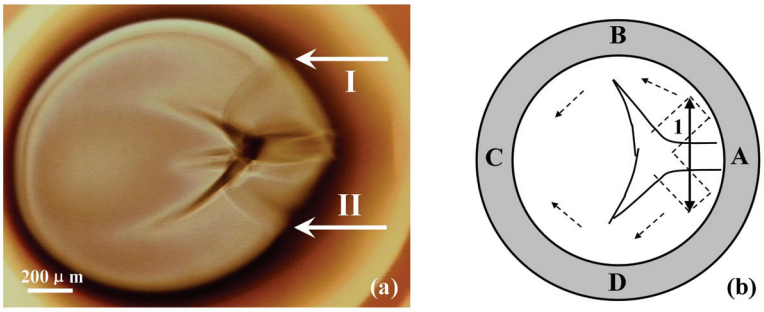

Fig. 21. (a) Oscillatory flow pattern in $NaBi(WO_4)_2$ melt, (b) The schematic diagram of the flow pattern

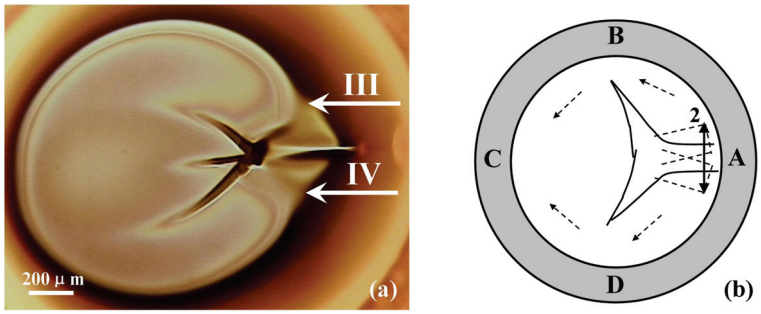

Fig. 22. (a) Flow pattern in $NaBi(WO_4)_2$ melt under 60 mT transverse magnetic field, (b) The schematic diagram of the flow pattern

In general, attention has seldom been paid to the growth of oxide single crystals in applied magnetic fields since their electrical conductivity is extremely low even in the melt. It is normally assumed that the effect of the magnetic field to be applied is negligible in an oxide melt. However, above experimental result shows that 60 mT static magnetic field is strong enough to affect the mass flow of oxide melt. It should be emphasized that the oscillation of the thermocapillary flow could be completely suppressed by the 60 mT magnetic field if the temperature difference applied on the loop decrease. The suppression of magnetic field on the oscillation flow might be due to the Lorentz force induced by the interaction of dissociated ions with magnetic field (W. Q. Jin, 2007).

6.2 Effect of rotating magnetic field on $Bi_{12}SiO_{20}$ crystal growth

In the following, the experiment results about bulk crystal growth by vertical zone-melting technique (VZM) in a rotation magnetic field (RMF) shall be demonstrated. Here $Bi_{12}SiO_{20}$ crystal is selected as model material due to its excellent photorefractive and electro-optical properties. More details about the RMF-VZM system is described in the reference (Y. Liu et al., 2010).

Fig. 23 shows the photographs of the $Bi_{12}SiO_{20}$ crystals grown by VZM. The crystal in Fig. 23(a) is grown with 25 mT and 50 Hz RMF and the one in Fig. 23(b) is obtained without RMF. A regular deep pattern with numerous curved lines is observed on the free surface

(upper part) of the as-grown single crystal obtained with RMF in Fig. 23(c). It is simplified as a schematic drawing in Fig. 23(d). Since such curved lines are observed only at the upper part of the as-grown crystal, they are in correlated with the free surface at the top end of the melt. By contrast with the same position of the single crystal grown in the normal condition without RMF shown in Fig. 23 (b), no similar pattern can be observed on the free surface of the same position. Therefore, it can be concluded that the appeared pattern is definitely induced by the applied RMF.

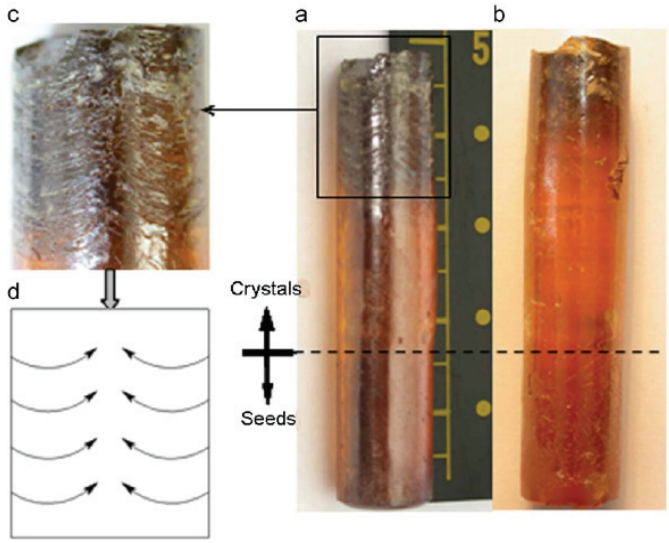

Fig. 23. $Bi_{12}SiO_{20}$ crystals grown with (a) and without (b) rotation magnetic field, the regular pattern (c) observed on the surface and its schematic drawing (d)

Optical microscopic observation reveals that the middle part of the crystal grown with RMF has no growth striations. On the other hand, a large number of growth striations could be clearly observed inside the crystal grown without RMF at the same position. This is due to the appearance of steady forced convection in the melt induced by magnetic field. As a result, the transport of heat and mass is enhanced and remains stable, and therefore the crystallographic perfection could be improved.

6.3 Improvement of crystallographic perfection in $Bi_{12}SiO_{20}$ crystal by axial vibration

The authors have experimentally investigated the effect of axial vibration on the free surface flows in a vertical Bridgman model under isothermal conditions (X. H. Pan, 2005a, 2005b). Steady forced flows are obtained on the free surface of the liquid phase driven by pure axial vibration. Based on this hinting, axial vibration is introduced into the $Bi_{12}SiO_{20}$ crystal growth in our laboratory (Y. Zhang et al., 2008, 2009), in order to suppress the unsteady thermocapillary or buoyancy convections. Some results are described in the following.

Axial vibration has been introduced in the growth of $Bi_{12}SiO_{20}$ single crystal by vertical Bridgman technique. The frequency of the axial vibration applied is 50 Hz and its amplitude varies. The quality of the $Bi_{12}SiO_{20}$ single crystal is identified by the high-resolution X-ray rocking curves as shown in Fig. 24. It can be found that the crystal grown with 70 μm

vibration has the strongest diffraction intensity and the smallest full-width at half-maximum (FWHM), indicating the highest crystal quality. This means that crystallographic perfection of oxide crystal can be effectively improved by axial vibration with proper amplitude.

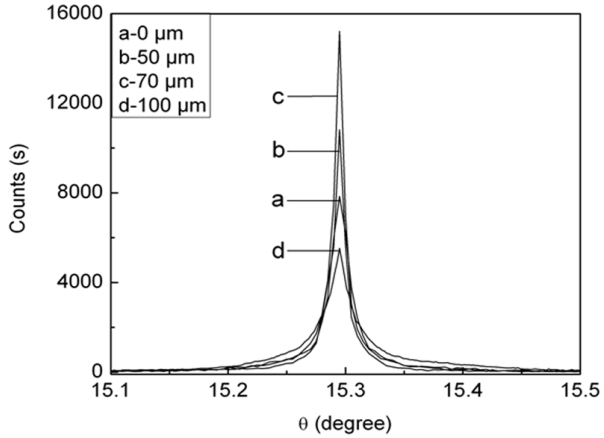

Fig. 24. X-ray rocking curves of $Bi_{12}SiO_{20}$ crystals grown by vertical Bridgman method with different vibration amplitudes

Fig. 25 shows the etch pit pattern of the as-grown $Bi_{12}SiO_{20}$ crystals by vertical Bridgman method. The etch pit density of the crystal grown without vibration is about $4.8\times10^4/cm^2$ (Fig. 25(a)). However, when an axial vibration of 70 μm amplitude is applied, the etch pit density of the crystal grown with vibration is only $2.2\times10^4/cm^2$ (Fig. 25(b)). This is attributed to the enhanced mass exchange and the diminished radial temperature gradient in front of the solid-liquid interface by vibration-induced forced convection.

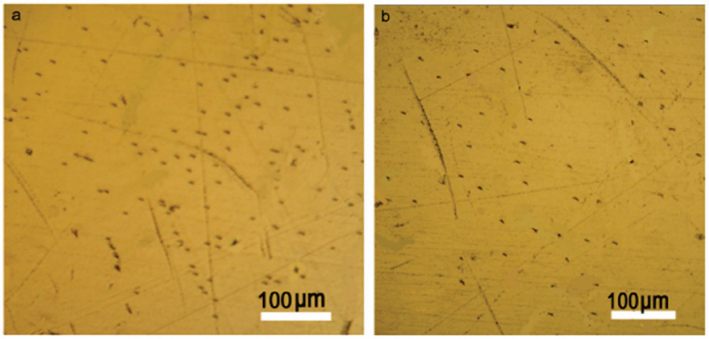

Fig. 25. Etch pit patterns of $Bi_{12}SiO_{20}$ crystals grown without vibration (a) and with vibration of 70 μm amplitude (b)

7. Summary and conclusions

The coupling of differential interference microscope and the Schlieren technique is an effective method to visualize the mass transport simultaneously with the growing interface

for oxide crystal growth. Besides the buoyancy and Marangoni convections induced by temperature gradient, diffusion-induced micro-convection in the boundary layer also exists. The style of mass transfer near the growing interface has great effect on the interfacial kinetics and the interfacial instability. The mass transport governed by pure diffusion can induce inhomogeneous concentration distribution along the growing interface of the single crystal and thus leading to morphological instability, where dendritic or skeletal shape occurs easily. Nevertheless, if the mass transport is governed by both convection and diffusion, the faceted interfacial shape is easy to maintain. The mass transport can be effectively improved by external forces such as magnetic field and vibration, and thus single crystal with high crystallographic perfection can be obtained.

8. Acknowledgements

The authors would like to thank their colleagues and collaborators. The author would also like to acknowledge the supports from National Natural Science Foundation of China under Grant Nos 50802105 and 50331040.

9. References

F. Rosenberger, (1983). Interfacial transport in crystal growth, a parametric comparison of convective effects. *Journal of Crystal Growth*, Vol.65, pp. 91-104

F. Rosenberger,(1993). Boundary layers in crystal growth-facts and fancy. *Progress in Crystal Growth and Material Characterization*, Vol.26, pp.87-98

F. Ai, W. Q. Jin, H. S. Luo, Y. Liu & X. H. Pan, (2009). Study on the buoyancy and surface tension convection of high-temperature oxide solution. *Materials Chemistry and Phsyics*, Vol.114, pp. 387-390

J. W. Cahn, W. S. Hilling & G. W. Sears (1964). The molecular mechanism of solidification. *Acta Metallurgica*, Vol.12, pp.1421-1439

P. R. Sahm & H. M. Tensi, (1981). Mass transport in the near vicinity of solidification fronts under microgravity. *Advances in Space Research*, Vol. 1, pp. 97-110

W. Q. Jin, (1983). Ph.D. Thesis, University of Tohoku, Sendai, Japan, P.179, in Japanese

W. Q. Jin, J. Y. Chen, W. S. Li & H. P. Yan, (1993). Development of optical system for high temperature in situ observation of oxides crystal growth. *Ferroelectrics*, Vol.142 pp.13-18

W. Q. Jin, J. Y. Chen & W. S. Li, (1993). High temperature in situ observation of the melt transfer process around growing $KNbO_3$ crystal. *Microgravity Quarterly*, Vol.3 pp.129-133

W. Q. Jin, Z. L. Pan, N. Cheng & Y. Hui, (1997). Boundary layer effect in crystal growth – comments on the optical in situ observation technique for melt crystal growth. *Journal of Inorganic Materials*, Vol. 12, pp. 279-285 (in Chinese)

W. Q. Jin, Z. L. Pan & Z. H. Liu, (1998). Effect of buoyancy-driven convection upon crystal growth of $KNbO_3$ in the melt. *Journal of Crystal Growth*, Vol. 191, pp. 760-766

W. Q. Jin, Z. L. Pan & C. Ning, (1999). Experiments on surface tension driven flow in high temperature oxide melting. *Space Forum*, Vol. 4, pp. 321-330

W.Q. Jin, X.A. Liang, Y. Hong, X.H. Pan & K. Tsukamoto, (2004). Study on thermocapillary convection in $Bi_{12}SiO_{20}$ melt. *Journal of Crystal Growth*, Vol. 271, pp. 302-306

W. Q. Jin, (2005). Diffusion effect in solidification. *Journal of Inorganic Materials*, Vol. 20, pp.42-46 (in Chinese)

W. Q. Jin, X. H. Pan, Y. Liu, Y. Hong, Y. F. Jiang & S. Yoda, (2006). Two-dimensional mass diffusion-induced bulk flow in a boundary layer of crystal growth. *Journal of Crystal Growth*, Vol. 293, pp. 198-202

W. Q. Jin, F. Ai, Y. Hong, H. S. Luo, Y. Liu & X. H. Pan, (2007). The attenuation of oscillatory thermocapillary convection in the oxide melt by a transverse magnetic field. *Science in China Series G*, Vol. 50, pp. 519-524

X. A. Liang, W. Q. Jin, Z. L. Pan & Z. H. Liu, (2000). Experimental measurement of temperature distribution across a loop-like heater. *Progress in Crystal Growth and Material Characterization*, Vol. 40, pp. 301-307

X. H. Pan &W. Q. Jin, (2005). Effect of axial vibration on free surface flows in cylindrical liquid. *Chinese Physics*, Vol. 14, pp. 422-426

X. H. Pan, (2005). Ph.D. Thesis, Shanghai Institute of Ceramics, CAS, Shanghai, China, P. 125, in Chinese

X. H. Pan, W. Q. Jin, Y. Hong & F. Ai, (2006). In situ observation of skeletal shape transition during BaB_2O_4 crystal growth in High-temperature solution. *Chinese Physics Letters*, Vol. 23, pp. 2269-2272

X. H. Pan, F. Ai, W. Q. Jin, Y. Liu & Y. Zhang, (2007). Morphologies of solid-liquid interface and surface steps during rapid growth of BaB_2O_4 single crystals. *Science in China Series G*, Vol. 50, pp. 539-545

X. H. Pan, W. Q. Jin, Y. Liu & F. Ai, (2008). Effect of surface tension-driven flow on BaB_2O_4 crystal growth from high temperature melt-solution. *Crystal Research and Technology*, Vol. 43, pp. 152-156

X. H. Pan, W. Q. Jin, Y. Liu & F. Ai, (2009). Solute distribution in $KNbO_3$ melt-solution and its effect on dendrite growth during rapid solidification. *Chinese Physics B*, Vol. 18 , pp. 699-703

Y. Hong, W. Q. Jin & X. H. Pan, (2004). Thermalcapillary convection in $NaBi(WO_4)_2$ melt. *Chinese Physics Letter*, Vol. 21, pp. 1986-1988

Y. Hong, W. Q. Jin, X. H. Pan, &Y. Shinichi,(2005). Effect of free surface deformation on thermocapillary convection in high Prandl number melt. *Journal of Crystal Growth*, Vol. 274, pp. 480-485

Y. Hong, W. Q. Jin, X. H. Pan & Y. Shinichi, (2006). Experimental study on marangoni convection and solidification in BaB_2O_4 melt. *International Journal of Heat and Mass Transfer*, Vol. 49, pp. 4254-4257

Y. Liu, Fei Aai, X. H. Pan, Y. Zhang, Y. F. Zhou & C. D. Feng, (2010). Effect of rotating magnetic field on $Bi_{12}SiO_{20}$ crystal growth by vertical zone-melting technique. *Journal of Crystal Growth*, Vol. 312, pp. 1622-1626

Y. Zhang, Y. Liu, W. Jiang, X. H. Pan, W. Q. Jin & F. Ai, (2008). Vertical Bridgman growth of $Bi_{12}SiO_{20}$ crystal with axial vibration. *Journal of Crystal Growth*, Vol. 310, pp. 5432-5436

Y. Zhang, Y. Liu, W. Jiang, X. H. Pan, W. Q. Jin, F. Ai & H. C. Wang, (2009). Effect of axial vibration on $Bi_{12}SiO_{20}$ crystal growth by Vertical Bridgman technique. *Crystal Research and Technology*, Vol. 44, pp. 248-252

Z. H. Liu, W. Q. Jin, Z. L. Pan & N. Cheng, (1998). Experiments on surface tension driven flow in high temperature oxide melt. *Journal of Inorganic Materials*, Vol. 13, pp. 113-116 (in Chinese)

Part 5

Advances in Bioengineering Aspects

24

Supercritical Fluid Application in Food and Bioprocess Technology

K. Khosravi-Darani[1] and M. R. Mozafari[2]
[1]Department of Food Technology Research, National Nutrition and Food Technology, Research Institute, Faculty of Nutrition Sciences and Food Technology, Shahid Beheshti University of Medical Sciences, P. O. Box: 19395-4741, Tehran,
[2]Department of Food Science, Faculty of Food Science and Technology, University Putra Malaysia, 43400 UPM, Serdang, Selangor,
[1]Iran
[2]Malaysia

1. Introduction

There are several old and new applications for the supercritical fluid (SCF) technology in bioprocessing, including the nonthermal cell inactivation (Dillow et al., 1999; Spilimbergo and Bertucco, 2003; Hong and Pyun, 2001), permeabilization (Aaltonen and Rantakyla, 1991), extraction of fermentation products (Bruno et al., 1993; Hampson and Ashby, 1999; Isenschmid et al., 1995), removal of biostatic agents and organic solvents from fermentation broth, SCF disruption of yeasts (Castor and Hong et al., 1995; Lin and Chen, 1994; Lin et al., 1992; Nakamura et al., 1994) and bacteria (Juhasz et al., 2003; Khosravi- Darani et al., 2004), destruction of industrial waste (Kim and Hong, 2001), fractionatation and purification of biopolymers (Khosravi- Darani et al., 2003), removal of chlorinated compounds from water, and treatment of lignocellulosic materials (Puri, 1983). Some products possibly produced by the SCF technology may be found in processes to obtain vitamin additives, de-alcoholized beverages, de-fat potato chips, and encapsulated liquids. For more information on the other examples, the readers are referred to the literature (King and Bott, 1993; Brunner, 2005; McHugh and Krukonis, 1994; Bertucco and Spilimbergo, 2001). Khosravi-Darani et al. have reviewed all aspects of the supercritical fluid extraction (SCE) in the downstream processing of bioscience (Khosravi-Darani and Vasheghani-Farahani, 2005).

There are also several applications for the SCF technology in food engineering including: extraction of compounds from natural products (the processing of hops, the extraction of caffeine, vanilla, beta-carotene, and vegetable oils), food sterilization, removal of undesired extractable (pesticides residues, hazardous chemicals from fish tissue, oil from dry-milled corn germ), and fractionation of cod liver oil (Bruno et al., 1993). Catalytic reactions in supercritical CO_2 have been receiving an increased attention during the last decade (Sarkari et al., 1993).

This chapter has focused on SCF special applications in the field of food biotechnology. The application of SCF is simple, inexpensive, and noninjurious to the structure and function of enzymes (Lin et al., 1992) and protein activities (Kamat et al., 1995; Zheng and Tsao, 1996; Kasche et al., 1988). The supercritical carbon dioxide (SC-CO_2) is the most commonly used

fluid. It's low critical temperature of 31.1°C and the pressure of 7.3 MPa make it an ideal medium for processing volatile products (Wells and DeSimone, 2001). The non-toxicity, non-flammability, as well as the selectivity of the process and the ease of recovery are the most important features. Most of SCFs are available in a relatively pure grade at a reasonable cost as compared with the industrial grade liquid solvents. Therefore, many subsequent downstream clean-up steps are unnecessary supercritical extraction (SCE). By replacing the SCE to avoid liquid extraction, O_2 is always very efficiently displaced from the matrix. This prevents oxidation and autoxidation reactions from becoming a problem, as they are often in liquid extraction schemes. This fact is a particular advantage in biotechnology since many important natural products and drugs are oxygen-sensitive (Teja and Eckert, 2000).

There are also some limitations in the SCF applications e. g. change of the phase equilibrium; alter of phase diagram of the solvent, difficult prediction and design of extraction conditions; necessity for addition of impurities as modifiers (called entrainers or cosolvents) to SCF in quantities up to 5(%v/v); impossible real time control by the most accurate equations of state, necessity to unfired pressure vessels; high initial capital outlay due to the high cost of compressors (Bruno et al., 1993). Other applications of the SCF in food biotechnology can be summarized as follows: removal of fat; alcohol recovery from wine (Guvenc et al., 1998); encapsulation of liquids (Heremans and Smeller, 1998), recovery of tocochromanols (vitamin E) and beta-carotene (provitamin A).

Particulate products can be also achieved by means of SCF processing e.g. concentrated powder after spraying of CO_2–liquid mixture into a spraying chamber at ambient conditions together with the substrate; also flash release of CO_2 from the liquid will result in the formation of small droplets. The prevention of oxidation processes and easier handling, dosage, and storage are among the purported advantages of this process (Brunner, 2005).

2. The effect of high pressure and temperature on food constituents

High pressure (100–1000 MPa) affects biological constituents and systems. Several physicochemical properties of water are modified, such as density, ionic dissociation, pH, and the melting point of ice. The pressure-induced unfolding, aggregation, enzyme inactivation (e.g., of ATPase) and gelation of food proteins occurred due to effect on non-covalent bonds and interactions. Chemical reactions, macromolecular trans-conformations, changes in the membrane structure and the melting point are enhanced under pressure . Several of these phenomena, are involved in the high inactivation ratio of most vegetative microbial cells: gram negative bacteria, yeasts, complex viruses, molds, and gram-positive bacteria, in this decreasing order of sensitivity to pressure. Other parameters like pressure, holding time, temperature and the composition of medium influence this resistance. The pH has little influence, but high salt or sugar concentrations and low water contents, exert very strong baro-protective effects. Many other articles have also dealt with the stability of proteins as a function of pressure (Zagrobelny and Bright, 1992; Athes et al., 1998) and particularly with that of enzymes (Degraeve and Lemay, 1997; Marie-Olive et al., 2000).

3. The recovery and purification of biological products

Vijayan et al. have broadly classified the process applications into three product segments: High-value, Low-volume (HVLV); Intermediate-value, Intermediate-volume (IVIV) and

Low-value, High-volume (LVHV) products (Vijayan et al., 1994). The production of HVHV has been found to be very favorable for the exploitation of the SFE technology. The types of foods processed include: flavor, fragrance, spice extracts, and essential oils from plants (Wang and Muttucumaru, 2002), animals, and other materials; hop extraction to produce alpha and beta acids as well as essential oils; purification and fractionation of aroma constituents. In fact, the advent of food processing as a modern industry has ushered in the use of food extractives rather than raw materials.

The food extractives of spices, called oleoresins, are used in the food processing industry for their appealing flavor and to improve the product quality. The selectivity of the extraction can be achieved using SC-CO_2 and the essential oils of pepper and ginger can be extracted without much contamination of non-volatile matter by the suitable selection of the extraction pressure and temperature of CO_2 (Nguyen et al., 1994). In the SCE of ginger, the oxygenated fraction can be much higher than that in steam-distilled oils. The ginger-oils in oleoresin of ginger can be extracted without any decomposition. The piperine can be extracted with insignificant loss with longer process times. The jasmine and vanilla absolutes from this process have desirable top notes with rounded flavor and are superior to those obtained by conventional process. Examples for IVIV include: the removal of caffeine from coffee and tea; the xanthins from cocoa; excess oil from fried foods and vegetable. Studies on reducing the cholesterol content of animal fats and the extraction of lipids are in progress. Separation of the polyunsaturated fatty acids (PUFA), notably eicosapentacnoic acid (EPA) and decosahexanoic acid (DHA), which are purported to have beneficial physiological activity, from a mixture of fatty acid and ethyl esters from fish oils is reported (Hammam, 1992). With respect to the SFE of LVHV products, there are some doubts as to whether it is competitive with traditional extraction methods, e.g., the oil production from vegetable seeds; the processing of grain flours to improve quality and fractionation of beef tallow. Table 1 shows some valuable extractives from natural materials in food industry.

The SFE process parameters including pressure and temperature variations have been measured by HPLC and GC/MS (Wang and Muttucumaru, 2002).

4. The inactivation of food related bacteria

The application of high pressure ranging from 100 to 1000 MPa, is one of the most promising methods for the food treatment and preservation at room temperature (Debs-Louka et al., 1999). High pressure inactivation of *E. coli* pressure resistant had been investigated in fruit juices and in low pH buffers. The results show that both parents and mutant strains become more pressure-sensitive in decreased pH and presence of organic acids. The high pressure treatment for 5–10 min under 300–600 MPa at 20–50°C allows the reduction of vegetative microbial cells by 4–5 log cycles. However, some enzymes, especially polyphenoloxidase in fruit juices, are more pressure-resistant and their inactivation needs additional approaches (Molin, 1983). The degradation of color and slight changes of flavor due to the higher content of dissolved oxygen in products are mentioned as an example of negative pressure effects (Knorr, 1995). Pasteurization of milk and the heat resistance of *Mycobacterium avium* subsp *paratuberculosis* (Lund et al., 2002) also vegetative and the latent form of other microorganisms have been reviewed (Sojka and Ludwig et al., 1997; Paidhungat et al., 2002; Raso et al., 1998). It seems evident that it was not possible to kill spores at room temperature with an extremely high operating pressure, up to 170 MPa. It was observed that there is an optimum range of temperature and pressure for stimulating

the germination of spores (Nakayama et al., 1996; Roberts and Hoover, 1996). Therefore, the coupled action of hydrostatic pressure and of specific temperature was investigated in order to activate spores and consequently to inactivate their vegetative forms in a second step with higher operating pressure (Hong et al., 1999). Ludwig et al. carefully studied the behavior of spores under different operative conditions of the high temperature and pressure and introduced a cycle-type treatment (Ludwig et al., 1994; 1997); this appeared to be more efficient than the double level pressure treatment. It was concluded that at higher temperature, faster germination is obtained, as well as a wider range of pressure is suitable to this scope. Salts, glucose, and amino acids were found to enhance the rate of germination. However, until now a complete inactivation of spores has not been achieved yet. The regression analysis of inactivation rates showed that pressurization at sub-zero temperatures (−20 and −10°C) enhanced the effects of pressure as pressurization at higher temperatures (i.e., pressurization at 190 MPa and −20°C gave the same effect as pressurization at 320 MPa and room temperature). The results imply that high pressure treatment at lower temperatures has a greater effect on food sterilization without destroying the original taste and flavor. Additional effects of sugars and salts on the inactivation of yeast are also described (Hashizume et al., 1995).

Many recent studies demonstrate that SC-CO_2 as a non-toxic and inexpensive gas can also be used for the inactivation of viruses (Fages et al., 1998) and pest control. It is a promising alternative method for the pasteurization and sterilization of foodstuff (particularly in the liquid phase), sterilization of thermosensitive substances, as well as thermally and hydrolytically sensitive polymeric materials in biomedical applications. Furthermore, application of SC-CO_2 seems to be attractive for its economical feasibility, as it needs very low pressure (lower than 20 MPa) compared to the so–called ultra high pressure treatment (200–700 MPa) (Bertucco and Vetter, 2001). A number of papers have been addressed to the inactivation of a wide range of microorganisms, bacteria, spores, and yeasts in physiological solutions by SCF (Watanabe et al., 2004; Erkmen, 2001; Spilimbergo et al., 2002; Clery-Barraud et al., 2004).

In the field of industrial applications, it is worthy to quote some recent publications that have dealt with the inactivation in complex substrates and solid food (Haas et al. 1989; Gould, 2003; Arreola et al., 1991; Erkmen, 2000; 2001). All these authors tested the efficiency of the SC-CO_2 mainly in natural foods (e.g. milk, fruit juice, and eggs) in a batch system. Spilimbergo has also checked with high pressure CO_2 on red orange juice of Sicily (Spilimbergo et al., 2002). Spores of *B. coagulans, B. subtilis, B. cereus, B. licheniformis, and Geobacillus stearothermophilus* were subjected to CO_2 treatment at 30–200 MPa and 35–65°C. All of the bacterial spores except the *G. stearothermophilus* spores were easily inactivated by the heat treatment. The treatment with CO_2 and 30 MPa of pressure at 95°C for 120 min resulted in 5-log-order spore inactivation. The activation energy required for the CO_2 treatment of *G. stearothermophilus* spores was lower than the activation energy for heating or pressure treatment (Matsuda et al., 2004). Lund et al. have studied heat resistance of *Mycobacterium avium* subsp *paratuberculosis* and related problems in milk pasteurization (Lund et al., 2002). Kamihira et al. found a sterilizing effect of SC-CO_2 on various microorganisms at 20.3 MPa and 35°C (water content of 70 to 90) (Kamihira et al., 1987). Dried cells were not sterilized when treated under the same conditions. Bruna evaluated the composition changes of strawberry puree during high pressure pasteurization (Bruna et al., 1994). The inactivation effect of the native microorganisms in raw milk and raw cream is nearly the same. Fat does not influence the inactivation. The inactivation of milk enzymes

phosphohexose isomerase, gama-glutamyltransferase, and alkaline phosphatase occurs as a result of SC treatment (Sojka and Ludwig, 1997; Ishikawa et al., 1997). Blickstad et al. (1981) reported the effect of CO_2 on pork microflora and found that increasing the partial pressure of CO_2 added to the packaging atmosphere and prolonged the shelf life of the meat.
Factors, such as temperature, pressure, and moisture, contribute to a more effective treatment by increasing the diffusivity of CO_2 (Isenschmid et al., 1995; Kamarei and Arlington, 1988; Schreck and Ludwig, 1997; Smelt, 1998). Within certain limits, a longer duration of exposure to CO_2 permits better sterilization; exposure time can be decreased by increasing the temperature (Lund et al., 2002). Microbial resistance to CO_2 also depends on the type of microorganism, the phase of growth, moisture, (Lin and Chen, 1994; Kamihira et al., 1987) and the suspension medium, the last of which can inhibit the bactericidal effect of compressed CO_2, especially in some food systems rich in proteins (Ishikawa et al., 1995). Lin et al. suggested that swollen cell walls, due to the presence of water, become more CO_2 permeable (Lin et al., 1994). Finally, though the use of the CO_2 sterilization offers cost and environmental advantages, there is no guarantee that a CO_2 sterilizer will receive FDA approval. The analysis of the CO_2 sterilization shows a lower cost per cubic foot ($6) than EtO ($19) because of the shorter cycle time, lower cost per load, and lack of regulatory constraints without negative environmental and health effects.

Products	SCF	T/ °C	P/ MPa
Lecithin and Soya oil	Near critical CO_2 + deodorized propane	--	8
Progestrone, Testostrone, Chlosterol	CO_2 with or without N_2O	35-60	8-25
Glycerides of fatty acid short chain	CO_2	40	31
Cholesterol	CO_2	40-60	8-12
Pure saturated triglycerides with acyl chain length of 12-36 carbons	CO_2	40	13-30
Lipids from egg yolk	CO_2 & (methanol or ethanol)	--	--
Fatty acid-ethyl esters derived from cod river oil	CO_2	50	15
cis-5, 8,11,14,17 EPA and Cis-4, 7, 10, 16, 19 DHA from menhaden oil	CO_2	--	--
PUFA from fungus *saprolengia parasitica*	CO_2	60	35

Table 1. Some examples of supercritical fluid extraction of valuable constituents from natural materials in food industry (Nguyen et al., 1994)

The CO_2 technology showed some disadvantages including high capital cost; space needed to store the CO_2 cylinders; design and build a prototype that satisfy the temperature, pressure, humidity, and agitation requirements for the CO_2 sterilization (Schreck and Ludwig, 1997). High pressure has the advantage of retaining taste, color, and texture much better than heat treatments and also affects food constituents; proteins, lipids, and starches may undergo conformational changes. In Japan, high pressure pasteurization of acidic foods, such as fruit juices and jam, is being practiced on an industrial scale. Such "cold" processing might also be utilized in a useful way in industrial cheese-making processes of

typical hard cheeses from "raw milk". With this process it could be possible to reduce the overall microbial load adverse to making cheese without modifying the subtle chemico-physical balance of milk. As pressure-treated milk shows modified properties during further processing, such as changed rennet or acid coagulation characteristics, coagulation time, and gel firmness. Further studies should be carried out to understand whether the structural changes of milk compounds could worsen cheese-making processes (Cuoghi, 1993). Also, the effect of high pressure on microorganisms and enzymes of ripening cheeses were studied. A significant decrease of total microbial count was obtained at the pressure above 400MPa. It was found that the inactivation of microorganisms was affected more by their initial number than by the type of cheese and its maturity. *E. coli* was completely inactivated in 400 MPa pressurized cheeses irrespective of their initial count. *Enterococci* were inactivated at 400 MPa, while the pressure of 600 MPa was needed to achieve this effect in a 2-week-old cheese. Yeasts and moulds were inactivated with 200 MPa. Aminopeptidases and endopeptidases of both cheese and its extract lost the catalytic abilities at 600 MPa irrespective of the type and ripening time of cheeses (Reps et al., 1994). On the whole, the SCF sterilization has been reported as a successful approach in the sterilization of several kinds of food including; fruits, juices, vegetables, jam, meat, milk, wine, liquid whole egg, natural pigments, yoghurt, and even chocolate (Hammam, 1992).

5. The use of semi-preparative SCF chromatography for the separation and isolation of flavor and food constitutes

Many successful applications of this technique for the analysis of triglycerides in butter fat and fish oil have been described. The coupling of SFC with thin layer chromatography resulted in a powerful method for identification of trace substances such as phenolic antioxidants (Flament et al., 1994).

6. The application of sc-co_2 in citrus processing

- *Debittering of citrus juices*. Kimball (1987) use SC-CO_2 to extract bitter triterpenoids, such as limonin from orange juice in which the pressure increase from 2.14 to 4.28 MPa was effective on limonin reduction. A change in the final pH, vitamin C, pulp content, amino acids, and percentage of acid could not be detected.
- *Extracting and /or concentration of citrus essential oils*. Mira et al. reported that it was possible to concentrate the flavor portion of citrus oils with SC-CO_2 at 70°C and 83 MPa. These conditions were optimum forminimizing the amount of flavors lost in extraction, which also resulted in low extraction yields (Mira et al., 1999).
- *Effect on quality attributes and microorganisms*. The prevention of undesirable flavors caused by microorganisms growing under low pH conditions is important. Therefore, the SC-CO_2 treatment of orange juice had the added benefit of reducing microbial numbers.

7. The SCF application as dispersion for biocatalysis

The advantage of using enzymes in the SCF include; completion of synthesis reactions in which water is a product, the increased solubilities of hydrophobic materials, greater thermo-stability of biomolecules, readily solvent recycling, integrated biochemical reactions,

and separations. Enzymes such as alpha amylase, glucose oxidase, lipase, and catalase retained their activities in the solution of high pressure CO_2 in water. All thermal and non-thermal methods to stabilize could have their own disadvantages. So, the researchers have focused on the applicability of SC in this process (Nakamura, 1990). Soybean lipoxygenase dissolved in Tris HCl buffer (0.01M; pH 9) was irreversibly inactivated by combined pressure (up to 650 MPa) and low temperature (−15 up to 35°C) treatment. The enzyme inactivation followed a first order reaction and the phase transition of water did not change the kinetic inactivation behavior.

8. The treatment of wastes of food industries

Reports have described the use of SCFs for the treatment of lignocellulosic materials, which are the major group of wastes of food industries e.g. straw and bran of corn and cereal, leaf and pomace of sugar cane, fruitwaste, etc. SCF treatment allows further utilization of lignocellulosic materials as a resource for chemicals, pulp, and energy (Puri, 1983). Pretreatment methods have been sought to remove lignin and to permit further utilization of carbohydrates contained in lignocellulosic materials. Several SCFs (e.g. SC-methanol, SC-acetone, and SC-ammonia) an alternative to chemical pretreatments, which use strong acids or bases. Ammonia-treated lignocellulosic materials were neutralized and buffered to a pH value of 4.8 before being incubated at 50°C with a fractionated and partially purified commercial crude cellulose preparation from *Trichoderma reesei*. Aliquots taken at various times were filtered before being analyzed for sugars by HPLC. Two long-term experiments were made with diets consisting of preparations of spent hops and a sample of apple pomace, incubated in the Rumen Simulation Technique (RuSiTech). A significant increase in the total volatile fatty acids and methane production was observed when the preparations of spent hops were incubated in separate bags rather than in mixtures with other components (Cansell et al., 1997). Lignin, cellulose, and their mixture were gasified with a nickel catalyst in SC-water at 673 K and 25 MPa. The gasification efficiency was low, but increased with the amount of the catalyst when softwood lignin was included in the feedstock. One possible mechanism is the catalyst being deactivated by tarry products from the reaction between cellulose and softwood lignin. Sawdust and rice straw were gasified under the same condition (Yoshida et al., 2004).

9. The SCF application as dispersion for biocatalysis

The use of the SCF as a dispersion for biocatalysis was described in 1985 and there is now a growing trend in using the SCF as a reaction media for enzymes. The advantage of using enzymes in the SCF include; synthesis reactions in which water is a product can be driven to completion, the increased solubilities of hydrophobic materials, greater thermo-stability of biomolecules in SCF, readily solvent recycling, integrated biochemical reactions and separations. CO_2 is the most widely used SCF, however, there is a growing interest in using other SCFs (e.g., ethylene, fluoroform, ethane, sulfur hexafluoride and near critical propane).

Enzymes such as alpha amylase, glucose oxidase, lipase and catalase retained their activities in the solution of high pressure CO_2 in water. Among the enzymatic reactions in SCF, the use of lipase shows most commercial promise. A SC-CO_2/H_2O mixture may be used as a reaction medium for either hydrolytic or synthetic reactions catalyzed by lipase and other

appropriate by hydrolases (Giebauf et al., 1999). In continuous reaction of acidolysis of triolein with stearic acid, the constants of the reaction and mass transfer such as rate constant, solubility, effective diffusivity, mixing diffusivity and mass transfer coefficient depend on temperature, pressure and flow velocity (Nakamura, 1990).
Immobilized *Candida antarctica* lipase B was successfully used as catalyst to synthesize butyl butyrate from butyl vinyl ester and 1-butanol in SC-CO_2) with excellent results. A clear enhancement in the synthetic activity and selectivity was observed with the decrease in fluid density for both liquids and SC-CO_2 media (Lozano et al., 2004). Also a commercial solution of free *Candida antarctica* lipase B (Novozyme 525L) was immobilized by adsorption onto 12 different silica supports modified with specific side chains (e.g. alkyl, amino, carboxylic, nitrile, etc.). The best results were obtained for the supports modified with non-functionalized alkyl chains and when the in water activity increased from 0.33 to 0.90. Immobilized derivatives coated with ionic liquids clearly improved their synthetic activity in SC-CO_2 by up to six times with respect to the hexane medium (Lozano et al., 2007).
Pseudomonas cepacea lipase (PCL) was used to catalyze the trans-esterification reaction between 1-phenylethanol and vinyl acetate in SC-CO_2. The catalytic efficiency of enzyme enhances by increasing pressure. Moreover SC sulphur hexafluoride (SCSF6) was used as reaction medium. Results showed high stability of the enzyme in this SC medium in comparison to those achieved in SC-CO_2 (Celia et al. 2005).
Thermal stability of proteinase of *Carica papaya* was tested at atmospheric pressure, SC-CO_2, nearcritical propane and dimethyl-ether. In SC-CO_2 at 300 bar thermal activation of the enzyme was improved in the comparison to ambient pressure. Activity of the enzyme decreased in propane and dimethyl-ether (300 bar). Addition of water in the system increased activity, which was incubated in SC-CO_2 for 24 h (Habulin et al. 2005).
Isoamyl acetate was synthesized from isoamyl alcohol in SC-CO_2 by enzymatic catalysis. Among several reactants, including acetic acid and two different acetates, acetic anhydride gave best yields. An esterification extent of 100% was obtained in continuous operation using acetic anhydride (acyl donor) and Novozyme 435 (enzyme) (Romero et al. 2005). Cocoa beans had been subjected to various pod storage periods prior to fermentation were analysed for pyrazines and SCE (Sanagi et al. 1997).

9.1 SCFs: puissant media for the modification of biopolymers

The use of SCFs media for polymer modification has been demonstrated (Yalpani 1993). Treatment of chitosan mixtures with glucose or malto-oligosaccharides in SC-CO_2 afforded the corresponding water soluble imine-linked, branched chitosan derivatives with high degrees of conversion. Treatment of starch, maltodextrins, cellulose acetate, poly(vinyl alcohol) and paper in SC-CO_2 and O_2 (19:1 v/v) led to the corresponding oxidized materials.

9.2 Gasification of straw

Bioconversion of lignocellulosics consists of substrate pretreatment by high pressure steam (for fractionation into cellulose, hemicellulose and lignin components), enzymatic hydrolyze, followed by fermentation of the liberated sugars to ethanol. The various technoeconomic models developed by network members were used to identify probable process schemes and determine technical "bottlenecks" (Saddler 1992).

9.3 Waste treatment

Waste treatment is one of the most important and urgent problems in environmental management around the world. SC-water oxidation has attracted attention for the treatment of industrial waste, especially toxic and refractory waste. In a study, SC-water oxidation with H_2O_2 was applied as the oxidant to the treatment of a model municipal solid waste containing proteins, fats, vitamins, fiber, and inorganic minerals. The effects of temperature, oxidant concentration, and reaction time on the decomposition of solid waste were investigated in a batch reactor with hydrogen peroxide over the temperature range of 673-823 K. (Mizuno et al. 2000). SC-water is very reactive, corrosive, and miscible with air and oxygen. An industrial process was describes the use of SC water to treat aqueous solutions containing organic compounds (Haas et al. 1989). The operation of a process based on SCF technology was described to treat waste of recombinant fermentation (Krishna et al.1986).

9.4 Particle formation

The rapid expansion of SCF is a promising new technology for particle formation and distribution of biodegradable polymeric (Debenedetti et al. 1993). Because of the extreme fragility of organic aerogels attempts are made to develop inorganic aerogels. Such microcellular polymers foams can be obtained directly by polymerization in a near critical diluent and SC drying in the same reactor vessel. In polymer industry, polymerization is stopped by adding a termination agent. The polymer solution was contacted with superheated steam to remove unreacted monomer and polymerization solvent (de solvent process). SC-CO_2 extraction can be alternative for the de-solvent process of polymer solutions. In fact SC-CO_2 can reduce the drying process due to its capability of complete recovery by depressurizing. In addition, SC-CO_2 can dissolve the typical polymerization solvents, *n*-hexane or toluene at higher pressures. The design of the de-solvent process requires quantitative information on the distribution of organic solvent between the polymer solution and the SC-CO_2 phase (Inomata et al. 1999).

9.4.1 Preparation of liposome

Liposomes are non-toxic (mostly) and effective in encapsulation (Mortazavi et al. 2007) and controlled release in food industry (Mozafari and Khosravi-Darani 2008). Manufacturing of liposome by SCF covers three separate methods including: (i) phospholipids solvation in a near critical fluid, mixture with a protein containing buffered solution (ii) decompression of solvated phospholipids prior to injection to solution, (iii) the critical fluid decompression technique in which phospholipids are first hydrated in an aqueous buffer, mixed with SCF, with the mixture being then submitted to decompression. Several parameters can improve the characteristics of the liposomes prepared with SCF ethane. Optimization studies would be necessary to examine whether liposomes of higher quality can be made using SCF technology. Also, other SCF should be tested (Frederiksen et al. 1997).

9.5 Production of different morphologies of biocompatible polymers

SC antisolvent method has great potential for processing of pharmaceuticals (Mosqueira et al. 1981; Steckel et al. 1997) and labile compounds such as proteins (Debenedetti et al 1993; Winters et al. 1999; Yeo et al. 1994; Yeo et al. 1993) and to obtain various morphologies of biopolymers (Bleich et al. 1996; Debenedetti et al. 1993; Dixon and Johnstone 1993;

Reverchon 1999; Subramanian et al. 1997), such as microspheres (Falk et al. 1997) threads, fibers, networks (Dixon and Johnstone 1993), sponges, foams, and films. One of the advantages of using SCF in polymer processing is the possibility of producing different solid shapes and structures at low temperature with a minimum amount of residual organic solvents. Also the process is environmentally safe and economic (Elvassore et al. 2001). A basic description of these techniques is reported by Bertucco and Pallado (2000).
The conformation of monomeric enzyme trypsin has been reported in SC-CO_2 (Zagrobelny and Bright 1992). To follow in situ conformation of trypsin (as a function of CO_2 density), steady state fluorescence spectroscopy was used. Zagrobelny showed that protein denaturation can occur during the fluid compression step and that the native trypsin is only slightly more stable (1.2 kcal/mol) than the unfolded form.

9.6 Purification of natural active copolymers

Conventional purification methods are not specific and must be repeated or combined for highly purification. Although, (immuno) affinity-based procedures are rapid and specific; but they are expensive, and reagents from biological origin are needed. Also the interactions involved between the product and the support are often strong and imply the use of rather denaturing reagents (either for the product or the support) to attain an efficient desorption yield (Lemay 2002). SCE has introduced as a more suitable method for purification of natural products. This technique helps to remove trace impurities in the synthetic active biocopolymers from maleic anhydride and pinene (Jarzebski and Malinowski 1995).

10. Supercritical fluid extraction in bioprocess technology

Recent investigations on the applications of SCE from post fermentation biomass or *in situ* extraction of inhibitory fermentation products as a promising method for increasing yield are reviewed (Khosravi-Darani and Vasheghani-Farahani 2005). Although SC-CO_2 is unfriendly and toxic, for some living cells, which precludes direct fermentation in dense CO_2, it does not rule out other useful applications for *in situ* extraction of inhibitory fermentation products and fractional extraction of biomass constituents due to the potential of system modification by physical parameters and addition of co-solvents to selectively extract compounds of varying polarity, volatility and hydrophilicity with no contamination.

10.1 Advantages and disadvantages of SCE especially for the biotechnology industries

The advantages of utilizing SCE have been well documented (Schultz et al., 1991). The application of SCF is simple, inexpensive, non- injurious to the structure and function of some enzymes (Lin et al., 1992) and protein activities (Juhasz et al., 2003; Kamat et al., 1995; Zheng and Tsao, 1996). Nowadays, SCE is a well-known unit operation, with some industrial as well as many lab and pilot scale applications. Introduction of SC-CO_2 to fermentation broth decreases the overall viscosity, facilitates the handling of the broth and enhances mass transfer from the liquid to the SC-phase. Randolph has summarized special advantages of SCE, especially for the biotechnology industries (1990):

- High diffusivity reduces mass transfer limitations from porous solid matrices
- Low surface tension allows penetration and wetting of pores to extract from cell
- selectivity of extraction due to sensitivity of solubility to changes in P and T

- Manipulating crystal size of solid compounds produced from SCFs by change in P and T
- Separating of compounds that cannot be distilled, owing to their thermal instability.
- Increased enhancement factors (ratio of actual solubility to ideal gas solubility)
- Low reactivity and toxicity of SC-CO_2 or ethane, and their gaseous state

The main disadvantages of SCE processes include low solubility of biomolecules in SCF and high capital costs. Furthermore, insufficient data exist on the physical properties of many bio-molecules, making prediction of phase behavior difficult. The addition of co-solvents may obviate the advantage of minimal solvent residues in the final product.

10.2 Supercritical extraction (SFE) from biomass

10.2.1 Post fermentation extraction of products

There are only a few reports using SFE on bacterial cell. SCFs are found to be useful in extracting desired materials from animal tissues, cells, and organs (Kamarei and Arlington, 1988). By varying the choice of SCF, experimental conditions, and biological source materials, one may obtain lipids, proteins, nucleotides, saccharides, and other desirable components or remove undesirable components (Kamarei and Arlington, 1988). Processing of lipid natural products by SCF has been reviewed (King, 2004). SCF can be applied for obtaining aromatic and lipid components from plant tissues (Kamarei and Arlington, 1988), lignin conversion (Avedesian, 1986), carotenoids extraction from carrots (Bath et al., 1995), tomato paste waste (Baysal et al., 2000) and microalgae (Mendes et al., 1995). The CO_2 extraction process is selective in the presence of chlorophyll a.

Moreover, there are some reports which describe the SFE of bacterial (Gharaibeh and Voorhees, 1996) and fungal lipids (Cygnarowicz et al., 1992) for use in the classification of them by fatty acid profiles. A simple two–step process was developed to extract and purify medium chain length polyhydroxyalkanoates (MCL-PHA) from bacterial cells (*Pseudomonas resinovorans*) grown on lard and tallow (Hampson and Ashby, 1999). The process consists of SCE of the lyophilized cells with CO_2 to remove lipid impurities, followed by chloroform extraction of the cells to recover the MCL–PHA. SFE conditions were varied as to T 40 – 100°C, P (13.78 – 62.05 MPa), and CO_2 flow rate (0.5 – 1.5 L/min, expanded gas). The results show that the two- step process saves time, uses much less organic solvent, and produces a purer MCL-PHA biopolymer than previous extraction and purification methods. Khosravi-Darani et al. (2003) have reported the equilibrium solubility of poly(hydroxybutyrate) (PHB) in SC-CO_2. The effects of the main parameters such as P, T, and solvent density on solubility were determined at different T (35 – 75°C) and P (12.2 – 35.5) MPa. Hejazi et al. (2003) reported the effects of process variables such as exposure time, P, T, volume of methanol as a modifier, and culture history on PHB recovery from suspended *R. eutropha* in buffer solution. In another report, Khosravi-Darani et al. extended this work to obtain maximum recovery with minimum energy consumption (2004). In this work PHB recovery was examined using a combination of supercritical disruption and chemical (salt and alkaline) pretreatments. Bacterial cells, treated in growth phase, exhibited less resistance to disruption than nutrient limited cells in the stationary phase. It was also found that the wet cells could be utilized to recover PHB, but purity of the product was lower than that obtained from freeze-dried cells. Pretreatment with a minimum of 0.4% wt NaOH was necessary to enable complete disruption with two repetitions of P release. Salt pretreatment was less effective; however, disruption was improved by the application of alkaline shock.

The use of SCE of biologically active compounds (chaetoglobosin A, mycolutein, luteoreticulin, 7,8–dihydro–7,8–epoxy–1–hydroxy–3–hydroxymethylxanthone–8–carboxylic

acid methyl ester, sydowinin B and elaiophylin) from the biomass has been compared with organic solvents extraction (methanol and dichloromethane). The extraction strength of SC-CO_2 alone appeared to be lower than that of dichloromethane. All the components of interest that were extractable with dichloromethane and methanol were also extractable with methanol-modified CO_2 (Cocks et al., 1995). A technique for the SC-CO_2 extraction of the fungal metabolite ergostrol in its free (non-conjugated) form was developed and applied to samples of flour moldy bread and mushrooms. The overall method showed an 83% recovery of free ergostrol for spiked bread flour (Young and Games, 1993).
Citric acid has successfully been separated from fermentation broth by a novel and unique purification process, which is characterized by organic solvent extraction and precipitation with compressed CO_2 as a poor solvent. Compressed CO_2 was then dissolved in acetone solution of crude citric acid to remove the residual impurities as precipitates using the anti-solvent effect of CO_2. Citric acid crystals could be obtained by the anti-solvent crystallization with CO_2 (Shishikura et al., 1992). Dry mouldy bran resulting from solid state fermentation of *Gibberella fujikuroi* were subjected to SCE. The extraction of the sterol by SCE was found to improve with the use of ethanol as entrainer. The solid material retained the gibberellic acid activity without any loss (Kumar et al., 1991). The solubility of cholesterol in SCFs have also been studied and the solubility is correlated by using equation of states (Hartono et al., 2001).
Extraction of ethanol from aqueous phase of a yeast fermentation broth has been described and a lower energy cost as compared to distillation has been reported (De Filippi and Moses, 1983). Shimshick reported the extraction of carboxylic acids from dilute aqueous media with SC-CO_2. The specific advantage of this application is the pH decrease of the aqueous phase, which results in a higher concentration of the free acids. This shift is necessary for effective extraction of the carboxylic acids (Shimshick, 1981). SC-CO_2 extraction has been reported to be more suitable for extraction of non-polar compounds with molecular weights less than 400. Griseofulvin is an antifungal antibiotic having a molecular weight of 353, making it amenable to SC-CO_2 extraction. The optimized conditions for SCE of griseofulvin from dried media after solid state fermentation were obtained (Saykhedkar and Singhal, 2004). Furthermore, SCF has been developed mainly for unit operation to recover intracellular enzymes, recombinant-DNA proteins and nucleic acids from microbial cell cultures (Khosravi-Darani, 2005, Castor and Hong, 1995).

10.2.2 In situ extraction from the biomass of microbial fermentation

In situ product removal is the fast removal of product from a producing cell thereby preventing its subsequent interference with cellular or medium components. Freeman and coworkers indicated future directions including application in situ extraction to a wider range of products and the developed methodologies, applicable under sterile conditions in the immediate vicinity of the producing cells (Freeman et al., 1993). End-product inhibition occurs in many fermentation processes and *in situ* removal of them typically enhances product formation rates, yields, and specificity (Christen et al., 1990; Gyamerah and Glover, 1996; Qureshi et al., 1998). Techniques that have been employed for *in situ* removal of fermentation products include liquid-liquid extractive fermentation (Adrian et al., 2000), use of selective membranes (Chang et al., 1992), cell recycling (Roca and Olsson, 2003), adsorption (Millitzer et al., 2002), microcapsule application (Stark et al., 2003) and vacuum fermentation (Qureshi et al., 1998). However, the intimate contact of an organic phase with the broth implies that the organic components of this phase may be present in the aqueous

phase at saturation levels. The disadvantage of liquid-liquid extraction is the residual of toxic solvent, which presents significant separation, purification, and environmental challenges (Job et al., 1989). Also membrane fermentation and adsorption vacuum fermentation are not cost-effective. Guvenc et al. (1998) demonstrated the feasibility of ethanol extraction from a post–fermentation broth using SC-CO_2. However, application of SC-CO_2 for *in situ* extractive fermentation has been limited by its inhibitory effect on the metabolism of a variety of yeasts and bacteria (Isenschmid et al., 1995; Van Eijs et al., 1988). This toxicity is attributed, in part, to the acidic pH (Toews et al., 1995) that results from the increased solubility of CO_2 at high partial Ps (Knutson et al., 1999). By buffering the medium and carefully controlling the compression and expansion conditions, the survival rate of cells increases. Van Eijs et al. developed an extraction procedure in which the *Lactobacillus plantarum* cell death was minimized (Van Eijs et al., 1988).

The impact of dense gases and SCF (N_2, CO_2, and ethane) on the carbohydrate consumption and ethanol formation by *Clostridium thermocellum* has been reported. Non–growing cells capable of metabolism were incubated at 60°C with cellobiose as a substrate in the presence of the three pressurized fluids. The rate and extent of ethanol production were similar in cell suspensions maintained at atmospheric and 6.9 MPa P under nitrogen (conventional method). Ethane at 6.9 MPa reduced the extent of ethanol production by less than 20% relative to the atmospheric control, whereas CO_2 at the same P reduced ethanol formation. The results suggest that pressurized hydrocarbons have benefits over SC-CO_2 for the *in situ* recovery of volatile microbial products (Knutson et al., 1999).

In situ extraction of acetone, butanol and ethanol from synthetic media, simulating the downstream processing of a *Clostridium acetobutylicum* fermentation broth has been described (Van Eijs et al., 1988). It was also observed that extraction yield is a close function of the extraction time. Also increased P helps to achieve higher yields (Guvenc et al., 1998).

The extractive fermentation of 2-phenylethyl alcohol, the rose aroma, coupling fermentation with *Kluyveromyces marxianus* and SC-CO_2 extraction has been reported (Fabre et al., 1999). Similar results show enhancement of 2-phenylethanol productivity by *Saccharomyces cerevisiae* in two-phase fed batch fermentation using solvent immobilization (Serp et al., 2003). Stark and coworkers reported the extractive bioconversion of 2-phenylethanol by *Saccharomyces cerevisiae* (2002). It has further been reported that furfural, a growth inhibitory byproduct, was successfully removed during fermentation of *clostridium* on sugars by introducing liquefied CO_2 at room T and 5.9 MPa (Sako et al., 1992).

Selection of biocompatible solvents is critical when designing bio-processing applications for the *in situ* biphasic extraction of metabolic end-products. The prediction of the biocompatibility of supercritical and compressed solvents is more complicated than that of liquid solvents, because their properties can change significantly with P and T. The activity of the anaerobic thermophilic bacterium, *Clostridium thermocellum*, was studied when the organism was incubated in the presence of compressed nitrogen, ethane, and propane at 333 K and multiple pressure (Jason et al., 2000)

10.2.3 Fractionation of cellular biomass

SC and near critical fluids are used to fractionate biomass materials such as microbial cells in two steps. In the first step, the biomass is exposed to elevated pressure SC or near critical fluid to bring about disruption of the biomass to liberate structural biomass constituents. In the second step, the disrupted biomass is subjected to a multiplicity of SC or near critical fluid extraction steps, with different solvation conditions used for each fraction. Thus,

fractionation of the biomass to obtain one or more compounds is effected (Castor and Hong, 1995). Different solvation properties are obtained using different Ts, Ps and/or modifier concentrations. Industrial applications are designed to take benefit of the very high selectivity of SCFs with attractive costs related to continuous operation: polymer fractionation, aroma production from fermented and distilled beverages, polyunsaturated fatty acids, active compounds from fermentation broth, pollution abatement on aqueous streams, etc (Perrut, 2000). SC and near critical CO_2 have been used to fractionate cellular biomass isolated from soil, air, water, swamps, hot springs, sea water, animal or plant (Castor et al., 1998).
A SCE procedure and a chromatographic separation/detection method were developed for the detection of earth-based microorganisms. The analytical results demonstrated the feasibility of using the reported techniques to detect the chemical signature of life in barren desert sand samples (Lang et al., 2002).
Another interesting application of SCF in biotechnology is detecting the presence of a microorganism in an environmental sample. In this strategy, after exposure of sample to SCF nucleic acid will be isolated from the microorganism and detecting the presence of a particular sequence of nucleic acid by hybridization and PCR method, the contamination will be identified (Nivens and Applegate, 1996).

11. Conclusion

Application of supercritical is a promising alternative method for the pasteurization and sterilization of foodstuff, thermo sensitive substances, as well as thermally and hydrolytically sensitive polymeric materials, e.g. polymeric particles for drug delivery or implants. Furthermore, application of SC-CO_2 seems to be attractive for its economical feasibility, as it needs very low pressure (lower than 20 MPa) compared to the so–called ultra high pressure treatment (200–700 MPa). Another special applications of SCFs in food processing include the decaffeination of green coffee beans, the production of hops extracts, the recovery of aromas and flavors from herbs and spices, the extraction and fractionation of edible oils and the removal of contaminants. These applications are now extended to new areas like formulation or specific chemical reactions, due to lightening environmental regulations; concern over the use of chemical solvents in food manufacturing; increased demand for higher quality products; increased cost of energy.
In the future, two areas of SCF applications in food industry are forecast for growth; the treatment of industrial wastes and the high value added products. So new application will developed e.g. novel processes for the disruption of microorganisms of therapeutic interest, the production of liposomes with implication to the cosmetic and pharmaceutical industries, and even a process to destroy and remove viruses effectively. The emergence of such a process brings real excitement and suggests that in the field of pharmaceutical and bioprocess industries, commercial applications may find their way to its implementation in the next decade.
Future trends in industrial development of SCFs include; legal issues which require banning organic solvents, quality consideration (raw material decontamination) for instance, pests from tropical products; the extraction of residues and toxins from food materials; as well as the deodorization and removal of fat, cholesterol, caffeine.
From the results of a number of extractions reported in literature can be concluded that by application of SC-CO_2 selective, extraction of several compounds from fermentation broth is

possible. Non polar compounds can be extracted at low energy costs by this procedure. The process is cost effective due to carrying out at fermentation temperature. If whole fermentation broth put in contact with SC-CO_2, may inactivate the microorganisms. These results offer the opportunity of in situ extraction of fermentation products with SC or sub critical (liquid) CO_2. Use of SCF for both the disruption and extraction simplifies the procedure, and minimizes equipment and labor needs, time, contamination and loss of yield. In fact, the entire process can be readily automated. The use of super or near critical fluids allows for easy removal of the solvent by depressurization. The use of SCF allows the control of extraction condition by variation of temperature, pressure or modifier solvents.
The finding that fermentation conditions influence the resistance of microbial cells to disruption should be further investigated. Studies of disruption kinetics and of the influence of cell morphology on kinetics of disruption are needed, and not information is available on disruption of mycelial organisms. The effects of thermal deactivation on cell properties and pre-incubation temperature on cell resistance to heat shock have received less attention. Further work is therefore required to characterize this interaction and relate it to changes in cell and broth properties.

12. References

Aaltonen, O. & Rantakyla, M. (1991). Biocatalysis in supercritical CO_2, *Chemical Technology,* Vol.21, pp. 240-248. ISSN 1744-1560

Adrian, T., Freitag, J. & Maurer, G. (2000). A novel high-pressure liquid-liquid extraction process for downstream processing in biotechnology: Extraction of cardiac glycosides. *Biotechnology and Bioengineering,* Vol.69, pp. 559-65. ISSN 0006-3592

Arreola, A.G., Balaban, M.O., Marshall, M., Peplow, A., Wei, C.I. & Scornell, J. (1991). Supercritical carbon dioxide effects on some quality attributes of single orange juice, *Journal of Food Science*, Vol.56, pp. 1030-1033. ISSN 0022-1147

Athes, V., Lange, R. & Combes, D. (1998). Influenec of polyols on the structural properties of *Kluyveromyces lactis* β-galactosidase under high hydrostatic pressure, *European Journal of Biochemistry,* Vol.255, pp. 206-212. ISSN 0021-924X

Avedesian, M.M. (1986). Apparatus and method involving supercritical fluid extraction; USP:4,714,591.

Baysal, T., Ersus, S. & Starmans, D.A.J. (2000). Supercritical CO_2 extraction of beta-carotene and lycopene from tomato paste waste. *Journal of Agricultural Food Chemistry*, Vol.48, pp. 5507-11. ISSN 1684-5315

Bertucco, A. & Pallado, P. (2000). Micronization of polysaccharide by a supercritical antisolvent techniques, In: *Supercritical fluid methods and protocols*: *Methods in biotechnology,* J.R. Williams & A. A. Clifford, (Ed.), pp. (193-200), Humana Press, ISBN 0896035719, Totowa.

Bertucco, A. & Spilimbergo, S. (2001). Treating microorganisms with High Pressure. In: *High Pressure Process Technology: Fundamentals and Applications*, A. Bertucco & G. Vetter (Ed.), pp. (626-630), Elsevier Science, Amsterdam. ISBN 139780444504982

Bertucco, A. & Vetter, G. (2001). *High Pressure Technology Fundamentals and Applications*, Elsevier, Amsterdam, 626-640. ISBN 139780444504982

Bleich, J. & Mueller, A. (1996). Production of drug based microparticles by the use of supercritical gases with the aerosol solvent extraction system (ASES) process. *Journal of Microencapsulation,* Vol.13, pp. 131-139. ISSN 0265-2048

Blickstad, E., Enfors, S.O. & Molin, G. (1981). Effect of hyperbaric carbon dioxide pressure on the microbial flora of pork stored at 4 or 140°C, *Journal of Applied Bacteriology,* Vol.50, pp. 493-504. ISSN 0021-8847

Brennecke, J. F. & Eckert, C. A. (1989). Phase equilibria for supercritical fluid process design. *AIChE Journal*, Vol. 35, pp. 1409-27. ISSN 0001-1541

Bruna, D., Istenesova, L., Volrich, M. & Cerovsky, M. (1994). Composition changes of strawberry puree during high pressure pasteurization. In: *High Pressures Food Science and Bioscience Chemistry*, S.I. Neil, (Ed.), pp. (248-253), The Royal Society of Chemistry, ISBN 139781855738232, UK.

Brunner, G. (2005). Supercritical fluids: technology and application to food processing, *Journal of Food Engineering,* Vol.67, pp. 21-33. ISSN 0260-8774

Bruno, T. J., Castro, C., Hamel, J. P. & Palavra, A. M. F. (1993).Supercritical fluid extraction of biological products. In: *Recovery Processes for Biological Materials*, J.F. Kennedy & J. Cabral, (Ed.), pp. (303-354), John Wiley and Sons, ISBN 10047193349X, New York.

Cansell, F., Rey, S. & Beslin, P. N. (1997). Thermodynamic aspects of supercritical fluids processing: applications to polymers and waste treatments, *Review on Institute France Petroleum,* Vol.53, pp. 71-98. ISSN n.d.

Castor, T. P. & Hong, G. P. (1995). Supercritical fluid disruption of and extraction from microbial cells, USP:5,380,826.

Castor, T. P., Chikarmane, H. M., Hong, G. T. & Shallice, C. (1998). Methods for fraction of biological-derived materials. USP:5,854,064.

Celia, E., Cernia, E., Palocci, C., Soro, S. & Turchet, T. (2005). Tuning *Pseudomonas cepacea* lipase (PCL) activity in supercritical fluids. *Journal of Supercritical Fluids,* Vol. 33. pp. 193-199. ISSN 0896-8446

Chang, C. J. & Randoplh, A. D. (1991). Separation of β-carotene mixtures precipitated from liquid solvents with high pressure CO_2, *Biotechnology Progress,* Vol.109, pp. 275-278. ISSN 8756-7938

Chang, H. N., Yang, J. W., Park, Y. S., Kim, D. J. & Han, K. C. (1992). Extractive ethanol production in a membrane cell recycle bioreactor. *Journal of Biotechnology,* Vol.24, pp. 329-43. ISSN 0168-1656

Clery-Barraud, C., Gaubert, A. & Masson, P. (2004). Combined effects of high hydrostatic pressure and temperature for inactivation of *Bacillus anthracis* spores, *Applied Environmental Microbiology,* Vol.70, pp. 635-637. ISSN 0099-2240

Cocks, S., Wrigley, S. K., Chicarelli-Robinson, M. I. & Smith, R. M. (1995). High-performance liquid chromatography comparison of supercritical fluid extraction and solvent extraction of microbial fermentation products. *Journal of Chromatography,* Vol. 697, pp. 115-22. ISSN: 0021-9673

Cuoghi, F. (1993). Use of high-pressure in the food-industry-cold sterilization of milk and influence on its properties, *Industrial Aliment,* Vol.32, pp. 956-964. ISSN n.d.

Cygnarowicz, P. M., O'Brien, D. J., Maxwell, R. J. & Hampson, J. W. (1992). Supercritical fluid extraction of fungal lipids using mixed solvents: experiment and modeling. *Journal of Supercritical Fluids*, Vol.5, pp. 24-30. ISSN 0896-8446

De Filippi, R. P. & Moses, J. M. (1983). Extraction of organics from aqueous solutions using critical fluid carbon dioxide. *Biotechnology and Bioengineering Symposium*, Vol.12, pp.205-19.

Debenedetti, P. G., Tom, J. W., Kwauk, X. & Yeo, S. D. (1993). Rapid expansion of supercritical solutions (RESS): fundamentals and applications. *Fluid phase Equilibria*, Vol. 82, pp. 311-321. ISSN 0378-3812

Debs-Louka, E., Louka, N., Abraham, G., Ghabot, V. & Allaf, K. (1999). Effect of compressed carbon dioxide on microbial cell viability, *Applied Environmental Microbiology,* Vol. 65, pp. 626-631. ISSN 0099-2240

Degraeve, P. & Lemay, P. (1997). High pressure-induced modulation of the activity and stability of *E. coli* β-galactosidase: potential applications, *Enzyme and Microbial Technology*, Vol. 20, pp. 550-557. ISSN 0141-0229

Denery, J. R., Dragull, K., Tang, C. S. & Li, Q. X. (2004). Pressurized fluid extraction of cartenoids from *Haematococcus pluvialis* and *Dunaliella salina* and kavalactones from piper methysticum, *Analytical Chimical Acta,* Vol. 501, pp. 175-181. ISSN 0003-2670

Dillow, A. K., Dehghani, F., Hrkach, J. S., Foster, N. R. & Langer, R. (1999). Inactivation of various microorganisms using carbon dioxide at high pressure, *Proceeding National Academic Science USA*, Vol. 96, pp. 10344-10348.

Dixon, D. J. & Johnstone, K. P. (1993). Formation of microporous polymer fibers and oriented fibrils by precipitation with a compressed fluid antisolvent. *Journal of Applied Polymer Science,* Vol.50, pp. 1929-1942. ISSN 0021-8995

Elvassore, N., Baggio, M., Pallado, P. & Bertucco, A. (2001). Production of different morphologies of biocompatible polymeric materials by supercritical CO_2 antisolvent techniques. *Biotechnology and Bioengineering,* Vol.73, pp. 449-457. ISSN 0006-3592

Erkmen, O. (2000). Effect of Carbon dioxide pressure on *Listeria monocytogenes* in physiological saline and foods, *Food Microbiology,* Vol.17, pp. 589-596. ISSN 0740-0020

Erkmen, O. (2001). Effect of high-pressure carbon dioxide on *Escherichia coli* in nutrient broth and milk, *International Journal of Food Microbiology,* Vol.65, pp. 131–135. ISSN 0168-1605

Fabre, C. E., Condoret, J. S. & Marty, A. (1999). Extractive fermentation of aroma with supercritical CO_2. *Biotechnology and Bioengineering,* Vol.64, pp. 392-400. ISSN 0006-3592

Fages, J., Poirier, B., Barbier, Y., Frayssinet, P., Joffret, M. L., Majewski, W., Bonel, G. & Larzul, D. (1998). Viral inactivation of human bone tissue using supercritical fluid extraction, *Asaio Journal,* Vol.44, pp. 289-293. ISSN 1058-2916

Falk, R., Randolph, T., Meyer, J. D., Kelly, R. M. & Manning, M. C. (1997). Controlled release of ionic pharmaceuticals from poly(L-lactide) microspheres produced by precipitation with a compressed antisolvent. *Journal of Controlled Release,* Vol.44, pp. 77-85. ISSN 0168-3659

Flament, I., Keller, U. & Wunsche, L. (1994). Use of semi-preparative supercritical fluid chromatography for the separation and isolation of flavor and food constitutes, In: *Supercritical Fluids Processing of Food and Biomaterials*, S.H. Rizvi, (Ed.), pp. (62-74), Chapman and Hall, ISBN 0751401846, Glasgow.

Frederiksen, L., Anton, K., Van-hoogevest, P., Keller, H.R. & Leuenberger, H. (1997). Preparation of liposomes encapsulating water-soluble compounds using supercritical carbon dioxide. *Journal of Pharmaceutical Science,* Vol.86, pp. 921-928. ISSN 0022-3549

Gharaibeh, A. A. & Voorhees, K. J. (1996). Characterization of lipid fatty acids in whole cell microorganisms using *in situ* SCF derivatization-extraction and gas chromatography mass spectrometry. *Analytical Chemistry,* Vol.68, pp. 2805-10. ISSN 0003-2700

Giebauf, A., Magor, W., Steinberger, D. J. & Marr, R. (1999). A study of hydrolases stability in supercritical carbon dioxide. *Enzyme and Microbial Technology* Vol.4, pp. 577-583. ISSN 0141-0229

Gould, G. W. (2003). Microbiological safety of new food preservation technologies, *Acta Alimentaria*, Vol.32, pp. 215-217. ISSN 0139-3006

Guarsie, G. B., Bertucco, A. & Pallado, P. (1994). CO_2 as a Supercritical Solvent in Fatty Acid Refining; Theory and Practice. In: *Supercritical Fluids Processing of Food and Biomaterials*, S.H. Rizvi, (Ed.), pp. (27-43), Chapman and Hall, ISBN 0751401846, Glasgow.

Guvenc, A., Mehmetoglu, U. & Calimli, A. (1998). Supercritical CO_2 extraction of ethanol from fermentation broth in a semi continuous system. *Journal of Supercritical Fluids*, Vol.13, pp. 325–9. ISSN 0896-8446

Gyamerah, M. & Glover, J. (1996). Production of ethanol by continuous fermentation and liquid-liquid extraction. *Journal of Chemical Technology and Biotechnology,*Vol.66, pp. 145–52. ISSN 0142-0356

Haas, G. J., Prescott, H. E. J., Dudley, E., Dik, R., Hintlian, C. & Keane, L. (1989). Inactivation of microorganisms by carbon dioxide under pressure. *Journal of Food Safety,* Vol.9, pp. 253-265. ISSN 1745-4565

Habulin, M., Primozic, M. & Knez, Z. (2005). Stability of proteinase form Carica papaya latex in dense gases. *Journal of Supercritical Fluids,* Vol. 33, pp. 27-34. ISSN 0896-8446

Hammam, H. (1992). Solubilities of pure liquids in supercritical carbon dioxide, *Journal of Supercritical Fluids*,Vol. 5, pp.101-106. ISSN 0896-8446

Hampson, J. W. & Ashby, R. D. (1999). Extraction of lipid-grown bacterial cells by supercritical fluid and organic solvent to obtain pure medium chain-length polyhydroxyalkanoates, *Journal of the American Oil Chemists' Society,* Vol.76, pp. 1371-1374. ISSN 0003-021X

Hartono, R., Mansoori, G. A. & Suwono, A. (2001). Prediction of solubility of biomolecules in supercritical solvents. *Chemical Engineering Science,* Vol.56, pp. 6949-58. ISSN 0009-2509

Hashizume, C., Kimura, K. & Hayashi, R. (1995). Kinetic-analysis of yeast inactivation by high-pressure treatment at low-temperatures, *Bioscience Biotechnology and Biochemstry,* Vol.59, pp. 1455-1458. ISSN 0916-8451

Hejazi, P. Vasheghani-Farahani, E. & Yamini, Y. (2003). Supercritical fluid disruption of *Ralstonia eutropha* for poly(β-hydroxybutyrate) recovery, *Biotechnology Progress,* Vol.19, pp. 1519-1523. ISSN 8756-7938

Heremans, K. & Smeller, L. (1998). Protein structure and dynamics at high pressure, *Biochimca Biophysica Acta,* Vol.1386, pp. 353-370. ISSN 1570-9639

Hong, S.I. & Pyun, Y.R. (2001). Membrane damage and enzyme inactivation of *lactobacillus plantarum* by high pressure CO_2 treatment, *International Journal of Food Microbiology,* Vol.63, pp. 19-28. ISSN 0168-1605

Hong, S. I., Park, V. & Pyun, Y. R. (1999). Nonthermal inactivation of *Lactobacillus planetarium* as influenced by pressure and temperature of pressurized carbon dioxide, *International Journal of Food Science and Technology,* Vol.34, pp. 125-130. ISSN 0950-5423

Ibanez, E., Lopez-Sebastian, S., Ramos, E., Tabera, J. & Reglero, G. (1997). Analysis of highly volatile components of foods by off-line SFE/GC, *Journal of Agricultural Food Chemistry,* Vol.45, pp. 3940-3943. ISSN 0021-8561

Ikushima, Y., Saito, N. & Goto, T. (1989). Selective extraction of oleic, linoleic and linolenic acid methyl esters from their mixtures with SC-CO_2 entrainer systems and a correlation of the extraction efficiency with a solubility parameter, *Industrial Engineering Chemical Research,* Vol.28, pp. 1364-1371. ISSN 0888-5885

Inomata, H., Honma, Y., Imahori, M. & Arai, K. (1999). Fundamental study of the de-solvating polymer solutions with supercritical CO_2. *Fluid phase equilibria,* Vol.158-160, pp. 857-867. ISSN 0378-3812

Isenschmid, A., Marison, I. W. & Von Stockar, U. (1995). The influence of pressure and temperature of compressed CO_2 on the survival of yeast cells, *Journal of Biotechnology,* Vol.39, pp. 229-237. ISSN 0168-1656

Ishikawa, H., Shimoda, M., Shiratsuchi, H. & Osajima, Y. (1995). Sterilization of microorganisms by supercritical CO_2 micro-bubble method, *Bioscience Biotechnology and Biochemistry,* Vol.59, pp. 1949-1950. ISSN 0916-8451

Ishikawa, H., Shimoda, M., Tamaya, K., Yonekura, A., Kawano, T. & Osajima, Y. (1997). Inactivation of Bacillus spores by supercritical carbon dioxide micro-bubble method, *Bioscience Biotechnology and Biochemistry,* Vol.61, pp. 1022-1023. ISSN 0916-8451

Jarzebski, A. B. & Malinowski, J. J. (1995). Potentials and Prospects for Application of Supercritical Fluid Technology in Bioprocessing, *Process Biochemistry,* Vol.30, pp. 343-352. ISSN 1359-5113

Jay, A. J., Steytler, D. C. & Knights, M. (1991). Spectrophotometric studies of food colors in near-critical carbon dioxide, *Journal of Supercritical Fluids,* Vol.4, pp. 131-141. ISSN 0896-8446

Job, C., Blass, E., Schertler, C., Straudenbauer, W.L. & Bunsenges, B. (1989). Problems concerning liquid liquid extraction of extracellular products directly from fermenter broths. *Physical Chemistry,* Vol.93, pp. 997–1000. ISSN n.d.

Juhasz, T., Szekely, E., Simandi, B., Szengyel, Zs. & Reczey, K. (2003). Recovery of a recombinant thermostable endoglucanase from *E. coli* using supercritical carbon dioxide cell disruption, *Chemical and Biochemical Engineering Q.,* Vol.17, pp. 131-34. ISSN 1846-5153

Kamarei, A. R. & Arlington, M. A. (1988). Supercritical fluid extraction of animal derived materials. USP: 4,749,522.

Kamat, E. J., Beckman, A. & Russell, J. (1995). Enzyme activity in supercritical fluids, *Critical Review on Biotechnology,* Vol.15, pp. 41-71. ISSN 0738-8551

Kamihira, M., Taniguchi, M. & Kobayashi, T. (1987). Sterilization of microorganisms with supercritical and liquid carbon dioxide, *Agricultural Biological Chemistry,*Vol.51, pp. 407-412. ISSN n.d.

Kasche, V., Schlothaucer, R. & Brunner, G. (1988). Enzyme denaturation in supercritical CO_2: stabilizing effects of S-S bonds during depressurization step, *Biotechnology Letter,* Vol.10, pp. 569-574. ISSN 0141-5492

Khosravi-Darani, K. & Vasheghani-Farahani, E. (2005). Application of supercritical fluid extraction in biotechnology, *Critical Review on Biotechnology,* Vol.25, pp. 1-12. ISSN 0738-8551

Khosravi-Darani, K., Vasheghani-Farahani, E., Shojaosadati, S. A. & Yamini, Y. (2004). The effect of process variables on supercritical fluid disruption of *Ralstonia eutropha* cells for poly(hydroxybutyrate) recovery, *Biotechnology Progress,* Vol.6, pp. 1757-1765. ISSN 8756-7938

Khosravi-Darani, K., Vasheghani-Farahani, E. & Yamini, Y. (2003). Solubility of polyhydroxy butyrate in supercritical carbon dioxide, *Journal of Chemical Engineering Data,* Vol.48, pp. 860-863. ISSN 0021-9568

Kim, K. H. & Hong, J. (2001). Supercritical CO_2 pretreatment of lignocellulose enhances enzymatic cellulose hydrolysis, *Bioresource Technology,* Vol.77, pp. 139-144. ISSN 0960-8524

Kimball, D.A. (1987). A research note on debittering of citrus juice using supercritical carbon dioxide, *Journal of Food Science,* Vol.52, pp. 481-482. ISSN 0022-1147

King, J. W. (2004). Advances in critical fluid technology for food processing, *Food Science and Technology Today*, Vol.14, pp. 186-191. ISSN 0950- 9623

King, M. B. & Bott, T. R. (1993). *Extraction of Natural Products Using Near-Critical Solvents,* Champman and Hall, pp. 981-987, ISBN, 0751400696, UK.

Knorr, D. (1995). High pressure effect on plant derived foods. In: *High Pressure Processing of Foods,* D. A. Leward, D. E. Johnston, R. G. Earnshaw, A. P. M. Hasting, (Ed.), pp.(123-140), Nottingham University Press, ISBN, 13: 9780813809441, UK.

Knutson, B. L., Strobel, H. J., Nokes, S. E., Dawson, K. A., Berberich, J. A. & Jones, C. R. (1999). Effect of pressurized solvents on ethanol production by the thermophilic bacterium *Clostridium thermocellum*. *Journal of Supercritical Fluids*, Vol.16, pp. 149-56. ISSN 0896-8446

Krishna, G., Czerkawski, J. W. & Breckenridge, G. (1986). Fermentation of various preparations of spent hops (*Humulus lupulus* L.) using the rumen simulation technique (Rusitec). *Agriculture Wastes,* Vol.17, pp.99-117. ISSN n.d.

Kumar, P. K. R. & Sankar, K. U. (1991). Lonsane BK. Supercritical fluid extraction from dry mouldy bran for the purification of gibberellic acid from the concomitant products produced during solid state fermentation. *Chemical Engineering Journal,* Vol.46, pp. 53-8. ISSN 1874-1231

Lang, Q. I., Cheng, F., Wai, C. M., Paszczynski, A., Crawford, R. L., Barnes, B., Anderson, T. J., Wells, R., Corti, G., Allenbach, L., Erwin, D. P., Assefi, T. & Mojarradi M. (2002). Supercritical fluid extraction and high-performance liquid chromatography-diode array electrochemical detection of signature redox compounds from sand and soil samples. *Analytical Biochemistry,* Vol.301, pp. 225-34. ISSN 0003-2697

Lemay, P. (2002). The use of high pressure for separation and production of bioactive molecules. *Biochimica et Biophysica Acta: Protein Structure and Molecular Enzymology* Vol.1595, pp. 357-366. ISSN 0006-3002

Lin, H. M. & Chen, L. F. (1994). Method for recovery of intracellular material by disruption of microbial cells with carbon dioxide under pressure, USP:5,306,637.

Lin, H. M., Yang, Z. & Chen, L. F. (1992). An improved method for disruption of microbial cells with pressurized carbon dioxide, *Biotechnology Progress,* Vol.15, pp. 41-71. ISSN 8756-7938

L'Italien, Y., Thibault, J. & LeDuy, A. (1989). Improvement of ethanol fermentation under hyperbaric conditions, *Biotechnology and Bioengineering,* Vol.33, pp. 471-476. ISSN 0006-3592

Lozano, P., Diego, T. D., Sauer, T., Vaultier, M., Gmouh, S. & Iborra, J. L. (2007). On the importance of the supporting material for activity of immobilized Candida antarctica lipase B in ionic liquid/hexane and ionic liquid/supercritical carbon dioxide biphasic media, *Journal of Supercritical Fluids,* Vol.40, pp. 93-100. ISSN 0896-8446

Lozano, P., Víllora, G., Gomez, D., Gayo, A. B., Sanchez-Conesa, J. A., Rubio, M. & Iborra, J. L. (2004). Membrane reactor with immobilized Candida antarctica lipase B for ester synthesis in supercritical carbon dioxide. *Journal of Supercritical Fluids,* Vol.29, pp. 121-128. ISSN 0896-8446

Ludwig, H., Gross, P., Scigalla, W. & Sojka, B. (1994). Pressure inactivation of microorganisms, *High Pressure Research,* Vol.12, pp. 193-197. ISSN n.d.

Ludwig, H. & Sokja, B. (1997). Release of dipicolinic acid and amino acids during high pressure treatment of *Bacillus subtilis* spores, *Pharmaceutical Industry,* Vol. 59, pp. 335-359. ISSN n.d.

Lund, B. M., Gould, G. W. & Rampling, A. M. (2002). Pasteurization of milk and the heat resistance of *Mycobacterium avium* subsp paratuberculosis: a critical review of the data, *International Journal of Food Microbiology,* Vol.77, pp. 135-145. ISSN 0168-1605

Majewski, W., Mengal, P., Perrut, M. & Ecalard, J. P. (1994). Supercritical Fluid Fractionation of Butter oil, In: *Supercritical Fluids Processing of Food and Biomaterials*, S.H. Rizvi, (Ed.), pp. (123-132), Chapman and Hall, ISBN 0751401846, Glasgow.

Marie-Olive, M. N., Athes, V. & Combes, D. (2000). Combined effects of pressure and temperature on enzyme stability, *High Pressure Research,* Vol.19, pp. 317-322. ISSN n.d.

Marongiu, B., Porcedda, S., Caredda, A., Piras, A., Mascia, V., Cadeddu, A. & Loddo, R. (2004). Isolation of *Juniperus phoenicea* volatiles by supercritical carbon dioxide extraction and bioactivity assays, *Journal of Essential Oil Research,* Vol.16, pp. 256-261. ISSN 1041-2905

Matsuda, T., Watanabe, K., Harada, T. & Nakamura, K. (2004). Enzymatic reactions in supercritical CO_2, carboxylation, asymmetric reduction and esterification, *Catalytic Today,* Vol. 96, pp. 103–111. ISSN n.d.

McHugh, M. A. & Krukonis, V.J. (1994). *Supercritical Fluid Extraction*: *Principles and Practice*, 2nd ed., Butterworths, 189-292, ISBN, 139780409900156, Boston.

Medina, A. R., Grima, E. M., Gimnezz, A. & Gonzalez, M.J.I. (1998). Downstream processing of algal polyunsaturated fatty acids, *Biotechnology Advance,*Vol.16, pp. 517-580. ISSN 0734-9750

Mendes, R. L., Fernandes, H. L., Coelho, J. P., Reis, E. C., Cabral, J. M. S., Novais, J. M. & Palabra, A. F. (1995). Supercritical CO_2 extraction of carotenoids and other lipids from *Chlorella vulgaris. Food Chemistry,* Vol.53, pp. 99-103. ISSN 0308-8146

Mesiano, A. J., Beckman, E. J. & Russell, A. J. (1999). Supercritical biocatalysis, *Chemical Review,* Vol. 99, pp. 623-633. ISSN n.d.

Millitzer, M., Wenzig, E. & Peukert, W. (2002). *In-situ* adsorption of biotechnologically produced macromolecules for optimisation of downstream processing. *Chemical Industrial Technology,* Vol. 74, pp. 152-5. ISSN 1474-1776

Mira, B., Blasco, M., Berna, A. & Subirats, S. (1999). Supercritical CO_2 extraction of essential oil from orange peel: effect of operation conditions on the extract composition, *Journal of Supercritical Fluids*, Vol.14, pp. 95-104. ISSN 0896-8446

Mizuno, T., Goto, M., Kodama, A. & Hirose, T. (2000). Supercritical water oxidation of a model municipal solid waste. *Industrial Engineering Chemical Research,* Vol.39, pp. 2807-2810. ISSN 0888-5885

Molin, G. (1983). The resistance to CO_2 of some food related bacteria, *European Journal of Applied Microbiology and Biotechnology,* Vol.18, pp. 214-221. ISSN 0175-7598

Mortazavi, S. M., Mohammadabadi, M. R., Khosravi-Darani, K. & Mozafari, M. (2007). Preparation of liposomal gene therapy vectors by a scalable method without using volatile solvents or detergents. *Journal of Biotechnology,* Vol.129, pp. 604-613. ISSN 0168-1656

Mosqueira, F. G., Higgins, J. J., Dunnill, P. & Lilly, M. D. (1981). Characteristics of mechanically disrupted bakers' yeast in relation to its separation in industrial centrifuges. *Biotechnology and Bioengineering,* Vol.23, pp. 335-343. ISSN 0006-3592

Mozafari, M.R., Khosravi-Darani, K., Gokce Borazan, G., Cui, J., Pardakhty, A. & Yurdugul, S. (2008). Encapsulation of food ingredients using, nanoliposome technology, *International Journal of Food Properties*, Vol. 11, pp.833–844. ISSN 1094-2912

Nagahama, K., Suzuki, J. & Suzuki, T. (1988). High pressure vapor liquid equilibria for the supercritical carbon dioxide, ethanol, and water system, In: *Proceedings of the 1st International Symposium on Supercritical Fluids*, M. Perrut, (Ed.), pp.(143–150), Nice, France.

Nakamura, K. (1990). Biochemical Reactions in Supercritical Fluids, *Trends in Biotechnology,* Vol.8, pp. 288-292. ISSN 0167-7799

Nakamura, K., Enomoto, A., Fukushima, H., Nagai, K. & Hakoda, M. (1994). Disruption of microbial cells by the flash discharge of high-pressure carbon dioxide, *Bioscience, Biotechnology and Biochemistry,* Vol.58, pp. 1297-1301. ISSN 0916-8451

Nakayama, A., Yano, Y., Kobayashi, S., Ischikawa, M. & Sakai, K. (1996). Comparison of pressure resistance of spores of six Bacillus strains with their heat resistances, *Applied and Environmental Microbiology,* Vol.62, pp. 3897-3900. ISSN 0099-2240

Nguyen, U., Evans, D. A. & Frakman, G. (1994). Natural antioxidants produced by supercritical extraction. In: *Supercritical Fluids Processing of Food and Biomaterials*, S.H. Rizvi, (Ed.), pp. (103-113), Chapman and Hall, ISBN 0751401846, Glasgow.

Nivens, D. E. & Applegate, B. M. (1996). Method for nucleic acid isolation using supercritical fluids. USP:5,922,536.

Paidhungat, M., Setlow, B., Daniels, W. B., Hoover, D., Parafragkou, E. & Setlow, P. (2002). 3Mechanism of induction of germination of *Bacillus subtilis* spores by high pressure, *Applied and Environmental Microbiology,* Vol.68, pp. 3172-3175. ISSN 0099-2240

Perrut, M. (2000). Supercritical fluid applications: Industrial developments and economic issues. *Industrial Engineering and Chemistry Research,* Vol.39, pp. 4531-35. ISSN 1520-5045

Puri, V. P. (1983) Explosive pretreatment of lignocellulosic residues with high pressure CO_2 for the production fermentation substrates, *Biotechnology and Bioengineering,* 26:3149-3161. ISSN 0006-3592

Qureshi, N., Maddox, I. S. & Friedl, A. (1992). Application of continuous substrate feeding to the acetone-butanol-ethanol fermentation relief of product inhibition using extraction, perstraction, stripping, and pervaporation. *Biotechnology Progress,* Vol.8, pp. 382-90. ISSN 8756-7938

Randolph, T. W. (1990). Supercritical fluid extractions in biotechnology. *Trends in Biotechnology*, Vol.8, pp. 78-82. ISSN 0167-7799

Raso, J., Barbosa-Canovas, G. & Swanson, B. G. (1998). Sporulation temperature affects initiation of germination and inactivation by high hydrostatic pressure of *Bacillus cereus*, *Journal of Applied Microbiology*, Vol.85, pp. 17-24. ISSN 1364-5072

Reps, A. Kolakowski, P. & Dajnowiec, F. (1994). The effect of high pressure on microorganisms and enzymes of ripening cheeses, In: *High Pressures Food Science and Bioscience Chemistry*, S.I. Neil, (Ed.), pp. (265-270), The Royal Society of Chemistry, ISBN 139781855738232, UK.

Reverchon, E. (1999). Supercritical anti-solvent precipitation of micro and nanoparticles. *Journal of Supercritical Fluids,* Vol.15, pp. 1-21. ISSN 0896-8446

Roberts, C. M. & Hoover, D. G. (1996). Sensitivity of *Bacillus coagulans* spores to combinations of high hydrostatic pressure, heat, acidity and nisin, *Journal of Applied Bacteriology,* Vol.81, pp. 363-368. ISSN 0021-8847

Roca, C. & Olsson, L. (2003). Increasing ethanol productivity during xylose fermentation by cell recycling of recombinant *Saccharomyces cerevisiae*. *Applied Microbiology and Biotechnology,* Vol.60, pp. 560-3. ISSN 0175-7598

Saddler, J. N. (1992). Biotechnology for the Conversion of Lignocellulosics. *Biomass Bioenergy,* Vol.2, pp. 229-238. ISSN 0961-9534

Sanagi, M. M., Hung, W. P. & Yasir, S. M. (1997). Supercritical fluid extraction of pyrazines in roasted cocoa beans effect of pod storage period. *Journal of Chromatography A,* Vol.785, pp. 361-367. ISSN: 0021-9673

Sarkari, M., Knutson, B. L. & Chen, C. H. (1993). Enzymatic catalysis in cosolvent modified pressurized organic solvents, *Biotechnology and Bioengineering,* Vol.65, pp. 258-264. ISSN 0006-3592

Saykhedkar, S. S., Singhal, R. S. (2004). Supercritical carbon dioxide extraction of griseofulvin from the solid matrix obtained after solid-state fermentation. *Biotechnology Progress,* Vol.20, pp. 818-24. ISSN 8756-7938

Schreck, C. & Ludwig, H. (1997). The inactivation of vegetative bacteria by pressure. In: *High Pressure Research in Biosciences and Biotechnology,* K. Heremans, (Ed.), pp. (37-59), Leuven University Press, ISBN, 9061868076, Belgium.

Schultz, K., Martinelli, E. E. & Mansoori, G. A. (1991). Supercritical fluid extraction and retrograde condensation application in biotechnology. In: *Supercritical Fluid Technology. Reviews in Modern Theory and Applications*, T.J. Bruni & F. Ely, (Ed.), pp. (451-78), CRC press, ISBN, 9780849368479,Boca Raton.

Serp, D., Von Stockar, U. & Marison, I.W. (2003). Enhancement of 2-phenylethanol productivity by *Saccharomyces cerevisiae* in 2 phase fed batch fermentation using solvent immobilization. *Biotechnology and Bioengineering,* Vol.82, pp. 103-10. ISSN 0006-3592

Shishikura, A., Takahashi, H., Hirohama, S. & Kunio, A. (1992). Citric acid purification process using compressed carbon dioxides. *Journal of Supercritical Fluids,* Vol.5, pp. 303-12. ISSN 0896-8446

Smelt, J. P. P. M. (1998). Recent advances in the microbiology of high pressure processing, *Trends Food Science and Technology,* Vol.9, pp. 152-157. ISSN 0924-2244

Sojka, B. & Ludwig, H. (1997). Effects of rapid pressure changes on the inactivation of *Bacillus subtilis* spores, *Pharmaceutical Industry,* Vol.59, pp. 436-438. ISSN n.d.

Spilimbergo, S. & Bertucco, A. (2003). Non-thermal bacterial inactivation with dense CO_2, *Biotechnology and Bioengineering,* Vol.84, pp. 627-638. ISSN 0006-3592

Spilimbergo, S., Elvassore, N. & Bertucco, A. (2002). Microbial inactivation by high-pressure, *Journal of Supercritical Fluids,* Vol.22, pp. 55-63. ISSN 0896-8446

Stark, D., Kornmann, H., Munch, T., Sonnleitner, B., Marison, I. W. & Von Stockar, U. (2003). Novel type of *in situ* extraction: use of solvent containing microcapsules for the bioconversion of 2-phenylethanol from L-phenylalanine by *Saccharomyces cerevisiae*. *Biotechnology and Bioengineering,* Vol.83, pp.376-85. ISSN 0006-3592

Stark, D., Munch, T., Sonnleitner, B., Marison, I. W., & Von Stockar U. (2002). Extractive bioconversion of 2-phenylethanol by *Saccharomyces cerevisiae*. *Biotechnology Progress,* Vol.18, pp. 514-23. ISSN 8756-7938

Steckel, H., Thies, J. & Mueller, B. W. (1997). Micronization of sterols for pulmonary delivery by supercritical carbon dioxide. *International Journal of Pharmaceutics,* Vol.152, pp. 99-110. ISSN 0378-5173

Subramanian, B., Rajewski, R. A. & Snavely, K. (1997). Pharmaceutical processing with supercritical carbon dioxide. *Journal of Pharmaceutical Science,* Vol.86, pp. 885-890. ISSN 0022-3549

Teja, A. S. & Eckert, C. A. (2000). Commentary on supercritical fluids: research and applications, *Industrial Engineering Chemical Research,* Vol.39, pp. 4442-4444. ISSN 0888-5885

Toews, K. L., Shroll, R. M., Wai, C. M. & Smart, N. G. (1995). pH-defining equilibrium between water and supercritical CO_2; Influence on supercritical extraction of organics and metal-chelates. *Analytical Chemistry,* Vol.67, pp. 4040-3. ISSN 0003-2700

Van Eijs, A. M. M., Wokke, J. M. P. & Ten Brink, B. (1988). Supercritical extraction of fermentation products. In: *Preconcentration and Drying of Food Materials, S.* Bruin, (Ed.), pp. (135-143), Elsevier , ISBN, 139780444429681, Amsterdam.

Vijayan, S., Byskal, D. P. & Buckley, L. P. (1994). Separation of oil from fried chips by a supercritical extraction process; an overview of bench-scale test experience and process economics, In: *Supercritical Fluids Processing of Food and Biomaterials*, S.H. Rizvi, (Ed.), pp. (74-92), Chapman and Hall, ISBN 0751401846, Glasgow.

Wang, L. & Muttucumaru, S. (2002). Separation of biosynthetic polyunsaturated fatty acid with supercritical fluids, *Biotechnology Annual Review,* Vol.8, pp. 167-181. ISSN 1387-2656

Watanabe, T., Furukawa, S. & Taj, S. (2004). High pressure carbon dioxide decreases the heat tolerance of the bacterial spores, *Food Science Technology Research*, Vol. 70, pp. 635-637. ISSN 1344-6606

Wells, S.L. & DeSimone, J. (2001). CO_2 technology platform: an important tool for environmental problems solving, *Angewandte Chemie-International Edition,* Vol.40, pp. 518-527. ISSN 1433-7851

Winters, M. A., Frankel, D. Z., Debenedetti, P. G., Carey, J., Devaney, M. & Przbycien, T. M. (1999). Protein purification with vapor phase carbon dioxide. *Biotechnology and Bioengineering,* Vol.62, pp. 247-258. ISSN 0006-3592

Yalpani, M. (1993). Supercritical fluids: puissant media for the modification of polymers and biopolymers, *Polymer*, Vol. 34, pp. 1102-1105. ISSN 0032-3861

Yamaguchi, K. & Murakami, M. (1986). Application of supercritical fluid extraction to aquatic organisms, *Journal of Japan Oil Chemists' Society,* Vol.35, pp. 260-265. ISSN 0513-398X

Yeo, S., Debenedetti, P. G., Sugunakar, Y. P. & Przbycien, T. M. (1994). Secondary structure characterization of micro-particulate insulin powders. *Journal of Pharmaceutical Science*, Vol. 83, pp. 1651-1656. ISSN 0022-3549

Yeo, S., Lim, G. B., Debenedetti, P. G. & Bernstein, H. (1993). Formation of micro-particulate protein powders using a supercritical fluid antisolvent. *Biotechnology and Bioengineering*, Vol.41, pp. 341-346. ISSN 0006-3592

Yoshida, T., Oshima, T. Y. & Matsumura, Y. (2004). Gasification of biomass model compounds and real biomass in supercritical water, *Biomass Bioenergy,* Vol.26, pp. 71-78. ISSN 0961-9534

Young, J. C. & Games, D. E. (1993). Supercritical fluid extraction and supercritical fluid chromatography of the fungal metabolite ergostrol. *Journal of Agricultural and Food Chemistry,* Vol. 41, pp. 577-81. ISSN 0021-8561

Zagrobelny, J. & Bright, F. V. (1992). In situ studies of protein conformation in supercritical fluids: Trypsin in carbon dioxide, *Biotechnology Progress,* Vol.8, pp. 421-423. ISSN 8756-7938

Zheng, Y. & Tsao, G. T. (1996). Avicel hydrolysis by cellulase enzyme in supercritical CO_2, *Biotechnology Letter,* Vol.18, pp. 451-454. ISSN 0141-5492

25

Moisture and Bio-Deterioration Risk of Building Materials and Structures

Hannu Viitanen
VTT
Finland

1. Introduction

During the service life of buildings, natural aging and eventual damage of materials due to different chemical, physical, and biological processes can take place. Ageing of the materials is one aspect of the environmental processes and involve different chemical, mechanical and biological reactions of the materials. Bio-deterioration, e.g. mould, decay and insect damage in buildings, is caused when moisture exceeds the tolerance of structures which may be a critical factor for durability and usage of different building materials.
Modelling of the development of mould growth and decay development is a tool for evaluate the eventual risk of ambient humidity or moisture conditions of materials for bio-deterioration of materials. The modelling can be used in combination of hygro-thermal analyses of building and building components.
Moisture availability is the primary factor controlling mould growth and decay development, but the characteristics of the substrate and environmental conditions determine the dynamics of the growth. However, moist materials may also dry and become wet again thus, resulting in fluctuating moisture conditions. Mould and decay problems in buildings are most often caused by moisture damage: water leakage, convection of damp air and moisture condensation, rising damp from the ground and moisture accumulation in the structure. Repeated or prolonged moisture penetration into the structure is needed for damage to develop.

2. Critical environmental conditions for bio-deterioration

There are several biological processes causing aging and damage to buildings and building components. This is due to natural ageing of materials but also caused by excessive moisture and damage of materials. For mould development, the minimum (critical) ambient humidity requirement is shown to be between RH 80 and 95 % depending on other factors like ambient temperature, exposure time, and the type and surface conditions of building materials (Table 1) For decay development, the critical humidity is above RH 95 %. Mould typically affects the quality of the surfaces and the adjacent air space with volatile compounds and spores. The next stage of moisture induced damage, the decay development, forms a serious risk for structural strength depending on moisture content, materials, temperature and time. The worst decay damage cases in North Europe are found in the floors and lower parts of walls, where water accumulates due to different reasons.

Type of organism	Damage / problem type	Humidity or moisture range (RH or MC %)	Temperature range (°C)
bacteria	bio corrosion of many different materials, smell, health problems	wet materials RH > 97 %	ca. -5 to +60
mould fungi	surface growth on different materials, smell and health problems	Ambient RH > 75 %, depends on duration, temperature and mould species	ca. 0 to +50
blue-stain fungi	blue-stain of wood permeability change of wood	Wood moisture content > 25 - 120 % RH > 95 %	ca. -5 to +45
decay fungi	different types of decay in wood (soft rot, brown rot or white rot), also many other materials can be deteriorated, Strength loss of materials.	Ambient RH > 95 %, MC > 25 - 120 %, depends on duration, temperature, fungus species and materials	ca. 0 to +45
algae and lichen	Surface growth of different materials on outside or weathered material.	wet materials also nitrogen and low pH are needed	ca. 0 to +45
insects	Different type of damage in organic materials, surface failures or strength loss.	Ambient RH > 65 % depends on duration, temperature, species and environment	ca. 5 to +50

Table 1. Organisms involving damages and defects of building components (Viitanen and Salonvaara 2001, Viitanen et al. 2003)

In Northern Europe, the roofs, floors and lower parts of walls are most often exposed to high humidity and potential attack by biodeterioration processes (Paajanen and Viitanen 1989, Viitanen 2001a, Kääriäinen et al. 1998) when also decay will develop. For the decay development, the humidity and moisture conditions will be higher than that for mould growth, and modelling of decay risk is a separate task. Mould growth is often typical in materials in exterior conditions. In damage conditions, however, different decay types can be found: brown rot, soft rot, and white rot. In buildings suffering from excessive moisture loading, brown rot is the most common decay type (Paajanen and Viitanen 1989, Viitanen 2001a).

The other a-biotic factors like UV radiation and quality of substrate (nutrients, pH, hygroscopicity, water permeability) are also significant for the growth of organisms. Different organisms, e.g. bacteria, fungi and insects, can grow and live in the building materials; microbiologically clean buildings probably do not exist, as some contamination begins as early as during the construction phase. The humidity / moisture conditions connected with temperature and exposure time are the most important factor for development of biological problems and damage in buildings.

The research and modelling of mould growth is most often performed under constant conditions when the ambient humidity conditions and microclimate will prevail for longer periods. Ayerst (1969) and Smith and Hill (1982) studied the effect of temperature and water

activity on germination and growth of selected mould fungi. They developed isopleths for the growth conditions of mould fungi on agar media. An isopleths is a boundary that defines all combinations of temperature and relative humidity that permit a particular mould growth rate. Grant et al. (1989) analysed and modelled the moisture requirements of some mould fungi isolated from dwellings. A certain succession, depending on the moisture requirements of different fungal species: primary, secondary and tertiary colonizers, was found.

Research with building materials will be better fitted to the moisture problems in buildings. Adan (1994) used a non-linear regression technique to model sigmoid curves describing vegetative fungal growth of *Penicillium chrysogenum* on gypsum board material. He used the time-of-wetness (TOW) as an overall measure of water availability for fungal growth under fluctuating humidity conditions. The TOW is defined by the ratio of the cyclic wet period (RH ≥ 80 %) and the cyclic dry period. The mould growth is a function of the effect of lowest humidity, time of wetness and high relative humidity frequency, and finally of periods of wet and dry conditions. He used Low Temperature Scanning Electronic Microscope LTSEM to analyse the growth and studied the effect of coatings and surface quality on the mould growth. He also evaluated the effect of distribution of growth density on test results. Clarke et al. (1998) developed a simulation model and tool for mould growth prediction in buildings based on an analysis of published data using growth limit curves for six generic mould categories. These limits have been incorporated within the ESP-r (building Energy Software) system for use in conjunction within combined heat and moisture flow simulation.

3. Modeling of development of mould growth

3.1 Mould growth on building materials

Modelling of mould growth and decay development based on humidity, temperature, exposure time and material will give tools for the evaluation of durability of different building materials and structures. The models make it possible to evaluate the risk and development of mould growth and to analyse the critical conditions needed for the start of growth of microbes and fungi. The model is also a tool to simulate the progress of mould and decay development under different conditions on the structure surfaces. This requires that the moisture capacity and moisture transport properties in the material and at the surface layer have been taken into account in the simulations. In practice there are even more parameters affecting mould growth, e.g. thickness of the material layers combined with the local surface heat and mass transfer coefficients. Therefore, the outcome of the simulations and in-situ observations of biological deterioration may not agree. One of the results of a newly finished large Finnish research project "Modelling of mould growth" is an improved and extended mathematical model for mould growth based on development of mould index in different materials under different exposure conditions (table 2).

Hukka and Viitanen (1999) and Viitanen et al. (2000) presented a model of mould growth which is based on duration of suitable exposure conditions required before microbial growth will start or the damage will reach a certain degree. Particular emphasis is focused on this time period, the so-called response time or response duration, in different humidity and temperature conditions for the start of mould growth (Figure 1). The model is based on the large laboratory studies on Scots pine and Norway spruce sapwood.

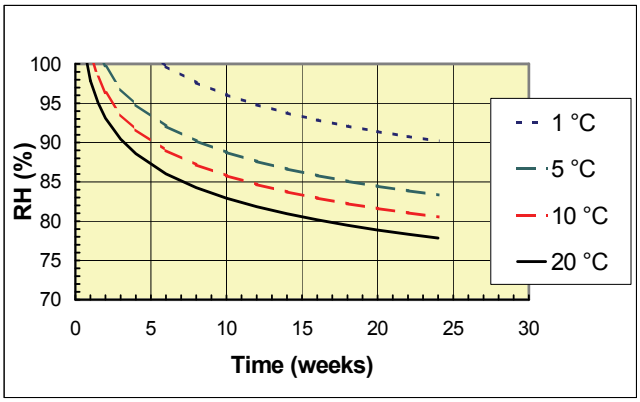

Fig. 1. Critical humidity (RH %), time (weeks) and temperature needed to start mould growth on pine sapwood (Viitanen 1996)

The growth of mould in this model was evaluated using the "mould index" scale shown in Table 2. The model can be used to evaluate the mould growth in different exposure conditions, and it can be introduced to building physic modeling to evaluate the performance of different structure. The model is not suitable for evaluate the development of decay, for which different models exist (Viitanen 1996, Viitanen et al. 2000).
The model describes also the dynamic nature of mould growth under varying temperature and humidity conditions as it gives the predicted mould index as a function of time. Simulation results with the model show that under fluctuating humidity, the mould index will decrease during low humidity or temperature periods, depending on the time periods (Figure 2). This kind of behaviour can also be found in the "Modelling of mould growth" study (Viitanen et al 2010).

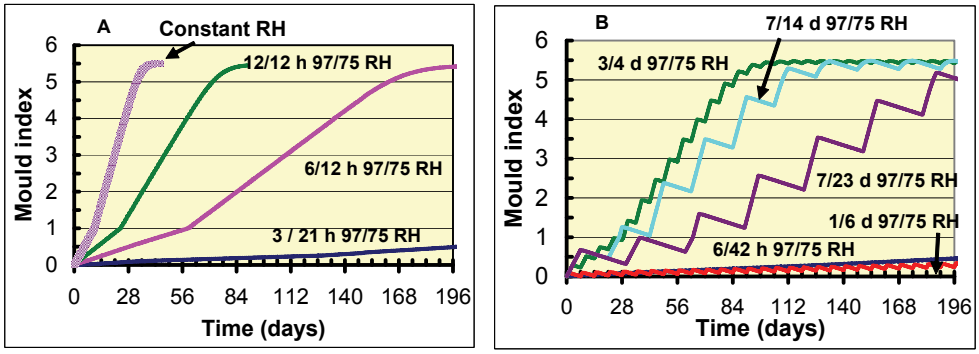

Fig. 2. Modelling the effect of varied fluctuating humidity conditions on the development of mould index in pine sapwood (Viitanen et al. 2000)

The original index is based on wood materials (Viitanen and Ritschkoff 1991a). New determinations for index levels 3 and 4 for other materials are presented using bold fonts and has been presented by Viitanen et al (2011a).

Index	Description of the growth rate
0	No growth
1	Small amounts of mould on surface (microscope), initial stages of local growth
2	Several local mould growth colonies on surface (microscope)
3	Visual findings of mould on surface, < 10 % coverage, or, **< 50 % coverage of mould (microscope)**
4	Visual findings of mould on surface, 10 - 50 % coverage, or, **>50 % coverage of mould (microscope)**
5	Plenty of growth on surface, > 50 % coverage (visual)
6	Heavy and tight growth, coverage about 100 %

Table 2. Mould index for experiments and modeling of mould growth on building materials

Sedlbauer (2001) studied different models to evaluate spore germination and growth of different mould species on different types of materials. He found, that the isopleths developed by growth of mould on an artificial medium can be used to evaluate the growth rate of different fungi. He used a hygrothermal model based on the relative humidity, temperature and exposure time needed for the spore germination of mould fungi based on the osmotic potential of spores. He analysed the effect of different climatic conditions on the spore moisture content and germination. He also evaluated the spore moisture content and germination time based on calculated time courses of temperature and relative humidity in various positions of the exterior plaster of an external wall using WUFI program (Sedbauer and Krus 2003). In Figure 3, a comparison of the critical conditions for mould growth assumed by some of mould growth models is shown. These curves represent lower limiting isopleths (humidity levels) for mould growth.

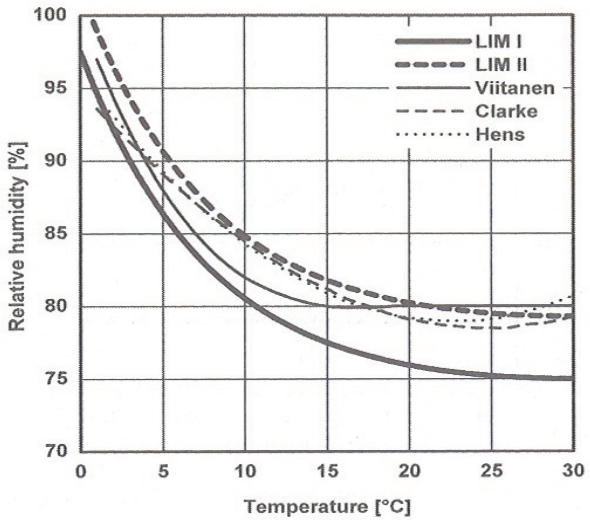

Fig. 3. Comparison of the LIM's of substrate class 1 (LIM I, biodegradable materials) and substrate class 2 (LIM II, porous materials) after Sedlbauer (2001) with data from results of building materials after Viitanen et al. (2000), Clarke et al. (1998) and Hens (1999)

The first version of the mould growth model was based on large laboratory studies with pine sapwood (Viitanen and Ritschkoff 1989). The mould growth intensities were determined at the constant conditions. In the later stages, studies in varied and fluctuated humidity conditions were performed and based on these studies, mould growth model (equation 1) was presented by Hukka and Viitanen 1999.

$$\frac{dM}{dt} = \frac{1}{7 \cdot \exp(-0.68 \ln T - 13.9 \ln RH + 0.14W - 0.33SQ + 66.02)} k_1 k_2 \quad (1)$$

where the factor k_1 represents the intensity of growth (Equation 3), W is the timber species (0 = pine and 1 = spruce) and SQ is the term for surface quality (SQ = 0 for sawn surface, SQ = 1 for kiln dried quality) based on Hukka and Viitanen (1999).
For other materials than wood the value SQ = 0 is used, which omits this factor. Numerical simulation is typically carried out using one hour time steps (climate data intervals) and hours are used in the equations instead of days.

$$k_1 = \begin{cases} 1 & \text{when } M \le 1 \\ \dfrac{2}{t_{M=3} / t_{M=1} - 1} & \text{when } M > 1 \end{cases} \quad (2)$$

In the equation, the factor $t_{M=1}$ is the time needed to start of the growth (M = 1, Table 2), and $t_{M=3}$ the time needed to reach the level M =3. The factor k_2 (Equation 3) represents the moderation of the growth intensity when the mould index (M) level approaches the maximum peak value in the range of 4 < M < 6.

$$k_2 = \max\left[1 - \exp\left[2.3 \cdot (M - M_{\max})\right], 0\right] \quad (3)$$

where the maximum mould index M_{max} level depends on the current conditions (Equation 4):

$$M_{\max} = 1 + 7 \cdot \frac{RH_{crit} - RH}{RH_{crit} - 100} - 2 \cdot \left(\frac{RH_{crit} - RH}{RH_{crit} - 100} \right)^2 \quad (4)$$

In Equation 4 RH_{crit} is the limit RH level to start the mould growth (Viitanen et al 2011a).
For other materials than wood, the model has to be modified. The new mould growth intensity factors are presented as relative values compared to those of the reference material pine by using Equations (5) and (6).

$$k_1 = \frac{t_{M=1,pine}}{t_{M=1}} \text{ when M < 1} \quad (5)$$

$$k_1 = 2 \cdot \frac{\left(t_{M=3,pine} - t_{M=1,pine}\right)}{t_{M=3} - t_{M=1}} \text{ when M} \ge 1 \quad (6)$$

where $t_{M=1}$ is the time needed for the material to start the growth (Mould index reaches level M = 1), and $t_{M=3}$ the time needed for the material to reach level M =3. The subscript $_{pine}$ refers to the value with the reference material pine.

The mould growth maximum values set restrictions for the growth and limit the index to realistic levels. For the new set of materials the equation of the maximum mould index level was written in form shown in equation 7 (Ojanen et al 2010, Viitanen et al 2011a):

$$M_{\max} = A + B \cdot \frac{RH_{crit} - RH}{RH_{crit} - 100} - C \cdot \left(\frac{RH_{crit} - RH}{RH_{crit} - 100} \right)^2 \quad (7)$$

In this equation the coefficients A, B and C can have values that depend on the material class. The new M_{max} has an effect on the factor k_2 (Equation 3) and it contributes to the simulation results. Table 4 presents the maximum levels of mould index values for different materials under different conditions. These results were classified to material sensitivity groups, presented both for growth intensities and maximum mould index levels. Table 3 gives the values for the growth intensity parameter k_1 classes and for the coefficients of the maximum mould index factors M_{max} and k_2. The factor RH_{min} represents the minimum humidity level for starting mould growth for each material group.

Sensitivity class	k_1		k_2 (M_{max})			RH_{min}
	M<1	M≥1	A	B	C	%
very sensitive, vs	1	2	1	7	2	80
sensitive, s	0.578	0.386	0.3	6	1	80
medium resistant, mr	0.072	0.097	0	5	1.5	85
resistant, r	0.033	0.014	0	3	1	85

Table 3. Parameters for the sensitivity classes of the updated mould model (Ojanen et al 2010, Viitanen et al 2011a)

Sensitivity class	Materials
Very sensitive	Pine sapwood
Sensitive	Glued wooden boards, PUR (paper surface), spruce
Medium resistant	Concrete, aerated and cellular concrete, glass wool, polyester wool
Resistant	PUR polished surface

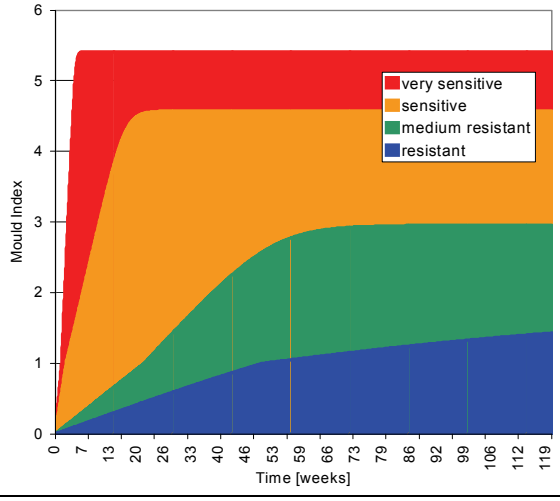

Table 4. Mould growth sensitivity classes and some corresponding materials in the research. The figure in table illustrates the predicted mould growth for the established sensitivity classes for constant conditions at 97 % RH and 22 C (Viitanen et al 2011)

The factors presented in Table 3 form the new basis for numerical simulation of mould growth on different material surfaces. These values will be applied in the following studies where the model performance will be evaluated.
Table 4 represents the tested materials, whose resulting mould indexes were used for the determination of k_1 for the respective classes. The k_1 classes were determined by using expert estimation for most suitable values.

3.2 Decline of the mould growth and mould index caused by frost or dry condition

As living organisms mould fungi need water and suitable temperature to grow. When conditions are unfavourable for fungi, activity of mould fungi will be inactivated depending on the extent of the frost or dryness and the time periods of unfavourable conditions. In Figure 4, the humidity and temperature conditions of microclimate for the favourable and unfavourable conditions for mould growth is shown. The rate of humidity and temperature and the time periods in favourable and unfavourable conditions will affect on the growth rate of mould. Especially the longer periods in low humidity or temperature will cause decline of the mould growth and development and even the decline of mould index.

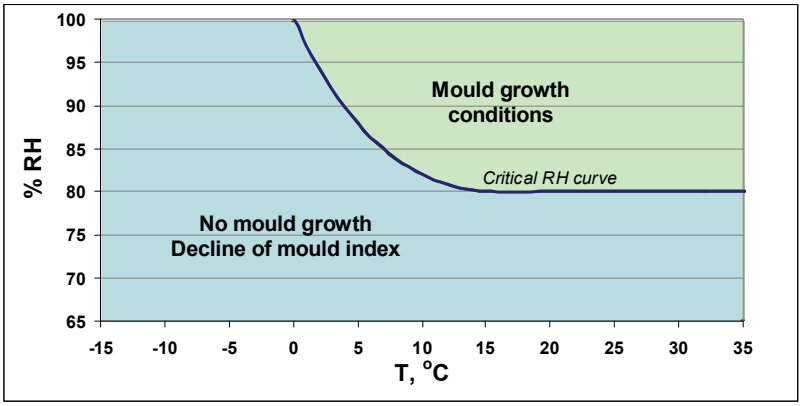

Fig. 4. Illustration of the regimes for the favourable and unfavourable conditions for mould growth (Viitanen et al 2011a)

The decline of mould growth on wooden surface has been modelled based on cyclic changes between two humidity conditions (Equation 8). The decline of mould index under different fluctuating conditions is modelled and shown in the figure 2.

$$\frac{dM}{dt} = \begin{cases} -0.00133, \text{when } t\text{-}t_1 \le 6 \text{ h} \\ 0, \text{when } 6 \text{ h} \le t - t_1 \le 24 \text{ h} \\ -0.000667, \text{when } t\text{-}t_1 > 24 \text{ h} \end{cases} \quad (8)$$

where M is the mould index and t is the time (h) from the moment t_1 when the conditions on the critical surface changed from growth to outside growth conditions (Hukka and Viitanen 1999).
Under long period seasonal variations of humidity conditions the decline of mould index may differ from that presented in Equation 8. Also the material may have a significant effect

on the decline process. The decline of mould index for other materials was presented using a constant, relative coefficient for each material (Equation 9).

$$\frac{dM}{dt}_{mat} = C_{mat} \cdot \frac{dM}{dt}_{0} \tag{9}$$

where $(dM/dt)_{mat}$ is the mould decline intensity for each material, $(dM/dt)_0$ is that for pine in the original model (Equation 9), and C_{mat} is the relative coefficient for mould index decline used in the simulation model. The original decline model for wood could be applied using these additional factors (Ojanen et al 2010, Viitanen et al 2011a).

The relative decline of mould for different materials was determined using laboratory experiments with walls (Ojanen et al 2010). The temperature and relative humidity conditions on the critical boundary layer between two different materials were monitored continuously. The mould index level of the material surfaces was determined with suitable intervals by opening the structure from three different parts. The experimental target conditions at the interface of the two materials are presented in Table 5.

These experimental walls had mould growth after the first warm and humid period ('Summer/autumn'). The mould decline was determined by the change of the mould index during the second period, a four month long 'Winter' period causing freezing temperatures at the critical boundary. The mould index values were determined for both material surfaces on each critical interface. Figure 11 presents the relative mould decline values (C_{mat}) solved from the observations in the experiments. The results include the detected mean, minimum and maximum mould index values.

Stage	**1**	**2**	**3**	**4**
Season	Summer/autumn	Winter	Spring	High exposure
Time, months	7	4	6	12
RH %	80 … 100	92 … 100	60 … 95	94 … 100
Temperature °C	27 … 18	-5 … +3	2 … 10	20 … 24

Table 5. Exposure conditions during the wall assemble test (Ojanen et al 2010)

The decline of mould intensity on different materials under unfavourable mould growth conditions could be presented as decline classes (Table 6). This classification is based on few measurements with relatively large scattering and it should be considered as the first approximation of these classes. It was found, that the decline was larger within wood

C_{eff}	**Description**
1.0	Pine in original model, short periods
0.5	Significant Relevant decline
0.25	Relatively low decline
0.1	Almost no decline

Table 6. Classification of relative mould index decline (Ojanen et al 2010)

4. Modeling of development of decay

4.1 Causes for decay damages in buildings

The excessive water into the building structure and materials is the basic cause to different bio-deterioration problems like decay. For instance, in washrooms water often penetrates through inside surfaces or pipe leakage into the structures causing long lasting high humidity conditions. In old wooden buildings, the floor has often been built above a cold ventilated basement or crawl space, where high humidity conditions may exist. If water is penetrated in the crawl space, the ventilation may not keep the floor dry and mould growth is obvious. If ventilation caps are closed, severe decay problems have been found, e.g. dry rot damage (Paajanen and Viitanen 1989, Kääriäinen et al. 1998).

In connection of the decay, also microbial contamination on the surfaces in the crawl space is typically much higher than inside the building. The level of fungal spores in the crawl space is about ten times as high as indoors. In crawl spaces, spore concentrations in a range of 10^3-10^5 colony-forming units per gram (cfu/g) of material are common. The levels have usually been highest on wood-based boards and on timber (Hyvärinen et al. 2002). In cases of heavy fungal colonisation, airborne spore concentrations of up to 10^3-10^4 cfu/m^3 have been detected.

The slab-on-ground structure without thermal insulation below the concrete slab has been used in old buildings. This type a floor is very sensitive for water damage and microbial growth. Especially in detached houses built between 1960 and 1980, wooden beams are often supported on concrete slabs on grade. Partial decay or insect damage is often found in the lower sill plate of exterior walls due to water penetration from the basement (Kääriäinen et al. 1998).

Decay is the more severe result of high moisture exposure of wooden structures when the materials are wet for long periods. According to laboratory studies, the growth of decay fungi and decay development can start when the ambient humidity level in the microclimate remains for several weeks above RH 95 – 100 % and moisture content of pine sapwood above 25 – 30 % (Viitanen and Ritschkoff 1991b, Morris et al 2006). According to experience, decay will develop when moisture content of wood exceeds the fibre saturation point (RH above 99.9 % or wood moisture content 30 %, but also the variation of conditions and temperature has an important effect.

4.2 Modeling the decay development

4.2.1 A model for decay development in pine sapwood

There is always a vide variation within the growth condition of different fungus species, and we need overall evaluation on the growth activity and decay development of a "typical" example fungi like typical decay fungi (e.g. *Coniophora puteana* or *Gloeophyllum sepiarium*). VTT has done comprehensive research in mould and decay growth and their numerical modelling on timber (Viitanen 1996, Viitanen et al 2003) presented a model of decay development in pine and spruce sapwood.

Later a new model was developed from the work presented in references Viitanen and Ritschkoff (1991b), Viitanen (1996), and Viitanen (1997). In these references, the decay growth of brown rot in spruce and pine sapwood is studied experimentally in different constant relative humidity and temperature conditions. In the present model, only the data of pine sapwood is considered. Based on the experimental findings presented in references, a model for variable conditions is proposed (Toratti et al 2009)). This model is a time stepping scheme. The development of decay is modelled with two consecutive processes:

a) Activation process:

This is termed as α parameter, which is initially 0 and gradually grows depending on the air conditions to a limit value of 1. This process is able to recover in favourable conditions (dry air) at a given rate (although no experimental evidence of recovery is available).

b) Mass loss process:

This occurs when the activation process has fully developed (α=1) otherwise it does not occur. This process is naturally irrecoverable.

These processes only occur when the temperature is 0..30 °C and the relative humidity is 95% or above. Outside these condition bounds, the activation process may recover, but the mass loss process is simply stopped. The activation process is as given in Equation 2. The recovery time (i.e. α recovers from a value of 1 back to 0) is assumed to be 17520 hours (2 years). Recovery takes place when the conditions are outside the bounds of the decay growth.

The model can be used for evaluation the exposure condition for the eventual risk of decay to develop. For example, recorded temperatures and relative humidity are given for the Helsinki area. This climate is shown in the figure 1 for a one year period. According to the model, this climate seems to induce a low mass loss of 1.1 % in 4 years (Figures 4 and 5). During the first year, no decay development will occur in untreated pine sapwood. After 3 and 4 years exposure, decay is expected to occur only to a very limited extent in the surface of unprotected pine sapwood. Under normal use conditions, the cladding is protected by paints or other coatings. The direct influence of water on the wood surface is very small, and decay development will be significantly retarded or even negligible.

$$\text{Activation process } \alpha = 0..1$$

$$\alpha(t) = \int_0^t d\alpha = \sum_0^t (\Delta\alpha) \text{ , where}$$

$$\Delta\alpha = \frac{\Delta t}{t_{crit}(RH,T)} \text{ or (in favorable conditions of decay)} \tag{10}$$

$$t_{crit}(RH,T) = \left[\frac{2.3T + 0.035RH - 0.024T \times RH}{-42.0 + 0.14T + 0.45RH}\right] \times 30 \times 24 \text{ [hours]}$$

The mass loss process proceeds the activation process, when α has reached 1(Eq. 11).

$$\text{Massloss process when } \alpha \geq 1$$

$$ML(t') = \int_{t\ at\ \alpha=1}^{t'} \frac{ML(RH,T)}{dt} dt = \sum_{t\ at\ \alpha=1}^{t'} \left(\frac{ML(RH,T)}{dt} \times \Delta t\right) \tag{11}$$

$$\frac{ML(RH,T)}{dt} = -5.96 \times 10^{-2} + 1.96 \times 10^{-4} T + 6.25 \times 10^{-4} RH \text{ [\% / hour]}$$

For advanced decay to develop, a significantly longer period is needed, and after a 10 years period, severe decay in unprotected and uncovered pine sapwood can be expected in the Helsinki area. The design of details has a strongly marked effect on the durability and

service life of wood structure. If there is a detail collecting the water, the moisture conditions are suitable for long time for decay to develop. If the structure and details are well planned so that there is no water sink and the structure can be dried after occasionally wetting, the conditions for decay development will not be reached, and there are actually no limits for the service life of wood.

4.2.2 Evaluation of decay risk in different part of Europe using decay model

The empirical wood decay model was run using the ERA-40 data for air temperature, humidity and precipitation at 6 hour intervals (Viitanen et al 2010b). ERA-40 is a massive data archive produced by the European Centre of Medium-Range Weather Forecasts (ECMWF). The reanalysis involves a comprehensive use of a wide range of observational systems including, of course, the basic synoptic surface weather measurements. The ERA-40 domain covers all of Europe and has a grid spacing of approximately 270 km. The nature of the data and the reanalysis methods of ERA-40 are described in detail in Uppala et al. [2005]. The evaluation of decay development in the model is based on the mass loss caused by the decay fungus. Within specified limitations, the mass loss is an applicable variable for evaluating the decay development in wood. The decay development model will give a general assumption of the effect of humidity, temperature and exposure time on the start and progress of the decay.

The resulting modelled mass loss in 1961-1970 at the calculation points of the ERA-40 grid were analyzed by a chart production software producing a maps of wood decay in Europe (Figure 7). First a map on decay risk protected from rain and then a map on decay risk of pine sapwood exposed to rain. A modification of the weather data was made so that the humidity of air was set to 100% during precipitation (at non-freezing temperatures) as this is thought to result in a full saturation in the wood surface.

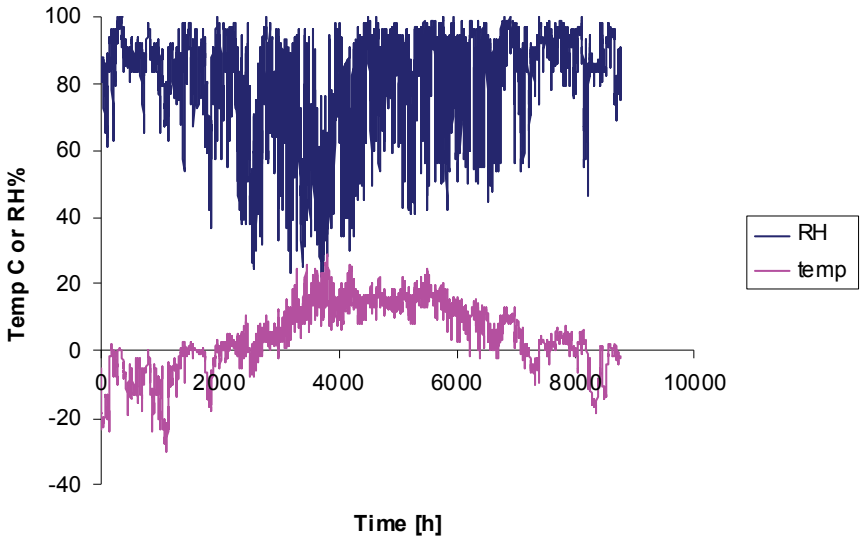

Fig. 5. Measured climate data (Helsinki) used in the decay model for one year (Viitanen et al 2010b)

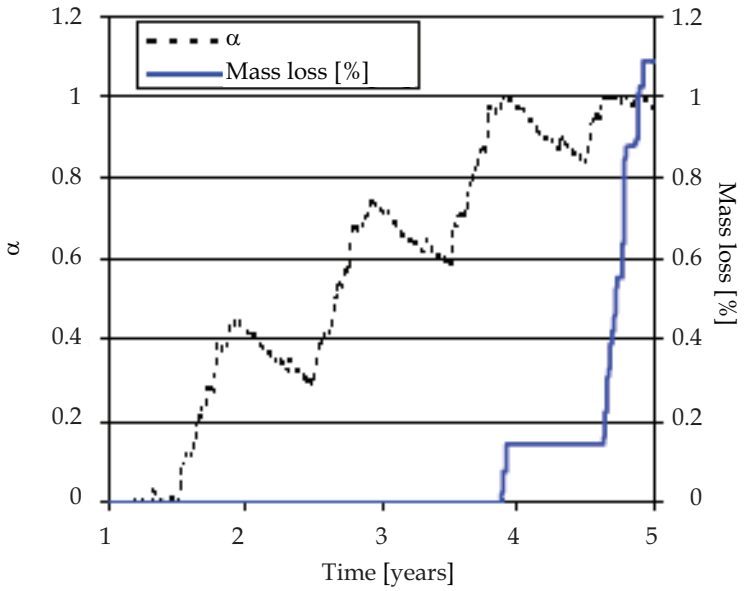

Fig. 6. No activation of growth or decay development during the first and second years, an activation of decay process after 4 years exposure may be expected (Viitanen et al 2010b)

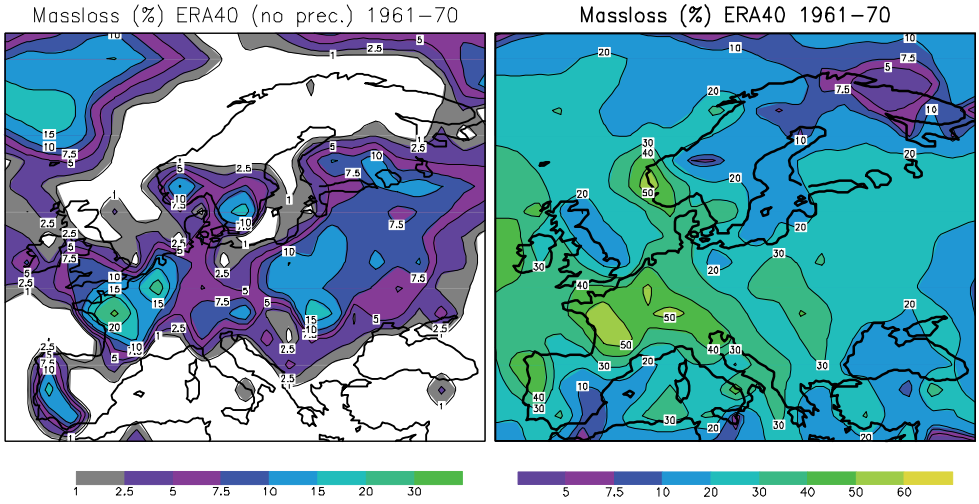

Fig. 7. a) Modelled mass loss (in %) of small pieces of pine wood that are protected from the rain or b) exposed to rain in 10 years in Europe (from [Viitanen et al. 2010b, 2011b)

The risk of decay activity in different part of Europe can be evaluated on the map. If we evaluate the decay activity rate in Helsinki to be 1, then the decay risk in north-western part of Portugal and in West Ireland is 2 times and in Atlantic part of France and Belgium it will

be between 2 and 2.5 times higher than that in Helsinki. In North Scandinavia it would be between 0.5 and 0.25, which will point out, the effect if climate on risk of decay development in outdoor structure varied vide within Europe. These coefficients can be used as one step to evaluate the effect of macroclimate conditions on service life of cladding and decking.
Another way to evaluate the macroclimate conditions is presented by Thelandersson et al (2011) using Meteonorm climate data. By calculating the daily dose and accumulating the dose for one year a measure of the risk of decay is obtained. This is made for several sites, and the result in terms of dosedays can be compared between the different sites. To be able to compare different sites, the dose was transferred to a relative dose by dividing it by the dose for the "base-station" Helsinki. Due to the variation of climate across Europe, relative doses between 0.6 (northern Scandinavia) and 2.1 (Atlantic coast in Southern Europe) were obtained.

5. Conclusion

There are several factors involved with the bio-deterioration of materials and buildings, and mathematic modelling that may help us to understand the complicated interaction of many factors. The presented numerical mould growth and decay development models are based on experimental results from several research projects. It is suitable for post-processing temperature and humidity data from any numerical simulation of hygrothermal conditions in building constructions. However, it must be kept in mind when performing the assessment that there is a great uncertainty coupled to this kind of analysis: the variation of the material sensitivities is high, estimation of a product sensitivity class is difficult without testing, the surface treatments may enhance or reduce growth potential, different mould species have different requirements for growth and the evaluation of the actual conditions in the critical material layers may include uncertainties. The best way to use the predicted mould growth and decay development as an assessment tool is to compare different solutions with each others: The solution with the lowest risk for the mould growth or decay development would most probably also have least other moisture related problems

6. Acknowledgment

This chapter is based on several research performed at VTT and other research institutes and universities.

7. References

Adan, O.C.G. 1994. On the fungal defacement of interior finishes. Eindhoven University of Technology. Thesis. Eindhoven, pp. 83-185.

Ayerst, G. 1969. The effects of moisture and temperature on growth and spore germination in some fungi. J. Stored Prod. Res. 5:127-141.

Clarke, J.A. Johnstone, C.M. Kelly, N.J. Mclean, R.C. Anderson, J.A., Rowan N.J. and Smith, J.E. 1998. A technique for prediction of the conditions leading to mould growth in buildings. Building and Environment 34 pp 515-521.

Grant, C., Hunter, C.A., Flannigan, B. and Bravery, A.F. 1989. The moisture requirements of moulds isolated from domestic dwellings. Internat. Biodet. 25:259-284.

Hens, H.L.S.C. 1999. Fungal defacement in buildings: A performance related approach. International Journal of Heating, Ventilation, Air-Conditioning and Refrigerating Research, Vol. 5, H 3, pp. 256-280

Hukka, A. and Viitanen, H. 1999. A mathematical model of mould growth on wooden material. Wood Science and Technology 33(6):475-485.

Hyvärinen, A., Meklin, T., Vepsäläinen, A. and Nevalainen, A. 2002. Fungi and actinobacterai in moisture-damaged building materials – concentrations and diversity, International Biodeterioration and biodegradation 49:27-37.

Kääriäinen, H., Rantamäki, J. and Tulla, K. Moisture Performance of Wooden Buildings. Feedback Knowledge of Actual Buildings. 1998. Espoo: Technical Research Centre of Finland. 85 p. (VTT Research Notes 1923). 63 p. + app. 14 p. (in Finnish).

Ojanen, T; Viitanen, H; Peuhkuri, R; Lähdesmäki, K; Vinha, J; Salminen, K. 2010. Mould growth modeling of building structures using sensitivity classes of materials. Thermal Performance of the Exterior Envelopes of Whole Buildings XI International Conference; (Buildingx XI), December 5-9, 2010, Clearwater Beach, Florida. Proceedings of Thermal Performance of the Exterior Envelopes of Whole Buildings XI International Conference (CD). DOE, BETEC, ASHRAE, Oak Ridge National Laboratory (ORNL) (2010), 10 p.

Paajanen, L. and Viitanen, H. 1989. Decay fungi in Finnish houses on the basis of inspected samples from 1978 to 1988. The International Research Group on Wood Preservation, IRG Doc. No: IRG/WP/1401. 4 p.

Sedlbauer, K. 2001. Prediction of mould fungus formation on the surface of/and inside building components. University of Stuttgart, Fraunhofer Institute for building Physics, Doctoral thesis. Stuttgart. Germany.

Sedlbauer K. and Krus, M. 2003. A new model for mould prediction and its application in practice. In Research in Building Physics. Ed. by Carmeliet, J. et al. Proc. of 2nd International conference on Building Physics

Smith, S.L. and Hill, S.T. 1982. Influence of temperature and water activity on germination and growth of Aspergillus restrictus and Aspergillus versicolor. Transactions of the British Mycological Society, Vol. 79, H 3, pp. 558-560.

Thelandersson, S.; Isaksson, T., Suttie, E., Früwald, E., Toratti, T., Grüell, G., Viitanen, H. and Jermer, J. 2011. Quantitative design guideline for wood outdoors above ground applications. Proceedings IRG Annual Meeting 2011, IRG/WP 11-20465

Toratti, T; Viitanen, H; Peuhkuri, R; Makkonen, L; Ojanen, T; Jämsä, S..2009. Modelling of durability of wooden structures. 4th International Building Physics conference IBPC 2009, Istanbul, Turkey, 15-18 June 2009. Istanbul Technical University. Istanbul, Turkey (2009), 127-134

Uppala, S.M., Kållberg, P.W., Simmons, A.J., Andrae, U., da Costa Bechtold, V., Fiorino, M., Gibson, J.K., Haseler, J., Hernandez, A., Kelly, G.A., Li, X., Onogi, K., Saarinen, S., Sokka, N., Allan, R.P., Andersson, E., Arpe, K., Balmaseda, M.A., Beljaars, A.C.M., van de Berg, L., Bidlot, J., Bormann, N., Caires, S., Chevallier, F., Dethof, A., Dragosavac, M., Fisher, M., Fuentes, M., Hagemann, S., Hólm, E., Hoskins, B.J., Isaksen, L., Janssen, P.A.E.M., Jenne, R., McNally, A.P., Mahfouf, J.-F., Morcrette, J.-J., Rayner, N.A., Saunders, R.W., Simon, P., Sterl, A., Trenberth, K.E., Untch, A., Vasiljevic, D., Viterbo, P., and Woollen, J. 2005: The ERA-40 re-analysis. Quarterly Journal. of the Royal Meteoroogical Society, 131, 2961-3012.

Viitanen, H. 1996. Factors affecting the development of mould and brown rot decay in wooden material and wooden structures. Effect of humidity, temperature and exposure time. Doctoral Thesis, Uppsala, The Swedish University of Agricultural Sciences, Department of Forest Products.

Viitanen, H. 1997. Critical time of different humidity and temperature conditions for the development of brown rot decay in pine and spruce. Holzforschung 51 (2): 99-106

Viitanen, H. 2001a. Biodegradation of cultural heritage, state of the art, Finland. ARIADNE Workshop: "Biodegradation of cultural heritage". Prague, December 10–15, 2001. Academy of Sciences of the Czech Republic, ITAM – ARCCHIP. 7 p.

Viitanen, H. and Ritschkoff, A. 1991a. Mould growth in pine and spruce sapwood in relation to air humidity and temperature. Uppsala. The Swedish University of Agricultural Scienses, Department of Forest Products. Report no 221. 40 p. + app. 9 p.

Viitanen, H. & Ritschkoff, A. 1991b. *Brown rot decay in wooden constructions. Effect of temperature, humidity and moisture*. Uppsala. Swedish University of Agricultural Scienses, Department of Forest Products. Report no 222. 55 p + appendix 2 p

Viitanen, H. and Salonvaara, M. 2001. Failure criteria. In Trechsel, E (Ed.). Moisture analysis and condensation control in building envelopes. American Society for Testing and Materials ASTM MNL40, pp. 66-80.

Viitanen, H., Hanhijärvi, A., Hukka, A. and Koskela, K. 2000. Modelling mould growth and decay damages Healthy Buildings. Espoo, 6 - 10 August 2000. Vol. 3. FISIAQ, 2000, pp. 341-346.

Viitanen, H., Ritschkoff, A-C., Ojanen, T. and Salonvaara, M. 2003. Moisture conditions and biodeterioration risk of building materials and structure. Proceedings of the 2nd International Symposium ILCDES 2003. Integrated Lifetime Engineering of Buildings and Civil Infrastructures, Kuopio, 1-3 Dec. 2003 RIL, VTT, RILEM, IABSE, ECCE, ASCE. Espoo (2003), pp. 151 – 156.

Viitanen, H; Vinha, J; Salminen K; Ojanen, T; Peuhkuri, R. Paajanen, L; Lähdesmäki, K. 2010a. Moisture and bio-deterioration risk of building materials and structures. Journal of Building Physics. 33 (3) 201-224.

Viitanen, H, Toratti, T. Makkonen, L. Peuhkuri, R. Ojanen, T. Ruokoloainen, L. and Räisänen, J. 2010b. Towards modelling of decay risk of wooden materials. Eur. J. Wood Prod. 68: 303-313.

Viitanen, H, Ojanen, T, Peuhkuri, R.; Vinha, J, Lähesmäki, K., Salminen, K. 2011 a. Mould growth modelling to evaluate durability of materials. 12th International Conference on Durability of Building Materials and Components. Conference Proceedings, Vol 1. 409 – 416.

Viitanen, H. Toratti, T, Makkonen, L. 2011b. Development of service life model for wooden structures. . 12th International Conference on Durability of Building Materials and Components. Conference Proceedings, Vol 1. pp 495 - 502.

26

The Release of Compounds from Microbial Cells

Marek Solecki
Technical University of Lodz
Poland

1. Introduction

Compounds present in the microbial cells are of great commercial value. Their separation requires disintegration of cell walls and cytoplasmic membranes. The disintegration of microorganisms on an industrial scale is carried out, among the others, in bead mills (Chisti & Moo-Young, 1986; Geciowa et al., 2002; Hatti-Kaul & Mattiasson, 2003). A bead mill is a container filled with beads that are set in circular motion by a rotating stirrer. Microorganisms dispersed in the liquid are disrupted due to the impact of beads. The mechanism of cell destruction is a result of combined action of normal and tangential forces. There are three basic types of this mechanism: collisions of beads, grinding and rolling performed by the beads. Disintegration is a very complex process. In this process, cell walls of microorganisms are disrupted, intracellular compounds are released and dissolved in the continuous phase, cell walls are subjected to microgrinding, the released macromolecular compounds are cut and the released enzymes interact. Rheological properties of the suspension and its continuous phase are changed.
Currie et al. (1974) described disintegration kinetics of microorganisms in the bead mill. The authors developed a linear model by comparing experimental data with results obtained during the disintegration process carried out in a high-pressure homogenizer (Hetherington et al., 1971). A logical model based on the analogy to the theory of gas kinetics was proposed by Melendres et al. (1998). They presumed that microorganisms could be destroyed due to collisions of dispersed beads of the packing. A phenomenological model based on the flow of suspension between two volumes was developed by Heim & Solecki (1998). The authors assumed that cells were disrupted while moving from a safe volume to the one in which no living microorganisms could exist. Basing on the sequence of events: cell disruption – the release of intracellular compounds, Melendres et al. (1993) developed a nonlinear model of the release of selected intracellular enzymes. Heim et al. (2007) described nonlinearity of the kinetics caused by changes in the disintegration conditions which was a result of the process run. Nonlinearity of the disintegration process resulting from subsequent decline of the biggest fractions of yeast cells was observed by Solecki (2009). Earlier, Whitworth (1974) described nonlinearity of cell disintegration kinetics in a suspension containing microorganisms (*Candida lipolytica*) which belonged to the same species and occurred in two morphological forms. The recently developed theory of random transformations of dispersed matter makes it possible to include in the description the fundamental phenomena observed during the process (Solecki, 2011). The aim of the study was to

develop, basing on this theory, a phenomenological model of microorganism disintegration in a bead mill and to present a mathematical description of the process which would include the effect of cell size on the rate of cell disintegration.

2. Theory

A basis for the theory of random transformations of dispersed matter and principles of constructing general phenomenological and mathematical models were presented by Solecki (2011). In the case of disintegration of microorganisms in bead mills, a material medium V(τ) is a suspension of microorganisms which fills the working mill chamber. The concept of material objects belonging to set *N* covers microbial cells dispersed in the liquid. A random transformation consists in cell disruption between circulating elements of the packing and release of intracellular compounds.
Basic conditions prevailing in space V of the mill chamber are safe for microbial cells. The process of random transformation of objects belonging to set *N* proceeds as follows.
In any instant τ (τ ≥ 0), p families of transformation volumes $V_{\gamma j}$ dispersed in space V are generated at random, where p is the natural number. During the process the number of generated families of volumes $V_{\gamma j}$ is big and can change in time according to Eq. (1).

$$p = f_3(\tau) \tag{1}$$

Volume $V_{\gamma ji}$ is the transformation space of the i-th cell of dispersed microorganisms which belongs to the j-th family. A set of the conditions in which a transformation proceeds at the intensity no less than γ_{ti}, occurring in this volume, will ensure the transformation of the i-th object from set *N*. The transformation consists in the change ς of cell properties (ς>0) belonging to the set of identified properties of microorganisms *Pr*. After the transformation an object from set *N* does not belong to set *N* any longer. In the case of disintegration of microbial cells in a bead mill, the set of systemic transformation conditions is limited mainly to the transforming action of mechanical factors. According to Eq. (2), space V is incomparably bigger than any i-th volume $V_{\gamma ji}$.

$$V_{\gamma ji} << V \tag{2}$$

The range of changes in transformation volumes $V_{\gamma ji}$ generated in space V is described by Eq. (3) in reference to the volume, and by Eq. (4) in view of the intensity of transformation conditions.

$$\left(V_{\gamma ji}\right)_{\min} \le V_{\gamma ji} \le \left(V_{\gamma ji}\right)_{\max} \tag{3}$$

$$V_{\gamma ji(\gamma_t = \gamma_{ti})} \le V_{\gamma ji(\gamma_t)} \le V\gamma_{\gamma ji(\gamma_t = \gamma_{t\max})} \tag{4}$$

Symbol γ_{tmax} denotes the highest intensity of transformation conditions which can be generated in space V.
As a result of relative movement, the i-th cell is introduced to appropriate transformation volume $V_{\gamma ji}$. This volume is limited by surface $F_{\gamma\alpha ji}$ belonging to it according to Eq. (5).

$$F_{\gamma\alpha ji} \in V_{\gamma ji} \tag{5}$$

On the other hand, volume $V_{\gamma ji}$ can be limited by surface $F_{\gamma\beta ji}$ when it is formed. This surface belongs to the transformation volume according to Eq. (6).

$$F_{\gamma\beta ji} \in V_{\gamma ji} \tag{6}$$

The i-th object is transformed immediately after translocation of all its points to the transformation volume $V_{\gamma ji}$. If volume $V_{\gamma ji}$ is bigger than the volume of the i-th object, then volume $V_{\beta ji}$ is formed in it. It is limited by surface $F_{\gamma\alpha ji}$ which does not belong to it according to Eq. (7)

$$F_{\gamma\alpha ji} \notin V_{\beta ji} \tag{7}$$

Space $V_{\beta ji}$ cannot include total unconverted material object belonging to set *N* for which an appropriate transformation volume is $V_{\gamma ji}$. Before being translocated to $V_{\beta ji}$, every i-th object must be first transformed in volume $V_{\gamma ji}$.

Volume $V_{\alpha i}$ is safe for the unconverted i-th object from set *N*. We assume that intensive stirring takes place in it. Its aim is to make the concentration of unconverted objects from set *N* uniform within appropriate volumes which are safe for them. Volume $V_{\alpha i}$ is composed of two parts: $V_{\alpha it}$ which is part of volume $V_{\alpha i}$ whose subsets can be transformed to volumes $V_{\gamma i}$ or $V_{\beta i}$; and $V_{\alpha ic}$ which is part of volume $V_{\alpha i}$ whose subsets are never transformed to other volumes. In the case of the bead mill, volumes $V_{\alpha ic}$ occur near all surfaces of the working chamber. These volumes are distant from the mill surface by the size of a cell, and the thickness of their layer is slightly smaller than the radius of the smallest bead in the packing. In volume $V_{\alpha ic}$ the i-th cell is fully safe. The quotient of volumes $V_{\alpha ic}$ to $V_{\alpha i}$, the quotient of the sum of volumes $V_{\gamma i}$ and $V_{\beta i}$ to $V_{\alpha it}$ and the rate of relative movement of the i-th cell to $V_{\gamma i}$ are the factors that determine efficiency of the system of transformation of the i-th cell in a given technical device. An increase of the first factor causes a decrease of the transformation efficiency. An opposite effect is caused by an increase of other factors.

For instance, studies were carried out to increase differences in the velocity of points on the surfaces of adjacent beads of the packing which circulates in the mill (Solecki, 2007). Such an effect was to be induced by the presence of immobile baffles between stirring disks of a classical mill. In many cases of geometric solution of the mill interior, because of introduction of the baffles the efficiency of microorganism disintegration was deteriorated (Solecki, 2007). The development of a narrow-clearance construction did not bring about elimination of classical mills equipped with multi-disk impellers from the market. Rate constants determined for the process of disintegration in the mill with a bell-shaped impeller were often lower than those determined for a classical mill in comparable process conditions (Solecki, 2007). Optimum operating conditions of narrow-clearance mills are obtained for smaller values of packing degree. In the case of a classical mill it is about 90%, while for the mill with a bell-shaped impeller 60%, and with a cylindrical stirrer only 40%.

Part of space V is composed of volume V_δ which is safe for microorganisms from set *N* (Solecki, 2011). No stirring takes place in it and neither it nor its subsets are transformed to other volumes. Between volumes V_α and V_δ microbial cells can migrate freely. For a correctly constructed mill chamber, volumes V_δ (these can be slots in the place where two elements meet) are negligibly small and insignificant from the technology point of view, particularly when the device is sterilized between subsequent processes. In further studies it was assumed that V_δ=0.

An ellipsoidal shape of microorganisms and their different sizes were assumed. The size of the i-th cell is described by the length of three mutually perpendicular axes c_{1i}, c_{2i} and c_{3i}, which satisfy relation (8).

$$c_{1i} = c_{2i} \le c_{3i} \tag{8}$$

Microorganisms were assumed to be much smaller than packing elements in the mill d_k according to Eq. (9).

$$c_{3i} << d_k \tag{9}$$

For the whole population of microorganisms subjected to disintegration it was assumed initially that cell walls had the same mechanical strength and that the compressibility of fluids protected by them was identical.

Microorganisms in the working mill chamber are disintegrated between two surfaces belonging to different solids. One of them is a single element of the packing, and the other one is another element of the packing or an element of the mill working chamber. This can be the external surface of the reservoir of diameter D_z, the surface of an impeller with disk diameter d_t or of its shaft of diameter d_w. Due to the relations in Eq. (9) through (12), it was assumed that all inner surfaces of the mill chamber and stirrer were planes.

$$d_k << D_z \tag{10}$$

$$d_k << d_w \tag{11}$$

$$d_k << d_t \tag{12}$$

It was assumed that microorganisms were destroyed as a consequence of disruption of cell walls caused mainly by compressive load which acted along the shorter cell axis c_{1i}. This assumption was made after analysis of the results of many experiments which included disruption of single yeast cells using micro-tools controlled by micromanipulators. Results of these experiments have not been published yet. Non-homogeneity of the structure, thickness and rigidity of cell walls causes that microorganisms compressed along the long axis are deformed asymmetrically and due to accumulated energy catapult from the hazardous zone. This property formed by the evolution guarantees a better survival rate of microorganisms in their environment. In the case of actions characterized by much higher dynamics than the typical one occurring in nature, the probability of cell destruction along the long axis can be significant. In such a case the above assumption simplifies the problem.

It is assumed that cell walls are disrupted when compounds inside the cell can flow out of it. This state is equivalent to cell disintegration – transformation of the object. Three stages are distinguished in the destruction of microorganisms (Solecki, 2009):

1. contact,
2. cell deformation,
3. disruption of cell walls.

At the first stage the cell of axis c_{1i} contacts two destroying surfaces. The cell is not deformed. Points of contact of solid bodies with the i-th cell are called the points of destruction. They form a single destruction system. The segment which connects destruction points of cell c_{1i} is defined as the destruction axis. At the second stage, when destroying

surfaces approach each other, the cell is deformed. The contact area of the cell with solid bodies described by diameter $d_{\delta i}$ increases. Walls of the cell with axis c_{1i} are disrupted when compression surfaces approach each other at the third stage to destruction distance $l_{\delta i\,\min}$ described by the relation given in Eq. (13).

$$l_{\delta i\,\min} < c_{1i} \tag{13}$$

From the point of view of random transformation, the first two destruction stages have no significance, providing naturally that the number of load cycles has no effect on the cell strength. Hence, it can be assumed that starting with instant $\tau=0$, all cells present in the suspension are so deformed that an arbitrarily small increase of deformation in the transformation volume causes their disruption. The distance of destruction is measured along the destruction axis. It was assumed that the cell-destroying surface contact area in the moment of cell wall disruption was represented by a spherical cap of diameter $\delta_{i\,max}$.

Disruption of cells dispersed in the liquid occurs once the cells have been translocated to destruction volume $V_{\gamma ji}$ which is in the place of formation of a single destruction system. The continuity of grinding surfaces was assumed for the set of points belonging to circular environment of diameter $\delta_{i\,max}$ around the point of destruction. At least one grinding surface has a spherical shape. Thus, in the mill two destruction elements can generate a single destruction axis or a set of axes which constitute a cylindrical surface. At the present stage of studies we make a simplified assumption that elements destroying microbial cells are perfectly rigid.

We consider the case of batch mill operation, when during the process the supply of microbial suspension is constant. Its volume is equal to V. The process is carried out for the known initial biomass concentration. The initial number of microorganisms is N_0. During the process no microbial cells are added from the outside (it is assumed that the disintegration process is carried out in sterile conditions) and no cells are removed to the outside. The time of disintegration is very short as compared to the life time of microorganisms and the time of formation of new cells in the process conditions. Hence, it can be assumed that function f_{13} which describes cell growth and function f_{14} describing elimination of cells different than that being a result of the transformation, satisfy equations (14) and (15).

$$f_{13}\left(N_0,\tau\right)=0 \tag{14}$$

$$f_{14}\left(N_0,\tau\right)=0 \tag{15}$$

In the case of disintegration of microorganisms in the bead mills the transformation consists in the disruption of microbial cell walls. In the process carried out in the bead mill, high levels of packing of the mill chamber and big rotational speed of the stirrer are applied. Because of a high level of packing the mill with beads and high intensity of their circulation resulting from high rotational speed of the stirrer, it was assumed that during the process:

1. the sum of all volumes $V_{\gamma i}$ is constant (Eq. (16)),

$$\bigcup_{i=1}^{n} V_{\gamma ji} = const \tag{16}$$

2. the sum of all volumes $V_{\beta i}$ is constant (Eq. (17)).

$$\sum V_{\beta i} = const \tag{17}$$

We also assume that the process of microbial disintegration is carried out in steady-state conditions during the whole process duration. The mill start-up is neglected.

3. A phenomenological model

Figure 1 shows a theoretical set of possibilities to generate the families of transformation volumes between two spherical surfaces. It is prepared on the basis of a description of the general phenomenological model presented by Solecki (2011).
Single microbial cells are reduced to material points which have, among the others, such properties as spatial shape, volume, mass, etc. On each vertical segment between $\overline{AC}$ and $\overline{BD}$, division of volume V(τ) is marked. This division is a result of forming transformation volume $V_{\gamma ji}$ for the i-th cell. We consider an arbitrary vertical segment $\overline{15}$. It is divided by dashed lines $\overline{RS}$, $\overline{GH}$ and $\overline{IJ}$ into four main parts. Volume $V_{\alpha ci}$ which is safe for cell N_i occupies interval $\langle 1,2)$. In this volume intensive stirring takes place. Neither the whole volume $V_{\alpha ci}$ nor any of its subsets can be transformed to other volumes. Interval $\langle 2,4)$ occupies volume $V_{\alpha ti}$. It is safe for cell N_i and intensive stirring is observed in it. Subsets of volume $V_{\alpha ti}$ can be transformed to volumes $V_{\gamma ji}$ and $V_{\beta ji}$. $V_{\gamma ji}$ is the transformation volume of object N_i and in Fig. 1 it occupies interval $\langle 3,4\rangle$. It includes surface $F_{\gamma\alpha ji}$ which separates it from volume $V_{\alpha ti}$. Volume $V_{\gamma ji}$ is also limited by surface $F_{\gamma\beta ji}$ belonging to it, in case it is formed. This occurs when $V_{\gamma ji}$ has the size big enough in relation to the object transformed in it. Volume $V_{\beta ji}$ occupies interval $(3,5\rangle$ and is inaccessible for non-transformed object N_i. Surface $F_{\gamma\alpha ji}$ which separates it from volume V_α does not belong to volume $V_{\beta ji}$. It was assumed that object N_i is the material point that has feature $(V_{\gamma i})_{min}$ among the others. This is the smallest transformation volume characteristic of a given object. Components of space V in Fig. 1 are defined by two parameters: the length of relevant vertical segments and color intensity which determines a functional relation. The family of volumes P_j is formed of a group of transformation volumes for various material objects from set *N* defined by segment $\overline{3'3"}$. For objects from set *N* of the smallest characteristic transformation volume $(V_{\gamma s})_{min}$, the division into $V_{\alpha ci}$, $V_{\alpha ti}$, $V_{\gamma ji}$ and $V_{\beta ji}$ is marked by continuous lines $\overline{R'S'}$, $\overline{G'H'}$ and $\overline{I'J'}$. For objects with the biggest characteristic transformation volume $(V_{\gamma b})_{min}$, the division into volumes with different properties is marked by dotted lines $\overline{R"S"}$, $\overline{G"H"}$ and $\overline{I"J"}$.
Like for the cell-disrupting spherical surface-spherical surface system, also for the spherical surface-plane surface system we can determine a map to generate volumes related to the cell transformation process.
To determine the set of possibilities of generating transformation volumes, it is essential to know results of morphological studies and strength tests of microorganisms dispersed in space V. The current development of computer techniques for microscopic image analysis causes that morphological studies are not a problem now. Studies on the strength of microbial cells were carried out by Mashmoushy et al. (1998), Shiu et al. (1999) and Svaldo-Lanero et al. (2007). In the case of the bead mill it is especially important to know destroying transformations in which cells are disrupted (Smith et al., 2000, Stenson et al., 2010). Mechanical stresses in *Saccharomyces cerevisiae* yeast cells caused by high hydrostatic pressure were tested by Hartman et al. (2006). Depending on the method by which the

process is carried out and according to a technical device selected, it is necessary to know the morphology of packing in the case of vibrating mixers and bead mill, the distribution of shearing forces and velocity of liquid flow through the valve in the case of high-pressure homogenizers, and finally the size of cavitation bubbles in the case of ultrasound homogenizers.

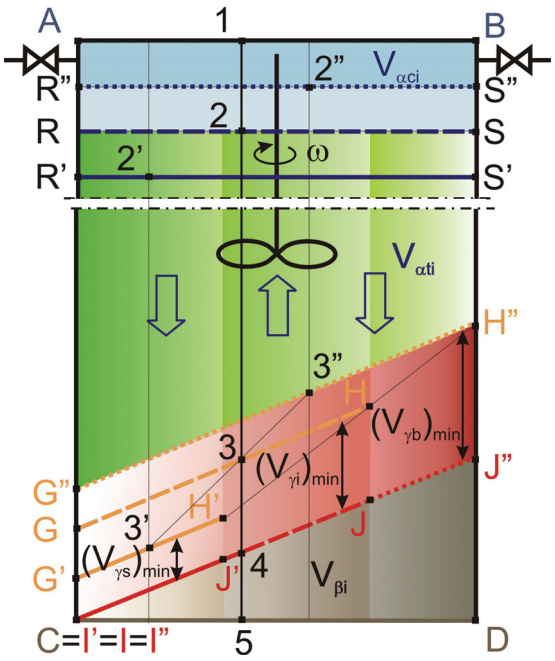

Fig. 1. The set of possibilities to generate a single family of transformation volumes and related volumes for microorganisms from set *N* dispersed in space V

In the case of cell disintegration in the bead mill packed with beads of the same diameter, p_s families of destruction volumes are formed by the spherical surface-spherical surface transformation system and p_p families by the spherical surface-flat surface transformation system. Numbers p_s and p_p are the natural numbers and their sum is equal to the number of transformation families p formed in space V. The phenomenological model consists of p_s layers of the first type shown in Fig. 1 and p_p layers of the second type specific of the spherical surface-flat surface system. The range of space divisions in subsequent layers encompasses only the divisions which were formed for one specified family of transformation volumes. If, for instance, two contacting spherical surfaces generate a transformation family, then the layer encompasses space divisions for all vertical segments from point H′ to point H″. On the other hand, if the distance between two spherical surfaces is such that the biggest axially compressed cell which is most susceptible to disintegration is disrupted, then in the component layer there will be a space division described (dotted lines) by the division of vertical segment passing through point G″. In a general case, for the i-th cell from set *N* the component layer will contain divisions marked on vertical segments from point 3′ to point 3″. The sum of all volumes contained in p layers is equal to V. By

analogy, phenomenological models can be constructed for other methods of microorganism disintegration: physical, chemical and biological.

In the phenomenological model of microorganism disintegration it was assumed that space V consisted of volumes V_{α}, V_{γ} and V_{β}. Additionally, volume V_{α} was divided into $V_{\alpha t}$ and $V_{\alpha c}$. Destruction volumes $V_{\gamma ji}$ are formed by circulating beads of the packing. The general and specific schematics of cell disruption between spherical surfaces were discussed in an earlier study (Solecki, 2011). The general scheme of cell disruption between the spherical and flat surface is shown in Fig. 2a. It covers all possible cases contained between segments $\overline{AC}$ and $\overline{BD}$ in Fig. 1, referring to the division of the volume of microbial suspensions into $V_{\alpha ji}$, $V_{\gamma ji}$ and $V_{\beta ji}$. After limiting deformation of the i-th cell, its walls are disrupted (Fig. 2a). The formed transformation volume $V_{\gamma ji}$ is limited by surface $F_{\gamma\alpha ji}$ (orange dashed line), surface $F_{\gamma\beta ji}$ (red dashed line), the spherical surface of packing element and the flat surface of the mill chamber. Volume $V_{\gamma ji}$ with the axis of symmetry OU includes limiting surfaces $F_{\gamma\alpha ji}$ and $F_{\gamma\beta ji}$. Surface $F_{\gamma\beta ji}$ limits volume $V_{\alpha ji}$, but it does not belong to this volume. The volume inaccessible for the i-th living cell $V_{\beta ji}$ is limited by the spherical plane and surface $F_{\gamma\alpha ji}$. The limiting surfaces do not belong to volume $V_{\beta ji}$. The axis of symmetry of volume $V_{\beta ji}$ is straight line OU.

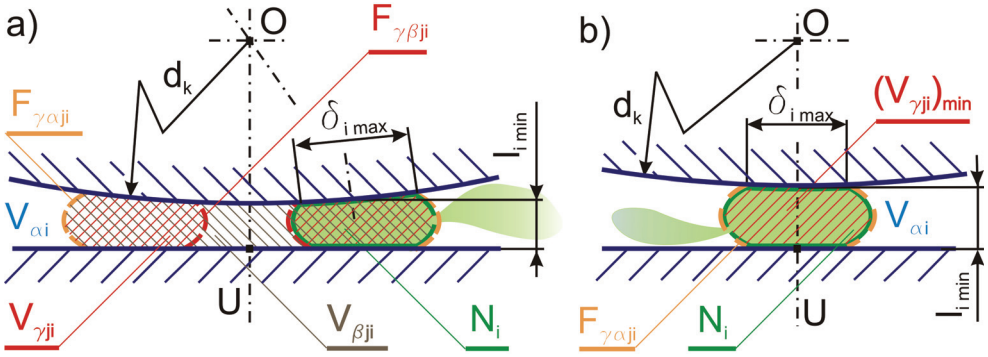

Fig. 2. The model of cell disruption during hitting with spherical elements: a) a general case – a non-axial impact, b) a particular case – an axial impact

In the specific case shown in Fig. 2b, the line of division of space V is in the AC position (Fig. 1) and volume $(V_{\gamma ji})_{min}$ is formed. It is limited by the spherical surface, flat surface and surface $F_{\gamma\alpha ji}$ (orange dashed line). The axis of symmetry of volume $(V_{\gamma ji})_{min}$ passes through points O and U.

It follows from the presented phenomenological model that it can encompass not only the working chamber of the mill but even the entire system of technical devices used to disintegrate microorganisms during continuous mill operation. Then volume $V_{\alpha c}$ is composed of suspension volume in the whole system connected to the working chamber including inlet and outlet reservoirs.

4. A mathematical model

The concentration of microorganisms introduced into space V is determined by the initial number of non-transformed cells N_0 in space V according to Eq. (18).

$$S = \frac{N_0}{V} \tag{18}$$

For process duration τ=0 volumes $V_{\gamma ji}$, $V_{\beta ji}$ and $V_{\alpha i}$ are formed in space V. Unconverted objects can be only in volume $V_{\alpha i}$ appropriate for them. Between safe volumes for particular cells of microorganisms from set *N* there is a relationship described by Eq. (19).

$$V_{\alpha b} \subset \ldots \subset V_{\alpha i} \subset \ldots \subset V_{\alpha s} \tag{19}$$

For the relation given in Eq. (19) equivalence can occur between Eq. (20) and Eq. (21).

$$\left(V_{\gamma s}\right)_{\min} = \left(V_{\gamma b}\right)_{\min} \Rightarrow V_{\alpha s} = V_{\alpha b} \tag{20}$$

$$\left(V_{\gamma s}\right)_{\min} < \left(V_{\gamma b}\right)_{\min} \Rightarrow V_{\alpha b} < V_{\alpha s} \tag{21}$$

In the case illustrated by Eq. (20) identical cells of microorganisms belonging to set *N* are uniformly dispersed in the whole volume $\bigcup V_{\alpha i}$. On the other hand, from the equivalence given in Eq. (21) follows the inequality of dispersion of the objects from set *N* in volume $\bigcup V_{\alpha i}$. Every additional surface $F_{\gamma\beta i}$ introduced in space V additionally separates volume $\bigcup V_{\alpha i}$ into two parts. They differ in the concentration of microorganisms which they contain. The process of ideal mixing ensures uniformity of the dispersion of objects from set *N* only within the volume limited by the surface of type $F_{\gamma\beta}$. In the case presented in Eq. (21), owing to relations given in Eq. (2) and (22) and uniform dispersion of elements of set *N* and volume $V_{\gamma ji}$ in space V, we can use mean concentration of dispersed material objects.

$$\left(V_{\gamma ji}\right)_{\min} << V \tag{22}$$

Hence, after starting the process, appropriate objects N_i of set *N* will be introduced at random to the formed volumes $V_{\gamma ji}$. Mean concentration of the transformed objects in the volume occupied by them is described by Eq. (23).

$$S_\alpha = \frac{N_0}{V_{\alpha\cup}} \tag{23}$$

In instant τ=0 of the process duration the number of unconverted objects N(τ) present in volume $\bigcup V_{\alpha i}$ is equal to the initial number of objects N_0, as described by Eq. (24).

$$N = N_0 \tag{24}$$

The number of cells $N_d(\tau)$ which were disrupted in instant τ=0 is given by Eq. (25).

$$N_d = 0 \tag{25}$$

The conversion rate of microorganisms X(τ) defined by the ratio of the number of disrupted cells N_d to the initial number of cells N_0 according to Eq. (26) is equal to 0.

$$X = \frac{N_d}{N_0} \tag{26}$$

At any time of the process duration τ the number of transformed microorganisms is N_d. The transformed cells can be in any place in space V. The number of living microorganisms present only in volume $\bigcup V_{\alpha i}$ is determined by Eq. (27).

$$N = N_0 - N_d \tag{27}$$

According to Eq. (28), after time τ of the process, microbial cells at mean concentration S_α determined by number N of unconverted cells in volume $\bigcup V_{\alpha i}$ are introduced to all volumes $V_{\gamma ji}$.

$$S_\alpha = \frac{N}{\bigcup_{i=1}^{n} V_{\alpha i}} \tag{28}$$

Naturally, the overall concentration of microorganisms in space V will be determined by Eq. (29). The concentration will be recorded, for instance, in the suspension samples taken from the mill and in the inlet or outlet reservoir.

$$S = \frac{N}{V} \tag{29}$$

The rate of conversion of microorganisms after time τ of the process is given by Eq. (26).
The increase of the number of transformed objects dN_d in all volumes $V_{\gamma ji}$ after arbitrarily short time interval dτ is specified by Eq. (30).

$$dN_d = S_\alpha dV \tag{30}$$

Volume dV displaced from $V_{\alpha ji}$ to $V_{\gamma ji}$ in time increment dτ depends on the size of limiting surface F through which dV is displaced and on the displacement rate u. This is described by Eq. (31).

$$dV = uFd\tau \tag{31}$$

Upon substitution of Eq. (28) and (31) to Eq. (30) we obtain Eq. (32) which describes the increase of objects transformed in volumes $V_{\gamma ji}$.

$$dN_d = kNd\tau \tag{32}$$

The process rate constant k of the transformation of microbial cells is described by Eq. (33).

$$k = \frac{F}{\bigcup_{i=1}^{n} V_{\alpha i}} u \tag{33}$$

Surface F is the sum of these parts of surface $F_{\gamma\alpha ji}$ through which microbial cells pass to volume $V_{\gamma ji}$.
Based on Eq. (33) the loss of non-transformed objects can be represented by Eq. (34).

$$dN = -k\left(N_0 - N_d\right)d\tau \tag{34}$$

5. Materials and methods

Microorganisms were disintegrated in a horizontal bead mill with a multi-disk impeller. The working chamber about 1 dm^3 in volume had the diameter of 80 mm. The impeller was equipped with six round disks 66 mm in diameter. They were mounted centrally on the shaft at a distance of 30 mm from each other. The mill was filled in 80% with ballotini of the diameter ranging from 0.8 to 1.0 mm. They were made of lead-free glass of specific density around 2500 kg/m^3. 50% water solution of ethylene glycol at the temperature 275 K was supplied to the cooling jacket of the mill. Experiments were carried out in the mill at periodic operating conditions (constant feed). Rotational speed of the impeller was 261.8 rad/s.
The experiments were performed for commercial baker's yeast *S. cerevisiae* produced by Lesaffre Bio-corporation (Wołczyn, Poland). The concentration of yeast suspension ranged from about 0.002 to over 0.17 g d.m./cm^3. Microorganisms were dispersed in the water solution containing 0.15 M NaCl and 4 mM K_2HPO_4.
The kinetics of cell disruption was determined on the basis of the count of living microorganisms present in the suspension samples. A computer-aided analysis of microscopic images (method I) was used. Cells were counted under the Olympus BX51 microscope (Olympus Optical Co.). Photographs were taken using a CCD digital camera of resolution 2576×1932×24 bit (Color View III, Soft Imaging System). Preparations were stained with methylene blue. Thom neu chamber (Paul Marienfeld & Co.) was used to count cells. Photographs were analyzed by means of a specialist software (analySIS 5, Soft Imaging System).
The amount of protein R dissolved in the continuous phase was determined by Bradford's method (1976) (method II). The supernatant was obtained after 20 min centrifugation at centrifugal force 34000 g. Measurements were made in a spectrophotometer at the wavelength 595 nm (Lambda 11, Perkin Elmer). A standard protein concentration curve prepared for bovine albumin (Albumin A 9647, Sigma) was applied.
The degree of release of intracellular compounds was analyzed also on the basis of light absorbance A in the supernatant (method III). The measurements were made using a Lambda 11 spectrophotometer (Perkin Elmer) at the wavelength λ = 260 nm (Middelberg et al., 1991; Heim & Solecki, 1998, 1999). Near the applied wavelength, spectral characteristics of RNA and DNA nucleic acids reach maximum values. The supernatant was obtained after centrifugation of the suspension in a 3K30 B centrifuge (Braun Biotech International) for 20 min at centrifugal acceleration of 34 000 g. The inside of the centrifuge was cooled down to 4°C.
In rheological investigations a RC 20 rotational rheometer (RheoTec) operating in a two-slot cylindrical tank – bell-shaped stirrer system was used. Measurements for the suspension of yeast cells and supernatant were made at the temperature 4°C. The degree of disintegration of microbial cells was changed from 0 to nearly 100%. Supernatant was obtained after 20 minute centrifugation of the suspension at centrifugal force 40 000 *g*.

6. Results and discussion

6.1 Disruption of microbial cells

In the case monogeneity of yeast cells the set of variable properties Vr of objects N is the empty set (Solecki, 2011). At such an assumption the loss of microorganisms dN_d in time interval $d\tau$ will be expressed by the right-hand side of Eq. (34) with an opposite sign. Kinetics of the disruption of microorganisms in holistic approach is described in Eq. (35).

$$dN_d = k(N_o - N_d)d\tau \tag{35}$$

Process rate constant k is described by Eq. (36).

$$k = \frac{F}{V_{\alpha\cup}}u \tag{36}$$

The sum of safe volumes $V_{\alpha\cup}$ for subsequent i-th material objects is given by Eq. (37).

$$V_{\alpha\cup} = \bigcup_{i=1}^{n} V_{\alpha i} \tag{37}$$

The regression line in Eq. (38) was obtained after integration of Eq. (35) by sides. The integration was preceded by the separation of variables. The regression line is often used to describe the disintegration kinetics of microbial cells in bead mills (Currie et al., 1974; Merffy & Kula, 1979; Limmon-Lason et al., 1976 Melendres et al., 1991; Garrido et al., 1994; Heim & Solecki, 1998; Solecki, 2007).

$$\ln\left(\frac{N_0}{N_0 - N_d}\right) = k\tau \tag{38}$$

A correlation between variables in Eq. (38) was investigated. For linear regression describing the kinetics of yeast cell disruption the values of coefficient R were higher than 0.9835. Although advantageous values of the coefficient were obtained, the analysis of rate constant showed significant changes of its value which accompanied changes in the suspension concentration (Fig. 4). They are described by Eq. (39) for the suspension concentration S>0.

$$k = a_1 S^2 + a_2 \tag{39}$$

When estimating the coefficients in Eq. (39), data for the rate constants much deviating from a model line for very low and low concentrations of the suspension were neglected. Table 1 gives values of the determined coefficients and significant results of statistical analysis.

Changes in the rate constant of cell disruption accompanying a change of the suspension concentration are induced by deviation of the process kinetics from linearity. Their character depends on biomass concentration. In general, three concentration ranges of yeast suspension with similar cell disruption process can be distinguished. These concentrations are very low, up to about 0.01 g d.m./cm^3, low – from about 0.01 to 0.10 g d.m./cm^3 and medium and high – exceeding 0.10 g d.m./cm^3. In Fig. 5, for selected biomass concentrations, the experimentally determined changes in the degree of yeast cell disruption are compared to the changes determined by the linear model (Eq. 38). At low concentrations of the suspension (S=0.08 g d.m./cm^3) the process is linear. At the initial stage of the process, at very low suspension concentrations (S=0.002 g d.m./cm^3), determined values of the rate constant are usually similar to the values obtained for low suspension concentrations. However, when the initial number of cells is small, the disruption rate decreases subsequently during the process. On the other hand, for medium and high concentrations (S=0.14 g d.m./cm^3) the process of microbial cell disruption at the initial stage is much slower than the model process. At the next stage of the process the cell disruption rate increases so that the process is much faster than in the case of low concentrations.

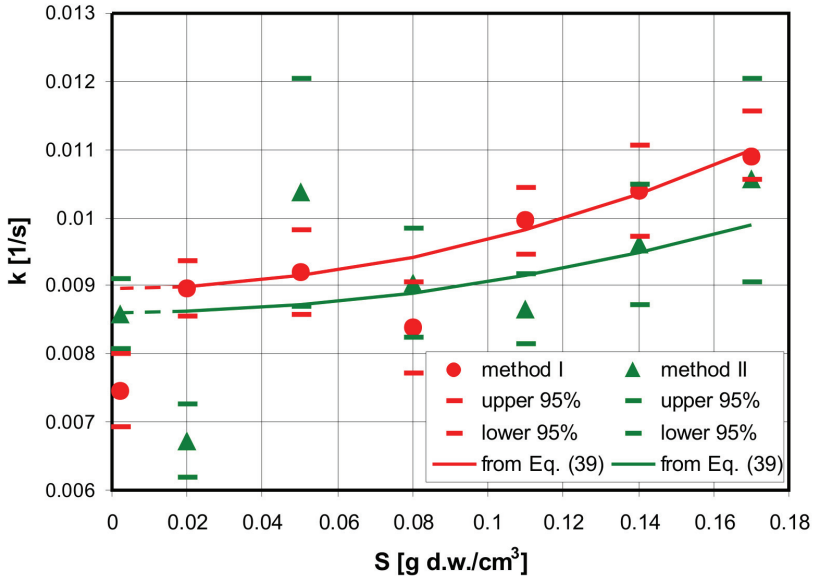

Fig. 3. Changes of rate constant determined for a linear model by method I (direct method based on computer-aided counting of cells under a microscope) and method II (indirect method based on measurement of the quantity of released protein)

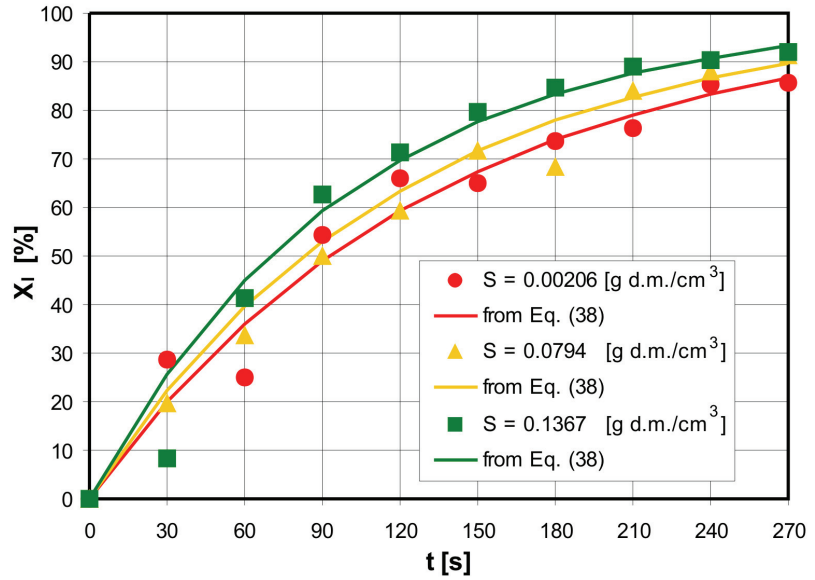

Fig. 4. The effect of suspension concentration on the cell disruption process

Method	a_1	a_2	n	R
	-	s^{-1}	-	-
I	0.070	0.00897	5	0,9948
II	0.045	0.0086	6	0,8812
III	0.125	0.0057	5	0,9786

Table 1. Results of the estimation of parameters in Eq.(39) for the analytical methods applied

Studies on yeast cell morphology revealed a significant differentiation of cell sizes. Selected parameters are given in Table 2. Size distributions of axes c_{1i} and c_{3i} are illustrated in Fig. 5. The process of microbial cell disruption was analyzed taking into account different cell sizes for two cases: in the first one the cells were determined by the short axis of the ellipsoid c_{1i}, while in the second one by mean diameter d_i.

Parameter	c_{1i}	c_{3i}	d_i	Elongation	Aspect ratio	Shape factor	Sphericity
unit	µm	µm	µm	–	–	–	–
min	3.314	4.020	3.643	1.004	1.010	0.846	0.503
max	8.007	9.433	8.686	1.432	1.439	1.126	0.992

Table 2. Chosen results of yeast morphology investigations

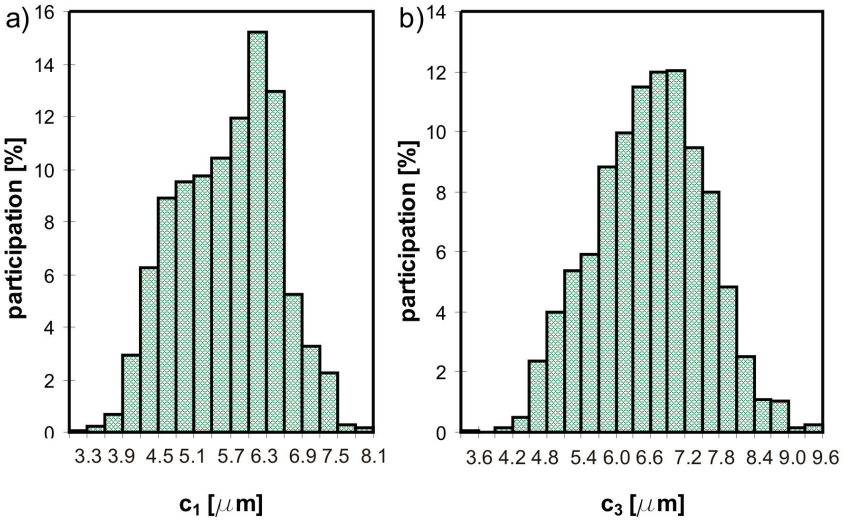

Fig. 5. Distribution of size of small and greater axis ellipsoid defining yeast cells

To model the disintegration process in relation to the size of yeast cells, for both cases mentioned above the set of cells was divided into m=12 size fractions. The effect of size fractions on the cell disruption kinetics was investigated using Eq. (35) to describe the disintegration of yeast cells from the given size fraction. This description allowed us to compare the process run in particular fractions with the process taken as whole. Results of the comparison of cell disruption kinetics for particular size fractions determined by mean

diameter d_i are illustrated in Fig. 6. Values of the rate constant determined for the biggest cell fraction are over 10 times higher than those determined for the smallest cell fraction. Based on the size analysis of undisrupted cells it was found that at a very small initial number of microorganisms during the process three biggest yeast cell fractions disappear successively: 9.5-10 μm, 9-9.5 μm and 8.5-9 μm. The process analyzed for size fractions determined by the short axis of the ellipsoid did not reveal any effect of the cell size on microorganism disruption kinetics. This result is a consequence of a significant differentiation of cell sizes determined by the short axis of the ellipsoid. Cells in the given fraction can have the shape almost spherical to ellipsoidal with the 1 : 1.4 axis ratio (Table 2). The same percent deformation along axis c_{1i} can be destructive for spherical cells but is still safe for much elongated cells.

Solecki (2011) considered the case of random transformation of objects from set N which differed by only one feature vr_1 having an important effect on the process. Eq. (40) describes the transformation of objects from an arbitrary interval $\zeta \in \langle 1, m \rangle$ taking into account the existence of the whole set N.

$$\frac{N_{0\zeta}}{N_0} dN_{d\zeta} = \frac{N_{0\zeta}}{N_0} k_\zeta \left(N_{0\zeta} - N_{d\zeta} \right) d\tau \tag{40}$$

Eq. (41) describes the transformation of objects of the entire set taking into consideration the division of set N into subsets.

$$\sum_{\zeta=1}^{m} \frac{N_{0\zeta}}{N_0} dN_{d\zeta} = \sum_{\zeta=1}^{m} \frac{N_{0\zeta}}{N_0} k_\zeta \left(N_{0\zeta} - N_{d\zeta} \right) d\tau \tag{41}$$

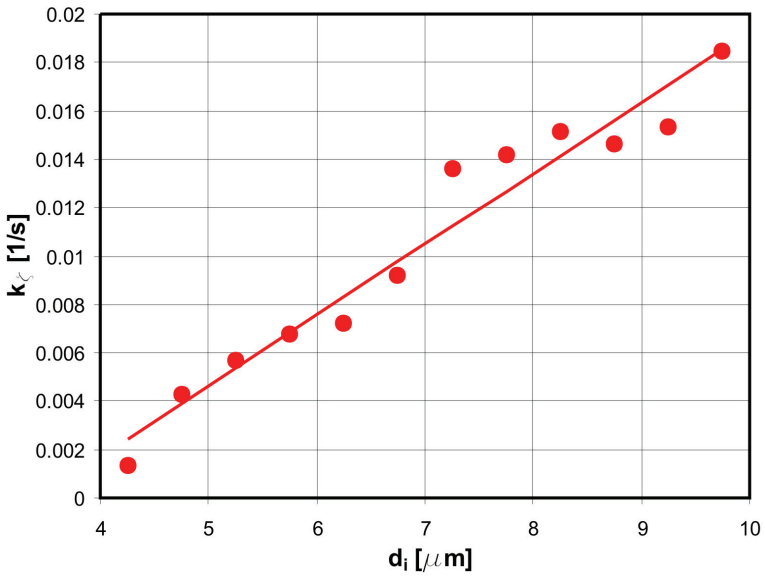

Fig. 6. The effect of cell size on the disintegration rate constant

After separating the variables in Eq. (41) and integration by sides, we get Eq. (42).

$$\sum_{\zeta=1}^{m} \frac{N_{0\zeta}}{N_0} \ln \frac{N_{0\zeta}}{N_{0\zeta} - N_{d\zeta}} = \sum_{\zeta=1}^{m} \frac{N_{0\zeta}}{N_0} k_\zeta \tau \tag{42}$$

Relations between rate constants in Eq. (35) and (40) are determined in Eq. (43).

$$\Phi \sum_{\zeta=1}^{m} \frac{N_{0\zeta}}{N_0} k_\zeta = k \tag{43}$$

Coefficient Φ is described by the relation given in Eq. (44).

$$\Phi = \ln \frac{N_0}{N_0 - N_d} \left(\sum_{\zeta=1}^{m} \frac{N_{0\zeta}}{N_0} \ln \frac{N_{0\zeta}}{N_{0\zeta} - N_{d\zeta}} \right)^{-1} \tag{44}$$

The process of disintegration in the mill is described by Eq. (42) as a total effect of disintegration of particular cell size fractions. The disintegration kinetics of microorganisms in particular fractions is linear. Differences in cell sizes do not cause nonlinearity of the process. Deviations from linearity shown for very low concentrations of the suspension are caused by the decay of subsequent cell size fractions during the process. Nonlinearity of the process obtained at a very small initial number of microorganisms in the suspension N_0 described by Eq. (42) is illustrated in Fig. 7.

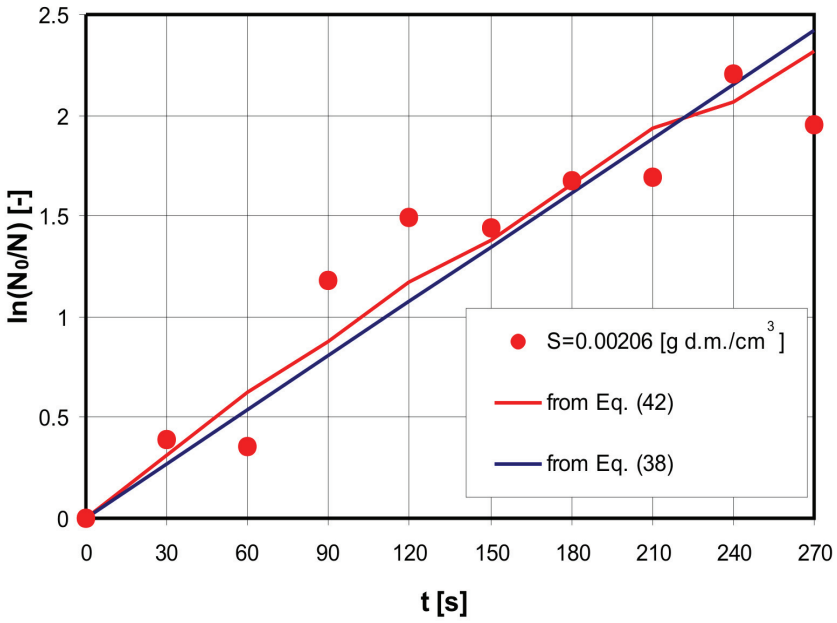

Fig. 7. The course of microbial cell disruption taking into consideration the effect of size fraction on the disintegration rate

Analysis of results of the process showed that at low concentrations of the suspension (0.05 g d.m./cm^3) the process was very well described by linear relation in Eq. (38) (R=0.9938). The presence of the biggest yeast cells until reaching over 90% disintegration was confirmed using the direct method. In the case of yeast cell concentration equal to 0.05 g d.m./cm^3, the initial number of cells is over 20 times bigger than in the case of cell concentration of 0.002 g d.m./cm^3. Hence, it is more probable that bigger cells will survive longer in the process at higher concentrations of the suspension.

The disintegration of microorganisms in the bead mill is a random transformation of dispersed matter. If the experiments were carried out for a single cell, it might have appeared that the degree of disintegration obtained in the first experiment would be 100%, in the second one also 100%, and in the third one e.g. 0%. From the investigations carried out for the suspension concentration equal to 0.05 g d.m./cm^3 it follows that if there are 2,355E9 cells dispersed at one time, after the process 0,2598E9 cells will remain alive on average. Hence, for an experiment carried out with a single cell, in 11 cases out of 100 experiments the result of disintegration at time τ=270 s will be 0% on average. It is probable, however, that in the process all cells will disintegrate. This probability decreases with an increase of the initial number of cells. Nonlinearity of the process caused by subsequent decay of objects from set N which are most susceptible to transformations can appear at every concentration of the suspension. This probability depends on the initial concentration of microorganisms in the suspension. For very low concentrations it is very big, while for high concentrations it is small. At a very small number of cells, a nonlinear process will be most probable, although it is not likely that the process will be linear. For a small and big number of cells, when no relations occur between the cells, a linear process is expected, but it may also happen that the process will be nonlinear. A result of this phenomenon are rate constants determined experimentally which are smaller than the values determined from the model and given by Eq. (39).

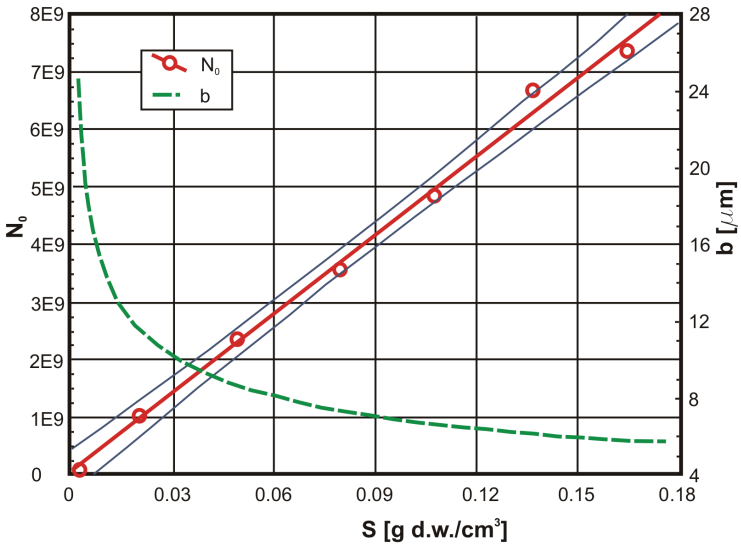

Fig. 8. Influence of suspension density on the distance between geometrical centres of adjacent cells (distribution of yeasts in the nodes of compact hexagonal network was assumed)

An increase of the initial number of yeast cells in the suspension causes an increase of rate constant k (Fig. 3) according to Eq. (39). Analysis of the phenomenological model of the process shows that this can be due to an increase of volume $V_{\gamma i}$ and consequently the growth of volume $V_{\beta i}$. When microorganisms are concentrated, the interrelations between cells are intensified. That was confirmed by the investigations of the effect of biomass concentration and degree of disintegration on distances between geometric centers of adjacent yeast cells (Heim & Solecki 1999; Heim et al., 2007). It was assumed that they are placed in the nodes of the compact hexagonal network. Eq. (45) describes relationships of the distances between centers of the adjacent microorganisms b with biomass concentration S and disintegration degree X (Heim et al., 2007).

$$b = \frac{a_4}{\left[S(1-X)\right]^{\frac{1}{3}}} + error \tag{45}$$

The analysis of yeast cell size distribution and distances between geometric centers of the cells indicated very significant intensification of relationships between the microorganisms, which follows an increase of the concentration of biomass. For instance, at the concentration 0.11 g d.m./cm^3 about 30% of the cells show higher value of parameter c_{1i} than distance b equal to about 6 μm. The increased intensity of cell interactions is confirmed also by the results of studies on rheological properties of the microbial suspension. It was proved that an increase of the initial concentration of microorganisms caused a decrease of apparent viscosity of the suspension. At the concentration 0.002 g d.m./cm^3 its value is close to that obtained for water, at 0.08 g d.m./cm^3 it is about 5 mPas, and at the concentration 0.17 g d.m./cm^3 it reaches 20 mPas.

During the disintegration of yeast cells significantly changed the rheological properties of the suspension. Interesting is a rapid decrease of the apparent viscosity at the initial stage of the process at τ=0-30 s, related to the destruction of a large number of spatial structures of yeast cells. The cell disruption rate increases at a later stage of the process. According to the results shown in Fig. 5, the rate of disintegration increases in the process time ranging from 30 to around 120 s.

The presented analysis of relationships refers to the suspension of yeast cells placed in an ordinary reservoir. The concentration of microorganisms in space V is generally described by Eq. (29). After supplying the suspension into the mill working chamber, the relationships between cells are further intensified. Particular cells N_i fill up only volumes $V_{\alpha i}$, while the continuous phase fills also volumes $V_{\gamma ji}$ and $V_{\beta ji}$. When the suspension is fed into the mill, the cells are filtered in volumes $V_{\alpha i}$. With the moment of starting the process, the suspension of mean concentration S_α is introduced to volume $V_{\gamma ji}$ according to Eq. (28).

The above analyses lead to a conclusion that an increase of volume $V_{\gamma i}$ which causes an increase of the cell disruption rate cannot be induced by yeast blocking by adjacent cells. Such an effect could be brought about by released intracellular compounds or some fragments of already disrupted cells. Nonlinearity of the process, which is revealed with an increase of suspension concentration, is described by Eq. (46) (Heim et al., 2007). It takes into account the concentration of the suspension of microorganisms and the change of distance between centers of adjacent cells which occurs during the process. A change of parameter b for a given concentration of the suspension is the measure of the number of disrupted cells and released intracellular compounds.

$$\ln\frac{N_0}{N} = k\left[1+\left(\frac{S}{b}\right)^{a_5}\right]t \tag{46}$$

The process rate for high suspension concentrations increases only at the second stage of the process, after over 30 s. At the initial phase, the process is slower than the disruption of microorganisms at the concentration of 0.05 g d.m./cm^3 (Fig. 4). Such a result was obtained at 0.11, 0.14 and 0.17 g d.m./cm^3. The decreased process rate is caused by inefficient operation of the packing in the working chamber. If packing of the cells is so dense as that described above, the approaching surfaces cause deformation of the compressed cell perpendicular to the destruction axis. A result is forcing out of adjacent cells from the hazardous zone and consequently, a decreased efficiency of the packing. In this case, the relative rate of cell supply does not only result from cell concentration and the dislocation rate of the suspension.

6.2 The release of intracellular compounds

In the case when cell disruption is equivalent to the release of intracellular compounds, the kinetics of protein release R from yeast cells is described by Eq. (47).

$$dR = k_{II}(R_m - R)d\tau \tag{47}$$

The values of absorbance obtained at a given concentration of individual samples were calculated into the amount of pure nucleic acid RNA released during the process from the cells. Its concentration in the continuous phase of the suspension after time of the process is denoted as C. The calculations were made after assuming mean values for nucleotides defined by Benthin et al. (1991). Taking into account the method of analysis of disintegrated microorganisms, a mathematical description of the process has the form of Eq. (48).

$$dC = k_{III}(C_m - C)d\tau \tag{48}$$

A maximum concentration of protein R_m and nucleic acids C_m was determined in separate experiments based on the quantities of released intracellular compounds specified for cell disintegration level ranging from about 98% to over 99%. Experiments performer at the disintegration range 0-90% are represented according to the method applied by the regression line given by Eq. (49) or Eq. (50), respectively.

$$\ln\left(\frac{R_m}{R_m - R}\right) = k_{II}\tau \tag{49}$$

$$\ln\left(\frac{C_m}{C_m - C}\right) = k_{III}\tau \tag{50}$$

When measuring method II was used, the values of coefficient R for data obtained in subsequent experiments were not smaller than 0.9605, while in the case of method III not smaller than 0.9826. The determined values of the rate constant of protein release are given in Fig. 3. Changes of this rate constant which proceed with concentration growth are in agreement with the dependence of yeast cell disruption rate constant on cell concentration. Rates constants of protein release at the highest concentration are about 1.5 times bigger

than the values obtained for the lowest yeast cell concentration. A similar relation and character of changes were obtained when the release of intracellular compounds was studied on the basis of absorbance measurements. Results of these experiments are illustrated in Fig. 9. At suspension concentration S>0 changes of the process rate constant in methods II and III are described by Eq. (39) and results of estimation are collected in Table 1. Data obtained by Bradford's method for concentrations 0.02 and 0.05 were deleted from statistical analyses; in the case of absorbance measurements data obtained for the lowest concentration of the suspension were omitted.

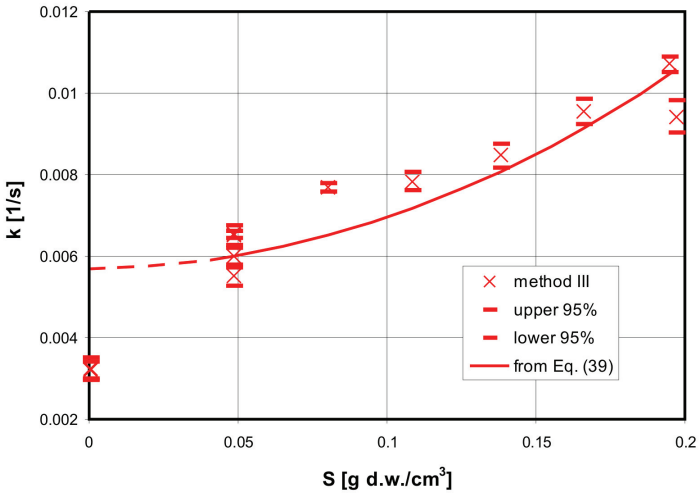

Fig. 9. Changes of rate constant determined for a linear model – method III

Results shown in Fig. 3 refer to biological material taken from one fermentation process, while these illustrated in Fig. 9 were obtained for yeast from a different fermentation process. In general, the results show that protein release is slower than microbial cell disruption. These observations are in agreement with results obtained by Middelberg et al. (1991) for *Escherichia coli* disintegrated in a high-pressure homogenizer. For such bacteria whose cellular structure is different than yeast cellular structure, the authors showed that the process tested on the basis of determination of the number of living microorganisms and absorbance of light with the wavelength 260 nm. According to Middelberg et al. (1991), the process of protein release measured also by Bradford's method is slower. Dependence of the release rate of intracellular compounds on the place of their location in cells was published by Hetherington et al. (1971). The authors report that during disintegration of *E. coli* cells the periplasmic enzymes are released faster than total protein, all cytoplasmic enzymes are released at the same rate as total protein, whereas membrane-bound enzyme slower.

The release of intracellular compounds during disintegration of microorganisms in the bead mill is shown in Figs 10 and 11. In general, the results are concordant with the results obtained in the experiments with cell disruption process. A decreased rate of protein release at the initial stage of disintegration is observed already at low suspension concentrations; it is higher than the decrease of cell disruption rate at medium and high concentrations of the suspension. Character of the process investigated on the basis of absorbance measurement is

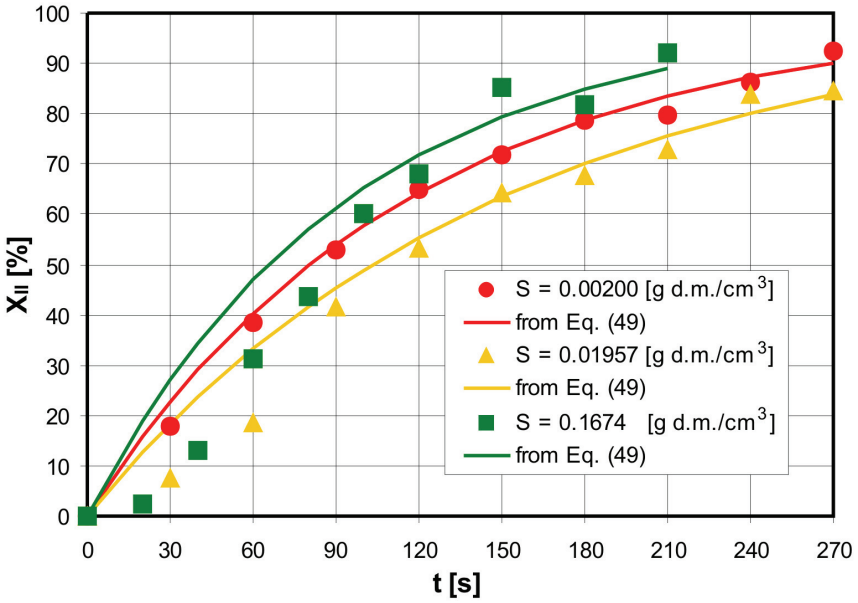

Fig. 10. The effect of suspension concentration on the protein release process

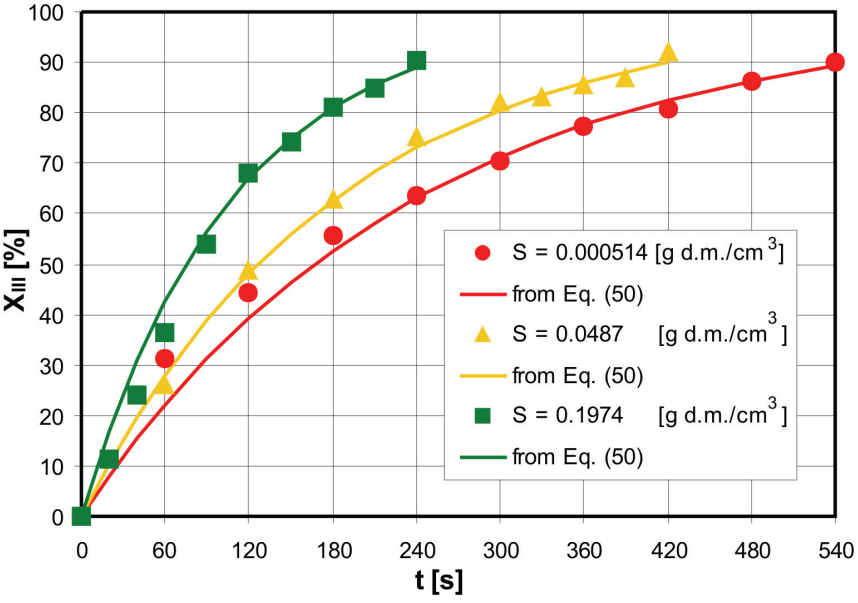

Fig. 11. The effect of suspension concentration on the intracellular compounds release process

close to the one obtained on the basis of determination of the number of living cells. In the case of high suspension concentrations the decrease of the intracellular compound release rate was not so significant as in the case of results obtained by the direct measuring method. The sequence of events: cell wall disruption – release of intracellular compounds, was used by Melendres et al. (1993) to describe nonlinear release of enzymes. This theory can be used in the description of total protein release. Eq. (35) can be written in the form of Eq. (51).

$$N_d = N_0\left(1 - e^{-kt}\right) \tag{51}$$

If protein release rate is proportional to that which can be released from disrupted cells, the increment of protein released in time dτ is described by Eq. (52).

$$dR = k_{II}(R_D - R)d\tau \tag{52}$$

Protein can be released only from disrupted cells. The maximum amount of protein R_D that can be released from cells disrupted in time τ is specified by Eq. (53).

$$R_D = R_m\left(\frac{N_d}{N_0}\right) \tag{53}$$

Upon substitution of Eq. (53) and Eq. (51) to Eq. (52) we obtain Eq. (54) for protein release in the process of microbial cell disruption.

$$dR = k_{II}\left[R_m\left(1 - e^{-k\tau}\right) - R\right] \tag{54}$$

Results illustrated in Fig. 4 show that differences in the process rates increase with an increase of the concentration of microorganism suspension. Character of changes of the rate constants determined on the basis of absorbance measurements is in agreement with that revealed on the basis of computer-aided analysis of microscopic images and Bradford's method (1976).

7. Conclusions

Disintegration of microorganisms in bead mills is the process of random transformation of organic matter dispersed in limited space. The general theory can be used to formulate a phenomenological model of the disintegration process and its mathematical description. They allow us to illustrate fundamental phenomena and mechanisms of the tested process. The presented method of modeling allows us to analyze many factors that have an influence on the kinetics of transformations, for instance such as different sizes, strength and morphological forms of cells.

The disintegration of microorganisms covers the process of cell disruption and subsequent release of intracellular compounds contained in the cells. The discussed results of experiments proved that the size of cells of microorganisms of the same species had an effect on microorganism disintegration rate. A subsequent loss of the biggest size fractions during the process causes nonlinearity of cell disruption kinetics. The probability of decay of the biggest cell size fractions at a very low concentration of microorganisms is very high. It decreases with an increase of the concentration of microbial suspensions.

In the packing of the mill working chamber, with an increase of the suspension concentration increases also intensity of intercellular relations due to filtering of

microorganisms in the space which is safe for them. At high and very high concentrations, cells deformed due to compression can force out adjacent cells from the destruction zone causing a decrease of the process rate at its initial stage. An increase of the rates of cell disruption and release of intracellular compounds at medium and high concentration of microbial suspensions can be caused by mutual blocking of cells, blocking of cells by fragments of disintegrated microorganisms or the interaction of released intracellular compounds. Results of the discussed investigations confirmed the dependence of compound release rates on the position of these compounds in a cell.

8. Acknowledgments

The study was carried out within the frames of the grant W-10/1/2011/Dz. St.

9. References

Benthin, S., Nielsen, J. & Villadsen, J. (1991). A Simple and Reliable Method for the Determination of Cellular RNA Content. *Biotechnology Techniques*, Vol.5, No.1, pp. 39-42 , ISSN 0951-208X

Bradford, M.M. (1976). A Rapid and Sensitive Method for the Quantitation of Microgram Quantities of Protein Utilizing the Principle of Protein-Dye Binding. *Analytical Biochemistry,* Vol.72, pp. 248-254, ISSN 0003-2697

Chen, J., Chen, H. and Gong, X. (1997). Mixotrophic and heterotrophic growth of *Haematococcus lacustris* and rheological behaviour of the cell suspensions. *Bioresource Technology,* Vol.62, pp. 19-24, ISSN 0960-8524

Chisti, Y. & Moo-Young, M. (1986). Disruption of microbial cells for intracellular products. *Enzyme and Microbial Technology,* Vol. 8, pp. 194–204, ISSN 0141-0229

Currie, J.A., Dunnil, P. & Lilly, M.D. (1972). Release of protein from bakers' yeast (*Saccharomyces cerevisiae*) by disruption in an industrial agitator mill. *Biotechnology and Bioengineering,* Vol.14, pp. 723-736, ISSN 0006-3592

Geciova, J., Bury, D. & Jelen, P. (2002). Methods for disruption of microbial cells for potential ues in the dairy industry – a review. *International Dairy Journal,* Vol. 12, pp. 541-553, ISSN 0958-6946

Garrido, F., Banerjee, U.C., Chisti, Y. & Moo-Young, M. (1994). Disruption of recombinant yeast for the release of β-galactosidase. *Bioseparation,* Vol.4, pp. 319-328, ISSN 0923-179X

Hatti-Kaul, R. & Mattiasson, B. (2003). Release of protein from biological host, in Hatti-Kaul, R. & Mattiasson, B. (eds), *Isolation and purification of proteins*, Marcel Deker, Inc, New York, Basel, pp. 22-49, ISBN 0-8247-0726-5

Hartmann, C., Mathmann, K. & Delgado, A. (2006). Mechanical stresses in cellular structures under high hydrostatic pressure. *Innovative Food Science and Emerging Technologies,* Vol.7, pp.1 – 12, ISSN 1466-8564

Heim, A., Kamionowska, U. & Solecki, M. (2007). The effect of microorganism concentration on yeast cell disruption in a bead mill. *Journal of Food Engineering,* Vol.83, pp. 121-128, ISSN 0260-8774

Heim, A. & Solecki, M. (1998). Disintegration of microorganisms in a circulating bed of balls. *Proceedings of World Congress on Particle Technology 3*, ISBN 0-85295-401-8, Brighton UK, July 1998

Heim, A. & Solecki, M., (1999). Disintegration of microorganisms in bead mill with a multi-disc impeller. *Powder Technology,* 105, 390-396, ISSN 0032-5910

Hetherington, P. J., Follows, M., Dunnill, P. & Lilly, M. D. (1971). Release of protein from baker's yeast (*Saccharomyces cerevisiae*) by disruption in an industrial homogeniser. *Transactions of the Institution of Chemical Engineers,* Vol.49, pp. 142–148, ISSN 0046-9858

Limon-Lason, J., Hoare, M., Orsborn, C.B., Doyle, D.J. & Dunnill, P. (1979). Reactor properties of a high-speed bead mill for microbial cell rupture. *Biotechnology and Bioengineering,* Vol.21, pp. 745-774, ISSN 0006-3592

Marffy, F. & Kula, M.R. (1974). Enzyme yields from cells of brewer's yeast disrupted by treatment in a horizontal disintegrator. *Biotechnology and Bioengineering*, Vol.16, pp. 623-634, ISSN 0006-3592

Mashmoushy, H., Zhang, Z. & Thomas, C.R. (1998). Micromanipulation measurement of the mechanical properties of baker's yeast cells. *Biotechnology Techniques,* Vol.12, No.12, pp. 925–929, ISSN 0951-208X

Melendres, A.V., Honda, H., Shiragam, N. & Unno, H. (1991). A kinetic analysis of cell disruption by bead mill. *Bioseparation,* Vol.2, pp. 231-236, ISSN 0923-179X

Melendres, A.V., Honda, H., Shiragami, N. & Unno, H. (1993). Enzyme release kinetics in a cell disruption chamber of a bead mill. *Journal of Chemical Engineering of Japan,* Vol.26 No.2, pp. 148-152, ISSN 0021-9592

Middelberg, A.P.J., O'Neill, B.K. & Bogle D.L. (1991). A novel technique for the measurement of disruption in high-pressure homogenization: studies on *E. coli* containing recombinant inclusion bodies. *Biotechnology and Bioengineering,* Vol.38, pp. 363–370, ISSN 0006-3592

Shiu, C. Zhang, Z. & Thomas, C.R. (1999). A novel technique for the study of bacterial cell mechanical properties, *Biotechnology Techniques,* Vol.13, pp. 707–713, ISSN 0951-208X

Smith, A.E., Moxham, K.E., Middelberg, A.P.J. (1998). On uniquely determining cell-wall material properties with the compression experiment, *Chemical Engineering Science,* Vol.53, pp. 3913-3922, ISSN 0009-2509

Smith, A.E., Zhang, Z. & Thomas, C.R. (2000). Wall material properties of yeast cells: Part 1. Cell measurements and compression experiments, *Chemical Engineering Science,* Vol.55, pp. 2031-2041, ISSN 0009-2509

Solecki, M. (2007). Yeast disintegration in a bead mill. *Chemical and Process Engineering*, Vol.28, 649-660, ISSN 02508-64

Solecki, M. (2009). Modeling of microorganism disintegration in spherical packing of a bead mill. *Proceedings of 5th International Conference for Conveying and Handlings of Particulate Solids*, ISBN 978-0858 259 065, Brisbane Australia, August 2009

Solecki, M. (2011). The theory of random transformation of dispersed matter. (unpublished)

Stenson, J.D., Ren, Y., Donald, A.M. & Zhang, Z. (2010). Compression testing by nanomanipulation in environmental scanning electron microscope. *Experimental Techniques*, Vol.34, No.2, pp. 60-62, ISSN 1747-1567

Svaldo-Lanero, T., Krol, S., Magrassi, R., Diaspro, A., Rolandi, R. Gliozzi, A. & Cavalleri, O. (2007). Morphology, mechanical properties and viability of encapsulated cells. *Ultramicroscopy,* Vol.107, pp. 913–921, ISSN 0304-3991

Whitworth, D.A. (1974). Hydrocarbon fermentation: protein and enzyme solubilization from *C. lipolytica* using an industrial homogenizert. *Biotechnology and Bioengineering,* Vol. 16, pp. 1399-1406, ISSN 0006-3592

27

Recovery of Biosynthetic Products Using Membrane Contactors

Carlo Gostoli
Department of Chemical Engineering, Alma Mater Studiorum – University of Bologna
Italy

1. Introduction

Membrane Contactors (MC) make possible to accomplish gas-liquid or liquid-liquid mass transfer operations without dispersion of one phase within another. The membrane acts as a mere physical support for the interface and does not contribute to the separation through its selectivity, the separation being primarily based on the principle of phase equilibrium.
Porous membranes with narrow pore size (typically in the range 0.02-0.2 μm) are used. One of the two phases enters the membrane pores and contacts the other phase at the pore mouth on the opposite side. Generally MC operations involve an aqueous phase and the membrane has hydrophobic character, however hydrophilic membranes can be used too [Kosaraju & Sirkar, 2007]. The key factor is that one of the two phases enters the pores whereas the other phase is kept outside. In the case of hydrophobic materials (Fig. 1), the membrane pores are filled by the non-polar phase or by the gas while the aqueous phase can not penetrate into the pores.

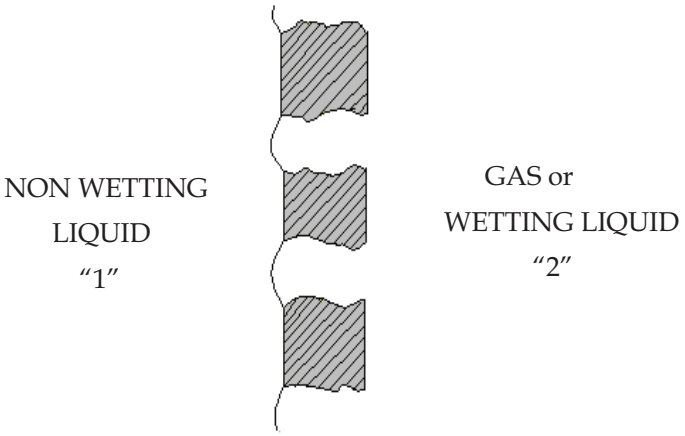

Fig. 1. The membrane contactor concept based on porous hydrophobic membrane in contact with an aqueous (non wetting) liquid at one side and a gas or organic (wetting) liquid at the other side

It is worth noting that the hydrophobicity of the materials is not a warranty for keeping the aqueous phase outside of the pores, indeed if a critical pressure value, called *breakthrough pressure*, is exceeded, the aqueous phase enters the membrane pores. The *breakthrough pressure* depends on the maximum pore size, d_P, the interfacial tension between the two phases, γ, the contact angle between the membrane and the two fluid, θ, according to the Young-Laplace equation (strictly valid for cylindrical pores):

$$\Delta P_c = \frac{4\gamma|\cos\theta|}{d_P} \tag{1}$$

As a consequence it is important to carefully control the operating pressures: the pressure of the aqueous phases has to be a bit higher than the pressure of the organic/gas phase, but lower than the breakthrough pressure. Selecting appropriate membrane materials and pore size it is possible to assure a pretty wide range of pressure for safe operations, for example PTFE or polypropylene membranes with nominal pore size of 0.2 μm exhibit a breakthrough pressure of nearly 3 bars for the water-air system. The discussion above can be extended to hydrophilic membranes; in that case the pores are filled by the aqueous phase, whose pressure has to be taken a bit lower than the gas/organic phase pressure, which in turn has to not overcome the breakthrough pressure, given again by Eq. (1). The choice between hydrophobic and hydrophilic membranes is dictated by the need to reduce the membrane resistance. As a rule the membrane pores should be filled by the phase in which the transferred species is most soluble. For example, if the species has higher affinity with the non polar or gas phase hydrophobic membrane will be preferred. If there is higher affinity with the polar phases the membrane will be hydrophilic.

MC have many advantages with respect to conventional mass transfer apparatuses: - membrane modules, in the form hollow fibres, provide interface areas per unit volume significantly greater than traditional devices, leading to more compact systems, - the interfacial area is well defined and remains constant regardless of the flow rates, whereas the design of the conventional devices is restricted by limitations in the relative flows of the two streams. - there is no mix of the two phases separate by the membrane and thus no need to separate the two phases downstream the process and no need of difference of density. - In addition MCs are easy in scale up and control, modular in design, flexible in operation.

Membrane contactors can be used for carrying out the recovery of bioconversion products from aqueous solutions by organic solvents, usually conduct in centrifugal devices, mixer-settler or columns. An additional advantage is relevant in this case: the operation can be performed in the presence of the living cells or enzymes that indeed do not get in direct contact with the solvent. The use of membrane based, dispersion free, solvent extraction for the recovery of bio-products, pioneered by Sirkar [Frank & Sirkar, 1987] has been well documented [Gawronski, 2000; Lazarova et al., 2002; Schlosser al., 2005].

Of course MCs present also some disadvantages: - no doubt the membrane represents an additional mass transfer resistance, and indeed overall mass transfer coefficients lower than those of conventional devices have been reported. However this drawback is well offset by the larger specific area, as a consequence the volumetric mass transfer coefficient for MCs is well above the values achievable in conventional devices. As in other membrane processes, problems my be the limited life time and fouling. However fouling my be less severe than in pressure driven processes; suspended solids and solutes are indeed not forced into the pores by convective flow, the species being transferred from one phase to the other by only diffusion.

2. Membrane and modules

Polymeric membranes were usually employed in membrane contactor studies and applications, because they are very competitive in performance and economics. Membranes with high hydrophobicity were preferred in most applications. Polypropylene (PP), polytetrafluoroethylene (PTFE), and polyvinylidenefluoride (PVDF) have been extensively used. Among these, microporous PTFE membrane shows excellent performance and stability, however, the application on industrial scale is limited, since PTFE membranes are available in flat sheet form rather than as hollow fibres. At present hollow fibre PP membranes exhibit the widest applications due to the good thermal and chemical stability, well-controlled porosity, and low cost. Recently increasing efforts have been devoted to develop ceramic membranes [Koonaphapdeelert et al., 2007, 2009; Li, 2007.], or hybrid membranes to get better chemical and thermal stability as well as higher mechanical strength. Membrane surface modification techniques to improve the hydrophobicity has also been investigated [Lv et al., 2011].

In principle both flat sheet membranes and hollow fiber can be used to make MC apparatuses. Fig. 2 shows the concept of a plate and frame module: it contains parallel membrane sheets with interposed spacers. Problems can arise from the susceptibility of the membrane to mechanical abrasion that required a careful design of the spacers and/or the use of supported membrane with an active layer, made for example of PTFE, and a woven or unwoven fabric. In this case the spacer in the active layer side can be substituted by a simple frame. Co-current flow is to be preferred to counter-current flow, in order to have a nearly constant pressure difference along the membrane, avoiding pressure inversion and membrane movement.

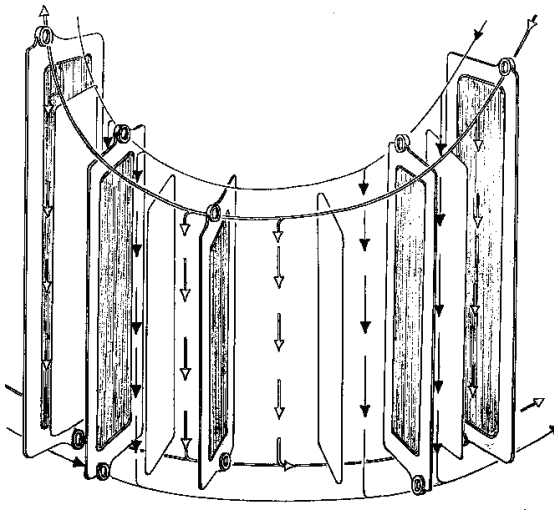

Fig. 2. The concept of plate & frame membrane contactors

The membrane area, a, per unit volume of these apparatuses is quite limited; assuming for example 1 mm the thickness of the fluid channels and 2 mm the thickness of the frames, the membrane area is a = 250 m^2/m^3. Taking into account the borders and the manifolds,

membrane area similar to or lower than conventional apparatuses can be estimated, so the main advantage of MC is lost. Plate and frame MC can be considered for particular applications, for example in air conditioning systems [Gaeta, 2003.], to reduce the pressure drop, or in the treatment of liquids containing suspended solids. Also spiral wound configuration has been proposed [Koschilowski et al., 2003].
Notwithstanding the larger availability of flat sheet membrane and its larger permeability, hollow fibers are generally preferred due to their high packing density. The basic hollow fibre module configuration with parallel flow of the streams is represented in Fig. 3. More complex configurations have been conceived in order to improve the mass transfer rate, as an example by inducing cross flow in the shell side [Drioli et al., 2006].

Fig. 3. Hollow fibre module

The fibre packing density can be characterized by the packing fraction, ϕ, representing the fraction of the cross section of the module occupied by the fibres. Denoting by N the number of fibres, d_o their outer diameter and d_S the shell diameter, we have:

$$\phi = N\left(\frac{d_o}{d_s}\right)^2 \tag{2}$$

Sometime the void fraction $\varepsilon = 1-\phi$ is used instead to characterize the packing density of the fibre bundle. The inner and outer membrane areas per unit volume (a_i and a_o respectively) are simply related to the packing fraction and diameters:

$$a_i = \frac{4\phi d_i}{d_o^2} \quad a_o = \frac{4\phi}{d_o} \tag{3}$$

In order to give an estimation of the membrane area per unit volume achievable with hollow fibres, let's consider a regular triangular arrangement of fibres with pitch 2s (Fig. 4). The cross section of the module appears formed by equilateral triangles of area $s^2\sqrt{3}$; each triangle contains 3/6 of circle, that's to say $3/6\pi d_i$ arc length, referring to the inner diameter, or $3/6\pi d_o$ referring to the outer diameter. The inner and outer membrane areas per unit volume are thus:

$$a_i = \frac{\pi}{2\sqrt{3}}\frac{d_i}{s^2} \quad a_o = \frac{\pi}{2\sqrt{3}}\frac{d_o}{s^2} \tag{4}$$

Or, referring to the dimensionless pitch:

$$\sigma = \frac{2s}{d_o} \tag{5}$$

$$a_i = \frac{2\pi}{\sqrt{3}\sigma^2}\frac{d_i}{d_o^2} \qquad a_o = \frac{2\pi}{\sqrt{3}\sigma^2}\frac{1}{d_o} \tag{6}$$

For a given pitch to diameter ratio, σ, the membrane area per volume is thus in inverse relation to the fibre size d_o, and very large areas can be obtained by narrow hollow fibres.

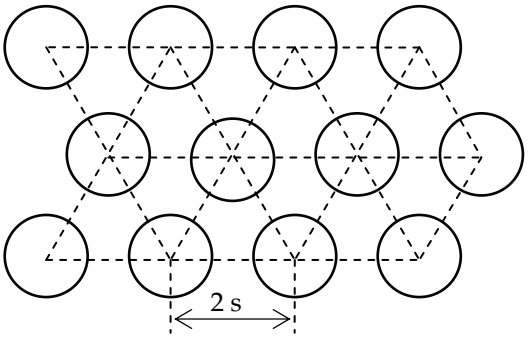

Fig. 4. Triangular array of fibres

Of course the maximum area is obtained when the fibres touch each other, i.e. for σ = 1. More realistic situations correspond to σ values about 1.5, for which the gap between the fibres is equal to the fibre radius. Tab. 1 reports the values of ai and ao achievable in triangular pitch with σ = 1.5, in hypothetical modules made with two well known, commercial PP hollow fibres.

	d_o mm	d_i mm	a_i m^2/m^3	a_e m^2/m^3
Accurel 0.6	1	0,6	967	1612
Celgard X40	0.3	0.2	3582	5373

Table 1. Membrane area per unit volume of modules made with Accurel or Celgard hollow fibres with pitch to diameter ratio σ = 1.5 (ϕ = 0.4)

Pitch of the triangular array and packing fraction are related by:

$$\phi = \frac{\pi}{2\sqrt{3}\sigma^2} \tag{7}$$

In particular the maximum packing, corresponding to σ = 1, is ϕ = 0.9, while σ =1.5 corresponds to ϕ = 0.4. Of course in commercial modules the hollow fibres are not arranged according to the regular array, as assumed above for illustrative purpose, however packing fraction in the range 0.4 – 0.5 are common and membrane area per unit volume are quite close to the values reported in Tab. 1.

3. Module design and module efficiency

Fig. 5 represents a counter-current mass transfer apparatus in which a species is extracted from an aqueous phase of flow rate W by a solvent of flow rate S. The flux N (*mol/m²s*)

across the interface in a section of the module in which the concentrations of the two streams are C_w and Cs is:

$$N = K_w(C_w - C_S / m) \tag{8}$$

in which K_w is the overall mass transfer coefficient based on the aqueous phase and m the partition coefficient.

$$m = \left[\frac{C_S}{C_w}\right]_{eq.} \tag{9}$$

For hollow fibres modules the flux can be referred to either the inner or outer surface of the fibres, provided that the mass transfer coefficient is defined accordingly.

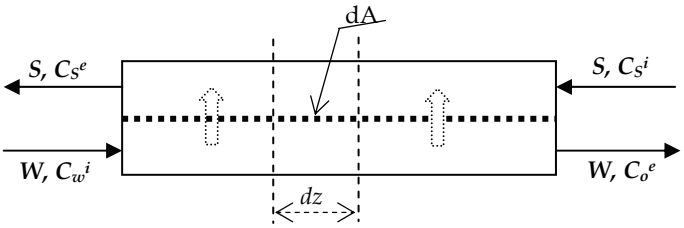

Fig. 5. Schematic of counter-current mass transfer apparatus. W and S are the flow rates of the aqueous and organic phases, C_w and C_S the respective concentrations

The design of the module is straightforward: we make a mass balance for the *dz* element of area *dA* (see Fig. 5):

$$W\frac{dC_w}{dA} = -K_w\left(C_w - C_S / m\right) \tag{10}$$

The membrane area A can be either the inner or outer surface of the fibres, as stated above. Since both Cw and Cs depend on the axial coordinate we must relate C_S to Cw, by the overall mass balance:

$$C_S = C_S^e + \frac{W}{S}\left(C_w^i - C_w\right) \tag{11}$$

After substitution and integration we have the membrane area:

$$A = \frac{W}{K_w}\frac{E}{E-1}\ln\frac{mC_w^i - C_S^e}{mC_w^e - C_S^i} \tag{12}$$

in which:

$$E = \frac{mS}{W} \tag{13}$$

represents the extraction factor.

Eq. (12) is useful in design problems, in which the inlet and exit concentrations of the two streams are given. When instead the module properties are given and we want relate the exit concentrations to the inlet ones, it is useful to introduce the module efficiency, defined as the ratio between the actual mass transfer occurring in the module and the maximum mass transfer corresponding to equilibrium between the water exit stream and the inlet solvent:

$$\eta = \frac{C_w^i - C_w^e}{C_w^i - C_S^i / m} \tag{14}$$

The efficiency is useful since it allows relating the overall amount of the species transferred to the inlet concentrations of the two streams. By a procedure similar to that followed above to obtain Eq. (12), the efficiency can be related to the overall mass transfer coefficient and membrane area:

$$\eta = \frac{1 - \mathrm{Exp}\left[-\frac{K_w A}{W}\left(1 - 1/E\right)\right]}{1 - \frac{1}{E}\mathrm{Exp}\left[-\frac{K_w A}{W}\left(1 - 1/E\right)\right]} \tag{15}$$

It is worth noting that efficiency approaches unity as the area goes to infinity, only if $E > 1$, while instead it approaches E if $E < 1$. Indeed in the former case the exit concentration of the aqueous stream approaches the value of equilibrium with the inlet solvent, whereas if $E < 1$, the exit concentration of the solvent approaches the value of equilibrium with the inlet aqueous stream. Finally Eq. (15) does not hold for the particular case of $E = 1$, in this case:

$$\eta = \frac{KA/W}{1 + KA/W} \tag{16}$$

Similar expression can be obtained for of co-current operation; in this case the efficiency, defined again by Eq. (14), is:

$$\eta = \frac{1 - \mathrm{Exp}\left[-\frac{K_w A}{W}\left(1 + 1/E\right)\right]}{1 + 1/E} \tag{17}$$

Of course co-current operation gives lower efficiency than counter-current operation.

3.1 Modelling of batch operation

In laboratory experiments, the membrane contactor and the reservoirs are usually arranged in closed system, in which the aqueous feed and the solvent are circulated through the module and the respective reservoirs, as represented in Fig. 6. Perfect mixing in the reservoirs and plug flow through the module are usually assumed. Apparently the system operates in unsteady state: the concentration of the aqueous phase, C_w, and the concentration of the organic phase, C_S, in the reservoirs change in time and eventually reach the equilibrium values corresponding to the partition coefficient. The module itself operates

in unsteady state, since the inlet concentrations are at any time equal to the concentrations prevailing in the reservoirs. Nevertheless, if the reservoir volumes are much larger than the module volume, or equivalently, the residence time in the module is negligible in the time scale of the experiment, the module can be considered to work in steady state, while the reservoirs work in unsteady state. This approach has been called pseudo steady state approximation and has been extensively used to analyze experiments intended to evaluate the overall mass transfer coefficient between the phases [D'Elia et al., 1986, Trébounet et al., 2006].

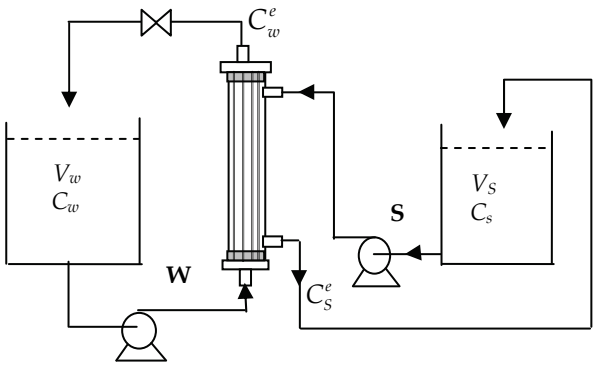

Fig. 6. Typical set-up of MC experiments

Based on the definition of module efficiency, Eq. (14), since the concentrations of the two streams entering the module are equal to the concentrations prevailing in the two reservoirs, the following mass balance equations hold, under the hypothesis of pseudo steady state:

$$V_w \frac{dC_w}{dt} = -W\eta\left(C_w - C_S / m\right) \tag{18}$$

$$V_w\left(C_w^0 - C_w\right) = V_S\left(C_S - C_s^0\right) \tag{19}$$

In principle V_w and V_S represent the volume of the two reservoir, but a better approximation is obtained considering V_w and V_S as total volumes of the two phases, comprehensive of the module and pipes volumes, even if these latter are generally quite small [Trébounet et al., 2006]. After integration and rearrangement we have:

$$\ln\frac{\left(1+1/R\right)C_w - C_w^0/R - C_S^0/m}{C_w^0 - C_S^0/m} = -\left[\frac{W\eta}{V_w}\left(1+\frac{1}{R}\right)\right]t \tag{20}$$

which in the case of extraction with initially pure solvent (C_S^0=0) simplifies to:

$$\ln\left[\left(1+\frac{1}{R}\right)\frac{C_w}{C_w^0} - \frac{1}{R}\right] = -\left[\frac{W\eta}{V_w}\left(1+\frac{1}{R}\right)\right]t \tag{21}$$

in which

$$R = \frac{mV_S}{V_w} \tag{22}$$

represents a sort of extraction factor for the whole operation, defined making reference to the phase volumes instead of stream flow rates, as in Eq. (13).
If the overall mass transfer coefficient as well as the volumes, flow rates and membrane area are known, we can calculate the module efficiency through Eq. (15), then the concentration of the aqueous phase vs. time through Eq. (20):

$$C_w = \frac{1}{R+1}\left\{\frac{C_w^0}{R} + \frac{C_S^0}{m} + \left(C_w^0 - \frac{C_S^0}{m}\right) Exp\left[-\frac{W\eta}{V_w}\left(1+\frac{1}{R}\right)t\right]\right\} \tag{23}$$

and eventually the concentration of the organic phase through Eq. (19).

$$C_S = C_s^0 + \frac{V_w}{V_S}\left(C_w^0 - C_w\right) \tag{24}$$

Alternatively the model can be used to evaluate the overall mass transfer coefficient from experiments. In this case the concentration of the two steams are measured vs. time, then the left side of Eq. (20) is plotted vs. time; from the slope of the straight line obtained we have the efficiency, eventually the mass transfer coefficient is calculated from eq. (15). The procedure has been reported in more details in the experimental section.

4. Mass transfer in hollow fibre contactors

Mass or heat transport for laminar flow in various geometries and under various boundary conditions was investigated by several authors, beginning with the classical work of Graetz for heat transfer in circular ducts with constant wall temperature [Knudsen & Katz, 1958]. Reference can be made to the work of [Siegel et al, 1958] for heat transfer in circular duct with uniform heat flux, [Hatton & Quarmby, 1962] for annular ducts and [Nunge and Gill, 1966] for a tube in tube heat exchanger. Various papers deal with haemodialysis in hollow fibre, for example [Davis & Parkinson, 1970; Gostoli & Gatta, 1980; Ding 2004].
The correct modelling of mass transfer in membrane contactors would require the simultaneous integration of the mass balance equations for the lumen and for the shell sides, the boundary conditions being equal flux at the membrane-fluid interfaces. However it is common practice to evaluate separately the individual mass transfer coefficients and to combine it in an overall mass transfer coefficient according to the resistance in series concept. The overall mass transfer coefficient embodies three contributions related to the tube and shell side boundary layers and to the diffusion through the membrane pores. Making reference to hydrophobic membranes, Eq. (25) holds in the case of aqueous feed flowing through the lumen:

$$\frac{1}{K_w} = \frac{1}{k_w} + \frac{1}{mk_m}\frac{d_i}{d_{lm}} + \frac{1}{mk_S}\frac{d_i}{d_0} \tag{25}$$

whereas for aqueous phase flowing through the shell we have:

$$\frac{1}{K_w} = \frac{1}{k_w} + \frac{1}{mk_m}\frac{d_0}{d_{lm}} + \frac{1}{mk_S}\frac{d_0}{d_i} \tag{26}$$

In both equations the mass transfer is referred to the actual interface: the inner surface of the fibres in the first case and the outer surface for aqueous feed flowing through the shell side.
Since in any case the membrane pores are filled by stagnant solvent, the mass transfer coefficient through the membrane is:

$$k_m = \frac{2D\varepsilon}{(d_0 - d_i)\tau} \tag{27}$$

Where ε is the membrane porosity, defined as the ratio between the cross sectional area of the pores and the total membrane area , and τ the tortuosity factor, taking into account that the diffusion path is longer than the membrane thickness due to the pores geometry. Typical values of tortuosity for the membranes mostly used are around 2. The diffusion coefficient, D, of the species in the solvent, if not available, can be estimated by predictive methods, for example the Wilke-Chang equation [Reid et al., 1978]. Mass transfer coefficients can be also evaluated experimentally by the Wilson plot method [Seara et al., 2007].

4.1 Mass transfer in hollow fibre lumen

The calculation of tube side mass transfer coefficient is well established, in that it represents the classical Graetz problem. Solutions are presented, as usual, in dimensionless form, as Sherwood number:

$$Sh = \frac{kd}{D} \tag{28}$$

vs. the Graetz number:

$$Gz = \frac{u_m d^2}{DL} = \mathrm{Re}\, Sc \frac{d}{L} \tag{29}$$

Graetz in 1885 developed an infinite series solution to the analogous problem of heat transfer under the condition of constant wall temperature [Knudsen & Katz, 1958]. The solution can be immediately applied to mass transfer with constant wall concentration, simply substituting the Sherwood and Smidth numbers to the Nuselt and Prandtl numbers. The Sherwood number approaches the limiting value Sh_∞=3.66 for low Graetz number, i.e. for long distance.
In the entry region (low distance) the Leveque approximation can be applied. It assumes that concentration gradients are limited to a thin layer near the wall. The result in term of average Sherwood number is:

$$Sh_0 = 1.615 \;\; Gz^{1/3} \tag{30}$$

All the relations reported in this work give the average Sherwood numbers, which are useful for design purposes. It should be remember that, in the entry zone, the local Sherwood number is 2/3 of the average value.
An interpolating formula is currently used instead of the infinite series solution for all the Graetz numbers [Knudsen & Katz, 1958]:

$$Sh = 3.66 + \frac{0.0668 \quad Gz}{1 + 0.04 \quad Gz^{2/3}} \tag{31}$$

An alternative expression for all the Gz values can be obtained combining the two asymptotic solutions as follows [Lipinski & Field, 2001]:

$$Sh = \left(Sh_{\infty}^{n} + Sh_{0}^{n} \right)^{1/n} \tag{32}$$

Satisfactory approximation is obtained for n = 3 or 4. For n = 3 Eq. (32) simplify to:

$$Sh = \left(49 + 4.21 Gz \right)^{1/3} \tag{33}$$

which can be used for all the Graetz number values, instead of the Eq. (31).
Fig. 7 reports the general behaviour: the asymptotic solution (Sh_{∞} = 3.66) is reached for Gz nearly 2, whereas the Leveque solution (entry length) applies for Gz > 50; in the transition zone Eq. (31) and Eq. (32) with n = 4 give the same results, however for large Gz Eq. (32) approaches the Leveque solution better than Eq. (31). In addition Eq. (32) can be applied not only to the present case, but to any situation in which two asymptotic solutions are available.

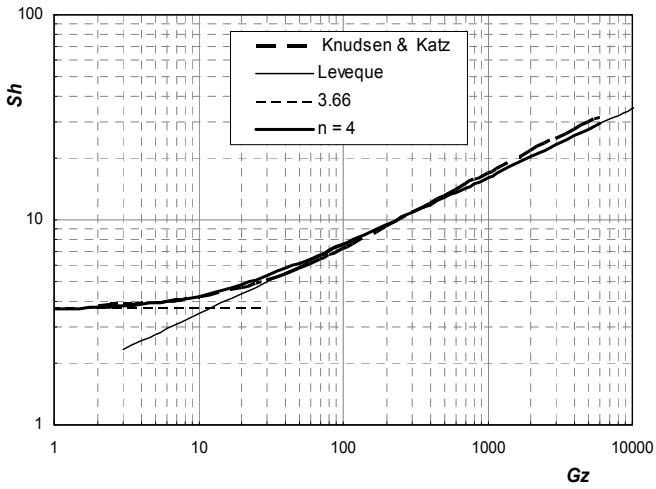

Fig. 7. Average Sherwood number vs. Graetz number for circular duct with constant wall concentration. Knudsen & Katz: Eq. (31), Leveque: Eq. (30), n = 4: Eq. (32)

Many papers suggested the use of Eq. (30), without any comment, tacitly assuming large values of Graetz Number, i.e. assuming the entry length longer than the module. This is correct in many cases, due to the low values of the diffusion coefficient in liquids; however, in very narrow hollow fibres also Graetz numbers in the transition zone are possible.
The Graez-Leveque theory showed in very good agreement with data in both heat and mass transfer experiments. Some authors reported mass transfer coefficients lower than the predictions at low flows (Gz<10). This is attributed to the slight polydispersity of the hollow

fibre diameters, which produces uneven flows [Wickramasinghe et al., 1992; Kreulen et al., 1993]. This effect is not relevant at larger flows.
The Graetz problem was solved also under the conditions of uniform wall flux; in the entry zone the expression similar to Eq. (30) is

$$Sh_0 = 1.953 \ Gz^{1/3} \tag{34}$$

whereas for long distance, i.e. low Graetz Number, the asymptotic value is Sh_∞=4.36. These values are nearly 20% larger than the Sherwood number calculated in the conditions of constant wall concentration. What condition better applies to the real situation can be questionable.

4.2 Mass transfer in the shell side

The calculation of shell side mass transfer coefficient is subject to more uncertainties, with respect to lumen side; correlations derived from experiments give different results and are often effective only for a specific module geometry and flow configuration, and thus are not very useful for evaluating new module designs [Lemanski & Lipscomb, 2001].
The theoretical models proposed can be roughly classified in the following categories i) regular packing of fibres, ii) single fibre, ii) random packing of fibres. The main features of the models will be briefly reviewed in the following.
Of interest to the problem at hand are also investigations of heat transfer in shell-and-tube exchangers in laminar flow. [Sparrow et al., 1961], developed an analytical solution to the governing equations for regular triangular and square tube arrangements with uniform wall heat flux. In an early work the same authors [Sparrow & Loeffler, 1959] derived the actual velocity profile for laminar flow between cylinders arranged in regular triangular or square arrays. Both the flow pattern and pressure drop depends strongly on the type of array for small spacing between the cylinders, but become independent of it for large spacing. Under these circumstances the velocity distribution around any one tube can be considered cylindrically symmetrical, so that an "equivalent annulus" model can be adopted, in which flow take place in a fictitious annular duct, which approximates the actual polygonal area surrounding each tube, as depicted in Fig. 8

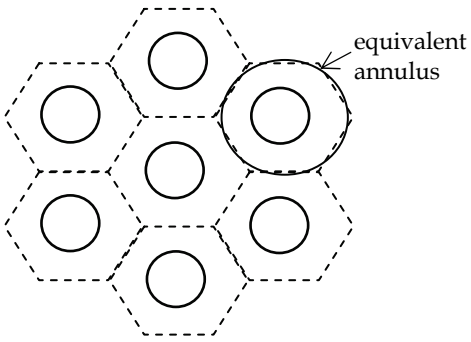

Fig. 8. The equivalent annulus approximation

Sparrow et al. showed that this simplified model can be used to describe the heat transfer for large spacing. For low spacing the model predicts asymptotic Nusselt numbers grater

than the actual ones for triangular array. From these results one can infer that the annulus model is reasonable for membrane contactors in which the fibres are not too closely spaced.
Shell side heat transfer in shell-and-tube exchangers in laminar flow were also modelled by [Miyatake & Iwashita, 1990] for triangular and square tube arrangements, but under the conditions of uniform wall temperature. The Authors developed a finite difference solution to the governing equations and presented correlations covering a broad range of Graetz numbers. Their correlations can be easily adapted to the equivalent mass transfer problem, see [Kreulen et al., 1993; Asimakopoulou & Karabela, 2006] who presented the modification for mass transfer as appendix of their works.
The comments are similar to the previous ones: heat (mass) transfer coefficients depends on the type of array for large packing density, but is almost independent of it for packing fraction less than 0.5; in this conditions the equivalent annulus formulation can be used with confidence.
A further condition for the validity of the annulus mode is a uniform distribution of the fluid, so that each fibre works in the same manner. This is an obvious, but rarely realised goal in module manufacture.
In real modules the hollow fibres are packed randomly rather than in regular array. Nevertheless, if the packing density is low, the random arrangement does not seriously invalidate the annulus model. In fact, for large spacing the flow pattern is actually independent of the type of array. Furthermore for a high packing density mass transfer is probably limited by channelling of the fluid through the irregularly arranged fibres. Therefore, it is questionable if greater accuracy would be provided by a more complicated model in which a regular array is assumed and peripheral variations are taken into account.
At this point we can say that the equivalent annulus formulation has to be preferred, for its simplicity, to models based on regular arrangement of fibres for low packing density. For high packing density (ϕ>0.5) probably the model fails, but models based on regular arrangement are expected to not work better.

4.2.1 The equivalent annulus formulation

The model assumes that around each tube, the flow take place in an annular duct bounded by a free surface of diameter d_a chosen so that the overall flow area is identical to that of the actual configuration, Fig. 9.

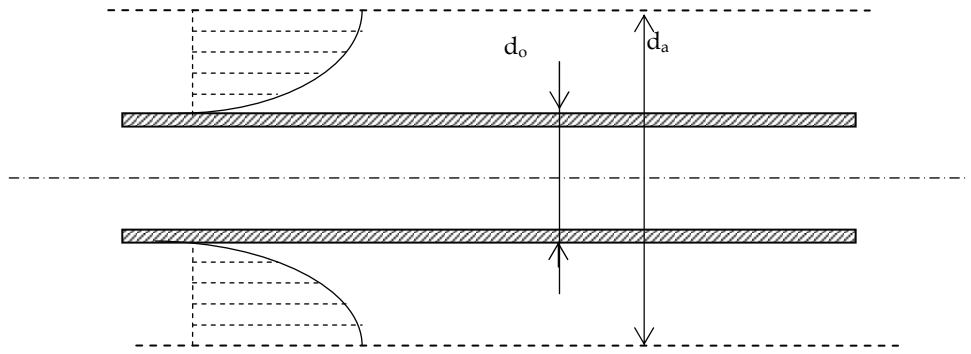

Fig. 9. A fibre with the surrounding fictitious annular duct

The outer diameter of the annulus is thus related to the packing fraction by:

$$d_a = \frac{d_o}{\sqrt{\phi}} \tag{35}$$

The maximum value $\phi = 0.9$ correspond to the situation in which the fibres are tangent to one other in a triangular array. As discussed before as ϕ approaches this value the model becomes inappropriate.
The velocity profile for fully developed laminar flow in the fictitious annular duct has been obtained by solving the equation of motion with the boundary conditions of zero velocity at the tube wall ($r = R_o = d_o/2$) and zero momentum flux at the external surface of the annulus ($r = R_a = d_a/2$). The velocity profile is given by:

$$u_{(r)} = \frac{u_m}{f(\phi)}\left[\ln\frac{r}{R_o} - \frac{\phi}{2}\left(\frac{r^2}{R_o^2} - 1\right)\right] \tag{36}$$

In which u_m is the average velocity, related to the pressure gradient by:

$$u_m = -\frac{1}{2\mu}\frac{dP}{dz}R_a^2 f(\phi) \tag{38}$$

And:

$$f(\phi) = \frac{\ln(1/\phi)}{2(1-\phi)} - \frac{3-\phi}{4} \tag{39}$$

It can be easily shown that Eq. (36) is equivalent to that obtained by Happel [Happel, 1959] for the so called "free surface model", one other name of the equivalent annulus model here described.
The steady state differential mass balance equation is

$$u_{(r)}\frac{\partial C}{\partial z} = D\frac{1}{r}\frac{\partial}{\partial r}\left(r\frac{\partial C}{\partial r}\right) \tag{40}$$

In which $u_{(r)}$ is local velocity, given by Eq. (36), D the diffusion coefficient, C the concentration of the diffusing species and z the axial coordinate.
Asymptotic solution for low z values (the entrance zone) can be obtained following the Leveque procedure, i.e. assuming that concentration gradient in the fluid are limited to a thin layer near the wall. Under the condition of constant wall concentration the average Sherwood number is:

$$Sh = 1.0178\left[\frac{1-\phi}{f(\phi)}\right]^{1/3} Gz^{1/3} \tag{41}$$

In which the Sherwood and Graetz numbers are defined making reference to the outer diameter of the tubes as characteristic length:

$$Sh = \frac{kd_o}{D} \quad Gz = \frac{u_m d_o^2}{Dz} \tag{42}$$

It will be noted that in the range $0.1 < \phi < 0.6$ the above equation (41) can be represented, with accuracy better than 99% by the expression linear in ϕ:

$$Sh \approx (1 + 2\phi) Gz^{1/3} \tag{43}$$

In passing also the Leveque-type solution under the condition of uniform wall flux is reported for completeness:

$$Sh = 1.23 \left[\frac{1-\phi}{f(\phi)} \right]^{1/3} Gz^{1/3} \tag{44}$$

The complete solution of Eq. (40) under the conditions of constant wall concentration was obtained by a finite difference method and is represented in Fig. 10 as average Sherwood number vs. Graetz number for different values of the packing fraction. Of course the numerical solution approaches the asymptotic solution, Eq. (41), for large Gz values, i.e. in the entrance zone, where the Leveque approximation applies. In Fig. 10 is also reported a line representing the Gz values above which the actual Sh differ less than 1% from the values calculated from Eq. (41), valid in the entrance zone. That line is represented by the interpolating formula:

$$Gz_{\lim} = 58\, e^{6.3\,\phi} \tag{45}$$

Apparently the length of the entry zone strongly depends on the packing fraction, ranging from nearly Gz = 100 for $\phi = 0.1$, to Gz =2500 for $\phi = 0.6$.

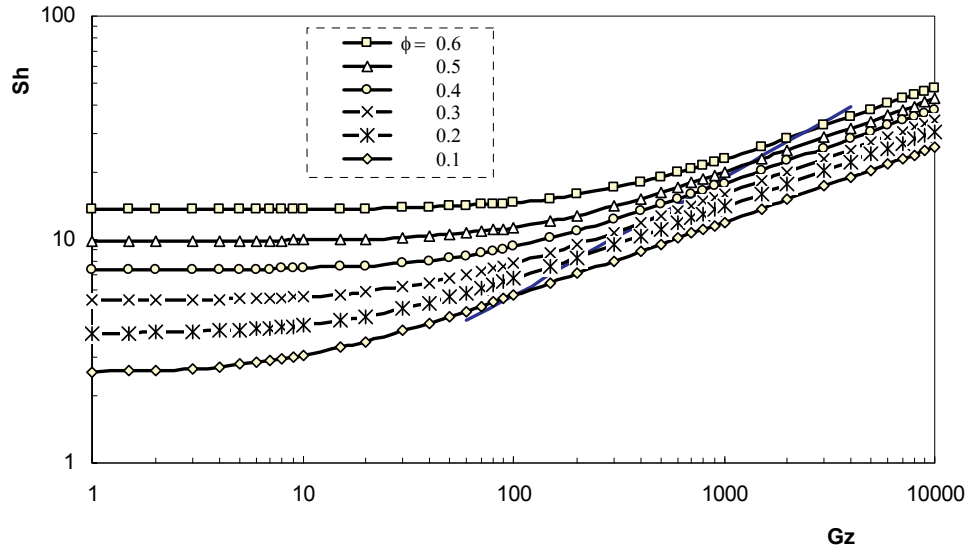

Fig. 10. Average Sherwood numbers for the equivalent annulus model under the conditions of constant wall concentration, for different values of the packing fraction ϕ

Fig. 10 shows that limiting values of Sh are approached for long distance, i.e. for low Graetz numbers. The dependence of these limiting values on the packing fraction ϕ, in the range $0.1<\phi<0.6$, is well described by the interpolation formula:

$$Sh_{\infty} = 1.93\, e^{3.29\,\phi} \tag{46}$$

The same qualitative behaviour was already observed for the solution of Eq. (40) under the conditions of uniform wall flux. In that case is possible to develop an analytical asymptotic solution also for large z values, i.e. low Gz, following a procedure similar to that reported in [Bird et al, 2007] for circular channel. The complete analytical solution was reported elsewhere [Gostoli & Gatta, 1980]. A more handy interpolation formula, for the range $0.1<\phi<0.65$, is here reported:

$$Sh_{\infty} = 2.08\, e^{3.3\,\phi} \tag{47}$$

The two solutions for low Graetz numbers are reported in Fig. 11, together with the data for triangular array, after [Miyatake & Iwashita, 1990]. Apparently the equivalent annulus formulation gives practically the same results as the more elaborated model of triangular array for packing fraction ϕ less than 0.45; only for larger packing fraction the deviation becomes substantial.

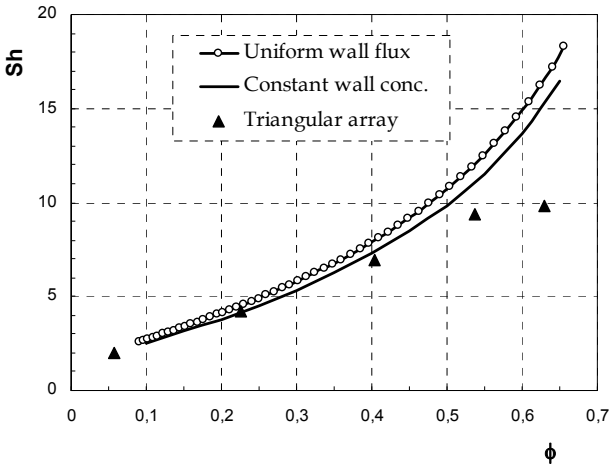

Fig. 11. Asymptotic Sherwood numbers (low Gz) for the equivalent annulus model under the conditions of uniform wall flux and constant wall concentration, compared with the data of [Miyatake & Iwashita, 1990] for triangular array

As for the tube side, a simple expression for all the Graetz number can be obtained combining the two asymptotic solutions (entrance zone and long distance) by Eq. (32).
By using n =3 in Eq. (32), Eq. (46) for long distance and the approximate expression (43) for the entrance zone the following, very handy expression is obtained:

$$Sh \approx \left[7.2\, e^{10\phi} + \left(1 + 2\phi\right)^3 Gz \right]^{1/3} \tag{48}$$

which is in pretty good agreement with the numerical solution reported in Fig. 10 and can be used for practical purposes instead of the exact values.

4.2.2 Discussion

The equivalent annulus model, presented in details in the previous section, gives a simple description of the mass transfer in the shell side, leading to an approximate explicit expression for the mass transfer coefficient, the Eq. (48), very handy for design and analysis of membrane contactors. As discussed above, for packing fraction up nearly 0.45, the model gives the same results of the more complicated models of regular arrangement in which the circumferential dependence of velocity and concentration are taken into account.

Of course its adequacy to describe mass transfer in actual apparatuses can be questioned.

The equivalent annulus model was compared to experimental results in [Asimakopoulou & Karabelas, 2006a, 2006b]. In their analysis only the entry length solution, Eq. (41), was considered. In the first paper the module used contained only 5 hollow fibres of outer diameter 0.3 mm with a very low packing fraction (ϕ = 0.093) and the agreement seemed satisfactory. In the second paper, aimed to investigate the effect of packing fraction, three further modules were used with packing fraction up to 0.4. The number of fibres contained in the modules was again quite limited, up to 68 and the modules were carefully hand made. The agreement between experiments and equivalent annulus model was again pretty good. The data showed a dependence on the packing fraction weaker than that predicted by Eq. (41), and the Authors suggested to use the simple expression $Sh = 1.45\ Gz^{0.33}$, to better represent the data in the range $0.093<\phi<0.4$. This equation corresponds to Eq. (41) or (42) for ϕ = 0.225, i.e. nearly the average value of the packing fractions tested.

Even if limited to the Leveque-type solution (the entrance zone), essentially the works of Asimakopoulou and Karabelas confirmed that the equivalent annulus adequately describes the mass transfer in small modules for packing fraction up to 0.4.

The situation in commercial modules, housing thousands of fibres, is somewhat more complicated. Many factors make the analysis complex and uncertain [Bao & Lipscomb, 2003]: 1) fibres are packed randomly in the module, 2) the fibres may not lie parallel to each other leading to a transverse flow component, 3) cross-flow regions are present near the entrance and exit ports, 4) fluid distribution into the bundle may not be uniform if the entrance and exit ports are not well designed. Finally the fibres are flexible and the arrangement may change with the flow.

Only the first factor, the effect of random fibre packing, received considerable attention. [Zheng et al, 2004] described the effect of randomness by a generalized free surface model, introducing a probabilistic distribution for the areas of the fictitious annuli circumventing each fibre. [Wu & Chen, 2000] used Voronoi tessellation to generate polygonal regions around each fibre. [Bao & Lipscomb G., 2002] modelled the fibre bundle as an infinite, spatially periodic medium. All the results indicate that channelling through randomly packed bundles reduces the average mass coefficient relative to regularly packed bundles, especially in the well developed limit.

A number of experimental correlations for shell side mass transfer appeared in literature, [Lipnizki & Field, 2001] provide an excellent summary and discussion. These correlations predict values that can be either much higher or much lower than the values calculated for regular and random fibres packings. This suggests that the other factors mentioned above can control the flow field. The presence of cross-flow regions due to shell port design or

non-parallel fibres may lead to higher than expected mass transfer coefficients. Poor fluid distribution may lead to lower than expected values. A number of apparent errors in the literature experimental correlations were also pointed out [Liang & Long, 2005].
The comparison of the models and correlations is also complicated by the different parameters used to characterize the packing as well as the different definition of the characteristic diameter. In this paper the outer fibre diameter d_o has been used in the definition of Reynolds and Sherwood numbers; many authors instead used the hydraulic diameter d_h, which depends on the packing fraction:

$$d_h = d_o\left(\frac{1}{\phi} - 1\right) \tag{49}$$

Both choices can be accepted, the outer diameter seems more rational to compare the performances of modules made with the same fibres, but with different packing density.

5. Biosynthetic vanillin

Vanillin (4-hydroxy-3-methoxy-benzaldehyde), the major organoleptic component of natural vanilla, is the most widely used flavour compound in food, cosmetics and pharmaceutical industries [Guzman, 2004]. Natural vanillin, obtained from *Vanilla* pods through a long and expensive process, can supply less than 1% of the market demand. Therefore, most of the vanillin employed is obtained through chemical synthesis from guaiacol or lignin [Ramachandra & Ravishankar, 2000]. The production of vanillin through microbial or enzymatic bioconversion of selected substrates such as ferulic acid or capsaicin is an interesting alternative, as the product can be labelled as "natural" according to the European and US legislation. Studies regarding the production of biotechnological vanillin have shown that several microorganisms have the potential of being used in the bioconversion of ferulic acid into vanillin, such as actinomycetes, *Pseudomonas spp*., *Bacillus spp*. and *Aspergillus spp.* [Walton et al., 2000]. Vanillin can also be obtained by an enzymatic process from capsaicin in two steps: capsaicin is converted by acilase to vanillylamine, which is then converted to vanillin by amine oxidase. [van den Heuvel et al., 2001]
The recovery of the product from the bioconversion broth is a key point of the whole process. As vanillin has toxic effect on bacterial cells and it can be further transformed to vanillyl alcohol or vanillic acid, the productivity can be potentially enhanced by in-situ removal of vanillin. The addition of adsorbent resins to the culture medium was proposed in the biotransformation of ferulic acid to vanillin by a *Streptomyces* sp. strain [Dongliang et al., 2007] in a fed-batch process. Pervaporation was also a proposed for product removal [Boddeker et al., 1997], however, owing to the low volatility, the vanillin flux was quite low at the bioconversion temperature. The aim of this work is to evaluate the potential of using membrane contactor technology for the recovery of vanillin from bioconversion broths in view of an integrated bioconversion – separation process.

6. Experimental

The partition coefficients of vanillin as well as of the substrates of the bioconversion (ferulic acid and vanillylamine) in various solvents were determined through batch experiments. The solvent selected was n-butyl acetate. This solvent allows the selective removal of the

produced vanillin from the bioconversion broth removing only a minor extent of the substrates. Indeed the partition coefficient of vanillin is 21 (at pH 7) whereas for ferulic acid it is 0.2 and for vanillylamine 0.01. As shown in Tab 2, the partition coefficient of vanillin depends on pH, making possible to counter-extract vanillin from the vanillin rich solvent phase by using alkaline water.

pH	7	8	9	10	12
m	21	15.8	10.4	4.4	0.02

Table 2. Partition coefficient of Vanillin between water and n- butyl acetate at various pH

Accurel® polypropylene hollow fibres, supplied by Membrana GmbH, Germany, with inner/outer diameter 0.6/1 mm and porosity 60% were used to build the module used in the experiments. The module contained 30 hollow fibres with overall area 158 cm^2 , the shell diameter was 10 mm, the packing fraction was thus $\phi = 0.3$.

The experimental set up is shown schematically in Fig. 6. The feed and the solvent were circulated counter-currently through the module and the respective reservoirs by two gear pumps with variable speed. The pressure of aqueous phase was kept a bit larger than that of the organic phase; to this purpose the feed reservoir was kept at a higher level with respect to the solvent reservoir. In addition a suitable overpressure (0.2-0.4 bar) can be created by a valve at the module exit. Both circuits were equipped with instruments for measuring the temperature and the flow rate during the experiments.

Small samples of the organic and aqueous phases were taken at various times and analyzed with HPLC reverse phase system, equipped with a Beckman Ultrasfere 4.6 mm x 250 mm ODS C18 column (particle diameter = 5 μm) , at 35°C. The mobile phase was composed of 70% H_20 added with 1% CH_3COOH and 30% CH_3OH added with 1% CH_3COOH; column temperature was 35°C, injection volume was 20 μL. The isocratic elution was performed for 16 minutes.

Four type of extraction experiments were performed: i) extraction from model solutions containing vanillin and ferulic acid or vanillylamine (the substrates of microbial and enzymatic conversion respectively), ii) extraction from the whole bioconversion broth, iii) extraction during bioconversion coupling bioconversion and separation, iv) counter-extraction of vanillin from the solvent by NaOH-water solution. The feed flowed either through the lumen or in the shell side. In all the experiments the temperature was 30°C and the pH was 7 in the extraction experiments and 12 in the counter extraction.

The bioconversion broth used in the experiments was obtained in a 3.5 L stirred tank bioreactor by *Pseudomonas fluorescens* BF13-1p at concentration 6 g/L with ferulic acid (2 g/L) as unique carbon source, at 30°C and pH 7.

7. Results

Typical results obtained in the extraction experiments are shown in Figs 12 and 13, in the first case the aqueous solution contained vanillin and ferulic acid, in the second one vanillin and vanillylamine.

Apparently vanillin was rapidly removed and reached the concentrations corresponding to the partition coefficient measured in batch experiments, whereas the ferulic acid or vanillylamine concentrations in the aqueous phase remained almost constant. The membrane

based solvent extraction is thus a good technique for the selective removal of vanillin without removing the substrates of the bioconversion.

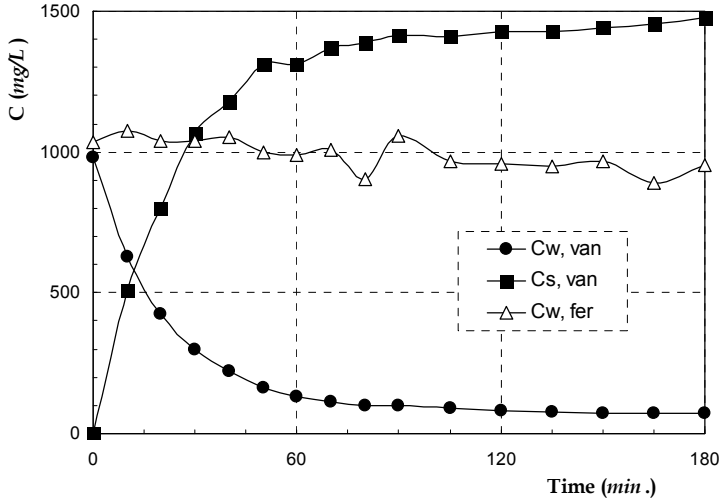

Fig. 12. Vanillin and ferulic acid concentrations vs. time in the extraction with buthyl-acetate. Feed shell side, feed volume 0.5 L, solvent volume 0.3 L, feed flow rate 45 L/h, solvent flow rate 25 L/h, pH 7

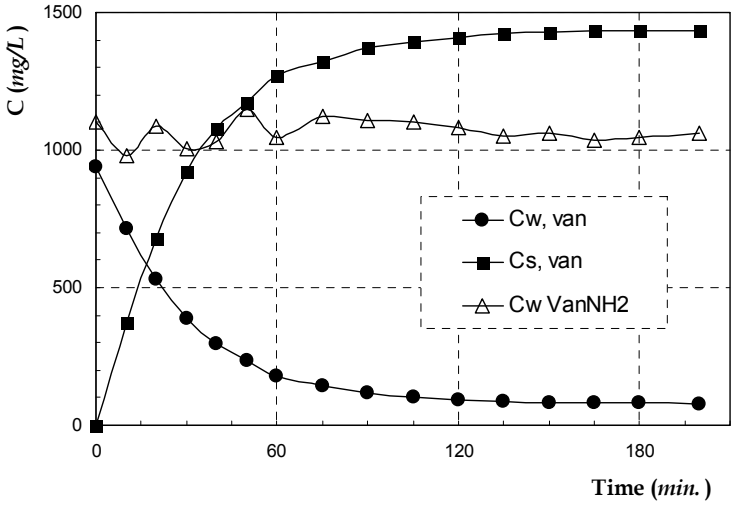

Fig. 13. Vanillin and vanillylamine concentrations vs. time in the extraction with buthyl-acetate. Feed shell side, feed volume 0.5 L, solvent volume 0.3 L, feed flow rate 45 L/h, solvent flow rate 25 L/h, pH 7

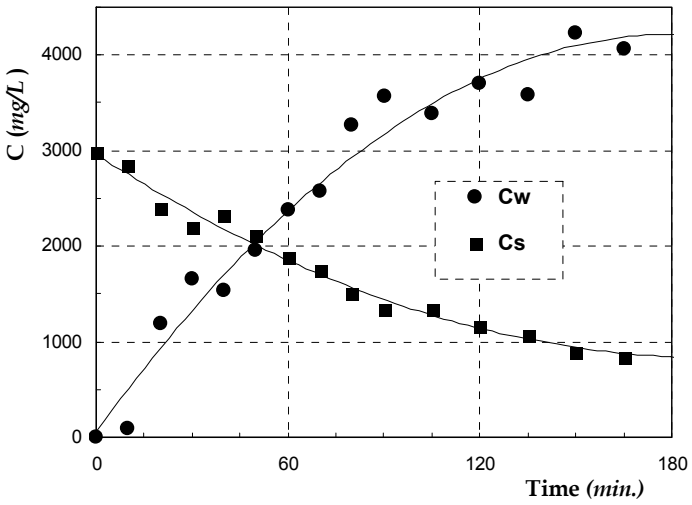

Fig. 14. Vanillin concentration in the organic and aqueous phases vs. time in the counter extraction from buthyl-acetate to water at pH = 12. Solvent tube side, solvent volume 0.5 L, water volume 0.3 L, solvent flow rate 25 L/h, feed flow rate 45 L/h

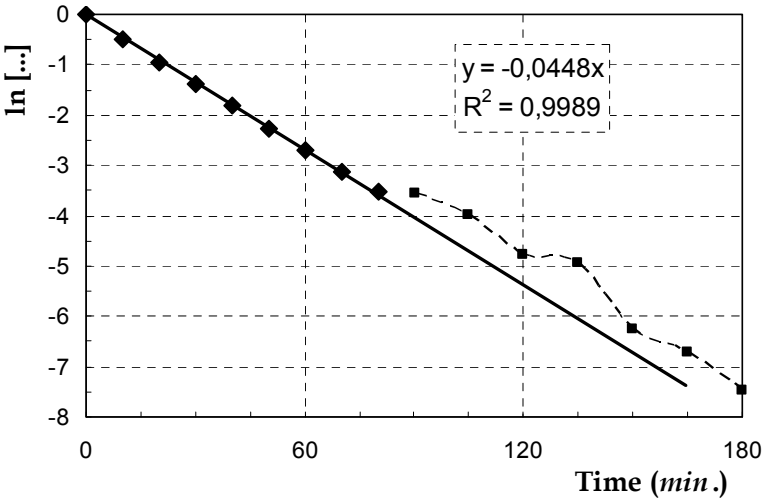

Fig. 15. Evaluation of the module efficiency through Eq. (20); same data as Fig. 13

Fig 14 refers to a counter-extraction experiment at pH 12, and reports the time course of the vanillin concentration in the organic and in the aqueous phases. Due to the favourable partition coefficient vanillin effectively moved towards the aqueous phase. The mass transfer was somewhat slower than in the extraction runs performed in similar conditions,

this behaviour can be clearly explained considering that, in this case, due to the partition coefficient value, the mass transfer resistance through the membrane was quite large.
The module efficiency was calculated from the vanillin concentration vs. time data as explained in the theoretical section (paragraph 3.1), i.e. plotting the left side of Eq. (20) vs. time. As shown in Fig. 15, which reports to the same data of Fig. 13, the data were well fitted by a straight line, of course only the points sufficiently apart from the equilibrium were considered, up to 90 minutes of experiment in this case.
From the slope of the straight (*0.0448*) the efficiency was calculated to be $E_{ff} = 2.8$ %, finally the overall mass transfer coefficient, calculated from Eq. (15) was $K_w = 1.3\ 10^{-5}$ *m/s*.
Tab. 3 summarizes the results obtained in the same way for all the extraction experiments. There is a pretty good agreement between the experimental and theoretical values of the mass transfer coefficients, which of course refers to the actual interface, the inner surface for aqueous feed flowing through the lumen, and the outer surface for aqueous feed in the shell.

W *(L/h)*	S *(L/h)*	η %	K_w *(m/s)*	$K_{w\ theor}$ *(m/s)*
		Feed tube side		
12	10	4.76	$1.4\ 10^{-5}$	$1.45\ 10^{-5}$
20	20	5.36	$1.6\ 10^{-5}$	$1.62\ 10^{-5}$
45	25	2.0	$1.5\ 10^{-5}$	$1.98\ 10^{-5}$
		Feed shell side		
20	35	4.52	$9.7\ 10^{-6}$	$7.6\ 10^{-6}$
45	25	2.77	$1.3\ 10^{-5}$	$9.2\ 10^{-6}$

Table 3. Module efficiency, experimental and theoretical values of the mass transfer coefficients in the extraction runs at different aqueous phase and solvent flow rates

The mass transfer coefficients were lower for feed flowing shell side with respect to the feed flowing through the lumen; however, it has to be considered that the interfacial area is substantially larger in the latter case, being the external surface of the fibres. As a result the mass transfer rates were comparable in the two cases.
The relative role played by the various mass transfer resistances involved were estimated from Eqs (25) or (26) based on the theoretical values of the individual mass transfer coefficients. In all cases the main resistance was associated to the aqueous phase boundary layer (70-80%). The membrane resistance too was appreciable (20-25%) while the solvent boundary layer played a minor role.
As expected, behaviour is different in counter-extraction. From the data of Fig. 14, the module efficiency was calculated to be nearly 0.9 and the membrane is responsible for 95% of the overall resistance; the solvent boundary layer played a minor role (nearly 5 %), whereas the aqueous phase mass transfer resistance was completely negligible. Of course in the counter-extraction hydrophilic membranes would be more convenient than the hydrophobic membranes used in this work.
Extraction experiments with the whole bioconversion broth gave nearly the same results, showing that fouling did not represent a serious problem. The coupling of the membrane contactor with the bioreactor exhibited good results for the enzymatic conversion of vanillylamine to vanillin. Fig. 16 reports one test performed as follows: in the first period

(up to 180 min) enzymatic conversion was performed in a conventional stirred tank reactor, the reactor was then connected to the hollow fibre module (as in Fig. 6). Apparently the vanillin was quickly transferred to the solvent and the reaction (vanNH2 → vanillin) proceeded with the same kinetics.

The results were not equally successful in the case of microbial conversion of ferulic acid to vanillin. After the start up of the extraction, the microbial activity seemed to stop almost at all. May be the solvent had a strong inhibitory effect, or the solvent itself was used as a substrate instead of ferulic acid; this point require further investigations.

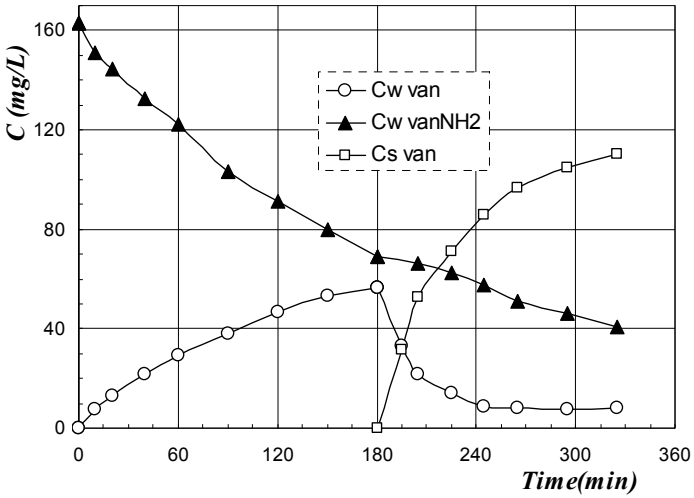

Fig. 16. Coupling extraction and enzymatic conversion

8. References

Asimakopoulou, A.G. & Karabelas, A.J., (2006a). Mass transfer in liquid–liquid membrane-based extraction at small fiber packing fractions, *Journal of Membrane Science* 271,151–162.

Asimakopoulou, A.G. & Karabelas, A.J., (2006b). A study of mass transfer in hollow-fiber membrane contactors - The effect of fiber packing fraction. *Journal of Membrane Science* 282, 430-441

Bao, L. & Lipscomb G.G., (2002). Mass transfer in axial flows through randomly packed fiber bundles with constant wall concentration, *Journal of Membrane Science* 204, 207–220

Bao, L. & Lipscomb G. G. (2003). Mass transfer in axial flows through randomly packed fiber bundles, In: *New Insights into Membrane Science and Technology: Polymeric and Biofunctional Membranes,* Bhattacharyya D. & Butterfield D.A. (Editors), pp. 5 – 26, Elsevier Science B.V., ISBN: 0-444-51175-X, Amsterdam.

Bird, R.B., Stewart, W.E. & Lightfoot, E.N. (2007). *Transport Phenomena*. John Wiley & Sons. ISBN: 978-0-470-11539-8, New York.

Boddeker, K.W; Gatfield, I.L.; Jahnig J. & Schorm C. (1997). Pervaporation at the vapor pressure limit: Vanillin, *Journal of Membrane Science* 137, 155-158.

D'Elia, N.A., Dahuron, L., Cussler, E.L., (1986). Liquid-Liquid extraction with microporous hollw fibres, *Journal of Membrane Science* 29, 309-319.

Devis H.R. & Parkinson G.V. (1970). Mass transfer from small capillaries with wall resistance in laminar flow regime, *Applied Sci. Research* 22(1), 20 – 30.

Ding,W.; He, L.; Zhao, G.; Zhang,H; Shu, Z.; Gao, D. (2004). Double porous media model for mass transfer of hemodialyzers. *International Journal of Heat and Mass Transfer* 47, 4849–4855.

Dongliang H.; Cuiqing, M.; Song ,L.; Lin, S.; Zang, Z.; Deng, Z. & Xu, P. (2007). Enhanced vanillin production from ferulic acid using adsorbent resin, *Appl. Microbiol Biotechnol* 74, 783-790

Drioli, E.; Criscuoli, A. & Curcio E. (2006). *Membrane contactors: fundamentals, applications and potentialities*, Elsevier, ISBN 0-444 52203 4, Amsterdam

Frank, G.T. & Sirkar, K.K. (1987). An integrated bioreactor-separator: in situ recovery of fermentation products by a novel membrane-based dispersion free solvent extraction technique. *Biotechnology and Bioengineering Symp*. 17, 303 - 316

Gaeta, S.N, 2003. Membrane contactors in industrial applications. Proc. of 1st Italy-Russia Workshop on membrane and membrane processes, Cetraro (I), 51-55

Gawronski, R. & Wrzesinska , B. (2000). Kinetics of solvent extraction in hollow-fiber contactors. *Journal of Membrane Science* 168 , 213–222

Gostoli, C. & Gatta A. (1980). Massa transfer in a hollow fiber dialyser, *Journal of Membrane Science* 6, 133 – 148.

Guzman, C. (2004). Vanilla, In *Handbook of herbs and spices, Vol. 2*, Peter K.V. (Ed.), pp. 322 – 354, Woodhead Publishing, ISBN: 1-85573-721-3, Cambridge, UK.

Happel, J. (1959). Viscous flow relative to arrays of cylinders. *AIChE Journal* 5, 174 – 177.

Hatton A.P. & Quarmby (1962). Heat transfer in the thermal entry length with laminar flow in annulus, *International Journal of heat and mass transfer* 5(19), 973 -980.

Knudsen, J.G. & Katz, D.L. (1958).*Fluid dynamics and heat transfer*, McGraw-Hill, ISBN, New York.

Koonaphapdeelert, S.; Li, K. (2007). Preparation and characterization of hydrophobic ceramic hollow fibre membrane. *Journal of Membrane Science* 291 (1–2), 70–76.

Koonaphapdeelert, S.; Zhentao Wu & Li, K. (2009). Carbon dioxide stripping in ceramic hollow fibre membrane contactors, *Chemical Engineering. Science*. 64, 1 - 8

Kosaraju, P.B. & Sirkar, K.K. (2007). Novel solvent-resistant hydrophilic hollow fiber membranes for efficient membrane solvent back extraction. *Journal of Membrane Science* 288, 41–50.

Koschilowski, J.; Wieghaus M. & Rommel M. (2003). Solar thermal driven desalination plants based on membrane distillation. *Desalination* 156, 295-304.

Kreulen, H.; Smolders, G.F.; Versteeg, G.F. &van Swaaij W.P.M. (1993). Microporous hollow fibre membrane modules as gas-liquid contactors. *Journal of Membrane Science* 78, 197-216.

Lazarova, Z., Syska, B. & Schugerl, K. (2002). Application of large scale hollow fiber membrane contactors for simultaneous extractive removal and stripping of penicillin G. *Journal of Membrane Science* 202, 151 – 164.

Li, K. (2007). Ceramic membranes for separation and reaction. *John Wiley,* ISBN 978-470-01440-0, Chichester.

Lemanski, J. & Lipscomb, G.G. (1001). Effect of shell-side flows on the performance of hollow-fiber gas separation modules. Journal of Membrane Science 195, 215–228.

Liang, T. & Long, R.L. (2005). Corrections to Correlations for Shell-Side Mass-Transfer Coefficients in the Hollow-Fiber Membrane (HFM) Modules. *Ind. Eng. Chem. Res. 44,* 7835-7843.

Lipnizki, F. & Field, R.W. (2001) Mass transfer performance for hollow fibre modules with shell-side axial feed flow: using an engineering approach to develop a framework, *Journal of Membrane. Science* 193, 195–208.

Lv, Y.; Yu, X.; Jia J.; Tu, S.T.; Yan, J. & Dahlquist, E. (2011). Fabrication and characterization of superhydrophobic polypropylene hollow fiber membranes for carbon dioxide absorption. *Appl Energy* doi:10.1016/j.apenergy.2010.12.038

Miyatake, O. & Iwashita, H. (1990). Laminar-flow heat transfer to a fluid flowing axially between cylinders with a uniform surface temperature, *Int. J. Heat Mass Transfer* 33 (3) 417–425

Nunge, R.J. & Gill W.N. (1966). An analytical study of laminar counter flow of double-pipe heat exchanger, *AIChE Journal* 12, 279 – 289.

Ramachandra Rao S. & Ravishankar G.A. (2000). Vanilla flavour: production by conventional and biotechnological routes. *J Sci Food Agric;* 80, 289-34

Reid R.C.; Prausnitz J.M. & Poling B.E. (1978) "*The properties of gas & liquids*", McGraw-Hill. ISBN 0-07-100284-7, New York.

Seara, J.F.; Uhìa F.J.; Jaime Sieres, J.S. & Campo, A. (2007). A general review of the Wilson plot method and its modifications to determine convection coefficients in heat exchange devices. *Applied Thermal Engineering* 27 2745–2757.

Schlosser, S.; Kertész, R. & J. Martàk J. (2005). Recovery and separation of organic acids by membrane-based solvent extraction and pertraction. An overview with a case study on recovery of MPCA. *Separation and Purification Technology* 41, 237–266.

Siegel, R.; Sparrow, E.M. & Hallman T.M. (1958). Steady laminar heat transfer in circular tube with prescribed wall heat flux, *Applied Sci. Research* A7(5), 386 – 392.

Sparrow, E.M. & Loeffler, A.L. (1959). Longitudinal laminar flow between cylinders arranged in regular array. *AIChE Journal* 5, 325 – 330.

Sparrow, E.M.; Loeffler, A.L. & Hubbard, H.A. (1961). Heat transfer in longitudinal laminar flow between cylinders. *Trans ASME, Journal of. Heat Transfer* 83, 415 – 422.

Trébounet, D.; Burgard, M. & Loureiro, J.M. (2006). Guidelines for the application of stationary model in the prediction of the overall mass transfer coefficient in hollow fiber membrane contactor. *Separation and purification Technology* 50, 97-106.

van den Heuvel R.H.H., Fraaije M.W., Laane C., van Berkel W.J.H., (2001) Enzymatic synthesis of vanillin, *J. Agric. Food Chem.* 49, 2954-2958.

Walton N.J., Narbad A, Faulds C.G. & Williamson G. (2000). Novel approaches to the biosynthesis of vanillin. *Curr. Opinion Biotechnol.* 11, 490-496

Wickramasinghe, S.R.; Semmens, M.J. & Cussler, E.L. (1992). Mass transfer in various hollow fiber geometries. *Journal of Membrane Science, 69, 235-250*

Wu, J. & V. Chen, V. (2000). Shell-side mass transfer performance of randomly packed hollow fiber modules, *Journal of Membrane Science*, 172, 59 – 74.

Zheng, J.M., Xu, Z.K., Li, J.M., Wang, S.Y. &Xu, Y.Y. (2004). Influence of random arrangement of hollow fiber membranes on shell side mass transfer performance: a novel model prediction. *Journal of Membrane Science* 236, 145–151

28

Taxol® Separation in a Simulated Moving Bed

Marco Aurelio Cremasco
Chemical Engineering School/ University of Campinas
Brazil

1. Introduction

Cancer is a public health concern worldwide that must be considered in various area of the knowledge. In USA, appear a million cases each year. In the South East of the Brazil, cancer is the second largest cause of death. The introduction of chemotherapy to combat the cancer results in significant tumors cure that didn't control with success by exclusive use of surgery and/or radiotherapy (Bonadonna, 1990). Researchers around the world have particular attention in the study of natural products as possible source of antineoplasic agents. Due to the diversity of the chemical structures founded in theses products, there are big chances to identify news molecules with anti-tumor activities (Cremasco & Starquit, 2010). The Taxol® (commercial name for Paclitaxel) discovery offers good points for this reasoning (Holanda et al., 2008).

According to Rhoads (1995), while many drugs act to disrupt the cancer cells, Taxol® paralyzes the internal structure. In the metaphase stage of cell replication, chromosome pairs split and move to the opposite ends of the cell and wait to become part of a daughter cell. Rhoads (1995) reported that these chromosomes were guided by the microtubules made of tubulin. These bundles of microtubules must be dismantled before the cell be divided. However, Taxol® prevents the cells from dividing further and essentially halts the cancer growth. It has been approved by the FDA, in the USA, for the treatment of advanced breast cancer, lung cancer, and refractory ovarian cancer. Taxol® is a diterpene compound (Figure 1).

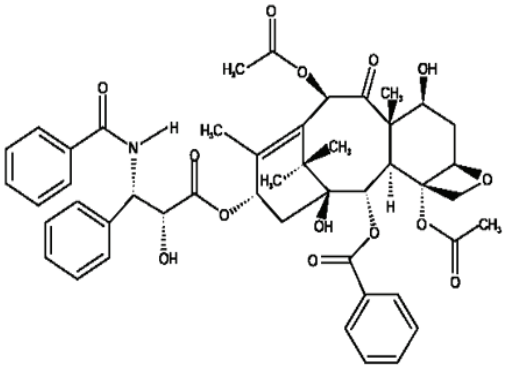

Fig. 1. Chemical structure of Taxol®

Taxol® is an extremely hydrophobic molecule. Its low solubility in water makes the administration of the drug difficult. The complexity of Taxol® rests primarily in its stereochemistry, which makes organic synthesis extremely difficult (Wu, 1999). Taxol® can be isolated from the bark of the Pacific yew (*Taxus brevifolia*). It also can be produced and recovered from the plant tissue culture (PTC) broth (Srinivasan, 1994). The presence of a number of structurally similar compounds in the source material for Taxol®, such as cephalomannine and baccatin, complicates the recovery and purification process (Wu, 1999). A major portion of the purification cost is due to the separation of Taxol® from a large number of taxanes with similar molecular structures. In this case, Taxol® separation and purification usually involves extraction, solvent portioning, and preparative HPLC purification to eliminate the hazardous solvents and the expense associated with pressure equipment (Wu, 1999). Conventional batch chromatography has been used for Taxol® separation from PTC broth (Wu et al., 1997). This technique, however, is expensive and has low yield and low productivity. A simulated moving bed (SMB), which saves solvent and increases the adsorbent utilization (Borges da Silva et al., 2006), can result in a more economical separation process. In a traditional SMB system, a series of fixed bed columns is connected to form a circuit (Figure 2).

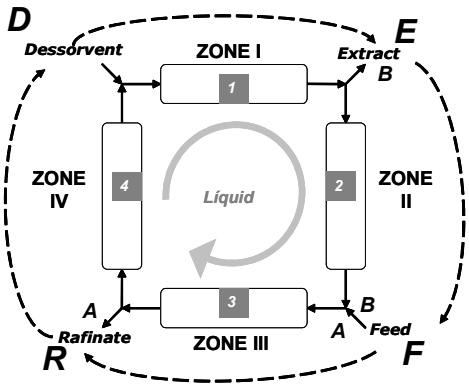

Fig. 2. Classical four zones SMB system (Cremasco & Starquit, 2010)

This circuit is divided into four zones by two inlet ports (feed and a solvent) and two outlet ports (a raffinate port, where the low-affinity mixture A is removed, and an extract port, where a high-affinity mixture B is removed). The inlet and outlet ports are periodically moved along the solvent flow direction by multiple-position valves, causing an apparent countercurrent movement between the liquid and the solid phase. As in batch chromatography, mixture A migrates faster than mixture B in the liquid flow direction (Ma & Wang, 1997). If the average feed port velocity is lower than the mixture A migration velocity and larger than mixture B migration velocity, then A will have a net velocity in the solvent flow direction relative to the feed port, while B will have a net velocity in the opposite direction. In this case, the standing wave approach says that mixture A adsorption wave remains stationary in zone IV, while its desorption wave stands in zone II. Solute B adsorption wave lies in zone III, adsorption wave lies in zone III, and its desorption wave stands in zone I (Ma & Wang, 1997). Figure 3 represents the standing wave approach for multicomponent system. In this figure, A, means low-affinity mixture; B, high-affinity

mixture; D means solvent flow; E, extract flow; F, feed flow; and R, raffinate flow (Cremasco & Starquit, 2010).

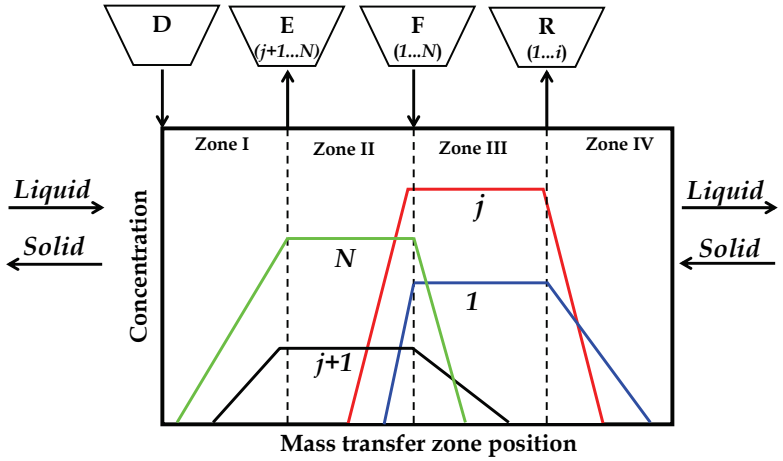

Fig. 3. Standing wave theory, non-equilibrium model (Cremasco et al., 2009a)

2. Theory

2.1 Standing wave analysis

For a system of N components in which the components are numbered from low to high affinity as 1, ... , j, j+1, ..., N (Figure 3); and in which a split is desired between component j and j+1, the standing wave equation are as follows (Cremasco et al., 2009a):

$$u^{I} - \left(1 + \psi\delta_{N}\right)\frac{L}{v} = -\beta_{N}^{I}\left(\frac{E_{b_N}^{I}}{L^{I}} + \frac{\psi v^{2}\delta_{N}^{2}}{L^{I}K_{f_N}^{I}}\right) = B_{N}^{I} \tag{1}$$

$$u^{II} - \left(1 + \psi\delta_{j}\right)\frac{L}{v} = \beta_{j}^{II}\left(\frac{E_{b_j}^{II}}{L^{II}} + \frac{\psi v^{2}\delta_{j}^{2}}{L^{II}K_{f_j}^{II}}\right) = B_{j}^{II} \tag{2}$$

$$u^{III} - \left(1 + \psi\delta_{j+1}\right)\frac{L}{v} = -\beta_{j+1}^{III}\left(\frac{E_{b_{j+1}}^{III}}{L^{III}} + \frac{\psi v^{2}\delta_{j+1}^{2}}{L^{III}K_{f_{j+1}}^{III}}\right) = B_{j+1}^{III} \tag{3}$$

$$u^{IV} - \left(1 + \psi\delta_{1}\right)\frac{L}{v} = -\beta_{1}^{IV}\left(\frac{E_{b_1}^{IV}}{L^{IV}} + \frac{\psi v^{2}\delta_{1}^{2}}{L^{IV}K_{f_1}^{IV}}\right) = B_{1}^{IV} \tag{4}$$

with:

$$\psi = \frac{1-\varepsilon}{\varepsilon} \tag{4}$$

$$\delta_j = \varepsilon_p + (1-\varepsilon_p)k_{pj} \tag{5}$$

To obtain the for port movement velocity, v, it is necessary to consider the dead volume from tubes that connect the columns, for example. This time is defined by

$$t_p = \frac{L}{v} + t_0 \tag{6}$$

L is mass transfer zone length (assume equal column effective length), t_0 is dead time in mass transfer zone k from

$$t_0 = \frac{V_0^k}{\varepsilon u^k A} \tag{7}$$

where V_0^k is dead volume in zone k. A is cross sectional column area; u^k, is the liquid interstitial velocity in zone k. From Figure 2

$$u^{III} - u^{I} = u_F \tag{8}$$

If one substitutes Eqs. (2) and (3) into Eq. (8), its results

$$t_p^2 - bt_p + c = 0 \tag{9}$$

with

$$b = t_0^{III} + t_0^{II} + \frac{\psi(\delta_{j+1} - \delta_j)L}{u_F - B_{j+1} + B_j} \tag{10}$$

$$c = t_0^{III} \times t_0^{II} + \frac{t_0^{II}(1+\psi\delta_{j+1})L - t_0^{III}(1+\psi\delta_j)L}{u_F - B_{j+1} + B_j} \tag{11}$$

The β values are determined from a pseudo-binary model, in which mixtures A and B are treated as single solutes A and B (Cremasco & Starquit, 2010). The four β values can be estimated from simple material balances around zones and mixing points. The following assumptions are made: (i) the concentration of solute A at the outlet of zone III is equal to its concentration at the raffinate port; (ii) the concentration of solute B at the inlet of zone II is equal to its concentration at the extract port; (iii) the ratio between the highest and the lowest concentrations for mixture (A or B) is the same in both adsorption and desorption zones. These assumptions lead to the following expressions:

$$\beta_1^{IV} = \ell n\left(\frac{C_A^R u^{III} - C_A^F u_F}{u^{II} C_A^E}\right) = \beta_j^{II} \tag{12}$$

$$\beta_N^{I} = \ell n\left(\frac{C_B^E u^{II} + C_B^F u_F}{u^{III} C_B^R}\right) = \beta_{j+1}^{III} \tag{13}$$

in which, in the pseudo-binary model (Cremasco & Wang, 2000),

$$C_A^F = \sum_{i=1}^{i=j} C_i^F \tag{14}$$

$$C_B^F = \sum_{i=j+1}^{i=N} C_i^F \tag{15}$$

$$C_A^R = \sum_{i=1}^{i=j} C_i^R \tag{16}$$

$$C_B^E = \sum_{i=j+1}^{i=N} C_i^E \tag{17}$$

The A and B mixture recoveries at the outlet ports are defined as

$$Y_A^{mix} = \frac{u_R C_A^R}{u_F C_A^F} \tag{18}$$

$$Y_B^{mix} = \frac{u_E C_B^E}{u_F C_B^F} \tag{19}$$

$u_R \equiv R/(\varepsilon A)$ and $u_E \equiv E/(\varepsilon A)$ are the equivalent raffinate and extract interstitial velocities. Mass balances for mixtures A and B are substituted into Eqs. (12) and (13) to give

$$\beta_1^{IV} = \beta_j^{II} = \ell n\left\{\left(\frac{u_E}{u^{II}}\right)\left(1 - Y_A^{mix}\right)^{-1}\left[\left(\frac{u^{III}}{u_R}\right)Y_A^{mix} - 1\right]\right\} \tag{20}$$

and

$$\beta_N^I = \beta_{j+1}^{III} = \ell n\left\{\left(\frac{u_R}{u^{III}}\right)\left(1 - Y_B^{mix}\right)^{-1}\left[\left(\frac{u^{II}}{u_E}\right)Y_B^{mix} + 1\right]\right\} \tag{21}$$

Substituting Eqs. (20) and (21) into (1) through (4), one obtains

$$u^I - \left(1 + \psi\delta_N\right)\frac{L}{v} = \ell n\left\{\left(\frac{u_R}{u^{III}}\right)\left(1 - Y_B^{mix}\right)^{-1}\left[\left(\frac{u^{II}}{u_E}\right)Y_B^{mix} + 1\right]\right\}\left(\frac{E_{b_N}^I}{L^I} + \frac{\psi v^2\delta_N^2}{L^I K_{f_N}^I}\right) = B_N{}^I \tag{22}$$

$$u^{II} - \left(1 + \psi\delta_j\right)\frac{L}{v} = \ell n\left\{\left(\frac{u_E}{u^{II}}\right)\left(1 - Y_A^{mix}\right)^{-1}\left[\left(\frac{u^{III}}{u_R}\right)Y_A^{mix} - 1\right]\right\}\left(\frac{E_{b_j}^{II}}{L^{II}} + \frac{\psi v^2\delta_j^2}{L^{II}K_{f_j}^{II}}\right) = B_j{}^{II} \tag{23}$$

$$u^{III} - \left(1 + \psi\delta_{j+1}\right)\frac{L}{v} = -\ell n\left\{\left(\frac{u_R}{u^{III}}\right)\left(1 - Y_B^{mix}\right)^{-1}\left[\left(\frac{u^{II}}{u_E}\right)Y_B^{mix} + 1\right]\right\}\left(\frac{E_{b_{j+1}}^{III}}{L^{III}} + \frac{\psi v^2\delta_{j+1}^2}{L^{III}K_{f_{j+1}}^{III}}\right) = B_{j+1}^{III} \tag{24}$$

$$u^{IV} - \left(1 + \psi\delta_1\right)\frac{L}{v} = -\ell n\left\{\left(\frac{u_E}{u^{II}}\right)\left(1 - Y_A^{mix}\right)^{-1}\left[\left(\frac{u^{III}}{u_R}\right)Y_A^{mix} - 1\right]\right\}\left(\frac{E_{b_1}^{IV}}{L^{IV}} + \frac{\psi v^2\delta_1^2}{L^{IV}K_{f_1}^{IV}}\right) = B_1{}^{IV} \tag{25}$$

In order to obtain the flow rates and the switching time for LMS, the linear standing wave analysis was used by following steps:

1. Find column and particle characteristics (D_b, L, V_0, ε, ε_p ,d_p).
2. Find the partition coefficient k_p (linear isotherm) for each solute and identify the less-retained mixture A= *1*, ..., *j* and the more-retained mixture B = *j+1*, ..., *N*.
3. Find rate parameters (D_{AB}, D_p, k_f, E_b). These constants can be from experimental data or from correlations founded in Literature. The values of k_f and E_b depend on the flow rate in zone k. The parameters associated with the corrections for mass-transfer effects, given in Eqs. (23) to (26) can be calculated from (Ma et al., 1996)

$$\frac{1}{K_{f_j}^k} = \frac{d_p}{6k_{f_j}^k} + \frac{d_p^2}{60\varepsilon_P D_{p_j}} \tag{26}$$

4. Fix the feed concentrations C_A^F and C_B^F.
5. Fix the mixture A yield at the raffinate port (Y_A^{mix}) and the mixture B yield at the extract port (Y_B^{mix}).
6. Choose a feed flow rate F.
7. Calculate the liquid apparent interstitial velocity in each zone and simulated adsorbent velocity using Eqs. (22) to (25), assuming $B_1 = B_j = B_{j+1} = B_N = 0$.
8. Calculate the flow-rate values dependent on mass transfer parameters using the velocities from step 6 and the information in step 3.
9. Calculate the new liquid apparent interstitial velocity in each zone k, and simulated adsorbent velocity.
10. Calculate the convergence criteria given by

$$\left[\sum_{k=1}^{k=4}\left(u_m^k - u_{m-1}^k\right)^2 + \left(v_m - v_{m-1}\right)^2\right]^{1/2} \le 0.1\times10^{-5} \tag{27}$$

    m is the iteration number, and k is the zone number.
11. To find zone flow rates and port switching time.

Notice that this strategy is directly applied for a binary mixture or for multicomponent mixture when the key-component for separation presents higher or lower affinity with sorbent when compared with other components in mixture. In case of key-component, in multicomponent mixture, that presents intermediary affinity (such as Taxol@ in mixture with other taxanes), it is necessary to know its final concentration (in raffinate or extract) for new definition of LMS' operational parameters. There are, basically, two ways to get this information: a) by experiments; b) by theoretical simulation. In this chapter, is presented the second form.

2.2 Adsorption process modeling

The modeling strategy chosen to represent the SMB process consisted of a dynamic modeling, in which each column was modeled individually by a general rate model. In order to obtain this mathematical model, some assumptions must be made: the flow rates are constant in each zone; the transversal cross section is constant for and through column; radial dispersion can be neglected; the axial dispersion coefficient is a function of solute and flow rate; the external mass transfer resistance is considered; solid phase is composed of

small spheres of uniform radius; the mobile phase is a dilute solution, so that Henry's law can be used to describe the sorbate uptake; the pore diffusion model describes the intra-particle transport mechanism; no chemical reaction occurs; initial concentration inside the column is zero. Based on the previous hypotheses, the adsorption process can be described by the following set of equations, for each solute in each column (Cremasco et al. 2009a, Cremasco & Starquit, 2010).

Solid Phase

$$\varepsilon_p \frac{\partial q_j^k}{\partial t} + \left(1-\varepsilon_p\right)\frac{\partial C_{p_j}^k}{\partial t} = \varepsilon_p D_{p_j} \frac{1}{r^2}\left(r^2 \frac{\partial q_j^k}{\partial r}\right) \tag{28}$$

$$C_{p_j}^k = k_{p_j} q_j^k \tag{29}$$

q_j is the solute j concentration in the liquid phase inside the particle pores (volume fraction ε_p), C_p is the solute concentration on the solid (volume fraction $1-\varepsilon_p$) , and indices k and j refer to solute and column, respectively. The initial and boundary conditions for solid phase are

$$t = 0;\ q_j^k = q_j^k\left(0, r\right) \tag{30}$$

$$r = 0;\ \frac{\partial q_j^k}{\partial r} = 0 \tag{31}$$

$$r = R;\ \varepsilon_p D_{p_j} \frac{\partial q_j^k}{\partial r} = k_{f_j}^k\left(C_j^k - q_j^k\big|_{r=R}\right) \tag{32}$$

Fluid Phase

$$\frac{\partial C_j^k}{\partial t} = E_{b_j}^k \frac{\partial^2 C_j^k}{\partial z^2} - u^k \frac{\partial C_j^k}{\partial z} - \psi \frac{6k_{f_j}^k}{d_p}\left(C_j^k - q_j^k\big|_{r=R}\right) \tag{33}$$

C_j is the solute j concentration in the fluid phase (volume fraction ε). The initial and boundary conditions for fluid phase are

$$t = 0;\ C_j^k = C_j^k\left(0, z\right) \tag{34}$$

$$z = 0;\ E_{b_j}^k \frac{\partial C_i^k}{\partial z} = u^k\left(C_j^k - C_{0_j}^k\right) \tag{35}$$

$$z = L;\ \frac{\partial C_j^k}{\partial z} = 0 \tag{36}$$

3. Taxol® separation case

The Taxol® separation simulation is based on laboratory-scale, four-column SMB founded in the Cremasco et al. (2009a, 2009b) as shown in Figure 4. Each column presents the same

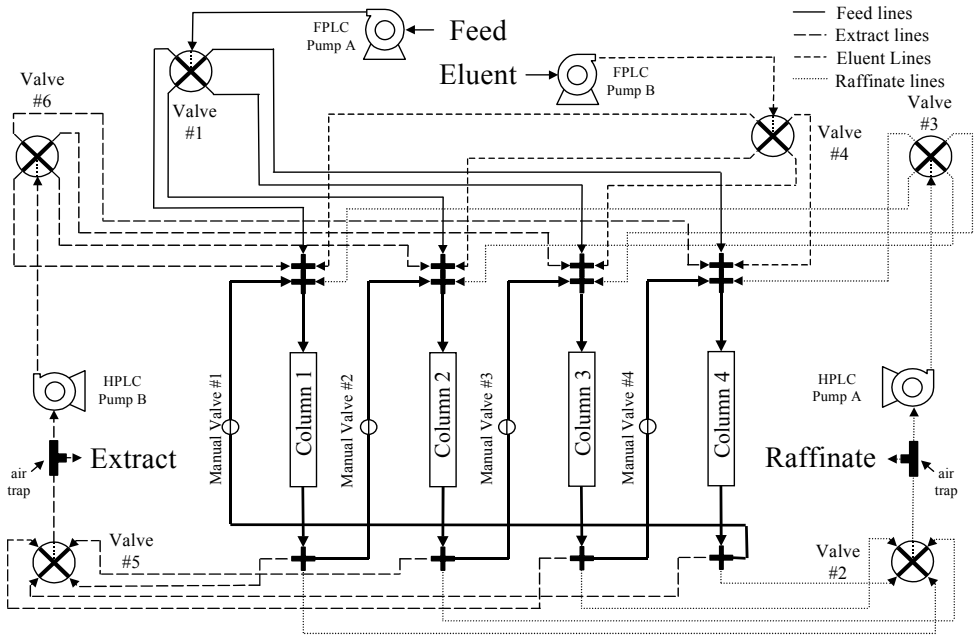

Fig. 4. SMB apparatus: valves system (Cremasco et al. 2009a, 2009b)

characteristics which are presented in Table 1. The system utilizes six eight-port rotary valves, four manual shut-off valves, and four pumps. The six rotary valves together determine the placement of the zones. Valve 1 determines where the feed enters (the column in zone I). Valve 2 determines where the raffinate is drawn. Valve 3 determines where the stream returns after the raffinate is drawn. Valve 4 determines where the desorbent enters. Valve 5 determines where the extract outlet occurs. Valve 6 determines where the recycle stream returns after the extract is drawn. The four manual shut-off valves provide a direct connection between consecutive columns when needed, and are closed to prevent back-flow when not needed. The four pumps consist of two Pharmacia LPLC pumps and two Waters HPLC pumps. The LPLC pumps provide the feed and desorbent flows. The HPLC pumps provide the recycle flow within the circuit. The raffinate pump (HPLC Pump A) provides the flow to Zone IV. The extract pump (HPLC Pump B) provides the flow to Zone II. The combined flow of the raffinate and desorbent pumps determines the flow rate of Zone I. The combined flow of the extract and feed pumps determines the flow rate of Zone III. The raffinate outlet flow rate is determined by the difference in the Zone III flow rate and the raffinate pump flow rate (Cremasco et al., 2009a).

D_b (cm)	L (cm)	V_0 (ml)	ε	ε_p	d_p (cm)
1.5	12.3	2.0	0.32	0.46	0.024

Table 1. Column and particle characteristics (Cremasco et al., 2009a)

The solution was formed by Taxol@ and three impurities, named Tr10, Tr18, and Tr21, based on their retention times in the HPLC chromatogram. Taxol@ had a retention time of 12 min.

The physical parameters are presented in Table 2, while the initial concentrations of the species are summarized in Table 3.

Taxanes	Tr10	Taxol	Tr18	Tr21
k_p (-)	82.52	40.03	38.67	15.09
$D_{AB}(10^4\ cm^2/\min)$	2.569	2.560	2.564	2.526
$D_p(10^4\ cm^2/\min)$	1.310	0.590	0.920	0.384

Table 2. Taxanes partition and diffusion coefficients (Cremasco et al., 2000a)

C^F_{Taxol} (ppm)	C^F_{Tr18} (ppm)	C^F_{Tr21} (ppm)	C^F_{Tr10} (ppm)
120.8	19.6	192.3	14.4

Table 3. Feed composition and SMB operating parameters for Run 1

4. Results and discussion

4.1 Run 1. Impurity separation that presents higher affinity with adsorbent

Following the standing wave strategy to get the SMB operational parameters, we have:

Step 1. Column and particle characteristics: Table 1.

Step 2. Partition coefficient k_p: Table 2. In this case, less-retained mixture A (less affinity with adsorbent): *i = 1= Tr21*; *i = 2 = Tr18; i = j =Taxol@;* more-retained mixture B (high with adsorbent): *i = j+1 = N = Tr10*.

Step 3. Mass transfer parameters: Table 2 for D_{AB} and D_p. The convective mass transfer coefficient is calculated by (Wilson & Geankoplis, 1966)

$$\mathrm{Sh}_j^k = \frac{1.09}{\varepsilon}\left(\mathrm{Pe}_{MP}^{1/3}\right)_j^k \tag{37}$$

with Sherwood number and molecular mass Peclet number for a particle defined by, respectively,

$$\mathrm{Sh}_j^k = \frac{k_{f_j}^k d_p}{D_{AB_j}} \tag{38}$$

$$\mathrm{Pe}_{MP_j}^k = \frac{u^k d_p}{D_{AB_j}} \tag{39}$$

and the axial dispersion coefficient calculated from (Chung & Wen, 1968),

$$\frac{E_{b_j}^k}{D_{AB_j}} = \frac{\varepsilon \mathrm{Pe}_{MP_j}^k}{0.2 + 0.0011\left(\mathrm{Re}_p^k\right)^{0,48}} \tag{40}$$

with particle Reynolds Number in zone k from

$$Re_p^k = \frac{u^k d_p}{\nu_B} \tag{41}$$

Step 4. From Table 3 and considering step 2: C_A^F = 322.7 ppm; C_B^F = 14.4 ppm.

Step 5. Y_A^{mix} = 0.999; Y_B^{mix} = 0.999.

Step 6. F = 0.10 ml/min (*initial*).

Step 11. After iterations in steps 6 up to 10, the operations parameters for Run 1 are presented in Table 4.

F (ml/min)	D (ml/min)	R (ml/min)	E (ml/min)	Q^I (ml/min)	Q^{II} (ml/min)	Q^{III} (ml/min)	Q^{IV} (ml/min)	t_p (min)
0.506	2.068	1.403	1.171	2.437	1.267	1.779	0.370	320.6

Table 4. Operational parameters for Run 1

Step 12. Adsorption process modeling. The numerical solution of the mass-balance equations, Eqs. 28 and 33, are obtained from VERSE-LC code (VErsatile Reaction Separation simulator for adsorption and Liquid Chromatography processes), developed at Bioseparation Laboratory, School of Chemical Engineering, Purdue University, with base on numerical code founded in Whitley (1990). The simulations are based on a detailed model and numerical solution of the model equations. These equations are formulated based on mass conservation principles and fundamental constitutive relations, and are discretized using orthogonal collocation on finite elements, and the DASPK solver is used in the time domain (Whitley, 1990; Berninger et al., 1991). This numerical method has been used in the studies of many adsorption systems (Ma et al., 1996; Ernest et al., 1997; Koh et al., 1998, Cremasco et al., 2001).

The characteristics of column and particle adsorbent are presented in Table 1. The intrinsic parameters (isotherms and diffusivities coefficients) are listed in Table 2, and the convective mass transfer coefficient and axial dispersion coefficient are given by Eqs. (37) and (40), respectively. Simulated curves of solutes concentration distribution along mass-transfer at the cyclic-steady state, for Run 1, are presented in Figure 5. This figure shows that adsorption wave of Tr21 lies between zones II and III, adsorption waves of Taxol® and Tr18 are, basically, in zone III, while the Tr10 adsorption wave lies in zone IV. The Tr21 desorption wave lies between zones III and IV, and desorption waves of Taxol® and Tr18 are between zones I and IV, while Tr10 desorption wave lies in zone I.

The computational elution curves for raffinate and extract are presented in Figure 6 and 7, respectively. These curves are based on the average product concentration, in which each data point was at end of each port switching time t_p. The species concentrations at end of the Run 1, for raffinate port as well as extract port, are from steady-state regime. The concentration values, in this case, are shown in Table 5. It is possible to see in this table that Taxol® is present in high concentration at raffinate port with 35.9% purity. However, in the raffinate is recovered the mixture A with 99.8% purity. In this case, the next separation step (Run 2) is considered a mixture as that one presents in Table 6, in which the focus is to separate the impurity Tr21.

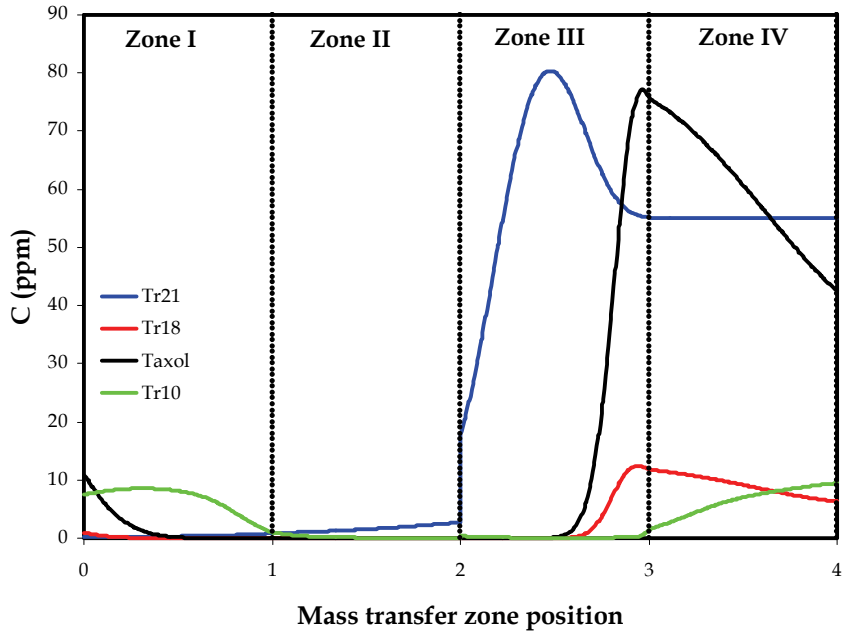

Fig. 5. Simulated curves of solutes concentration distribution along mass-transfer at the cyclic-steady state for Run 1

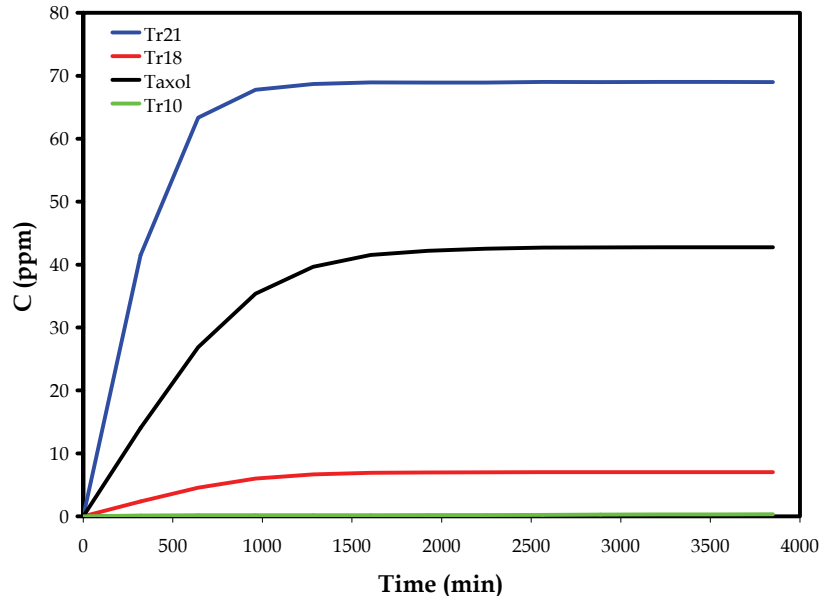

Fig. 6. Theoretical elution curves at raffinate port: Run 1

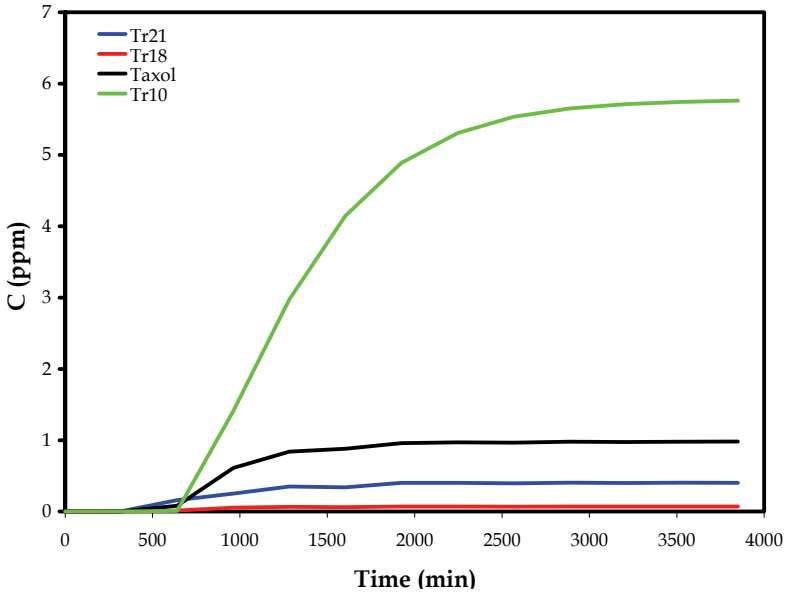

Fig. 7. Theoretical elution curves at extract port: Run 1

	C_{Tr21} (ppm)	C_{Tr18} (ppm)	C_{Taxol} (ppm)	C_{Tr10} (ppm)
Raffinate	69.00	7.01	42.74	0.33
Extract	0.40	0.07	0.98	5.76

Table 5. Feed composition and SMB operating parameters for Run 2

C^F_{Taxol} (ppm)	C^F_{Tr18} (ppm)	C^F_{Tr21} (ppm)
42.74	7.01	69.00

Table 6. Species concentration at steady-state regime for Run 1

4.2 Run 2. Impurity separation that presents less affinity with adsorbent

The same way for Run 1, we have:

Step 1. Same of Run 1.

Step 2. Partition coefficient k_p: Table 2. In this case, less-retained mixture A (less affinity with adsorbent): *i = 1= j = Tr21*; more-retained mixture B (high with adsorbent) *i = j+1 = Tr18; i = N =Taxol@;*

Step 3. Same of Run 1.

Step 4. From Table 3 and considering step 2: C^F_A = 69.00 ppm; C^F_B = 49.75 ppm.

Step 5. Y^{mix}_A = 0.9999 Y^{mix}_B = 0.9999.

Step 6. F = 0.10 ml/min (*initial*).

Step 11. After iterations in steps 6 up to 10, the operations parameters for Run 2 are presented in Table 7.

F (ml/min)	D (ml/min)	R (ml/min)	E (ml/min)	Q^{I} (ml/min)	Q^{II} (ml/min)	Q^{III} (ml/min)	Q^{IV} (ml/min)	t_p (min)
0.439	1.557	0.663	1.333	2.073	0.740	1.179	0.516	215.3

Table 7. Operational parameters for Run 2

Step 12. Adsorption process modeling. Same of Run 1.
Simulated curves of solutes concentration distribution along mass-transfer at the cyclic-steady state, for Run 2, are presented in Figure 8. This figure showed that TR 21 adsorption wave is, basically, in zone III, and its desorption wave is in zone I and IV. For Tr18 and Taxol®, the adsorption waves are between zones I and IV, and their desorption wave are in zone II.

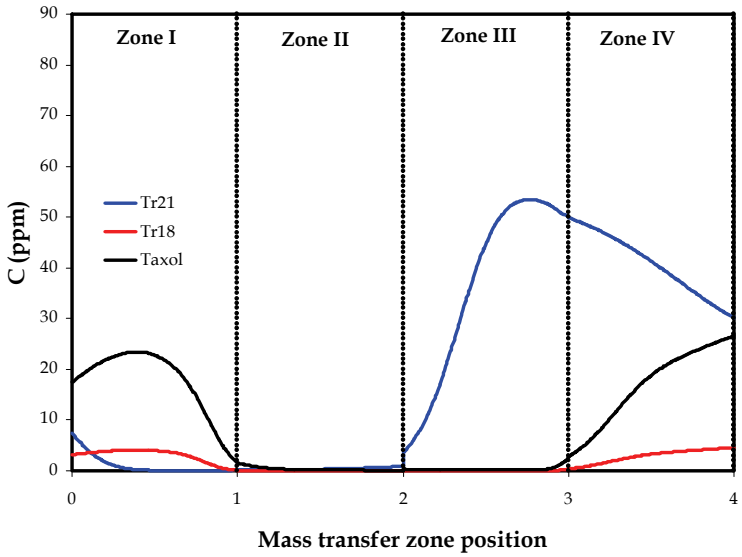

Fig. 8. Simulated curves of solutes concentration distribution along mass-transfer at the cyclic-steady state for Run 2

The computational elution curves for raffinate and extract are presented in Figure 9 and 10, respectively. These curves are based on the average product concentration, in which each data point was at end of each port switching time t_p. The species concentrations at end of the Run 2, for raffinate port as well as extract port, are from steady-state regime. The concentration values, in this case, are shown in Table 8. From this table, there is recover of 93.3% purity of mixture B with. However, the Taxol@ presents 83% purity.

	C_{Tr21} (ppm)	C_{Tr18} (ppm)	C_{Taxol} (ppm)
Raffinate	43.50	0.05	0.50
Extract	0.53	2.21	13.33

Table 8. Species concentration at steady-state regime for Run 1

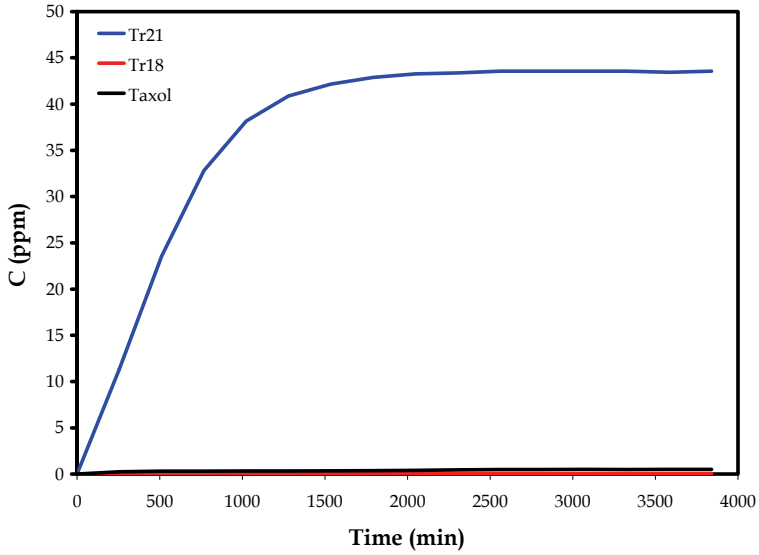

Fig. 9. Theoretical elution curves at raffinate port: Run 2

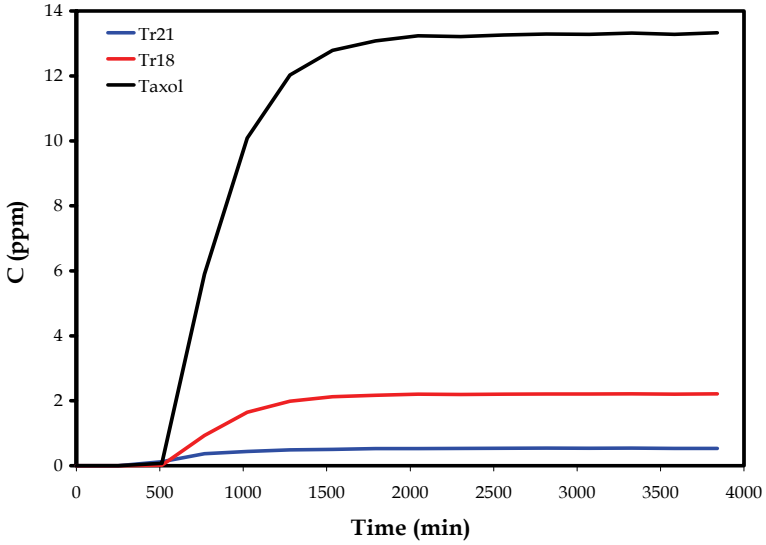

Fig. 10. Theoretical elution curves at extract port: Run 2

C^F_{Taxol} (ppm)	C^F_{Tr18} (ppm)	C^F_{Tr21} (ppm)
42.74	7.01	69.00

Table 9. Feed composition and SMB operating parameters for Run 2

4.3 Run 2 – Alternative: SMB with eight columns

With the goal to increase the Taxol@ purity, it is possible to simulate the performance of experimental system, now, with eight columns, considering two columns in each mass transfer zone. The standing wave analysis strategy (SWA) is basically the same presented before; the difference is to consider 2L instead L in the SWA model. After to apply the strategy presented in section 4.2, the operations parameters for Run 2 with eight columns are presented in Table 10.

F (ml/min)	D (ml/min)	R (ml/min)	E (ml/min)	Q^{I} (ml/min)	Q^{II} (ml/min)	Q^{III} (ml/min)	Q^{IV} (ml/min)	t_p (min)
0.758	2.635	1.144	2.250	3.512	1.262	2.020	0.877	126.3

Table 10. Operational parameters for Run 2 with eight columns

Simulated curves of solutes concentration distribution along mass-transfer at the cyclic-steady state, for Run 2, with 8 columns, are presented in Figure 11. This figure showed basically the behavior founded in Run 2 with 4 columns: Tr21 adsorption wave is in zone III, and its desorption wave is in zone I and IV. For Tr18 and Taxol®, the adsorption waves are in between zone I and IV, and their desorption waves are in zone II.

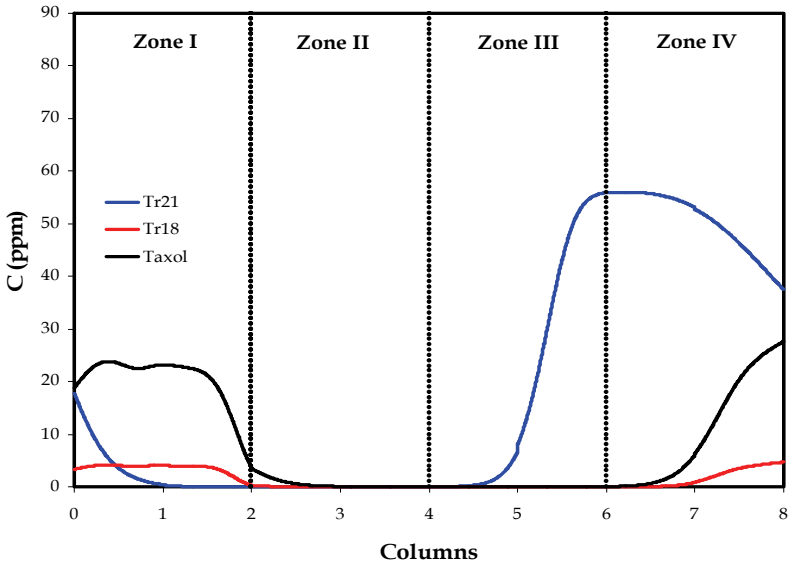

Fig. 11. Simulated curves of solutes concentration distribution along mass-transfer at the cyclic-steady state, for Run 2 with 8 columns

The computational elution curves for raffinate and extract are presented in Figure 12 and 13, respectively. These curves are based on the average product concentration, in which each data point was at end of each port switching time t_p. The species concentrations at end of the Run 2 with 8 columns, for raffinate port as well as extract port, are from steady-state regime. The concentration values, in this case, are shown in Table 11.

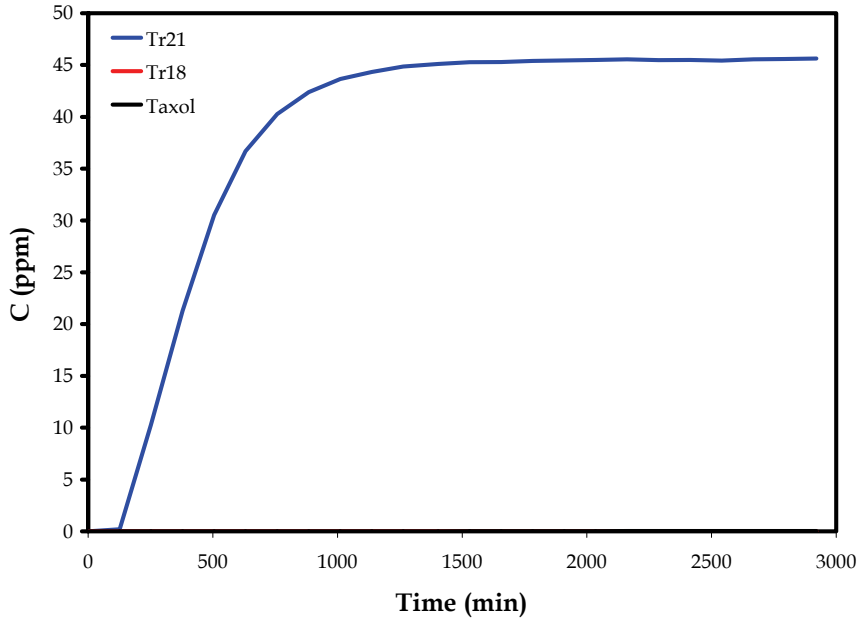

Fig. 12. Theoretical elution curves at raffinate port: Run 2

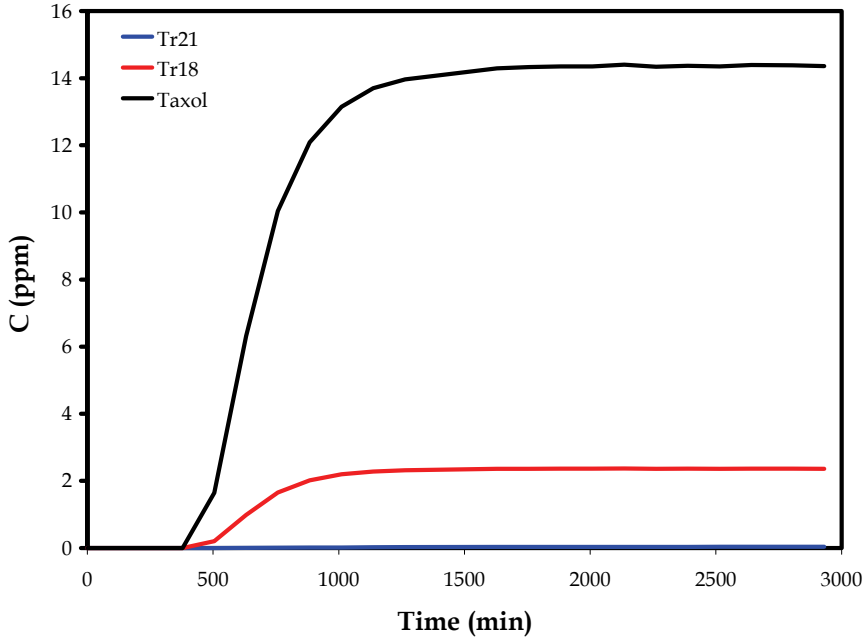

Fig. 13. Theoretical elution curves at extract port: Run 2

	C_{Tr21} (ppm)	C_{Tr18} (ppm)	C_{Taxol} (ppm)
Raffinate	45.63	0.00	0.03
Extract	0.03	2.36	14.38

Table 11. Species concentration at steady-state regime for Run 2 with eight columns

Figure 12 shows that after switching ten times the valves position. Tr21 is already reaching the cyclic steady-state at raffinate port, with concentration showed in Table 11. In the other hands, the extract port is characterized by Taxol@ (Figure 13). From Table 11, there is recover of 99.8% purity of mixture B. However, the Taxol@ presents 85.7% purity. Despite on the increase of mixture B purity with columns number increase, the improvement of Taxol@ purity is not relevant. In fact, Taxol@ and Tr18 are difficult to separate using the chosen adsorbent, because the selectivity between the two solutes is close to one ($\alpha_{Taxol,Tr18} = k_{Taxol}/k_{Tr18} = 1.035$).

5. Conclusion

This chapter showed that a multicomponent and complex system, such as taxane mixture, can be treated as a pseudo-binary model, in which mixtures A (low-affinity mixture) and B (high-affinity mixture) are considered as single solutes A and B. In this case, it is possible to use the standing wave design to specify zone flow rates and switching time. The numerical simulation of SMB offers predictive results, pointing to two separation steps of Taxol® from impurities at least. It was analyzed the influence of column numbers in Taxol® separation, in which purity improvement was not relevant with number-of-column increase (4 to 8). In this case, the purity increase is governed by the selectivity between Taxol® and other solute.

6. Acknowledgment

The author acknowledges the financial support obtained from CNPq (Proc. n. 01/08101-3) for this research project.

7. Nomenclature

A	- cross sectional column area;	L^2
C	- solute concentration in the mobile phase;	ML^{-3}
C_p	- superficial solid intra-particle concentration;	ML^{-3}
C_0	- column injection concentration;	ML^{-3}
D	- eluent (desorbent) flow rate;	L
D_b	- column diameter;	L
D_{AB}	- free diffusion coefficient;	L^2T^{-1}
d_p	- average particle diameter;	L
D_p	- effective diffusion coefficient;	L^2T^{-1}
E	- extract flow rate;	L^3T^{-1}

E_b	- axial dispersion coefficient;	L^2T^{-1}
F	- feed flow rate;	L^3T^{-1}
k_f	- film mass transfer coefficient;	LT^{-1}
$1/K_f$	- global mass transfer resistance;	T
k_p	- equilibrium partition constant;	-
L	- zone length;	L
q	- intra-particle liquid phase concentration;	ML^{-3}
Q	- zone flow rate;	L^3T^{-1}
R	- raffinate flow rate;	L^3T^{-1}
R	- average particle radius;	L
t_P	- switching period;	T
t_0	- dead time;	T
u	- SMB liquid superficial velocity;	LT^{-1}
v	- apparent adsorbent simulated velocity;	LT^{-1}
V_0	- dead volume;	L^3
Y	- recovery.	-

Greek letters

β	- mass transfer correction in the standing wave analysis;	-
δ	- adsorption velocity;	-
ε	- bed porosity;	-
ε_p	- particle porosity;	-
ψ	- bed porosity ratio.	-

Subscripts

A	- pseudo-solute A (low-affinity);	-
B	- pseudo-solute B (high-affinity);	-
D	- desorbent;	-
E	- extract;	-
F	- feed;	-
j	- specie j;	-
k	- mass transfer zone k;	-
R	- raffinate;	-
I, II, III, IV	- mass transfer zones I, II, III, IV.	-

Superscripts

E	- extract;	-
F	- feed;	-
k	- mass transfer zone k;	-
max	- maximum value;	
R	- raffinate;	-
I, II, III, IV	- mass transfer zones I, II, III, IV.	-

8. References

Berninger, J. A.; Whitley, R. D., Zhang, X., and L. Wang, N.-H. (1991), A versatile model for simulation of reaction and nonequilibrium dynamics in multicomponent fixed-bed adsorption processes, *Comput. Chem. Eng.*, 15, 749-768.

Bonadonna, G. (1990), Does chemotherapy fulfill its expectation in cancer treatment?, *Ann. Oncol.*, 1, 11-21.

Borges da Silva, A. A., Ulson de Souza, A. A., Rodrigues, A. E.; Ulson de Souza, and S. M. A. (2006), Glucose isomerization in simulated moving bed reactor by *Glucose isomerase*, *Brazilian Arch. Biol.*, 49 (3), 491 – 502.

Chung, S. F., and Wen, C. Y. (1968), Longitudinal dispersion of liquid flowing through fixed and fluidized beds, *AIChE J*, 14, 857-866.

Cremasco, M. A., and Wang, N.-H. L. (2000), Ternary separation of amino acid in simulated moving bed, Part I: design strategy, *Proceedings of XIV Chilean Chem. Eng. Meeting*, CD ROM, Santiago, Chile.

Cremasco, M. A., Wu, D.-J., and Wang, N.-H. L. (2000), Estimation of partition coefficient and mass-transfer parameters of taxanes, (in Portuguese) *Proceedings of XIII Brazilian Chem. Eng. Meeting*, CD ROM, Aguas de São Pedro, Brazil.

Cremasco, M.A., Hritzko, B.J., Xie, Y., and Wang, N.-H. L. (2001), Parameters estimation for amino acids adsorption in a fixed bed by moment analysis, *Brazilian J. Chem. Eng.*, 18 (2), 207-218.

Cremasco, M.A., Hritzko, B.J., and Wang, N.-H. L. (2009a), Experimental purification of paclitaxel from a complex mixture of taxanes using a simulated moving bed, *Brazilian J. Chem. Eng.*, 26 (1), 207-218.

Cremasco, M.A., Starquit, A., and Wang, N.-H. L. (2009b), Separation of L-tryptophan present is an aromatic amino acids mixture in a four-columns simulated moving bed: experimental and simulation studies, *Brazilian J. Chem. Eng.*, 26 (3), 611-618.

Cremasco, M. A., and Starquit, A. (2010), Modeling for Taxol® separation in simulated moving bed, *Brazilian Arch. Biol.*, 53 (6), 1433 – 1441.

Ernest, M .V. Jr., R. D. Whitley, Z. Ma, and Wang, L. N.-H. (1997), Effect of mass action equilibria on fixed bed multicomponent ion exchange dynamics, *Ind. Eng. Chem. Res.*, 36, 212-226.

Holanda, C. M. C. X., Oliveira, H. E., Rocha, L. G., Spyrides, M. H. C., Aragão, C. F. S., and Medeiros, A. C. (2008), Effect of Paclitaxel (Taxol®) on the biodistribution of sodium pertechnetate ($Na^{99m}TcO_4$) in female *wistar* rats, *Brazilian Arch. Biol.*, 51 (Special number), 191 – 196.

Koh, J-H., Wankat, P.C., and Wang, L. N.-H. (1998), Pore and surface diffusion and bulk-phase mass transfer in packed and fluidized beds, *Ind. Eng. Chem. Res.*, 37, 228-239.

Ma, Z.; R.D Whitley, R. D., and Wang, L. N.-H. (1996), Pore and surface diffusion in multicomponent adsorption and liquid chromatography systems, *AIChE J.*, 42 (5), 1244-1262.

Ma, Z., and Wang, N.-H. L. (1997), Standing wave analysis of SMB chromatography: linear systems, *AIChE J.*, 43, 2488-2507.

Rhoads, D.N. (1995), *The recovery of Taxol from plant tissue culture media*, BSc Thesis, Purdue University, West Lafayette, USA.

Srinivasan, V., Pestchanker, L., Moser, S., Hirasuna, T.J., Taticek, R., and Shuler, M.L., (1994), Taxol production in bioreactors: Kinetics of biomass accumulation, nutrient uptake, and Taxol production by cell suspensions of *Taxus baccata*, *Biotechnol. Bioeng*., 47, 666-676.

Whitley, R. D. (1990), *Dynamics of nonlinear multicomponent bhromatography – Interplay of mass transfer, intrinsic sorption kinetics, and reaction,* Ph. D. Thesis, Purdue University, West Lafayette, USA.

Wilson, E.J., and Geankoplis, C.J. (1966), Liquid mass transfer at very low Reynolds numbers in packed beds, *Ind. Eng. Chem. Fundam*., 5, 9-14.

Wu, D.-J, Ma, Z., Au, B.W. ,and Wang, N.-H, L. (1997), Recovery and purification of Paclitaxel using low-pressure liquid chromatography, *AIChE J*., 3 (1), 232-242.

Wu, D-J. (1999), *Development of simulated moving bed chromatography processes for biochemical purification,* Ph. D. Thesis, Purdue University, West Lafayette, USA.

Part 6

Advances in Chemical Engineering Aspects

29

A Review of Mass Transfer Controlling the Reaction Rate in Heterogeneous Catalytic Systems

Raweewan Klaewkla, Matthias Arend and Wolfgang F. Hoelderich
Chemical Technology and Heterogeneous Catalysis, University of Technology RWTH Aachen, Worringer Weg 1, 52074 Aachen, Germany

1. Introduction

Mass transfer limitations play an important role on the rate of reaction; the rate of conversion and product formation, including in the catalytic systems. In a homogeneous catalytic reaction in which all substances (reactant(s), product(s), and catalyst) are in the same phase, the effect of mass transfer between phases is mostly negligible. In a heterogeneous catalytic reaction; however, the catalyst is usually in a different phase from the reactant(s). Commonly the catalyst is in the solid phase embedded in the reacting species which usually are in the liquid or gaseous phase. Consequently, the reaction rate is principally relied on the mass transfer or diffusion between these phases.
A lot of efforts have been made, due to the important roles of mass transfer effects on the reaction rate. The main purpose for this chapter is to apply the basic restriction of mass transfer on the heterogeneous catalytic reaction. The illustrations based on the literature reviews in the heterogeneous catalytic processes are conducted for elucidation.
Since the reaction catalyzed by solid catalysts occurs when the reactant molecules come in contact with the active sites, which are usually located inside the catalyst pores. In other words, the catalytic reaction is taken place after the reactant molecules diffuse through the fluid layer surrounding the catalyst particles (external diffusion or film diffusion), then through the pore with in the particle (internal diffusion). The internal diffusion of the molecules competes with the reaction; at the same time, the external mass transfer is dependent on the stagnant film thickness and the activity on the outer layer. Hence, the diffusion of molecules is not only hindered by the other molecules, but also by the physical hindrances. The classical seven steps for a catalytic reaction (Fig. 1), i.e. (1) diffusion of the reactants from the bulk phase (boundary layer) to the external surface of the catalyst pellet (film diffusion or interphase diffusion), (2) diffusion of the reactant from the pore mouth through the catalyst pores to the immediate vicinity of the internal catalytic surface; the point where the chemical transformation occurs, (pore diffusion or intraparticle diffusion), (3) adsorption of reactants on the inner catalytic surface, (4) reaction at specific active sites on the catalyst surface, (5) desorption of the products from the inner surface, (6) diffusion of the products from the interior of the pellet to the pore mouth at the external surface, and (7) diffusion of the products from the external pellet surface to the bulk fluid (interphase diffusion), are generally used as the key for explanation.

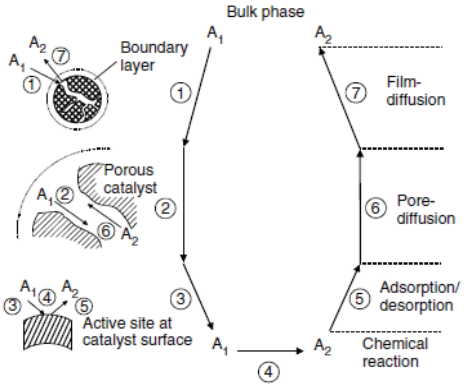

Fig. 1. Individual steps of a simple, heterogeneous catalytic fluid–solid reaction $A_1 \rightarrow A_2$ carried out on a porous catalyst (Dittmeyer & Emig, 2008)

The adsorption, surface reaction, and desorption are sequential steps. However, when a chemical reaction occurs on a surface, the rate of mass transfer to the reactive surface (intraparticle diffusion) is in steady state and equal to the rate of the reaction.

If diffusion or mass transfer steps (steps 1, 2, 6, and 7) are very fast, there is no resistance for the mass transfer from the bulk to the particle surface and from the particle surface to the active site in the pore. The concentration around the catalyst sites is supposed to be the same as that of the bulk one. Under these conditions, the mass transferring steps do not affect the reaction rate. The rate of reaction can be calculated from the reaction mechanism assuming that the concentration at the catalyst site is the same as that of the bulk.

If diffusion from the bulk to the catalyst surface is slow, e.g. the reactants are in the gas phase while the catalyst is in the solid phase, then the external mass transfer resistance is high and becomes an important factor with respect to the overall reaction rate. Nevertheless, the external mass transfer resistance is strongly depended on the flow conditions, e.g. temperature, pressure, and superficial velocity, in the reactor and the particle size of the catalyst (Fogler, 2006a). Varying these parameters can help to reduce the external mass transfer resistance.

In case of the internal diffusion effects are significant and there is no external mass transfer resistance then the concentration profile would vary across the catalyst pellet.

In this chapter, the influences of the mass transfer, i.e. external and internal diffusion, controlling the rate of heterogeneous catalysis reaction are focused. The important factors for mass transfer such as the flow rate conditions (temperature, pressure, and solvent) and the catalyst deactivation are discussed. The types of reactors effecting the enhancement of the mass transferring rate are also communicated. The objective is to summarize the main concepts and formulas for the rate of reaction, which identified to be limited by the mass transfer resistance.

2. Influences of external mass transfer

When a chemical reaction occurs on an active surface, the rates of intraparticle diffusion and chemical reaction are in steady state and simultaneously take place. For a given component "*A*", the reaction rate can be defined as:

$$r_A = k_{cA}\left(x_A^b - x_A^s\right) \tag{1}$$

where r_A (mol L^{-2} t^{-1}) is the reaction rate of the component "A", k_{cA} (mol L^{-2} t^{-1}) is the mass transfer coefficient in a binary system, $x_A{}^b$ is the mole fraction of species "A" in gas bulk, and $x_A{}^s$ is the mole fraction of species "A" in equilibrium with adsorbed "A" (Löffler & Schmidt, 1977).

In order to measure r_A, the value of ($x_A{}^b$ - $x_A{}^s$) must be small. In other words, the mass transfer resistance must be small compared to the surface reaction resistance which can be neglected. Löffler & Schmidt (1975) illustrated that in order to determine the reaction rates with only 10% error due to mass transfer, the Damköhler number (Da) should be less than 0.1. For a first order reaction, Da can be calculated with:

$$Da = \frac{r_A / k_c}{\left(x_A^b - \frac{r_A}{k_c}\right)} \tag{2}$$

The value of Da is varied between zero and infinity (the higher value of r_A/k_c than $x_A{}^b$ is physically impossible). In a system in which Da is higher than 3, the reaction becomes mass transfer controlled. And the rate measured under these conditions should represent a measurement of k_c. Using the heat and mass transfer analogy and the correlation presented by Kyte et al. (1953) with elimination of the insensitive term, the mass transfer coefficient for the natural convection to horizontal wires becomes:

$$k_c \sim T^{0.5} D_w^{-1} \tag{3}$$

where T and D_w represent in temperature (K) and wire diameter (cm), respectively. When the temperature difference between gas and catalyst is small, the forced convection is the main mechanism for mass transfer. The mass transfer coefficient "k_c" presented by Bird et al. (2002) can be calculated as:

$$k_c \sim v^{0.3} T^{0.5} D_w^{-0.7} P^{-0.3} \tag{4}$$

where v is the gas velocity and P is the pressure.

The mass transfer coefficient, k_c, can be calculated by the correlations of the experimental data (Satterfield, 1970 as cited in Forni, 1999), between the Sherwood ($Sh = k_c D_p / D_{AB}$), Schmidt ($Sc = \mu/(\rho D_{AB})$, and Reynolds ($Re = D_p \rho u_s / \mu$) numbers. Wherein, "k_c" is the mass transfer coefficient for the system in which the reactant is the liquid phase (for the mass coefficient of a gaseous reactant "k_g", it can be calculated from the relationship of $k_g = k_c/RT$). "D_p"(cm) is the diameter of the catalyst particle. "D_{AB}"(cm^2 s^{-1}) is the diffusion coefficient or diffusivity of component "A" in component "B". "ρ" (g cm^{-3}) and "μ" (Pa s) are the density and viscosity of the fluid, respectively. "u_s" (cm s^{-1}) is the superficial flow rate of the fluid referred to the overall cross section of the catalyst bed, which is calculated in the absence of the catalyst. These correlations are in the terms of the Colburn "J" factor (i.e. J_D) as a function of the Reynolds number:

$$J_D = \frac{Sh}{ReSc^{1/3}} \tag{5}$$

J_D is a function of the Reynolds number. For the gaseous reactants whereby 3 < Re < 2000 and the interparticle void fraction (ϵ) of the bed of the particles 0.416 < ϵ < 0.788, J_D can be calculated as:

$$J_{D\epsilon} = 0.357 Re^{-0.359} \tag{6}$$

For the liquid reactants by which 55 < Re < 1500 and 0.35 < ϵ < 0.75:

$$J_{D\epsilon} = 0.25 Re^{-0.31} \tag{7}$$

and for the liquid reactants with 0.0016 < Re < 55

$$J_{D\epsilon} = 1.09 Re^{-0.67} \tag{8}$$

For a heterogeneously catalysed reaction, the reactants can be in the different phases (gas and liquid); in other words, comprising of the binary diffusion, the pressure of the gaseous reactant(s) influences the reaction rate as in the term of D_{AB}. By means of the solubility of gaseous reactant(s) in the liquid phase affects a higher reaction rate then improves the conversion.
Additionally, a higher reaction temperature influences the sorption processes on the catalyst surface, subsequently influences the reaction rate. The equations for predicting the gas, liquid, and solid diffusivities as the function of temperature and pressure are given in Table 1. It should be noted that the Knudsen, liquid, and solid diffusivities are independent of the total pressure.

Phase	Order of Magnitude ($cm^2\ s^{-1}$)	Temperature and Pressure Dependences [a]	Eq.
Gas			
- Bulk	10^{-1}	$D_{AB}(T_2,P_2) = D_{AB}(T_1,P_1)\frac{P_1}{P_2}\left(\frac{T_2}{T_1}\right)^{1/2}$	(9)
- Knudsen	10^{-2}	$D_A(T_2) = D_A(T_1)\left(\frac{T_2}{T_1}\right)^{1/2}$	(10)
Liquid	10^{-5}	$D_{AB}(T_2) = D_{AB}(T_1)\frac{\mu_1}{\mu_2}\left(\frac{T_2}{T_1}\right)^{1/2}$	(11)
Solid	10^{-9}	$D_{AB}(T_2) = D_{AB}(T_1)exp\left[\frac{E_D}{R}\left(\frac{T_2-T_1}{T_1T_2}\right)\right]$	(12)

[a] μ_1 and μ_2 are liquid viscosities at temperatures T_1 and T_2, respectively; E_D is the diffusion activation energy

Table 1. Diffusivity relationships for gases, liquid, and solid (Fuller et al. 1966; Reddy & Doraiswamy, 1967; Perry & Green, 1999, as cited in Fogler, 2006a)

For a binary mixture, the single diffusivity D_{AB} can be evaluated from the experimental data related to the Schmidt number. However, most practical reactions involve multicomponent mixtures, of which rigorous handling is more complicated. Since the flux of a given chemical

species "j" (N_j) is driven not only by its own concentration gradient, but also by those of all the other species. For ideal gas mixtures, the kinetic theory leads to the Maxwell-Stefan equation as demonstrated in Eq. (13) (Maxwell, 1866; Stefan, 1871, as cited in Froment & Bischoff, 1979):

$$N_j = -\sum_{k=1}^{N-1} C_i D_{jk} \nabla y_k + y_i \sum_{k=1}^{N} N_k, \quad j = 1,2,...,N-1 \tag{13}$$

in which the last term accounts for bulk flow of the mixture. The exact form of D_{jk} depends on the system under study. The technique for solving the equation is done by using matrix methods.

In an empirical binary mixture of ideal gases, the diffusivity can be expressed in terms of the chemical potential gradient (μ_i) (Krishma & Wesselingh, 1997). Under isothermal conditions with a constant pressure of a species "i", referred to the Maxwell-Stefan equation, the diffusivity "D" can be derived from:

$$-\frac{y_1}{RT} \nabla_{T,p} \mu_1 = \frac{y_2 N_1 - y_1 N_2}{C_t D} \tag{14}$$

where y_1 and y_2 are the mole fractions of the species "1" and "2", C_t is total molar concentration of the fluid mixture (mol m^{-3}), and D is defined as the Maxwell-Stefan diffusivity ($m^2\ s^{-1}$).

For a non-ideal fluid mixture, the component activity coefficients are introduced to express the left member of Eq. (14) as:

$$-\frac{y_1}{RT} \nabla_{T,p} \mu_1 = \left(1 + y_1 \frac{\partial \ln \gamma_1}{\partial y_1} \right) \nabla x_1 = \Gamma \nabla y_1 \tag{15}$$

where γ_1 is the activity coefficient of species "1" (dimensionless) and Γ is the thermodynamic correction factor portraying the non-ideal behavior. Combining of Eq. (14) and (15) after introducing $y_2 = (1 - y_1)$, Eq. (16) is obtained:

$$N_1 - y_1 N_t = C_t D \Gamma \nabla y_1 \tag{16}$$

For highly non-ideal mixtures, the thermodynamic factor Γ strongly depends on the mixture composition and vanishes in the region of the critical point.

For gaseous mixtures at low to moderate pressures and for thermodynamically ideal liquid mixtures, the thermodynamic factor Γ is equal to 1 and the Maxwell-Stefan diffusivity is independent of composition.

For highly non-ideal liquid mixtures, the thermodynamic factor Γ strongly depends on the composition of the mixture. An empirical formula for the composition dependence is:

$$D = (D_{(x_1 \to 1)})^{x_1} (D_{(x_1 \to 0)})^{(1-x_1)} \tag{17}$$

where the bracketed terms are the infinite dilution values of the Maxwell-Stefan diffusivity at either ends of the composition range and x_1 is the liquid mole fraction of the species "1".

The mechanistic picture developed for the diffusion in a two-component system can be extended to the general multicomponent cases, analogous to Eq. (14) as:

$$-\frac{y_i}{RT}\nabla_T \mu_i = \sum_{\substack{j=1 \\ j\neq 1}}^{n} \frac{y_j N_i - y_i N_j}{C_t D_{ij}} = \sum_{\substack{j=1 \\ j\neq 1}}^{n} \frac{y_j J_i - y_i J_j}{C_t D_{ij}}, \quad i = 1,2,....,n \tag{18}$$

where the second equality holds irrespective of the reference velocity frame chosen for the diffusion process.
The examples for the heterogeneous catalysis which are strongly limited by the external mass transfer are the oxidation of alkanes (C_2 – C_4) (Hiam et al., 1968 as cited in Löffler & Schmidt, 1977) and ammonia decomposition (Löffler & Schmidt, 1976)

3. Influences of internal mass transfer

In a heterogeneously catalysed reaction, the mass transfer of the reactants first takes place from the bulk fluid to the external surface of the pellet (Fogler, 2006b). The reactants then diffuse from the external surface into and through the pores within the pellet to the catalytic surface of the pores, in which the reaction occurs. Generally, the overall reaction rate is affected by the external surface diffusion only for the low temperature process (Thomas & Thomas, 1997). Under high temperature conditions, a total pressure difference across the pore usually presents, generating a forced flow in pores. Depending on the catalyst pore size, three diffusion modes can be observed (Forni, 1999). When the pore diameter d_p is much larger than the mean free path "λ" of the diffusing molecules, the diffusion takes place in the usual way as observed outside the pores (bulk or molecular diffusion). When $d_p \approx \lambda$, the diffusing molecules hit the pore walls more frequently than the other molecules (Knudsen diffusion). In addition, in the microporous solids, such as zeolites, the pore diameter of which is close to the size of the reactant molecule. Thus, the reactant molecules can only diffuse in the pores by remaining constantly in contact with the pore walls (surface or configurational diffusion).
According to the mole balance for diffusion and reaction inside the catalyst pellet as described by Fick's law, the internal diffusion rate "N_A" (mol cm^{-2} s^{-1}) is defined as:

$$N_A = -D_e\left(\frac{\partial C_A}{\partial z}\right) \tag{19}$$

where C_A is the number of moles of component "A" per unit of the open pore volume, z is the diffusion coordinate, with the effective diffusion coefficient (diffusivity) D_e (cm^2 s^{-1}) is given by:

$$\frac{1}{D_e} = \frac{1}{D_{b,e}} + \frac{1}{D_{k,e}} \tag{20}$$

where $D_{b,e}$ and $D_{k,e}$ are the effective diffusion coefficients for bulk and Knudsen diffusions, respectively. $D_{b,e}$ and $D_{k,e}$ can be calculated using the equations as demonstrated by Satterfield (1970) as:

$$D_{b,e} = \frac{D_b \theta}{\tau} \tag{21}$$

$$D_{k,e} = 1.94 \times 10^4 \frac{\theta^2}{\tau S_g \rho_p}\sqrt{\frac{T}{M}} \tag{22}$$

where D_b (cm^2 s^{-1}) is the bulk diffusion coefficient, θ is the internal void fraction of the solid particle, τ is the tortuosity factor of the pores, S_g (cm^2 g^{-1}) is the specific surface area of the catalyst, ρ_p (g cm^{-3}) is the particle density, T (K) is the reaction temperature, and M (g mol^{-1}) is the molecular mass of the diffusing species.

In a multicomponent system, the Maxwell-Stefan equation is more generally used than the Fick's law for providing the diffusivity data. The interesting example is the application of the Maxwell-Stefan equation for diffusion in zeolites (Kapteijn et al., 2000). The extended approach to describe the surface diffusion of the adsorbed molecules for an *n*-components mixture is started with Eq. (23) (Krishna, 1990, 1993a, 1993b, as cited in Kapteijn et al., 2000):

$$-\nabla\mu_i = RT\sum_{\substack{j=1\\ j\neq 1}}^{n}\theta_j\frac{u_i-u_j}{D_{ij}^s} + RT\frac{u_i}{D_i^s}, \quad i=1,2,...,n \tag{23}$$

where $\nabla\mu_i$ is the force acting on the species "i" tending to move along the surface with a velocity u_i . The first term on the right-hand side reflects the friction exerted by adsorbate "j" on the surface motion of species "i", each moving with velocities u_j and u_i with respect to the surface, respectively. The second term reflects the friction between the species "i" and the surface. D_{ij}^s and D_i^s represent the Maxwell-Stefan surface diffusivities. The fractional surface occupancies are given by "θ_i":

$$\theta_i = \frac{q_i}{q^{sat}} \tag{24}$$

where q_i represents the loadings of component "i" in zeolite and q^{sat} is referred to the saturation loading (molecules per unit cell or mol kg^{-1}).

Eq. (23) has been successfully applied to describe the transient uptake in zeolites, such as the single-component adsorption on MFI-type zeolites (silicalite-1 and ZSM-5 etc.), carbon molecular sieves, and in zeolitic membrane permeation.

For a first-order catalytic reaction, the reaction rate r_A (mol cm^{-3} s^{-1}) referred to the unit volume of catalyst particle is given by:

$$r_A = k_s S_v C_A \tag{25}$$

where k_s (cm s^{-1}) is the reaction rate constant and S_v (cm^2 cm^{-3}) is the surface area per unit particle volume. For a spherical catalyst pellet with a radius r_1 (cm) (Fig. 2), the profile of the reactant concentration as a function of radius can be calculated using a mass balance of which referred to the spherical shell thickness d_r and r (Fogler, 2006b).

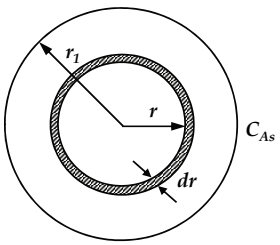

Fig. 2. Shell balance on a catalyst pellet

The integration is easily managed by introducing a dimensionless term known as Thiele modulus (Φ), Eq. (26).

$$\Phi = r_1 \sqrt{\frac{k_s S_v C_{As}^{V-1}}{D_e}} \tag{26}$$

where C_{As} is the reactant concentration at the external particle surface and ν is the reaction order. The parameter Φ represents the ratio of reactivity over diffusivity of the reacting species. For first-order reactions, Φ is independent of reactant concentration. The result of the integration is implicit as:

$$C_A = \frac{C_{As}}{r \sinh \Phi} \sinh\left(\frac{r\Phi}{r_1}\right) \tag{27}$$

For a low value of Φ, the concentration everywhere inside the pore is high. In other words, the diffusion coefficient is very high as compared to the reaction rate. The concentration is uniform across the pore and almost equal to the surface concentration C_{As}. The reaction rate in comparison to the diffusion rate is very low. Hence, one can say that the surface reaction is the rate determining step for a reaction having a low value of Φ.

For a high value of Φ, the reaction rate is fast compared to the diffusion rate. The internal diffusion rate results in the distinctive concentration gradients. Therefore, the reaction rate is evaluated based on the concentration existing at each spatial position inside the pore, not at the surface.

In comparison the relationship between diffusion and reaction limitations, the internal effectiveness factor eta (η) is defined (Pushpavanam, 2009).

$$\eta = \frac{\text{actual reaction rate}}{\text{reaction rate assuming no diffusion resistance}} \tag{28}$$

The magnitude of the effectiveness factor is range from 0 to 1. For a first-order reaction, the effectiveness factor can be derived from:

$$\eta = \frac{-r_A}{-r_{As}} = \frac{-r_A \times \text{volume of catalyst particle}}{-r_{As} \times \text{volume of catalyst particle}} \tag{29}$$

For a spherical particle:

$$\frac{4}{3}\pi r_1^3 r_A = 4\pi r_1^2 N_A = 4\pi r_1^2 D_e \left(\frac{dC_A}{dr}\right)_{r=r_1} \tag{30}$$

Combination of Eq. (30) and (27) results in:

$$\frac{4}{3}\pi r_1^3 r_A = 4\pi r_1^2 D_e \left[\frac{C_{As}\Phi}{r_1}\left(\frac{1}{Tgh\Phi} - \frac{1}{\Phi}\right)\right] \tag{31}$$

For the absence of any diffusion resistance:

$$\frac{4}{3}\pi r_1^3 r_{As} = \frac{4}{3}\pi r_1^2 C_{As} k_s S_v \tag{32}$$

Substitution of Eq. (31) and (22) in (29) results in:

$$\eta = \frac{3D_e\Phi}{r_1^2 k_s S_v}\left(\frac{1}{Tgh\Phi} - \frac{1}{\Phi}\right) \tag{33}$$

Using the definition of Φ in Eq. (26), then Eq. (30) becomes:

$$\eta = \frac{3}{\Phi}\left(\frac{1}{Tgh\Phi} - \frac{1}{\Phi}\right) \tag{34}$$

On the other hand:

$$\eta = \frac{3}{\Phi}\left(\Phi \coth\Phi - 1\right) \tag{35}$$

The dependence of η on Φ for the first-order reaction is shown in Fig. 3.

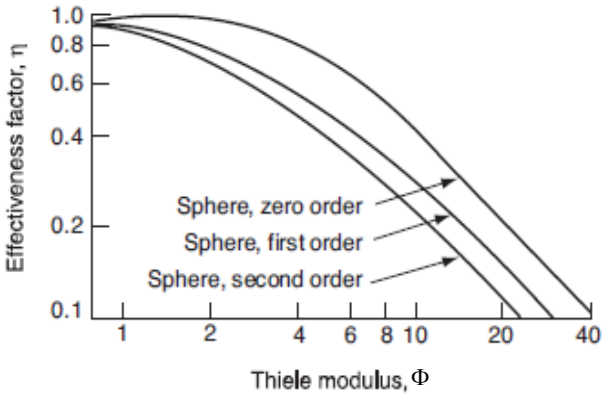

Fig. 3. Effectiveness (η) of a catalyst as a function of Thiele modulus (Φ) for the spherical particles (Fogler, 2006b)

In many circumstances, one is interested to identify the step, determining the reaction rate. The Weisz–Prater criterion (C_{WP}) is used to measure the rate of reaction in order to determine whether the internal diffusion is limiting the reaction. This criterion can be calculated with the following equation:

$$C_{WP} = \eta\Phi^2 = 3\left(\Phi \coth\Phi - 1\right) \tag{36}$$

For $C_{WP} << 1$, there is no diffusion limitation and consequently no concentration gradient exists within the pellet. However, for $C_{WP} >> 1$, the reaction is tremendously limited by the internal diffusion.

4. Effect of the catalyst deactivation on mass transfer

The rate of heterogeneous catalytic reaction usually decreases with the time-on-stream due to the catalyst deactivation. The catalyst deactivation takes place by means of several reasons; for example, the products or by-products produced in the system plug the catalyst pores, subsequently, limit the mass transfer process from the external pore mouth to the internal catalyst surface. In some cases, the foreign molecules, such as coke, are formed under the reaction conditions, deposit on the active surface (fouling or poisoning), and then render the catalyst activity. The presence of an appropriate solvent can assist to prevent or reduce these deactivation problems.
Generally, there are three categories of deactivation mechanisms of which the loss of the catalytic activity is traditionally divided (Fogler, 2006c), i.e. sintering or aging, fouling or coking, and poisoning.

4.1 Deactivation by sintering (aging)

Deactivation by sintering is the loss of the catalytic activity due to the loss of the active surface area or of a crystal phase transformation resulting from a prolonged exposure to high temperature conditions. The active surface area may be lost either by crystal agglomeration and growth of the metals deposited on the support or by narrowing or closing of the pores inside the catalyst pellet. A change in the surface structure may also result from either surface recrystallization or the formation or elimination of surface defects (active sites). The reforming of alkanes over platinum on alumina is an example of catalyst deactivation as a result of sintering.
Deactivation by sintering, in some cases, is a function of the mainstream gas concentration. The most commonly used is the second order with respect to the present activity:

$$r_d = k_d a^2 = -\frac{da}{dt} \tag{37}$$

where a is the catalyst activity as the function of time, $a(t)$, and k_d is the constant for the sintering decay.
The amount of sintering is usually measured in the term of the active area of the catalyst, S_a:

$$S_a = \frac{S_{a0}}{1 + k_d t} \tag{38}$$

4.2 Deactivation by coking or fouling

Deactivation by coking or fouling is commonly involved in the reactions of hydrocarbons, such as catalytic reforming, hydrogenation, oxidation etc. The decay mechanism results from a carbonaceous (coke) material depositing on the surface of the catalyst. The amount of coke on the surface after a certain time can be found with the following empirical relationship (Voorhies, 1945 as cited in Fogler, 2006c):

$$C_C = A t^n \tag{39}$$

where C_C is the concentration of carbon on the surface (g m^{-2}) while n and A are fouling parameters, which are the functions of feed rate. This expression can be used for a wide variety of catalysts and feed streams.

4.3 Deactivation by poisoning

Deactivation by this mechanism occurs when the poisoning molecules (*P*) become irreversibly chemisorbed on active sites (*S*), thereby reducing the number of sites available for the main reaction. The poisoning molecule can be a reactant and/or a product in the main reaction, or it may be an impurity in the feed stream. The reaction rate for poisoning is:

$$r_d = k_d^{'} C_P^m a^q = 2\frac{da}{dt} \tag{40}$$

where m and q are the reaction orders.

5. Effect of reactor types on mass transfer

As the result of the kinetics data obtained from the integral reactors under the conditions which limited by mass and heat transfer cannot be used for formulating the meaningful kinetic expressions. In other words, for any kinetic measurements, modeling, and the typical approaches to the reactor rate calculations, the mass transfer limitation is always assumed to be of less effect that can be negligible. An appropriate type of reactor characteristically helps to enhance the mass transferring rate of the system. Accordingly, the design of any reactor generally concerns on the need for eliminating heat and mass transfer effects or accounting them in the suitable manner.

Several types of reactors exist for the heterogeneous catalytic reactions. These include fixed bed reactors, tubular catalytic wall reactors, and fluidized bed reactors. However, for gas-liquid-solid reactions, the reactor types (e.g. trickle bed reactor or bubble column reactor) are usually developed for the specific reaction conditions (Levenspiel, 1999).

The continuous flow-through reactors/plug flow reactor (tubular and column) are widely used for the heterogeneous systems. The tubular reactors permit a vigorous heat exchange in the reaction zone and ensure a uniform residence time for all particles in the flow. Whereas, the column reactors are structurally less suited for vigorous heat exchange and therefore are used in those cases where an addition (or removal) of heat to the reaction zone is either unnecessary or is carried out on a limited scale. In column reactors, it is very important to have a uniform distribution of flow through the cross section of the column. In such a case, the flow-through reactors are usually equipped with the circulation loops for recycling any substances which are unreacted.

The reactors in which the diffusional effect can be precisely predicted are the tubular flow or plug-flow reactor (PFR). These reactors are sometimes filled with the solid packing (packed-bed reactor, PBR), in order to accelerate the mass transfer between phases and reduce the variation in residence time of the reactant particles. In multiphase catalytic reaction, PBR is regularly used as a model reactor. The PBR can be operated either with a continuous gas or in a distributed liquid phase (trickle operation; in which the catalyst is stationary, so called trickle-bed reactor (TBR)) or with a distributed gas and a continuous liquid phase (bubble operation; in which the catalyst is suspended in the liquid phase) flowing through a packed bed of the catalyst, so called fixed-bed like reactor (FBR). The directions of gas and liquid flows in the system, i.e. cocurrent downflow, cocurrent upflow, and countercurrent flow (Fig. 4 (A) - (C)), are considered as one of the most important factors.

An alternative reactor type is the slurry reactor, a vessel in which the gaseous reactant is dispersed into a liquid phase containing the suspended solid catalyst. At high ratio of fluid-

feed flow rate to the reactor diameter, the gas-liquid-solid reactor is often termed an ebullating-bed (a high solid concentration type of fluidized bed reactor in which catalyst particles are held in suspension by the upward movement of the liquid reactant and gas flow), Fig. 4 (D), or bubble column reactor, as a low solid concentration, Fig. 4 (E).

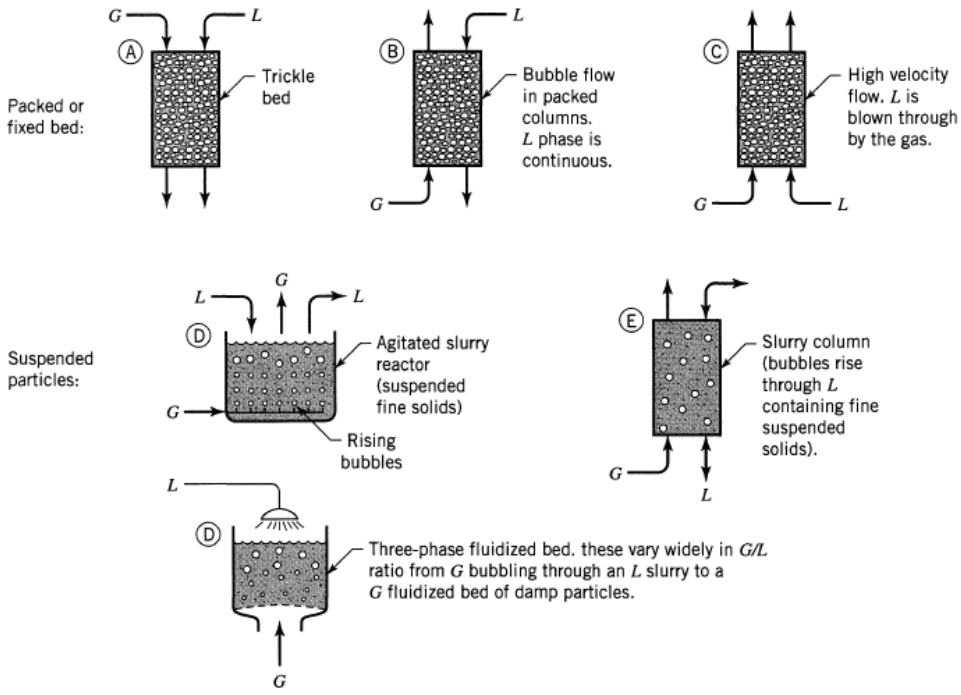

Fig. 4. Various types of reactors with direction of gas (G) and liquid (L) flows for the reactions catalyzed by the solid catalysts (Levenspiel, 1999)

Some special chemical reactor types are fluidized (Fig. 5. (A)) and moving (Fig. 5 (B)) bed reactors, which have characteristics that set them apart from the other reactors. The advantages of these reactors include the possibility of a continuous intake of fresh solid phase and removal of depleted solid phase, a high rate of heat exchange, the lack of dependence of the speed of the fluidizing agent (gas, vapour, or liquid), and a wide range of properties of solid particles (including suspensions and pastes) and fluidizing agents. However, the use of reactors with fluidized and moving beds is limited. This is because they do not ensure a uniform residence time of the particles of the two phases in the beds, and do not preserve the solid-phase properties. In addition, they require the powerful recovery equipment for fines.

5.1 Slurry reactor

The three phase (gas and liquid as the reactants with solid as the catalyst) catalytic slurry reactors are commonly used in industry for a wide variety of processes, such as oxidation, hydrogenation, carbonylation, and pollution control (Ramachandran & Chaudhari, 1980). A

number of steps such as gas-liquid mass transfer, liquid-solid mass transfer, intraparticle diffusion, and chemical reaction are involved for the reaction. A useful concept for analyzing these kind of heterogeneous catalysis reactions is the overall effectiveness factor (Ω) which incorporated the effects of all transport resistances (internal and external).

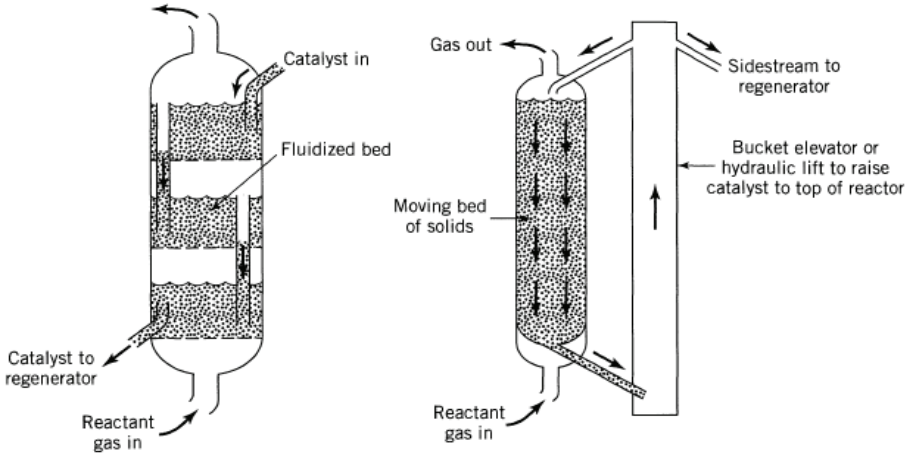

Fig. 5. Fluidized-bed (a) and moving-bed (b) reactors (Levenspiel, 1999)

For the first-order reaction in which a gas phase containing reactant "A" is continuously bubbled through the agitated slurry (a semibatch reactor), the overall effectiveness factor for a slurry reactor is defined as (Fogler, 2006b):

$$\Omega = \frac{\text{actual overall rate of reaction}}{\text{reaction rate if entire surface area is exposed to the bulk concentration}} \tag{41}$$

The actual overall rate of the reaction can be expressed in terms of the rate per unit volume, r_A, the rate per unit mass, r_A', and the rate per unit surface area, r_A'', which are related by the equation:

$$-r_A = -r_A^{'}\rho_b = -r_A^{''}S_a\rho_b \tag{42}$$

The overall rate of reaction in terms of the bulk concentration C_{Ab} is:

$$-r_A^{''} = \Omega\left(-r_{Ab}^{''}\right) = \Omega k_1^{''}C_{Ab} \tag{43}$$

The rates of reaction based on surface and bulk concentrations are related by:

$$-r_A = \Omega\left(-r_{Ab}\right) = \eta\left(-r_{As}^{''}\right) \tag{44}$$

where:

$$-r_{As}^{''} = k_1^{''}C_{As} \tag{45}$$

$$-r''_{Ab} = k''_1 C_{Ab} \tag{46}$$

with the effectiveness "η" can be calculated as Eq. (35).

5.2 Fixed-bed reactor

For external mass transfer-limited reactions in a PBR, the rate of reaction at any points in the bed is (Fogler, 2006b):

$$-r'_A = k_c a_c C_A \tag{47}$$

where the correlation for the mass transfer coefficient k_c is directly proportional to the flow rate and inversely proportional to the particle diameter (D_p) The factor a_c (m^2 m^{-3}) is the external surface area of the catalyst per volume and defined as:

$$a_c = \frac{6(1-\Phi)}{d_p} \tag{48}$$

Consequently, for the external mass transfer-limited reactions, the reaction rate is inversely proportional to the particle diameter.

For reactions which are controlled by the internal diffusion, the rate of reaction varies inversely with the particle diameter and exhibits exponential temperature dependence; however, it is independent on the velocity.

The multiphase catalytic PBR operated with the trickle operation (TBR) are widely used in the petroleum and petrochemical industry, especially, when processing with the heavy petroleum fraction, such as in hydrocracking, hydrodesulphurization, hydrogenation, etc. In a TBR, different flow regimes can exist, depending on the physical properties of the gas and liquid phases, the flow rates, and the nature and size of the catalyst packing (Lemcoff et al., 1988). The retention of liquid in the packed-bed or liquid hold up is an important parameter in the performance of a TBR. The partial catalyst wetting is a common phenomenon found in TBR (Satterfield, 1975, as cited in Sakornwimon & Sylvester, 1982). This may result from a poor liquid distribution caused by a faulty design of the liquid distributor or from an inadequate ratio between reactor and particle diameter. The fraction of the external surface of a particle wetted by the liquid or external wetting efficiency, has an important effect on the rate of reaction in a TBR.

For the interphase mass transfer, the evaluation is generally considered at the equilibrium conditions (Lu et al., 1984, as cited in Lemcoff et al., 1988).

For the intraphase mass transfer, in case of partial internal wetting, the gaseous reactant will partly diffuse into the dry pores. Therefore, it affects the diffusion of gas and solute in liquid within the catalyst pores. The total molar flux of a component (N_j) in a porous media can be described in terms of diffusion ($N_j{}^D$) and viscous fluxes ($N_j{}^V$) in the gas phase, and of a surface flux ($N_j{}^\sigma$) at the gas-solid interface:

$$N_j = N_j^D + N_j^v + N_J^\sigma \tag{49}$$

The total diffusion flux, $N_j{}^D$, involves both the molecular and Knudsen diffusion (Mason et al., 1967; Feng & Stewart, 1973, as cited in Lemcoff et al., 1988), whilst, the viscous flux, $N_j{}^V$, can be described in terms of the Darcy law:

$$N_j^v = -x_j \frac{B_0 C}{\mu} \nabla P \tag{50}$$

where B_0 is the viscous permeability of the porous media. The surface diffusion is commonly represented by the Fick's law equation:

$$N_j^\sigma = -D_j^\sigma \nabla C_j^\sigma \tag{51}$$

where $C_j{}^\sigma$ is the surface concentration of species "j".
When the molecular size becomes comparable to that of the pore, the rate of solute diffusion in liquids within porous media is reduced. Thus, diffusion is related to an exclusion phenomenon and a hydrodynamic drag effect. Then the total molar flux is suggested with the use of Fick's law equation:

$$N_j = -D_{e,j}^L \nabla C_j + x_j N \tag{52}$$

where $D_{e,j}{}^L$ represents the effectiveness coefficient, x_j is the molar fraction and N is the molar flux of the component "j".
$D_{e,j}{}^L$ is given by:

$$D_{e,j}^L = D_{b,j}^L \varepsilon K_p \frac{K_r}{\tau} \tag{53}$$

where $D_{b,j}{}^L$ is the bulk diffusivity in free solution, ε is the particle porosity, K_p is the equilibrium partition coefficient and K_r is the fractional reduction of diffusivity resulting from the proximity of the pore wall.
At equilibrium:

$$K_p = (1-\lambda)^2 \tag{54}$$

where λ is the ratio of molecular diameter to pore diameter. When the solvent molecule is also comparable:

$$K_p = \frac{(1-\lambda_{solute})^2}{(1-\lambda_{solvent})^2} \tag{55}$$

The parameter K_r is the function of the solute diameter, $K_r = K_r(\lambda)$, which correlated to:

$$\log K_r = -2.0\lambda \tag{53}$$

The overall effectiveness factor for the partially wetted catalyst pellet (η_0) is presented in several literatures; however, they all are related to the relationship of the following equation (Lemcoff et al., 1988):

$$\eta_0 = f\eta_w + (1-f)\eta_d \tag{56}$$

where η_w and η_d are the overall effectiveness factors for a pellet completely covered by liquid and gas, respectively, and f is the external wetting efficiency. The solutions of this

effectiveness factor depend on the limiting phase (gas or liquid) and completion of wetting in the catalyst pellet, which the more detail are documented elsewhere (as cited in Lemcoff et al., 1988; Sakornwimon & Sylvester, 1982).

6. Conclusion

In a gas-liquid reaction catalysed by a porous-solid catalyst, one of the most important key parameters which influence the catalyst activity and selectivity is the mass transfer between the multiphases. The reactants which are typically in the gaseous and liquid phase diffuse through the boundary layer (external diffusion), then through the catalyst pore mouths into the internal catalytic surface (internal diffusion). After adsorption on the active surface, the reaction occurs on the specific active sites. Subsequently, the formed products desorb and diffuse to the catalyst pore mouths and finally to the bulk phase.

Numerous reactions are limited by the step of external or internal diffusion. The reaction depends on the parameters involving the diffusion coefficient between gas and liquid phase (D_{AB}), the size of the catalyst particle, the pore size diameter, the diffusive surface area, the physical properties (density and viscosity) of the fluids, and the flow conditions (temperature, pressure, and flow rate) of the gas and liquid reactants. The relationships of these parameters are analogous between heat and mass transfer, which can be written as in the dimensionless terms, e.g. Sherwood, Schmidt, and Reynolds numbers. However, these correlated equations are limit in explanation for the multicomponent mixtures; as a result, the Maxwell-Stefan equation is more widely used. Subsequently, the mass transfer factors, e.g. molar flux and effectiveness factors can be determined.

The rate of catalytic reaction regularly decreases with time, due to catalyst deactivation. This deactivation occurs because of three main mechanisms: sintering, fouling, and poisoning. Different deactivation mechanisms affect catalytic rate in different ways.

Different flow characteristics in different reactor types influence the mass transfer between different phases. Hence, for a selection and invention the catalytic reactor, besides the factors, i.e. ensuring a given yield include the volume, flow rate, heat-exchange surface, rate of catalyst substitution, and various structural parameters (particularly in the case of high-pressure reactors), the obligatory need involves the use of experimental data on the kinetics of reactions, catalytic poisoning, and the rates of heat and mass transfer (particularly the effectiveness factor).

For reactions involving gaseous, liquid, and solid (as the catalyst) phases, a high interface area can be achieved by dispersing one of the reactants as in the TBR or bubble operation reactor. The partial catalyst wetting is a common phenomenon found in TBR, which is an important effect on the rate of catalytic reaction. In order to calculate the overall effectiveness factor, the important step is to consider the phase of reactant which limits the catalyst wetting.

7. References

Bird, R.B., Stewart, W.E. & Lightfoot, E.N. (2002). *Transport Phenomena* (2nd Edition), pp. 679-689, John Wiley & Son, ISBN 0-471-41077-2, New York

Dittmeyer, R. & Emig, G. (2008). Simultaneous Heat and Mass Transfer and Chemical Reaction. In: *Handbook of Heterogeneous Catalysis*, Vol.1, G. Ertl, H. Knözinger, F.

Schüth, J. Weitkamp, (Eds.), pp. 1727-1784, ISBN-13: 978-3-527-31241-2, Wiley-VCH, Weinheim

Fogler, H.S. (2006a). External Diffusion Effects on Heterogeneous Reactions, In: *Elements of Chemical Reaction Engineering*, N.R. Amundson (Ed), pp. 757-801, Prentice-Hall Inc., ISBN 0-13-047394-4, New Jersey

Fogler, H.S. (2006b). Diffusion And Reaction, In: *Elements of Chemical Reaction Engineering*, N.R. Amundson (Ed), pp. 813-852, Prentice-Hall Inc., ISBN 0-13-047394-4, New Jersey

Fogler, H.S. (2006c). Catalysis and Catalytic Reactors, In: *Elements of Chemical Reaction Engineering*, N.R. Amundson (Ed), pp. 645-738, Prentice-Hall Inc., ISBN 0-13-047394-4, New Jersey

Forni, L. (1999) Mass Transfer in Catalytic Reactions. Catalysis Today, Vol.52, No.2-3, (September 1999), pp. 147-152, ISSN: 0920-5861

Froment, G.F. & Bischoff, K.B. (1979). *Chemical Reactor Analysis and Design*, pp 143-177, John Wlley & Sons. Inc., ISBN 0-471-02447-3

Kapteijn, F., Moulijn, J.A., Krishna, R. (2000). The Generalized Maxwell-Stefan Model for Diffusion in Zeolites: Sorbate Molecules with Different Saturation Loadings. *Chemical Engineering Science*, Vol. 55, Issue 15, (August 2000), pp 2923-2930, ISSN 0009-2509

Krishna, R. & Wesselingh, J.A. (1997). The Maxwell-Stefan Approach to Mass Transfer. *Chemical Engineering Science*, Vol. 52, No.6, (February 1997), pp 861-911, ISSN 0009-2509

Kyte, J.R., Madden, A.J. & Piret, E.L. (1953). Natural-Convection Heat Transfer at Reduced Pressure. *Chemical Engineering Progress*, Vol.49, No.12, pp. 653-662, ISSN 0360-7275

Lemcoff, N.O., Cukierman, A. L., & Martínez, O.M. (1988), Effectiveness Factor of Partially Wetted Catalyst Particles: Evaluation and Application to the Modeling of Trickle Bed Reactors, *Catalysis Reviews, Science and Engineering*, Vol.30, No.3, (August 1988), pp. 393-456, ISSN: 1520-5703 (electronic) 0161-4940 (paper)

Levenspiel, O. (1999). Part III: Reactions Catalyzed by Solids, *Chemical Reaction Engineering* (3rd Edition), pp. 367-516, John Wiley & Sons Inc, ISBN 0-471-25424-X, New York

Löffler, D.G., Schmidt, L.D. (1975). Catalytic Activity and Selectivity on Heterogeneous Surfaces with Mass Transfer. *AIChE Journal*, Vol.21, No.4, (July 1975), pp. 786-791, ISSN 0360-7275

Löffler, D.G., Schmidt, L.D. (1976). Kinetics of NH3 Decomposition on Polycrystalline Pt. *Journal of Catalysis*, Vol.41, No.3, (March 1976), pp. 440-454, ISSN 0021-9517

Löffler, D.G., Schmidt, L.D. (1977). Influence of External Mass Transfer on Catalytic Reaction Rates on Metals. *Industrial and Engineering Chemistry Fundamentals*, Vol.16, No.3, (August 1977), pp. 362-366, ISSN 0196-4313

Pushpavanam, S. (2009). Mass Transfer Effects in Chemical Reactions. pp. 7.1-7.28, Narosa Publishing House, Retrived from http://203.199.213.48/1357

Ramachandran, P.A. & Chaudhari, R.V. (1980). Overall Effectiveness Factor of a Slurry Reactor for Non-Linear Kinetics. *The Canadian Journal of Chemical Engineering*, Vol.58, No.3, (June 1980), pp. 412-415, ISSN 1939-019X

Sakornwimon, W. & Sylvester, N.D. (1982), Effectiveness Factors for Partially Wetted Catalysts in Trickle-Bed Reactors, *Industrial and Engineering Chemistry Process Design and Development*, Vol.21, No.1, (January 1982), pp. 16-25, ISSN: 0196-4305

Satterfield, C.N. (1970). *Mass Transfer in Heterogeneous Catalysis*, MIT Press (MA), ISBN 0-26-219062-1, Cambridge

Thomas, J.M. & Thomas, W.J. (1997). *Principles and Practice of Heterogeneous Catalysis*, VCH, ISBN 03-527-29288-8, Weinheim, New York

30

Role of Mass Transfer in Phase Transfer Catalytic Heterogeneous Reaction Systems

P. A. Vivekanand and Maw-Ling Wang
Department of Environmental Engineering, Safety and Health
Hungkuang University; Shalu District, Taichung 43302 Taiwan,
Republic of China

1. Introduction

Conventional techniques [1] for removing the constraints of mutual insolubility of aqueous phase with organic phase are industrially unattractive and polluting. A plausible technique now widely known as ''phase transfer catalysis" (PTC) has emerged as a broadly useful tool [2–7] in solving the predicament of insolubility of aqueous phase with organic phase. In this methodology, involving a substrate (in the organic layer) and an anionic reagent or a nucleophile (in the aqueous layer), reacting anions are continuously introduced into the organic phase. Currently, PTC is an important choice in organic synthesis and is widely applied in the manufacturing processes of specialty chemicals, such as pharmaceuticals, perfumes, dyes, additives, pesticides, and monomers. Further, the recent tendency toward "green and sustainable chemistry" has again attracted strong attention to this technique [8-13]. In the last five decades, a steadily increasing number of papers and patents dealing with phase transfer topics and related to their applications have been published in the literature [14-30].
It is understood that the complicated nature of the PTC system stems from the two mass-transfer steps and two reaction steps in the organic and aqueous phases. In addition, the equilibrium partitions of the catalysts between two phases also affect the reaction rate. The difficulty in realizing the mass-transfer rates of catalysts between two phases is probably due to the uneasy identification of the catalyst (or intermediate product) during reactions. Inoue *et al.* [31] investigated mass transfer accompanied by chemical reaction at the surface of a single droplet. They studied the mass-transfer effect for both neglecting and accounting for the mass-transfer resistance in the continuous phase.
Wang and Yang [32] investigated the dynamic behavior of phase transfer- catalyzed reactions by determining the parameters accounting for mass transfer and the kinetics in a two-phase system. However, the main disadvantage of PTC in the industrial application of soluble phase-transfer catalyst (PTC) applications, such as quaternary ammonium salts, is the need to separate the catalysts from the reaction mixture and its subsequent reuse or disposal. Hence, from industrial point of view, polymer-anchored catalyst is more desirable in order to simplify catalyst separation from the reaction mixture and its reuse thereby the need for complex chromatographic techniques can be avoided for product separation and isolation [33–38]. To circumvent the problem of separation of catalyst from the reaction mixture, for the first time Regen [39] reported anchoring the phase transfer catalysts to a polymer backbone and suggested the name "Triphase Catalysis". Quaternary onium salts,

crown ethers and cryptands have all been immobilized on various kinds of supports, including polymers (most commonly (methylstyrene-costyrene) resin crosslinked with divinylbenzene), alumina, silica gel, clays, and zeolites [40–51]. Kinetics of triphase phase-transfer-catalyzed reactions [52] are influenced by (i) mass transfer of reactant from bulk liquid to catalyst surface; (ii) diffusion of reactant through polymer matrix to active site; (iii) intrinsic reaction rate at active site; (iv) diffusion of product through polymer matrix and mass transfer of product to external solution; (v) rate of ion exchange at active site. In heterogeneous conditions, for a proper mass transfer to occur, both the liquid phases should be in contact with catalyst. Thus, mass transfer of reactant from bulk solution to catalyst surface and mass transfer of the product to the bulk solution are the significant steps involved. The reaction mechanism of these PTC's system is often complicated and several factors affect the conversion of reactants. With all these antecedents, in this chapter, a kinetic and mathematical model of phase-transfer catalysis concerning mass transfer with various organic reactions will be presented. An extensive detail has been made on the effects of mass transfer in the PTC reaction systems. Further, it is proposed to present the diffusion resistance of an active phase-transfer catalyst in the organic phase and mass-transfer resistance between the droplet and the bulk aqueous phase.

2. Influence of mass transfer in various PTC assisted organic reactions

2.1 O-Alkylation

Previously, we reported a simplified model [53] to predict the dynamic behavior of the allylation for 2, 4, 6-tribromophenol catalyzed by tetra-*n*-butylammonium bromide. The intermediate product viz., of tetra-*n*-butylammonium 2,4,6-tribromophenoxide ((C_6H_2)-Br_3OBu_4N) was successfully identified [54]. Kinetic run was started by dissolving a known quantity of potassium hydroxide and 2,4,6-tribromophenol in water. The solution was then introduced into the reactor, which was thermostated at the desired temperature. A measured quantity of allyl bromide and diphenyl ether (internal standard), were dissolved in the chlorobenzene solvent and then added to the reactor. To start the reaction, tetra-*n*-butylammonium bromide (TBAB) was then added to the reactor. Aliquot samples (0.8 mL) were collected from the reactor at regular intervals of time. After the separation of organic phase from aqueous phase, 0.1 mL of the organic-phase sample was immediately diluted with 4.5 mL of methanol and the sample was analyzed by HPLC analysis. A general schematic diagram of phase-transfer catalysis for the allylation of 2, 4, 6-tribromophenol is presented in Scheme 1.

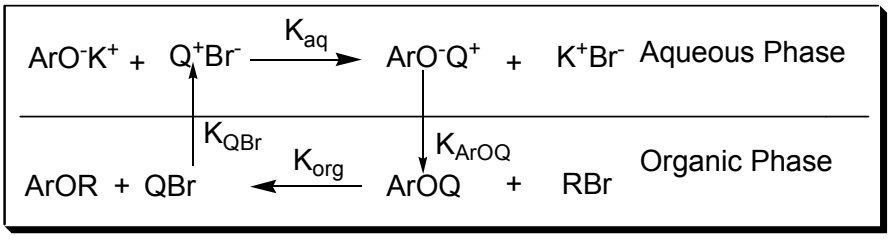

Scheme 1. O-Alkylation of 2,4,6-tribromophenol under PTC Conditions

where the parameters, K_{aq}, K_{org}, K_{ArOQ} and K_{QBr} are given in the Nomenclature section.

In order to formulate a mathematical model to describe the dynamic behavior of the two-phase reaction shown above, a two-film theory is employed to consider the mass transfer of the catalysts between two phases. Hence, those equations which model the two-phase reaction are presented below. The rate of change for ArOQ in the organic phase is the difference of mass-transfer rate and organic-phase reaction rate.

$$\frac{dC_{ArOQ}^{org}}{dt} = K_{ArOQ}A\left(C_{ArOQ}^{aq} - \frac{C_{ArOQ}^{org}}{m_{ArOQ}}\right) - K_{org}C_{RBr}^{org}C_{ArOQ}^{org} \tag{1}$$

The rate of change for ArOQ in the aqueous phase is the difference of aqueous-phase reaction rate and mass transfer rate.

$$\frac{dC_{ArOQ}^{aq}}{dt} = K_{org}C_{ArOK}^{aq}C_{QBr}^{aq} - K_{ArOQ}Af\left(C_{ArOQ}^{aq} - \frac{C_{ArOQ}^{org}}{m_{ArOQ}}\right) \tag{2}$$

Similarly, the rate of change for QBr either in the organic phase or in the aqueous phase is obtained as shown in (3) and (4).

$$\frac{dC_{QBr}^{org}}{dt} = K_{org}C_{ArOQ}^{org}C_{RBr}^{org} - K_{QBr}A\left(C_{QBr}^{org} - m_{QBr}C_{QBr}^{aq}\right) \tag{3}$$

$$\frac{dC_{QBr}^{aq}}{dt} = K_{QBr}Af\left(C_{QBr}^{org} - m_{QBr}C_{QBr}^{aq}\right) - K_{aq}C_{ArOK}^{aq}C_{QBr}^{aq} \tag{4}$$

The reaction rate of ArOK in the aqueous phase is

$$\frac{dC_{ArOK}^{aq}}{dt} = -K_{aq}C_{ArOK}^{aq}C_{QBr}^{aq} \tag{5}$$

The reaction rate of RBr in the organic phase is

$$\frac{dC_{RBr}^{org}}{dt} = -K_{org}C_{ArOQ}^{org}C_{RBr}^{org} \tag{6}$$

In the above equations, "f" is defined as the ratio of the volume of organic phase (V_0) to the volume of aqueous phase (V_a), *i.e.*

$$f = \frac{V_o}{V_a} \tag{7}$$

The distribution coefficients of catalysts m_{ArOQ} and m_{QBr} are defined as

$$m_{ArOQ} = \frac{C_{ArOQ}^{org(s)}}{C_{ArOQ}^{aq(s)}} \tag{8}$$

$$m_{QBr} = \frac{C_{QBr}^{org(s)}}{C_{QBr}^{aq(s)}} \tag{9}$$

where the superscript "s" denotes the characteristics of the species at the interphase.
The conversion of allyl bromide (RBr) is defined as X,

$$X = 1 - \frac{C_{RBr}^{org}}{C_{RBr,0}^{org}} \tag{10}$$

where the subscript "0" denotes the initial concentration of allyl bromide. The total number of moles of catalyst (Q_o) and the total number of moles of 2,4,6-tribromophenol (E_o) initially are

$$Q_0 = V_o\left(C_{ArOQ}^{org} + C_{QBr}^{org}\right) + V_a\left(C_{ArOQ}^{aq} + C_{QBr}^{aq}\right) \tag{11}$$

$$E_0 = V_o\left(C_{ArOQ}^{org} + \left[C_{RBr,0}^{org} - C_{RBr}^{org}\right]\right) + V_a\left(C_{ArOK}^{aq} + C_{ArOQ}^{aq}\right) \tag{12}$$

The initial conditions of the above equations are

$$\begin{aligned} &C_{QBr}^{org} = 0,\ C_{QBr}^{aq} = C_{QBr,0}^{aq},\ C_{RBr}^{org} = C_{RBr,0}^{org};\ t = 0 \\ &C_{ArOQ}^{org} = 0,\ C_{ArOQ}^{aq} = 0,\ C_{ArOK}^{aq} = C_{ArOK,0}^{aq};\ t = 0 \end{aligned} \tag{13}$$

The parameters m_{QBr}, m_{ArOQ}, $K_{QBr}A$, $K_{ArOQ}A$, K_{aq} and K_{org} for the allylation of 2,4,6-tribromophenol in a two phase catalyzed reaction [54] are as follows:

$$m_{QBr} = 7.1 \times 10^{-2} - 0.56 C_{QBr}^{aq} \tag{14}$$

$$m_{ArOQ} = (8.02 + 0.05T) + (78.33T - 1165) C_{ArOQ}^{aq} \tag{15}$$

$$K_{QBr}A = 2.69 \qquad \text{min}^{-1} \tag{16}$$

$$K_{ArOQ}A = 3.84 + 0.06T \qquad \text{min}^{-1} \tag{17}$$

$$K_{aq} = 3.2 \times 10^{7} \exp\left[\frac{-4840}{T + 273.16}\right] \qquad M^{-1}\,\text{min}^{-1} \tag{18}$$

$$K_{org} = 3.3 \times 10^{9} \exp\left[\frac{-7016}{T + 273.16}\right] \qquad M^{-1}\,\text{min}^{-1} \tag{19}$$

After a small induction period, the concentration of ArOQ is kept at a constant value and hence, the pseudo-steady-state hypothesis (PSSH) can be made in the system under investigation, i.e.,

$$\frac{dC_{ArOQ}^{org}}{dt} = \frac{dC_{ArOQ}^{aq}}{dt} = 0 \tag{20}$$

Thus, (1) and (2) become

$$C_{ArOQ}^{aq} = \left(\frac{1}{m_{ArOQ}} + \frac{K_{org} C_{RBr}^{org}}{K_{ArOQ}A}\right) C_{ArOQ}^{org} \tag{21}$$

$$K_{aq}C_{ArOK}^{aq}C_{QBr}^{aq} = K_{ArOQ}Af\left(C_{ArOQ}^{aq} - \frac{C_{ArOQ}^{org}}{m_{ArOQ}}\right) \tag{22}$$

Eliminating C^{aq}_{ArOK} from (21) and (22), we obtain

$$C_{QBr}^{aq} = \frac{fK_{org}C_{RBr}^{org}}{K_{aq}C_{ArOK}^{aq}}C_{ArOQ}^{org} \tag{23}$$

In a similar way, the following equation is held for QBr:

$$\frac{dC_{QBr}^{org}}{dt} = \frac{dC_{QBr}^{aq}}{dt} = 0 \tag{24}$$

From (3), (4), and (23), we have

$$C_{QBr}^{org} = \frac{K_{org}C_{ArOQ}^{org}C_{RBr}^{org}}{K_{QBr}A} + m_{QBr}C_{QBr}^{aq} \tag{25}$$

Substituting (23) into (25)

$$C_{QBr}^{org} = K_{org}C_{ArOQ}^{org}C_{RBr}^{org}\left[\frac{1}{K_{QBr}A} + \frac{m_{QBr}f}{K_{aq}C_{ArOK}^{aq}}\right] \tag{26}$$

Combining (11),(21), (23), and (26), we have

$$C_{ArOQ}^{org} = \frac{Q_o}{V_o}\left\{1 + \frac{1}{fm_{ArOQ}} + \frac{K_{org}C_{RBr}^{org}}{fK_{ArOQ}A} + \left(1 + fm_{QBr} + \frac{k_{aq}C_{ArOK}}{K_{QBr}A}\right)\frac{K_{org}C_{RBr}^{org}}{K_{aq}C_{ArOK}^{aq}}\right\}^{-1} \tag{27}$$

Applying the Damkohler numbers of ArOQ and QBr, respectively, as

$$Da_{A_{rOQ}} = \frac{K_{org}C_{RBr}^{org}}{K_{ArOQ}A} = \frac{K_{org}(1-X)C_{RBr,0}^{org}}{K_{ArOQ}A} \tag{28}$$

$$Da_{QBr} = \frac{K_{aq}C_{ArOK}^{aq}}{K_{QBr}A} \tag{29}$$

The concentration of ArOK in the aqueous phase can be obtained from the material balance of 2,4,6-tribromophenol, which is shown in (12). As shown in (28) and (29), the Damkohler number indicates the ratio of the chemical reaction rate to the mass-transfer rate of the catalyst. An effective fraction of catalyst, η, which is defined as the ratio of the observed two-phase reaction rate to the organic-phase reaction rate with catalyst completely used, is given as

$$\eta = \frac{K_{app}C_{RBr}^{org}}{K_{org}\left(\frac{Q_0}{V_o}\right)C_{RBr}^{org}} = \frac{V_oC_{ArOQ}^{org}}{Q_0} \tag{30}$$

where

$$K_{app} = K_{org} C_{ArOQ}^{org} \tag{31}$$

Thus, η can be expressed as

$$\eta = \frac{1}{1 + \frac{\alpha}{f} + (1+\beta)R} \tag{32}$$

where

$$\alpha = \frac{1}{m_{ArOQ}} + Da_{ArOQ} \tag{33}$$

$$\beta = fm_{QBr} + Da_{QBr} \tag{34}$$

$$R = \frac{K_{org} C_{RBr}^{org}}{K_{aq} C_{ArOK}^{aq}} \tag{35}$$

The parameters "α" and "β" reflect the effects of the equilibrium distribution of catalysts between two phases and the mass transfer of catalysts across the interphase. "R" is a ratio of the reaction velocity in the organic phase to that of velocity in the aqueous phase. Thus, the concentrations of ArOQ and QBr either in the organic phase or in the aqueous phase can be represented by the following equations:

$$C_{ArOQ}^{org} = \frac{\frac{Q_0}{V_o}}{1 + \frac{\alpha}{f} + (1+\beta)R} \tag{36}$$

$$C_{ArOQ}^{aq} = \left(\frac{Q_0}{V_o}\right)\eta\alpha \tag{37}$$

$$C_{QBr}^{org} = \left(\frac{Q_0}{V_o}\right)\eta\beta R \tag{38}$$

$$C_{QBr}^{aq} = \left(\frac{Q_0}{V_o}\right)\eta f R \tag{39}$$

By solving the nonlinear algebraic equations of (11), (12), (32), (36), (37), (38), and (39) with the specified parameters or the operating conditions, the simulation results for f = 1 are given in Figures 1-3.

As given in (28) and (29), the Damkohler number (D_a) is defined as the ratio of the reaction rate to the mass transfer rate. From the plot of D_a *vs.* the conversion of allyl bromide, it is obvious that the Damkohler number of ArOQ, which also depends on the initial concentration of allyl bromide, is much less than unity for the whole range of conversion

(Figure 1). Thus, the reaction rate of the organic-phase reaction is much lower than the mass-transfer rate of ArOQ. Hence, the mass-transfer resistance of ArOQ from the aqueous phase to the organic phase is negligible when compared with the reaction rate in the organic phase. In addition, the Damkohler number of ArOQ increases with the increase of temperature for a certain value of conversion. This is attributed to the increase in the organic phase reaction rate at a higher temperature while the resistance of mass transfer of ArOQ is very small.

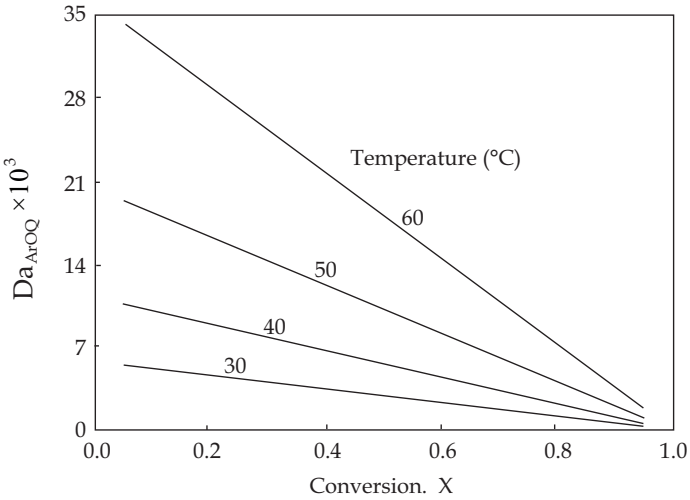

Fig. 1. Dependence of the ratio of the reaction to the mass transfer rate for ArOQ (Da_{ArOQ}) on conversion (X) at different temperatures: 0.7 g of allyl bromide, 3.0 g of 2,4,6-tribromophenol, 0.2 g of TBAB catalyst, 1.0 g of KOH, 50 mL of H_2O, 50 mL of chlorobenzene. (Adapted from Ref. [53], by permission)

The order of magnitude of the Damkohler number of QBr (Da_{Br}) for the whole range of conversion is about unity (Figure 2). These results reflect the fact that the mass-transfer rate of QBr from the organic phase to the aqueous phase is slightly larger than the reaction rate in the aqueous phase. A plot of R value, which denotes the relative reactivity of the organic phase to the aqueous phase *vs.* conversion, is given in Figure 3. The R value is less than unity. In combining the results from Figures 1-3, the step of the organic-phase reaction is confirmed as the rate-determining step of the whole reaction quantitatively rather than qualitatively by other investigators in the published documents.

From the plot of η *vs.* X, it was found that about 75-90% of the catalyst exists in the form of ArOQ remaining in the organic phase. Further, we found that the concentration of ArOQ in the organic phase increases when the initial amount of catalyst added to the reactor increases. Some of the salient features of the study are:

i. The reaction system was simulated by the proposed model in conjunction with the system parameters, such as mass-transfer coefficients of catalysts, distribution coefficients of catalysts and the intrinsic reaction rate constants either in the organic phase or in the aqueous phase.
ii. The Damkohler numbers, which directly reflect the relative rate of chemical reaction to the mass transfer of the catalysts, are defined.

iii. The mass-transfer resistance of catalysts from the aqueous phase to the organic phase is negligible.

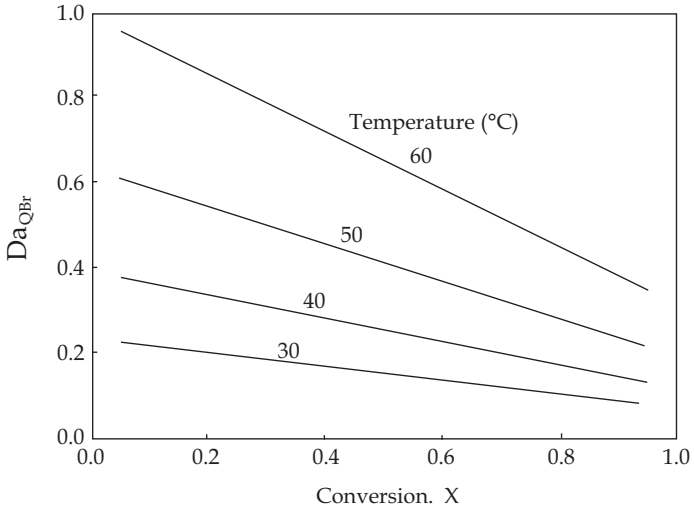

Fig. 2. Dependence of the ratio of the reaction to the mass transfer rate for QBr (Da_{QBr}) on conversion (X) at different temperatures: 0.7 g of allyl bromide, 3.0 g of 2,4,6-tribromophenol, 0.2 g of TBAB catalyst, 1.0 g of KOH, 50 mL of H_20, 50 mL of chlorobenzene. (Adapted from Ref. [53], by permission)

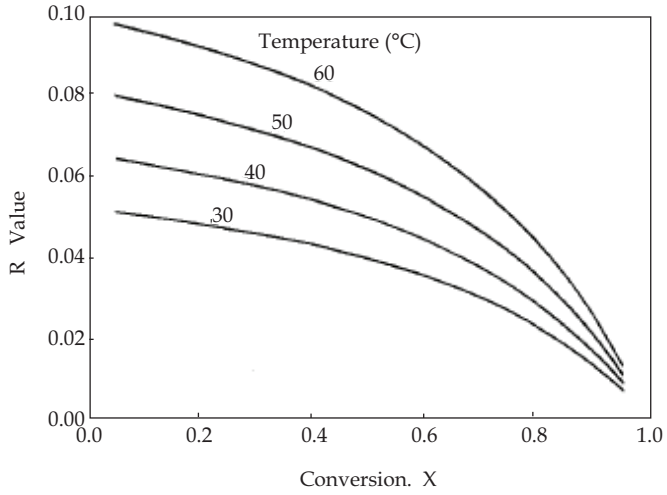

Fig. 3. Dependence of the ratio of the organic-phase reaction to the aqueous-phase reaction rate (R value) on conversion (X) at different temperatures: 0.7 g of allyl bromide, 3.0 g of 2,4,6-tribromophenol, 0.2 g of TBAB catalyst, 1.0 g of KOH, 50 mL of H_20,50 mL of chlorobenzene. (Adapted from Ref. [53], by permission)

Later, we investigated the reaction of 2,4,6-tribromophenol with allyl bromide catalyzed by triphase catalyst (polymer supported tributylamine chloride) in an organic/alkaline solution [55]. The apparent reaction rates were observed to obey the pseudo-first-order kinetics with respect to the organic reactant when excess 2,4,6-tribromophenol was used. Also, a kinetic model in terms of the intrinsic reactivity and intra-particle diffusion limitations for a spherical catalyst is proposed to describe the triphase catalytic reaction system. The pseudo-steady-state approach to the mass balance equation was employed to get the solution. The effective diffusivity of the reactants within the catalyst was obtained from this model and used to predict the observed reaction rate. The apparent reaction rate constants were measured at various agitation speeds using 40-80 mesh of catalyst. Kinetic results indicate that the mass-transfer resistance outside the catalyst can be neglected for agitation speeds higher than 600 rpm (Figure 4)

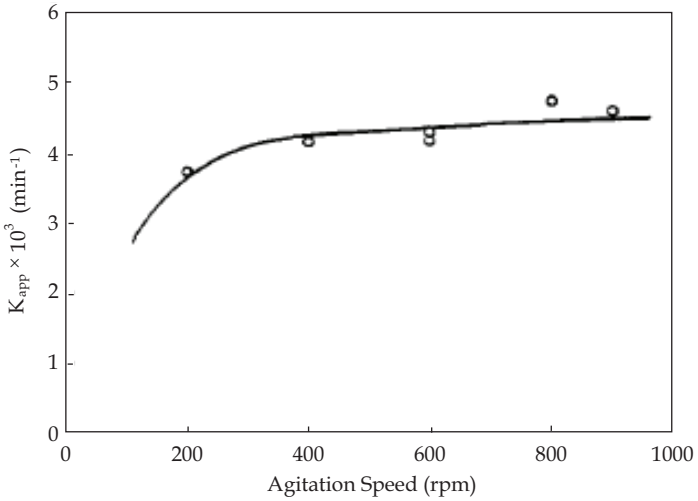

Fig. 4. Effects of the agitation speed on the apparent reaction rate constant: 9.06 x 10^{-3} mol of 2,4,6-tribromophenol; 50 mL of water; 1.567 mole ratio of allyl bromide to 2,4,6-tribromophenol; 1.97, mole ratio of KOH to 2,4,6-tribromophenol; 0.488 g of catalyst pellet (40-80 mesh); 50 mL of chlorobenzene; 50 °C. (Adapted from Ref. [55], by permission)

2.2 Substitution reaction between hexachlorocyclotriphosphazene and sodium 2,2,2-trifluoro-ethoxide

Effects of mass transfer and extraction of quaternary ammonium salts on the conversion of hexachlorocyclotriphosphazene were investigated in detail [56]. Initially, a known quantity of sodium hydroxide, trifluoroethanol, and tetra-*n*-butylammonium bromide were introduced into the reactor which was thermostated at the desired temperature. Measured quantities of phosphazene reactant, $(NPCl_2)_3$ and *n*-pentadecane (internal standard) were dissolved in chlorobenzene solvent at the desired temperature. Then, the organic mixture was added into the reactor to start a kinetic run. An aliquot sample was withdrawn from the reaction solution at the chosen time. The sample (0.5 mL) was immediately added to 3 mL of

hydrochloric acid to quench the reaction and then the organic-phase contents are analyzed quantitatively by GC using the method of internal standard.
In organic reactions which are driven by S_N2 mechanism under phase transfer catalysis conditions, the substrate and the nucleophile react directly *via* a transittion state to product. The system can be explained by first order reaction by plotting ln $[(NPCl_2)_3]$ *vs.* time, which results in a straight line. Thus, the system can be expressed as:

$$-\frac{d[(NPCl_2)_3]_o}{dt} = k_{o,app}[(NPCl_2)_3]_o \tag{40}$$

where,

$$k_{o,app} = k[QOCH_2CF_3]_o \tag{41}$$

The fixed value of $k_{0,,app}$ is called the pseudo-steady-state first-order reaction rate constant. The series reaction of the organic phase was explained by the S_N2 mechanism [57, 58]. The reaction expressions can be written as:

$$(NPCl_2)_3 + QOCH_2CF_3 \xrightarrow{k_o} N_3P_3Cl_5(OCH_2CF_3) + QCl \tag{42}$$

$$N_3P_3Cl_5(OCH_2CF_3) + QOCH_2CF_3 \xrightarrow{k_1} N_3P_3Cl_4(OCH_2CF_3)_2 + QCl \tag{43}$$

$$N_3P_3Cl_4(OCH_2CF_3)_2 + QOCH_2CF_3 \xrightarrow{k_2} N_3P_3Cl_3(OCH_2CF_3)_3 + QCl \tag{44}$$

$$N_3P_3Cl_3(OCH_2CF_3)_3 + QOCH_2CF_3 \xrightarrow{k_3} N_3P_3Cl_2(OCH_2CF_3)_4 + QCl \tag{45}$$

$$N_3P_3Cl_2(OCH_2CF_3)_4 + QOCH_2CF_3 \xrightarrow{k_4} N_3P_3Cl\ (OCH_2CF_3)_5 + QCl \tag{46}$$

$$N_3P_3Cl\ (OCH_2CF_3)_5 + QOCH_2CF_3 \xrightarrow{k_5} (NP\ (OCH_2CF_3)_2)_3 + QCl \tag{47}$$

Thus, the reaction rate can be expressed as,

$$\frac{dy_1}{dy_0} = -1 + k_1 * \frac{y_1}{y_0} \tag{48}$$

$$\frac{dy_2}{dy_0} = k_1 * \frac{y_1}{y_0} - k_2 * \frac{y_2}{y_0} \tag{49}$$

$$\frac{dy_3}{dy_0} = k_2 * \frac{y_2}{y_0} - k_3 * \frac{y_3}{y_0} \tag{50}$$

$$\frac{dy_4}{dy_0} = k_3 * \frac{y_3}{y_0} - k_4 * \frac{y_4}{y_0} \tag{51}$$

$$\frac{dy_5}{dy_0} = k_4 * \frac{y_4}{y_0} - k_5 * \frac{y_5}{y_0} \tag{52}$$

$$\frac{dy_6}{dy_0} = k_5 * \frac{y_5}{y_0} \tag{53}$$

where the dimensionless variables and parameters are defined as

$$y_0 = \frac{[(NPCl_2)_3]_o}{[(NPCl_2)_3]_o^0}$$

$$y_1 = \frac{[N_3P_3Cl_5(OCH_2CF_3)]_o}{[(NPCl_2)_3]_o^0}$$

$$y_2 = \frac{[N_3P_3Cl_4(OCH_2CF_3)_2]_o}{[(NPCl_2)_3]_o^0}$$

$$y_3 = \frac{[NPCl_3(OCH_2CF_3)_3]_o}{[(NPCl_2)_3]_o^0}$$

$$y_4 = \frac{[N_3P_3Cl_2(OCH_2CF_3)_4]_o}{[(NPCl_2)_3]_o^0}$$

$$y_5 = \frac{[N_3P_3Cl\ (OCH_2CF_3)_5]_o}{[(NPCl_2)_3]_o^0}$$

$$y_6 = \frac{[(NP(OCH_2CF_3)_2)_3]_o}{[(NPCl_2)_3]_o^0}$$

and

$$k_1^* = \frac{k_1}{k_0}, \qquad k_2^* = \frac{k_2}{k_0}, \qquad k_3^* = \frac{k_3}{k_0}, \qquad k_4^* = \frac{k_4}{k_0}, \qquad k_5^* = \frac{k_5}{k_0}$$

where $[(NPC1_2)_3]_O^0$ represents the initial concentration of reactant $(NPC1_2)_3$ in the organic phase and $k_o^* = 1$.

In general, eq. 48-53 can be solved with the following initial conditions of y_i.

$$y_0 = 1, \qquad y_1 = y_2 = y_3 = y_4 = y_5 = y_6 = 0 \tag{54}$$

The solutions are

$$y_{n+1} = \sum_{l=o}^{n+1} \frac{(\prod_{i=0}^{n} k_i^*) y_0^{k_l^*}}{\prod_{\substack{i=0 \\ i \neq l}}^{n+1} (k_i^* - k_l^*)}; \qquad n = 0,1,2,3,4 \tag{55}$$

$$y_6 = \sum_{l=0}^{5} \frac{k_5^* (\prod_{i=0}^{4} k_i^*)(y_o^{k_l^*} - 1)}{k_l^* \prod_{\substack{i=0 \\ i \neq l}}^{5} (k_i^* - k_l^*)} \quad (56)$$

From eqs 55 and 56, the concentrations of the distributed products, $N_3P_3C1_{6-y}(OCH_2CF_3)_y$, y = 1-6, including the intermediate and final products, are thus determined.

In order to follow the kinetics of phase-transfer catalyzed reactions, it is necessary to sort out the rate effects due to equilibria and anion-transfer mechanism for transfer of anions from the aqueous to the organic phase *i.e.*, the concentration of $QOCH_2CF_3$ would remain constant if Q^+ concentration in the organic phase remained constant throughout the entire course of a kinetic run and the equilibrium constant *K* is very small.

$$QOCH_2CF_{3\ org} + Cl^-_{\ aq} \underset{}{\overset{k}{\rightleftharpoons}} QCl_{\ org} + {}^-OCH_2CF_{3\ aq} \quad (57)$$

Many experimental runs were carried out to examine the Q^+ values and K values. More than 99.5% of Q^+ stay in the organic phase and K value was calculated to be less than $1x10^{-2}$. Therefore, the concentration of $QOCH_2CF_3$ in the organic phase remains constant. Based on this experimental evidence, those factors affecting the reaction are discussed in the following sections.

In PTC systems, it is recognized that the rate-determining step is controlled by the chemical reaction in the organic phase. In systems involving fast mass-transfer rate of catalyst between two phases, the influence of mass transfer on the reaction can be neglected. However, on varying the concentration of $(NPCl_2)_3$, the apparent reaction rate constant values also changes (Table 1). Further, the value of $k_{0.5/\ 2}$, defined as the ratio of the $k_{o,app}$ value using 0.5 g of $(NPCl_2)_3$ to the $k_{o,app}$ value using 2 g of $(NPCl_2)_3$, is increased for increasing reaction temperature. This phenomenon indicates that the present reaction system is both controlled by chemical kinetics and mass transfer.

Organic reactions, which are controlled by purely chemical reaction kinetics, will be independent of the mass of the reactant on the conversion. The effect of the mass of $(NPCl_2)_3$ in presence of different phase transfer catalysts, on the conversion is shown in Table 2. Only in the presence of TEAC the reaction is controlled purely by chemical reaction kinetics. On the other hand other reactions, with different kinds of catalysts, are both controlled by chemical reaction kinetics and mass transfer. A higher influence of mass transfer on the reaction rate is confirmed by higher value of $k_{0.5/2}$.

	$k_{0,app}$, min^{-1} mass of reactant, $(NPCl_2)_3$, g						
Temp. °C	**0.5**	**1.0**	**1.5**	**2.0**	$k_{1.5/2}$	$k_{1/2}$	$k_{0.5/2}$
20	0.36	0.27	0.21	0.17	1.24	1.59	2.11
30	0.58	0.40	0.31	0.24	1.29	1.67	2.42
40	0.87	0.75	0.52	0.31	1.67	2.42	2.81

[a]Reaction conditions: 7 g of $HOCH_2CF_3$, 0.0059 mol of $(NPCl_2)_3$, 3 g of NaOH, 20 mL of water, 9.6×10^{-5} mol of TBAB, 50 mL of chlorobenzene.

Table 1. Effects of Mass Transfer on the Reaction System[a]. (Adapted from Ref. [56] by permission)

	$k_{0,app}$, min^{-1} $(NPCl_2)_3$, g				Relative Reactivity	Q^+ in chlorobenzene with adding	Q^+ in chlorobenzene with out adding	Apparent extraction constants with out addding
PTC	0.5	1.0	1.5	2.0	$k_{0.5/2}$	*ROH*,[b] %	*ROH*,[c] %	ROH, E_{app}[d]
TEAC	0.022	0.022	0.033	0.022	1.00	Trace	0	0
BTMAC	0.039	0.038	0.034	0.033	1.18	4.67	0	0
CTMAB	0.26	0.19	0.17	0.14	1.86	100	4.1	3.7
Aliq.336	0.32	0.25	0.19	0.14	2.3	100	100	∞
BTEAC	0.28	0.23	0.19	0.16	1.75	19.20	0	0
TBAB	0.36	0.27	0.21	0.17	2.10	100	18	18
BTBAB	0.39	0.29	0.22	0.18	2.16	100	31	51

([a]0.0059 mol of $(NPCl_2)_3$, 7 g of $HOCH_2CF_3$, 3 g of NaOH, 9.6 x 10^{-5} mol of PTC, 50 mL of chlorobenzene, 20 mL of water, 20 °C; [b]7 g of $HOCH_2CF_3$,3 g of NaOH, 9.6 x 10^{-5} mol of PTC, 50 mL of chlorobenene, 20 mL of water, 20 °C; [c]3 g of NaOH, 9.6 x 10^{-5} mol of PTC, 50 mL of chlorobenene, 20 mL of water, 20 °C. [d]E_{app}= $[QY]_o/[Q^+]/[Y^-]_a$)

Table 2. Effects of Catalysts on the Relative Reactivities[a]. (Adapted from Ref. [56], by permission)

	$k_{0,app}$, min^{-1} $(NPCl_2)_3$, g				Rel. Reactivity	No PTC reaction	H 0 C H 2 C F 3 extracted in solvent	Dielectric constant (temp, °C)	App. extraction const.
PTC	0.5	1.0	1.5	2.0	$k_{0.5/2}$	$(NPCl_2)_3$ %	+/-	ε	E_{TBAB}
1,2-Dichloroethane	0.82	0.59	0.45	0.30	2.73	5	+	10.36(25)	6.1
Chlorobenzene	0.36	0.27	0.21	0.17	2.10	8	-	5.6(25)	<0.1
Dichloromethane	0.36	0.26	0.19	0.14	2.57	5	+	9.08(20)	35
Benzene	0.11	0.09	0.08	0.071	1.55	2	+	2.28(20)	<0.001
Toluene	0.14	0.11	0.095	0.07	2.00	4	+	2.37(25)	<0.001
Hexane	0.046	0.046	0.041	0.04	1.10	0	+	1.89(20)	<0.001
Chloroform	0.059	0.059	0.047	0.043	1.53	2	+	4.8(20)	47

[a] E_{TBAB}= $[QBr]_o/[Q+]_a[Br^-]_a$. Reaction conditions: $HOCH_2CF_3$ = 7 g, T BAB = 9.6 x 10^{-5} mol, solvent = 50 mL, H_2O = 20 mL, NaOH = 3 g, temp = 20 °C

Table 3. Effects of Solvents on the Relative Reactivities[a]. (Adapted from Ref. [56], by permission)

We measured the percentage of quaternary ions in the organic phase of the chlorobenzene/NaOH aqueous system with or without adding $HOCH_2CF_3$ (Table 3). From the reaction mechanism it is clear that either the catalyst QOR or QX may stay within the organic phase or the aqueous phase. We attribute the competition of QOR with QX to stay within the organic phase is due to the addition of $HOCH_2CF_3$. It is obvious that the addition of the organophilic substance will make the quaternary cation move into the organic phase.

As a consequence, the preferential extraction of $-OCH_2CF_3$ into the organic phase by the quaternary cation catalyst is responsible for the efficiency of the reaction. The apparent extraction constant, E_{app},, is thus an index for reflecting the mass transfer effect. Thus, a larger value of E_{app} implies that the two-phase reaction is dominated by the effects of mass transfer.

Influence of solvents on the rate of the reaction was examined by employing seven different solvents under PTC conditions (Table 3). The order of relative activities of the solvents is dichloroethane > chlorobenzene > dichloromethane > benzene > toluene > chloroform > hexane. Higher values of $k_{0.5/2}$ imply a significant influence of the mass transfer on the reaction rate.

From the Arrhenius plot of $k_{0,app}$ of *vs.* 1/T for different initial concentration ratios of NaOH and $HOCH_2CF_3$, the activation energy, E_a, was obtained and presented in Table 4. Thus, the effects of mass transfer and chemical reaction kinetics on the conversion depend highly on the reactant concentrations of NaOH and $HOCH_2CF_3$.

$HOCH_2CF_3$ (g)	NaOH (g)	E_a (kcal/mol)
14	2.5	11.4
7	7	19.0
7	3	7.1

Table 4. Energy of activation at various amounts of NaOH and $HOCH_2CF_3$. (Adapted from Ref. [56], by permission).

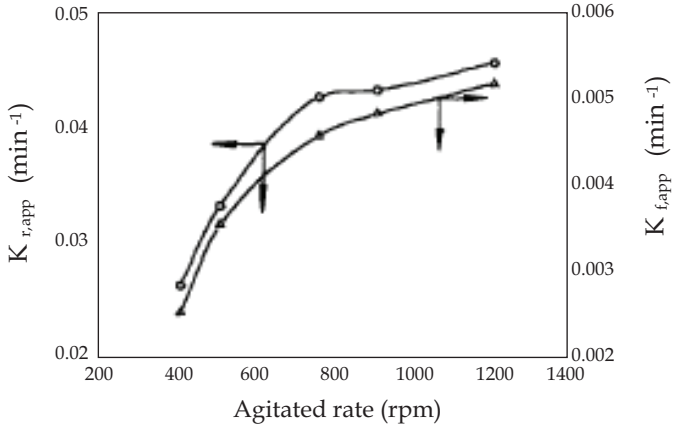

Fig. 5. Dependence of the apparent reaction rate constants $k_{r,app}$ and $k_{f,app}$ on the agitated rate; 7 g of $HOCH_2CF_3$,0.0059 mol of $(NPCl_2)_3$, 3 g of NaOH, 20 mL of H_20, 0.175 mequiv of catalyst, 50 mL of chlorobenzene, 20 °C. (Adapted from Ref. [59], by permission)

Further, the kinetics and the mass transfer behaviors of synthesizing polytrifluoroethoxycyclotriphosphazene from the reaction of 2,2,2-trifluoroethanol with hexachlorocyclotriphosphazene by triphase catalysis in an organic solvent / alkaline solution were studied [59]. In general, the reaction mechanism of the triphase catalysis is: (1) mass transfer of reactants from the bulk solution to the surface of the catalyst pellet,

(2) surface or intrinsic reaction of reactants with active sites, and (3) diffusion of reactants to the interior of the catalyst pellet (active sites) through pores. It was found that the diffusional limitation involves both ion diffusion and organic reactant diffusion within the catalyst pellet. The mass transfer limitation influences the triphase reaction rate. The displacement reaction rate of $(NPCl_2)_3$ in the organic phase was limited by the particle diffusion and the intrinsic reactivity together. The film diffusion of the aqueous phase in the ion-exchange step is the main rate limiting factor. The mass transport of the ion-exchange step in the aqueous phase was not improved by increasing the concentration of $NaOCH_2CF_3$. The effect of the agitation speed on the conversion of hexachlorocyclotriphosphazene is shown in Figure 5. The reaction follows a pseudofirst-first-order rate law. Rate constants increased with the agitation rate up to 750 rpm and increased only slightly up to 1200 rpm.

2.3 C-Alkylation

The essential condition for a reaction to occur is the effective collision of reactant molecules, even in the phase transfer catalysis system. Recently, Vivekanand and Blakrishnan [29] investigated the effect of varying stirring speed on the rate of the reaction of C-alkylation of dimedone by dibromoethane in the range 200–800 rpm under PTC conditions (Scheme 2). The experimental results show that the rate constants increase with the increase of stirring speed from 200 to 600 rpm. Further increase in the speed of agitation had practically no effect on the rate of reaction (Fig. 6). This is because the interfacial area per unit volume of dispersion increased linearly with increasing the stirring speed till 600 rpm is reached and there after there is no significant increase in the interfacial area per unit volume of dispersion with the corresponding increases in the speed. Consequently, increasing the stirring speed changes the particle size in the dispersed phase. At stirring speeds of 700 and 800 rpm, nearly constant rate constant values were observed. This is not because the process is necessarily reaction rate-limited, but because the mass transfer has reached a constant value. Thus, Fig. 6 is indicative of an interfacial mechanism rather than Starks' extraction mechanism. Chiellini et al. [60] observed a continuous increase in the rate of ethylation of PAN, even up to stirring speeds of 1950 rpm, for which an interfacial mechanism was proposed. Similar observations were made under various phase transfer catalytic reactions and an interfacial mechanism was proposed [41,61–64].

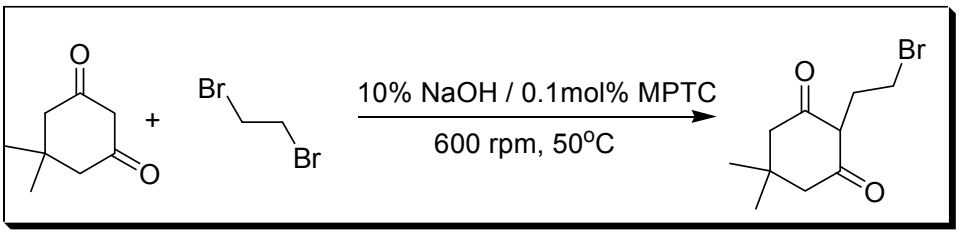

Scheme 2. C-Alkylation of dmedone under PTC conditions

2.4 N-Alkylation

The synthesis of 1-(3-phenylpropyl)-pyrrolidine-2,5-dione was successfully carried out [23] from the reaction of succinimide with 1-bromo-3-phenylpropane in a small amount of KOH and organic solvent solid–liquid phase medium under phase-transfer catalysis (PTC)

almost water-free conditions (Scheme 3). For a solid-liquid phase reaction system, agitation increases the kinetic energy of the system and tends to speed up the reaction until a limiting factor is reached. After this the reaction rate is not affected by increasing stirring rates. Therefore, the effect of the agitation speed on the conversion and the reaction rate was studied in the range of 0-1200 rpm. As shown in Figure 7, the experimental data of the reaction kinetics follows the pseudo-first-order rate law and passes the origin point of a straight line for each experimental run. The apparent rate constants (k_{app}) were obtained from the slope of the straight lines. There was a significant increase in the apparent rate constant values from 0 to 200 rpm, but it remained at an almost constant value from 200 to 1200 rpm. This phenomenon indicated less influence of the external mass transfer resistance on the reaction beyond 200 rpm. Thus, the organic-phase reaction is obviously a rate determining step at 200-1200 rpm. All subsequent reactions were set at 1200 rpm to assess the effect of various factors on the rate of reaction.

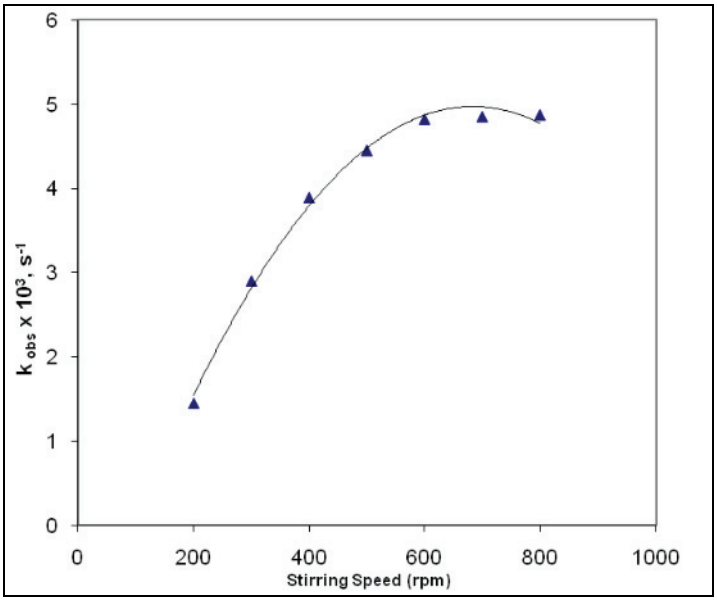

Fig. 6. Dependence of k_{obs} on stirring speed in the C-alkylation of dimedone. (Adapted from Ref. [29], by permission)

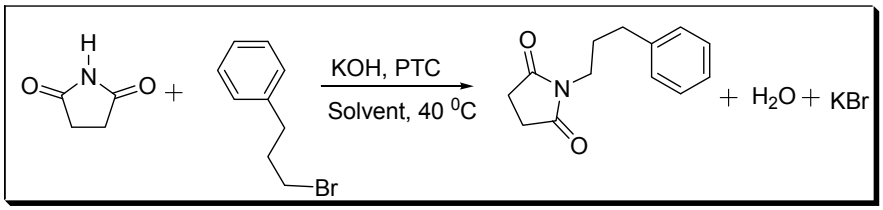

Scheme 3. *N*-alkylation of Succinimide with 1-bromo-3-phenylpropane under S-L-PTC conditions

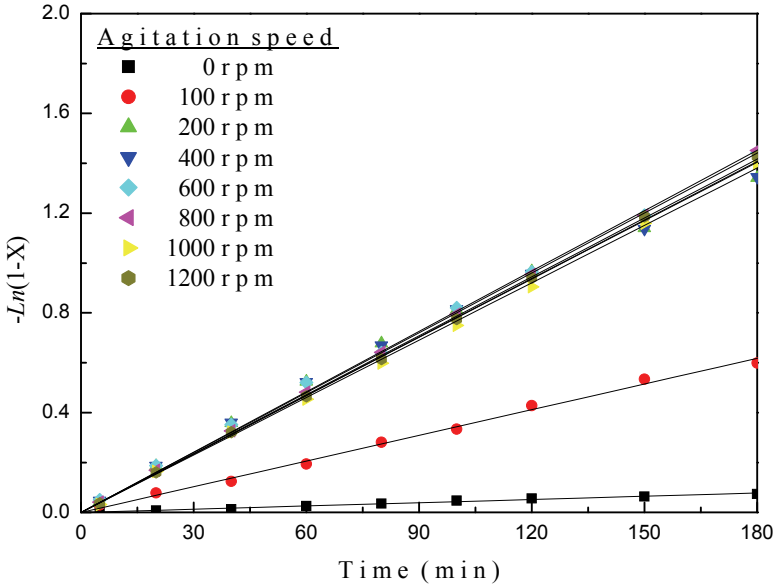

Fig. 7. Plot of -ln(1 - X) of 1-bromo-3-phenylpropane versus time with various agitation speeds; 9.0 × 10^{-2} mol of succinimide, 1 g of KOH, 0.4 g of TOAB, 6.0 × 10^{-3} mol of 1-bromo-3-phenyl-propane, 50 mL of cyclohexanone, 0.3 g of internal standard (naphthalene), 40 °C. (Adapted from Ref. [23], by permission)

2.5 S-Alkylation

The reaction between sodium sulfide and *n*-bromobutane to synthesize di-*n*-butyl sulfide was carried out for in an organic solvent/alkaline solution two-phase medium under phase transfer catalysis (PTC) conditions [65]. The overall reaction is presented in Scheme 4. In the two-phase reaction, mass transfer resistance is an important factor in affecting the reaction rate. In general, either the organic or the aqueous solution can be dispersed in smaller droplet size by agitating the two-phase solution, so, the contact area of two phases is increased with higher agitation speed. The flux of the two-phase mass transfer is also highly dependent on the flow condition (e.g. agitation speed). Fig. 8 shows the dependence of the apparent rate constant ($k_{app,1}$) on the agitation speed. For agitation speeds less than 350 rpm, both mass transfer and reaction resistance are important in determining the overall reaction rate. In this work, the reaction rate does not significantly change for agitation speeds larger than 350 rpm, and the mass transfer resistances of the active catalyst between the two phases are the same for agitation speed over 350 rpm. Hence, it is obvious that the reaction in organic phase is the rate-controlling step for agitation speed larger than 350 rpm under the standard reaction conditions. Below 50 rpm, the reaction rate is quite low because the two-phase solutions do not mix well and layering is clearly observed. Over 100 rpm, the ivory-white dispersion phase occurs. However, the phenomenon of constancy of the reaction rate constant over a certain agitation speed widely exists in PTC reactions, which are formulated based on an extraction model. Wang and Tseng [66], Jayachandran et al. [67], Park et al. [68], Wang and Wu [69] and Do and Chou [70], proposed the agitation speeds

from 200 to 800 rpm. This threshold value changes with changes in the reaction parameters, e.g. the two-phase surface tension will be changed using different organic solvents or adding cationic surfactants, so the maximum two-phase mass transfer rate will be changed under different agitation speeds.

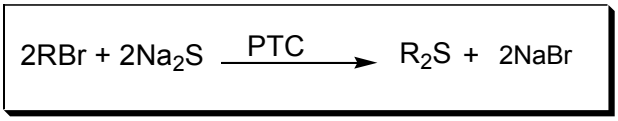

Scheme 4. Thioether synthesis under phase-transfer catalysis conditions

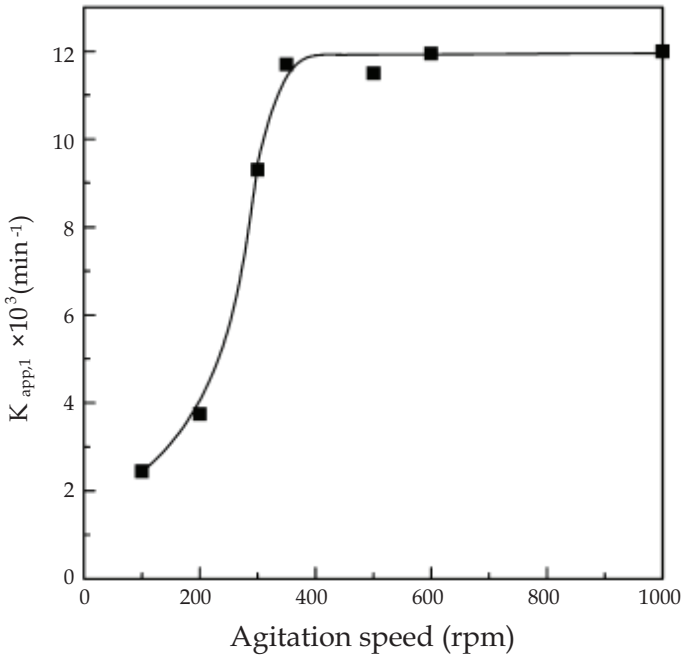

Fig. 8. Effect of the agitation speed on the apparent rate constant ($k_{app,1}$) in the organic phase; 7 g of sodium sulfide, 10 ml of water, 0.15 mmol of TBAB, 4 mmol of n-bromobutane, 40 ml of n-hexane, 40 °C. (Adapted from Ref. [65], by permission)

2.6 Dichlorocyclopropanation

Mass transfer between two phases in a phase-transfer catalysis system is important in affecting the conversion or the reaction rate. From the point of kinetics, changing the agitation speed can influence both the mass transfer rate, which relates to the mass transfer coefficient and the interfacial area between two phases, and the reaction rate. Increasing the agitation speed leads to increase both the mass transfer coefficient and the interfacial area, thus enhancing the mass transfer rate. The effects of varying stirring on the rate constants of the dicholorocarbene addition reactions were documented in the literature [40, 71-73].

The kinetics of dichlorocarbene addition to 1,7-octadiene have been studied under phase transfer catalytic conditions [74] using aqueous sodium hydroxide as the base and tetrabutylammonium chloride as a phase transfer catalyst (Scheme 5). In this work, the effect of agitation speed on the conversion for the reaction carried out at low alkaline concentration (30% NaOH) is shown in Fig. 9. No other byproducts were obtained during or after the reaction. The conversion is highly dependent on agitation speeds less than 800 rpm, above which the conversion is not influenced by increasing the agitation speed. The corresponding rate constant values with various agitation speeds are given in Table 5. Increasing the agitation speed leads to increase both the mass transfer coefficient and the interfacial area, thus enhancing the mass transfer rate. A similar trend was observed by Vivekanand and Balakrishnan [75] in the kinetic study of dicholorocarbene addition to indene catalyzed by triphase catalyst, where the rates were found to be independent of stirring speed >400 rpm.

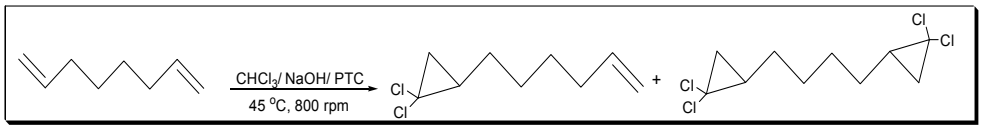

Scheme 5. Dichlorocarbene addition to 1,7-octadiene under PTC conditions

Agitation speed (rpm)	$k_{app\ 3} \times 10$ ($min^{-1}\ M^{-2}$)
200	0.26
400	0.88
600	1.90
700	2.58
800	3.29
100	3.41

Table 5. Effect of the agitation speed on the $k_{app,3}$ value at low NaOH concentration: 10 mmol of 1,7-octadiene, 20 ml of chloroform, 0.2 mmol of tetrabutylammonium chloride (TBAC), 6 g of NaOH, 14 ml of water, 40 °C. (Adapted from Ref. [74], by permission)

2.7 Esterfication

Dutta *et.al.* [76] reported kinetics of esterification of phenol derivatives *viz.,* phenol, *m*-cresol and resorcinol in alkaline solution catalyzed by polystyrene supported tri-*n*-butyl phosphonium ion under pseudo-first order conditions (Scheme 6). Kinetic results presented are interpreted in terms of three rate processes *i.e.* mass transfer of benzoyl chloride (organic substrate) to the catalyst surface, diffusion of the substrate through the polymer matrix and intrinsic reactivity at the active sites. The reaction engineering aspects have been addressed from experimentally observed rate determining phenomena as complimented by the theory of diffusive mass transfer in porous catalyst.

The order of reactivity of different phenol derivatives: resorcinol< *m*-cresol< phenol. Apparent rate constants were found to increase up-to 800-1000 rpm (stirring speed) for different phenols, beyond which the k_{app} values were found to be remain constant. They reported that catalysts with particle size lower than 70μm do not enhance the rate. This is

attributed to low mass transfer of reactants from the bulk phase to the particle surface and hence the reaction rate is reduced. However the reaction rate is better than the uncatalyzed reaction. In presence of highly active catalyst, mass transfer from the bulk phase to the surface of the catalyst particle can be rate controlling step. They reported that the mass transfer of benzoyl chloride from the bulk organic phase to the surface of the catalysts depends on the contact between the polymer particles and organic droplets, both of which are suspended in a continuous phase of aqueous sodium phenolate. Authors interpreted the kinetic results in terms of three aspects *viz.*, i) mass transfer of benzoyl chloride to the catalyst surface, ii) diffusion of benzoyl chloride through polymer matrix, and iii) intrinsic reactivity at the active sites.

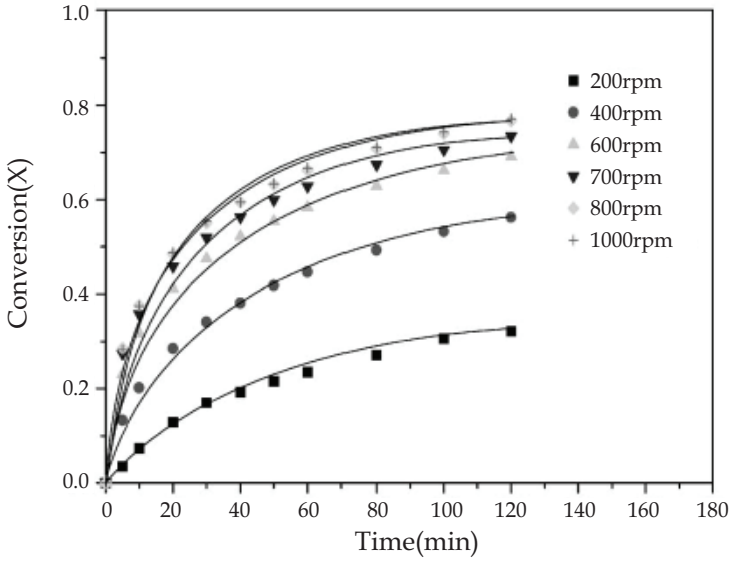

Fig. 9. Effect of the agitation speed on the conversion of 1,7-octadiene at low alkaline concentration (30% NaOH): 10 mmol of 1,7-octadiene, 20 ml of chloroform, 0.2 mmol of tetrabutylammonium chloride (TBAC), 6 g of NaOH, 14 ml of water, 40 °C. (Adapted from Ref. [74], by permission)

Esterifcation of benzyl chloride with sodium acetate to form benzyl acetate and sodium chloride were carried out under tri-phase conditions using polymer supported tributylmethylammonium chloride as the phase transfer catalyst [77]. The investigation focused on the determination of external mass transfer coefficient from the liquid bulk phases to the surface of the catalyst in tri-phase catalytic systems. Special emphasis was placed on the equipment (rotating disk contactor, RDC) which has been conceived and designed for this purpose. Determination of mass transfer coefficient involves an analysis of the various regimes of solid-liquid systems with the solid not soluble in the liquid phase. Esterfication was found to be mass transfer controlled at low agitation speeds and it was found to be characterized by considerable non-catalytic reaction and effects due to dispersion associated with the catalyst. Nevertheless, it was possible to determine the external mass transfer coefficient as a function of the bulk agitation speed. The mass transfer

coefficient increases with the increasing agitation rate indicated the dependence of the mass transfer coefficient on the agitation rate.

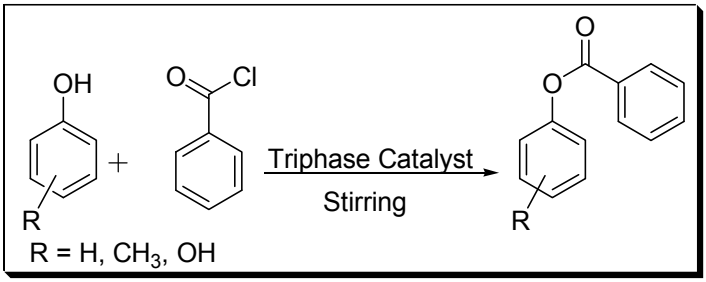

Scheme 6. Esterfication of substituted phenols under PTC conditions

3. Conclusion

Conventional technologies for multiphase organic reactions were largely uneconomical and polluting and hence were commercially not feasible. In recent years, several new techniques have emerged that use homogeneous or heterogeneous catalysts such as phase transfer catalysts, supported metal catalysts, biocatalysts etc. Among various types of catalysts, phase transfer catalysts have attracted more and more attention. It facilitates inter-phase transfer of species, making reactions between reagents in two immiscible phases possible.

Many organic synthetic applications based on PTC have shown great success. The present chapter has hence concentrated on the PTC reactions, *viz.,* alkylation reactions, esterfication reactions, dichlorocarbene addition reactions etc., using both soluble and immobilized forms of the catalyst. By its very nature, PTC involves interphase transport of species, neglecting which can grossly over predict the conversion of a PTC mediated reaction. Hence, greater emphasis has been given to present the role of mass transfer in PTC-assisted reactions. Nevertheless, there are definitely numerous catalytic reactions still waiting to be discovered and hence, opportunity for major discovery will remain vibrant for a very long time indeed. The new designs for microwaves and ultrasound assisted PTC reactions and the relevant mass transfer data is most essential to understand the design and scale-up of these emerging technologies in industries. It is hoped that this chapter will spur further research in this area, whose applications in the manufacture of organic intermediates and fine chemicals seems almost unlimited.

4. Acknowledgments

We gratefully acknowledge support of this work by the National Science Council, Taiwan (NSC), under several grants. Further, we would like thank numerous students and postdoctoral scientists who have worked on these projects.

5. Nomenclature

A = Mass-transfer area between organic and aqueous phase, cm^2/cm^3

X = Conversion of allyl bromide

C_{ArOQ}^{org} = Concentration of ArOQ in organic phase, M

C_{ArOQ}^{aq} = Concentration of ArOQ in aqueous phase, M

C_{QBr}^{aq} = Concentration of QBr in aqueous phase, M

C_{QBr}^{org} = Concentration of QBr in organic phase, M

C_{ArOK}^{aq} = Concentration of ArOK in aqueous phase, M

C_{ArOR}^{org} = Concentration of ArOR in organic phase, M

C_{RBr}^{org} = Concentration of RBr in organic phase, M

E_o = Initial moles of 2,4,6-tribromophenol

f = V_o / V_a

K_{aq} = Reaction rate constant of the aqueous phase, M^{-1} min^{-1}

K_{org} = Reaction rate constant of the organic phase, M^{-1} min^{-1}

K_{ArOQ} = Mass-transfer coefficient of ArOQ from aqueous to

K_{QBr} = Mass-transfer coefficient of QBr from organic phase

m_{QBr} = Distribution coefficient of QBr $\left(\frac{C_{QBr}^{org(s)}}{C_{QBr}^{aq(s)}}\right)$

m_{ArOQr} = Distribution coefficient of ArOQ $\left(\frac{C_{ArOQ}^{org(s)}}{C_{ArOQ}^{aq(s)}}\right)$

V_a = volume of aqueous phase, L

V_o = Volume of organic phase, L

t = Time in minutes

6. References

[1] F.M. Menger, Chem. Soc. Rev. 1 (1972) 229.
[2] C.M. Starks, C.L. Liotta, M. Halpern, Phase Transfer Catalysis, Chapman & Hall Publications, New York, 1994.
[3] E.V. Dehmlow, S.S. Dehmlow, Phase Transfer Catalysis, third ed., VCH, New York, 1993.
[4] G.D. Yadav, S.V. Lande, Adv. Synth. Catal. 347 (2005) 1235.
[5] M. Makosza, ARKIVOC 4 (2006) 7.
[6] J.P. Jayachandran, C. Wheeler, B.C. Eason, C.L. Liotta, C.A. Eckert, J. Super. Fluids, 27 (2003) 179.
[7] H. M. Yang, H. S. Wu, Catal. Rev. 45 (2003) 463.
[8] T. Ooi, M.Takahashi, K. Doda, K. Maruoka, J. Am. Chem. Soc. 124 (2002) 7640.
[9] D. Y. Kim, S. C. Huh, E.J. Park, Org. Lett. 4 (2002) 545.
[10] M. Benaglia, M. Cinquini, F. Cozzi, G. Tocco, Tetrahedron Lett. 43 (2002) 3391.
[11] M. Ueno, H. Hisamoto, T. Kitamori, S. Kobayashi, Chem.Commun. (2003) 936.
[12] R. H. Fan, X. L. Hou, Org. Biomol. Chem. 1 (2003) 1565.
[13] N. Ohtani, T. Ohta, Y. Hosoda, T.Yamashita, Langmuir, 20 (2004) 409.
[14] W.P. Weber, G.W. Gokel, Phase Transfer Catalysis in Organic Synthesis, Springer-Verlag, New York, 1977.

[15] Y. Sasson, R. Neumann, Handbook of Phase Transfer Catalysis, Chapman & Hall, New York, 1997.
[16] C.M. Starks, Am. Chem. Soc. Symp. 326 (1985) 1.
[17] H.H. Freedman, Pure Appl. Chem. 586 (1986) 857.
[18] W.E. Keller, Phase-transfer reactions, Fluka-Compendium 1 1986.
[19] W.E. Keller, Phase-transfer reactions, Fluka-Compendium 2 1987. .
[20] M. L. Wang, T. H. Huang, J. Chem. Eng. Japan, 36 (2003) 231.
[21] M. L. Wang, T. H. Huang, Ind. Eng. Chem. Res. 43 (2004) 675.
[22] M. L.Wang, T. H. Huang, W. T. Wu, Chem. Eng. Commun. 191 (2004) 27.
[23] M. L. Wang, C. J. Chen, Org. Process Res. Dev. 12 (2008) 748.
[24] M. L.Wang, C. J. Chen, Org. Process Res. Dev. 14 (2010) 737.
[25] M. L. Wang, G. S . Prasad, J. Tai. Inst. Chem. Eng. 41 (2010) 81.
[26] Y. H. Tseng, M. L.Wang, J. Tai. Inst. Chem. Eng. 42 (2011) 129.
[27] P. A. Vivekanand, T. Balakrishnan, Cat. Commun. 10 (2009) 687.
[28] P. A. Vivekanand, T. Balakrishnan, Appl. Catal. A: Gen. 364 (2009) 27.
[29] P. A. Vivekanand, T. Balakrishnan, Cat. Commun. 10 (2009) 1371.
[30] P. A. Vivekanand, T. Balakrishnan, Cat. Commun. 10 (2009) 1962.
[31] K. Inoue, F. Nakashio, Chem. Eng. Sci. 34 (1979) 191.
[32] M. L. Wang, H. M. Yang, Chem. Eng. Sci. 46 (1991) 619.
[33] A. Akelah, A. Moet (1990) Functionalized polymers and their applications. Chapman and Hall, New York
[34] P. Hodge, D. C. Sherington (1988) Synthesis and separations using functionalized polymers. Wiley, New York
[35] A.R. Kiasa, R. Badri, B. Zargar, S .Sayyahi, J Org Chem. 73 (2008) 8382.
[36] P. H. H. Hermkens, H. C. J. Ottenhejm, D. Rees, Tetrahedron 52 (1996) 4527.
[37] L. A.Thomson, J. A. Ellmann, Chem Rev. 96 (1996) 555.
[38] S. Desikan, L. K. Doraiswany Ind Eng Chem Res 34 (1995) 3524.
[39] S. L. Regen J Am Chem Soc 97(1975) 5956.
[40] E. V. Dehmlow, S.S. Dehmlow Phase transfer catalysis. Verlag Chemie, Weinheim (1993).
[41] C. M. Starks, C. L. Liotta, M. Halpern, Phase-transfer catalysis, fundamentals, applications, and industrial perspectives. Chapman and Hall, New York (1994).
[42] S. L .Regen, J Am Chem Soc 98 (1976) 6270.
[43] S. L. Regen, J. J. Besse, J Am Chem Soc 101 (1979) 4059.
[44] M. Tomoi, W. T. Ford, J Am Chem Soc 103 (1981) 3828.
[45] V. Ragaini, G. Colombo, P. Barzhagi, Ind Eng Chem Res. 27 (1988) 1382.
[46] P. Schlunt, P. C. Chau, J Catal. 102 (1986)348.
[47] O. Arrad, Y. Sasson, J Org Chem 55 (1990) 2952.
[48] W. T. Ford, J. Lee, M. Tomoi, Macromolecules 15 (1982) 1246.
[49] P. Tundo, P. Venturello, E. Angeletti, J Am Chem Soc 104 (1982) 6551.
[50] S. D. Naik, L.K. Doraiswamy AIChE J (1999) 612.
[51] D. E. Bergbreiter, J. Tian, C. Hongfa, Chem. Rev. 109 (2009) 530.
[52] M. Tomoi, W. T. Ford, J. Am. Chem. Soc. 102 (1980) 7141.
[53] M. L Wang, H. M. Yang, Ind. Eng. Chem. Res. 30 (1991) 631.
[54] M. L.Wang, H. M. Yang, Ind. Eng. Chem. Res. 29 (1990) 522.
[55] M. L. Wang, H. M. Yang, Ind. Eng. Chem. Res. 30 (1991) 2384.
[56] M. L.Wang, H. S. Wu, J. Org. Chem. 55 (1990) 2344.

[57] M. F. Sorokin, V. K. Latov, Kinet. Catal. (USSR) (1966) 35.
[58] J. L. Schmutz, H. R. Allcock, Inorg. Chem. 14 (1975) 2433.
[59] M. L. Wang, H. S. Wu, J. Poly. Sci. Part A: Poly. Chem. 30 (1992)1393.
[60] R. Solaro, S. D. Antone, E. J. Chiellini, J. Org. Chem. 45 (1980) 4179.
[61] T. Balakrishnan, W. T. Ford, Tetrahedron Lett. (1981) 4377.
[62] M. Rabonivitz, Y. Sasson, M. Halpern, J. Org. Chem. 48 (1983) 1022.
[63] P. A. Vivekanand, M. L. Wang, Ultrason. Sonochem. 18 (2011) 1241-1248, doi:10.1016/j.ultsonch.2011.02.002
[64] V. Rajendran, M. L. Wang, J. Mol. Catal. A: Chem. 288 (2008) 23.
[65] M. L. Wang, Y. H. Tseng, J. Mol. Catal., A: Chem. 203 (2003) 79.
[66] M. L. Wang, Y. H. Tseng, J. Mol. Catal., A: Chem. 179 (2002) 17.
[67] J. P. Jayachandran, T. Balakrishnan, J. Mol. Catal., A: Chem. 152 (2000) 91.
[68] S. W. Park, H. S. Yoon, S. B. Park, I. J. Sohn, J. Polym. Sci., A: Polym. Chem. 38 (2000) 3059.
[69] M. L. Wang, H. S. Wu, R. Soc. Chem. (1991) 841.
[70] J. S. Do, T. C. Chou, Ind. Eng. Chem. Res. 29 (1990) 1095.
[71] W. P. Reeves, R. G. Hilbrich, Tetrahedron 32 (1976) 2235.
[72] M. L. Wang, W. H. Chen, F. S. Wang, J. Mol. Catal. A: Chem. 236 (2005) 65.
[73] M. L. Wang, Z. F. Lee, Bull. Chem. Soc. Jpn. 79 (2006) 80.
[74] M. L. Wang, Y. M. Hsieh, R.Y. Chang, J. Mol. Catal., A: Chem. 198 (2003) 111.
[75] P. A. Vivekanand, T. Balakrishnan, Cat. Lett. 13 (2009) 1587.
[76] N. N. Dutta, A. C. Ghosh, R. K. Mathur, Phase-Transfer Catalysis, Chapter 20, pp 261–276, ACS Symposium Series, Vol. 659, 1997.
[77] H. J. Glatzer, S. Desikan, L. K. Doraiswamy, Chem. Eng. Sci., 53 (1998) 2431.

31

Transport of Ultradispersed Catalytic Particles Through Bitumen at Upgrading Temperatures

Herbert Loria and Pedro Pereira-Almao
Chemical & Petroleum Engineering Department, University of Calgary
Canada

1. Introduction

Mass transfer and deposition of fine particles in cylindrical channels has received considerable attention for a long time due to its practical significance and direct application in industry. For example, this knowledge is helpful in aerosol classification and its deposition under electrical fields, formation of deposits in heat exchangers and pipelines, hydrodynamic field chromatography, thrombus formation in organs and, many other areas (Adamczyk and Van De Ven, 1981). Recently, this phenomenon has gained particular importance on the dispersion of ultradispersed catalysts for heavy crude oil and bitumen hydroprocessing due to its practical significance and direct application (Pereira-Almao et al., 2007; Galarraga and Pereira-Almao, 2010; Loria et al., 2011).

Ultradispersed catalysts have been studied for heavy oil and bitumen hydroprocessing as an alternative for typical supported catalysts. An advantage when comparing ultradispersed catalysts to supported ones, in the case of heavy oil and bitumen hydroprocessing, is that the former could be easily incorporated into the reaction media to flow together with the feedstock to be treated, in this manner residence times can be longer than those conventionally used for hydroprocessing (Pereira-Almao et al., 2005; Pereira-Almao, 2007).

Recent publications (Loria et al., 2009b, 2009c, 2010) have demonstrated the feasibility of the transport of ultradispersed particles based on their motion through diverse viscous media enclosed in horizontal cylindrical channels. Time-dependent, two and three-dimensional convective-dispersive models, which simulated the transient deposition and suspension of ultradispersed particles immersed in viscous media inside a horizontal cylinder, were developed, solved and experimentally validated. In addition, a study on the effect of the fluid medium properties over the dispersion coefficient was performed. The dispersion coefficient is a proportionality constant that serves to quantify the particle concentration due to convection and dispersion and should be expressed as a function of the properties of the fluid medium (Loria et al., 2010).

The solution of the previously mentioned models provides a particle concentration profile along the horizontal channel, as well as information regarding the critical particle size that allows particles to remain suspended in the fluid medium enclosed in this geometry. This knowledge can be applied in the previously referred ultradispersed catalysis of heavy crude oils and bitumen. In these systems, it is important to ensure that catalytic particles remain suspended in the fluid medium in order to make use of their catalytic activity and also, to

obtain the conditions for which these particles will sediment in order to recover and reuse them in recirculation systems.
The present study intends to show the application of the convective-dispersive models in cases that involve the storage and transport of catalytic particles immersed in bitumen at upgrading temperatures (340 -380° C) inside cylindrical geometries.
The main objective of this paper is to employ the previously developed models as tools for interpretation of cases of interest for the heavy oil and bitumen industry. The modelling parameters of these systems can be based on those employed in the validation experiments for the convective-dispersive models (Loria et al., 2009b, 2009c, 2010), since physical properties from particles and fluids used in the experiments were deliberately chosen to be similar as those that catalytic particles and bitumen would have at upgrading temperatures.
The first part of this paper deals with a large scale application of the two-dimensional convective-dispersive model (Loria et al., 2009b, 2009c). Since this model predicts the particle concentration profile enclosed in a circumference, it can be applied to the cross-sectional part of a spherical storing tank. In this section, the concentration profile of molybdenum trioxide (MoO_3) catalytic particles immersed in bitumen enclosed in a 4 m diameter spherical tank is studied.
The second section of this paper is related to the three-dimensional convective-dispersive model (Loria et al., 2010). This model simulates the transient deposition and suspension of particles immersed in a fluid travelling through a horizontal cylindrical channel and provides the particle concentration profile along the channel. In this case, simulations involving a pipe of 100 m length and 101.6 cm diameter transporting MoO_3 catalytic particles immersed in bitumen were carried out.
The simulations took into account different particle diameters, ranging from 1 to 1500 nm and different temperatures, ranging from 340 to 380° C. The bitumen's physical properties (density and viscosity) vary with respect to the different studied temperatures and are essential inputs of the convective-dispersive model. In order to obtain these properties; a previously developed thermodynamic model for their calculation (Loria et al., 2009a) was employed.

2. Two-dimensional transport of particles through viscous fluid media

2.1 Two-dimensional convective-dispersive model to predict the concentration profile of particles immersed in viscous media

When a particle settles down in a liquid medium, it accelerates until the forces that cause the sedimentation equilibrate with the resistance or drag forces offered by the medium. Once this equilibrium is achieved, the particle has a constant sedimentation velocity called terminal sedimentation velocity (v_{pT}) which can be represented by (Ramalho, 1983):

$$v_{pT} = \frac{g\left(\rho_p - \rho_L\right)d_p^2}{18\mu_L}, \tag{1}$$

where g is the acceleration due to gravity, ρ_p is the density of the particle, ρ_L is the density of the liquid, d_p is the diameter of the particle and μ_L is the viscosity of liquid medium. Equation 1 is also known as the Stokes' law for the sedimentation of discrete particles.
A continuity equation for the particle concentration in a fluid medium can be obtained by carrying out a mass balance on a differential element of volume. Considering that particle

concentration (C_P) varies with time (t), that the effective dispersion coefficient (D_E) is constant, that the particle concentration inside a cylindrical channel is modelled as a function of the position of the particles in the cross-section of the cylinder and the time, $C_P = C_P(r, \theta, t)$, that the angular velocity of the particle (v_θ) is small compared to the radial velocity (v_r) and that this radial velocity can be obtained by projecting the vertical terminal velocity of the particle into the radial direction ($v_r = v_{PT}\cos\theta$); then the continuity equation in cylindrical coordinates can be written as (Bird et al., 2007):

$$\frac{\partial C_P}{\partial t} + v_{pT}\cos\theta\frac{\partial C_P}{\partial r} = D_E\left[\frac{1}{r}\frac{\partial}{\partial r}\left(r\frac{\partial C_P}{\partial r}\right)+\frac{1}{r^2}\frac{\partial^2 C_P}{\partial \theta^2}\right]. \tag{2}$$

D_E is called the effective dispersion coefficient because the transport of the particles from high concentrated areas to low concentrated ones is, in this case, due to their mixing with the liquid bulk (Franco, 2008) and it is called effective because includes the motion effects caused by the particles and the gravity force in all directions. It distinguishes from the diffusivity coefficient in the sense that diffusivity is determined by the molecular properties of the particles and the fluid in which they are immersed, whereas the dispersion coefficient is determined by the particle properties and fluid conditions. Generally, in atmospheric transport, dispersive flux dominates the diffusive flux.

In the beginning of the process ($t = 0$) all particles are well dispersed inside the cross section of the cylindrical channel. This means that particle concentration is uniform everywhere inside the cross-section of the cylindrical channel. This concentration is the initial concentration of the particles (C_{P0}).

$$\text{At } t = 0,\ C_P(r, \theta, 0) = C_{P0},\ 0 < r < R,\ 0 < \theta < 2\pi. \tag{3}$$

In the vertical axis there are symmetry boundary conditions that can be represented as:

$$\text{At } \theta = 0,\ \frac{\partial C_P}{\partial \theta} = 0\ ,\ 0 < r < R. \tag{4}$$

$$\text{At } \theta = \pi,\ \frac{\partial C_P}{\partial \theta} = 0\ ,\ 0 < r < R. \tag{5}$$

In the centre of the cylindrical channel the particle concentration does not vary with respect to the radius around all the angles:

$$\text{At } r = 0,\ \frac{\partial C_P}{\partial r} = 0\ ,\ 0 < \theta < 2\pi. \tag{6}$$

The walls of the channel represent a physical boundary where there is no mass exchange between the interior and exterior of the cylinder. This is an insulation boundary that will prevent any particle from leaving the channel, gathering all settled particles at the bottom. The insulation boundary means that there is no convective or dispersive flux across that boundary. This can be represented by:

$$\text{At } r = R,\ -D_E\frac{\partial C_P}{\partial r} + \left(v_{pT}\cos\theta\right)C_P = 0\ ,\ 0 < \theta < 2\pi. \tag{7}$$

The convective-dispersive model is a linear second order parabolic partial differential equation; this equation can be solved by a large variety of numerical methods: finite differences, finite element, finite volume, characteristics methods, discontinuous Garlekin methods, etc. A numerical solution based in the finite element method was used to solve this equation. This solution presented good convergence and stability properties due to the regular grid structure and its flexibility with respect to the adaptation to the geometry domain. Computational fluid dynamics software was used in order to apply the method.

2.2 Effect of the fluid medium properties on the dispersion coefficient

Two of the parameters which are necessary input data for the numerical solution of the convective-dispersive model are v_{pT} and D_E. They can be obtained from experimental physical parameters. The calculation of v_{pT} can be performed directly from equation 1. However; the effective dispersion coefficient of the particles, D_E, cannot be obtained directly from any formula, the best way to obtain this value is to perform an adjustment of this parameter using concentration values from experimental data.

In a previous work (Loria et al., 2009c), a study to observe the variation of the dispersion coefficient with respect to the changes of the properties of the fluid medium was performed. For this study the experimental data collected from Fe_2O_3 nanoparticles immersed in different mixtures of water and glycerol was used.

Figure 1 shows the behaviour of the dispersion coefficient with respect to an increase of density and viscosity of the fluid medium. It can be observed that as the fluid medium becomes denser and more viscous the dispersion coefficient decreases. The particles gradually decrease their capability to move as the fluid medium becomes denser and more viscous; thus, the particles lose their ability to go from high concentrated areas to low concentrated ones, causing a decrease of the dispersion coefficient. These experimentally obtained dispersion coefficients showed a tendency to increase when the conditions were more favourable for sedimentation, that is, low density and viscosity

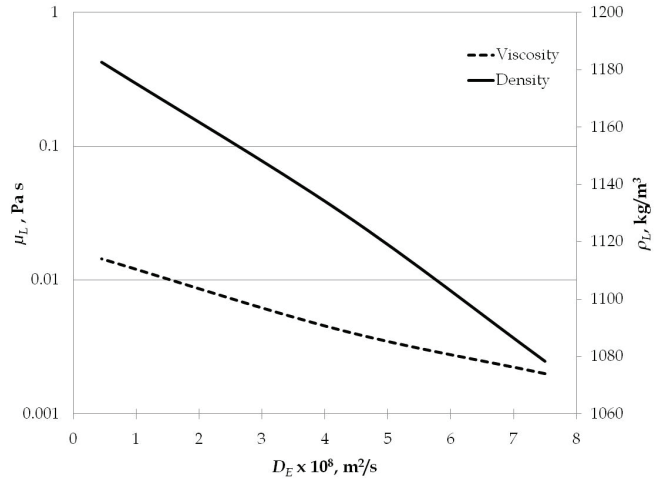

Fig. 1. Dispersion coefficient (D_E) as a function of the viscosity (μ_L) and density (ρ_L) of the fluid medium in the cross-section of a horizontal cylinder

Literature data related to cross-sectional dispersion coefficients in horizontal channels is scarce. The dispersion coefficient obtained in this research could be compared to the diffusion coefficients obtained by (d'Orlyé et al., 2008). They studied diffusion coefficients of maghemite particles (γ-Fe_2O_3) dispersed in an aqueous solution of nitric acid. They performed diffusion coefficient measurements for nanometric particles (< 10 nm) based on the results of dynamic light scattering experiments in the cross-section of horizontal capillary tube. They obtained diffusion coefficients in the order of 10^{-11} m^2/s, which varied three orders of magnitude from the D_E values obtained in this work. This difference is probably due to the use of particles smaller than 10 nm, the employment of capillary tubes of 50 μm of diameter and the use of dynamic light scattering results for the calculation of particle concentrations since dynamic light scattering is a technique primarily designed for particle size measurement.
Dispersion coefficients with similar orders of magnitude as the ones obtained in a previous work (Loria et al., 2009c) carried out with submicron particles (10^{-8} -10^{-9} m^2/s) were found by (Robbins, 1989; Massabò et al., 2007). However, these results are not comparable with this work since they performed their calculations in a packed column based on concentration measurements that were generated by the computational simulation of a continuous tracer injection experiment in a vertical cylindrical geometry.

2.3 Ultradispersed catalytic particles immersed in bitumen at upgrading temperatures stored inside a spherical tank

In this section, the two-dimensional convective-dispersive model is applied to a large scale case which involves the storage of MoO_3 catalytic particles immersed in Athabasca bitumen, at upgrading conditions (340-380 °C), inside a 4 m diameter spherical tank.
The objectives of this study are: to find the critical particle diameter for its suspension, and to calculate the deposited mass of the catalytic particles at the bottom of the tank once the steady state has been reached.
The density (ρ_L) and viscosity (μ_L) of the Athabasca bitumen at five different temperatures ranging from 340 to 380 °C were employed in the following simulations. These physical properties were calculated with thermodynamic models for the prediction of density and viscosity of heavy crude oil and bitumen, details of these models were presented by (Loria et al., 2009a). Table 1 shows the densities and viscosities of Athabasca bitumen in the range 340 to 380 °C, these values were obtained with the previously mentioned thermodynamic models.

T, °C	ρ_L, kg/m³	μ_L, cP
340	884.7	2.71
350	877.2	2.42
360	869.4	2.38
370	856.4	2.27
380	843.7	2.17

Table 1. Densities and viscosities of the Athabasca bitumen in the range 340 to 380 °C

MoO_3 (ρ_p = 4700 kg/m³ (Perry, 1997)) particle diameters which were used for the simulations ranged from 1 to 1500 nm. In total fourteen different particle diameters were studied: 1, 10, 50, 100, 150, 200, 250, 300, 400, 500, 750, 1000, 1250 and 1500 nm.

The initial MoO_3 particle concentration (C_{P0}) applied to all the simulations was 1.2526 mol/m^3. A common concentration unit employed in ultradispersed catalysis for hydroprocessing is ppm (parts per million or g/m^3). In this case, 1.2526 mol/m^3 are equivalent to 180.3 ppm. This particle concentration is within the same magnitude order as those that have been proposed for ultradispersed catalysis for hydroprocessing (Pereira-Almao, 2007).

The calculation of the dispersion coefficient that was used for these simulations was based on the results that were obtained when the two-dimensional convective-dispersive model was validated with Fe_2O_3 particles immersed in mixtures of water and glycerol (Loria et al., 2009c). These data were used since particle properties and concentrations in addition to the fluid medium characteristics used in those experiments are similar to those employed in the simulations carried out in this section.

The dispersion coefficient calculation was carried out in the following way: polynomial interpolations were applied to the data from Figure 1 (μ_L and ρ_L vs. D_E); then, for each temperature a pair of D_E values were obtained (one based on μ_L and the other in ρ_L) and their average was recorded; finally, the 5 different D_E average values (corresponding to each one of the studied temperatures and ranging from 4.9 - 5.6 × 10^{-8} m^2/s) were averaged and the final D_E value was obtained. The D_E value obtained from these calculations resulted to be 5.33 × 10^{-8} m^2/s.

A total of 70 different simulations were carried out in this section (based on the 14 different particle diameters and 5 different temperatures). Computational fluid dynamics was used to perform the simulations; each simulation was carried out up to a time of 1 × 10^8 s (27778 h), a time long enough to reach the steady state in each one of them. 2508 grid points were employed for the solution of each simulation and their computing time was around 60 s

A point of interest in this study is the critical particle diameter for deposition; that is, the particle diameter from which particles with higher sizes will be deposited and particles with lower sizes will remain suspended. In order to measure this new parameter, the following analysis was conducted.

The normalized maximum particle concentration, which is the concentration that is found at the bottom of the circumference after the simulation time (steady state) divided by the initial concentration, was calculated for each simulation. When the normalized maximum concentration tends to the initial one (normalized concentration = 1), it means that there is no particle deposition at the bottom of the circumference.

This normalized maximum particle concentration was plotted against the particle diameter in order to observe at which particle diameter the maximum particle concentration becomes significant. Figure 2 represents the behaviour of the normalized maximum particle concentration at different particle diameters and temperatures.

As temperature increases for a specific particle diameter, the normalized maximum concentration increases. Also, as the particle diameter increases, the normalized maximum concentration increases for a constant temperature. It can also be observed that a change in particle diameter have a more pronounced effect over the normalized maximum concentration than a change in temperature.

In the particle diameter axis, there is a zone for values lower than 150 nm where the normalized maximum concentration is equal to the initial one independently of the studied temperature. This means that MoO_3 particles smaller than 150 nm will remain suspended in the Athabasca bitumen after a long period of time (1 × 10^8 s) in the range of temperatures from 340 to 380 °C.

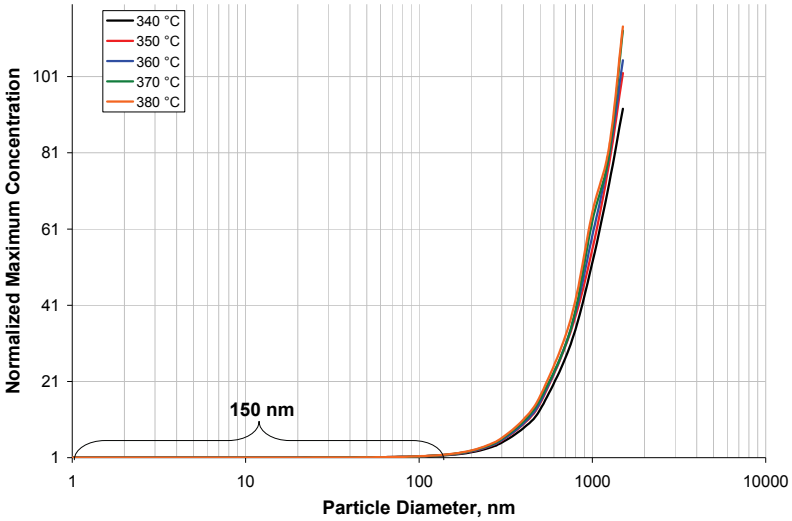

Fig. 2. Effect of the particle diameter and temperature on the deposition of MoO_3 particles immersed in Athabasca bitumen enclosed in a spherical tank of 4 m diameter

In order to calculate the deposited mass of the catalytic particles at the bottom of the spherical tank once the steady state has been reached, the following procedure was employed.

Assuming that the deposited particles filled a small gap of height H at the bottom of the spherical tank of radius R, its volume (V_P) can be calculated by:

$$V_P = \frac{1}{3}\pi H^2 (3R - H) \tag{8}$$

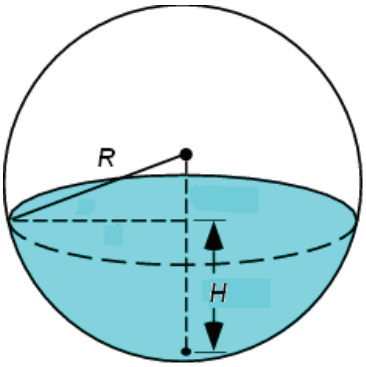

Fig. 3. Gap of height H at the bottom of a spherical tank of radius R

Assuming that the height of this small gap is approximately H = 6.5 cm (based on the simulation results), the volume of the gap (V_P) for a sphere of 2 m of radius is 1.73 $\times 10^{-3}$ m^3.

Since particle concentration in this part of the tank after a long period of time is already known from the simulation results, i.e. the maximum particle concentration ($C_{P\max}$), then the deposited mass (M_P) is:

$$M_P = C_{P\max} V_P \tag{9}$$

On the other hand, the total mass of the immersed particles inside the tank (M_{PT}) is:

$$M_{PT} = C_{P0}\left(\frac{4}{3}\pi R^3\right). \tag{10}$$

Considering that the initial particle concentration (C_{P0}) in the simulation was assumed to be 180.3 ppm or 1.2526 mol/m^3; the total particle mass immersed in a spherical tank of 2 m of radius is 6.042 kg.
The percentage of deposited particles at the bottom of the spherical tank ($\%M_{dep}$) can be calculated by:

$$\%M_{dep} = \frac{M_P}{M_{PT}} \times 100 \cdot \tag{11}$$

Table 2 and Figure 4 show the percentage of deposited particles at the bottom of the spherical tank ($\%M_{dep}$) at different temperatures and particle diameters.

			%Mdep		
***dp*, nm**	**340 °C**	**350 °C**	**360 °C**	**370 °C**	**380 °C**
1500	0.476	0.525	0.542	0.582	0.588
1250	0.375	0.402	0.413	0.415	0.425
1000	0.269	0.287	0.305	0.325	0.349
750	0.158	0.175	0.178	0.179	0.192
500	0.070	0.079	0.080	0.084	0.089
400	0.045	0.050	0.051	0.054	0.057
300	0.025	0.028	0.029	0.030	0.032
250	0.018	0.020	0.020	0.021	0.022
200	0.012	0.014	0.014	0.014	0.015
150	0.009	0.009	0.009	0.010	0.010
100	0.007	0.007	0.007	0.007	0.007
50	0.005	0.006	0.006	0.006	0.006
10	0.005	0.005	0.005	0.005	0.005
1	0.005	0.005	0.005	0.005	0.005

Table 2. Percentage of deposited particles at the bottom of the spherical tank ($\%M_{dep}$) containing MoO_3 particles immersed in Athabasca bitumen at different temperatures

Figure 4 demonstrates that the percentage of deposited particles at the bottom of the tank is less than 0.02%, when particle diameters below 200 nm are employed; and, when particle diameters in the range 200 – 1500 nm are used, the percentage of deposited particles is between 0.02 and 0.6 %.

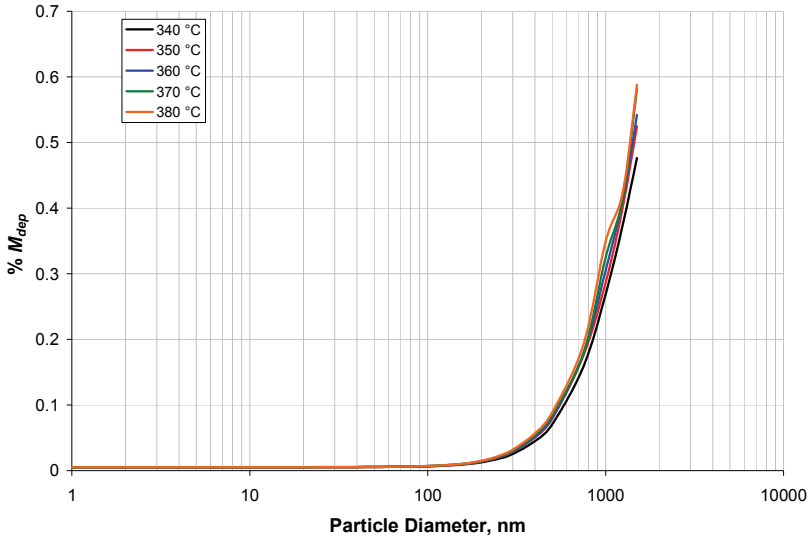

Fig. 4. Percentage of deposited particles at the bottom of the spherical tank (%M_{dep}) at different temperatures and particle diameters for the deposition of MoO_3 particles immersed in Athabasca bitumen enclosed in a spherical tank of 4 m diameter

3. Three-dimensional transport of particles through viscous fluid media

3.1 Three-dimensional convective-dispersive model to predict the concentration profile of particles immersed in viscous media

3.1.1 Axial varticle velocity

The first step to develop the three-dimensional convective-dispersive model is to obtain the flow velocity profile since particle velocity in this direction depends on it. This profile can be obtained from the Navier-Stokes equations. Consider a laminar incompressible fluid that travels inside a horizontal cylinder of radius R and length L. The force (F) pushing the liquid through the cylinder is the change in pressure (ΔP) multiplied by the cross-sectional area of the cylinder (A):

$$F = -\Delta P A \,. \tag{12}$$

This force is oriented in the same direction of the motion of the liquid:

$$\Delta P = P_{out} - P_{in} \,,\; P_{out} < P_{in}. \tag{13}$$

If the cylinder is long enough, then the flow through the cylinder is known as fully developed velocity profile, this means that there are not velocity components in the radial (v_r) and angular direction (v_θ) and the velocity in the longitudinal direction (v_z) is only a function of the radial coordinate (r).

Assuming a fully developed velocity profile at steady state, that the gravity force is not the force causing the motion and its effect is negligible, that the pressure decreases linearly across the length of the cylinder, that the axial velocity (v_z) is finite at $r = 0$ and that there is a

no slip boundary condition at the cylinder wall; then, the following parabolic velocity profile can be obtained:

$$v_z(r) = \frac{\Delta P}{4\mu_L L} R^2 \left(1 - \frac{r^2}{R^2}\right). \tag{14}$$

Equation 14 is known as the Poiseuille's flow inside cylinders. The volumetric flux (Q) inside the cylinder can be calculated using the following procedure:

$$Q = \int_A \mathbf{n} \cdot \mathbf{v} dA = 2\pi \int_0^R v_z(r) r dr = \frac{\pi \Delta P R^4}{8\mu_L L}. \tag{15}$$

where **n** is the unit vector normal to the velocity vector (**v**). The mean axial velocity ($\overline{v}_z$) is the volumetric flux divided by the cross-sectional area:

$$\overline{v}_z = \frac{2\pi \int_0^R v_z(r) r dr}{\pi R^2} = \frac{\Delta P R^2}{8\mu_L L}. \tag{16}$$

If the particles travelling through a horizontal cylinder are small enough as compared with the size of the cylinder radius, it can be considered that they travel at the same velocity of the fluid. Unlike liquid molecules present in a Poiseulle's flow, a solid spherical discrete particle of radius (r_p) cannot approach the slow flowing area close to the wall (Fung, 1993; Michaelides, 2006). Considering this assumption its average velocity can be calculated by:

$$\overline{v}_z(r_p) = \frac{2\pi \int_0^{R-r_p} v_z(r) r dr}{\pi (R - r_p)^2} = \frac{\Delta P R^2}{8\mu_L L}\left[2 - \left(1 - \frac{r_p}{R}\right)^2\right]. \tag{17}$$

If $r_p << R$, then

$$\overline{v}_z(r_p) = \frac{\Delta P R^2}{8\mu_L L} = \overline{v}_z. \tag{18}$$

Thus, the axial velocity of the particles can be represented by the Poiseuille's flow equation.

3.1.2 Analysis of the particle concentration inside a horizontal cylindrical channel

Particle concentration in a fluid medium can be obtained by carrying out a mass balance for particles present in a differential element of the system. In order to develop a convective-dispersive model which simulates the transport of particles travelling through a fluid medium, the mass balance for particles present in a differential element of a cylinder presented in Section 2.1 can be employed. Consider a laminar incompressible flow which contains particles that flow inside a horizontal cylinder of radius R and length L. The mass balance equation that represents this problem is the following (Bird et al., 2007):

$$\frac{\partial C_P}{\partial t} + \left(v_r \frac{\partial C_P}{\partial r} + v_\theta \frac{1}{r}\frac{\partial C_P}{\partial \theta} + v_z \frac{\partial C_P}{\partial z}\right) = D_E \left[\frac{1}{r}\frac{\partial}{\partial r}\left(r \frac{\partial C_P}{\partial r}\right) + \frac{1}{r^2}\frac{\partial^2 C_P}{\partial \theta^2} + \frac{\partial^2 C_P}{\partial z^2}\right]. \tag{19}$$

The settling of particles affects the distribution of the particle concentration at each point of the horizontal cylinder. Thus, the particle concentration inside the horizontal channel will be modelled as a function of the position of the particles inside the channel and the time: $C_P = C_P(r, \theta, z, t)$.

Equation 19 can be simplified by assuming that the angular velocity of the particle (v_θ) is small compared to the radial velocity (v_r). Thus, v_θ can be neglected. Equation 19 can be written as:

$$\frac{\partial C_P}{\partial t} + \left(v_r \frac{\partial C_P}{\partial r} + v_z \frac{\partial C_P}{\partial z} \right) = D_E \left[\frac{1}{r} \frac{\partial}{\partial r} \left(r \frac{\partial C_P}{\partial r} \right) + \frac{1}{r^2} \frac{\partial^2 C_P}{\partial \theta^2} + \frac{\partial^2 C_P}{\partial z^2} \right]. \tag{20}$$

As in Section 2.1, the radial particle velocity (v_r) is considered to be the projection of the vertical terminal velocity of the particle (v_{pT}) into the radial direction:

$$v_r = v_{pT} \cos\theta = \frac{g\left(\rho_p - \rho_L\right) d_p^2}{18 \mu_L} \cos\theta. \tag{21}$$

In the case of the axial velocity (v_z), it has been shown that it can be represented by the Poiseuille's flow. Equation 20 can now be expressed as:

$$\frac{\partial C_P}{\partial t} + \left[v_{pT} \cos\theta \frac{\partial C_P}{\partial r} + \frac{\Delta P}{4 \mu_L L} R^2 \left(1 - \frac{r^2}{R^2} \right) \frac{\partial C_P}{\partial z} \right] = D_E \left[\frac{1}{r} \frac{\partial}{\partial r} \left(r \frac{\partial C_P}{\partial r} \right) + \frac{1}{r^2} \frac{\partial^2 C_P}{\partial \theta^2} + \frac{\partial^2 C_P}{\partial z^2} \right]. \tag{22}$$

Initially ($t = 0$), it is assumed that the cylinder only contains the fluid travelling through it and there are no particles present inside the cylindrical channel.

$$\text{At } t = 0, \; C_P(r, \theta, z, 0) = 0, \quad 0 \le r \le R, \; 0 \le \theta \le 2\pi, \; 0 \le z \le L. \tag{23}$$

If an open system is considered, at the entrance of the channel ($z = 0$) the suspension of solid particles has a homogeneous constant initial concentration (C_{P0}).

$$\text{At } z = 0, \quad C_P(r, \theta, 0, t) = C_{P0}, \quad 0 \le r \le R, \; 0 \le \theta \le 2\pi. \tag{24}$$

At the exit of the channel ($z = L$) the convection dominates the mass transport; this implies that the concentration gradient due to dispersion in a perpendicular direction to this boundary is negligible. This condition eliminates the need of specifying a concentration or a fixed value for the flux at the outlet boundary, since both of them are unknown. Mathematically this condition can be represented by:

$$\mathbf{n} \cdot \left(-D_E \nabla C_P \right) = 0 \Rightarrow \mathbf{e}_z \cdot \left[-D_E \left(\mathbf{e}_r \frac{\partial C_P}{\partial r} + \frac{\mathbf{e}_\theta}{r} \frac{\partial C_P}{\partial \theta} + \mathbf{e}_z \frac{\partial C_P}{\partial z} \right) \right] = 0, \tag{25}$$

where **n** is the normal vector to the plane at the outlet of the cylinder, $\mathbf{e}_z$, in this case. Solving the dot product, it is found that:

$$\text{At } z = L, \; \frac{\partial C_P}{\partial z} = 0, \quad 0 \le r \le R, 0 \le \theta \le 2\pi. \tag{26}$$

In the vertical axis there are symmetry boundary conditions that can be mathematically represented as:

$$-D_E\left(\frac{1}{r}\frac{\partial C_P}{\partial \theta}\right)+v_\theta C_P=0. \tag{27}$$

Previously it was assumed that the angular velocity of the particle (v_θ) is neglected, therefore:

$$\text{At } \theta=0,\ \frac{\partial C_P}{\partial \theta}=0\ ,\quad 0\le r\le R,\ 0\le\ z\le L. \tag{28}$$

$$\text{At } \theta=\pi,\ \frac{\partial C_P}{\partial \theta}=0\ ,\quad 0\le r\le R,\ 0\le z\ \le L. \tag{29}$$

The particle concentration is finite along the radial direction for all the angles and lengths:

$$\text{At } 0\le\ r\ \le R,\ C_P=\textit{finite}\ ,\quad 0\le\theta\le 2\pi,\ 0\le z\le L. \tag{30}$$

The walls of the channel represent a physical boundary where there is no mass exchange between the interior and exterior of the cylinder. This is an insulation boundary that will prevent any particle from leaving the channel and gather all them at the bottom. The insulation boundary means that there is no convective or dispersive flux across that boundary. This can be represented by:

$$-D_E\left(\frac{\partial C_P}{\partial r}\right)+v_r C_P=0\ . \tag{31}$$

Then:

$$\text{At } r=R,\ -D_E\frac{\partial C_P}{\partial r}+\left(v_{pT}\cos\theta\right)C_P=0\ ,\quad 0\le\theta\le 2\pi,\ 0\le z\le L. \tag{32}$$

The convective-dispersive model is a linear second order parabolic partial differential equation. A numerical solution based in the finite element method was used in this work. Computational fluid dynamics software was used to apply the method.

3.2 Effect of the fluid medium properties on the dispersion coefficient

This section is dedicated to study the variation of the dispersion coefficient (D_E) respect to changes in the properties of the fluid medium and the initial concentration of particles. For this study, experimental data collected from a previous work (Loria et al., 2010) was employed.

Figure 5 shows the behaviour of the dispersion coefficient with respect to an increase of density and viscosity of the fluid medium. It can be observed that as the fluid medium becomes denser and more viscous the dispersion coefficient decreases because particles lose their ability to move from high concentrated areas to low concentrated ones.

Figure 6 shows the variation of the dispersion coefficient with respect to a change of the fluid velocity. It can be observed that as fluid velocity increases the dispersion coefficient decreases. In this case an increase in the fluid velocity causes an increase in the axial velocity of the particles, enhancing their ability to remain suspended and reducing their capacity to move from high concentrated areas to low concentrated ones, causing a decrease in the dispersion coefficient.

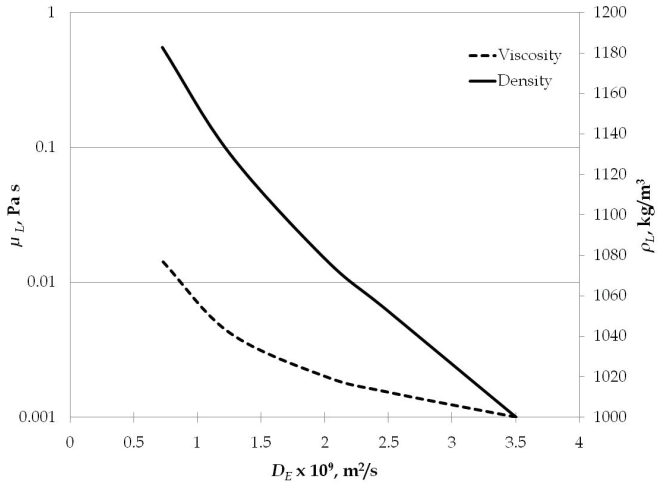

Fig. 5. Dispersion coefficient (D_E) as a function of the viscosity (μ_L) and density (ρ_L) of the fluid medium in a horizontal cylinder

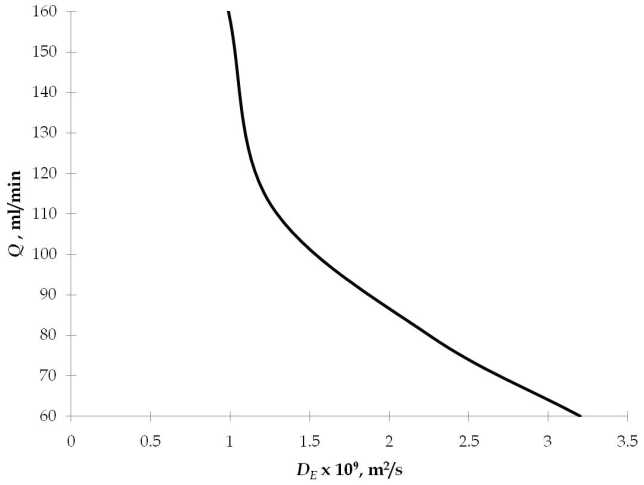

Fig. 6. Dispersion coefficient (D_E) as a function of the fluid velocity (Q) of the fluid medium in a horizontal cylinder

Several works regarding axial dispersion coefficients in horizontal channels were found in the reviewed literature. Nevertheless, large part of this literature is advocated to aerosol particles flowing through airways. For instance, Zhang et al. (2005) and Schulz et al. (2000) have studied the aerosol particle dispersion coefficients to determine how many and where these particles are deposited in the human respiratory system. Giojelli et al. (2001) have focused their attention to study the dispersion coefficients for aerosol particles separation from biogas produced by sludge coming from wastewaters. The typical orders of magnitude

for dispersion coefficients employed in the previously described processes were around 10^{-4} m^2/s, which is not by any means comparable to the ones obtained in the previously referred work (Loria et al., 2010), since totally different materials are involved in the mass transfer of the studied phenomena.

The dispersion of a solute in a laminar Poiseuille's flow to measure diffusion coefficients of proteins and macro-molecules was studied by Bello et al.(1994). Their experimental measurements of the diffusion coefficients gave values that varied from 10^{-8} to 10^{-11} m^2/s. Even though these results are closer to the dispersion coefficients calculated the work from Loria et al. (2010), they cannot serve as a standard of comparison, since the diameter of these molecules is reduced to a few nanometers and the vessels where these authors evaluated the diffusion coefficients were capillaries with 50 to 100 μm of inner diameter.

3.3 Ultradispersed catalytic particles immersed in bitumen at upgrading temperatures transported through a pipeline

This section is dedicated to the application of the three-dimensional convective-dispersive model to a large scale case which involves the transport of MoO_3 catalytic particles immersed in Athabasca bitumen, at upgrading conditions (340-380 °C), through a pipe of 100 m length and 101.6 cm diameter.

The simulations in this section have two different goals. The first is to find the critical diameter to avoid particle deposition. The second is to calculate the deposited particle mass at the bottom of the pipe once the steady state has been reached.

As in the previous section, the density (ρ_L) and viscosity (μ_L) of the Athabasca bitumen at five different temperatures ranging from 340 to 380 °C were employed in the simulations for this section. These physical properties of the Athabasca bitumen at the temperatures of interest were shown in Table 1.

In this section, twelve different MoO_3 particle diameters were used for the simulations: 1, 10, 50, 100, 150, 200, 250, 300, 400, 500, 1000 and 1500 nm. The initial MoO_3 particle concentration (C_{P0}) that was applied to all the simulations was 1.2526 mol/m^3, equivalent to 180.3 ppm.

A fluid velocity (Q) of 30000 ml/min (5×10^{-4} m^3/s or 272 bbd) was chosen in order to have a large volumetric flux and, also, to maintain a laminar regime inside the pipe. Taking into account that the pipe diameter is d = 101.6 cm, the mean axial velocity ($\overline{v}_z = Q/(\pi\, d^2/4)$) is 6.17×10^{-4} m/s. This value permits the calculation of the fluid Reynolds number ($Re = \rho_L\, \overline{v}_z\, d/\mu_L$) which estimates if a fluid is laminar or turbulent.

Table 3 shows the different values of the fluid Reynolds number for the Athabasca bitumen transported through a pipe at the 5 different studied temperatures. Also, Table 3 shows the pressure drop (ΔP) between the ends of the pipe which was calculated using Equation 18.

T, °C	ρ_L, kg/m³	μ_L, cP	ΔP, mPa	Re
340	884.7	2.71	5.18	204
350	877.2	2.42	4.63	227
360	869.4	2.38	4.55	229
370	856.4	2.27	4.34	236
380	843.7	2.17	4.15	244

Table 3. Fluid Reynolds numbers and pressure drop between the ends of the pipe at the 5 different studied temperatures

Table 3 reports fluid Reynolds numbers <2100 and small values of pressure drop between the ends of the cylinder which demonstrates that a laminar flow is maintained across the pipe at any of the 5 different studied temperatures. Generally, a fluid is laminar if the Reynolds number is between 0 and 2100 (Bird et al., 2007).

The calculation of the dispersion coefficient that was employed for these simulations was based on the results that were obtained when the three-dimensional convective-dispersive model was validated with Fe_2O_3 particles immersed in mixtures of water and glycerol (Loria et al., 2010). These results were taken into account because particle properties and concentration as well as the fluid medium characteristics and axial velocities used in that experiments are similar to those present in the simulations carried out in this section.

The dispersion coefficient calculation was carried out in a similar way as in Section 2.3: polynomial interpolations were carried out with the data from Figure 5 and Figure 6 (μ_L and ρ_L vs. D_E and $\overline{v}_z$ vs. D_E); then, for each temperature three different values of D_E were obtained (based on μ_L, C_{P0} and in $\overline{v}_z$) and their average was recorded; finally, the 5 different D_E average values (corresponding to each studied temperature and ranging from 2.1 - 2.18 × 10^{-9} m^2/s) were averaged and the final D_E value was obtained. The D_E value obtained from these calculations resulted to be 2.14 × 10^{-9} m^2/s.

A total of 60 different simulations were carried out in this section (based on the 12 different particle diameters and 5 different temperatures). Computational fluid dynamics was used to perform the simulations; each simulation was carried out up to a time of 1.5 × 10^7 s (4167 h), a time long enough to reach the steady state in each one of them. 9878 grid points were employed for the solution of each simulation and their computing time was around 240 s.

One subject of interest in this study is the critical particle diameter for deposition. In order to measure this parameter, the following analysis was conducted.

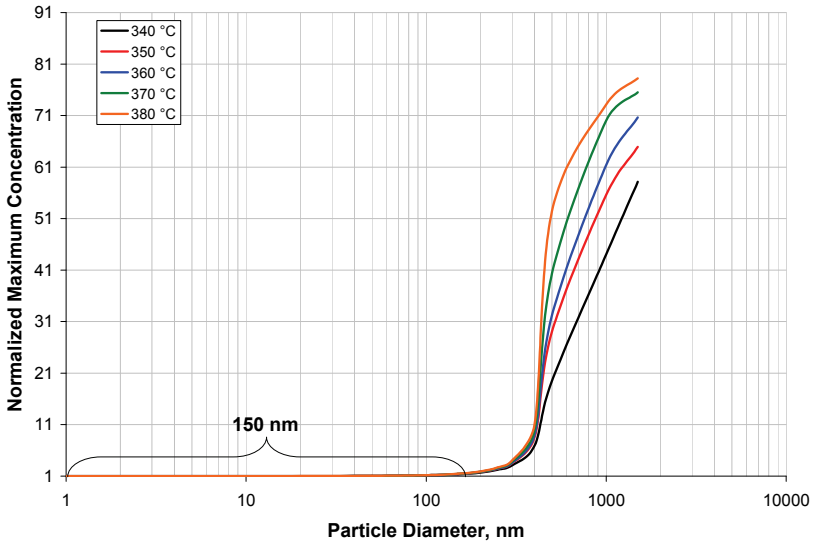

Fig. 7. Effect of the particle diameter and temperature on the deposition of MoO_3 particles immersed in Athabasca bitumen flowing through a pipe

The normalized maximum particle concentration, which in this case is the concentration that is found at the exit bottom of the horizontal cylinder after the simulation time (steady state) divided by the initial concentration, was calculated for each simulation. This normalized maximum particle concentration was plotted against the particle diameter in order to observe at which particle diameter the maximum particle concentration becomes significant. Figure 7 represents the behaviour of the normalized maximum particle concentration at different particle diameters and temperatures.

As temperature increases for a specific particle diameter, the normalized maximum concentration increases and as the particle diameter increases, the normalized maximum concentration increases for a specific temperature. It can also be observed that a change in particle diameter have a more pronounced effect over the normalized maximum concentration than a change in temperature.

In the particle diameter axis, there is a zone for values lower than 150 nm where the normalized maximum concentration is equal to the initial independently of the temperature. This means that MoO_3 particles smaller than 150 nm will remain flowing through the Athabasca bitumen after a long period of time (1.5×10^7 s) in the range of temperatures from 340 to 380 °C.

The following procedure was employed for the calculation of the deposited mass of the catalytic particles along the bottom of the pipe once the steady state has been reached.

Assuming that the deposited particles filled a small horizontal section of height H at the bottom of a cylinder of radius R and length L, its volume (V_P) can be calculated by:

$$V_P = L\left[\cos^{-1}\left(\frac{R-H}{R}\right)R^2 - \sqrt{H(2R-H)}(R-H)\right]. \tag{33}$$

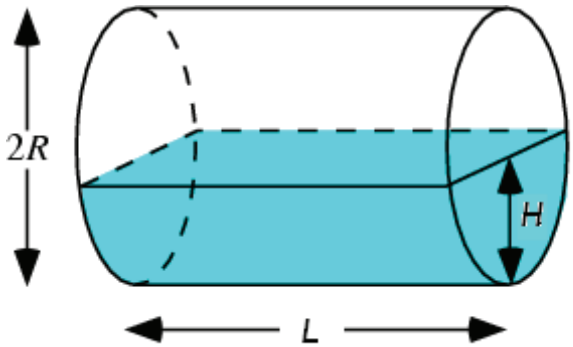

Fig. 8. Horizontal section of height H at the bottom of a cylinder of radius R and length L

Assuming that the height of this small gap is approximately H = 3.5 cm (based on graphics from the simulations), the volume of the small horizontal section (V_P) for a cylinder of 101.6 cm of radius and 100 m of length is 0.871 m^3.

The average particle concentration ($\bar{C}_{P\max}$) at the bottom of the channel and across the length L of the cylinder after a long period of time ($t = 1.5 \times 10^7$ s) can be estimated by:

$$\bar{C}_{P\max} = \frac{\int_0^L C_P(L)\,dL}{L}. \tag{34}$$

The different concentrations along the bottom of the cylinder can be retrieved from the simulation results; with these data the integral in Equation 34 can be evaluated using the Simpson's rule for the solution of numerical integrals (Carnahan et al., 1969).
The mass of particles deposited at the bottom of the channel (M_P), enclosed in the partial volume (V_P) with height H, is:

$$M_P = \bar{C}_{P\max} V_P . \tag{35}$$

On the other hand, the total mass of particles that entered to the tank (M_{PT}) after a long period of time (t = 1.5 × 10^7 s) can be estimated by:

$$M_{PT} = QC_{P0}t . \tag{36}$$

Considering that the initial particle concentration (C_{P0}) in the simulation was assumed to be 180.3 ppm or 1.2526 mol/m^3 and that the volumetric flux is Q = 5 × 10^{-4} m^3/s, the total particle mass that entered to the cylinder after 1.5 × 10^7 s was 1352 kg. The percentage of deposited particles at the bottom of the spherical tank (%M_{dep}) can be calculated by Equation 11.

	%M_{dep}				
d_p, **nm**	**340 °C**	**350 °C**	**360 °C**	**370 °C**	**380 °C**
1500	0.488	0.565	0.615	0.657	0.681
1000	0.372	0.484	0.534	0.610	0.637
500	0.142	0.203	0.218	0.264	0.327
400	0.056	0.067	0.070	0.076	0.084
300	0.029	0.031	0.032	0.034	0.035
250	0.022	0.023	0.024	0.024	0.025
200	0.017	0.018	0.018	0.019	0.019
150	0.015	0.015	0.015	0.015	0.015
100	0.013	0.013	0.013	0.013	0.013
50	0.012	0.012	0.012	0.012	0.012
10	0.012	0.012	0.012	0.012	0.012
1	0.012	0.012	0.012	0.012	0.012

Table 4. Percentage of deposited particles at the bottom of the horizontal cylinder (%M_{dep}) containing MoO_3 particles immersed in Athabasca bitumen at different temperatures

The percentage of deposited particles at the bottom of the spherical tank (%M_{dep}) at different temperatures and particle diameters is shown in Table 4 and Figure 9.
In Figure 9, it can be observed that after the studied time, less than 0.1 % of the total mass of particles, with diameters lower than 400 nm, has been deposited; whereas the percentage of deposited particles, with diameters in the range 400 – 1500 nm, is between 0.1 and 0.68 %.

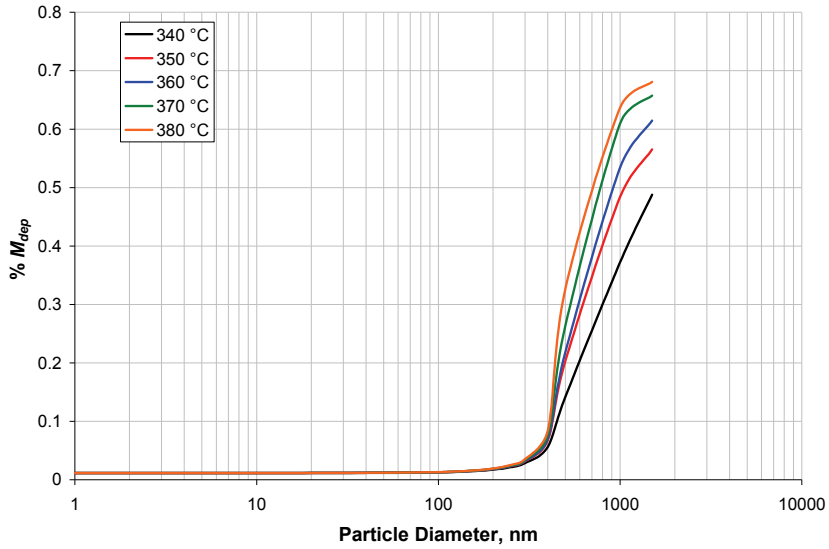

Fig. 9. Percentage of deposited particles at the bottom of the cylindrical channel (%M_{dep}) at different temperatures and particle diameters for the deposition of MoO_3 particles immersed in Athabasca bitumen flowing through a pipe

4. Conclusion

The results from these simulations unveiled the particle diameter and fluid medium properties that are necessary to ensure particle suspension and mobility in bitumen. In the case of the spherical storage tank simulation, it was found that MoO_3 particles smaller than 150 nm will remain suspended in bitumen at temperatures from 340 to 380 °C after a long period of time (27778 h) Also, it was shown that the percentage of deposited particles at the bottom of the tank after this period of time is less than 0.02 % when particles diameters below 200 nm are utilized.

Regarding the simulations applied to the flow of particles through a horizontal pipeline, the results demonstrated that particles smaller than 150 nm will remain flowing through bitumen after a long period of time (4167 h) in the range of temperatures from 340 to 380 °C. In addition, the modelling results showed the percentage of settled particles at the bottom of the cylinder after this period of time when a particle deposition scenario is presented. It was observed that less than 0.1 % of the total mass of particles (that passed through the cylinder during this time), with diameters lower than 400 nm, were deposited at the bottom.

Based on these results, it seems that when MoO_3 catalytic particles with diameters lower than 400 nm (nanometric range) are immersed in bitumen either in a stagnant or a flow scenario, almost all the particles will remain suspended in the system. Therefore, this kind of particles could be employed as ultradispersed catalysts for bitumen hydroprocessing reactions. It would be interesting to compare these models with experimental data from real systems; however, on line tools for the particle concentration measurement would have to be developed in order to achieve this objective.

5. Acknowledgment

This work was supported in part by the National Council for Science and Technology of Mexico, The Alberta Ingenuity Centre for In Situ Energy funded by the Alberta Ingenuity Fund and the industrial sponsors: Shell International, ConocoPhillips, Nexen Inc, Total Canada and Repsol-YPF, and The Schulich School of Engineering at the University of Calgary, Canada.

6. References

Adamczyk, Z. & Van De Ven, T. G. M. (1981). Deposition of Particles under External Forces in Laminar Flow through Parallel-plate and Cylindrical Channels. Journal of Colloid and Interface Science, Vol. 80 No. 2 pp. 340-356

Bello, M. S., Rezzonico, R. & Righetti, P. G. (1994). Use of Taylor-Aris Dispersion for Measurement of a Solute Diffusion Coefficient in Thin Capillaries. Science, Vol. 266 No. 5186 pp. 773-776

Bird, R. B., Stewart, W. E. & Lightfoot, E. N. (2007). Transport Phenomena, J. Wiley, New York

Carnahan, B., Luther, H. A. & Wilkes, J. O. (1969). Applied Numerical Methods, Wiley, New York

d'Orlyé, F., Varenne, A. & Gareil, P. (2008). Determination of Nanoparticle Diffusion Coefficients by Taylor Dispersion Analysis using a Capillary Electrophoresis Instrument. Journal of Chromatography A, Vol. 1204 No. 2 pp. 226-232

Franco, A. (May, 2008). Transport Phenomena, Available from http://www.sc.ehu.es/sbweb/fisica/transporte

Fung, Y. C. (1993). Biomechanics: Mechanical Properties of Living Tissues, Springer, New York

Galarraga, C. E. & Pereira-Almao, P. (2010). Hydrocracking of Athabasca Bitumen Using Submicronic Multimetallic Catalysts at Near In-Reservoir Conditions. Energy & Fuels, Vol. 24 No. 4 pp. 2383-2389

Giojelli, B., Verdier, C., Hihn, J. Y., Béteau, J. F. & Rozzi, A. (2001). Identification of Axial Dispersion Coefficients by Model Method in Gas/Liquid/Solid Fluidised Beds. Chemical Engineering and Processing, Vol. 40 No. 2 pp. 159-166

Loria, H., Pereira-Almao, P. & Satyro, M. (2009a). Prediction of Density and Viscosity of Bitumen Using the Peng-Robinson Equation of State. Industrial & Engineering Chemistry Research, Vol. 48 No. 22 pp. 10129-10135

Loria, H., Pereira-Almao, P. & Scott, C. E. (2009b). A Model To Predict the Concentration of Dispersed Solid Particles in an Aqueous Medium Confined inside Horizontal Cylindrical Channels. Industrial & Engineering Chemistry Research, Vol. 48 No. 8 pp. 4088-4093

Loria, H., Pereira-Almao, P. & Scott, C. E. (2009c). A Model To Predict the Concentration of Submicrometer Solid Particles in Viscous Media Confined inside Horizontal Cylindrical Channels. Industrial & Engineering Chemistry Research, Vol. 48 No. 8 pp. 4094-4100

Loria, H., Pereira-Almao, P. & Scott, C. E. (2010). Model To Predict the Concentration of Ultradispersed Particles Immersed in Viscous Media Flowing through Horizontal Cylindrical Channels. Industrial & Engineering Chemistry Research, Vol. 49 No. 4 pp. 1920-1930

Loria, H., Trujillo-Ferrer, G., Sosa-Stull, C. & Pereira-Almao, P. R. (2011). Kinetic Modeling of Bitumen Hydroprocessing at In-Reservoir Conditions employing Ultradispersed Catalysts. Energy & Fuels, *In Press*

Massabò, M., Catania, F. & Paladino, O. (2007). A New Method for Laboratory Estimation of the Transverse Dispersion Coefficient. Ground Water, Vol. 45 No. 3 pp. 339-347

Michaelides, E. E. (2006). Particles, Bubbles & Drops: Their Motion, Heat and Mass Transfer, World Scientific, New Jersey

Pereira-Almao, P. (2007). Fine Tuning Conventional Hydrocarbon Characterization to Highlight Catalytic Upgrading Pathways, Proceedings of Variability of the Oil Sands Resource Workshop, Lake Louise, AB, May 1-4, 2007

Pereira-Almao, P., Hill, J., Wang, J. & Vasquez, A. (2005). Ultra Dispersed Catalyst for Processing Heavy Hydrocarbon Fractions, Proceedings of AICHE, 2005 Spring National Meeting, Atlanta, GA, USA

Pereira-Almao, P. R., Ali-Marcano, V., Lopez-Linares, F. & Vasquez, A. (2007).Ultradispersed Catalysts Compositions and Methods of Preparation. WO 2007/059621 A1, 2007.

Perry, R. H. (1997). Perry's Chemical Engineers' Handbook, McGraw-Hill, New York

Ramalho, R. S. (1983). Introduction to Wastewater Treatment Processes, Academic Press, New York

Robbins, G. A. (1989). Methods for Determining Transverse Dispersion Coefficients of Porous Media in Laboratory Column Experiments. Water Resources Research, Vol. 25 No. 6 pp. 1249-1258

Schulz, H., Brand, P. & Heyder, J. (2000). Particle Deposition in the Respiratory Tract, In: Particle-Lung Interactions, P. Gehr and J. Heyder, (Ed.), 229-290, Marcel Dekker, New York

Zhang, Z., Kleinstreuer, C., Donohue, J. F. & Kim, C. S. (2005). Comparison of Micro- and Nano-size Particle Depositions in a Human Upper Airway Model. Journal of Aerosol Science, Vol. 36 No. 2 pp. 211-233

32

Measurement of Liquid Velocity and Liquid Distribution in a Packed Bed Using Electrical Resistance Tomography

H. D. Doan and A. Lohi
Department of Chemical Engineering, Ryerson University, Toronto, ON, Canada

1. Introduction

Packed beds are widely used in industrial mass transfer operations, including absorption, stripping, adsorption and distillation. The packing material offers a large surface area available for heat and mass transfer between gas-liquid or fluid-solid phases for a given volume. Distillation, absorption, adsorption and extraction are typical applications of packed columns. In the design of a packed column, the averaged mass transfer coefficient is usually used and assumed to be constant at all locations in the column. This is due to the fact that studies of mass transfer in a packed bed are generally based on a macroscopic approach. In this approach, the averaged mass transfer coefficient is determined based on the conditions of the inlet and outlet streams without consideration of local fluid dynamic and local mass transfer at different locations within the bed. Local mass transfer in a packed bed is in fact dependent on local liquid velocity. The local mass transfer coefficient thus varies with locations in the packed bed due to the variation of velocity and the random nature of liquid spreading in the bed. Therefore, the use of the averaged mass transfer coefficient often renders uncertainty in design and scaling-up of a packed column.

Among different methods, dissolution (Kumar et al., 1977; Sedahmed et al., 1996; Guo and Thompson, 2001) and gas absorption (Aroonwilas et al., 2003; Linek et al., 2001) are the two popular methods that have been used to obtained the average mass transfer coefficient. More recently, direct measurements of the local mass transfer coefficient in a packed bed was developed using an electrochemical technique (Gostick et al., 2002), and a mathematical model for local mass transfer coefficient in a packed bed was proposed (Dang-Vu et al., 2006a). The mass transfer coefficient is strongly dependent on liquid distribution in a packed bed. Liquid distribution is in turn dependent on the packing size and type, and the design of the liquid distributor.

Several studies on liquid velocity and distribution in a packed column have been carried out using different techniques, such as: liquid collecting method (Hoek et al., 1986; Kouri and Sohlo, 1996; Dang-Vu et al., 2006b), tracing method (Macias-Salinas and Fair, 1999; Inglezakis et al., 2001), conductance probe (Tsochatzidis et al., 2002), and tomographic measurements (Loser et al., 1999; Reinecke and Mewes, 1997; Yin et al., 2002; Bolton et al., 2004; Ruzinsky and Bennington, 2007). The liquid collecting method has been used widely to investigate liquid distribution in a packed column due to its simplicity in measurements

(Hoek et al., 1986; Kouri and Sohlo, 1996; Farid and Gunn, 1978; Kunjummen et al., 2000). In this method, liquid is collected in an array of cells or concentric cylinders at the bed outlet. The liquid collecting duration is also recorded. Liquid velocity obtained from the measured liquid volume is then used to quantify the liquid distribution in the bed. However, the liquid velocity obtained from the liquid collecting method is an axially aggregated flow through the packed bed at a certain radial location, which doesn't reveal the local liquid distribution at various axial distances along the bed. Therefore, in the present study measurements of liquid distribution and velocity at various axial distances in a packed bed were carried out, using electrical resistance tomography (ERT). The ERT system can quantify the liquid distribution and liquid velocity in the packed bed without disturbing the flow field since it is a non-intrusive technique. In addition, measurements at different locations in the packed bed can be measured simultaneously without the need for changing the bed height, which is of advantage over the liquid collecting method.

2. Experimental method

2.1 Apparatus for the electrical resistance tomography

The experimental apparatus consists of a 0.3-m diameter column filled with 2.0-cm polypropylene spheres as shown in Figure 1. The packed bed height of 6 times the column diameter was used. An ERT system (model P2000, Industrial Tomography Systems Ltd., Manchester, UK) was used to measure the flow pattern at 6 axial positions in the packed bed using 6 electrode planes (P1 to P6) located at equal-distance of 0.30 m apart along the axial direction of the bed. In order to avoid disturbance to the flow, electrodes were installed flush with the inside wall of the column. At each electrode plane, 16 stainless-steel electrodes (1.0 cm x 2.0 cm) were arranged at equal distance one to another on the perimeter of the column (Figure 2). All electrodes on the 6 planes were connected to a data acquisition system for data collection. Experiments were performed with a high conductivity tracer (a sodium chloride solution) introduced into the liquid inlet to create a high conductivity front that moved through the packed bed.

In the present study, an electric current was applied to two neighbouring electrodes (e.g. electrodes 1 and 2), and then voltages were measured from the remaining pairs of neighbouring electrodes (e.g. 3 and 4; 5 and 6 .etc...). The electric current was then applied through the next pair of electrodes and the voltage measurements were repeated. Measurements were made within each plane separately and concurrently. 104 individual voltage measurements were collected from each of the 6 planes of electrodes every 100 ms (sampling interval). Those 104 measurements constitute a measurement set. The number of samples per frame (the number of measurement sets that were taken to produce an average frame of data) was set at 8. From the voltage measurements, the ITS System 2000 software uses a linear back-projection image-reconstruction algorithm to convert the data to tomograms that showed the distribution of liquid flow on a 2D plane.

Both upward and downward flow modes were used in the experiments. For the upward flow mode, water was pumped continuously from a holding tank to the bottom of the column. The liquid flow rate was monitored by a rotameter (Model F-45750-LHN12, Fabco Co., Maple, Ontario, Canada). A 0.5% wt salt solution (conductivity = 9.95 $mS.cm^{-1}$) was used as the high conductivity tracer. Five liquid flow rates from 8.83 – 12.6×10^{-4} $m^3.s^{-1}$ (14–20 gpm) were used in the experiments. When the water flow rate in the column had reached a steady state, a 1L aliquot of the tracer solution was injected into the liquid inlet stream to the

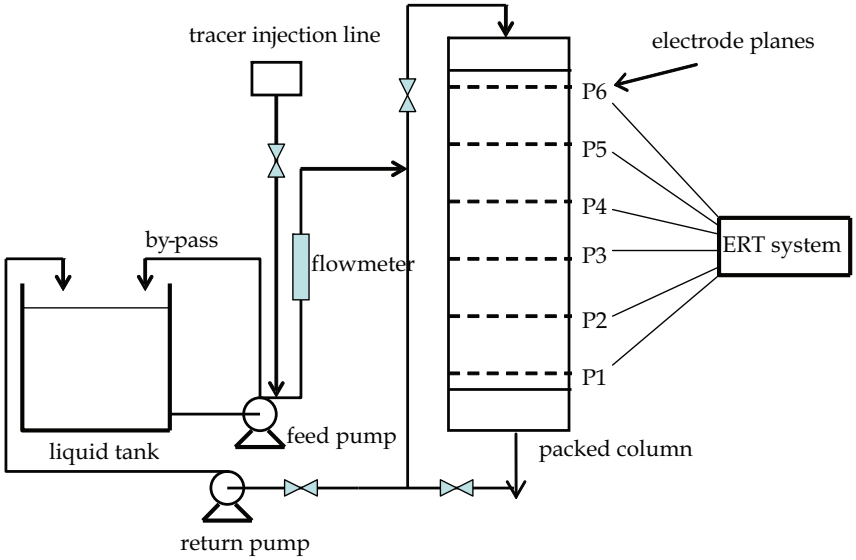

Fig. 1. Schematic diagram of the experimental set-up for ERT

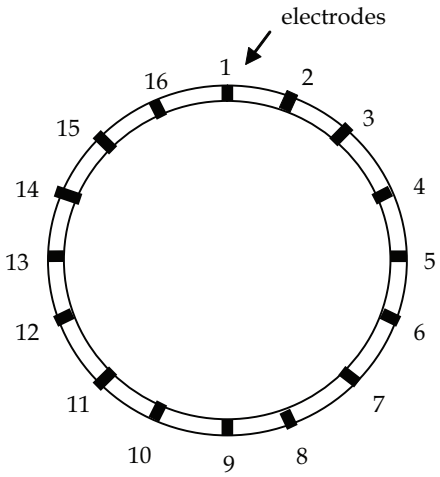

Fig. 2. Arrangement of the electrodes on the column wall

column. A reference in the ERT system was taken before the injection of the tracer. This reference acted as a base line from which the increase in the conductivity was observed when the tracer reached the electrodes. This reference conductivity was about 1.00 mS.cm^{-1}. The ERT system recorded the conductivity profiles at 6 planes along the column simultaneously.

For the downward flow mode, water was pumped to the top of the column. A 1.5% wt salt solution (conductivity = 29.9 mS.cm^{-1}) was used as the tracer for better conductivity measurements due to the liquid hold up and channelling that tended to dilute the tracer

more. Similar conductivity measurement procedure to that for the upward flow was used at various flow rates from 5.05 – 7.57×10^{-4} m^3.s^{-1} (8–12 gpm).
Following the acquisition of data from the boundary of the object to be imaged it is necessary to process this data using an appropriate image reconstruction algorithm. For an ERT system the reconstructed image will contain information on the cross-sectional distribution of the electrical conductivity of the contents within the measurement plane. A square grid with 20 x 20 = 400 pixels represents the vessel interior cross-section. Some of these pixels will lie outside the vessel circumference and the image is therefore formed from the pixels inside the vessel. The circular image is constructed using 316 pixels from the 400 pixel square grid as shown in Figure 3 (ITS System 2000 Version 6 User's Manual, Industrial Tomography System Ltd., Manchester, UK).
The conductivity values of individual pixels can be exported to an Excel file for further analysis. From the time elapse between the advancement of the conductivity peak of an individual pixel from one plane to the next one, the local liquid velocity was determined. From the values of the local velocities, the liquid distribution factor was calculated using Equation (1) below. These values were then compared with the values obtained from the liquid collecting method that is described in the following section.

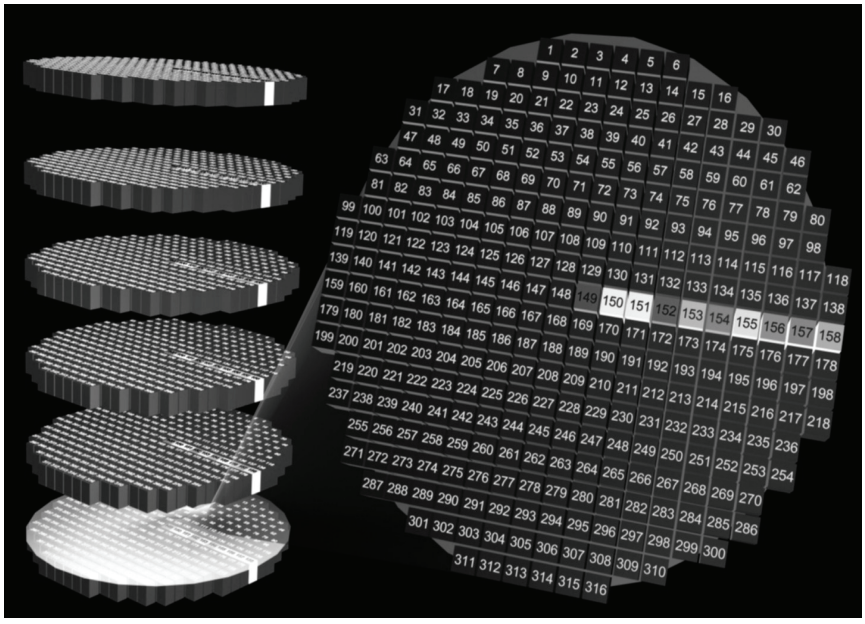

Fig. 3. ERT grid of 316 pixels for the image reconstruction

2.2 Apparatus for the liquid collecting method

In the investigation of liquid distribution, the same 0.3 m diameter PVC column filled with 2.0-cm polypropylene spheres as shown in Figure 1 was used. However, a liquid collector was added to the column as shown in Figure 4. For liquid distribution measurements using the liquid collecting method, only water was used. Two liquid flow rates of 5.05×10^{-4} m^3.s^{-1} and 7.57×10^{-4} m^3.s^{-1} (8 gpm and 12 gpm) were used. For a comparison with the ERT method,

in which only liquid was used, the gas blower was turned off in these experiments. Liquid flowing down the bed was collected in a collector with 39 tubes of 25.4-mm diameter. The tubes were arranged circularly at four different radial positions as shown in Figure 5.

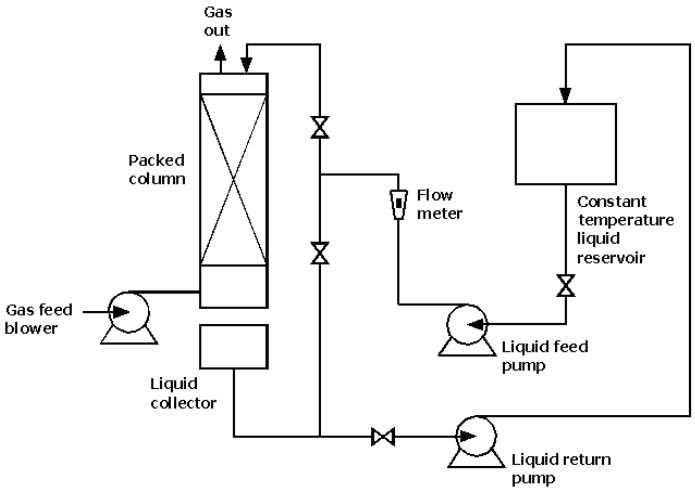

Fig. 4. Experimental set-up for the liquid collecting method

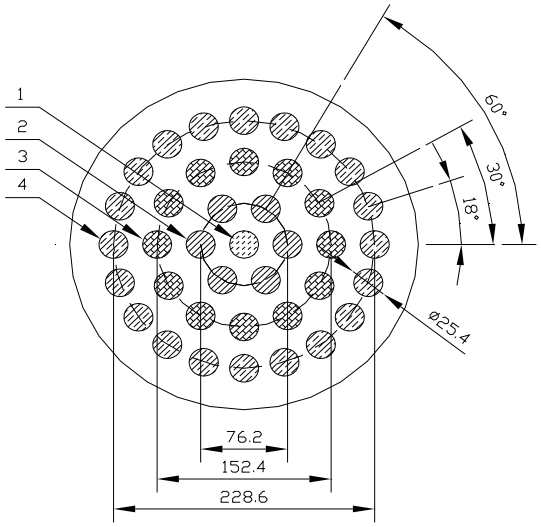

Fig. 5. Schematic diagram of the arrangement of in the liquid collecting tubes: 1. Center section with 1 tube; 2. Inner section I with 6 tubes; 3. Inner section II with 12 tubes; and 4.Outer section with 20 tubes (dimension unit: mm)

Measurements were carried out at three axial levels from the top of the packing: 0.3, 0.6 and 0.9 m. These are equivalent to the ratios of the packing height to the column diameter, x/D,

of 1, 2 and 3. The wall flow was separated from the bulk flow in the packing by an annular ring on the inside wall of the column at the packing support level and collected in a separate container so that it did not interference with the local liquid flow through the packing to the liquid collector described above.
In order to quantify liquid distribution in the packed bed, a liquid distribution factor was used and defined as below (Dang-Vu et al., 2006b):

$$M_F = \frac{1}{n}\sqrt{\sum_{i=1}^{n}\left(1-\frac{V_i}{V_{AVG}}\right)^2} \tag{1}$$

where M_F is the liquid distribution factor, n is the number of liquid collecting tubes, V_i is the liquid velocity to individual collecting tubes and V_{AVG} is the averaged liquid velocity

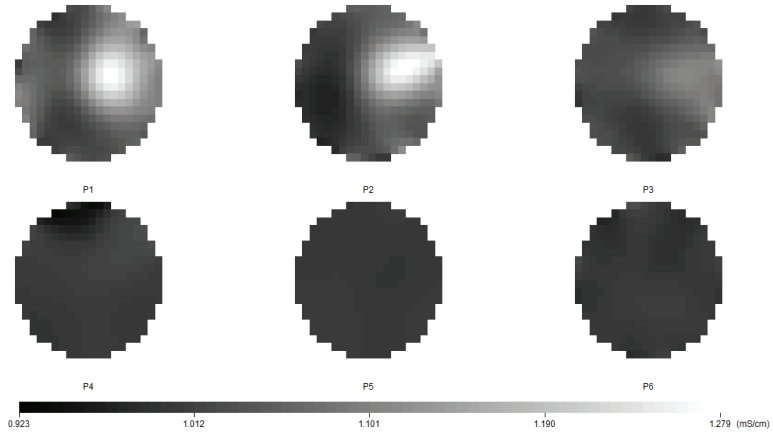

6(a)

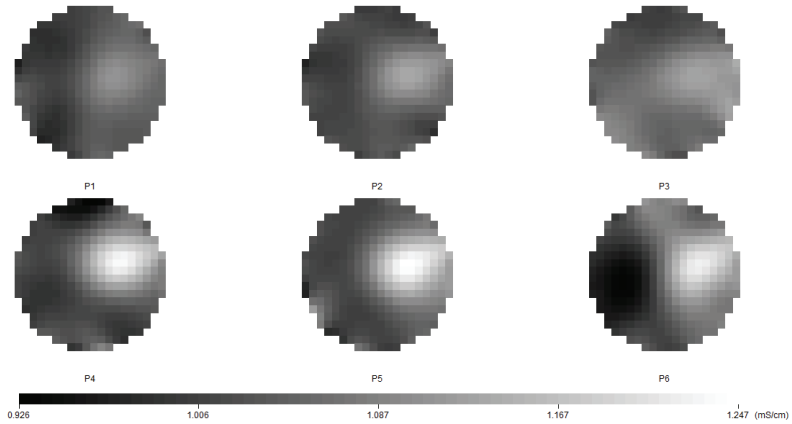

6(b)

Fig. 6. Tomographic images of the conductivity at various planes for upward flow

3. Results and discussion

3.1 Upward flow profile

For the upward flow mode, the high conductivity tracer moved upward with the bulk flow and passed plane 1 to plane 6, consecutively, after the tracer injection. The advancement of the tracer upward through the column can be seen in the tomograms in Figures 6(a) and 6(b). The shade of a region in a tomogram indicates the conductivity of that region in accordance with the conductivity scale in mS/cm as shown below the tomograms.

Some time after the tracer injection, the high conductivity solution reached planes 1 and 2 as indicated by the light spots in the tomograms for P1 and P2 in Figure 6(a). The tomograms at planes 3 to 6 still have a dark shade indicating a low conductivity of the bulk water stream since the tracer solution didn't reach to those planes yet. As time went by, the tracer solution moved farther upward to P4, P5 and P6 as can be seen by the high conductivity regions (light shade) in Figure 6(b) while the conductivities at P1, P2 and P3 decreased (dark shade at those planes) since the tracer solution had moved out of those regions.

Using the mean conductivity data across a plane, conductivity peaks can be identified when the tracer has reached successive planes as shown in Figure 7. The distance between the peaks represent the time for the tracer to move between the planes. From the conductivity peaks and the time elapsed between two peaks, the liquid velocity from one plane to the next one was determined. It was noted that in the upward flow mode, a steady flow and a more even distribution of conductivity across a plane were obtained. The velocities at different planes are comparable to one another and the average velocity throughout the packed bed. This might be due to the fact that the liquid almost moved up the column in a plug flow pattern. The flow pattern wasn't distorted by liquid hold-up or liquid channelling. The ERT measurements of the liquid velocity were within 5% with the interstitial velocities calculated from the averaged liquid flowrate measured by a flowmeter and the bed porosity (Figure 8).

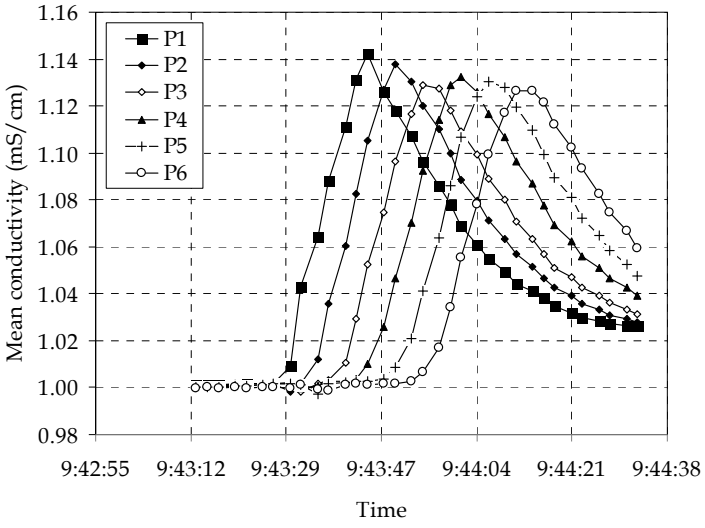

Fig. 7. Mean conductivity at various planes for the upward flow

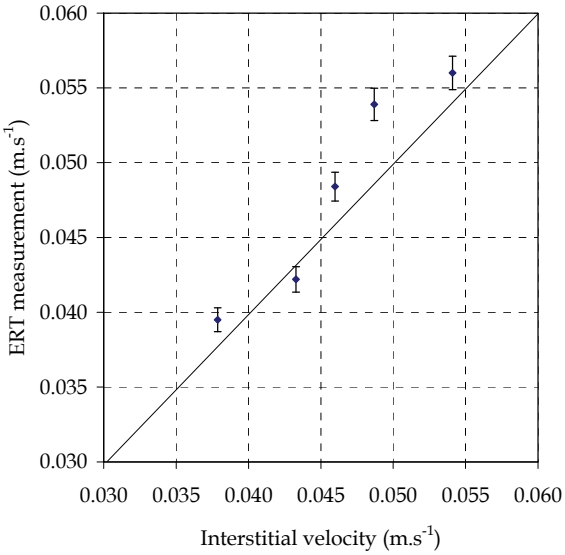

Fig. 8. Comparison of liquid velocity measured by the ERT and the flowmeter

3.2 Trickle flow profile

Tomograms for the trickle flow mode are shown in Figures 9(a) and 9(b). In addition, the variations of the mean conductivities at individual planes with time are presented in two separate graphs, for clarity, in Figures 10(a) and (b). Tomographic images were recorded at six different heights downstream from the top of the column. The high conductivity tracer moved from plane 6 (P6) downwards to plane 1 (P1) after injection, as indicated by the high conductivity regions of light shade in the tomograms in Figures 9(a) and 9(b). When the column is operated in the trickle flow mode, the advancement of the high conductivity plane was not as clear as those obtained with the upward flow. The tomograms show successive increases in conductivity from plane 6 (P6) at the top of the bed to plane 1 (P1) at the bottom of the bed. However, the high conductivity liquid remains at a plane for a period longer than that observed with the upward flow mode. At times, high conductivity profiles of multiple planes overlapped since the high conductivity front didn't move from one plane to another in pulses, i.e. no distinctive peaks at individual planes at different time steps. Less pronounced and broader mean conductivity distribution was observed as shown in Figures 10(a) and (b). This might be due to liquid hold-up in the packed bed under the trickle flow mode. Liquid tends to linger in the void space of the packing before moving downward the column.

For the trickle flow, the conductivity peaks were not very distinctive from one plane to another. Therefore, liquid residence time in the column was used as an indicator for the liquid flow. A theoretical residence time was also calculated using the interstitial liquid velocity, which was determined from the average flow rate measured by a flowmeter and the void fraction of the bed. The ERT-measured residence time was shorter at a higher flow rate, as expected. The residence time determined from the ERT data also followed a trend similar to that of the theoretical residence time, as shown in Figure 11. For varied liquid flowrates from 5.05 – 7.57×10^{-4} m^3.s^{-1}, the theoretical residence times were about 1.5 -2.0

times those predicted from the ERT data. It appeared that the deviation between the two residence times increased with liquid flow rate. The theoretical residence time based on the volumetric flow rate measurement and the bed void volume was unable to account for the effect of the liquid hold–up, the liquid channelling and the wall flow in the packed bed. In addition, it is relevant to note that the theoretical residence time was based on the whole void space, and the liquid was assumed to fill all the void space in the packed bed before eluting out at the bottom of the column. As a result, the residence time tended to be long. On the other hand, the actual liquid flow might have channelled through the packed bed; hence, by-passed some of the void space resulting in a shorter residence time as shown by the ERT measurement. This might be considered as an advantage of the ERT system in capturing the real flow distribution in the packed bed.

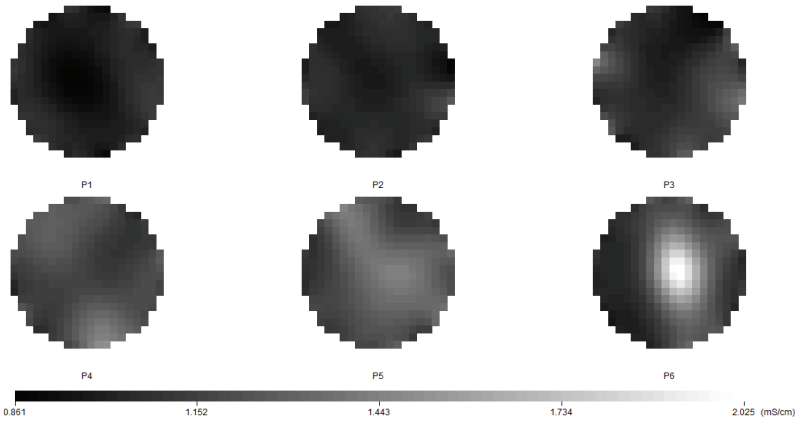

9(a)

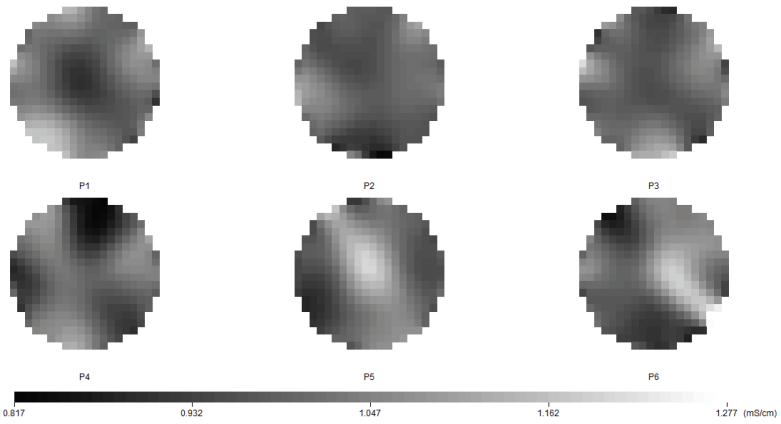

9(b)

Fig. 9. Tomographic images of the conductivity at various planes for trickle flow

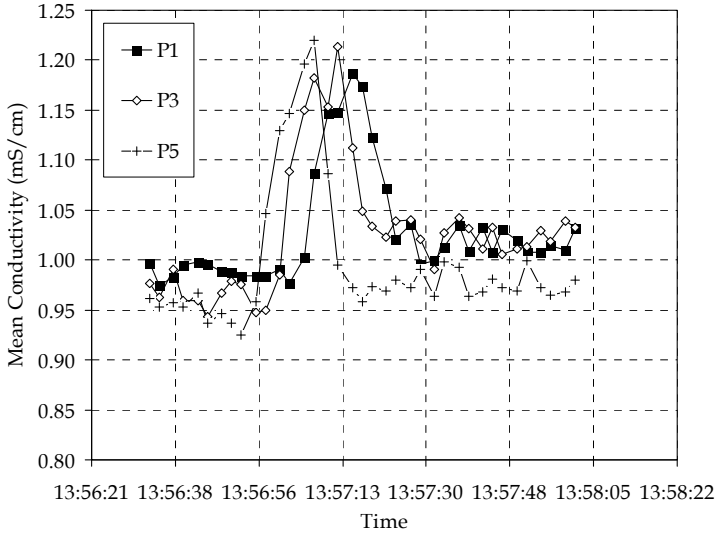

10(a)

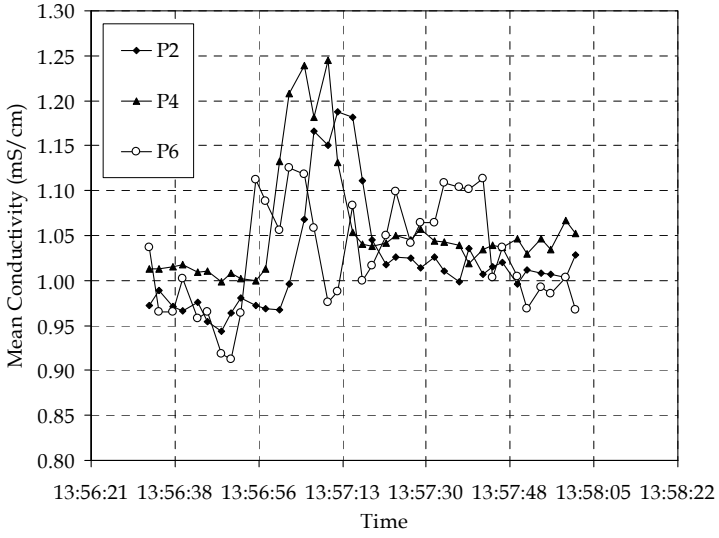

10(b)

Fig. 10. Mean conductivity at various planes for the trickle flow

Liquid distribution factors estimated by Equation (1) using the liquid velocities obtained by the liquid collecting method and the ERT method at two liquid flowrates are plotted in Figure 12. As can be seen in Figure 12, the liquid distribution factor obtained from the ERT technique follows a similar trend of that obtained from the liquid collecting method. This indicates that the ERT method was suitable for the measurement of liquid distribution in a packed column. Moreover, the ERT method allows for measurements of liquid distribution at multiple axial

distances concurrently. This is an advantage over the liquid collecting method, which can only measure the aggregated liquid distribution at one bed height at a time.

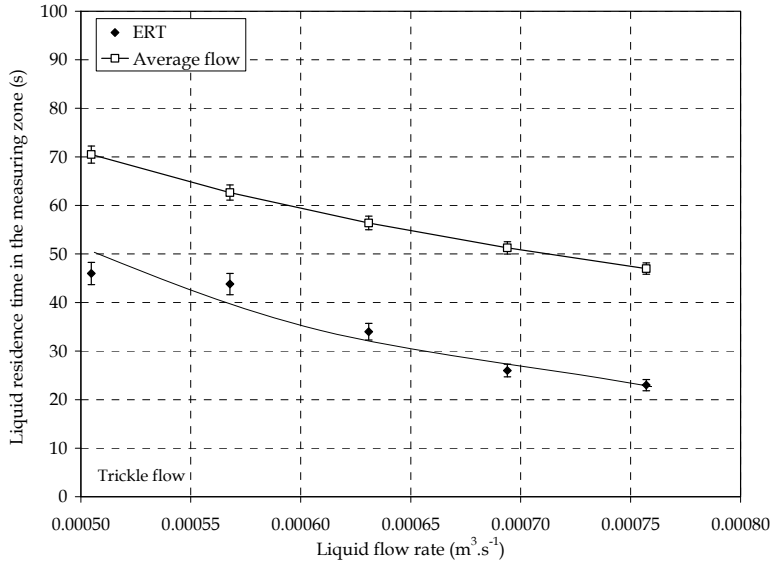

Fig. 11. Liquid residence times estimated from the ERT measurements and the calculated values from the average flowrate measured by a flowmeter

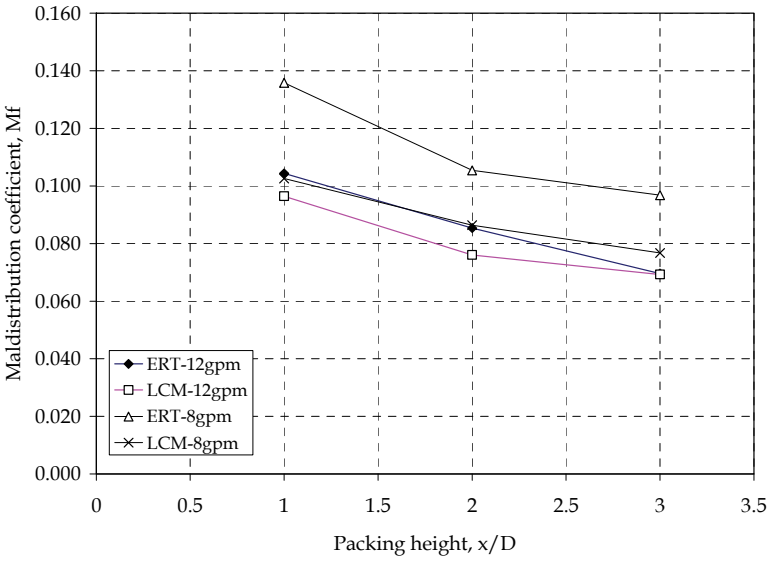

Fig. 12. Liquid distribution factor obtained by the liquid collecting method and the ERT technique

As can be seen in Figure 12, the liquid distribution factor decreased with the bed height and liquid flowrate, as expected. This is in agreement with the results obtained and reported by other researchers (Hoek et al., 1986; Kouri and Sohlo, 1996; Dang-Vu et al., 2006b). At both liquid flowrates, the liquid distribution factors obtained by the ERT method are higher than those obtained by the liquid collecting method. This might be due to the fact that the number pixels used in the ERT method was 316, i.e. the cross-sectional area of the column was divided into 316 segments, while the number of liquid collecting tubes was only 39. The liquid streams collected in the collecting tubes covered a significant portion of the cross-sectional area of the column as compared with the local velocities obtained by the ERT method. Therefore, the liquid streams collected in the liquid collecting method were averaged out resulting in a more even liquid distribution as indicated by the lower liquid distribution factor.

Figures 13 and 14 show the distribution of liquid conductivity over the whole cross-section of the column at the top plane (P6) and at P4 that was at 60 cm downward the column from P6. The axes labelled as direction are the two directions enclosing the cross-section of the column with the column center being at the center of the bar graph. As can be seen in these figures, liquid conductivity was more even at plane 4, indicating a better liquid distribution at this plane. When the tracer was introduced into the top of the column, it trickled down the column with the main liquid flow. There was some level of liquid mal-distribution at the top section of the packed bed. Therefore, the liquid distribution was less even, as indicated by a higher level of variation of the liquid conductivity at top plane (P6) with a standard deviation of 0.149 as compared with the value of 0.062 at P4. Moreover, this also indicates that the liquid conductivity measured by the ERT method could be used as an indicator for liquid distribution at various axial distances along the packed bed

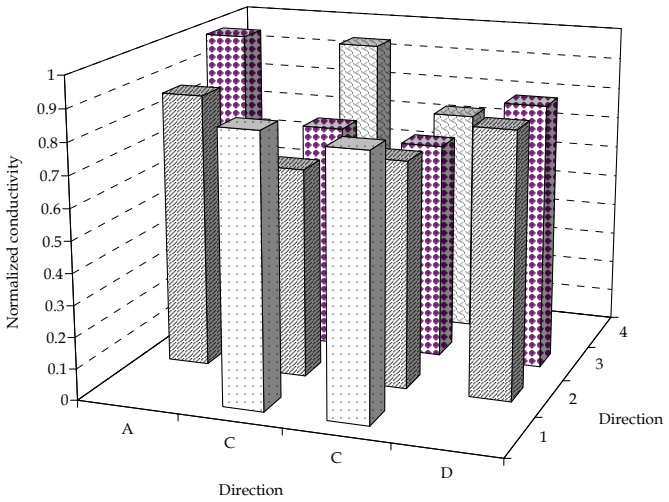

Fig. 13. Distribution of the conductivity across the column area at top plane (or P6)

4. Conclusion

In the present study, the ERT system was successfully applied to measure liquid flow distribution at varied axial distances along a packed bed without disturbing the flow profile.

In the upward flow mode, the liquid velocity and flow rate measured by the ERT system agreed to the velocity measured independently by a flow meter within 5%. A qualitative view of the images generated by the ERT system also provides information on the distribution within each plane. In addition, the ERT system could be used to capture radial and axial liquid maldistribution as well as liquid channelling in a trickle flow mode. For the trickle flow mode, the liquid residence time measured by the ERT method followed a similar trend of that calculated from the interstitial liquid velocity, which was determined from the liquid flowrate to the column and the packed bed characteristics. However, the calculated liquid residence time was about 1.5 – 2 times higher than that measured by the ERT method. This indicates the capability of the ERT method to capture the effect of liquid channelling, liquid hold-up and the wall flow on the actual liquid flow in a packed bed. The calculated superficial velocity is inaccurate since it is only true under an ideal condition with a perfect liquid distribution in the packed bed, which doesn't exist in reality.

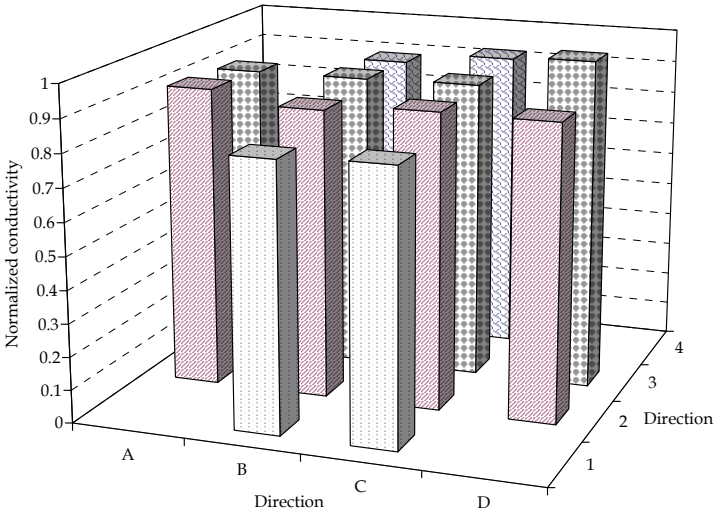

Fig. 14. Distribution of the conductivity across the column area at plane 4 (or P4 at 60 cm down the column from top plane)

5. Acknowledgement

Financial support from the National Science and Engineering Research Council of Canada (NSERC) for the purchase of the ERT system used in this project is highly appreciated. In addition, we would like to thank T. Vu and A. Nguyen for their assistance in the laboratory.

6. References

Aroonwilas, A.; Chakma, A.; Tontiwachwuthikul, P. & Veawab, A. (2003). Mathematical modeling of mass transfer and hydrodynamics in CO_2 absorbers packed with structured packings. *Chem. Eng. Sci.* Vol. 58, pp. 4037 – 4053.

Bolton, G. T.; Hooper, C.W.; Mann, R. & Stitt, E.H. (2004). Flow distribution and velocity measurement in a radial flow fixed bed reactor using electrical resistance tomography. *Chem. Eng. Sci.* Vol. 59, pp. 1989 – 1997.

Dang-Vu, T.; Doan, H.D. & Lohi, A. (2006a). Local mass transfer in a packed bed: Experiments and Model. *Ind. Eng. Chem. Res.* Vol. 45, pp. 1097-1104.

Dang-Vu, T.; Doan, H.D.; Lohi, A. & Zhu, Y. (2006b). A new liquid distribution factor and local mass transfer coefficient in a random packed bed. *Chem. Eng. J.* Vol.123, pp. 81 – 91.

Farid, M. M. & Gunn, D.J. (1978). Liquid distribution and redistribution in packed columns--II. Experimental. *Chem. Eng. Sci.* Vol. 33, pp. 1221 – 1231.

Gostick, J.; Doan, H.D.; Lohi, A. & Pritzker, M. (2002). Investigation of local mass transfer in a packed bed using a limiting current technique. *Ind. Eng. Chem. Res.* Vol. 42, pp. 3626 – 3634.

Guo, G. & Thompson, K.E. (2001). Experimental analysis of local mass transfer in packed beds. *Chem. Eng. Sci.* Vol. 56, pp. 121 – 132.

Hoek, P. J.; Wesselingh, A. & Zuiderweg, F.J. (1986). Small scale and large scale liquid maldistribution in packed columns. *Chem. Eng. Res. Des.* Vol. 64, pp. 431 – 449.

Inglezakis, V. J.; Lemonidou, M. & Grigoropoulou, H.P. (2001). Liquid holdup and flow dispersion in zeolite packed beds. *Chem. Eng. Sci.* Vol. 56, pp 5049 – 5057.

Kouri, R.J. & Sohlo, J. (1996). Liquid and gas flow patterns in random packings. *Chem. Eng. J.* Vol. 61, pp. 95 – 105.

Kumar, S.; Upadhyay, S.N. & Mathur, V.K. (1977). Low Reynolds number mass transfer in packed beds of cylindrical particles. *Ind. Eng. Chem. Process Des. Dev.* Vol. 16, pp. 1 – 8.

Kunjummen, B.; Prasad, T.S. & Sai, P.S.T. (2000). Radial liquid distribution in gas-liquid concurrent downflow through packed beds. *Bioproc. Eng.* Vol. 22, pp. 471 – 475.

Linek, V.; Moucha, T. & Rejl, F.J. (2001). Hydraulic and mass transfer characteristics of packings for absorption and distillation columns: Rauschert-Metal-Sattel-Rings. *Trans. IChemE* Vol. 79(A), pp. 725 – 732.

Loser, T.; Petritsch, G. & Mewes, D. (1999). Investigation of the two-phase countercurrent flow in structured packings using capacitance tomography, Proceedings of the 1st World Congress on Industrial Process Tomography, pp. 354– 361, Buxtion, Greater Manchester, April 14-17, 1999.

Macias-Salinas, R. & Fair, J.R. (1999). Axial mixing in modern packings, gas and liquid phases: I. single-phase flow. *AIChE J.* Vol. 45, pp. 222 – 239.

Reinecke, N. & Mewes, D. (1997). Investigation of the two-phase flow in trickle-bed reactors using capacitance tomography. *Chem. Eng. Sci.* Vol. 52, pp. 2111 – 2127.

Ruzinsky, F. & Bennington, C.P.J. (2007). Aspects of liquor flow in a model chip digester measured using electrical resistance tomography. *Chem. Eng. J.* Vol. 130, pp. 67 – 74.

Sedahmed, G. H.; El-Kayar, A.M.; Farag, H.A. & Noseir, S.A. (1996). Liquid solid mass transfer in packed beds of Raschig rings with upward two-phase (gas-liquid) flow. *Chem. Eng. J.* Vol. 62, pp. 61 – 65.

Tsochatzidis, N. A.; Karabelas, A.J.; Giakoumakis, D. & Huff, G.A. (2002). An investigation of liquid maldistribution in trickle beds. *Chem. Eng. Sci.* Vol. 57, pp. 3543 – 3555.

Yin, F.; Afacan, A.; Nandakumar; K. & Chuang, K.T. (2002). Liquid holdup distribution in packed columns: gamma ray tomography and CFD simulation. *Chem. Eng. Proc.* Vol. 41, pp. 473 – 483.

33

Mass Transfers Within Emulsions Studied by Differential Scanning Calorimetry (DSC) - Application to Composition Ripening and Solid Ripening

D. Clausse[1], A. Drelich[1] and B. Fouconnier[2]
[1]*EA 4297 Transformations Intégrées de la Matière Renouvelable, Université de Technologie de Compiègne;*
[2]*Departamento de Ingeniería de Procesos y Hidráulica, Universidad Autónoma Metropolitana;*
[1]*France*
[2]*México*

1. Introduction

In this chapter mass transfer within simple, mixed and multiple emulsions will be considered. Simple emulsions are made of either water droplets dispersed within an oil phase (W/O) or oil droplets dispersed within an aqueous phase (O/W). Mixed emulsions are obtained by mixing gently to avoid coalescence, two simple emulsions the composition of the droplets being different. Finally, multiple or double emulsions are obtained by dispersing either a simple emulsion (W/O) in an aqueous phase to get what is referred as W/O/W emulsion or by dispersing a simple emulsion (O/W) in an oil phase to get an O/W/O emulsion.

These systems are known to be instable and their evolution towards bulk separated phases is the result of coalescence of the droplets due to different main mechanisms as Ostwald ripening, flotation, aggregation, sedimentation or creaming. This evolution can be considerably reduced by adding in their formulations either surfactants or/and particles. Thus, kinetic stability can be obtained. In that case other mechanisms can be studied, mechanisms that traduce an evolution of the systems as well but breakdown of the emulsions is not the result of the evolution understudy. It is this kind of evolution due to mass transfer that will be studied in this chapter. The bibliography will be done in each part dealing with the different kinds of emulsions considered.

First mass transfer in simple emulsions will be described. For these systems a not very well known mass transfer can be the result of the coexistence of still liquid droplets and yet solid ones at a temperature below the solid/liquid equilibrium temperature. This situation is the result of nucleation phenomena that create a delay for the formation of a solid germ that will induce the solidification of the droplets at different temperatures during the regular cooling of the emulsion. Another phenomenon leading to mass transfer in these systems is obtained by adding a material in the oil phase in a W/O emulsion, material that will diffuse and react

chemically with the water of the dispersed droplets. Following this process, an example of hydrate formation will be described.
In mixed emulsions the transfer is due to the difference of composition between the two populations of droplets. The phase wherein they are dispersed plays the role of a liquid membrane and should this membrane be permeable to one of the material present in the droplets a mass transfer occurs as it can be observed in a direct osmosis device.
In multiple emulsions, the situation is very similar of the one observed in mixed emulsions, except that the phases involved in the mass transfer are the dispersed droplets in the globules (primary emulsion) and the continuous phase wherein the globules are dispersed. A difference in the composition between these two kinds of phases lead to a mass transfer, the material of the globules playing in that case the role of a liquid membrane.
Different techniques have been used to detect this kind of mass transfer in emulsions. They are based on the phenomena linked with the mass transfer, mainly: solidification and changes of the composition and the sizes of the phases involved in the mass transfer. Therefore classical techniques as spectroturbidimetry, light scattering, conductivimetry and rheology have been used. In this chapter the results obtained by using a technique that has been developed for charactering emulsions and their evolution due to mass transfer will be thoroughly described. The referred technique called DSC for Differential Scanning Calorimetry is described in the next section. Afterwards the results dealing with simple, mixed and multiple emulsions will be described.

2. Differential scanning calorimetry for studying mass transfer within emulsions

The test consists in submitting an emulsion sample, the volume of which being a few mm^3, to a regular cooling and heating performed in a Differential Scanning Calorimeter, the volume of the cell being a few mm^3. The emulsion samples are taken time to time from the mother emulsion wherein mass transfers are expected to occur at ambient temperature.
During the cooling of a pure material, the droplets dispersed in the emulsions are expected to freeze. Due to the need to the formation of a solid germ that requires a certain amount of energy, the freezing temperatures are lower than the melting ones and the theory shows they are scattered around a mean temperature T^* referred as the most probable freezing temperature of the droplets. The energy released during the droplets freezing is evidenced on the obtained freezing curve as a peak showing a bell shape if the polydispersity is low. Should the emulsion contains a rather large range of droplet sizes, the freezing curve will show more than one signal and the shape could be asymmetrical. The apex temperature of the signal that gives T^* can be correlated to the mean droplet size. On the contrary, as there is no delay in the melting phenomenon, all the droplets (whatever their size) will melt at the same temperature, which is the one observed for a bulk material. More theoretical developments of these phenomena can be found in literature (Clausse et al., 2005). Typical experimental results are given thereafter.
Figures 1 shows typical cooling curves obtained by DSC of pure water (Figure 1a) dispersed in W/O emulsions. For comparison, DSC of bulk water is given on Figure 1b. These curves represent the basic data needed to interpret the results obtained by DSC on emulsions. For a bulk material, its solidification will give a signal at a temperature higher than the one obtained for dispersed material (-18°C for bulk water and -39 °C for dispersed water). Between the melting temperature T_m and the freezing temperature T_c, the material still

liquid is said to be under cooled. The degree of undercooling is defined by $\Delta T = T_m - T_c$. For water, this degree is around 20°C for bulk water of a few mm^3 and around 40°C for a population of microsized droplets. Another point to stress is that the shape of the signals is also different. This can be attributed to the way the material solidifies, very rapidly in a bulk sample or progressively in a dispersed phase as it has been indicated previously.

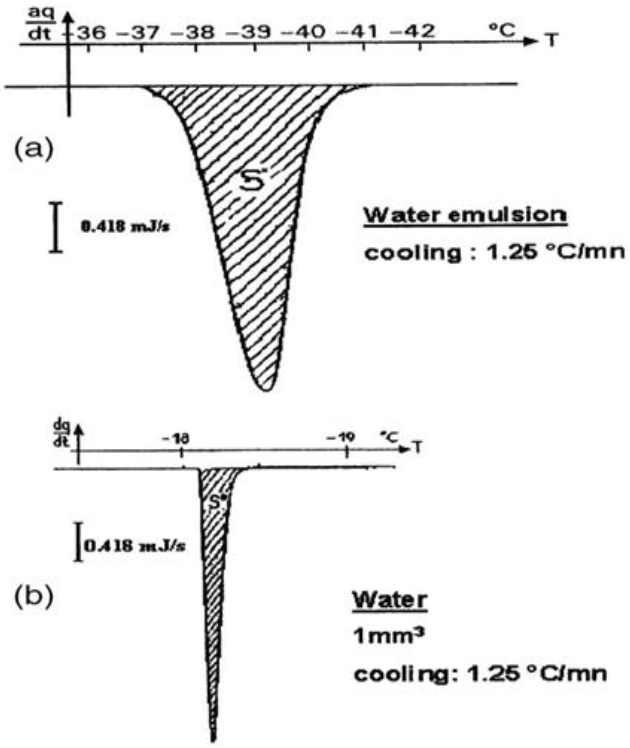

Fig. 1. Cooling curves for water dispersed in an emulsion (a) and for bulk water (b)

From the electrical power dq/dt registers by the calorimeter it is possible to deduce the enthalpy power dh/dt involved by the freezing or melting of the sample. On using rather low scanning rate temperature less than 2K/min, dh/dt can be approximated by dq/dt. Therefore by a previous calibration done with pure materials, the area of the signal correctly delimited permits to determine ΔH, the total heat involved in the liquid-solid transition. This quantity divided by the energy involved per mass unit Δh permits to know the mass m involved in the transition. Δh for the freezing is different for the melting one due to the net influence of the temperature specially for water due to a rather high difference between the values of the heat capacities of ice and liquid water. Nevertheless this quantity can be estimated from data on heat capacities values and as far comparison of areas of signals are done, this point is not a problem by itself. Furthermore when it is possible the amount of material involved in the transition can be determined by the area of the melting signal at a known temperature at which Δh is found in the literature. Should a mass transfer induces a change of the initial mass m(t=0) of a material, the following of the area A(t) of either the

freezing signal or the melting signal allows to evaluate the transferred material z or the ratio of non-transferred material y. They will be given by the following equations:

$$z = m(t=0) - m(t) = \frac{\left[\Delta H(t=0) - \Delta H(t)\right]}{\Delta h} = A(t=0) - A(t) \quad (1)$$

$$y = \frac{m(t)}{m(t=0)} = \frac{\Delta H(t)}{\Delta H(t=0)} = \frac{A(t)}{A(t=0)} \quad (2)$$

Should the material contain additives, the cooling curves obtained will be different and dependent on the amount of solute present (Figure 2). For two compounds A+B forming solutions in all proportions and showing an eutectic point, the freezing curves show either one or two signals as it is shown on figure 2 for 6 compositions shown by dotted lines in the phases diagram T versus composition x given as molar fraction of component B in the solutions. Line starting from A_0^e represents the A solidification points versus composition and line starting from B_0^e, the B solidification points versus composition, E being the eutectic point of the binary. When a solution is dispersed within an emulsion the solidification of the droplets shows different results depending on the composition. A composition different from the eutectic point E, separates the sequence of the events. This point indicated as ε on the graph is found at the intersection of two lines that give the most probable solidification temperatures of A for x<xε and the most probable solidification temperatures of B for x>xε. The circles mimic the contents of the droplets regards to the solid materials present. They are drawn in front of the respective signals shown by DSC. For example for droplets the composition of which being given by dotted line 2, the cooling curve shows two signals, one showing the partial solidification of A and at a lower temperature the total solidification of the droplet, namely the solidification of B and the solidification of the remaining A still liquid. As it can be seen on the diagram, the signals shift with the composition. The temperature of the apex of the first signal observed gives the most probable solidification temperature as it was yet described for dispersed pure material. The heating curve represented on the figure 2 by the line 1* for the composition represented by the dotted line 1, shows the eutectic melting followed by the progressive melting of component A until its complete dissolution when the equilibrium line is reached. This diagram is a schematic one for the case considered, solutions that can be mixed in all proportions and that show an eutectic point. In this chapter mixtures of hexadecane and tetradecane that enter in this case will be considered. Generally, especially for water + salt, the diagram is limited as far very concentrated solution in B being impossible to reach. That is the case for water + NaCl, solutions or water +urea solutions also treated in this chapter.

For the purpose of studying mass transfer that induces changes in the composition of the droplets, only the lines that give the most probable solidification temperature of either A or B will be considered. This curve will be referred as the calibration curve that gives the most probable freezing temperature T* versus the composition of the droplets. The undercooling given by the interval of temperatures between the equilibrium lines, and the lines that give the most probable solidification temperatures is not a constant as the figure lets assuming, but in fact it is changing with the composition and the drawing of the calibration curve needs to study samples of various compositions as it will be described later on. Determining the temperature from the freezing signal allows determining the composition of the droplets and therefore from the knowledge of the formulation of the emulsions and by doing a

material balance, the amount of material transferred can be determined. When it is possible another way to follow the transfer is to determine the areas of the freezing or better the melting signals for the droplets for which the composition does not vary, the transfer being from these droplets to the other droplets of different composition. The way these determinations are done will be more thoroughly described in the sections dealing with.

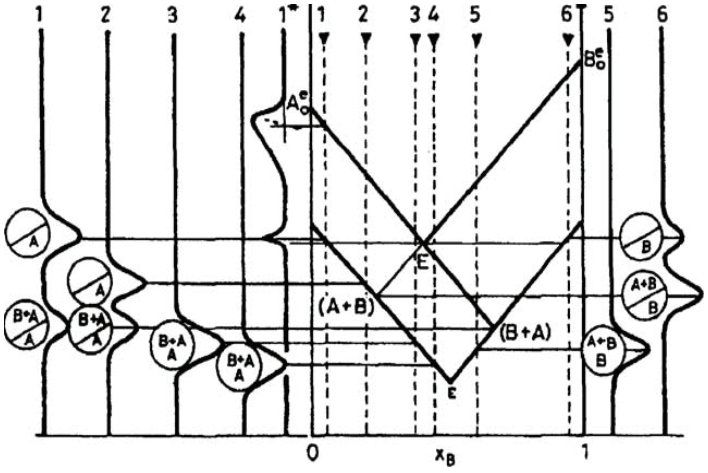

Fig. 2. Cooling and heating curves for a solution A+B dispersed within an emulsion

To summarize two ways for quantifying the mass transfer will be used. One from the determination of y (equation 2) and the other one from the calibration curve T^* versus the composition of the droplets made of A+B due to the transfer.

3. Mass transfer within simple emulsions. Solid ripening in W/O emulsions

An example is given by the mass transfer between yet solid droplets and still liquid ones due to under cooling phenomena. This transfer not very well known but that has to be taken into account when during the storage of the emulsion, the temperature reaches values below the melting ones, is referred as solid ripening as far the equilibrium state in these conditions is all the dispersed material solid (Clausse et al. 1999b). The other type is encountered when a material is added in the continuous phase of an emulsion. It is expected to diffuse and to react chemically with the material of the dispersed droplets. At the end a stable solid material is also obtained. Formation of solid hydrates in petroleum industry is a typical example of such a situation. It is this kind of transfer that is described thereafter.

An example of such solid ripening giving rise to the formation of a hydrate is illustrated by the study of trichlorofluoromethane (CCl_3F) hydrate formation in W/O emulsions. CCl_3F is a volatile liquid poorly soluble in water and forms a hydrate under mild conditions at 8.5°C and 1 bar. Therefore, CCl_3F appeared to be a good candidate in order to mimic the conditions of gas hydrate formation in W/O emulsions as a model system (Jakobsen et al. 1996; Fouconnier et al. 1999, 2006). The solid hydrate phase is formed inside the dispersed droplets as the result of a chemical reaction between CCl_3F molecules and water molecules present in the droplets. Actually, CCl_3F molecules are initially dissolved in the oily

continuous phase and diffuse through the W/O interface to be encapsulated by water molecules into a crystalline hydrate phase of structure II. In this chapter, it is described how to study the CCl_3F hydrate formation by DSC.

3.1 Emulsion preparation

The emulsions were prepared using Exxol D80 (a mixture of aliphatic and cycloaliphatic hydrocarbons from C_{10} to C_{13}) and mixed with trichlorofluoromethane as the continuous oil phase (Fouconnier et al., 2002). The emulsifier, berol 26 (tetraoxyethylene nonyl-phenyl ether, C_9-Ph-$E0_4$), was added to the oil phase at a concentration of 4% by volume. The amount of CCl_3F is incorporated in the oil in stoechiometric proportion according to the hydrate formation reaction: $CCl_3F + 17\ H_20 \rightarrow CCl_3F(H_2O)_{17}$. The dispersed phase was composed of aqueous saline solutions of calcium chloride at different concentrations by weight. Nevertheless, in order to diminish the evaporation of volatile CCl_3F and also to prevent the emulsion breaking, a primary emulsion made of Exxol D80, berol 26 and the saline solution was firstly prepared. The dispersion was obtained at 10000 rpm by means of a homogenizer Polytron PT 3000 during 10 minutes. The CCl_3F was finally added under gentle mixing to the emulsion stored at 0°C and kept at this temperature until utilization. The final emulsions were 60/40 water to oil ratio.

3.2 Mechanisms of hydrate formation in W/O emulsions

Jakobsen et al. were the first to study CCl_3F hydrate formation in W/O emulsions by dielectric spectroscopy (Jakobsen et al., 1996). During experiments, the emulsions were under constant stirring and the hydrate formation was detected with an induction period at 4.5°C but took place spontaneously at 3°C. The induction period was attributed to an insufficient undercooling, a reduced contact between CCl_3F and water molecules, the energy added to the system by stirring and inhomogeneous mixing during the initial period due to the addition of CCl_3F in the emulsion. The shift of temperature between 8.5°C and 3°C was attributed to the freezing depression point due to the presence of NaCl in the dispersed aqueous phase and the effect of undercooling in emulsions as it has been described in section 2.

The authors modeled the kinetics of the CCl_3F formation as followed.

$$CCl_3F_{(oil)} \rightarrow CCl_3F_{(aqueous\ phase)} \quad (a)$$

$$CCl_3F + 17\ H_2O \rightarrow CCl_3F.(H_2O)_{17} \quad (b)$$

$$CCl_3F + 17\ H_2O\ \Re\ CCl_3F.(H_2O)_{17} \quad (c)$$

The reaction (a) represents the diffusion of CCl_3F from the oil phase to the aqueous dispersed phase. The reaction (b) represents the slow formation of the hydrate considering that cavities of structure II are forming. The reaction (c) represents the autocatalytic formation of the hydrate.

Jakobsen et al. showed that the diffusion of CCl_3F molecules from the oil phase to the aqueous phase is the rate-limiting step. They also speculated that the surfactant can act as a barrier to the diffusion of the hydrate forming specie.

We also studied a similar dispersed system by DSC, $CaCl_2$ was also used, and it is worth noting that in our conditions of study it was impossible to detect the hydrate formation

during the cooling of the emulsions or by storing them at low temperatures for a long period. The conditions of CCl_3F hydrate formation by DSC were different from those used by Jakobsen. There was no agitation and furthermore the emulsions understudied were really stable. During the cooling of the emulsions, it was only observed the crystallization of aqueous droplets as bell shape signals at temperatures below -40°C as the droplets contained salt. Hydrate formation was not detected during the cooling.

Therefore, in order to evidence the conditions of the CCl_3F hydrate formation in W/O emulsions, a study using DSC and X-ray diffraction has been undertaken (Fouconnier et al. 2006). It has been concluded that a high degree of undercooling results in a spontaneous ice formation in the droplets during cooling of the emulsions. It has been showed by X-ray diffraction that the hydrate formed during subsequent heating of the emulsions as soon as the ice was beginning to melt. A mechanism of hydrate formation based on the shell model was then proposed as illustrated in figure 3.

During the heating of the emulsion, when the ice begins to melt, the droplet can be viewed as a core of ice surrounding by a saline solution. During the progressive melting of ice, the hydrate forms leading to the formation of a shell around the droplet. When the ice is completely melts, the hydrate formation is stopped and a shell of hydrate phase is in equilibrium with a concentrated saline solution since salt does not participate to the hydrate formation. Finally, when the hydrate dissociates, the remaining saline solution is progressively diluted until reaching the initial composition of the dispersed solution when the hydrate is completely dissociated.

From this simplified model it was then possible to study the hydrate formation within W/O emulsions and the effect of salts upon the hydrate formation.

It is described in next paragraph how to interpret the heating of DSC curves and for example, how to determine the quantity of hydrate formed.

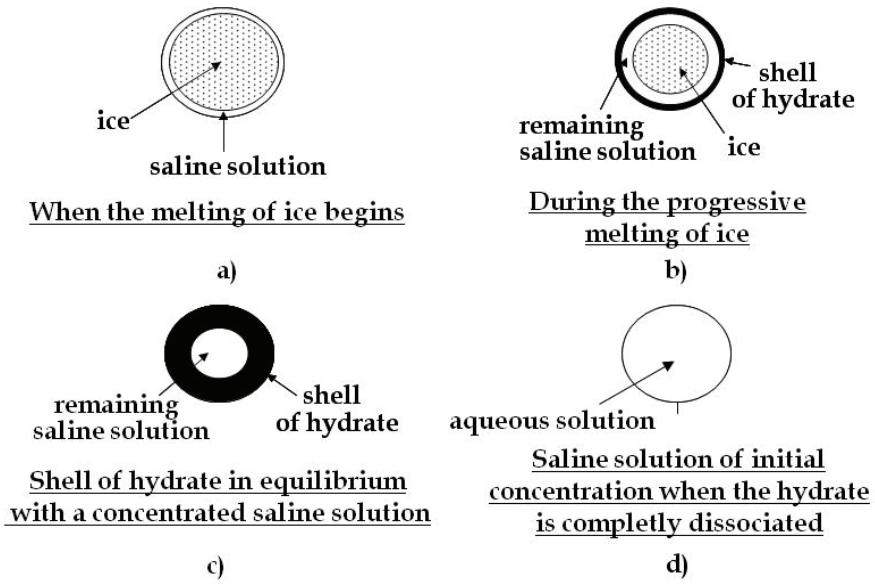

Fig. 3. Schematic representation of the droplet composition at different temperatures

3.3 DSC measurements and determination of the amount of hydrate formed

Figure 4 report the DSC heating curves of two emulsions with and without CCl_3F after being cooled down since -90°C. Both emulsions were prepared with aqueous solutions of $CaCl_2$ at a concentration of 6.8 wt%. On the DSC curves, the signal I at -52°C is attributed to the eutectic fusion of the water-calcium chloride binary system. Signals II and III represent the progressive melting of ice as it has been described in section 2. An additional signal IV only appears for the emulsion containing CCl_3F and it is attributed to the dissociation of hydrate.

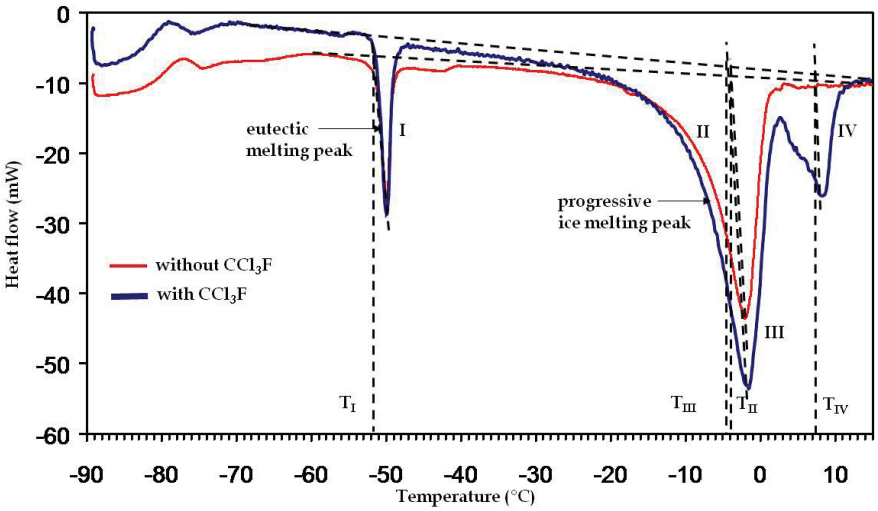

Fig. 4. DSC curves of emulsions with and without CCl_3F containing initially saline solutions of 6.8 wt% $CaCl_2$

It has been observed from the DSC and X-ray diffraction analysis that the hydrate dissociates progressively like melting of ice in presence with salt as the line 1* of the figure 2 shows. Therefore, the temperature of hydrate dissociation has been determined as the solid-liquid equilibrium temperatures of water-salt systems (Fouconnier et al. 2002).

The temperatures of the end of progressive ice melting (T_{II}, T_{III}) and the hydrate dissociation temperature (T_{IV}) are obtained by taking the intersection between the baseline of DSC curves and a line parallel to the greatest slope line of the eutectic peak, going through the node of each endothermic peak. The corresponding temperatures are given by the projection of the intersection points (dotted lines) on the temperature axis. Doing so, the temperatures of the end of the melting of ice (or solid-aqueous solution equilibrium temperature) are of -4.7°C and -4°C for the emulsion with and without CCl_3F respectively. The temperature of the hydrate dissociation is 7.5°C. It can be observed that the temperature of the end of ice melting in reference to the emulsion containing CCl_3F is slightly lower than the one of the emulsion without CCl_3F. This shift of temperature is attributed to the formation of hydrate. When hydrate forms, water molecules are engaged in the hydrate structure resulting in the concentration of the saline solution inside the emulsion droplets.

Once stated how to determine the temperatures of the hydrate dissociation as function of salt concentration and by considering that the hydrate phase is in equilibrium with a

remaining saline solution when ice is completely melted, it is possible to carry out a mass balance using the temperatures of ice-aqueous solution equilibrium and by using the water-$CaCl_2$ equilibrium curve. Such mass balance is illustrated by the study of an emulsion containing a dispersed $CaCl_2$ aqueous solution of 20 wt%. For comparison, the equivalent emulsion without CCl_3F was also studied.
Figure 5a presents the DSC curves for emulsions with and without CCl_3F. Figure 5b shows the water-$CaCl_2$ equilibrium curve.

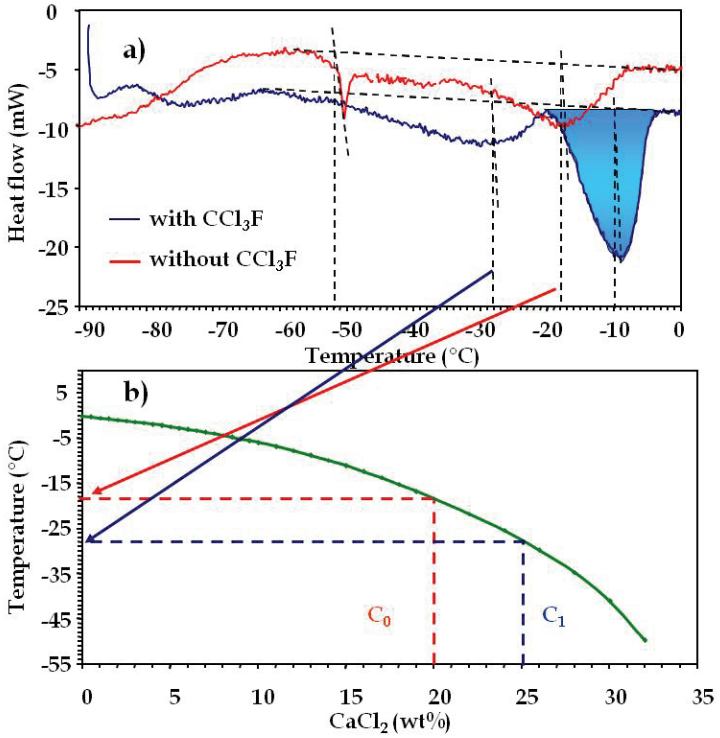

Fig. 5. a) DSC curves of emulsions with and without CCl_3F containing initially saline solutions of 20 wt% $CaCl_2$. b) Equilibrium curve of the water-$CaCl_2$ binary system

The temperatures of ice-saline solution equilibrium were determined as described previously and are T = -28°C for the emulsion containing CCl_3F and T = -18°C for the emulsion without CCl_3F. These temperatures are then reported on the equilibrium curve of the water-$CaCl_2$ system. Therefore, T = -28°C corresponds to a hydrate phase in equilibrium with a saline solution of 25 wt% of $CaCl_2$ and T = -18°C corresponds to the dispersed saline solution of 20 wt% used for the emulsion preparation.
On the other hand, the mass fraction φ of aqueous phase of the emulsion was needed to carry out the mass balance. According to the formulation of the emulsion, the mass fraction φ is given by the following relation where $m_{aqueous,\ E}$ and $m_{oil\ phase,\ E}$ are the mass of the dispersed saline solution and the mass of the oil phase (CCl_3F + berol + Exxol D80) respectively.

$$\varphi = \frac{m_{aqueous\ phase,E}}{m_{oil\ phase,E} + m_{aqueous\ phase,E}} = 0.624 \quad (3)$$

The emulsion sample was also weighted before introducing it inside the calorimeter head. In this example, the mass sample was m_s = 0.2111g. From this data it was possible to determine the mass of the aqueous phase inside the emulsion sample as

$$m_{aqueous\ phase,S} = m_S \times \varphi = 0.1317\,g \quad (4)$$

which finally gave 0.1054 g of water in the emulsion sample.
Finally, by knowing that the saline solution concentrated from 20 wt% to 25 wt% due to hydrate formation, it can be deduced that 75% of mass water does not participate to the reaction. Therefore, the number of mole of water engaged in the hydrate structure can be deduced from the equation (5).

$$n_{water} = \frac{m_{water\ engaged}}{M_{water}} = \frac{0.1054 \times (1 - 0.75)}{18} = 1.4638 \times 10^{-3}\,mol \quad (5)$$

The mass of hydrate crystallized $m_{hydrate}$ during the progressive melting of ice is calculated via equation (6) considering structure II of hydrate ($CCl_3F.(H_2O)_{17}$).

$$m_{hydrate} = \frac{n_{water\ engaged}}{17} \times M_{hydrate} = 3.8190 \times 10^{-2}\,g \quad (6)$$

where $M_{hydrate}$ = 443.5 g.mol^{-1} is the molar weight of the CCl_3F hydrate.
Furthermore, it was also possible to determine the hydrate dissociation energy. The hydrate dissociation peak was integrated via the calorimeter software. Therefore, the corresponding energy released during the dissociation of hydrate divided by the mass calculated as described before, gave the specific dissociation energy of the hydrate. In this example, the specific dissociation energy was determined as 166.1 J.g^{-1} at -10°C (Fouconnier et al. 2002).
The CCl_3F hydrate model has been also used to understand the mechanism of hydrate formation in emulsion (Dalmazzone et al. 2002). It has been demonstrated that DSC is a suitable technique to detect the hydrate formation via the solid-liquid transitions involved and to predict the hydrate formation zone by the determining the temperature of hydrate dissociation as a function of salt concentration.
This model has been used to study methane hydrate formation in drilling muds (Dalmazzone et al. 2002). It has been demonstrated that the CCl_3F hydrate formation can modeled gas hydrate formation in applied systems. Studies of gas hydrate formation by DSC can be found in literature (Koh et al, 2002; Karrat & Dalmazzone, 2003; Lachance et al., 2008; Dalmazzone et al. 2009, Davies et al., 2009) and it must be also emphasized that DSC has been developed to be directly used in offshore in order to predict the zone of gas hydrate formation (Le Parlouër et al. 2004).

4. Mixed emulsions

Mixed emulsions are obtained by gently mixing two simple emulsions containing droplets of different composition (Figure 6). Mixed emulsions are well-suited model systems to study

transfer mechanisms across liquid membranes (Li, 1968; Colinart et al., 1984; Noble & Stern, 1995). For instance, these systems allow to model transport processes between two oil phases separated by an aqueous membrane in the case of oil-in-water (O/W) emulsions and between two aqueous phases separated by an organic membrane in the case of water-in-oil (W/O) emulsions.

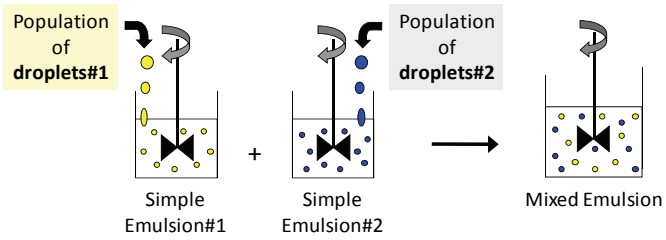

Fig. 6. Schematic representation of mixed emulsion preparation

The mass transfers due to a gradient composition between the different phases present in the emulsion lead to a modification of the composition of the droplets by dilution and the decrease of the amount of pure droplets by transfer (Figure 7).

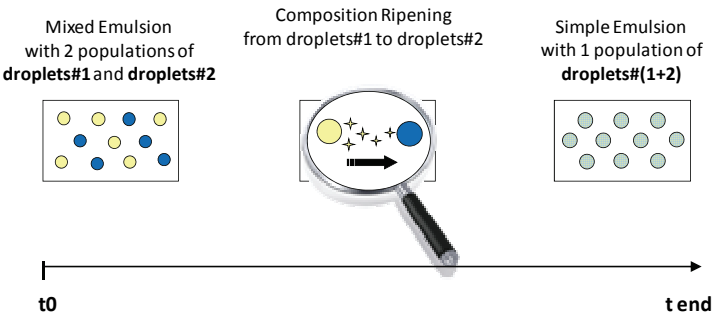

Fig. 7. Schematic representation of the droplet composition with time in mixed emulsion

Many studies evidenced the composition ripening that takes place in mixed emulsion by measuring the rate of mass exchange between two kinds of water droplets with solute dispersed in oil media or two populations of hydrocarbon droplets dispersed in aqueous phase. In the case of this study, we propose to describe in this chapter the pure water mass transfer to aqueous solute solution droplets in W/O mixed emulsion and the transfer of tetradecane to hexadecane droplets in O/W mixed emulsion.

4.1 DSC measurements and determination of water mass transfer in W/O mixed emulsions

The goal of the work reported (Clausse et al., 1995; 1999; 2008; Sacca et al., 2008) is to evidence the composition ripening that takes place in W/O mixed emulsions and to measure the rate of water exchange between pure water droplets and aqueous solute (urea or NaCl) droplets dispersed in oil medium. The effect of the emulsion stabilizing agent, as emulsifier or particles, on the kinetics of water transfer was investigated and discussed.

4.1.1 Emulsion preparation

The W/O mixed emulsions, for which water transfer is expected, were obtained by a simple manual mixing of equal masses of two W/O simple emulsions. First, W/O simple emulsions were made of 20 wt% (or 30 wt%) of pure water droplets or 20 wt% (or 30 wt%) of aqueous solute solution droplet dispersed in continuous phase consisting in variable mixtures of paraffin oil and pure vaseline paste. The aqueous solution consists in a urea solution (concentration of 20 wt% or 30 wt%) or a NaCl solution (concentration of 20 wt%). The emulsification was realized with a high speed homogeneizer at 50°C-60°C due to the higher viscosity of the aqueous solutions compared to pure water. To study the influence of the stabilizing agent, the W/O simple emulsions were stabilized employing different surfactants in the oil continuous phase, as the lipophilic lanolin emulsifier (8 wt%) and the nonionic Span 80 surfactant (3 wt%). To study the influence of solid particles, the W/O simple emulsions were solely stabilized by hydrophobic Aerosil R711 silica particles (0.1 wt% to 3 wt%). Then, the W/O mixed emulsion was obtained by mixing equal masses of the W/O simple emulsions prepared in the same conditions and with the same stabilizing agent. The W/O resultant mixed emulsion is a mixture of 10wt% (or 15 wt%) of pure water and 10 wt% (or 15 wt%) of aqueous solute solution droplets dispersed in oil media.

4.1.2 DSC measurements - results and discussion

In the case of W/O mixed emulsion constituted at time zero of two kinds of water droplets, two broad exothermic peaks are observed on DSC curves, corresponding to the crystallization of pure water droplets and of aqueous solution of solute droplets.

In the case of W/O mixed emulsions containing pure water droplets and aqueous urea solution droplets stabilized by lanolin surfactant, the DSC cooling curves (Figure 8) indicate two solidification peaks corresponding to the freezing signal I of pure droplets at T* = -39°C (Figure 8a) and the freezing signal II of aqueous urea solution droplets with a concentration of 30 wt% at T* = -60°C (Figure 8b). DSC cooling curves point out a noticeable decrease with time of the signal I area characteristic of pure water droplets freezing (Figure 8c;d). In addition, DSC cooling curves show a shift with time towards higher temperature of the signal II corresponding to the solidification of water+urea droplets. Therefore these results evidence that there is no urea transfer and that water has been transported from the pure water droplets towards the water+urea droplets, causing their dilution, according to the calibration curve of this system reported on Figure 9. Finally, only one signal at around T = -48°C is observed 65 min after the mixing and no more evolution has been observed after that time (Figure 8e). This unique signal assumed that there are no more pure water droplets whereas the water+urea droplets are still present and their dilution having reached a maximum. From the knowledge of the dependence of the water+urea droplets freezing temperature versus the urea composition (Figure 9), it was deduced that the unique signal observed at T* = -48°C is characteristic of the freezing of 15 wt% urea solution droplets. This final composition is in agreement with the initial W/O mixed emulsion obtained by mixing equal masses of each W/O simple emulsion containing 30% pure water of droplets and 30% of aqueous urea solution droplets. The evolution of pure water moles numbers in mixed emulsion was deduced from the surface area of the solidification signal I of pure water (using the Equation 2) (Figure 10).

It appears that the transfer is rather fast at the beginning in agreement which the fact that the gradient of concentration is maximum at t=0. Afterwards the experimental results obtained from four different emulsions are scattered in a relative large range that shows the problem of reproducibility. More controlled size droplets would certainly improve the reproducibility.

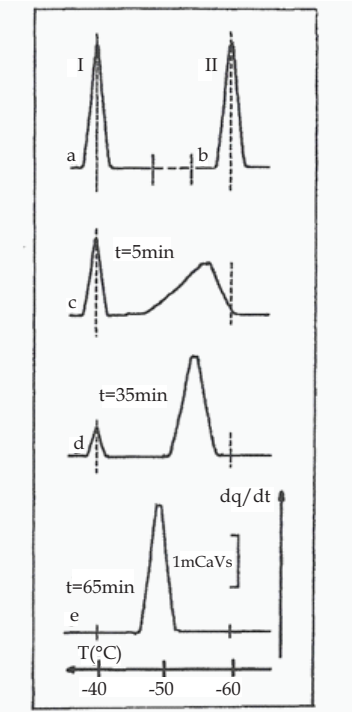

Fig. 8. DSC cooling curves of W/O mixed emulsion with pure water droplets and water+urea droplets dispersed in oil media at successive time intervals c) t=5min; d) t=35min; e) t=65min

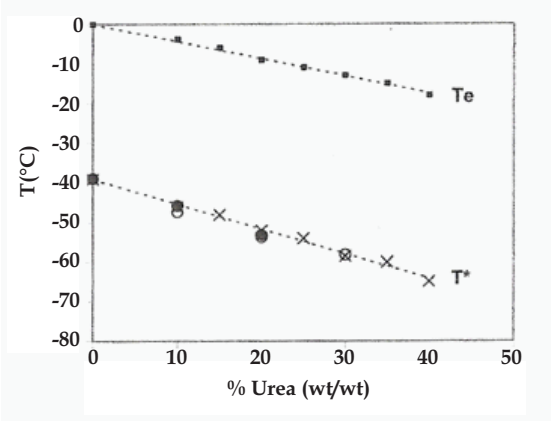

Fig. 9. Freezing temperature of urea solution versus urea concentration. Te: equilibrium freezing temperature of the urea solution in bulk; T*: most probable freezing temperature of the micro-sized droplets of urea solution dispersed in oil media

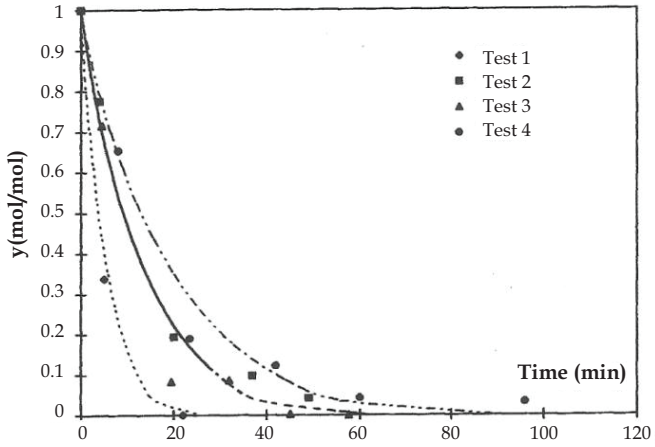

Fig. 10. Ratio y of pure water moles numbers non-transferred in W/O mixed emulsion with pure water droplets and water+urea droplets dispersed in oil media versus time

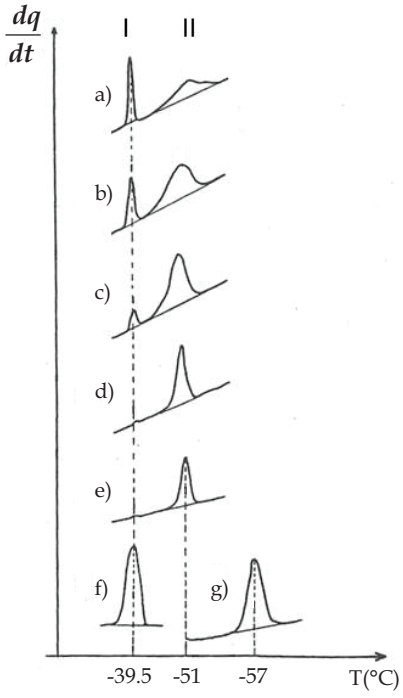

Fig. 11. DSC cooling curves of W/O mixed emulsion with pure water droplets and water+NaCl droplets dispersed in oil media at successive time intervals a) t = 2 min; b) t = 25 min; c) t = 43 min; d) t = 62 min; e) t = 82 min

In the case of W/O mixed emulsions containing pure water droplets and aqueous NaCl solution droplets stabilized by lanolin surfactant, the DSC cooling curves (Figure 11) indicate a solidification signal I at T* = -39.5°C corresponding to freezing of pure water droplet (Figure 11f) and a solidification signal II relative to the freezing of aqueous NaCl solution droplets with a concentration of 20 wt% at T* = -67°C (Figure 11g). With time, DSC cooling curves show the area of the solidification signal I of pure water droplets decreases whereas the freezing signal II appears to broaden first and then to be more and more narrow (Figure 11a-e). Therefore these results evidence the decrease of the amount of pure water droplets in mixed emulsion by a dilution of the water+NaCl droplets due to water coming from the pure water droplets. When the DSC cooling curves do not change any longer after 82 min, the signal I has practically disappeared and a well defined signal II observed at around T* = -51°C is noticeable (Figure 11e). This unique signal evidence that the complete water mass transfer is achieved: no more pure water droplets are still present and the water+NaCl droplets are diluted as much as possible. From the knowledge of the phase diagram of the water+NaCl emulsified system, and the melting temperature of the final droplets population, it was deduced that the unique signal observed at T* = -51°C is characteristic of the freezing of 10 wt% aqueous NaCl solution droplets. This final composition is in agreement with the formulation of the W/O mixed emulsion. The evolution of the percentage of pure water moles numbers in mixed emulsion was deduced from the surface area of the solidification signal I of pure water (using the Equation 2) (Figure 12).

In that case as well, it appears that the transfer is rather fast at the beginning. Furthermore, the time involved to reach equilibrium is very close to the one observed for the water+urea system, around 60min.

In the case of W/O mixed emulsions containing pure water droplets and aqueous urea solution droplets stabilized by hydrophobic silica particles instead of a surfactant, the DSC curves (Figure 13) indicate a solidification signal I at T* = -37°C very close to what was observed for the freezing of pure droplets (Figure 13a) and a solidification signal II at T* = -52.6°C characteristic of the freezing of aqueous urea solution droplets with a

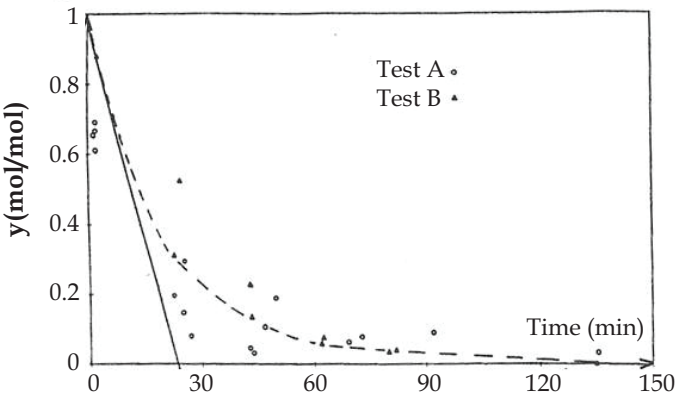

Fig. 12. Ratio y of pure water moles numbers non-transferred in W/O mixed emulsion with pure water droplets and water+NaCl droplets dispersed in oil media, versus time

concentration of 20 wt% (Figure 13b). DSC curves show that the evolution of the solidification signal occurs similarly to what is observed in the case of W/O mixed emulsions stabilized by a surfactant. Therefore these results evidence that aqueous urea solution droplets are diluted by the transfer of water from pure water droplets which progressively disappear from the mixed emulsion, in agreement with the previous studies presented. DSC cooling curves show no modification of the unique solidification peaks observed from 3h 15min (Figure 13e) characteristic of the complete water mass transfer. Similar experiments were performed on W/O mixed emulsions prepared in the same condition but containing pure water droplets and aqueous urea solution droplets stabilized by the nonionic Span 80 surfactant. Same evolutions of the solidification signals are observed, but the unique solidification peaks resulting for complete water mass transfer is observed after 1 hour of evolution.

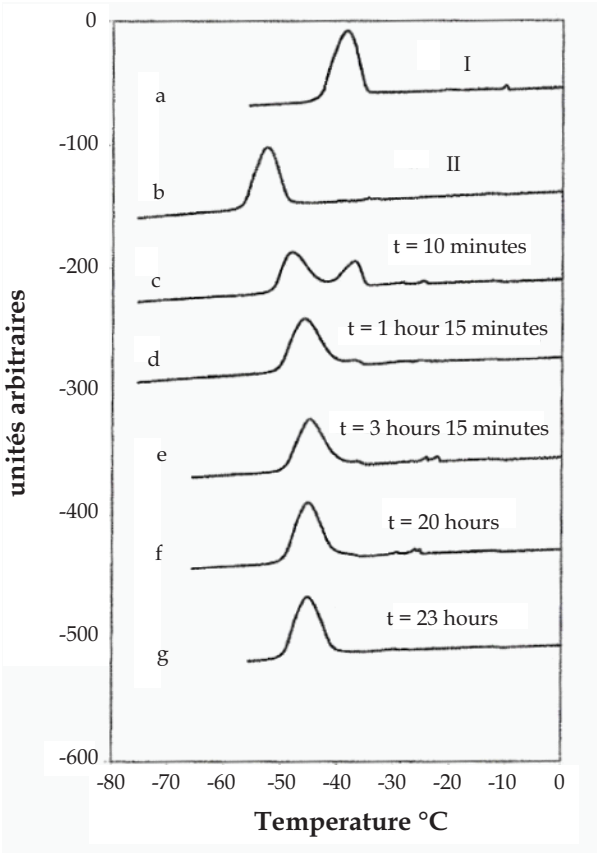

Fig. 13. DSC cooling curves of W/O mixed emulsion with pure water droplets and water+urea droplets dispersed in oil media and stabilized by hydrophobic silica particles at successive time intervals a) corresponding W/O simple emulsion of water+urea droplets at t=0; b) corresponding W/O simple emulsion of pure water droplets; c) t = 10min; d) t = 1 hours 15 min; e) t = 3 hours 15 min; f) t = 20 hours; g) t = 23 hours

This work shows a water mass transfer through the oil media from the pure water droplets to the aqueous droplets containing a solute, causing their dilution. The transfer mechanism found is in agreement with the solution-diffusion model. This mechanism supposed that water can be solubilized in the oil medium and can also diffuse in this oil medium due to the composition discrepancy between the droplets that creates a chemical potential gradient. According to thermodynamic considerations, water transfer is expected to transfer from pure water droplets (highest water chemical potential) towards water+solute droplets (lowest water chemical potential), and not the reverse. The results show that the characteristic time scale for water transport through the oil media can span about one hour in presence of surfactant. The kinectics of composition ripening seems to depend on parameters of emulsion formulation as the surfactant type and concentration, the solute type and concentration, and the presence of solid particles in the oil media. The mass transfer process is attributed to the great exchange area available in the emulsion and furthermore to the essential presence of surfactants. Although, the role of these parameters is not yet clearly established. These results evidence that the presence of silica particles in the oil media does not stop but slow down the water mass transfer, in comparison to a surfactant. These results suggest that the mechanism of mass transfer in presence of solid particles might be different of the solution-diffusion model previously proposed.

4.2 DSC measurements and determination of tetradecane mass transfer in O/W mixed emulsion

The objective of the work presented (Avendano-Gomez et al., 2000; Avendano-Gomez, 2002; Clausse et al., 2002b; Drelich, 2009) is to study the composition ripening that takes place in O/W mixed emulsions and to measure the rate of oil exchange between n-tetradecane and n-hexadecane droplets dispersed in aqueous phase. The influence of surfactant concentration, surfactant nature, amount of salt and presence of solid particles on the rate of oil exchange is also studied and discussed.

4.2.1 Emulsion preparation

The O/W mixed emulsion was prepared by gently mixing two O/W simple emulsions. Firstly, O/W simple emulsions of tetradecane and n-hexadecane were prepared separately with a concentration of 40 wt% of the oil phase with the same surfactant type and concentration and homogenized with a high speed blender at 20 000 rpm. To study the influence of the surfactant, the O/W simple emulsions were stabilized employing different surfactant aqueous systems, as the non ionic surfactant Tween 20 and the ionic surfactant Brij 35. The different surfactant aqueous systems were prepared with two surfactant concentrations of 2 wt % and 4 wt%, corresponding to a higher concentration than their respective critical micellar concentration. To study the influence of the presence of salt, the O/W simple emulsions were prepared with aqueous solution containing an amount of NaCl (1 wt% and 2 wt%) added to the Tween 20 surfactant (2 wt%). To study the influence of solid particles, the O/W simple emulsions were stabilized by a mixture of hydrophilic Aerosil A200 (2 wt%) and hydrophobic Aerosil R711 (2 wt%) silica particles. Then, the O/W mixed emulsion was obtained by mixing equal masses of the O/W simple emulsions. The O/W resultant mixed emulsion is a mixture of 15 wt% of pure n-tetradecane and 15 wt% of pure n-hexadecane droplets dispersed in 70 wt% of surfactant aqueous phase.

4.2.2 DSC measurements – results and discussion

In the case of O/W mixed emulsion constituted at time zero of two populations of oil droplets of different nature, two broad exothermic peaks are observed on DSC curves, corresponding to the crystallization of each population of oil droplets.

In the case of O/W emulsions containing n-tetradecane droplets and n-hexadecane droplets stabilized by a surfactant, the DSC curves (Figure 14) indicate a first broad exothermic signal I at T* = -2°C for the solidification of the n-hexadecane droplets, a second broad exothermic signal II at T* = -17°C corresponding to the freezing of the n-tetradecane droplets, and a narrow exothermic peak at T_c = -22°C related to the crystallization of the aqueous continuous phase. DSC curves (Figure 15) show an evolution of the two oil solidification peaks with time: an area reduction of the solidification signal II of pure tetradecane droplets and a displacement of the solidification signal I of n-hexadecane towards lower temperatures. The area reduction of the solidification peak II of pure n-tetradecane droplets is related to the amount decrease of pure n-tetradecane droplets with time. The displacement of the solidification signal I of n-hexadecane droplets towards lower temperature is related to the composition modification of the n-hexadecane droplets by the n-tetradecane dilution with time, according to the calibration curve reported on Figure 16. These evolutions evidence a preferential and global oil exchange from the tetradecane droplets towards the n-hexadecane droplets. In addition, the DSC curves reveal only one solidification peak and no change in the crystallization temperature of the dispersed phase obtained after some hours of emulsion evolution. This unique signal suggests that the mass transfer between the oils droplets is complete. The crystallization temperature of the last unique signal is observed at around T* = -10°C and corresponds to a composition of 50% in mass of n-hexadecane in the droplets according the calibration curve (Figure 16). The initial O/W mixed emulsion containing the same mass ratio of tetradedacne/n-hexadecane, the resulting composition due to a mixture between the tetradecane and the n-hexadecane droplets is 50% of n-hexadecane. Therefore, the final n-hexadecane composition within the

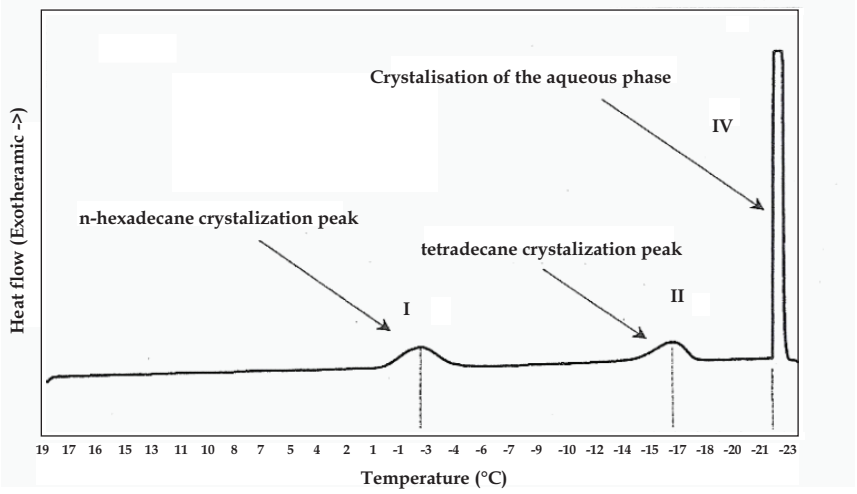

Fig. 14. DSC curves of solidification of O/W mixed emulsion with n-tetradecane droplets and n-hexadecane droplets dispersed in aqueous phase

droplets is in agreement with the value expected. The results indicate the time to reach the total oil transfer is 16 hours with 2% of Brij 35 and only 3 hours and 30 minutes with 4% of Brij 35 (not represented), 24 hours with 2% of Tween 20 (Figure 15a right) and only 6 hours with 4% of Tween 20 (Figure 15a left). The result shows that the mass transfer is achieved after 31 h and 30 minutes of evolution when droplets are dispersed in aqueous phase containing 2% of NaCl and 2% of Tween 20 (Figure 15b). The evolution of pure tetradecane moles numbers in mixed emulsion was deduced from the surface area of the solidification signal I of pure tetradecane (using the Equation 2) (Figure 17).

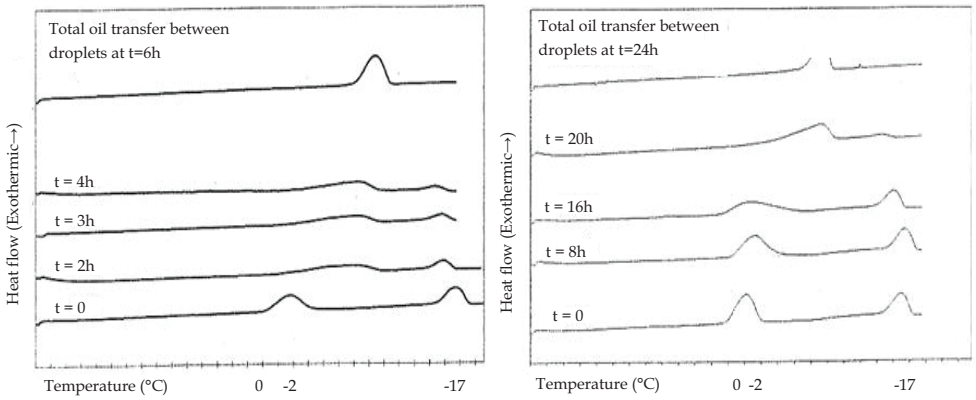

(a)

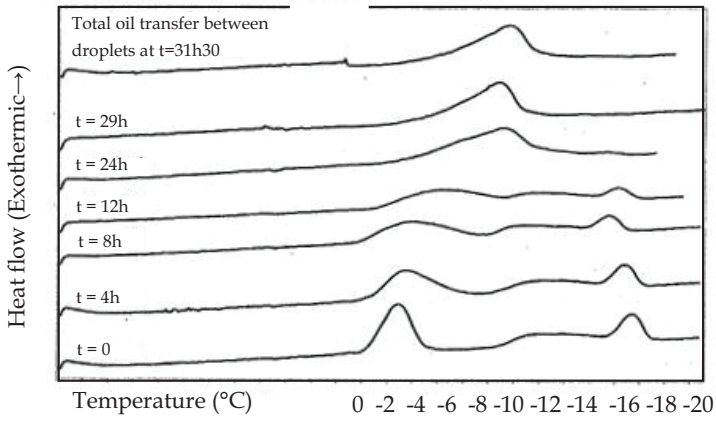

(b)

Fig. 15. DSC curves showing the solidification of O/W mixed emulsion containing 15 wt% of n-tetradecane droplets and 15 wt% of n-hexadecane droplets dispersed in an aqueous phase with a) 4 wt% (left) and 2 wt% (right) of Brij 35, b) 4 wt% (left) and 2 wt% (right) of Tween 20 surfactant and c) 2 wt% of NaCl and 2 wt% of Tween 20 surfactant, at successive time intervals

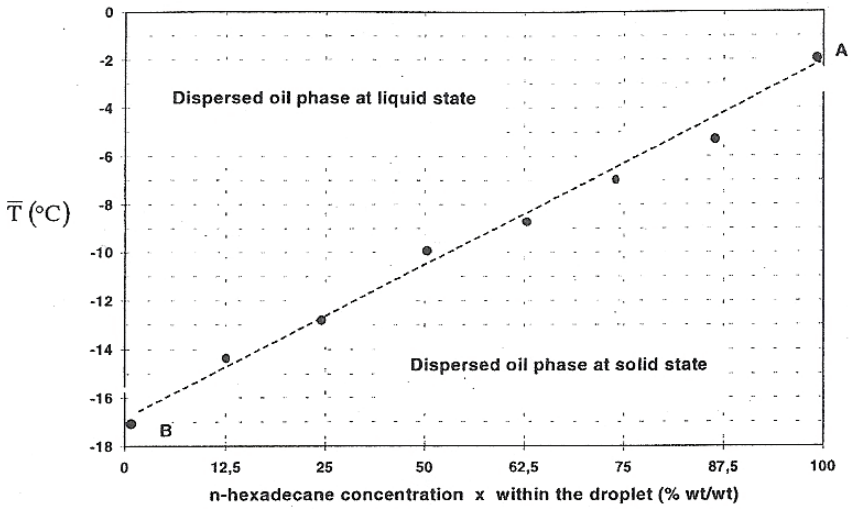

Fig. 16. Calibration curve giving the most probable crystallization temperature as a function of n-tetradecane/n-hexadecane oil droplets dispersed in aqueous phase

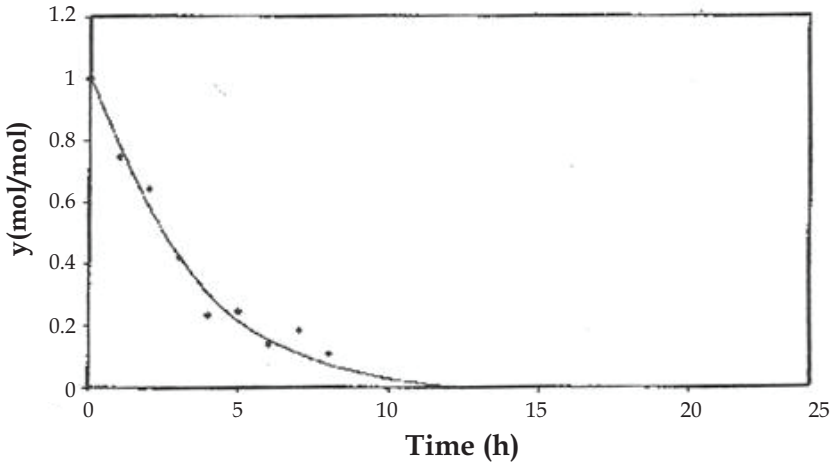

Fig. 17. Ratio y of pure tetradecane moles numbers non-transferred in O/W mixed emulsion with n-tetradecane droplets and n-hexadecane droplets dispersed in aqueous surfactant phase versus time

In the case of O/W emulsions stabilized by silica particles, the DSC curves (Figure 18) show no evolution of the solidification signals of oil droplets observed during a time scale of 13 days. These results suggest that no modification of the droplets oil composition occurred during this time scale. These evolutions evidence silica particles not permit to a mass transfer between tetradecane and n-hexadecane.

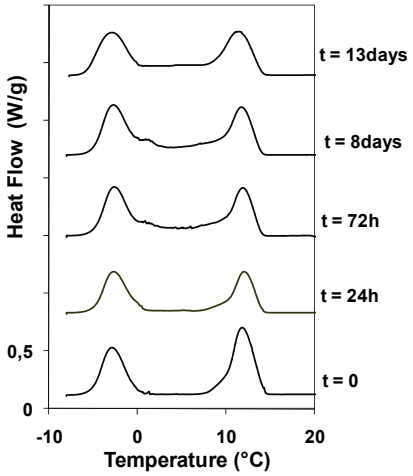

Fig. 18. DSC curves showing the solidification of solid-stabilized O/W mixed emulsion containing 20 wt% of n-tetradecane droplets and 20 wt% of n-hexadecane droplets, at successive time intervals

This work shows a preferential mass transfer from the tetradecane to the n-hexadecane droplets in agreement with the literature. Many studies evidenced the importance of the solubility of the oil dispersed phase in water on the direction and the rate of oil exchange through the continuous water phase (Taisne et al., 1996; Binks et al., 1998; 1999). Indeed, it was demonstrated that the Tween 20 surfactant enhances the solubility of the tetradecane rather than the hexadecane (McClement et al., 1995; Weiss et al., 2000). The results show that the characteristic time scale for oil exchange between tetradecane and n-hexadecane droplets kinetics can span a wide range from seconds to several hours in presence of surfactant. The kinectics of composition ripening seems to depend on parameters of emulsion formulation as the surfactant type, the surfactant concentration, and the amount of salt and the presence of solid particles in the aqueous phase. The results show that the rate of oil exchange between droplets is faster when the non-ionic surfactant concentration is higher, in agreement with the literature (McClement et al., 1993c; Binks et al., 1998; 1999). On the contrary, the amount of salt added into the continuous phase slows down the rate of oil transfer as it was evidenced by McClement et al. (McClement et al., 1993c), and the presence of solid particles seems to block the oil exchange (Drelich et al., 2011). These results suggest that oil transfer may enhanced by the excess of surfactant micelles in the continuous phase. Mechanism of micelle transportation and solubilization of the oil through the continuous phase was proposed in the literature (McClement et al., 1992; 1993a; 1993b, 1993c; Binks et al., 1998; 1999; Elwell et al., 2004).

4.3 Model of kinetics of composition ripening

The mechanism of composition ripening has to be considered when a composition gradient exists within the emulsion under study. To model the mass transfer, the mixed emulsions are pictured as: two oil phases of different nature compartmented and separated by a plane liquid aqueous membrane or two aqueous phases of different composition compartmented and separated by a plane liquid membrane made of oil (Figure 19).

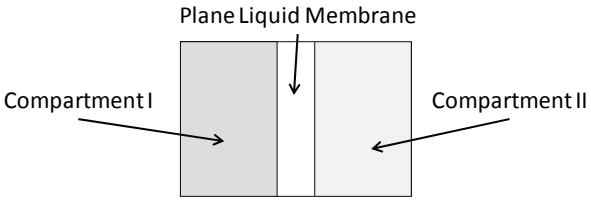

Fig. 19. Picture of mixed emulsion in the model of mass transfer

It has been demonstrated in the presented work and in the literature that the transport of pure water in W/O mixed emulsion or the transfer of pure tetradecane in O/W mixed emulsion is increased when surfactant making micelles is present as the micelles can incorporated the transferred molecules and facilitate their transport through the continuous media. To quantify the transfer, the flux J is introduced and expressed in terms of chemical potential gradient $\overline{grad\mu}$ according to the following equation:

$$\vec{j} = -L \times \overline{grad}\mu \tag{7}$$

With L being the factor related to the transferred material diffusion coefficient and the transferred material concentration in the membrane. By using this model, it has been possible to express the changes of the number of material moles in the compartment I containing pure material, $n_1^I(t)$ versus time t. This number decreases versus time ,the material being transferred between two populations of droplets in direction of the decreasing chemical potential. For example, water being transferred from the pure water droplet to the water+solute droplets or tetradecane being transferred from the pure tetradecane droplets to the hexadecane droplets. A mathematical treatment and thermodynamic considerations developed (Clausse et al., 1995a) allow obtaining the following relation:

$$V^t\left[n_1^I(t=0)^{1/3} - n_1^I(t)^{1/3}\right] - \left[n_1^I(t=0)^{4/3} - n_1^I(t)^{4/3}\right] = 2n_1^{II}v_1^{2/3}(V_0^I)^{1/3}\frac{L_D}{\ddot{d}} \tag{8}$$

In this equation, V and v are the total volume and the molar volume, respectively, and L_p and $\ddot{d}$ are the permeability coefficient and the mean diameter of the droplets, respectively. Furthermore, n_1 and n_2 are the moles numbers of water and solute or the moles numbers of tetradecane and hexadecane, respectively. L_p is a parameter difficult to know as it is linked to unknown parameters such as the width of the equivalent membrane, the water diffusion coefficient or the tetradecane diffusion coefficient and the water concentration or the tetradecane concentration in the membrane. Nevertheless, it is possible from this model to predict the lapse of time necessary to reach equilibrium, when all the pure water molecules has migrated from the pure water droplets to the water+solute droplets, or when the tetradecane molecules has migrated from the pure tetradecane droplets to the diluted hexadecane droplets. This point is reached when $n_1^I(t) = 0$. Similar treatments dealing with water transfer within multiple emulsions have been given in the literature (Clausse et al., 1995b; Potier et al., 1992).

In each studied case, the water transport in W/O mixed emulsion and the tetradecane transfer in O/W mixed emulsion, experimental results are fairly well fitted by the model proposed. Although this model is not perfect, it gives the main physical parameters to be

considered and it could be improved by taking account the changes of the characteristics of the emulsion with time due to the transfer, and the emulsifier influence.

5. Multiple emulsions

Multiple or double emulsions are systems in which a liquid phase is dispersed into globules which in turn are dispersed into another immiscible liquid phase (Garti & Lutz, 2004; Benichou et al., 2007). The liquid phase dispersed as microdroplets in the globules is called the internal phase whereas the liquid phase in which are dispersed the globules is called the external phase. Therefore a multiple emulsion contains three liquids phases and are classified as either Water-in-Oil-in-Water (W/O/W) emulsions or Oil-in-Water-in-Oil emulsions (O/W/O) (Pal, 2011; Muschiolik, 2007). The inner dispersed droplets are separated from the external phase by a layer of the globules phase (Garti & Lutz, 2004).
Multiple emulsions are liquid carriers for entrapped and release of active or reactive molecules in pharmaceutics, cosmetics, food and industrial applications. Nevertheless, W/O/W multiple emulsions are more studied because they have higher potential to become commercial products than O/W/O multiple emulsion (Benichou & Aserin 2007). For instance, in cosmetics the release of an encapsulated drug inside an aqueous globule of a W/O/W emulsion can be directly liberated by breaking of the globules via mechanical stress (Muguet et al., 2001; Tejado et al., 2001). In pharmaceutics, drugs can be protected by the membrane until it reaches its target and then released by controlled release (Garti & Lutz, 2004; Hai & Magdassi, 2004; Tejado et al., 2005). Controlled release can by operated via swelling of the globules (or Ostwald swelling) which consists in an increase in size of the inner dispersed droplets due to a difference of chemical potential on both sides of the membrane leading to a water mass transfer from the external phase to the internal phase (Geiger et al., 1998; Grossiord & Stambouli, 2007; Lutz et al., 2009). As a consequence, the volume of the oily globules increases and when the resistance of the membrane becomes insufficient, the globule breaks liberating the active compound.
In water waste treatments which also involve W/O/W emulsions, the toxic compound present in the external phase has to diffuse through the membrane to be entrapped in the inner droplets. In such separation processes, selectivity of the membrane is an important parameter (Kentish & Stevens, 2001; Kumbasar, 2009). Indeed when a compound has to be extracted from a solution containing a variety it is important that only the compound to be extracted diffuses through the membrane. In order to promote selectivity of the membrane, a carrier can be added into the membrane phase (Venkatesan & Meera Sheriffa Begum, 2009; Ng et al., 2010). A carrier is a molecule which can form a complex with the toxic compound at the external interface and transport it to the internal phase where the toxic compound will be entrapped (Hasan et al., 2006; Frasca et al., 2009). High selectivity means that the carrier holds a good affinity with the toxic compound in order to exclusively transport it through the membrane (Kaghazchi et al., 2006).
In separation applications, the instability of the multiple emulsions can reduce significantly the efficiency of the process. Indeed, if Ostwald swelling or coalescence of the globules occurs, such mechanisms can lead to the break of the globules. The extracted molecule is then directly released in the external phase which ruins the extraction process (Yan & Pal, 2001, 2004; Mortaheb et al., 2008).
If O/W/O multiple emulsions have been less extensively studied, they can also finds potential applications in food, cosmetics and controlled delivery drugs (Benichou et al.,

2007; Mishra & Pandit, 1989; Laugel et al., 1998, 2000; Yu et al., 2003). They are found also in application in separation processes of hydrocarbons (Krishna et al., 1987; Garti & Kovacs, 1991). In controlled drug delivery applications the challenge consists in the control of the diffusion of the entrapped active molecule (Grossiord et al., 1998). The active matter can diffuse and migrate through the membrane via an osmotic pressure gradient and it can be almost difficult to retain the active molecule inside the inner phase upon prolonged storage, all the more as the emulsifier can form micelles (Benichou et al., 2007). Micelles are capable of solubilizing the active molecule and facilitate the transport of active matter from the internal interface to the external interface.

One can see that developing potential applications of multiple emulsions requires a good understanding of the mass transfer mechanisms but besides measuring kinetics of mass transfer, it is also important to take into account formulation aspects of the emulsion which have also a direct influence on the mass transfer.

W/O/W emulsions entrapping different compounds, urea or $MgSO_4$ have been studied by using the DSC techniques presented in this chapter (Potier et al., 1992; Raynal et al., 1994 Raynal et al, 1993). As case of study we propose to describe the release of tetradecane within an O/W/O multiple emulsion studied by DSC. It is described how to detect the variations of composition of the external oil phases during time as well as the evolution of the emulsion with time. The influence of formulation parameters such as surfactant concentration and mass ratio of the internal phase on the evolution of the emulsion are also discussed.

5.1 Emulsion preparation

The tetradecane/Water/hexadecane ($O_1/W/O_2$) multiple emulsions were prepared in a two-step emulsification method (Avendaño-Gomez et al., 2005). Firstly, primary simple emulsions O_1/W were prepared. Tetradecane was dispersed into an aqueous solution in which was previously dissolved Tween 20. Different concentrations of Tween 20 have been investigated, 2 wt%, 4 wt% and 7 wt%. Tetradecane was then slowly dripped into the aqueous phase under agitation using an Ultra Turrax mixer at a speed of 20,000 rpm. All the O_1/W emulsions prepared contained a tetradecane/water ratio of 2/3. The primary emulsions were then sonicated during 10 min. The droplet size distribution was measured using Coulter counter technique and the mean size of tetradecane droplets for all primary emulsion was about 5 μm. In a second step, 19 g of each primary O_1/W emulsion was mixed gently in 10.7 g of the hexadecane external phase containing 1 g of Abil EM 90 as surfactant and 0.1 g of decanol as co-surfactant. Each primary emulsion was incorporated slowly in the hexadecane using a Rayneri blender at a speed of 50 rpm and the emulsions were kept under gentle agitation until the duration of the experiments. The globule size of the emulsions was then determined by using a Cannon Microscope and the mean diameter was about 1000 μm for the all emulsions prepared.

5.2 DSC measurements - results and discussions

Figure 20 presents an example of the evolution of DSC curves obtained for the $O_1/W/O_2$ multiple emulsions understudied. The DSC curves are characteristic of a multiple emulsion containing 2 wt% of Tween 20 in the aqueous membrane. On this figure, the initial DSC curve was obtained by submitting the emulsion after 1 minute of its preparation and presents 3 peaks of crystallization. At that time it can be considered that the transfer has not yet started and the three peaks of crystallization corresponds to the crystallization of the

three phases composing the multiple emulsion. The signal at around -18°C represents the crystallization of the aqueous phase by breakdown of undercooling. This signal is characteristic of bulk water crystallization as it has been described in section 2. Even if the aqueous phase is dispersed as a multitude of globules their size of 1 mm is not sufficiently tiny enough to involve nucleation delays like those observed in W/O emulsions droplets of a few μm^3. Therefore the behavior of crystallization of aqueous globule looks like the crystallization of water bulk phase. The exothermic peak at 17°C which initial part of the signal is sharp is attributed to the bulk hexadecane crystallization. The hexadecane crystallizes at 17°C but with a very little degree of subcooling, the melting temperature of hexadecane being of 18°C. The third bell shape peak is attributed to the crystallization of the tetradecane dispersed droplets. The temperature is -12.8°C and is given by the apex of the peak which means that nearly 50% of the droplets are crystallized.

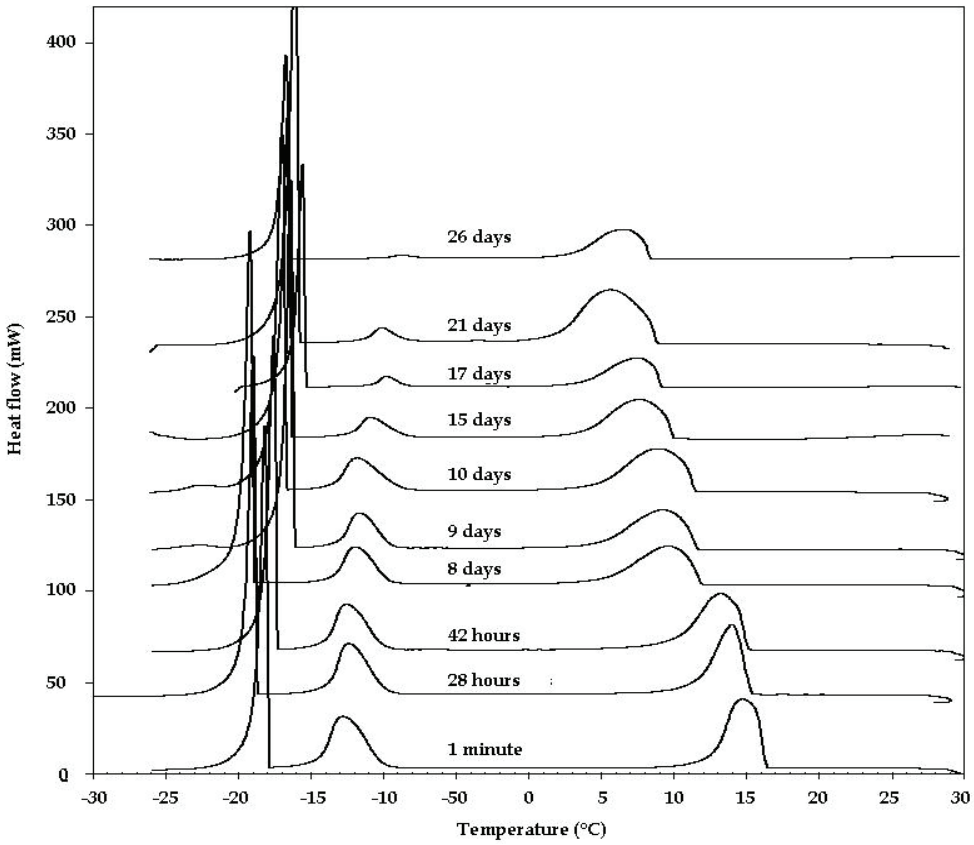

Fig. 20. Evolution of the DSC curves of an $O_1/W/O_2$ multiple emulsion containing 2 wt% of Tween 20 in the aqueous membrane

Figure 20 also shows a clearly evolution with time of the crystallization peaks of the internal phase and the external phase. Actually, the crystallization peak of the tetradecane exhibits a

progressive decrement in intensity whereas the temperature of the crystallization peaks of hexadecane decreases progressively from 17°C to 10°C. From these results it can be deduced that tetradecane releases gradually over time. On the ultimate DSC curve, the crystallization peak of tetradecane disappears which means that the globules are empty and total tetradecane has been transferred in the external phase. Consequently the external phase composition has changed over time from pure hexadecane to a given tetradecane-hexadecane composition when the transfer ends, passing through different intermediate compositions.

Using equation 2, it is then possible to determine the percentage y of tetradecane still entrapped at time t. The values of y versus time and obtained for different amounts of Tween (2, 4 and 7%) are reported on figure 21.

The emulsions initially contained the same amount of encapsulated tetradecane and it can be easily observed that the kinetics depend on the amount of Tween 20 contained in the membrane. The higher the concentration of surfactant, the higher is the release of tetradecane. Nevertheless, it must be emphasized that tetradecane is gradually released through the aqueous membrane and that no globule breaking was observed during the life-time of the multiple emulsion.

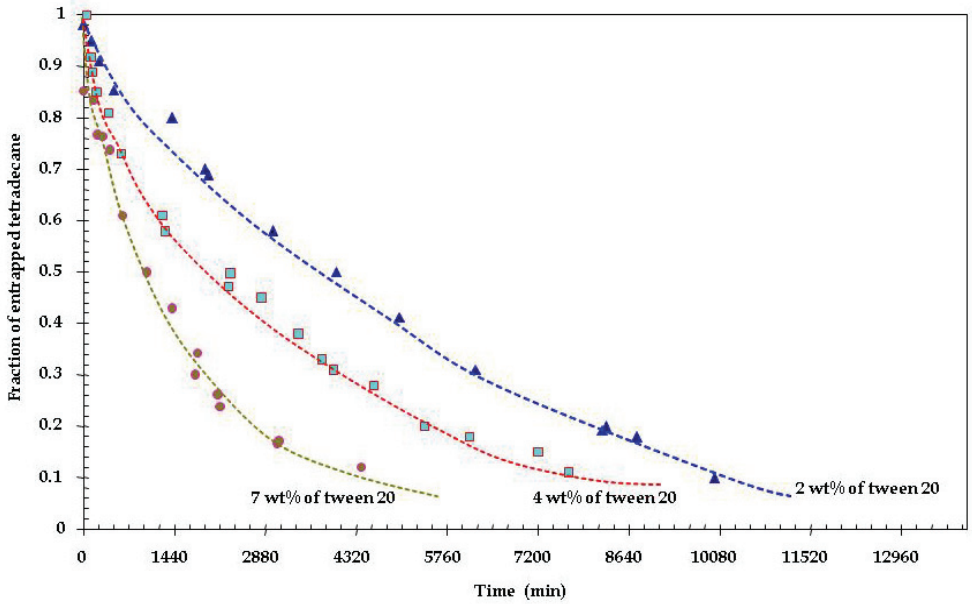

Fig. 21. Evolution of the quantity of tetradecane encapsulated in the globules with time at different concentrations of Tween 20 in the aqueous membranes phase

5.3 Model of kinetics of tetradecane release

First a model based on the expressions of the flux of tetradecane versus chemical potential gradient has been used (Avendano, 2002). A solubilisation – diffusion model has been developed and the comparison with the experimental data has shown theoretical release times higher: 50% released in 4000 minutes (experiment) and 5000 minutes (model).

Therefore an improved model using the shrinking core model commonly applied to heterogeneous reactions (Stambouli et al., 2007) has been developed. The model has been modified and applied to the multiple emulsions under studied. Owing to the fact that the structure of multiple emulsions is complex and in order to simplify the mathematical treatment of the model, it has been assumed that the internal droplets of tetradecane form only one virtual drop encapsulated in an aqueous spherical shell which represents the membrane. The shrinking model and the typical concentration profile for diffusive transport of tetradecane through the membrane are described in figure 22. For clarity reasons let us define first of all, the notations used in the description of the kinetics model: C_I represents the pure tetradecane into the internal virtual drop. C_{II}, is the tetradecane concentration in the external phase (tetradecane + hexadecane). C'_I is the tetradecane concentration at the interface in the aqueous phase at interface I. C'_{II} is the tetradecane concentration in the aqueous phase at the interface II. C′(r) is the tetradecane concentration in the aqueous phase at radius r. r_I and r_{II} are the radius of the internal virtual tetradecane drop and the radius of the aqueous globule respectively.

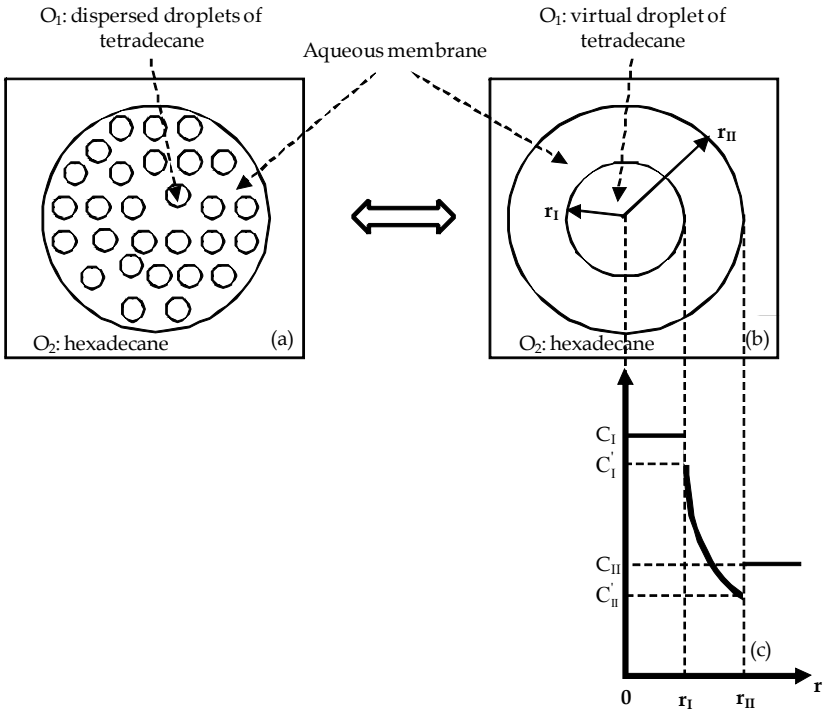

Fig. 22. (a) Schematic representation of the tetradecane/water/oil emulsion. (b) A multiple globule containing a virtual drop of tetradecane surrounding by a spherical aqueous membrane shell. (c) Profile of tetradecane concentration in the emulsion

Two partition coefficients can be defined as the ratios between the concentration of tetradecane concentration in the aqueous membrane phase and the oily phases I and II considering that equilibrium is assumed at both water/oil interfaces I and II.

$$K_1 = \frac{C'_{\mathrm{I}}}{C_{\mathrm{I}}} \tag{9}$$

$$K_2 = \frac{C'_{\mathrm{II}}}{C_{\mathrm{II}}} \tag{10}$$

For simplification, it is considered that the internal dispersed droplets of tetradecane are immobile inside the aqueous globules and are able to release tetradecane in the external phase through the membrane. Therefore, it is assumed that the release of tetradecane occurs via a pure molecular diffusion or pure micellar diffusion.
The expression of the tetradecane flow through the aqueous spherical membrane shell of radius r is expressed as equation (11) where D_e is the effective diffusion coefficient of tetradecane in the aqueous membrane phase.

$$J(r) = -4\Pi r^2 D_e \left(\frac{dC'}{dr} \right) \tag{11}$$

From mass balance equations and integration between $r=r_1$ and $r=r_2$ assuming that the volume of the aqueous membrane does not vary during the tetradecane release, the time t of release can be expressed by the following equation

$$t = \frac{\rho_T (r_{\mathrm{I}}^0)^2}{2D_e \Delta C^*} \left[(Z_0 - x)^{\frac{2}{3}} - (1-x)^{\frac{2}{3}} + 1 - Z_0^{\frac{2}{3}} \right] \tag{12}$$

where $\Delta C^* = C'_I - C'_{II}$; ρ_T and V_T are respectively the density of tetradecane and the volume of the virtual tetradecane phase I ; $Z_0 = \left(\frac{r_{II}^0}{r_I^0} \right)^3$, $y = \frac{r_I}{r_I^0}$ where r_I^0 is the initial radius of the virtual tetradecane droplet.
If we considered the time t_1 at which the internal tetradecane phase is completely release, ($r_1=0$ and $x= 1$), then t_1 is expressed as

$$t_1 = \frac{\rho_T \left(r_I^0 \right)}{2D_e \Delta C^*} \left[(Z_0 - 1)^{\frac{2}{3}} + 1 - Z_0^{\frac{2}{3}} \right] \tag{13}$$

Finally it is possible to write the time t of release in the equivalent following form as

$$t = \frac{t_1}{\left[(Z_0 - 1)^{\frac{2}{3}} + 1 - Z_0^{\frac{2}{3}} \right]} \left[(Z_0 - x)^{\frac{2}{3}} - (1-x)^{\frac{2}{3}} + 1 - Z_0^{\frac{2}{3}} \right] \tag{14}$$

Taking into account the value of Z_0 from equation 15, it was possible by using equation (14) where t_1 is the fitting parameter and the least-squares method to obtain the best fitting of the experimental data relating to the tetradecane release x versus time.

$$Z_0 = \left(\frac{r_{II}^0}{r_I^0} \right)^3 = \frac{0.282 + 0.326}{0.282} \tag{15}$$

Where 0.282 and 0.326 are the volume fractions of the tetradecane phase and the membrane aqueous phase in the multiples emulsions respectively.

Figure 23 presents the experimental and the model results obtained from a multiple emulsion containing 2 wt% of Tween 20 in the membrane phase. The model fits well the experimental data. It is worth noting that the model also fits the experimental data for the multiple emulsions containing 4 and 7 wt% of Tween 20 in the aqueous membrane phase. The time t_1 of complete release of tetradecane has been derived from the three formulations and it was obtained, t_1= 875h, t_1= 451h and t_1= 318h for 2, 4 and 7 wt% of Tween 20 respectively. In the model, the values of $\frac{D_e \Delta C^*}{\rho_T}$ were fitted using equation 12 using $r_I^0 = 0.387mm$ calculated from Z_o ($r_{II}^0 = 1mm$). The values of the effective diffusion coefficient obtained were compared to those of literature (Mandal et al, 1985) and a difference was observed. However, the order of magnitude of the effective diffusion coefficient is in a good agreement with the literature data. Therefore, it can be concluded that the tetradecane release is strongly dependent from the Tween 20 concentration and occurs by a micellar transport mechanism. The difference observed between the diffusion coefficients from the model and literature may be due to the simplifications made for developing the model. A more accurate model can be proposed but new empirical parameters are needed.

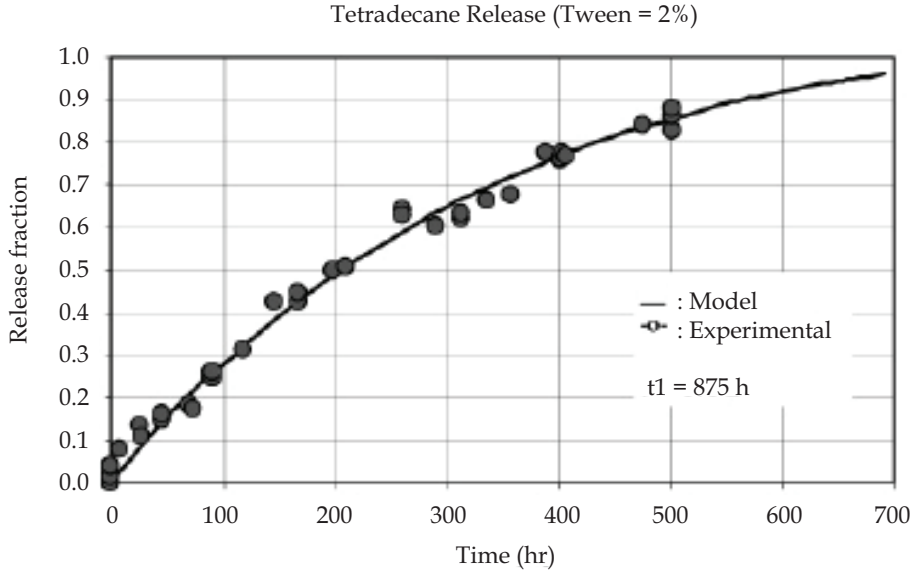

Fig. 23. Tetradecane release obtained from the model and compared to the experimental data. Example of an emulsion containing 2 wt% of Tween 20 in the aqueous membrane

6. Conclusion

Mass transfers occurring within different kinds of emulsions, simple, mixed and multiple, have been described in this chapter. Almost of the examples given are dealing with mass transfer occurring at ambient temperature between phases of different composition. Focus has been made about the results obtained by submitting time to time an emulsion sample to a cooling and heating cycle during which freezing and melting of the phases concerned by the mass transfer are registered through the energies involved in the liquid – solid transition thanks to a differential scanning calorimeter. The amount of the transferred mass is deduced either from the freezing or melting of the pure material droplets A or from the calibration curve that gives the freezing temperature of the droplets made of A+B, versus the composition. This DSC technique appears to be suitable to study this kind of phenomenon as far it permits to follow the transfer and furthermore to get the kinetic of the transfer. Doing so a model of the transfer can be set up and the mechanisms involved can be described. It appears that the mechanism to be considered is a solution – diffusion transfer facilated by micelles that entrapped the compound to be transferred. Therefore a control release can be set up through the formulation of the emulsion. Another type of mass transfer has been described that induces solid ripening as the result of the mass transfer. The case of hydrate formation has been given as an example. The mass transfer due to the diffusion of a material in the oil phase of a W/O emulsion, induces the formation of a solid compound, namely an hydrate, when this compound chemically reacts with water of the dispersed water. Here as well, the DSC technique appears to be suitable but due to overlapping of transitions dealing with water and hydrate a complementary technique is needed. That shows the limit of the DSC technique that needs net liquid-solid transitions and a reduced overlapping of the transitions. To conclude these studies show the great advantage to use emulsions for having mass transfer in a rather short time due to the total high surface area of exchange and the presence of micelles. Therefore, these systems can be considered to set up separation processes, the emulsions being seen as liquid membranes systems or as mini reactors for getting chemical reactions between compounds. Nevertheless a control of the formulation of the emulsions in order to get kinetically stable emulsions at least during the process involved is needed.

7. References

Ariyaprakai, S. & Dungan, S. R. (2010). Influence of surfactant structure on the contribution of micelles to Ostwald ripening in oil-in-water emulsions. *Journal of Colloid and Interface Science*, Vol. 343, No. 1, (March 2010) pp. 102-108 ISSN 0021-9797

Avendano-Gomez, J.; Grossiord, J.L. & Clausse, D. (2000). Composition ripening in o/w emulsions. *Entropie*, Vol. 36, No. 224-25, (September 1999) pp. 110-116 ISSN 0013-9084

Avendaño-Gomez, J. (2002).Etude par calorimétrie du mûrissement de composition dans une émulsion mixte H_1-H_2/eau et une émulsion multiple H_1/eau/H_2. Thèse de Doctorat de l'Université de Technologie de Compiègne, France

Avendaño-Gomez, J. R.; Grossiord, J.L. & Clausse, D. (2005). Study of mass transfer in oil–water–oil multiple emulsion by differential scanning calorimetry. *Journal of Colloid and Interface Science*, Vol. 290, No. 2, (October 2005) pp. 533-545 ISSN 0021-9797

Benichou, A.; Aserin, A. & Garti, N. (2007). O/W/O double emulsions stabilized with WPI-polysaccharide conjugates. *Colloids and surfaces A: Physicochem. Eng. Aspects*, Vol. 297, No. 1-3, (April 2007) pp. 211-220 ISSN 0927-7757

Benichou, A. & Aserin, A. (2007). Recent developments in O/W/O multiple emulsions, In: *Multiple Emulsion: Technology and Applications,* A. Aserin, pp. (165-208), John Wiley and Sons Inc. ISBN 978-0-470-17093-9, Hoboken, USA

Binks, B. P.; Clint, J.H.; Fletcher, P.D.I. & Rippon, S. (1998). Kinetics of swelling of oil-in-water emulsions. *Langmuir*, Vol. 14, No. 19, (September 1998) pp. 5402-5411 ISSN 0743-7463

Binks, B. P.; Clint, J.H.; Fletcher, P.D.I. & Rippon, S. (1999). Kinetics of swelling of oil-in-water emulsions stabilized by different surfactants. *Langmuir*, Vol. 15, No. 13 (June 1999) pp. 4495-4501 ISSN 0743-7463.

Capek, I. (2004). Degradation of kinetically-stable o/w emulsions. *Advances in Colloid and Interface Science*, Vol. 107, No. 2-3, (March 2004) pp. 125-155 ISSN 0001-8686

Clausse, D. (1985). Caractérisation des propriétés thermodynamiques d'une émulsion. Détermination de la température et de l'enthalpie de changement d'état de la phase dispersée. *Revue Générale de Thermique*, Vol. 279, pp. 263-268 ISSN 0035-3159

Clausse, D.; Pezron, I. & Gauthier, A. (1995a). Water transfer in mixed water-in-oil emulsions studied by differential scanning calorimetry. *Fluid Phase Equilibria*, Vol. 110, No. 1-2, (September 1995) pp.137-150 ISSN 0378-3812

Clausse, D.; Pezron, I. & Raynal, S. (1995b). Water transfer within multiple W/O/W Emulsions at a fixed subambiant temperature. *Cryo-Letters*, Vol. 16, No. 4, (July-August 1995), pp. 219-230 ISSN 0143-2044

Clausse, D.; Pezron, I. & Behaeghel, A. (1999a). Water transfer between water and water+NaCl droplets in emulsions, *Journal of Dispersion Science and Technology*, Vol. 20, No. 1-2, (1999a) pp. 315-326 ISSN 0193-2691

Clausse, D.; Pezron, I. & Komunjer, L. (1999b). Stability of W/O and W/O/W emulsions as a result of partial solidification. *Colloids and Surface A: Physicochemical and engineering Aspects*, Vol. 152, No. 1-2, (July 1999) pp. 23-29 ISSN 0927-7757

Clausse, D.; Fouconnier, B. & Avendaño-Gomez, J. R. (2002b). Ripening phenomena in Emulsions - A calorimetry investigation. *Journal of Dispersion Science and Technology*, Vol. 23, No. 1-3, pp. 379-391 ISSN 0193-2691

Clausse, D.; Gomez, F.; Pezron, I.; Komunjer, L. & Dalmazzone, C. (2005). Morphology characterization of emulsions by differential scanning calorimetry. *Advances in Colloid and Interface Science*, Vol. 117, No. 1-3, (December 2005) pp. 59-74 ISSN 0001-8686

Clausse, D.; Pezron, I.; Gomez, F.; Dalmazzone, C.; Sacca, L. & Drelich, A. (2008). Differential Scanning Calorimetry as a tool for following emulsion evolution in microgravity conditions from the MAP-Project FASES. *Journal of the Japan Society of Microgravity Application*, Vol. 25, No. 3, pp. 227-230

Colinart, P.; Delepine, S.; Trouve, G. & Renon, H. (1984). Water transfer in emulsified liquid membrane process. *Journal of membrane Science*, Vol. 20, No. (August 1984) pp. 167-187 ISSN 0376-7388

Dalmazzone, D.; Kharrat, M.; Lachet, V.; Fouconnier, B. & Clausse, D. (2002). DSC and PVT measurements of methane and trichlorofluoromethane hydrate dissociation equilibria in highly concentrated calcium chloride solutions and water-in-oil emulsions. *Journal of thermal Analysis and Calorimetry*, Vol. 70, (February 2002) pp. 493-505 ISSN 1418-2874

Dalmazzone, D.; Hamed, N. & Dalmazzone, D. (2009). DSC measurements and modelling of the kinetics of methane hydrate formation in water-in-oil emulsion. *Chemical Engineering Science*, Vol. 64, No. 9, (May 2009) pp. 2020-2026 ISSN 0009-2509

Davies, S. R.; Hester, K. C.; Lachance, J. W.; Koh, C. A. & Sloan, E. D. (2009). Studies of hydrate nucleation with high pressure differential scanning calorimetry. *Chemical Engineering Science*, Vol. 64, No. 2, (January 2009) pp. 370-375 ISSN 0009-2509

Drelich, A. (2009). Emulsions formulées avec des particules de silice : caractérisation, stabilité, transfert de matière. Thèse de Doctorat de l'Université de Technologie de Compiègne, France

Drelich, A.; Gomez, F.; Grossiord, J. L.; Clausse, D. & Pezron, I. (2011). to be published.

Elwell, M.W.; Roberts, R.F. & Coupland, J.N. (2004). Effect of homogenization and surfactant type on the exchange of oil between emulsion droplets. *Food Hydrocolloids,* Vol. 18, No. 3, (May 2004) pp. 413-418 ISSN 0268-005X

Fouconnier, B.; Legrand, V.; Komunjer, L.; Clausse, D.; Bergfoldt, L. & Sjöblom, J. (1999). Formation of trichlorofluoromethane hydrate in w/o emulsions studied by differential scanning calorimetry. *Progress in colloid & polymer science*, vol. 112, pp. 105-108 ISSN 0340-255X

Fouconnier, B.; Manissol, Y.; Dalmazzone, D. & Clausse, D. (2002). Study of trichlorofluoromethane hydrate formation in W/O emulsions : dissociation energy and equilibrium with salt + water solutions. *Entropie*, Vol. 38 No. 239-240, (August 2002) pp. 72-77 ISSN 0013-9084

Fouconnier, B.; Komunjer, L.; Ollivon, M.; Lesieur, P.; Keller, G. & Clausse, D. (2006). Study of CCl_3F hydrate formation and dissociation in W/O emulsion by differential scanning calorimetry and X-ray diffraction. *Fluid Phase Equilibria*, Vol. 250, No. 1-2, (December 2006) pp. 76-82 ISSN 0378-3812

Frasca, S.; Couvreur, P.; Seiller, M.; Pareau, D.; Lacour, B.; Stambouli, M. & Grossiord, J. L. (2009). Paraquat detoxication with multiple emulsions. *International Journal of Pharmaceutics*, Vol. 380, No.1-2, (October 2009) pp 142-146 ISSN 0378-5173

Grossiord, J. L. & Stambouli, M. (2007). Potentialities of W/O/W Multiple Emulsions in Drug Delivery and Detoxification, In: *Multiple Emulsion: Technology and Applications,* A. Aserin, pp. (209-234), John Wiley and Sons Inc. ISBN 978-0-470-17093-9, Hoboken, USA

Garti, N. & Kovacs, A. (1991). Facilitated emulsion liquid membrane separation of complex hydrocarbon mixtures. *Journal of Membrane Science*, Vol. 56, No. 3, (March 1991) pp. 239-246 ISSN 0376-7388

Garti, N. & Lutz, R. (2004). Recent progress in double emulsion, In: *Emulsions: Structure Stability and Interactions*, D. N. Petsev, pp. (557-667), Elsevier. ISBN 0-12-088499-2, Oxford, UK

Geiger, S.; Tokgoz, S.; Fructus, A.; Jager-Lezer, N.; Seiller, M.; Lacombe, C. & Grossiord, J. L. (1998). Kinetics of swelling–breakdown of a W/O/W multiple emulsion: possible mechanisms for the lipophilic surfactant effect. *Journal of Controlled Release*,Vol. 52, No. 1-2, (March 1998) pp. 99-107 ISSN 0168-3659

Grossiord, J. L.; Seiller, M. & Silva-Cunha, A. (1998). Obtaining multiple emulsions, In : Multiple emulsions : structure, properties and applications, M. Seiller, J. L. Grossiord, pp. 57-80, Edition de santé. ISBN 2-86411-119-5, Paris, France.

Hai, M. & Magdassi, S. (2004). Investigation on the release of fluorescent markers from w/o/w emulsions by fluorescence-activated cell sorter. *Journal of Controlled Release*, Vol. 96, No. 3-18, (May 2004) pp. 393-402 ISSN 0168-3659

Hasan, M. A.; Selim, Y. T. & Mohamed, K. M. (2006). Removal of chromium from aqueous waste solution using liquid emulsion membrane. *Journal of Hazardous Materials*, Vol. 168, No. 2-3, (September 2009) pp. 1537-1541 ISSN 0304-3894

Jakobsen, T.; Sjöblom, J. & Ruoff, P. (1996). Kinetics of gas hydrate formation in W/O-emulsions the model system trichlorofluoromethane/water/non-ionic surfactant studied by means of dielectric spectroscopy. *Colloids and Surfaces A: Physicochemical and Engineering Aspects*, Vol. 112, No. 1, (July 1996) pp. 73-84 ISSN 0927-7757

Jiao, J. & Burgess, D. J. (2003). Ostwald ripening of water-in-hydrocarbon emulsions. *Journal of Colloid and Interface Science*, Vol. 264, No. 2, (August 2003) pp. 509-516 ISSN 0021-9797

Kaghazchi, T.; Kargari, A.; Yegani, R. & Zare, A. (2006). Emulsion liquid membrane pertraction of L-lysine from dilute aqueous solutions by D2EHPA mobile carrier. *Desalination*, Vol. 190, No.1-3, (April 2006) pp. 161-171 ISSN 0011-9164

Kentish, S. E. & Stevens, G. W. (2001). Innovations in separation technology for the recycling and re-use of liquid waste streams. *Chemical Engineering Journal*, Vol. 84, No. 2, (October 2001) pp. 149-159 ISSN 1385-8947

Kharrat, M. & Dalmazzone, D. (2003). Experimental determination of stability conditions of methane hydrate in aqueous calcium chloride solutions using high pressure differential scanning calorimetry. *Journal of Chemical Thermodynamics*, Vol. 35, No. 9, (September 2003) pp. 1489-1505 ISSN 0021-9614

Koh, C. A.; Westacott, R.E.; Zhang, W.; Hirachand, K.; Creek, J. L. & Soper, A. K. (2002). Mechanisms of gas formation and inhibition . *Fluid Phase Equilibria*, Vol. 194-197, (March 2002) pp. 143-151 ISSN 0378-3812

Krishna, R.; Goswami, A. N. & Sharma, A. (1987). Effect of emulsion breakage on selectivity in the separation of hydrocarbon mixtures using aqueous surfactant membranes. *Journal of Membrane Science*, Vol. 34, No. 2, (1987) pp. 141-154 ISSN 0376-7388

Kumbasar, R. A. (2009). Extraction and concentration study of cadmium from zinc plant leach solutions by emulsion liquid membrane using trioctylamine as extractant. *Hydrometallurgy*,Vol. 95, No.3-4, (February 2009) pp. 290-296 ISSN 0304-386X

Lachance, J. W.; Dendy Sloan, E. & Koh C. A. (2008). Effect of hydrate formation/ dissociation on emulsion stability using DSC and visual techniques. *Chemical Engineering Science*, Vol. 63, No. 15, (August 2008) pp. 3942-3947 ISSN 0009-2509

Laugel, C.; Baillet, A.; Youenang Piemi, M. P.; Marty, J. P. & Ferrier, D. (1998). Oil–water–oil multiple emulsion for prolonged delivery of hydrocortisone after topical application: comparison with simple emulsion. *International Journal of Pharmaceutics*, Vol. 160, No.1, (January 1998) pp. 109-117 ISSN 0378-5173

Laugel, C.; Rafidison, P.; Potard, G.; Aguadisch, L. & Baillet, A. (2000). Modulated release of triterpenic compounds from a O/W/O multiple emulsion formulated with dimethicones: infrared spectrophotometric and differential calorimetric approaches. *Journal of Controlled Release*, Vol. 63, No.1-2, (January 2000) pp. 7-17 ISSN 0168-3659

Le Parlouër, P.; Dalmazzone, C.; Herzhaft, B.; Rousseau, L. & Mathonat, C. (2004). Characterisation of gas hydrate formation using a new high-pressure micro-DSC. *Journal of Thermal Analysis and Calorimetry*, Vol. 78, No. 1, (2004) pp. 165–172 ISSN 1388–6150

Li, N. N. (1968). Membrane separation process. US Patent 3 410 794

Lutz, R.; Aserin, A.; Wicker, L. & Garti, N. (2009). Release of electrolytes from W/O/W double emulsions stabilized by a soluble complex of modified pectin and whey protein isolate. *Colloids and Surfaces B: Biointerfaces*, Vol. 74, No. 1, (November 2009) pp. 178-185 ISSN 0927-7765

Mandal, A. B.; Gupta, S. & Moulik S. P. (1985). Characterization of Tween-20 and Tween-80 micelles in aqueous medium from transport studies. *Indian Journal of chemistry*, Vol. 24A, No. 8, pp. 670-674 (1985) ISSN 0376-4710

McClements, D. J.; Dungan, S. R.; German, J. B. & Kinsella, J. E. (1992). Oil exchange between oil-in-water emulsion droplets stabilised with a non-ionic surfactant. *Food Hydrocolloids*, Vol. 6, No. 5 (November 1992) pp. 415-422 ISSN 0268-005X

McClements, D. J.; Dungan, S. R.; German, J. B. & Kinsella, J. E. (1993a). Evidence of Oil Exchange between Oil-in-Water Emulsion Droplets Stabilized by Milk Proteins. *Journal of Colloid and Interface Science,* Vol. 156, No. 2 (March 1993) pp. 425-429 ISSN 0021-9797

McClements, D. J.; Dungan, S. R.; German, J. B. & Kinsella, J. E. (1993b). Factors which affect oil exchange between oil-in-water emulsion droplets stabilized by whey protein isolate: protein concentration, droplet size and ethanol. *Colloids and Surfaces A: Physicochemical and Engineering Aspects,* Vol. 81, No. 13 (December 1993) pp. 203-210 ISSN 0927-7757

McClements, D. J. & Dungan, S. R. (1993c). Factors that affect the rate of oil exchange between oil-in-water emulsion droplets stabilized by a non-ionic surfactant: droplet size, surfactant concentration, and ionic strength. *Journal of Physical Chemistry*, Vol. 97, No. 28 (July 1993) pp. 7304-7308 ISSN 0022-3654

Mishra, B. & Pandit, J. R. (1989). Prolonged release of pentazocine from multiple O/W/O emulsions. *Drug Development Industrial Pharmacy,* Vol. 15, No. 8, pp. 1217-1230 (1989) ISSN: 0363-9045

Mortaheb, H. R.; Aminia, M. H.; Sadeghiana, F.; Mokhtarania, B. & Daneshyara, H. (2008). Study on a new surfactant for removal of phenol from wastewater by emulsion liquid membrane. *Journal of Hazardous Materials*, Vol. 160, No. 2-3, (December 2008) pp. 582-588 ISSN 0304-3894

Muschiolik, G.; (2007). Multiple emulsions for food use. *Current Opinion in Colloid & Interface Science,* Vol. 12, (August 2007) pp. 213-220 ISSN 1359-0294

Muguet, V.; Seiller, M.; Barratt, G.; Ozer, O.; Marty, J. P. & Grossiord, J. L. (2001). Formulation of shear rate sensitive multiple emulsions. *Journal of control release*, Vol. 70, No. 1-2 (January 2001) pp. 37-49 ISSN 0168-3659

Ng, Y. S.; Jayakumar, N. S. & Hashim, M. A. (2010). Performance evaluation of organic emulsion liquid membrane on phenol removal. *Journal of Hazardous Materials*, Vol. 184, No.1-3, (December 2010) pp. 255-260 ISSN 0304-3894

Noble, R. D. & Stern, A. A. (1995). Membrane separation technology: Principle and application, In: , R. D. Noble & A. A. Stern, Elsevier Science ISBN 044481633X, Amsterdam, The Netherlands

Tedajo, G. M.; Seiller, M.; Prognon, P. & Grossiord, J. L. (2001). pH compartmented W/O/W multiple emulsion: a diffusion study. *Journal of control release*, Vol. 75, No. 1-2 (July 2001) pp. 45-53 ISSN 0168-3659

Tedajo, G. M. et al. (2005). Release of antiseptics from the aqueous compartments of a W/O/W multiple emulsion. *International Journal of Pharmaceutics*, Vol. 288, No. 1, 6 (January 2005) pp. 63-72 ISSN 0378-5173

Venkatesan, S. & Meera Sheriffa Begum, K.M. (2009). Emulsion liquid membrane pertraction of benzimidazole using a room temperature ionic liquid (RTIL) carrier. *Chemical Engineering Journal*, Vol. 148, No. 2-3, (May 2009) pp. 254-262 ISSN 1385-8947

Yan, J. & Pal, R. (2001). Osmotic swelling behavior of globules of W/O/W emulsion liquid membranes. *Journal of Membrane Science*, Vol. 190, No.1, (August 2001) pp. 79-91 ISSN 0376-7388

Yan, J. & Pal, R. (2004). Effects of aqueous-phase acidity and salinity on isotonic swelling of W/O/W emulsion liquid membranes under agitation conditions. *Journal of Membrane Science*, Vol. 244, No.1-2, (November 2004) pp. 193-203 ISSN 0376-7388

Pal, R. (2011). Rheology of simple multiple emulsions. *Current Opinion in Colloid & Interface Science,* Vol. 16, No. 1, (February 2011) pp. 41-60 ISSN 1359-0294

Potier, L.; Raynal, S.; Seiller, M.; Grossiord, J.L. & Clausse, D. (1992). Study state transitions within multiple W/O/W emulsions using calorimetry (DSC). *Thermochimica Acta*, Vol. 204, No. 1, (July 1992) pp. 145-155 ISSN 0040-6031

Potier, L. (1993). Etude par calorimétrie des changements d'état dans une émulsion multiple E/H/E : Application aus transferts de solvant entre deux phases aqueuses. Thèse de Doctorat de l'Université de Technologie de Compiègne, France

Raynal, S.; Potier, L.; Garcia, S. & Clausse, D. (1992). Etude par analyse Enthalpique Différentielle de la surfusion et de la sursaturation de solutions aqueuses d'urée. *Proceeding ACAT*, Vol. 23

Sacca, L.; Drelich, A.; Gomez, F.; Pezron, I. & Clausse, D. (2008). Composition Ripening in Mixed Water-in-oil Emulsions Stabilized with Solids Particles. *Journal of Dispersion Science and Technology*, Vol. 29, N° 7, (2008) pp. 948-952 ISSN 0193-2691

Stambouli, M.; Avendano-Gomez, J. R.; Pezron, I.; Pareau, D.; Clausse, D. & Grossiord, J. L. (2007). Modelization of the release from a tetradecane/water/hexadecane multiple emulsion: Evidence of significant micellar diffusion. *Langmuir*, Vol. 23, No. 3, (January 2007) pp. 1052-1056 ISSN 0743-7463

Taisne, L.; Walstra, P. & Cabane, B. (1996). Transfert of oil between emulsion droplets. *Journal of Colloid and Interface Science,* Vol. 184, No. 2 (December 1996) pp. 378-390 ISSN 0021-9797

Weiss, J.; Cancelliere, C. & McClements, D.J. (2000). Mass Transport Phenomena in Oil-in-Water Emulsions Containing Surfactant Micelles: Ostwald Ripening. *Langmuir*, Vol. 16 No. 17, (August 2000) pp. 6833-6838 ISSN 0743-7463

Yu, S. C.; Bochot, A.; Le Bas, G.; Chéron, M.; Mahuteau, J.; Grossiord, J. L.; Seiller, M. & Duchêne, D. (2009). Effect of camphor/cyclodextrin complexation on the stability of O/W/O multiple emulsion. *International Journal of Pharmaceutics*, Vol. 261, No. 1-2, (August 2003) pp. 1-8 ISSN 0378-5173

34

Mass Transfer - The Skeleton of Purification Processes

Behnam Khoshandam
Semnan University
Iran

1. Introduction

The purification or generally separation processes play a major role in a chemical, petrochemical, oil and gas industry. After producing a synthetic material usually a purifying section should be designed. The purification processes contain broad units of absorption/ desorption, distillation, liquid-liquid extraction, leaching, humidification/dehumidification, drying, adsorption/desorption, evaporation, membrane and crystallization. Processing design of these units is one of duties of chemical engineers and for this reason literatures related to purification are taught to chemical engineers as different courses on unit operations and separation processes.

The basic rules of mass transfer are as skeleton of different separation or purification processes. Concentration gradient of one or more constituents in a media can force the molecules to transfer in different directions based on Fick's first law of diffusion. Creating a convection form in flow of molecules using different ways in industrial units helps the molecules transportation and in other word the purification rate. Of course to this scenario addition of other phases also should be considered. Addition of a phase or an excess media to the first media produces the problem of passing molecules from the interface between phases and answer to the question of how much molecules are able to pass the interface dam. Therefore in this stage phase equilibrium coming from thermodynamics can help us to answer the question. Using different equilibrium data in handbooks helps us to construct the equilibrium curves.

On the other hand, different contact processes of crosscurrent, countercurrent and cocurrent of different phases create operating line or operating curve that can show the conditions of flows pass next to each other in mass exchanger equipment. Stagewise and differential types of contact are two usual forms of phase contact in mass exchanger equipments. The equipments used these forms of contacts are tray and packed towers and number of theoretical trays and the height of packed beds are two processing parameters that need to be calculated in separation processes.

Many good literatures have been published on separation processes. Different units have been studied in a valuable book under the title "Mass Transfer Operations" (Treybal, 1955) and added others as well, (McCabe et al., 1956), (Pavlov et al., 1979), (Henley et al., 1981), (Hines & Maddox, 1985), (Khoury, 1995) and (Geankoplis, 2003). The analysis of different separation processes was carried out from the same point of view. The processes were

studied in details in mentioned references and usually the classification of separation processes was carried out based on phases concerned in units, for example in transfer between gas and liquid phases, humidification, gas absorption and distillation processes were presented. But it seems classifying the units into two broad branches of 'absorption-like' and 'desorption-like' processes can be helpful on discussion of the main aspects of mass transfer. Therefore in the present chapter, separation units taking place in towers (tray or packed-bed type) are discussed based on a common view point and set into two broad branches. The transfer of molecules presented in a phase to the other phase is investigated from dense point of view of phases. Different separation processes are divided to 'absorption-like' processes and 'desorption-like' processes and a similar analysis procedure for units contain in each category is explained. This method of analysis of separation processes maybe helpful for undergraduate students of chemical engineering and also graduate students to make a common sense between different purification techniques.
In this chapter after dividing the different units into 'absorption-like' and 'desorption-like' processes in the second section, staged processes philosophy is brought in section three and followed with a brief discussion on thermodynamics of processes in section four. Operating line or curve related to processes will be discussed in the fifth section and it follows with staircase construction in sixth section. Different equilibrium diagrams and the strategy of using difference points in process calculations will be discussed in seventh section and section eight contains the calculation of packed bed height. The chapter will be ended through a conclusion section at last.

2. 'Absorption-like' and 'Desorption-like' purification processes

There are different processes that can be applied in purification of products obtained in a chemical industry. Fig. 1 shows different separation processes that can be taking place in tray, packed-bed towers or both. Classification can be carried out based on phases presented in the processes but these processes can be classified into two big branches of 'absorption-like' and 'desorption-like' processes as well. But before explaining these two branches it needs to describe the mass transfer basis of the purification processes.

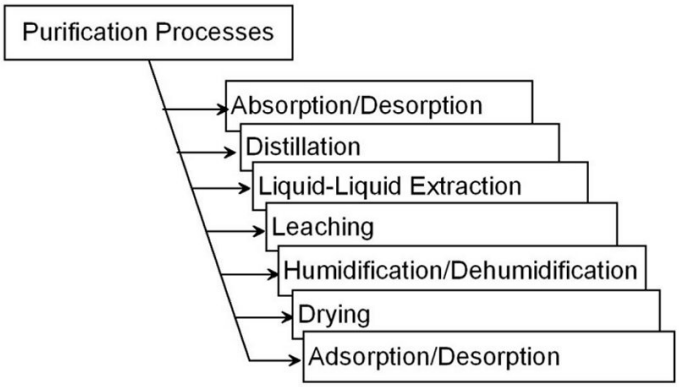

Fig. 1. Classification of purification processes that takes place in tray, packed-bed towers or both

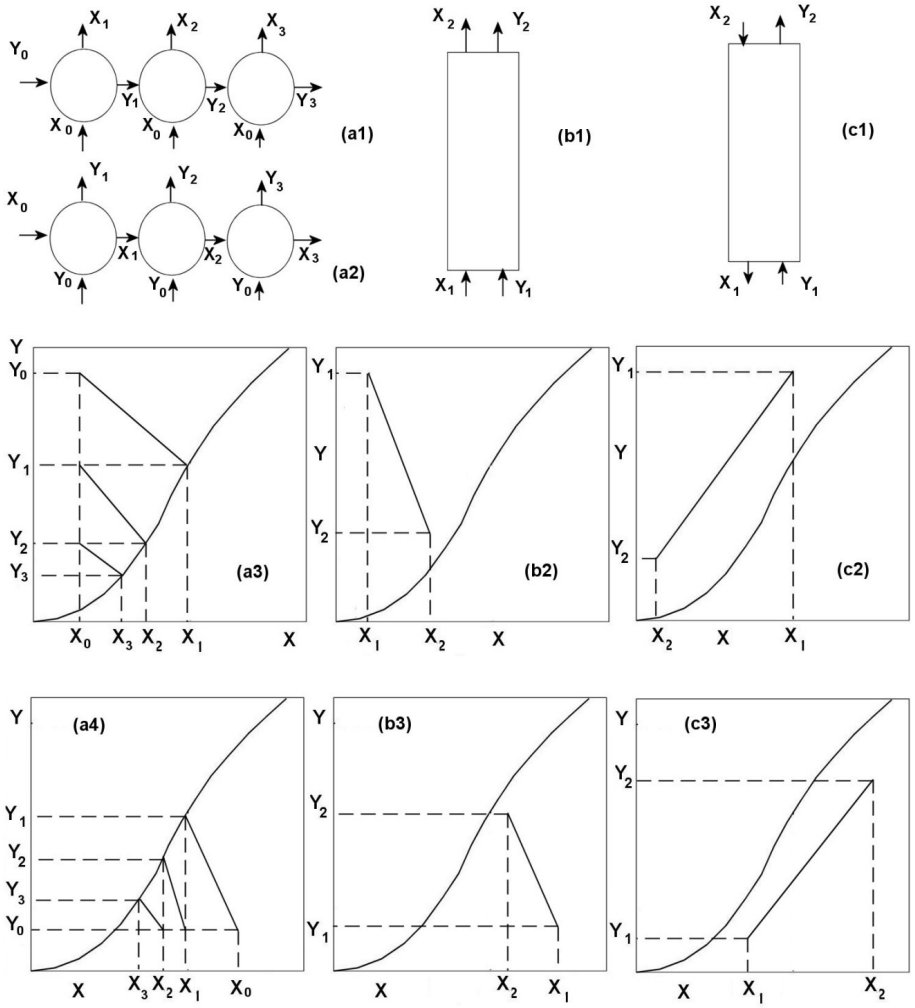

Fig. 2. Processes used in purification and variation of transferring component concentration in absorption-like and desorption-like processes; (a1, a3) crosscurrent flow, absorption-like process; (a2, a4) crosscurrent flow, desorption-like process; (b1, b2) cocurrent flow, absorption-like process; (b1, b3) cocurrent flow, desorption-like process; (c1, c2) countercurrent flow, absorption-like process; (c1, c3) countercurrent flow, desorption-like process

Usually on diffusion and transfer of a constituent through a phase to the interface produced in contact with other phases two cases can be considered. In the first case the constituent molecules move through a less dense phase to the interface and from interface to other phase contain denser material due to the first phase. This case is called as 'absorption-like' process and can contain different processes of absorption, dehumidification and adsorption. But sometimes the molecules move from a dense phase to less dense other phase and it is called a 'desorption-like' processes. Desorption, humidification, leaching and drying processes

can fall in this group. Distillation process that contains rectifying and stripping sections together in a tower is set in 'desorption-like' processes group. Usually Liquid-liquid extraction also falls in 'desorption-like' processes group.
Transferring mass of a component is occurred when there is a difference in component chemical potential between phases. This is a thermodynamics fact of mass transfer. The assumptions simplify this fact into measurable parameter of concentration of component in different phases. The concentration of a component i can be translated as mole or mass concentration (as mole or mass of i to volume which is shown as C_i or ρ_i, respectively), mole or mass fractions (as mole to total moles that is shown as x_i or y_i and as mass to total masses that is shown as ω_i) and partial pressure for gaseous components (as pressure of i that is shown as p_i).
From processing point of view, the differences between purification processes can be categorized in two ways of 'phases contact form' and 'component transferring form'. The contact between phases depends on direction of streams to and from the separator and can be divided into crosscurrent, cocurrent and countercurrent flows. The component transferring form also specifies the way of mass transfer and as mentioned it divides to absorption and desorption-like processes. The operation of different processes is determined from form of varying the component concentrations in streams passing the equipment due to the equilibrium condition from component transferring point of view. The variation of concentrations can be presented as an operating line and the conditions at equilibrium between phases are referred as equilibrium curve. Fig. 2 shows different contact form of phases in purification processes and the form of locating operating line and equilibrium curve in each case generally. All purification processes often fall into different cases shown in Fig. 2. The parameters X and Y show mole fraction of transferring component to mole fraction of non-transferring component and sometimes called as mole ratios. [X=x/(1-x) and Y=y/(1-y)]

3. Staged processes philosophy

Transfer of a component from one phase to another phase can be occurred using the following driving forces:

a. Temperature driving force- In this case transferring heat or energy from outside the system to the desire phase causes moving the component molecules from bulk of the phase to the interface between phases and then to the other phase. Batch distillation and drying are examples of this case.
b. Concentration driving force- Increasing concentration gradient helps the component molecules to transfer more (higher mass flux) from bulk condition to the interface and through other phase. In drying process, using a gas stream with low humidity helps the drying of solid to carry out better. The reason is to impose higher humid concentration difference between bulk of the solid and the gas bulk that consequently causes the mass transfer rate to be increased.
c. Concentration and thermal driving forces simultaneously- Using energy and increasing concentration gradient simultaneously cause the transport of component molecules to be higher than cases when to impose each driving force individually. If mass and heat transfer carry out simultaneously, large number of molecules get the chance to move to the interface and be separated. In drying process using heat transfer to the solid surface and a gas medium with low humidity help the moisture inside solid to be separated more and efficiently.

d. Hydraulic driving force- Imposing the pressure gradient using decreasing the total pressure in one phase forces the molecules that move more and faster to the interface and be separated. Drying of a moist solid in a vacuum gas media is a good example in this case that as we expect the moisture molecules are separated faster and more in comparison with the cases that vacuum condition not be used.

On the other hand, for mass transfer to carry out better some conditions can be used to increase mass flux from increasing the mass transfer coefficient viewpoint. Reaching this condition is available from using higher turbulence conditions and consequently increasing the Reynolds number. But in the present section the focus is done on increasing driving forces.

The processes that are used for purification in chemical industries need at least two phases to contact each other and this contact should be performed in a contactor or mass exchanger equipment. What is important in contacting phases is that during the course of separation of components transferring molecules causes the concentration gradient to be decreased along the time and the system of finite volume from two phases gets closer to the equilibrium condition just at temperature and pressure of the system. The question is that 'is the equilibrium available really what we need?'. It maybe true sometimes but not often. What needs to do is contacting phases more and more or in other words stage by stage. Each stage can be considered as a control volume that mass transfer taking place on it. Imposing different operating conditions of temperature and pressure in each stage can impose different equilibrium conditions that can be accessible and the flows leaved the stage can be reached them theoretically. Therefore each stage is called as a 'theoretical stage' and the separation processes sometimes are called 'staged processes'.

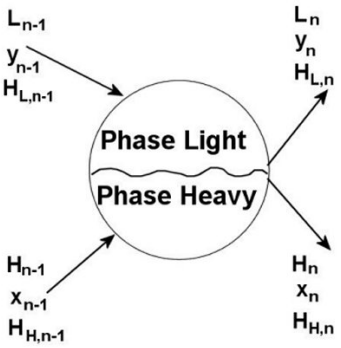

Fig. 3. Schematic of a theoretical stage n

Fig. 3 shows a stage as a control volume in separation processes generally. As it is shown two streams from two phases enter the stage with known flow rates, compositions and enthalpies (noted as L, y and H_L in light phase and H, x, H_H in heavy phase, respectively) and after getting the equilibrium condition at temperature and pressure of the stage, two streams made from two phases leave the stage. To get the desire conditions for the flows leave the stage, a set of stages is often used. Therefore the streams enter the stage 'n' coming from stage 'n-1' and stage numbers are brought as subscripts of flow characteristics.

What happened on the stage, as mentioned, are the contact and consequently the component transfer between phases. Transport of mass between phases contains the phenomena of mass transfer inside a phase from bulk to the interface, passing the interface,

and finally transfer of mass to the bulk of other phase. Fig. 4 shows two phases of L and H in contact with each other, schematically. As it is shown in Fig. 4a in contact between two phases L and H, a phase interface that is a nonhomogeneous phase contains surfaces with constant properties in border zone is generated in reality. The normal vector, n shows the direction that properties in the phase interface are varied. Fig.4b is a theoretical equivalent figure that Gibbs suggested and used a geometrical interface (called Gibbs' interface) to replace the phase interface. Based on this model, the properties of homogeneous phases L and H are constant at top and bottom of the geometrical interface, respectively.

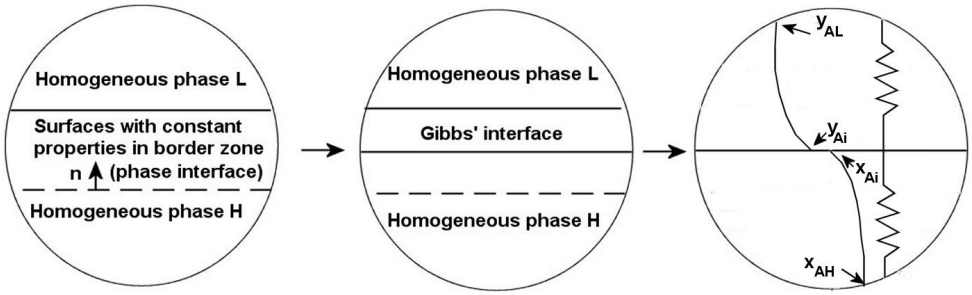

Fig. 4. Two phases L and H in contact each other; (a) In reality; (b) The model suggested by Gibbs for contacting two immiscible phases [taken from (Luikov, 1980)]; (c) The resistances against mass transfer in each phase and concentration gradients

In purification processes it needs to transfer a component or number of components from one phase to the other phase. By considering the model proposed by Gibbs, transfer of a component should be carried out from bulk of a phase to geometrical interface, equilibrium should be existed between phases on interface, and then transfer of component is occurred from interface to the bulk of other phase. The resistances against mass transfer from bulk to bulk are shown in Fig.4c. The component A mole fraction decreases from y_{AL} at bulk to y_{Ai} at geometrical interface in phase L side. The A mole fraction at interface in phase H side, x_{Ai} is in equilibrium with y_{Ai} and can be calculated from equilibrium data. Finally a concentration gradient through phase H is seen as shown in Fig. 4c. As it is obtained logically, equality of component A chemical potentials in two phases L and H (μ_{AL} and μ_{AH}) is not meaning the equality of mole fractions in equilibrium condition at interface.

Knowing about resistances against mass transfer in contacting phases helps the engineer as a separation equipment designer to decide carefully on design of stages in terms of residence time of phases on stage and level of turbulency needs on phases to get the equilibrium condition for the streams leaved the stage. The phase with higher resistance shows the controlling step in mass transfer and needs to have more turbulency in mass exchanger.

Analysis on resistances can be carried out from writing the flux of mass transfer in respect of cases that can be considered as 'equimolar counterdiffusion' or mass transfer through 'stagnant nondiffusing components'. Indeed the classification can be performed as conditions of high or low mass transfer flux. In low mass transfer flux and in the case of 'equimolar counterdiffusion', the flux of component A can be formulated similar to convective heat transfer flux as

$$N_A = k'_y(y_{AL} - y_{Ai}) = k'_x(x_{Ai} - x_{AH}) \quad (1)$$

where N_A is the convective mass transfer flux, k'_y and k'_x are the convective mass transfer coefficients in light and heavy phases, respectively, y_{AL} and y_{Ai} are the mole fractions of component A in the bulk and interface side of light phase, and x_{Ai} and x_{AH} are the component A mole fraction at interface side and bulk of heavy phase, respectively. Equation (1) can be figured as an analog electrical relation of voltage=(resistance)(current). The mole fraction differences play as voltage or driving force, flux as the current, and finally inverse of convective mass transfer coefficients as resistances. From equation (1) the operating line for a theoretical stage can be derived as

$$-\frac{k'_x}{k'_y} = \frac{y_{AL} - y_{Ai}}{x_{AH} - x_{Ai}} \quad (2)$$

The above operating line is passed from two points of (x_{AH}, y_{AL}) and (x_{Ai}, y_{Ai}) with a negative slope of $-k'_x/k'_y$. The operating line, MN is shown in Fig. 5. As it is seen the point N shows mole fractions on interface and is located on the equilibrium curve.

Equation (1) can also be written based on overall mass transfer coefficients of K'_y and K'_x, but only one problem remains that 'what type of mole fractions should be used compatible with x_{AH} and y_{AL}?'. Therefore when the driving force is written based on the mole fraction difference in phase-L, y_{AL} is considered for the concentration at starting point of mass transfer and we should consider a mole fraction at the end of way of mass transfer in bulk of the phase-H and equivalent with x_{AH}. This value can be called y_A^*, a mole fraction in phase-L in equilibrium with x_{AH} on equilibrium curve, as shown in Fig. 5. This procedure can be taken for overall driving force based on phase-H as well. Consequently, the flux relation based on the overall driving force is written as follows

$$N_A = K'_y(y_{AL} - y_A^*) = K'_x(x_A^* - x_{AH}) \quad (3)$$

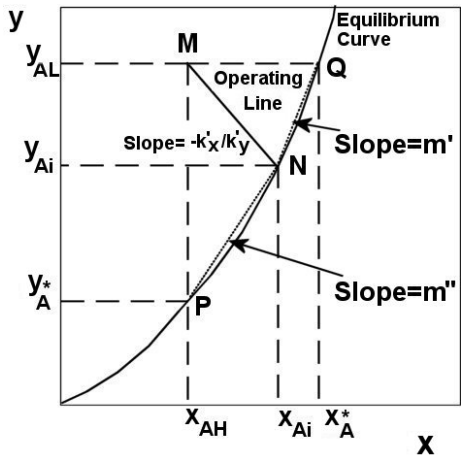

Fig. 5. The operating line of a theoretical stage, line MN

The overall driving force, mole fraction difference, based on light phase can be written mathematically as

$$y_{AL} - y_A^* = (y_{AL} - y_{Ai}) + (y_{Ai} - y_A^*) \tag{4}$$

By setting equivalent relations for driving forces using equations (1), (3) and Fig. 5 and after simplifying we have

$$\frac{1}{K_y'} = \frac{1}{k_y'} + \frac{m''}{k_x'} \tag{5}$$

This relation shows that the overall resistance against mass transfer is equal the resistance in light phase plus m˝ times the resistance in heavy phase.
Analogous following relation can be derived if the overall driving force is written based on the heavy phase

$$\frac{1}{K_x'} = \frac{1}{k_x'} + \frac{1}{m' k_y'} \tag{6}$$

Equations (5) and (6) have been derived in the case of equimolar counterdiffusion that for diffusion of component A through stagnant component, other relations can be derived (Geankoplis, 2003).

4. Thermodynamics

The aim of studying thermodynamics of different processes is obtaining the equilibrium condition that we assume in theoretical ideal conditions that can be accessible in the interface between phases. Therefore this condition is ideal and is not available in real operation of units. Usually the concentration of separated constituent in a less dense phase can be drawn versus its concentration in the second phase and called as the equilibrium curve. For using better from equilibrium curves in separation processes, dimensionless concentrations as weight or mole fractions are used. Sometimes when gaseous phase considered as a light phase, the partial pressure can be used as concentration.
Thermodynamics probably is the principal part of analysis of separation processes. This part directly is connected to physical and chemical properties of materials and needs to be investigated experimentally before using any mathematical models to predict the equilibrium data. We are facing with a broad subject in thermodynamics called 'phase equilibria' and as it is noted intellectually in the valuable book of 'The properties of gases and liquids' (Poling, Prausnitz, & O'Connell, 2001), working on this part of science needs more attention as experimentally investigation, careful using reliable data published in literatures and using mathematical models that give reliable results. For this reason in this section a brief discussion on phase equilibria is presented. Vapor-liquid, liquid-liquid, solid-liquid, gas-liquid and gas-solid equilibria are discussed in this section.

4.1 Vapor-liquid equilibria (VLE)

At the equilibrium between vapor and liquid phases, for a mixture with m-components, the following relation is written between fugacity of each component i, f_i, as

$$f_i^v = f_i^l \quad , (i = 1, 2, ..., m) \tag{7}$$

where superscripts v and l show vapor and liquid phases, respectively. Simplifying the above equation using equivalent relations for right and left hand sides gives

$$y_i \Phi_i P = x_i \gamma_i f_i^0 \tag{8}$$

where y_i and x_i are mole fractions of component i in the vapor and liquid phases, respectively, Φ_i and γ_i are the fugacity and activity coefficients of component i in the vapor and liquid phases, respectively, P is the total pressure in vapor phase and f_i^0 is the standard-state fugacity. Replacing an equivalent value for standard-state fugacity, the following relation is obtained

$$y_i \Phi_i P = x_i \gamma_i P_i^{sat} \exp\left[\int_0^{P_i^{sat}} (Z_i - 1) \frac{dP}{P} + \frac{1}{RT} \int_{P_i^{sat}}^{P} V_i dP \right] \tag{9}$$

where P_i^{sat} is the vapor pressure of pure i, Z_i is the vapor-phase compressibility factor, V_i is the liquid-phase molar volume, R is the universal gas constant and T is the absolute temperature.

The simplest form of governing equation on VLE is the Raoult's law which is suitable to low pressure and considers ideality for both liquid (γ_i=1) and vapor (Z_i=1, Φ_i=1) phases. Indeed it assumes that the liquid molar volume is negligible or $P \cong P_i^{sat}$. The Raoult's law is written as

$$y_i P = x_i P_i^{sat} \tag{10}$$

The LHS of this equation shows partial pressure of component i in the vapor phase, P_i. For a binary system, this relation can be written for two components of 1 and 2 as

$$\begin{aligned} P_1 &= x_1 P_1^{sat} \\ P_2 &= x_2 P_2^{sat} \end{aligned} \tag{11}$$

It depicts that at the constant temperature, the partial pressure of each components has a linear function of mole fraction in liquid phase. Summation of partial pressures on both components makes the total pressure versus x_1 curve (the bubble-point curve). In Raoult's law partial pressure curves for two components and the bubble-point curve are linear, but some real mixtures show deviations from Raoult's law. If these curves do not show the linear behavior and lie above the Raoult's law lines, the system shows positive deviations from Raoult's law and there are negative deviations when curves lie below the Raoult's law lines. These behaviors come from both liquid and vapor phase non-idealities. Based on equation (9), in liquid phase the non ideality comes from γ_i and integral of V_i and in the vapor phase two terms of Φ_i and integral containing Z_i cause the deviations.

But at low pressures, ideality assumption for the real liquid mixtures sometimes is not true and in this case

$$y_i P = x_i \gamma_i P_i^{sat} \tag{12}$$

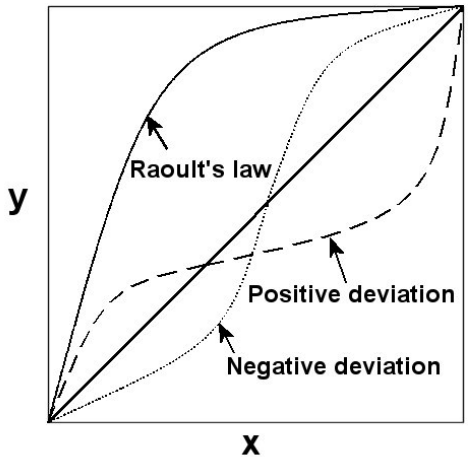

Fig. 6. Equilibrium curves obtained from Raoult's law and non-ideal situations of positive and negative deviations from Raoult's law

If $\gamma_i>1$, the system shows positive deviations and vice versa the negative deviations are seen for the case when $\gamma_i<1$. It should be noted that occurrence of azeotropes ($y_i=x_i$) sometimes causes the deviations to occur. A significant difference in vapor pressures or bubble points of pure components or very close vapor pressures of pure constituents of mixture can generate azeotropes. Fig. 6 shows the equilibrium curves in ideal (using Raoult's law) and non-ideal (positive and negative deviations) situations. As it is seen the azeotropes occurred in non-ideal situations.

4.2 Liquid-liquid equilibria (LLE)

Liquid-liquid equilibria can be described from the term of miscibility on two liquid phases. When two liquid phases are mixed, it can produce one phase from miscible liquid phases or two immiscible phases in equilibrium with each other. Two liquid phases often have partial miscibility in each other. It means that under some operating conditions of pressure, temperature and composition, they are miscible and produce one final phase or immiscible and show a two-phase region. Temperature, pressure and composition are variables that can affect the miscibility of liquid phases. Through these, the pressure is less important on liquid phases, and mostly the Tx diagram is considered to show the behavior of mixed liquids.

The region of homogeneous liquid solution and two-phase zone schematically are shown in Fig. 7. As it is shown, in the region outside the dome-shaped curve, two liquid phases are miscible and one homogeneous phase is made but inside the curve a two-phase region is produced. A mixture of two liquids that lies inside the dome, is not produced a stable single phase and splits into two liquid phases in equilibrium with each other that each one has its own composition.

For binary systems, outside the dome-shaped curve, one homogeneous phase is existed and based on the phase rule; there are 3 degrees of freedom ($2-\pi+m$ for an m-components system with π phases). It means that for each point outside the dome zone; pressure, temperature and composition of the mixed liquids should be fixed to obtain all properties of one produced phase. On the other hand, inside the dome zone; the degree of freedom is

calculated as 2 and by fixing pressure and composition or pressure and temperature, the other properties of resultant phases are fixed. With this discussion, each point like E, inside the dome zone splits into two phases with compositions at B and A that obtained from drawing a horizontal line passing through the point, called tie line, as depicted in Fig. 7. As it is seen, two phases produced at B and A are rich phases that each one is enriched of one constituent. The lever rule is applied to calculate the ratio of total moles in two phases as well.

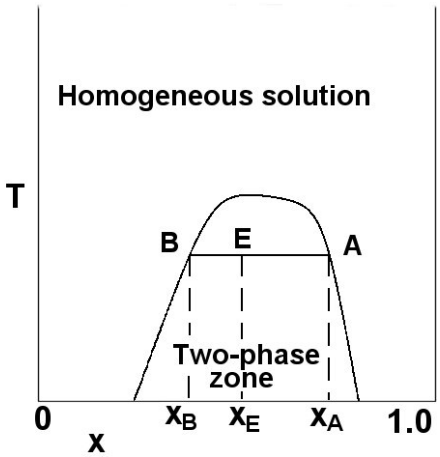

Fig. 7. Schematic of a Tx diagram for liquid-liquid equilibria

But application of liquid-liquid equilibria in separation processes needs the condition when at least a system of three components presents. Two liquid phases have partial miscibility in each other and the third constituent is miscible in two mentioned liquids completely. This is a usual case in separation processes. Therefore in this case an equilateral triangular diagram is used to show where we are in separation process. A triangular diagram schematically is shown in Fig. 8a. Each of three apexes is shown a pure component and a point inside triangle shows a ternary mixture. If the point lies inside the dome zone it is not a stable mixture and splits into two phases that each one is enriched from one constituent. Outside the dome zone, there is only one homogeneous phase and on the sides AC and BC of the triangle, binary systems are presented. The compositions of each point inside the triangle are obtained from drawing perpendiculars to each side. Length of perpendicular to each side of the triangle shows the value of composition opposite to the side and ratio of length of each perpendicular to summation of them shows the mass or mole fraction of components. The tie line passes through a point M inside the dome zone can show the compositions of phases produced at D and E as presented in Fig. 8a.

For simplicity, the equilibrium data can be plotted on a rectangular coordinates graph as well. As it is shown in Fig. 8b each rectangular coordinate shows the mass or mole fraction of one component. In this figure the liquid phase at point E is rich from transferring component C and its mass fraction is shown as y_E, the mass fraction of C in liquid phase at point D is shown as x_D and finally the mass fraction of component C in unstable liquid mixture at point M is depicted as z_M.

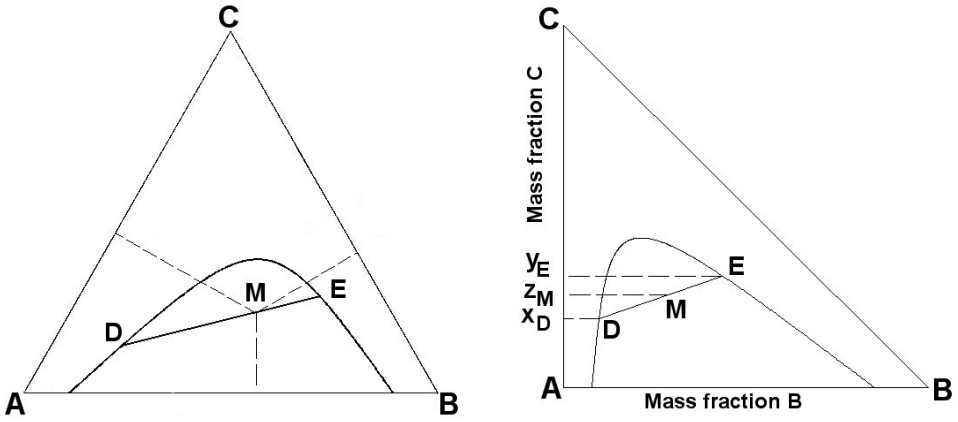

Fig. 8. Liquid-liquid equilibrium; (a) Equilateral triangular coordinates; (b) Rectangular coordinates

4.3 Solid-liquid equilibria (SLE)

The solubility of a solid into a liquid is a parameter that depends upon equilibria existed between solid and liquid phases. A solid phase can be dissolved into a specified liquid phase completely or it can be partially dissolved under some conditions of pressure and temperature.

The solubility of a solid in a liquid depends upon intermolecular forces between solid and liquid, the melting point and enthalpy or entropy of fusion of the solid. Between two different solids demonstrating the same intermolecular forces with a liquid, the solid with higher melting point and higher enthalpy of fusion has lower solubility. But when a solute trapped inside a solid matrix (marc) immiscible in the liquid solvent, it is assumed that the equilibrium mole fraction of solute in solvent or the solubility is complete and a ternary system like what investigated in the liquid-liquid equilibria should be analyzed.

Therefore the SLE ternary systems are considered to include one solid phase immiscible in liquid solvent phase and a solute trapped in the solid matrix. The equilateral triangular diagrams are used to show the equilibrium between different components. Usually the solute can be dissolved into solvent completely and there is a limit for solid matrix to keep solute inside its porous structure. Fig. 9 shows a typical equilateral triangular diagram in which different components are set on each apex and show the marc (A), pure solvent (C) and pure solute (B). The curve *abcde* in the diagram shows the limit between two and three phases. The left side demonstrates the three phase region that three components are distinguishable. In this region a mixture of three phases contains more solid matrix than other two components. Also the region in the right side of the curve belongs to the mixtures with two phases. One phase is rich from the solid matrix (points b, c and d) and another is rich from liquid solvent (points b′, c′ and d′). All the solute is distributed between these two phases. Indeed as it is seen for the phase rich from the solid matrix that located on the curve, there are significant amounts of solvent and solute trapped in the porous structure of the solid.

If the solid matrix does not adsorb the solute molecules, the concentration of solute inside pores is the same as that inside the phase rich from the solvent in equilibrium with.

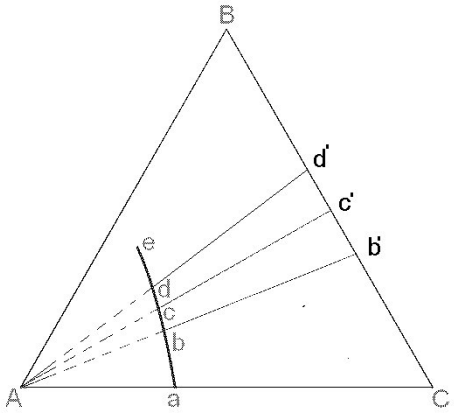

Fig. 9. Equilibrium in solid-liquid system

4.4 Gas-liquid equilibria

Equilibrium between a gas and a liquid can be studied from two different viewpoints. In first case, a constituent of gas phase can be transferred to the liquid phase and in other word it can dissolve into the liquid. In this case the limitation for the gas solubility in liquid is the matter of fact and needs to be studied. But the second case is regarded as transfer of liquid constituent into the gas phase and the transport of molecules is continued to make a saturated gas from the liquid constituent molecules.

Each case is really depending upon operating conditions of temperature and pressure and also concentrations of other components presented in the system. Thermodynamic relationships can describe the relation between different parameters affecting equilibrium state but the reliable results in each case need to be obtained experimentally.

The solubility of a gas constituent through a liquid phase is depending to the temperature and increasing the temperature decreases the solubility. Also increasing pressure in gas phase helps the gaseous molecules to dissolve better in the liquid. When gaseous molecules dissolve in liquid phase a broad range of mixtures can be studied from a pure initial liquid to a pure liquid produced from gaseous constituent molecules. Obtaining the solubility of a component in liquid depends on interaction between solute and solvent molecules as well and this subject has been investigated in thermodynamics of ideal and non-ideal solutions. Based on what obtained in this scope, the molecules of similar group of materials e.g. alcohols, alkanes, alkenes etc interact each other normally like molecules of pure materials individually and in other word can produce an ideal solution. But when the molecules constituting solute and solvent be different from each other and belong to different groups, they can interact each other differently and produce non-ideal solutions. The Raoult's law predicts the behavior of ideal solutions very well but when solutions show a non-ideal behavior it fails. In non-ideal solutions the partial pressure of gaseous component in gas phase is not proportional with component mole fraction in the liquid phase with proportionality coefficient of component vapor pressure but in this case if solute molecules dissolve limited into the liquid phase, the Henry's law is governed and is written as

$$\bar{P}_i^* = H_i x_i \tag{13}$$

where $\bar{P}_i^*$ is the partial pressure of component i (=Py_i) and H_i is the Henry's constant for component i. Fig. 10 shows the curve f_i^v versus x_i in general form as $\bar{P}_i^*$ is replaced with f_i^v based on the Henry's law.

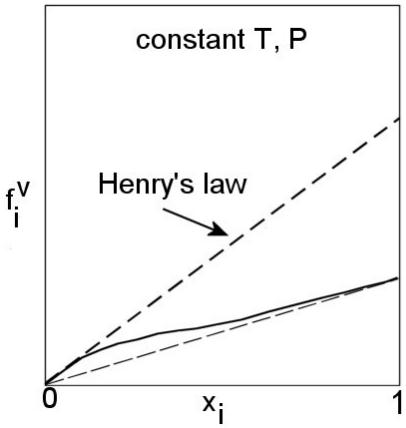

Fig. 10. Henry's law for dilute solution behaviors

4.5 Gas-solid equilibria

When two phases of solid and gas contacted each other, the final amount of gas molecules inside the gas phase and those attached to the solid surfaces depends on equilibria between phases. The equilibrium in this case means that reaching a partial saturation of unsaturated forces at the surface of solid phase from the way of interaction with the gas molecules in gas phase (Rudzinski, Steele, & Zgrablich, 1997). Different interactions between gas molecules in the gas phase and solid surface molecules can be occurred and gas molecules can interact with each other when adsorbed on the solid surface as well.

To obtain a proper equilibrium relation between fraction of coverage of a solid (θ) and the pressure of a gaseous adsorbate (p), it needs to know microscopic phenomenon of covering the solid surface by gas molecules and all phenomena happened in gas molecules adsorption. Different forces occurred between molecules, effect of operating conditions on molecular interactions and many other subjects should be studied. The gas molecules can be adsorbed physically (physisorption) or chemically (chemisorption) to the solid surface. The forces between molecules in physisorption are of Van der Waals type when in chemisorption, chemical bonds which are much strong (>0.5 eV energy per each molecule adsorbed) are occurred between molecules. Search to find a good equilibrium model [θ=θ(p)] that called an 'adsorption isotherm' needs to consider different assumptions on coverage of solid surface by monolayer/multilayer of gas molecules, homogeneity of solid surface, interaction of gas molecules located on the solid surface and etc. Assumption of monolayer or multilayer coverage of solid surface by gas molecules depends upon the type of forces between gas and solid molecules. In physisorption processes, multilayer of gas molecules can be produced on the solid surface though monolayer of gas molecules is made in the case of chemisorption. Homogeneity of solid surface results producing the uniform

sites for gas molecules to be adsorbed energetically. Other subject needs to be studied is the answer to this question that how strong be the forces between solid and gas molecules in adsorbing sites. In other word do the gas molecules can slide on solid surface and are mobile or they fixed on sites and localized.

For gas molecules or adsorbate to be localized on the solid surface, the energy between solid molecules on the surface and adsorbate should be higher than thermal energy of kT (where k is the Boltzmann constant and T is the absolute temperature). High value of T means that the energy for surface diffusion is in a range that causes the adsorbed molecules to move on the solid surface and be mobilized. In this case (monolayer localized adsorption), the Langmuir model and Fowler-Guggenheim model are used. Different models were also presented for monolayer mobile adsorption. The Volmer and Hill-de Boer isotherms are considered in this case. The BET (Brunauer, Emmet,Teller) and FHH (Frenkel, Halsey, Hill) isotherms were also presented in the case of multilayer localized adsorption. In isotherms mentioned, the solid surface is assumed to be ideal and homogeneous but in reality this assumption cannot be true most of the times. The structure of solid surface and presence of different compounds and phases are characteristics of non-homogeneity of solid surface. In real cases three isotherms of Freundlich, Dubinin-Radushkevich and Temkin were used more in monolayer adsorption. A good collection of different researches on solid-gas equilibria was presented in ref. (Rudzinski, Steele, & Zgrablich, 1997).

Based on what happened in reality on the solid surface and the gas adsorbed, different mathematical models were presented. Through models proposed, some were used widely. Langmuir isotherm model applying to monolayer localized adsorption is obtained from equating rates of adsorption and desorption of the gas molecules on the solid surface and finally the following equation is obtained

$$V = \frac{V_m bp}{1 + bp} \tag{14a}$$

where V is the total volume adsorbed, V_m is the volume of the gas required to form a completed unimolecular layer on the adsorbent surface ($\theta = V/V_m$ is the fraction of solid surface covered by the gas molecules), b is defined as the adsorption equilibrium constant (ratio of adsorption to desorption rate constants) and p is the gas pressure. The adsorption equilibrium constant, b, is a function of temperature and materials that play as solid adsorbent and the gaseous adsorbate. The Langmuir model can be written as another form as

$$q = \frac{QK_L C}{1 + K_L C} \tag{14b}$$

where q is the equilibrium concentration of adsorbate in solid phase as mass adsorbate per mass adsorbent, Q is the maximum adsorbate concentration in solid phase as mass adsorbate per mass adsorbent, K_L is the equilibrium constant and C is the adsorbate concentration in the fluid phase as moles per volume. The Langmuir isotherm is shown in Fig. 11a.

Brunauer, Emmet and Teller (BET) developed the method used to get the Langmuir isotherm for multilayer adsorption on the solid surface. In this model only the first layer of adsorbate is localized on solid sites based on adsorption forces between adsorbent-adsorbate molecules. The second, third and other layers interact as condensation-like process. The BET isotherm can generate S-shaped equilibrium curve and is written as

$$V = \frac{V_m c p}{(p_o - p)\left[1 + (c-1)p / p_o\right]} \tag{15}$$

where p_o is the vapor pressure of adsorbate liquid and c is a constant that can be defined as

$$c = e^{(E_1 - E_L)/RT} \tag{16}$$

where E_1 and E_L are heat of adsorption in the first layer and heat of condensation in other layers, respectively, and T is the absolute temperature. Other form of BET model is written as

$$q = \frac{QK_L p}{\left[1 - (p/p_o)\right]\left[1 + K_L p + (p/p_o)\right]} \tag{17}$$

The BET isotherm based on the above equation is brought as Fig. 11b. Derivation of two models proposed above was based on kinetic arguments but a semiempirical isotherm model that is used frequently belongs to Freundlich. This equation is written in power form mathematically as

$$V = V_m b p^{1/n} \tag{18}$$

where n is a constant. The other form for Freundlich model can be written as

$$q = K_F p^{1/n} \tag{19}$$

where K_F is a constant. The Freundlich model of adsorption can be drawn as two types shown in Fig. 11(a and c) for values n>1 and n<1, respectively. For n=1 this relation can show a linear type of adsorption isotherm as well but the favorable isotherms are considered as shown in Fig. 11a.

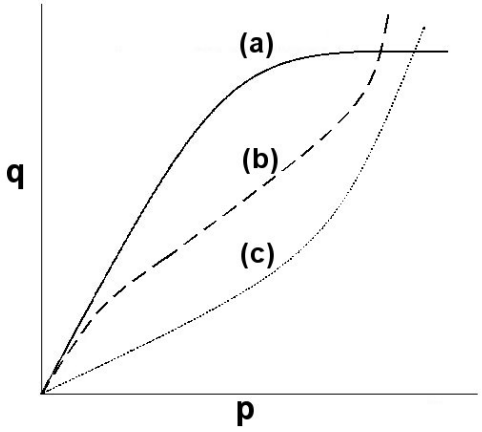

Fig. 11. Different isotherms; (a) The Langmuir and Freundlich (n>1) isotherms; (b) The BET isotherm; (c) The Freundlich isotherm (n<1)

5. Operating behavior of flows inside a separator

After obtaining equilibrium data carefully, the first step of separation process analysis means analysis of operating behavior of flows inside separating vessel (tray or packed-bed towers) that should be studied. Behavior of flows passes inside separators is dependent directly on the flow form and contact type of phases. In this section operating lines or curves are obtained from mass balance equations in different contact forms of crosscurrent, cocurrent and countercurrent flows inside multistage and differential separators.
Before investigating the different contact types, it needs to define different notations used for flow streams. We consider that in separation processes that often two phases contact each other; one phase can be assumed as light phase in comparison with other phase that can be called heavy phase, i.e. in adsorption process gas or liquid phase plays the role as light phase and solid phase as a heavy phase. Therefore letters L and H are used for light and heavy phases, respectively. For simplicity on writing formulations, the stagnant part of streams are defined as L_s through light and H_s through heavy phases (their units are as, kg or kmole of stagnant component/time). The mole or mass fraction of separating component in light and heavy phases defined as y and x, respectively. Number of each stage is brought as indices for flows leaving the stage. Definition of two parameters also is useful in formulating mass balance equations and finally the operating behavior of the process. X and Y are defined as mole/ mass fraction of transferring component to mole/mass fraction of stagnant components. As mentioned before the relation between y and Y is as follows

$$Y = \frac{y}{1-y} \tag{20}$$

A similar relation is defined for relation between x and X.

5.1 Crosscurrent form of contact

This form of contact is used on different processes of leaching, adsorption and liquid-liquid extraction. In crosscurrent operation one phase contacts with the streams of other phase in constant properties. This kind of contact causes keeping high driving force in each stage and consequently high mass transfer rate. Fig. 12 shows an absorption-like process that operates in a crosscurrent form of operation, schematically. The mass balance equation for stage n is written as

$$H_s X_0 + L_s Y_{n-1} = H_s X_n + L_s Y_n \tag{21}$$

After simplifying, the operating line is obtained as follows

$$-\frac{H_s}{L_s} = \frac{Y_n - Y_{n-1}}{X_n - X_0} \tag{22}$$

Lines with negative slopes of $-H_s/L_s$ are operating lines in this form of contact. In Fig. 12 the flow rates of heavy phase are assumed to be the same to the all stages but they may be different and consequently parallel operating lines are not obtained necessarily.
As it is seen the mole fraction of transferring component in light phase is decreased in each stage and using higher flow rate for heavy phase causes the higher purification to be happened.

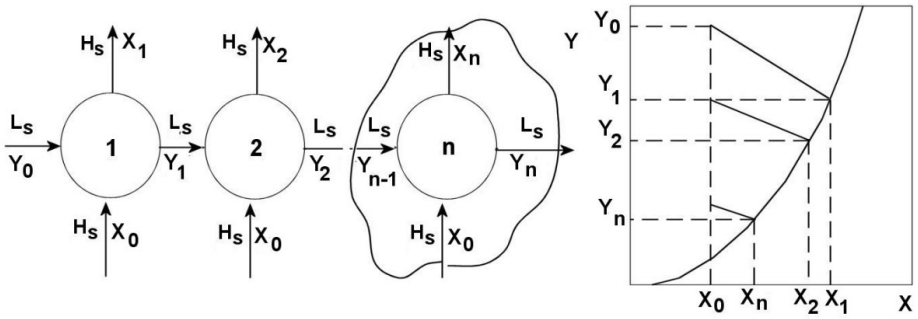

Fig. 12. A schematic of multistage crosscurrent contact and operating lines

5.2 Cocurrent form of contact

The flow direction of two phases is the same in cocurrent form of contact and the mass transfer driving force is decreased along the contactor from input to output section. A schematic of a contactor with cocurrent contact form is shown in Fig. 13. The mass balance equation in this case is written as

$$L_s Y_1 + H_s X_1 = L_s Y_2 + H_s X_2 \tag{23}$$

The operating line can be obtained by arranging this equation as

$$-\frac{H_s}{L_s} = \frac{Y_2 - Y_1}{X_2 - X_1} \tag{24}$$

The slope of operating line in this case is negative and the flow properties tend to approach the equilibrium conditions.

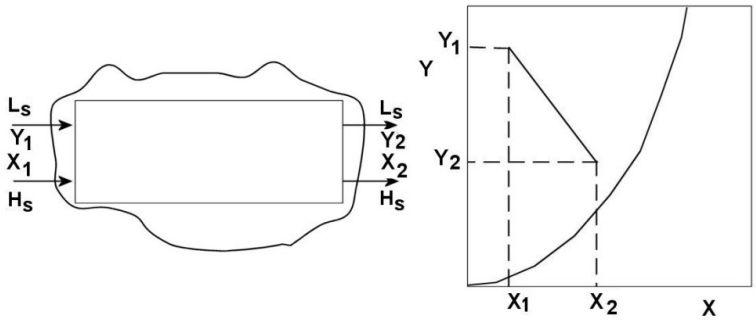

Fig. 13. A schematic of a contactor with cocurrent contact form in the case of absorption-like processes

5.3 Countercurrent form of contact

This type of contact has a good performance in comparison with other types. In this type two phases flow in opposite directions in the contactor. Therefore the driving force for mass transfer will be high enough to prepare a good purification condition in each stage. A

schematic of this process is shown in Fig. 14 and the mass balance equation for the loop shown in this figure can be written as

$$L_s Y_1 + H_s X_2 = L_s Y_2 + H_s X_1 \tag{25}$$

Therefore the operating line in this case is written as follows

$$\frac{H_s}{L_s} = \frac{Y_2 - Y_1}{X_2 - X_1} \tag{26}$$

The slope of operating line in this case is positive as it is seen in Fig. 14.

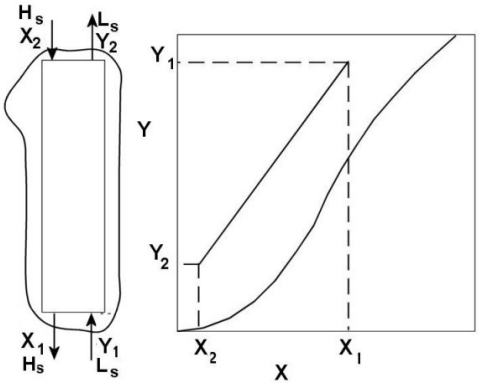

Fig. 14. A contactor with countercurrent flow in absorption-like process

6. Staircase construction

Calculating number of plates in a tray tower as a processing design parameter is investigated in this section. Two kinds of problems can be created relating with staircase construction. Sometimes a chemical engineer wants to design a tray tower and find the number of plates. In this case operating line or curve is known and number of theoretical plates can be calculated. But in number of cases a tray tower with fixed number of plates is existed and operation in tray tower should be arranged in such a way that we have fixed known number of plates. Therefore in this section two kinds of problems we are facing that are discussed and analyzed.

6.1 Known operating conditions, unknown number of plates

In the case of known operating conditions of temperature, pressure and compositions of the streams at two ends of the contactor a staircase construction can be used to find number of stages. Fig. 15 shows an absorption-like operation with known operating line and equilibrium curve. A staircase construction is shown in the figure from top to bottom or vice versa to find the number of theoretical stages as 6.

6.2 Known number of plates, unknown operating conditions

Sometimes the purification process should be carried out in an available contactor with a known number of plates and the operating conditions are unknown. In this case the

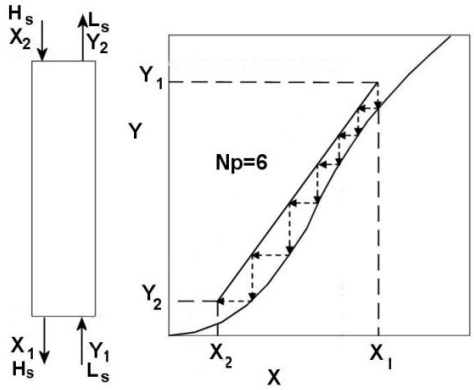

Fig. 15. A contactor with countercurrent flow form in the case of absorption-like process, known mole fractions for input and output streams and unknown number of stages

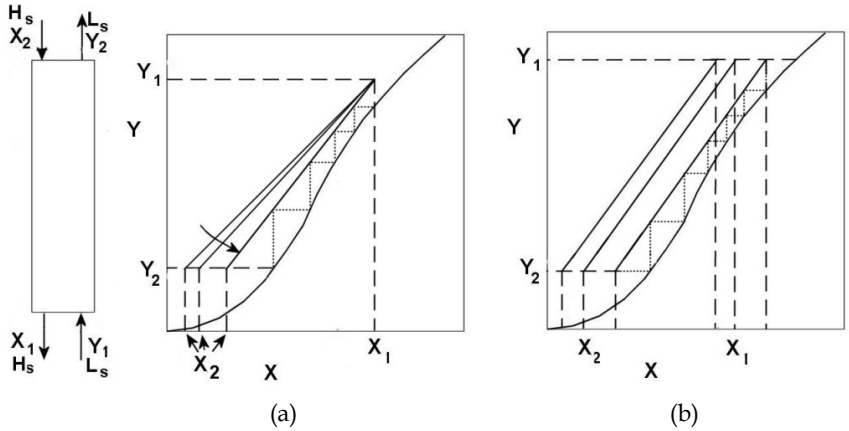

Fig. 16. An absorption-like process; (a) Known three mole ratios (X_1, Y_1 and Y_2) and five theoretical stages; (b) Known flow rates (L_s, H_s), two mole ratios (Y_1, Y_2) and six theoretical stages

calculations are performed using the trial and error method. Usually four parameters are necessary to fix the operating line of the process, but in the present case three of them are known with number of theoretical stages in the contactor. Four parameters necessary to fix the operating line may be the mole fractions of transferring component at top and bottom of the contactor in the heavy and light phases. Sometimes two mole fractions with known values of heavy and light phase flow rates are given. What important in these type of problems is that always trial and error method should be used to fix the conditions of the mass exchanger equipment.

In the usual cases the mole fraction of transferring component in the stream rich from it, stream necessary to carry out the purification and the desire stream after purification are known. Fig. 16a shows an absorption-like process that is expected to be carried out in a tray tower with five stages, countercurrently, with known mole ratios at section one (X_1, Y_1) and

Y_2 at the section two. With known number of stages and using the known mole ratios and the method of trial and error, X_2 should be guessed and checked the number of stages. This computational procedure is continued to obtain the correct number of stages. Fig. 16b shows the case when two mole ratios of Y_1 and Y_2 and the flow rates (known slope of operating line) are known. In this case the operating line keeps sliding to get the correct number of stages.

7. Different equilibrium diagrams and strategy of using difference points

Depending on different separation processes and different contact forms of phases, different equilibrium diagrams seem to be useful. The formulations that are carried out on each process as the mass and heat balance equations, often force the process calculations to be done using different equilibrium diagrams. Part of calculations usually related to converting different types of equilibrium data to each other.

In distillation operation, the Hxy diagram (phase enthalpies versus transferable mole fraction) sometimes is used as equilibrium diagram. The liquid-liquid extraction and leaching process calculations can be carried out in triangular diagrams or rectangular diagrams e.g. Nxy diagrams in leaching (N is in mass of solid matrix, marc per mass of liquid mixture; x and y are in mass of solute per mass of liquid mixture in heavy and light phases, respectively). The NXY diagram is used in liquid-liquid extraction when it assumes that a solvent is added to the feed solution and the transferable component is miscible in it (N is in mass of solvent added per mass of mixture with no solvent; X and Y are in mass of solute per mass of solvent free mixture in heavy and light phases, respectively). Fig. 17 shows different equilibrium diagrams which their tie lines are generated from usual equilibrium

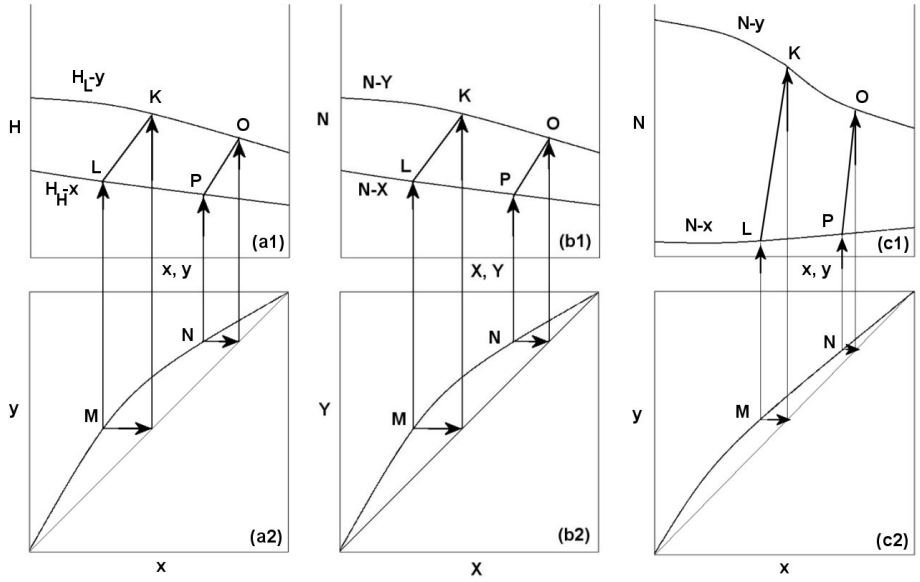

Fig. 17. Useful equilibrium diagrams; (a1, a2) Hxy diagram useful in distillation operation when using the Ponchon-Savarit method for binary systems; (b1, b2) NXY diagram used in liquid-liquid extraction; (c1, c2) Nxy diagram used in leaching operation

curves. As it is shown each point on xy or XY diagrams (e.g. M or N) can be converted to a tie line (KL or OP) on equilibrium curves laid on the top.

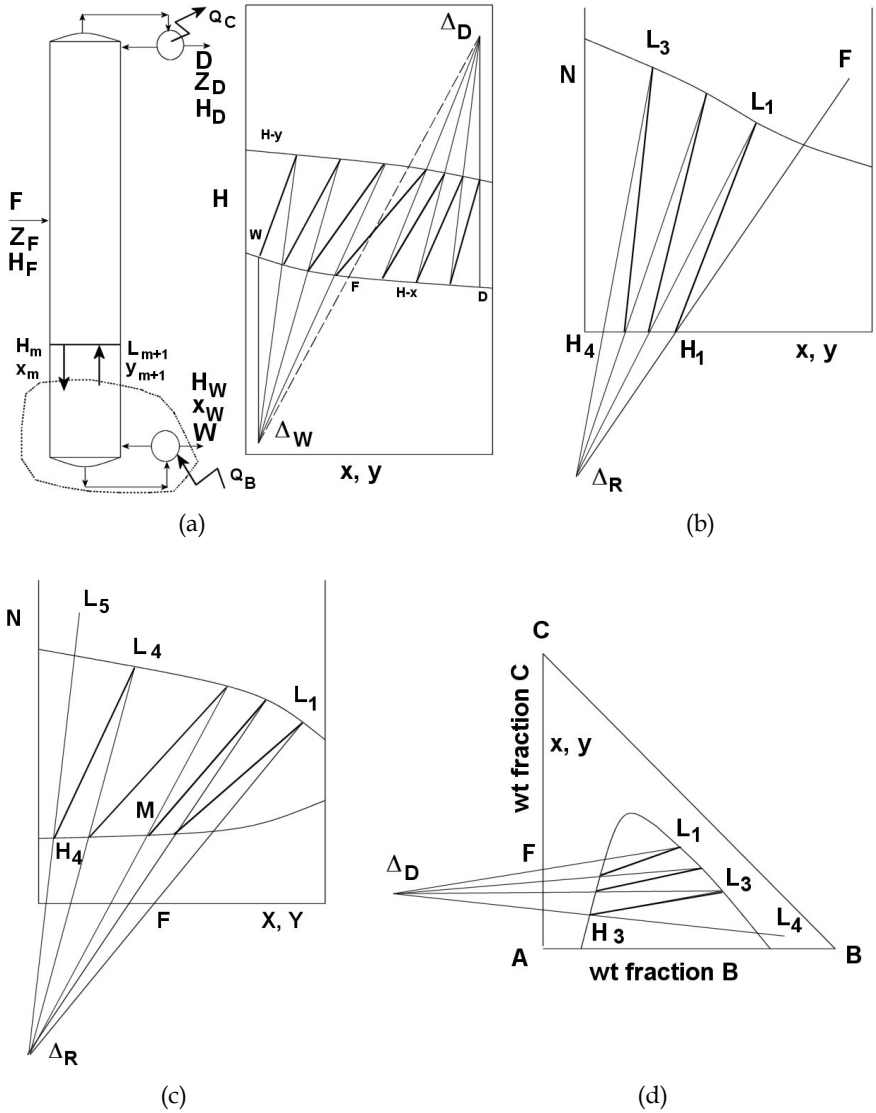

Fig. 18. Using difference point to carry out the processing calculations graphically (tie lines are shown as bold and other lines show the operating lines) (a) Distillation tower with 7 stages; (b) Leaching process with 3 stages; (c) Liquid-liquid extraction in 4 stage process (NXY equilibrium diagram); (d) Liquid-liquid extraction in 3 stage process (rectangular coordinates, C is the transferable component and B is the solvent used to separate C from its mixture with A)

Strategy of using difference points is used in separation processes with countercurrent form of contact to analyze the operations graphically. This plan is produced from this reality that the difference between total flow rates or component flow rates of two phases passed next to each other is constant. It means that as it is shown in Fig. 18a in distillation process for the loop shown between stage m and the bottom product of the column, total mass balance and component mass balance equations can be written as

$$\begin{aligned} H_m - L_{m+1} &= W \\ H_m x_m - L_{m+1} y_{m+1} &= W x_W \end{aligned} \tag{27}$$

where H, L and W are the flow rates of heavy phase, light phase and bottom product, respectively. The notations x and y are the mole fractions and m shows the stage number. As it is seen these equations can be written for all stages between feed tray and bottom of the tower and it means that the differences are constant. A similar equation can be added for heat balance and in that case the difference between energies is constant as well. The important subject is that in liquid-liquid extraction and leaching process when the contact form is countercurrent such equations can be developed and using a difference point to carry out the process calculations graphically seems to be necessary. Such points are brought in Fig. 18 for different processes of distillation, leaching and liquid-liquid extraction. The method that used to find number of stages graphically was described completely in ref. (Treybal, 1955).

8. Packed bed height

Differential form of contact is a usual method to contact phases in different separation processes. High surface area for contacting phases, less pressure drop, simplicity and low cost are the factors that cause this type of mass exchanger to be more useful. Height and number of transfer units are of important parameters that need to be calculated in packed bed contactors. During contact between phases along the height of the tower, concentration of separating component in two phases changes continuously and this type of mass transfer changes the rate of two streams as well. Sometimes transport of mass is occurred in the case of transfer into stagnant components e. g. absorption of ammonia from air with water, and sometimes it occurred as equimolar countertransfer e. g. in distillation process.

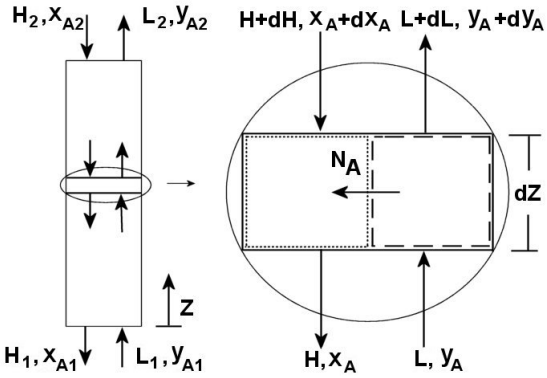

Fig. 19. A schematic of packed bed tower (left) and an element of tower in z-direction (right)

A schematic of packed bed tower is shown in Fig. 19. The two phases of L and H flow inside the tower in countercurrent form. L and H show the flow rates as kmol/(time)(tower cross sectional area). The mass balance equation on one element, dZ from the tower as shown in RHS of Fig. 19 can be simplified as

$$d(Ly_A) = d(Hx_A) \tag{28}$$

The mass balance equation on phase-L can be written as well

$$-N_A dS = d(Ly_A) \tag{29}$$

where dS is the total surface area that mass can be transferred from it, in dZ element, per tower cross sectional area.
In packed beds dS can be calculated from its relation with packing specific area, a and dZ as

$$dS = a\,dZ \tag{30}$$

The packing specific area is defined as total surface area of packing per volume of tower. A proper relation can be written for flux of component A e.g. in the case of equimolar countertransfer in low mass transfer rate based on overall mass transfer coefficient in light phase the following relation can be written

$$N_A = K'_y(y_A - y^*_A) \tag{31}$$

The flow rate L is assumed to be constant in the case of equimolar countertransfer. Replacing dS from equation (30) and N_A from equation (31) into equation (29) and considering L as a constant

$$-K'_y(y_A - y^*_A)\,a\,dZ = L\,dy_A \tag{32}$$

By separating the variables and integration the following equation is obtained

$$Z = \int_0^Z dZ = \int_{y_{A1}}^{y_{A2}} \frac{L}{K'_y a}\frac{dy_A}{(y^*_A - y_A)} \tag{33}$$

If $H_{OL} = L/K'_y a$ and is defined as height of the transfer units for the overall mass transfer coefficient and is assumed to be constant, the following equation is obtained from equation (33)

$$Z = H_{OL}\int_{y_{A1}}^{y_{A2}} \frac{dy_A}{y^*_A - y_A} \tag{34}$$

The value of integral is defined as the number of transfer units, N_{OL} as

$$N_{OL} = \int_{y_{A1}}^{y_{A2}} \frac{dy_A}{y^*_A - y_A} \tag{35}$$

In the case when transfer of component through stagnant components takes place and for low mass transfer rate, the K coefficients should be used to define flux relation and equation (31) should be replaced with

$$N_A = K_y(y_A - y_A^*) = \frac{K_y'}{(1-y_A)_{*M}}(y_A - y_A^*) \tag{36}$$

where

$$(1-y_A)_{*M} = \frac{(1-y_A)-(1-y_A^*)}{\ln\frac{1-y_A}{1-y_A^*}} \tag{37}$$

Indeed when component A transfers through stagnant components, e.g. absorbing ammonia from air using water, flow rate L cannot be assumed as a constant and it can be formulated as

$$L = \frac{L_s}{1-y_A} \tag{38}$$

where L_s is part of the light phase flow rate that is nontransferable or stagnant. Replacing new values for N_A and L from equations (36) and (38), respectively, into equation (29), other relations are produced for height of packed bed and number of transfer units.
When the rate of mass transfer is high, using F coefficient as mass transfer coefficient is usual and other form of definition of N_A is needed. The governing equations in this case have been presented in ref. (Hines & Maddox, 1985).

9. Conclusion

In the present chapter it tried to figure out a mass transfer sense related to more useful purification processes in chemical industries. A common sense in different processes was obtained based on classifying all separation processes into two broad categories of absorption-like and desorption-like processes. This classification can help the reader to get a similar sense when see separation processes individually. Referring denser phase as a heavy phase in comparison with the second phase causes the processing calculations to be simplified and categorized easily. The basic concepts of mass transfer were used to describe what happened in the interface between two phases and a brief discussion on the phase equilibria was used to generate equilibrium curves.
Also it tried to bring a good summary on significant processing calculations in different contact forms of phases and finally the calculations on two mass exchangers of tray towers and packed-bed columns were presented briefly.

10. References

Geankoplis, C. J.; (2003). *Transport Processes And Separation Process Principles*, New Jersey, Prentice Hall PTR.

Henley, E. J.; & Seader, J. D. (1981). *Equilibrium-Stage Separation Operations In Chemical Engineering*, John Wiley & Sons.

Hines, A. L.; & Maddox, R. N. (1985). *Mass Transfer Fundamentals and Applications,* Prentice Hall.

Khoury, F. M.; (1995). *Predicting The Performance Of Multistage Separation Processes*, Houston, Gulf Publishing Company.

Luikov, A. V.; (1980). *Heat and Mass Transfer,* Moscow, Mir Publisher.

McCabe, W. L.; Smith, J. C., & Harriott, P. (1956). *Unit Operations Of Chemical Engineering,* McGraw Hill.

Pavlov, K. F.; Romankov, P. G., & Noskov, A. A. (1979). *Examples And Problems To The Course Of Unit Operations Of Chemical Engineering*, Moscow, Mir Publisher.

Poling, B. E.; Prausnitz, J. M., & O'Connell, J. P. (2001). *The Properties Of Gases And Liquids,* McGraw Hill.

Rudzinski, W.; Steele, W. A., & Zgrablich, G. (1997). *Equilibria And Dynamics Of Gas Adsorption On Heterogeneous Solid Surfaces*, Elsevier.

Treybal, R. E.; (1955). *Mass Transfer Operations,* McGraw Hill.

35

Microdroplets for the Study of Mass Transfer

Young Hoon Choi, Young Soo Song and Do Hyun Kim
Departmenet of Chemical and Biomolecular Engineering, KAIST
South Korea

1. Introduction

As the development in the microfabrication technology in the last two decades has allowed the easy fabrication of microchannels with low cost, many studies have been conducted on the transport of fluid and the realization of various functions using fluids (Whitesides, 2006; Dittrich et al., 2006). The realization of the microchannel-based fluidic system and the relevant study are called microfluidics. In the scale in which microfluidics is concerned, the surface force is dominant over the body force, since the surface-to-volume ratio is large. The dominant influence of the surface force allows the production as well as the movement and control of micro-sized droplets in a microchannel. This study area is called droplet-based microfluidics (Beebe et al., 2002; Kim, 2004; Stone et al., 2004). Droplet-based microfluidics is expected to enable chemical and biological applications such as particle synthesis (Frenz et al., 2008), microextraction (Mary et al., 2008), and protein crystallization (Zheng et al., 2003). In a general microfluidics system, the Reynolds number (Re) is very small as 0.1-10, and thus the fluid forms a laminar flow. Such a laminar flow makes it difficult for two different fluids to be mixed with each other. However, if droplets are used, different fluids can be mixed with each other, because an internal circulation flow takes place in the droplets (Tice et al., 2003).
This chapter describes the microextraction based on the droplet-based microfluidics. Firstly, we will explain the electrohydrodynamic droplet generation and control technology in the aqueous two-phase system (ATPS) that we employed for the study, and the application of the generated droplets to microextraction. In particular, we were able to control the rate of extraction, which was impossible in the previous extraction methods, and analyzed the microextraction behaviour by simulating the phenomena based on a simple dissolving model.

1.1 Droplet-based microfluidics

The technology that is firstly required in droplet-based microfluidics is the method to generate droplets in a microchannel. Droplet generation is related with capillary number (Ca), which is the ratio of viscous force to interfacial tension (Squires & Quake, 2005). In a macroscopic system, droplets can be easily generated by vigorously shaking immiscible fluids, but the size distribution is very wide. In a microfluidics system, on the contrary, droplets are generated by various controllable methods so that the size distribution can be limited. Microfluidic methods for forming droplets can be either passive or active. Most methods are passive, relying on the flow field to deform the interface and promote the

natural growth of interfacial instability (Christopher & Anna, 2007). Specially designed geometries that affect the streams or externally applied forces are used to generate droplets in the microfluidic systems depending on the characteristics of the immiscible fluids such as viscosity, interfacial tension, wettability to the material surface and other electric properties. Flow rates of the dispersed phase (Q_d), continuous phase flows (Q_c) and their ratio (Q_d/ Q_c) are the parameters that can be controlled during the droplet formation operation. Three common techniques that are often used for generation of droplet in microfluidic system are dispersing fluid in a continuous phase with the configuration of co-flowing stream, cross-flowing in T-junction and flow-focusing as shown in Figure 1 (Anna et al., 2003). These techniques are feasible particularly for fast generation of droplets of oil/water two-phase system with uniform size distribution.

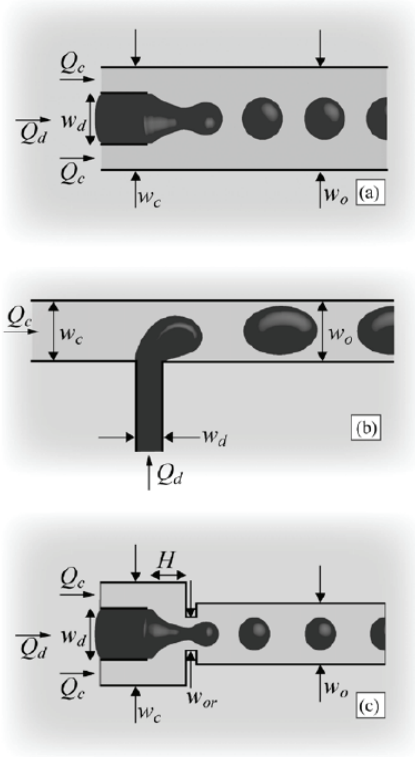

Fig. 1. Illustrations of the three main microfluidic geometries of methods used for droplet formation. (a) Co-flowing streams, (b) crossflowing streams in a T-shaped junction, and (c) elongational flow in a flow focusing geometry. In each case the widths of the inlet and outlet streams are indicated. It is assumed that the device is planar with a uniform depth h. (Anna et al., 2003)

Different from the passive methods, the active methods generate droplets by applying various external forces. Electrohydrodynamic methods are the most frequently used for the active generation. Although electrohydrodynamic methods require electrodes to apply an

electric field, they have the advantages that the electric signals can be easily controlled and there is not a concern for fatigue fracture since there is not a moving part. Electrohydrodynamic methods can be used not only for the generation of droplets but also for their control, and thus there can be many applications of the methods. Several applications of EHD method have been reported in droplet-based microfluidic system. Ozen et al. (Ozen et al., 2006a, 2006b) formed monodisperse droplets using the EHD instability of the interface between two liquids and analyzed the stability in the case where the fluids are assumed to be leaky dielectric. EHD generation of a single droplet in an aqueous two-phase system (ATPS) which has high salt concentrations in both phases was also reported (Song et al., 2007; Choi et al., 2008). The results are considered in Section 2.1.

Generated droplets should be manipulated properly for further utilization in the same microfluidic system. This includes manipulation of droplets by breakup, sorting and coalescence, etc. Various techniques have been published for the effective manipulations of droplet in the microfluidic systems. For breakup of generated droplets, geometry of the microchannels has been specially designed (Link et al., 2004; Ménétrier-Deremble & Tabeling, 2006) and electrical field has been applied for the control (Choi et al, 2006). Tan et al. reported sorting of droplets through controlling the bifurcating junction geometry and the flow rates of the daughter channels (Tan et al., 2008). Ahn et al. developed dielectrophoretic manipulation of droplets for high-speed microfluidic sorting devices (Ahn et al., 2006). Prakash et al. demonstrated synchronization of bubble movements via planar fluidic resistance ladder network (Prakash & Gershenfeld, 2007). An active method of controlling charged droplets electrically was reported by Link et al (Link et al., 2006). Coalescence of droplets is essential for the reaction of molecules confined in different droplets and thus it has been extensively studied including the mechanism and methodology for microfluidic systems (Bremond et al., 2008; Zagnoni & Cooper, 2009; Tan et al., 2007; Ahn et al., 2006).

1.2 Microextraction in microfluidic systems

Microextraction has been developed and widely applied as an efficient tool for molecular transport in microfluidic devices, taking the advantages of small dimension such as stable and continuous operation without the need of shaking and settling as in conventional extraction system and enhanced separation caused by large interfacial distance and short diffusion time. Several research results on microfluidic extraction of metal ion complexes within organic-aqueous two-phase system have been published by Kitamori's group (Tokeshi et al., 2000a, 2000b; Surmeian et al., 2002; Hisamoto et al., 2003). Kitamori's group realized microextraction in the microfluidic system by forming a laminar flow with two or more fluids in a microchannel and using the interfaces between different fluids. When the microextraction is realized in a droplet-based microfluidic system, a more rapid mass transfer can be expected than in a laminar flow-based system because the ratio of the interfacial area between the different fluids per the unit volume is larger. As an example of the droplet-based microextraction, Xu et al. (Xu et al., 2008) demonstrated extraction of succinic acid from *n*-butanol to aqueous droplets containing sodium hydroxide. Mary et al. studied the extraction of a solute from the continuous phase and purification where the solute transport was in the opposite direction (Mary et al., 2008). Castel et al. (Castell et al., 2008, 2009) reported continuous molecular enrichment in a microfluidic system aided by the vortex within segmented droplets and developed liquid-liquid phase separator which turns segmented flow to continuous flow. These examples of droplet-based microfluidics indicate

that droplets not only help mass transfer through the droplet surface but also mix the fluids be means of the circulation flow inside them and serve as carriers of fluids by themselves. These properties show that droplets can be used for microextraction as well as microreaction.

1.3 Aqueous two-phase system

In this study, we employed aqueous two-phase system (ATPS) to realize the microextraction in the microfluidic system. The liquid-liquid system, called ATPS or aqueous biphasic system was first studied by a Swedish biochemist P. Å. Albertsson (Albertsson, 1986). ATPS has become a powerful tool for separation of a range of biomaterials, including plant and animal cells, microorganisms, fungi, virus, chloroplasts, mitochondria, membrane vesicles, proteins, and nucleic acids. It can also be an appealing system for microfluidic droplet application, since the two phases are all aqueous (Walter et al., 1985; Hatti-Kaul, 2000). An ATPS consists of two immiscible phases formed by dissolving two incompatible polymers, such as poly(ethylene glycol) and dextran, or one polymer and an appropriate inorganic salt, or a cationic surfactant and a salt. The phase separation, which finally leads to equilibrium, is thought to be due to the incompatible physicochemical properties of components. Thus one phase is predominantly rich with one component and the second phase is enriched by the other component. ATPS is highly advantageous because the high water content (usually 70-90%) provides biocompatibility and selectivity for the stable pre-concentration of hydrophilic molecules with relatively low interfacial tension compared to that of organic/water two-phase system. It can be a versatile partitioning system for the separation of many kinds of dyes, metal ions, silica particles, proteins and cells (Walter & Johansson, 1986; Walter et al., 1991). Various factors such as concentration and type of phase-forming polymer or salts and the choice and addition of affinity ligands can affect the distribution of a solute over the two phases, thus giving more flexibility for the customized systems.

Several applications of ATPS into microfluidic systems have been reported for continuous partitioning of cells (Yamada et al., 2004; Nam et al., 2005), taking the advantage of PDMS (polydimethylsiloxane)-compatibility avoiding swelling problem that is commonly caused when organic/water two-phase system is applied to PDMS microfluidic device. The ATPS-based partitioning systems developed in these research works have almost same protocol because the direction and configuration of mass transfer where the material being extracted is transported from one phase to the other are almost identical with those of the two-phase system based on oil and water. Although laminar nature of liquid-liquid flow in microfluidic channel makes continuous separation possible, control of the interface has been known as a difficult task because the immiscible nature of the two liquid phases causes competition between interfacial tension and the viscous force. As Dreyfus et al. reported (Dreyfus et al., 2003), only in a certain regime of flow rates of liquid phases, stratified structure of flows, that is necessary for continuous microextraction, can be maintained.

2. Droplet generation and manipulation

In this chapter, electrohydrodynamic droplet generation in aqueous two-phase microflow and manipulation of ATPS droplets are discussed. ATPS droplets usually have electrophoretic mobility due to the presence of anions. If the interfacial tension is sufficiently high, the interface can respond to the applied d. c. electric field based on the same reason. Though much lower than that of organic/aqueous two-phase system, interfacial tension in tetrabutylammonium bromide (TBAB)/ammonium sulfate(AS) ATPS is relatively high

(about 4-5 dyne/cm) compared to that of common ATPS formed with poly(ethylene glycol) and dextran (10^{-4} to 0.1 dyne/cm). Thus the interface readily responds to the external electric field in microchannels. The fabricated microfluidic device has a T-junction at which the two-phase flow may have the configuration that can generate dispersed droplets by the electric potential difference applied. The threshold voltage necessary for the electrohydrodynamic droplet generation depends on pH due to the degree of dissociation and charge accumulation. Electrokinetic control of droplet break-up and switching of droplet movement direction were also demonstrated based on the same electrophoretic mobility of ATPS droplets. Volume of broken droplets and the direction of droplet movement were effectively controlled by the applied DC electric field. In addition, simple manipulatin of ATPS droplets was demonstrated in the microchannels that are branched at the end.

2.1 Electrohydrodynamic generation of droplets

The ATPS for the droplet generation was prepared by dissolving TBAB and AS in water by 15 and 30%, respectively, by stirring the solution well. The prepared solution is left still for more than 12 hours so that it can be divided into two phases by the difference in the specific gravity. After separating the stable phases, TBAB-rich phase and AS-rich phase were individually introduced at the inlets of the microfluidic system by syringe pump, which controlled the flow rates of each phase independently. The microfluidic system in Figure 2 was fabricated by using the general PDMS replica. The ratios of flow rate of TBAB-rich phase to AS-rich phase were fixed at 0.133 and 0.156 in which the two streams were laminar as shown in figure. In these ratios, the more viscous TBAB-rich phase occupied about half of the channel width, but from T-junction one branched channel was totally occupied by TBAB-rich phase and the other branched channel by TBAB-rich phase and AS-rich phase together. Application of an electric field in this state through the electrodes shown in Figure 2 causes the change in the interface as in Figure 3, as the AS-rich phase is drawn in the direction toward the positive electrode. The interface at the center of T-junction was deformed to the positive electrode, which is located at the outlet where only TBAB-rich phase was flowing out. At the same time, the interface in the part of the channel connected to the negative electrode was also deformed due to the temporary change in volumetric flow

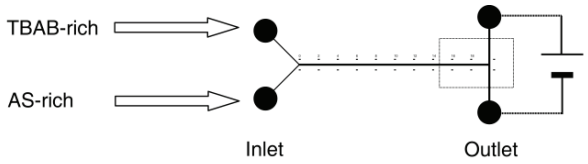

	Width (mm)	Depth (mm)	Length (mm)
Main channel	200	100	20
Inlet branch	100	100	5
Outlet branch	100	100	5

Fig. 2. Schematic illustration of the device for electrohydrodynamic generation of droplets and the dimensions of the channels

rate of AS-rich phase. When the electric pulse signal was switched off, the interface returned to its original shape. When the applied voltage was increased, the deformation of AS-rich phase became larger and small volume of AS-rich phase was detached from main AS-rich phase stream forming a droplet dispersed in TBAB-rich phase Figure 4.

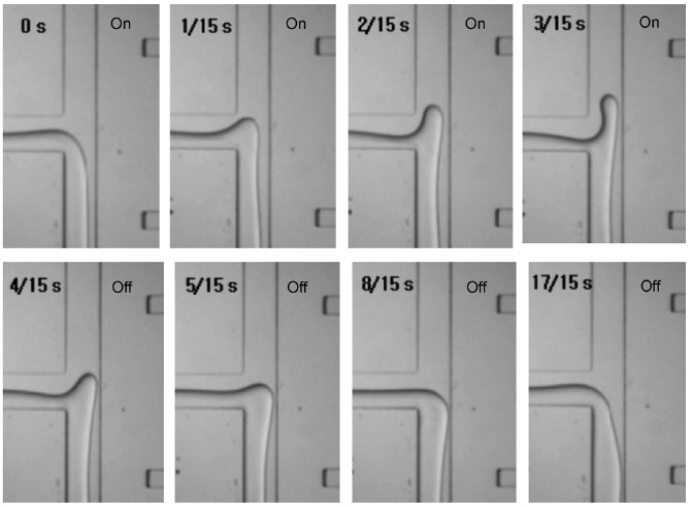

Fig. 3. Change of interface configuration by d.c. 12 V electric pulse application. The electric pulse was applied from 0 second to 4/15 second (200 ms) as shown in the first four pictures. The positive electrode is located at the end of the channel on the upward side

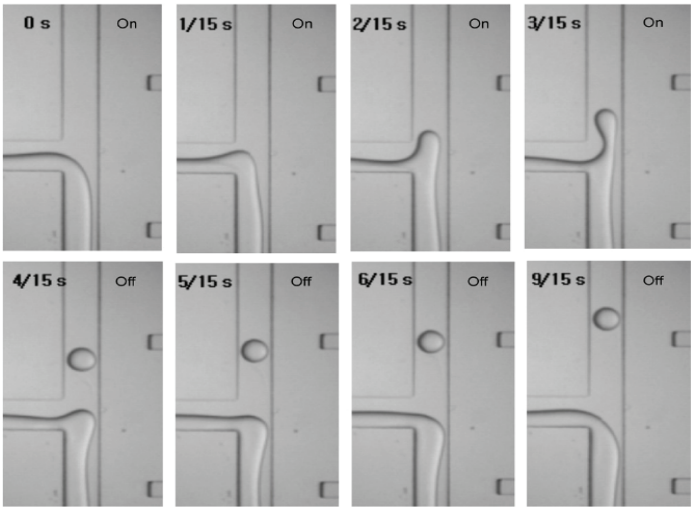

Fig. 4. Generation of a single droplet 20 V electric pulse application. The electric pulse was applied from 0 second to 4/15 second (200 ms) as shown in the first four pictures. The positive electrode is located at the end of the channel on the upward side

The higher potential difference of electric pulse results in generation of multiple droplets with different volume in each droplet, usually the first droplet being the largest in diameter as shown in Figure 5. During switching-on of the electric pulse, the droplets have bell-shapes and are attracted to the positive electrode in a way similar to electrophoretic motion, while the spherical droplets flow freely with continuous phase after switching off. The number of droplets generated is controlled by the change in the magnitude and duration of a d.c. electric pulse as shown in Figure 6. Longer pulse at higher voltage usually generated more droplets.

Capillary number of this particular droplet-generation can be calculated. The capillary number for the ATPS microfluidic system is $Ca=\eta_{TBAB}\cdot U_{AS}/\sigma$ where U_{AS} is the speed of the AS-rich phase η_{TBAB} is the continuous TBAB-rich phase viscosity, σ is two-phase interfacial tension. For example, when the ratio of TBAB-rich phase flow rate to that of AS-rich phase is 0.133, their actual flow rates were 0.133μl/min and 1μl/min, respectively. With 40cP (4×10^{-3} kg/m·sec) of η_{TBAB}, 1.7×10^{-3} m/s of U_{AS} and the 5dyne/cm (5×10^{-3} N/m), the calculated Ca is 1.36×10^{-3}. This number falls between the range of Ca studied by Jullien et al., (4×10^{-4} and 2×10^{-1}) (Jullien et al., 2009) where droplet breakup may occur in microfluidic T-junctions. This method of droplet generation has the advantage that the time and frequency of droplet generation can be controlled using the electric signals without a moving part, different from the piezoelectric method (Ziemecak et al., 2011). Moreover, the droplet generation using ATPS can be achieved at a very low electric potential when compared with that of the other electrichydrodynamic methods using different two-phase systems.

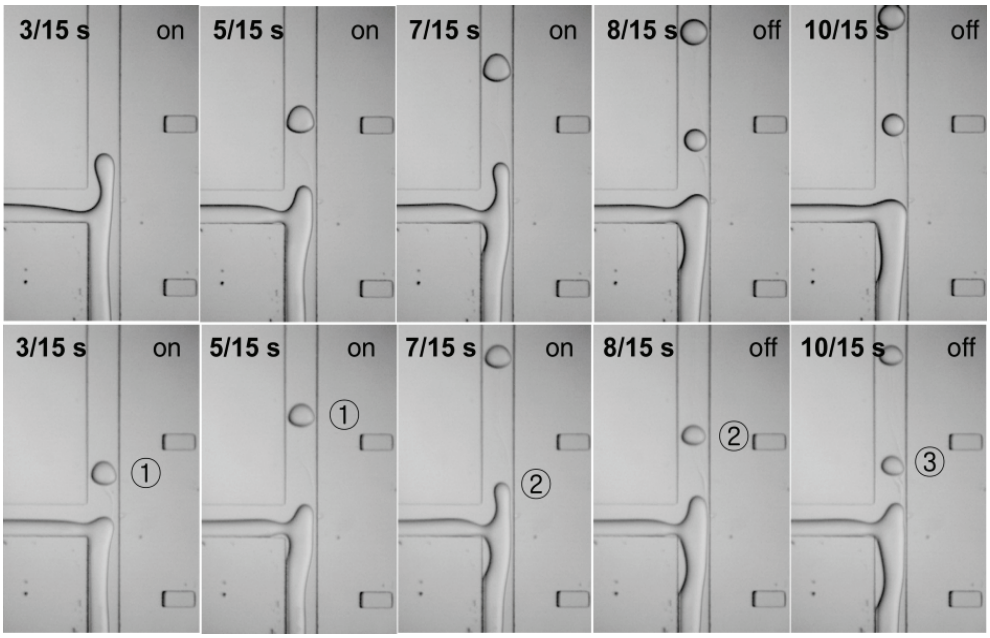

Fig. 5. Multiple-droplet generation by electric pulse application. Two (first row) and three (second row)-droplet generation by electric field application. Two drops are generated by a 20 V, 500 ms pulse (above). Three drops are generated by a 20 V, 800 ms pulse

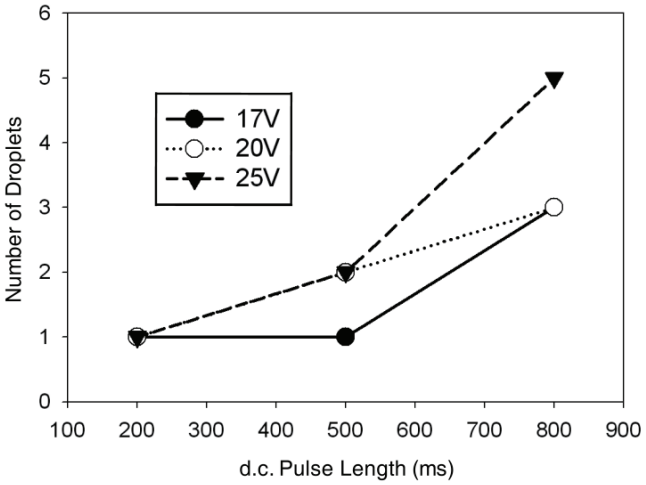

Fig. 6. Number of generated droplets controlled by the mode of electric pulse application. The number of droplets generated is controlled by the change in the magnitude and duration of a d.c. electric pulse. Longer pulse at higher voltage usually generated more droplets

2.2 Electrohydrodynamic manipulation of droplets

Manipulation of droplet movement is an essential technique for the availability of a microfluidic system to transport a certain droplet to the desired part of the system. Since passive manners for droplet transportation have limitation of complex channel design and flow rate control, active manners are usually preferred. For instance, Ahn et al. developed dielectrophoretic manipulation of droplets for high-speed microfluidic sorting devices (Ahn et al., 2006). Active method of controlling charged droplets electrically was reported by Link et al (Link et al. 2006). In line with these previous studies, the method to manipulate the movement of droplets of TBAB/AS ATPS in the microfluidic channels was developed, separating and directing the droplets of specific number into desired part of the device from the sequential flow of droplets, by applying the programmed d. c. electric field which was synchronized with the droplet frequency.

In this study, droplets were produced passively by shear force at the Y-junction where the two streams first contact with each other in the microfluidic device of the design shown in Figure 7. For the period without electric field, droplets flow toward outlet 1 because the branched channel that leads to outlet 1 is shorter than that toward outlet 2 as shown in Figure 7, thus it has higher pressure gradient. For the period with electric field on, droplets are attracted toward outlet 2 due to the electric attraction. In this way, a specific droplet can be selectively separated from the line of droplets that flows through the channel. Figure 8 shows the result of the experiment where the generated droplets were sent to the outlet 1 and outlet 2 alternatively by applying electric signals in a certain interval. As shown in these results, the electrohydrodynamic transport is a convenient method for handling droplets inside microfluidic devices without any moving part. The control of direction is possible only by changing the pulse signals with a simple switching on and off program. This simplicity will allow the realization of complicated and multi-functional microfluidic system based on aqueous two-phase droplets.

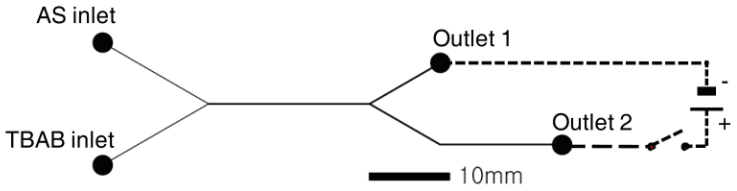

	Width (μm)	Depth (μm)	Length (mm)
Inlet channel	100	100	15
Main channel	200	100	20
Outlet 1	200	100	10
Outlet 2	200	100	25

Fig. 7. Y-branched microfluidic device design for the droplet transport experiment

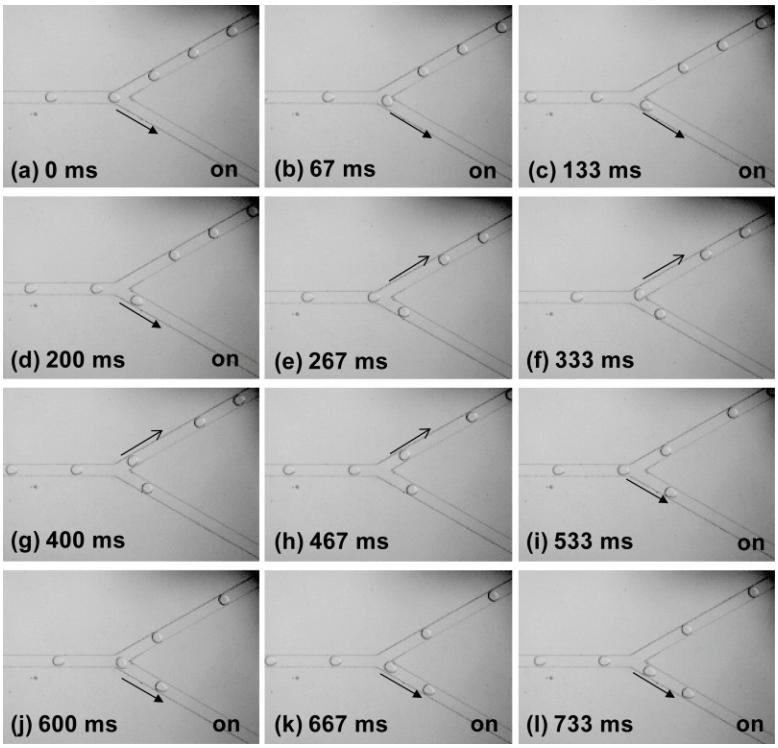

Fig. 8. Transport of a droplet into the desired channel by the application of electric pulses

3. Aqueous two-phase droplet-based microextraction

This chapter is about microfluidic extraction systems based on droplet of aqueous two-phase system (ATPS). Fast mass transfer between continuous phase and dispersed droplet is demonstrated by microextraction of ruthenium red within a microfluidic device which can also generate droplets with electrohydrodymanic method. By comparing brightness data of known concentrations of ruthenium red droplets with those of droplet of interest, change of ruthenium red concentration was traced along the microextraction channel, resulting in good agreement with Fick's diffusion model, and more details are found at Choi et al., 2010. It is also suggested the method for cessation of microextraction which is essential for controlling solute concentration inside a droplet by means of the electrohydrodynamic manipulation of droplet movement direction demonstrated in Section 2.1. Droplets of different ruthenium red concentration were moved to branched channels designed for each of the droplet to move to desired place of microfluidic system for further reaction. The microextraction system based on ATPS droplets has extensive potential to be used in effective and convenient mass transfer of solutes which have different solubility with advantage of handling discrete volume of liquid of desired concentration.

3.1 Microextraction kinetics

This section is devoted to the ATPS droplet-based microfludics system for ruthenium red extraction. The microextraction kinetics in the microfluidic system was analyzed. As shown in Figure 9, we fabricated the microfluidic system that consisted of the droplet-generation part and the extraction part to which a microchannel of 70 mm belonged. The length of the microchannel, 70 mm, was determined by considering the convergence of the ruthenium red concentration in the droplet after the sufficient extraction. The feed flow rates of ammonium sulfate **(**AS)-rich phase and tetrabutylammonium bromide (TBAB)-rich phase into droplet-generation part are kept at 5.04μl/min and 0.14 μl/min, respectively. In the microextraction part, ruthenium red-containing TBAB-rich phase is introduced to the main microextraction channel, as shown in Figure 4.1a and b schematically, at the flow rate of 0.24μl/min.

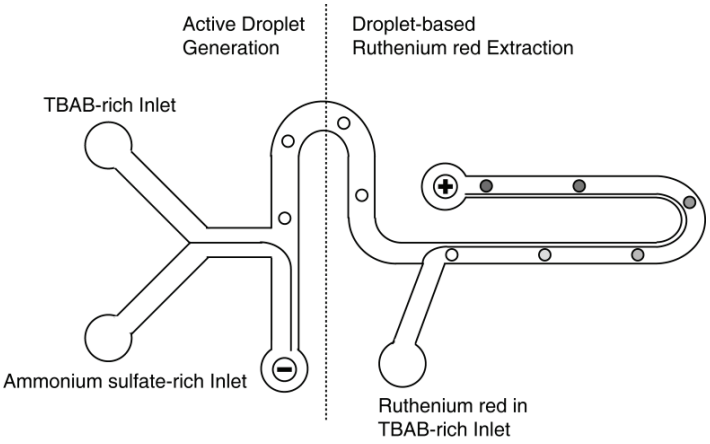

Fig. 9. The schematic diagram of the microfluidic system for the analysis of kinetics of microextraction of ruthenium red

The flow rate combination is selected carefully to have appropriate pressure drop and width of each stream, especially at the T-junction in droplet-generation part and at the junction where ruthenium red stream is introduced in microextraction part. Six kinds of ruthenium red-containing TBAB-rich phases were prepared by dissolving ruthenium red in the TBAB-rich phase with the concentration of 0.05, 0.07, 0.09, 0.11, 0.13 and 0.15% (w/w). Ruthenium red of which molecular weight is 786.36, has the structural formula of $[(NH_3)_5Ru\text{-}O\text{-}Ru(NH_3)_4\text{-}O\text{-}Ru(NH_3)_5]Cl_6$. It is dispersed in the TBAB-rich phase as solid particles, but is highly soluble in AS-rich phase as indentified by its color.

In this study, the extraction of ruthenium red from the TBAB-rich phase to the AS-rich phase droplet was assumed as the combination of two different processes for the analysis. The first process was the dissolution of the ruthenium red in the TBAB-rich phase at the As-rich phase surface up to the saturated concentration. This process was required because ruthenium red existed in the TBAB-rich phase as solid particles dispersed due to its low solubility in that phase. The general equation for the process involving dissolution of dispersed solid particles can be written as (Mary et al., 2008; Xu et al., 2008)

$$\frac{\partial C_s}{\partial t} = k_{diss}\left(C_{sat} - C_s\right) \tag{1}$$

where C_s denotes the concentration at the surface of the droplet, C_{sat}, the concentration when saturated, and k_{diss}, the dissolution rate coefficient. Integrating above equation gives C_s as a function of time as follows:

$$C_s = C_{sat}\left(1 - \exp(-k_{diss}t)\right) \tag{2}$$

The next process required was the spread of the dissolved ruthenium red over the AS-rich droplet in the direction of the droplet center. This second process can be described with the one-dimensional model of simple diffusion with spherical coordinate system:

$$\frac{\partial C_{in}}{\partial t} = D\frac{1}{r^2}\frac{\partial}{\partial r}\left(r^2\frac{\partial C_{in}}{\partial r}\right), \tag{3}$$

where C_{in} and D denote the concentration of solute inside the droplet and the effective diffusion coefficient, respectively. This model assumes no internal motion of the fluid in the droplet. The concentration in the continuous phase is assumed to be constant because TBAB-rich phase with fixed concentration of ruthenium red is continuously fed to the microextraction device.

The boundary conditions at r=0 and r=R for this equation are specified as

$$\frac{\partial C_{in}}{\partial r} = 0 \qquad \text{at } r = 0, \tag{4}$$

$$C_{in} = C_s = C_{sat}\left(1 - \exp(-k_{diss}t)\right) \qquad \text{at } r = R. \tag{5}$$

The initial condition is

$$C_{in} = 0 \qquad \text{at } t = 0 \text{ for all } r. \tag{6}$$

The first boundary condition (Eq. 4) assumes symmetry at the center of the droplet. In the second boundary condition (Eq. 5), C_{sat} is the concentration on the surface of the droplet at saturation, which corresponds to the product of concentration of ruthenium red in TBAB-rich phase and distribution coefficient between two phases. Although concentration in the TBAB-rich phase is known and assumed to be constant, the distribution coefficient is not available. After sufficiently long extraction time, the droplet will be saturated with solute and the concentration will correspond to C_{sat}. In this work, it is assumed that the extraction time is long enough and the final concentration at the end of extraction is considered to be C_{sat}. Solving Eq. 3 using the previously described boundary conditions gives the radial distribution of concentration in the droplet at each time of concentration measurement. The C_{avg} inside the droplet at each time interval can be calculated. The model validity was verified by comparing the C_{avg} with the experimental result.

Because the information about C_{sat}, k_{diss} and D is required to solve the equation numerically, here we briefly introduce the method to calculate these parameters. The measured concentration of ruthenium red at 70 mm position which is the end of the microchannel was chosen as C_{sat} in each experiment. The k_{diss} value was determined as 0.09 (sec^{-1}) by fitting experimental results from the entire microextraction process and applied to solve the equation with five different C_{sat} (We have used the same C_{sat} for experiments of 0.13 and 0.15% (w/w) assuming that the C_{sat} has reached its solubility limit). Diffusion coefficient of ruthenium red in AS-rich phase, D, was measured by using 'T-sensor' developed by Kamholtz et al. (Kamholtz et al., 1999) Solutions of simple diffusion model with experimental results are shown in Figure 10. Here, C_{out} is the concentration of ruthenium red in the continuous TBAB-rich phase. Time-dependent simulation results are in good agreement with the experimental results except the lowest concentration results (C_{out}=0.05% (w/w)) in their initial time stage where simulation overestimates the concentrations. One explanation for this error may be that in the early stages of microextraction, the ruthenium red is mainly in the region near the surface of the droplet which is excluded in the brightness measurement especially when the concentration of ruthenium red is very low. As the extraction process continues, more ruthenium red is diffused to the region belonging to the brightness measurement, and simulation shows better agreement with experimental result.

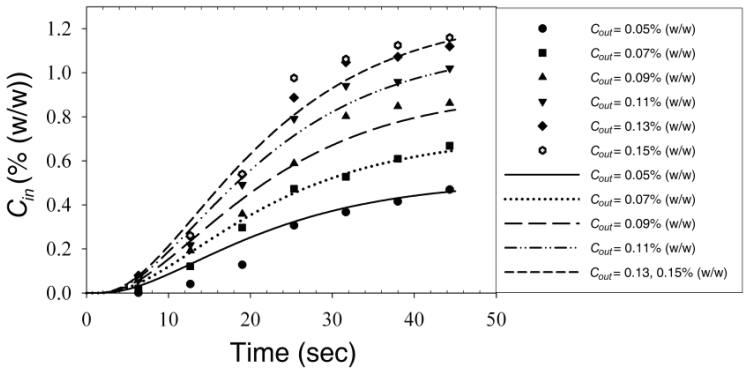

Fig. 10. Comparison of the experimental (e0.05, e0.07, e0.09, e0.11, e0.13 and e0.15) and theoretical data (s0.05, s0.07, s0.09, s0.11, s0.13 and s0.15) of the droplet-based microextraction kinetics

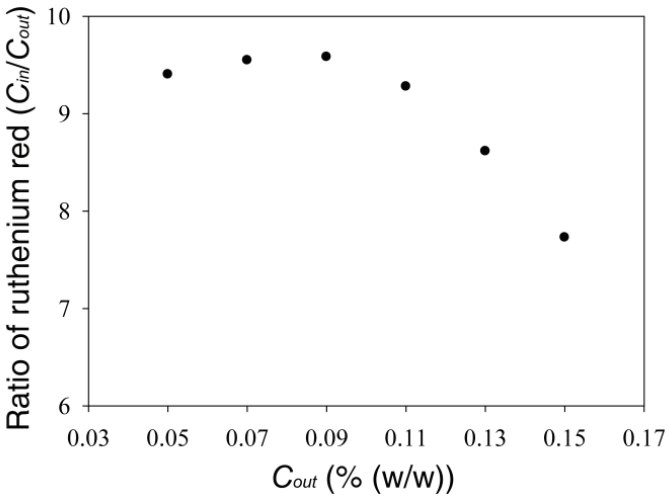

Fig. 11. Ratio of the ruthenium red concentration in the droplet at the 45 seconds of microextraction to that of continuous TBAB-rich phase initially introduced to the microextraction device

Figure 11 shows the ratio of the concentration of ruthenium red in the droplet after 45 seconds of microextraction to that of the continuous TBAB-rich phase fed initially. In the first three cases of low ruthenium red concentrations (0.05, 0.07 and 0.09% (w/w)) in TBAB-rich phase, the ratio is almost constant. However, the ratio decreases, as the concentration of ruthenium red of the TBAB-rich phase increases for high range of concentration of ruthenium red. This suggests that there exists the solubility limit of ruthenium red in the AS-rich droplet above which the concentration cannot increase independent of the concentration in the TBAB-rich phase. The solubility limit of ruthenium red in the AS-rich phase droplet, corresponding to C_{out} of 0.13 and 0.15% (w/w), is about 1.15% (w/w) in this experiment.

3.2 Microextraction control

In the previous section, the microextraction was performed using the droplet-based microfluidic system. When a macroscopic system is realized in a microfluidics system, various functions that are impossible in a macroscopic system can be realized. This section describes the method to stop the microextraction before reaching the equilibrium by moving the droplet from the ruthenium red-containing TBAB-rich phase stream to the pure TBAB-rich phase stream using the EHD force. This function enables to obtain a droplet of a specific concentration of a substance without any other additional treatments in a microfluidics system in which the process for chemical reaction or analysis is integrated following microextraction. In the previous Section 3.1, the time-dependent profile of microextraction process was derived from the experimental and simulation results, and thus stopping of microextraction was possible using the carefully designed microextraction device and the droplet-motion guiding techniques. The microextraction device that was designed by considering this function consisted of two branched channels at the position of 10 and 20 mm from the junction of the ruthenium red injection where microextraction begins, as

shown in Figure 12. The branched channels were arranged to have an angle of 45° so that droplets can readily move toward the branched channels. AS-rich phase that forms laminar flow with TBAB-rich phase in the droplet-generation part of the device is fed at the flow rate 5.4 μl/min. The droplet produced in the droplet-generation part of the device moves to microextraction part, and then extraction starts at the junction where TBAB-rich phase with ruthenium red concentration of 0.29 (%, w/w) is injected. Only when the droplet crosses the streamlines and is fully surrounded by the ruthenium red containing TBAB-rich phase, isotropy of microextraction is guaranteed. To force droplet to enter the ruthenium red stream, the microchannel that has a narrow cross section was fabricated as shown in Figure 13 a. Because the flow rate of the main TBAB-rich phase, which initially carries the AS-rich droplet, is kept at 0.24 μl/min, smaller than that of ruthenium red solution (0.51 μl/min), the droplet moves toward the ruthenium red solution due to the pressure difference. Microextraction continues until the d. c. electric pulse with the duration of 200 ms is applied at the end of the branched channel. At that moment the droplet departs ruthenium red-containing TBAB-rich phase by approaching the electrode located at each end of the branched microchannel and microextraction is terminated.

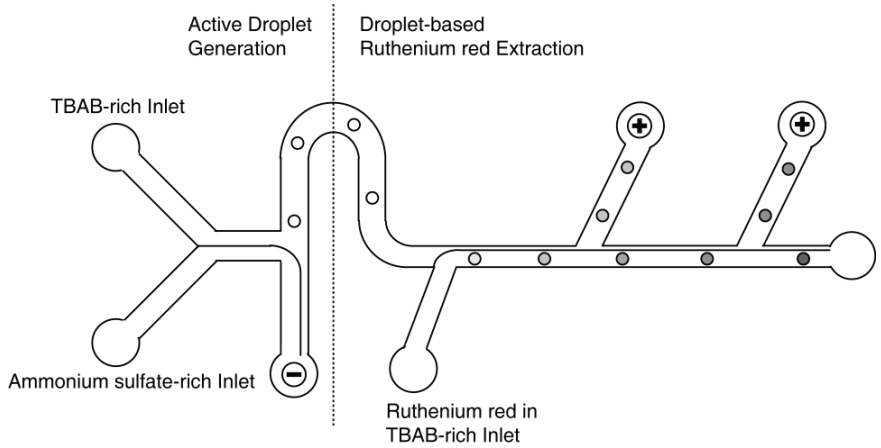

Fig. 12. The schematic diagram of the microfluidic system for microextraction control. Droplets can moved to one of the two branched channels by applied electric pulse after cessation of microextraction

As shown in Figure 13 b and c, the thresholds located at 10 and 20 mm positions serve as leaping boards for the droplet. When d. c. electric potential is not applied, the droplet moves freely, following its streamline over the threshold as shown in Figure 13 b. When electric potential is applied on the electrode at the end of the branched channel, the droplet changes its direction at the junction so that it leaves the flow stream of ruthenium red-containing TBAB-rich phase and jumps into the branched channel with increased speed due to the electrophoretic effect as shown in Figure 13 c. The concentrations of droplets at the first and second branched microchannel when microextraction is terminated are 0.12 and 0.24 (%, w/w) and corresponding concentrations which have been predicted by simulation are 0.11 and 0.28 (%, w/w), which shows that the droplet-based microextraction can be terminated depending on the needs in a process, even before reaching the equilibrium state.

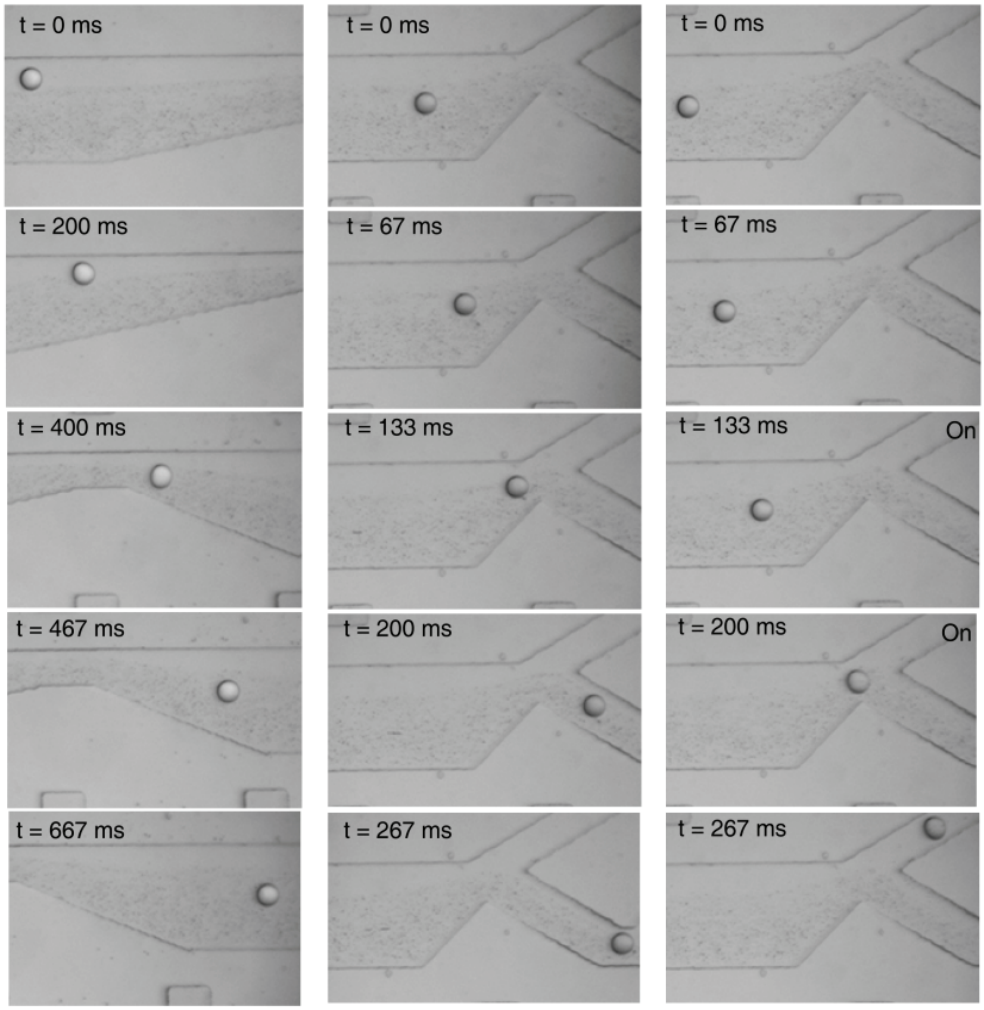

Fig. 13. Microextraction control and manipulation of droplet within the microextraction system shown in Figure 4.1b. (a) Beginning of microextraction: The AS-rich phase droplet is dipped into the ruthenium red-containing TBAB-rich phase at the narrowed part of the microchannel and starts microextraction. (b) The first branched channel at the position of 10 mm from the starting point of microextraction. In this case shown in the picture, the electric pulse is not applied so that the droplet can move continually through the microextraction channel. (c) The second branched channel at the position of 20 mm from the starting point of microextraction. The applied electric pulse changes the movement direction of the droplet toward the branched channel so that the microextraction is stopped and the droplet can move to other part of the microfluidic system

4. Conclusion

In this study, the microfluidic system based on the aqueous two-phase system (ATPS) droplets was developed. Taking advantage of the benefits that microfluidics can provide, this study was focused on the mass transfer between two liquid-liquid phases. Droplets generated and manipulated in microfluidic system can provide unique opportunities to handle fluids in a segmented flow, offering novel platform of miniaturized system for chemical and biological processes. The two-phase that has been employed in this experimental work is the ATPS formed by tetrabutylammonium bromide (TABA)/ammonium sulfate (AS). Among the numerous possible liquid-liquid two-phase systems available, only a few of them can be operated in microfluidic system both in the stratified laminar flow and in segmented droplet-based flow. This unique feature comes from the moderate interfacial tension between the TBAB-rich phase and AS-rich phase.

Generation of TBAB/AS ATPS droplets by electrohydrodynamic method was studied. Initially fed as laminar flow, the AS-rich phase was destabilized and eventually dispersed as droplets in the continuous TBAB-rich phase at the T-junction in the microfluidic system when the d. c. electric potential difference was applied as pulses. Based on the pH dependency of the threshold electric voltage required to generate a single droplet, the electrophoretic mobility of the AS-rich phase in TBAB-rich phase was discussed and a model for the mechanism was suggested. Applying the same electrohydrodynamic principle, manipulation of droplet movement direction was demonstrated in a different microfluidic device. This technique can be a fundamental method for the operation of the ATPS-based microfluidic system.

TBAB/AS ATPS droplet-based microextraction was also investigated. Ruthenium red was successfully extracted from the TBAB-rich phase to the AS-rich phase droplet in the microfluidic extraction device. The mass transportation between the two liquid phases was discussed assuming two different steps, from the continuous phase to the droplet surface and from the droplet surface to the center of the droplet, applying diffusion equation for each step. Further, the method for stopping microextraction which is essential for controlling solute concentration inside a droplet was suggested by means of the electrohydrodynamic manipulation of droplet movement direction. Here showed is just one example of TBAB/AS ATPS droplet-based microextraction. The compatibility of TBAB/AS ATPS with stable biological materials and other water-soluble inorganic molecules can provide potentials for further application in chemistry and biology. It is expected that the next applications of this ATPS in microfluidic should be in the analysis of charged biomolecules, separation of surface-treated nanoparticles and reaction of inorganic molecules in coordinate chemistry.

In addition, future development of ATPS droplet handling technique will add the merits of this microfluidic system. For example, precisely controlled coalescence of ATPS droplets can lead to reaction of the reactants confined inside the droplets. Appropriate surface treatment of the microfluidic device and proper fabrication which takes the phase properties into account can enable one to alternate the flow pattern from segmented flow to continuous flow depending on the need of the process. Application of additives that can give affinity for efficient separation and aqueous three-phase system which allows more variety can be considered as the topics for future research. Alternative aqueous two-phase-forming materials which can be used for multi-phase system in low concentrations

can widen the application in which relatively susceptible biological molecules are involved.

5. References

Ahn, K., Kerbage, C., Hunt, T. P., Westervelt, R. M., Link D. R. & Weitz, D. A. (2006). Dielectrophoretic manipulation of drops for high-speed microfluidic sorting devices. *Applied Physics Letters*, Vol. 88, No.2, art. no. 024104, pp. 1-3

Ahn, K., Agresti, J., Chong, H., Marquez, M. & Weitz, D.A. (2006) Electrocoalescence of drops synchronized by size-dependent flow in microfluidic channels. *Applied Physics Letters*, Vol.88 No.26, art. no. 264105

Albertsson, P.-Å. (1986) *Partition of Cell Particles and Macromolecules, 3rd Ed.*, Wiley, New York

Anna, S. L., Bontoux, N. & Stone, H. A. (2003). Formation of dispersions using ''flow focusing'' in microchannels. *Applied Physics Letters*, Vol.82, No.3, pp. 364-366

Beebe, D. J., Mensing, G. A. & Walker, G. M. (2002). Physics and applications of microfluidics in biology, *Annual Review of Biomedical Engineering*, Vol.4, pp.261-286

Bremond, N., Thiam, A. R. & Bibette, J. (2008). Decompressing emulsion droplets favors coalescence, *Physical Review Letters*, Vol.100, No. 2, art. no. 024501

Castell, O. K., Allender, C. J. & Barrow, D. A. (2008). Continuous molecular enrichment in microfluidic systems, *Lab on a Chip - Miniaturisation for Chemistry and Biology*, Vol. 8, No. 7, pp. 1031-1033

Castell, O. K., Allender, C. J. & Barrow, D. A. (2009). Liquid-liquid phase separation: Characterisation of a novel device capable of separating particle carrying multiphase flows, *Lab on a Chip - Miniaturisation for Chemistry and Biology*, Vol.9, No.3, pp. 388-396

Choi, Y. H., Song, Y. S. & Kim, D. H. (2006) Proceedings of the 10th International Conference on Miniaturized Systems for Chemistry and Life Sciences (μTAS2006), T. Kitamori, H. Fujita, S. Hasebe (Eds.) pp. 95-97, CHEMINAS, Tokyo, Japan

Choi, Y. H., Song, Y. S. & Kim, D. H. (2008) Electrohydrodynamic generation and transport of a single or multiple droplets of aqueous two-phase system in microfluidic device, *AIP Conference Proceedings*, Vol.1027, pp. 1006-1008

Choi, Y. H., Song, Y. S. & Kim, D. H. (2010). Droplet-based microextraction in the aqueous two-phase system, *Journal of Chromatography A*, Vol.1217, pp. 3723-3728

Christopher, G. F. & Anna, S. L. (2007). Microfluidic methods for generating continuous droplet streams, *Journal of Physics D: Applied Physics*, Vol. 40, No.19, art. no. R01, pp. R319-R336

Dittrich, P. S., Tachikawa, K. & Manz, A. (2006) Micro total analysis systems. Latest advancements and trends, *Analytical Chemistry*, Vol. 78, No.12, pp. 3887-3907

Dreyfus, R., Tabeling, P. & Willaime, H. (2003) Ordered and disordered patterns in two-phase flows in microchannels, *Physical Review Letters*, Vol.90, No.14, pp. 144505/1-144505/4

Frenz, L., Harrak, A. E., Pauly, M., Bégin-Colin, S., Griffiths, A. D. & Baret, J. (2008). Droplet-based microreactors for the synthesis of magnetic iron oxide nanoparticles, *Angewandte Chemie International Edition*, Vol.47, pp.6817-6820

Hatti-Kaul, R. (2000) *Aqueous Two-Phase Systems: Methods and Protocols*, Humana Press, Totowa, New Jersey

Hisamoto, H., Shimizu, Y., Uchiyama, K., Tokeshi, M., Kikutani, Y., Hibara, A. & Kitamori, T. (2003). Chemicofunctional membrane for integrated chemical processes on a microchip, *Analytical Chemistry*, Vol. 75, No.2, pp. 350-354

Jullien, M.-C., Tsang Mui Ching, M.-J., Cohen, C., Menetrier, L. & Tabeling, P. (2009) Droplet breakup in microfluidic T-junctions at small capillary numbers, *Physics of Fluids*, Vol.21, No.7, art. no. 072001

Kamholz, A. E., Weigl, B. H., Finlayson, B. A. & Yager, P. (1999). Quantitative analysis of molecular interaction in a microfluidic channel: The T-sensor, *Analytical Chemistry*, Vol.71, No.23, pp. 5340-5347

Kim, D. H. (2004). Microfluidic systems: state of the art, *Korean Chemical Engineering Research*, Vol. 42, pp.375-386

Link, D. R., Anna, S.I ., Weitz, D. A. & Stone, H. A. (2004). Geometrically Mediated Breakup of Drops in Microfluidic Devices, *Physical Review Letters*, Vol.92, No.5, pp. 545031-545034

Link, D. R., Grasland-Mongrain, E., Duri, A., Sarrazin, F., Cheng, Z., Cristobal, G., Marquez, M. & Weitz, D. A. (2006). Electric control of droplets in micro-fluidic devices, *Angewandte Chemie - International Edition*, Vol.45, No.16, pp. 2556-2560

Mary, P., Studer, V. & Tabeling, P. (2008). Microfluidic droplet-based liquid-liquid extraction, *Analytical Chemistry*, Vol.80, pp.2680-2687

Ménétrier-Deremble, L. & Tabeling, P. (2006). Droplet breakup in microfluidic junctions of arbitrary angles, *Physical Review E - Statistical, Nonlinear, and Soft Matter Physics*, Vol.74, No.3, art. no. 035303

Nam, K.-H., Chang, W.-J., Hong, H., Lim, S.-M., Kim, D.-I. & Koo, Y.-M. (2005). Continuous-flow fractionation of animal cells in microfluidic device using aqueous two-phase extraction, *Biomedical Microdevices*, Vol.7, No.3, pp. 189-195

Ozen, O., Aubry, N., Papageorgiou, D. T. & Petropoulos, P. G. (2006). Electrohydrodynamic linear stability of two immiscible fluids in channel flow, *Electrochimica Acta*, Vol.51, No.25, pp. 5316-5323

Ozen, O., Aubry, N., Papageorgiou, D. T. & Petropoulos, P. G. (2006). Monodisperse drop formation in square microchannels, *Physical Review Letters*, Vol.96, No.14, art. no. 144501, pp. 1-4

Prakash, M. & Gershenfeld, N. (2007). Microfluidic bubble logic, *Science*, Vol.315, No.5813, pp. 832-835

Song, Y. S., Choi, Y. H. & Kim, D. H. (2007). Microextraction in a tetrabutylammonium bromide/ammonium sulfate aqueous two-phase system and electrohydrodynamic generation of a micro-droplet, *Journal of Chromatography A*, Vol.1162, pp. 180-186.

Squires, T. M. & Quake, S. R. (2005). Microfluidics: Fluid physics at the nanoliter scale, *Reviews of Modern Physics*, Vol.77, No.3, pp. 977-1026

Stone, H. A., Stroock, A. D. & Ajdari, A. (2004). Engineering flows in small devices: microfluidics toward a lab-on-a-chip, *Annual Review of Fluid Mechanics*, Vol.36, pp.381-411

Surmeian, M., Slyadnev, M. N., Hisamoto, H., Hibara, A., Uchiyama, K. & Kitamori, T. (2002). Three-layer flow membrane system on a microchip for investigation of molecular transport, *Analytical Chemistry*, Vol.74, No.9, pp. 2014-2020

Tan, Y.-C., Ho, Y. L. & Lee, A. P. (2007). Droplet coalescence by geometrically mediated flow in microfluidic channels, *Microfluidics and Nanofluidics*, Vol.3, No.4, pp. 495-499

Tan, Y.-C., Ho, Y. L. & Lee, A. P. (2008) Microfluidic sorting of droplets by size, *Microfluidics and Nanofluidics*, Vol.4, No.4, pp. 343-348

Tice, J. D., Song, H., Lyon, A. D. & Ismagilov, R. F. (2003). Formation of droplets and mixing in multiphase microfluidics at low values of the Reynolds and the capillary numbers, *Langmuir*, Vol.19, pp.9127-9133

Tokeshi, M., Minagawa, T. & Kitamori, T. (2000). Integration of a microextraction system on a glass chip: Ion-pair solvent extraction of Fe(II) with 4,7-diphenyl-1,10-phenanthrolinedisulfonic acid and tri-n-octylmethylammonium chloride, *Analytical Chemistry*, Vol.72, No.7, pp. 1711-1714

Tokeshi, M., Minagawa, T. & Kitamori, T. (2000). Integration of a microextraction system: Solvent extraction of a Co-2- nitroso-5-dimethylaminophenol complex on a microchip, *Journal of Chromatography A*, Vol.894, No. 1-2, pp. 19-23

Xu, J. H., Tan, J., Li, S. W. & Luo, G. S. (2008). Enhancement of mass transfer performance of liquid-liquid system by droplet flow in microchannels, *Chemical Engineering Journal*, Vol.141, No.1-3, pp. 242-249

Walter, H., Brooks, D. E. & Fisher, D. (Eds.) (1985). *Partitioning in Aqueous Two Phase Systems: Theory, Methods, Uses and Applications to Biotechnology*, Academic Press, Orlando, FL.

Walter, H. & Johansson, G. (1986). Partitioning in aqueous two-phase systems: An overview, *Analytical Biochemistry*, Vol.155, No.2, pp. 215-242

Walter, H., Johansson, G. & Brooks, D. E. (1991). Partitioning in aqueous two-phase systems: Recent results, *Analytical Biochemistry*, Vol.197, No. 1, pp. 1-18

Whitesides, G. M. (2006). The origins and the future of microfluidics, *Nature*, Vol. 442, pp.368-373

Yamada, M., Kasim, V., Nakashima, M., Edahiro, J. & Seki, M. (2004). Continuous cell partitioning using an aqueous two-phase flow system in microfluidic devices, *Biotechnology and Bioengineering*, Vol.88, No.4, pp. 489-494

Zagnoni, M. & Cooper, J. M. (2009). On-chip electrocoalescence of microdroplets as a function of voltage, frequency and droplet size, *Lab on a Chip - Miniaturisation for Chemistry and Biology*,Vol. 9, pp. 2652-2658

Zheng, B., Roach, L. S. & Ismagilov, R. F. (2003). Screening of protein crystallization conditions on microfluidic chip using nanoliter-size droplets, *Journal of the American Chemical Society*, Vol.125, pp.11170-11171

Ziemecak I., Steijn V., Koper G. J. M., Rosso M., Brizard A. M., Esch J. H. & Kreutzer M. T. (2011). Monodisperse hydrogel microspheres by forced droplet formation in aqueous two-phase system, *Lab on a Chip - Miniaturisation for Chemistry and Biology*, Vol.11, pp. 620-624